FIFTH RECENT ADVANCES IN QUANTITATIVE REMOTE SENSING

Editor
José A. Sobrino

VNIVERSITAT ID VALÈNCIA

FIFTH RECENT ADVANCES IN QUANTITATIVE REMOTE SENSING

Auditori de Torrent, Spain
18 – 22 September 2017

Editor

José A. Sobrino
Global Change Unit
Universitat de València, Spain

FIFTH RECENT ADVANCES IN QUANTITATIVE REMOTE SENSING
Edited by
José A. Sobrino
Universitat de València, Spain

Publication: G. Sòria

Preface

The Fifth International Symposium on Recent Advances in Quantitative Remote Sensing, was held in Torrent, Spain from 18 to 22 September, 2017. It was sponsored and organized by the Global Change Unit (GCU) from the Image Processing Laboratory (IPL), University of Valencia (UVEG), Spain. Other sponsors include:

- City Council of Torrent (Spain);
- L'Auditori Torrent (Spain);
- European Space Agency (ESA);
- National Aeronautics and Space Administration (NASA);
- Airbus Defence & Space;
- EOLAB;

This Symposium addressed the scientific advances in quantitative remote sensing in connection with real applications. Its main goal was to assess the state of the art of both theory and applications in the analysis of remote sensing data, as well as to provide a forum for researcher in this subject area to exchange views and report their latest results. In this book 89 of the 262 contributions presented in both plenary and poster sessions are arranged according to the scientific topics selected. The papers are ranked in the same order as the final programme.

To conclude, I would particularly like to thank the participants who have contributed to constructive discussions and the members of the International Scientific Committee, who greatly contributed to select the papers presented at the Symposium providing an attractive scientific programme. The success is also due to the efforts made by the Organizing Committee. Many thanks to all of them.

<div align="right">

José A. Sobrino
Symposium Chairperson
Global Change Unit,
Universitat de València

</div>

Valencia, 2018

International Scientific Committee:

Chairperson:
J. A. Sobrino   University of Valencia, Spain

Members*:*
G. Asrar   University of Maryland, USA
F. Baret   INRA, Avignon, France
M. Berger   ESA/ESRIN, Italy
G. Chehbouni   IRD, France
D. Ghent   University of Leicester, UK
A. Gillespie   University of Washington, USA
R. O. Green   NASA, JPL, Pasadena, USA
G. Gutman   NASA, Washington, D. C., USA
A. Huete   University of Technology, Sydney Australia
Y. Kerr   CESBIO, Toulouse, France
Z.-L. Li   University of Strasbourg, France
S. Liang   University of Maryland, USA
M. Menenti   Delft University of Technology, The Netherlands
J. Moreno   University of Valencia, Spain
F. Nerry   University of Strasbourg, France
A. Olioso   INRA, Avignon, France
F. Prata   NILU, Norway
J. Privette   NOAA, NCDC, USA
S. Quegan   University of Sheffield, UK
M. Rast   ESA/ESRIN, Italy
A. Royer   University of Sherbrooke, Canada
Z. Su   University of Twente, The Netherlands
E. Vermote   NASA, GSFC, USA
Z. Wan   ERI, UCSB, USA
J. P. Wigneron   INRA, Bordeaux, France
Y. Yu   NOAA, USA
P.J. Zarco-Tejada   JRC European Commission, Italy

Organizing Committee:

Chairperson:
P. Gómez   Symposium, Torrent, Spain

Members*:*
B. Franch   University of Maryland, USA
S. García   University of Valencia, Spain
J. Gomis   University of Valencia, Spain
J. C. Jiménez-Muñoz   University of Valencia, Spain
Y. Julien   University of Valencia, Spain
C. Mattar   University of Aysén, Chile
R. Oltra   University of Valencia. Spain
D. Skoković   University of Valencia, Spain
G. Sòria   University of Valencia, Spain

iv

CONTENTS

viii

x

Evaluation of multisource LAI time series for crop assessment

Manuel Campos-Taberner[1*], Francisco Javier García-Haro[1], Francesco Nutini[2], Gonçal Grau-Muedra[1], Gustau Camps-Valls[3], Roberto Confalonieri[4], Carlo Girardelli[4], Lorenzo Busetto[2], Luigi Ranghetti[2], Dimitrios Katsantonis[4], Dimitris Stavrakoudis[5], Chara Minakou[5], Beatriz Martínez[1], Sergio Sánchez-Ruíz[1], María Amparo Gilabert[1], Luca Gatti[6], Massimo Barbieri[6], Francesco Collivignarelli[6], Francesco Holecz[6], Daniela Stroppiana[1], Mirco Boschetti[1]

[1]*Environmental Remote Sensing Group (UV–ERS), Earth Physics and Thermodynamics Department, Faculty of Physics, Universitat de València, Dr. Moliner 50, 46100 Burjassot, Spain.*
[2]*Institute for Electromagnetic Sensing of the Environment, Italian National Research Council, Via Bassini 15, 20133 Milan, Italy.*
[3]*Image Processing Laboratory (IPL), Universitat de València, Catedrático A. Escardino, 46980 Paterna,València, Spain.*
[4]*Cassandra Lab, Università degli Studi di Milano (Italy)*
[5]*Hellenic Agricultural Organization—Demeter, Institute of Plant Breeding and Genetic Resources, 57001 Thermi, Thessaloniki, Greece.*
[6]*Laboratory of Forest Management and Remote Sensing, School of Forestry and Natural Environment, Aristotle University of Thessaloniki, 54124 Thessaloniki, Greece.*
[7]*Sarmap, Cascine di Barico 10, 6989 Purasca, Switzerland.*
*manuel.campos@uv.es

ABSTRACT- *The aim of this work is to assess the utility of combining Sentinel-2A and Landsat (Landsat-7 ETM+ and Landsat-8 OLI) LAI time series for rice crop monitoring. LAI maps were produced in three countries (Italy, Spain and Greece) using state-of-the-art machine learning algorithms trained on simulated radiative transfer modelling data specifically generated to characterize rice features. Retrievals were focused on rice areas using a rice mask obtained with Sentinel-1A data. The availability of both Landsat-7/8 and Sentinel2-A imagery in 2016 allowed to generate a very dense temporal data set of high resolution LAI maps, useful to monitor crop development at field level. The intercomparison between Sentinel-2A and Landsat-8 estimates showed high spatial consistency between estimates over the three areas. Direct validation was performed with in situ LAI measurements acquired in coordinated field campaigns, revealing a good accuracy and correlation in all cases. These results suggest that a very frequent time series of LAI at high resolution can be obtained from a multi-sensor approach to better outline rice-growing behavior. The use of combined curves of LAI can be exploited to identify agronomical dynamics (management and crop phenology) for the retrieval of phenological stages, and monitoring vegetation production or deriving multitemporal training sets for mapping purposes. In particular it is also illustrated as the anomalous drops in LAI time series can help identifying problems/damages at field level due to the effects of plant diseases or other factors.*

1 INTRODUCTION

Information of the actual development crop status is a fundamental element in crop monitoring and modelling studies. Crop monitoring is necessary to identify the onset of stress conditions, which require agro-practises in order to mitigate their impact on crop yield. In this framework, leaf area Index (LAI) estimation at high spatial resolution is key information for assessing vegetation status.

LAI can be estimated from remote sensing using statistical, physical, or hybrid methods (Camps-Valls *et al*., 2011). Pure statistical methods extract patterns and trends from a data set, and try to understand the underlying physical laws ruling the relationships between them. Physically-based methods are based on the physical knowledge describing the interactions between incoming radiation and vegetation though radiative transfer models (RTMs).

For their part, hybrid methods couple statistical non-parametric with physically-based methods. Hybrid methods rely on inverting a database generated by a radiative transfer model exploiting the generality of RTMs and the flexibility and computational efficiency of non-parametric non-linear regression methods. The advantage of hybrid approaches is that a broad range of land cover situations can be simulated (e.g., up to hundred thousands), leading to a data set much bigger than what can be collected during a field campaign and the RTM can be inverted in a flexible and accurate manner with machine learning methods.

In relation with biomass and crop yield estimation, LAI estimates can be assimilated in crop models (Confalonieri *et al*., 2009) by means of forcing and/or recalibration techniques (Dorigo *et al*., 2007; Busetto *et al*., 2017). Derive and assimilate accurate LAI estimates improves the accuracy of grain yield estimates (Curnel *et al*., 2011) and an operational application of this workflow for rice was successfully demonstrated in Asia in the framework of the RIICE (Remote sensing-based Information and Insurance for Crops in Emerging economies) project (http://www.riice.org/) where rice yield is estimated from the Oryza2000 model by assimilating LAI maps derived from synthetic aperture radar (SAR) images (Holecz *et al*., 2013). Similarly, LAI has been used assessment in the framework of the ERMES (an Earth obseRvation Model based RicE information Service) project (http://www.ermes-fp7space.eu/) with the aim of developing a prototype of Copernicus down-stream services assimilating Earth observation (EO) and *in situ* data on crop modeling dedicated to the rice sector.

This work provides a general overview of the Landsat-7/8 and Sentinel-2A LAI estimates derived through a hybrid retrieval methodology and used for crop assessment from multisource LAI time series in the framework of the ERMES.

2 MATERIALS

2.1 Study areas

In this work, we used the ERMES study areas which are located in Italy, Spain and Greece. The Italian study area belongs to the Lomellina rice district (south-western Lombardy region). The Spanish study area is located in the rice district of Valencia (east of Spain), and the Greek study area is located in the rice district of Thessaloniki, which is the main rice cultivation area for Greece. Within each study area, rice is a common crop with a long tradition and economic value.

2.2 Field data

In the framework of the local ERMES field activities, LAI ground measurements were conducted over the study areas. In Spain, Italy and Greece, 32, 16 and 10 ESUs (elementary sampling units) were selected. The temporal frequency of the campaigns was approximately 7–10 days starting from the very beginning of rice emergence (early June) up to the maximum green rice LAI development (mid-August). A range of 18–24 measurements over every ESU was taken following the guidelines and recommendations of the Validation of Land European Remote sensing Instruments (VALERI) protocol. LAI measurements were acquired using a dedicated smartphone app (PocketLAI) which has shown similar estimates obtained using plant canopy analyzers (e.g., LAI-2000) and DHP (digital hemispherical photography) over rice fields (Campos-Taberner *et al*., 2016a)

2.3 Remote sensing data

In this study Landsat-8 Operational Land Imager (OLI) and Landsat-7 Enhanced Thematic Mapper (ETM+) surface reflectance data at 30-m spatial resolution were used during the 2016 rice season over the three study areas. Images were available every 16 days in Italy and Greece, and every seven and nine days in Spain. In adition, Sentinel-2A Level 1C data (top-of-atmosphere reflectances) were used in the same period over the three study areas providing information every 10 days in 13 bands in the visible, near infra-red and short wave infra-red spectrum at a 10, 20 and 60 m spatial resolution depending on the band.

The remote sensing data used in this study was completed by Sentinel-1A data which were used during the 2016 European rice season over the aforementioned rice areas. Both Sentinel-1A and Sentinel-2A were downloaded from the ESA Sentinels Scientific Data Hub, while Landsat-7/8 images were downloaded through the United States Geological Survey (USGS) Earth Resources Observation and Science (EROS) Center Science Processing Architecture (ESPA).

3 RETRIEVAL METHODOLOGY

In this work we derive LAI from optical remote sensing surface reflectance (Landsat-7/8 and Sentinel-2A) by inverting the PROSAIL radiative transfer model (Jacquemoud *et al*., 2009) (see Figure 2). PROSAIL simulates surface reflectance of the vegetated surface of interest (in our case, rice crops in the tropics) in the range of 400 to 2500 nm. For this purpose, PROSAIL uses a set of bio-chemical and structural parameters at canopy and leaf levels.

PROSAIL was run 2000 times following a specific parameterization for rice (Campos-Taberner *et al*., 2016b;2017) in order to obtain a database composed of surface reflectance corresponding to each optical remote sensing product and the associated LAI values.
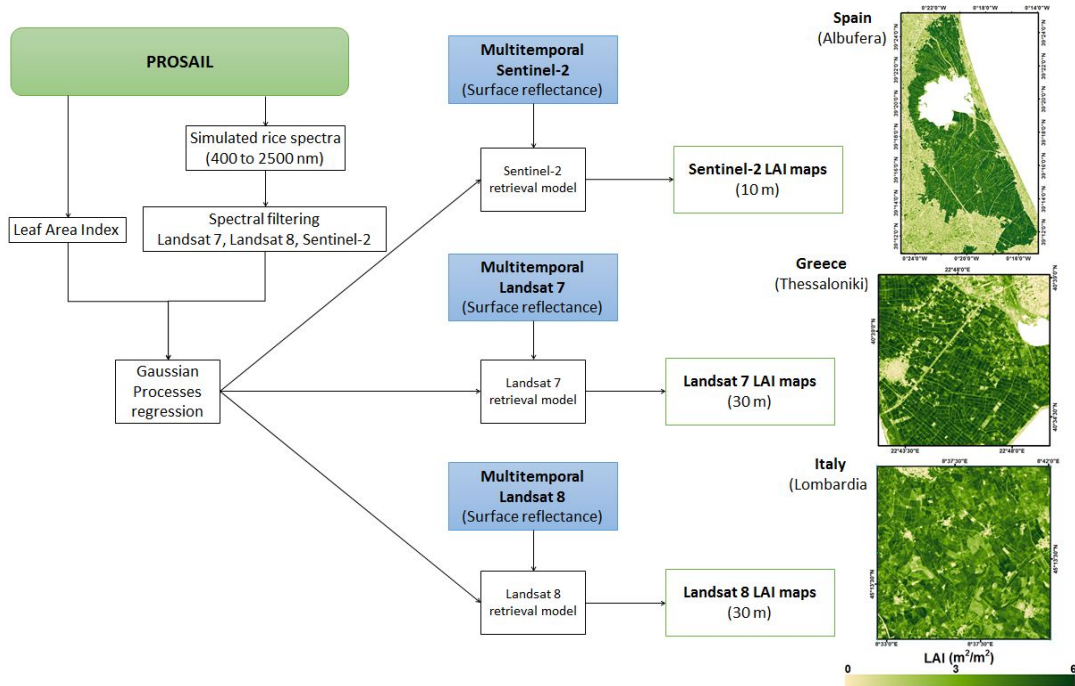
Figure 1. Hybrid retrieval methodology including some examples of the estimated decametric LAI maps.

The simulated database was then used for training a Gaussian process regression (GPR) (Rasmussen and Williams, 2006) model which has proven to be an efficient and robust machine learning non-linear regression tool for bio-physical parameter retrieval (Campos-Taberner, *et al.*, 2015). In addition, Rice maps derived from Sentinel-1A data were derived following a multi-temporal rule-based methodology (Nelson *et al.*, 2014) and subsequently used as masking layer for LAI retrieval.

3 RESULTS

Decametric LAI retrievals were obtained over the three rice areas during the 2016 rice season applying the retrieval methodology to both multitemporal Landsat-7/8 and Sentinel-2A imagery. Six Sentinel-2A surface reflectance spectral bands were used during the retrieval process: blue, green, red, near infrared and the two short wave infrared channels. These channels were selected to enhance the consistency with Landsat-7/8 data (Campos-Taberner *et al.*, 2017) allowing thus the creation of a robust multi-sensor retrieval. The obtained estimates were validated with *in situ* LAI measurements collected in the three countries using the PocketLAI. The root mean squared error (RMSE), mean error (ME), mean absolute error (MAE) and coefficient of determination (R^2) were computed in order to assess the accuracy of

the retrievals, bias and goodness-of-fit. Good accuracy and high correlation were found in all cases, revealing an overall RMSE of 0.61 and 0.69 as well as $R^2=0.90$ and $R^2=0.95$ in the case of Landsat-7/8 and Sentinel-2A LAI retrievals, respectively (see Figure 2 and Figure 3).
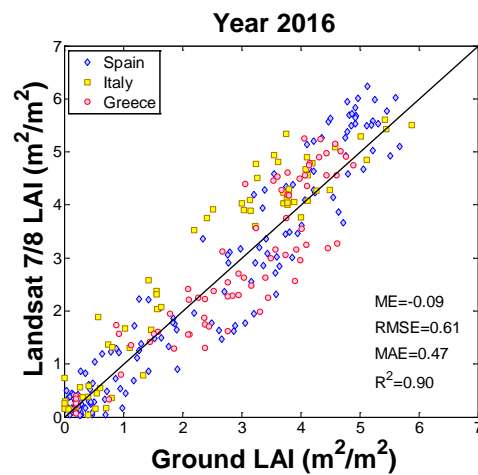
Figure 2. Scatter plots of Landsat-7/8 estimated LAI values versus *in situ* LAI measurements during the 2016 rice season.

Year 2016
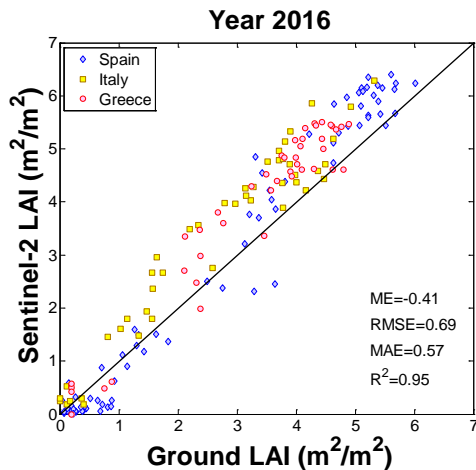
Figure 3. Scatter plots of Sentinel-2A estimated LAI values versus *in situ* LAI measurements during the 2016 rice season.

The use of combined curves of LAI can be exploited to identify agronomical dynamics (management and crop phenology) for the retrieval of phenological stages, and monitoring vegetation production or deriving multitemporal training sets for mapping purposes. In particular, anomalous drops in LAI time series can help identifying problems/damages at field level due to the effects of plant diseases or other factors. For example, Figure 4 shows the temporal evolution of two Sentinel-2A rice pixels (healthy and damaged). It can be seen the anomalous temporal LAI evolution over the same field which is related with rice crop disease.
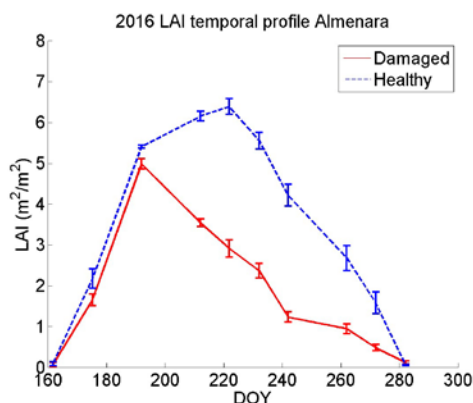
Figure 4. Sentinel-2 LAI evolution within a rice field. Blue line corresponds to a healthy rice pixel whereas the red one corresponds to a damaged pixel.

4 CONCLUSIONS

This study presented multi-source LAI retrieval from decametric Landsat-7/8 and Sentinel-2A data over three European rice areas in the 2016 rice season. The approach relies on the inversion of the PROSAIL RTM with Gaussian process regression on rice fields detected by using Sentinel-1A data. The methodology allows us to retrieve a dense temporal dataset of LAI maps which is fundamental to perform expert crop monitoring and also to improve crop model estimations exploiting assimilation techniques. This multi-sensor approach is suitable to fill gaps in the time series mainly due to the presence of clouds, obtaining thus a more reliable time series for precision agriculture applications and rice monitoring.

REFERENCES

Busetto, L., Casteleyn, S., Granell, C., Pepe, M., Barbieri, M., Campos-Taberner, M., Casa, R., Collivignarelli, F., Confalonieri, R., Crema, A., García-Haro, F. J., Gatti, L., Gitas, I. Z., González-Pérez, A., Grau-Muedra, G., Guarneri, T., Holecz, F., Katsantonis, D., Minakou, C., Miralles, I., Movedi, E., Nutini, F., Pagani, V., Palombo, A., Paola, F. D., Pascucci, S., Pignatti, S., Rampini, A., Ranghetti, L., Ricciardelli, E., Romano, F., Stavrakoudis, D. G., Stroppiana, D., Viggiano, M., Boschetti, M., 2017, Downstream services for rice crop monitoring in europe: From regional to local scale. *IEEE Journal of Selected Topics in Applied Earth Observations and Remote Sensing*, pp. 1–19.

Campos-Taberner, M., Garcia-Haro, F., Moreno, A., Gilabert, M., Sanchez-Ruiz, S., Martinez, B., Camps-Valls, G., 2015, Mapping leaf area index with a smartphone and Gaussian processes, *Geoscience and Remote Sensing Letters, IEEE*, **12**, 2501–2505.

Campos-Taberner, M., García-Haro, F.J., Camps-Valls, G., Grau-Muedra, G., Nutini, F., Crema, A., Boschetti, M., 2016b, Multitemporal and multiresolution leaf area index retrieval for operational local rice crop monitoring, *Remote Sensing of Environment*, **187**, 102 – 118.

Campos-Taberner, M., García-Haro, F.J., Confalonieri, R., Martínez, B., Moreno, l., Sánchez-Ruiz, S., Gilabert, M. A., Camacho, F., Boschetti, M., Busetto, L., 2016a, Multitemporal monitoring of plant area index in the valencia rice district with Pocketlai. *Remote Sensing*, **8**(3), 202.

Campos-Taberner, M., García-Haro, F.J., Camps-Valls, G., Grau-Muedra, G., Nutini, F., Busetto, L., Katsantonis, D., Stavrakoudis, D., Minakou, C., Gatti, L., Barbieri, M., Holecz, F., Stroppiana, D., & Boschetti, M., 2017, Exploitation of SAR and optical Sentinel data to detect rice crop and estimate seasonal dynamics of leaf area index, *Remote Sensing*, **9**(7), 248.

Camps-Valls, G., Tuia, D., Gómez-Chova, L., Jiménez, S., & Malo, J., 2011, Remote sensing image processing. Synthesis Lectures on Image, Video, and Multimedia Processing (Morgan & Claypool Publishers).

Confalonieri, R., Rosenmund, A. S., Baruth, B., 2009, An improved model to simulate rice yield. *Agronomy for Sustainable Development*, **29**, 463–474.

Curnel, Y., de Wit, A.J., Duveiller, G., Defourny, P., 2011, Potential performances of remotely sensed LAI assimilation in WOFOST model based on an OSS Experiment. *Agricultural and Forest Meteorology*, **151**, 1843–1855.

Dorigo,W., Zurita-Milla, R., deWit, A., Brazile, J., Singh, R., & Schaepman, M., 2007, A review on reflective remote sensing and data assimilation techniques for enhanced agroecosystem modelling, *International Journal of Applied Earth Observation and Geoinformation*, **9**, 165–193.

Holecz, F., Barbieri, M., Collivignarelli, F., Gatti, L., Nelson, A., Setiyono, T.D., Boschetti, M., Manfron, G., Brivio, P.A., Quilang, J., et al., 2013, An operational remote sensing based service for rice production estimation at national scale. In Proceedings of the Living Planet Symposium, Edinburgh, UK, 9–13 September 2013.

Jacquemoud, S., Verhoef, W., Baret, F., Bacour, C., Zarco-Tejada, P.J., Asner, G.P., François, C., Ustin, S.L., 2009, PROSPECT + SAIL models: A review of use for vegetation characterization. *Remote Sensing of Environment*, **113**, S56–S66.

Nelson, A., Setiyono, T., Rala, A., Quicho, E., Raviz, J., Abonete, P., Maunahan, A., Garcia, C., Bhatti, H., Villano, L., et al., 2014, Towards an operational SAR-Based rice monitoring system in ASIA: Examples from 13 demonstration sites across Asia in the RIICE project. *Remote Sensing*, **6**, 10773–10812.

Development of sea surface temperature retrieval algorithm for the Chinese Gaofen-5 data

Yuanyuan Chen [1,2], Si-Bo Duan [1] and Zhao-Liang Li [1,3]

[1] *Key Laboratory of Agri-informatics, Ministry of Agriculture/Institute of Agricultural Resources and Regional Planning, Chinese Academy of Agricultural Sciences, Beijing, 100081, P. R. China*

[2] *Key Laboratory of Cultivated Land Use, Ministry of Agriculture, P. R. China; Chinese Academy of Agricultural Engineering, Beijing, 100121*

[3] *ICube (UMR7357), UdS, CNRS, 300 Bld Sébastien Brant, CS10413, Illkirch, 67412, France*

Correspondence: lizhaoliang@caas.cn

ABSTRACT: *Sea surface temperature (SST) is a key geophysical parameter at the ocean–atmosphere boundary. One commonly used method to estimate SST based on remote sensing measurements is the split-window algorithm. However, some assumptions and approximations, which do not appear to reflect the reality, were used to derive the linear split-window algorithm. Reviewing the publications in the recent years on the SST retrieval, the algorithm of SST determination is usually developed by recalculating the algorithm coefficients for the new sensors. Little attention has been paid on exploring the theoretical improvement of split-window algorithm. The goal of this paper is to investigate the assumptions and approximations used in the derivation of split-window technique and develop the SST retrieval algorithm for the Gaofen-5 (GF-5) satellite, which is scheduled to be launched in the second half of 2017. Two revised equations of these assumptions and approximations were created. Combining the revised equations, a nonlinear SW algorithm was obtained that could be simplified to the quadratic split-window equation. Based on the simulated data, the developed algorithm gives a SST retrieval accuracy of RMSE = 0.34 K. The main difference of this study from the previous research is that this paper focuses more on building our theoretical understanding of the semi-empirical quadratic split-window equation.*

KEY WORDS: *Sea surface temperature*; *Split-window*; *Revision*; *Gaofen-5*

1. INTRODUCTION

Sea surface temperature (SST) is required for many environmental applications, such as monitoring the thermal pollution from nuclear power and climate change (Chen et al., 2003; Jangid et al., 2017). Researchers have long investigated the use of remote sensing data to retrieve SST. The split-window method is at present the most popular method for SST estimation. One approximation used in the derivation of split-window method is the first-order Taylor approximation of the Planck function (Prabhakara et al., 1974). Another assumption is that the atmospheric equivalent temperatures in the two adjacent thermal infrared (TIR) channels were regarded as the same ($T_{ai} = T_{aj}$) (Sobrino et al., 1991). Notably, there are certain restrictions for these assumptions. The first-order Taylor approximation of the Planck function requires that the difference among the temperatures, that are the at-sensor brightness temperature T_i, atmospheric equivalent temperature T_{ai} and the SST in the radiative transfer model (RTM), is small. In addition, the hypothesis $T_{ai} = T_{aj}$ does not appear to reflect reality. This paper focuses on investigating these assumptions and developing SST retrieval algorithm for the coming Gaofen-5 (GF-5) satellite.

The GF-5 satellite is the fifth satellite of China High-resolution Earth Observation System project, scheduled to be launched in the second half of 2017. The multiple spectral-imager (MSI) is a payload onboard this satellite, observing the earth almost at nadir with the spatial resolution of 40-meter for two TIR channels (labeled as $CH_{10.8}$ and $CH_{11.95}$). Figure 1 shows the spectral response functions of GF-5/MSI split-window channels.

2. METHOD

Based on the RTM, the following equation can be obtained by using Taylor's expansion of the Planck function,

$$T_i = T_{ai} + \tau_i(T_s - T_{ai}) + \Delta T_i \qquad (1)$$
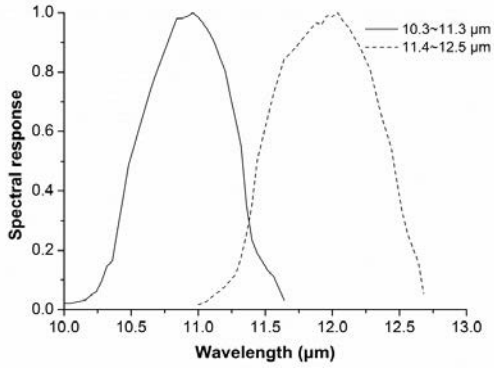
Figure 1. Spectral response functions of Gaofen-5 split-window channels.

where τ_i is the transmittances through the atmosphere from the surface to the satellite in channel i, T_s is the sea surface temperature (SST), ΔT_i is the error in T_i caused by linearizing the Planck function. In the published literature, ΔT_i is small and always be neglected (Prabhakara et al., 1974; Sobrino et al., 1991). Writing Eq. (1) for two channels i and j, Eq. (2) can be derived,

$$T_s = T_i + A(T_i - T_j) + \Delta T_{s1} + \Delta T_{s2} \qquad (2)$$

where $\Delta T_{s1} = - \Delta T_i - A(\Delta T_i - \Delta T_j)$ with $A = (1 - \tau_i) / (\tau_i - \tau_j)$, $\Delta T_{s2} = A_a(T_{ai} - T_{aj})$ with $A_a = - (1 - \tau_i) (1 - \tau_j) / (\tau_i - \tau_j)$. ΔT_{s1} is the error of T_s retrieval caused by linearizing the Planck function and ΔT_{s2} is the impact of the hypothesis $T_{ai} = T_{aj}$ on T_s retrieval.

In order to evaluate the influence of ΔT_{s1} and ΔT_{s2} on T_s retrieval, 81 profiles from TIGR 2000 database were selected as input to execute the radiative transfer simulation procedure. These 81 profiles remain representative of a worldwide description of the atmosphere with the near surface air temperature (T_0) 236.25-303.41 K and the total water vapor content (W) 0.09-5.69 g/cm^2. The atmospheric radiative transfer model MODTRAN was used to simulate the atmospheric upwelling radiance and the atmospheric transmittance considering a nadir viewing. Using these parameters, according to the RTM, the total radiance was calculated with 5 surface temperatures: $T_0 - 5$ K, $T_0 - 2$ K, T_0 K, $T_0 + 2$ K and $T_0 + 5$ K. Then the brightness temperature can be obtained by inverting the Planck function. The atmospheric equivalent temperature can be obtained from the atmospheric upwelling radiance. According to the simulated data, ΔT_{s1} and ΔT_{s2} in Eq. (2) were calculated.

The range of ΔT_{s1} is about -0.4~0.5 K. If the linearization of Planck function were used, a root mean square error (RMSE) of 0.1 K and a bias of -

0.06 K can be obtained for T_s retrieval. To reduce or eliminate the error, the second-order derivative of Taylor expansion of Planck function was considered. Based on the simple mathematical manipulation, We found, there is a good linear relationship between ΔT_i and $\dfrac{(T_s - T_i)^2 \tau_i}{T_i(1 - \tau_i)}$, with sufficient accuracy of T_i (RMSE lower than 0.01 K) for both channels, as shown in Figure 2. Thus, the revision of ΔT_i was given,

$$\Delta T_i = \alpha_i \frac{(T_s - T_i)^2 \tau_i}{T_i(1 - \tau_i)} \qquad (3)$$

where α_i is the regression coefficient, which is 1.40 for $CH_{10.8}$ and 1.21 for $CH_{11.95}$, respectively.

(a)

(b)
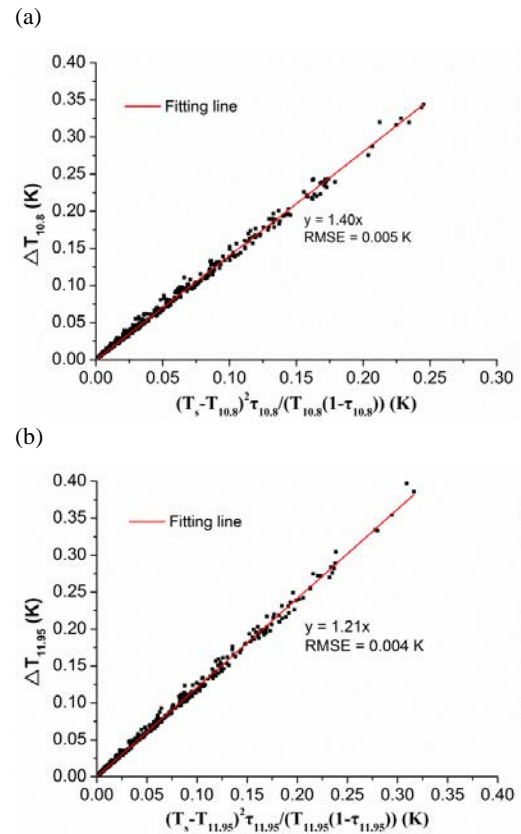
Figure 2. Parameterization of ΔT_i using $(T_s - T_i)^2 \tau_i / (T_i (1 - \tau_i))$ for Gaofen-5 TIR channels centered at (a) 10.8 μm and (b) 11.95 μm. Here, T_s is the sea surface temperature, T_i is the simulated brightness temperature, τ_i is the transmittance and ΔT_i is the error of linearization of Planck function.

According to the expression of ΔT_{s2}, if the hypothesis of $T_{ai} = T_{aj}$ is adopted, ΔT_{s2} would be 0. However, according to the values of $T_{a10.8}$ and $T_{a11.95}$, ΔT_{s2} ranges from about -6~2 K, as displayed in Figure 3. We can see that the $T_{ai} = T_{aj}$ hypothesis can produce the RMSE of 1.74 K and bias of -0.88 K for the SST estimation. In fact, the linear dependence, not the equal relationship, exists between $T_{a10.8}$ and $T_{a11.95}$, as shown in Figure 4.

$$T_{a11.95} = aT_{a10.8} + b \qquad (4)$$
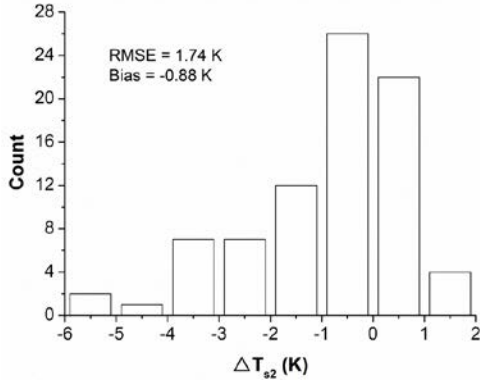
Figure 3. Histogram of error caused by the hypothesis of $T_{a10.8} = T_{a11.95}$ for SST retrieval. Here, $T_{a10.8}$ and $T_{a11.95}$ are the atmospheric equivalent temperatures in Gaofen-5/MSI split-window channels.
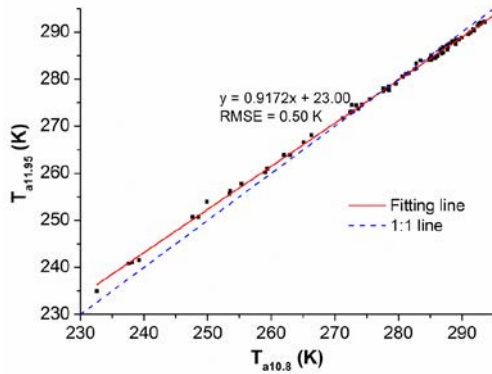
Figure 4. The linear dependence of the atmospheric equivalent temperatures for Gaofen-5 split-window channels.

Writing Eq. (1) with ΔT_i substituted by Eq. (3) for two channels of CH$_{10.8}$ and CH$_{11.95}$, one can get,

$$SST - T_{10.8} = (M-1)(T_{10.8} - T_{11.95}) + (M-1+N)T_{11.95} \quad (5)$$

where
$$M = \frac{A_4}{2(A_1 - A_2 \frac{T_{10.8}}{T_{11.95}})} \qquad \text{and}$$

$$N = \frac{\sqrt{A_4^2 + 4(\frac{A_1}{T_{10.8}} - \frac{A_2}{T_{11.95}})(A_5 T_{10.8} + A_6 T_{11.95} + A_3)}}{2(A_1 \frac{T_{11.95}}{T_{10.8}} - A_2)}$$

, with

$$A_1 = \frac{a\alpha_{10.8}(1 - \tau_{11.95})\tau_{10.8}}{1 - \tau_{10.8}},$$

$$A_2 = \frac{\alpha_{11.95}(1 - \tau_{10.8})\tau_{11.95}}{1 - \tau_{11.95}},$$

$$A_3 = b(1 - \tau_{10.8})(1 - \tau_{11.95}),$$

$$A_4 = 2(A_1 - A_2) - a(1 - \tau_{11.95})\tau_{10.8} + (1 - \tau_{10.8})\tau_{11.95},$$

$$A_5 = -A_1 + a(1 - \tau_{11.95}) \text{ and } A_6 = A_2 - (1 - \tau_{10.8}).$$

According to the calculated result, M ranged from 0.9620~0.9941, close to 1. The first term of Eq. (5) (i.e., $(M-1)(T_{10.8} - T_{11.95})$) is thus small even if multiplied by the maximum of $(T_{10.8} - T_{11.95})$ (approximately 4 K). While the second term (i.e., $(M - 1 + N)T_{11.95}$) makes the main contribution to Eq. (5), because of the large value of $T_{11.95}$. Taking the structure of the split-window algorithm into consideration, the relationship between $(M - 1 + N)T_{11.95}$ and $(T_{10.8} - T_{11.95})$ was investigated. As shown in Figure 5, $(M - 1 + N)T_{11.95}$ can be parameterized using $(T_{10.8} - T_{11.95})$, with RMSE = 0.30 K.
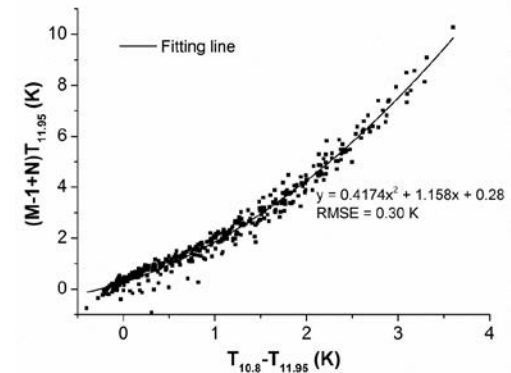
Figure 5. The relationship between $(M - 1 + N)T_{11.95}$ in Eq. (5) and the difference of the brightness temperatures in split-window channels $(T_{10.8} - T_{11.95})$.

Based on the above analysis, Eq. (5) can be simplified as:

$$SST - T_{10.8} = A(T_{10.8} - T_{11.95})^2 + B(T_{10.8} - T_{11.95}) + C \tag{6}$$

where A, B and C are the algorithm coefficients. Using the least-square fitting method, $A = 0.4253$, $B = 1.123$ and $C = 0.28$ were obtained for GF-5 data, with RMSE = 0.30 K.

3. RESULTS

This section aims to assess the general applicability of the developed quadratic split-window algorithm (Eq. (6)) to different atmospheric conditions. Therefore, another dataset was established using 23 atmosphere profiles with a nearly uniform distribution of W. For these profiles, W is ranging from 0.12~5.56 g/cm^2 and T_0 is within 232.25~303.15 K. Again, MODTRAN model was used to simulate the atmospheric parameters in the thermal radiation process and at-sensor brightness temperatures with the surface temperatures ranging from $T_0 - 5$ K, $T_0 - 2$ K, T_0 K, $T_0 + 2$ K and $T_0 + 5$ K. Based on 115 simulated situations (23 profiles * 5 surface temperatures), the SST was calculated using Eq. (6). A RMSE of 0.3 K and a bias of 0 K were obtained. Among the difference between the truth and the retrieved SST, 93.04% of the error is within ±0.5 K and 76.52% is within ±0.3 K.

4. CONCLUSIONS

Some assumptions and approximations, that are the linearization of Planck function and the same atmospheric equivalent temperatures in two adjacent split-window channels, were used in the derivation of split-window algorithm. These assumptions and approximations were investigated in this paper. Two revisions of the assumptions and approximations were then created for GF-5/MSI data. Based on these two revisions, the quadratic split-window algorithm suitable for GF-5/MSI TIR data was developed. The developed algorithm was evaluated using another simulated dataset. A RMSE of 0.3 K and a bias of 0 K, implying the satisfactory accuracy, were obtained. Performing an analysis of the developed algorithm in a future period when the GF-5 satellite data is available would be valuable.

REFERENCES

Chen, C., Shi, P. and Mao, Q., 2003, Application of remote sensing techniques for monitoring the thermal pollution of cooling-water discharge from nuclear power plant. *Journal of Environmental Science and Health*, **38**, 8, 1659-1668.

Jangid, B. P., Kumar, P., Raju, A. and Kumar, R., 2017, Significance of high resolution GHRSST on prediction of Indian Summer Monsoon. *Advances in Space Research*, 1-11.

Prabhakara, C., Dalu, G. and Kunde, V. G., 1974, Estimation of sea surface temperature from remote sensing in the 11-13μm window region. *Journal of Geophysical Research*, **79**, 5039-5044.

Sobrino, J. A., Coll, C. and Caselles, V., 1991, Atmospheric corrections for land surface temperature using AVHRR channels 4 and 5. *Remote Sensing of Environment*, **38**, 19-34.

Bathymetry of Suez Canal and the Temsah Lake Using WorldView-2 imagery

Ahmed Elsharkawy[1], Mohamed Elhabiby[2], Naser El-Sheimy[3]

[1] Military Technical College, Phone: 002-02-24031982, Email: ashawky@mtc.edu.eg

[2] Public Works Department, Faculty of Engineering, Ain Shams University, Cairo, Egypt.

[2] Email: mmelhabi@ucalgary.ca

[3] Dept. of Geomatics Engineering, University of Calgary, Calgary, Alberta, T2N 1N4

[3] Email: elsheimy@ucalgary.ca

ABSTRACT (In this research paper the relative bathymetry of the Suez Canal Water way and the Temsah Lake will be derived using the new bands of the WorldView-2 satellite. The non-linear model introduced by (Stumpf et al. 2003) will be used to examine the role of each of the new bands and their expected improvement in the quality of the classification of the bottom types and the relative depths.

For this purpose a calibration process will take place first by converting digital numbers into radiance then to reflectance values. Dark pixel correction will be applied to account for atmospheric and sun-glint effects then six different ratios will be used to derive relative bathymetry of the study area.

1 INTRODUCTION

Typically, bathymetric charts are generated from ship-borne sounding surveys with single- or multi-beam echo sounders, in which they can operate to depths more than 500 m. State-of-the-art acoustic multi-beam, swath-mapping systems can achieve 6 m spatial resolution and about 8 cm depth accuracy in 200 m water depth (Su et al. 2008). However, in case of shallow water, ship-borne surveys may not be the proper solution for the following reasons:

- The survey will be time consuming and expensive, as the survey swaths are narrow.
- It may not be feasible to survey waters shallower than 2–3 m deep because of sound saturation or/and inaccessibility of survey vessels.

Recently, airborne bathymetric LiDAR (Light Detection And Ranging), introduced an optimum solution for the mapping of shallow coastal waters. The only limitations occur with this relatively new technology are; the high cost of operation and that the amount of maximum penetration of LiDAR systems is greatly dependent upon water transparency. Average penetration depth for most of currently operated systems are in the range of 30 meters, LADS (Laser Airborne Depth Sounder) developed by Tenix LADS Corporation is an exception where penetration depth reaches 70 meters. Also, most systems can reach up to 4 meters spatial resolution with 20 cm accuracy (Su et al. 2008). In 2012, Optech developed CZMIL, coastal zone mapping and imaging LiDAR. CZMIL is an innovative airborne coastal zone mapping system that integrates bathymetric LiDAR, with a hyper-spectral imaging system and digital metric camera to produces simultaneous high-resolution 3D data and imagery of the beach and shallow water seafloor (www.optech.ca/Optech_News_Release_CZMIL-120507.html).

Optical remote sensing was also introduced as an alternative solution for bathymetric applications. David R. Lyzenga, first introduced a model for shallow water depth estimation using a single band from aerial photography (Lyzenga 1978). This model was then expanded to multi-spectral satellite imagery using a non-linear bathymetric inversion model (Stumpf et al. 2003). According to Beer's law, the basic physical principles underlying the retrieval of bathymetric information from optical remote sensing images are:

- Light attenuation in the water column increases exponentially as depth increases.
- Additionally, attenuation varies by wavelength, resulting in less attenuation and greater depth penetration in the blue region of the visible spectrum than the green or red regions (Lyzenga 1978; Lyzenga 1981).

These two properties are the basis for optically-derived bathymetry from multispectral, passive sensors. In the next section a brief summary of these two properties and how they can be applied to finally derive water depth of shallow waters will be introduced.
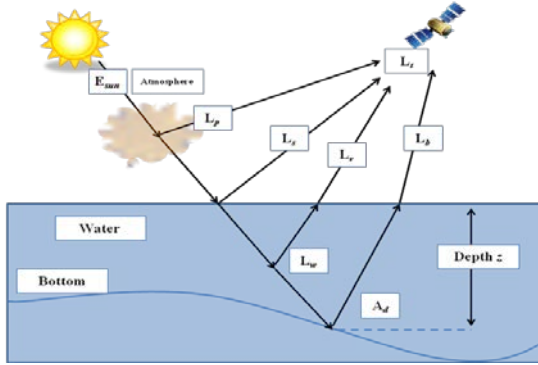
Figure 1 Four main components of the total radiance (Jensen 2007)

2 Bathymetric Models for Optical Multi-spectral Imagery

According to (Jensen 2007), the total upwelling radiance (L_t) recorded by the remote sensor consists of four components, as shown in Figure 1.

$$L_t = L_b + L_v + L_s + L_p \qquad \textbf{Eq. 1}$$

Where, (L_p), atmospheric path radiance, is a function of atmospheric scattering, including both Rayleigh (molecular) scattering and Mie (aerosol) scattering, **(L_v), subsurface volumetric radiance,** results from volume scattering from the water and its organic/inorganic constituents like sediment and chlorophyll. **(L_s), Specular radiance,** is the reflection from the water surface, including possible sun-glint effects. Finally, **(L_b), the bottom radiance,** is the energy reflected from the seabed, which integrates the information about water depth and bottom characteristics.

In order to retrieve water depth information from the total radiance, bottom radiance (L_b), has to be extracted from the total radiance (L_t). Atmospheric correction and sun-glint removal are applied first to remove (L_p) and (L_s), then deep water correction is accomplished to remove (L_v) (Lyzenga 1978; Lyzenga 1981; Stumpf et al. 2003).

As long as, the bottom radiance (L_b) equals zero for deep water, then the measured total radiance over optically-deep water (L_∞) includes the joint effects of subsurface volumetric radiance (L_v), specular radiance (L_s), and atmospheric path radiance (L_p). After atmospheric and sun-glint corrections, the deep water radiance (L_∞) only contains subsurface volumetric radiance (L_v) (Su et al. 2008). Assuming that the values of (L_v) of shallow and deep waters will not change, then we can use optically deep water radiance (L_∞) recorded by the remote sensor to correct the subsurface volumetric radiance (L_v) in shallow water.

Based on Beer's Law, (Lyzenga 1978; Lyzenga 1981) introduced a simple radiative transfer model for shallow waters:

$$L = L_\infty [\ 1\text{-}\ exp(\text{-}gz)\ ] + A_d\ exp(\text{-}gz) \qquad \textbf{Eq. 2}$$

Where, $L = L_t - L_p - L_s$, is the measured radiance after atmospheric and sun-glint corrections, L_∞ is deep water radiance (equivalent to volumetric radiance L_v), A_d is the upwelling spectral radiance directly reflected from the bottom before interacting with the overlying water column, g is a two-way attenuation coefficient, and z is depth. Rearranging this equation, putting z in the left hand side, results in the equation of the bathymetric inversion model for a single spectral band as follows:

$$z = g^{\text{-}1}\ [\ ln(A_d \text{-} L_\infty) - ln(L \text{-} L_\infty)] \qquad \textbf{Eq. 3}$$

Later on, Lyzenga developed a new bathymetric inversion model using more than one band as follows:

$$z = a_o + \sum_{i=1}^{N} a_i \ln[L(\lambda_i) - L_\infty(\lambda_i)] \qquad \textbf{Eq. 4}$$

Where, a_i are the constant coefficients, N is the number of spectral bands, $L(\lambda_i)$ is the remote sensing radiance after atmospheric and sun-glint corrections for spectral band λ_i, and $L_\infty(\lambda_i)$ is the deepwater radiance for spectral band λ_i.

The model explained in Eq. 4 referred to as the log-linear inversion (or deepwater correction) model, this model has been extensively used for estimating water depths from optical multi-spectral remote sensing imagery (Su et al. 2008).

In 2003, (Stumpf et al. 2003) proposed a non-linear bathymetric inversion model based on a log-transformed band ratio:

$$z = m_1 \frac{\ln(nL(\lambda_2))}{\ln(nL(\lambda_1))} - m_o \qquad \textbf{Eq. 5}$$

Where, m_0, m_1, and n are constant coefficients for the model, and L (λ_1) and L (λ_2) are the atmospheric and sun-glint corrected remote sensing radiances for bands λ_1 (short wave length), and λ_2 (long wave length) (Stumpf et al. 2003).

When two bands are used, with different water absorptions, the log values change with depth and the whole ratio will change. If we abide to retain the shorter wave length in the nominator and the longer wave length in the denominator so the log ratio will increase as the depth increase. This ratio will compensate for the implicitly for variable bottom type (Stumpf et al. 2003), but changes in depth affect the high absorption band more. As a result, the effect of change in ratio because of depth is much greater than

that caused by change in bottom reflectance. Generally, (Stumpf et al. 2003) demonstrated that their non-linear inversion model is more robust and accurate than the conventional log-linear inversion model for relatively deep areas. This is why we will utilise this method with worldview-2 imagery to examine the role of the new bands in bathymetry.

Blue light (450-510 nm) can penetrate clear down to 30 m depth, and thus serves as the optimum spectral band from which to extract depth information (Su et al. 2008). Worldview-2 provides a new band; costal blue (400-450 nm), with higher capability of penetrating water (Globe 2009). Also, the yellow band (585-625 nm) will be examined as the longer wavelengths attenuate rapidly in water.

The main assumption for both aforementioned models is based on the assumption that water optical properties are spatially homogeneous, which results in uniformity in water quality over the area of study. In addition, both models assume that the ratio of bottom reflectance's is the same for different types of bottoms in the same scene. In general, high water clarity and uniform bottom types are two vital conditions, that must be met for reliable depth retrieval from optical multispectral imagery (Su et al. 2008). In this research the relative depths of part of the water way of the Suez Canal and the over polluted Temsah Lake will be derived from the worldview-2 imagery, using the non-linear bathymetric inversion model derived by Stumpf.

3 Data description

Lake Temsah has a nearly triangular shape with elongated sides extending East-West. The lake is small and shallow. It has a surface area of about 8 square kilometers with an average depth of only 11 meters and containing about 90 million cubic meters of water. The lake is surrounded by industrial workshops for shipyards, domestic areas, recreational beaches and agricultural lands. The Suez Canal pathway is deep, about 24 m depth, but narrows about 300-360 m wide at water level. Figure 2 illustrates a false color image for the area of study.

Unlike the Canal pathway, Temsah Lake receives a great deal of untreated domestic and industrial waste discharges and agricultural drainage return flows. Consequently, the lake and its beaches exhibit serious water quality problems in many locations. Moreover, the substantial amounts of sediment loads, which enter the lake, produce higher accumulation rates and seriously obstruct lake transportation (Donia 2011).

A water quality index, WQI, is a mathematical way of summarizing multiple properties into a single value. This index values are ranging between 0 and 100, with higher numbers indicating lower quality water. (Donia 2011), introduced one of the standers WQI chart for

the Temsah Lake and it used in this study to demonstrate the differences in water quality across this region.

Figure 2 Temsah Lake and Canal Suez water way
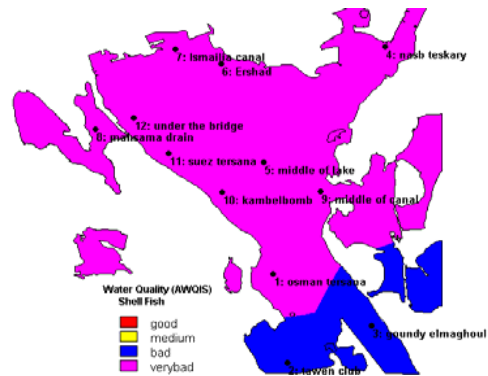
Figure 3 A WQI for the Temsah Lake,(Donia 2011)

The figure above shows that almost all the lake water quality is considered very bad except the southern region of the lake that is considered better quality but still bad.

4 Methodology

Generally, any imagery will be used in a radiometric/spectral analysis must be converted to spectral radiance at a minimum, or top of atmosphere reflectance in order to account for the variation in the relative positions between the sun, the Earth and the satellite to obtain absolute values for the NDVI ratios can be applied in any other scene (Updike and Comp 2010). Converting the Digital Numbers (DN) to Top

of Atmosphere (ToA) reflectance is a two-step process. First DNs are converted to ToA radiance values. Then these radiance values are then converted to reflectance values (Observation 2010).

4.1 Conversion to Top-of-Atmosphere Spectral Radiance

According to (Globe 2009), WorldView-2 products are delivered to the customer as radiometrically corrected image pixels. The values of these pixels are calculated as a function of the amount of the spectral radiance enters the telescope aperture and the instrument conversion of that radiation into a digital signal. Therefore, image pixel data are unique to WorldView-2 and should not be directly compared to imagery from other sensors in a radiometric/spectral sense. Instead, image pixels should be converted to a top-of-atmosphere spectral radiance at a minimum. Top-of-atmosphere spectral radiance is defined as the spectral radiance entering the telescope aperture at the WorldView-2 altitude of 770 kms. The conversion from radiometrically corrected image pixels to spectral radiance uses the following general equation for each band of a WorldView-2 product (Updike and Comp 2010):

$$L_{\lambda_{pixel,band}} = \frac{K_{band} \cdot q_{pixel,band}}{\Delta\lambda_{band}} \qquad \text{Eq. 6}$$

Where, $L_{\lambda_{pixel,band}}$ are the top-of-atmosphere spectral radiance image pixels [W.m^{-2}.sr^{-1}.μm^{-1}], K_{band} is the absolute radiometric calibration factor [W.m^{-2}.sr^{-1}.count^{-1}] for a given band, $q_{pixel,band}$ are the given radiometrically corrected image pixels [counts] and $\Delta\lambda_{band}$ is the effective bandwidth [μm] for a given band

Both K_{band} and $\Delta\lambda_{band}$ can be found in the image metadata files (*.IDM) attached with the WorldView-2 product under the names (absCalFactor) and (effectiveBandwidth) respectively. The following table summarize both of these quantities for both the panchromatic and the eight multi-spectral bands.

4.2 Conversion to Top-of-Atmosphere Spectral reflectance

Right now we have the ToA spectral radiance. However, this top-of-atmosphere spectral radiance varies with Earth-Sun distance, solar zenith angle, topography, bi-directional reflectance distribution function (BRDF-the target reflectance varies depending on the illumination and observation

geometry), and atmospheric effects (absorption and scattering) (Updike and Comp 2010). As mentioned earlier that converting multispectral data into reflectance before performing spectral analysis techniques such as band ratios, Normalized Difference Vegetation Index (NDVI), matrix transformations, etc., is a must. For each scene the distance between the sun and earth in astronomical units, the day of the year (Julian date), and solar zenith angle must be known.

Table 1 Absolute Radiometric Calibration and Effective Bandwidth for the Given Bands

Band name	K_{band} W.m^{-2}.sr^{-1}.count^{-1}	$\Delta\lambda_{band}$ μm
C	9.30E-03	4.73E-02
B	1.78E-02	5.43E-02
G	1.36E-02	6.30E-02
Y	6.81E-03	3.74E-02
R	1.10E-02	5.74E-02
R-E	6.06E-03	3.93E-02
NIR1	1.22E-02	9.89E-02
NIR2	9.04E-03	9.96E-02

$$JD = int[356.25 \cdot (year + 4716)] + int[30.6001 \cdot (month + 1)] + day + \frac{UT}{24} + (2 - int(\frac{year}{1000}))$$
$$+ int\left(\frac{int(\frac{year}{1000})}{4}\right) - 1524.5 \qquad \text{Eq. 7}$$

$$D = JD - 2451545.0 \qquad \text{Eq. 8}$$

$$g = 357.529 + 0.98560028 * D \qquad \text{Eq. 9}$$

$$d_{ES} = 1.00014 - 0.01671 \cdot cos(g) - 0.00014 \cdot cos(2g) \qquad \text{Eq. 10}$$

The Earth-Sun distance will be in Astronomical Units (AU) and should have a value between 0.983 and 1.017. For the WorldView-2 launch date, October 8, 2009 at 18:51:00 GMT corresponds to the Julian Day 2455113.285; the Earth-Sun distance is 0.998987 AU. At least six decimal places should be carried in the Earth-Sun distance for use in radiometric balancing or top-of atmosphere reflectance calculations (Updike and Comp 2010). The average solar Zenith angle has to be calculated for the whole scene at the time of acquisition according to the following equation:

$$\theta_s = 90.0 - sunEL \qquad \text{Eq. 11}$$

Where, sunEl value can be found in the same file *.IDM. Now we can convert the radiance values to ToA reflectance values using the following equation.

$$\rho_{\lambda_{pixel,band}} = \frac{L_{\lambda_{pixel,band}} \cdot d_{ES}^2 \cdot \pi}{E_{sun\lambda_{band}} \cdot cos\,(\theta_s)}$$ Eq. 12

Where

$\rho_{\lambda_{pixel,band}}$ are the ToA reflectance values

$L_{\lambda_{pixel,band}}$ are the ToA radiance values

d_{ES} is the Earth-Sun distance in Astronomical Units (AU)

$E_{sun\lambda_{band}}$ WorldView-2 Band-Averaged Solar Spectral Irradiance (Updike and Comp 2010)

θ_s The average solar Zenith angle

The traditional NDVI ratio will be used to generate a mask to separate the water body of the study area, as in Figure 4. C/RE, C/Y, B/Y, C/G, B/G and G/Y ratios will be used to derive relative bathymetry of the study area using the non-linear bathymetric inversion model derived by Stumpf.
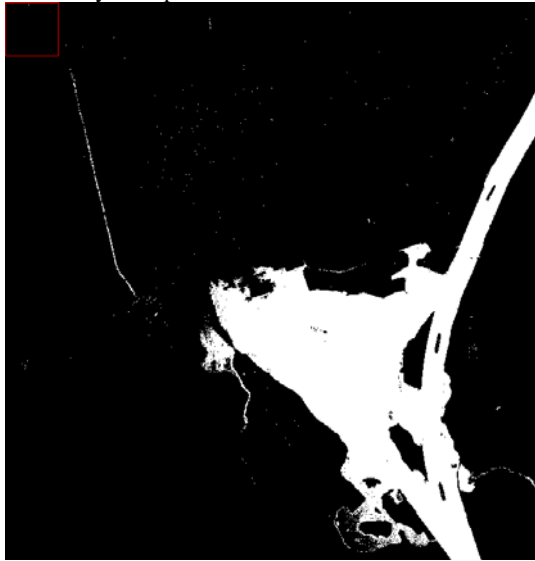
Figure 4 Masked area of study

Ideally, atmospheric effects must be removed together with the water column correction in order to achieve radiometric values that are only representative of the sea depth and to make the upwelling response from different bottom types homogeneous (Deidda and Sanna 2012). Moreover, if sun-glint is present, the effect of the sun beams reflecting on the sea surface, it has to be corrected. Knowing that, the upwelling radiance of NIR bands have very low values even for shallow waters. Subsequently, dark pixel subtract will be applied to account for sun-glint and atmospheric effects by subtracting the Min. value in the NIR bands

for a deep water area from the reflectance values for all other visible band.

5 RESULTS AND DISCUSSION

The available data about the depth of Suez Canal and the Temsah Lake indicates that the dominant depth of the Suez Canal water way is about 24 meters, and an average of 11 meters for the Temsah Lake. No DEM data was available for this site, so the analysis of this result will be depending on the aforementioned information and considering the environmental condition of this area. As discussed before the logarithmic ratio will increase as the depth increase, if we apply this rule on the given results will leads to un realistic results. For instance, considering C/R-E result, if we start with a depth of 24 meters at the blue range (1.033-1.07) will lead to a nominal depth of 46 m at the brown range (1.0885-1.11) which is not true.

The reason behind this result is the water quality and bottom type condition of the water way of the Suez Canal and the Temsah Lake. The water way of Suez Canal is much better than the one exist in the Temsah Lake as it is always running water has two sources of fresh water coming from both the Red sea and the Mediterranean Sea. Moreover, the bottom type is homogeneous sand with small gravel, which follows the main assumptions for the bathymetry derivation from satellite imagery; shallow water with homogenous bottom and clear water. But in case of the Temsah Lake results, the bottom of the lake suffer from a lot of sediments coming from the water way plus enormous domestic pollution from the ship yards, the agriculture land and domestic waste water. This pollution affects both water quality and bottom type.

Based on visual comparison, C/RE, C/Y and C/G give better results compared the other ratios, as they were able to separate between two homogeneous ranges (the green and the blue) to depicts both 4-5 meters and 24 meters depth ranges respectively for the water way. Moreover, these ratios give a distinct three ranges for the Temsah Lake (red, cyan and brown) all of them have an average depth of 11 meters, but with different bottom types; the more the ratio value the more sediments and impurities.

	0.9969-1.033
	1.033-1.070
	1.070-1.0771
	1.0771-1.0885
	1.0885-1.100

C/RE

	0.988-1.015
	1.015-1.041
	1.041-1.050
	1.050-1.059
	1.059-1.068

C/Y

	0.975-1.001
	1.001-1.028
	1.028-1.037
	1.037-1.045
	1.045-1.054

B/Y

	0.988-1.001
	1.001-1.021
	1.021-1.028
	1.028-1.033
	1.033-1.041

C/G

	0.978-1.003
	1.003-1.014
	1.014-1.016
	1.016-1.020
	1.020-1.029

B/G

	0.982-1.008
	1.008-1.014
	1.014-1.021
	1.021-1.027
	1.027-1.034

G/Y
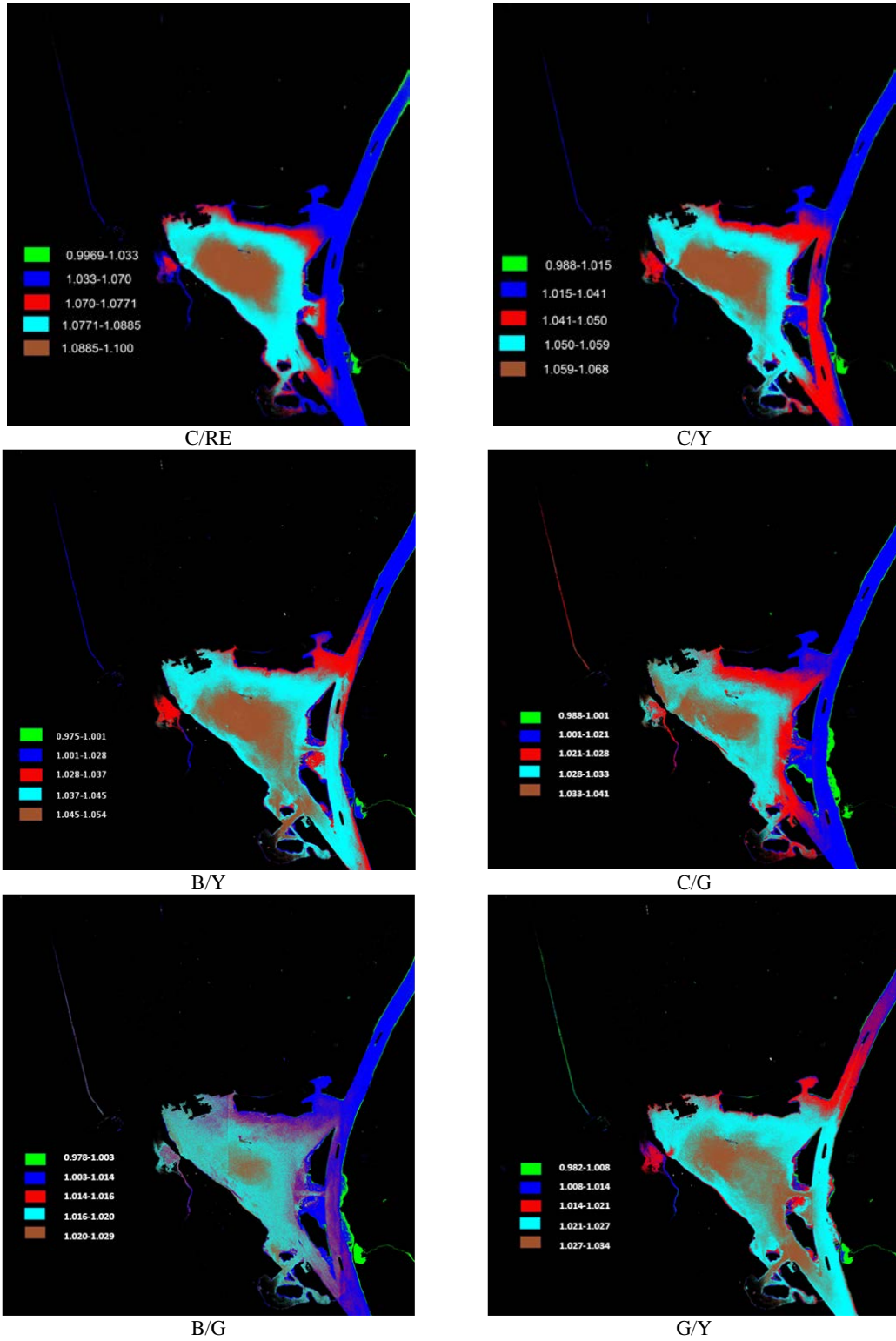
Figure 5 Relative non-linear bathymetric inversion results

6 REFERENCES

Deidda, M. and G. Sanna (2012). "Pre-processing of high resolution satellite images for sea bottom classification." Italian Journal of Remote Sensing-Rivista Italiana Di Telerilevamento **44**(1): 83-95.

Donia, N. (2011). "Water quality management of lake Temsah, Egypt using geographical information system (GIS)." INTERNATIONAL JOURNAL OF ENVIRONMENTAL SCIENCE AND ENGINEERING (IJESE) **2**: 1-8.

Globe, D. (2009) "The Benefits of the 8 Spectral Bands of WorldView-2." White Paper, 12.

Globe, D. (2009). DigitalGlobe Core Imagery Products Guide. D. Globe.

Jensen, J. R. (2007). Remote sensing of the environment: An earth resource perspective. Upper

Saddle River,NJ, Prentice Hall.

Lyzenga, D. R. (1978). "Passive remote sensing techniques for mapping water depth and bottom features." Aplied Optics **Vol. 17**(No. 3): 5.

Lyzenga, D. R. (1981). "Remote sensing of bottom reflectance and water attenuation parameters in shallow water using aircraft and Landsat data." International Journal of Remote Sensing **2**(1): 71-82.

Observation, T. Y. C. f. E. (2010). "Converting Digital Numbers to Top of Atmosphere (ToA) Reflectance." from http://www.yale.edu/ceo.

Stumpf, R. P., K. Holderied and M. Sinclair (2003). "Determination of water depth with high-resolution satellite imagery over variable bottom types." Limnology and Oceanography **48**(1): 547-556.

Su, H. B., H. X. Liu and W. D. Heyman (2008). "Automated Derivation of Bathymetric Information from Multi-Spectral Satellite Imagery Using a Non-Linear Inversion Model." Marine Geodesy **31**(4): 281-298.

Updike, T. and C. Comp (2010). Radiometric Use of WorldView-2 Imagery. D. Globe.

Clouds eliminated from AVHRR/2 images with cloud and snow

Zhu Ji , Chen Guizhu, Shang Guofei

College of Town-Country Planning and Land Resources, Hebei GEO University, Shijiazhuang, 050031, Hebei, China.
zhorse74@163.com

ABSTRACT-*Generally, clouds and snow are mixed in one image together, the clouds are difficult to be identified from the image. Here, clouds were divided into high clouds, medium clouds, low clouds and thin clouds. They were identified and eliminated according to respective thresholds, which were obtained from experiments basing on AVHRR/2 data over Qinghai-Tibet Plateau. In the light of visual inspection, it can be found that the results of cloud elimination were reliable and accurate.*

KEY WORDS-*Cloud elimination, Qinghai-Tibet Plateau, AVHRR/2 data*

1 INTRODUCTION

Qinghai-Tibet Plateau is high and vast, and often covered with clouds all year around. Then, the pollution of clouds can be often seen in AVHRR/2 images of the plateau, and reduce the accuracy of their mapping. Therefore, the pollution of clouds must be eliminated from those AVHRR/2 images before the mapping of the AVHRR/2 images. Generally, if clouds and snow are mixed in one image together, the clouds are difficult to be eliminated from the image. Turner et al. detected clouds from AVHRR/2 images successfully in Antarctica (Turner, 2001). This is a good achievement of cloud elimination from images with cloud and snow together. His method is used here as a reference of cloud elimination. However, with respect to surface features, Qinghai-Tibet plateau is very different from Antarctica, so Turner's method of cloud elimination cannot be used unchangeably on the plateau, and a new method of cloud elimination needs to be found for the AVHRR/2 images over Qinghai-Tibet Plateau. In addition, the focus here is how to practically eliminate clouds from AVHRR/2 images, rather than the mechanism of cloud elimination. Therefore, the mechanism of cloud elimination is not studied deeply in the work.

In 1981, AVHRR/2 sensors were first used on board the satellite of NOAA-7, and can extend moderate resolution data of remote sensing to 30 years ago, and provide the data of high temporal resolution.

2 STUDY AREA AND DATA

2.1 Study Area

The study area is Qinghai–Tibet Plateau in southwest China, with a latitude and longitude of about 26□–40□ and 73□–105□ respectively, and an area and altitude of about 2,500,000 km2 and 4000–5000 m respectively. It has abundant snow cover and glaciers

all year round. The meltwaters of these snow and glaciers are the main runoff sources of the upper reaches of many great rivers. Fig.1 shows the location and terrain of the plateau.

2.2 Data

In this research, the used AVHRR/2 data come from National Satellite Meteorological Center, China Meteorological Administration, and are daily data of time series, which have been geometrically corrected and geo-located. Their boundaries are about 17°00′36″N-41°00′00″N, 65°00′18″E-105°59′42″E.

The AVHRR/2 sensors have totally 5 channels, whose NO.1 and NO.2 channels are visible and near-infrared bands respectively, and NO.3 is middle-infrared band, and NO.4 and NO.5 are all thermal infrared bands. In addition, their spatial resolution is about 1100m.
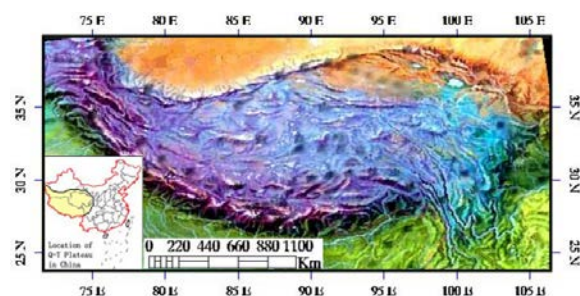
Fig.1. Location and terrain of Qinghai-Tibet Plateau

3 THE CLOUD DETECTIONS OF AVHRR/2 IMAGES

Before removing cloud pollution, the cloud pixels must be identified from AVHRR/2 images. Generally, cloud is easy to be separated from

most of ground objects in remote sensing images, because there are great differences between the spectral features of cloud and other ground objects. But, the spectral features of cloud are very similar to those of snow in visual band, and then the cloud is not easy to be separated from the snow in remote sensing images.

Here, clouds were divided into high clouds, medium clouds and low clouds, difference ways were used to identify them respectively in remote sensing images. The process of cloud identification is as Fig.2.
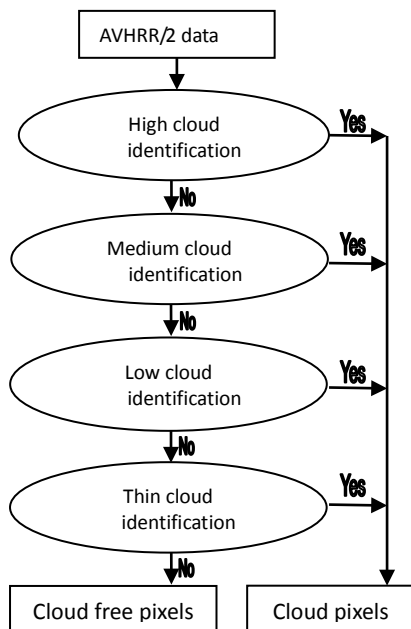
Fig.2. The flow chart of cloud detection

3.1 The Detection of High Clouds Using NO.4 Channel

High clouds are mainly comprised of little ice crystal. The temperature of cloud Hop is obviously lower than that of ground, because the high cloud is in a very high altitude. According to this difference of temperature, the high clouds can be easily separated from other ground objects. The spectra of thermal infrared depend on the temperatures of the ground objects, thus the data of the thermal infrared can be used to identify the high clouds (Oleson, 1985). In the work, the data of NO.4 channel were chosen for detecting the high clouds from the AVHRR/2 images of Qinghai-Tibet Plateau. Using the AVHRR/2 data in 1995, 1998 and

2006 years in experiments, it was found that a pixel would be a cloud pixel if the brightness temperature of NO.4 channel was lower than 250K, that is, T4 < 250K.

3.2 The detection of medium clouds using NO.1, NO.3 and NO.4 channels

Medium clouds are mainly comprised of little ice crystal and supercooled water, and their reflectance is fairly high. The data of the NO.3 channels include reflective energy and emissive energy. Generally, the medium clouds can be identified basing on the difference of brightness temperatures between NO.3 and NO.4. In practice, bare land may be confused with medium clouds in the identification of medium clouds. In order to eliminate the interference of the bare land, the data of NO.1 channel was used to identification of medium clouds. Finally, the identification models of medium clouds are

$$\begin{cases} T3-T4=15K \\ CH1<0.28 \end{cases} \tag{1}$$

where T3 and T4 are the brightness temperature of NO.3 channel and NO.4 channel respectively, CH1 is the reflectance of NO.1 channel.

3.3 The detection of low clouds using NO.3 and NO.4 channels

In images which have snow and clouds together, it is very difficult to eliminate low clouds. Turner et al. has successfully eliminated low clouds using NO.3 channel in the Antarctic continent (Turner, 2001). But, in Qinghai-Tibet Plateau, the results of cloud elimination is not good if only NO.3 channel was used in the identification of low clouds. Here, NO.4 channel is also used in the identification for improving the removing results of low clouds. In light of the experiments using the AVHRR/2 data in 1995, 1998 and 2006 years, the identification models of low clouds can be obtained as follow.

$$\begin{cases} T34=T3-T4<15K \\ T34/T4>0.035 \end{cases} \tag{2}$$

3.4 The detection of thin clouds using NO.4 channel and NO.5 channel

Thin clouds can keep out a part of spectral radiation from the earth's surface into a sensor, however, the other part of the spectral radiation can still reach the sensor. Consequently, ground objects under thin clouds can be seen in remote sensing images, but not clearly. The thin clouds certainly reduce the accuracy of mappings, and should be eliminated before the mappings.

Yamanouchi et al. found that thin clouds can be identified through brightness temperature differences between NO.4 channel and NO.5 channel (Yamanouchi, 1987). In his research, the differences between NO.4 and NO.5 were used to identify the thin clouds. The results of experiments indicate that if the brightness temperature differences of a pixel are more than 2.2K, that is, T4-T5＞2.2K, the pixel is labeled as a cloud pixel.

4 THE ELIMINATION OF CLOUD PIXELS FROM AVHRR/2 IMAGES

After cloud detection is complete for a AVHRR/2 image, each cloud pixel of the AVHRR/2 image is substituted with its corresponding cloud-free pixel in another AVHRR/2 image (namely a referenced AVHRR/2 image) taken temporally closest to the substituted AVHRR/2 image among all referenced AVHRR/2 images in which all pixels corresponding to the substituted pixel are cloud-free. Nevertheless, the temporal difference between a referenced image and substituted image should be limited within a certain time, such as 7 or 10 days.

5 COMPARISON BETWEEN CLOUD ELIMINATED IMAGES AND THEIR SOURCE IMAGES

According to the visual inspection of the cloud eliminated result above, the pollution of clouds can be eliminated from AVHRR/2 images, but snow cover still stayed in them. The following figures can indicate the comparison between clouds eliminated images and their source images (Fig.3, Fig.4, Fig.5, and Fig.6).
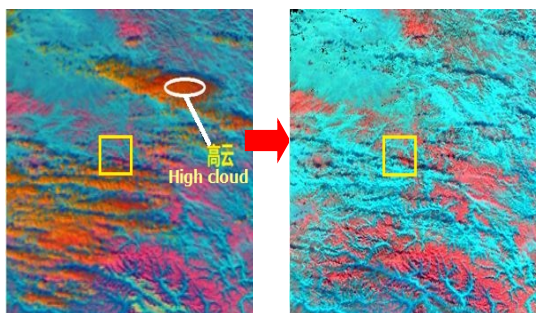
Fig.3 Comparison between high cloud eliminated image and its source image (The left is the source image, where the pixels of high clouds are jacinth, such as the pixels in the white circle. The right is the high cloud eliminated image)
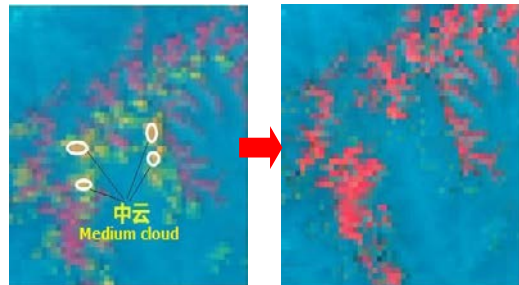
Fig.4 Comparison between medium cloud eliminated image and its source image (The left is the source image, where the pixels of medium clouds are yellow, such as the pixels in the white circles. The right is the high cloud eliminated image)
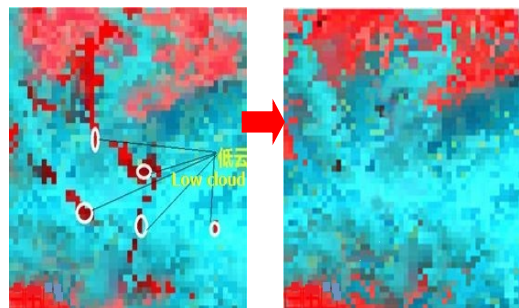
Fig.5 Comparison between low cloud removed image and its source image (The left is the source image, where the pixels of low clouds are deep red, such as the pixels in the white circles. The right is the low cloud removed image)
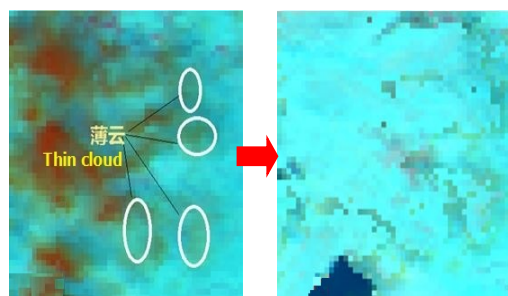
Fig.6 Comparison between thin cloud removed image and its source image (The left is the source image, where the pixels in the white circles are the pixels of thin clouds. The right is the thin cloud removed image)

6 CONCLUSIONS

Qinghai-Tibet Plateau is high and vast, and often covered with clouds all year around. Then, the pollution of clouds often appears in AVHRR/2 images of the plateau, and reduces the accuracy of their mapping. Generally, clouds and snow are mixed in one image together, the clouds are difficult to be identified

from the image. Here, clouds were divided into high clouds, medium clouds, low clouds and thin clouds. They were identified and removed according to appropriate thresholds respectively, which were obtained from experiments basing on AVHRR/2 data over Qinghai-Tibet Plateau. In light of visual inspection, it can be found that the results of cloud elimination were reliable and accurate.

In 1981, AVHRR/2 sensors were first used on board the satellite of NOAA-7. The method of cloud elimination is found for the AVHRR/2 images, then, the images can be used in practice, and moderate resolution data of remote sensing can extend to 30 years ago.

REFERENCES

Turner, J., G. Marshall, J., and Ladkin, R. S., 2001, An operational real-time cloud detection schime for use in the Antarctic based on AVHRR data, International Journal of Remote Sensing, 22(15): 3027-3046.

Oleson, F.S., and Grassl, H., 1985, Cloud detection and classification over oceans at night with NOAA-7, International journal of Remote Sensing, 6: 1435-1444.

Yamanouchi, T., Suzuki, K., and Kawaguchi, S., 1987, Detection of clouds in Antarctica from infrared multispectral data of AVHRR, Journal of the Meteorological Society Of Japan, 65: 949-962.

Towards a complete spectral reflectance uncertainty model for Field Spectroscopy

M. Jiménez, O. Gutiérrez de la Cámara, A. Moncholí, F. Muñoz
Área de Sistemas de Teledetección - Instituto Nacional de Técnica Aeroespacial (INTA).
Cta. de Ajalvir s/n Torrejón de Ardoz 28850, Spain
jimenezmm@inta.es; gutierrezcao@inta.es; moncholiea@inta.es; fmunoz@isdefe.es

ABSTRACT- *To improve the reliability of spectral libraries acquired by field spectroscopy, the uncertainty of the spectral reflectance measured must be estimated and reported, taken into account as many important sources of uncertainty as possible. This work presents the initial approach to establish a complete model of uncertainty of field spectroscopy measurements that ensures the traceability chain. The first two steps towards this objective are presented: on one hand, the framework and the sources of uncertainty to create the model are reviewed, on the other hand, with the intention to be aware of the uncertainty values that can result due to environmental conditions, some empirical data using two field spectroradiometers were undertaken. Type A standard statistical methods were applied for spectral reflectance measurements acquired with a dual system of two ASD FieldSpec3 spectroradiometers over two uniform and invariant surfaces. The reproducibility in environmental ambient were evaluated measuring under variable of solar and atmospheric conditions. For VNIR region, where spectroradiometer performs better, an average of 5% of uncertainty were gathered. For SWIR region both sources, environmental and instrumental rise to 12% of uncertainty.*

1 INTRODUCTION

In optical Earth Observation satellites, ground truth data acquired by field spectroscopy plays a major role in sensor calibration, product validation, and image analysis. In all these activities, the uncertainty and traceability requirements demanded for field spectroscopy have increased substantially.

Uncertainty estimation is fundamental for data quality evaluation and data interoperability. In this sense, the Guide to the Expression of Uncertainty in Measurement (GUM), developed by the *Joint Committee for Guides in Metrology* (JCGM) and the *Bureau International des Poids et Mesures* (BIPM), provides guidance on how to determine, combine and express uncertainty. The GUM became a standard guide in 2009, and confirmed in 2015, by *International Organization of Standardization* (ISO) and the *International Electrotechnical Commission* (IEC). For Earth Observation community, the main principles of the GUM were implemented by the *Quality Assurance Framework for Earth Observation* (QA4EO) project. One of the last initiatives that are making progress in this implementation is the project *Metrology for Earth Observation and Climate* (MetEOC), funded by the *European Metrology Research Programme*. MetEOC is developing new infrastructure and methods to allow higher, traceable, accuracy to be delivered to the European calibration and validation community.

Field spectroscopy has undergone to a remarkable growth over the past two decades in terms of use and application for different scientific disciplines. To improve the reliability of the spectral libraries acquired, the uncertainty of the spectral reflectance must be estimated and reported, taken into account as many important sources of uncertainty as possible.

This work presents the initial approach to establish a complete model of uncertainty for field spectroscopy measurements that ensures the traceability chain. In this paper, the first two steps towards this objective are presented. On one hand, the framework and the sources of uncertainty to create the model are reviewed. On the other hand, with the intention to be aware of the uncertainty values that can result due to environmental conditions, some empirical data using two field spectroradiometers were undertaken.

2 FIELD SPECTROSCOPY BACKGROUND

Field spectroscopy is the measurement of high resolution spectral radiance or irradiance in the field to derive the reflectance or emissivity spectral signatures of Earth's surface targets under natural environmental conditions (Milton et al., 2009). In comparison with imaging spectroscopy, the sensing instrument in the field can remain fixed over the subject of interest for much longer, and the path length between the instrument and the object being measured is reduced

The main applications of field spectroscopy are: to relate spectral curves with bio-physical and bio-chemical process; to predict the most favorable

spectral, radiometric, and viewing geometry configuration and the optimum time to carry out a particular remote sensing task; to calibrate, validate and simulate remote sensing data and products.

The rugged and portable spectroradiometers developed in recent years, measures spectral radiance using a fiber-optic bundle, with the possibility to attach different optics. Manufacturers basically offer two kinds of spectroradiometers: (1) small, light devices to work only in the visible and rear infrared VNIR (350–1000 nm), with levels of the signal to noise ratio (SNR) around 250:1; and (2) bigger and heavier devices that work in the entire solar spectrum, with actively cooled short wave infrared (SWIR) detectors (1000–2500 nm) and SNR around 1000:1. The typical spectral configuration is to have a full width half maximum (FWHM) of nearly 3 nm in the VNIR spectral region, and a FWHM of nearly 10 nm in the SWIR.

Single beam, where the same instrument is used to measure both the target and the reference panel spectral radiance, is the most widely used acquisition methodology. Even in a cloudless sky and low solar zenith angles, the most simultaneous radiance acquisition between the panel and target is recommended. In Dual beam, one spectroradiometer measures the radiance of the target and the second one measures the Sun irradiance using a cosine receptor, reference panel or an integrating sphere.

3 TOWARDS THE UNCERTAINTY MODEL

An uncertainty measurement model is a mathematical expression were all the input quantities that are required to obtain a measurand are associated in an algorithm. Following the GUM, each quantity has a standard uncertainty associated, which can be combined using the Law of Propagation of Uncertainty to obtain the final uncertainty.

These uncertainties are grouped into two categories, depending on the method used to estimate its value: Type A, which are the uncertainties evaluated by statistical processes; and Type B, the uncertainties evaluated by non-statistical processes.

The National Physical Laboratory (NPL) considers eight fundamental steps to establish an uncertainty model (Woodliams at al., 2014):

 a) Understanding the problem
   a1: Describing the traceability chain
   a2: Writing down the calculation equations
   a3: Considering the sources of uncertainty
 b) Determining the formal relationships
   b4: Creating the measurement equation
   b5: Determining the sensitivity coefficients
   b6: Assigning uncertainties
 c) Propagating the uncertainties

   c7: Combining and propagating uncertainties
   c8: Expanding uncertainties

Follow these eight steps, ensures the development of the complete uncertainty model for a measurand. Furthermore, determining a simplified version of the uncertainty model and then adding complexity in stages later on, as the problem becomes better understood is recommended.

In the particular case of field spectroscopy, the spectral reflectance obtained by field spectroradiometers is the measurand. The first approximation in the simplified model generation, is to review the main sources of uncertainty for spectral reflectance.

3.1 Sources of Uncertainty

The main sources of uncertainty for spectral reflectance measured by field spectroscopy can be grouped into five categories: the equipment performance, the methodology of measurement, the sampling strategy, the properties of the surface, and the environmental conditions.

Regarding the equipment performance, radiometric and spectral calibration is usually accomplished by the manufacturer. Thus, Type B uncertainty estimations is supplied. Furthermore, the radiometric and spectral calibration characteristics of field spectroradiometer can be periodically evaluated in the laboratory by Type A repeatability procedures (Anderson et al., 2011). In addition, Type A reproducibility procedures for environmental effects and configuration possibilities have also be evaluated. Likewise, in case of the use of reference panel, integrating sphere or cosine receptor to derive irradiance in the field, the radiometric calibration is on the manufacturer's side, but radiometric and angular characteristics must be evaluated by Type A repeatability procedures. Regarding the methodology, the time between target and panel measurements is a critical parameter for spectral reflectance accuracy using single spectrometer, especially in no clear-skies conditions. In the case of dual system, the intercalibration between the two spectroradiometeres is the critical parameter. In addition, the illumination and observation geometries have to be taken into account. Concerning sampling strategy, the size of the target, the number of samples and the sampling type, can vary considerably the spectral reflectance estimation. Concerning surface properties, the lambertian degree and uniformity of the surface, are the most important sources of uncertainty. Regarding environmental conditions, the most important sources are: sun position, sky cloud coverage, atmospheric water vapor and aerosols presence, and the adjacency effects because of surrounding elements.

Further steps to be taken in subsequent work, will determine the formal relationships between the elements and the sensitivity coefficients for each source. Then, uncertainty assigned will be combined and propagated. However, prior to these steps and with the aim to quantify the impact of environmental factor to the total uncertainty, a test was conducted trying to leave fixed the rest of the sources.

4 THE TEST: SOME EMPIRICAL DATA

As an initial approach to become aware of the uncertainty range that we can find in field spectroscopy measurements, a test was carried out with two field spectroradiometers measuring two invariant surfaces in several days with different illumination and atmospheric conditions.

The field spectroradiometers are two ASD FieldSpec3 (PAnalytical, CO, USA) that measures incoming radiance using a fiber optic which is adaptable with a fore optic lens. It has a spectral range from 350 to 2500 nm, with a 3 nm spectral resolution and a sampling interval of 1.4 nm in the VNIR spectral regions and 10 nm and 2 nm in the SWIR.

Figure 1 shows the test setup installed on the rooftop of one of the buildings at National Institute of Aerospace Technology (INTA, Madrid) facility. Over a table, two very uniform and invariant surfaces: one dark (5% reflectance) and one bright (50% reflectance) were placed. Two white reference panels were also placed. The two spectroradiometers were mounted in a trolley close to the table. The spectroradiometers´ laptops were situated in the upper part of the trolley, and the spectroradiometers itself in the lower part covered for direct sunlight. All the components that are placed over the table (tripods, fibre optic, and a camera for hemispherical sky pictures) that can produce adjacency effect in the radiance signal are covered or painted in black.
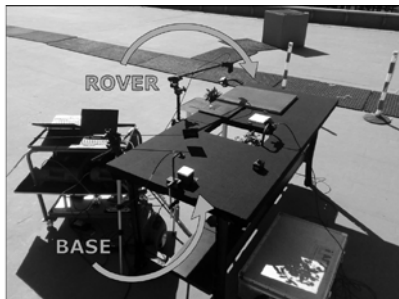
Figure 1. Picture of the test elements and setup on the rooftop of the building at National Institute of Aerospace Technology (INTA, Madrid)

4.1 Data acquisition and processing

With the premise to have single and dual spectral reflectance measurements at the same moment, the measurement protocol was designed following the procedure proposed by Bachmann (Bachmann et al., 2012). One spectroradiometer (The Rover) measures both surfaces and one reference panel before and after each surface, turning the tripod´s arm. The other one (The Base), is fixed looking a second reference panel measuring thrice for each surface acquisition: the first measurement was simultaneously to the first Rover measurement over the panel, for the intercalibration of the spectroradiometers; the second measurement is acquired simultaneously to the Rover target measurement for surface reflectance estimation; and the last one, is simultaneously to the other Rover panel measurement, but with the panel covered to remove direct irradiance component, measuring diffuse irradiance. All the spectroradiometers measurements are made in radiance mode, saving five files repetitions for each sample over target or panel.

Seven days of acquisitions were carried out. For each day, both surfaces were measured from 10:00 to 13:00 (local time) every 15 minutes, stepped up the measurements in occasions subject to cloud presence. Both spectroradiometer were connected to electrical power supply, and they were turned on one hour before the beginning of data acquisition. Measurements were acquired directly with the fiber optic (FOV 25º). In order to avoid any shadow appearance over the target or panel, the Rover fiber is nadir-oriented and held 20 cm above the target and the panel, which has 12x12 cm size. The Base is 10º tiled from nadir and held 5 cm above the panel, which in this case is only 6x6 cm size to be able to cover the whole panel for direct sunlight.

For both surfaces, the hemispherical conical reflectance factor (HCRF) was calculated in single and dual mode using Python in-house programme. In case of single mode, HCRF was calculated with the panel interpolated radiance between the before and after acquisitions. In dual mode, the data of Rover and Base panels was used directly, because had simultaneous triggering.

The solar radiation diffuse-to-global ratio (DGR) was calculated for each surface acquisition with the ratio between the simultaneous measurement of Base panel covered from direct sunlight and the Rover panel measurement.

Although the uncertainty calculations have to follow the Law of Propagation procedures recommended by the GUM, for this test quantification the uncertainty calculations was carried out following the procedure proposed by Pinto (Pinto et al., 2012), that takes into account statistical fluctuation of the data following, as well, GUM recommendations. A total uncertainty is

the summation of a repeatability uncertainty and a called "various uncertainty".

The repeatability uncertainty is the experimental standard deviation of the global uncertainty. The global uncertainty can calculate an overall standard deviation, which takes into account the dispersion of the data of all sampling points, according to the following equation (1):

$$\sigma_{global} = \sqrt{\frac{1}{k \times (n-1)} \times \left[\sum_1^n (x_n - \overline{x_1})^2 + \sum_1^n (x_n - \overline{x_2})^2 + \cdots + \sum_1^n (x_n - \overline{x_k})^2 \right]} \quad (1)$$

where: k is the number of sampling points; n is the number of repetitions on each point; xn is the value obtained from the repetition n; and xk is the mean value for point k.

The "various uncertainty" is calculated using all the panel measurements using this equation (2)

$$\sigma_{various} = \sqrt{\left(\frac{1}{k-1}\right) \times \sum_1^k (x_k - \bar{x})^2} \quad (2)$$

where: k is the number of points; xk is the mean of the reference plate at point k; and $\bar{x}$ is the mean plate for k points

4.2 Results

From the seven measurement days, we have two completely clear-sky, one day with no clouds but with saharian dust intrusion, and the rest with varying conditions of clouds presence. During those seven days, a total of 74 measurements for each surface were recorded. Removing a few acquisitions made it with thick clouds standing on the way, 60 of the total were acquired with direct sunlight or cirrus clouds, and their get into the uncertainty calculations.

The total uncertainty for bright and dark surfaces in single and dual mode are presented in Figure 2. Noticing that in single mode the acquisitions of panel and target was nearly simultaneously, minor differences are found between the two modes, as expected. For both surfaces, the uncertainty is about 5 % in the visible part of spectrum, where the bigger impact of solar radiation and atmospheric constituents take place. In case of dark surface the uncertainty reach 10 % in the NIR part mainly due to adjacency effects. The rise to 10 % and above in the SWIR part of the spectrum, is mainly due to lower signal to noise ratio of the spectroradiometer.
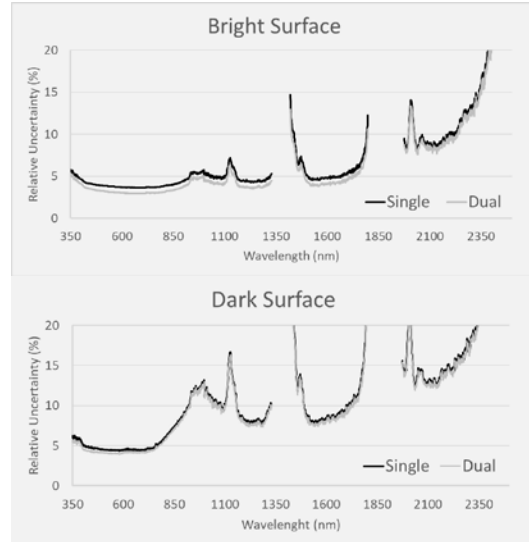
Figure 2. Total uncertainty for bright and dark surfaces in single and dual mode.

Looking in detail to the reference panel measurements for both spectroradiometers, the impact on the uncertainty resulting from the solar zenith angle variation and different levels of diffuse to global ratio were evaluated.

Figure 3 shows the standard deviation values obtained for the Rover and Base measurements over the reference panel corresponding to the two days with clear-sky conditions. Measuring in both days from 10:00 to 13:00 (local time), the solar zenith angle varies from 0.4 to 1 radians. It can be seen, that into this medium solar zenith angle variation range, avoiding very low or very angles, only a soft correlation is achieved.
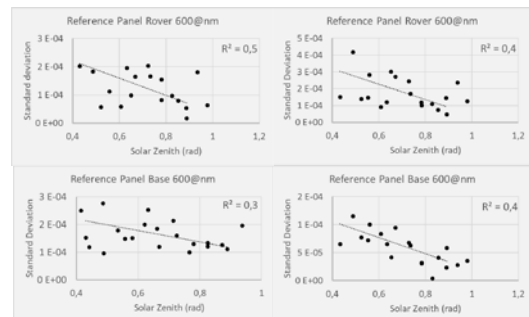
Figure 3. Standard deviation values obtained for the Rover and Base spectroradiometers measurements over the reference panel plotted against solar zenith angle (in radians). Corresponding to the two days with clear-sky conditions

Figure 4 shows the standard deviation values obtained for the Rover and Base measurements over the reference panel corresponding to all the measurements selected for the calculations: Those measurements includes a wide range of illuminations conditions, indicated by variation of the diffuse to global ratio from 0.05 to 0.25 at 600nm wavelenght. In this case, no correlation was found between standard deviation and diffuse to global ratio.
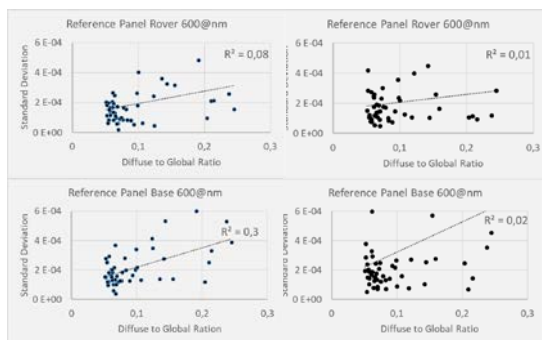
Figure 4. Standard deviation values obtained for the Rover and Base spectroradiometers measurements over the reference panel plotted against diffuse to global radiation, corresponding to all the measurements selected for the calculations.

5 CONCLUSIONS

The uncertainty values for spectral reflectance measurement by field spectroscopy due to variations in illumination and atmospheric conditions were estimated by Type A procedures. For VNIR region, where spectroradiometer performs better, an average of 5% of uncertainty were gathered. For SWIR region both sources, environmental and instrumental, reach to 12%.

Only a small correlation were found between standard deviation of reference panel radiance measurement and solar zenith angle. No correlation was found between standard deviation of reference panel radiance measurement and diffuse to global ratios.

6 REFERENCES

K. Anderson, J. L. Dungan, and A. MacArthur, "On the reproducibility of field-measured reflectance factors in the context of vegetation studies," *Remote Sens. Environ.*, vol. 115, pp. 1893–1905, 2011.

C. M. Bachmann, M. J. Montes, C. E. Parrish, R. A. Fusina, C. R. Nichols, R.-R. Li, E. Hallenborg, C. A. Jones, K. Lee, J. Sellars, S. A. White, and J. C. Fry, "A dual-spectrometer approach to reflectance measurements under sub-optimal sky conditions," Opt. Express 20, 8959–8973 (2012).

Joint Committee for Guides in Metrology Working Group 1 (JCGM/WG 1). (2008). *Guide to the Expression of Uncertainty in Measurement*

E. J. Milton, M. E. Schaepman, K. Anderson, M. Kneubuhler, and N.Fox, "Progress in field spectroscopy," *Remote Sens. Environ.*, vol. 113, Suppl. 1, pp. S92–S109, 2009.

C. T. Pinto, F. J. Ponzoni, R. M. de Castro, and D. J. Griffith. Spectral uniformity evaluation of reference surfaces for airborne and orbital sensors absolute calibration. Revista Brasileira de Geofisica (2012) 30(3): 263-275.

E. Woolliams, A. Hueni, J. Gorrono. (2014) Intermediate Uncertainty Analysis for Earth Observation (Instrument Calibration). NPL Training Course Textbook. Available online: http://www.emceoc.org/ documents/uaeo-int-trg-course.pdf

Interest of VNIR directional measurements for parameterizing the TIR directional anisotropy

Zunjian Bian[1], Jean-Louis Roujean[2], Mark Irvine[1], Jean-Pierre Lagouarde[1],

[1.] *INRA, UMR 1391 ISPA, F-33140 Villenave d'Ornon, France*
[2.] *Météo France CNRM-UMR3589, F-31057 Toulouse, France*
Corresponding author: jean-pierre.lagouarde@inra.fr

ABSTRACT- *VNIR (visible and near infrared) reflectances as well as Land Surface Temperature (LST) measurements in the TIR (thermal infrared) domain are both prone to directional anisotropy (DA) effects. Simple models are needed to correct remotely-sensed data from these effects. Two candidate parametric models first proposed by Roujean (2000), referred to as R_{2000}, in the VNIR and by Lagouarde and Irvine (2008) in the TIR, referred to as RL, are first presented. Both required two parameters to be fitted, in particular a k coefficient related to canopy structure. Their generalization is made, using a large data base generated with the deterministic multilayer model SCOPE developed by Van der Tol et al. (2009) which allows to simulate DA in a large range of wavelengths. The canopy is assumed to be 'spherical' and the input data -meteorological forcing, water availability, LAI, hot spot parameter- are chosen for representing a large range of conditions that can practically be met. We show that DA in the red is most related to TIR DA, and we finally propose a simple parameterization of the k coefficient against LAI. This is a significant progress, as it now makes R_{2000} and RL models tools requiring only one parameter to be fitted for practical applications.*

1 INTRODUCTION

VNIR (visible and near infrared) as well as TIR (thermal infrared) radiation measurements are both prone to directional anisotropy (DA) effects. In the VNIR spectral domain, such effects for vegetation canopies are originating from multi-scale variability of spectral properties andand . Generally, a canopy owns a complex structure that causes a radiation beam to follow different trajectories according to the illumination properties. As a result, the relative proportion of sunflecks and shadows in the field of view of a remote sensing instrument are at the root of sizeable directional effects. For the same physical, reasons, a TIR signal will be also impacted. However, in the TIR domain, energy transfers combine with radiative processes to determine the surface temperature of the leaves, which makes DA also dependent of meteorological forcing and water status of the plants (Duffour et al., 2016a). Hitherto, the appraisal of this was already widely explored both based on experimental efforts and modeling approaches (see reviews in Paw U, 1992; Lagouarde et al., 2000; Verhoef et al., 2007; Menenti et al., 2008). Particularly, the SCOPE model (e.g. Van der Tol, 2009) is a coupled radiative-energy transfer multi-layer model aiming at studying the determinism of DA (Duffour et al., 2015). The model represents a test-bed for examining the response of DA to varying physical properties, though limited to the treatment of homogeneous canopies. Nevertheless, simpler approaches seems mandatory in the lack of detailed information on the target with objective to processing massive remotely sensed data sets contaminated by DA. Nowadays, the context is the forthcoming space mission THRISNA devoted to collect TIR measurements at high spatio-temporal as a cooperation between France and India throughout their respective spatial agencies, CNES and ISRO. This paper presents the scientific work achieved so far as a candidate to fullfill the mission demand. Two simple parametric models mimicking DA are presented with possible applications in both VNIR and TIR spectral domains.

2 THE TWO CANDIDATE MODELS

2.1 The VNIR Roujean 2000 model

This model (referred hereafter as R_{2000} below) is based on a physically-based development to treat VNIR data (e.g. Roujean, 2000):

$$\rho(\theta_v, \theta_s, \varphi) = \rho_{HS} e^{kf} \qquad (1)$$

with

$$f = \sqrt{tan^2\theta_s + tan^2\theta_v - 2tan\theta_s tan\theta_v cos\varphi} \qquad (2)$$

θ_s and θ_v solar and viewing angles, φ relative viewing - solar azimuth. Roujean (2000) suggested to take k = LAI/4, which corresponds to spherical canopies.

2.2 The TIR RL model

The RL (RL stands for 'Roujean Lagouarde') model has been adapted in the TIR from R_{2000} (Lagouarde and Irvine, 2008; Duffour et al., 2016b):

$$\Delta T(\theta_v, \theta_s, \varphi) = \Delta T_{HS} \frac{exp(-kf) - exp(-kf_N)}{1 - exp(-kf_N)} \quad (3)$$

The TIR anisotropy ΔT is defined as the difference between of-nadir and nadir viewing surface temperature. ΔT_{HS} is the value when viewing hot spot. By replacing ΔT by the reflectance ρ, this model can be extended to the VNIR domain (both are referred to as RL_{TIR} and RL_{VNIR} below):

$$\rho(\theta_v, \theta_s, \varphi) = \rho_{HS} \frac{exp(-kf) - exp(-kf_N)}{1 - exp(-kf_N)} \quad (4)$$

3 METHODOLOGY

Directional anisotropy is simulated with SCOPE model (see Duffour et al., 2016 for details) for a selection of SENTINEL 2 bands (490, 560, 665, 705, 783, 865 and 1610 nm) and in the TIR. Following Duffour et al. (2015, 2016a), SCOPE input data have been prescribed to describe a wide range of conditions that can practically be met. A spherical canopy structure is assumed, which corresponds to a random distribution of leaf inclination and orientation. LAI values are taken within the range [0.5, 1.0, 1.5, 2.0, 3.0 5.0]. The hot spot parameter q defined as the ratio between leaf size and canopy height takes the values [0.01, 0.05, 0.1, 0.50], while the vegetation height is taken to 1 meter. For meteorological forcing, we consider scenarios for 4 dates above 2 ICOS stations that are Auradé (43.56°N, 1.05 °E, DOYs 79 and 174) and Avignon (43.91°N, 4.88 °E, DOYs 118 and 147). Simulations are performed at 13:00 LST, which is today the time of orbit pass envisaged for the future satellite mission TRISHNA. Finally, cases of dry/wet soil/vegetation have been crossed using 2 values of maximum of carboxylation Vcmo, 25 and 125 $\mu mol \cdot m^{-2} \cdot s^{-1}$ (for dry and wet vegetation), and 2 values of soil resistance to vapor transfer r_{ss}, 200, 2000 $s \cdot m^{-1}$ (for wet and dry, respectively). Gathering all these input data allows to built 384 SCOPE simulations per wavelength.

R_{2000} and RL models are then fitted on each SCOPE simulated data within the principal plane ±3° in azimuth. Privileging the principal plane - instead of using all azimuthal directions - for the fit is justified by the fact that the magnitude is the largest and the hot spot effect is the best sampled. The fit is operated in two manners:
- '1-parameter fit': ρ_{HS} and ΔT_{HS} fitted with k prescribed, k = LAI/4
- '2-parameters fit': ρ_{HS} and ΔT_{HS} fitted, simultaneously with k

The overall polar plots of DA in the whole directional space can then be reconstructed using the parameters retrieved in the principal plane. A illustration is provided at the end of the proceedings (see color plate) for R_{2000} and RL models against SCOPE for one case study (LAI = 1.5, q = 0.1, Vcmo= 25 $\mu mol \cdot m^{-2} \cdot s^{-1}$, rss= 200 $s \cdot m^{-1}$, Auradé for DOY 174). The polar plots first reveal the magnitude of anisotropy effects in the whole directional space. The discrepancies between the models are a narrower and more intense hot spot peak with SCOPE.

The innovative work here is finding new value of k determined as the best parameterization with LAI.

4 GENERALIZATION OF THE R_{2000} MODEL IN THE VNIR

Figure 1 displays the comparisons on all viewing directions (0 ≤ φv < 360, 0 ≤ θv ≤ 60) between SCOPE-simulated and R_{2000} reflectances fitted keeping 1- (Fig. 1 c,d) and 2- (Fig. 1 a,b) parameters free, for the 865 nm red (Fig. 1a,c) and 865 nm near infrared (Fig. 1 b,d) wavelengths. Fig. 1 shows that using k = LAI/4 as initially proposed by Roujean (2000) fails for NIR, and that the red band provides the highest correlation. This is confirmed by the analysis of similar fits made for the other SENTINEL channels (not presented here).

The relationships between k and LAI were then investigated for each wavelength. Only relationships for red and NIR are presented in Figure 2. For each LAI, the k values obtained for the 4 dates and the 4 q values are mixed (16 points). Most of the dispersion of the points is explained by the variability of hot spot parameter q, with only little impact of the date. (i.e. k(LAI) curves very close to each other for a given q value). As q remains difficult to estimate and as no robust way for estimating q from remotely-sensed data has been proposed up to now, we looked for a unique k(LAI) function for each wavelength A double-exponential function was tested to explain the relationship between k and LAI (Fig. 2). The following revealed the more suited:

$$k = \beta(1 - e^{\alpha \cdot LAI}) \quad (5)$$

Now combining Eq. (1) and (4) makes R_{2000} a 1-parameter model (ρ_s), provided LAI is known. Its performance was evaluated by fitting it on the same dataset (Fig. 3). The loss of performance of the new R_{2000} parameterization compared to the direct '2-parameters fit' is marginal. Performance is optimum in the Red and SWIR at 1.61 µm. We also notice that the k = LAI/4 parametirzation fails, particularly for 560, 783 and 865nm wavelengths.
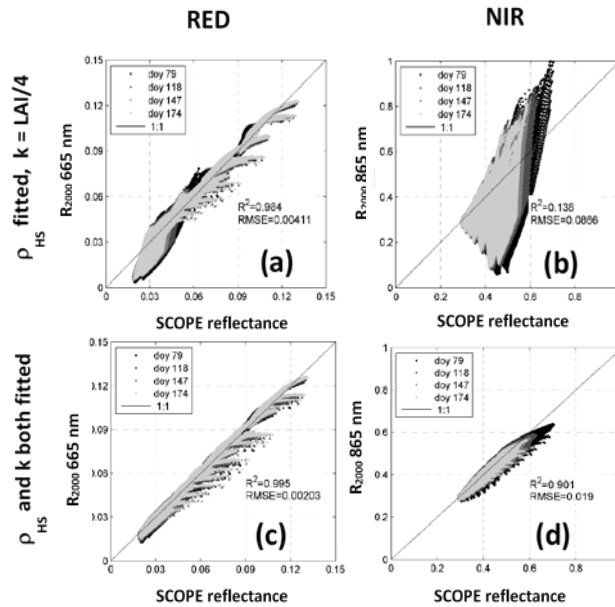
Figure 1. Comparison of R$_{2000}$ fits against SCOPE simulated data for two fitting strategies in red (665 nm) and NIR (885 nm) wavelengths.
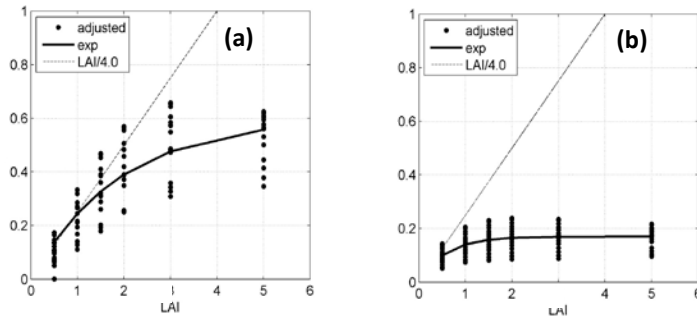
Figure 2. Parameterization of the relationship between k and LAI for Red 665 nm (a) and NIR 865 nm (b).
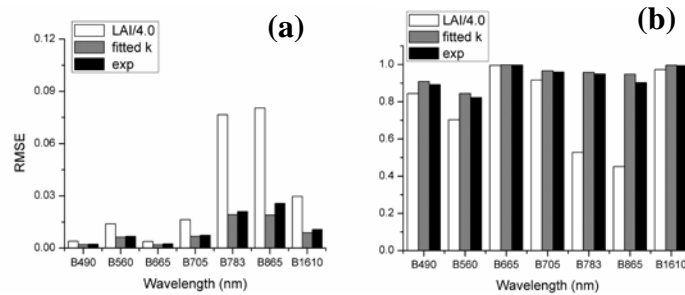
Figure 3. Performance of the R$_{2000}$ model with $k = LAI/4.0$ (white) and $k = \beta(\lambda)\ (1 - e^{\alpha(\lambda).LAI})$ (black) compared to SCOPE fitted with k free (grey) for SENTINEL 2 bands (490nm, 560nm, 665nm, 705nm,783nm, 865nm, and 1610nm)

5 GENERALIZATION OF THE RL MODEL IN VNIR AND TIR

Canopy structure is a primary driver of directional anisotropy for both TIR and VNIR, and it largely governs the k coefficient values. It is therefore interesting to evaluate if the k retrieved in the VNIR bands could be also suitable in the TIR. For this purpose we fitted the RL_{TIR} model in 3 ways:

- ΔT_{HS} and k_{TIR} are let free and fitted together against SCOPE-simulated data
- ΔT_{HS} is let free and k_{TIR} is prescribed to LAI/4
- ΔT_{HS} is let free and k_{TIR} is from the value of k_{VNIR} retrieved from the fit of RL_{VNIR} for each SCOPE simulation. As they correspond to vegetation channels most currently available on Earth Observation satellites, only 2 wavelengths have been considered in this exercise: red and NIR at 665 and 865 nm respectively.

The results are shown in Fig. 4. A similar good agreement is found when ΔT_{HS} and k_{TIR} are let free (Fig. 4a) and when ΔT_{HS} is let free and k_{TIR} is given the value of k_{VNIR} retrieved in the red (Fig. 4c). The quality of the relationship decreases when k_{TIR} is prescribed to LAI/4 (Fig. 4b) or at 865 nm. The k_{VNIR} values retrieved from the R_{2000} model were also tested, but they revealed slightly less performant than RL_{VNIR} (results not presented here).
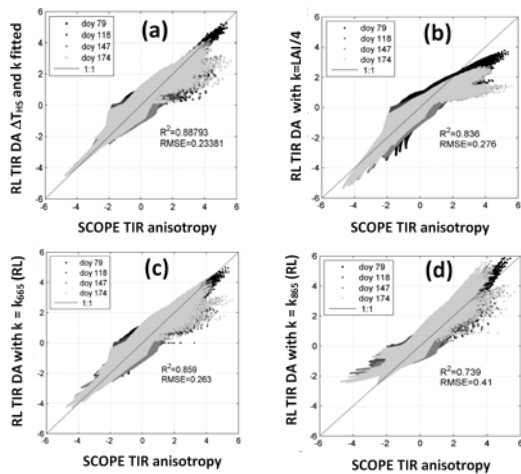
Figure 4. Comparison of fits of RL_{TIR} model against SCOPE-simulated directional anisotropy. In all cases, the parameter ΔT_{HS} is let free. The parameter k is let free (a), or prescribed to LAI/4 (b), to its value retrieved for red (c) or NIR (d) wavelength.

It is interesting to compare the values of k retrieved for each of the 384 fits in the TIR with RL_{TIR} model against those retrieved in the red (665 nm) and NIR (865 nm) with the RL_{VNIR} model. Figure 5 clearly shows that there exists a rather strong correlation in the red contrary to NIR.
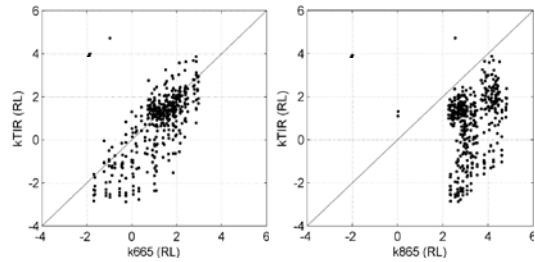
Figure 5. Comparison of k values retrieved with RL model in the TIR (k_{TIR}) against values k_{665} and k_{865} in the red and NIR

This led us to analyze the relationship between k_{665} and LAI (Fig. 6). As previously we note an important scatter behavior mainly related to the variations in the hot spot parameter q. A simple linear relationship $k = \alpha LAI + \beta$ is estimated in the red. We found $\alpha = 0.41$ and $\beta = 0.19$.
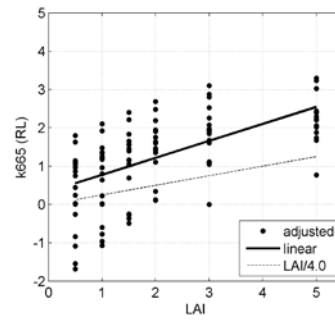
Figure 6. Parameterization of the relationship k(LAI) in RL_{VNIR} model for red 665 nm.
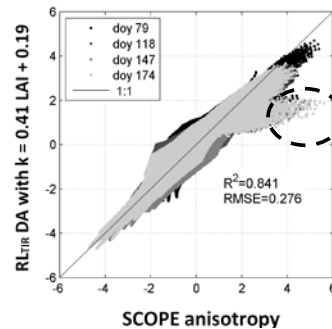
Figure 7. Comparison of the generalized RL_{TIR} model with SCOPE-simulated directional anisotropy.

To check its robustness, the RL_{TIR} model with $k = 0.41$ $LAI + 0.19$ was finally fitted against the 384 SCOPE simulations of the dataset. The results is presented in Fig. 7. The overall agreement is quite good and comparable to the fit obtained when letting both ΔT_{HS} and k_{TIR} free, as confirmed by R^2 (0.841 and 0.888) and RMSE (0.276 and 0.234) statistics. The discrepancy observed for high values of anisotropy (surrounded by a dotted circle in Fig. 7) corresponds to the particular case of hot spots with low q values.

6 CONCLUSION

The two parametric R_{2000} and RL models of directional anisotropy in the VNIR and TIR respectively have been consolidated and generalized against SCOPE simulated data. For both of them, the similarity of anisotropy in the red (at 665 nm) and in the TIR has been exploited in order to propose simple parameterizations of k coefficient against LAI. This is a significant progress, as it now makes R_{2000} and RL models tools requiring only one parameter, either ρ_{HS} or ΔT_{HS}, to be fitted. Because LAI is a product easily accessible from space, this is likely to facilitate practical applications in the future. Nevertheless *a priori* prescribing either ρ_{HS} or ΔT_{HS} still remains difficult as discussed by Duffour et al. (2016b) and methodologies have to be developed for this purpose.

The study has been conducted assuming spherical canopies. A generalization to other structures (planophile, erectophile) remains to be investigated.

Finally a validation against field data is also necessary. Ongoing UAV experiment at the laboratory based on the use of light cameras (GoPro filtered in red and NIR, OPTRIS for TIR) should provide robust data very soon for that purpose.
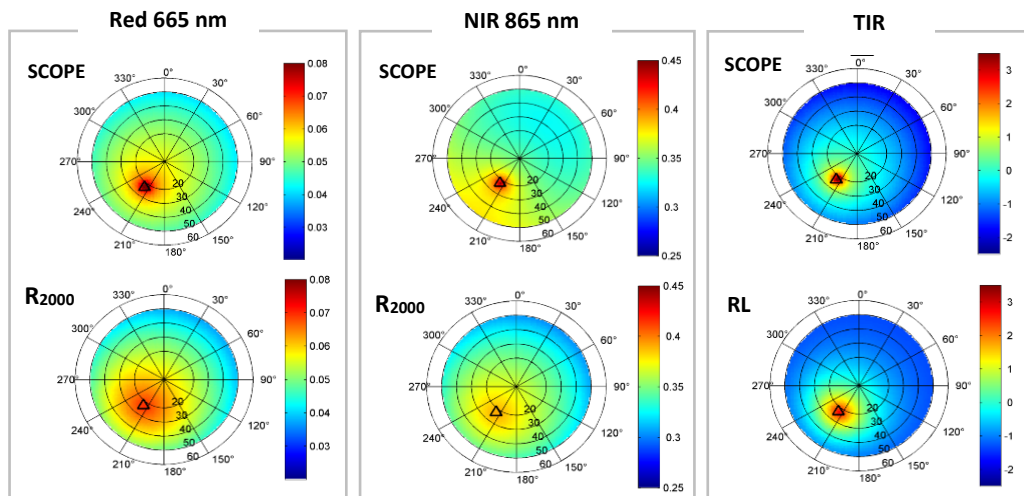
Example of fits of R_{2000} and RL models against SCOPE simulations
(LAI = 1.5, q = 0.1, Vcmo = 25, rss = 200, Auradé DOY 174)

7 REFERENCES

Duffour C., Olioso A., Demarty J., Van der Tol C., Lagouarde J.-P., 2015. An evaluation of SCOPE: a tool to simulate the directional anisotropy of satellite-measured surface temperatures. *Remote Sens. Environ.,* 158, 362-375.

Duffour C., Lagouarde J.-P., Olioso A., Demarty J., Roujean J.-L., 2016a. Driving factors of the directional variability of thermal infrared signal in temperate regions. *Remote Sens. Environ.* 177 (2016) 248–264.

Duffour C., Lagouarde J.-P., Roujean J.-L. 2016b. A two parameter model to simulate thermal infrared directional effects for remote sensing applications. *Remote Sensing of Environment* 186 (2016) 250–261.

Lagouarde J.-P., Ballans H., Moreau P., Guyon D., and Coraboeuf D., 2000. Experimental study of brightness surface temperature angular variations of Maritime Pine *(Pinus Pinaster)* stands, *Remote Sens. Environ.*, vol. 72, no. 1, pp. 17–34.

Lagouarde J.-P. and Irvine M., 2008. Directional anisotropy in thermal infrared measurements over Toulouse city centre during the CAPITOUL measurement campaigns: first results. *Meteorology and Atmospheric Physics*, special issue CAPITOUL. 102, 173-185, DOI: 10.1007/s00703-008-0325-4.

Menenti M., Jia L., and Li Z.-L., 2008. Multi-angular thermal observations of terrestrial vegetation, in *Advances Land Remote Sensing*, S. Liang, Ed. New York, NY, USA: Springer-Verlag, 2008, pp. 51–93.

Paw U K. T., 1992. Development of models for thermal infrared radiation above and within plant canopies," *ISPRS J. Photogram. Remote Sens.*, vol. 47, no. 2/3, pp. 189–203.

Roujean, J.-L., 2000. A parametric hot spot model for optical remote sensing applications. *Remote Sensing of Environment.* 71, 197–206. DOI : 10.1016/S0034-4257(99)00080-2

Van der Tol, C., Verhoef, W., Timmermans, J., Verhoef, A., and Su, Z., 2009. An integrated model of soil-canopy spectral radiances, photosynthesis, fluorescence, temperature and energy balance. Biogeosciences, 6, 3109–3129.

Verhoef W., Jia L., Xiao Q., and Su Z., 2007. Unified Optical-Thermal Four-Stream Radiative Transfer Theory for Homogeneous Vegetation Canopies. *IEEE Trans. Geos. and Remote Sens.*, Vol. 45, No. 6, 1808-1822.

Improving GIS-based monthly air temperature maps with satellite-derived land surface temperature

Mira M.[1], Ninyerola M.[2], Batalla M.[3], Pesquer L.[3], Pons X.[1]

(1) GRUMETS Research Group. Department of Geography, Edifici B, Universitat Autònoma de Barcelona, 08193 Bellaterra, Spain.
(2) GRUMETS Research Group. Department of Animal Biology, Vegetal Biology and Ecology, Universitat Autònoma de Barcelona, 08193 Bellaterra, Spain.
(3) GRUMETS Research Group. CREAF, Edifici C, Universitat Autònoma de Barcelona, 08193 Bellaterra, Spain.
maria.mira@uab.cat, miquel.ninyerola@uab.cat, meritxell.batalla@uab.cat,
xavier.pons@uab.cat, meritxell.batalla@uab.cat

ABSTRACT - *This study proposes an empirical methodology for mapping monthly air temperature (T_{air}) (minimum and maximum) using meteorological data, geographic information and monthly land surface temperature (LST) derived from satellite data. Two sources of data for monthly LST estimates during daytime and nighttime were considered: 1) MOD11B3 and MYD11B3 products from the Moderate Resolution Imaging Spectroradiometer (MODIS), with a pixel size of 5600 m, and 2) the product from the Along Track Scanning Radiometer-2 (ATSR-2), or from the Advanced Along Track Scanning Radiometer (AATSR) (both with an spatial resolution of about 0.05°). The study period included June and December from 2003 to 2011. The analysis considered the spatial interpolation improvements in different land uses (Forests, Agricultural and livestock, and Urban areas) and different degrees in the orographic complexity of Catalonia (northeast of the Iberian Peninsula). Meteorological stations were weighted, in the calibration step, based on information from the quality masks of LST data. The best T_{air} models were obtained when regression included remote sensing LST and geographical variables, especially for minimum Tair and over Forests and Rugged lands. In general, the improvement was more important (in terms of reducing uncertainty) for the estimation of monthly minimum T_{air}, than for the estimation of monthly maximum T_{air}. Minimum T_{air} was better estimated using nighttime LST (RMS differences up to 0.3 K), as well as maximum T_{air} on winter, while on summer was better estimated with daytime LST. A simpler model, which did not include the topographic wetness index and the cost distances, provided similar T_{air} estimates.*

1 INTRODUCTION

Monitoring and definition of the climate and meteorology of a specific geographic region are essential for the knowledge of the spatial and temporal patterns of the surface air temperature (T_{air}), defined as the temperature measured by a thermometer exposed to the air in a place protected from the direct solar radiation (WMO, 1992), normally located at about 1.5 m above the ground. The T_{air} is a key climatic and meteorological variable that makes it possible to quantifying processes at surface level. In fact, it is involved in many environmental processes such as energy flows, actual and potential evapotranspiration, water stress, and species distribution (Prihodko and Goward, 1997). It can therefore be used, for example, as an input parameter in weather and climate models.

T_{air} is usually measured at meteorological stations, which provide point data, spatially characterized by the density and distribution of the network of available stations. However, in many cases (especially in large and heterogeneous areas) it is necessary to have a continuous or quasi-continuous surface of the T_{air}.

Remote sensing is the only methodology that effectively evaluates the spatial distribution of land surface variables on a regional and global scale. Thanks to the technological developments in the latest generation of spectral band sensors in the thermal infrared region (8-14 μm) (e.g., Sentinel-3, MODIS, ASTER, AATSR, AVHRR) the capacity of existing Earth observation programs has improved. These sensors incorporate new spectral measurement channels of and provide much better spatial and spectral resolution than just a few decades ago. Likewise, the long historical satellite data series that exist today (Landsat, over 40 years, NOAA-AVHRR, over 30 years, MODIS, 16 years) make it possible to combine climate cartography based on data from meteorological stations with satellite information (Vicente-Serrano *et al.*, 2004; Sun *et al.*, 2005; Cristóbal *et al.*, 2008; Hengl *et al.*, 2012). In this sense, there are in the literature a variety of studies

that introduce the land surface temperature (LST) estimated with remote sensing data (Cristóbal *et al.*, 2008; Hengl *et al.*, 2012). However, it is not usual to find jobs that use extensive time series.

The present work has the general aim of progressing in the understanding and prediction of future environmental changes. The main objective is to improve the monthly T_{air} spatial estimates (minimum and maximum) currently provided by GIS-based models that combine statistical (multiple regression) and spatial (interpolation) approximations from meteorological data, incorporating LST from satellite data as a predictor. In this study, a long and robust time series (from 2003 to 2011) is considered, both from data from conventional meteorological observations and from remote sensing data, also integrating geographic factors such as altitude, continentality, etc. and that also takes into account images from different satellites. As a secondary objective, the changes in the estimates of the T_{air} at the spatial and temporal levels are evaluated, considering the analysis of data corresponding to the different times of the year analyzed, as well as the differentiation between land cover and the orographic complexity. The area of study is Catalonia, located at the northeast of the Iberian Peninsula.

2 MATERIAL

The database includes concurrent measurements from satellite data (daytime and nighttime LST), field measurements of meteorological stations (T_{air}) and geographic data for the summer (June) and winter (December) months from 2003 to 2011.

2.1 Meteorological station data

The meteorological data were provided by the Spanish National Meteorological Agency (AEMET) and the Catalan Meteorological Service (SMC). These data were previously subjected to a rigorous quality control, making a selection according to several objective criteria (stability of the time series, cross validation test, etc.), together with the expert knowledge (quality of the series of the meteorological stations, proper location, etc.).

The T_{air} has been observed around 5 h - 6 h (minimum) and 15 h - 16 h (maximum), although there is some variability depending on the location and time of the year. It is considered an average of 195 stations in each image, varying between a minimum of 180 and a maximum of 212 depending on the time of year. The accuracy of the estimates is 0.1 K.

2.2 Other geographic data

The model also considers geographic information derived from a digital elevation model and other geographic variables, such as altitude, latitude, continentality (Euclidean distance and cost distance to the sea), potential solar radiation and a topographic wetness index (Böhner *et al.*, 2002).

2.3 Satellite data

As monthly data of daytime and nighttime LST were considered 1) the products MOD11B3 and MYD11B3 of the Moderate Resolution Imaging Spectroradiometer (MODIS) of NASA and 2) the product hereafter called "ATCDR" corresponding to data of the Along Track Scanning Radiometer-2 (ATSR -2) or the European Space Agency's (ESA) Advanced Along Track Scanning Radiometer (AATSR).

The acquisition time of the images on the study area is detailed in Table 1. The nominal spatial resolution of both products is approximately 6 km (5568 km for MODIS and 0.05 degrees for ATSR-2 and AATSR). However, the images were adapted to 90 m of spatial resolution by means of bilinear interpolation (or the nearest neighbour, in the case of quality masks of MODIS products) for inclusion in the regression models.

Table 1. Average local time of acquisition of the satellite images, after considering all the images and pixels of the study area.

Product	Daytime	Nighttime
ATCDR	10:26	21:24
MOD11B3	11:11	21:59
MYD11B3	13:08	2:04

3 METHODOLOGY

Although different spatial interpolation techniques exist, we opted to apply a methodology based on the multiple regression analysis combined with the spatial interpolation of the regression residuals by the inverse of the weighted distance (Ninyerola *et al.*, 2000, 2005; Sun *et al.*, 2005). The multiple regressions provide a predictive model of the climatic variable (T_{air}) from the variables that influence the climate of the zone (the geographic variables and the LST). The result is a potential map obtained from the equation of adjustment of the regression that reflects the general behaviour of the climate. Once this potential mapping is available, it is possible to interpolate the residuals of the regression itself to bring the potential surface closer to the observed data, and therefore, in general, for the entire mapped territory. In other words, the use

of the variance not explained by the regression model allows, once combined with the potential map, to obtain the most realistic maps possible. The residuals (difference between the value predicted by the regression model and the value observed in the meteorological stations) show the local aspects of the climate since they quantify how particular is that climatology with respect to the general model.

Several reliability indexes were used to describe the thematic quality of each map. For the calculation of these indices it is indispensable to reserve a set of stations (set of validation or test) that allows comparing them with the values estimated from the set of adjustment stations. Cross-validation leave-one-out was applied in the present study. This process allows to preserve to the maximum the predictive capacity of the models and to obtain an average reliability index.

The statistical variables analysed in this study are the root mean square error (RMSE) and the coefficient of determination (R^2).

The stations included in the model were weighted in the calibration, based on the LST quality bands information, according to the criteria established in Table 2 and Table 3. Further, stations were classified according to the land cover (*Forests*, *Agricultural and livestock*, and *Urban areas*) and the orographic complexity, which are based on the standard deviation of the altitude within a radius of 10 km (*Flatlands*, deviation <150 m; *Middle ground*, between 150 and 250 m; *Rugged lands*, > 250 m). Different complexities for the model were considered as well, by considering all independent variables (hereafter called "complex model") or all variables except the topographic wetness index and the cost distances to the Mediterranean and the Cantabric sea (hereafter called "simple model").

Table 2. Weighting of the meteorological stations according to the uncertainty (δ) of the LST product from ATCDR.

ATCDR	
δLST (K)	Weighting (%)
≤ 1	100
>1 y ≤1.2	90
>1.2 y ≤1.4	80
>1.4 y ≤1.6	70
>1.6 y ≤1.8	60
>1.8 y ≤2.0	50
>2.0 y ≤2.3	40
>2.3 y ≤2.6	30
>2.6 y ≤3.0	20
>3.0	10

Table 3. Weighting of the meteorological stations according to the quality masks provided by the MOD11B3 and MYD11B3 products. QC-LST: "QC_Mandatory_QA_flag"; QC-Emis: "QC_Emis_error_flag".

QC-LST	QC-Emis	Weighting (%)
1	1,2,3,4	100
3	1	70
3	2	50
3	3	30
3	4	10

4 RESULTS

4.1 General observations for the regression coefficients

For the estimation of the minimum T_{air}, solar radiation was not considered as a dependent variable, since in most cases its inclusion was not significant (p>0.05), and regression coefficients were even negative, inverting the natural relationship of the T_{air} with the solar radiation (since at higher radiation is expected higher T_{air}).

The regressions obtained for the estimation of the maximum T_{air} during winter presented a general tendency to not include the topographic wetness index when considering the LST, nor the cost distance to the Mediterranean when considering the nighttime LST. However, for the estimation of the minimum T_{air} such exclusion only occurred occasionally.

When the LST implied an improvement in the T_{air} estimation, a larger coefficient was obtained for that variable. On the other hand, its value decreased (or was practically zero), when the improvement was smaller or non-existent.

4.2. Performance from models with a set of common meteorological stations

The improvements observed in the T_{air} estimation by including the LST an independent variable are summarized in Table 4, as well as the difference observed by considering a daytime or nighttime LST product. As a result, the LST product providing the best estimates of T_{air} (in terms of *RMSE*) is detailed in Table 5. Further, mention that the R^2 had a maximum value of 0.95 and a mean value of 0.90 and 0.83 for the maximum and minimum T_{air}, respectively. There were no large differences in R^2 (<0.02) in the models that did not include the LST or between the models obtained for summer or winter.

Table 4. Maximum (mean) difference in the RMSE of T_{air} observed during years 2003-2011 on models with 80 common meteorological stations.

Month	$RMSE_{noLST} - RMSE_{withLST}$ (K)		$RMSE_{LSTd} - RMSE_{LSTn}$ (K)	
	Max	Min	Max	Min
June	0.16 (0.11)	0.15 (0.10)	-0.15 (-0.07)	0.15 (0.10)
Dec.	0.12 (0.04)	0.3 (0.2)	0.13 (0.02)	0.3 (0.17)

Table 5. Product providing the best estimates of T_{air} (in terms of *RMSE*). Results from regressions considering 80 common meteorological stations for years 2003-2011.

Month	Max	Min
June	MYDd	ATCDRn
Dec.	MYDn	ATCDRn

Table 6. Maximum (mean) difference in the *RMSE* of T_{air} observed during years 2003-2011 on models considering all meteorological stations in the fitting step but considering only stations included within each class in the validation step.

		N	$RMSE_{noLST} - RMSE_{withLST}$ (K)	
			Max	Min
			June / Dec.	June / Dec.
Land cover	Forests	33-38	0.3 (0.17) / 0.19 (0.08)	0.3 (0.16) / 0.4 (0.3)
	Agric. and livestock	99-110	0.06 (0.04) / 0.03 (0.009)	0.11 (0.07) / 0.13 (0.06)
	Urban areas	44-59	0.07 (0.04) / 0.09 (0.04)	0.10 (0.07) / 0.3 (0.19)
Orographic complexity	Flatlands	120-131	0.07 (0.04) / 0.04 (0.006)	0.16 (0.10) / 0.2 (0.15)
	Middle ground	33-46	0.16 (0.09) / 0.05 (0.015)	0.08 (0.05) / 0.3 (0.15)
	Rugged lands	26-34	0.16 (0.12) / 0.4 (0.19)	0.17 (0.04) / 0.5 (0.2)

Table 7. Maximum (mean) differences in statistics obtained with the "simple" and the "complex" model. Model results for years 2003-2011 by considering all meteorological stations and LST estimates from the product indicated in Table 5.

Month	$RMSE_{simple} - RMSE_{complex}$ (K)		$R^2_{simple} - R^2_{complex}$	
	Max	Min	Max	Min
June	0.15 (0.08)	0.03 (0.017)	-0.04 (-0.07)	-0.004 (-0.010)
Dec.	0.018 (0.04)	0.04 (0.011)	-0.001 (-0.03)	-0.005 (-0.016)

Table 8. Maximum (mean) values for T_{air} observed during years 2003-2011 on models with all meteorological stations.

Month	$RMSE_{noLST} - RMSE_{withLST}$ (K)		RMSE (K)		R^2	
	Max	Min	Max	Min	Max	Min
June	0.10 (0.05)	0.08 (0.05)	1.2 (1.1)	1.5 (1.2)	0.945 (0.922)	0.918 (0.852)
Dec.	0.04 (0.03)	0.2 (0.10)	1.3 (0.09)	1.3 (1.3)	0.947 (0.888)	0.899 (0.822)

4.3 Performance by considering all meteorological stations

The improvements on the T_{air} estimates observed when introducing the LST in the models, for each land cover and orographic complexity class, is summarized in Table 6. Table 7 presents the performance differences between models of different complexity, and Table 8 the overall performance.

5 DISCUSSION

The low significance of the solar radiation coefficient in the models is attributed to the arrangement of the meteorological stations in the geographical space, most of them located in flat areas. This causes little variability and does not capture the relationship in the models.

Except for the maximum T_{air} on summer, the nighttime LST product provided a higher accuracy than the daytime LST product both for maximum and minimum T_{air}. As already shown by Zeng *et al.* (2015) for the estimation of the daily T_{air}, the ability of the nighttime LST to estimate the maximum monthly T_{air} is demonstrated, whereas the majority of the studies do not use to explore this possibility (Vancutsem *et al.*, 2010).

The usefulness of remote sensing LST data on T_{air} estimation is demonstrated by the improvement observed (in terms of *RMSE*) in relation to the performance provided by the classical T_{air} models. It is higher for minimum T_{air} on winter (being up to 0.3 K),

and lower for maximum T_{air} on summer (being up to 0.12).

Further, the improvement is more significant over *Forests* and *Rugged lands*, which is an encouraging result, given the few ground data available in such type of surfaces. Furthermore, we also observed that the improvement provided by the inclusion of the LST is more important than that provided by the inclusion of more geographic variables into the model.

6 CONCLUSIONS

The incorporation of T_{air} satellite estimates into the monthly T_{air} predictive models implies a significant improvement, especially for minimum and maximum T_{air} estimates on winter time. In conclusion, the LST provides additional information regarding the thermal inversion phenomenon, not reflected so far by geographic variables or terrain measures, probably due to the few meteorological stations located on Rugged lands.

As an added value, the present work will be important for updating and improving the "Digital Climate Atlas of Catalonia" developed by the Universitat Autònoma de Barcelona and available online (*http://www.creaf.uab.cat/miramon/Index_en.htm*).

8 REFERENCES

Böhner, J., Köthe, R., Conrad, O., Gross, J., Ringeler, A., and Selige, T., 2002, Soil regionalisation by means of terrain analysis and process parameterisation. In: Micheli, E., Nachtergaele, F., Montanarella, L. [Ed.]: Soil Classification 2001. European Soil Bureau, Research Report No. 7, EUR 20398 EN, Luxembourg. pp.213-222.

Cristóbal, J., Ninyerola, M., and Pons, X., 2008, Modeling air temperature through a combination of remote sensing and GIS data. Journal of Geophysical Research - Atmospheres. 113:D13106.

Hengl, T., Heuvelink, G.B.M., Tadic, M.P., and Pebesma, E.J., 2012, Spatio-temporal prediction of daily temperatures using time-series of MODIS LST images. Theoretical and Applied Climatology, **107**(1), 265-277.

Ninyerola, M., Pons, X., and Roure, J.M., 2000, A methodological approach of climatological modelling of air temperature and precipitation through GIS techniques. International Journal of Climatology, **20**, 1823-1841.

Ninyerola, M., Pons, X., and Roure, J.M., 2005, Atlas Climático Digital de la Península Ibérica. Metodología y aplicaciones en bioclimatología y geobotánica. 44 pp. Universitat Autònoma de Barcelona, Bellaterra. http://opengis.uab.es/wms/iberia/pdf/acdpi.pdf

Prihodko, L., and Goward, S.N., 1997, Estimation of air temperature from remotely sensed surface observations. Remote Sensing of Environment, **60**, 335-346.

Sun, Y.J., Wang, J.F., Zhang, R.H., Gillies, R.R., Xue, Y., and Bo, Y.C., 2005, Air temperature retrieval from remote sensing data based on thermodynamics. Theoretical and Applied Climatology, **80**, 37-48.

Vancutsem, C., Ceccato, P., Dinku, T., and Connor, S.J., 2010, Evaluation of MODIS land surface temperature data to estimate air temperature in different ecosystems over Africa. Remote Sensing of Environment, **114**, 449-465.

Vicente-Serrano, S.M., and Heredia-Laclaustra, A., 2004, NAO influence on NDVI trends in the Iberian Peninsula (1982–2000). International Journal of Remote Sensing, **25**, 2871-2891.

World Meteorological Organization, 1992, Measurement of temperature and humidity (R.G. Wylie and T. Lalas). Technical Note No. 194, WMO-No. 759, Geneva.

Zeng, L.L., Wardlow, B.D., Tadesse, T., Shan, J., Hayes, M.J., Li, D.R., and Xiang, D.X., 2015, Estimation of daily air temperature based on MODIS land surface temperature products over the corn belt in the US. Remote Sensing, **7**, 951-970.

Evaluation of the surface soil moisture over alpine vegetation region of Tibetan Plateau

Long Xia[1], Xiaoning Song[1, *], Pei Leng[2], Yawei Wang[3], Yanbin Hao[4], Yanfen Wang[4]

[1.]College of Resources and Environment, University of Chinese Academy of Sciences, Beijing 100049, China;

[2.]Key Laboratory of Agri-Informatics, Ministry of Agriculture/Institute of Agricultural Resources and Regional Planning, Chinese Academy of Agricultural Sciences, Beijing 100081, China;

[3.]Department of geography, Ludwig- Maximilians-Universität München(LMU),80337, Germany;

[4.]College of Life Sciences, University of Chinese Academy of Sciences, Beijing 100049, China

[*]Corresponding to whom should be addressed: songxn@ucas.ac.cn

ABSTRACT- *Surface soil moisture (SSM), as an important surface process parameter, plays a very important role in water resources management, crop growth, land degradation, vegetation coverage and global climate change research. In this study, the Moderate-resolution Imaging Spectroradiometer (MODIS) products from 2008 to 2010 over alpine vegetation region of Tibetan Plateau are selected, including MOD11A2 Land surface temperature (LST) 8 days synthetic product and MOD13A2 Normalized differential vegetation index (NDVI) 16 days synthetic product, to construct the LST-NDVI triangle feature space. Then, the linear interpolation and nonlinear interpolation methods are both used to estimate the SSM at the regional scale. Finally, the error analysis between retrieval SSM and ground measured SSM was carried out to explore the applicability of the two methods in the alpine vegetation area of the Tibetan Plateau, and the temporal and spatial variation of soil moisture in the study area was also analysed. The results show that the accuracy of the nonlinear interpolation method is significantly higher than the linear interpolation method. The Root mean square error (RMSE) between the estimated SSM and the ground measured data of the linear interpolation method is 0.1007m3/m3, and the correlation coefficient R is 0.5637 compared with the nonlinear interpolation method with RMSE of 0.0752m3/m3and R of 0.6344. At the same time, there is a consistent regional soil moisture distribution with a decreasing trend from west to east of two retrieval methods.*

1 INTRODUCTION

Surface soil moisture (SSM) plays a fundamental role in controlling the exchange of water and heat energy between the land surface and the atmosphere. The electromagnetic energy emitted and reflected by soil surface is measured to study the relationship between remote sensing information and SSM, and to establish the information model between SSM and remote sensing data, so as to retrieve the soil moisture information (Chen et al., 2012).

Bowers and Smith (1972) found that the absorption amplitude of water in the absorption band was linearly related to soil moisture content. Dalal (1986) accurately estimated the soil moisture information of a large number of soil samples by using the moisture absorption values measured in the near infrared band. Kahle (1977) studied the thermal inertia model, and proposed different methods to solve one-dimensional heat conduction equation, and combined

with remote sensing data to solve the thermal inertia inversion of large area. Watson (1982) proposed a physical analytical equation for retrieving soil thermal inertia using remote sensing data, combined with meteorological data and soil moisture profile calculation, the soil moisture was successfully retrieved.

While the development of soil moisture is retrieved by visible near infrared and thermal infrared remote sensing, the methods of combining the two were applied. Price (1990) proposed the concept of triangular space, and if there were enough pixels in the area with the clouds and water being removed, the spatial distribution of LST and vegetation index or vegetation coverage tends to converge into a triangle or trapezoid, which is called the LST- vegetation index feature space. Carlson et al. (1995) found that soil moisture and LST and vegetation index changes are non-linear and established a polynomial model to

describe the relationship of the three. Sandholt et al. (2002) proposed the Temperature vegetation drought index (TVDI) to represent the status of soil moisture on the base of LST-NDVI triangle feature space, and Goward et al. (2002) established the linear relationship between TVDI and soil moisture for the SSM retrieval.

In the LST-NDVI feature space, the slope indicates that there is the lowest soil moisture for different vegetation types in the situation of the highest temperature, and we call this "dry edge". Meanwhile, the bottom edge of the triangle indicates that the soil moisture is sufficient and will not become a limiting factor for vegetation growth at the same temperature, which we call "wet edge". SSM can be interpolated between the "dry edge" and "wet edge" in the LST-NDVI feature space, and the interpolation method can be divided into linear interpolation and nonlinear interpolation.

Whether SSM is linear or nonlinear in LST-NDVI feature space remains to be studied. Since the linear interpolation method is simple, most researchers tend to use it while the nonlinear interpolation is complex, which is seldom used. This study aims to analyse the application of linear interpolation and nonlinear interpolation in regional SSM retrieval, and to analyse the temporal and spatial variation of SSM in the study area.

2 STUDY AREA AND DATA

2.1 Description of study area

The source area of the Yellow River (SAYR, 95°50′E-103°30′E and 32°20′N-36°10′N) is located in the northeast of the Tibetan Plateau with an average elevation of 4065m., as shown in Figure 1.
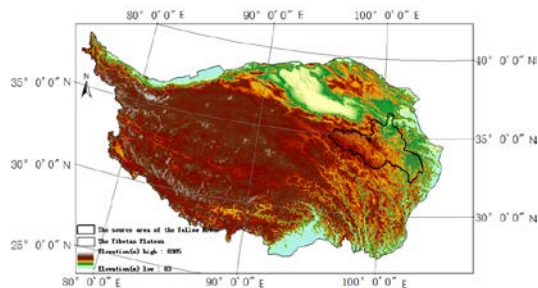
Figure 1. The location of study area

The landform of the SAYR is complex, and the vegetation types are diverse, Most of the area is covered with alpine vegetation types, such as alpine shrubs, alpine meadows, alpine grasslands, etc.

Furthermore, the south and southeast of the SAYR is characterized by cold and semi-humid climate features, while the northern and western regions show a cold and arid to semi-arid climate pattern. The mean annual average air temperature is about 5℃, and the annual precipitation varies between 320 and 750mm over the study area.

2.2 MODIS data

MODIS is currently equipped on two satellites: Terra and Aqua. The two satellites cooperate with each other to observe the entire earth surface every 1~2 days, and obtain the observation values of 36 bands. These data are widely used in the dynamic processes of the global land, ocean and atmosphere. The MODIS standard data products of MOD11A2 known as 8 days synthetic products of LST with a spatial resolution of 1 km and MOD13A2 known as 16 days synthetic products of NDVI with a spatial resolution of 1 km are selected in this study.

2.3 Ground measured data

The Cold and Arid Regions Environmental and Engineering Research Institute, Chinese Academy of Sciences (CARRERI, CAS) and the Faculty of Geo-Information Science and Earth Observation of the University of Twente (ITC) have installed an extensive soil moisture monitoring network in the east of the SAYR, as shown with red triangle in Figure 2. The network consists of 20 stations to monitor the soil moisture (5 cm deep) and can easily validate the satellite derived SSM.
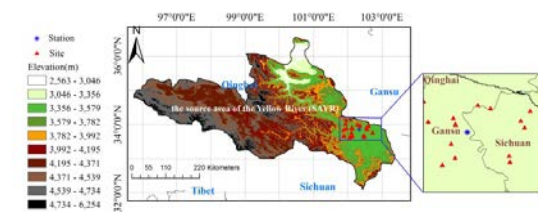
Figure 2. 20 Soil moisture sites operated by CARRERI and ITC in SAYR

3 METHODOLOGIES

3.1 LST-NDVI triangle feature space

It is found that the spatial relationship between NDVI and LST is triangle when the research area is large enough, and the land cover type changes from bare soil to complete vegetation cover, and the soil moisture changes from drought to moist as shown in Figure 3. In the LST-NDVI feature space, point A

represents the condition of dry bare soil with a high value of LST and low value of NDVI; point B represents the condition of wet bare soil with a low value of LST and low value of NDVI; point C represents that vegetation is completely covered, and soil moisture is adequate with a low value of LST and high value of NDVI. Moreover, the slope indicates that there is the lowest soil moisture for different vegetation types in the situation of the highest temperature, and we call this "dry edge". Meanwhile, the bottom edge of the triangle indicates that the soil moisture is sufficient and will not become a limiting factor for vegetation growth at the same temperature, which we call "wet edge".
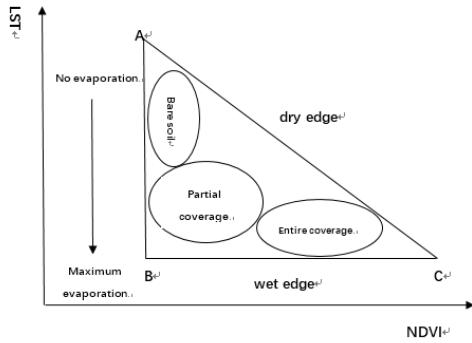
Figure 3. LST-NDVI feature space

3.2 Linear interpolation method

Sandholt proposed the Temperature vegetation drought index (TVDI) to represent the status of soil moisture on the base of LST-NDVI triangle feature space as expressed:

$$TVDI = \frac{T - (a_2 + b_2 \times NDVI)}{(a_1 + b_1 \times NDVI) - (a_2 + b_2 \times NDVI)} \quad (1)$$

Where T represents the LST of any pixel, a_1, b_1 and a_2, b_2 are respectively linear fitting coefficients of dry edges and wet edges. The value of TVDI varies from 0 to 1, and the larger the TVDI value is, the lower the SSM of the pixel is; the smaller the TVDI value is, the higher the SSM is. Then, we can know the dry and wet distribution of the study area by TVDI, but we don't know exactly how much relative water content is in the soil so that we need to convert TVDI into SSM.

Goward et al found that the LST-NDVI feature space can be regarded as the contours of soil moisture in this region. The intersection point of each contour in this region is approximately straight line compared to the wet edge, so we can describe the slope of the straight line and soil moisture with unitary linear relationship as expressed:

$$M = M_w - (M_w - M_d) \times TVDI \quad (2)$$

Where M is the SSM of one pixel; M_w is the maximum SSM of wet edge, and we can regard it as 1; M_d is the minimum SSM of dry edge, which can be calculated by fitting the slope value of dry edge equation and the minimum SSM.

3.2 Polynomial nonlinear interpolation method

SSM can be interpolated between the wet and dry edge conditions in the LST-NDVI feature space. In addition, the interpolation method can be divided into linear interpolation and nonlinear interpolation. Carlson found that soil moisture and LST and vegetation index changes are non-linear and established a polynomial model to describe the relationship of the three as expressed:

$$M_c = \sum_{i=0}^{i=2} \sum_{j=0}^{j=2} a_{ij} NDVI^{(i)} LST^{(j)} \quad (3)$$

Where Mc is the SSM, a_{ij} are polynomial coefficients.

4 RESULTS AND ANYLYSIS

The results show that, as shown in Table 1, the retrieval SSM, estimated by both linear and nonlinear interpolation method in the LST-NDVI feature space, is larger than the ground measured data. At the same time, the absolute error and the RMSE between the estimated SSM and the ground measured data of the nonlinear interpolation method are less than the linear interpolation method, which shows that the nonlinear interpolation method is more accurate.

Table 1. Error analysis of two methods

Method	absolute error	RMSE	R
Linear interpolation method	0.0015	0.1007	0.5637
Nonlinear interpolation method	0.0004	0.0752	0.6344

The correlation coefficient R obtained by the nonlinear interpolation method is 0.6344 greater than the linear interpolation method of 0.5637 as shown in Figure 4, which shows that the nonlinear interpolation method has better fitting effect with the ground measured data. In general, the polynomial model is better than the drought index model in terms of computational accuracy and fitting results. In general, the nonlinear interpolation method is better than the linear interpolation method in the calculation accuracy and the fitting result in this study.

Linear interpolation method

Nonlinear interpolation method
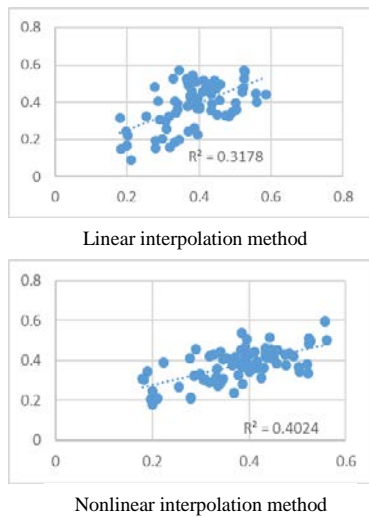
Figure 4. The correlation coefficient analysis between the estimated SSM and the ground measured data of two methods
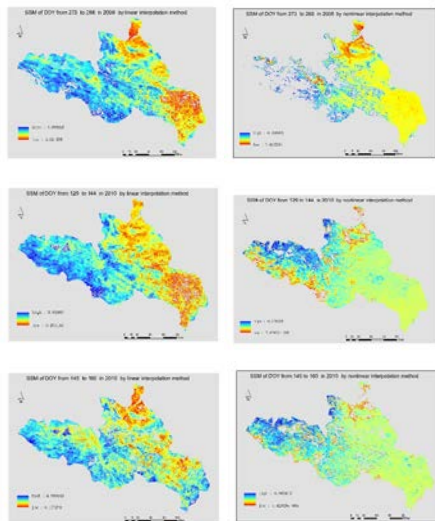
Figure 5. SSM (m3/m3) retrieval by linear(left) and Nonlinear interpolation methods (DOY, Day of the year)

As shown in Figure 5, the soil moisture retrieved by the two models is basically consistent in the regional distribution. Furthermore, from east to west, there is a trend of SSM value from high to low, and there is higher in the West and southwest, while it's lower in the northeast and southeast. Also, soil moisture changes slightly over time throughout the central region.

5 SUMMARY AND CONCLUSIONS

SSM plays a considerable role in various hydrological models, meteorological studies and ecological applications. This study takes the SAYR covered with alpine vegetation in the northeast of Tibetan Plateau as the research area, and LST-NDVI feature space has been constructed using MODIS LST and NDVI products from 2008 to 2010. Then combined with the ground measured data from CARRERI, the SSM has been retrieved by both linear interpolation and polynomial nonlinear interpolation methods. Finally, the results show that the trend of SSM distribution in the two models is basically consistent; in addition, the accuracy of polynomial nonlinear interpolation method is higher than that of linear interpolation method, which is more appropriate for SSM retrieval over alpine vegetation region of Tibetan Plateau.

ACKNOWLEDGEMENT

REFERENCES

Chen S.-L., Liu Y.-B., & Wen Z.-M., 2012, Satellite retrieval of soil moisture: An overview. *Advances in Earth Science*, 27, 1192-1203.

Bowers S. A., & Smith S. J., 1972, Spectrophotometric determination of soil water content. *Soil Science Society of America Proceedings*, 36, 978-980.

Dalal H., 1986, Simultaneous determination of moisture, organic carbon, and total nitrogen by infrared reflectance spectrometry. *Soil Science Society of America Journal*, 50, 120-123.

Kahle A. B., 1977, A simple thermal model of the earth's surface for geologic mapping by remote sensing. *Journal of Geophysical Research*, 82, 1673-1680.

Watson K., 1982, Regional thermal inertia mapping from an experimental satellite. *Geophysics*, 47, 1681-1687.

Price J. C., 1990, Using spatial context in satellite data to infer regional scale evapotranspiration. *IEEE Transaction on Geoscience and Remote Sensing*, 28, 940-948.

Carlson T. N., Gillies R. R., & Schmugge T. J., 1995, An interpretation of methodologies for indirect measurement of soil water content. *Agricultural and Forest Meteorology*, 77, 191-205.

Sandholt I., Rasmussen K., & Andersen J. A., 2002, A simple interpretation of the surface temperature/vegetation index space for assessment of surface moisture status. *Remote Sensing of Environment*, 79, 213-224.

Goward S. N., Xue Y., & Czajkowski K. P., 2002, Evaluating land surface moisture conditions from the remotely sensed temperature/vegetation index measurements: an exploration with the simplified simple biosphere model. *Remote Sensing of Environment*, 79, 225-242.

Quantitative Monitoring of the Grazing Intensity in Temperate Meadow Steppe based on Remote Sensing Data

Dawei Xu[a], Baorui Chen[a], Ruirui Yan[a], Yuchun Yan[a], Xinbo Sun[b], Lijun Xu[a], Xiaoping Xin[a],[*]

[a]*Hulunber Grassland Ecosystem Observation and Research Station, Institute of Agricultural Resources and Regional Planning, Chinese Academy of Agricultural Sciences, Beijing 100081, China*

[b]*Key Laboratory of Crop Growth Regulation of Hebei Province, Agricultural University of Hebei, Baoding 071001, China*

Email:418xdw@163.com

CONTACT: Xiaoping Xin, xinxiaoping@caas.cn Chinese Academy of Agricultural Sciences, Beijing

ABSTRACT: Grazing intensity (GI) is difficult to measure accurately because of the diversity of grazing livestock, mobility of the grazing space and uncertainty of the grazing time. Thus, GI monitoring is often qualitative, and few studies have quantitatively monitored GI. In this paper, models of GI and the Normalized Difference Vegetation Index (NDVI), GI and the above ground biomass (AGB) were established using a controlled GI experiment based on grassland ecology measurements and remote sensing. The accuracy of the model was evaluated using GI values estimated based on AGB samples and the principle that AGB is similar for the same GI in the same type of grassland. The GI of temperate meadow grassland was quantitatively simulated based on NDVI without field measurements. The results show that it is feasible to simulate GI based on NDVI, the simulation results were influenced by different climate conditions, especially for precipitation in each year. Most of the study area was heavily grazed, except a few pastures with rational utilization (0.23-0.46 Au·ha^{-1}), and in many cases, continuous heavy grazing occurred for many years without cultivation.

1 INTRODUCTION

The grassland ecosystem in China includes 400 million hectares of various grasslands that account for approximately 41.7% of the total land area, making it the largest terrestrial ecosystem in the country (Ren et al., 2008). Additionally, it serves important ecological and productive functions (Hoffmann et al., 2016). Grazing, which has a long history in China, is one of the most important types of grassland utilization (Kawamura et al., 2005). However, 90% of the available natural grassland is degraded to different degrees (Harris, 2010), the monitoring studies of grazing intensity (GI) have generally been qualitative, and quantitative monitoring remains a challenge (Li et al., 2016). GI refers to the number of livestock per unit area in a given period, and it is an important index that reflects the degree of grazing utilization. The conventional method of grassland ecosystem monitoring is based on the following characteristics: (1) this method requires considerable manpower and material resources to investigate livestock populations and distributions, which not suitable for a wide range to estimate, and (2) grazing experiments have been designed according to the GI, plot area and grazing time in a large number of scientific studies.

Remote sensing has recently become one of the main technologies for large-scale grassland research and has a wide range of applications in the grassland resource surveying and mapping. Currently, quantitative GI monitoring using remote sensing technology is mainly based on establishing models between GI and a selected index (Kawamura et al., 2005), such as above ground biomass (AGB) (Li et al., 2016), net primary production (NPP) (Hunt and Miyake, 2006), vegetation index (VI) (Green et al., 2016), etc. This method could be further improved; for instance, the GI data that were used for modelling were generally obtained via investigation or statistical data, and these data were often associated with inherent error; how to make full use of previously measured and known GI values by scientific studies; the error in GI estimates can be magnified because of the error associated with the inversion of AGB, NPP, etc.

2 MATERIALS AND METHODOLOGY

2.1 Study Area

The study area is located in Xieertala, Hailar District of Hulunber, Inner Mongolia autonomous region, China (Fig. 1). The precipitation and temperature in the study area are moderate, and the climate is temperate continental. The annual precipitation generally averages 300-400 mm and is mainly concentrated in June to September.
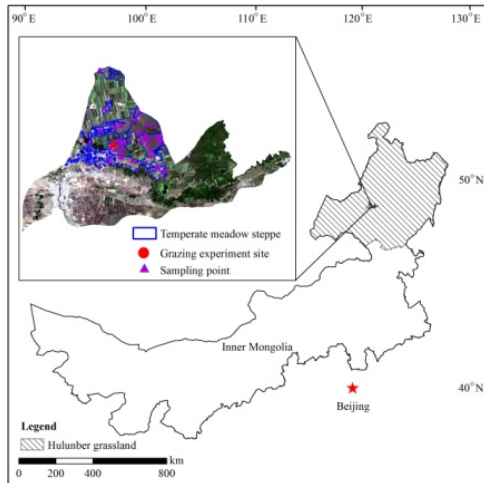
Fig. 1. Location of the study area

The frost-free period is typically 110 d, and the mean annual air temperature is -4 to 1°C. The soil is chernozem or chestnut soil with a medium fertility level. The main types of land cover in the study area are grassland, cropland, residential land, roads, water, forest, etc. The grassland types include temperate meadow steppe, temperate steppe, mountain meadow, and lowland meadow, and the main types of grassland utilization are grazing, cutting and fencing.

2.2 Methodology

2.2.1 Controlled GI Experiment

The controlled GI experiment was established in 2009 (Fig. 2). A randomized block design with three replications was used. Each replication included six grazing gradients: 0 (G0.00), 0.23 (G0.23), 0.34 (G0.34), 0.46 (G0.46), 0.69 (G0.69), and 0.92 (G0.92) AU·ha^{-1} (where 1 AU = 500 kg of adult cattle). Eighteen plots of 5 ha (300 m × 167 m) were fenced, and the total area was 90 ha. The six grazing gradients included 0, 2, 3, 4, 6, and 8 head of young cattle in each plot. Thus, a total of 69 head of cattle were used, and each cattle weighed 250-300 kg. The cattle stayed in a plot throughout the entire grazing period from June to October.

2.2.2 GI inversion and evaluation

A total of 10 images from 2010 to 2016 were used in this study, including nine images from HJ-1A and HJ-1B data obtained from the China Centre for Resources Satellite Data and Applications (www.cresda.com) and one Landsat5 TM image obtained from the United States Geological Survey (http://glovis.usgs.gov) because there were too many clouds in the HJ-1A and HJ-1B images. AGB (fresh weight and dry weight) data were collected from 17 July 2016 to 31 July 2016.
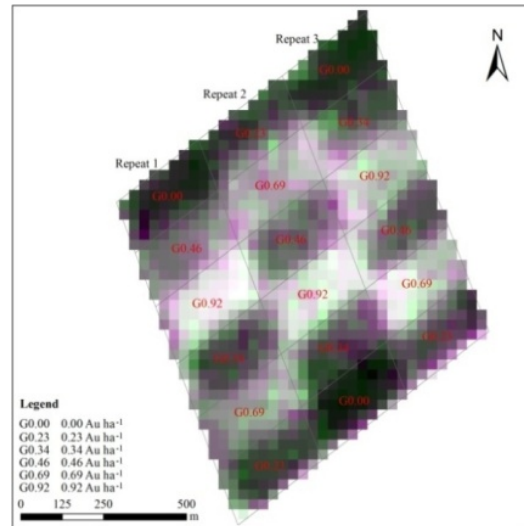
Fig. 2. Controlled grazing intensity experiment

The fresh weight was determined in 1 m×1 m quadrats, and the dry weight was calculated after drying for 48 hours at 65°C to constant weight in an oven. A total of 178 samples were collected in the controlled GI experiment, and each plot had 9-10 quadrats. Additionally, 100 samples were collected outside of the controlled GI experiment but in the study area.

The pure pixels in each plot were selected in the controlled GI experiment by visual interpretation. Additionally, the variations in NDVI under different GIs were compared to determine the best time to establish the model between GI and NDVI. The NDVI was computed as follows:

$$NDVI = \frac{R_{NIR} - R_{RED}}{R_{NIR} + R_{RED}} \qquad (1)$$

where R_{NIR} is the surface reflectance in the near infrared region and R_{RED} is the surface reflectance in the red region.

It is difficult to measure the GI accurately because of the diversity of grazing livestock, mobility of the grazing space and uncertainty of grazing times. The model between GI and AGB (fresh weight and dry weight) was established based on data from 178 quadrats in the controlled GI experiment. The model was used to calculate the GI based on 100 samples collected outside of the controlled GI experiment. The GI values calculated by the model of GI and AGB were regarded as true values based on the principle that AGB is similar for the same GI and in the same type of grassland. The GI values calculated by the model between GI and NDVI were then evaluated using measured values. Finally, the GI in temperate meadow steppe was inverted based on the NDVI, which was directly derived from remote sensing images.

3. RESULTS AND ANALYSIS

3.1 The GI simulation model

The relationship between GI and NDVI can be established in two ways based on the controlled GI experiment. The first approach is to use the average pixel-based NDVI of each grazing plot (Fig. 3; y = -0.241x+0.700, R^2=0.954, N=18), and the second it to use the NDVI of each pixel at each grazing gradient (Fig. 4; y = -0.242x+0.701, R^2=0.911, N=40). The results indicate that NDVI can be used to evaluate GI because both methods yielded R^2 values greater than 0.9; thus, strong correlations exist between GI and NDVI. The second linear model was used in this paper because the average NDVI eliminated some of the differences in the individual NDVI values.

$$y = -0.2414x + 0.7006$$
$$R^2 = 0.954$$
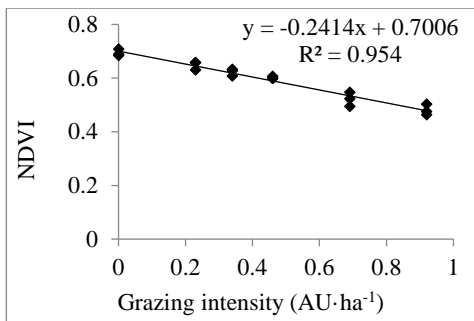
Fig. 3. Relationship between GI and pixel-averaged NDVI of each grazing plot

$$y = -0.2422x + 0.701$$
$$R^2 = 0.9117$$
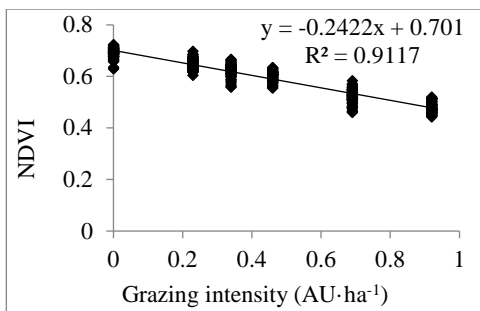
Fig. 4. Relationship between GI and NDVI in each pixel and at each grazing gradient

3.2 Accuracy Verification

The GI values calculated via inversion using the GI and AGB model were regarded as the true values. The GI values simulated using the GI and NDVI model were compared to the true values, and a regression analysis was performed. The R^2, RMSE and relative error values were used as accuracy evaluation indexes. As shown in Fig. 5, the simulation results were similar to the true values, with R^2 values of 0.799 and 0.816 for fresh weight and dry weight, respectively, and RMSE values of 0.178 AU·ha^{-1} and 0.166 AU·ha^{-1}. Additionally, the

relative errors were between -20% and 20% and accounted for 60% and 66% of the total error. All evaluation indexes suggest that the simulation results of the GI and NDVI model were accurate based on their agreement with true values.
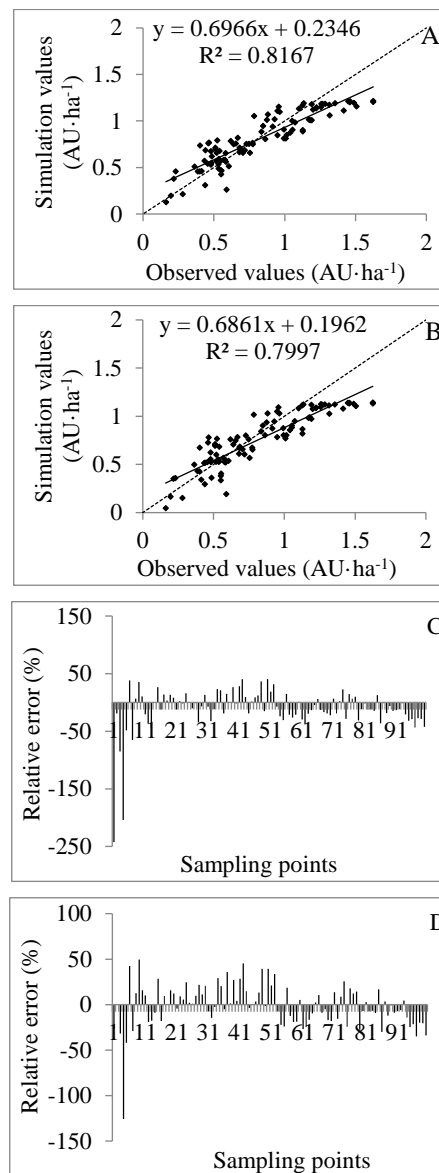
Fig. 5. Comparisons of simulated GI based on NDVI and true values based on AGB sampling (fresh weight and dry weight): relationships between simulated GI and fresh weight (A) and dry weight (B) NDVI and the relative error between simulated GI and fresh weight (C) and dry weight (D) NDVI
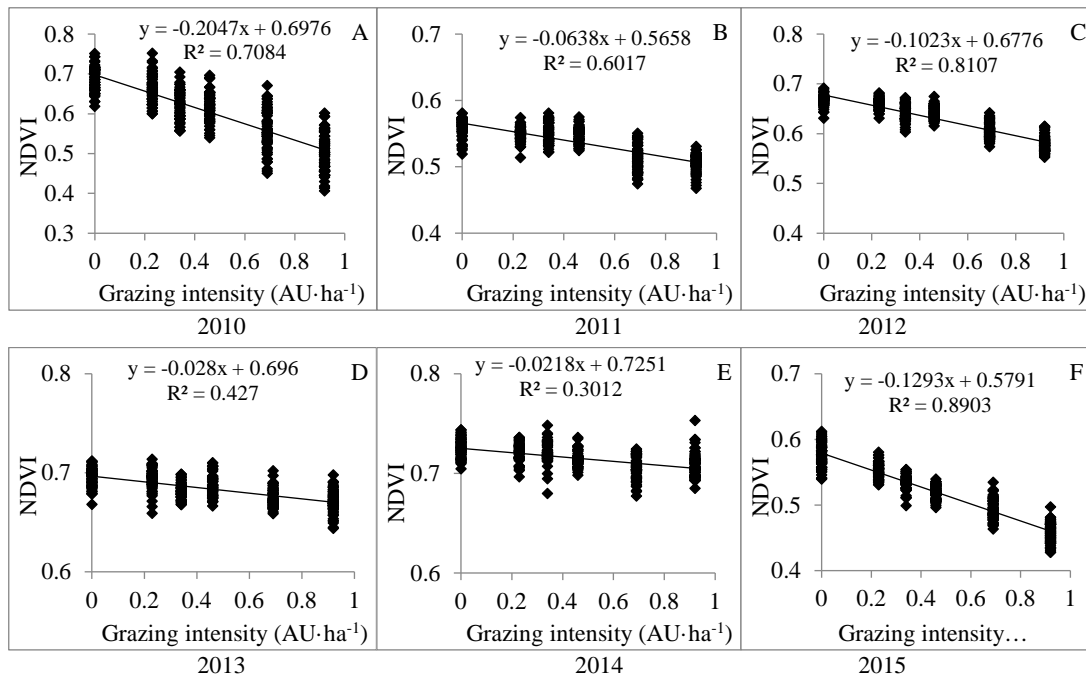
Fig. 6. Relationships between GI and NDVI in each pixel and for each grazing gradient from 2010 to 2015

3.3 Model differences in different climates

The previous analysis showed that GI could be feasibly estimated from NDVI. However, if the climate changes annually, the relationship of GI and NDVI will change in a corresponding manner? NDVI was negatively correlated with GI in July 2010 to 2015 based on the previous method (Fig. 6), but R^2 differences were observed in different years, including relatively small differences in 2013 (0.301) and 2014 (0.427) and larger differences in 2015 (0.890) and 2012 (0.810).

3.4 Mapping the grazing intensity

The map of GI in the study area is shown Fig. 7. Based on the linear model between GI and NDVI, the GI values were suitable at 0.23 AU·ha-1 to 0.46AU·ha^{-1} in the same controlled GI experiment according to the community height, density, coverage, biomass, etc. (Yan et al., 2010, 2015). As a result, most grazing areas were heavily grazed from 2010 to 2016, and few areas were reasonably grazed. The average GIs in the study area were 0.97 AU·ha^{-1}, 1.14 AU·ha^{-1}, 0.80 AU·ha^{-1}, 3.07 AU·ha^{-1}, 3.75 AU·ha^{-1}, 1.15 AU·ha^{-1}, and 1.31 AU·ha^{-1} from 2010 to 2016. Additionally, the simulation results were not ideal in 2013 and 2014 based on the low R^2 values between GI and NDVI, which may have been due to the higher-than-average precipitation conditions during the growing seasons in those years.

4. CONCLUSION AND DISCUSSION

Previous studies have successfully identified the signals of grazing impacts on grassland using remote sensing data (Numata et al., 2007), and some studies suggested that no direct relationship could be established between the development of vegetation cover and animal-based GI at the community level (Röder et al., 2008). However, NDVI adequately reflects the interactions associated with the climate-plant-animal relationship; thus, it can be used to characterize the temporal evolution of the green biomass in natural grassland (Junges et al., 2016). The simulation results based on NDVI inversion were generally good based on accuracy verification; however, the values were underestimated when the GI exceeded 0.96 AU·ha^{-1}. This problem can be solved by increasing the interval of the grazing gradient.

The growth of vegetation was affected by climatic conditions. The simulation accuracy decreased as the precipitation during the growing season increased because vegetation differences were small when high precipitation occurred in the arid area. Among the climatic variables in arid and semi-arid environments, precipitation variability has been found to be the primary determinant of vegetation dynamics (Paudel and Andersen, 2010), and a previous study found that most of the variation in production (75%) was explained by growing season precipitation at both grazed and un-grazed sites (Yang et al., 2012). This finding is consistent with those of this paper.
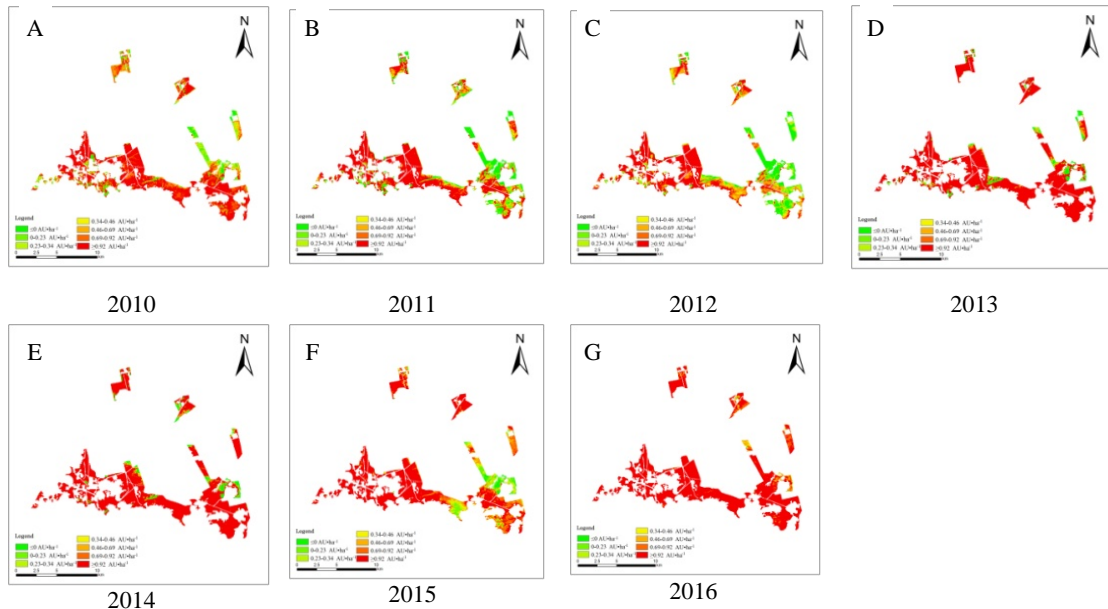
Fig. 7. Map of the grazing intensity in the study area from 2010 to 2016(A, B, C, D, E, F, and G)

The average area of reasonable grazing was only 4.89% of the total area from 2010 to 2016, and the area of heavy grazing was 83.43% of the total area, while the lightly grazed area was only 11.68% of the total area. The heaviest grazing in the study period was observed in 2016, when heavily grazed areas accounted for 98.84% of the total area. The lightest grazing in the study period occurred in 2012, when the heavily grazed area accounted for 64.67% of the total area. Most of the study area was heavily grazed, except a few pastures with rational utilization, and continuous grazing often occurred for many years without cultivation. Both the GI and grazing management system are key factors that affect grassland vegetation (Ren et al., 2015). Grazing patterns and the GI must be adjusted to ensure the sustainable utilization of grassland, and such adjustment methods include rotational grazing, rest grazing, etc.

REFERENCES

Green, S., Cawkwell, F., Dwyer, E., 2016. Cattle stocking rates estimated in temperate intensive grasslands with a spring growth model derived from MODIS NDVI time-series. International Journal of Applied Earth Observation and Geoinformation.52, 166-174.

Harris, R. B., 2010. Rangeland degradation on the Qinghai-Tibetan plateau: A review of the evidence of its magnitude and causes. Journal of Arid Environments.74(1), 1-12.

Hoffmann, C., Giese, M., Dickhoefer, U., Wan, H. W., Bai, Y. F., Steffens, M., Liu, C. Y., Butterbach-Bahl, K., Han, X.G., 2016. Effects of grazing and climate variability on grassland ecosystem functions in Inner Mongolia: Synthesis of a 6-year grazing experiment. Journal of Arid Environments.135, 50-63.

Hunt, E. R., Miyake, B.A., 2006. Comparison of stocking rates from remote sensing and geospatial data.Rangeland Ecology & Management. 59(1),11-18.

Junges, A. H., Bremm, C., Fontana, D. C., de Oliveira, C. A. O., Schaparini, L. P., Carvalho, P. C. D., 2016. Temporal profiles of vegetation indices for characterizing grazing intensity on natural grasslands in Pampa biome. Scientia Agricola. 73(4), 332-337.

Kawamura, K., Akiyama, T., Yokota, H., Tsutsumi, M., Yasuda, T., Watanabe, O., Wang, S. P., 2005.Quantifying grazing intensities using geographic information systems and satellite

remote sensing in the Xilingol steppe region, Inner Mongolia, China.Agriculture Ecosystems & Environment. 107(1), 83-93.

Kelliher, F. M., Henderson, H. V., Cox, N. R., 2017. The uncertainty of nitrous oxide emissions from grazed grasslands: A New Zealand case study.Atmospheric Environment.148, 329-336.

Li, F., Zheng, J. J., Wang, H., Luo, J. H., Zhao, Y., Zhao, R. B., 2016.Mapping grazing intensity using remote sensing in the Xilingol steppe region, Inner Mongolia, China.Remote Sensing Letters. 7(4), 328-337.

Numata, I., Roberts, D. A., Chadwick, O. A., Schimel, J., Sampaio, F. R., Leonidas, F. C., Soares, J. V., 2007. Characterization of pasture biophysical properties and the impact of grazing intensity using remotely sensed data. Remote Sensing of Environment. 109(3), 314-327.

Paudel, K. P., Andersen, P., 2010. Assessing rangeland degradation using multi temporal satellite images and grazing pressure surface model in Upper Mustang, Trans Himalaya, Nepal.Remote Sensing of Environment. 114(8), 1845-1855.

Ren, H. Y., Han, G. D., Ohm, M., Schonbach, P., Gierus, M., Taube, F., 2015. Do sheep grazing patterns affect ecosystem functioning in steppe grassland ecosystems in Inner Mongolia? Agriculture Ecosystems & Environment.213, 1-10.

Ren, J. Z., Hu, Z. Z., Zhao, J., Zhang, D. G., Zhang, D. G., Zhang, D. G., 2008. A grassland classification system and its application in China.Rangeland Journal. 30(2), 199-206.

Röder A., Udelhoven, T., Hill, J., del Barrio, G., Tsiourlis, G., 2008. Trend analysis of Landsat-TM and -ETM+ imagery to monitor grazing impact in a rangeland ecosystem in Northern Greece.Remote Sensing of Environment.112(6), 2863-2875.

Yan, R. R., Xin, X. P., Yan, Y. C., Wang, X., Zhang, B. H., Yang, G. X., Liu, S. M., Deng, Y., Li, L. H., 2015. Impacts of Differing Grazing Rates on Canopy Structure and SpeciesComposition in Hulunber Meadow Steppe.Rangeland Ecology & Management. 68(1), 54-64.

Yan, R. R., Xin, X. P., Zhang, B. H., Yan, Y. C., Yang, G. X.,2010. Influence of Cattle Grazing Gradient on Plant Community Characteristics in Hulunber Meadow Steppe. Chinese Journal of Grassland, 32(3), 62-67.

Yang, X. H., Guo, X. L., Fitzsimmons, M., 2012.Assessing light to moderate grazing effects on grassland production using satellite imagery.International Journal of Remote Sensing.33(16), 5087-5104.

Improvement of the T$_S$-NDVI feature space of the TVDI method on spatio-temporal variation drought monitoring in karst areas

Hongbo Yan[1,2]，Guoqing Zhou[*2]， ，Fengfeng Yang [3]， Xianjian Lu[1,2]

[1]*College of Geomatics and Geoinformation, Guilin University of Technology, Guilin, China; 2009019@glut.edu.cn*

[2] *Guangxi Key Laboratory of Spatial Information and Geomatics, Guilin University of Technology, Guilin, China; gzhou@glut.edu.cn*

[3] *Hebei Research Institute of Construction & Geotechnical Investigation Co., Ltd., Shijiazhuang; ffengyang2018@yeah.net*

ABSTRACT: The temperature vegetation dryness index (TVDI) is an effective optical remote sensing method to monitor regional surface soil moisture status. However, due to the disturbance of multiple factors, the correlation coefficient of the dry and wet edge of the Ts-NDVI space of the traditional TVDI method is quite low and unstable in karst areas. Thus, this paper tried to improve the accuracy of the TVDI method by adding DEM correction to the Ts-NDVI feature space to monitor soil moisture in the karst area of Guangxi, China. After DEM correction to the Ts-NDVI feature space of the TVDI method, the change rules of the dry and wet edge correlation coefficients with NDVI values were obtained using multiple correlation analysis. The correlation coefficient of the dry edge with the increasing of NDVI value presents the two parabola forms of distribution while the wet edge correlation coefficient is positively correlated with NDVI, and the accuracy of the Ts-NDVI space of the TVDI method was improved obviously in the study area.

KEYWORDS: *Remote sensing; DEM correction; Surface soil moisture; Ts-NDVI feature space; TVDI; Karst*

1 INTRODUCTION

Surface soil moisture (SSM) is one of the key factors which affect the climate and ecological environment in Karst areas. There is a close relationship between SSM and energy exchange among hydrosphere, atmosphere and biosphere, and SSM has a powerful control on the land surface evapotranspiration, carbon cycle and water migration. What's more, SSM has great influence on the growth of crops, land degradation and vegetation cover, etc. Study on SSM of the Karst area is of great importance to the drought and flood disaster monitoring, evaluation of crop growth and ecological environment problems analysis and solving in Karst areas.

SSM can be measured to some degree by all regions of the electromagnetic spectrum, and SSM retrieval methods can be divided into 2 big categories: optical remote sensing methods and microwave remote sensing methods. Each has its own advantages and disadvantages. Temperature vegetation drought index (TVDI) is one of the most representative optical remote sensing methods put forward by Sandholt (2002), which considered comprehensively the effect of vegetation index (VI) and surface temperature (Ts) on soil moisture, using Ts-NDVI feature space to retrieval SSM. At present, TVDI is the most widely studied and used method for SSM retrieval in optical remote sensing (Kimura, 2007; Hosseini, 2011; Zhang, 2014). Many scholars have carried on research, verification, improvement and perfection to the TVDI

method. For example: Vicente-Serrano et al. (2004) used AVHRR and ETM+ data in the north of Spain to verify the accuracy and applicability of TVDI. Holzman et al. (2014) used MODIS data in four agricultural experimental regions of the Argentine Pampas to verify the accuracy and applicability of the TVDI model. Kimura（2007）improved the fitting method of the dry and wet edge equation of TVDI, and proposed an improved TVDI index. Hosseini et al. (2011) used MODIS data to analyze the soil moisture based on EVI-LST and NDVI-LST, and found that the SSM retrieval accuracy based on EVI-LST was higher. Zhao et al. (2011) improved the TVDI model from multiple perspectives by using different methods. Considering the situation of water shortage in Northwest China, Li et al. (2012) used the modified soil adjusted vegetation index (MSAV) to replace the normalized difference vegetation index (NDVI) for SSM retrieval, and the TVDI method was further improved. However, due to the disturbance of multiple factors, the traditional TVDI method doesn't fit karst areas, and the correlation coefficient of the dry and wet edge of the Ts-NDVI space is quite low and unstable according to the researches. Therefore, this paper aimed to improve the fitting accuracy of the wet and dry edge of the Ts-NDVI space of the TVDI method by adding DEM corrections especially for the Karst area, in order to improve SSM retrieval accuracy in Karst area.

2 MATERIALS AND METHODS

2.1 The study area

Guangxi (20°54′ ~ 26°20′ N, 104°29′ ~ 112°04′ E), located in the southwest of China's coastal areas, covers approximately 236.7 thousand square kilometers (see Fig. 1). It is surrounded by mountains and plateau, north of Nanling Mountains, west of Yunnan Guizhou Plateau and close to south Tropical Oceans. The geographical environment of the study area is complex, with more mountains and less land. Hills and mountains account for 70.8% of the area. The geographical distribution is north high and south low, from northwest to Southeast tilt, and Underground Rivers are developed.
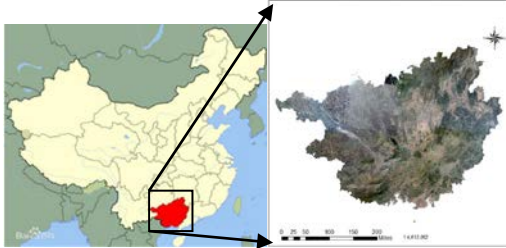
Fig.1 the study area

The study area is a typical subtropical monsoon climate with warm temperature. The average annual precipitation is of 1086 ~ 2755mm but uneven distributed. The soil types in Guangxi are mainly ferrisol, which is widely distributed in the subtropical regions of the world. The study area of Guangxi has a typical Karst landform distribution, with karst mountain areas of 9.8×104 km², accounting for 41% of the whole region. In the slope soil region of Karst, because the soil is shallow and infiltration performance is strong, the surface runoff of the slope is very little. Thus the SSM distribution is not directly proportional to the rainfall.

2.2 data sets

(1) MODIS/Terra data products: The 3rd level MODIS/Terra LST, NDVI and reflectance data products (1-km MOD11A2, 1-km MOD13A2 and 0.5-km MOD09A1) included in the study are obtained from the United States Geological Survey (USGS), download from **http://glovis.usgs.gov/**. The MOD11A2 product (global 8-day 1 km surface temperature/emissivity data), MOD13A2 product (global 1 km 16-day vegetation index data) and MOD09A1 product (global 0.5 km 8-day reflectance data) include the data from February to April and August to October of 2009. To unify the resolution, the 16-day surface temperature/emissivity data are calculated from the mean values of the 8-day data.

(2) DEM data: ASTER GDEM -v2 data is selected which is the product of the new generation earth observation satellite of Terra by NASA. The data covers all land areas from latitude of 83°N to 83°S, and the elevation accuracy is 30 meters. There are 38 images in the study area of Guangxi. The data was obtained from the website of **http://www.gscloud.cn.**

2.3 The method

2.3.1. The traditional TVDI model

Land surface temperature (Ts) and vegetation index (VI) are significantly negatively correlated, and the slope and intercept of the Ts / NDVI diagram differed with types of vegetation coverage in the same atmospheric and surface moisture conditions, and this is the Ts-NDVI feature space (Lambin and Ehrlich., 1996) (Fig.2).
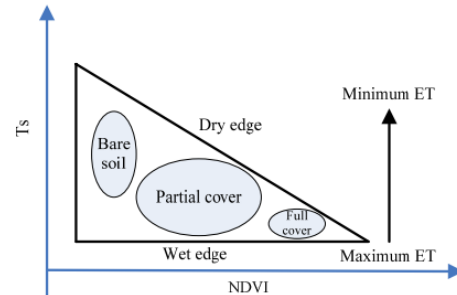
Fig.2 The ideal Ts-NDVI triangle space

On this basis, TVDI was proposed by Sandholt in 2002 for SSM retrieval, which can be expressed as follows:

$$TVDI = (T_S - T_{S\,min})/(T_{S\,max} - T_{S\,min}) \quad (1)$$

In Formula (1), T_S represents the surface temperature of any pixel, $T_{S\,min}$ indicates the lowest surface temperature in the same NDVI, and $T_{S\,max}$ represents the highest surface temperature in the same NDVI.

$$T_{S\,min} = (a_1 + b_1 NDVI) \quad (2)$$

$$T_{S\,max} = (a_2 + b_2 NDVI) \quad (3)$$

Formula (2) and (3) are called wet edge equation and dry edge equation respectively. a_1 and b_1 are coefficients of the wet edge equation, and a_2 and b_2 are coefficients of the dry edge equation. According to the principle of TVDI, the bigger the TVDI value, the closer to the dry edge of the NDVI/Ts feature space, and the less SSM, and vice versa.

2.3.2. Topographic correction to the TVDI model

SSM retrieval using TVDI method is mainly affected by the two factors of surface temperature and

vegetation coverage. However, other factors such as the topography and atmospheric conditions will cause a certain impact on the SSM retrieval accuracy. In this paper, the ground elevation were used to correct the temperature in order to effectively eliminate the impact of solar radiation and atmospheric background differences.

The elevation correction model formula is as follows:

$$T_2 = T_1 + m_1 \cdot H \tag{4}$$

In formula (4), T_2 represents the modified surface temperature, T_1 represents the surface temperature before correction, m_1 represents the level affected by elevation, usually with the constant of -0.6km/ºC，H represents the DN value of the image and the elevation of each pixel.

3. DATA PROCESSING AND ANALYSIS

MODIS data of the study area in the year of 2009 (12 groups) were processed, using the software platforms of ENVI5.1 and MRT (MODIS Reprojection Tool). ENVI5.1 and MRT were used to preprocess MODIS images, including extraction, mosaic, projection and resampling, etc. In the preprocessing procedure, bilinear interpolation method was used in resampling for 1000m resolution, and the Lambert Azimuthal was selected in the projection mode. The correlation between NDVI and Ts, noise removal and elevation data processing of ASTER GDEM V2 were dealt with IDL programming. The surface temperature Ts was obtained by the method of split window algorithm using band 31 and 32 of the MODIS data.

3.1 The traditional Ts-NDVI space

The traditional Ts-NDVI space can be obtained according to formula (1) to formula (3) in section 2.3, and the results are as follows (see table 1, table 2 and Fig.3).

As can be seen from table 2, the relative coefficient of the wet edge in quite low, especially in August the correlation coefficient R^2 is only 0.34 (Fig. 3).

3.2 Topographic correction to the Ts-NDVI space

The low fitting correlation coefficient of the wet edge in the traditional Ts-NDVI feature space of the TVDI method has direct relation with Karst landform, which makes rain infiltration rate fast, resulting the SSM retrieval by TVDI model is not consistent with the actual soil moisture after rainfall, and the retrieval model distorted. By the addition of topographic correction in the TVDI method, the low correlation coefficient of the wet edge can be improved effectively, and the SSM retrieval accuracy can be improved.

Table1. The dry edge fitting equations of the Ts-NDVI space

Time	Fitting equation	correlation coefficient(R^2)
Feb.2009	y=-16.4002x+312.380	0.85
Mar.2009	y=-21.0066x+315.675	0.90
Apr.2009	y=-26.6305x+324.940	0.95
Aug.2009	y=-17.9828x+321.198	0.89
Sep.2009	y=-24.0018x+321.443	0.89
Oct.2009	y=-13.6965x+312.947	0.92

Table2. The wet edge fitting equations of the Ts-NDVI space

Time	Fitting equation	correlation coefficient(R^2)
Feb.2009	y=15.8921x+276.582	0.57
Mar.2009	y=26.7310x+263.809	0.77
Apr.2009	y=42.4722x+255.526	0.75
Aug.2009	y=8.60516x+284.003	0.34
Sep.2009	y=10.8663x+283.655	0.71
Oct.2009	y=8.33422x+284.514	0.57
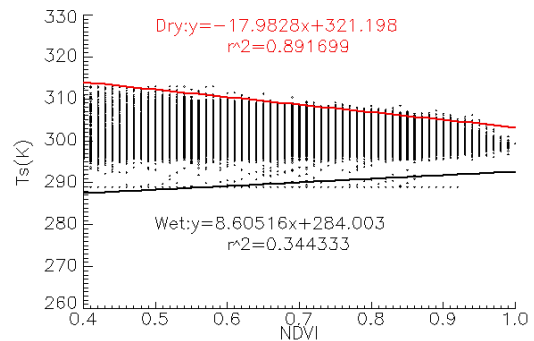
Fig. 3 The traditional Ts-NDVI space in Aug. 2009

According to the formula (1) to (4) in section 2.3, DEM topographic correction was added to T_S, and the fitting coefficients of the dry and wet edge after modified were obtained. Take the data in Oct.2009 for example (Fig.4 and Fig.5). It is indicated from figure 4 that the correlation coefficient curve of the dry edge after DEM correction showed a parabolic rise with the increase of the NDVI values, while that of the wet edge showed a significant increase in the low vegetation area, and decreased with the increase of the vegetation coverage (Fig.5). The correlation coefficient is highest in NDVI=0.3 then decreased gradually according to Fig.5. It shows a high correlation between topographic correction and the fitting coefficients of the wet edge in low vegetation areas.
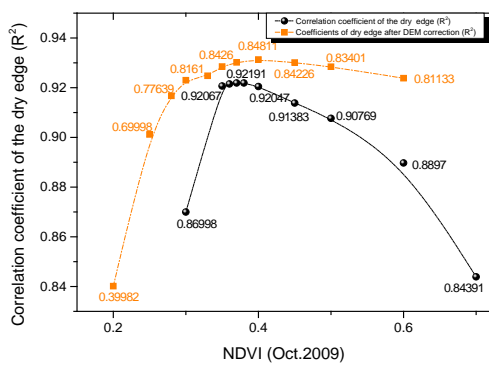
Fig.4 Fitting coefficients of the dry edge before and after DEM correction
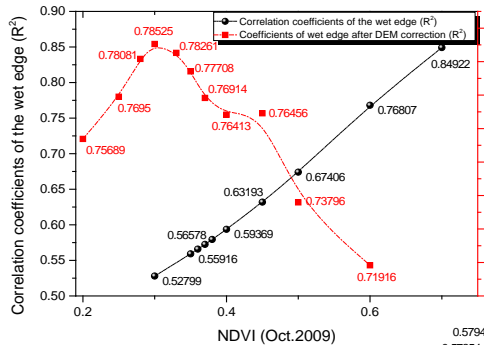
Fig.5 Fitting coefficients of the wet edge before and after DEM correction

It can be concluded from Fig.4 and Fig.5 that: the fitting coefficient of the wet edge can be improved obviously by adding DEM correction in the low vegetation cover areas, but with the increase of vegetation coverage, the applicability decreased.

4 CONCLUSIONS

TVDI is an effective index from optical remote sensing imagery as retrieval surface soil moisture. However, the traditional Ts-NDVI space of the TVDI method does not fit karst areas. In order to improve the accuracy of SSM retrieval through TVDI in Karst areas, the Ts-NDVI feature space of TVDI was analyzed and improved by adding DEM correction to modify the surface temperature, and good results were obtained. The change rules of the dry and wet edge correlation coefficients with NDVI values were obtained using multiple correlation analysis: The correlation coefficient of the dry edge with the increasing of NDVI value presents the two parabola forms of distribution. The wet edge correlation coefficient is positively correlated with NDVI, and the accuracy was improved obviously. The implementation process of the TVDI method has been optimized after DEM correction.

REFERENCES

Holzman, M.E., Rivas, R. and Piccolo, M.C., 2014, Estimating soil moisture and the relationship with crop yield using surface temperature and vegetation index. Int. J. Appl. Earth Obs. Geoinf., 8, 181-192.

Hosseini,M., and Saradjian,M.R., 2011, Muft-index-based soil moisture estimation using MODIS images. International Journal of Remote Sensing, 32(21), 6799-6809.

Kimura, R., 2007, Estimation of moisture availability over the Liudaogou river basin of the Loess Plateau, Using new indices with surface temperature. Journal of Environments, 10, 1-10.

Lambin, E. F., and D. Ehrlich., 1996, The surface temperature –vegetation index space for land cover and land-cover change analysis. International Journal of Remote Sensing, 17, 463- 487.

Li, X., Song, X. and Zhou, X., 2012, Study on methods of monitoring soil moisture by remote sensing in semi-arid areas. Geography and Geo-Information Science, 26(1), 90-93.

Sandholt, I., Rasmussen K, and Andersen J., 2002, A simple interpretation of the Surface temperature/ vegetation index space for assessment of surface moisture status. Remote sensing of environment, 79(2), 213-224.

Vicente-Serrano, S. M., Pons-Fernández, X. and Cuadrat-Prats, J.M., 2004, Mapping soil moisture in the central Ebro river valley (northeast Spain) with Landsat and NOAA satellite imagery: a comparison with meteorological data. Int. J. Remote Sensing, 25 (20), 4325-4350.

Zhao, J., Zhang, X. and Liao, C. et al., 2011, TVDI based soil moisture retrieval from remotely sensed data over large arid areas. Remote Sensing Technology and Application, 26(6), 742-750.

Zhang, D., Tang, R., Zhao, W. et al., 2014, Surface soil water content estimation from thermal remote sensing based on the temporal variation of land surface temperature. Remote Sensing, 6 (4), 3170-3187.

Theoretical basis for retrieval of leaf area index from normalized derivatives of red-edge reflectance with application to Sentinel-2

Richard Fernandes[1], Khalid Omari[1], Francis Canisius[1], Nadia Rochdi[2]
[1]*Canada Centre for Remote Sensing, Natural Resources Canada*
[2]*Alberta Terrestrial Imaging Centre*
Richard.fernandes@canada.ca, Khalid.omari@canada.ca, francis.canisius@canada.ca,
nadia.rochdi@atic.uleth.ca

ABSTRACT - *The relationship between leaf area index and normalized derivative of red-edge reflectance is derived and evaluated using simulated reflectance using the FLIGHT radiative transfer model and measurements over corn and soybean fields. The relationship applies within the red-edge between 710nm and 760nm, where sensitivity to the ratio of leaf reflectance to albedo is small. An algorithm for leaf area index retrieval using Sentinel 2 is developed using this relationship. The algorithm performs comparably to published empirical regression with the measured dataset (i.e. RMSE 0.68) with weak sensitivity to factors such as acquisition geometry, clumping, leaf angle distribution and leaf chlorophyll concentration.*

1 INTRODUCTION

Leaf area index (L) is defined as half the live foliage surface area per unit horizontal ground area. LAI is an essential climate variable and routinely derived using both empirical and physically based algorithms applied to multispectral satellite imagery. Measurements suggest strong (e.g. standard error 0.58), species and chlorophyll independent relationships between L and simple transformations of the normalized difference of reflectance in the red-edge (i.e. 690nm to 800nm) (Dash and Curran, 2004; Gitelson, 2005; Vina et al. 2011).

This paper develops a theoretical basis for the relationship between LAI and the normalized derivative of red-edge reflectance (N) given by

$$N(\lambda, \Omega_0, \Omega_1) = \frac{\partial ln R(\lambda, \Omega_0, \Omega_1)}{\lambda} \quad (1)$$

where R is canopy bi-directional reflectance for directions Ω_0, Ω_1 at wavelength λ. The basis is then used to develop and algorithm for retrieving LAI from red-edge bands corresponding to the Sentinel 2 Multispectral Imager and evaluated using measurements over corn and soybean fields.

2 THEORY

2.1 Black Soil Canopies
Assuming black soil and spatially uniform foliage single scattering albedo (ω), canopy reflectance is given by (omitting angles) (Huang et al. 2007):

$$R_{bs}(\lambda) = i_0 \rho_1(\lambda) \omega(\lambda) \frac{1 - p_2(\lambda)\omega(\lambda)\Delta(\lambda)}{1 - p_2(\lambda)\omega(\lambda)} \quad (2)$$

where i_0 is canopy interceptance, ρ_k, p_k are canopy escape and recollision probabilities after k^{th} scattering respectively and assuming these probabilities are constant for $k \geq 3$:

$$\Delta = 1 - \frac{p_1}{\rho_1}\frac{\rho_2}{p_2} - \frac{p_1}{\rho_1}(\rho_3 - \rho_2)\omega - \frac{p_1}{\rho_1}(p_3 - p_2)\omega^2 \quad (3)$$

The wavelength dependence of ρ_1 is determined solely by ζ, the ratio of foliage reflectance to ω (Stenberg and Manninen, 2015). Figure 1 indicates that between 710nm and 760nm, $\left|\frac{\partial ln\omega}{\lambda}\right| \gg \left|\frac{\partial ln\zeta}{\lambda}\right|$ so that combining Equations 1 and 2 gives: (4)

$$N_{bs} = \frac{\partial ln\omega}{\partial \lambda}\left[\frac{1}{1 - p_2\omega} - \frac{p_2\omega}{1 - \Delta p_2\omega}\left(\Delta + \omega\frac{\partial\Delta}{\partial\omega}\right)\right] \quad (4)$$

To relate N_{bs} to L from Lewis et al. (2007):

$$p_2 = a_0(\zeta, LAD, \Phi) + a_1(\zeta, LAD, \Phi)p_\infty(\Phi) \quad (5)$$

where a_0, a_1 are constants, *LAD* is leaf angle distribution , Φ is clumping index and (Stenberg, 2007):

$$p_\infty = 1 - \frac{\int_0^{\frac{\pi}{2}}[1 - \exp(-\Phi L)]sin\theta cos\theta d\theta}{L} \quad (6)$$

Equations 4, 5, 6 provide a mathematical relationship between N_{bs} and L termed the 'complete' model.

2.2 Multispectral Application
For a contribution R_s from soil collided fluxes:

$$N_{bs} = N\frac{1 - \frac{\partial R_s}{\partial \lambda}/\frac{\partial R}{\partial \lambda}}{1 - R_s/R} \quad (7)$$

Solving Equations 4,5 and 6 for L requires , ρ_k , p_k for $1 \leq k \leq 3$, ω, Φ, a_0, a_1. These requirements are

onerous for multi-spectral data where the number of wavelengths where N is observed is limited.

Simulations from PROSPECT5b (Feret et al., 2008) over a wide range of leaf parameters indicates that between 710nm and 760nm, ζ is primarily determined by the 'n;' parameter related to leaf structure while ω is primarily determined by leaf chlorophyll and dry matter concentrations (C_{ab}, C_m).
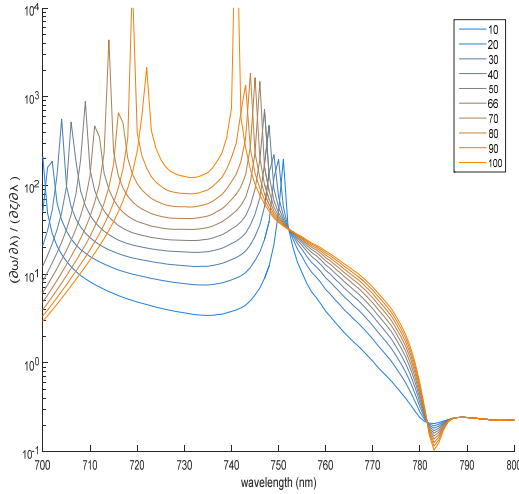
Figure 1. $(\partial \ln\omega/\partial\lambda)/(\partial \ln\zeta/\partial\lambda)$ based on PROSPECT5b
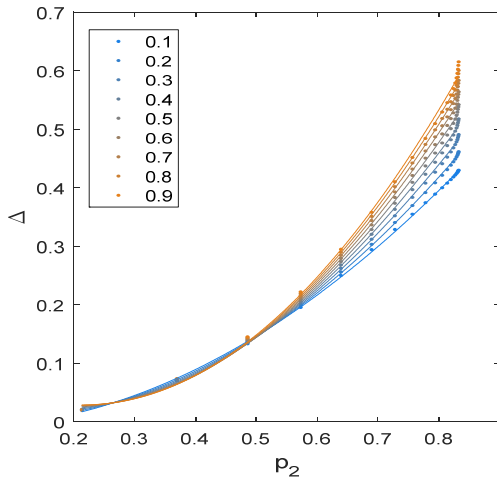
Figure 2. Relationship between Δ and $\Delta + \omega\frac{\partial\Delta}{\partial\omega}$ and p2 for $\zeta = 0.5$.

For homogenous canopies with horizontal bi-Lambertian leaves ρ_k , p_k can be expressed as analytic functions of L and ζ . In this case, as Figure 2 indicates, given ω both Δ and $\Delta + \omega\frac{\partial\Delta}{\partial\omega}$ can be approximated by a single quadratic:

$$\Delta(n,\omega) \approx \Delta(n,\omega) + \omega\frac{\partial\Delta}{\partial\omega} \approx b_0(n,\omega) + b_1(n,\omega)p_2 + b_2(n,\omega)p_2^2 \qquad (8)$$

Combing Equation 4 and 8 allows the relationship N_{bs} and p_2 to be parameterzied only by n, C_{ab} and C_m

$$N_{bs} = \frac{\partial \ln\omega}{\partial\lambda}\sum_{k=0}^{\infty}(1 - \Delta(n,\omega)^k)p_2^k\omega^k \qquad (9)$$

Equation 9 is termed the 'approximate' model

3 VALIDATION

3.1 Black Soil Theory

Simulations from the FLIGHT radiative transfer model (North, 1996) coupled with PROSPECT5b based on a wide range of parameters (Table 1) corresponding to homogenous canopies were used to validate the black soil theory. For each group of simulations sharing the same n, C_{ab} and C_m, Equation 4 of the complete model was inverted to estimate p_2 using the FMINCON routine in MATLAB. Additionally, the approximate model was used to estimate both p_2 and L after calibrating a_0, a_1 over all simulations in a group. Again, the FMINCON routine was used to solve for p_2 and a_0, a_1 in Equations 9 and 3 respectively

Table 1. FLIGHT/PROSPECT5 parameter indicated as start value:step:end value.

Parameter	Units	Range
Ω_0	deg.	10:10:60
Ω_1	deg.	0
L	-	0.5:0.5:10
$diam.$	cm	1,5,10
LAD	-	Planophile, Erectophile, Spherical
C_{ab}	μgcm⁻²	10:10:100
C_{ar}	μgcm⁻²	0.2*C
C_w	gcm⁻²	0.01
C_{dm}	gcm⁻²	0.002:0.0036:0.02
C_{bp}	-	0:0:0
n	-	1:0.3:2.5

3.2 Measurements

The multispectral application was validated using measurements from the CALMIT dataset reported in Gitelson et al. (2005) and Vina et al. (2011). The data consisted of in-situ measurements of (L, R ,soil reflectance ρ_s, C_{ab}, leaf reflectance R_l) at 3 fields over 3 growing seasons resulting in a total of 190 corn and 104 soybean samples. Both Φ and n were estimated from studies of similar crops assuming they did not change over time (Haboudane et al., 2002; Liu et al. 2013). C_m, dry matter, and ω were estimated by inverting PROSPECT5 to match R_l given C_{ab} and n.
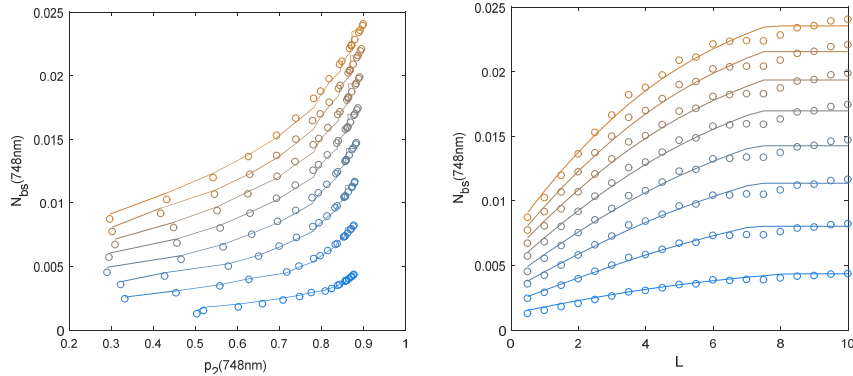
Figure 3. FLIGHT/PROSPECT5 (circles) for leaf chlorophyll concentrations from 10 µgcm^{-2} (blue) to 80 µgcm^{-2} (orange) and (lines) fitted approximate models.

The theory was validated using two different approaches for estimating p_2 The first approach inverted the approximate model (Equation 9) using measured values of leaf optical properties to estimate p_2 using a single red-edge wavelength for all data. In practice leaf optical properties and soil reflectance are not known. N_{bs} was estimated by Equation 7 using:

$$R_s \approx exp(-2\Phi L)\rho_s \qquad (10)$$

with measured values of Φ, L and ρ_s.

In both cases a_0, a_1 were hold-out calibrated data for the same species but with prior estimates Φ.

In the second approach the approximate model was inverted simultaneously using two wavelengths, closely approximated by the normalized difference of Sentinel2 Multispectral Imager Bands 4 and 5 (for 728nm) and 5 and 6 (for 748nm), to estimate both leaf optical properties and p_2 given N. To avoid soil correction, a polynomial relationship was fit between p_2 and N for dense canopies (initial estimate of p_2>0.5) and then used with hold-out measurements to calibrate a relationship between L and N that was then applied for all targets.

4 RESULTS

4.1 Black Soil Theory

Figure 3 shows results for a typical red-edge wavelength from which it is observed:

i)   The relationship between N_{bs} and L is concave saturating at ≈ 6 .

ii) The relationship between N_{bs} and L shows substantial sensitivity to C_{ab}.

iii) The relationship between N_{bs} and p_2 is approximately quadratic before saturation.

iv) The approximate model provides good agreement with simulations of N_{bs} and L.

4.2 Measurements

Figure 4 shows results validating the approximate theory using multispectral measurements for one wavelength (735nm). For both species, L is retrieved with comparable accuracy (root mean square error (rmse) 0.31 for corn, 0.10 for soybean).

Figure 5 shows results validating the multispectral application of the approximate theory for Sentinel 2 MSI bands. The retrieval of p_2 follows the relationship with L suggested by Equation 4 but shows evidence of convergence to a single minimum value of p_2. L is retrieved with an rmse of 0.31 for corn and 0.10 for soybean.

These results suggest that the theoretical basis of the simplified model applies in the red-edge and may be useful for developing retrieval algorithms for L.

5 CONCLUSIONS

The normalized derivative of bi-directional reflectance measurements in the red-edge was shown to be related to both L and leaf chlorophyll concentration using an analytical model. The model first relates the second recollision probability, p_2, to the black soil normalized derivative and then relates p_2 to L . The model was verified with both simulated and measured datasets leading to the conclusion that relationship between the normalized red-edge derivative and L is, in general, sensitive to leaf chlorophyll concentration.

The analytical model was used to develop a proof-of-concept inversion algorithm using two red-edge normalized derivatives. The algorithm retrieved L with accuracies similar to the uncertainty of in-situ measurements but required calibration of the p_2 versus L relationship by species. Further studies are required to determine the sensitivity of this calibration to canopy architecture and to verify the end-to-end performance of the algorithm.
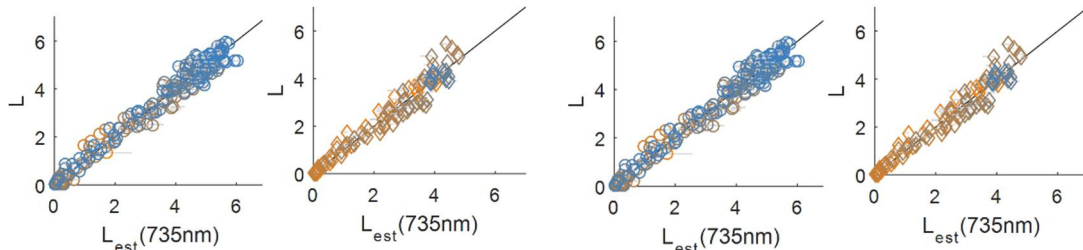
Figure 4. In-situ L versus estimated corn (left) and soybean (right) L using approximate model with observed ω and ρ$_s$. Colours indicate leaf chlorophyll from 10 µgcm^{-2} (blue) to >60 µgcm^{-2} (orange).

Figure 4. In-situ *L* versus estimated corn (left) and soybean (right) *L* using approximate model with observed ω and ρ_s. Colours indicate leaf chlorophyll from 10 µgcm^{-2} (blue) to >60 µgcm^{-2} (orange).
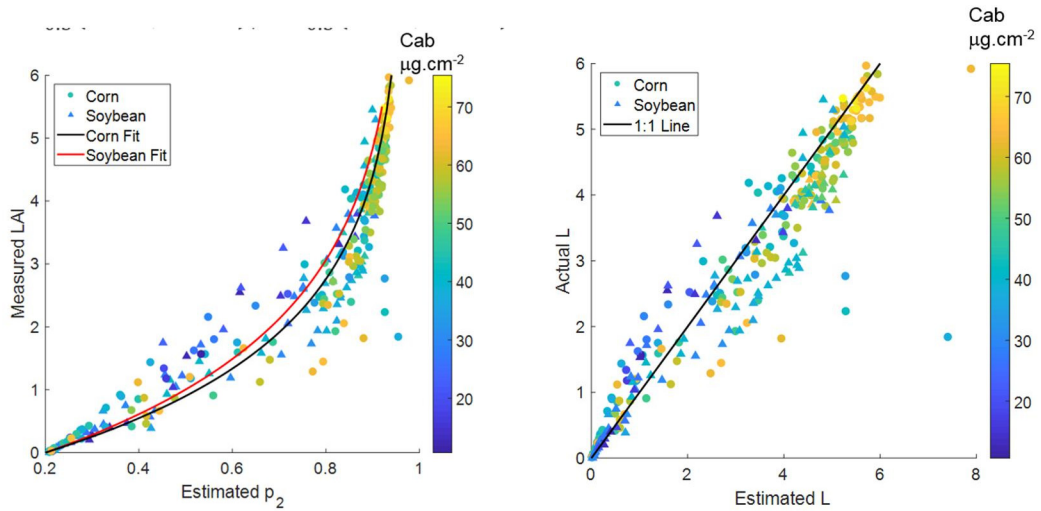
Figure 5. In-situ *L* versus estimated p_2 (left) and *L* (right) for both corn and soybean canopies based on inverting the approximate model using two red-edge bands without knowledge of ω or ρ_s.
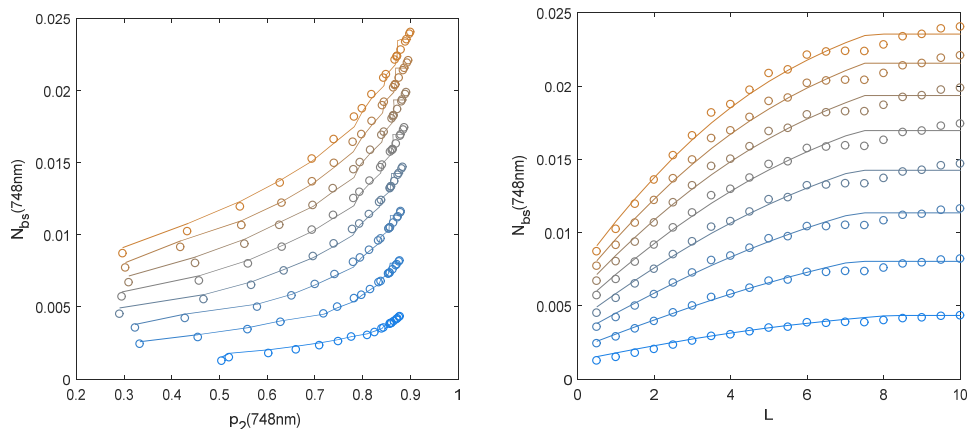
Figure 6. FLIGHT/PROSPECT5 (circles) for leaf chlorophyll concentrations from 10 µgcm^{-2} (blue) to 80 µgcm^{-2} (orange) and (lines) fitted approximate models.
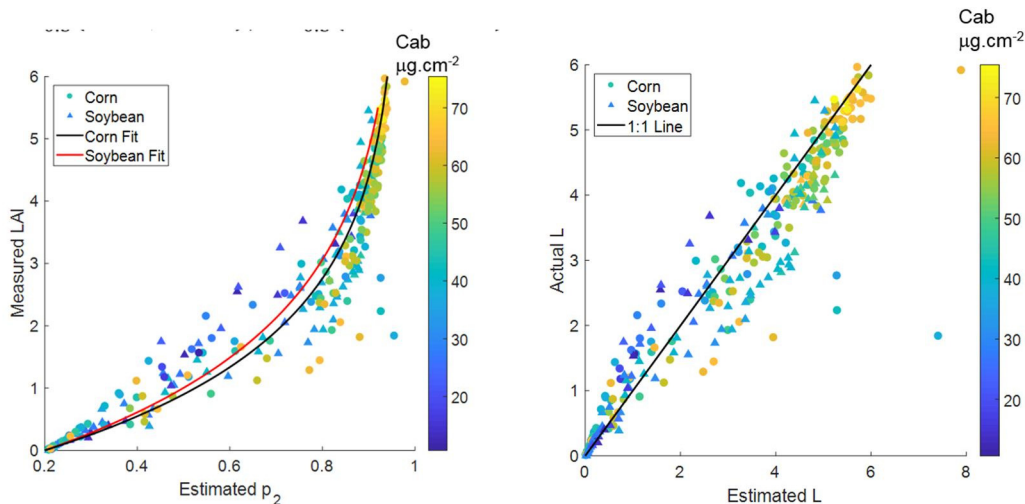
Figure 7. In-situ L versus estimated p_2 (left) and L (right) for both corn and soybean canopies based on inverting the approximate model using two red-edge bands without knowledge of ω or $ρ_s$.

6 ACKNOWLEDGEMENTS

7 REFERENCES

Dash, J. and Curran, P.J, 2004, The MERIS terrestrial chlorophyll index. *International Journal of Remote Sensing*, **25**, pp. 5403–5413.

Féret J.B., François C., Asner G.P., Gitelson A.A., Martin R.E., Bidel L.P.R., Ustin S.L., le Maire G., & 675 Jacquemoud, S, 2008, PROSPECT-4 and 5: advances in the leaf optical properties model separating photosynthetic pigments. *Remote Sensing of Environment*, **112**, pp. 3030-3043.

Gitelson, A.A., Viña, A., Ciganda, V., Rundquist, D.C. and Arkebauer, T.J, 2005, Remote estimation of 691 canopy chlorophyll content in crops. *Geophysical Research Letters*, **32**, L08403, http://dx.doi.org/10.1029/2005GL022688.

Haboudane, D., Miller, J. R., Tremblay, N., Zarco-Tejada, P. J., and Dextraze, L. ,2002, Integrated narrow-band vegetation indices for prediction of crop chlorophyll content for application to precision agriculture. *Remote Sensing of Environment*, **81**, pp. 416-426.

Huang, D., Knyazikhin, Y., Dickinson, R.E., Rautiainen, M., Stenberg, P., Disney, M.I., et al., 2007, Canopy 719 spectral invariants for remote sensing and model applications. *Remote Sensing of Environment*, **106**, pp. 106-122.

Lewis, P., Disney, M., Knyazikhin, Y. Quaife, T. and Schull, M, 2007, Modelling canopy reflectance with spectral invariants. In "*Proceedings of the ISPRS Working Group VII/1 Workshop ISPMSRS'07: Physical Measurements and Signatures in Remote Sensing*" March 12-14, 2007 Davos, Switzerland Editor(s): Michael Schaepman, Shunlin Liang, Nikée Groot and Mathias Kneubühler , Volume XXXVI-7/C50.

Liu, J., Pattey, E., and Admiral, S., 2013, Assessment of in situ crop LAI measurement using unidirectional view digital photography. *Agricultural and Forest Meteorology*,**169**, pp. 25-34.

North, P. R. J., 1996, Three-dimensional forest light interaction model using a Monte Carlo method. *IEEE Transactions on Geoscience and Remote Sensing*, **34**, 946.956.

Stenberg, P, 2007, Simple analytical formula for calculating average photon recollision probability in vegetation canopies. *Remote Sensing of Environment* , **109**, pp. 221–224.

Stenberg, P. and Manninen, T, 2015, The effect of clumping on canopy scattering and its directional properties: a model simulation using spectral invariants. *International J. Rem. Sens.,* **36**, pp. 5178-5191.

Viña, A., Gitelson, A.A., Nguy-Robertson, A.L. and Peng, Y, 2011, Comparison of different vegetation 806 indices for the remote assessment of green leaf area index of crops. Remote Sensing of Environment, **15**, pp. 3468-3478

Annual dynamics of shortwave radiation reflected from bare soils in Europe

Jerzy Cierniewski[1], Jakub Ceglarek[1], Cezary Kaźmierowski[1], Jean-Louis Roujean[2]

[1]*Department of Soil Science and Remote Sensing of Soils, Adam Mickiewicz University in Poznań, 61-680 Poznań, Poland*

[2]*Météo-France/CNRS, 31057 Toulouse Cedex, France*

Email addresses: ciernje@amu.edu.pl, jakub.ceglarek@amu.edu.pl, cezark@amu.edu.pl, jean-louis.roujean@meteo.fr

ABSTRACT *Smoothing rough ploughed soils increases their albedo, which results a lower amount of shortwave radiation being absorbed by their surface layer. That surface emits less long-wave radiation, leading to a reduction in its temperature, which in turn can affect the climate. This paper presents a multistage procedure for quantification the annual dynamics of shortwave radiation reflected from air-dried bare soils within arable lands of the European Union (EU) and its associated, Norway and Switzerland. The soils, being in conventional tillage, were treated as bare, formed by a plough (Pd) and a harrow (Hs), when the major crops were planted there. Information about the areas of the soils and periods when they are bare was obtained from vectorised and rasterized geostatistical datasets. This procedure takes into account the spatial diversity of the soils characterized by thousands of reflectance spectra stored in the European Lucas Top Soil Database. These spectra were used to predict the half-diurnal albedo variation of the soils on a given day of the year. The shortwave radiation reaching the examined soils was obtained from satellite data of the SEVIRI instrument. It was found that the maximum of radiation levels reflected from the soils occur between the beginning of April and the end of May. During these periods, the radiation reflected from the soils formed by Pd and Hs can reach about 220 and 250 PJ/d in the western part of the EU, 150 and 190 PJ/d in the central part and up to 280 and 330 PJ/d in the southern part.*

1 INTRODUCTION

The broadband blue-sky albedo of bare soil depends on relatively stable features over time (the content of soil organic matter, iron oxides and carbonates), as well as the states of salinity, moisture and roughness, which change dynamically due to agricultural practices on arable lands (Cierniewski *et al*. 2015). Smoothing rough ploughed soils increases their albedo, which results in a lower amount of shortwave radiation absorbed by their surface layer. That surface emits less long-wave radiation, leading to a reduction in its temperature, which in turn can affect the climate (Desjardins 2010, Farmer and Cook 2013).

This paper presents a multistage procedure that aims to quantify the annual dynamics of shortwave radiation reflected from bare soils within the European Agricultural Region, where its major crops are cultivated. It is assumed that these soils, being in conventional tillage, are bare when the crops are planted until the crops reach the ground cover, which can significantly change the bare soil's reflectance features. The soils are in two extreme roughness states formed by a plough and a smoothing harrow and are air-dried.

2 METHODS

The study area is the European Agricultural Region (EAR) according to the Major World Crop Areas and Climate Profiles (USDA, 1994), limited to the current countries of the European Union (EU) along with its associated countries (Switzerland and Norway). The EAR was analysed as divided into its western (W), central (C), and southern (S) sub-regions (Fig. 1).

In the first stage of the procedure, using digital georeferenced datasets with a resolution of 5x5 arc minutes (Monfreda et al. 2008), it was determined where and in what areas the major crops (barley, wheat, maize, potato, rye, sugar beet and rapeseed) are cultivated in each sub-region. Using datasets from the crop calendar of Sacks et al. (2010), the planting dates of the individual crops was ascertained. Then, using datasets from the National Center for Atmospheric Research (https://ncar.ucar.edu) and the growing degree days (a tool measuring heat accumulation to predict plant development rates), an evaluation was made as to when the selected crops would reach approximately 15% ground cover. It was assumed, as Baumardner et al. (1986) argued, that spectral reflectance from fields with lower crop cover could be treated the same as the reflectance from bare soil.
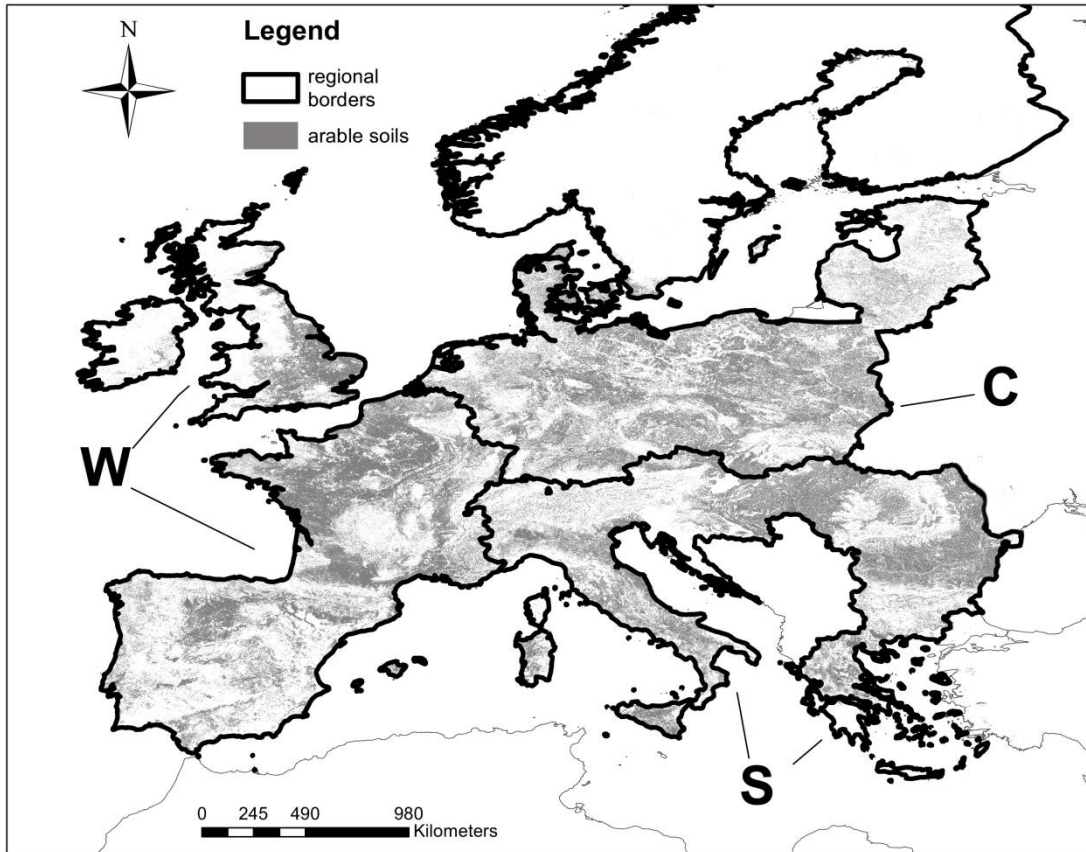
Figure 1. Sub-regions – western (W), central (C) and southern (S) – where arable soils covered by the major crops can be bare.

In the second stage of the procedure, to determine the soil units that the delineated arable areas belong to, a digital soil map (ESDB v2.0 2004), classified as major reference groups according to the World Reference Base for Soil Resources (WRB), was superimposed on the croplands class taken from a land cover map (GlobCover 2009).

In the third stage, the soil units that occupied more than 5% area of the arable soils in a given sub-region were characterized by the reflectance spectra of all the soil samples that were located in their contours. The spectra were obtained from the European *Lucas* Top Soil Database (Tóth et al. 2013).

These average spectra of the analysed sub-regions were used in the fourth stage to calculate the half-diurnal albedo α variation of the bare soils within W, C and S. Their overall soil α level at a given roughness condition under the $\theta_s = 45°$ (α_{45}) was calculated as in the paper proposed by Cierniewski et al. (2017):

$$\alpha_{45} = 0.33 - 0.1099T_{3D} - 5795.4x_{574} - 510.2x_{1087} + 7787.2x_{1355} + 12161x_{1656} + 6932.8x_{698} \qquad (1)$$

where T_{3D} is the roughness index defined as the ratio of the real surface area within its basic unit to its flat horizontal area (Taconet et al. 2007), and x is the reflectance data transformed to its second derivative for a specified wavelength: 574, 698, 1087, 1355 and 1656 nm. Meanwhile, α_{θ_s} under $\theta_s < 75°$ was calculated as:

$$\alpha_{\theta_s} = \alpha_{45}[1 + s_\alpha(\theta_s - 45)], \qquad (2)$$

where s_α expresses the slope of the α increases in this θ_s range:

$$s_\alpha = 0.000000626 + 0.0043HSD^{-1.418}, \qquad (3)$$

where HSD is the roughness index expressing the standard deviation of a soil surface area within its basic unit (Taconet et al. 2007). The half-diurnal α variation of the soil units relative to θ_s, taking into account their

roughness, was expressed in the full θ_s range up to 90° by the formula:

$$\alpha_{\theta_S} = \frac{a + c\theta_S^{0.5}}{1 + b\theta_S^{0.5}}, \qquad (4)$$

where a, b and c are fitting parameters. This equation was individually fitted to the average half-diurnal α distributions of the bare soils, using TableCurve 2Dv5.01software, assuming that each of them was shaped by a plough (Pd) and smoothing harrow (Hs) within W, C and S. It was assumed that the roughness of the soils formed by Pd and Hs was described by HSD values of 25 and 5 mm, and T_{3D} values of 1.5 and 1.05, respectively.

In the fifth stage, the α_{θ_s} distributions of the soils representing W, C and S, originally fixed for every tenth day of the year in the θ_s function, were transformed to the function of solar local time, which allowed the calculation of the average values of the diurnal albedo of the soils (α_d).

In the sixth stage, using 3 channels of the satellite SEVIRI instrument (related to 0.6, 0.8 and 1.6 µm), the amounts of shortwave radiation (Ri_d) reaching three places characterizing W, C and S every day in 2011 (in increments of one hour) in clear and cloudy conditions were determined. These amounts were obtained by a modified method implemented in the Land-SAF project proposed by Gautier et al. (1980) and Frouin et al. (1989). To smooth the impact of highly variable atmospheric conditions the daily Ri_d values for W, C and S were averaged over the year by a non-linear *Erfc Peak* equation implemented in TableCurve 2D v5 software as no. 8008 (Systat software Inc., USA). Finally, Ri_d values were converted to TJ/km^2. Multiplying the bare soil areas within W, C and S by the averaged diurnal albedo of soils formed by Pd and Hs values, as well as Ri values, the diurnal amount of shortwave radiation reflected from the sub-regions throughout the year was estimated (Rr_d).

3 RESULTS AND DISCUSION

It was found that the total soil areas for cultivation of the major crops within W, C and S sub-regions is about 229, 231 and 197 thousands square kilometres, respectively (Fig. 1). Taking into account the Eurostat data from 2013 (ec.europa.eu/eurostat) that the above areas are in the conventional tillage in the proportions: 56%, 69% and 74%, it was determined that the research areas within W, C and S are 128 160, and 146 thousands km^2, respectively.

The share of the WRB major soil groups covering at least 90% of each sub-region is shown in Table 1. *Cambisols* and *Luvisols* have a dominant share, 66% and 56%, in W and C, respectively.

Table 1. The proportion of the WRB major soil group areas within the sub-regions: western (W), central (C) and southern (S).

Soil units	W Area (%)	W No. of contours	C Area (%)	C No. of contours	S Area (%)	S No. of contours
Albeluvisols	4.1	303	4.2	345	–	–
Arenosols	–	–	4.7	407	–	–
Cambisols	43.0	2503	22.4	1386	28.8	1360
Chernozems	–	–	–	–	19.2	254
Fluvisols	8.9	596	9.3	612	10.7	304
Gleysols	–	–	4.2	389	–	–
Leptosols	8.2	627	–	–	3.3	633
Luvisols	22.8	1105	34.0	1429	14.7	715
Phaeozems	–	–	3.1	121	11.1	267
Podzols	–	–	9.9	903	–	–
Regosols	2.9	247	–	–	–	–
Vertisols	–	–	–	–	3.1	107
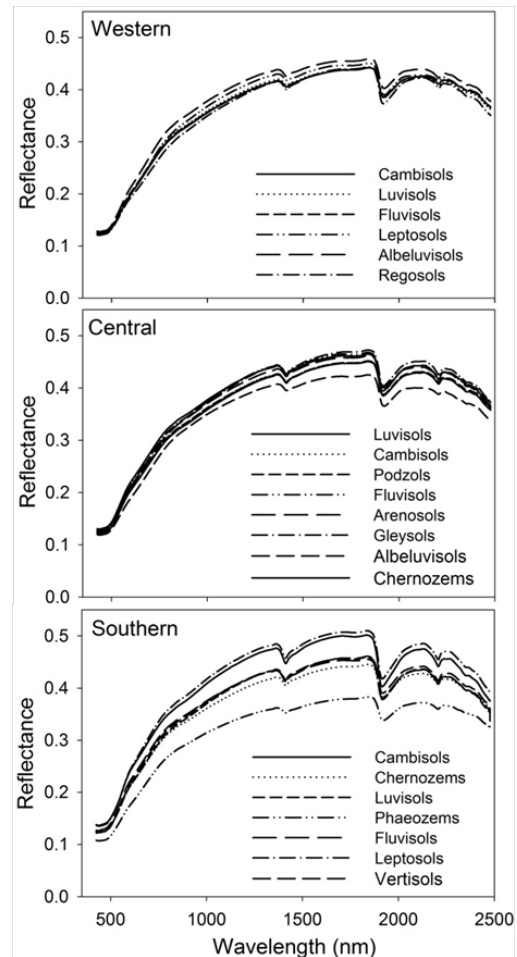
Figure 2. Averaged spectra of the WRB major soil groups within the analysed sub-regions.

Although the proportion of *Cambisols* in S is larger than in W and C, the proportion of *Luvisols* is in third position behind *Chernozems*. Laboratory reflectance spectra relating to 2,482, 2,373, and 968

soil samples taken from W, C and S, respectively, were used to characterize the reflectance features of the soil major groups within these sub-regions. The greatest diversity of the soil spectral reflectance is shown by the averaged major soil groups in S, where their lowest reflectance refers to *Regosols*, and the highest to *Cambisols* (Fig. 2). Meanwhile, the smallest difference in this reflectance is revealed by the main groups in W. The averaged spectra describing all the soils that cover the studied sub-regions clearly show the higher reflectance of S than W and C (Fig. 3). The average diurnal α_d of the soils shaped by Hs is 14-22% higher than the same soils formed by Pd throughout the year within all the sub-regions (Fig. 4a).
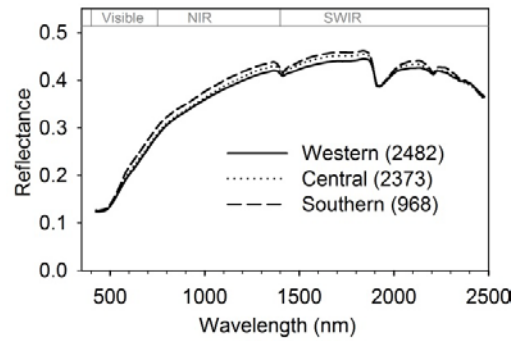
Figure 3. Averaged spectra of all the WRB major soil groups within the analysed sub-regions.
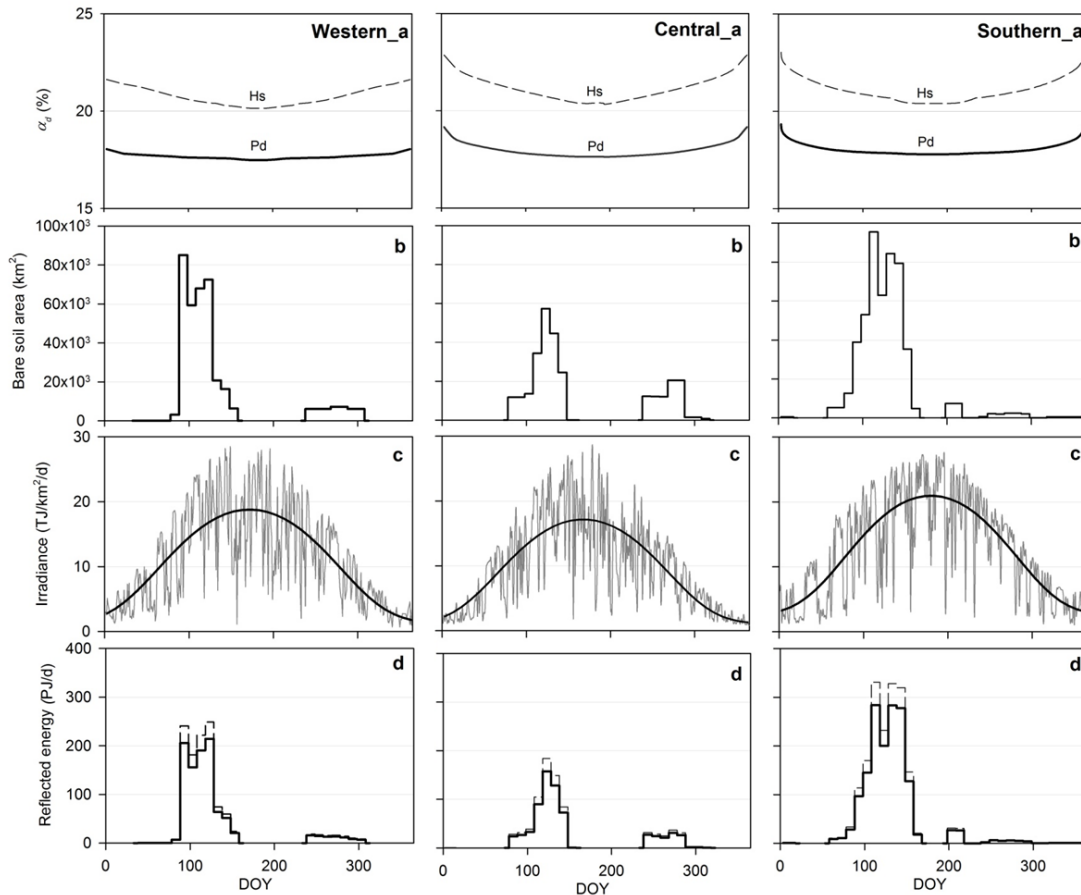
Figure 4. Annual variations in: (a) – average diurnal albedo (α_d) of the averaged bare soils formed by a plough (Pd) and a smoothing harrow (Hs) within the western (W), central (C) and southern (S) sub-regions; (b) – areas of the bare soils within the sub-regions; (c) – real (grey line) and averaged (black line) amount of shortwave radiation (Ri_d) reaching the soils within the sub-regions (d) – real amount of diurnal shortwave radiation reflected from one square kilometre of the soils within the sub-regions (Rrb_d), formed by Pd (black solid line) and Hs (grey dashed line).

Spring peaks of the bare soil areas, about 85,000 and 60,000 km^2, were found within W and C around the 95th day of the year (DOY) (5-April) and the 125th DOY (5-May), respectively (Fig. 4b). The largest spring peak, reaching 95,000 km^2, was established within S around the 110th DOY (20-April). Significantly smaller autumn peaks of the bare soil areas within W, C, and S, reaching 10,000, 20,000 and less than 5,000 km^2, respectively, were found around the 280th DOY (7-October). Within S in summer around the 210th DOY an additional area of bare soils was found measuring 10,000 km^2. The diurnal amount of shortwave radiation (Ri_d), reaching the sub-regions in 2011 varied from about 2 TJ/km^2 around the beginning of the astronomical winter to 17, 19, and 21 TJ/km^2 for C, W and S, respectively, at the beginning of the astronomical summer (Fig. 4c).

The spring maxima of the radiation that can be reflected from the bare soils (Rr_d) in W, C and S were predicted from the beginning of April to the end of May at 90-125th DOY, 120-140th DOY and 110-150th DOY, respectively (Fig. 4d). During these periods, Rrd related to the soils formed by Pd and Hs can reach in these periods about 220 and 250 PJ/d in W, 150 and 190 PJ/d in C and up to 280 and 330 PJ/d in S. At the turn of summer and autumn, between 240th DOY and 280th DOY (from the end of August to the beginning of October), the radiation amount reflected from bare soils formed by Pd and Hs can only reach 20-25 PJ/d in W and 25-30 PJ/d in C. The radiation in this period in S can be almost imperceptible. In contrast, in summer around the end of July, the radiation in S can reach 25 and 30 PJ/d for Pd and Hs, respectively.

4 CONCLUDING REMARKS

The results presented in this paper show a clear annual variation of the amount of shortwave radiation reflected from bare soils within arable lands in the European Union (EU).

It was found that the greatest amount of radiation could be reflected from the soils from the beginning of April to the end of May. This instantaneous radiation amount relating to soil shaped by a smoothing harrow and plough was estimated at 250 and 220 PJ/d, respectively, for the western part of the European Union, 190 and 150 PJ/d for the central part and 330 and 280 PJ/d for the southern part.
This study indicates that the quantitative relationship between the reflectance of soils and their blue-sky albedo variation requires further research on arable lands in larger areas to evaluate the impact of bare soil reflection on a global scale.

5 REFERENCES

Baumgardner, M.F., Silva, L.F., Biehl, L.L., Stoner, E.R., 1986. Reflectance Properties of Soils. *Advances in Agronomy*. **38**, 1–44. doi:10.1016/S0065-2113(08)60672-0

Cierniewski, J., Karnieli, A., Kaźmierowski, C., Królewicz, S., Piekarczyk, J., Lewińska, K., Goldberg, A., Wesołowski, R., Orzechowski, M., 2015, Effects of soil surface irregularities on the diurnal variation of soil broadband blue-sky albedo. *IEEE Journal of Selected. Topics in Applied Earth Observations and Remote Sensing*, **8**, 493–502.

Cierniewski, J., Ceglarek, J., and Kaźmierowski, C., 2017, Predicting the diurnal blue-sky albedo variation of soils with given roughness using their hyperspectral reflectance spectra obtained under laboratory conditions. 10th EARSeL SIG Imaging Spectroscopy Workshop, Zurich, Switzerland, 19-21 April, 2017. *Remote Sensing (in preparation)*

Desjardins, R. L., 2010, The impact of agriculture on climate change. Proceedings NABC 21st Conference on Adapting Agriculture to Climate Change Symposium, Saskatoon, SK, Canada, National Agricultural Biotechnology Council, 29–39.

Farmer, G. T., and Cook, J., 2013, Climate Change Science: A Modern Synthesis, vol. 1. The Physical Climate, Springer, 564 pp.

Frouin, R., Lingner, D. W., Gautier, C., Baker, K. S., Smith, R. C., 1989. A simple analytical formula to compute clear sky total and photosynthetically available solar irradiance at the ocean surface. *Journal of Geophysical Research*. **94** (C7), 9731-9742.

Gautier, C., Diak, G., Masse, S., 1980. A simple physical model to estimate incident solar radiation at the surface from GOES satellite data. *Journal of Climate and Applied Meteorology*. **19**, 1005-1012.

Monfreda, C., Ramankutty, N., and Foley J. A., 2008, Farming the planet. Part 2: Geographic distribution of crop areas, yields, physiological types, and net primary production in the year 2000. *Global Biochemical Cycless 22,* GB 1022, doi: 10.1029/2007GB002947.

Sacks, W. J., Deryng, D., Foley, J. A., and Ramankutty, N., 2010, Crop planting dates: an analysis of global patterns. *Global Ecology and Biogeography*, **19**, 607-620.

Taconet, O., Ciarletti, V., 2007, Estimating soil roughness indices on a ridge-and-furrow surface using stereo photogrammetry. *Soil and Tillage Research,* 93, 64–76.

USDA, 1994, Major World Crop Areas and Climatic Profiles. World Agricultural Outlook Board, U.S. Department of Agriculture. Agricultural Handbook No. 664.

TRISHNA : a new high resolution thermal infrared Indo-French mission concept

Jean-Pierre Lagouarde [1], Bimal K. Bhattacharya [2], Philippe Crébassol [3], Philippe Gamet [3]

[1.] *INRA, UMR 1391 ISPA, F-33140 Villenave d'Ornon, France*

[2.] *Space Applications Centre, ISRO, Ahmedabad, India*

[3.] *CNES, 18 av. Edouard Belin, F-31401 Toulouse, France*

Corresponding author: jean-pierre.lagouarde@inra.fr

ABSTRACT- *The water cycle and energy budget at the Earth surface tightly interact with the climate change processes. Their monitoring as well as a number of practical applications (agriculture, soil and water quality assessment, irrigation and water resource management, etc...) require surface temperature measurements to be available at local scale. Such is the goal of the Indo-French high spatio-temporal TRISHNA mission (Thermal infraRed Imaging Satellite for High-resolution Natural resource Assessment). The scientific objectives of the mission are first presented. The definition of the mission specifications is supported by research work aiming at a better understanding of the surface temperature signal. Recent advances in this field are briefly reviewed, in particular original results dealing with the impact of directional anisotropy and of atmospheric turbulence on surface temperature measurements. Progress in modelling of surface fluxes is also discussed. The main specifications of the mission are then described and the trade-offs made for defining the revisit, the spatial resolution, the overpass time, the spectral bands and the orbit justified. The baseline of the mission is finally given.*

1 INTRODUCTION

It is now widely recognized that humans interact strongly and rapidly with the environment at all spatial and temporal scales through agricultural practices, landscape organisation, urbanization, emissions of pollutants and greenhouse gases (IPCC 2014). These interactions affect the water and carbon cycles and climate processes. Exchanges of water, CO_2 and energy between the surface and the atmosphere largely drive a number of processes such as vegetation growth, soil moisture dynamics, ocean circulation, biogeochemical cycles, etc... which, in turn, exert a strong feedback on climate. Many of the processes involved are primarily governed by water and energy budgets where the land and sea surface temperatures (LST and SST) appear as key signatures. As they are largely uncorrelated to the other observable surface variables, the surface temperatures provide new information to describe the processes and to drive models. The spatial variability of the surface requires that the complexity of both physical and biological processes involved must be assessed at small scale which corresponds to the scale at which decisions concerning water management or implementation of policies devoted to the mitigation of climate change effects are effective. In addition, surface fluxes show short-time scale variability, which requires frequent observations. Spatial systems combining both high spatial resolution and revisit capacities, which do not exist today, are therefore needed in thermal infrared (TIR), especially as SENTINEL-2 and RESOURCESAT missions now provide high quality complementary data in the optical domain.

After several advanced studies (MISTIGRI, Lagouarde et al., 2013; THIRSTY, Crebassol et al., 2014) in partnership with other agencies, the French CNES and Indian Space Research Organization (ISRO) are in the process of defining a new satellite mission, TRISHNA (for Thermal infraRed Imaging Satellite for High-resolution Natural resource Assessment) combining a high spatial resolution (about 50 m) and high revisit capacities (3 days) in the TIR with global coverage.

The scientific objectives of the mission are first presented. Research work has been conducted to consolidate the mission specifications and recent results are briefly illustrated. The base line of the mission is finally summarized.

2 SCIENTIFIC OBJECTIVES

Two primary scientific objectives drive the mission, (i) ecosystem stress and water use and (ii) coastal and continental waters, with four complementary goals: (iii) urban, (iv) solid earth/geology, (v) cryosphere and (vi) atmosphere.

2.1 Ecosystem stress and water use (design driver)

LST provides a key information on actual evapotranspiration (AET) of vegetation (agricultural crops as well as natural surfaces), a critical term of the water cycle. Water used by agriculture represents about 70% of the water consumption at global scale. Many countries face drought problems, making water

stress detection and irrigation optimization techniques necessary for a better management of water resources. Important applications are therefore expected in crop production monitoring for assessment of food security for example. As CO_2 and water transfer processes in plants are intimately related, and as water is the vector of many dissolved nutrients and/or pollutants within the soil, LST can help to monitor biogeochemical cycles with applications to water quality and soil pollution. Improved estimation of AET should facilitate the closure of watershed water budgets (infiltration, runoff, river flow, etc.) Other application can be found in ecology (e.g. mapping of microclimates, permafrost melting etc.).

2.2 Coastal and inland waters (design driver)

High spatio-temporal resolution SST is expected to better assess the sub-mesoscale activity in coastal areas in relation with the variability of ecosystem productivity. As for continental biosphere, it will improve the estimation of gas fluxes (CO_2, CH_4) at the air-sea interfaces. Applications for coastal zone monitoring and management deal with water quality, algae blooms, fish resource, fresh water resurgences and water discharges (e.g. pollutants, thermal plumes etc.) among others. Additionally to similar applications for inland waters, the surface temperature of lakes has been defined as an essential climate variable by GCOS (Global Climate Observing System). The study of sea ice (extent, growth/decay of ice, feedback with climate) will also benefit from TRISHNA data.

2.3 Urban

In the context of an increase of urban world population and of an increase of heat waves as a consequence of climate change, more and more efforts are devoted to the characterization of urban heat islands (UHI) and to their possible mitigation or heat action plans for comfort of inhabitants (by 'greening' of the city, urban planning or control of air conditioning energy consumption for instance). Improved flux estimations should also provide better inputs for urban and peri-urban hydrology studies.

2.4 Solid Earth

TRISHNA should contribute to the monitoring volcanic activity (prediction of eruptions, lava flow The detection of thermal anomalies should fi applications for detection of peat or coal fir geothermal exploration or possibly as earthquak precursors, among others.

2.5 Cryosphere

Apart from polar regions, the monitoring of snow and ice and the monitoring of glacial high altitude lakes in mountainous regions is particularly important as the snow and glacier melt runoff represents a perennial source of water for river basins. This is crucial for India which is partly dependent on Himalayan cryosphere.

2.6 Atmosphere

Different information on atmosphere (water vapour or precipitable water content) and clouds (type, height) can be derived from thermal infrared for improving surface radiative budgets.

3 RECENT RESEARCH RESULTS

3.1. Impact of atmospheric turbulence on LST

The atmospheric turbulence near the surface generates LST temporal fluctuations. Using high frequency TIR imagery over different surfaces (pine stands, corn, bare soil), it has been shown that their intensity and frequency depend on the characteristics of the turbulent flow and that their impact on LST depends on the spatial resolution of sensors (Lagouarde et al., 2015). High frequency structures in the surface boundary layer correspond to typical scales of a few meters linked to the size of the surface roughness elements. Fluctuations in LST associated with these structures are similar in the mechanical domain to the "waves" or "honamis", which propagate over wheat fields under the influence of wind, and are smoothed out for decametric pixels (50-100 m). Low frequency structures within the planetary boundary layer, conversely, have typical scales of several hundred meters and can trigger significant fluctuations both in time and in amplitude on pixels of smaller size.

The departure from the mean of a LST time series illustrates the possible error made on an instantaneous satellite measurement (Figure 1) at the 50 m resolution. Provided an assumption of ergodicity of the LST signal is done, simulations performed at the laboratory with the Large Eddy Simulation (LES) model ARPS have confirmed the experimental results and provide a simulation of the expected errors depending on the spatial resolution at which a satellite measurement is performed (Figure 2).
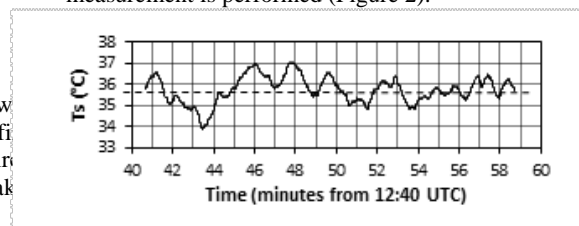
Figure 1. Time trace of the LST acquired at 10 Hz over a corn field (Bilos, SW France) at a resolution of 50 m. The departure of LST from the average (doted line) illustrates the possible uncertainty on satellite measurements.
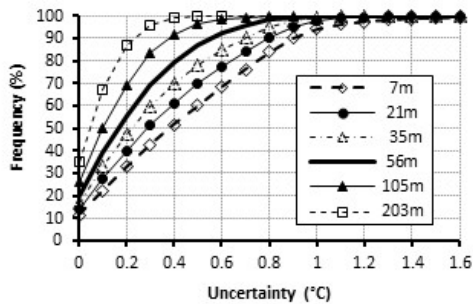
Figure 2. Cumulative uncertainty histograms (in absolute value) at various resolutions for a maritime pine cover from Large Eddy Simulations. The measurement error decreases inversely with spatial resolution (for example, the error is less than ±0.4°C for 98 % of measurements at a resolution of 203 m, but for only 80 % and 60 % of them at resolutions of 56 and 21 m).

3.2 TIR directional anisotropy

LST measurements are prone to significant directional anisotropy effects. We define anisotropy as the difference between temperatures observed in oblique and nadir viewing angles. Experimental work based on airborne thermal imaging camera measurements allowed us to illustrate directional effects in the TIR domain for all azimuth viewing directions and on a range of zenith viewing angles up to 60° on forest and urban canopies (Lagouarde et al., 2000, 2008). Significant hotspot effects have been characterized. They are explained by the fact that when the surface is viewed exactly in the direction of the Sun, the sensor only sees sunlit elements, leading to a undesired or spurious peak in temperature.

Modeling efforts are conducted to simulate directional anisotropy through various approaches (a review can be found in Verhoef et al., 2007). Combining 3D canopy models with radiative and energy transfer allows to simulate anisotropy for complex surfaces such as urban areas or row crops (Krayenhoff and Voogt, 2007). Multilayer radiative and energy transfer coupled models, such as SCOPE (Van der Tol, 2009) are more adapted to continuous and homogeneous canopies (Duffour et al., 2015). But their complexity makes none of these approaches well suited to an operational processing of satellite data. For this purpose attempts are made to develop simpler parametric models (Vinnikov et al., 2012; Duffour et al. 2016). All the above-mentioned models can help to provide guidelines in the phase of mission specifications definition (Figure 3). Nevertheless, a better assessment of TIR directional anisotropy is needed because it still remains a concern for delivering robust operational products.

3.3 Surface fluxes modelling

Important research is conducted on surface flux models for estimation of evapotranspiration. Different approaches are developed, either based on surface energy budget using one- or multi-source models and referred to as 'residual methods', or on scaling AET in a two-dimension LST-vegetation parameter space referred to as 'contextual methods' (a review can be found in Lagouarde and Boulet, 2016). The numerous examples of satellite-derived AET maps given in literature demonstrate the potential of these methods (Mallick et al., 2009; Bhattacharya et al., 2010; Anderson et al., 2012). The EVASPA platform (EVapotranspiration Assessment from SPAce) brings several algorithms all together to provide an ensemble simulation, which allows not only computing AET but also deriving its uncertainty (Gallego-Elvira et al., 2013). As LST measurements from space are available only once a day at satellite overpass and for cloud-free conditions, monitoring of seasonal water budgets requires extrapolation (reconstitution of the diurnal cycle) and interpolation (gap-filling between two successive images) steps (Delogu et al., 2012). The evaporative fraction (the ratio between latent heat flux and available energy) or stress index (the ratio between latent heat flux and potential evaporation) are the supports currently used for the temporal interpolation. Research is currently made to propose alternative more efficient supports such as surface humidity or meteorological models outputs for instance.
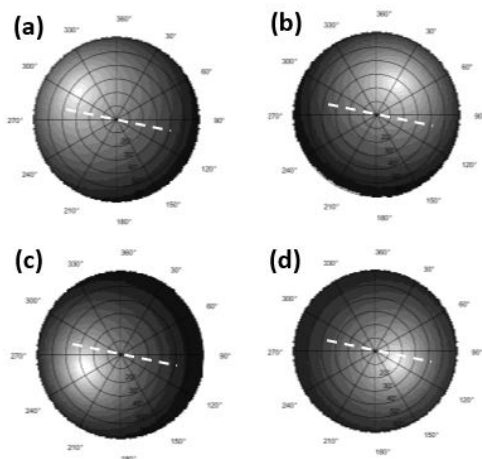
Figure 3. Qualitative modelled anisotropy for May, 21st using the Duffour parametric approach. The hot spot peak appears in white. It depends on location and time: Bordeaux 10:00 and 13:00 solar time (a and b), idem for Bangalore (c and d). The white dotted line indicates a scan line.

4. MAIN MISSION SPECIFICATIONS

4.1 Revisit

A daily revisit would be the optimum (i) to minimize the impact of uncertainty of LST due to atmospheric turbulence on the accuracy of AET retrievals and (ii) to cope with the high probability of clouds in many parts of the world. However, for a single satellite mission, the revisit is also severely constrained by the swath angle required for the global coverage of Earth. Orbit studies show that a reasonable scan angle lower than 35° can only be obtained with 3 day-revisit.

4.2 Spatial resolution

A high spatial resolution is required to access small size fields. Several papers in literature argue for a resolution lower than 100 m. An analysis of the size of fields in a typical agricultural landscape in the South West of France led us to recommend a 50 m resolution at nadir, corresponding to about a hundred meters at the swath edges. In many places of India, the very fragmented landscape makes 50m at least mandatory (Eswar et al., 2013). However, at lower resolution, the atmospheric turbulence induced uncertainty may increase significantly (see section 3.1). Technical constraints are also to be considered, in particular the size of existing detectors with respect to the swath to be covered. The final trade-off is a 50m spatial resolution at nadir.

4.3 Overpass time

The specification of overpass time results from a trade-off of 4 constraints :

- Models show that the best accuracy of AET retrievals is obtained for a LST acquisition around 1 pm (Delogu et al., 2012).
- The sensitivity of time d(LST)/dt is minimum (close to 0 °C/hour) when LST reaches its maximum around solar noon. This makes more robust the comparison of instantaneous satellite-retrieved AET against integrated values derived from surface or meteorological models at time steps of around half an hour. For comparison, around 10:00 (solar time), the variation of LST is about 4 °C/hour.
- Surface temperature measurements over water bodies should ideally be performed late enough in the night, to remove inertia effects of a thin surface layer heated by solar radiation the previous day. The night overpass time being delayed by 12 hours, a daytime 1 pm overpass is preferred whereas an earlier overpass (~10:00 as for Landsat) would be less adapted for summer months for instance.
- For mid latitudes, the hot spot being situated in a plane perpendicular to the scan line (provided the orbit inclination at Equator adequately chosen, see figure 3) the impact of TIR directional anisotropy is limited. This is not true for the inter-tropical zone.

An overpass around 1 pm is finally recommended.

4.4 Orbit

For the 3 day orbit first selected for TRISHNA (666 km) a point at ground is always observed in the same viewing geometry. A consequence is that, in inter-tropical zone, the hot spot may affect some regions during several months per year. The lack of any robust model of hot spot makes difficult using LST data and derived fluxes obtained in such conditions. An alternative orbit with a 8 day-revisit (761 km) is considered which sub-cycles 3/2/3 could provide at least 2 hot spot free data out of 3 in the inter-tropical zone.

4.5 Sensitivity

Because of the intrinsic atmospheric turbulence induced uncertainty on LST, a NeDT better than 0.3 K @ 300 K is useless for continental surfaces. This value has still to be confirmed for water bodies.

4.6 Spectral bands

In the TIR domain, two bands centered on 10.3 and 11.5 µm (with about 1 µm banwidth) have been chosen in the atmospheric window above 10 µm to apply the split-window method. Two additional bands in the 8-9.4 µm window have been selected to perform the temperature - emissivity separation using the TES method (after Gillespie et al., 1998): they are centered at 8.6 and 9.1 µm (~0.35 µm banwidth). A end-to-end simulator is used to determine the exact shape of TIR spectral filters.

Moreover, in response to scenarios considering the possibility of flying a thermal instrument along with VNIR data provided by other systems (such as Sentinel, Landsat, etc…), a study (not detailed here) has been conducted to demonstrate that it is mandatory to embark both TIR and VNIR/SWIR instruments on the same platform.

In the VNIR domain, the classical red and near-infrared vegetation bands at 0.650 and 0.860 µm are mandatory. A green band (0.555 µm) will be used for coastal applications and snow discrimination (through NDSI). A blue band at 0.485 µm will allow cloud discrimination. A band at 1.38 µm to detect cirrus and high thin clouds is highly desirable. These last two bands will be acquired at a degraded resolution (100 or even 200 m) to limit the downward data volume. Finally a SWIR band is needed to address aerosol characterization and related incident shortwave radiative forcing, snow discrimination and albedo estimation. 1.650 and 2.130 µm are still debated.

5. CONCLUSION

The summary of the baseline is as follows:
Resolution : 50 m (nadir (<100 edges of swath)
Revisit : 3 observations for any ground location per 8 days period (using the 3 sub-cycles of a 8 day-orbit at 761 km)
Coverage : global
NeDT : 0.3 K
TIR bands : 8.6 and 9.1 µm (with Δλ ~0.35 µm), 10.3 and 11.5 µm (with Δλ ~1.0 µm)
VNIR bands : 0.485, 0.555, 0.650 and 0.860 µm mandatory, 1.38 µm highly desirable. Possible degradation of the spatial resolution for blue (0.485) and cirrus (1.38) bands.
SWIR band : 1.650 or 2.130 µm (being studied)
Two preliminary studies of TIR instrumental concepts are currently being conducted. They are based on two different concepts, a classical scanner and a step and stare instrument.
TRISHNA is currenty in a A phase till end 2019. It will be followed by a one-year B phase. The launch could be foreseen at the 2023-2025 horizon.

7. REFERENCES

Anderson M.C., Allen R.G., Morse A., Kustas W.P., 2012. Use of Landsat thermal imagery in monitoring evapotranspiration and managing water resources *Rem. Sens. Environ.* 122 (2012) 50–65.

Bhattacharya, B. K., Mallick, K., Patel, N. K., and Parihar, J. S, 2010. Regional clear sky evapotranspiration over agricultural land using remote sensing data from Indian geostationary meteorological satellite, *J. Hydrol.*, 387, 65–80.

Crebassol, P., Lagouarde J.-P., Hook S., 2014. THIRSTY Thermal InfraRed SpaTial System. IEEE Geos. Remote Sens. Symp., 3021–3024. http://dx.doi.org/10.1109/IGARSS.2014.6947113.

Delogu E., Boulet G., Olioso A., Coudert B., Chirouze J., Ceschia E., Le Dantec V., Marloie O., Chehbouni G., Lagouarde J.-P., 2012. Reconstruction of temporal variations of evapotranspiration using instantaneous estimates at the time of satellite overpass. *Hydrology and Earth System Sciences*, 16, 2995–3010. doi:10.5194/hess-16-2995-2012

Duffour C., Olioso A., Demarty J., Van der Tol C., Lagouarde J.-P., 2015. An evaluation of SCOPE: a tool to simulate the directional anisotropy of satellite-measured surface temperatures. *Rem. Sens. Environ.,* 158, 362-375.

Duffour C., Lagouarde J.-P., Olioso A., Demarty J., Roujean J.-L., 2016a. Driving factors of the directional variability of thermal infrared signal in temperate regions. *Remote Sens. Environ.* 177 (2016) 248–264.

Duffour C., Lagouarde J.-P., Roujean J.-L. 2016b. A two parameter model to simulate thermal infrared directional effects for remote sensing applications. *Rem. Sens. Environ.* 186 250–261.

Eswar, R., Sekhar, M., Bhattacharya, B.K., 2013. A simple model for spatial disaggregation of evaporative fraction: comparative study with thermal sharpened land surface temperature data over India. *J. of Geophys. Research: Atmospheres*, 118 (21): 12,029-12,044.

Gallego-Elvira B., Olioso A., Mira M., Reyes-Castillo S., Boulet G., Marloie O., Garrigues S., Courault D., Weiss M., Chauvelon P., Boutron O., 2013. EVASPA (EVapotranspiration Assessment from SPAce) tool: An overview. *Procedia Environmental Sciences*, 19, 303–310. DOI: 10.1016/j.proenv.2013.06.035

Gillespie, A., Rokugawa, S., Matsunaga, T., Cothern, J.S., Hook, S., and Kahle, A., 1998. A temperature and emissivity separation algorithm for Advanced Spaceborne Thermal Emission and Reflection Radiometer (ASTER) images, *IEEE Trans. Geosci. Remote Sensing*, 36 (4), 1113-1126.

Krayenhoff, E. S., & Voogt, J. A., 2007. A microscale three-dimensional urban energy balance model for studying surface temperatures. *Boundary-Layer Meteorology*, 123, 433−461.

Lagouarde J.-P. and Boulet G., 2016. Energy Balance of Continental Surfaces and the Use of Surface Temperature, Chapter 10, 323 – 362. *In:*Land Surface Remote Sensing in Continental Hydrology, N. Baghdadi and M. Zribi Ed., ISTE Editions, ISBN : 9781785481048.

Lagouarde J.-P., Irvine M., Dupont S., 2015. Atmospheric turbulence induced errors on measurements of surface temperature from space. *Remote Sens. Environ.*, 168, 40-53.

Lagouarde J.-P., Bach M., Sobrino J.A., Boulet G., Briottet X., Cherchali S., Coudert B., Dadou I., Dedieu G., Gamet P., Hagolle O., Jacob F., Nerry F., Olioso A., Ottlé C., Roujean J.L., Fargant G., 2013. The MISTIGRI Thermal Infrared project: scientific objectives and

mission specifications. *Int. J. Remote Sens.*, 34 (9-10), 3437-3466.

Lagouarde J.-P., Ballans H., Moreau P., Guyon D., and Coraboeuf D., 2000. Experimental study of brightness surface temperature angular variations of Maritime Pine *(Pinus Pinaster)* stands, *Remote Sens. Environ.* 72 (1), 17–34.

Lagouarde J.-P. and Irvine M., 2008. Directional anisotropy in thermal infrared measurements over Toulouse city centre during the CAPITOUL measurement campaigns: first results. *Meteorology and Atmospheric Physics*, special issue CAPITOUL. 102, 173-185, DOI: 10.1007/s00703-008-0325-4.

Mallick K., Bhattacharya B. K., Rao V.U.M., Reddy D.R., Banerjee S., Venkatesh H., Pandey V., Kar G., Mukherjee J., Vyas S. P., Gadgil A. S., Patel N.K., 2009. Latent heat flux estimation in clear sky days over Indian agroecosystems using noontime satellite remote sensing data. *Agric. For. Meteorol.* 149 1646–1665.

Van der Tol, C., Verhoef, W., Timmermans, J., Verhoef, A., and Su, Z., 2009. An integrated model of soil-canopy spectral radiances, photosynthesis, fluorescence, temperature and energy balance. *Biogeosciences*, 6, 3109–3129.

Verhoef W., Jia L., Xiao Q., and Su Z., 2007. Unified Optical-Thermal Four-Stream Radiative Transfer Theory for Homogeneous Vegetation Canopies. *IEEE Trans. Geos. and Remote Sens.*, Vol. 45, No. 6, 1808-1822.

Vinnikov, K.Y., Yu, Y., Goldberg, M.D., Tarpley, D., Romanov, P., Laszlo, I., Chen, M., 2012. Angular anisotropy of satellite observations of land surface temperature. *Geophys. Res. Lett.* 39, L23802. http://dx.doi.org/10.1029/2012GL054059.

Quantitative analysis of thermal infrared multi-angle polarized characteristics of water

Xia Zhang, Guo-fei Shang*, Zhen Li, Ai-qing Guo
Institute of land resources and urban and rural planning, Hebei GEO University, Shijiazhuang City, Hebei Province, China, 050000
Zhangx396@nenu.edu.cn   Huai An Road No. 136, Shijiazhuang, Hebei Province,China

ABSTRACT- *The thermal radiation of water is polarized and the study of the thermal infrared polarized characteristics of water is the foundation of the detection of thermal infrared polarized remote sensing, and also significant theoretical support for water remote sensing interpretation. In this paper, quantitative analysis of the influence of the detection angle, the azimuth angle, the wave band, the temperature and their interactions in different polarized conditions on the thermal infrared polarized characteristics of water has been made by the orthogonal experimental design and spectrum analysis. The results show that, the polarized brightness temperature of water decreases with the increase of the detection angle and increases with the temperature rises. There is a parabolic distribution between the polarized brightness temperature and the azimuth angle, and the peak of the parabola is located near the azimuth angle of 180 °. The polarized brightness temperature in the four wave bands is different and presents distinct characteristics in different detection conditions. The interaction between the temperature and the detection angle has an extremely significant effect on the thermal infrared polarized characteristic of water. It provides new ideas and methods for remote sensing technology to monitor the water, having crucial theoretical significance and practical value for making full use of the polarized information and promoting the development of quantitative remote sensing.*

1 INTRODUCTION

Water is one of the most important research objects in Geosciences (R.-F. Zhao, 2005). In recent years, many achievements have been made in the study of the reflection polarization of water (Y.-F. Lv, 2012). However, the thermal infrared polarized detection of water still belongs to a new research direction in remote sensing, which has great potential of application and development.

Scientists in this field at home and abroad have carried out some tentative research work and achieved plenty of considerable results. It is found that water is the only one in the natural background which has more obvious thermal radiation polarized characteristic than others (B.Ben Dor, 1992). Analysis of the influence of the detection angle and the state of water on the thermal radiation polarized characteristic of water has been made (Shaw 2001, 2007) to point out that it can provide more effective information for the application of thermal radiation polarized remote sensing with the observation of a larger detection angle. X.-B. Sun (2010) has pointed out the great theoretical significance of research on the thermal infrared polarized detection of water.

But there are still a lot of problems in the spectrum database construction and quantitative research on the influencing factors and their interactions of thermal radiation polarization of water. The study of polarized spectrum is the foundation of the study of thermal radiation polarized image of water. This study can accumulate basic scientific data for thermal radiation polarized remote sensing and provide references for the design and development of the platform and sensor of polarized remote sensing.

2 THEORETICAL BASIS AND EXPERIMENTAL CONDITIONS

2.1 Theoretical basis

Malus first discovered the polarization of light. Maxwell had established the electromagnetic theory of light, which is essentially proved to be polarized (Y.-B. Liao, 2003). Fresnel had found that in the process of reflection and refraction, the light would produce polarization (H.-F. Zeng,2012). By the Fresnel formula of thermal radiation, as the two orthogonal polarized components of the thermal radiation of the reflection on the surface of the two kinds of media have polarization, the degree of absorption of the two is different according to the principle of energy conservation. So the absorption will also change the polarized characteristics of light. Combined with Kirchhoff's law, good at absorbing is also good at thermal radiation, so the thermal radiation will also have polarization characteristics, which is the physical basis of thermal radiation polarized detection.

2.2 Experimental Conditions

The platform is BPDF measuring platform (as shown in Figure 1), which refers to the Bidirectional Polarized-reflectance Distribution Function. The measuring instruments are: CE312-1b thermal infrared radiometer (as shown in Figure 2), and thermal infrared polarizer (3-18μm). The BPDF platform, the thermal infrared radiometer and the thermal infrared polarizer are combined into a thermal radiation multi-angle polarized detector. Others in the temperature measurement are using three thermometers, they are the first-class standard thermometer, the second-class standard thermometer and the weather thermometer respectively.

Figure 2. The thermal infrared radiometer

3 INFLUENCING FACTORS ANALYSIS OF POLARIZATION OF WATER

It is discussed from four aspects of the detection angle, azimuth angle, wave band and temperature in the analysis of the factors affecting the thermal radiation polarization of water.

3.1 The effect of detection angle

It can be seen from Figure 3 that the detection angle has a certain influence on the polarized brightness temperature of water. It shows that the polarized brightness temperature decreases with the increase of the detection angle, and the larger the detection angle is, the faster the rate of descent is.

Figure 1. BPDF measuring platform
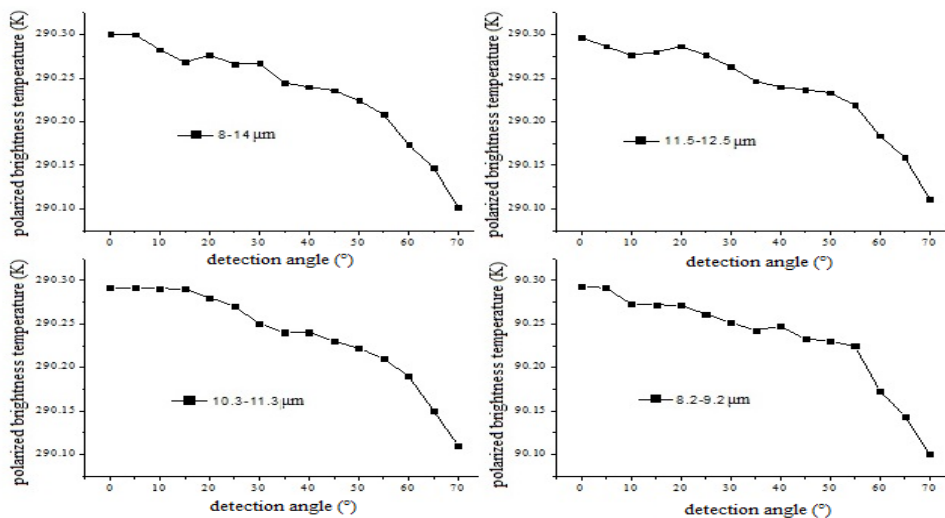
Figure 3. The polarized brightness temperature of water varies with detection angle

3.2 The effect of azimuth angle

It can be seen from the Figure 4 that the polarized brightness temperature of water in the four bands with azimuth angle is very similar, which is basically parabolic and the peak of the parabola is near the

azimuth angle of 180 degrees.
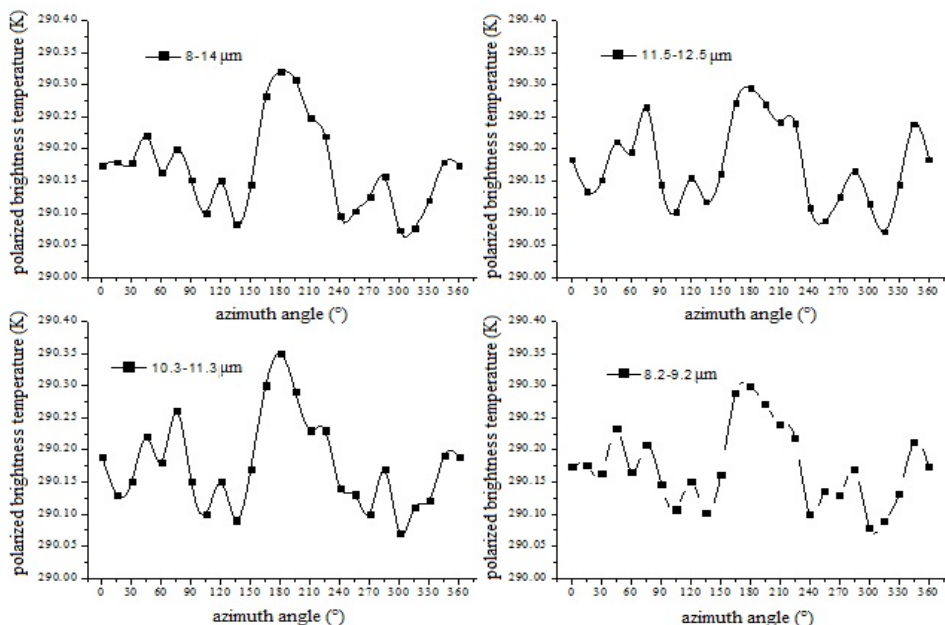
Figure 4. The polarized brightness temperature of water varies with azimuth angle

3.3 The effect of wave band

It can be seen from the Figure 5 that the polarized brightness temperature of water varies with different wave bands and combined bands and presents distinct characteristics in different detection conditions.
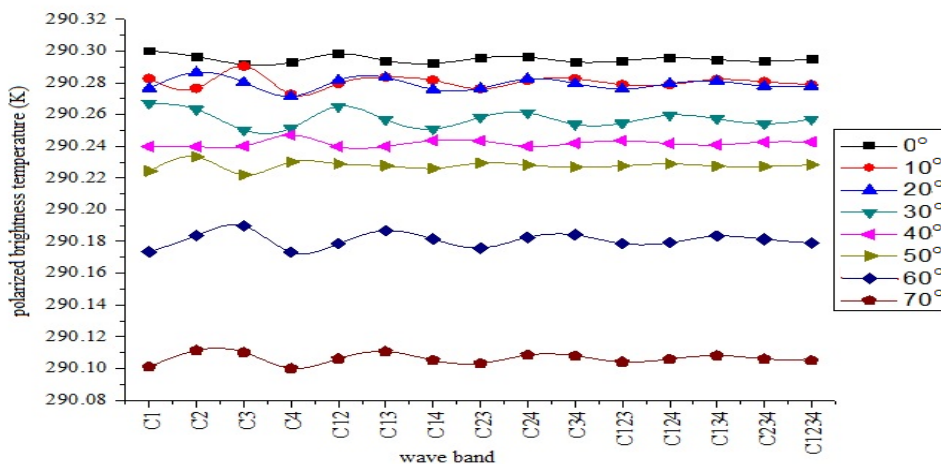
Figure 5. The polarized brightness temperature of water varies in different wave bands

3.4 The effect of temperature

It can be seen from the Figure 6 that the polarized brightness temperature of water is monotonically increasing with the temperature rises. The curve is smooth and the polarized spectrum in the four wave bands is almost completely coincident.
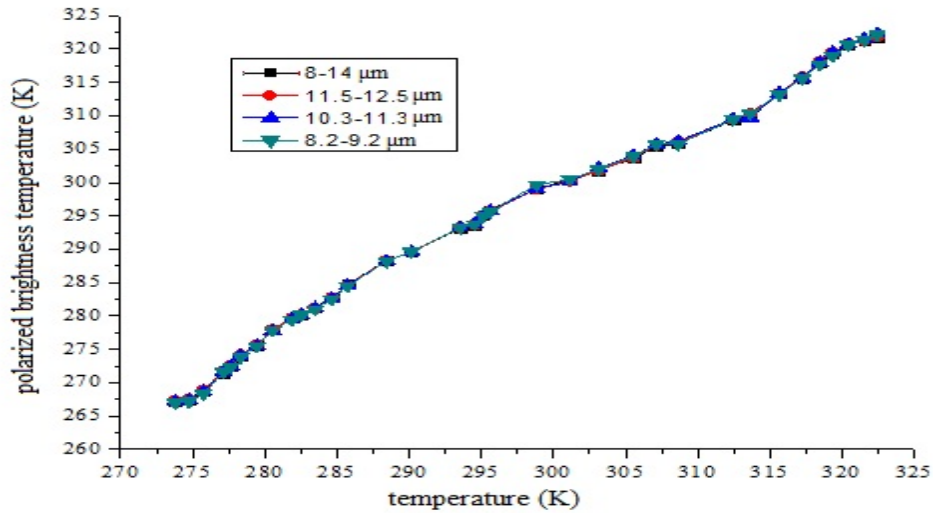
Figure 6. The polarized brightness temperature of water varies with temperature

4 INTERACTIONS ANALYSIS OF POLARIZATION OF WATER

In order to make study of the effect of interactions, an orthogonal experiment has been designed in this paper.

Table 1. The factor-level orthogonal experimental design of water

Level \ Factor	Temperature (A)	Wave band (B)	Azimuth angle (C)	Detection angle (D)
1	25℃	10.3-11.3μm	180°	40°
2	45℃	8.2-9.2μm	0°	60°

In the orthogonal experiment design of water (as shown in Table 1), there are four factors and each factor has two levels. The arrangement of factors and interactions is shown in the orthogonal experimental design L_{16}（2^{15}）header design of water (as shown in Table 2).

In the experiment, each factor and interaction is occupying one column and only the first, the second, the fourth, and the eighth columns of factor A, B, C, and D are arranged in the experiment. The interactions do not schedule any experiments.

Table 2. The orthogonal experimental design L_{16}（2^{15}）header design of water

Column Number	1	2	3	4	5	6	7	8	9	10	11	12	13	14	15
Factor	A	B	AB	C	AC	BC		D	AD	BD		CD			

According to the experimental design scheme, the thermal radiation polarized data of water under different combination of factors and levels is obtained. With the polarized brightness temperature as the evaluation index, we have got the difference between the factors and the interactions of these factors.

The primary and secondary relationship between the factors and the interactions is obtained by means of range analysis. The influence of the factors and the interactions on the thermal radiation polarized characteristics of water is determined by variance analysis and significance test.

According to N.-Z. Zhao (2008), if the F value of a factor (or interaction) is greater than 1% of F on the table, the impact of this factor is extremely significant, which is recorded as "**". If it is between 5% and 1% of F, the impact of this factor is significant, which is recorded as "*". If it is between the values of 20% and 5% of F, it has a certain effect, which is recorded as "(*)". If it is less than 20% of F on the table, it can be considered that the factor does not have much impact. The results of variance analysis in different polarization conditions are shown in Table 3 to Table 5.

Table 3. The result of variance analysis in 0° polarization angle

Source of Variance	Sum of Square	Degrees of Freedom	F	Sig.	Significance
A	108.913	1	12069.469	0.000	**
D	46.800	1	5186.232	0.000	**
AD	11.415	1	1265.013	0.000	**
CD	0.132	1	14.625	0.012	(*)
AC	0.076	1	8.469	0.033	(*)
Error	.045	5			
Sum	1393351.938	16			

Table 4. The result of variance analysis in 45° polarization angle

Source of Variance	Sum of Square	Degrees of Freedom	F	Sig.	Significance
A	105.574	1	3539.011	0.000	**
D	50.307	1	1686.367	0.000	**
AD	11.878	1	398.180	0.000	**
Error	.149	5			
Sum	1392715.173	16			

Table 5. The result of variance analysis in 90° polarization angle

Source of Variance	Sum of Square	Degrees of Freedom	F	Sig.	Significance
A	106.159	1	1771.088	0.000	**
D	51.161	1	853.543	0.000	**
AD	13.502	1	225.257	0.000	**
CD	0.257	1	4.288	0.093	(*)
Error	.300	5			
Sum	1392255.173	16			

The results of variance analysis show that the influencing factors and interactions on the polarized characteristics of water are basically the same in the conditions of 0 ° , 45 ° and 90° polarization angle. Both of the temperature, the detection angle and their interaction have extremely significant impact on the polarized brightness temperature. But there are still differences on the interactions of different factors. The interaction between the detection angle and the azimuth angle has some influence on the polarized

brightness temperature in the 0 ° and 90 ° polarization angle and the interaction between the temperature and the azimuth angle has some influence on the polarized brightness temperature in the 0 ° polarized conditions. Other interactions have no significant impact.

5 CONCLUSION

In this paper, the polarized characteristics of water have been discussed from the influencing factors and their interactions. From the study above, we can draw some general conclusions on this problem.

(1) The polarized brightness temperature of water decreases with the increase of detection angle, and the larger the detection angle is, the faster the rate of descent is.

(2) There is a parabolic distribution between the polarized brightness temperature and the azimuth angle, and the peak of the parabola is located near the azimuth angle of 180 °.

(3) The polarized brightness temperature varies in the four wave bands and presents distinct characteristics in different detection conditions.

(4) The polarized brightness temperature increases monotonically with the temperature rises.

(5) The interactions among these factors do exist and the influence varies in different polarized conditions. The interaction between the temperature and the detection angle has an extremely significant effect on the thermal infrared polarized characteristics of water.

REFERENCES

Zhao Ruo-fa, Guo Huadong, Wang Weimin. Study on the progress of passive microwave remote sensing in soil moisture evolution. Journal of Remote Sensing Technology and Application, 2005,20 (1): 49-57.

Lv Yunfeng. Polarization characteristics of water body. Northeast Normal University, 2012.

B.Ben-Dor. Polarization properties of targets and backgrounds in the infrared. Proc SPIE.1992, 1971:68-76.

Shaw.J. A. Polarimetric measurements of long-wave infrared spectral radiance from water. Appl. Opt.,2001,40(33):5985–5990.

Shaw J A. A survey of infrared polarization in the outdoors.SPIE,2007,66601:66610.

Sun Xiao-bing, Quao Yan-li, Hong Jin. Research Progress of Visible and Infrared Polarization Remote Sensing Technology and Its Application. Journal of Atmospheric and Environmental Optics, 2010, 5(3): 175-188.

Liao Yan-biao. Polarization optics. Beijing: Science Press. 2003.

Zeng Hai-fang. Research on the Key Technology of Infrared Polarization Imaging. Nanjing Science and Technology University, 2012.

Zhao Nai-Zhuo, Zhang Jing-Qi,Zhao Yun-sheng,et al. Quantitative Analysis of Interactions between Factors Influencing Polarized Reflection of Loess. Acta Pedologica Sinica. 2008,45(2),380-383.

FENYX

A. Corrales Sierra, J. Ortiz Muñoz, N. Seoane Vieira, B. Calvo Moral, J.A. Gómez Sánchez, B. Marqués Balaguer
Aerial Platforms for Research. INTA
corralessa@inta.es

ABSTRACT - *Aerial Platforms for Research (PAI) is a unique infrastructure conceived as a comprehensive measurement capability. It provides support to the requests and needs of the atmospheric, remote sensing and R&D scientific instrumentation communities. From 2008 to 2011, 12 organizations members of EUFAR worked together on the COPAL project (COmmunity heavy PAyload Long endurance instrumented aircraft for tropospheric research and geosciences), with the objective to provide the scientific community with a high payload and long endurance aircraft (HPLE). From 2016-2020 the Strategic Plan of the infrastructure identified as one of its key weaknesses the obsolescence of the C212, core of the ICTS. With the objective of avoid this obsolescence and guarantee the future of the Spanish airborne research, the Spanish Ministry of Economy, Industry and Competitiveness has approved the funds required for the acquisition and modification of a new heavy payload long endurance instrumented aircraft: FENYX.*

1 INTRODUCTION

An Aerial Research Platform (PAI, initials in Spanish) is an aircraft modified for the installation and operation of scientific instrumentation, able to perform flight campaigns to carry out scientific experiments and testing equipment and systems within the Earth's atmosphere.

INTA (National Institute for Aerospace Technology) has three PAI: two C-212-200 aircraft, manufactured by CASA, and a motorglider Stemme S15, modified and adapted for scientific use. These aircraft provide support for the needs of the community Flight Test trials, atmospheric research, data collection from remote sensing/observation of the Earth and tests for the development and qualification of new scientific instrumentation, among others.

The Spanish Ministry of Economy has recognized the PAI of INTA as ICTS (Singular Scientific and Technological Infrastructure). It is an infrastructure conceived so as to acquire data from aerial platform for scientific applications.

The ICTS consists of an air segment, which includes these three aerial platforms, the onboard scientific instrumentation and auxiliary systems necessary to perform data acquisition campaigns. The ground segment of the ICTS, is composed of the airfield, home-base of the ICTS, with the aeronautical infrastructure for the safe operation of the aircraft: control centre for operations, runway, taxiway, platforms, hangars, guidance for navigation, etc. Also, includes, a computer network, workshops, warehouses, laboratories, offices, etc. The ground segment also includes all the necessary instrumentation to acquire complementary field data of the data taken from the air, weather station,

instrumentation calibration and maintenance of sensors, modules for the analysis and validation of data, etc.

The data obtained by the instrumentation of PAI can be on occasion complex and unique due to their format, variable measurements, measurement technique, etc. The PAI team offers to its users the necessary support to interpret the generated data and to extract the useful information.

The complete system is offered to the national and international scientific community through partnerships, as a commercial transaction, within the framework of projects Horizon 2020, etc.

2 THE ORIGIN OF PROJECT FENYX: COPAL

The leading European countries in research with airborne facilities, each have different types of aerial research platforms. These countries are integrated through the EUFAR program (www.eufar.net); this enables the European scientific community access to the most suitable aerial platform for their experiment, regardless of the country to which it belongs.

EUFAR is an Infrastructure Integration Initiative (I3), which began during the 6th framework program, and currently comprises 24 European institutions that operate over 30 instrumented aircraft. Spain participates with the PAI of INTA.

The EUFAR instrumented aircraft fleet is composed of more than 30 aircraft with operating speeds from 30 to 200 m/s, payloads of between 80 and 4500 kg and a ceiling of operation that reaches up to 21 km. All of them with a flight range not exceeding that of five hours.

Due to the limiting factor of space and weight on the current European research aircraft fleet, the integration of new instrumentation is always difficult

and sometimes even impossible. A new aircraft with a large capacity and autonomy, allows for the development of new technologies, as well as the expansion of the operational capabilities of the current European research aircraft fleet.

For the construction and commissioning of this new platform called COPAL (COmmunity heavy-PAyload Long endurance Instrumented Aircraft for Tropospheric Research in Environmental and Geo-Sciences), which aims to provide the scientific community with an aerial platform for research of troposphere loads and autonomy, unique in Europe, able to reach and operate anywhere in the world such as remote oceanic or continental and polar regions. This will provide an unprecedented opportunity to countries which, do not operate these types of platforms but have the scientific potential to develop research papers by making use of the observations and measurements from the instrumented aircraft, allowing for the development of new multidisciplinary international experiments.

The participants in this program were universities and research centres devoted to the study of the atmosphere, some aircraft operators, most of them members of EUFAR.

Spain actively participated in COPAL, being in charge of the technical part of the project: definition of the aircraft, study of costs, selection of the operator of the aircraft and the data operator.

Selection of aircraft: three aircraft were selected (A-400M, C-130 and the C-295), the option preferred by the majority of the members of the project was the C-130, similar to the American aircraft.

After the feasibility study, which took place between 2007 and 2011, and which was financed through ESFRI, insufficient funding was found for the implementation of this new aircraft.

3 FENYX: PROJECT DESCRIPTION

As previously indicated, the European scientific community does not currently have an aerial platform of great autonomy and load for testing in the troposphere, this type of platform vital in flight campaigns associated with specific research projects related to climatic, chemical and large scale meteorological studies.

FENYX aims to develop a new aircraft that will have capacity to carry more than 6 tons of instrumentation for a maximum of 8 hours. The choice of the payload, is associated with the operation of least cost and greatest benefit to research. In this way, the wide ranging capabilities of FENYX increase the likelihood of obtaining adequate scientific demand (approximately) that of close to 10 hours of autonomy with more than 5 tons of maximum payload.

FENYX will in addition include significant advantages, such as the existence of a rear doorway, this greatly facilitates the loading and unloading of bulky and heavy equipment for operations of STOL (Short Take Off and Landing) characteristics, which make it possible to operate in remote areas. On the other hand, the turboprop, the velocity range of the aircraft is less than that of a turbo fan, which is of great benefit when it comes to the collecting of samples, data or images in flight

Various initiatives at the European level GMES (Global Monitoring for Environment and Security) and around the world have launched a plan to establish a system for observation of the Earth (GEOSS, Global Earth Observation System of Systems), agreed to by more than sixty Nations, which together with the initiatives of the European Commission, are proof of the importance which these observation initiatives have acquired.

To install the scientific equipment, the aircraft must undergo several modifications, such as:

- ✓ Capacity to install scientific instrumentation:
  a. Pods under the wings
  b. Holes on the fuselage
  c. Capacity for equipment installation on the windows
  d. LIDAR holes
  e. Remote sense holes.
- ✓ New avionic system
- ✓ Electrical power for scientific equipment
- ✓ Tube for air data probe
- ✓ Cabin configuration for 8 different scientific experiments
- ✓ FTI
- ✓ Pressure taps throughout the cabin, available for the 8 possible scientific groups
- ✓ Button camera types.
- ✓ Ice core sampling

With these observation systems, aerial platforms play a fundamental role as a unique tool in the fields of remote sensing and atmospheric research for the realization of in situ measurements as well as a privileged place of observation of the Earth. This new platform creates the possibility of investigations in remote areas of the continent or ocean areas away from the coast and specifically, in the polar areas

The phases referred to in the project are:

3.1 Specification.

To launch this new ICTS research platform, the documentation generated during the COPAL project

would be used as a reference. As well as data collected from current users. This lays out the technical characteristics which a research platform should have, as well as: an analysis of costs of acquisition, modification, operation and maintenance, scientific equipment and the aircraft operator requirements and, where appropriate operator of data, updating said study with updated information provided by the manufacturer and by the scientific community. From there, proceed to write the specifications of the aircraft and technical documentation that determines the characteristics that must be met to fulfil the requirements of the scientific community

3.2. The modifications that are necessary for the insertion of the scientific instrumentation.

The aircraft will be a platform for research and for this purpose must be installed with the scientific equipment needed for the campaigns. It will be necessary to design and implement the modifications to the aircraft (structural, electrical, communications...) that will allow for the housing of the instrumentation on board.

3. Certification of modifications.

All aircraft must have a certificate of airworthiness, which ensures that it is safe for flight. This certificate should take into account both the aircraft and the modifications.

4 EXPANSION OF CAPACITY FOR SCIENTIFIC APPLICATIONS

We plan to base the aircraft in Galicia, in particular at the CIAR (Rozas Airborne Research Center).

Infrastructure with these capabilities, ready to be deployed and operated anywhere in the world, will allow the scientific community, local, national and international, to make atmospheric studies in situ, of meteorological variables, pollution, climate change, remote sensing or observation of the Earth, microbiology, or development of new instrumentation. The existence and availability of the PAI infrastructure allows us to react and respond to certain catastrophic events that occur with relative frequency, and thus mitigate their effects on the society and its economy. A good example was the international reaction to the eruption in April 2010 of the Icelandic volcano Eyjafjallajökull. The combined effect of the ash cloud and winds dragged the particles onto the continent and resulted in the immediate closure of airspace to commercial flights, which, in turn, triggered a crisis for the transportation of people and goods, creating a situation of chaos without precedent in the recent history of the continent. Researchers in the field

grouped together to discuss and agree on coordinated actions to the dramatic situation created by the ash. In particular, centres and institutes of the European Consortium EUFAR - European Facility for Airborne Research in Environmental and Geo-sciences, reacted by planning and coordinating flights to collect data within the critical areas, established protocols of interpretation, procedures concerning the sharing of data and the results of its analysis. One of the most important conclusions was the determination that the concentration of ash in the atmosphere was 1000 times lower than that predicted by the British numerical model. Once established the upper limit of the concentration of particles was compatible with the safe operation of the aircraft, it was possible to finally re-open the air space to commercial operations.

Another example are the flights carried out to integrate manned and unmanned aircrafts into the same airspace, within the framework of the SESAR project.

Apart from the value of having the appropriate means to react to crises associated with disasters natural or those caused by human activity, a new platform with features such as those already described, expand the capacity for data collection, in both quantitative and qualitative terms, being able to perform the flight paths most appropriate and cover larger areas, as well as acquire more parameters for longer and with less uncertainty, thereby increasing productivity and efficiency, in scientific terms, of the infrastructure.

In addition, the commissioning of a platform so complex and costly, will facilitate the creation and development in its environment of technology based companies, highly specialized in servicing the needs of onboard instrumentation, companies which in turn will benefit from access to the facilities of the Centre (CIAR) to carry out their tests, test instrumentation or debug their hardware or software solutions. A paradigm of this model is the complex of companies of scientific instrumentation development that emerged on the outskirts of Boulder, Colo., when the enclave was chosen as a base of operations for large U.S atmospheric research aircraft, and today, are the world reference within the sector.

The new platform will also allow new aeronautical equipment and prototypes to be tested in flight before being accepted and implemented in commercial aircraft.

The policy of the major aircraft manufacturers is not to use any equipment which has not previously demonstrated and been qualified for aeronautical use, thus hampering the entry of new suppliers to the market, so this aircraft may be used as a test bench for those entrepreneurs with the aim of developing

equipment, eliminating barriers, improving competition and densifying the industrial fabric of the aeronautical sector.

5 CONCLUSIONS

The Aerial Research Platforms, ICTS-PAI, are important tools for the realization of a large part of the projects within certain scientific fields, in particular those related to environment (both from the aspect of atmospheric and Earth observation), being an essential element in many scientific branches for obtaining data from land or air.

This new aircraft will not only ensure the permanence in the long term of the ICTS, but will also broaden the already existing capabilities (autonomy, payload, range, ceiling...), both at the national level and in Europe.

With this new aircraft, studies can be performed in any part of the Earth's atmosphere below its flight ceiling (25,000 ft), reaching remote areas such as polar or desert regions, areas unreachable with aircraft available today.

This increased research capacity will increase our knowledge of the characteristics and operation of the atmosphere that surrounds us, and those characteristics and phenomena that occur on the Earth's surface, providing data that will be applicable to many fields of study, many of them in close relationship with the environment, enabling us to better understand the current situation , its evolution, what are the threats that cause degradation, etc.; that will enable us to react actively to promote its preservation and eventually, will lead to an improvement in the quality of life of the society.

Other areas to benefit will be companies from within the private sector that are undertaking research projects in collaboration with bodies of research to

expand knowledge of aircrafts, for example aerodynamic studies, noise or icing. For example, the European Commission recently approved a grant for the PHOBIC2ICE project, which involved Airbus Defence and Space, INTA and the CSIC, in collaboration with agencies from other countries, to study new materials, coatings and treatments that may reduce the formation of ice on aircraft, thus increasing their safety. The new aircraft will expand our currently existing capabilities to carry out these types of projects.

In addition, the FENYS aircraft would have capacity to integrate up to 8 different groups of researchers, which would encourage collaboration between national or international groups, as well as the transfer of knowledge. Due to the coexistence on board of several scientific groups, this encourages a multidisciplinary research (for example, performing microbiological studies whilst simultaneously taking weather or atmosphere physics data) and international cooperation, and can carry out flights with different groups from different countries

6 THANKS

Analysis of new vegetation index from GF-5 satellite simulation data

Ziyang Zhang[1, 2], Bo-Hui Tang[1, 2, *], Zhao-Liang Li[1, 2, 3], Ronglin Tang[1, 2], and Hua Wu[1, 2]

[1.] State Key Laboratory of Resources and Environmental Information System, Institute of Geographic Sciences and Natural Resources Research, CAS, Beijing, 100101, China.
[2.] University of Chinese Academy of Sciences, Beijing, 100049, China.
[3.] Key Laboratory of Agri-informatics, Ministry of Agriculture/Institute of Agricultural Resources and Regional Planning, Chinese Academy of Agricultural Sciences, Beijing 100081, China.
* Corresponding to whom should be addressed: tangbh@igsnrr.ac.cn

ABSTRACT

This paper aims to evaluate the potential of newly developed indices for retrieving leaf water content (LWC) from GF-5 satellite simulation data. In this study, PROSPECT model was selected to calculate leaf reflectance from 400nm-2500nm, and the range of the parameters in the model was set based on LOPEX93. 6 band reflectance was calculated from the GF-5 spectral response function (SRF) and simulated reflectance in PROSPECT. In order to find LWC sensitive band, the standard deviation was introduced to analyse the degree of dispersion of the reflectance along with the change of LWC. Simulation analysis shows that bands 5 and 6 are sensitive bands of leaf water content. To further analyse the influence of different combination of bands, new indices are extracted from Normalized difference vegetation index (NDVI), difference vegetation index (DVI), ratio vegetation index (RVI) under 11 band combinations. Polynomial regression was used to establish the relationship between the vegetation index and the leaf water content. Coefficient of determination (R^2) was used to evaluate the strength of the relationship. In the end, data in LOPEX93 was used to evaluate the accuracy of the predicted LWC from the index. RMSE was employed to do the accuracy assessment. We find that DVI (4, 5) is the best index to retrieve leaf water content from GF-5 data. The results show that the retrieval accuracy can be as high as 0.0007g/cm^2.

1 INTRODUCTION

Leaf water content is one of the main controlling factors of the photo synthesis, respiration and biomass in plant leaves, Spatial and temporal variability of leaf water content is critical for monitoring drought risk, diagnosing plant diseases and insect pests, predicting wildfires and estimating crop yields (M. E. Bauer, 1986; B.Datt 1999; H. G. Jones 1998; Yanosky, T. M 2005). Traditional measurement of water content of vegetation, which compares the difference in weight between fresh and dry leaves to address leaf water content, can only be carried out manually at field scale. (F. M. Danson 2004). Remote sensing, on the other hand, provides a means to monitor water content of vegetation at large scale with flexible spatial and temporal resolution (H. Erjr 1989). Leaf water content has been widely retrieved using spectral data collected in the visible, near infrared and shortwave infrared (VNIR and SWIR) Thomas et al. studied the relationship between water content and spectral reflectance of vegetation leaves by obtaining the reflectance spectra of different leaf water content(Thomas 1971). They found that the reflectance of vegetation leaves increased with the decrease of leaf water content. And reflectance at 1450nm and 1930nm are significantly correlated with leaf water content. Carter found that reflectance at 1450 nm, 1950 nm, and 2500 nm was most sensitive to leaf water content changes(Carter 1991);Sims found that the reflectance at the 950 ~ 970 nm and 1150 ~ 1260 nm was related strongly to the leaf water content(Sims 2003). Zhang found that the solar spectral reflectance indicated a leaf water absorption zone near 970nm, 1200nm, 1450nm, 1930nm and 2500nm, at which reflectance can be used for the estimation of leaf water content (Zhang 2006). Based on this water sensitive wavebands, combined with the absorption and scattering characteristics of visible light, near infrared and shortwave infrared reflectance, the vegetation moisture index model of different types such as moisture stress index (MSI), water index (WI), normalized difference water index (NDWI), global

water moisture index(GWMI)are put forward. Based on the above research, in order to extract the water content index of LWC, we should first carry out the analysis of leaf water content sensitive index to find out which band is suitable for LWC retrieval.

GF-5 satellite is launched for the main use of Chinese Ministry of Environmental Protection .The satellite also carries the most sensors, has the highest spectral resolution in National Science and Technology Major Project. The satellite data can be used to monitor aerosols, terrestrial vegetation, urban heat islands and other environmental factors. In this paper, we use the radiative transfer model of vegetation leaves to simulate reflectance under different LWC, Analyse the sensitive band of LWC. Based on the classical vegetation index and the GF-5 SRF, the remote sensing LWC vegetation index based on GF-5 data is established.

2.1 Use of model

Leaf reflectance was first simulated by the PROSPECT model. PROSPECT model is a radiative transfer model obtained by simulating the upwards and downwards radiation flux of the leaf. With a few parameters as input, it is able to simulate the reflectance and transmittance of the blade from $0.4\mu m$ to $2.5\mu m$. The parameters such as chlorophyll content, carotene content, leaf structure parameters, brown pigment content and dry matter content were kept constant. The leaf water content was changed in steps to simulate the change of leaf reflectance under different leaf water content.

2.2 Parameter range

In the data simulation process, the first step is to set the value of the parameters. In order to make the value of the parameters closer to the true leaf content of the biochemical substance, the parameter values in the PROSPECT model in this paper are derived from the average measured values for the 1993 LOPEX93 experiment. In which, different types of leafy plant species were collected at two different times.The values of each input parameters were determined according to the biochemical content of 70 leaves in the experiment. In order to carry out the sensitive band analysis of LWC, the most frequent value was selected as the fixed value of other non-essential parameters. It is noteworthy that, for example, the dry matter content of different leaves is very different, the most frequent value of this parameter is around 0.004 g / cm^2, but the maximum value reaches 0.014 g / cm^2, so the most frequent value is chosen as the representation to simulate the reflectance. (Table 1).

Table 1. The values of parameters according to LOPEX 93'

leaf structure parameter	1.5
chlorophyll a+b content	$40 \mu g/cm^2$
carotenoids content	$13 \mu g/cm^2$
brown pigments concentration	0
Leaf water content	0.011-$0.05 g/cm^2$ ($0.001 g/cm^2$ as step)
dry matter content	0.004 g/cm^2

At the same time, we used the reflectance measured in the LOPEX93 experiment as the validation dataset. The simulation results and accuracy of the calibration group were evaluated by 330 sets of measurement data in this experiment. For the calibration group, a standard deviation of the reflectance of the sample with 40 different water contents was used to find the band suitable for retrieval. The simulated hyperspectral reflectivity and calculated band reflectance under 40 different LWC are also displayed in Figure 1.
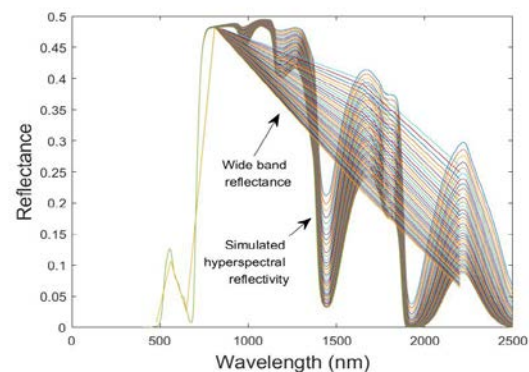
Figure 1. The simulated hyperspectral reflectivity and calculated wide band reflectance under 40 different LWC.

2.4 GF-5 band reflectance

In order to obtain the wide band reflectance of the satellite based sensor, we used the spectral response function of GF-5 to convolve the simulated hyperspectral reflectance. The GF-5 satellite sensor has a visible short-wave infrared region with band1 (400 to 520 nm), band 2 (520 to 600 nm), band 3 (620 to 680 nm), band 4 (760 to 860 nm), band 5 (1550 nm to 1750 nm), band 6 (2080 ~ 2350nm). The spectral response function of band 4, for example, can be seen in Figure 2.
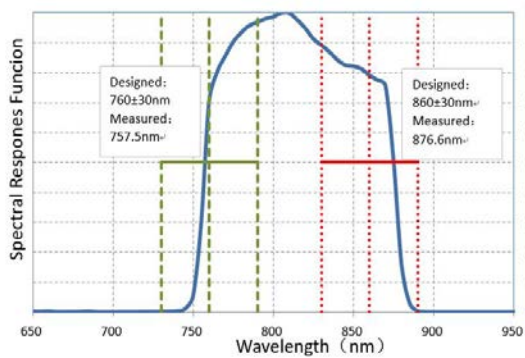
Figure 2. 4th band spectral response function of the sensor on GF-5 satellite

2.5 Data analysis

In order to find a sensitive band, the standard deviation was introduced to analyse the degree of dispersion of the reflectance along with the change of LWC. The greater the degree of dispersion, the more sensitive it is. Band reflectance in both sensitive bands and insensitive bands were used as the input of the new vegetation index to calculate the vegetation index.

In the field of remote sensing applications, the vegetation index has been widely used to qualitatively and quantitatively assess vegetation cover and its growth vigor. Because the spectral index can effectively reduce the scattering effect of vegetation leaves on single spectral band reflectivity. Therefore, the vegetation LWC index is established by using the combination of absorption and scattering characteristics of different leaf segments. In this paper, we use the three vegetation index types, namely, the ratio vegetation index model, the difference vegetation index model and the normalized difference vegetation index model. According to the results of band sensitivity analysis, a total of 11 combinations of the following can be obtained. (Table 2)

Polynomial regression was used to establish the relationship between the vegetation index and the leaf water content. Coefficient of determination (R^2) was used to evaluate the strength of the relationship. In the end, data in LOPEX93 was used to evaluate the accuracy of the predicted LWC from the index. RMSE was employed to do the accuracy assessment

3 RESULT

The standard deviation of the simulated reflectivity does not change much in band 1 to band 4. Indicating that in these bands, changes in water content cannot cause a large change in reflectivity, so these bands are leaf water content insensitive bands. In band 5 and band 6, however, the standard deviation of the reflectance is large, indicating that the two bands are the sensitive band.

Table 2. Three vegetation index under different band combinations

BAND	NDVI	DVI	RVI
1+5	$NDVI_{(1, 5)}$	$DVI_{(1, 5)}$	$RVI_{(1, 5)}$
2+5	$NDVI_{(2, 5)}$	$DVI_{(2, 5)}$	$RVI_{(2, 5)}$
3+5	$NDVI_{(3, 5)}$	$DVI_{(3, 5)}$	$RVI_{(3, 5)}$
4+5	$NDVI_{(4, 5)}$	$DVI_{(4, 5)}$	$RVI_{(4, 5)}$
1+6	$NDVI_{(1, 6)}$	$DVI_{(1, 6)}$	$RVI_{(1, 6)}$
2+6	$NDVI_{(2, 6)}$	$DVI_{(2, 6)}$	$RVI_{(2, 6)}$
3+6	$NDVI_{(3, 6)}$	$DVI_{(3, 6)}$	$RVI_{(3, 6)}$
4+6	$NDVI_{(4, 6)}$	$DVI_{(4, 6)}$	$RVI_{(4, 6)}$
5+6	$NDVI_{(5, 6)}$	$DVI_{(5, 6)}$	$RVI_{(5, 6)}$
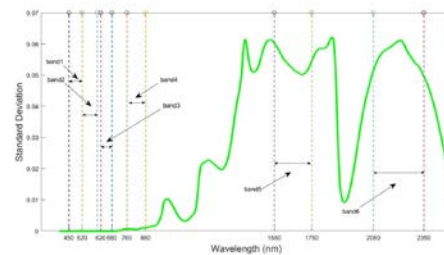
Figure 3. The standard deviation curve of reflectance in different band

Three classic vegetation index models NDVI, DVI, RVI, were introduced to calculate the corresponding new vegetation index. As mentioned above, band 1 to band 4 are not sensitive to leaf water content changes, so here band 1 to band 4 are combined with band 5 and band 6, respectively, there are 11 ways to combine the wide band reflectance in total. According to 11 band combinations, the correlation coefficients between simulated water content and simulated wide-band reflectance are shown in the following table. At the same time, according to the LOPEX93 experiment, the regression results were verified using the water content and spectral measurements of 330 samples in the experiment. RMSEs are also shown in the table below and in Figure 4-6. The result shows that NDVI (4, 5), DVI (2, 6), RVI (4, 5) are the best to retrieve leaf water content.

Table 3. R² between vegetation index and leaf water content, RMSE between real LWC and predicted LWC in LOPEX93 regressed by index.

INDEX	NDVI		RVI		DVI	
BAND	R2	RMSE	R2	RMSE	R2	RMSE
1+5	0.758	0.248	0.758	1.185	0.992	0.639
2+5	0.999	0.021	0.997	0.154	0.993	0.06
3+5	0.981	0.104	0.981	0.542	0.992	0.275
4+5	0.998	0.012	0.993	0.089	0.993	0.007
1+6	0.935	0.109	0.932	0.358	0.974	0.191
2+6	0.999	0.014	0.989	0.046	0.976	0.021
3+6	0.994	0.042	0.988	0.142	0.975	0.076
4+6	0.99	0.013	0.975	0.066	0.974	0.006
5+6	0.996	0.012	0.989	0.086	0.368	0.011
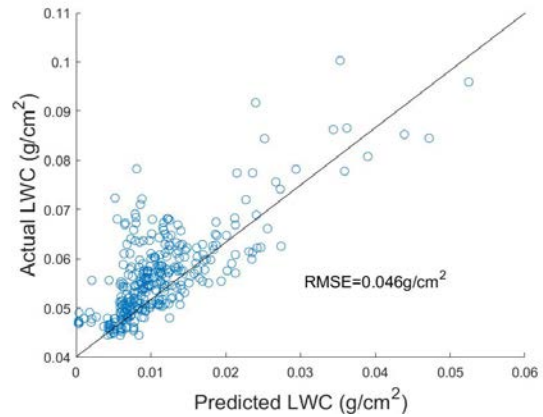
Figure 6. RMSE of RVI at the band combination of 2 and 6.

4 CONCLUSION

In this paper, new vegetation index using the combination of 11 band reflectance simulated from GF-5 sensor has been proposed to retrieve LWC. The vegetation leaf model PROSPECT model have been used to simulate the hyperspectral reflectance. LOPEX 93 dataset was used for accuracy validation.

To analyse the sensitive of the spectral reflectance to the change of LWC, change of standard deviation of the reflectance with LWC respect to wavelength has been calculated. The results show that the spectral reflectance at band 5 and band 6 are sensitive to the variation of LWC.

Three vegetation indices, normalized difference vegetation index (NDVI), ratio vegetation index (RVI) and difference vegetation index (DVI), have been used to retrieve the LWC. Comparisons of the retrieval LWC showed that the DVI combined by band 4 and band 5 is the best with RMSE of 0.007 g/cm².

Figure 4. RMSE of DVI at the band combination of 4 and 5.
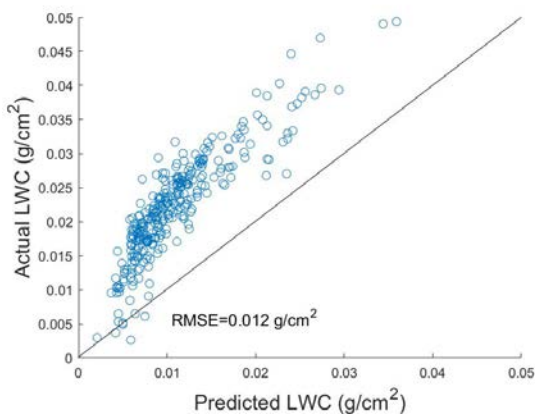
Figure 5. RMSE of NDVI at the band combination of 4 and 5.

REFERENCES

Aldakheel, Y. Y. and F. M. Danson. "Spectral Reflectance of Dehydrating Leaves: Measurements and Modelling." *International Journal of Remote Sensing* 18, no. 17 (1997): 3683-3690.

Bauer, Marvin E., Craig S. T. Daughtry, Larry L. Biehl, Edward T. Kanemasu and Forrest G. Hall. "Field Spectroscopy of Agricultural Crops." *IEEE Transactions on Geoscience & Remote Sensing* GE-24, no. 1 (1986): 65-75.

Carter, Gregory A. "Primary and Secondary Effects of Water Content on the Spectral Reflectance of Leaves." *American Journal of Botany* 78, no. 7 (1991): 916-924.

Ceccato, Pietro, Stéphane Flasse, Stefano Tarantola, Stéphane Jacquemoud and Jean Marie Grégoire. "Detecting Vegetation Leaf Water Content Using Reflectance in the Optical Domain." *Remote Sensing of Environment* 77, no. 1 (2001): 22-33.

Cheng, T., B. Rivard and A. Sánchez-Azofeifa. "Spectroscopic Determination of Leaf Water Content Using Continuous Wavelet Analysis." In *Geoscience and Remote Sensing Symposium*, 659-670, 2010.

Colombo, R., M. Meroni, A. Marchesi, L. Busetto, M. Rossini, C. Giardino and C. Panigada. "Estimation of Leaf and Canopy Water Content in Poplar Plantations by Means of Hyperspectral Indices and Inverse Modeling." *Remote Sensing of Environment* 112, no. 4 (2008): 1820-1834.

Danson, F. M. and P. Bowyer. "Estimating Live Fuel Moisture Content from Remotely Sensed Reflectance." *Remote Sensing of Environment* 92, no. 3 (2004): 309-321.

Datt, B. "Remote Sensing of Water Content in Eucalyptus Leaves." *Australian Journal of Botany* 47, no. 6 (1999): 909-923.

Gerber, F., R. Marion, A. Olioso, S. Jacquemoud, B. Ribeiro Da Luz and S. Fabre. "Modeling Directional–Hemispherical Reflectance and Transmittance of Fresh and Dry Leaves from 0.4μm to 5.7μm with the Prospect-Visir Model." *Remote Sensing of Environment* 115, no. 2 (2016): 404-414.

Jones, H. G. and F. Tardieu. "Modelling Water Relations of Horticultural Crops: A Review." *Scientia Horticulturae* 74, no. 1–2 (1998): 21-46.

Jr, E. Raymond Hunt and Barrett N Rock. "Detection of Changes in Leaf Water Content Using near- and Middle-Infrared Reflectances ☆." *Remote Sensing of Environment* 30, no. 1 (1989): 43-54.

Sims, Daniel A and John A Gamon. "Estimation of Vegetation Water Content and Photosynthetic Tissue Area from Spectral Reflectance: A Comparison of Indices Based on Liquid Water and Chlorophyll Absorption Features." *Remote Sensing of Environment* 84, no. 4 (2003): 526-537.

Thomas, J. R, L. N Namken, G. F Oerther and R. G Brown. "Estimating Leaf Water Content by Reflectance Measurements." *Agronomy Journal* 63, no. 6 (1971): 845-847.

Yi, Qiuxiang, Fumin Wang, Anming Bao and Guli Jiapaer. "Leaf and Canopy Water Content Estimation in Cotton Using Hyperspectral Indices and Radiative Transfer Models." *International Journal of Applied Earth Observations & Geoinformation* 33, no. 33 (2014): 67-75.

Zhang, Jiahua and Wenjuan Guo. "Quantitative Retrieval of Crop Water Content under Different Soil Moistures Levels." *Proc Spie* 6411, (2006): 64110D-64110D-9.

A Temperature and Emissivity Retrieval Algorithm Based on Atmospheric Offset Characteristic from Low emissivity Hyperspectral Thermal Infrared Data

CHEN Mengshuo[1], Wu Hua[1,2], Jiang Xiaoguang[1,3,*], Li Zhaoliang[4], QIAN Yonggang[3], Wang Ning[3]

1. University of Chinese Academy of Sciences, Beijing 100190, China
2. The State Key Laboratory of Resources and Environmental Information System, Institute of Geographical Sciences and Natural Resources Research, Chinese Academy of Sciences, Beijing, 100101, China
3. Key Laboratory of Quantitative Remote Sensing Information Technology, Academy of Opto-Electronics, Chinese Academy of Sciences, Beijing 100094, China
4. Key Laboratory of Agri-informatics, Ministry of Agriculture/Institute of Agricultural Resources and Regional Planning, Chinese Academy of Agricultural Sciences, Beijing 100081, China;
*Corresponding author: xgjiang@ucas.ac.cn

Abstract Land surface temperature and emissivity separation (TES) is a key problem in thermal infrared (TIR) remote sensing. Many TES algorithms have been proposed and have been validated on natural surface materials. However, when applied on low emissivity materials, the retrieval accuracy still needs to be improved. Aiming at the problem of stronger coupling between land surface and atmosphere in the retrieval of low emissivity materials, a method for quickly estimating relative accurate initial LST are proposed on the basis of atmospheric absorption. And through exploring the offset characteristic of atmospheric downward radiance, a temperature/emissivity retrieval algorithm based on atmospheric offset characteristic are proposed from hyperspectral thermal infrared data. The results show that the accuracy of first guess temperature estimated with new method is well improved compared with the traditional method for low emissivity materials. By using the estimated first guess temperature, a comparison between the proposed TES algorithm and iterative spectrally smooth temperature and emissivity separation (ISSTES) is further carried out in this paper. The accuracy of proposed TES algorithm is about 0.4K better than ISSTES for low emissivity materials, which means the proposed algorithm can weaken the influence of the error of atmospheric downward radiance. In addition, the proposed algorithm just involves several groups of channels, which make the computation efficiency be higher than ISSTES. In conclusion, the proposed algorithm can provide an accurate and fast TES for low emissivity materials.

Index Terms--Land surface temperature and emissivity, hyperspectral thermal infrared, low emissivity

1. INTRODUCTION

Land surface temperature (LST) and Land surface emissivity (LSE) are important physical parameters for characterization of surface state. LST is vital in the physical processes of surface energy and water balance at local through global scales(Li, Z. L,2013, Friedl, M. A,2002, Anderson, M. C.,2008, Hashimoto, H.,2008) and also widely used in a variety of fields include evaporation(Salvucci, G. D,1997, Kalma, J,2008), urban heat island[7]climate modelization(Gillespie, A,1998). LSE is important for studies of soil development and erosion, bedrock mapping, resource exploration and so on(Gillespie, A,1998, Li, Z. L,2013, Vaughan, R. G.,2003). The most efficient method to investigate the LST and LSE over a local/global region is utilizing the remotely sensed hyperspectral thermal infrared (TIR) data. While the retrieval of LST and LSE is carried out from the at-surface radiance, since N observed equations need to calculate N emissivity with one temperature, the core issue is how to solve the ill-posed problem in temperature-emissivity separation (TES). Up to now, many TES methods have been proposed for solving the problem, such

as iterative spectrally smooth temperature and emissivity separation (ISSTES)(C. C. Borel,1998), the automatic retrieval of temperature and emissivity using spectral smoothness method (ARTEMISS)(C. C. Borel,1998), downward radiance residual index (DRRI) method(Xinghong Wang,2008), stepwise refining algorithm of temperature and emissivity separation(Cheng Jie,2008), linear spectral emissivity constraint temperature and emissivity separation(Ning Wang,2011). For natural surface materials (such as water, vegetation and soil) which have high emissivity in the thermal infrared band, various kinds of uncertainty have small impact on retrieval results [16]. The existing hyperspectral thermal infrared surface temperature/emissivity retrieval algorithm has achieved good accuracy(Wan, Z,1997, Sobrino, J. A,2001).

However, except for natural surface materials, ground targets also includes metal materials (such as steel), artificial materials (aluminum foil, ceramic tiles, glass, etc.), low emissivity coatings, which are made up of relatively low emissivity materials, those objects are closely linked with human activities and have a wide range of applications. Some research also pointed out that retrieval algorithm could not recover LST with the nominal accuracy, especially for the surfaces with lower emissivity(Boonmee, M,2007).The possible reasons are as follows: (1) For low emissivity materials, because of the land-atmosphere coupling problem, the accuracy of retrieval results could reduce with the influence of the instrument noise and the uncertainties in atmospheric downward radiance. From Qian yg' work(Qian, Y.,2016), the uncertainty in atmospheric downward radiance dominate the large retrieval error of low emissivity materials. (2) The existed ways of estimation of initial temperature like brightness temperature method are not suitable for low-emissivity materials. In term of a nonlinear problem, an initial temperature has a large difference with actual LST will lead to efficiency decrease or failure to search the result. In this paper, by exploring the absorption characteristics of atmospheric downward radiance,

an algorithm is proposed from hyperspectral thermal infrared data to retrieve the temperature and emissivity for low emissivity materials. In this paper, the low emissivity is defined as the value of emissivity is low on whole spectra, since when high value band exists, the band can be used for retrieving a high accuracy result.

2. METHODOLOGY

2.1 Radiative transfer equation

In TIR domain (8~14 μ m), ignoring the scattering effect of atmosphere and assuming a local thermodynamic equilibrium, the at-sensor radiance measured by an instrument can be described by atmospheric radiative transfer equation (RTE)(Zhao-Liang Li,1999).

$$L(\lambda) = L_g(\lambda)\tau(\lambda) + L_\uparrow(\lambda)$$
$$L_g(\lambda) = \varepsilon(\lambda)B(\lambda, T_s) + (1 - \varepsilon(\lambda))L_\downarrow(\lambda) \quad (1)$$

Where $L(\lambda)$ and $L_g(\lambda)$ is the radiance measured at sensor and at ground in wavelength λ, $\varepsilon(\lambda)$ is the land surface emissivity, $B(\lambda, T)$ is the Planck's function at land surface temperature T, $L_\uparrow(\lambda)$ and $L_\downarrow(\lambda)$ is upward and downward atmospheric radiance.

According to the radiative transfer equation, the land surface emissivity can be estimated as:

$$\varepsilon(\lambda) = \frac{L_g(\lambda) - L_\downarrow(\lambda)}{B(\lambda, T) - L_\downarrow(\lambda)} \quad (2)$$

2.2 A temperature and emissivity retrieval algorithm based on atmospheric absorption feature

Experiments found the atmospheric downward radiance spectrum's integral offset phenomenon when water vapor profile and temperature profile have estimation error (Figure 1), on the basis of the assumption that downward radiance's offset at atmospheric absorption peak/valley channels is approximately invariant, this paper attempts to weaken the influence of uncertainty of atmospheric downward radiance through the adjacent atmospheric absorption peak/valley channel's difference, then achieve an rather

accurate initial temperature, finally the LST and LSE will be extracted. The specific process is as follows.

According to the equation (1), calculate the difference of at-ground radiance at atmospheric absorption peak/valley channels:

$$L_g(\lambda_{peak}) - L_g(\lambda_{valley}) = [\varepsilon(\lambda_{peak})B(\lambda_{peak}, T_s) - \varepsilon(\lambda_{valley})B(\lambda_{valley}, T_s)]$$
$$+ [(1 - \varepsilon(\lambda_{peak}))L_\downarrow(\lambda_{peak}) - (1 - \varepsilon(\lambda_{valley}))L_\downarrow(\lambda_{valley})]$$

(3)

Where $L_g(\lambda_{peak})$ and $L_g(\lambda_{valley})$ are the at-ground radiance at atmospheric absorption peak/valley channel, $L_\downarrow(\lambda_{peak})$ and $L_\downarrow(\lambda_{valley})$ are the atmospheric downward radiance, $\varepsilon(\lambda_{peak})$ and $\varepsilon(\lambda_{valley})$ are the emissivity.

Additional constraints are required for extracting the LST and LSE from equation (2). For hyperspectral thermal infrared data, assuming that surface emissivity in adjacent channels are approximately equal, and the self-radiance in the adjacent channels due to the small wavelength variation are also assumed approximately equal.

$$\varepsilon(\lambda_{peak}) \approx \varepsilon(\lambda_{valley})$$
$$\varepsilon(\lambda_{peak}) \cdot B(\lambda_{peak}, T) \approx \varepsilon(\lambda_{valley}) \cdot B(\lambda_{valley}, T)$$

(4)

By the above assumptions, according to the equation (2), the average emissivity between peak/valley channels can be calculated as:

$$\varepsilon(\lambda) = 1 - \frac{L_g(\lambda_{peak}) - L_g(\lambda_{valley})}{L_\downarrow(\lambda_{peak}) - L_\downarrow(\lambda_{valley})}$$

(5)

The initial temperature can be estimated as:

$$T_{initial} = B^{-1}(\lambda_{valley}, \frac{L_g(\lambda_{valley}) - [1 - \varepsilon(\lambda_{valley})]L_\downarrow(\lambda_{valley})}{\varepsilon(\lambda_{valley})})$$

(7)

Based on the acquired initial temperature, the process of the retrieval of LST and LSE is as follows:

According to the radiative transfer equation, the land surface emissivity can be estimated as:

$$\varepsilon(\lambda, T_{opt}) = \frac{L_g(\lambda) - L_\downarrow(\lambda)}{B(\lambda, T_{opt}) - L_\downarrow(\lambda)}$$

(8)

An approach is that the emissivity at adjacent channels are approximately invariant, the

equivalent emissivity at two adjacent channels can be presented as:

$$\overline{\varepsilon}_{i,opt} = \left[\varepsilon_i(\lambda_{peak}, T_{opt}) + \varepsilon_i(\lambda_{valley}, T_{opt}) \right] / 2$$

(9)

An index is defined to find the best-fitting temperature T_{opt} by computing the difference of the measured minus the simulated radiance at two adjacent channels:

$$Rdiff_i = \left[L_{g_{i,m}}(\lambda_{peak}) - L_{g_{i,m}}(\lambda_{valley}) \right] - \left[L_{g_{i,fit}}(\lambda_{peak}, T_{opt}, \overline{\varepsilon}_{i,opt}) - L_{g_{i,fit}}(\lambda_{valley}, T_{opt}, \overline{\varepsilon}_{i,opt}) \right],$$
$$L_{g_{i,fit}}(\lambda, T_{opt}, \overline{\varepsilon}_{i,opt}) = \overline{\varepsilon}_{i,opt}B(\lambda, T_{opt}) + (1 - \overline{\varepsilon}_{i,opt})L_\downarrow(\lambda)$$

(10)

Where $L_{g_{i,m}}(\lambda_{peak})$ and $L_{g_{i,m}}(\lambda_{valley})$ are the measured at-ground radiance at atmospheric absorption peak/valley channels, $L_{g_{i,fit}}(\lambda_{peak}, T_{opt}, \overline{\varepsilon}_{i,opt})$ and $L_{g_{i,fit}}(\lambda_{valley}, T_{opt}, \overline{\varepsilon}_{i,opt})$ are the simulated at-ground radiance at atmospheric absorption peak/valley channels, $\overline{\varepsilon}_{i,opt}$ are the equivalent emissivity at adjacent channels.

The above formula can be expanded as:

$$Rdiff_i = \left[L_{g_{i,m}}(\lambda_{peak}) - L_{g_{i,m}}(\lambda_{valley}) \right] -$$
$$\left[\overline{\varepsilon}_{i,opt}(B(\lambda_{peak}, T_{opt}) - B(\lambda_{valley}, T_{opt})) + (1 - \overline{\varepsilon}_{i,opt})(L_\downarrow(\lambda_{peak}) - L_\downarrow(\lambda_{valley})) \right]$$

(11)

Obviously, when atmospheric downward radiance has error (Figure 1), by separating the offset error from correct downward radiance, above equation can be written as:

$$Rdiff_i = \left[L_{g_{i,m}}(\lambda_{peak}) - L_{g_{i,m}}(\lambda_{valley}) \right] -$$
$$\left[\overline{\varepsilon}_{i,opt}(B(\lambda_{peak}, T_{opt}) - B(\lambda_{valley}, T_{opt})) + (1 - \overline{\varepsilon}_{i,opt})(L_\downarrow(\lambda_{peak}) - L_\downarrow(\lambda_{valley})) \right] -$$
$$(1 - \overline{\varepsilon}_{i,opt})\left[\Delta L_\downarrow(\lambda_{peak}) - \Delta L_\downarrow(\lambda_{valley}) \right]$$

(12)

Where $\Delta L_\downarrow(\lambda_{peak})$ and $\Delta L_\downarrow(\lambda_{valley})$ are the downward radiance's offset at atmospheric absorption peak/valley channels.

Since the downward radiance's offset is approximately the same at adjacent channels, i.e.:

$$\Delta L_\downarrow(\lambda_{peak}) \approx \Delta L_\downarrow(\lambda_{valley})$$

(13)

Obviously, the equation (11) is equivalent to equation (12), which means this method can weaken the error of atmospheric downward radiance, thereby increasing the accuracy of the retrieval results. The criterion (cost function) is defined as the square root of the sum of square of index at several adjacent channel groups.

$$\sigma(T_{opt}, \varepsilon_{opt}) = \min \sqrt{\sum_{i=1}^{N} Rdiff_i^2} \qquad (14)$$
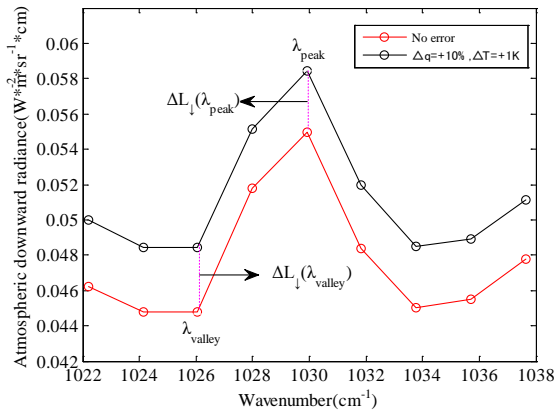
Figure 1.   The atmospheric downward radiances

Table 1 The selected channel groups for retrieval

#	$\lambda_{valley}(cm^{-1})$	$\lambda_{peak}(cm^{-1})$	#	$\lambda_{valley}(cm^{-1})$	$\lambda_{peak}(cm^{-1})$
1	1134.06	1135.99	9	1209.28	1211.21
2	1139.85	1135.99	10	1215.06	1211.21
3	1162.99	1164.92	11	1216.99	1218.92
4	1166.85	1164.92	12	1222.78	1224.71
5	1172.63	1174.56	13	1226.64	1224.71
6	1176.49	1174.56	14	1234.35	1236.28
7	1195.78	1197.71	15	1242.07	1243.99
8	1199.64	1197.71	16	1247.85	1243.99

3.   DATA

In this paper, to simulate hyperspectral thermal infrared data corresponding to various atmospheric situations and land surface types. Several atmospheric profiles are chosen from TIGR (Thermodynamic Initial Guess Retrieval) constructed by the Laboratoire de Meteorologie Dynamique (LMD) (Chedin, A,1985, Achard,

V.1991, Chevallier, F,1998). The TIGR database contains 2311 typical atmospheric profiles which define a 40-layer atmosphere and contain the following data for each layer: altitude, pressure, temperature, water vapor density. The profiles with relative humidity at any layer greater than 90% or at two consecutive layers greater than 85% were considered to be cloudy (Galve J M, 2008). Firstly, we select 1413 cloudless atmospheric profiles; secondly, taking into account the principle of uniform distribution of water vapor, 195 atmospheric profiles are chosen from cloudless atmospheric profiles for simulation. The bottom temperature of the selected profiles varies from 250K to 309K, atmospheric total precipitable water (TPW) nearly equally distributes between 0.10~5.56 g/cm^2.

Subsequently, the corresponding atmospheric transmittance, atmospheric downward radiance and atmospheric upward radiance are calculated with the MODTRAN 5.0, which is developed by AFRL/VSBT（Air Force Research Lab, Space Vehicles Directorate）and Spectral Sciences, lnc.. Since MODRAN 5.0 can provide high spectral resolution as fine as 0.1 cm-1 and well suited for simulating hyper-spectral TIR radiances. It is used to simulate the atmospheric parameters located in atmospheric windows from 800 cm-1 to 1250 cm-1(8-12.5 μm). To better cover the real situation, the spectral resolution is set as 4 cm-1 (FWHM) and a spectral sampling interval is 2 cm-1 according to the parameter settings of ABB Bomem MR304.

10 types of representative high/low emissivity materials are chosen to generate the simulated hyperspectral TIR data for analysis. The emissivity spectra of these materials are downloaded from University of California, Santa Barbara (UCSB) spectral library and Johns Hopkins University (JHU) spectral library are shown in Figure 4. For each surface material at each atmospheric condition, the reasonable ranges of LSTs in the simulation were set according to the bottom temperature (Ta) of the selected profiles, and LST varied from Ta-10K to Ta +15K in steps of 5K.
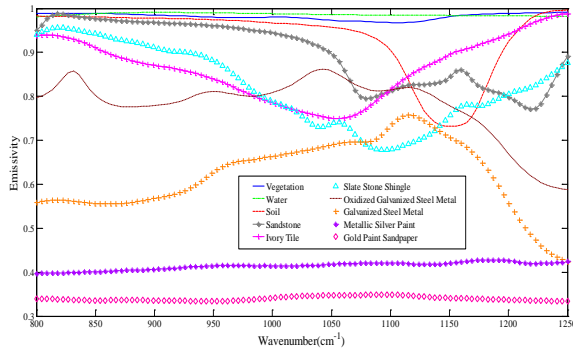
Figure 2. Emissivity spectrum of ten materials

Table 2 Emissivity characteristics of ten materials

Material name	Abb.	Mean of the spectral emissivity at chosen channels	Difference of the spectral emissivity at chosen channels
Water	WA	0.98675	0.00029
Vegetation	VE	0.98310	0.00003
Soil	SO	0.89189	0.00534
Sandstone	AS	0.82190	0.00329
Ivory Tile	IT	0.94064	0.00223
Slate Stone Shingle	SSS	0.80413	0.00330
Oxidized Galvanized Steel Metal	OGSM	0.67795	0.00395
Galvanized Steel Metal	GSM	0.56384	0.00584
Metallic Silver Paint	MSP	0.42317	0.00037
Gold Paint Sandpaper	GPS	0.33766	0.00020

4. RESULTS

The accuracy of algorithm is characterized by root-mean-square error (RMSE) of temperature and RMSE of relative emissivity errors:

$$RMSE_{LST} = \sqrt{\frac{\sum_{i=1}^{M}(LST_{ret,i} - LST_{true})^2}{M}} \quad (8)$$

$$RMSE_{LSE} = \sqrt{\frac{\sum_{j=1}^{M}\sum_{i=1}^{N}\left(\left(LSE_{ret,i[j]} - LSE_{true,i[j]}\right)\Big/LSE_{true,i[j]}\right)^2}{M \times N}} \quad (9)$$

Where LST_{ret} and LST_{true} are the retrieved and true temperature, respectively. N is band number. M is total number of measurements.

4.1 Modeling accuracy

To analyze the effect of the difference of emissivity at adjacent channels, the retrieval is carried out on data without error. As shown in Figure 3, all materials' retrieval errors are less than 0.05K for temperature and 0.64% for emissivity and the accuracy of materials with rather high emissivity is higher than rest materials'. The largest error and the smallest error for temperature is shown in AS with 0.05K and in VE also WA with 0.03K, respectively. The largest and the smallest error for emissivity is shown in GSM with 0.64% and SSS with 0.44%, respectively. The reason is that more dramatic spectral changes at adjacent channels cause larger modeling error.
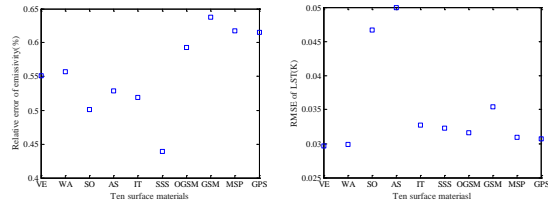
Figure 3. The effect of assumption on LST/LSE separate

4.2 Sensitivity analysis

4.2.1 Instrument noise

To investigate the influences of instrument noise on the accuracy of retrieval results, different levels of noise equivalent differential temperature (NEΔT) of 0.05, 0.10, 0.15, and 0.20K are added to the land surface brightness temperature of simulated ground-leaving radiance. For each level of NE△T, the random noise is simulated 1000 times as an array of Gaussian distributed random numbers with mean of 0 and standard deviation of the value of NE△T. As shown in Figure 4, natural surface materials have better retrieval accuracy than the rest materials, which means the influence of instrument noise is lager on relative low emissivity materials. With increase of NEΔT, the errors of LST and LSE will also increase.

Compared to the high emissivity materials, the increase of retrieval error for low emissivity materials is larger. With NEΔT varying from 0.05K to 0.2K, the error of LST increases about 0.24K and the error of LSE increases 0.63% for VE and WA, the error of LST increases 0.5K and the error of LSE increases 1.4% for GPS.
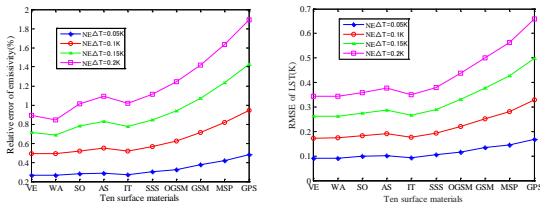
Figure 4. Influence of NEΔT on LST/LSE

4.2.2 Atmospheric downward radiance

Generally, in the process of TES, the atmospheric downward radiance is the input parameter. However, there is no effective way to estimate the actual downward radiance. When it is calculated by using atmospheric radiative transfer model with atmospheric sounding data, the miscalculation of the water vapor and temperature will result in offset error. Compared with high emissivity materials, low emissivity materials' TES are easy to be influenced by the error. To analyze the sensitivity of the atmospheric downward radiance error, the temperature and moisture profiles of the selected 195 atmospheric profiles from TIGR database are shifted by 1 K and 10% (△T=1K, △q=10%) and -1 K and -10% (△T=-1K, △q=-10%), respectively. The shifted profiles are used for generated the downward radiance containing error with MODTRA 5. Then the error-free ground-leaving radiance and the error-added downward radiance are used as input parameters for TES.

As shown in Figure 5, for high emissivity materials (such as IS, WA and VE), the retrieved LSTs are similar between the error-free and error-added downward radiances. The reason is that the atmospheric downward radiance takes a little part in at-surface radiance for high emissivity materials, there is a slightly effect of atmospheric downward radiance error on LST compared to low emissivity materials. However, the error-added downward

radiance is used in the calculation of LSE which leads to a slightly increase of retrieval emissivity error. Meanwhile, with the decrease of emissivity, the retrieval error will increase and the retrieval accuracy of high emissivity materials is much higher than low emissivity materials. The lower spectral emissivity and larger difference of spectral emissivity make the errors of SO and AS are larger than other high emissivity materials. The largest error is shown in GPS with 3.6K and 13.07%. It is obvious that the atmospheric downward radiance error has a larger influence on low emissivity materials.
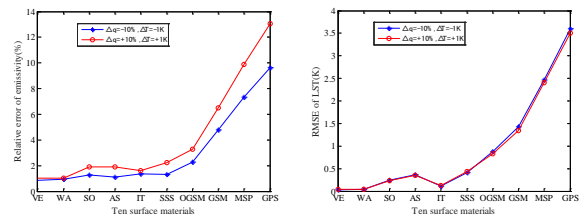
Figure 5. Influence of atmospheric downward radiance error on LST/LSE

4.3 Comparison with ISSTES

In this section, experiment is carried out to estimate the performance of the proposed method and the maximum brightness temperature method on estimating initial temperature. The maximum brightness temperature is calculated with the follow formula with setting maximum emissivity as 0.95.

$$T_{initial} = \max(B_\lambda^{-1}(L_g(\lambda), 0.95))$$

Both instrument noise and downward radiance error are taken into consideration. The NEΔT of 0.2K is added to observed data and the downward radiance is simulated with the shifted atmospheric profiles (△T=1K, △q=10% and △T=-1K, △q=-10%). As shown in figure 6, the new method for estimating initial temperature can achieve much better accuracy when applied on low emissivity materials.
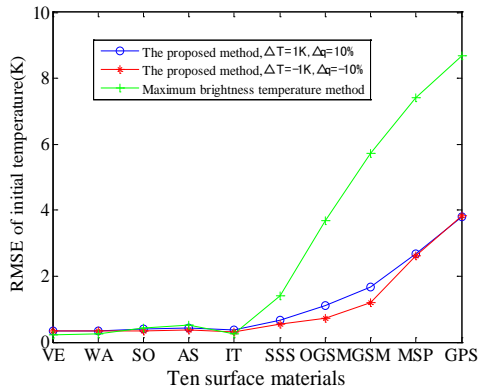
Figure 6.   Comparison of the RMSE of initial temperature calculated by two methods on different materials

The accuracy comparison of the proposed algorithm and ISSTES is carried out and the retrieval of both two methods begins with initial LST calculated by the proposed method. In this section, both instrument noise and downward radiance error are taken into consideration. The NEΔT of 0.2K is added to observed data and the downward radiance is simulated with the shifted atmospheric profiles ($\triangle$T=1K, $\triangle$q=10% and $\triangle$T=-1K, $\triangle$q=-10%). As shown in Figure 6, for high emissivity materials, the accuracy of two algorithms is basically similar; for low emissivity materials, the proposed algorithm is better and the accuracy is about 0.4K better for GPS. This is because the incorrect downward radiance has larger influence on low emissivity materials and the proposed algorithm can weaken this influence. In addition, the proposed algorithm takes 40.5h and the ISSTES takes about 407.1h which means the proposed method has higher computing efficiency.
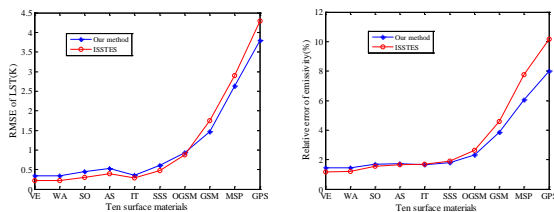
Figure 7.   The accuracy of our method and ISSTES method

5.   CONCLUSIONS

In this study, a temperature and emissivity retrieval algorithm based on atmospheric absorption feature is proposed. On basis of the assumption that the downward radiance's offsets at atmospheric absorption peak/valley channels are approximately invariant, the algorithm can weaken the influence of the atmospheric downward radiance error and separates the LST and LSE. The result shows: (1) the new method for estimating initial temperature can achieve much better accuracy when applied on low emissivity materials. (2) The proposed method shows certain improvement in the retrieval of low emissivity materials and great improvement in computing efficiency.

6.   REFERENCES

Achard, V. (1991). Trois problemes cles de l'analyse 3d de la structure thermo-dynamique de l'atmosphere par satellite : mesure du contenu en ozone; classification des masses d'air; modelisation hyper rapide du transfert radiatif. Arqueología Espacial, págs. 173-188.

Anderson, M. C., Norman, J. M., Kustas, W. P., Houborg, R., Starks, P. J., & Agam, N. (2008). A thermal-based remote sensing technique for routine mapping of land-surface carbon, water and energy fluxes from field to regional scales. Remote Sensing of Environment, 112(12), 4227-4241.

Boonmee, M. (2007), Land Surface Temperature and Emissivity Retrieval from Thermal Infrared Hyperspectral Imagery. Dissertation, Rochester Institute of Technology.

C. Borel. Error analysis for a temperature and emissivity retrieval algorithm for hyperspectral imaging data. International Journal of Remote Sensing, 2008, 29(17-18):5029-5045.

C. C. Borel. Surface emissivity and temperature retrieval for a hyperspectral sensor. Geoscience and Remote Sensing Symposium Proceedings. IGARSS '98. IEEE International, 1998, 1:546-549.

Chedin, A., Scott, N. A., Wahiche, C., & Moulinier, P. (1985). The improved initialization inversion method: a high resolution physical method for temperature retrievals from satellites of the tiros-n series.Journal of Applied Meteorology, 24(2), 128-143.

Cheng Jie, Liu QinHuo, Li XiaoWen, et al. Correlation-based temperature and emissivity separation algorithm. Science in China Series D: Earth Sciences, 2008, 51(3):357-369.

Chevallier, F. (1998). A neural network approach for a fast and accurate computation of a longwave radiative

budget. Journal of Applied Meteorology, 37(11), 1385-1397.

Friedl, M. A. (2002). Forward and inverse modeling of land surface energy balance using surface temperature measurements. Remote Sensing of Environment, 79(2–3), 344-354.

Galve J M, Coll C, Caselles V, et al. An Atmospheric Radiosounding Database for Generating Land Surface Temperature Algorithms [J]. IEEE Transactions on Geoscience & Remote Sensing, 2008, 46(5):1547-1557.

Gillespie, A., Rokugawa, S., Matsunaga, T., Cothern, J. S., Hook, S., & Kahle, A. B. (1998). A temperature and emissivity separation algorithm for advanced spaceborne thermal emission and reflection radiometer (aster) images. IEEE Transactions on Geoscience & Remote Sensing, 36(4), 1113-1126.

Hashimoto, H., Dungan, J. L., White, M. A., Yang, F., Michaelis, A. R., & Running, S. W., et al. (2008). Satellite-based estimation of surface vapor pressure deficits using modis land surface temperature data.Remote Sensing of Environment, 112(1), 142-155.

Kalma, J. D., Mcvicar, T. R., & Mccabe, M. F. (2008). Estimating land surface evaporation: a review of methods using remotely sensed surface temperature data. Surveys in Geophysics, 29(4-5), 421-469.

Li, Z. L., Tang, B. H., Wu, H., Ren, H., Yan, G., & Wan, Z., et al. (2013). Satellite-derived land surface temperature: current status and perspectives. Remote Sensing of Environment, 131(131), 14-37.

Li, Z. L., Wu, H., Wang, N., Qiu, S., Wan, Z., & Tang, B. H., et al. (2013). Land surface emissivity retrieval from satellite data. International Journal of Remote Sensing, 34(9-10), 3084-3127.

Ning Wang, Hua Wu, Françoise Nerry, et al. Temperature and Emissivity Retrievals From Hyperspectral Thermal Infrared Data Using Linear Spectral Emissivity Constraint. IEEE Transactions on Geoscience & Remote Sensing, 2011, 49(4):1291-1303.

Qian Y, Wang N, Ma L, et al. Evaluation of Temperature and Emissivity Retrieval using Spectral Smoothness Method for Low-Emissivity Materials[J]. IEEE Journal of Selected Topics in Applied Earth Observations & Remote Sensing, 2016:1-9.

Qian, Y., Wang, N., Ma, L., Chen, M., Wu, H., & Liu, L., et al. (2016). Evaluation of temperature and emissivity retrieval using spectral smoothness method for low-emissivity materials. IEEE Journal of Selected Topics in Applied Earth Observations & Remote Sensing, 9(9), 4307-4315.

Salvucci, G. D. (1997). Soil and moisture independent estimation of stage‐two evaporation from potential evaporation and albedo or surface temperature. Water Resources Research, 33(1), 111-122.

Sobrino, J. A., Raissouni, N., & Li, Z. L. (2001). A comparative study of land surface emissivity retrieval from noaa data. Remote Sensing of Environment, 75(2), 256-266.

Tomlinson, C. J., Chapman, L., Thornes, J. E., & Baker, C. (2011). Remote sensing land surface temperature for meteorology and climatology: a review. Meteorological Applications, 18(3), 296–306.

Vaughan, R. G., Calvin, W. M., & Taranik, J. V. (2003). Sebass hyperspectral thermal infrared data: surface emissivity measurement and mineral mapping. Remote Sensing of Environment, 85(1), 48-63.

Wan, Z., and Z.-L. Li (1997), A physics-based algorithm for retrieving land-surface emissivity and temperature from EOS/MODIS data. IEEE Transactions on Geoscience and Remote Sensing, 35(4):980–996.

Xinghong Wang, Xiaoying OuYang, Bohui Tang, et al. A New Method for Temperature/Emissivity Separation from Hyperspectral Thermal Infrared Data. Geoscience and Remote Sensing Symposium. IGARSS 2008. IEEE International, 2008, 3: 286 - 289.

Zhao-Liang Li, F. Becker, M.P. Stoll, et al. Evaluation of Six Methods for Extracting Relative Emissivity Spectra from Thermal Infrared Images. Remote Sensing of Environment, 1999, 69(3):197-214.

Hyperspectral indices for investigating the biochemical properties of vegetation

Agnieszka Jenerowicz, Agata Orych, Piotr Walczykowski, Mateusz Gralewicz
Military University of Technology, Faculty of Civil Engineering and Geodesy, Geodesy Institute, Department of Remote Sensing, Photogrammetry and Imagery Intelligence, gen. S. Kaliskiego 2, 00-908 Warsaw, Poland
agnieszka.jenerowicz@wat.edu.pl, agata.orych@wat.edu.pl,piotr.walczykowski@wat.edu.pl

ABSTRACT - *The main areas of interest for remote sensing research, had always been concerned with environmental studies. Significant technological developments of remote sensing techniques have greatly enhanced the quality of data acquired to determine the state of vegetation and predicting crop yields. One of the most significant technological advances of remote sensing had been the invention and popularisation of hyperspectral technologies. Such sensors make it possible to acquire continuous data about a phenomenon, generating accurate spectral characteristics. The data, obtained from hyperspectral measurements can be used to describe the growth and biochemical state of a plant and determine the source of vegetation stress. For this purpose, the spectral reflectance coefficients and vegetation indices are used. Vegetation indices allow not only to assess the overall state of vegetation but also to estimate the presence of particular minerals present in the plants or soil. The paper includes a thorough review of hyperspectral vegetation indices as well as some example measurements and results conducted by the Authors. The presented research aims to determine the possibility of using chosen hyperspectral indices to identify spectral variability within the plants due to changes to its biochemical state.*

1 INTRODUCTION

Remote sensing is a rapidly growing area of science. Research carried out by scientists lead to the discovery of new applications and modernisation of many areas of life. One of the areas in which remote sensing was applied is a system for assessing the state of vegetation and predicting crop yields.

In the 70's remote sensing started to be actively used for agriculture and since then many researchers around the world have been applying remote sensing techniques for different purposes (Brenchley, 1968; Huete, 1988; Sivakumar & Hinsman, 2003; Zarco-Tejada et al., 2005). In recent years, scientific and technical improvements have increased the potential use of remote sensing data for precision agriculture, mainly to support the quantification of spatial and temporal changes of vegetation (Fitzgerald et al., 2006; Ahamed et al., 2011; Heim et al., 2015; Lehmann et al., 2015).

The application of remote sensing in precision agriculture is based on the interaction of the electromagnetic radiation with vegetation and soil-usually, the reflected radiation is measured (Jenerowicz & Woroszkiewicz, 2016). All methods used in remote sensing for vegetation identification, crop- prediction, biomass monitoring are based on the assumption that vegetation stress, crop production are influenced by measurable biophysical parameters such

as chlorophyll, water content and content of different microelements, e.g. nitrogen, phosphorus, etc., and its variations, in which can be identified in remotely-sensed images through the use of spectral reflectance characteristics and spectral indices (vegetation indices) (Zurita-Milla et al., 2009; Rembold et al., 2013; Muramatsu et al., 2015).

Traditionally spectral reflectance coefficients are measured with spectroradiometers which allow for discrete measurements. A high accuracy characterises spectral reflectance coefficients obtained with such devices, but they can be obtained only from one point of the investigated object at any given time, which is extremely problematic when the structure of the investigated object is not homogenous or is changing in time. Methods based on spectrometric measurements can be very time-consuming. Therefore image-based methods are used more and more often, especially the hyperspectral technology (Walczykowski et al., 2016a). Hyperspectral technology allows acquiring continuous data about the phenomenon so that we get a very accurate spectral reflectance characteristics. Hyperspectral vegetation indices allow not only to overall assess the state of vegetation but also to estimate the presence of a particular mineral in plants or soil. Such remote sensing capability is applied in precision agriculture and lead to the modernisation of examination of the biochemical plants status.

The presented research aims to determine the possibility of using chosen hyperspectral indices to identify spectral variability within the plants due to changes to its biochemical state.

2 METHODOLOGY

2.1 Sensor used, and experiment set up

The sensor used for this research is a Headwall MicroHyperspec A-series VNIR 327-band pushbroom sensor. The sensor acquires hyperspectral imagery continuously line by line with a 1.9 nm spectral bandwidth in the 380- 1000 nm range. The camera can be easily mounted on an Unmanned Aerial Vehicle (Walczykowski et al., 2016b)- Fig.1.

Fig. 1. Headwall MicroHyperspec A-series VNIR 327-band pushbroom sensor

Imagery is acquired using moving the camera over the test field using a slider system mounted on an especially designed measuring station (Walczykowski et al., 2013). The station consists of a mobile frame, which can be moved in the vertical plane and a sensor arm which can be moved in three directions (X, Y, and Z). Therefore it is possible to carry out experiments in constant, repeatable conditions. Throughout the experiment, the sensor was located 1.5m above the imaged scene, and the entire scene was illuminated using well-dispersed lighting.

To ensure proper exposition and so a high quality of the acquired images, a radiometric calibration of the sensor was conducted using a Zenith Lite 95% reference panel.

The experiment was conducted in two series:
(I) 28.08.2016- 26.09.2016
(II) 26.09.2016-26.10.2016.

In order to complete the task plant samples, i.e. bean- Fig.2, were grown and treated with various fertilizers, i.e. pure water, biohumus, nitro- chalk, ammonium nitrate, potassium chloride, lime, magnesium sulphate, agricultural lime, LUBOFOS (is a complex, granulated fertilizer, it contains: ammonia nitrogen mineral acid-soluble phosphorus pentoxide, potassium oxide, total sulphur trioxide, a variety of micronutrients, such as: boron, copper, manganese, and zinc), and FOSTAR (it contains: nitrogen and phosphorus pentoxide) - Table 1.
Then, at regular intervals, hyperspectral imaging was obtained.

Fertilizer	Fertilizers dose	
	I serie	II serie
nitro- chalk	0.4 g	0.1 g
LUBOFOS	2.4 g	0.6 g
lime	2.4 g	0.6 g
ammonium nitrate	0.4 g	0.1 g
potassium chloride	1.6 g	0.4 g
biohumus	40 ml/ week	40 ml/ week
magnesium sulphate	20 ml (3%)	4 ml (3%)
water	2 x 40 ml / week	2 x 40 ml/ week
agricultural lime	2.4 g	0.6 g
FOSTAR	20 ml	4 ml

Table 1. Doses of fertilisers used in the experiment

All fertilisers were regularly applied (every seven days) in the form of aqueous solution in order to accelerate the process.

2.2 Data processing

Plant samples were grown using various fertilisers, which were administered at regular intervals throughout the growth process.
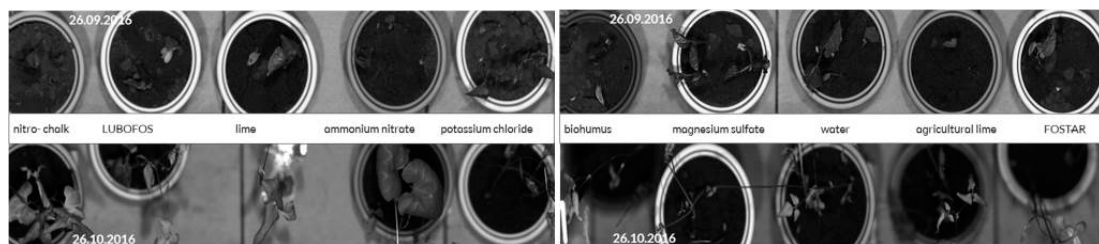
Fig. 2. Plants used in the second series of experiment

The hyperspectral imagery was obtained systematically creating a large dataset for performing multitemporal analyses.

All hyperspectral images were pre-processed with radiometric correction, i.e. Empirical Line Calibration (Smith & Milton, 1999), to obtain correct spectral reflectance coefficients for all acquired spectral bands.

Next, all hyperspectral images were filtered with Minimum Noise Fraction Transform (MNF) (Green et al., 1988)-first 37 components of MNF transform were used, the rest was considered as noise.

After radiometric calibration and noise reduction, the spectral reflectance characteristics of every plant in each data set were obtained. Moreover, the hyperspectral vegetation indices, i.e. hyperspectral Red Edge Normalized Difference Vegetation Index (1) (Gitelson & Merzlyak, 1994), and indices for nitrogen (2), phosphorus (3), and potassium (4) content (Özyiğit & Bilgen, 2013) were calculated.

$$NDVI_{705} = \frac{R_{750} - R_{705}}{R_{750} + R_{705}} \qquad (1)$$

$$\begin{aligned} N = {} & - 0.426 - 630R_{647} + 296R_{680} \\ & + 517R_{651} - 569R_{675} + 244R_{654} \\ & + 66.4R_{609} + 44.5R_{76} - 141R_{727} \\ & - 280R_{669} + 86.4R_{721} + 381R_{676} \end{aligned} \qquad (2)$$

$$\begin{aligned} K = {} & 0.759 - 417R_{646} + 410R_{651} - 458R_{669} \\ & + 147R_{682} + 140R_{417} + 423R_{410} \\ & + 334R_{670} + 1059R_{460} - 716R_{468} \\ & - 410R674 + 225R_{658} - 480R_{463} \\ & + 164R_{422} + 178R_{676} + 256R_{411} \end{aligned} \qquad (3)$$

$$P = 0.0316 + 42.5R_{680} - 42.6R_{675} \qquad (4)$$

As a result, eight measurements in two-time series were performed. Then all hyperspectral data were processed (spectral reflectance characteristics of investigated samples were obtained, and hyperspectral vegetation indices were calculated) and analysed.

3 RESULTS

In order to determine the influence of selected fertilisers on the condition of bean, first spectral reflectance characteristics from the hyperspectral data were obtained and analysed. Preliminary analysis was made by spectral curves, which allowed to examine individual spectral ranges regarding changes caused by applied fertilisers- Fig. 3.

The analysis of spectral reflectance characteristics had shown the downward trend of the chlorophyll content in the bean as it grows. The tested samples show that the use of biohumus and phosphorus has an adverse effect on chlorophyll content, while the use of lime and ammonium nitrate significantly minimises the decrease of chlorophyll along with the plant's growth.

Next, the hyperspectral vegetation indices were calculated. First, the hyperspectral NDVI was calculated- Fig. 4. Obtained results show similar tendency as when analysing spectral reflectance curves. The measurement showed that the highest value of NDVI was obtained for ammonium nitrate and the lowest for biohumus. The reference sample (the plant fertilised only with pure water) was significantly reduced - its value decreased from 0.34 to 0.12, which confirms the legitimacy of the fertiliser application- Fig. 5. The chart below shows that not every fertiliser has a good effect on the beans tested.
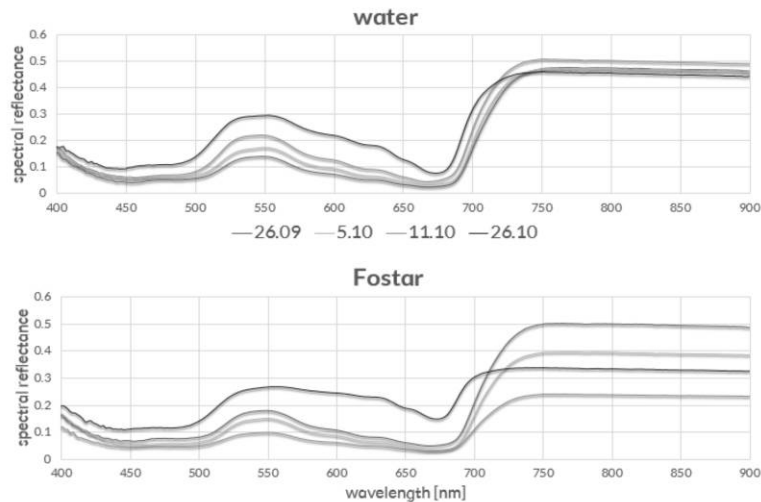
Fig. 3. Spectral reflectance characteristic of plant fertilised with water, and FOSTAR
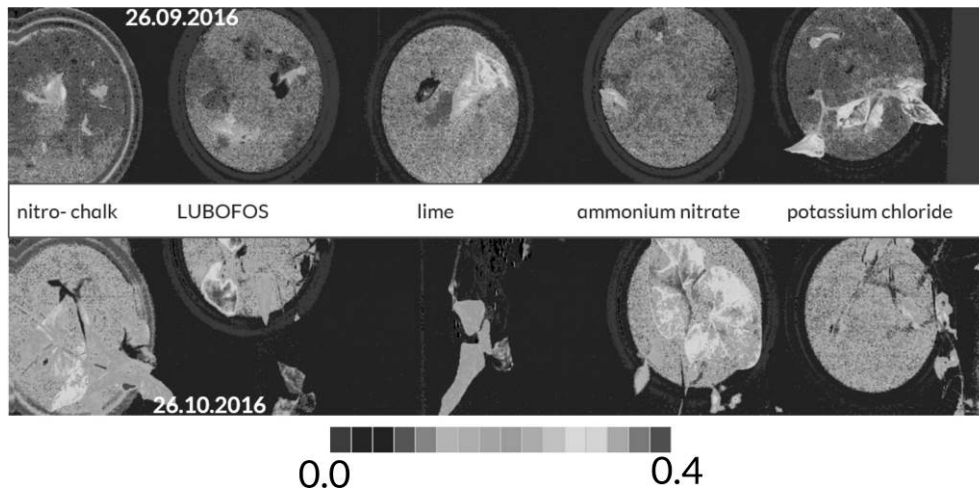
Fig. 4. Results of NDVI for some plant samples
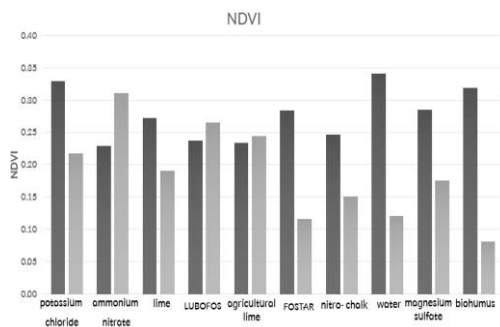
Fig. 5. Temporal NDVI changes: 26.09.2016,
and 26.10.2016

Next, the hyperspectral indices for nitrogen, phosphorus- Fig. 6, and potassium content were calculated.

Based on the analysis of the results can be observed an increase in the content of tested minerals for all plant samples. However, the last measurement shows the significant decrease in values due to death of plants.
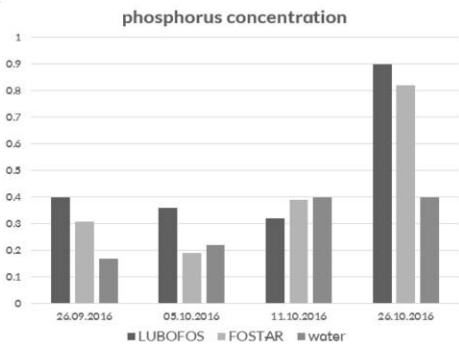
Fig. 6. Temporal phosphorus concentration changes
for some plant samples

4 SUMMARY AND CONCLUSIONS

The research was conducted using a Headwall hyperspectral pushbroom A-Series VNIR sensor in controlled laboratory conditions. Plant samples were grown using various fertilisers, which were administered at regular intervals throughout the growth process. The hyperspectral imagery was obtained systematically creating a large dataset for performing multitemporal analyses.

The performed analyses made it possible to identify the relationship between the value range of selected indices and plant health.

Only some fertiliser have the positive effect on plants health, i.e. lime, nitro- chalk, LUBOFOS, ammonium nitrate, and potassium chloride.

Vegetation indices allow not only to overall assess the state of vegetation but also to estimate the presence of a particular mineral in plants or soil. Therefore, the future work should include more spectral indices and very accurate analyses of plant state.

The obtained data made it possible to obtain spectral reflectance curves of all of the measures plants as well as to calculate chosen hyperspectral vegetation indices. The performed analyses made it possible to identify the relationship between the value range of selected indices and plan health. Such remote sensing capabilities are extremely useful in precision agriculture and can lead to advances in the examination of the biochemical properties of plants.

5 ACKNOWLEDGEMENTS

6 REFERENCES

Ahamed, T., Tian, L., Zhang, Y. , Ting, K.C., 2011, A review of remote sensing methods for biomass feedstock production, *Biomass and Bioenergy*, Volume 35, Issue 7, July 2011, 2455-2469.

Brenchley, G.H., 1968, Aerial Photography for the Study of Plant Diseases, *Annual Review of Phytopathology*, Vol. 6: 1 -20.

Fitzgerald, G.J., Lesch, S.M., Barnes, E.M., Luckett, W.E., 2006, Directed sampling using remote sensing with a response surface sampling design for site-specific agriculture, *Computers and Electronics in Agriculture*, Volume 53, Issue 2, September 2006, 98-112.

Gitelson, A.A., M.N. Merzlyak, 1994, Spectral Reflectance Changes Associated with Autumn Senescence of Aesculus Hippocastanum L. and Acer Platanoides L. Leaves. Spectral Features and Relation to Chlorophyll Estimation. *Journal of Plant Physiology* 143:286‑292.

Green, A. A., Berman, M., Switzer, P., Craig, M. D., 1988, A transformation for ordering multispectral data regarding image quality with implications for noise removal: *IEEE Transactions on Geoscience and Remote Sensing*, v. 26, no. 1, p. 65-74.

Heim, R.H.-J., Jürgens, N., Große-Stoltenberg, A., Oldeland, J., 2015, The Effect of Epidermal Structures on Leaf Spectral Signatures of Ice Plants (Aizoaceae)", *Remote Sens*. 2015, 7, 16901-16914.

Huete, A., 1988, A soil-adjusted vegetation index (SAVI), *Remote Sensing of Environment*, 25, 295-309.

Jenerowicz A, Woroszkiewicz M., 2016, The pansharpening of satellite and UAV imagery for agricultural applications. In: Neale CMU, Maltese A, editors. Proc SPIE 9998, Remote Sensing for Agriculture, Ecosystems, and Hydrology XVIII. 2016. p. 99981S.

Lehmann, J.R.K., Große-Stoltenberg, A., Römer, M. and Oldeland, J., 2015, Field Spectroscopy in the VNIR-SWIR Region to Discriminate between Mediterranean Native Plants and Exotic-Invasive Shrubs Based on Leaf Tannin Content, *Remote Sens*. 2015, 7, 1225-1241.

Muramatsu, K., Furumi, S., Daigo, M., 2015, Algorithm developing of gross primary production from its capacity and a canopy conductance index using flux and global observing satellite data", Proc. SPIE 9637, Remote Sensing for Agriculture, Ecosystems, and Hydrology XVII, 96371A.

Özyiğit, Y., Bilgen, M., 2013, Use of Spectral Reflectance Values for Determining Nitrogen, Phosphorus, and Potassium Contents of Rangeland Plants, *Journal of Agricultural Science and Technology*, 15(Supplementary Issue), pp. 1537–1545.

Rembold, F., C. Atzberger, I. Savin, Rojas, O., 2013, Using Low Resolution Satellite Imagery for Yield Prediction and Yield Anomaly Detection, *Remote Sensing* 5: 1704–1733.

Sivakumar, M.V.K., Hinsman, D. E., 2003, Satellite Remote Sensing and GIS Applications in Agricultural Meteorology and WMO Satellite Activities, Proceedings of a Training Workshop held 7-11 July 2003 in Dehra Dun, India, 1-22.

Smith, G. M., Milton, E. J., 1999, The use of the empirical line method to calibrate remotely sensed data to reflectance, *International Journal of Remote Sensing*. Taylor & Francis, 20(13), pp. 2653–2662.

Walczykowski P, Jenerowicz A, Orych A., Siok K., 2016a, Determining spectral reflectance coefficients from hyperspectral images obtained from low altitudes. *ISPRS - Int Arch Photogramm Remote Sens Spat Inf Sci*. 2016 Jun 20; XLI-B7:107–10.

Walczykowski, P., Orych, A., Dąbrowski, R., 2013, Designing a modern Measuring Station for obtaining spectral response characteristics in laboratory conditions, in The 1st Research Conference In Technical Disciplines, November, 18. - 22. 2013, pp. 121–124.

Walczykowski, P., Siok, K., Jenerowicz, A., 2016b, Methodology for determining optimal exposure parameters of a hyperspectral scanning sensor, *International Archives of the Photogrammetry, Remote Sensing and Spatial Information Sciences* - ISPRS Archives, XLI-B1, pp. 1065–1069.

Zarco-Tejada, P., Berjón, A., López-Lozano, R., Miller, J., Martín, P., Cachorro, V., et al., 2005, Assessing vineyard condition with hyperspectral indices: leaf and canopy reflectance simulation in a row-structured discontinuous canopy, *Remote Sensing of Environment*, 99, 271- 287.

Zurita-Milla, R., G. Kaiser, J. G. P. W. Clevers, W. Schneider, Schaepman,M. E., 2009, Downscaling time series of MERIS full resolution data to monitor vegetation seasonal dynamics, *Remote Sensing of Environment* 113, Elsevier Inc. 1874–1885.

Mineral identification and classification by combining hyperspectral VNIR-SWIR and multispectral TIR data

Li Ni[1,*], WangminYing[2, 3], Wan Li[2, 3], Hua Wu[2, 3,*]

[1] *Key Laboratory of Digital Earth Science, Institute of Remote Sensing and Digital Earth, Chinese Academy of Sciences, Beijing 100094, China;*

[2] *State Key Laboratory of Resources and Environment Information System, Institute of Geographic Sciences and Natural Resources Research, Chinese Academy of Sciences, Beijing 100101, China*

[3] *University of Chinese Academy of Sciences, Beijing 100049, China*

*Corresponding author: wuh@lreis.ac.cn

ABSTRACT- *Hyperspectral data, which have fine continuous spectrum, have been recognized to be more suitable for the detailed identification and classification of land surface, especially for minerals. However, the mineral identification and classification often use spectral data just within 0.4-2.5um from VNIR to SWIR at present, which may limit accuracies and capabilities in a certain extent particularly for silicate and carbonate. To improve mineral identification and classification accuracy and realize fine mapping, this paper tries to make full use of the different spectrum of complementary remote sensing information by combining hyperspectral VNIR-SWIR reflectance and multispectral TIR emissivity together. Firstly, the reflectance and emissivity spectrum for several typical minerals, such as kaolinite, alunite, calcite, quartz and ilmenite, are well analyzed to find the optimum diagnosed characteristics. Four algorithms, i.e. spectral angle mapping (SAM), spectral feature fitting (SFF), orthogonal subspace projection (OSP) and adaptive Coherence/cosine Estimator (ACE), are selected in the experiment. Compared with the results using hyperspectral data alone, the introducing of multispectral TIR data in identification and classification has improved accuracies for both the simulated and real data. The overall accuracies are improved about 4-13% for the simulated data and about 1-5% for the real data by using different algorithms. Those improvements prove that the spectral diagnosed characteristics in TIR region helps to identify and classify minerals. The combining use of those data has a great potential application value for minerals identification and classification in the near future.*

1 INTRODUCTION

In the early 1980s, the emergence of hyperspectral remote sensing data enabled the acquisition of data with increased number of spectral bands and higher spectral resolution has certainly given significant impacts on objects' classification (Goetz, 1985). Hyperspectral data's narrow bandwidth and contiguous spectral facilitate to distinguish and classify minerals more accurately (Ramesh et al., 2017).

At present, minerals and rocks' indentation is mainly based on the spectral features in the visible near-infrared (VNIR) region range 400-2500um, and these features are related to certain chemical composition and lattice structure of minerals and rocks (Cloutis, 1996).

The alteration minerals contain a large number of Fe^{2+}, Fe^{3+}, OH^-, CO_3^{2-} and other ions or groups of ions, it is the electronic transition, vibration and rotation of these ions makes minerals display special spectral absorption and reflection features in VNIR and short-wave infrared (SWIR) spectrum (Zhang, 2012). Rocks are composed of different minerals and their spectral characteristics are much more complex, essentially the mixture of minerals' spectrum (Gila 2016).

Hyperspectral data can't detect the vibration intensity of the minerals and rocks across the VNIR-SWIR region, which limited the ability of mineral indentation and classification. For example, most abundant minerals have special spectral feature in thermal infrared (TIR) region range 8-14 μm (Charlotte, 2011). The silicon-oxygen bond (Si-O) stretching vibrations in feldspars and quartz, as well as in other silicates, exhibit spectral features in the TIR region. And TIR remote sensing data can also provide some distinction amongst $Al-OH^-$, $Mg-OH^-$ bearing minerals, carbonates and so on (Gila, 2014). In TIR region, the radiance of the object is mainly from itself, so basis of mineral identification and classification is its emissivity (Li, 2013).

The reflectance spectra of rocks are nonlinearly mixed with the reflectance spectra of their inner minerals, while the emissivity spectra have the characteristics of linearly mixing. Under the condition of good spatial resolution, linearly spectral unmixing method can be used to unmix targets and identify minerals (Gillespie, 1992; Thomson 1993).

TIR remote sensing, combined with VNIR–SWIR hyperspectral remote sensing, is becoming a promising method for environmental studies. This paper realizes the minerals identification and classification by combining hyperspectral VNIR-SWIR and multispectral TIR data, and the accuracy comparison of four classification methods are summarized.

2 METHODOLOGY

2.1 Classification methods based on spectral feature

The identification and classification of mineral in visible/ near-infrared region based on reflectivity of the objects, while in thermal infrared region is the emissivity. Temperature emissivity separation method (TES) was used to acquire the mineral emissivity from thermal infrared data (Gillespie et al., 1998). In order to verify whether the thermal infrared data can help improve mineral identification and classification accuracy, four algorithms, i.e. spectral angle mapping (SAM), spectral feature fitting (SFF), orthogonal subspace projection (OSP) and adaptive Coherence/cosine Estimator (ACE), are selected in the experiment.

The SAM is a classification method that determines spectral similarity between the test spectra and reference spectra by treating them as vectors in an N-dimensional space (Kruse et al., 1993). The similarity of the two spectra is determined by calculating the angle between the two vectors in the image. The smaller the angle, the more similar the two spectra. SFF is one of the algorithms nowadays used for satellite spectral analysis about recognition and classification, which is based on spectral absorption feature (Clark et al., 1990). The envelope line of the test spectra and the reference spectra should be removed before spectra matching, and then least squares method is used to fit curve. Root mean square error is used to evaluate the matching degree between two spectra. OSP algorithm is based on the mixed linear model, which divides the mixed pixels into interest endmember (target) and non-interest endmember (background). The mineral is identified by enhancing the characteristics of the target and suppressing the background features (Harsanyi and Chang, 1994). ACE algorithm takes both the statistical model and subspace projection model into account. It assumes that the background's covariance structure is the same regardless of target existence. While the variance is different, which directly affects the area proportion of the target in background (Kraut et al., 2005). The similarity between the test spectra and the reference spectra is determined by calculating the cosine square of the angle between two spectra in whitening space.

2.2 Simulated data introduction

Eight minerals and rocks were selected from the United States Geological Survey (USGS) Spectral Library and the Johns Hopkins University (JHU) Spectral Library as the targets to be classified. It consists of five minerals and three rocks (Table 1).

Table 1 Eight targets of simulated data

Category	Name	Description
1	Alunite	$NaAl_3(SO_4)_2(OH)_6$, Sulfate minerals
2	Calcite	$CaCO_3$, Carbonate minerals
3	Kaolinite	$Al_2Si_2O_5(OH)_4$, Silicate minerals
4	Montmo-rillonite	$(Na\ Ca)_{0.33}(Al\ Mg)_2Si_4O_{10}(OH)_{20}$, Silicate minerals
5	White mica	$KAl_2(Si_3Al)O_{10}(OH\ F)_2$, Silicate minerals
6	Gneiss	Feldspar, quartz, mica
7	Marble	Calcite, dolomite
8	Qurtz	Quartz

Table 2 The proportion of mixed endmember in seven tests

Dataset	Soil	Category1	Category2
1	-	-	-
2	0-5%	-	-
3	0-5%	0-5%	0-5%
4	0-10%	0-10%	0-10%
5	0-10%	0-15%	0-15%
6	0-20%	0-20%	0-20%
7	0-20%	0-25%	0-25%

Considering the spectral response function of Hyperion hyperspectral data and ASTER multispectral data, the spectral curves of eight targets were respectively processed. Hyperion data collects spectra in 242 continuous spectral channels covering the wavelength range 356-2578nm, and 155 channels were considered according to actual situation. ASTER thermal infrared data has a high spatial resolution, and cover the wavelength range 8125-1165nm in thermal infrared bands. Figure 1 shows the reflectivity of eight targets in the Hyperion band and the emissivity in ASTER thermal infrared band, respectively.

Considering the existence of mixed endmember in remote sensing image, especially the images with low spatial resolution, the linear spectral mixture model was used to mix targets.
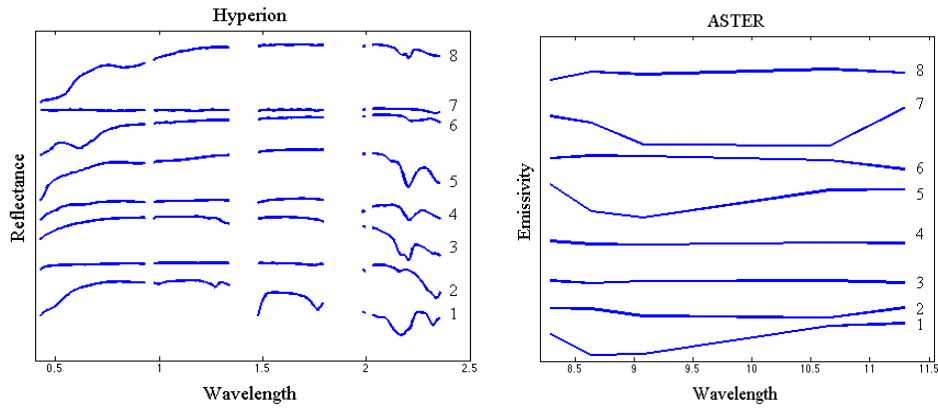
Figure 1 The reflectivity and emissivity of eight targets
(1- alunite,2- calcite,3- kaolinite,4- montmorillonite,5- white mica,6- gneiss,7- marble,8- quartz
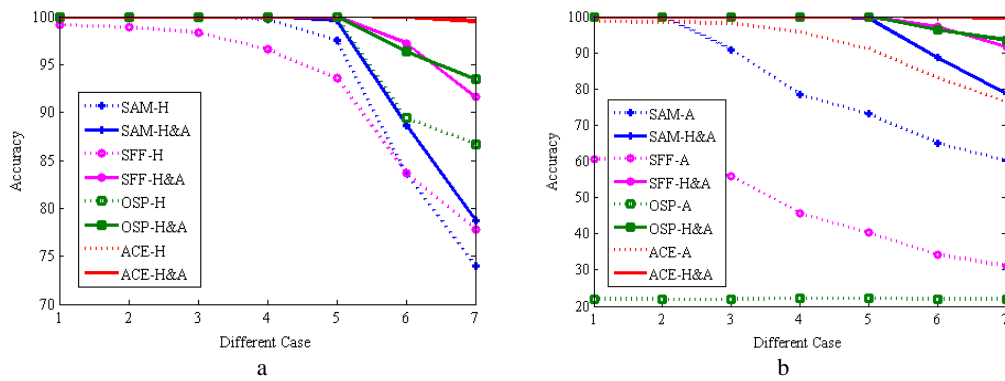
Figure 2 a: The comparison results between Hyperion data (dashed) and combination data (solid)
b: The comparison results between thermal infrared data（dashed）and combination data（solid）

Here, soil endmember, Alunite endmember (category 1) and calcite endmember (category 2) were mixed into seven datasets. Table 2 shows the proportion of each endmember in seven datasets, and the distribution of them is uniform. What's more, each test was also processed by considering spectra response function of Hyperion data and ASTER thermal infrared data.

3 RESULTS

3.1 The comparison and analysis of classification accuracy of simulated data

Four classification methods are used to classify the seven sets of simulated data respectively, each set of data included hyperspectral Hyperion data, ASTER thermal infrared data and combination data of both. Figure 2 (a) and Figure 2 (b) show the comparison results between Hyperion data and combination data, thermal infrared data and combination data, respectively. For the overall accuracy of the four methods, the accuracy of ACE is higher, and the other three methods are equal. Compared with using

hyperspectral data solely, the accuracies are improved of different level for four classification methods in the use of combination of data classification. While SFF increase the most, SAM and OSP take second place, and ACE was not significantly improved.

The accuracies of different classification methods are all improved under the condition of different mixing degree, the same classification and evaluation system, which effectively prove the contribution of thermal infrared data, also prove that the combining use of the VNIR-SWIR hyperspectral data and TIR multispectral data improve the accuracy of mineral identification and classification effectively.

3.2 The comparison and analysis of classification results of simulated data

The confusion matrix precision classification and ROC curve evaluation are used to analyze classification results of the seven set of simulated data. Table 3 shows the overall classification accuracy of the four classification methods and the detailed classification accuracy of each category. The identification accuracy of rocks is lower than that of

minerals, especially marble and quartzite, for the reason that the rocks contain a variety of minerals. The introduction of thermal infrared data is helpful to improve the classification accuracy of SFF method, especially the accuracy of calcite, white mica, marble and quartzite. ROC curve is a method to evaluate the result of classification besides confusion matrix calculation. The more the ROC curve bends in the upper left direction, the better the classification performance of the model. Fig 3 show the ROC curve of hyperspectral data and hyperspectral classification combined with thermal infrared data with four classification methods, all of the ROC curve method is to be near the top left corner after combing the thermal infrared data, which means the better classification result.

The simulation experiments prove that the TIR data is still an effective supplement for VNIR and SWIR data in mineral identification and classification, which can be improved on accuracy by both complementary on the spectrum. OSP and ACE methods based on spatial projection transform are relatively good for identification and classification because of the effective suppression of background spectra and noise. Though not better than OSP and ACE, traditional SAM and SFF classification method have their own advantages, SFF method is suitable for minerals with obvious absorption characteristics, while SAM can effectively distinguish minerals with spectral shape differences.

Table 3 classification accuracy of simulated data using four classification methods

	SAM				SFF				OSP				ACE			
	Hyperion		Combined		Hyperion		Combined		Hyperion		Combined		Hyperion		Combined	
OA	74.00		78.75		77.83		91.59		86.70		93.43		99.57		99.50	
classes	Prod.	User	Prod.	User	Prod.	User	Prod.	User	Prod.	User	Prod.	User	Prod.	User	Prod.	User
1-alunite	77.38	100.00	80.71	100.00	87.69	100.00	82.71	100.00	99.22	94.31	100.00	85.58	99.78	100.00	99.56	100.00
2-calcite	69.36	93.21	71.28	86.82	15.98	100.00	89.38	96.93	98.69	94.85	99.19	96.56	99.80	99.90	99.49	99.90
3-kaolinite	89.13	86.01	89.22	87.55	88.08	98.98	89.35	98.80	96.83	99.44	95.02	100.00	99.95	99.10	99.86	99.10
4-montmorillonite	93.73	36.11	94.06	42.88	90.19	63.09	91.10	84.03	99.92	82.67	86.56	100.00	99.59	99.75	99.59	99.92
5-white mica	88.99	88.16	90.63	89.05	40.22	100.00	86.41	97.40	75.82	100.00	97.69	99.58	97.28	100.00	98.10	100.00
6-gneiss	89.55	89.48	89.96	89.09	81.62	100.00	96.60	98.84	100.00	56.78	100.00	72.60	99.51	99.84	99.43	100.00
7-marble	40.45	100.00	56.89	100.00	99.39	60.90	100.00	81.66	57.38	100.00	85.98	100.00	100.00	99.31	100.00	98.87
8-quartz	58.99	100.00	59.71	100.00	24.10	100.00	65.83	100.00	92.45	93.80	93.88	99.62	97.48	100.00	95.68	100.00
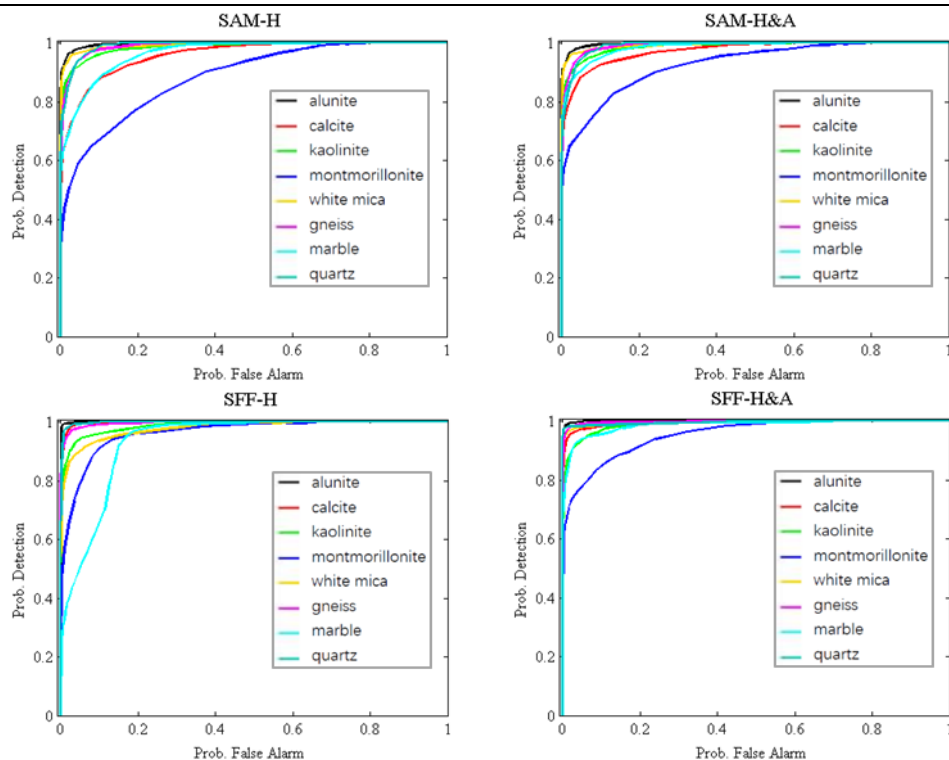
Fig 3a   ROC curve of hyperspectral data(left) and hyperspectral classification combined with thermal infrared data(right) with four classification methods
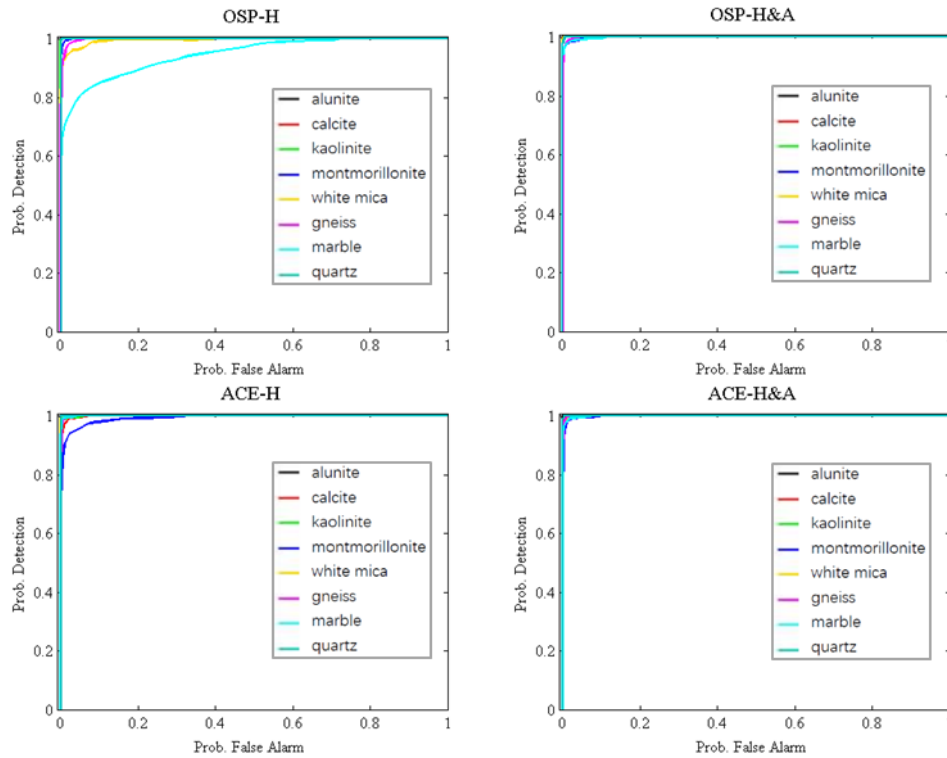
Fig 3b ROC curve of hyperspectral data(left) and hyperspectral classification combined with thermal infrared data(right) with four classification methods

4 CONCLUSION

This paper analyzes the spectral characteristics of the reflectance spectrum in VNIR-SWIR and the emissivity spectrum in TIR of minerals, and then point four methods being used to realize the minerals identification and classification by combining hyperspectral VNIR-SWIR and multispectral TIR data. Seven groups of experiments with different degree of mixing simulation of the mineral effectively prove that TIR multispectral data complemented with VNIR-SWIR hyperspectral data in the observed spectrum can improve identification accuracy. In addition, the four identification and classification methods used in the experiment are compared, and the accuracy comparison and application of each classification method are summarized.

ACKNOWLEDGMENT

REFERENCES

Charlotte A B, Liu J G, Philippa J M., 2011, Hyperspectral remote sensing for mineral exploration in Pulang, Yunnan Province, China. *International Journal of Remote Sensing*, 32(9): 2409-2426.

Clark R N, Gallagher A J, Swayze G A., 1990, Material absorption band depth mapping of imaging spectrometer data using a complete band shape least-squares fit with library reference spectra. *Proceedings of the Second Airborne Visible/Infrared Imaging Spectrometer (AVIRIS) Workshop. JPL Publication,* 2: 4-5.

Cloutis E A, 1996, Hyperspectral geological remote sensing: evaluation of analytical techniques. *International Journal of Remote Sensing*, 17: 2215-2242.

Gila N, Veronika K, Petr R, et al., 1992, Mineral Classification of Land Surface Using Multispectral LWIR and Hyperspectral SWIR Remote-Sensing Data. A Case Study over the Sokolov Lignite Open-Pit Mines, the Czech Republic. *Remote sensing,* 6: 7005-7025.

Gila N, Yaron O, Eyal B D., 2016, Integration of Hyperspectral Shortwave andLongwave Infrared Remote-Sensing Data for Mineral Mapping of Makhtesh Ramon in Israel. *Remote sensing,* 8:318.

Gillespie A R., 1992, Spectral mixture analysis of multispectral thermal infrared images. *Remote Sensing of Environment,* 42(2): 137-145.

Gillespie A, Rokugawa S, Matsunaga T, et al., 1998, A temperature and emissivity separation algorithm for Advanced Spaceborne Thermal Emission and Reflection Radiometer (ASTER) images. *Geoscience and Remote Sensing, IEEE Transactions on*, 36(4): 1113-1126.

Goetz A F H., 2009, Three decades of hyperspectral remote sensing of the Earth: A personal view. *Remote Sensing of Environment*, 113: S5-S16.

Harsanyi J C, Chang C I., 1994, Hyperspectral image classification and dimensionALIty reduction: an orthogonal subspace projection approach. *Geoscience and Remote Sensing, IEEE Transactions on*, 32(4): 779-785.

Kruse F A, Lefkoff A B, Boardman J W, et al., 1993, The spectral image processing system (SIPS)—interactive visuALIzation and analysis of imaging spectrometer data. *Remote sensing of environment*, 44(2): 145-163.

Li Z L, Tang B H, Wu H, et al., 2013, atellite-derived land surface temperature: Current status and perspectives. *Remote Sensing of Environment*, 131: 14-37

Ramesh N A, Amba S, Ramesh H T., 2017, EXhype: A tool for mineral classification using hyperspectral data, *ISPRS Journal of Photogrammetry and Remote Sensing*, 106-118.

Thomson J L, SALIsbury J W., 1993, The mid-infrared reflectance of mineral mixtures (7–14 μm). *Remote Sensing of Environment*, 45(1): 1-13.

Zhang T T, Liu F., 2012, Application of Hyperspectral Remote Sensing in Mineral Identification and Mapping. *2nd International Conference on Computer Science and Network Technology,* 103-106.

Determining spatial resolution variability of hyperspectral pushbroom sensors

Agata Orych, Agnieszka Jenerowicz, Diana Zach

Military University of Technology, Faculty of Civil Engineering and Geodesy, Geodesy Institute, Department of Remote Sensing, Photogrammetry and Imagery Intelligence, gen. S. Kaliskiego 2, 00-908 Warsaw, Poland

agata.orych@wat.edu.pl, agnieszka .jenerowicz@wat.edu.pl

ABSTRACT - *Spatial resolution is one of the most important parameters in determining the quality of electro-optical remote sensing sensors. The spatial quality of a sensor can be described by one of two values - the GRD (Ground Resolved Distance) and GSD (Ground Sampling Distance). The GSD is a purely theoretical value, an approximate value of ground resolution, which determines the size of a pixel on the ground. GRD is described as the smallest detail possible to determine in the image. For single band remote sensing sensors this value will be constant for a given sensor-imaged object distance, with the GRD value directly proportional to this distance. This however is not always the same for hyperspectral sensors, which acquire data simultaneously in many narrow bands of the electromagnetic spectrum. The purpose of this paper was to determine the spectral quality of imagery acquired in different bands, and to define in which spectral band we can accomplish the best spatial resolution and in which spectral bands the worst. The spatial resolution variability in different spectral bands was examined. A selection of different calibration targets were used to obtain the required data. The best values of spatial resolution were obtained for imagery from the red spectral bands. The worst values of spatial resolution were obtained for imagery from the blue spectral range.*

1 INTRODUCTION

Non-satellite remote sensing sensors are becoming a very popular tool for acquiring high quality remote sensing data for many applications. With the rapid developments in sensors, their miniaturisation and drops in production costs, data acquired using low-cost UAV systems and light-weight sensors is becoming more and more popular for many applications (Dabrowski et al., 2014, Fryskowska et a;., 2016), such as forestry (Feng et al., 2015), precision agriculture (Grenzdörffer, et al., 2008), monitoring cultural heritage (Kedzierski et al., 2014), environmental studies, and pollution monitoring (Orych et al., 2014). There had also been similar developments with more complex and advanced sensors, such as hyperspectral pushbroom scanners. Such sensors can be mounted on aerial platforms (both traditional and unmanned aerial vehicles) or, using specialized terrestrial transport systems, operated in field or laboratory conditions. They are usually characterized by very high spectral and spatial resolutions, which makes the acquired data a very valuable source of information about the investigated objects. The way in which hyperspectral sensors are designed and constructed, usually means that all spectral bands are obtained by optically splitting the radiation incident on the sensor lens, registering very fine spectral information on the detector array (Cocks et al., 1998). The optical properties of the radiation incident on the array are not constant between different wavelengths. This can lead to slightly blurred and noisy images being obtained in different bands, which is especially visible when acquiring data in laboratory conditions (Walczykowski et al., 2016). The aim of this paper was to develop a methodology for determining the spatial resolution variability between different spectral bands of a pushbroom hyperspectral sensor.

Fig. 1. Headwall MicroHyperspec A-series VNIR 327-band pushbroom sensor

2 METHODOLOGY

2.1 Sensor Used

The sensor used for this research is a Headwall MicroHyperspec A-series VNIR 327-band pushbroom sensor, that acquires hyperspectral imagery continuously line by line. This hyperspectral scanner acquired imagery data in 327 spectral channels with a 1.9 nm spectral bandwidth in the 380- 1000 nm range.

The camera can be easily mounted on an Unmanned Aerial Vehicle due to it's relatively small dimension and small weight - 0,68kg (Walczykowski et al., 2016)- Fig.1.

2.2 Experiment set up

Imagery is acquired by means of moving the camera over the test field using a slider system mounted on an especially designed measuring station (Walczykowski et al., 2013). The station consists of a mobile frame, which can be moved in the vertical plane and a sensor arm which can be moved in the X, Y and Z directions. Such a design allows for smooth and safe operation of all measuring devices and more importantly allows precise positioning of sensors and light at the same distance from the test object during all subsequent measurements.

By being able to position the measuring instrument with such precision, it is possible to carry out experiments in constant, repeatable conditions. Throughout the experiment, the sensor was located 1.5m above the imaged scene, with movement occurring only in one direction - along the central axis of the imaged targets. The entire scene was illuminated using well dispersed lighting. To ensure good exposition and so a high quality of the acquired images, a radiometric calibration of the sensor was conducted using a Zenith Lite SG3151 95% reference panel.

2.3 Measurement method

The methodology is based on acquiring a series of scans of an especially designed calibration field, consisting of a number of different spatial resolution calibration targets such as a Siemens Star, bar targets and slanted edges (Fig. 2).

These targets were selected to give the possibility of determining resolutions using different methods:

- manually - visual analysis of the bar targets,

- semi-automatically - using the Siemen's Star

- automatically - using MTF on the Slanted Edge (Orych, 2015).

Additionally, the use of these targets made it possible to examine the variations in resolutions relative to the location on the focal plane.

The impact of the acquisition parameters of the camera on the spatial resolution variations had also been investigated.

Fig. 2. Especially designed calibration field: slanted edge test, Siemen's star test and two bar targets
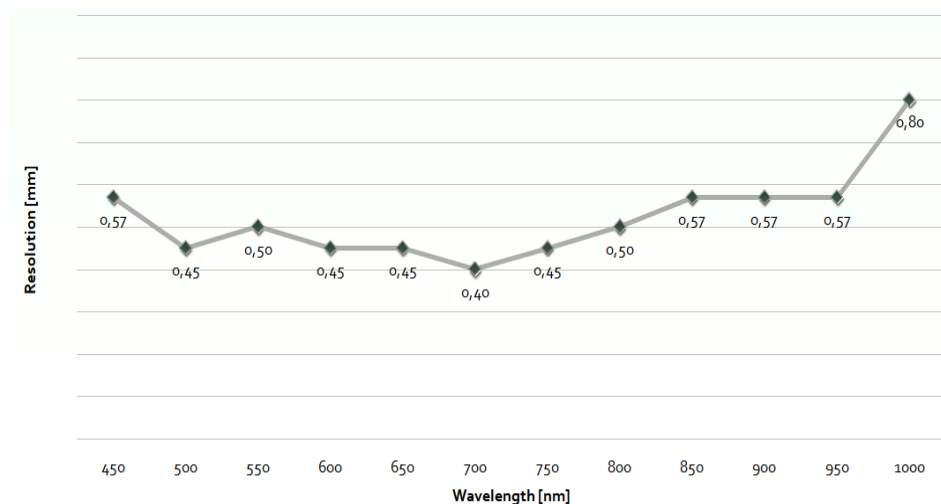
Fig. 3. Spatial resolution determined in bands of chosen wavelength using the hyperspectral pushbroom sensor

3 RESULTS

Spatial resolution was determined using all four of the above targets. The obtained data made it possible to determine the scale of differences in spatial resolution between all of the 327 spectral bands.

As seen in the figure below- Fig. 3 the best spatial resolution was recorded for the red spectral bands. The worst values of spatial resolution were obtained in the blue spectral range.

This information could be used to determine the optimal methodology for obtaining future datasets for different applications.

4 ACKNOWLEDGEMENTS

5 REFERENCES

Cocks, T., Jenssen, R., Stewart, A., Wilson, I. and Shields, T., 1998, October. The HyMapTM airborne hyperspectral sensor: the system, calibration and performance. In Proceedings of the 1st EARSeL workshop on Imaging Spectroscopy (pp. 37-42). EARSeL.

Dabrowski, R., Delis, P. and Wyszynski, M., 2014, January. Analysis of the possibility of using a video camera as a UAV sensor. In Environmental Engineering. Proceedings of the International Conference on Environmental Engineering. ICEE (Vol. 9, p. 1). Vilnius Gediminas Technical University, Department of Construction Economics & Property.

Feng, Q., Liu, J. and Gong, J., 2015. UAV remote sensing for urban vegetation mapping using random forest and texture analysis. *Remote sensing*, 7(1), pp.1074-1094.

Fryskowska, A., Kedzierski, M., Grochala, A., Braula, A. 2016. Calibration of Low Cost RGB and NIR Uav Cameras. *International Archives of the Photogrammetry, Remote Sensing and Spatial Information Sciences*, 817-821.

Grenzdörffer, G.J., Engel, A. and Teichert, B., 2008. The photogrammetric potential of low-cost UAVs in forestry and agriculture. *The International Archives of the Photogrammetry, Remote Sensing and Spatial Information Sciences*, 31(B3), pp.1207-1214.

Kedzierski, M., Fryskowska, A. 2014. Terrestrial and aerial laser scanning data integration using wavelet analysis for the purpose of 3D building modeling. *Sensors*, Volume: 14 Issue: 7 Pages: 12070-12092

Orych, A., 2015. Review of methods for determining the spatial resolution of uav sensors. *The International Archives of Photogrammetry, Remote Sensing and Spatial Information Sciences*, *40*(1), p.391.

Orych, A., Walczykowski, P., Jenerowicz, A. and Zdunek, Z., 2014. Impact of the cameras radiometric resolution on the accuracy of determining spectral reflectance coefficients. *The International Archives of Photogrammetry, Remote Sensing and Spatial Information Sciences*, 40(1), p.347.

Walczykowski, P., Jenerowicz, A., Orych, A. and Siok, K., 2016. DETERMINING SPECTRAL REFLECTANCE COEFFICIENTS FROM HYPERSPECTRAL IMAGES OBTAINED FROM LOW ALTITUDES. *The International Archives of Photogrammetry, Remote Sensing and Spatial Information Sciences*, pp.107-110.

Walczykowski, P., Siok, K. and Jenerowicz, A., 2016. METHODOLOGY FOR DETERMINING OPTIMAL EXPOSURE PARAMETERS OF A HYPERSPECTRAL SCANNING SENSOR. *The International Archives of Photogrammetry, Remote Sensing and Spatial Information Sciences*, pp.1065-1069.

Fair comparison of NDVI time series reconstruction methods using the TISSBERT datase

Y. Julien, J. A. Sobrino, G. Sòria, J.-C. Jimenez-Muñoz, D. Skokovic, J. Gomis
Global Change Unit, Image Processing Laboratory, Parque Científico, Universidad de Valencia, C/ Catedrático Jose Beltran n°2, 46980 Paterna, Spain.
yves.julien@uv.es

ABSTRACT - *Cloud presence and residual atmospheric contamination introduce artefacts in available NDVI time series. Numerous methods are available in the scientific literature to reconstruct such time series, although the validation of these methods has been problematic. Here, we used more than 30 years of daily global data from NOAA-AVHRR satellite series to simulate test and reference time series for time series reconstruction method validation. We tested various models (Gaussian, Cauchy, Log-normal, and Gamma) to retrieve cloud-free and cloud-contaminated NDVI daily statistics, as well as cloud presence probability, at daily resolution and global scale. We then synthesized 15 years of daily global cloud-free and cloud-contaminated NDVI, and termed this validation dataset TISSBERT (Time Series Simulation for Benchmarking of Reconstruction Techniques). We finally applied widely used approaches (IDR, HANTS, Savitsky-Golay, asymmetric Gaussian, double logistic) to reconstruct the TISSBERT cloud contaminated NDVI time series, which we compared with the TISSBERT cloud-free NDVI time series. This comparison shows that, despite geographical differences, all methods tend to fail where they are most needed, that is in polar, tropical and subtropical areas. The TISSBERT dataset is freely available to the scientific community upon demand.*

1 INTRODUCTION

When working with remotely sensed vegetation indices time series, one would hope working with clean time series, such as the red curve in figure 1, although available data usually show a noisier yearly distribution such as the blue and orange crosses (fig. 1). Therefore, one has first to reconstruct the time series before any application. However, existing reconstruction methods (among many others: Julien and Sobrino, 2010; Roerink et al., 2000; Jönsson and Eklundh, 2004) have been poorly validated, due to the lack of all-year cloud-free data.

We present here the TISSBERT (Time Series Simulation for Benchmarking of Reconstruction Techniques) dataset, built for such validation, as well as a preliminary comparison of 5 different NDVI time series reconstruction methods (IDR [Julien and Sobrino, 2010]; HANTS [Roerink et al., 2000], Savitsky-Golay, asymmetric Gaussian, and double logistic [Jönsson and Eklundh, 2004]).

2 DATA AND METHODS

The Long-Term Data Record Version 4 (LTDR-V4) dataset (Pedelty et al., 2007) consists of daily observations from the NOAA-AVHRR instruments during the period 1981-2013, with a spatial resolution of 0.05°. We used reflectances in red and near-infrared bands to estimate NDVI, and QA (Quality Assessment) data to retrieve cloud and land/sea mask information. A few dates (22) with obvious georeferenciation errors were removed from the analysis.
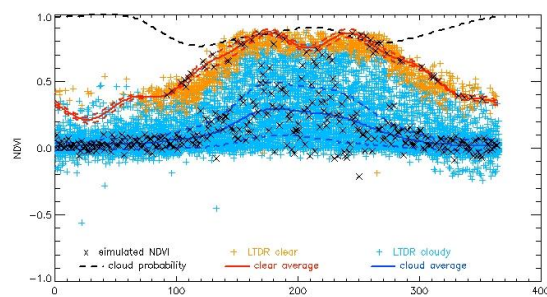
Figure 1. Yearly distribution and statistics of NDVI for a given LTDR-V4 vegetated pixel.

In a first step, we selected randomly 10 000 pixels to assess the validity of the approach. We tested different models for data distribution (Gaussian, Cauchy, Log-normal, and Gamma) for 10 000 randomly selected pixels. The best model (Gaussian) was chosen for pixel by pixel retrieval of cloud presence probability, cloud-free NDVI and cloud-contaminated average and standard deviation values. Statistics were then summarized through a 8th harmonic model fit into HDF files.

We then synthesized 15 years of daily global TISSBERT cloud-free (reference) and cloud-contaminated (test) for validation purposes.

We finally applied 5 different NDVI time series reconstruction (IDR [Julien and Sobrino, 2010]; HANTS [Roerink et al., 2000], Savitsky-Golay, asymmetric Gaussian, and double logistic [Jönsson and Eklundh, 2004]) to the TISSBERT test time series, and assessed their performance through RMSE.

3 TISSBERT DATASET

The Gaussian distribution was the best model for cloud-contaminated data, although a discrete Gaussian distribution was chosen for cloud-free data, to decrease the influence of mislabelled observations (Fig. 2).
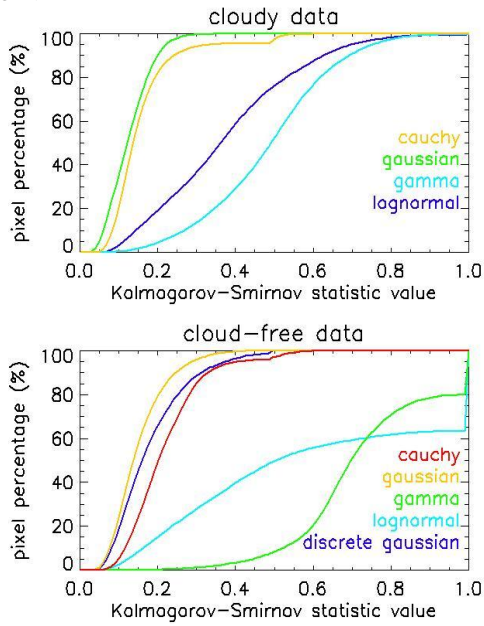
Figure 2. Histogram of Kolmogorov-Smirnov test values for different statistical distribution of NDVI values.

In most cases, the 8th order harmonic fit led to a reliable summary of TISSBERT parameter yearly behaviour (Fig. 3). High correlations (> 0.90) were obtained in most places, except for the case of cloud-free standard deviations, for which correlations are of the order of 0.60.
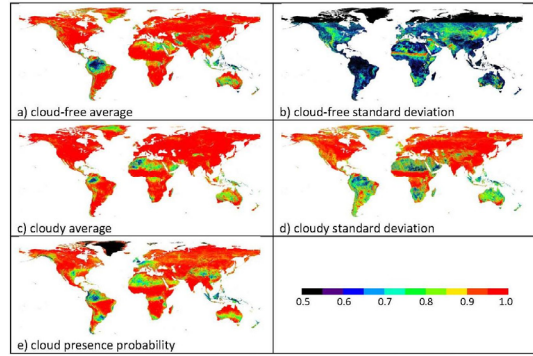
Figure 3. Pearson's correlation coefficient for TISSBERT parameters fit with 8th order Fourier formulation.

Figure 4 shows samples of TISSBERT parameters for given DOYs throughout the year. Cloud-free average maps show the expected seasonal variations, mirroring cloud contaminated maps, the latter with noticeably lower NDVI values.

4 COMPARISON

All methods present high errors (RMSE > 0.02) in the tropics and in temperate to boreal areas, where cloud presence is higher (Fig. 5).
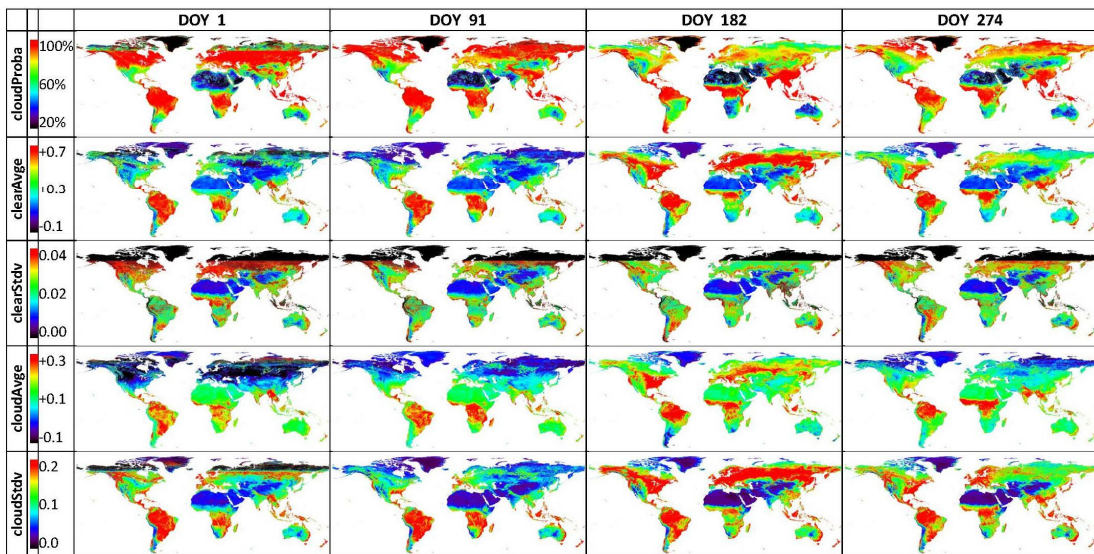
Figure 4. TISSBERT parameter values for DOYs 1 (1st of January), 91 (1st of April), 182 (1st of July), 274 (1st of October) in NDVI units, except for cloudProba parameter, in percentage.
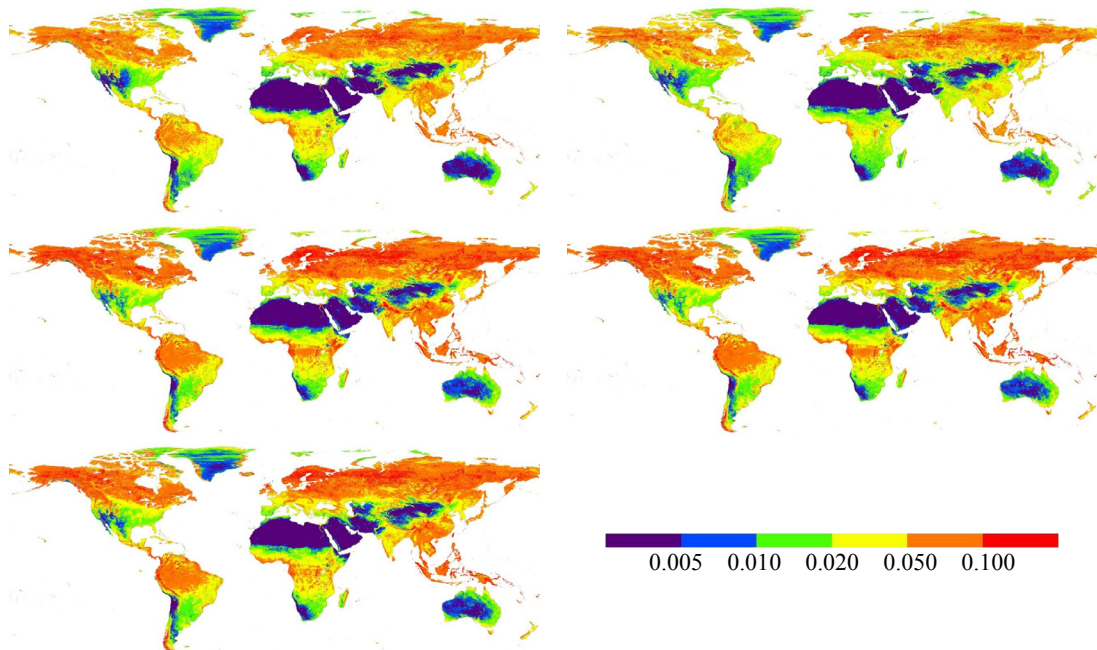
Figure 5. RMSE for (from left to right, top to bottom) IDR, HANTS, Savitsky-Golay, asymmetric Gaussian, and double logistic reconstruction methods.

In other words, all methods fail where their presence is most needed, and therefore there is room for improvement of the reconstructing methods. HANTS method shows the lowest RMSE when using either summarized or raw TISSBERT data for test and reference time series synthesis (Fig. 5), especially in highly vegetated areas, although the observed RMSE is higher than the acceptability limit of 0.02 NDVI units.

5 DISCUSSION AND CONCLUSIONS

The TISSBERT validation dataset is built on several assumptions:

- accuracy of LTDR-V4 cloud masking: fig. 1 shows that some errors exist, which may lead to an overestimation of the retrieved standard deviations,
- stability of the land cover over more than 30 years: for most places, this assumption holds at this coarse spatial resolution,
- low influence of phenology: when taking it into account, the approach led to the same results, due to the higher influence of the atmosphere on the observations variability

Although these assumptions are strong, the LTDR-V4 dataset is by far the longest daily NDVI record available, and was therefore used for building the TISSBERT validation data, which shows a good reliability for most of the globe. The preliminary validations shown above indicate HANTS as the best choice for time series reconstruction, although only the RMSE statistic was considered here, while assessing reconstruction methods accuracy in timing and amplitude of events may lead to different conclusions.

REFERENCES

Julien, Y. and Sobrino, J. A. (2010). Comparison of cloud-reconstruction methods for time series of composite NDVI data, Remote Sensing of Environment, 114 (2010) 618–625.

Roerink, G. J., Menenti, M. and Verhoef, W. (2000). Reconstructing cloudfree NDVI composites using Fourier analysis of time series, International Journal of Remote Sensing, 2000, Vol. 21, No. 9, 1911-1917.

Jönsson, P., and Eklundh, L. (2004). TIMESAT — A program for analyzing time-series of satellite sensor data, Computers and Geoscience, 30, 833−845.

Pedelty, J., Devadiga, S., Masuoka, E., Brown, M., Pinzon, J., Tucker, C., et al. (2007). Generating a long-term land data record from the AVHRR and MODIS instruments, IEEE International Geoscience and Remote Sensing Symposium (IGARSS), 2007, pp. 1021-1025, doi:10.1109/IGARSS.2007.4422974.

Remote detection of human-induced evapotranspiration in the Songhua River Basin of China

H. Chen[1, 2], W.C. Zhang[1, *]

[1] *Key Laboratory of Digital Earth Science, Institute of Remote Sensing and Digital Earth, Chinese Academy of Sciences, Beijing 100094, China.*
[2] *University of Chinese Academy of Sciences, Beijing 100049, China.*
[*]Corresponding author: zhangwc@radi.ac.cn

ABSTRACT - *Accurate estimation and numerical simulation of human-induced ET are difficult to parameterize in hydrologic models, usually attributed to the lack of data and understanding of their physical mechanisms and impacts. As most land surface models (LSMs) can only simulate ET under natural climate conditions, here we hypothesize instead of that discrepancies in ET estimates should be expected in some cases and can be applied to measure the effect of anthropogenic influences in developed river basins. ET output from four LSMs, Noah, MOSAIC, VIC and CLM in GLDAS-1, and GRACE-inferred ET from a water budget with the same precipitation from GLDAS-1 meteorological forcing, monitored runoff, and total water storage change (TWSC), combined with two remote sensing based ET products (MODIS and AVHRR) as the observed ET (Obs-ET) were utilized to detect human-induced ET changes over the Songhua River basin (SRB) of China. Comparison between monthly mean Obs-ET estimates (2003-2013) and GLDAS-modelled ET indicated that human-induced ET has shown the negative effect due to wetland degradation from April to June and the positive effect due to groundwater irrigation in summer months. And Obs-ET (443.6±15.4 mm/yr), considerably lower than GLDAS-modelled ET (489.3±51.4 mm/yr), suggested that human activities contribute to about 10% decrease in ET over the SRB. And human-induced ET has shown a larger proportion in the wet period (e.g., 2013, about 31%) and a lower proportion in the dry period (e.g., 2008, about 7%). The uncertainty of the estimated and the Obs-ET were also examined.*

1 INTRODUCTION

As a critical component of the terrestrial hydrological cycle, evapotranspiration (ET), plays an important role in water exchanges and energy flow across the land-biosphere-atmosphere interactions at global, regional and basin scales. ET is not only influenced by natural variability, but also by human activities such as irrigation or reservoir impoundment (Lo and Famiglietti et al., 2013; Pokhrel et al., 2015). However, accurate estimation and numerical simulation of human-induced ET are difficult to parameterize in hydrologic models, usually attributed to the lack of data and understanding of their physical mechanisms and impacts (Hanasaki et al., 2008; Tang et al., 2008; Rodell et al., 2011).

Many kinds of ET estimation methods have been proposed, for examples: (1) remote sensing (RS)-based ET estimations, such estimations mainly based on Priestley-Taylor, Penman-Monteith algorithm or residual of surface energy budget models for monitoring spatiotemporal variability of ET by using vegetation index-based data: Leaf Area Index (LAI) or Normalized Difference Vegetation Index (NDVI) or land surface temperature (LST), i.e., MODIS and AVHRR ET products (Mu et al., 2007; Zhang et al., 2010), (2) LSMs ET products followed energy/water balance and calculated how vegetation canopy and soil moisture impact ET respectively, e.g., Noah (Ek et al.,

2003), Mosaic (Koster and Suare, 1994), Variable Infiltration Capacity (VIC) (Liang et al., 1994) and Common Land Model (CLM) (Dai et al., 2003), (3) networks of ET monitoring stations, e.g., eddy covariance (EC) towers, and (4) the Global Climate Model (GCM)-based ET products, generated by coupling atmospheric model with the land and ocean surface models. And another estimation technique is a terrestrial water budget. i.e., total precipitation minus the sum of ET and net runoff equals the change in water storage (Ramillien et al., 2006). Since 2002, Satellite gravity measurements from Gravity Recovery and Climate Experiment (GRACE) have provided quantitative measurement of terrestrial water storage changes with unprecedented accuracy, which track water movement at regional scale rather than point-scale observation and are now enabling closure of this equation (Long et al., 2014).

In this study, as most land surface models (LSMs) can only simulate ET under natural climate conditions, here we hypothesize instead of that discrepancies in ET estimates should be expected in some cases and can be applied to measure the effect of anthropogenic influences in developed river basins (Castle et al., 2016; Pan et al., 2017). ET output from four LSMs, Noah, Mosaic, VIC and CLM in GLDAS-1, and GRACE-inferred ET from a water budget with the same precipitation from GLDAS-1 meteorological

forcing, monitored runoff, and total water storage change (TWSC), combined with two remote sensing based ET products (MODIS and AVHRR) as the Observed ET (Obs-ET) to detect human-induced ET changes over the Songhua River basin (SRB) of China.

The reminder of this paper was organized as follows: Section 2 presents the study region, methodologies and data sets used (e.g., GRACE data, LSMs estimations, and other RS-based ET products). The results and discussions were given in Section 3 and followed the concluding remarks of the study in the final section 4.

2 MATERIALS AND METHODS

2.1 Study Region
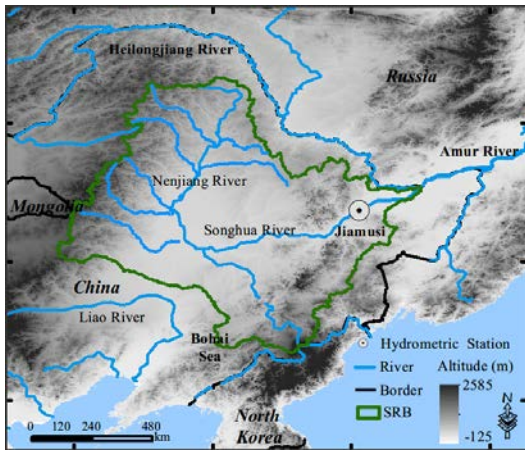
Fig.1 Location map of the SRB, showing DEM, river networks, and the outlet of the SRB-Jiamusi hydrometric station utilized in this study.

The SRB, one of the seven major river catchments in China with the area of 557,000 km^2, located in the far northeast of China, is extremely sensitive to climatic change because of its mid- and high- latitude location, which stretches from 41º42' to 51º38'N and 119º52' to 132º31'E (see Figure 1), across the provinces of Heilongjiang, Jilin, Liaoning and Inner Mongolia. It is surrounded by three mountains, and the Songnen Plain is in the central and southwest part of the basin (Meng et al., 2012). The predominant climate of the SRB belongs to the typical north temperate monsoon climate with cold & long winters and hot & rainy summers. The long-term annual average rainfall is approximately 500 mm, ranges from 400 mm in the southern plains to 700-900 mm in southeast mountains (Li et al., 2014) and about 60-80% of which falls during four months (June - September) (Mu et al., 2012). In addition, numbers of wetlands and permafrost zones are widely distributed over the basin.

2.2 GRACE-derived ET by a water budget approach

A water budget approach with the observed precipitation, net streamflow and GRACE-derived TWS changes was employed to simulate ET as described in equation (1), and the TWS changes for a certain period of a time (e.g., 1 month) can be computed as the backwards difference of TWSA, in this study, the double difference derivative in equation (2) was utilized to derived $\Delta S/\Delta t$ (Long et al., 2014).

$$ET = P - Q - \Delta S/\Delta t \qquad (1)$$

$$\Delta S/\Delta t \approx (TWSA(t+1) - TWSA(t-1))/2\Delta t \qquad (2)$$

where P is precipitation, Q is catchment discharge and ΔS is catchment water storage change over a certain time interval (Δt).

2.3 Human-induced ET estimations

The ensemble of ET outputs from four LSMs, Noah, Mosaic, VIC and CLM in GLDAS-1 were used as modelled ET (Mod-ET), which was supposed to not include the impacts of anthropogenic activities on ET. The GRACE-inferred ET from a water budget with the same precipitation from GLDAS-1 meteorological forcing, monitored streamflow of Jiamusi Station, and TWS changes, combined with two remote sensing based ET products (MODIS and AVHRR) are integrated as the Obs-ET, which were considered resulting from the combined natural and anthropogenic impacts. Comparison between the Mod-ET and Obs-ET were conducted to detect human-induced ET changes (2003-2013) over the Songhua River Basin of China.

2.3 Materials

In this study, three different GRACE-derived TWSA solutions over the SRB from 2003 to 2013, namely the gridded GRACE SH solutions from three sources: (1) Center for Space Research (CSR), (2) GeoForschungsZentrum Potsdam (GFZ), (3) Jet Propulsion Laboratory (JPL), were used to estimate TWS changes. These datasets were open to public as 1°×1° data anomalies relative to a mean time baseline from 2004 through 2009. Scale factors were provided separately to account for signal loss during processing related to truncation to degree and order 60 and application of a 300 km Gaussian smoothing filter. The TWSA solutions have some missing data (e.g., January 2011, May 2012), a simple linear interpolation was adopted for interpolation.

For the LSMs based ET productions, here, four LSMs (VIC, Noah, CLM, MOSAIC) of GLDAS-1 (Koster and Suarez, 1992; Liang et al., 1994; Ek et al.,

2003; Rodell et al., 2004) outputs in 1°×1° grids from NASA were utilized. Two ET productions obtained from remotely sensed products based on the MODIS and AVHRR spanning from 2003 through 2013 were also used.

The precipitation data mentioned above was obtained from the forcing dataset of the GLDAS-1 in 1°×1° format. And the observed streamflow data of the Jiamusi hydrometric station, obtained from the Heilongjiang Province Hydrological Bureau for the long-term study period, were used in estimating net flow of the study region.

3 RESULT AND DISCUSSION

3.1 GRACE-derived TWS changes and variations
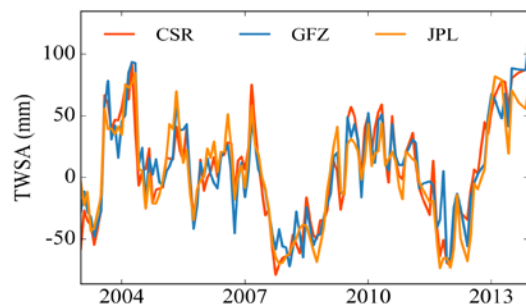
Fig. 2 Monthly TWSA solutions of the SRB from 2003 to 2013.
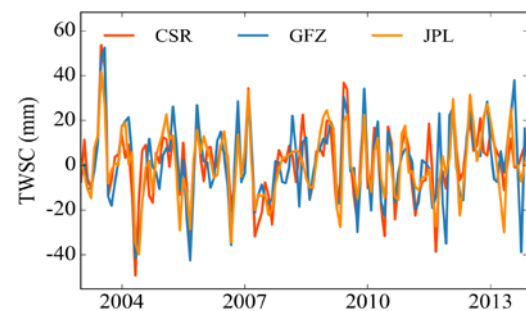
Fig. 3 Monthly TWSC time series over the SRB derived from GRACE TWSA for the period of 2003-2013.

Comparisons of monthly time-series of TWSA (spatially averaged over the SRB) derived from the three different data processing centres with different approaches indicated a high consistency (Fig. 2) with correlation coefficients ranging from 0.91 to 0.93 under the significant level of P<0.001. These consistencies gave us confidence in the use of the average GRACE TWSA time series for further estimations. As for the TWSA time series, here the averaged result of the various solutions was used to quantitatively assess the TWS variations, the variation

rate was estimated to be 1.22 ± 2.22 mm/yr from 2003 to 2013. In general, the GRACE-derived TWS changes for the SRB went through a dry period from 2004 to 2008 with the estimated change rate of TWS about -15.90 ± 4.23 mm/yr and a wet period from 2009 to 2013 about 6.91 ± 7.49 mm/yr. However, none evident trend can be recognized in the TWS variations over the region for the study period since the TWS remained comparatively stable for the whole watershed within such a short period.

Fig. 3 shows the TWS changes derived from TWSA time series by using a double difference derivative approach, their average values were used for GRACE-derived ET estimations further.

3.2 Human-induced ET over the SRB

Under the hypothesize instead of that discrepancies in ET estimates should be expected in some cases and can be applied to measure the effect of anthropogenic influences in developed river basins, the monthly ET can be estimated with difference data sources.
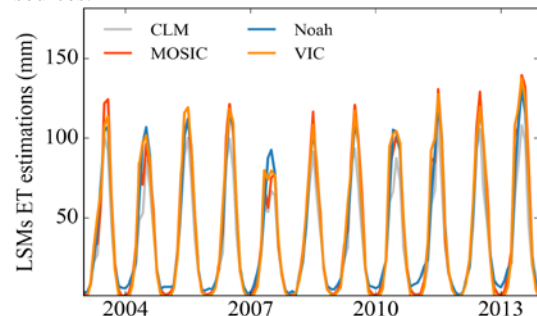
Fig. 4 Monthly ET estimations from LSMs of the SRB from 2003 to 2013.
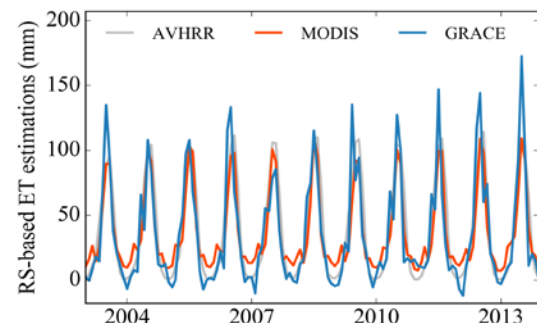
Fig. 5 Monthly ET estimations from the MODIS, AVHRR and GRACE satellites of the SRB from 2003 to 2013.
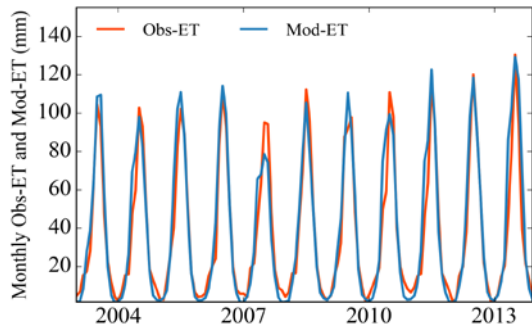
Fig. 6 Monthly Mod-ET and Obs-ET time series of the SRB from 2003 to 2013.

Fig. 4 and 5 presented the monthly ET estimations from four LSMs products and three satellite remote sensing-based simulations over the SRB for the study period 2003-2013, respectively. Fig. 6 showed the averaged Mod-ET and Obs-ET for deriving human-induced ET. Firstly, results demonstrated the validity of GRACE satellites to track the amplitude and phase of ET over the SRB (Fig. 5). Satellite-based ET were generally consistent (R = 0.86-0.91) with each other for the period of Feb 2003-Nov 2013. And for the LSMs ET estimations, also showed good consistency both in phase and amplitude. The discrepancies between Mod-ET and Obs-ET were estimated as human-induced ET. Obs-ET (443.6±15.4 mm/yr), considerably lower than Mod-ET (489.3±51.4 mm/yr), indicated that human activities contribute to about 10% decrease in ET over the SRB. Result also showed that the human-induced ET has shown a larger proportion in the wet period (e.g., 2012-2013, about 31%) and a lower proportion in the dry period (e.g., 2007-2008, about 7%). The proportions were calculated with the yearly Mod- and Obs-ET estimations (which was not presented in the paper), however, the large difference of proportion of human-induced ET between the wet and dry period may be attributed to rainfall in the region.
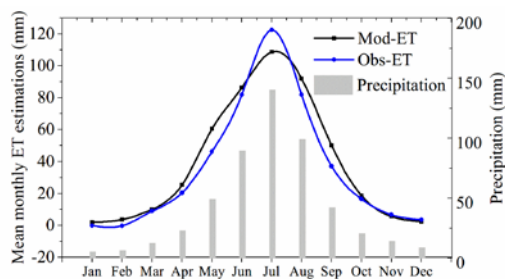
Fig. 7 Monthly mean Mod-ET, Obs-ET estimations and precipitation of the SRB from 2003 to 2013.

Fig. 7 presented the monthly mean Mod-ET, Obs-ET and precipitation of the SRB. Comparison between

Obs-based monthly mean ET estimates and Mod-ET indicated that human-induced ET has shown the negative effect which may be attributed to wetland degradation (i.e., large-area transformation from wetlands to croplands (Mao et al., 2014)) from April to June and the positive effect due to groundwater irrigation in summer months (Zhang et al., 2007), which can be detected by GRACE, but not by LSMs. However, the human-induced ET variations under multiple driving factors are complicated, which is worthwhile for further exploration in the future.

3.3 Uncertainty

The estimated Human-induced ET proportions were affected by a series of uncertainties inherited from both data processing schemes and propagation of model errors. Theoretically, the uncertainty of the estimated human-induced ET changes can be estimated as follows: first of all, the uncertainty in the simulations of ET changes with different LSMs were manifested but to what levels kept unknown. In terms of the RS-based ET estimations, each solution has their accuracy assessment, for instance, the AVHRR ET products agree well (root mean square error (RMSE) = 13.0-15.3 mm month^{-1}; R²= 0.80-0.84) with observed tower fluxes from globally representative land cover types (Zhang et al., 2010). Additionally, high uncertainty in GRACE-derived TWS changes caused by the coarse spatial resolution of GRACE measurements and different post-processing approaches being adopted may also be a source of an ET estimation uncertainty (Long et al., 2014) in this study, however, as a preliminary attempt, we do believe the results with good enough reliability.

4 CONCLUSION

This study addresses the potential of GRACE-based TWS changes data in water budget calculations, combining with LSMs ET estimations to detect human-induced ET changes over the SRB of China. Firstly, GRACE offers an important measure in monitoring water storage changes due to both climatic and human factors at regional scales. However, many problems are yet to be resolved for improvements. Secondly, this approach may provide a new way for isolating and quantifying human impacts on components of water cycles, e.g., ET, groundwater storage changes, and the LSMs may also benefit from this study for improving model simulations.

ACKNOWLEDGMENTS

mission of NASA's Earth Science Division and archived and distributed by the Goddard Earth Sciences (GES) Data and Information Services Center (DISC).

REFERENCES

Castle, S. L., Reager, J. T., Thomas, B. F., Purdy, A. J., Lo, M., & Famiglietti, J. S., et al., 2016, Remote detection of water management impacts on evapotranspiration in the colorado river basin. *Geophysical Research Letters*, 43(10), 5089-5097.

Dai, Y., Zeng, X., Dickinson, R. E., Baker, I., Bonan, G. B., & Bosilovich, M. G., et al., 2003, The common land model. *Bull.amer.meteor.soc*, -1(8), 1013-1023.

Ek, M. B., Mitchell, K. E., Lin, Y., Rogers, E., Grunmann, P., & Koren, V., et al., 2003, Implementation of noah land surface model advances in the national centers for environmental prediction operational mesoscale eta model. *Journal of Geophysical Research Atmospheres*, 108(D22), GCP 12-1.

Hanasaki, N., Kanae, S., Oki, T., Masuda, K., Motoya, K., & Shirakawa, N., et al., 2008, An integrated model for the assessment of global water resources. 2. applications and assessments. *Hydrology & Earth System Sciences*, 12(4), 1027-1037.

Koster, R. D., & Suarez, M. J., 1992, Modeling the land surface boundary in climate models as a composite of independent vegetation stands. *Journal of Geophysical Research: Atmospheres*, 97(D3), 2697-2715.

Koster, R. D., & Suarez, M. J., 1994, The components of a 'svat' scheme and their effects on a gcm's hydrological cycle. *Advances in Water Resources*, 17(1–2), 61-78.

Liang, X., Lettenmaier, D. P., Wood, E. F., & Burges, S. J., 1994, A simple hydrologically based model of land surface water and energy fluxes for general circulation models. *Journal of Geophysical Research Atmospheres*, 99(D7), 14415–14428.

Lo, M. H., & Famiglietti, J. S., 2013, Irrigation in california's central valley strengthens the southwestern u.s. water cycle. *Geophysical Research Letters*, 40(2), 301-306.

Long, D., Longuevergne, L., & Scanlon, B. R., 2014, Uncertainty in evapotranspiration from land surface modeling, remote sensing, and grace satellites. *Water Resources Research*, 50(2), 1131–1151.

Pan, Y., Zhang, C., Gong, H., Yeh, P. J. F., Shen, Y., Guo, Y., ... & Li, X., 2017, Detection of human-induced evapotranspiration using GRACE satellite observations in the Haihe River basin of China. *Geophysical Research Letters*, 44(1), 190-199.

Li, F., Zhang, G., & Xu, Y. J., 2014, Spatiotemporal variability of climate and streamflow in the Songhua River Basin, northeast China. *Journal of hydrology*, 514, 53-64.

Long, D., Shen, Y., Sun, A., Hong, Y., Longuevergne, L., Yang, Y., ... & Chen, L., 2014, Drought and flood monitoring for a large karst plateau in Southwest China using extended GRACE data. *Remote sensing of environment*, 155, 145-160.

Mao, D., Wang, Z., Li, L., Song, K., & Jia, M., 2014, Quantitative assessment of human-induced impacts on marshes in Northeast China from 2000 to 2011. Ecological engineering, 68, 97-104.

Meng, D., & Mo, X., 2012, Assessing the effect of climate change on mean annual runoff in the Songhua River basin, China. *Hydrological Processes*, 26(7), 1050-1061.

Mu, Q., Heinsch, F. A., Zhao, M., & Running, S. W., 2007, Development of a global evapotranspiration algorithm based on modis and global meteorology data. *Remote Sensing of Environment*, 111(4), 519-536.

Mu, X., Li, Y., Gao, P., Shao, H., & Wang, F., 2012, The runoff declining process and water quality in Songhuajiang River catchment, China under global climatic change. *CLEAN–Soil, Air, Water*, 40(4), 394-401.

Pokhrel, Y. N., Koirala, S., Yeh, P. J. -., Hanasaki, N., Longuevergne, L., & Kanae, S., et al., 2015, Incorporation of groundwater pumping in a global land surface model with the representation of human impacts. *Water Resources Research*, 51(1), 78-96.

Ramillien, G., Frappart, F., Güntner, A., Ngo-Duc, T., Cazenave, A., & Laval, K., 2006, Time variations of the regional evapotranspiration rate from gravity recovery and climate experiment (grace) satellite gravimetry. *Water Resources Research*, 42(10), W04427.

Rodell, M., Houser, P., Jambor, U., Gottschalck, J., 2004. The global land data assimilation system. *Bulletin of the American Meteorological Society*, 85(3): 381.

Rodell, M., Mcwilliams, E. B., Famiglietti, J. S., Beaudoing, H. K., & Nigro, J., 2011, Estimating evapotranspiration using an observation based terrestrial water budget. *Hydrological Processes*, 25(26), 4082–4092.

Tang, Q., Rosenberg, E. A., & Lettenmaier, D. P., 2009, Use of satellite data to assess the impacts of irrigation withdrawals on upper klamath lake, *oregon.*, 6(1), 617-627.

Zhang, G., Deng, W., Yang, Y. S., & Salama, R. B., 2007, Evolution study of a regional groundwater system using hydrochemistry and stable isotopes in Songnen Plain, northeast China. Hydrological Processes, 21(8), 1055-1065.

Zhang, K., Kimball, J. S., Nemani, R. R., & Running, S. W., 2010, A continuous satellite-derived global record of land surface evapotranspiration from 1983 to 2006. *Water Resources Research*, 46(9), 109-118.

Urban Green Land Water Consumption Analysis with Remote Sensing Technology in Beijing City

Di Suchuang [1,5], Li Zhao-liang [2,3,4], Tang Ronglin [2*],
Pan Xingyao [1,5], Liu Honglu[1,5], Yong Niu[6]

1. Beijing Water Science and Technology Institute, China;

2. Institute of Geographic Sciences and Natural Resources Research, China;

3. ICube, UdS, CNRS, France;

4. Chinese Academy of Agricultural Sciences, China;

5. Bejing Engineering Research Center for Non-conventional Water Resources Utilization and Water Saving, China;

6. College of Forestry, Shandong Agricultural University, China;

* Email：trl_wd@163.com

ABSTRACT – The water consumption of green land in a large region was difficult to attain through traditional methods and a practical method was developed using different sources of remote sensing data. Four major procedures were included as follows: (1) The green land area was derived from the high spatial resolution RapidEye imagine using Stratified Classification method. (2) The primary vegetation types of green land were identified using Object-oriented Classification method. (3) Regional green land ET was inversed based on multi-temporal Landsat8 imagines using the Surface Energy Balance Algorithm for Land (SEBAL) model. (4) Water consumption patterns for different vegetation were analysed, and regional water consumption was estimated. The case study was performed in the northwestern region of Beijing City with an area of 147.5 km^2. The green land area was 56.87 km^2, and the deciduous broadleaf forest area was the largest among 6 vegetation types. The total quantity of water consumption for green land in study region in the growing period was 41.52 Mm^3. The quantity of water consumed for different vegetation types from high to low were deciduous broadleaf forest, mixed green space, grassland, evergreen needleleaf forest, golf course, and aquatic vegetation, and the values were 17.43 Mm^3, 13.52 Mm^3, 4.74 Mm^3, 3.81 Mm^3, 1.24 Mm^3, 0.79 Mm^3, respectively.

1 INTRODUCTION

Urban green land is an important component for an ecological and livable civic environment and accurately estimating regional water consumption is meaningful for water management and irrigation scheduling. Traditional methods such as Lysimeter measurements, sap flow measurements, as well as water balance measurements were accurate, but when they were applied to estimate regional water consumption, uncertainties were raised by spatial interpolation. Many kinds of Evapotranspiration (ET) estimation models were developed to estimate regional ET based on remote sensing products, such as the Surface Energy Balance Algorithm for Land (SEBAL, Bastiaanseen et al., 1998), the Surface Energy Balance System (SEBS, Su, 2002), the Surface Temperature – Vegetation Index space (Jiang and Islam, 2001, Tang et al.,2010), Penman-Monteith hybrid models (Mu, et al., 2011, Di et al., 2015) and Temporal Variations models (Lu et al., 2013). The managers could dynamically monitor regional water consumption with

lower cost on nearly real-time using these models, however, there were two major limitations(Li et al., 2009): (1) up scaling errors based instantaneous ET; (2) no thermal-infrared data under cloudy conditions. This works aimed to develop a new method to estimate water consumption for different kinds of green land based on the land cover classification methods and SEBAL model. Accordingly, the new method was applied in the northwest part of Beijing City, the vegetation types were identified and the water consumption quantity was estimated by regional ET results on typical days and interpolating method.

2. STUDY AREA AND DATA

The study area focused within the northwest part of central urban area in Beijing City and the total area was about 147.5 km^2 (Fig.1). The main land covers included buildings, roads, water body, green land, bare soil. The green land vegetation types included deciduous broadleaf forest (DBF), evergreen needleleaf forest (ENF), mixed green space (MGS), golf course (GC), grassland (GL), aquatic vegetation

(AV). The regions where green land were widely distributed included National Olympic Forest Park, Summer Palace, Yuanmingyuan Park, Bajia Park, Haidian Park, Betucheng Park. Besides, green lands were also widely distributed along the main roads and in the residential regions.

The two types of multiple–spectral imagines used in the study included the RapidEye imagine and Landsat8 imagines. The RapidEye imagine was used to classify land covers and to identify green land vegetation types for the high spatial resolution (5 m). The RapidEye imagine was generated on Jun. 10th, 2009. Landsat8 imagines were used for inversing the regional ET. The multi-spectral datasets were acquired by both the Operational Land Imager (OLI) and by the Thermal Infrared Sensor (TIRS). Landsat8 images in four periods were used and they were generated on May 12th, Jun.13th, Sep.1st and Oct. 3rd in 2013.
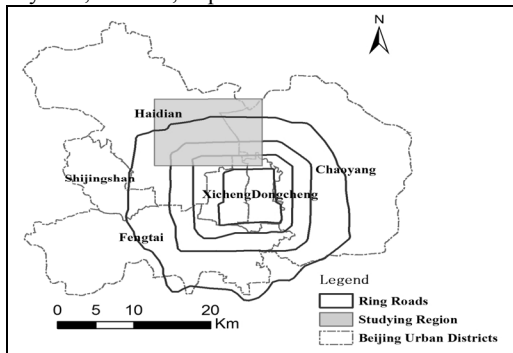
Fig.1 Location of the studying region

3. METHODOLOGY

3.1 Technology roadmap

Firstly, remote sensing imagines were pre-processed and these procedures were included such as: radiance correction, geometric correction, calculating key parameters such as NDVI and surface temperature. Secondly, the main research content might be divided into two parts: one was concerning land cover classification and vegetation identification and the other was regarding the multi-temporal regional ET reversion. The total regional water consumption quantity was attained based on these above results.

3.2 Green land classification and vegetation type identification

The stratified classification method was used in the study and a decision tree was built, as shown in Fig. 3. Water area and no water area could be partitioned according to NIR reflectance values. Vegetation area and no vegetation area could be partitioned by NDVI. For the similar spectral feature of bare soil and built-up (including roads), they were hard to be

distinguished only accounting for the spectral reflectance value and the spatial feature should be taken into account.
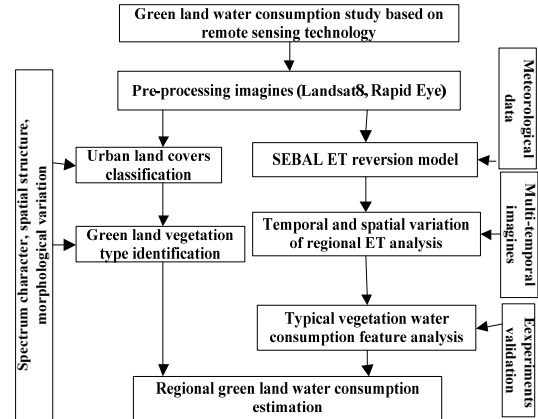
Fig. 2 Flow chart of green land water consumption estimation in the study
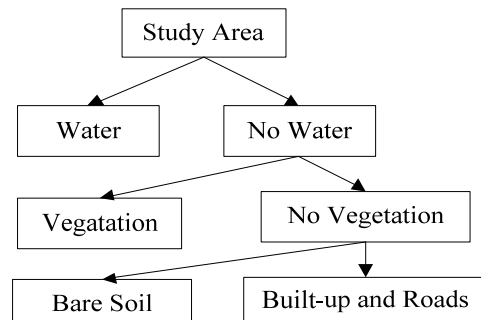
Fig. 3 Decision tree for stratified classification
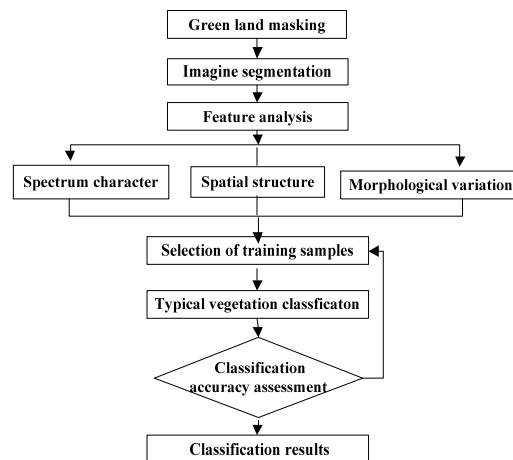
Fig. 4. Vegetation identification by Object-oriented classification method

The green land vegetation types included deciduous broadleaf forest, evergreen needleleaf forest, mixed green space, golf course, grassland, aquatic vegetation. The spectral features of these vegetation types are similar and they would not be identified using only spectral information.

The object-oriented classification method was used and it would integrate the spectral information, the structural information as well as the morphological information in classification. Firstly, these imagines were segmented into lots of units with similar features. Secondly, these units were classified using supervised classification method and training samples.

3.3 Regional ET reversing method

The Surface Energy Balance Algorithm for Land (SEBAL) model had been widely used to inverse the land surface ET (Bastiaanseen, 2000, Zeng et al., 2008) and it was based on physical surface energy balance theory. In the SEBAL model, the input data include visible band images, near infrared band imagines, thermal infrared band imagines, as well as meteorological data such as air temperature and weed speed. The output results included net surface solar radiation, soil heat flux, sensible heat flux and latent heat flux which was closely related with ET. The instantaneous ET was transformed to attain daily ET using the fixed ratio interpolation method. The processes for the SEBAL model were shown in Fig. 5.

Water consumption quantity was estimated according to the areas of vegetation types and average ET values which were derived on typical days.

4. RESULTS AND DISCUSSION

4.1 Green land classification and typical vegetation identification

According the stratified classification results, the green land area was approximately 56.87 km^2 accounting for 38.6% of the total study region. The areas for built-up land and roads, green land, water, bare soil were 84.30 km^2, 56.87 km^2, 3.79 km^2 and 2.54 km^2, respectively. To evaluate the accuracy of the stratified classification results, 100 random sampling points were generalized and the classification results were compared with the investigation results. The total accuracy was 94%.

According to the object-oriented classification results, the deciduous broadleaf forest area was the maximum in the green land region and its value was 23.24 km^2 which accounted for 40.9% of the total green land region and 15.8 % of studying region. The areas for the evergreen needleleaf forest, aquatic vegetation, grassland, golf course, and mixed green space, were 5.31 km^2, 0.82 km^2, 8.63 km^2, 1.45 km^2, and 17.42 km^2, respectively.
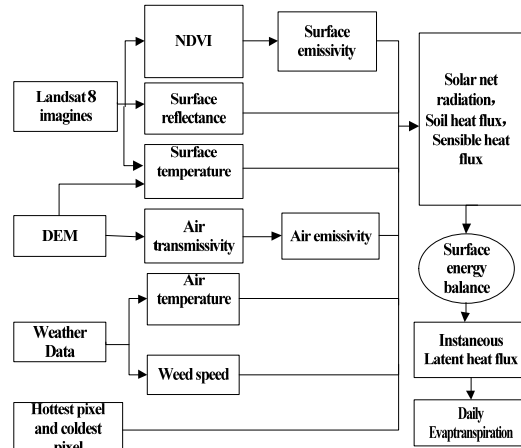
Fig. 5 Flow chart for applying SEBAL model to inverse ET
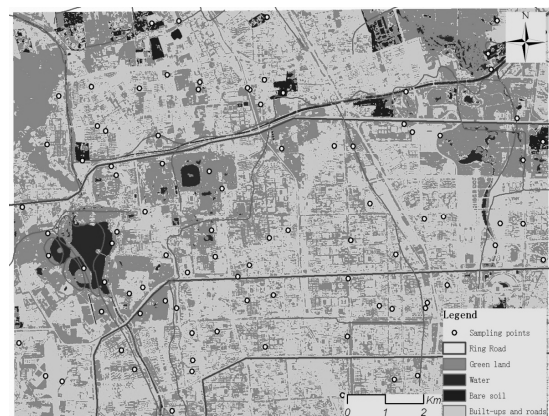
Fig.6 Classification results for different land cover types
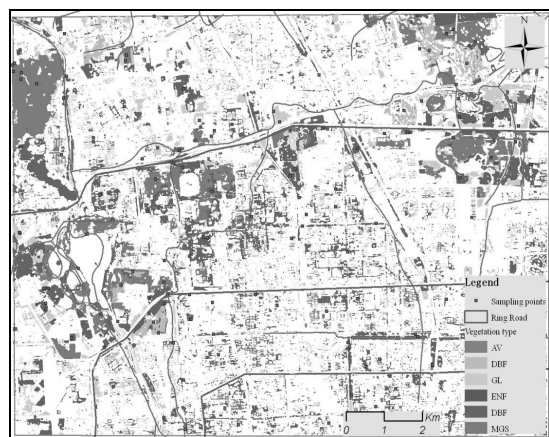
Fig.7 Classification results for different vegetation types

4.2 Regional ET reversion results

The regional daily ET values were reversed using the SEBAL model on 4 typical days (May 12th, Jun. 13th, Sep. 1st and Oct. 3rd in 2013) and the regional ET spatial distribution patterns were shown as Fig.8.

The ET values for different land covers were analysed based on the reversed daily regional ET maps. The average daily ET values for different land covers from high to low were water body, high-density vegetation areas, low-density vegetation areas, no vegetation areas such as built-up area and roads.

Spatially, The ET values within the region between the 5th ring road and the 4th ring road were considerably higher than in other regions because green land and water bodies were more abundant. Temporally, the days on which the mean regional ET values ranked from high to low maps were Sep. 1st, followed by May 12th, Oct. 3rd and Jun. 13th.

4.3 Comparison of reversed and measured ET values for typical quadrats

The reversed ET values on typical days were extracted from the ET maps and the measured ET values were from sap flow measurements or from water balance measurement. Four quadrets were selected in Bajia Park and the vegetation types included *Populus, Salix babylonica, sabina chinensis, Ophiopogon japonicus, Poa annua*. The differences between the reversed and the measured ET values ranged from -2.0 to 2.5 mm/d, and the mean value was 0.1 mm/d. The relative errors ranged from -33.9% to 94.3%, and the mean relative error is 7.9%. The coefficient of determination is 0.1392. The errors were mainly caused by mixed pixels and the detailed information on green land was generalized due to the coarse spatial resolution of Landsat8 imagines.

4.4 Water consumption patterns for different vegetation and regional water consumption quantity

4.4.1 Water consumption patterns for different vegetation

Base on the vegetation type classification map and the reversed daily ET maps, the variation curves of seasonal water consumption might be generated by selecting typical sample points and by extracting the ET values on typical days and 14 sampling points were selected. The ET values from water bodies sampling points were much higher than green land area and they ranged from 6.2 mm/d to 7.9 mm/d. The mean ET value for water bodies was 7.2 mm/d. The average daily ET values for different vegetation from high to low were aquatic vegetation, golf courses, mixed green space, deciduous broadleaf forest, evergreen needleleaf forest, grassland and the average daily ET values were 5.3 mm/d, 4.7mm/d, 4.3 mm/d, 4.1mm/d, 3.9 mm/d and 3.0mm/d, respectively.

Fig.8 Reversed Daily ET
(A. May 12th, B. Jun.13th, C. Sep. 1st, D. Oct. 3rd)
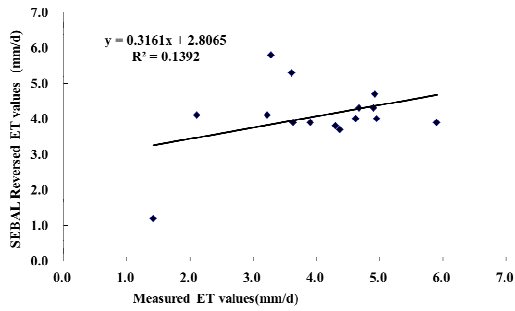
Fig. 9 Comparison between measured ET values and reversed ET values

According to the sampling points, the average ET values for different vegetation types and water bodies were shown in Fig.10. The change trends of seasonal ET curves for different vegetation types and water bodies were similar and they were like a group of sine lines. The highest ET values appeared on Sep.1st and the lowest ET values appeared on Jun.13th. The curve of deciduous broadleaf forest crossed the curve of mixed green space and the curve of evergreen needleleaf forest, because the ET values for these vegetation types in some periods were similar.
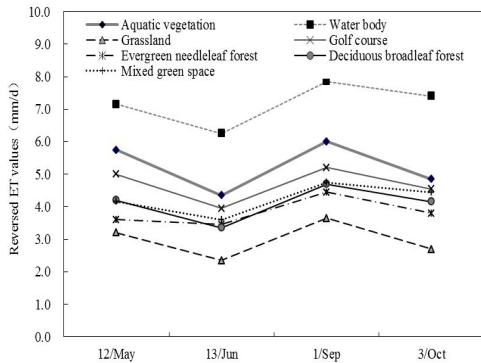
Fig. 10 Reversed ET change trends for different vegetation

4.4.2 Region water consumption quantity estimation

The reversed daily ET values on typical days for representative vegetation types and the vegetation classification results were used to attain the quantity of the water consumed in the growing season and two assumptions accompanied this extrapolation. (1) The monthly average ET value for typical vegetation might be presented by the ET value on a typical day. (2) Due to the influence of the cloud coverage, there were no available imagines in July and August and the monthly average ET values in the two months were interpolated from the ET values in June and September.

The monthly water consumption was attained by multiplying the areas that were derived from the RapidEye imagine, daily ET values for typical vegetation which were derived from the reversed ET maps and the number of days in the month. By summarizing the monthly water consumption, the total quantity for water consumed by green land in the growing season was attained.

The quantities of the water consumed by the green land in different months are shown in Fig.11 and the total quantity is 41.52 Mm^3 in the growing season. The highest value appeared in September with the value of 7.79 Mm^3 and the minimum value appeared in June with the value of 5.65 Mm^3. According to the statistical results, the deciduous broadleaf forest consumed the most water with the value of 17.43 Mm^3 followed by the mixed green space with the value of 13.52 Mm^3, the grassland with the value of 4.74 Mm^3, the evergreen needleleaf forest with the value of 3.81 Mm^3, the golf courses with the value of 1.24 Mm^3 and the aquatic vegetation with the value of 0.79 Mm^3.
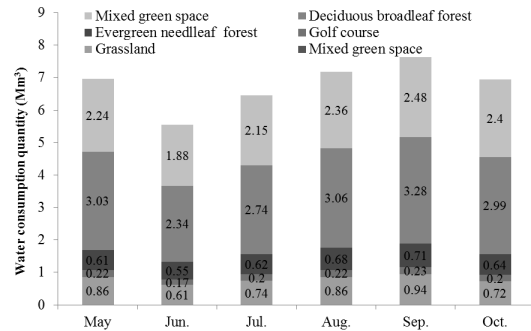
Fig. 11 Water consumption by different vegetation in different months

Based on the water consumption characteristics of typical vegetation, the green land areas extracted from remote sensing imagines, and the investigation data, Di et al. (2012) estimated that the water consummated by the green land was about 161 Mm^3 and the total green land area is approximately 197.3 km^2 within the 5th ring road in Beijing urban area. Supposing the water consumption is proportional to the area of green land, the water consumption would be 46.41 Mm^3 by Di's method, accounting for a green land area of 56.87 km^2 in the study region. The difference between the result from Di's method and the result from our method is 11.8%.

5. CONCLUSION

Remote sensing technology is of crucial importance for urban green land classification and regional water consumption estimation in large regions. In this article, this case study was carried out in the northwest region of Beijing City and the study area covered

approximately 147.5 km^2. This study was based on high resolution remote sensing imagines, meteorological data and water consumption experiment results. The following processes were included: (1) the green land region was derived from a high spatial-resolution RapidEye imagine using Stratified Classification method; (2) vegetation types were identified using Object-oriented Classification method;(3) the daily ET values were reversed using the Surface Energy Balance Algorithm for Land (SEBAL) model; (4) the regional ET spatial patterns and the water consumption temporal patterns for different vegetation were analysed based on multi-temporal daily ET maps, and the total quantity of water consumption in the study region was estimated.

The area of green land was 56.87 km^2 accounting for 31% of the urban area. Furthermore, the green land was divided into 6 classes: deciduous broadleaf forest, evergreen needleleaf forest, mixed green space, golf course, grassland, and aquatic vegetation and the areas were 23.24 km^2, 5.31 km^2, 0.82 km^2, 8.63 km^2, 1.45 km^2, and 17.42 km^2, respectively.

The regional daily ET values were reversed using the SEBAL model on 4 typical days (May 12th, Jun.13th, Sep.1th and Oct.3th in 2013) and the ET spatial distribution patterns were analysed. The average daily ET values for different types of vegetation from high to low were aquatic vegetation, golf course, mixed green space, deciduous broadleaf forest, evergreen needleleaf forest, and grassland, and the average daily ET values were 5.3 mm/d, 4.7mm/d, 4.3 mm/d, 4.1mm/d, 3.9 mm/d, and 3.0mm/d respectively. Compared with the water consumption experiment of the typical vegetation, the mean relative error for reversed ET values based on the SEBAL model was approximately 7.9%.

Through temporal interpolation, the total water consumption quantity for the green land in the study region in the growing period was attained and the value was 41.52 Mm^3.The quantity of water consumed for different vegetation types from high to low were deciduous broadleaf forest, mixed green space, grassland, evergreen needleleaf forest, golf course,and the aquatic vegetation, and the values were 17.43 Mm^3, 13.52 Mm^3, 4.74 Mm^3, 3.81 Mm^3, 1.24 Mm^3, and 0.79 Mm^3, respectively.

Although, the estimation error is relatively small compared with the measured data and other related research results, further work will be done to reduce uncertainty by estimating the ET values in sub-pixel scale according to the area contribution of different land covers. Therefore, the regional ET results are expected to be more accurate and to be more helpful in urban water resource management.

7、REFERENCES

Bastiaanseen, W. G. M., 2000, SEABAL-based sensible and latent heat fluxes in the irrigated Gediz Basin, Turkey. J*ournal of Hydrology*, 229: 87-100.

Bastiaanssen, W. G. M., M. Menenti, R. A. Feddes and A. A. M. Holtslag, 1998, A Remote Sensing Surface Energy Balance Algorithm for Land (SEBAL) 1. Formulation. *Journal of Hydrology*, 212-213: 198-212.

Di, S., Z.-L. Li, R. Tang, H. Wu, B. Tang, and J. Lu, 2015, Integrating two layers of soil moisture parameters into the MOD16 algorithm to improve evapotranspiration estimations. *International Journal of Remote Sensing*, 36(19): 4953-4971.

Di, S., W. Wu, H. Liu and X. Pan, 2012, Greenland water consumption estimation and evapotranspiration inversion within 5th Ring Road in Beijing city. *Transactions of the Chinese Society of Agricultural Engineering*, 28(10): 98-102. (in Chinese)

Jiang, L. and S. Islam, 2001, Estimation of surface evaporation map over Southern Great Plains using remote sensing data. *Water Resource Research*, 37: 329-340.

Li, Z.-L., R. L. Tang, Z. Wan, Y. Bi, C. Zhou, B. Tang, G. Yan and X. Zhang, 2009, A review of current methodologies for regional evapotranspiration estimation from remotely sensed data. *Sensors*, 9: 3801-3853.

Lu, J., R. L. Tang , H.Tang and Z.-L. Li, 2013, Derivation of daily evaporative fraction based on temporal variations in surface temperature, air temperature, and net radiation. *Remote Sensing*, 5: 5369-5396.

Mu, Q., M. Zhao and S. W. Running, 2009, Improvements to a MODIS global terrestrial evapotranspiration algorithm. *Remote Sensing of Environment*, 115(8): 1781-1800.

Tang, R. L., Z.-L. Li, and B. H. Tang, 2010, An application of the Ts-VI triangle method with enhanced edges determination for evapotranspiration estimation from MODIS data in arid and semi-arid regions: implementation and validation. *Remote Sensing of Environment*, 114(4): 540-551.

Zeng L., K. Song, B. Zhang and J. Du, 2008, Applying Landsat Data and SEBAL Model to Inverse Regional Evapotranspiration and Its Parameters Estimation. *Remote Sensing Technology and Application*, 2008, 23(3), 255-263. (in Chinese)

Effect of cloud on daily evapotranspiration estimation using the constant global shortwave irradiance ratio method

Yazhen Jiang[1], Xiaoguang Jiang[1,2,3], Ronglin Tang[2,1,*], Zhao-Liang Li[4], Yuze Zhang[1], Cheng Huang[1],Chen Ru[1]

1. University of Chinese Academy of Sciences, Beijing 100049, China;
2. State Key Laboratory of Resources and Environment Information System, Institute of Geographic Sciences and Natural Resources Research, Chinese Academy of Sciences, Beijing 100101, China;
3. Key Laboratory of Quantitative Remote Sensing Information Technology, Academy of Opto-Electronics, Chinese Academy of Sciences, Beijing 100094, China;
4. Key Laboratory of Agri-informatics, Ministry of Agriculture/Institute of Agricultural Resources and Regional Planning, Chinese Academy of Agricultural Sciences, Beijing 100081, China;
* Authors to whom correspondence should be addressed: tangrl@lreis.ac.cn

ABSTRACT- *Upscaling instantaneous evapotranspiration (ET) retrieved at a specific time of satellite overpass to daily ET is a key issue in regional scale applications for planning water resources and monitoring water use efficiency. The constant global shortwave irradiance ratio method which keeps the ratio of instantaneous incoming shortwave solar radiation to daily value as constant is reported to be robust in obtaining daily ET. However, the method is usually used in clear days, and the study about the cloud effect on daily ET estimation trough this method is rare. This study concentrated on the shortwave cloud radiative effect (CRESW; W/m^2) on daily ET estimation through the constant global shortwave irradiance ratio method. The CRESW was defined as the difference between the downward global irradiance measurements for cloud-sky (satellite overpass moment is clear) and for corresponding ideal clear-sky conditions. The selected clear-sky conditions from field data was also regraded as reference. Then daily ET was obtained by upscaling instantaneous ET obtained at satellite overpass time using the temporal upscaling method at cloud-sky, ideal clear-sky and selected clear sky conditions. Compared with observed daily LE, the upscaled LE at selected clear sky condition had a bias of $6.3W/m^2$, a RMSE of 14.5 W/m^2; at cloud-sky condition had a bias of 8.2 W/m^2, a RMSE of 18.4 W/m^2, with estimation error increased. Compared with daily ET obtained at ideal clear sky condition, the upscaled daily ET reduced, and the reduction amount has an exponential increase with the CRESW.*

1. INTRODUCTION

Evapotranspiration (ET) can be used to express the vegetation water consumption and reflect the surface moisture effectively (Courault et al., 2005; Anderson et al., 2012; Tang et al., 2013). Daily ET is more significant among many practical applications in the fields of water management, drought monitoring and climate change study, compared to the instantaneous ET resulted from remote-sensing based models at the time of satellite overpass (Li et al., 2009). Therefore, the remotely sensed instantaneous ET must be upscaled temporally to obtain ET integration over a longer time scale (e.g. days, months to years).

In order to accommodate the temporal scaling challenges encountered by remote sensing based ET models, techniques have been proposed and applied by various researchers to upscale instantaneous ET to daily value (Brutsaert & Sugita, 1992; Chávez et al., 2008; Delogu et al., 2012; Cammalleri et al., 2014). The constant global shortwave irradiance ratio method which keeps the ratio of instantaneous incoming shortwave solar radiation to daily value as constant is reported to be robust in obtaining daily ET (Ryu et al., 2012; Niel et al., 2012; Xu et al., 2015). However, the

temporal upscaling method is usually used in the clear-sky days, and the study about the cloud effect on daily ET estimation trough this method is rare. The issue comes, that the cloud coverage is a prominent phenomenon in many parts of the world and the mean cloud cover per day even exceed 60% in the humid tropics (Bussieres & Goita, 1997). Thus, extrapolating instantaneous ET only under all-sky clear condition has limited applicability for operational remote sensing applications.

In fact, it is practicable to quantify the effect of cloud cover using some schemes (Jackson et al., 1983). In Long's study (2000; 2006), shortwave cloud radiative effect (CRESW; W/m^2) is defined as the difference between the downward global irradiance measurements for cloud-sky and for corresponding ideal clear-sky conditions. The presence of clouds denotes a main decrease in irradiance at the surface, although other factors such as increased column water vapor amount or aerosol optical depth changes may also contribute to the difference. The cloudy days expressed by irradiance reduction have been validated as heavily overcast days using measurements. Therefore, an elaborate understanding of the cloud

effect is essential and feasible in exactly obtaining daily ET.

This study concentrates on shortwave cloud radiative effect on daily ET estimation through the constant global shortwave irradiance ratio method.

2. STUDY SITE AND DATA

2.1 Study site

This study was carried out at the Yucheng station （36.8291° N, 116.5703° E, located in the southwest of Yucheng County, Shandong Province in North China）. The Yucheng station is a part of the Chinese terrestrial ecosystem flux network and aims at measuring long-term exchange of carbon dioxide, water vapor, and heat between the land and the atmosphere. The climate here is the subhumid and monsoon climate with a mean annual temperature of 13.1 ℃ and precipitation of 528 mm. The soil is sandy loam, and the land cover types near the station primarily consist of crop (winter-wheat and summer-corn rotation), bare soil, tree and water.
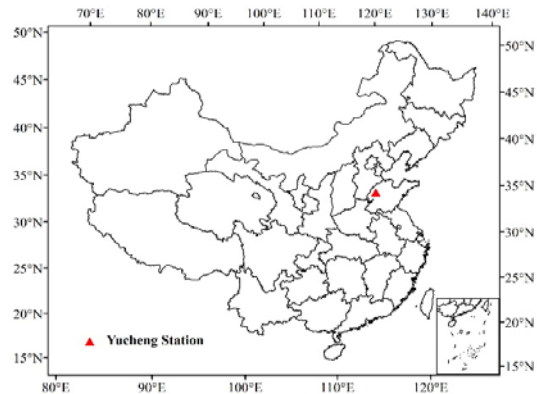
Figure 1. The location of study site

2.2 In situ measurements

The measurements from the Yucheng station needed in this study contain meteorological variables, radiation data, and flux data from late April 2009 to late October 2010. Meteorological variables, including air temperature, wind speed, relative humidity and atmospheric pressure, were measured at the height of 2.93 m during the growth period of wheat and at 4.2 m during the growth period of corn. Radiation data, including downwelling and upwelling shortwave and longwave radiations, were acquired from a CNR-1 radiometer installed at the height of 3.98 m. Flux data H and LE were measured by an Eddy Covariance (EC) system. The height of the EC facility was 2.7 m and 3.75 m during the growth period of wheat and the growth period of corn, respectively. G was estimated

from a single HFP-01 soil heat flux plate at 2 cm below the surface without considering heat transfer for the 2cm storage layer above the plate.

All of the meteorological variables and the EC measurements were are recorded as a 30-min average, so there are 48 records in a day for each variable. It is noted that 5 min averaged data of downwelling shortwave radiations are contained for clear sky identification.

2.3 Remote sensing data

Remote sensing data used in this study are from the MODIS Terra satellite, including the calibrated radiance product (MOD021KM), the land surface temperature and emissivity product (MOD11_L2), the surface reflectance product (MOD09GA), the geolocation product (MOD03) and the cloud mask product (MOD35). These data are downloaded from the Atmosphere Archive and Distribution System Web (https://ladsweb.nascom.nasa.gov/data/search.html). Of the 36 spectral channels of the MODIS sensor, two visible bands and five near-infrared bands have spatial resolutions of 250 m and 500 m, respectively, and the rest thermal infrared bands have a spatial resolution of 1000 m.

3. METHODS

3.1 The method for the instantaneous LE calculation

In this paper, the calculation of instantaneous LE is performed using the following equation (Boegh et al., 2002):

$$LE = (\rho c_p / \gamma) \frac{e_s^* - e_a}{r_s + r_{ae}} \qquad (1)$$

where e_s^* is the saturated vapour pressure at the evaporating front evaluated on the basis of the surface temperature, kPa; e_a is the vapour pressure of the air above the canopy, kPa, r_s is the surface resistance, s/m; r_{ae} is the aerodynamic resistance, s/m.

For the calculations of the aerodynamic resistance (r_{ae}) and surface resistance (r_s), the study uses the method proposed by Boegh et al (2002). The input parameters are surface temperature (T_s), net radiation (R_n), soil heat flux (G), air temperature (T_a), and air humidity (e_a).

3.2 The temporal upscaling method

In the constant global shortwave irradiance ratio method, the ratio of instantaneous incoming shortwave solar radiation to daily value keeps constant, which is equal to the ratio of instantaneous ET to the daily ET, namely

$$\frac{ET_i}{ET_d} = \frac{Rs_i}{Rs_d} \qquad (2)$$

where Rs is the incoming shortwave solar radiation; the subscript i and d represent instantaneous and daily time scale, respectively.

In the ideal clear-sky days, the ration of instantaneous incoming shortwave solar radiation to daily value is expressed like this (Bisht et al., 2005; Hou et al., 2014)

$$\frac{Rs_i}{Rs_d} = \frac{\pi}{2}\sin(\pi\left(\frac{t_{overpass} - t_{rise}}{t_{set} - t_{rise}}\right)) \qquad (3)$$

where t_{set}, t_{rise} and $t_{overpass}$ are the time for sunset, sunrise and overpass of satellite.

3.3 Clear-sky selections from shortwave irradiance measurements

The clear-sky shortwave is a maximum at local solar noon, diminishing to zero at night. The primary factor determining the magnitude at any given time is the solar zenith angle (Long et al., 2006). Thus, for a given solar zenith angle we expect the total shortwave to fall within a nominal range of values for clear sky. We use the method proposed by Long et al (2000) to identify clear sky moments.

The first test is to normalize the total shortwave data by a power law function of the cosine of the solar zenith angle:

$$Rs_N = Rs_\downarrow / \mu_0^b \qquad (4)$$

where $Rs_\downarrow$ is the downwelling total shortwave; Rs_N is the normalized total shortwave; μ_0 is the cosine of the solar zenith angle; and b is a constant.

Maximum and minimum limits are set, and only normalized values falling inside this range are tentatively labeled as clear. This, as a first cut, eliminates periods of obvious positive and negative cloud effect. Figure 2 shows the 5-min total shortwave and normalized date May 20, 2009. Values used in this comparison are 1.31 for the constant b, 1150 W/m² for the maximum limit, 900 W/m² for the minimum limit.
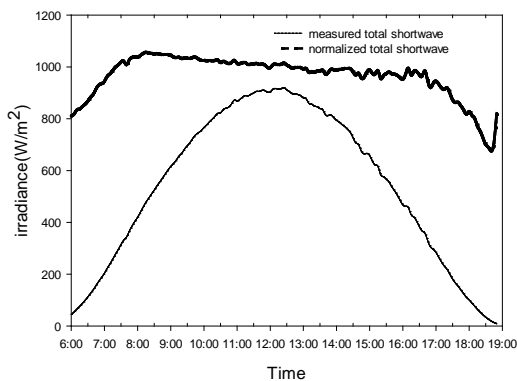
Figure 2. Measured and normalized shortwave irradiance

Next, the temporal changes in total shortwave irradiance are studied. For clear periods, the change in irradiance is small over short periods of time compared to changes due to cloud effects. Thus, the change in measured total shortwave to the corresponding change in top-of atmosphere irradiance ($F_{\downarrow T}$) is compared.

For clear sky, the absolute change in $R_{S\downarrow}$ over a short time must be less than the absolute change in $F_{\downarrow T}$. We use a limit envelope based on $F_{\downarrow T}$ and the solar zenith angle in this test for clear sky (Figure 3).
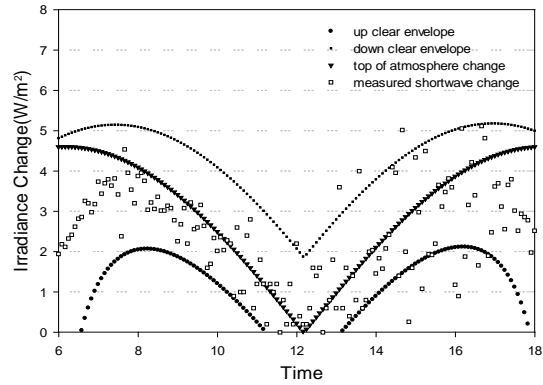
Figure 3. Illustration of the change in irradiance with time

In order to account for the uncertainties and noise of these measurements, we use minimum and maximum values which are less than and greater than, respectively, the value of the absolute change of $F_{\downarrow T}$ with the time (Eq. (5)).

$$MAX = |\Delta F_{\downarrow T} / \Delta t| + Cu_0$$

$$MIN = |\Delta F_{\downarrow T} / \Delta t| - \left[Rt(u_0^{cos\theta} + 0.1)/u_0\right] \qquad (5)$$

Using the clear-sky identification method, 77 cloud-sky (satellite overpass moment is clear) days and 45 totally clear-sky days were selected.

3.4 The shortwave cloud radiative effect

The shortwave cloud radiative effect (CRESW; W/m²) is determined using downward global irradiance measurements (5-min averages), recorded at the surface. All situations in terms of cloud cover and cloud type were considered to determine the CRESW, which is defined as the difference between the downward global irradiance measurements for cloud-sky (satellite overpass moment is clear) and for corresponding ideal clear-sky conditions.

$$CRESE = Rs_{cloud} - Rs_{clear} \qquad (6)$$

Over long time averages or large spatial domains, the CRESW is always negative because clouds reflect more radiation than clear-sky, implying that less solar radiation reaches the surface.

4 RESULTS AND DISCUSSIONS

4.1 The instantaneous ET calculation from MODIS data and field data

Figure 4 shows the instantaneous ET (LE, used interchangeably hereafter) estimated using remote sensing data and part meteorology data of MODIS/Terra overpass times over 77 cloud-sky days and 45 totally clear-sky day. The estimated instantaneous LE was compared with the instantaneous LE observations corrected by the Bowen Ration (BR) method to close the energy imbalance of EC measurements. The instantaneous LE of cloud-sky days was overestimated a little by a small bias of $1.5 W/m^2$ and a root mean square error (RMSE) of 37.6 W/m^2. The instantaneous LE of selected clear-sky days was undervalued by a bias of $-32.31.5 W/m^2$ and a RMSE of 48.9 W/m^2.

Then daily LEs at cloud-sky, ideal clear-sky and selected clear-sky conditions were obtained by upscaling the instantaneous LEs obtained at satellite overpass time using the constant global solar radiation ratio method.
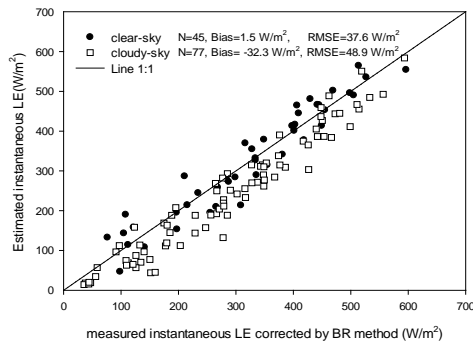
Figure 4. Comparison of the estimated instantaneous LE and the measured value corrected with the BR method

4.2 Upscaling results at cloud-sky and selected clear-sky conditions

Daily LEs obtained through the constant global solar radiation ratio method at cloud-sky and selected clear-sky conditions were compared with the measured Daily LEs corrected with the BR method in Figure 5.

Figure 5 demonstrates that both the daily LEs at cloud-sky days and selected clear-sky days were underestimated. The upscaled and observed daily LEs at the selected clear-sky days produced a significant linear relation, with a low bias of $-6.3 W/m^2$, and a RMSE of 14.5 W/m^2. The estimation bias related to cloud-sky days was $-8.2 W/m^2$ and the RMSE was 18.4 W/m^2. Narrowed statistical bias and RMSE of daily LE at clear-sky days revealed superior performances of the temporal upscaling method at and the upscaling results at cloud-sky condition had higher estimation deviation.
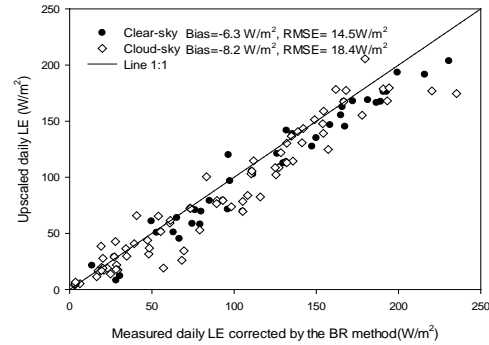
Figure 5. Comparison of the upscaled daily LEs and the measured value corrected with BR method at cloud-sky and selected clear-sky conditions

4.3 The shortwave cloud radiative effect on daily evapotranspiration estimation

According to the definition of shortwave cloud radiative effect (CRESW), we can obtain the CRESW of 77 cloud-sky days, namely the difference between the downward global solar irradiance measurements for 77 cloud-sky and for corresponding ideal clear-sky conditions. Based on the constant global solar radiation ratio method, we acquired daily LE which is hypothetical value for ideal clear-sky days.
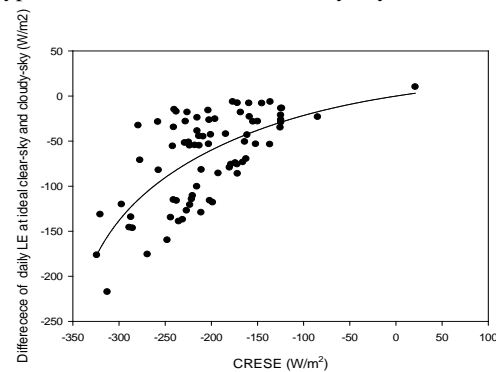
Figure 6. The relationship of the CRESW and the difference between daily LE upscaled at cloud-sky days and corresponding ideal clear-sky days

Figure 6 illustrates the relationship of the CRESW and the difference between daily LE upscaled at 77 cloud-sky days and corresponding ideal clear-sky days from the same instantaneous LE. Compared with daily LE obtained at ideal clear-sky condition, the upscaled daily ET at cloud-sky condition reduced, and the reduction amount has an exponential relation with the CRESW. The exponential relationship was not very significant, which was due to the fact that the CRESW is defined as the difference between the downward global irradiance measurements for cloud-sky and for corresponding ideal clear-sky conditions,

ignoring some cloud effect caused from the column water vapor amount or aerosol optical depth changes.

Meanwhile, it is notable that the instantaneous LEs of MODIS/Terra overpass times over 77 cloud-sky days and 45 totally clear-sky day was both estimated using remote sensing data and part meteorology data in this study. The parameter retrievals required for the LE calculation have some deviations, which would affect the daily LE upscaling from the instantaneous, namely the behaviour of the temporal upscaling method to some extent.

5 CONCLUSION

This study evaluated the shortwave cloud radiative effect (CRESW; W/m^2) on daily LE estimation upscaled through the constant global shortwave irradiance ratio method. The CRESW is defined as the difference between the downward global irradiance measurements for cloud-sky and for corresponding ideal clear-sky conditions. The selected clear-sky conditions from field data was also as reference. Daily ET was obtained by upscaling instantaneous ET obtained at satellite overpass time using the constant global solar radiation ratio method at different conditions, respectively. Compared with observed daily LE, the upscaled LE at selected clear-sky condition had a bias of $6.3 W/m^2$, a RMSE of 14.5 W/m^2; at cloud-sky had a bias of $8.2 W/m^2$, a RMSE of $18.4 W/m^2$, with estimation error increased. Compared with daily LEs obtained at ideal clear-sky condition, the upscaled daily ET at cloudy-sky days reduced, and the reduction amount has an exponential increase with the CRESW.

6. REFERENCES

Anderson, M. C., Kustas, W. P., Alfieri, J. G., Gao, F., Hain, C., & Prueger, J. H., et al., 2012, Mapping daily evapotranspiration at Landsat spatial scales during the bearex'08 field campaign. *Advances in Water Resources*, 50, 162–177.

Bisht, G., Venturini, V., Islam, S., & Jiang, L. E., 2005, Estimation of the net radiation using MODIS (Moderate Resolution Imaging Spectroradiometer) data for clear sky days. *Remote Sensing of Environment*, 97(1), 52-67.

Boegh, E., Soegaard, H., & Thomsen, A., 2002, Evaluating evapotranspiration rates and surface conditions using landsat tm to estimate atmospheric resistance and surface resistance. *Remote Sensing of Environment*, 79(2–3), 329-343.

Brutsaert, W., & Sugita, M., 1992, Application of self-preservation in the diurnal evolution of the surface energy budget to determine daily evaporation. *Journal of Geophysical Research: Atmospheres,* 97(D17), 99-104.

Bussieres, N., Goita, K., 1997, Evaluation of strategies to deal with cloudy situation in satellite evapotranspiration algorithm. Proceedings of the third International Workshop NHRI symposium 17, 16-18 October 1996, NASA, Goodard Space Flight Center, Greenbelt, Maryland, USA: 33-43.

Cammalleri, C., Anderson, M.C., Kustas, W.P., 2014, Upscaling of evapotranspiration fluxes from instantaneous to daytime scales for thermal remote sensing applications. *Hydrology and Earth System Sciences,* 18, 1885-1894.

Chávez, J.L, Neale, C.M.U, Prueger, J.H., Kustas, W.P., 2008, Daily evapotranspiration estimates from extrapolating instantaneous airborne remote sensing ET values. *Irrigation Sciences*, 27(1), 67-81.

Courault, D., Seguin, B., Olioso, A., 2005, Review on estimation of evapotranspiration from remote sensing: from empirical to numerical modeling approaches. *Irrigation and Drainage systems*, 19(3), 223-249.

Crago, R.D. (1996). Conservation and variability of the evaporative fraction during the daytime. *Journal of Hydrology*, 180(1-4), 173-194.

Delogu, E., Boulet, G., Olioso, A., Coudert, B., Chirouze, J., Ceschia, E., Le Dantec, V., Marloie, O., Chehbouni, G., Lagouarde, J.P., 2012, Reconstruction of temporal variations of evapotranspiration using instantaneous estimates at the time of satellite overpass. *Hydrology and Earth System Sciences,* 16, 2995-3010.

Hou, J., Jia, G., Zhao, T., Wang, H., & Tang, B., 2014, Satellite-based estimation of daily average net radiation under clear-sky conditions. *Advances in Atmospheric Sciences*, 31(3), 705.

Jackson, R. D., Hatfield, J. L., Reginato, R. J., Idso, S. B., & Pinter, P. J.,1983, Estimation of daily evapotranspiration from one time-of-day measurements. *Agricultural Water Management,* 7(1-3), 351-362.

Li, Z-L., Tang, R., Wan, Z., Bi, Y., Zhou, C., Tang, B-H., Yan, G., Zhang, X. (2009). "A review of current methodologies for regional evapotranspiration estimation from remotely sensed data. " *Sensors*, 9, 3801–3853.

Long, C. N., & Ackerman, T. P., 2000, Identification of clear skies from broadband pyranometer measurements and calculation of downwelling shortwave cloud effects. *Journal of Geophysical Research-Atmosphere.,* 105(D12), 15609-15626.

Long, C. N., Ackerman, T. P., Gaustad, K. L., & Cole, J. N. S., 2006, Estimation of fractional sky cover from broadband shortwave radiometer measurements." *Journal of Geophysical Research. D11204 Doi/jd, 111*(D11), 1937-1952.

Niel, T. V., & Mcvicar, T. R., 2012, Upscaling latent heat flux for thermal remote sensing studies: comparison of alternative approaches and correction of bias. *Journal of Hydrology,* 468(4), 35-46.

Ryu, Y., Baldocchi, D. D., Black, T. A., Detto, M., Law, B. E., & Leuning, R., et al, 2012, On the temporal upscaling of evapotranspiration from instantaneous remote sensing measurements to 8-day mean daily-sums. *Agriculture. Forest Meteorology,* 152(1), 212-222.

Tang, R., Li, Z. L., & Sun, X, 2013, Temporal upscaling of instantaneous evapotranspiration: an intercomparison of four methods using eddy covariance measurements and MODIS data. *Remote Sensing and. Environment,* 138(6), 102-118.

Xu, T., Liu, S., Xu, L., Chen, Y., Jia, Z., & Xu, Z., et al. ,2015, Temporal upscaling and reconstruction of thermal remotely sensed instantaneous evapotranspiration. *Remote Sensing,* 7(3), 3400-3425.

Study on the spatiotemporal variations of terrestrial water storage and its relation to precipitation and NDVI over the Tibetan Plateau during 2003-2015

Qilun Li[1, 2], Wanchang Zhang[1, *], Ning Nie[3], Jinping Liu[1, 2], Hao Chen[1, 2]

[1] *Key Laboratory of Digital Earth Science, Institute of Remote Sensing and Digital Earth, Chinese Academy of Sciences, Beijing 100094, China*

[2] *University of Chinese Academy of Sciences, Beijing, 100049, China*

[3] *State Key Laboratory of Pollution Control and Resource Reuse, School of the Environment, Nanjing University, Nanjing 210023, China*

Email addresses: liql@radi.ac.cn; *Corresponding author: zhangwc@radi.ac.cn

Abstract - *Tibetan Plateau, the headwater of most Asian rivers, has a crucial influence on the water resources of the whole Asia, especially in the east and south of Asia. As an important component of the water cycle, terrestrial water storage (TWS) changes greatly affect regional water supply and demand situation. Since launched in 2002, the Gravity Recovery and Climate Experiment (GRACE) satellite mission has provided quantitative measurement of TWS changes on global and regional scales. In this study, the spatiotemporal variations of TWS anomaly, derived from GRACE satellite data during 2003-2005, over the Tibetan Plateau were investigated by using a least square regression model and Pearson correlation coefficient. Then we detected the relation between water cycle and carbon cycle, with TWS anomaly, the precipitation data from the Tropical Rainfall Measurement Mission (TRMM), and the Normalized Difference Vegetation Index (NDVI) data from Moderate Resolution Imaging Spectroradiometer (MODIS). This study revealed that yearly TWS anomaly of the Tibetan Plateau had been undergoing a continuous decreasing trend with a rate of approximately -0.87 cm/yr (2.187×10^{10} m^3/yr). Also, it showed a high correlation with precipitation both in spatial and temporal distribution; for the entire study area, there was an average time lag of about 26.7 days between precipitation and TWS anomaly. In the meantime, both TWS changes and precipitation had a pretty high correlation with NDVI ($R^2 = 0.66$ and $R^2 = 0.79$, respectively).*

1 INTRODUCTION

As an important component of the hydrologic cycle, Terrestrial Water Storage (TWS) change is a comprehensive reflection of accumulated precipitation, evapotranspiration, runoff and groundwater processes (Chen et al., 2009). TWS change is very valuable for the management of agriculture water and regional water resources, which is a prominent problem in the present and future. Although TWS changes, including changes in surface water, ground water, soil moisture, evapotranspiration, snow and ice sheets, can be measured by in-situ observations with a pretty high accuracy, it is difficult to obtain an extensive region due to the small coverage area and limited distribution of in-situ observation stations (Rieser et al., 2010).

Under the demands for direct observations of large-scale TWS change, the Gravity Recovery and Climate Experiment (GRACE) mission was launched, jointly by National Aeronautics and Space Administration (NASA) and German Aerospace Center (DLR), in March 2002. GRACE is the first satellite dedicated to measure the earth's time-variable gravity changes, and has continuously observed more than 10 years for global gravity changes (Tapley et al.,2004). Studies have proved that the time-variable gravity changes are related to water mass redistributions on a short-time scale, which represents TWS changes (Hu et al., 2006; Rieser et al., 2010). To date, GRACE data has been used in amount of studies to investigate TWS change, ground water storage. (Rieser et al., 2010; Rodell et al., 2009; Seyoum & Milewski, 2016; Hu et al., 2006; Xu et al., 2013).

Precipitation, the recharge source of TWS, plays a major role in the water balance. Therefore, we compared the spatiotemporal variations of TWS changes from GRACE and the precipitation data from TRMM over the Tibetan Plateau in this study. In addition, this study also investigated whether there was a statistically significant correlation between plant growth and water storage, with the data sets of NDVI from MODIS, precipitation from TRMM, and TWSA.

2 STUDY AREA AND DATA

2.1 Study area

The Tibetan Plateau, located in the southwest of China between 26°N-39°N and 73°E-104°E, as shown in Fig.1, covers an area of about 2.6×10^6 km^2, accounting for 26.8% of the total land area of China. The average elevation of the Tibetan Plateau is about 4-5km.

2.2 GRACE data

In this study, the monthly GRACE Release 5.0 (RL05) data from January 2003 to December 2015 were used (available at http://grace.jpl.nasa.gov/) (Swenson &

Wahr, 2006) based on the spherical harmonic coefficients from the Centre of Space Research (CSR).
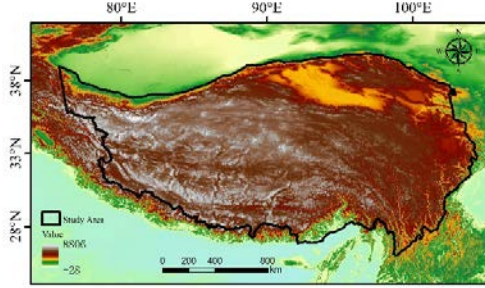
Fig.1. Geographic map showing the topography and location boundaries of the Tibetan plateau

In data processing, the degree 2 order 0 coefficients were replaced by the solutions from Satellite Laser Ranging (Cheng et al., 2015) and the degree 1 coefficients were estimated using the method from Swenson et al. (Swenson et al., 2008). A glacial isostatic adjustment (GIA) correction (Geruo et al., 2013), a destriping filter and a 300 km wide Gaussian filter was applied to the data. Mean monthly solution from January 2004 to December 2009 was removed from each solution. Then these smoothed spherical harmonic coefficients were converted into 1 degree gridded data. And finally, the gridded GRACE data was scaled using the gridded scaling dataset provided by Landerer and Swenson (Landerer & Swenson, 2012) to restore much of the energy loss in the truncation and filtering. The scaled GRACE TWS Anomaly (TWSA) was expressed in centimeter of Equivalent Water Height (EWH).

2.3 Precipitation data and NDVI data

Precipitation data was collected from the TRMM 3B43 V7 monthly gridded precipitation product, the widely-used satellite precipitation measurement product, with spatial resolution of 0.25 degree (available at https://pmm.nasa.gov/TRMM). The NDVI data was collected from MODIS MOD13A3 V5 product, with spatial resolution of 1 km (available at https://lpdaac.usgs.gov/dataset_discovery/modis). In order to keep the consistency of spatial resolution, the TRMM precipitation data and the MOD13A3 NDVI data were resampled by bilinear interpolation into 1 degree, and then the comparative analyses were conducted.

3 METHODOLOGY

3.1 Spherical harmonic expressions of TWSA

The GRACE spherical harmonic coefficients were converted into EWH, which represented the TWSA, given by Equation (1):

$$\Delta h(\theta,\varphi) = \frac{2a\rho_{ave}\pi}{3\rho_{water}} \sum_{l=0}^{N} \sum_{m=0}^{l} \frac{2l+1}{1+k_l} w_l \tilde{P}_{lm}(\cos\theta)$$

$$\times [\Delta C_{lm} \cos(m\varphi) + \Delta S_{lm} \sin(m\varphi)] \qquad (1)$$

where $\Delta h(\theta,\varphi)$ is the EWH value, a=6378136.3 m is the radius of the earth at the equator, ρ_{ave}=5517 kg/m^3 is the average density of the Earth, ρ_{water}=1000 kg/m^3 is the density of pure water, N=60 is the maximum spherical harmonic degree, l and m are the degree and order of spherical harmonic, θ and φ are the co-latitude and longitude, k_l is the degree l elastic load Love number of the Preliminary Reference Earth Model, ΔC_{lm} and ΔS_{lm} are the spherical harmonic coefficients from GRACE, $\tilde{P}_{lm}(\cos\theta)$ is the l degree and m order normalized associated Legendre polynomial. And w_l is the Gaussian smoothing factor, which can be computed by:

$$w_0 = \frac{1}{2\pi}$$
$$w_1 = \frac{1}{2\pi}\left[\frac{1+e^{-2b}}{1-e^{-2b}} - \frac{1}{b}\right]$$
$$w_{n+1} = -\frac{2n+1}{b} w_n + w_{n-1}$$
$$b = \frac{\ln(2)}{[1-\cos(r/a)]} \qquad (2)$$

where r=300 km denotes the soothing radius.

3.2 Analysis methods

In this study, a least square regression model was used to fit the TWSA and precipitation time series given by:

$$y(t) = A \cdot \sin[2\pi \cdot (t - \varphi)/T] \qquad (3)$$

The Pearson correlation coefficient R was used to analyze the relation among TWS, precipitation and NDVI.

$$R = \sqrt{\frac{\sum_{i=1}^{N}(X_i - \bar{X})^2 \cdot (Y_i - \bar{Y})^2}{\sum_{i=1}^{N}(X_i - \bar{X})^2 \cdot \sum_{i=1}^{N}(Y_i - \bar{Y})^2}} \qquad (4)$$

4 RESULTS AND ANALYSIS

The spatial distribution of monthly average TWSA in the Tibetan Plateau was calculated using the GRACE-derived TWSA from January 2003 to December 2015. From Fig.2, there is a significant difference in TWSA among different months. During the period from January to May, the TWSA in the northwestern part of the Tibetan Plateau remains basically in equilibrium, and only the TWSA in the Middle Kunlun Mountain Nature Reserve has a small surplus, with a maximum of 6 cm. The closer to the southeast, the lower the TWS, with the lowest value of -17 cm. During the period from June to September, affected by the southwest monsoon, the Tibetan Plateau comes into rainy season, and precipitation increases significantly.
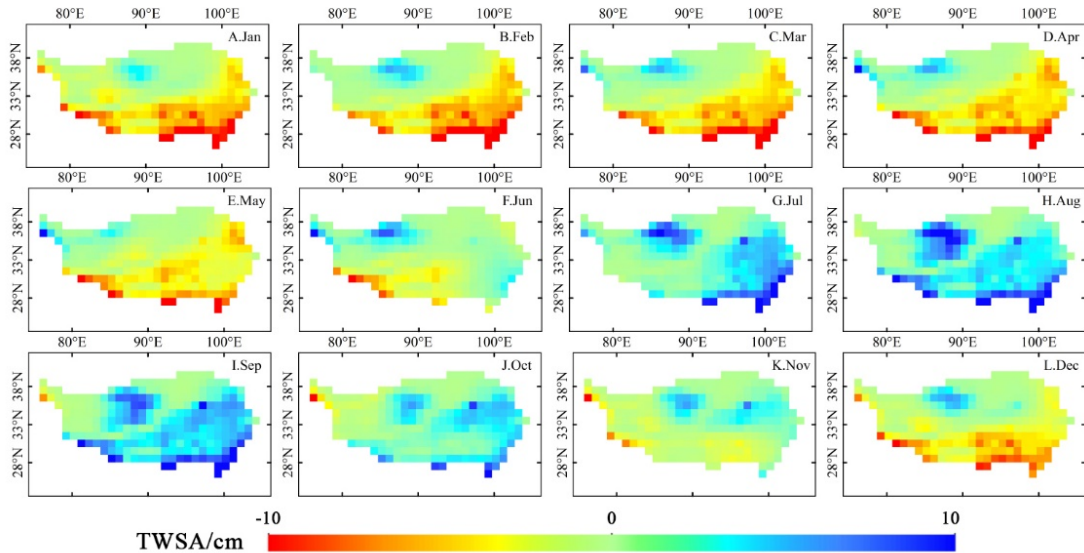
Fig.2. Spatial distribution of monthly average TWSA in the Tibetan Plateau during 2003-2015

The TWSA in vast majority of the Tibetan Plateau shows a substantial surplus, and the maximum appears in the southeast reached 16 cm. From October to December, the rainy season is completely over, with no precipitation supplement, and because of the steep mountains in southern region, the surface water runs off rapidly, which makes the TWSA significantly reduce even reaching -8 cm.
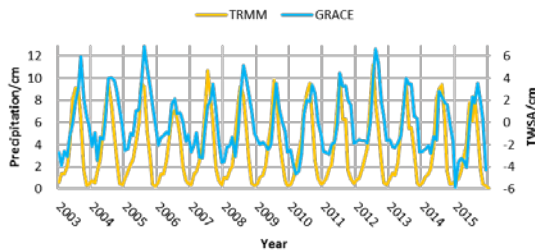
Fig.3. Temporal comparison between monthly precipitation and TWSA

Fig.3 illustrated a temporal comparison between monthly precipitation from TRMM and GRACE-derived TWSA. It indicated that the yearly TWSA had been undergoing a continuous decreasing trend with significant seasonal fluctuation for the entire study region during 2003-2015, with the change rate estimated to be about -0.87 cm/yr (2.187×10^{10} m^3/yr). Also, it could be found that peak value and valley value of TWSA had a good consistency with precipitation, which indicated that the seasonal variation of TWSA in the Tibetan Plateau was in line with the seasonal regularity of precipitation. After applying regression model to the time series of TWSA and precipitation as shown in Table 1, we found there was an average time lag of approximately 26.7 days between precipitation and TWSA, suggesting that it took about one months until a temporal gravity observation could detect a precipitation event. This phenomenon was mainly caused by soil interception, as well as regulation and storage of lake and groundwater (Xu et al., 2013).

Table 1. Annual initial phase, amplitude and period of precipitation and TWSA in the Tibetan Plateau (Formula and variable names are shown in Equation (3))

Production	Initial Phase (φ/d)	Amplitude (A/cm)	Period (T/d)
Precipitation	194.80	4.06	365.02
TWSA	221.5	3.14	364.80

As shown in Fig.4, the spatial distribution of correlation coefficients between monthly precipitation and one-month-delay TWSA presented the relative higher values compared with other combinations, which indicated the existence of the time lag.
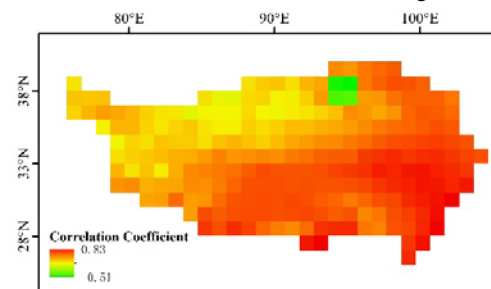
Fig.4. Spatial correlation between monthly precipitation and one-month-delay TWSA

Meanwhile, TWSA changes in the north of the Tibetan Plateau were especially different from the other regions both in spatiotemporal distribution and variation trend, while there was nothing special in precipitation, thus it showed a negative correlation. The correlation coefficient between TWS and precipitation in the Tibetan Plateau presented a declining trend from southeast to northwest. In most regions, the correlation coefficients were greater than 0.5 and the maximum reached 0.83, while Qaidam Basin, in the northern Tibetan Plateau, showed a significant negative correlation with the value of -0.51. The main reason for this spatial distribution was that the precipitation was abundant in the southeastern region, which led to the variations of TWS. Perennial little rain in the Qaidam Basin, and because of terrain factors, long sunshine time, strong evaporation (Su et al., 2015), rapid loss of water storage, so that the TWS and precipitation were negatively correlated in this area.

Furthermore, by calculating the monthly average of TWS, precipitation, NDVI in the Tibetan Plateau, the comparisons between them were shown in Fig.5. From Fig.5A and Fig.5B, it can be found that both TWSA and precipitation had a pretty high correlation with NDVI ($R^2 = 0.66$ and $R^2 = 0.79$, respectively), which confirmed that the growth pattern of vegetation was closely related to the distribution of precipitation and TWSA over the Tibetan Plateau. Compared with TWSA, precipitation had a relative higher correlation to NDVI. The analysis results indicated that precipitation had the most direct impact on NDVI in the Tibetan Plateau, which meant that plants were more likely to obtain water directly from precipitation. While soil moisture, surface and groundwater, *etc.* were not the main factors of vegetation growth. Additionally, the highest correlation coefficient of 0.93 between precipitation and one-month-delay NDVI in Fig.5C indicated that the vegetation growth had a lag effect of 1 month to precipitation, due to the infiltration of precipitation through the soil, plant roots absorption process.

5 CONCLUSIONS

This study analyzed the variations of TWSA both in the spatial and temporal scale over the Tibetan Plateau, and compared the spatiotemporal relation among TWSA, precipitation and NDVI by using a least square regression model and Pearson correlation coefficient. Results showed that the TWSA in the northwestern part of the Tibetan Plateau was almost in the stable state near to zero for the study period, while in the southeastern region the TWSA reacted to extreme losses in the dry season and surpluses in the rainy season. Meanwhile, it indicated that a continuous decreasing trend in the yearly TWSA with significant seasonal fluctuation over the study region, with the change rate of approximately

-0.87 cm/yr (2.187×10^{10} m^3/yr).

In addition, we found there was an average time lag of about 26.7 days between precipitation and TWSA. The correlation coefficients between TWSA and precipitation showed a declining trend from southeast to northwest, with correlation coefficients in most regions were greater than 0.5 and the maximum reached 0.83.

Furthermore, it could be found that both TWSA and precipitation had a pretty high correlation with NDVI ($R^2 = 0.66$ and $R^2 = 0.79$, respectively), and the vegetation growth had a lag effect of 1 month to precipitation. In order to further reveal the interrelationship between water cycle and carbon cycle in the Tibetan Plateau, more statistical methods and more datasets should be used to analyze in future work.
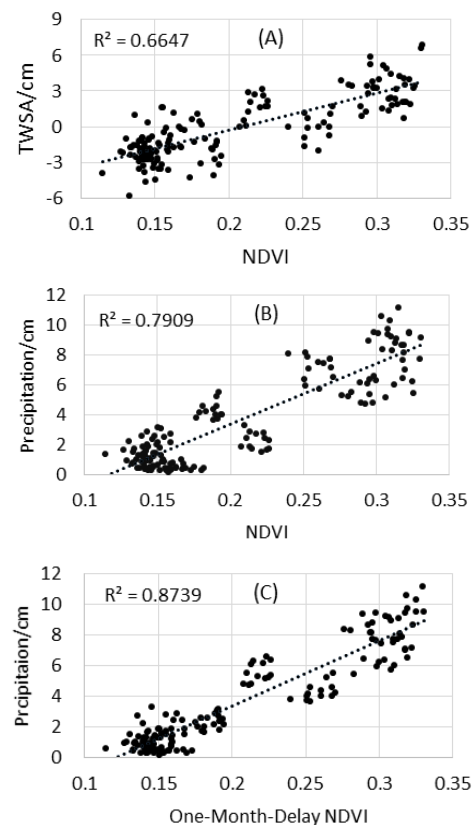
Fig.5. Comparisons between monthly NDVI and precipitation, TWSA in Tibetan Plateau. A-C represented the comparison of TWS and NDVI, precipitation and NDVI, precipitation and one-month-delay-NDVI, respectively.

REFERENCES

Chen, J. L., Wilson, C. R., Tapley, B. D., Yang, Z. L., & Niu, G. Y., 2009, 2005 drought event in the Amazon River basin as measured by GRACE and estimated by climate models. *Journal of Geophysical Research Solid Earth, 114*(B5), B05404.

Rieser, D., Kuhn, M., Pail, R., Anjasmara, I. M., & Awange, J., 2010, Relation between GRACE-derived surface mass variations and precipitation over Australia. *Australian Journal of Earth Sciences, 57*(7), 887-900.

Tapley, B. D., Bettadpur, S., Watkins, M., & Reigber, C., 2004, The gravity recovery and climate experiment: Mission overview and early results. *Geophysical Research Letters, 31*(9), 4 PP.

Hu, X. G., Chen, J., Zhou, Y., Cheng, H., & Liao, X., 2006, Seasonal water storage change of the Yangtze River basin detected by GRACE. *Science in China: Earth Science, 49*(5), 483-491.

Rodell, M., Velicogna, I., & Famiglietti, J. S., 2009, Satellite-based estimates of groundwater depletion in India. *Nature, 460*(7258), 999-1002.

Seyoum, W. M., & Milewski, A. M., 2016, Monitoring and comparison of terrestrial water storage changes in the northern high plains using GRACE and in-situ based integrated hydrologic model estimates. *Advances in Water Resources, 94*, 31-44.

Xu, M., Ye, B. S., & Zhao, Q., 2013, Temporal and spatial pattern of water storage changes over the yangtz river basin during 2002-2010 based on grace satellite data. *Progress in Geography*, 32(1), 68-77.

Swenson, S., & Wahr, J., 2006, Post‐processing removal of correlated errors in GRACE data. *Geophysical Research Letters, 33*(8), 2006.

Cheng, M., Ries, J. C., & Tapley, B. D., 2015, Variations of the Earth's figure axis from satellite laser ranging and GRACE. *Journal of Geophysical Research Solid Earth, 116*(B1).

Swenson, S., Chambers, D., & Wahr, J., 2008, Estimating geocenter variations from a combination of GRACE and ocean model output. *Journal of Geophysical Research Atmospheres, 113*(B8), 194-205.

Geruo, A., Wahr, J., & Zhong, S., 2013, Computations of the viscoelastic response of a 3-D compressible Earth to surface loading: an application to Glacial Isostatic Adjustment in Antarctica and Canada. *Geophysical Journal International, 192*(2), 557-572.

Landerer, F. W., & Swenson, S. C., 2012, Accuracy of scaled GRACE terrestrial water storage estimates. *Water Resources Research, 48*(4), 4531.

Xu, P. K., & Zhang, W. C., 2013, Inversion of terrestrial water storage changes in recent years for qinghai-tibetan plateau and yarlung zangbo river basin by grace. *Journal of Water Resources & Water Engineering*, 24(1), 23-29.

Su, Z. X., 2015, Estimating Water Storage Variations in Qaidam Basin Using GRACE Data. (Master Thesis) *China University of Geosciences (Beijing)*, Beijing, China.

Integrating different satellite-based models to improve global terrestrial evapotranspiration with a generalized regression neural network

Meng Liu[1,2], Rong-Lin Tang[1,2*], Zhao-Liang Li[1,2,3], YunJun Yao[4], Guangjian Yan[4]

1. State Key Laboratory of Resources and Environment Information System, Institute of Geographic Sciences and Natural Resources Research, Chinese Academy of Sciences, Beijing 100101, China;
2. University of Chinese Academy of Sciences, Beijing 100049, China;
3. Key Laboratory of Agri-informatics, Ministry of Agriculture/Institute of Agricultural Resources and Regional Planning, Chinese Academy of Agricultural Sciences, Beijing 100081, China;
4. State Key Laboratory of Remote Sensing Science, School of Geography, Beijing Normal University, Beijing 100875, China;

*Authors to whom correspondence should be addressed: trl_wd@163.com

ABSTRACT - *Combining surface evaporation and plant transpiration, evapotranspiration is critical to surface water and heat balance as it links water, carbon cycles and energy exchange. Lots of ET models have been developed to estimate global terrestrial evapotranspiration at present. An existing problem is that there are large model uncertainties among different models. In this study, a generalized regression neural network method was used to integrate five global satellite-based models (MOD16, RRS-PM, PT-JPL, MS-PT and Semi-empirical model) to improve the accuracy of global ET estimates for nine different vegetation types. Compared to individual satellite-based models, the integrated model with a generalized regression neural network produced significantly decreased bias (less than 2 W/m^2) and root-mean-square error (the maximum of the decrease could reach almost 37 W/m^2) for the validation. The integrated model probably could explain 53%-73% of the land surface ET change at 242 eddy covariance global flux sites and it had an improved performance for global ET estimation over long-time series.*

1 INTRODUCTION

As the main process parameter of water and energy exchange in hydrosphere, atmosphere and biosphere, evapotranspiration (ET) is defined as the water being converted from liquid to gaseous and from land surface to atmosphere, which combines the coinstantaneous surface evaporation and plant transpiration (Allen et al., 1998; Li et al., 2009; Wang and Dickinson, 2012). Nowadays, lots of studies have been developed on evapotranspiration models and showed that different models have large uncertainties (Chen et al., 2014; Chen et al., 2015; Yao et al., 2014). In this study, a generalized regression neural network method was used to integrate five global satellite-based models (MOD16, RRS-PM, PT-JPL, MS-PT and Semi-empirical model) to improve the accuracy of global ET estimates for nine different vegetation types.

2 DATA SOURCES AND METHODS

2.1 Data

In this paper, observational data from 242 global flux tower sites, MODIS NDVI (MOD13A2, 16-day, spatial resolution 1km) and MODIS LAI (MOD15A2, 8-day, spatial resolution 1km) during 2000 to 2009,

were used to estimate land surface ET at global flux tower sites for different satellite-based models. The observational data included daily air temperature, maximum air temperature, minimum air temperature, solar radiation, surface net radiation, soil heat flux, vapor pressure, relative humidity, wind speed, sensible heat flux and ET. These global sites included nine different vegetation covers: cropland (CRO, 35 sites), deciduous broadleaf forest (DBF, 28 sites), deciduous needleleaf forest (DNF, 4 sites), evergreen broadleaf forest (EBF, 19 sites), evergreen needleleaf forest (ENF, 62 sites), mixed forest (MF, 11 sites), grass and other types (GRA, 57 sites), shrubland (SHR, 17 sites) and savanna (SAW, 9 sites). The ground-measured flux data, where eddy covariance (ECOR) methods are used to measure the exchanges of energy between terrestrial ecosystems and the atmosphere, were used to validated and evaluated the results.

2.2 Methods

At present, scholars have carried out a serious of researches about evapotranspiration models, products and regional application. According to the precious researches, most traditional evapotranspiration algorithms were based on physical models such as one

source or two source models (Wang and Dickinson, 2012), Penman-Monteith approach (Penman, 1948; Monteith, 1965), Priestley-Taylor approach (Priestley and Taylor, 1972) and so on. For these approaches, many physical parameters were required and calibrations were generally needed in different regions.

The MOD16 model was developed based on the Penman-Monteith equation by Mu et al. in 2011. The total ET is the sum of interception evaporation (ET_i), canopy transpiration (ET_c) and soil evaporation (ET_s) (Mu et al., 2011). The soil evaporation conclude and unsaturated soil evaporation and saturated wet soil evaporation. The model was a modified version of the model published in 2007 by Mu et al. (Mu et al., 2007).

The RRS-PM model was developed by Yuan et al. in 2010. It is also developed based on the Penman-Monteith equation. Based on the model published in 2007 by Mu et al., Yuan et al. revised the algorithm parameters, improved calculation of the vegetation cover fraction by using EVI, and modified the air temperature constraint for vegetation conductance (Yuan et al., 2010).

The PT-JPL model was developed based on the Priestley and Taylor equation by Fisher et al. in 2008. The total ET is the sum of interception evaporation (ET_i), canopy transpiration (ET_c) and soil evaporation (ET_s). Both atmospheric moisture (RH and VPD) and eco-physiological constraints (FPAR and LAI) were introduced in the model without using any ground-based observed data (Fisher et al., 2008).

The MS-PT model which based on the Priestley and Taylor equation was developed by Yao et al. in 2013. It estimates ET from four components: saturated wet soil evaporation, unsaturated wet soil evaporation, vegetation transpiration, and evaporation from vegetation interception. In the model, the surface soil moisture constraints were parameterized by using the apparent thermal inertia derived from DT and vegetation transpiration was estimated by the N95 model. By reducing the atmospheric inputs of PT-JPL algorithm, the revised model inputs only contains Rn, air temperature, DT, and NDVI (Yao et al., 2013).

The Semi-empirical model (UMD) was developed by Wang et al. (Wang et al., 2010). To solve the problem that there is no method can monitor trends of the surface latent heat flux for decades, the semi-empirical algorithm was developed to estimate global ET on a multi-decadal time scale, which adds empirical coefficients to the Penman equation and uses wind speed to calculate aerodynamics impedance. By using shortwave radiation, temperature, wind speed, water vapor pressure deficit, relative humidity deficit and satellite derived NDVI, ET were estimated over

global scale. This model works well in different climate conditions.

Generalized regression neural networks (GRNNs), which is the generalization of probabilistic neural networks and radial basis function networks, were proposed by Specht in 1991 (Specht, 1991). The advantage of GRNNs is that they can approximate the surfaces inherent in arbitrary sample datasets, and have special properties that "these networks do not require iterative training to calculate estimates directly from training data". At present, GRNNs have been widely used in many fields such as adaptive control, system identification, time series prediction and pattern recognition (Leung et al., 2000; Xiao et al., 2009; Xiao et al., 2012). The network structure and weight of GRNNs are determined by the input parameters of GRNNs. The only free parameter is its smoothing parameter σ. Therefore, the training of GRNNs is to determine the optimal solution of the smoothing parameter σ.

3 RESULTS AND DISCUSSION

The GRNNs integrated results underestimated ET for all types. For CRO, the results of the RRS-PM were the worst, and the results of the two PT-based models were significantly better than the results of the two PM-based models. All individual models underestimate ET. For DBF, the results of different models were similar. The results of the two PM-based models were not as good as the results of the two PT-based models. The two PM-based underestimated ET, while the two PT-based models and the semi-empirical model overestimated ET. For DNF, the results of the semi-empirical model were worse with the largest bias and RMSE and the highest R^2. For EBF, the results of the two PM-based models were better than those two PT-based models. For ENF, the results of the MS-PT model were better with smaller bias and RMSE. For GRA, the results of the UMD model were the best. The results of the two PT-based models were significantly better than those of the two PM-based models. The PT-JPL model and UMD model overestimated ET while other three models underestimated ET. For MF，the MS-PT model had the smallest RMSE, the MOD16 model had the smallest bias, and the UMD model had the highest R^2. For SAW, the results of the RRS-PM model were worse with larger bias and RMSE. The MOD16 had the smallest bias and the largest RMSE. For SHR, the results of the UMD model were the best. Except RRS-PM underestimated ET, other models all overestimated ET.
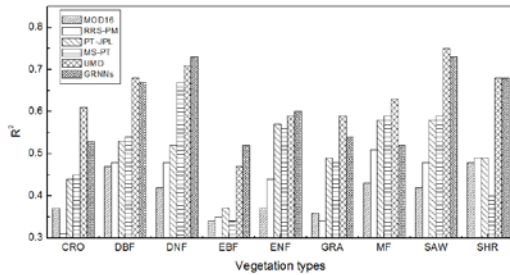
Fig. 1 The R^2 of estimated ET of six models and ground-measured ET for different vegetation types.
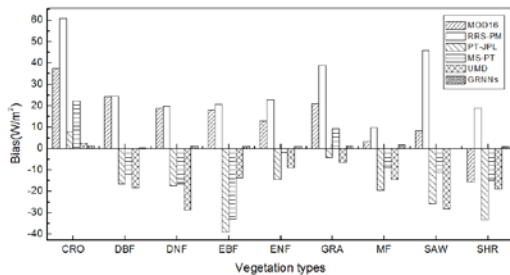
Fig. 2 The averaged biases of ground-measured ET versus estimated ET of six models for different vegetation types.
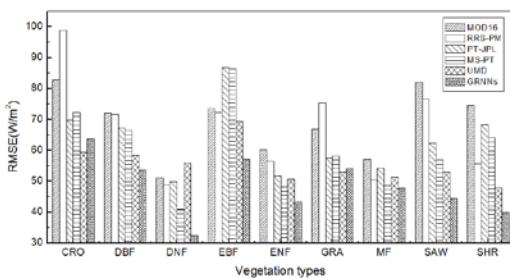
Fig. 3 The averaged RMSEs of estimated ET of six models for different vegetation types.

In general, for individual models, the R^2 of UMD were the best. Except EBF, R^2 of other types of UMD were greater than 0.5. Through integrating by GRNNs, R^2 were all greater than 0.5 for all nine types. For CRO, DBF, GRA and SAW, the R^2 of the integrated ET were worse than the UMD model, but better than other four methods. For MF, the R^2 of the integrated ET was worse than the two PT-based models and the UMD model. For most types, the results of the two PT-based models were better than those of the two PM-based models. The bias of the integrated ET were all below 2W/m^2. Except CRO and GRA, the RMSEs of the integrated ET by GRNNs performed better than

the individual models. For CRO and GRA, the RMSEs of the integrated ET were a little greater than that of the UMD model. Through integrating, the estimated ET were significantly improved on the whole.

4 CONCLUSIONS

For different vegetation types, the integrated results were better than those from the five satellite-based models. Compared to each of the five satellite-based models, the integrated model with a generalized regression neural network produced significantly decreased bias (less than 2 W/m^2) and root-mean-square error (RMSE, the maximum of the decrease could reach almost 37 W/m^2) for the validation. The correlation coefficient in the validation for the integrated model was lower than the best of the single model for five vegetation types. The integrated model probably could explain 53%-73% of the land surface ET change at 242 eddy covariance global flux sites and on the whole it had an improved performance for global ET estimation over long-time series.

REFERENCES

Allen, R. G., Pereira, L. S., Raes, D., and Smith, M., 1998, Crop evapotranspiration-Guidelines for computing crop water requirements. FAO Irrigation and drainage paper 56, FAO, Rome.

Chen, Y., Xia, J., Liang, S., et al., 2014, Comparison of satellite-based evapotranspiration models over terrestrial ecosystems in China. *Remote Sensing of Environment*, 140, 279-293.

Chen, Y., Yuan, W., Xia, J., et al, 2015, Using Bayesian model averaging to estimate terrestrial evapotranspiration in China. *Journal of Hydrology*, 528, 537-549.

Fisher, J. B., Tu, K. P., Baldocchi, D. D., 2008, Global estimates of the land-atmosphere water flux based on monthly AVHRR and ISLSCP-II data, validated at 16 FLUXNET sites. *Remote Sensing of Environment*, 112(3): 901-919.

Leung, M. T., Chen, A. S., Daouk, H., 2000, Forecasting exchange rates using general regression neural networks. *Computers & Operations Research*, 27(11): 1093-1110.

Li, Z.-L., Tang, R. L., Wan, Z., Bi, Y., Zhou, C., Tang, B. H., Yan, G. J., and Zhang, X., 2009, A Review of Current Methodologies for Regional Evapotranspiration Estimation from Remotely Sensed Data. *Sensors*, 9, 3801-3853.

Monteith, J. L., 1965, Evaporation and environment. Symposia of the Society for Experimental Biology, 19(19), 205-234.

Mu, Q., Heinsch, F. A., Zhao, M., et al., 2007, Development of a global evapotranspiration algorithm based on MODIS and global

meteorology data. *Remote Sensing of Environment*, 111(4): 519-536.

Mu, Q., Zhao, M., and Running, S. W., 2011, Improvements to a MODIS global terrestrial evapotranspiration algorithm. *Remote Sensing of Environment*, 115, 1781-1800.

Penman, H. L., 1948, Natural evaporation from open water, bare soil and grass. Proceedings of the Royal Society of London A: Mathematical, Physical and Engineering Sciences. The Royal Society, 193(1032): 120-145.

Priestley, C. H. B., Taylor, R. J., 1972, On the assessment of surface heat flux and evaporation using large-scale parameters. *Monthly weather review*, 100(2): 81-92.

Specht D. F., 1991, A general regression neural network. *Neural Networks*, *IEEE Transactions on,* 2(6): 568-576.

Wang, K., Dickinson, R. E., Wild, M., et al, 2010, Evidence for decadal variation in global terrestrial evapotranspiration between 1982 and 2002: 1. Model development. *Journal of Geophysical Research: Atmospheres (1984–2012)*, 115, D20112.

Wang, K., and Dickinson, R. E., 2012, A review of global terrestrial evapotranspiration: Observation, modeling, climatology, and climatic variability. *Reviews of Geophysics*, RG2005, 50(2), 1-54.

Xiao, Z., Liang, S., Wang, J., et al., 2009, A temporally integrated inversion method for estimating leaf area index from MODIS data. *Geoscience and Remote Sensing, IEEE Transactions on*, 47(8): 2536-2545.

Xiao, Z., Wang, J., Liang, S., et al, 2012, Variational retrieval of leaf area index from MODIS time series data: examples from the Heihe river basin, north-west China. *International journal of remote sensing*, 33(3): 730-745.

Yao, Y. J., Liang, S. L., Cheng, J., Liu, S., Fisher, J. B., and Zhang X., et al., 2013, MODIS-driven estimation of terrestrial latent heat flux in China based on a modified Priestley–Taylor algorithm. *Agricultural and Forest Meteorology*, 171, 187-202.

Yao, Y., Liang, S., Li, X., Hong, Y., Fisher, J. B., Zhang, N., et al., 2014, Bayesian multi-model estimation of global terrestrial latent heat flux from eddy covariance, meteorological, and satellite observations. *Journal of Geophysical Research: Atmospheres*, 119(8), 4521-4545.

Yuan, W. P., Liu, S., Yu, G, Bonnefond, J. -M., Chen, J., Davis, K., et al., 2010, Global estimates of evapotranspiration and gross primary production based on MODIS and global meteorology data. *Remote Sensing of Environment*, 114, 1416-1431.

Ten-day gross primary production (GPP) using SEVIRI/MSG data in the framework of LSA SAF project

B. Martínez, S. Sánchez-Ruiz, M. Campos-Taberner, F.J. García-Haro, M.A. Gilabert
Departament de Física de la Terra i Termodinàmica, Facultat de Fisica, Universitat de València. Dr. Moliner, 50, 46100-Burjassot (España).
e-mail: beatriz.martinez@uv.es

ABSTRACT- *The main goal of this paper is to provide a ten-day GPP product from MSG/SEVIRI data in the framework of the EUMETSAT/LSA SAF project. The proposed algorithm to derive GPP from MSG/SEVIRI relies on the Monteith approach, which is driven by the flux density of photosynthetically active radiation (PAR), the fractional absorption of that flux (f_{APAR}) and the light-use efficiency (ε), through the assimilation of the LSA SAF products. ε is operationally parameterized as a function of a maximum value ($ε_{max}$) and a factor (C_{ws}), which accounts for the reduction of photosynthetic activity in case of short-term water stress. The C_{ws} uses the daily actual evapotranspiration (DMET, LSA-302) and the reference evapotranspiration (DMETREF, LSA-303) LSA SAF products. A quality assessment of the MSG GPP product is carried out by means of a site-level comparison using GPP estimates from FLUXNET La Thuile synthesis eddy covariance (EC) data. Moreover, an inter-comparison with other satellite similar derived products, such as MODIS GPP (MOD17A2) and FLUXCOM GPP products is achieved. Results have shown as the intra-annual variability at the EC fluxes towers has been well reproduced by the MSG GPP estimates, particularly over the dry season where more influence on the canopy due to water stress is expected. The comparison at regional scale has indicated similar discrepancies between MSG-MODIS and MSG-FLUXCOM products that those derived between MODIS-FLUXCOM.*

1 INTRODUCTION

The main goal of this paper is to provide a ten-day gross primary production (GPP) product over Europe and Africa from the integration of SEVIRI/MSG products in the framework of the EUMETSAT/LSA SAF (http://lsa-saf.eumetsat.int) for 2012.

GPP from SEVIRI data is estimated using Monteith's light use efficiency (LUE) concept (Monteith, 1972). This concept provides the theoretical basis for most models of GPP relying on optical remote sensing and considers GPP as proportional to the incoming photosynthetically active radiation (PAR), the fractional absorption of that flux (f_{APAR}) and the light-use efficiency (ε). The accuracy of the GPP products based on the proposed approach is highly dependent on the f_{APAR}, and the down-welling surface shortwave radiation flux (Gilabert et al., 2015). One of the major source of uncertainty in the GPP model is LUE parameter (ε) since it depends on meteorological data (also through the use of some variables such as evapotranspiration, precipitation, etc., which are needed to account for the reduction in efficiency due to water stress). Since water availability and radiation are known as main potential climatic constraints to vegetation productivity in many areas of Europe and Africa, special attention is paid to capture the GPP response under dry conditions by controlling the water shortage limitations.

2 METHODS

To derive the ten-day MSG/GPP estimates, first the gross primary production on a daily basis is computed as:

$$\text{GPP} = \varepsilon_{\max} C_{\text{ws}} f_{\text{APAR}} \text{PAR} \qquad (1)$$

where daily down-welling surface shortwave radiation flux (DIDSSF) MSG product (LSA-201) is used to derive the PAR (i.e., 0.46DIDSSF (Iqbal, 1983)) and the daily f_{APAR} (MDFAPAR) (LSA- 407). Second, ε is operationally parameterized as a function of a maximum value ($ε_{max}$), which is downregulated by an estimator related with water stress (C_{ws}). Overall, optimized $ε_{max}$ values can range between 0.55–3.5 g MJ^{-1} (Garbulsky et al., 2010). Three values have been assigned to the main ecosystems types: a value of 1.8 g MJ^{-1} is given to deciduous broadleaf forest (DBF), 1.5 g MJ^{-1} to evergreen needleleaf forest (ENF) and 1.2 g MJ^{-1} to remaining ecosystems types (Garbulsky et al., 2010). GPP was not computed for desert areas.

The water stress factor (C_{ws}) is parameterized as a simplified local water budget proposed by (Maselli et al., 2009) for Mediterranean ecosystems and applied satisfactorily over Spain (Gilabert et al., 2015). C_{ws} accounts for the limited photosynthetic activity in case of short-term water stress based on actual (AET) and

potential (PET) evapotranspiration, both cumulated over a two-month period for forests and shrublands, and one-month period for grasslands. A variant of this parameterization is proposed in the MSG GPP algorithm as follows:

$$C_{ws} = 0.6 + 0.4 \frac{AET}{ET0} \qquad (2)$$

where ET0 is the reference evapotranspiration. C_{ws} can vary between 0.6 (when short-term water shortage reduces photosynthesis to 60% of its potential value) and 1 (when there is no such reduction, as it occurs in irrigated crops).

The ten-day MSG/GPP estimates are calculated by averaging the 10 subsequent and consecutive daily GPP observations. All daily observations are considered in the averaging except those with poor quality. The 10-day estimates are only computed when there is a minimum of three daily GPP data.

3 MATERIALS

3.1 PAR

PAR is the photosynthetically active radiation in the 0.4–0.7 µm spectral range and is computed as the 46% of daily irradiation (Iqbal, 1983). Daily irradiation images for Europe and Africa are provided from the daily down-welling radiation flux (DIDSSF) MSG product (LSA-201) at 3.1 km spatial resolution (sub-satellite point) for the year 2012. It essentially depends on the solar zenith angle, on cloud coverage and, to a lesser extent, on atmospheric absorption and surface albedo (LSA SAF, 2012).

The MSG DIDSSF product is computed by integrating the downward surface solar flux (DSSF) product every 30 minutes over a whole day. The validation results of DSSF using *in situ* data from six European ground measurement stations (Geiger et al., 2008) throughout two years showed a difference between instantaneous satellite estimates and ground measurements of about 40 and 110 W m^{-2} for clear and cloudy sky conditions, respectively. A more thorough validation of the MSG DSSF product was carried out in Spain (Moreno et al., 2013). The resulting statistics from this validation showed a bias of -0.12 MJ m^{-2} (rMBD of about 1%) and a mean absolute difference of 1.0 MJ m^{-2} (rMAD of 6%) in terms of daily global irradiation.

3.2. f_{APAR}

f_{APAR} is the fraction of PAR that is absorbed by leaves and provides a link between the canopy function, i.e. its energy absorption capacity, and its structure and condition. The MSG f_{APAR} product (MDFAPAR, LSA-407) delivered by the LSA SAF network was used as input. It has a 3.1 km spatial resolution (sub-satellite point) and daily frequency over the geostationary MSG grid (García-Haro et al., 2015). The MDFAPAR product is based on a linear relationship between the Renormalized Difference Vegetation Index (RDVI), computed from clear-sky top of the canopy reflectances in the red (R_R) and near infrared (R_{NIR}) bands for an optimal angular geometry in the solar principal plane. Observed deviations between MSG f_{APAR} and other f_{APAR} products were in the order of about 0.1 for f_{APAR} (García-Haro et al., 2015).

In this study, the f_{APAR} time series are filtered and reconstructed using an optimized LOESS method (Moreno et al., 2014; Gilabert et al., 2015).

3.3 C_{ws}

The daily C_{ws} is computed using the daily actual evapotranspiration LSA SAF product (DMET, LSA-302) and the reference evapotranspiration (ET0). The latter corresponds to the evapotranspiration from a clearly defined reference surface and is also provided by the LSA SAF (DMETREF, LSA-303), using an algorithm based on fundamental physical principles as close to the Food and Agricultural Organization of the United Nations (FAO) reference surface as possible. ET0 estimates depend on the daily short-wave radiation at the surface derived from MSG/SEVIRI by the LSA SAF (DIDSSF, LSA-203). The C_{ws} parameterization based on the assimilation of different MSG/SEVIRI products, enhances synergy and the internal consistency of the family of products.

4 RESULTS

The performance of the resulting ten-day GPP estimates is assessed by site-level comparisons using GPP estimates from eddy covariance (EC) towers and a consistency analysis against alternative GPP products available from independent remote sensing global data, such as MODIS GPP (MOD17A2) and global flux fields from the Max Planck Institute (MPI) (FLUXCOM products).

4.1 Direct comparison with *in situ* GPP estimates.

Daily GPP data from 18 EC flux towers were downloaded from the global Fluxes Database Cluster data set (FLUXNET). The purity of a 5 km × 5 km pixel using the 1 km Global Land Cover 2000 (GLC2000) to select adequate sites for comparing MSG GPP and EC estimates without bias due to surface spatial heterogeneity was analyzed. Then, sites presenting one landcover fraction greater than 80% were directly selected, while the rest were assessed visually using Google earth tool (Table 1).

Table 1. Statistics of the MSG GPP direct comparison between MSG GPP and GPP EC. The mean bias error (MBE), mean absolute error (MAE) and root mean square error (RMSE) are given in g m^{-2} day^{-1}, and their relative values (rMBE, rMAE and rRMSE) in %. The correlation coefficient (r) is also shown.

SITE ID	MBE (rMBE)	MAE (rMAE)	RMSE (rRMSE)	r
CZ-BK1	−1.3 (−27)	1.8 (38)	2.5 (52)	0.84
DE-SfN	0.002 (0.1)	1.4 (40)	1.9 (51)	0.78
FI-Let	−2.5 (−32)	2.7 (34)	3.2 (40)	0.78
FI-Hyy	−1.8 (−25)	2.2 (30)	2.6 (37)	0.74
FI-Sod	2.2 (44)	2.3 (46)	2.9 (60)	0.74
IT-Lav	−2.6 (−38)	2.7 (39)	3.6 (53)	0.85
DE-Hai	−1.2 (−26)	2.2 (49)	3.1 (69)	0.82
DE-Lnf	−1.8 (−36)	3.0 (60)	4.3 (86)	0.71
IT-Col	−0.4 (−9)	1.6 (37)	2.1 (48)	0.92
DK-Sor	−2.8 (−46)	3.1 (51)	4.5 (74)	0.89
BE-Vie	−1.5 (−25)	2.2 (36)	2.9 (47)	0.75
FR-Pue	0.8 (23)	1.5 (45)	2.1 (61)	0.69
DE-Gri	−0.4 (−9)	1.8 (38)	2.5 (52)	0.81
IT-MBo	−0.7 (−16)	1.7 (39)	2.5 (57)	0.87
SN-Dhr	−0.9 (−38)	1.2 (47)	2.2 (86)	0.91
ES-LMa	−0.04 (−2)	1.0 (47)	1.2 (55)	0.56
ZA-Kru	−0.9 (−22)	1.4 (36)	2.0 (52)	0.77
DE-Geb	0.4 (18)	1.5 (64)	2.4 (99)	0.63

The RS GPP products generally present similar pattern. For ENF, one of the most productive vegetation types considered in the present study (CZ-BK1, DE-SfN, FI-Let, FI-Hyy, FI-Sod, IT-Lav), a mean bias error (MBE) lower than 40% is observed in most of the towers (Table 1) with a very good agreement between MSG GPP and EC GPP values (r>0.7). A lower overall error and bias (RMSE=2.87 g m^{-2} day^{-1} and MBE=−1.17 g m^{-2} day^{-1}) are obtained when considering all ENF sites (Figure 1), observing a better agreement at EC GPP values lower than 7.0 g m^{-2} day^{-1} (distribution close to the one-to-one line). For the DBF flux towers, moderate (r=0.69 for FR-Pue) to very good agreement (r=0.92 for IT-Col) was observed between MSG GPP and EC GPP. The MSG GPP estimates agree with MODIS and FLUXCOM values, but the high EC GPP levels were not reached (e.g. DN-Lnf and Dk-Sor) giving an overall negative bias and RMSE= 3.38 g m^{-2} day^{-1} when all DBF towers were considered. For BE-Vie, DK-Sor, De-Lnf and DE-Hai discrepancies between the GLC2000 and the information provided by the tower (Table 1) were observed. These discrepancies were also presented for the grassland (De-Gri, IT-MBo and SN-Dhr) and the savanna EC towers (ES-LMa, ZA-Kru). For grasslands towers IT-MBo and De-Gri, a good agreement was observed (correlation up to 0.9 for IT-MBo). A higher agreement (RMSE=2.18 g m^{-2} day^{-1}; MBE=-0.57 g m^{-2} day^{-1}) between the MSG GPP and EC GPP estimates is observed when the ENF and DBF towers are excluded (Figure 1c). An overall error of

2.79 g m^{-2} day^{-1} with a bias lower than one between the MSG GPP and EC GPP estimates when considering all sites is obtained.
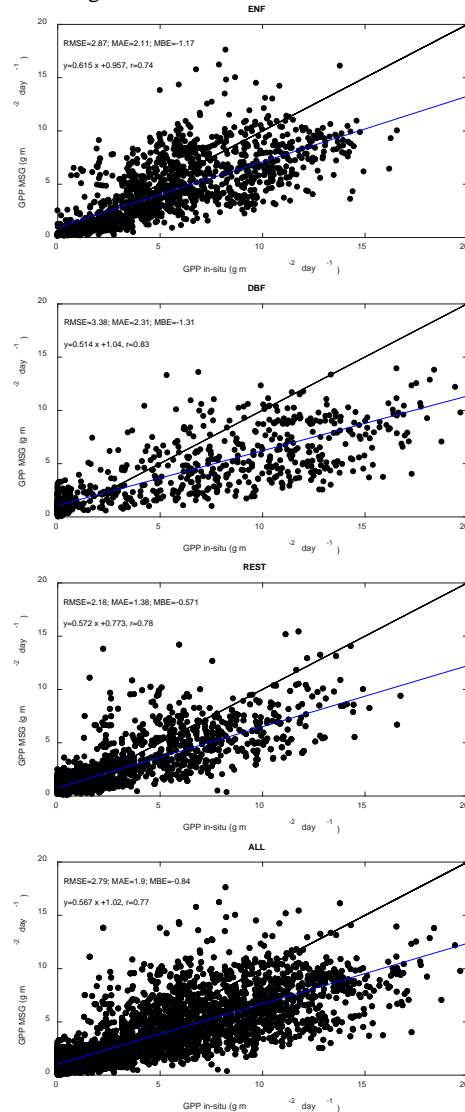
Figure 1. Evaluation of the MSG GPP against *in situ* EC GPP for the sites according to ENF, DBF, rest of land covers and all land covers together. The black lines show the one-to-one ratios, whereas the blue lines are the fitted ordinary least square regression.

4.2 Consistency checking with synergistic global satellite carbon product.

The overall RMSE (Figure 2) over the considered period are computed between the MSG and MODIS and the MSG and FLUXCOM GPP products. The RMSE between MODIS and FLUXCOM GPP values is also computed (bottom Figure 2).
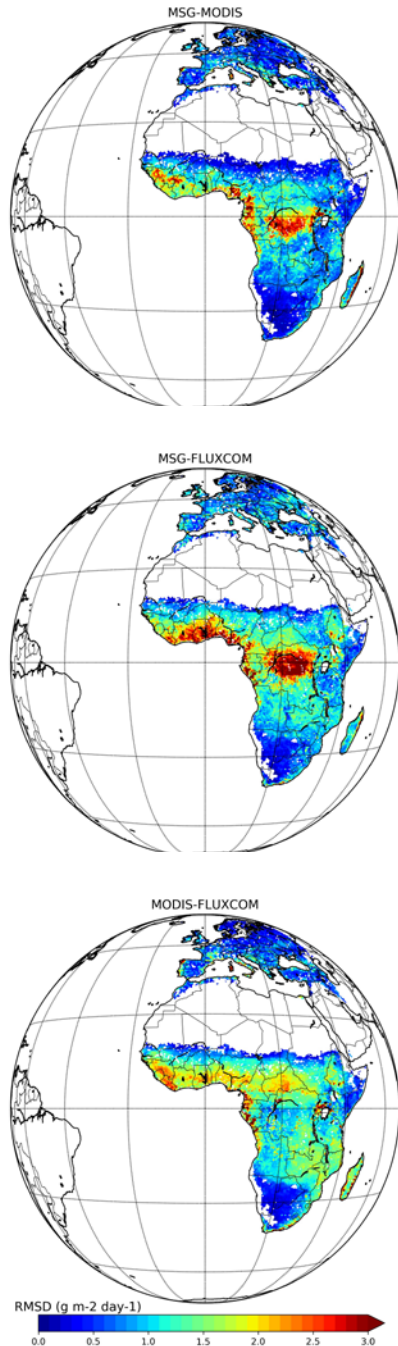
Figure 2. RMSD and MBD (in g m^{-2} day^{-1}) between MSG-MODIS (top), MSG-FLUXCOM (centre) and MODIS-FLUXCOM (bottom).

The results show that the MSG GPP provides RMSE and MBE values regarding the other reference products (MODIS and FLUXCOM) of the same order than those observed between MODIS and FLUXCOM over Europe. The major differences with MSG relies on the GPP estimates over tropical forests in central Africa, with RMSE values up to 3.0 g m^{-2} day^{-1}. Nevertheless, MODIS and FLUXCOM provides higher differences over semi-arid, savanna and transitional woodlands (e.g. RMSE and MBE values up to 2.0 g m^{-2} day^{-1}).

Table 2. Statistics for the inter-comparison of the MSG GPP at 10-day and MODIS with EC GPP data. The MBE and RMSE are in g m^{-2} day^{-1}. The correlation coefficients (r) are presented.

SITE ID		MBE	RMSE	r
CZ-BK1	MSG$_{10day}$	−1.3	2.1	0.91
	MODIS	-1.4	1.9	0.93
DE-SfN	MSG$_{10day}$	− 0.11	1.2	0.86
	MODIS	-0.02	1.9	0.84
FI-Let	MSG$_{10day}$	−2.5	2.9	0.90
	MODIS	-2.4	2.8	0.84
FI-Hyy	MSG$_{10day}$	-1.7	2.3	0.74
	MODIS	-1.7	2.1	0.85
FI-Sod	MSG$_{10day}$	2.2	2.3	0.85
	MODIS	-0.5	0.9	0.89
IT-Lav	MSG$_{10day}$	-2.6	3.4	0.89
	MODIS	-3.0	3.8	0.86
DE-Hai	MSG$_{10day}$	-1.1	2.7	0.87
	MODIS	-1.4	2.8	0.92
DE-Lnf	MSG$_{10day}$	-1.6	4.0	0.75
	MODIS	-2.1	3.8	0.87
IT-Col	MSG$_{10day}$	-0.3	1.8	0.96
	MODIS	-0.3	2.3	0.91
DK-Sor	MSG$_{10day}$	-2.7	4.4	0.93
	MODIS	-3.2	4.6	0.94
BE-Vie	MSG$_{10day}$	-1.5	2.5	0.79
	MODIS	-1.9	2.4	0.91
FR-Pue	MSG$_{10day}$	0.7	1.7	0.75
	MODIS	2.2	3.2	0.75
DE-Gri	MSG$_{10day}$	-0.5	1.9	0.89
	MODIS	-1.5	2.6	0.90
IT-MBo	MSG$_{10day}$	-0.7	2.3	0.91
	MODIS	-0.9	1.7	0.95
SN-Dhr	MSG$_{10day}$	-0.9	2.1	0.93
	MODIS	-1.4	2.8	0.92
ES-LMa	MSG$_{10day}$	-0.1	0.9	0.61
	MODIS	-0.4	1.1	0.54
ZA-Kru	MSG$_{10day}$	-1.0	1.7	0.88
	MODIS	-0.5	1.6	0.89
DE-Geb	MSG$_{10day}$	0.4	1.9	0.71
	MODIS	0.05	1.4	0.84

The MSG GPP provides similar or lower errors than MODIS at nine of the eighteen sites (Table 2). In general, an underestimation is observed for the three RS products, being larger at the most productive DBF and ENF sites, such as DK-Sor, DE-Hai, DE-Lnf and

FI-Let. In general, a good agreement is observed between the MSG GPP and EC GPP estimates when the GPP MSG is re-sampled to 10-day (Figure 3). The computed statistics are in agreement with those derived for the MODIS product. MBE errors lower than 1.0 g m^{-2} day^{-1} are obtained for the grasslands and savannas EC towers. Lowers errors are obtained for the ENF EC sites (CZ-BK1, De-SfN, FI-Let, FI-Sod and IT-LAv) than for the DBF sites (De-Hai, DE-Lnf, IT-Col, DK-Sor, BE-Vie).

The annual spatial patterns for MSG, MODIS, and FLUXCOM GPP (Figure 4) are compared. The three estimates agree reasonably well, although differences are significant in some areas. Specifically, there is a good agreement in Europe and North and South Africa, but MSG GPP is lower than FLUXCOM and MODIS over Central Africa. The largest differences occur in Equatorial areas covered by tropical forest where MODIS and FLUXCOM estimates are around 3500 g m^{-2} yr^{-1}, while annual MSG GPP is below 3000 g m^{-2} yr^{-1}.

Figure 3. Temporal profiles for MODIS, MSG GPP at 10-day and EC GPP (scaled at 10-day).
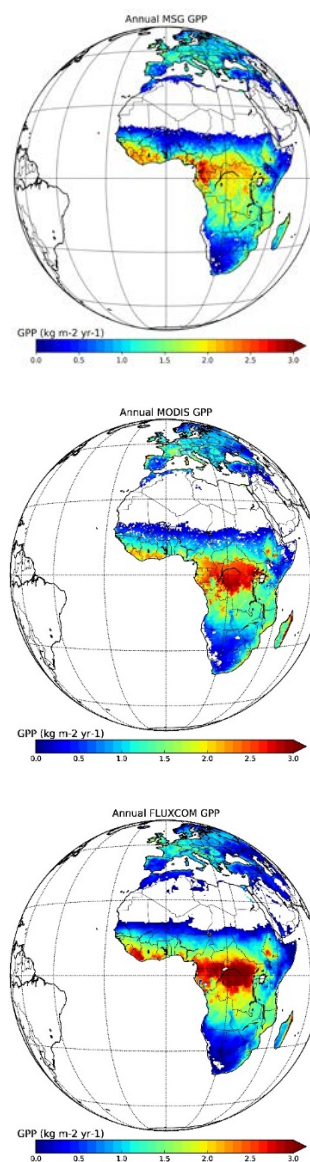
Figure 4. Annual GPP estimates for MSG, MODIS and FLUXCOM.

5 CONCLUSIONS

The resulting GPP product (MSG GPP) was assessed by direct site-level comparison with GPP from eddy covariance data (EC GPP). MSG GPP presented rMBE lower than 40% for the most forest vegetation types with a very good agreement (r>0.7) between EC GPP and MSG GPP. The comparison with MOD17A2 and FLUXCOM has revealed good agreement among products over Europe and North and South Africa.

6 ACKNOWLEDGMENTS

7 REFERENCES

Garbulsky, M.F., et al., 2010. Patterns and controls of the variability of radiation use efficiency and primary productivity across terrestrial ecosystems. *Glob. Ecol. Biogeogr.*, 19, 253–267.

García-Haro, F.J., Camacho, F., Martínez, B., Meliá, J. 2015. Validation Report Vegetation Parameters (VEGA), SAF/LAND/UV/VR_VEGA/2.0.

Geiger, B., Meurey, C., Lajas, D., Franchistéguy, L., Carrer, D., Roujean, J-L. 2008. Near real time provision of downwelling shortwave radiation estimates derived from satellite observations. Meteorological Applications, 2008, 15, 411-420.

Gilabert, M.A., et al., 2015. Daily GPP estimates in Mediterranean ecosystems by combining remote sensing and meteorological data. *ISPRS Journal of Photogrammetry and Remote Sensing*, 102, 184–197.

Iqbal, M., 1983. An Introduction to Solar Radiation. Academic Press, Toronto, 390pp.

LSA SAF. 2012. Algorithm Theoretical Basis Document (ATBD) for Down-welling Surface Shortwave Flux (DSSF). SAF/LAND/MF/A TBD_DSSF/1.0.

LSA SAF. 2016. Algorithm Theoretical Basis Document for Vegetation parameters (VEGA). SAF/LAND/UV/VR_VEGA/2.0.

Maselli, F., Papale, D., Puletti, N., Chirici, G, Corona, P., 2009. Combining remote sensing and ancillary data to monitor the gross productivity of water-limited forest ecosystems. *Remote Sens. Environ.* 113, 657–667.

Monteith, J.L., 1972. Solar radiation and productivity in tropical ecosystems. *J. Appl. Ecol.* 9, 747–766.

Moreno, A., Gilabert, M.A., Camacho, F., Martínez, B. 2013. Validation of daily global solar irradiation images from MSG over Spain. *Renew. Energy*, 60, 332–342.

Moreno, A., García-Haro, F.J., Martínez, B., Gilabert, M.A., 2014. Noise reduction and gap filling of fAPAR series using an adapted local regression filter. *Rem. Sens.* 6, 8238–8260.

Calibration of BIOME-BGC through remote sensing and meteorological ground data for the estimation of net carbon fluxes in Comunitat Valenciana

S. Sanchez-Ruiz[1], M. Chiesi[2], L. Fibbi[2], F. Maselli[2], A. Moreno[3], B. Martinez[1], M. Campos-Taberner[1], F. J. Garcia-Haro[1], A. Carrara[4], M. A. Gilabert[1]

1Departament de Fisica de la Terra i Termodinamica, Facultat de Fisica, Universitat de Valencia, Dr. Moliner, 50. 46100-Burjassot, Spain
2IBIMET-CNR, Via Madonna del Piano, 10. 50019-Sesto Fiorentino, Italy
3Numerical Terradynamic Simulation Group, University of Montana, 59812-Missoula, USA
4Fundacion CEAM, Parc Tecnologic, Charles Robert Darwin, 14. 46980-Paterna, Spain
sergio.sanchez@uv.es

ABSTRACT – *Particular attention must be paid to the estimation of carbon fluxes between biosphere and atmosphere in Mediterranean regions such as Comunitat Valenciana since an increase in the intensity and the duration of droughts has been reported. A production efficiency model (PEM) driven mostly by remotely sensed data was used to estimate monthly gross primary productivity (GPP), GPP_{PEM}, in two sites where eddy covariance (EC) towers were placed (ES-CPa, a shrubland; and ES-ES1, an evergreen needleleaf forest). GPP_{PEM} was validated against GPP from EC sites, GPP_{EC}, (R = 0.93 and RMSE = 15 g m^{-2} month^{-1} in ES-CPa, R = 0.71 and RMSE = 30 g m^{-2} month^{-1} in ES-ES1). Several simulations were performed by the biogeochemical model BIOME-BGC with different effective soil depth (z_e) values and monthly GPP (GPP_{BGC}) and respirations were obtained. GPP_{BGC} series were compared to GPP_{PEM} ones, which were taken as a reference, and the z_e that obtained the minimum RMSE were selected (40 cm and 65 cm respectively for ES-CPa and ES-ES1). Optimized GPP_{BGC} presented a better agreement with GPP_{EC} than default GPP_{BGC} (i.e. with z_e = 100 cm). Finally, optimum BIOME-BGC outputs were used to estimate net ecosystem exchange and it was validated against EC observations (R 0.74 = and RMSE = 16 g m^{-2} month^{-1} in ES-CPa, R = 59 and RMSE = 30 g m^{-2} month^{-1} in ES-ES1).*

1 INTRODUCTION

Vegetation productivity in Mediterranean regions such as Comunitat Valenciana is being affected by the increase in the intensity and the duration of droughts (Kovats et al., 2014). Particular attention to the estimation of carbon fluxes in these regions must therefore be paid.

Gross primary productivity (GPP) has already been estimated by production efficiency models (PEMs) driven by a combination of remote sensing and ground data in this kind of regions (Gilabert et al., 2015; Maselli et al., 2009; Sanchez-Ruiz et al., 2017). However, ecosystems simulation biogeochemical models such as BIOME-BGC (Running and Hunt, 1993; White et al., 2000) are needed for the estimation of net carbon fluxes and have been applied in Mediterranean regions too (Chiesi et al., 2007; Maselli et al., 2009). BIOME-BGC needs a considerably big amount of inputs that can be divided into drivers (meteorological time series and site data) and parameters (ecophysiological data). A particular site physical property that is not usually available at spatially distributed level is the effective soil depth (z_e), that is, the soil depth which plant roots can reach. Water storage depends on z_e and precipitation, which is concentrated in short periods of time in Comunitat Valenciana.

The present study aims at calibrating BIOME-BGC in terms of z_e for the estimation of net carbon fluxes in Comunitat Valenciana. To do this, monthly GPP series for the 2005-2012 period simulated by BIOME-BGC with different z_e are compared to the ones obtained by a PEM driven mostly by remotely sensed data. The latter are taken as a reference and the optimum z_e are selected. Next the optimized BIOME-BGC outputs are used to estimate net ecosystem exchange (NEE). Both GPP and NEE are validated against eddy covariance (EC) data in two sites.

2 STUDY AREA AND SITES DESCRIPTION

Comunitat Valenciana is a Spanish region located in the eastern part of the Iberian Peninsula (between 37.8500 ° and 40.7833 ° in latitude, and -1.5833 ° and 0.5167 ° in longitude). Altitude ranges between 0 m.a.s.l. and 1839 m.a.s.l. with mountains covering

most of its surface. Climate is mostly typical Mediterranean with a NW-SE gradient in air temperature and precipitations concentrated in spring and especially in autumn. During the study period (2005-2012), mean annual air temperature and averaged annual precipitation varied spatially from 12 ºC to 18 ºC and from 270 mm year^{-1} to 940 mm year^{-1}, respectively. According to the Third Spanish Forest Inventory (NFI3), the most abundant species in Comunitat Valenciana are *Pinus halepensis* Mill. and *Quercus ilex* L. among trees, and *Thymus spp.* and *Rosmarinus officinalis* L. in the case of shrubs.

Figure 1 shows a vegetation type map of the study area elaborated from SIOSE (IGN, 2011) data and a zoom in the surroundings of the two study sites.

Descriptive information of the two study sites where EC towers are placed is reported in Table 1.

3 DATA

3.1 Used data

Daily net ecosystem exchange data measured in the two EC towers abovementioned were downloaded from the European Carbon Database Cluster (http://www.europe-fluxdata.eu).

The Spanish Meteorological Agency (AEMet) provided in situ daily measurements of cumulated precipitation and maximum and minimum air temperature from meteorological stations distributed throughout the study area for the period 2005-2012.

SEVIRI product LSA-09 (daily integrated down-welling surface shortwave flux, DIDSSF) was downloaded from the LSA-SAF Server (http://landsaf.meteo.pt/) for the 2007-2012 period when available. Otherwise LSA-07 (down-welling surface shortwave flux estimated every 30 minutes, MDSSF) was downloaded instead. Details on these products can be found in "Product User Manual Down-welling Surface Shortwave Flux (DSSF)," (2011).

MODIS products MCD43A1 and MCD43A2 (Schaaf et al., 2002) for the period 2005-2012 were retrieved from the online Reverb, courtesy of the NASA EOSDIS Land Processes Distributed Active Archive Center (LP DAAC), USGS/Earth Resources Observation and Science (EROS) Center, Sioux Falls, South Dakota, reverb.echo.nasa.gov.

The global 3 arc second digital elevation model from the Shuttle Radar Topography Mission (SRTM) (Farr et al., 2007) was downloaded from http://edcftp.cr.usgs.gov/pub/data.

Soil clay, sand and silt content maps (Ballabio et al., 2016) were downloaded from the European Soil Database (http://esdac.jrc.ec.europa.eu/resource-type/european-soil-database-soil-properties).
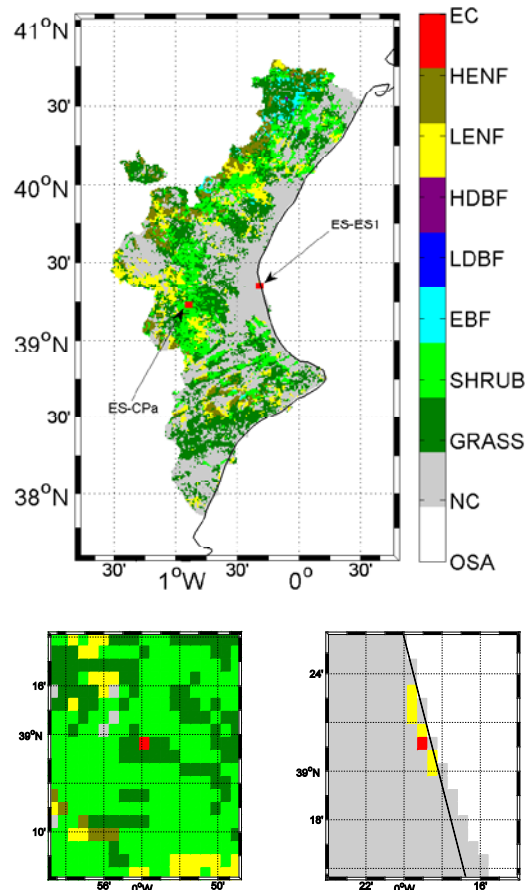
Figure 1. Vegetation type map of Comunitat Valenciana (top). Zooms on ES-CPa (bottom left) and ES-ES1 (bottom right). OSA (out of study area), NC (non-classified), GRASS (grassland), SHRUB (shrubland), EBF (evergreen broadleaved forest), LDBF (low altitude deciduous broadleaved forest), HDBF (high altitude deciduous broadleaved forest), LENF (low altitude evergreen needleleaved forest), HENF (high altitude evergreen needleleaved forest), and EC (eddy covariance site). The altitude threshold was set at 800 m.

Table 1. Descriptive information of the study sites and period of EC data availability. *h* is the altitude above the sea level, PRE is the averaged annual precipitation, and *T* is the mean annual air temperature.

Site	ES-CPa	ES-ES1
Lat (º)	39.2242	39.3448
Lon (º)	-0.9031	-0.3200
h **(m)**	810	5
PRE (mm)	470	550
T **(ºC)**	13	18
Vegetation type	SHRUB	LENF
Data period	2009-2011	2005-2006

3.2 Data preprocessing

Daily GPP (GPP$_{EC}$) was calculated from the EC observations obtained according to Reichstein et al., (2005) methodology. Both GPP$_{EC}$ and NEE (NEE$_{EC}$) were summed up to monthly values.

Daily cumulated precipitation and maximum and minimum air temperature images were obtained by ordinary kriging from the in situ measurements provided by AEMet. Mean air temperature images were calculated from maximum and minimum ones.

DIDSSF was integrated from MDSSF when not available. 1-km global incoming solar radiation images were obtained through the application of artificial neural networks (ANN) to the precipitation and air temperature images abovementioned. Both DIDSSF and the ANN-derived solar radiation were previously validated (Moreno et al., 2013, 2011). A relationship between them was found and it was used to fill DIDSSF gaps and the whole 2005-2006 period.

All images were reprojected to a 1-km spatial resolution latitude/longitude regular grid.

4 METHODS

4.1 Production efficiency model

A Monteith-like PEM described by equation (1) was used to calculate daily GPP (GPP$_{PEM}$) estimates in the two EC sites:

$$GPP_{PEM} = PAR \, f_{APAR} \, \varepsilon_{max} \, \varepsilon_{T} \, \varepsilon_{W} \qquad (1)$$

where PAR (MJ m^{-2} day^{-1}), the photosynthetically active (400 – 700 nm) radiation, was calculated as the 46 % of daily global incoming solar radiation; f_{APAR}, the fraction of PAR absorbed by vegetation canopy, was estimated according to the Roujean and Breon (1995) algorithm; ε_{max} is the maximum light use efficiency set as 1.2 g MJ^{-1}; ε_{T} is the TMIN_scalar used in MOD17 algorithm (Running and Zhao, 2015); and ε_{W} is the water stress coefficient used in CASA (Potter et al., 1993).

DIDSSF images were used to calculate PAR. MCD43A1 and MCD43A2 were used to calculate f_{APAR} and a gap filling and noise reduction filter (Moreno et al., 2014) was applied before the final lineal interpolation to obtain daily values. In the case of ES-ES1, due to the proximity of different water bodies surrounding the tower, f_{APAR} was estimated from MOD13Q1 (Didan and Huete, 2015), 16-day NDVI at 250-m spatial resolution, through Myneni and Williams (1994) equation. The minimum air temperature images were used to calculate ε_{T}. The mean air temperature images and the DIDSSF ones were used to calculate ε_{W} through the Jensen and Haise (1965) equation using the precipitation images as actual evapotranspiration proxies (Maselli et al.,

2009). Monthly GPP$_{PEM}$ estimates were obtained by sum of the daily values.

4.2 BIOME-BGC

BIOME-BGC (Running and Hunt, 1993; White et al., 2000) is a biogeochemical model able to estimate all main vegetation processes in a terrestrial ecosystem finding a quasi-climax equilibrium condition. Daily maximum and minimum air temperature and precipitation series were used to simulate daylight average air temperature and daylight average partial pressure of water vapor through MT-CLIM (Thornton et al., 2000). The same input series, the resulting ones, and the daily incoming solar radiation ones were used as inputs for BIOME-BGC together with the ecophysiological parameters obtained by Chiesi et al. (2007) for Mediterranean ecosystems. Monthly GPP (GPP$_{BGC}$) and growth (R_{gr}), maintenance (R_{mn}), and heterotrophic (R_{het}) respirations series were simulated with different z_e for the two EC sites.

4.2.1 Effective soil depth calibration

BIOME-BGC was run with 40 different z_e values for each EC site. z_e values ranged from 5 cm to 200 cm by 5 cm steps. GPP$_{BGC}$ series were compared to the GPP$_{PEM}$ ones and the z_e that obtained the minimum RMSE was selected.

4.2.2 Net ecosystem exchange

The optimum BIOME-BGC outputs in terms of z_e were used to calculate NEE and it was validated against EC measurements.

In the case of ES-CPa, since the growth of SHRUB in this kind of regions is limited, it can be assumed that the ecosystem is close to equilibrium and NEE can be calculated from optimized BIOME-BGC outputs using Equation (2):

$$NEE_{BGC} = GPP_{BGC} - R_{gr} - R_{mn} - R_{het} \qquad (2)$$

In the case of ES-ES1, an actual volume ($V_A = 146$ m^3 ha^{-1}) estimation was extracted from NFI3 for the nearest plot that contained the same species. Next BIOME-BGC outputs were corrected using this value in Equation (3) (Maselli et al., 2009) to calculate actual NEE:

$$NEE_{A,BGC} = GPP_{BGC} \, FC_A / FC - R_{gr} \, FC_A / FC - R_{mn} \, V_A / V_P - R_{het} \, V_A / V_P \qquad (3)$$

where FC$_A$ and FC are, respectively, the actual and potential forest cover, and V_P the potential volume. The latter can be calculated from BIOME-BGC output dead stem carbon, while the forest covers can be calculated using V_A, V_P, and BIOME-BGC output maximum LAI through Beer's law.

5 RESULTS

5.1 Identification of optimum z_e

RMSE between GPP$_{PEM}$ and GPP$_{BGC}$ as a function of the z_e used in BIOME-BGC simulations is shown in Figure 2 for the two EC sites. Optimum effective soil depths of 40 cm and 65 cm were found for ES-CPa and ES-ES1, respectively, always shallower than the default one (100 cm).
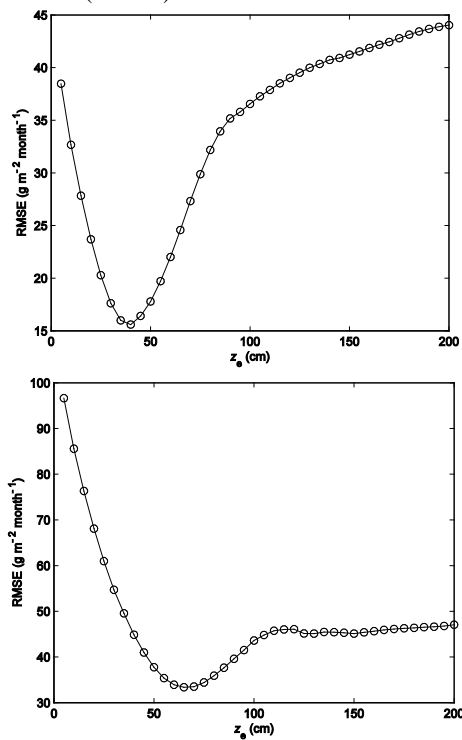
Figure 2. RMSE between GPP$_{PEM}$ and GPP$_{BGC}$ as a function of z_e for ES-CPa (top) and ES-ES1 (bottom).

Table 2. Statistics of the validation of GPP and NEE against EC data in the two sites. MBE, MAE, and RMSE are expressed in g m^{-2} month^{-1}. Correlations (R) are statistically significant at 95 % confidence level.

ES-CPa				
	R	**MBE**	**MAE**	**RMSE**
GPP$_{EC}$ / GPP$_{PEM}$	0.93	7	12	15
GPP$_{EC}$ / GPP$_{BGC,100}$	0.67	40	40	50
GPP$_{EC}$ / GPP$_{BGC,40}$	0.84	6	18	20
NEE$_{EC}$ / NEE$_{BGC,40}$	0.74	-10	12	16
ES-ES1				
	R	**MBE**	**MAE**	**RMSE**
GPP$_{EC}$ / GPP$_{PEM}$	0.71	7	17	30
GPP$_{EC}$ / GPP$_{BGC,100}$	0.54	30	40	50
GPP$_{EC}$ / GPP$_{BGC,65}$	0.55	3	30	40
NEE$_{EC}$ / NEE$_{A,BGC,65}$	0.59	-13	20	30

5.2 Validation at EC sites

The results of the validation of estimated carbon fluxes against EC data are gathered in Table 2. Regarding GPP, GPP$_{PEM}$ generally presents the best results except that minimum MBE is obtained by GPP$_{BGC}$ using the optimum z_e. The use of the optimum z_e always improved the results in the case of GPP$_{BGC}$, especially reducing the errors. The accuracy achieved for NEE is generally lower than that for GPP due to the difficulties in correctly simulating all respiration processes.

Scatterplots of simulated GPP and NEE *vs* EC data are shown in Figure 2.

6 DISCUSSION AND CONCLUSIONS

A PEM mainly driven by remotely sensed data was used to estimate monthly GPP$_{PEM}$ in two EC sites. Then monthly GPP$_{BGC}$ and respirations were simulated by BIOME-BGC using 40 different z_e values. The high correlations and low errors obtained by the validation of GPP$_{PEM}$ against EC data justified its use as a reference to compare to GPP$_{BGC}$ and select the optimum z_e by the minimum RMSE criterion. The obtained z_e, 40 cm and 65 cm respectively for ES-CPa and ES-ES1 were coherent with the vegetation type, i.e. a shallower depth for the less productive SHRUB and a deeper depth for the more productive LENF, and always improved the statistics with respect to default $z_e = 100$ cm when compared to EC data. Finally the optimum BIOME-BGC outputs were used to estimate NEE and NEE$_A$ and they were validated against EC measurements. Reasonably good correlations were obtained, although errors were rather high. Effective soil depth revealed itself as a critical variable for the simulation of water budget by BIOME-BGC. Since water storage capacity depends on it, the importance of z_e is even higher in the studied semiarid Mediterranean areas due to the concentration of annual precipitation in short periods of time. The air temperature and precipitation time series had to be corrected before using them because a disagreement was found when comparing with the measurements taken at the EC towers. This must be taken into account if this methodology is applied at spatially distributed level, especially in high altitude areas. The regional modelling of net carbon fluxes also requires spatially distributed estimates of woody biomass (Maselli et al., 2009). Such estimates can be derived from a V_A map that is currently being obtained by the integration of ground and remotely sensed data for the study area.
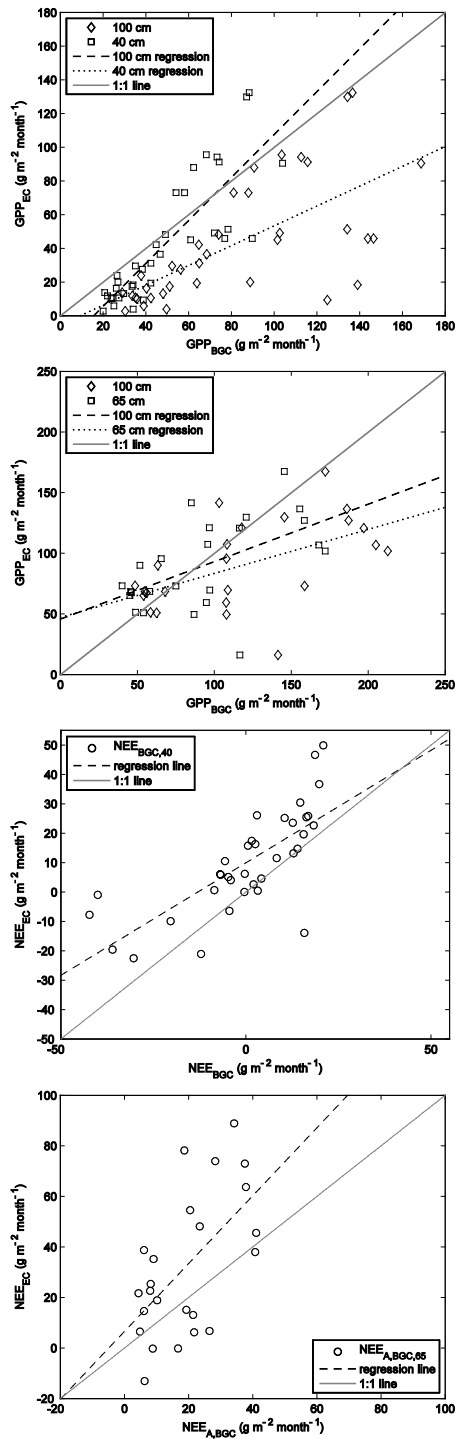
Figure 2. From top to bottom: GPP$_{EC}$ *vs* GPP$_{BGC}$ in ES-CPa, GPP$_{EC}$ *vs* GPP$_{BGC}$ in ES-ES1, NEE$_{EC}$ *vs* NEE$_{BGC}$ in ES-CPa, NEE$_{EC}$ *vs* NEE$_{A,BGC}$ in ES-ES1.

8 REFERENCES

Ballabio, C., Panagos, P., Monatanarella, L., 2016. Mapping topsoil physical properties at European scale using the LUCAS database. Geoderma 261, 110–123. doi:10.1016/j.geoderma.2015.07.006

Chiesi, M., Maselli, F., Moriondo, M., Fibbi, L., Bindi, M., Running, S.W., 2007. Application of BIOME-BGC to simulate Mediterranean forest processes. Ecol. Modell. 206, 179–190. doi:10.1016/j.ecolmodel.2007.03.032

Didan, K., Huete, A., 2015. MOD13Q1 MODIS/Terra Vegetation Indices 16-Day L3 Global 250m SIN Grid. NASA EOSDIS Land Processes DAAC. doi:10.5067/MODIS/MOD13Q1.006

Farr, T., Rosen, P., Caro, E., Crippen, R., Duren, R., Hensley, S., Kobrick, M., Paller, M., Rodriguez, E., Roth, L., Seal, D., Shaffer, S., Shimada, J., Umland, J., Werner, M., Oskin, M., Burbank, D., Alsdorf, D., 2007. The shuttle radar topography mission. Rev. Geophys. 45. doi:10.1029/2005RG000183.1.INTRODUCTION

Gilabert, M.A., Moreno, A., Maselli, F., Martínez, B., Chiesi, M., Sánchez-Ruiz, S., García-Haro, F.J., Pérez-Hoyos, A., Campos-Taberner, M., Pérez-Priego, O., Serrano-Ortiz, P., Carrara, A., 2015. Daily GPP estimates in Mediterranean ecosystems by combining remote sensing and meteorological data. ISPRS J. Photogramm. Remote Sens. 102, 184–197. doi:10.1016/j.isprsjprs.2015.01.017

IGN, 2011. Documento Técnico SIOSE 2011.

Jensen, M.E., Haise, H.R., 1965. Estimating evapotranspiration from solar radiation. J. Irrig. Drain. Div. 89, 15–41.

Kovats, R.S., Valentini, R., Bouwer, L.M., Georgopoulou, E., Jacob, D., Martin, E., Rounsevell, M., Soussana, J.F., 2014. Climate Change 2014: Impacts, Adaption, and

Vulnerability. Part B: Regional Aspects. Contribution of Working Group II to the Fifth Assessment Report of the Intergovernmental Panel of Climate Change.

Maselli, F., Chiesi, M., Moriondo, M., Fibbi, L., Bindi, M., Running, S.W., 2009. Modelling the forest carbon budget of a Mediterranean region through the integration of ground and satellite data. Ecol. Modell. 220, 330–342. doi:10.1016/j.ecolmodel.2008.10.002

Maselli, F., Papale, D., Puletti, N., Chirici, G., Corona, P., 2009. Combining remote sensing and ancillary data to monitor the gross productivity of water-limited forest ecosystems. Remote Sens. Environ. 113, 657–667. doi:10.1016/j.rse.2008.11.008

Moreno, Á., García-Haro, F., Martínez, B., Gilabert, M.A., 2014. Noise Reduction and Gap Filling of fAPAR Time Series Using an Adapted Local Regression Filter. Remote Sens. 6, 8238–8260. doi:10.3390/rs6098238

Moreno, A., Gilabert, M.A., Camacho, F., Martínez, B., 2013. Validation of daily global solar irradiation images from MSG over Spain. Renew. Energy 60, 332–342. doi:10.1016/j.renene.2013.05.019

Moreno, A., Gilabert, M.A., Martínez, B., 2011. Mapping daily global solar irradiation over Spain: A comparative study of selected approaches. Sol. Energy 85, 2072–2084. doi:10.1016/j.solener.2011.05.017

Myneni, R.B., Williams, D.L., 1994. On the relationship between FAPAR and NDVI. Remote Sens. Environ. 49, 200–211. doi:10.1016/0034-4257(94)90016-7

Potter, C.S., Randerson, J.T., Field, C.B., Matson, P.A., Vitousek, P.M., Mooney, H.A., Klooster, S.A., 1993. Terrestrial ecosystem production: A process model based on global satellite and surface data. Global Biogeochem. Cycles 7, 811–841.

Product User Manual Down-welling Surface Shortwave Flux (DSSF), 2011.

Reichstein, M., Falge, E., Baldocchi, D., Papale, D., Aubinet, M., Berbigier, P., Bernhofer, C., Buchmann, N., Gilmanov, T., Granier, A., Grunwald, T., Havrankova, K., Ilvesniemi, H., Janous, D., Knohl, A., Laurila, T., Lohila, A., Loustau, D., Matteucci, G., Meyers, T., Miglietta, F., Ourcival, J.-M., Pumpanen, J., Rambal, S., Rotenberg, E., Sanz, M., Tenhunen,

J., Seufert, G., Vaccari, F., Vesala, T., Yakir, D., Valentini, R., 2005. On the separation of net ecosystem exchange into assimilation and ecosystem respiration: review and improved algorithm. Glob. Chang. Biol. 11, 1424–1439. doi:10.1111/j.1365-2486.2005.001002.x

Roujean, J., Breon, F., 1995. Estimating PAR Absorbed by Vegetation from Bidirectional Reflectance Measurements. Remote Sens. Environ. 51, 375–384.

Running, S., Hunt, E., 1993. Generalization of a forest ecosystem process model for other biomes, BIOME-BGC, and an application for global-scale models. Scaling Physiol. Process. Leaf to globe. doi:10.1016/B978-0-12-233440-5.50014-2

Running, S.W., Zhao, M., 2015. User's Guide: Daily GPP and annual NPP (MOD17A2/A3) Products NASA Earth Observing System MODIS Land Algorithm. Version 3.0.

Sanchez-Ruiz, S., Moreno, A., Piles, M., Maselli, F., Carrara, A., Running, S., Gilabert, M.A., 2017. Quantifying water stress effect on daily light use efficiency in Mediterranean ecosystems using satellite data. Int. J. Digit. Earth 10, 623–638. doi:10.1080/17538947.2016.1247301

Schaaf, C.B., Gao, F., Strahler, A.H., Lucht, W., Li, X., Tsang, T., Strugnell, N.C., Zhang, X., Jin, Y., Muller, J.-P., Lewis, P., Barnsley, M., Hobson, P., Disney, M., Roberts, G., Dunderdale, M., 2002. Global albedo, BRDF and nadir BRDF-adjusted reflectance products from MODIS. Remote Sens. Environ. 83, 135–148.

Thornton, P.E., Hasenauers, H., White, M.A., 2000. Simultaneous estimation of daily solar radiation and humidity from observed temperature and precipitation: an application over complex terrain in Austria. Agric. For. Meteorol. 104, 255–271.

White, M.A., Thornton, P.E., Running, S.W., Nemani, R.R., 2000. Parameterization and Sensitivity Analysis of the BIOME–BGC Terrestrial Ecosystem Model: Net Primary Production Controls. Earth Interact. 4, 1–85. doi:10.1175/1087-3562(2000)004<0003:PASAOT>2.0.CO;2

Reconstructed glacier mass balance in the past few decades with the latest GRACE and GLDAS products over the Yarlung Zangbo River Basin, China

Jinping Liu [1, 2], Wanchang Zhang [1, *]

[1]*Key Laboratory of Digital Earth Science, Institute of Remote Sensing and Digital Earth, Chinese Academy of Sciences, No. 9 Dengzhuang South Road, Haidian District, Beijing, China, 100094, liujp@radi.ac.cn (J.P. Liu), zhangwc@radi.ac.cn (W.C. Zhang);*
[2]*University of Chinese Academy of Sciences, Beijing, China, 100049;*
Email addresses: liujp@radi.ac.cn; *Corresponding author: zhangwc@radi.ac.cn

Abstract - *Glacier mass balance (GMB) monitoring is not only crucial for water resource management but also essential for understanding the glacier response to climate change over the Yarlung Zangbo River Basin (YZRB). The long-term GMB series from 1980 to 2014 was reconstructed at monthly and yearly scales based on GRACE and GLDAS products, and two indirect approaches were adopted to examine the rationality of the reconstructed time series under the poor condition of field data availability over the YZRB. Good correlation was found between GRACE-based terrestrial water storage change (TWSC) and GLDAS-based TWSC at both monthly and yearly scales, but one year time lag (lag-1) of GLDAS-based TWSC compared to GLDAS-based TWSC was adjusted to establish the good correlation with GRACE-based TWSC at yearly scale over the YZRB. The reconstructed GMB series revealed two periods of decreasing trend for the years from 1980 to 1994 and from 1998 to 2014. In particular, less accumulation in cold months (i.e. JAN, FEB, MAR, APR, OCT, NOV, and DEC) and more ablation in warm months (i.e. MAY, JUN, JUL, AUG, and SEP) was found in the latter period compared to the former one, which suggested an overall decreasing tread of reconstructed GMB time series for the YZRB. The reconstructed GMB time series not only offer a unique opportunity for understanding the varying characteristics of GMB in the YZRB during the past decades, but also provide a new perspective for estimating the glacier water resource in other large watersheds under the global changes.*

1 INTRODUCTION

Glacier mass balance (GMB) is considered as the most important bridge and tie linking the meteorology and water resources (Zhu et al., 2017). However, traditional direct and continuous mass balance measurements for the glaciers in an extensive region are extremely difficult due to the inaccessibility of glaciers for logistical difficulties and maintains in high altitude mountainous region, especially for the YZRB due to its unique geographical location (Nie et al., 2016). Pioneer studies have suggested that strong relationships existed between annual GMB and minimum glacier-wide albedo derived from Moderate Resolution Imaging Spectro-radiometer (MODIS) (Dumont et al., 2012; Sirguey et al., 2016). However, optical remote sensing is of a notable weakness that the imagery is easy to be affected by cloud, which greatly weakens the relationship, moreover, for estimation of GMB of a glacier, successive field observations of GMB are needed, which makes this approach unpractical.

With the success launch of the GRACE (Gravity Recovery and Climate Experiment) satellite and the advances of GLDAS (Global Land Data Assimilation System) products, studies of terrestrial/ground water storage (TWS) variations and GMB by using these two data products have been implemented in the past decade (Chen et al., 2009; Rodell and Famiglietti, 2002; Zhu et al., 2017; Zeng et al., 2012). Aiming to take the best use of hydro-meteorological variables from GRACE and GLDAS products, in association with the relevant approaches proposed by pioneer studies, this study attempted to estimate and reconstruct long term monthly and yearly GMB over the YZRB from 1980 to 2014 under water balance principle for the closed watershed YZRB.

2 STUDY REGION, DATA AND METHODOLOGY

2.1 Study region

Located in 27º49′-31º7′N and 82º1′-97º6′E, the Yarlung Zangbo River Basin (YZRB) with an total area of approximately 25×10^4 km^2 is one of the highest river basins in the world with an average elevation higher than 4600 m above sea-level (Liu et al., 2014) (Fig.1). Because of its location in the Yarlung Zangbo Suture Zone, within which enormous transportation channels carry moisture from the Indian Ocean to the inner region of the Qinghai-Tibet Plateau, the YZRB plays an important role as a precipitation

generation mechanism over the Qinghai-Tibet Plateau, where many maritime and continental glaciers developed with abundant solid (*i.e.* glaciers and snow cover) and liquid (stream flow) water resource in China (Nie et al., 2016). According to Chinese Glacier Inventory, within the YZRB, there are approximately 10,816 glaciers (14,493 km^2), which accounts for 29% and 23% of total glaciers in Tibetan Plateau and China, respectively (Yao et al., 2010).

2.2 Data

2.2.1 GRACE Products and Processing

Among various TWS anomaly (TWSA) products, three GRACE level-3 Release-05 (RL05) products are widely used to estimate the regional and global water storage variations, which are provided by University of Texas Center for Space Research (CSR), Jet Propulsion Laboratory (JPL), and Geo Forschungs Zentrum (GFZ), respectively. All these products are in 1°×1° spatial resolution and at monthly time scales. Prior to any analysis, the scale factor, provided separately with the GRACE RL05 products, should be applied firstly to reduce the correlated errors in post-processing caused by truncation, destriping and Gaussian smoothing filter (Swenson and Wahr, 2006). Uncertainties caused by instrument and post-processing do exist in each product and by far no direct method can assess them (Swenson and Wahr, 2006; Yi and Sun, 2014), therefore these three GRACE products of the YZRB from April 2002 to December 2014 were compared to determine an optimal combined solution. In this study, the TWSA products with the missing data were linearly interpolated to derive TWS change (TWSC) time series (Nie et al., 2016).

2.2.2 GLDAS Data and Processing

To estimate the GMB, the change of soil moisture (SMC), canopy water storage (CWSC), snow water equivalent (SWEC) need to be deducted respectively from TWSC. In this study, the monthly hydrologic variables, SM, CWS, and SWE with spatial resolution of 1°×1°, were obtained from four hydrologic models (CLM, MOSAIC, NOAH, and VIC) in GLDAS products for the YZRB during 1980-2014, monthly averaged change of SM, CWS, and SWE (Non-glacier covered regions) obtained from these four hydrologic models were considered as the "real vaiables" of the studied hydrologic processes. Since the above mentioned hydrologic variables were not simulated in the south and north polar regions, thus they can't not be processed in the same way as done to GRACE products (*i.e.* truncation to 60th degree and order, smoothing with a Gaussian filter of 300 km in radius), otherwise numerious errors might be introduced into their spherical harmonic coefficients. Hydrologic variables, i.e. rainfall (P), snowfall (S), evapotranspiration (E), surface runoff (Qs), and subsurface runoff (Qsb) derived from all four hydrologic models of GLDAS were also used to deduce TWSC (noted as TWSC-GLDAS) through water balance principle over the closed YZRB. Additionally, it is worthwhile to note that the monthly and yearly TWSC and GMB were not reconstructed during 1995-1997 for the unnatural trends in the simulated hydrologic variables of GLDAS during the period (Nie et al., 2016).

2.2.3 Datasets Used to Evaluate the Reconstructed GMB Series

Three approaches were adopted to directly/indirectly evaluate the reconstructed GMB datasets for the YZRB.
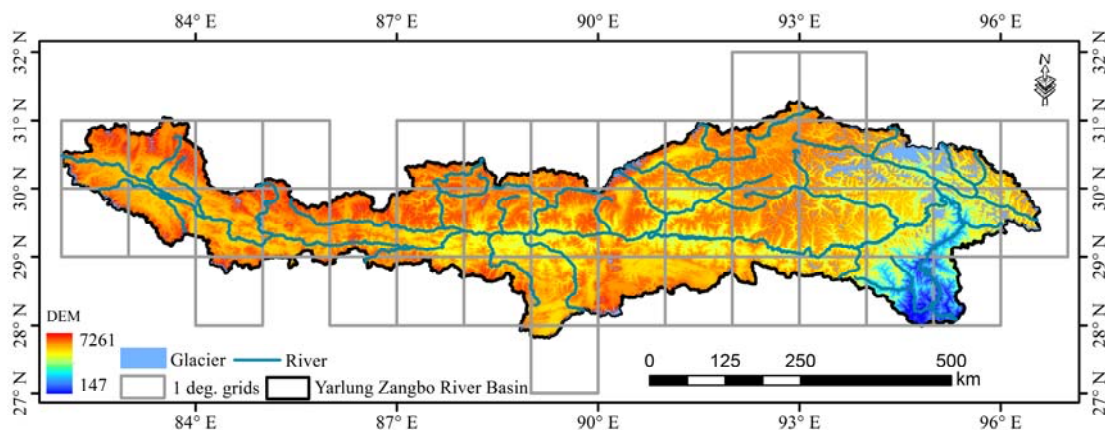
Fig.1 Geographic location and topographic map of the YZRB. Glacier locations and GRACE pixels covering the study region used for various estimations were also presented in the figure

The datasets utilized for this purpose include The Second Chinese Glacier Inventory datasets (SCGI, Version 1.0), the China Precipitation and Temperature Analysis Products (CPTAP) and Land-Use/Cover-Change (LUCC) maps. The first two datasets were used for analyzing the change trend of precipitation and temperature over glacier-covered areas, and the last one was for detecting the change of glacier covered extent (GCE) during the study periods. The CPTAP, produced and routinely calibrated by the National Meteorological Information Center (NMIC) and the China Meteorological Administration (CMA) based on approximately 2472 meteorological stations across China (Chen et al., 2008; Shen et al., 2010), with the spatio-temporal resolution of 0.5°×0.5°/daily were used to understand the precipitation and temperature variations over the glacier-covered areas of the YZRB during 1980-2014. The SCGI dataset, with overall accuracy about 96.7% for glacier area inventory, was provided by Cold and Arid Regions Science Data Center at Lanzhou (Guo et al., 2015), which was used as the glacier boundary for the corresponding period. According to SCGI, the glacier accounted for approximately 4.6% of the total area of the YZRB. The LUCC datasets, derived through artificial visual interpretation primarily based on Landsat TM/ETM imageries, were provided by Data Center for Resources and Environmental Sciences, Chinese Academy of Sciences (RESDC). Seven LUCC maps of the YZRB for 1980, 1990, 1995, 2000, 2005, 2010, and 2015 respectively are available presently, among which the LUCC maps for 1980, 1995, and 2015 were selected to detect the GCE changes over the YZRB during the studied periods.

2.3 Methodology

2.3.1 Reconstruct Glacier Mass Balance

Theoretically, if the water consumption for human activities is less enough to be neglected, the water balance equation for the YZRB can be expressed as:

$$TWSC_n = TWSA_n - TWSA_{n-1} = P_n + S_n - E_n - Qs_n - Qsb_n \quad (1)$$
$$TWSC_m = TWSA_{(m,12)} - TWSA_{(m-1,12)} = P_m + S_m - E_m - Qs_m - Qsb_m \quad (2)$$

where P, S, E, and Q denote accumulative rainfall, snowfall, actual evapotranspiration and runoff, respectively. n and m represent a specific month and a certain year, respectively. $TWSA_n$ and $TWSA_{n-1}$, as well as $TWSA_{(m,12)}$ and $TWSA_{(m-1,12)}$ denote the basin-scale averaged TWSA for the month n and $n-1$, as well as basin-scale averaged TWSA in December of the year m and $m-1$, respectively.

According to Equation 1 and 2, various linear regression models were established between GRACE-based TWSC and different combinations of hydro-meteorological variables (*e.g.* P, S, P+S-E, and P+S-

Qs) (Nie et al., 2016; Zeng et al., 2012). Among them, an optimal linear regression model was identified by R^2 and employed to reconstruct the TWSC over the YZRB during 1980-2014. The GMB during 1980-2014 can be expressed as Equation 3:

$$GMB = TWSC_{re} - SCC_{gl} - SWEC_{ng} \quad (3)$$

where $TWSC_{re}$ denotes the reconstructed TWSC series; SCC_{gl} stands for the sum of SMC and CWSC based on GLDAS datasets; and $SWEC_{ng}$ for the change of SWE over the non-glacier covered regions.

2.3.2 Evaluating the Reconstructed Glacier Mass Balance

Unfortunately, *in-situ* GMB measurements or similar research are not available for validating the reconstructed GMB series over the YZRB. Although validating long-term GMB datasets is very difficult, the variation trend of GMB in time series might be indirectly assessed by climatic indices and glacier-cover extent (GCE) owning to strong sensitivity of GMB to precipitation and temperature. In general, an increase (a decrease) of GCE usually indicates glacial accumulation (ablation). Therefore, the two indirect approaches were employed to evaluate the reconstructed long-term GMB series in present study.

3 RESULTS AND DISCUSSION

3.1 TWS Changes (TWSC) during 2003-2014

3.1.1 GRACE-based TWSA

To obtain the GRACE-based TWSC, the monthly TWSAs series, derived from CSR, JPL and GFZ as well as their average were calculated over the YZRB during 2003-2014 (Fig.2). The TWSAs variations illustrated with the dataset from different data processing centers exhibited strong annual cycles and generally coincide well with each other. In particular, the correlation coefficients (noted as CC) between three TWSAs series range from 0.96 to 0.98 at the significance level of α<0.001. Table 1 lists the annual amplitudes, annual phase, and variation trend of different GRACE-based TWSAs datasets and their average over the YZRB during 2003-2011, among which the uncertainties in annual amplitudes, annual phase and variation trend of different GRACE products have been estimated as two standard deviations (95% confidence interval) after errors in monthly datasets were propagated in the least squares fit procedure (Feng et al., 2014). High consistency among annual amplitudes, annual phase and variation trend of different GRACE products as seen in Table implied that the averaged series of TWSAs from CSR, JPL and GFZ can be used to deduce the TWSC in the following sections.

146
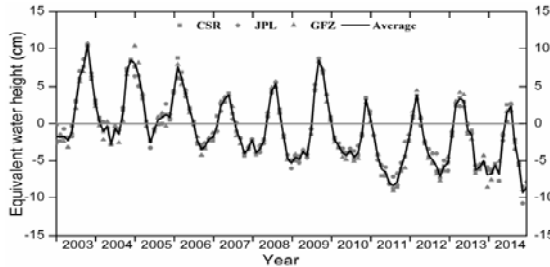
Fig.2 GRACE-based monthly TWSAs over the YZRB during 2003-2014

Table 1. Annual amplitudes, phases and variation trend of TWSAs from different GRACE products and their average series during 2003-2014

GRACE product	Annual amplitude (cm)	Annual phase (degree)	Annual trend (cm/yr)
CSR	4.29 ± 0.40	227.68 ± 7.48	-0.72 ± 0.08
JPL	4.28 ± 0.37	225.50 ± 9.22	-0.77 ± 0.08
GFZ	4.69 ± 0.38	227.05 ± 7.00	-0.73 ± 0.08
Average	4.55 ± 0.35	226.10 ± 7.31	-0.75 ± 0.07

3.1.2 Comparisons of TWSC from GRACE and GLDAS

According to Equation 1 and 2, the monthly and yearly TWSC-GRACE and TWSC-GLDAS datasets were computed during 2003-2014. Good correlation between these two datasets at monthly scale with the CC about 0.67 at the significance level of $\alpha<0.001$, as exhibited in Fig.3, suggested reliability of the approach utilized.
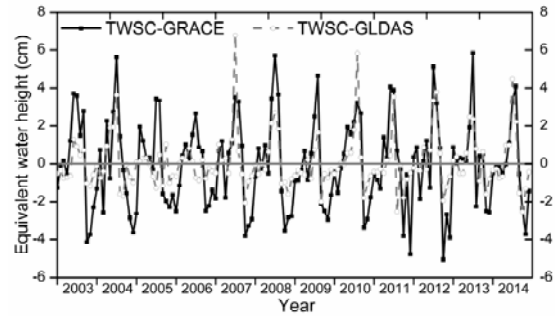
Fig.3 Comparison of monthly basin-scale averaged TWSC-GRACE and TWSC-GLDAS series during 2003-2014

While a rather low correlation for these two datasets at yearly scale with the CC only about 0.30 (not shown) was detected. However, we think that it was probably caused by accumulated errors of the hydrologic variables (see Equation 3). It should be noted that GRACE has the advantage of capturing human-induced TWSC signals, while the hydrologic variables in GLDAS are susceptible to the quality of forcing data (Nie et al., 2016). Therefore, further exploration to reconstruct more reliable and longer-term TWSC series based on the GRACE-based TWSC by means of different combinations of hydrologic variables might be an effective alternative.

3.2 Reconstruct GRACE-based TWSC for 1980-2014 over the YZRB

The CCs between TWSC-GRACE and the different combinations of hydro-meteorological variables (*e.g.* P, S, E, Qs, Qsb, and P+S-E-Qs) derived from GLDAS were calculated based on Pearson correlation analysis at both monthly and yearly scales, the results obtained were listed in Table 2.

Table 2. Correlations of the basin-scale averaged TWSC-GRACE with different combinations of hydro-meteorological variables

	Hydrologic variables	Monthly		Yearly (No time lag)		Yearly (one year lag)	
		CC	Sig.	CC	Sig.	CC	Sig.
TWSC-GRACE	P+S	0.73	$\alpha<0.001$	0.37	-	-0.41	-
	E	0.68	$\alpha<0.001$	0.33	-	-0.12	-
	Qs	0.72	$\alpha<0.001$	0.38	-	-0.37	-
	Qsb	0.37	$\alpha<0.001$	0.35	-	-0.3	-
	Qs+Qsb	0.62	$\alpha<0.001$	0.37	-	-0.34	-
	P+S-E	0.73	$\alpha<0.001$	0.38	-	-0.58	$\alpha<0.1$
	P+S-E-Qs	0.69	$\alpha<0.001$	0.35	-	-0.63	$\alpha<0.05$
	P+S-E-Qsb	0.75	$\alpha<0.001$	0.37	-	-0.68	$\alpha<0.05$
	P+S-Qs	0.73	$\alpha<0.001$	0.36	-	-0.41	-
	P+S-Qsb	0.74	$\alpha<0.001$	0.37	-	-0.44	-
	P+S-E-Qs-Qsb	0.67	$\alpha<0.001$	0.30	-	-0.75	$\alpha<0.01$
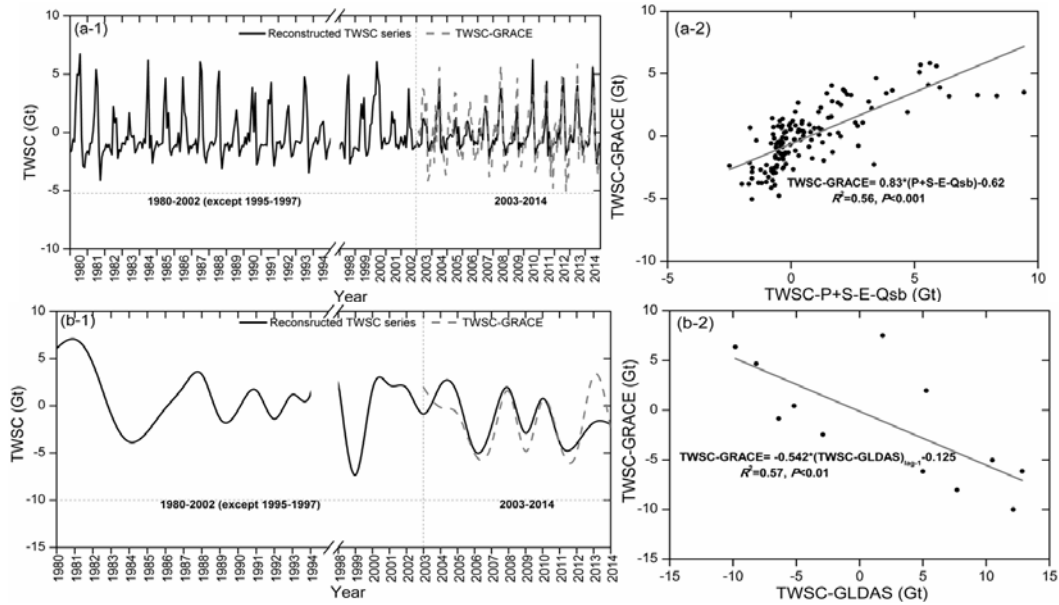
Fig.4 Monthly reconstructed TWSC based on "P+S-Qsb" (noted as "TWSC-P+S-Qsb") and TWSC-GRACE (a-1 and -2); yearly reconstructed TWSC based on "P+S-E-Qs-Qsb" and TWSC-GRACE (b-1 and -2)

Notably, at the yearly scale, higher correlations between TWSC-GRACE and the combinations of hydrologic variables were found in comparisons with one year time lag between them, probably can be explained by instantaneous measurements of GRACE-based TWSA and overestimation of runoff (Qs+Qsb) in GLDAS datasets. From Table 2, it can be found that the combination of hydrologic variables "P+S-E-Qsb" most closely correlated with TWSC-GRACE at monthly scale, while the combination of hydrologic variables "P+S-E-Qs-Qsb" derived from TWSC-GLDAS with one year time lag has the highest correlation with TWSC-GRACE at the yearly scale. On the basis of above analysis, the monthly and yearly TWSC datasets for 1980-2014 were reconstructed and the results were shown in Fig.4. It can be seen that significant seasonal signals with the annual amplitude of 1.84±0.26 Gt during 1980-1994 and 1.56±0.24 Gt during 1998-2014 at monthly scale (Fig.4a-1,-2) and additional yearly TWSC series exhibited a decreasing trend both during 1980-1994 and 1998-2014 (Fig.4b-1,-2).

3.3 Reconstructed long-term GMB series during 1980-2014

3.3.1 Reconstructed Seasonal Variability of GMB over the YZRB

The long-term monthly GMB series, calculated according to Equation 3, was shown in Fig.5a. Significant seasonal cycles with annual amplitude of 2.45±0.31 Gt during 1980-1994 and annual amplitude

of 2.31±0.24 Gt during 1998-2014 at monthly scale can be clearly recognized, which suggested a relative larger fluctuation in GMB during 1980-1994 than that during 1998-2014. Monthly mean GMB in different periods (Fig.5b) revealed less accumulation in the cold seasons (JAN, FEB, MAR, APR, OCT, NOV and DEC) and generally more ablation in the warm ones (MAY, JUN, JUL, AUG, and SEP) during 1998-2014 compared to 1980-1994. Overall, the glaciers within the YZRB presented a negative mass balance during 1980-2014.
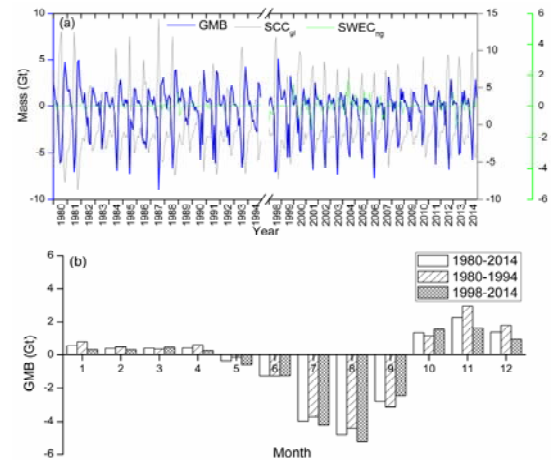
Fig.5 Monthly GMB (blue), SCCgl (gray) and SWECng (green) over the YZRB reconstructed during 1980-2014 (a); Mean GMB at each month of a year in different periods (b)

3.3.2 Reconstructed Inter-annual Variability of GMB over the YZRB

Based on Equation 3, the yearly GMB series during 1980-2014 was obtained over the YZRB (Fig.6).
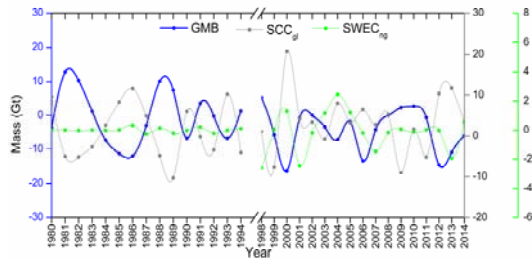
Fig.6 Yearly GMB (blue), SCCgl (gray), and SWECng (green) over the YZRB reconstructed during 1980-2014

Decreasing trends of GMB for YZRB in both periods 1980-1994 (-0.24 Gt/yr) and 1998-2014 (-0.18 Gt/yr) at monthly scale and its annual mean for periods of 1980-1994 (-0.26 ± 7.93 Gt/yr) and 1998-2014 (-4.36 ± 6.36 Gt/yr) (mean ± one standard deviation), respectively, were revealed. Correspondingly, it can be expected that precipitation (temperature) regimes should exhibit decreasing (an increasing) trend over GCE for the studied period, which may indirectly examine the reliability of the reconstructed GMB.

3.4 Indirect Evaluation of the Reconstructed GMB

3.4.1 Response of GMB to Precipitation and Temperature

Fig.7a presented annual precipitation over GCE of the YZRB, a general decreasing trend during 1980-2014 with annual precipitation fluctuated with an increasing trend (1.74 mm/yr) during 1980-1994 and following a significant decreasing trend during 1998-2014 at a level of 0.1, can be seen evidently. While for annual temperature, as exhibited in Fig.7b, a significant increasing trend occurred during 1980-2014, in particular, the change rate of annual mean temperature during 1998-2014 was larger than that during 1980-1994. The GMB of the YZRB was well corresponded to the temperature and precipitation changes in the studied periods under the context of climate changes.

3.4.2 Change of GCE Derived from LUCC

Fig.8 gives the spatial distribution of different land use types in different years, from which we can see that GCE had a significant decreasing trend from 1980 to 2015, especially in the east of the YZRB. The glacier areas in 1980, 1995, and 2015 were 10010.65 km^2, 8448.71 km^2, and 7668.73 km^2, respectively, which suggested about 15.6% decreasing (-1561.94 km^2)

during 1980-1995 and about 9.2% (-779.98 km^2) during 1995-2015, which is highly consistent with the continuous decreasing of GMB during 1980-1994 and during 1998-2014. Additionally, the decreased GCE primarily converted to unutilized land with a proportion of 41.8% during 1980-1994 and with a proportion of 37.9% during 1998-2014 through change detection statistics in ENVI software.
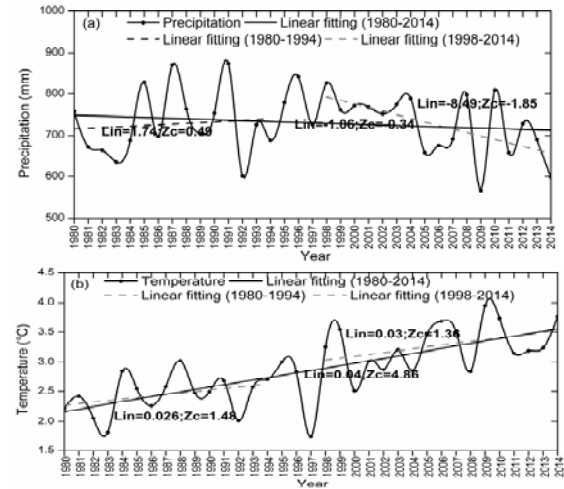
Fig.7 Inter-annual change trends of precipitation (a) and temperature (b) over the YZRB during 1980-2014. Lin denotes linear trend and Zc for Mann-Kendall test statistics
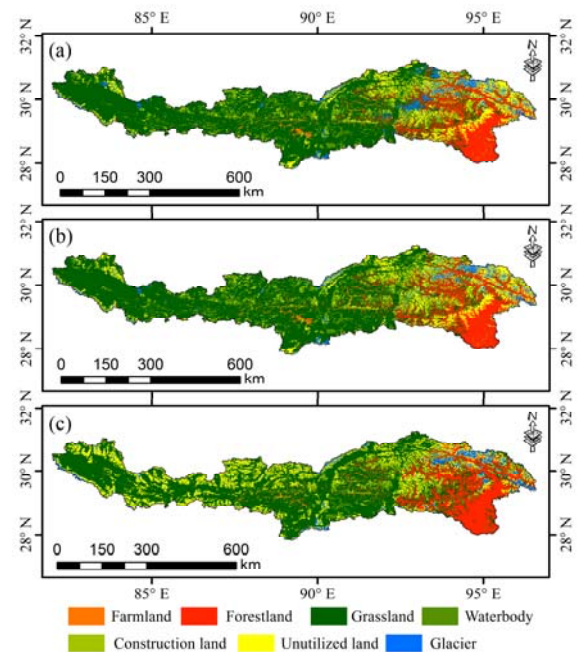
Fig.8 Comparison of GCE in LUCC for the year of 1980 (a), 1995 (b), and 2015 (c)

4 CONCLUSION

With GRACE-based TWSA and GLDAS datasets, the long-term seasonal and inter-annual variability of GMB were reconstructed over the YZRB during 1980-2014. High consistency among three GRACE-based monthly TWSA datasets with correlation coefficients ranging from 0.96 to 0.98 demonstrated the reliability of these two products. However, strongest negative correlations were found between TWSC-GRACE and TWSC-GLDAS with one year time lag from 2003 to 2014. For GMB within the YZRB reconstructed, generally less accumulation in cold months and more ablation in warm months during 1998-2014 than that during 1980-1994 characterized the general treads of GMB variations over the past few decades. Inter-annual variations of GMB presented a decreasing trend during both 1980-1994 and 1998-2014, but smaller GMB during the latter period than that during the former period furtherly revealed that glaciers have accelerated ablation over the YZRB during 1980-2014 under the background of increasing temperature and decreasing precipitation.

No doubt errors do exist in the reconstructed GMB series as presented in this study. Those errors might be resulted from the defects of simple regression model utilized in this study, or from the simulation uncertainty of hydrologic variables in GLDAS datasets, the instrument error and post-processing error of GRACE-based TWSA series, or even by the neglected groundwater change. However, we do believe the reconstructed GMB series and analysis results offer an opportunity and a new perspective for understanding the characteristics of GMB variations over the YZRB in the past few decades.

ACKNOWLEDGEMENTS

REFERENCES

Chen, J. L., Wilson, C. R., Blankenship, D., & Tapley, B. D. 2009. Accelerated Antarctic ice loss from satellite gravity measurements. *Nature Geoscience, 2*, 859-862.

Chen, M., Shi, W., Xie, P., Silva, V. B. S., Kousky, V. E., Wayne Higgins, R., & Janowiak, J. E. 2008. Assessing objective techniques for gauge-based analyses of global daily precipitation. *Journal of Geophysical Research: Atmospheres, 113*.

Dumont, M., Gardelle, J., Sirguey, P., Guillot, A., Six, D., Rabatel, A., & Arnaud, Y. 2012. Linking glacier annual mass balance and glacier albedo retrieved from MODIS data. *The Cryosphere, 6*, 1527-1539.

Feng, W., Lemoine, J. M., Zhong, M., & Hsu, H. T. 2014. Mass-induced sea level variations in the Red Sea from GRACE, steric-corrected altimetry, in situ bottom pressure records, and hydrographic observations. *Journal of Geodynamics, 78*, 1-7.

Guo, W., Liu, S., Xu, J., Wu, L., Shangguan, D., Yao, X., . . . Liu, Q. 2015. The second Chinese glacier inventory: data, methods and results. *Journal of Glaciology, 61*, 357-372.

Liu, Z., Yao, Z., Huang, H., Wu, S., & Liu, G. 2014. Land use and climate changes and their impacts on runoff in the Yarlung Zangbo river basin, China. *Land Degradation & Development, 25*, 203-215.

Nie, N., Zhang, W., & Deng, C. (2016). *Responses of water resource of the Yarlung Zangbo River Basin to climate changes and glacier-snow fluctuations in recent years.* Paper presented at the IOP Conference Series: Earth and Environmental Science.

Nie, N., Zhang, W., Zhang, Z., Guo, H., & Ishwaran, N. 2016. Reconstructed Terrestrial Water Storage Change (ΔTWS) from 1948 to 2012 over the Amazon Basin with the Latest GRACE and GLDAS Products. *Water Resources Management, 30*, 279-294.

Rodell, M., & Famiglietti, J. S. 2002. The potential for satellite-based monitoring of groundwater storage changes using GRACE: the High Plains aquifer, Central US. *Journal of Hydrology, 263*, 245-256.

Shen, Y., Feng, M., Zhang, H., & Gao, F. 2010. Interpolation methods of China daily precipitation data. *Journal of Applied Meteorological Science, 21*, 279-286.

Sirguey, P., Still, H., Cullen, N. J., Dumont, M., Arnaud, Y., & Conway, J. P. 2016. Reconstructing the mass balance of Brewster Glacier, New Zealand, using MODIS-derived glacier-wide albedo. *The Cryosphere, 10*, 2465-2484.

Swenson, S., & Wahr, J. 2006. Post-processing removal of correlated errors in GRACE data. *Geophysical Research Letters, 33*.

Yao, T., Li, Z., Yang, W., Guo, X., Zhu, L., Kang, S., . . . Yu, W. 2010. Glacial distribution and mass balance in the Yarlung Zangbo River and its influence on lakes. *Chinese Science Bulletin, 55*, 2072-2078.

Yi, S., & Sun, W. 2014. Evaluation of glacier changes in high‐mountain Asia based on 10 year GRACE RL05 models. *Journal of Geophysical Research: Solid Earth, 119*, 2504-2517.

Zeng, Z., Piao, S., Lin, X., Yin, G., Peng, S., Ciais, P., & Myneni, R. B. 2012. Global evapotranspiration over the past three decades: estimation based on the water balance equation combined with empirical models. *Environmental Research Letters, 7*, 014-026.

Zhu, C., Lu, Y., Shi, H., & Zhang, Z. 2017. Spatial and temporal patterns of the inter-annual oscillations of glacier mass over Central Asia inferred from Gravity Recovery and Climate Experiment (GRACE) data. *Journal of Arid Land, 9*, 87-97.

Net Primary Productivity Modelling and its Analysis of spatial and temporal patterns in Temperate Grassland, Northern China

Fen Zhao [1,2,3], Bin Xu [3,*], Xiuchun Yang [3], Lang Xia [3], Yunxiang Jin [3], Jinya Li [3], Jian Guo [3], Ge Shen [3]

1. Institute of Geographic Sciences and Natural Resources Research, Chinese Academy of Sciences，Beijing 100101, China

2. Graduate University of Chinese Academy of Sciences， Beijing 100049, China

3. Key Laboratory of Agri-Informatics of Ministry of Agriculture, Institute of Agricultural Resources and Regional Planning, China Academy of Agriculture Sciences, Beijing 100081, China

zhaof.15b@igsnrr.ac.cn; xubin@caas.cn; yangxiuchun@caas.cn; xialang2012@163.com; jinyunxiang@caas.cn;lijinya_caas@hotmail.com;guojianxiaobai@163.com;shenge_yanzhou@163.com

ABSTRACT - Precise and rapid estimation of grassland productivity has an important significance for evaluating regional ecological carrying capacity, utilizing natural resources reasonably. In this study, based on MODIS remote sensing data, meteorological data and ground measured data, the light utilization efficiency (LUE) parameter of CASA model was optimized, and the optimized model was used to estimate and analyze net primary productivity (NPP) and its spatio-temporal distribution of Xilingol Grassland between 2005 and 2014. The results indicated that: (Ⅰ) Maximum LUE was calculated to be 0.539 g_C.MJ^{-1} for Xilingol grassland according to the least error criterion. (Ⅱ) Measurement validation showed good performance of optimized model in research area, with R^2 of 0.72 and mean relative estimation error of 0.29. (Ⅲ) NPP of Xilingol grassland decreased from northeast to southwest gradually. Accordingly, the NPP in different grassland types was as follows: the eastern meadow grassland > the central typical grassland > the western desert grassland. (Ⅳ) The total annual NPP showed a rising trend during 2005-2014, increasing from 156.67 g_C.m^{-2}.a^{-1} in 2005 to 186.53 g_C.m^{-2}.a^{-1} in 2014. Precipitation and temperature were found to be the dominant climatic factors that controlled the interannual variability in NPP. In terms of research area, temperature appeared to control NPP only in regions where precipitation was scarce, in other words, the rise of temperature has little effect on NPP when precipitation was sufficient.

1 INTRODUCTION

Grassland ecosystem is one of the most important types of terrestrial ecosystems on the planet. As an important parameter of grassland ecosystem functioning and the carbon cycle, grassland NPP is the foundation of material cycle and energy flow, as well as the most direct indicator of grassland's ecological status and services (Ruppert et al, 2014). Global and regional estimation of grassland NPP is of great importance for the management and protection of grassland resource. Specially, the research of regional grassland production is importance of evaluating ecosystem carrying capacity, using and developing grassland resource reasonably, and providing decision support for grassland management departments.

Grassland NPP refers to the remainder subtracting autotrophic respiration from the total amount of organic matter fixed by grassland vegetation. A number of methods have been adopted to obtain grassland NPP, among of these, the method based on measured data is traditional and less used in view of time and energy consuming and non-spatial continuity. In the current research, model-based method is commonly applied for estimating grassland NPP. Models for grassland NPP estimate can be categorized into three groups: climate-related statistical models such as Miami model, Thornthwaite Memorial model, Chikugo model; process-based models, such as BIOME-BGC model, CENTURY model, TEM model, CARAIB model; light use efficiency models, such as CASA model, GLO-PEM model, C-Fix model, TURC model. Light use efficiency models based on remote sensing data, can estimate NPP in different spatio-temporal resolutions and explore dynamic changes in NPP. Compared with other models, it can simulate vegetation NPP more efficiently and accurately.

CASA (Carnegie-Ames-Stanford Approach) model is the most commonly used light use efficiency model for estimating grassland NPP, which fully considers the environment conditions and vegetation characteristics. In addition, it estimates NPP directly instead of subtracting autotrophic respiration from GPP, thus is relatively simpler and more efficient for calculating NPP. CASA model was developed based on Monteith's equation (Potter et al. 1993; Field et al.1995), using remote sensing data, meteorological data and ground data to simulate vegetation NPP. In recent years, there have been several studies into regional grassland NPP with CASA model (Bradford et al., 2005; Zhang et al., 2008). While previous researchers have mainly obtained model parameters from references, few studies have modified and optimized model parameters aimed at specific region. Additionally, due to lacking of measured data, model validation proved to be the issue. Therefore, more detailed analysis need to done aimed at specific ecosystem or region. The objectives of this study were to estimate and validate NPP of Xilingol grassland from 2005 to 2014 using optimized CASA model, and further analyze its spatio-temporal distribution.

2 Materials and Methods

2.1 Study area

This study was conducted in the Xilingol grassland, located in the central part of Inner Mongolia at 41°35′ ~ 46°46′ N, 111°09′ ~ 119°58′ E. Xilingol grassland is a typical temperate grassland of northern China and the sensitive zone in response to climate change, with an arid and semiarid temperate continental monsoon climate. The elevation varies from 800 m to 2000 m, with higher elevation in South than that in North as a whole. The total area of the Xilingol grassland is 192,512 km^2, accounting for 95.03% of the total land area of Xilingol. The map of grassland resources in China at a 1:1,000,000 scale shows that the vegetation types in the grassland are meadow grassland, typical grassland and desert grassland ranging from east to west (Fig.1).

2.2 Data

2.2.1 Field Sampling Data

The field sampling was conducted in ungrazing region every July and August from 2005 to 2014, to obtain the maximal aboveground biomass in the growing season. The sampling sites, with an area of at least 1 km^2, were chosen to represent typical vegetation communities. To obtain the actual aboveground biomass of herbs, all the aboveground plants in three or four plots (1 m × 1 m) were harvested to measure

their fresh weight. As to shrubs in the homogeneous grassland, one plot (10 m × 10 m) was sampled to obtain the aboveground biomass, then the sum of the weights in three or four plots were calculated. Finally, by drying fresh grass in the laboratory and averaging the dry weight of both the herbs and shrubs in three or four plots at the sampling site, the field sampling dataset can be obtained. In view that there were few unnatural disturbances in ungrazing region, the aboveground biomass was transferred into aboveground NPP by the conversion coefficient of 0.45. The total NPP was estimated based on aboveground NPP and the ratio between the underground and aboveground NPP. The estimated total NPP could be used for model parameter optimization and model validation.
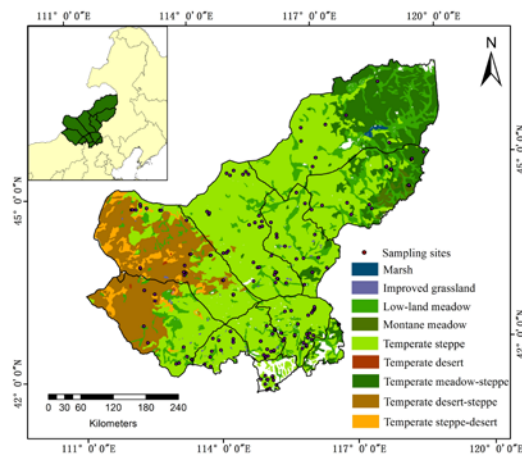
Fig.1. Location of the study area and grassland types

2.2.2 Remote Sensing Data

In this study, MODIS 8-day composited surface reflectance product (MOD09A1) with a resolution of 500 m was selected to invert the parameters for CASA model, MODIS 8-day composited FPAR product (MOD15A2) and PSNnet (net photosynthesis) product (MOD17A2) with a resolution of 1 km were used for model validation. There were seven bands in 8-day composited surface reflectance product, of which, band 1 (Red 620~670nm) and band 2 (NIR 841~876nm) were used to calculate the Normalized Difference Vegetation Index (NDVI), band 2 (NIR 841~876nm) and band 6 (NIR 841~876nm) were used to calculate the Land Surface Water Index (LSWI).

2.2.3 Meteorological Data

The meteorological data used in this study was provided by the China Meteorological Data Sharing Service System, including ground climatological daily

dataset and radiation daily dataset. Few meteorological stations in the Xilingol grassland, especially radiation stations, couldn't meet the conditions of interpolation, so 35 ground meteorological stations in the the Xilingol grassland and surrounding districts were selected for interpolation after taking full consideration of stations distribution. To be consistent with the remote sensing data, these data should be 8-day composited as well, then ANUSPLINE software was used in the interpolation process of the 8-day composited meteorological data. In consideration of the model demand, the outputs from the ANUSPLINE software were 8-day mean temperature, 8-day precipitation, 8-day solar radiation with 500 m spatial resolution.

2.3 CASA model

CASA model is the most commonly used light use efficiency model, in which vegetation NPP is mainly determined by vegetation absorbed photosynthetic Active Radiation (APAR) and light use efficiency (ε):

$$NPP(x,t) = APAR(x,t) * \varepsilon(x,t) \tag{1}$$

$$APAR(x,t) = SQL(x,t) * 0.5 * FPAR(x,t) \tag{2}$$

$$\varepsilon(x,t) = T_{\varepsilon 1}(x,t) * T_{\varepsilon 2}(x,t) * W_{\varepsilon}(x,t) * \varepsilon_{max} \tag{3}$$

where $NPP(x, t)$ is the net primary productivity (g_C m^{-2} 8-day^{-1}) fixed by green vegetation at pixel x in t time, $APAR(x, t)$ is the amount of absorbed photosynthetic active radiation (MJ m^{-2} 8-day^{-1}) at pixel x in t time, and $\varepsilon(x, t)$ represents the actual light use efficiency (g C MJ^{-1}) of pixel x in t time. $SOL(x, t)$ is total solar radiation (MJ m^{-2}) of pixel x in t 8-day, $FPAR(x, t)$ is the absorbed fraction of photosynthetic active radiation (PAR) absorbed by vegetation canopy, constant 0.5 stands for the fraction of total solar radiation that can be used by vegetation (0.4 ~ 0.7μm). $T_{\varepsilon 1}(x,t)$ and $T_{\varepsilon 2}(x,t)$ are environmental stresses which reflect the reduction of light use efficiency caused by temperature factor, $W_{\varepsilon}(x,t)$ is the environmental stress which indicates the reduction of light use efficiency caused by moisture factor, ε_{max} is the maximum light use efficiency in an ideal condition.

2.3.1 FPAR

The original CASA model used the MODIS/NDVI to invert FPAR, but this algorithm cannot accurately calculate the actual ground vegetation FPAR. Although the FPAR has a significantly linear relationship with both NDVI and RVI, previous research has proved that estimations using the FPAR - NDVI relationship have tended to estimate FPAR on the high side, while estimations using the FPAR - RVI relationship have tended to estimate FPAR on the low side. Therefore,

the above two methods were combined to optimize traditional estimation, and the mean of the two FPAR values calculated using NDVI and RVI value was taken for FPAR estimation in this study, as follows:

$$FPAR(x,t) = \frac{(NDVI(x,t) - NDVI_{min}) * (FPAR_{max} - FPAR_{min})}{(NDVI_{max} - NDVI_{min})} + FPAR_{min} \tag{4}$$

$$FPAR(x,t) = \frac{(SR(x,t) - SR_{min}) * (FPAR_{max} - FPAR_{min})}{(SR_{max} - SR_{min})} + FPAR_{min} \tag{5}$$

$$SR(x,t) = \frac{1 + NDVI(x,t)}{1 - NDVI(x,t)} \tag{6}$$

$$FPAR(x,t) = \frac{FPAR(x,t)_{NDVI} + FPAR(x,t)_{SR}}{2} \tag{7}$$

where $FPAR_{max}$ and $FPAR_{min}$ are constants with values of 0.950 and 0.001 respectively; $NDVI_{max}$ and $NDVI_{min}$ are the maximum and minimum Normalized Difference Vegetation Index respectively; and SR_{max} and SR_{min} are the maximum and minimum Ratio Vegetation Index respectively.

2.3.2 Environmental stresses

Temperature stress factor $T_{\varepsilon 1}(x,t)$ refers to the effect to vegetation productivity caused by biochemical function under the condition of low temperature and high temperature, Temperature stress coefficient $T_{\varepsilon 2}(x,t)$ refers to the diminishing tendency of light use efficiency when environment temperature $T(x,t)$ changes from optimum temperature $T_{opt}(x,t)$ to maximum or minimum temperature, can be calculated as follow:

$$T_{\varepsilon 1}(x,t) = 0.8 + 0.02 * T_{opt}(x) - 0.0005 * [T_{opt}(x)]^2 \tag{8}$$

$$T_{\varepsilon 2}(x,t) = \frac{1.184}{1 + e^{0.2*[T_{opt}(x) - 10 - T(x,t)]}} * \frac{1}{1 + e^{0.3*[-T_{opt}(x) - 10 + T(x,t)]}} \tag{9}$$

Moisture stress factor (W_{ε}) reflects the water influence on photosynthesis, was usually estimated based on the amounts of potential evapotranspiration and actual evapotranspiration in previous research. In this study, we proposed an simple approach using a satellite-derived water index to estimate W_{ε}. Short wave infrared band (SWIR) is sensitive to the soil water and vegetation water content, so near infrared band (NIR) and short wave infrared band (SWIR) are combined to invert land surface water index (LSWI) (Xiao et al., 2005). LSWI values range from -1 to 1, with the increase of soil water or vegetation water content, SWIR absorption increases and reflection decreases, resulting in LSWI values increased.

$$W_\varepsilon = \frac{1 + LSWI}{1 + LSWI_{max}} \tag{10}$$

$$LSWI = \frac{\rho_{NIR} - \rho_{SWIR}}{\rho_{NIR} + \rho_{SWIR}} \tag{11}$$

where $LSWI_{max}$ is the maximum LSWI within the vegetation growing season for individual pixels, ρ_{NIR} and ρ_{SWIR} are the reflectivity in NIR and SWIR band respectively.

2.3.3 ε_max

As the critical parameter of CASA model, maximum light use efficiency is affected by various factors (e.g. geographic location, climate, vegetation type). Based on the least error criterion between the observed and estimated NPP, we obtained the optimum ε_{max} for the northern temperate grassland in China (Yu et al., 2009).

$$E(x) = \sum_{i=1}^{j} (m_i - n_i \varepsilon_{max})^2 \tag{12}$$

Where, $E(x)$ is the error between the observed and estimated NPP, j is the number of observed NPP, m_i represents observed NPP of the i sampling plot, and $n_i = APAR(x) \times T_\varepsilon(x) \times W_\varepsilon(x)$. Equation 12 can also be expanded as follows:

$$E(x) = \sum_{i=1}^{j} m_i^2 - 2\sum_{i=1}^{j} m_i n_i \varepsilon_{max} + \sum_{i=1}^{j} n_i^2 m_i^2 \tag{13}$$

which is hyperbolic equation, $E(x)$ is minimum when maximum light utilization efficiency was calculated to be 0.539 g_C.MJ^{-1} for Xilingol grassland according to the above formula.

3. Results

3.1 Validation of the CASA model

Using the reserved observed data (approximately 20% of the total samples), we calculated the root-mean-square error (RMSE) and mean relative estimation error (REE) between the estimated NPP and the actual NPP to evaluate the accuracy of the model. In addition, we used actual NPP for validating the precision of the MODIS 8-day NPP. It turned out that R^2 between estimated NPP and the actual NPP was 0.72 (P < 0.001), higher than R^2 between MODIS NPP and the actual NPP (Fig.2). By calculating the mean relative estimation error (REE) between estimated NPP and the actual NPP, we concluded that accuracy of optimized model could reach 71%, superior to the performance of MODIS NPP in study area.
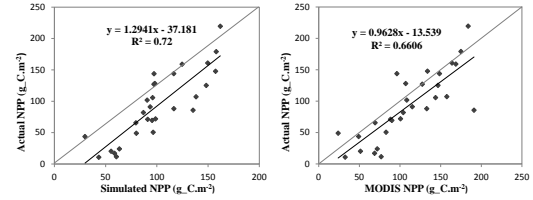
Fig.2. The relationships between actual and simulated/MODIS NPP

3.2 Spatial distribution of NPP

During 2005 to 2014, the annual mean NPP of Xilingol grassland estimated by CASA model was 161.23 g_C.m^{-2}.a^{-1} with a remarkable spatial heterogeneity. As can be seen from the spatial distribution map, NPP decreased from northeast to southwest gradually, the region with NPP great than 400 g_C.m^{-2}.a^{-1} mainly distributed in northeast of Xilingol, NPP ranged from 100 to 200 g_C.m^{-2}.a^{-1} in the central region, and was generally less than 100 g_C.m^{-2}.a^{-1} in the southwest region (Fig.3). As a whole, NPP in study area mostly focused on the range from 50 to 200 g_C.m^{-2}.a^{-1}, accounting for 80 percent of total pixels. However, there was a small amount of pixels with NPP great than 400, below 2%.
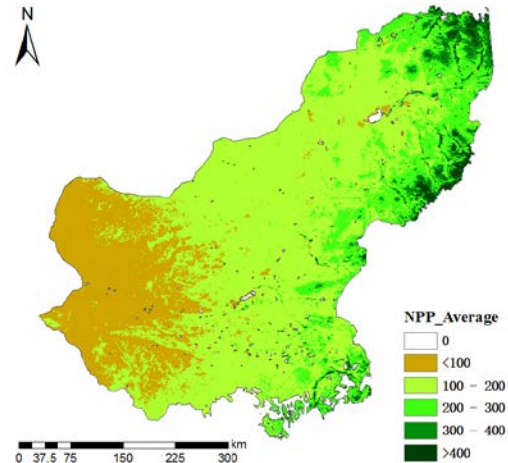
Fig.3. Spatial distribution of annual average NPP during 2005 to 2014

Other than obvious spatial heterogeneity, vegetation productivity differed in biomes. On the whole, the average annual NPP of different grassland types followed an order of: eastern meadow steppe > middle temperate steppe > western desert steppe. Specifically, the average annual NPP of montane meadow was 413.97 g_C.m^{-2}.a^{-1}, far above the annual NPP of temperate meadow-steppe (246.38 g_C.m^{-2}.a^{-1}). Temperate steppe-desert had the lowest productivity,

with average annual NPP of 80.02 g_C.m^{-2}.a^{-1}. The annual NPP in montane meadow, emperate meadow-steppe and low-land meadow were higher than the average value of study area, while temperate steppe, temperate meadow-steppe, temperate steppe-desert and temperate desert owned lower annual NPP compared with average level.

3.3 Interannual variation in NPP

The annual fluctuation of the NPP was observed, ranging from 120.01 g_C.m^{-2}.a^{-1} in 2007 to 187.57 g_C.m^{-2}.a^{-1} in 2008 (Fig.4). During 2005 to 2014, NPP presented increasing trend with a rate of 3.89 g_C.m^{-2}.a^{-1}. During the years 2008, 2012, 2013 and 2014, annual NPP of temperate grassland was higher than multi-year average, with values of 193.49 g_C m^{-2} yr^{-1}, 190.83 g_C m^{-2} yr^{-1}, 178.08 g_C m^{-2} yr^{-1} and 193.84 g_C m^{-2} yr^{-1}, respectively.
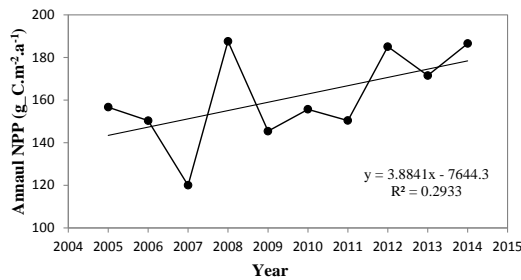
Fig.4. Interannual variation of NPP during 2005 to 2014

As we know, precipitation and temperature are the two most commonly factors to NPP on interannual scales. By analyzing the interannual variations of these two climate variables and correlation with NPP, we found precipitation had a higher correlation with NPP than temperature in temperate grassland. During ten years, precipitation showed a significant increasing trend in accordance with NPP. There was relatively little precipitation in 2007, thus lower productivity compared with other years. Although precipitation in 2012 was far above that in 2008, there was lower NPP in 2012 than 2008. The reason for this phenomenon was that low temperature counteracted some effect of high precipitation on NPP in 2012. This suggested that the combined effects of precipitation and temperature were responsible for the annual variations in NPP on northern temperate grassland.

The spatial pattern of NPP trends during 2005-2014 was shown in Fig.5, of which, only about 10% grid cells showed negative annual NPP trends. NPP exhibited increasing trend in most parts of Xilingol grassland, and significantly decreased in southwest of

East Ujimqin and West Ujimqin, as well as Xilinhot. By grassland types, the NPP trend of temperate meadow-steppe (4.26 g_C m^{-2} yr^{-1}), improved grassland (4.09 g_C m^{-2} yr^{-1}) and temperate steppe (3.98 g_C m^{-2} yr^{-1}) were higher than overall level in study area, while annual NPP in montane meadow (2.08 g_C m^{-2} yr^{-1}) and temperate desert (2.83 g_C m^{-2} yr^{-1}) showed relatively low tendency.
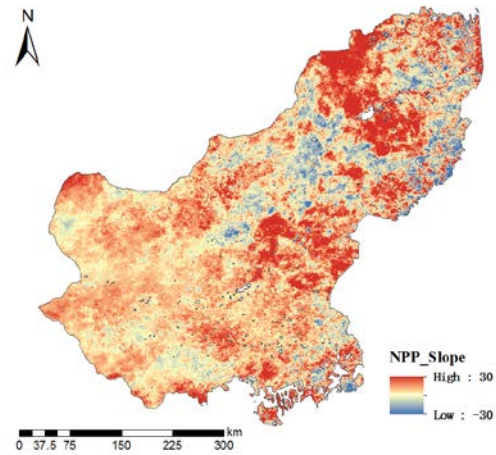
Fig.5. Spatial distribution of NPP interannual tendency during 2005 to 2014

3.4 Temporal variation of NPP within the year

Based on 8-day NPP of multi-year average, we conducted that the growing season ranged from mid-April to early October in the northern temperate grassland, and NPP peaked in about 209th day with 8-day NPP 12.38 g_C m^{-2}. Xilingol grassland began to turn green in mid-April and accumulate biomass with the temperature and precipitation increasing. Up until early October, grassland entered the period of wilt, and productivity declined.
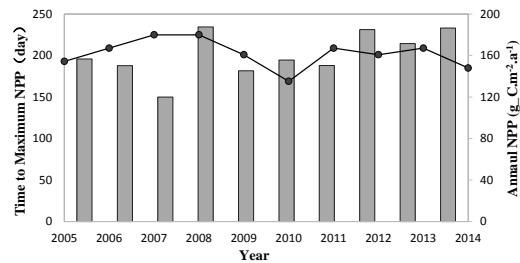
Fig.6. Temporal variation of 8-day NPP from 2005 to 2014

In view of the difference in climate factor, the time to maximum NPP in different years was inconsistent (Fig.6). For example, the maximum NPP occurred in

about August 13th for the year 2007, while June 18th in 2010. The variation curve of 8-day NPP was consistent with that of 8-day precipitation, especially in growing season. However, temperature played a more important role than precipitation in the period of greening up in temperate grassland. The temperature of time to greening up and wilting tended to zero, this also meant that vegetation in northern temperate grassland accumulated biomass when temperature above zero.

4. Discussions and Conclusions

In this study, we optimized maximum light use efficiency for improving the simulation accuracy of regional productivity. Maximum light utilization efficiency was calculated to be 0.539 g_C.MJ^{-1} for Xilingol grassland according to the least error criterion. Measurement validation showed good performance of the optimized model in research area, with an overall coefficient of determination of 0.72 and mean relative estimation error of 0.29. Due to the shortage of measured data, the value of maximum light use efficiency has always been controversial, our results will be a good reference on the research about temperate grassland.

The combined effects of precipitation and temperature were responsible for the annual variations in NPP on northern temperate grassland. Specifically, temperature appeared to play an even greater role in NPP for the regions where precipitation was scarce, in addition, the rise of temperature has little effect on NPP when precipitation was sufficient. In other words, sufficient precipitation could counteract some effect of high temperature. As to the sequential variation within the year, the curve of 8-day NPP was consistent with that of 8-day precipitation, especially in growing season. However, temperature played a more important role than precipitation in the period of greening up in temperate grassland. The temperature of time to greening up and wilting tended to zero, this also meant that vegetation in northern temperate grassland accumulated biomass when temperature above zero.

REFERENCES

Bradford J. B., Hicke J. A., Lauenroth W. K.. The relative importance of light-use efficiency modifications from environmental conditions and cultivation for estimation of large-scale net primary productivity. Remote Sensing of Environment, 2005, 96(2): 246-255.

Field, C.B., Randerson J.T., Malmstrom C.M., et al. Global net primary production: Combining ecology and remote sensing. Remote Sensing of Environment, 1995. 51(1): 74-88.

Olson, R. J., Johnson, K. R., Zheng, D. L., and Scurlock, J. M. O., 2001, Global and Regional Ecosystem Modeling: Databases of Model Drivers and Validation Measurements. (Environmental Sciences Division)

Potter C.S., Randerson J.T., Field C.B., et al.. Terrestrial ecosystem production A process model based on global satellite and surface data. Global Biogeochemical Cycles, 1993, 7(4): 811–841.

Ruppert J.C., Linstadter A.. Convergence between ANPP estimation methods in grasslands - A practical solution to the comparability dilemma. Ecological Indicators, 2014(36): 524-531.

Xiao X., Zhang Q.Y., Scott S., et al. Satellite-based modeling of gross primary production in a seasonally moist tropical evergreen forest. Remote sensing of environment, 2005, 94(1): 105-122.

Yu D., Shao H., Shi P., et al. How does the conversion of land cover to urban use affect net primary productivity? A case study in Shenzhen city, China. Agricultural and Forest Meteorology. 2009, 149(11): 2054–2060.

Zhang Y., Yu Q., Jiang J., et al. Calibration of Terra/MODIS gross primary production over an irrigated cropland on the North China Plain and an alpine meadow on the Tibetan Plateau. Global Change Biology, 2008, 14(4): 757–767.

Remote sensing monitoring of greenup date and its correlation with meteorological factors in the Xilingol grasslands of northern China

J. Guo[1,2], X. Yang[1], J. Niu[2], Y. Jin[1], B. Xu[1], G. Shen[1], W. Zhang[1], and Y. Zhang[1]

[1] *Key laboratory of Agri-informatics of the Ministry of Agriculture, Institute of Agricultural Resources and Regional Planning, Chinese Academy of Agricultural Sciences, Beijing 100081, PR China;*

[2] *School of Ecology and Environment, Inner Mongolia University, Hohhot 010021, PR China;*
guojianxiaobai@163.com, yangxiuchun@caas.cn

ABSTRACT -*This study examined greenup in the Xilingol grasslands of northern China. A double logistic function was used to reconstruct a time series of SPOT-VEGETATION (VGT) Normalized Difference Vegetation Index (NDVI) from 1999 to 2012. The dynamic threshold method was used to monitor the greenup date by remote sensing. 68% of the ground monitoring results were consistent with the remotely-sensed greenup date. For the sample plots, the root-mean-square error (RMSE) of the greenup date measured by remote sensing was 8.7 d. The greenup date of temperate grassland, comprising 66.4% of the total grassland area, is usually in mid to late April, with some variability (standard deviation = 18.45 d). Based on the linear trend analysis of each pixel, only 13.9% of the pixels showed a significant change over the 14-year time series. However, the linear trend increased from the southeast to the northwest, and 57% of the pixels demonstrated earlier greenup. Across the whole region, the linear trend showed an average rate of change of -1.5 d/10 a. The correlations at seven meteorological stations were statistically significant (p<0.05). The average correlative value of deterministic factors was 0.54. The partial correlation coefficients between greenup date and temperature prior to seedling establishment were negative at five stations, among which three stations exhibited significant negative correlations. Partial correlation coefficients between greenup date and precipitation prior to seedling establishment were negative at all eight stations, and five of these exhibited significant negative correlations.*

1 INTRODUCTION

Global warming has led to observable changes in the greenup date of grassland vegetation (Myneni, 1997). In recent years, researches on climate change have become more and more important, and scholars have paid more and more attention to the research on phenology. Phenology has become the frontier fields of global climate change research. The greenup date is the beginning of plant growth season, which is one of the important stages, and plays an important role in plant growth. Remotely-sensed greenup date reflects the regional scale surface vegetation growth. It is regional vegetation phenology calculated according to time series vegetation index, based on the change of vegetation index curve.

Traditional phenology has the characteristics of objective and accurate. But in addition to some countries in Europe, most of the countries and regions lack of wide coverage, long time series of plant phenology observation data. It was difficult to analyse large-scale vegetation phenology (Chen and Wang, 2009). Remote sensing has been applied to the monitoring and research of vegetation phenology, which has broadened the means and field of vegetation phenology research and promoted the study of global

change (Schwartz, 1998).Remote sensing data has been widely used in the study of large-scale vegetation activities, especially for the relatively simple structure of grassland ecosystem.

Time series data based on high time resolution remote sensing data (such as NOAA/AVHRR, MODIS, SPOT-VGT) can accurately reflect the large scale vegetation phenological characteristics (Wei, 2013).Phenology initially applied mainly in the service of agricultural production development. The development of remote sensing technology to agricultural phenology provides a new monitoring method. Remote sensing monitoring has played an important role in agriculture season forecast, crop's monitoring and control of plant diseases and insect pests (Zhang, et al., 2002; Friedl, et al., 2002; Mark, et al., 2001).Vegetation index has been widely used in vegetation classification, the dynamic changes of vegetation, vegetation phenological study, etc. (Hou, et al., 2004; Walker, et al., 2014; Nan, et al., 2012; Hmimina, et al., 2013).

At present, vegetation phenological studies has focused on the effects of climate warming on vegetation (Piao and Fang, 2003; Xu, et al., 2015). More and more researchers began to pay close attention to vegetation

phenology, but under the background of global climate change and the shortage of coverage phenological observation station, herbaceous vegetation phenology researches were relatively insufficient, lacked of large scale grassland phenological monitoring research based on remote sensing.

China, as a country of abundant grassland resources, possesses around 400,000,000 hectares of various natural grasslands, which account for about 41.7% of China's total land area. A deeper understanding of the spatiotemporal characteristics of these changes and their response to climate factors is of great importance in guiding the start time of grazing and in helping explore the effects of the grassland ecosystem on the global carbon cycle. Using remote sensing methods, the greenup date of grassland vegetation monitoring was characterized by rapidness and broad coverage, and has a prospect of wide applications.

2 MATERIALS AND METHODS

2.1 Study area

Xilingol League is located in the central part of Inner Mongolia, between 41°35' and 46°46'N and 111°09' and 119°58'E. This area comprises natural pastures that are among the highest in quality in northern China, and the total grassland area is 192,512 km^2, representing 95.03% of the total area of the region. The Xilingol grassland is primarily dominated by temperate meadow steppe, temperate steppe and temperate desert steppe (Fig.1). The league has a wide range of grassland types, some continuity in spatial distribution and certain typicality and completeness in type. Therefore, the study area is representative and can better study the characteristics of remote sensing phenology.
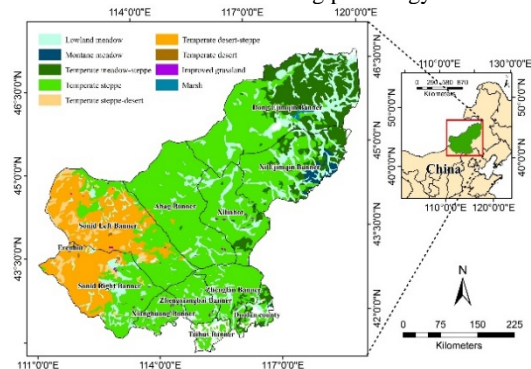
Fig.1. The location map of Xilingol League, China

2.2 Dataset

The remote sensing data were SPOT VGT S10 products with a 1km spatial resolution for the period from 1999 to 2012 from the VITO（http://free.vgt.vito.be/）. The NDVI was developed using the Maximum Value

Composition (MVC). A double logistic function was used to reconstruct the NDVI time series.

Ground-based monitoring greenup date data came from Grassland Monitoring and Supervision Center Ministry of Agriculture, PR China and the Xilinhot Meteorological Experimental Station for Animal Husbandry. The former included 162 sample plots, 426 quadrats from 2010-2012 distributed in Sonid Right Banner, Boarder Yellow Banner, Xilinhot and Dong Ujimqin Banner. The later included typical species greenup date like *Leymus chinensis* and *Stipa krylovii* from 2000-2012.

Meteorological data used in this study included temperature and precipitation data were downloaded from Climatic Data Center, National Meteorological Information Center, China Meteorological Administration (http://data.cma.cn). There are eight national weather stations in the study area. Because there were some abnormal data value and the missing value, we need to do some data quality control work like time anomaly test, space anomaly value test, high and low outliers test, missing value substitution, etc.

2.3 Determination of vegetation greenup date

TIMESAT is a software package that can analyse remote sensing time series data (Jönsson, 2004). It can filter and reconstruct NDVI time series and then extract the vegetation greenup date. TIMESAT includes three methods of data reconstruction such as Savitzky Golay filter (S-G), Asymmetric Gaussian function filter (A-G) and Double Logistic function filter (D-L). By importing NDVI time series data into the TIMESAT software, we can check every pixel`s reconstructed results in the preview data interface. We chose some representative area in temperate meadow steppe, temperate steppe and temperate desert steppe and test different filtering method to reconstruct NDVI time series.

We found D-L method was similar to A-G method and S-G method considered the peak more. D-L method and A-G method could achieve NDVI time series curve smoothing, meanwhile too much information would not lose. D-L method and A-G method had similar reconstruct result which were better than S-G method. This paper selected D-L method to reconstruct NDVI s time series.

Threshold method is a high efficient method by defining a threshold size. Greenup date results extracted by this method is relatively accurate, but it was easy to receive subjective influence for different researchers and threshold values. Comparing with fixed threshold method, dynamic threshold method had better practicability in spatiotemporal characteristics.

We used the following dynamic threshold method model:

$$NDVI_{lim} = (NDVI_{max} - NDVI_{min}) \times C \quad (1)$$

NDVI$_{lim}$ is the dynamic threshold; and NDVI$_{max}$ and NDVI$_{min}$ are respectively the maximum and minimum NDVI values in the annual NDVI cycle; C is a coefficient.

Combined with the ground-based monitoring data, considering distribution of extract the greenup date after a large number of tests, we used 25% threshold to extract the greenup date.

3 RESULTS

3.1 Spatial-temporal pattern of grasslands greenup date in Xilingol league

Xilingol League grassland area is large and the meteorological factors distribution has obvious spatial differences. Due to climate change and human activities, the grassland greenup date has certain change rules (Chen, et al., 2005). A lot of research has shown that this area remotely-sensed greenup date had advanced trend. But the change trend of vegetation greenup date in space distribution was complex and regional heterogeneity.

3.1.1 Verification of the remotely-sensed greenup date monitoring results

The remotely-sensed greenup date monitoring results were verified using data derived from ground-based monitoring of 162 sample plots from 2010 to 2012, among which 11 sample plots belongs to the outliers. After eliminating these 11 sample plots, we used 151 samples plots for verification of the remotely-sensed greenup date monitoring results. 68% of the ground monitoring results were consistent with the remotely-sensed greenup date. 7 sample plots remotely-sensed monitoring results differed by 30d from ground-based monitoring results, among which 5 sample area belonged to the temperate desert steppe. 22 sample plots remotely-sensed monitoring results differed by 20d from ground-based monitoring results, among which 13 sample area belonged to the temperate desert steppe. We found in temperate desert steppe the threshold value for monitoring greenup date was not high accuracy. The Root Mean Square Error (RMSE) is used to evaluate the effectiveness of the extraction method. RMSE represents the deviation between the remotely-sensed ground-based monitoring results and reflects the accuracy of the dynamic threshold method.

The calculation formula of RMSE is as follows:

$$RMSE = \sqrt{\frac{\sum_1^n \left(O_i - P_i\right)^2}{n}} \qquad (2)$$

n is the total number of samples, and O$_i$ is the remotely-sensed monitoring greenup date, and P$_i$ is the ground-based monitoring greenup date.

For the sample plots, the RMSE of the greenup date measured by remote sensing was 8.7d. The time series data interval used in this paper is 10d, so it was reasonable and feasible to extract the remote sensing monitoring results in the study area through the dynamic threshold method.

The remotely-sensed greenup date monitoring results were also verified using ground-based monitoring data derived from the Xilinhot meteorological experimental station for animal husbandry. After eliminating outliers and missing values, we found 11 among 17 sample plots results were consistent with the remotely-sensed greenup date. From dominant species verification results, the accuracy was about 69%. So dominant species greenup date could better represent the region greenup date. When working in the field observation, quadrat`s greenup date could be judged according to dominant species.

3.1.2 Spatial patterns of vegetation remotely-sensed greenup date

According to the spatial pattern of the multi-year mean remotely-sensed greenup date (Fig.2), the greenup date in most areas occurred between early April and mid May. They were delayed from the south to the north. The spatial pattern of vegetation growth was affected by complex meteorological factors. Vegetation was sensitive to water and heat conditions during growth in Xilingol league grasslands. The higher temperature and more precipitation during growth season, the earlier vegetation greenup.
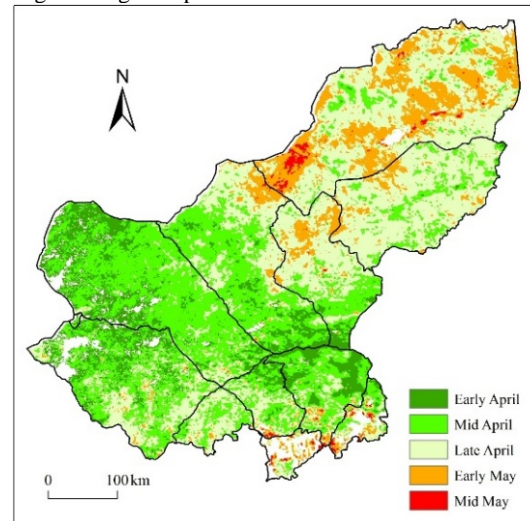
Fig.2 Mean greenup date during 1999-2012

Tab.1 shows the multi-year mean greenup date of every grassland type. Temperate desert steppe greenup date concentrated in early April and mid April, mainly distributed in central and north Sonid Left Banner and northwest Sonid Right Banner. Temperate steppe greenup date concentrated in mid April and late April,

mainly distributed in southeast Sonid Right Banner, east Sonid Right Banner, Abag Banner, Xilinhot, west West Ujimqin Banner, local west East Ujimqin Banner, Xianghuang Banner, Zhengxiangbai Banner and Zhenglan Banner. Temperate meadow steppe greenup date concentrated in late April and early May, mainly distributed in central and north Sonid Left Banner and northwest Sonid Right Banner.

Tab.1 Mean greenup date of every grassland type (%)

Mean greenup date	early April	mid April	late April	early May	mid May
temperate desert steppe	35.88	53.57	10.18	0.36	0.02
temperate steppe	9.2	36.39	42.49	10.93	0.99
temperate meadow steppe	1.46	13.06	59.97	24.99	0.51

3.1.3 Spatial patterns of trends in vegetation remotely-sensed greenup date

Linear trend of greenup date research(Fig.3) showed that 57% of pixels were advanced, 43% of pixels were delayed, the average change trend was -1.5d/10a, 8% of pixels` trend were significant advanced, 5.9% of pixels` trend were significant delayed. Linear trend increased from southeast to northwest, overall, the role of climate change on Xilingol league area grassland has promote greenup date in advance. The trend in Warm meadow steppe was small, about 80% of the pixels` trend were within ±10d/10a, 43% of pixels` trend in warm grasslands and warm desert grasslands were greater than 10d/10a .
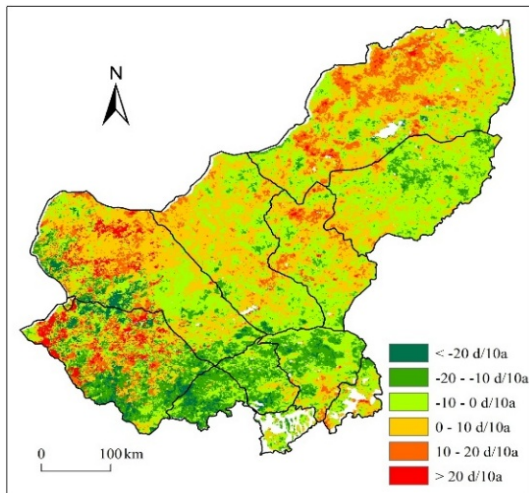
Fig. 3 The greenup date trend

3.2 Remotely-sensed greenup date in relation to meteorological factors

Xilingol league area grasslands greenup date were significant negative correlation with the temperature and precipitation (Tab. 2). Specifically, the average of greenup date and temperature of partial correlation coefficient was -0.18, 5 sites were negatively correlated, 3 sites were significant negative correlated. The average of greenup date and precipitation of partial correlation coefficient was -0.58, 8 sites were negatively correlated, 5 sites were significant negative correlated. Most of the sites, temperature and precipitation worked at the same time. The average regression coefficient between greenup date and temperature and precipitation was 0.54, 7 sites were significantly related.

Tab. 2 The partial correlation and regression coefficient of greenup and temperature and precipitation

meteorological stations	partial correlation		regression coefficient
	temperature	precipitation	
East Ujimqin Banner	-0.386	-0.743[**]	0.423[*]
Erenhot	0.853[**]	-0.663	0.648[*]
Naran-Bulag	-0.69[**]	-0.165	0.502[*]
Abag Banner	0.102	-0.65[**]	0.278
Sonid Left Banner	0.408	-0.862[**]	0.686[**]
Zhu Rihe	-0.683[**]	-0.665[*]	0.518[*]
West Ujimqin Banner	-0.89[**]	-0.097	0.654[*]
Xilinhot	-0.162	-0.825[**]	0.606[**]

** and * indicate that the correlation is significant at the 0.01 and 0.05 levels, respectively.

4 CONCLUSION AND DISCUSSION

4.1 Conclusion

We monitored the grassland greenup date through 25% dynamic threshold method in Xilingol league. The accuracy was 68% through 162 sample plots of ground monitoring data during 2010 to 2012, the remotely-sensed greenup date `s RMSE was 8.7 days.

The greenup over this area occurred between early April and mid May. They were delayed from the south to the north. Linear trend of greenup date research showed that 57% of pixels were advanced, the average

change trend was -1.5d/10a, 13.9% of pixels` trend were significant changed. Linear trend increased from southeast to northwest, overall, the role of climate change on Xilingol league area grassland had promoted greenup date in advance. The trend in warm desert grasslands were greater than in Warm meadow steppe.

Collectively, these results demonstrate that increasing precipitation and higher temperatures can advance the greenup date. Further analysis showed that, in relatively wet regions, increase in temperature promoted greenup, while the effect of precipitation was more important in dry regions.

4.2 Discussion

The datasets used in the present study were remote sensing data and ground observed data. The nature of the remote sensing information determines that there is uncertainty in data acquisition, processing, and analysis. For ground observed data, such as vegetation greenup date, there is relatively strong subjectivity in the estimation process, and different persons may obtain different greenup date. Thus, there is also uncertainty in the ground observed data. Therefore, it is crucial to eliminate the data uncertainty as much as possible.

The ground verification sample pilots distributed unevenly. Some areas had no observation data and some observation data of region may not have continuous data. For the high accuracy monitoring greenup date, it is necessary to make more continuous observations.

5 REFERENCES

Chen, X. Q., Hu, B, Yu, R., 2005, Spatial and Temporal Variation of Phenological Growing Season and Climate Change Impacts in Temperate Eastern China. *Global Change Biology*, 11, 1118~1130.

Chen, X. Q., and Wang L. H., 2009, Progress in Remote Sensing Phenological Research. *Progress in Geography*, 1, 33-40.

Friedl, M, A, Mclver D K, Hodges, J., 2002, Global land-cover mapping from MODIS: algorithms and early results. *Remote Sensing of Environment*, 83, 287-302.

Hmimina, G., Dufrene, E., Pontailler, J. Y., et al., 2013, Evaluation of the potential of MODIS satellite data to predict vegetation phenology in different biomes An investigation using ground-based NDVI measurements. *Remote Sensing of Environment*, 132, 145-158.

Hou, X. and Gao S., et al., 2014, Extracting grassland vegetation phenology in North China based on cumulative SPOT-VEGETATION NDVI data. *International Journal of Remote Sensing*, 9, 3316-3330.

Mark, R., Rick, C., Mick, C., et al. Long-term studies of vegetation dynamics. *Science*, 2001, 5530, 650-655.

Myneni, R. B., Keeing, C. D., Tucker, C. J., et al. ,1997, Increase growth in the northern high latitude from 1981 to 1991. *Nature*, 386, 698-702.

Nan, C., Piao, S. L., Chen, A. C., et al., 2012, Spring vegetation green-up date in China inferred from SPOT NDVI data a multiple model analysis. *Agricultural and Forest Meteorology*, 165, 104-113.

Piao, S. L. and Fang, J. Y., 2003, Seasonal Changes in Vegetation Activity in Response to Climate Changes in China between 1982 and 1999. *Acta Geographica Sinica*, 1, 119-125.

Song, C. Q., You, S. C., Ke, L. H., et al., 2011, Spatio-temporal variation of vegetation phenology in the Northern Tibetan Plateau as detected by MODIS remote sensing. *Chinese Journal of Plant Ecology*, 2011, 853-863.

Walker, J. J., Beurs, K. M., Wynne, R. H., et al., 2014, Dryland vegetation phenology across an elevation gradient in Arizona, USA, investigated with fused MODIS and Landsat data. *Remote Sensing of Environment*, 1, 85-97.

Wei, J. L., 2013, Progress of Remote Sensing in Ecological Phenology. *Urban Geotechnical Investigation & Surveying*, 4, 104-107.

Xu, Y. J., Dai, J. H., Wang, H. J., et al., 2015, Variations of main phenophases of natural calendar and analysis of responses to climate change in Harbin in 1985-2012. *Geographical Research*, 9, 1662-1674.

Youngkeun S., John, B., Yukihiro, M., 2013, Drought impact assessment from monitoring the seasonality of vegetation condition using long-term time-series satellite images a case study of Mt. Kenya region. *Environmental Monitoring and Assessment*, 185, 4117-4124.

Zhang, X., Sohlberg, R. A., Townshend, J. R., et al., 2002, Detection of land-cover changes using MODIS 250m data. *Remote Sensing of Environment*, 83, 336-350.

Using MODIS time series data to estimate grass production and its spatial-temporal variation in Beijing-Tianjin sandstorm source region, China

JIN Yunxiang[1], YANG Xiuchun[1], LI Zhemin[2], QIN Zhihao[1], ZHANG Hongbin[3], XU Bin[1]

1.Key Laboratory of Agri-Informatics of Ministry of Agriculture, Institute of Agricultural Resources and Regional Planning, Chinese Academy of Agricultural Sciences, Beijing 100081, China
2.Agricultural Information Institute, Chinese Academy of Agricultural Sciences, Beijing 100081, China
3.Rural Energy & Environment Agency, Ministry of Agriculture, Beijing, 100125, China
Email addresses: jinyunxiang@caas.cn; xubin@caas.cn

ABSTRACT - *Sandstorms involve strong winds that blow sand and dust such that the air visibility declines. Northern China, including Beijing and Tianjin, have seriously suffered from sandstorms at the end of the 20th century. Grass production is not only an essential material base for maintaining grassland ecosystems but also an important parameter for assessing the condition of the grassland ecosystems. This study established a remote sensing estimation model with MODIS NDVI data and field survey data from 2000 to 2010 in Beijing-Tianjin sandstorm source region (BTSSR). We estimated grass production from 2000 to 2010 and assessed the change of grass production both temporally and spatially. The results showed that: (1) The optimal model was established by exponential function model. The MRE and the precision of the model were 0.288 and 71.2% respectively. The average total grass production was 33.13 million tons, and the yield of grass production was 986.59 kg/ha. (2) Grass production exhibited significant spatial heterogeneity in BTSSR and decreased from the southeast to the northwest. (3) Grass production in most of BTSSR exhibited a positive increase trend over the past decade. Grass production significantly increased in the drought grassland desertification control region and the HunShanDaKe sandy land region. Accurate measurements of grass production and its temporal and spatial variation are important for utilization and protection of grassland resources, and this study is meaningful and reference for the evaluation of grassland management strategies in China.*

1 INTRODUCTION

Sandstorms involve strong winds that blow sand and dust such that the air visibility declines. These storms are caused by arid climates and desertification; they are also an important indicator of the ecological and environmental conditions of northern China. North China, including Beijing and Tianjin, experienced strong sandstorms at the end of the 20th century. According to statistics, the Beijing and Tianjin regions experienced more than 10 sandstorms, floating dust and blowing sand from March to April of 2000 (Qin et al., 2012). China proposed the Beijing and Tianjin sandstorm source control project in June 2000, and it was completely implemented by 2002. The first-stage construction lasted 10 years (2001-2010) and was intended to inhibit land desertification in the Beijing and Tianjin regions, improve the ecological environment, and perform United Nations Convention to Combat Desertification. The project aimed to optimize the ecological environment of the capital and control zone and to inhibit the expansion of desertification. The sandstorms were notably reduced; thus, the ecological environment of Beijing and its peripheral regions was greatly improved through vegetation protection, tree planting and seeding,

converting grain plots back to forests, and controlling minor watersheds, grasslands, and ecological immigrants. After the project was implemented, the ecological impacts and their effects on governance gained attention. The sandstorm source control project of Beijing and Tianjin was an ecological restoration project whose purpose was to ensure the survival and development of humans. To date, most studies showed that the project had a positive effect (Wang et al., 2007; Yang and Ci, 2008; Yin and Yin, 2010).

The major aim of the sandstorm source control project was to restore the vegetation of forests and grasslands. The underlying theory of the project was that the variation of land utilization promotes the variation in ecosystem functions. Thus, vegetation, soil, water and climate would be impacted. Grass production is an important indicator of the vegetation restoration effect. Thus, the increase or decrease of grass production can be used to assess the success or failure of ecological restoration programs. Grass production is the material basis for preserving grassland ecosystems and is the most direct indicator of grassland conditions. It is important guiding significance for impacts of the Beijing and Tianjin sandstorm source control project to understand the

spatial-temporal distribution and variation of grass production.

Remote sensing technology provides a novel method for monitoring grass production. The main advantages of remote sensing monitoring are the macroscopic scale, speed and efficiency. Remote sensing provides timely grassland information for grassland management and decision-making. For instance, the normalized difference vegetation index (NDVI) of remote sensing data products (e.g., Advanced Very High Resolution Radiometer (AVHRR), Moderate Resolution Imaging Spectroradiometer (MODIS), or Landsat-TM/ETM+) is extensively applied to dynamic spatial-temporal monitoring of grassland vegetation (Gaitán et al., 2013; Kang et al., 2007; van Leeuwen et al., 2006; Wylie et al., 2002). Based on MODIS data and the corresponding ground-based data in 2005, Xu et al. (2008) divided the entire country into 6 different grassland zones to establish estimation models of grass production; they explored the spatial distribution of grass production in China. Piao et al. (Piao et al., 2007) established an above-ground biomass statistical model using national grassland resource inventory data and the AVHRR-NDVI time series dataset; then, they estimated the distribution of above-ground biomass carbon stocks in China's grasslands from 1982 to 1999.
Researchers have studied the dynamics variation of vegetation in small regions of the Beijing and Tianjin sandstorm source control project (He and Lv, 2003; Zhang et al., 2012; Zhao et al., 2011). In addition, aspects of the project's engineering, as well as its ecological and economic impacts, have been studied (Hu et al., 2012; Wang et al., 2007; Wang et al., 2013). Several studies have documented the vegetation restoration conditions, and few studies have monitored grass production using remote sensing technology in the Beijing and Tianjin sandstorm source region. In this study, we estimated the grass production between 2000 and 2010 and assessed the impacts of the Beijing and Tianjin sandstorm source control project. The results provide scientific evidence for ecological protection and management.

2 MATERIAL AND METHODS

2.1 Study area

The Beijing and Tianjin sandstorm source region stretches from Darhan Muminggan United Banner of Inner Mongolia in the west to Pingquan County of Hebei Province in the east and from Dai County of Shanxi Province in the south to East Ujimqin Banner of Inner Mongolia. The region is located at 109°30'-119°20'E and 38°50'-46°40'N, and it covers 75 counties (banners, municipalities and districts) of 5

provinces (autonomous regions and municipalities directly under the central government), including Beijing, Tianjin, Hebei, Shanxi and Inner Mongolia. The total area is 458,000 km^2: approximately 700 km from east to west and 600 km from south to north. The area comprises plains, mountains and plateaus. The annual mean temperature is 4-7.5°C and the annual mean precipitation is 250-470 mm. Significant differences of temperature and precipitation occur in different areas. Overall, the project region has a temperate continental climate. The natural vegetation primarily includes *Stipa grandis* P. Smirn, *Stipa krylovii* Roshev and *Artemisia frigida* Willd.

The study area has 15 grassland types (see Fig. 1 for the grassland types at a scale of 1:1,000,000), such as temperate steppe, temperate meadow steppe and temperate desert steppe. The grassland covers an area of 401,000 km^2 and accounts for approximately 87.6% of the total land area. The study area is divided into four zones based on climate, soil and vegetation(Yang et al., 2014): the northern arid grassland desertification control zone (NAGDCZ), with a desertification area of 27,815 km^2; the Hunshandake sandy land control zone (HSLCZ), with a desertification area of 48,567 km^2; the farming-pastoral area of desertificated land control zone (FADLCZ), with a desertification area of 13,712 km^2; and the water conservation zone of Yan hills and mountains (WCZYHM), with a desertification area of 11,745 km^2 (Fig. 1).
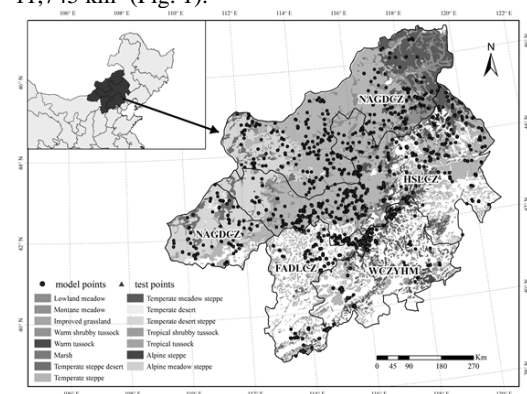
Fig. 1 Spatial distribution of grassland types and sampling sites in four zones.

2.2 Field data

The ground sample plot data were obtained from the authors' multi-year field survey and the large-scale field campaign organized by the Grassland Monitoring and Supervision Center Ministry of Agriculture, P. R. China, from 2005 to 2010. Sampling occurred at the peak of the vegetation growing season, from July to August. The size of the sample plots of herbaceous plants and stunted brushwood was 1 m×1 m, while

that of the sample plots for shrubs was 10 m×10 m. The major vegetation species included *Leymus chinensis* Trin., *Stipa grandis* P. Smirn, *Artemisia frigida* Willd., *Reaumuria soongorica* Pall. and *Lespedeza bicolor* Turcz.. All herbaceous plants were harvested to measure their fresh weight. For shrubs, we sorted the plants into three groups according to their sizes (large, medium and small) and harvested the green parts, along with the branches of the same year (Jin et al., 2014). For most of the sampling sites, we selected three plots (1 m×1 m) as one sample site; the distances between plots were more than 250 m, and the areas between the sampling sites were at least 1 km2. The precise geographical coordinates were recorded as field data. Because the quality of the field data might influence the accuracy of the models (Yang et al., 2007), we conducted strict verification and standardization of the field data in accordance with the grassland types and the multi-year conditions of the sampling plots. Then, we eliminated abnormal data in the field dataset to obtain 2,327 field samples (Fig. 1).

2.3 Remote sensing data

The remote sensing data were obtained from the MOD09Q1 data products on NASA's website (http://modis.gsfc.nasa.gov/). The data were the 8-day synthetic reflectivity product data with a spatial resolution of 250 m. The data were collected during the peak growth period of the grassland from 2000 to 2010 (from the last ten days of July through the first ten days of September). The data were processed by the MODIS Reprojection Tools (MRT) software, including projection conversion, format conversion and mosaicking. Based on the characteristics of the study area and biomass studies, we used NDVI as the remote sensing data. The NDVI was calculated using red and near-infrared bands of MODIS reflectance data from 2000 to 2010. The NDVI was calculated as follows:

$$NDVI = \frac{\rho_{NIR} - \rho_R}{\rho_{NIR} + \rho_R} \qquad (1)$$

ρ_{NIR} and ρ_R were the reflectances of the red and near-infrared bands.

According to the sampling time and geographical coordinates of the field data, we calculated the mean NDVI within a circular area of each site using geographic information system (GIS), with 3-4 pixels per mean NDVI. Then, we built the database for the grass production and NDVI within the corresponding period.

2.4 Establishment and verification of estimation models

According to the database of the grass production and NDVI from 2005 to 2010, we randomly selected 80%

of the field data to establish models and 20% of the field data to verify the models. We developed statistical models using the statistical regression method, including the unary linear regression model, logarithmic function model, power function model and exponential function model. Based on the reserved verification data, the MRE and precision were calculated to evaluate the models, as shown in equations (2)-(3). Finally, we used the determination coefficient (R^2) and precision to confirm the optimal model.

$$MRE = \sqrt{\frac{\sum \left[(Y_i - Y_i')/Y_i\right]^2}{N}} \qquad (2)$$

$$precision = (1 - MRE) \times 100\% \qquad (3)$$

3 RESULTS AND DISSCUSION

3.1 Model Establishment

We obtained 1,878 field data to establish models and 449 field data to verify the models based on the grass production and NDVI spatial database. The unary linear regression model, logarithmic function model, power function model and exponential function model were developed using SPSS software. The optimal model for remote sensing data and grass production was determined with R^2 and precision.
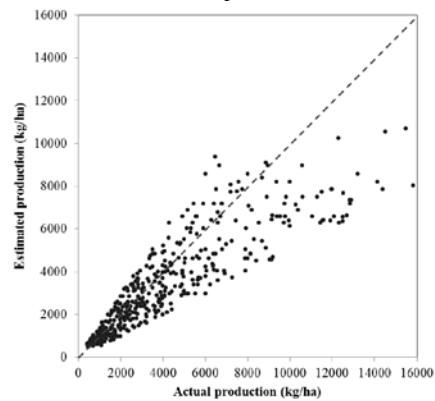
Fig. 2 Relationship between the estimated and the actual grass production

The correlation coefficient of the exponential function model was highest in the study region, and R^2 was 0.460. A good relationship existed between the estimated and the actual grass production on the basis of the exponential model (Fig. 2). Each point was distributed within the periphery of the 1:1 line. The MRE was 0.288, and the precision of the model was 71.2%; thus, the model could estimate the grass production in the Beijing and Tianjin sandstorm source region at the macro scale. Figure 2 showed that the low grass production zones were concentrated, while the high grass production zones were decentralized.

Therefore, the estimation error of the high grass production zone was larger than that of the low grass production zone.

3.2 Spatial-temporal distribution of grass production

Because the model was based on fresh grass yields, the actual calculated grass production was converted via the conversion factor for the dry-fresh ratio. This conversion factor is referenced in 'Grassland Resources of China' (Veterinary, Department of Animal Husbandry, 1996). Based on the optimal exponential function model, we estimated the grass production in the Beijing and Tianjin sandstorm source region from 2000 to 2010 during the peak growth season. The average total grass yield was 33,130,000 tons, and the average unit production was 986.59 kg/ha.

Based on the average grass production in the Beijing and Tianjin sandstorm source region, obvious spatial differences occurred to the grass production (Fig. 3). The spatial distribution exhibited a gradual increase from the northwest to the southeast. (1) Because of the humid climate and the abundant rainfall in the water conservation zone of Yan hills and mountains, the grassland vegetation had favourable growth conditions; the grass production was over 2000 kg/ha, which was the highest in the study area. The average grass production was 2951.3 kg/ha over the 10-year period. The annual variation of grass production was relatively stable (CV=8.53%). After the sandstorm source control project of Beijing and Tianjin was implemented, the grass production increased in the decade and reached a maximum of 3282.9 kg/ha in 2006. (2) The range of the grass production of the farming-pastoral area of desertificated landcontrol zone was between 1000 kg/ha and 2500 kg/ha, and the average grass production was 1230.8 kg/ha over the 10-year period. The annual variation of grass production fluctuated to some extent (CV=15.43%). In this zone, the grass production reached a maximum of 1514.7 kg/ha in 2006. (3) The middle of the Hunshandake sandy land control zone had the maximum grass production, ranging from 1000 kg/ha to 2000 kg/ha. The western part of this zone had lower grass production, i.e., below 500 kg/ha. The average grass production was 930.0 kg/ha over the 10-year period in this zone. The annual variation of grass production was larger (CV=19.68%). The grass production increased more in the intermediate stage of the project than in the early stage and declined in the last stage. The maximum grass production occurred in 2003, while the minimum of approximately 641.5 kg/ha occurred in 2009. (4) Because of the arid climate and shortage of rainfall, the grass production was the lowest in the northern arid grassland desertification control zone, particularly

in the grassland desertification zone; the average grass production was 650.4 kg/ha over the 10-year period. The annual variation of grass production greatly fluctuated (CV=21.93%). The grass production increased from 2000 to 2006; the maximum grass production of approximately 866 kg/ha occurred in 2003. The grass production largely declined from 2007 to 2010 (excluding the year 2008) and accounted for approximately 70% of the average grass production over the period.
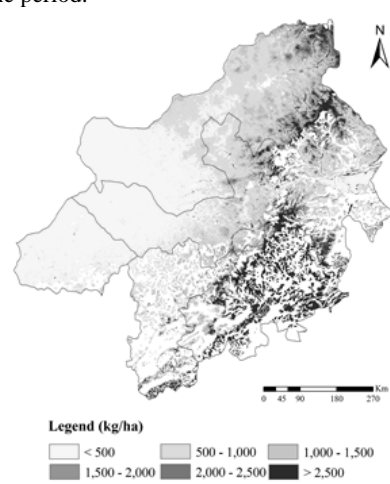
Fig. 3 The 11-year-averaged grass production between 2000 and 2010

We selected the grassland types with more than 5000 km^2 to analyse the grass production variations in grassland types in the Beijing and Tianjin sandstorm source region between 2000 and 2010 (Fig. 4). The annual grass production fluctuated to some extent. The grass production of different grassland types increased from 2000 to 2006 and fluctuated from 2007 to 2010. Because the northern regions of China suffered severe droughts in 2007 and 2009 (Barriopedro et al., 2012; Piao et al., 2010), the grass production notably declined in 2007 and 2009. The droughts might be one of the reasons that the grass production declined during the later phase of the project. The grass production of warm shrubby tussock was higher than the other grassland types. The annual variation of warm shrubby tussock was stable (CV=5.6%), and the average production of warm shrubby tussock was 2983.94 kg/ha over the 10-year period. The temperate meadow steppe grasslands were the second-most productive grassland, with an average production of 1968.56 kg/ha. The maximum production of these two grassland types (i.e., warm shrubby tussock and temperate meadow steppe) occurred in 2006. The grass production of the temperate steppe and the lowland meadow were in the mid-production range. The temperate steppe covered the largest area,

accounting for 49.5% of the grassland area. The average grass production of the temperate steppe was 792.43 kg/ha, and the annual variation was unstable (CV=20.4%). The desert steppe had the lowest grass production. The average grass production of the temperate steppe desert and temperate desert steppe were 233.94 kg/ha and 254.34 kg/ha, respectively. Meanwhile, the maximum values of the grass production for the temperate steppe, the lowland meadow, the temperate steppe desert and the temperate desert steppe occurred in 2003.
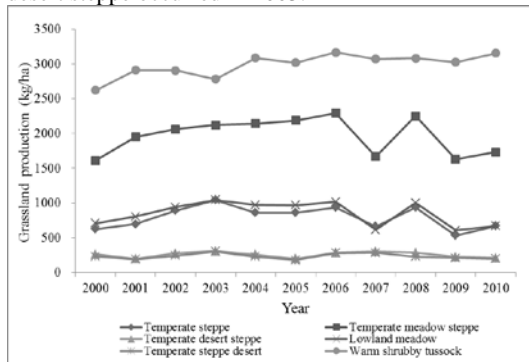
Fig. 4 The interannual variation of grass production in different grassland types

4 CONCLUSIONS

Based on the grassland ground sample plot data in the Beijing and Tianjin sandstorm source control region and MODIS remote sensing data (NDVI), we developed statistical models for grass production. Moreover, we explored the spatial-temporal distribution of grass production in the Beijing and Tianjin sandstorm source control region from 2000 to 2010. We modelled the grassland growth conditions at the macro scale, which provided a reference for the evaluation of the project. The results indicated the following: (1) The exponential function model established with the NDVI and grass production was the optimal model. The MRE was 0.288, and the precision of the model was 71.2%. The average total grass yield was 33,130,000 tons over the project period, and the average unit production was 986.59 kg/ha. (2) The spatial distribution of the grass production exhibited obvious differences in which the production increased from the northwest to the southeast. From the highest to lowest production, the areas with grass production were the water conservation zone of Yan hills and mountains > the farming-pastoral area of desertificated land control zone > the Hunshandake sandy land control zone > the northern arid grassland desertification control zone. (3) Interannual variations of grass production were apparent. The grass production presented a stable increase from 2000 to 2006, while it fluctuated

between 2007 and 2010. The interannual variations notably differed among the four zones. The production of the grassland desertification control zones (Hunshandake sandy land control zone and northern arid grassland desertification control zone) exhibited larger annual variations than the other zones.

According to the analysis of the grass production in the Beijing and Tianjin sandstorm source control region over the project period, the grass production clearly increased in some areas of the region; thus, the project had an important impact. Based on the outcome of the first-stage construction of the Beijing and Tianjin sandstorm source control project, the grassland management must be further strengthened. Overgrazing may result in decreased vegetation and enhanced wind erosion that restricts the recovery of grassland (Shinoda et al., 2011). Therefore, the methods of livestock production should be effectively improved to cultivate high-quality pasture and to assess the livestock carrying capacity in the context of grass production and ultimately reverse the trend of grassland degradation.

6 REFERENCES

Gaitán, J.J., Bran D., Oliva, G., Ciari, G., et al., 2013, Evaluating the performance of multiple remote sensing indices to predict the spatial variability of ecosystem structure and functioning in Patagonian steppes. *Ecological Indicators*, **34**, 181-191.

He, Q. and Lv, D.R., 2003, Monitoring vegetation cover change in east Hunshandake sandy land with Landsat TM and ETM+ and its possible causes. *Remote Sens. Technol. Appl.*, **6**, 353-359.

Hu, J., Ye, H.Y., Wang, D.M. et al., 2012, Study on ecological and economic benefits evaluation of Beijing-Tianjin sandstorm sources control project in Beijing city. *Journal of Beijing University of Agriculture*, **4**, 38-42.

Jin, Y.X., Yang, X.C., Qiu J.J., et al., 2014, Remote Sensing-Based Biomass Estimation and Its Spatio-Temporal Variations in Temperate Grassland, Northern China. *Remote Sensing*, **6**, 1496-1513.

Kang, L., Han, X.G., Zhang, Z.B., et al., 2007, Grassland ecosystems in China: review of current knowledge and research advancement. *Philosophical Transactions of the Royal Society B-Biological Sciences*, **362**, 997-1008.

Piao, S., Ciais, P., Huang, Y., et al., 2010, The impacts of climate change on water resources and agriculture in China. *Nature*, **467**, 43-51.

Piao, S., Fang, J., Zhou, L., 2007, Changes in biomass carbon stocks in China's grasslands between 1982 and 1999. *Global Biogeochemical Cycles*, **21**, B2002.

Shinoda, M., Gillies, J.A., Mikami, M., et al., 2011, Temperate grasslands as a dust source: Knowledge, uncertainties, and challenges. *Aeolian Research*, **3**, 271-293.

Van, Leeuwen, W.J.D., Orr, B.J., Marsh, S.E., et al., 2006, Multi-sensor NDVI data continuity: Uncertainties and implications for vegetation monitoring applications. *Remote Sens Environ*, **100**, 67-81.

Veterinary, Department Of Animal Husbandry, 1996, Rangeland Resources of China. (Beijing, China: China Science and Technology Press), pp. 188-207.

Wang, G.Y., Innes, J.L., Lei, J.F., et al., 2007, China's forestry reforms. *Science*, 1556-1557.

Wang, L.Q., Qiao, N. and Kang, R.B, 2013, Review of the research on ecological effects and evlaluation of sandstorm source control project in and around Beijing and Tianjin. *Forestry economics*, 13-17.

Wylie, B.K., Meyer, D.J., Tieszen, L.L. et al., 2002, Satellite mapping of surface biophysical parameters at the biome scale over the North American grasslands: A case study. *Remote Sens Environ*, **79**, 266-278.

Xu, B., Yang, X.C., Tao, W.G., et al., 2008, MODIS-based remote sensing monitoring of grass production in China. I*nt J Remote Sens*, **29**, 5313-5327.

Yang, X., Xu, B., Jin, Y., et al., 2014, Remote sensing monitoring of grassland vegetation growth in the Beijing-Tianjin sandstorm source project area from 2000 to 2010. *Ecological Indicators*, DOI: 10.1016/j.ecolind.2014.04.044.

Yang, X.C., Xu, B., Zhu, X.H., et al., 2007, Models of grass production based on remote sensing monitoring in northern agro-grazing Ecotone. *Geogr. Res.*, 213-221.

Yang, X.H. and Ci, L.J., 2008, Comment on why large-scale afforestation efforts in China have failed to solve the desertification problem. Environ. *Sci. Technol.*, **20**, 7722-7723.

Yin, R.S. and Yin, G.P., 2010., China's primary programs of terrestrial ecosystem restoration: initiation, implementation, and challenges. *Environ. Manag.*, **3**, 429-441.

Yunbin, Q., Zhongbao, X., Yang, Y. et al., 2012, Spatiotemporal variation of sandstorm and its response to vegetation restoration in Beijing-Tianjin sandstorm source area. *Transactions of the Chinese Society of Agricultural Engineering*, **24**, 196-204.

Zhang, G.L., Dong, J.W., Xiao, X.M. et al., 2012, Effectiveness of ecological restoration projects in Horqin sandy land, China based on SPOT-VGT NDVI data. *Ecol. Eng.*, 20-29.

Zhao, L., Zhang, L.G., Yu, W.L. et al., 2011, The annual variation of aboveground biomass of undergrowth vegetation and its impact factors in the area of conversion of cropland to forest in Duolun County. *J. Inner Mongolia Forestry Sci. Technol.*, **1**, 14-27.

Three decades of NOAA-AVHRR data to assess vegetation dynamics in the Iberian Peninsula and the Balearic Islands: the IBERIAN NDVI dataset.

N. Martin-Hernandez*[a], S.M. Vicente-Serrano[a], S. Beguería [b], C. Azorin-Molina[c], F. Reig[a], J. Zabalza[a],

[a]*Pyrenean Institute of Ecology (Spanish National Research Council), Zaragoza, Spain;*
[b]*Aula Dei Experimental Station (Spanish National Research Council), Zaragoza, Spain;*
[c]*Department of Earth Sciences, University of Gothenburg, Sweden.*
*nmartin@ipe.csic.es, svicen@ipe.csic.es

ABSTRACT - *We have processed the complete afternoon 1.1-km spatial resolution NOAA – AVHRR daily images available since 1981 to develop a NDVI dataset for the Iberian Peninsula and the Balearic Islands. We developed an automatic processing approach that includes an accurate calibration using post-launch calibration coefficients, geometric and topographic corrections, cloud removal, temporal filtering and bi-weekly composites by maximum value composite. We also corrected inhomogeneity between AVHRR/2 and AVHRR/3 by means of a cross calibration with the GIMMS3g dataset. The resulting product has been the IBERIAN NDVI dataset, which was compared with other existing NDVI products. For this purpose we used the GIMMS3g bi-weekly NDVI with 8-km resolution, the SMN-VHP weekly product at 4-km pixel resolution and the monthly MODIS NDVI product at 1-km of spatial resolution. We chose Mann-Kendall and Theil-Sen tests to calculate the significance of the trends and the magnitude of change of the NDVI datasets. We found high resemblance of the seasonal and annual NDVI trends from the IBERIAN NDVI and the other three datasets. The IBERIAN NDVI dataset allows retrieving NDVI changes at longer temporal coverage (1981 – 2015) than MODIS and higher spatial resolution (1.1-km) than GIMMS and SMN.*

1 INTRODUCTION

Remote sensing data allows extracting spatial and temporal information about environmental variables. The Normalized Difference Vegetation Index (NDVI) reflects the difference of the light absorption by vegetation in the red and infrared regions of the electromagnetic spectrum (Rouse et al., 1974), which is directly related to the photosynthetic activity and it provides indirect information on the vegetation activity, total biomass and vegetation coverage (Tucker, 1979).

The NDVI is highly useful to assess spatial and inter-annual changes in the vegetation activity and it has been widely used to assess long term changes in vegetation over the past decades (Fensholt, 2012). The images from the Advanced Very High Resolution Radiometer (AVHRR) data from the National Oceanic and Atmospheric Administration (NOAA) polar-orbiting satellites are the longest and continuously available record to monitor vegetation dynamics and they have been widely analysed to retrieve NDVI and to develop long term databases of this index (Beck et al, 2011).

There are different NDVI datasets available at the global scale, obtained from the AVHRR imagery, as the Global Inventory Modelling and Mapping Studies (GIMMS) (Tucker et al., 2005) or the Mediterranean Extended One-Km AVHRR Data Set (MEDOKADS) NDVI dataset (Koslowsky and Friedrich, 2005). There are also other NDVI products from other sensors as the Moderate-Resolution Imaging Spectroradiometer (MODIS) on-board the Terra satellite and the Long Term Data Record (LTDR), which combines NDVI data from different sensors including both the AVHRR and MODIS (Dardel et al., 2014).

Nevertheless, these products usually are affected by a low spatial resolution (e.g. 64 km^2 per pixel in the case of the GIMMS dataset), or they are covering a short period (e.g. MODIS since 2000). NOAA-AVHRR images are available from 1981 at the spatial resolution of 1.1 km at the Nadir. We have used this data to develop a high spatial resolution and long-temporal coverage since 1981.

2 DATA AND METHODS

Firstly, we processed the NOAA-AVHRR images and obtained the called IBERIAN NDVI dataset for Iberian Peninsula and the Balearic Islands. Secondly, we did a comparison between the new dataset and other three NDVI products: the GIMMS3g, the Smoothed NDVI (SMN) -both of them were also obtained from the AVHRR sensor- and the MODIS dataset.

2.1 The IBERIAN NDVI dataset

The IBERIAN NDVI dataset is a set of semi-monthly images (two per month) with 1,1-km spatial resolution at nadir obtained from the processing of the original AVHRR data collected from the High Resolution Picture Transmission (HRPT) receiving ground station (available at National Institute for Aerospace Technology (INTA), Maspalomas, Canary Islands, Spain hhttp://www.inta.es/index.asp).

The processing of approximately 2 Tb of images included radiometric calibration with post-launch calibration coefficients for the afternoon satellites: NOAA-7, 8, 9, 11, 14, 16, 18, and 19 (Rao and Chen, 1995; NOAA's User Guide, Roben 2009), inter-satellite normalization to NOAA-9 (Trishchenko et al., 2002 and 2009), automatic geometric correction using 97 Ground Control Points to the European 1979 UTM zone 30º (between 35ºN and 44ºN and 11º W and 5ºE), visual revision and a non-lambertian topographic correction (Teillet, 1982).

Moreover, a cloud removal process was included: the algorithm described in Azorin-Molina et al. 2013 uses the five bands of the AVHRR sensor and identify between cloud, snow-ice and clear ground pixels to compute the daily cloud masks. Thereafter, the NDVI was obtained using the Channel 1 (Red) and Channel 2 (Near-Infrared) top-of-the-atmosphere reflectance (ρ), according to:

$$NDVI = \rho_{NIR} - \rho_{Red} / \rho_{NIR} + \rho_{Red} \qquad (1)$$

Semi-monthly NDVI values were obtained by means of a maximum composite method (Huete, 1985) with the purpose of reducing atmospheric effects. Data gaps were filled by means of regression models and a fitting correlation procedure using the NDVI of the semi-monthly periods before and after the date of interest, based on Quarmby et al. (1993) and also the semi-monthly series were temporally filtered by means of a maximum filter to reduce noise.

Finally, we deal with the limitations of the instruments due to the AVHRR/3 sensor introduced in 2000 has different characteristics than AVHRR/2. Friedrich and Koslowsky (2009) highlight that uncertainty in the data obtained from AVHRR instruments can be introduced by changes in spectral characteristics rather than by real vegetation changes. In addition, the authors said that corrections presented by Trishchenko are useful to normalize the information but are not enough to correct the AVHRR/3 characteristics in NDVI time-series.

In the same line, Pinzon and Tucker (2014) applied a correction for the AVHRR instruments to generate the GIMMS3g NDVI dataset (1981 – 2015). We corrected the inhomogeneity between AVHRR/2 and AVHRR/3 in the IBERIAN NDVI dataset by means of a cross calibration with the GIMMS3g dataset. We only applied the correction for the AVHRR/3 data from 2000 to 2015.

2.2 The AVHRR – GIMMS3g NDVI dataset

The GIMMS3g product consists in semi-monthly maximum NDVI value composite images at 8-km of spatial resolution for the period 1981 - 2015. It has been corrected for cloud cover, atmospheric correction, volcanic aerosols, sensor degradation, inter-satellite differences and solar and viewing angle effects due to satellite drift (Tucker et al., 2005, Pinzon and Tucker, 2014). Data is available at https://ecocast.arc.nasa.gov/data/pub/gimms/3g.v1/; last accessed October 2017

2.3 The AVHRR – SMN dataset

The Smoothed NDVI (SMN) is a product used in the calculation of the Vegetation Health Product (VHP), which is calculated at a weekly time scale at 4-km of spatial resolution. It is available since 1981 but it contains temporal gaps. The dataset is smoothed for cloud removal and adjusted using the Empirical Distribution Function statistical technique in order to correct sensor degradation, satellite orbital drift and to reduce aerosols (Kogan et al., 2011). The dataset is available at https://www.star.nesdis.noaa.gov/smcd/emb/vci/VH/vh_ftp.php; last accessed October 2017.

2.4 The MODIS NDVI dataset

From the MODIS instrument that starts to work in 2000 we chose the available monthly NDVI data resampled from 250m to 1-km spatial resolution called MOD13A3.005. (https://lpdaac.usgs.gov/dataset_discovery/modis/modis_products_table/mod13a3; last accessed October 2017).

2.5 Comparison analyses

In order to compare the new dataset with the other three products, we adapted the IBERIAN NDVI dataset as follows:

a) IBERIAN NDVI was resampled to 8x8km pixel resolution as GIMMS and the period 1982 – 2014 was selected.

b) IBERIAN NDVI was resampled to 4x4-km of grid size as SMN. This product has temporal gaps so we compared only the common available images for both datasets during the period 1982 – 2014.

c) IBERIAN NDVI images for the period 2004 – 2014 were selected to compare with the MODIS NDVI images. Both datasets have 1x1-km spatial resolution.

The comparison was based on the calculation of the annual, seasonal and monthly NDVI averages graphically displayed and also on a correlation analysis using Pearson's correlation, for each dataset and for all the pixels of the study area.

Furthermore, we determined the NDVI trends of the four datasets. To conduct the trend significance (p<0.05) we used the non-parametric Mann-Kendall test (Lanzante, 1996) positive values of tau indicated a trend of increasing NDVI and negative values decreasing NDVI. To identify which areas show the major changes we chose the Theil-Sen slope estimator (Sen, 1968) to obtain the magnitude of change. The results are displayed in annual and seasonal maps that allow determining the trend significance of change in NDVI for the four datasets.
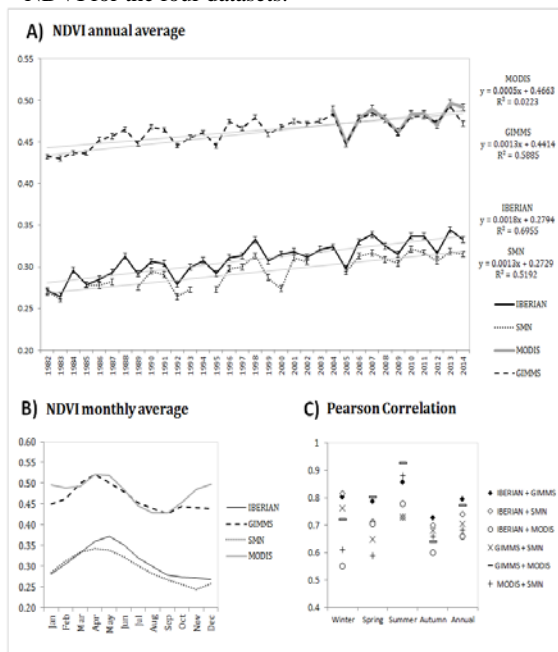
Figure 1. (A) NDVI annual average. (B) NDVI monthly average. (C) Pearson correlation between datasets.

3 RESULTS

In general, all the datasets exhibit an increase in the NDVI trends during the last decades for the Iberian Peninsula and the Balearic Islands. In figure 1 the graphics shown the average NDVI for the entire study area and allows comparing the information between datasets.

The evolution of the NDVI over the years is shown in figure 1.A. The temporal behaviour of average NDVI from the IBERIAN NDVI product (thin black line) has a similar trend as the annual NDVI averages of the GIMMS (dashed line), MODIS (thick grey line) and SMN (dotted line) datasets. All of them exhibit an increase in vegetation activity for the common period. It is notice that the NDVI temporal series from the IBERIAN dataset has the same scale as the SMN product but lower than the GIMMS and MODIS values.

The monthly NDVI averages for the whole study area (figure 1.B) show similar patterns for three of four datasets. The GIMMS and SMN show a pic of the vegetation activity on April while IBERIAN monthly pic is on May. Alternatively, the MODIS dataset exhibits higher average values during the mentioned both months and also show higher values on December and January.

Pearson's annual and seasonal correlations between datasets in figure 1.C show the relationship between pair of datasets. We used all the pixels of the study area from each dataset to observe the general temporal behaviour. The highest correlation values are found on summer and the lowest on winter. The most similar correlations are the annual and autumn ones and the less are the winter and spring values. The correlation between GIMMS and IBERIAN datasets show high annually and seasonally correlation values (about 0.8). For the IBERIAN and SMN the correlation values are near 0.7 and finally, there is more variability in the correlation values between IBERIAN and MODIS.

The resulting spatial patterns of NDVI trends are shown in figure 2. In order to simplify the interpretation we grouped the information in five categories: Significant positive change (dark blue), No significant positive change (blue), No significant and no change (white), Not significant negative change (red), Significant negative change (dark red).

The annual maps (first column of maps in figure 2.A, B and C) exhibit a significant increase in NDVI (mostly in blue) in the majority of the Iberian Peninsula and the Balearic Islands for the analysed periods 1982 – 2014 (in A and B) and 2004-2014 (in C).

The comparison between IBERIAN and GIMMS datasets in figure 2.A for the period 1982 – 2014 exhibit that the seasonal resulting maps also show an increase in the NDVI trends, predominantly in blue. Although there are few local areas in red that exhibit a decrease in the NDVI trends as for example in the Guadalquivir basin on spring.

The figure 2.B exhibits the comparison between IBERIAN and SMN datasets. There is a good adjustment between trends on winter and the significance of change differs on spring, summer and autumn. The south-western areas of the Iberian Peninsula present more negative significant magnitude of change on spring in the SMN product and more positive significant change on autumn maps than in the IBERIAN corresponding maps.

A) IBERIAN and GIMMS at 8x8 km (1982 – 2014)

B) IBERIAN and SMN at 4x4 km (1982 – 2014)

C) IBERIAN and MODIS at 1x1 km (2004 – 2014)
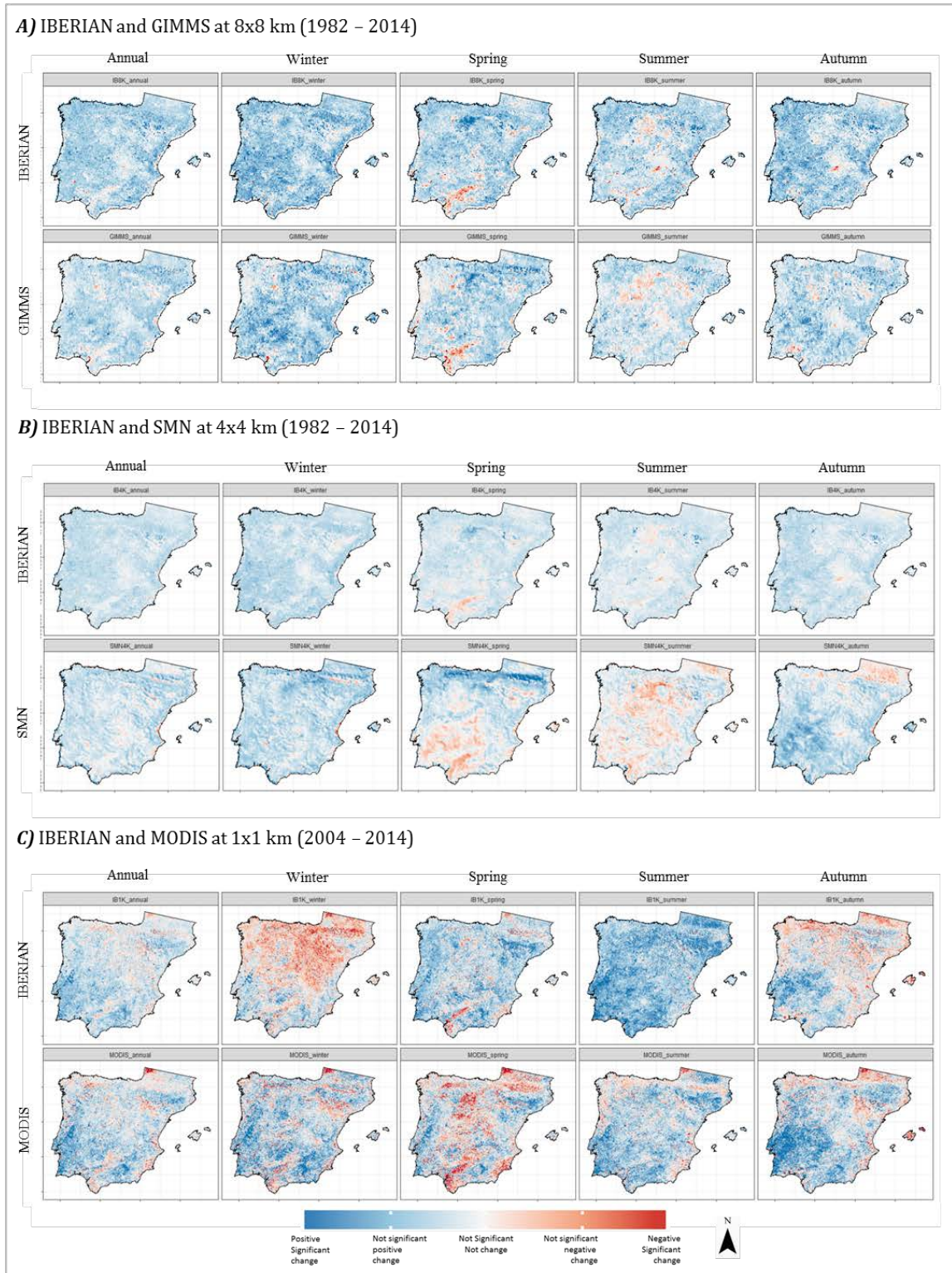
Figure 2. NDVI annual and seasonal significant magnitude of change.

171
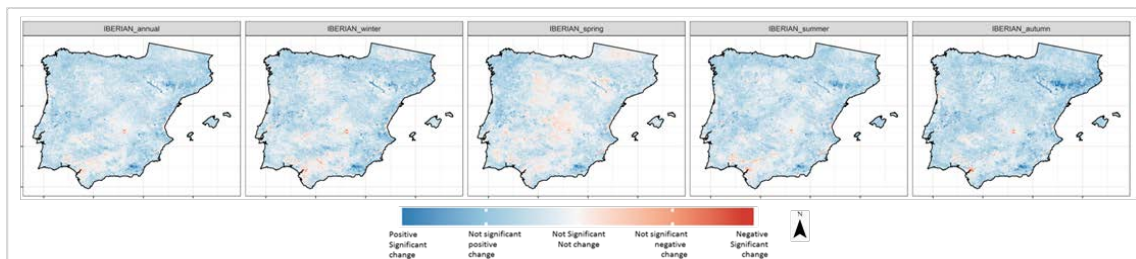
Figure 3. NDVI annual and seasonal significant magnitude of change for the period 1982 – 2014 at 1,1-km spatial resolution.

On the other hand, the summer maps show negative significant magnitude of change (red) in large part of the territory meanwhile for the IBERIAN dataset the results are not significant or have a positive significant change.

Alternatively, the IBERIAN-MODIS comparison annual maps for the period 2004 – 2014 in figure 2.C show that the main increase of the NDVI values is recorded in the south-western part of the Iberian Peninsula for the IBERIAN dataset. The main decrease is exhibited in some parts of the Ebro and Guadalquivir river basins and also in the south-eastern part of the Iberian Peninsula. The seasonal maps present a good adjustment between the IBERIAN and MODIS dataset on autumn, the trends differs on spring and summer and does not adjust on winter for the northern part of the Iberian Peninsula due to the IBERIAN dataset exhibit more negative significant changes than MODIS.

Finally, the figure 3 shows the annual and seasonal NDVI significant magnitude of change for the IBERIAN dataset at 1,1-km² spatial resolution between 1982 and 2014.

4 CONCLUSIONS

In this study we have developed a NDVI dataset (1981 – 2015) with 1.1 km² resolution. We have showed that the processing methods developed and the algorithms used with the original NOAA-AVHRR images are useful to obtain a dataset that enables determining changes in the vegetation activity over the last three decades across The Iberian Peninsula and the Balearic Islands.

We have compared the performance of the new dataset with the other datasets to identify trends. It is notice that the comparison between GIMMS and IBERIAN shows the best agreement in the NDVI trends. The increases and decreases are found in approximately the same areas but the amount of significant or not significant trends are more accurately localized in the IBERIAN maps.

The main advantage of the IBERIAN NDVI dataset is that allows retrieving changes in the inter-annual variability of NDVI values at longer and continuous temporal coverage (1981 – 2015) than MODIS and higher spatial resolution (1.1-km) than GIMMS and SMN datasets.

REFERENCES

Azorin-Molina, C., Baena-Calatrava, R., Echave-Calvo, I., Connell, B. H., Vicente-Serrano, S. M., & López-Moreno, J. I., 2013, A daytime over land algorithm for computing AVHRR convective cloud climatologies for the Iberian Peninsula and the Balearic Islands. *International Journal of Climatology*, 33, 2113-2128.

Beck, H. E., McVicar, T. R., van Dijk, A. I., Schellekens, J., de Jeu, R. A., & Bruijnzeel, L. A., 2011, Global evaluation of four AVHRR–NDVI data sets: Intercomparison and assessment against Landsat imagery. *Remote Sensing of Environment*, 115, 2547-2563.

Dardel, C., Kergoat, L., Hiernaux, P., Mougin, E., Grippa, M., & Tucker, C. J., 2014, Re-greening Sahel: 30 years of remote sensing data and field observations (Mali, Niger). *Remote Sensing of Environment*, 140, 350-364.

Fensholt, R., & Proud, S. R., 2012, Evaluation of earth observation based global long term vegetation trends-Comparing GIMMS and MODIS global NDVI time series. *Remote sensing of Environment*, 119, 131-147.

Friedrich, K., & Koslowsky, D., 2009, Inter-comparison of MEDOKADS and NOAA/NASA pathfinder AVHRR land NDVI time series. *Recent advances in remote sensing and geoinformation processing for land degradation assessment*, 8, 103.

Kogan, F., Guo, W., & Jelenak, A., 2011, Global vegetation health: long-term data records. *In Use of Satellite and In-Situ Data to Improve Sustainability,* 247-255, Springer Netherlands.

Koslowsky, D., Billing, H., & Friedrich, K., 2005, MEDOKADS: a long-term data set for detection and monitoring of desertification risks in the Mediterranean. *Remote sensing and geoinformation in the assessment and monitoring of land degradation and desertification*, Trier, Germany, 191-198.

Pinzon, J. E., & Tucker, C. J., 2014, A non-stationary 1981–2012 AVHRR NDVI3g time series. *Remote Sensing*, 6, 6929-6960.

Robel J, 2009, NOAA KLM user's guide – satellite and data description of NOAA's polar orbiting satellites from NOAA-15 and later, Feb 2009 revision. (https://data.noaa.gov/dataset/noaa-polar-orbiting-operational-environmental-satellites-poes-radiometer-data; last accessed October 2017)

Rouse, J. W., Haas, R. H., Schell, J. A., and Deering, D.W., 1974, Monitoring vegetation systems in the great plains with ERTS, Third ERTS Symposium, NASA SP-351 I:309-317.

Trishchenko, A. P., 2009, Effects of spectral response function on surface reflectance and NDVI measured with moderate resolution satellite sensors: Extension to AVHRR NOAA-17, 18 and METOP-A. *Remote Sensing of Environment*, 113, 335-341.

Trishchenko, A. P., Cihlar, J., & Li, Z., 2002, Effects of spectral response function on surface reflectance and NDVI measured with moderate resolution satellite sensors. *Remote Sensing of Environment*, 81, 1-18.

Tucker, C. J., 1979, Red and photographic infrared linear combinations for monitoring vegetation. *Remote sensing of Environment*, 8, 127-150.

Tucker, C.J., Pinzo, J.E., Brown, M.E., Slayback, D.A., Pak, E. W., Mahoney, R., … & El Saleous, N., 2005, An extended AVHRR 8-km NDVI dataset compatible with MODIS and SPOT vegetation NDVI data. *International Journal of Remote Sensing*, 26, 4485-4498.

Teillet, P.M., Guindon, B., Goodeonugh, D.G., 1982, On the slope-aspect correction of multispectral scanner data. *Canadian Journal of Remote Sensing*, 8, 84-106

Lanzante, J. R., 1996, Resistant, robust and non-parametric techniques for the analysis of climate data: theory and examples, including applications to historical radiosonde station data. *International Journal of Climatology*, 16, 1197-1226.

Sen, P. K., 1968, Estimates of the regression coefficient based on Kendall's tau. *Journal of the American Statistical Association*, 63, 1379-1389.

Land-cover classification using multi-source data

Q.Wu[a,b], R.F. Zhong[a,b,*], W.J. Zhao[a,b], K. Song[a,b], L.M. Du[a,b]
a. Beijing Advanced Innovation Center for Imaging Technology, Capital Normal University, Beijing 100048, China; b. College of Resource Environment and Tourism, Capital Normal University, Beijing 100048, China
Email: wuqiong_0108@126.com; *zrf@cnu.edu.cn

ABSTRACT - *Land cover and its change are one of the important factors of global environmental change. The new GF-2 satellite provides abundant spectral features and texture information, and airborne light detection and ranging (LiDAR) provides accurate three-dimensional coordinates at a finer scale. Fusing these data has the potential to improve land cover classification. In the article, we selected the random forest (RF) as a classifier. The spectral bands of GF-2, normalized difference vegetation index (NDVI), normalized digital surface model (nDSM) derived from LIDAR data, and their gray-level co-occurrence matrix (GLCM) textures including mean, variance, homogeneity, contrast, dissimilarity, entropy, second moment and correlation were generated to create seven scenarios with different combination of RF input variables. We estimated the classification performance on GF-2 data, compared and assessed the individual and combined contributions of GF-2 and LiDAR data with regard to classification accuracy using fusion data. GF-2 data alone or the fusion of GF-2 data and other sources can provide relatively good classification mapping accuracy in complex urban environments. The classification accuracy of fused data from the GF-2 and LiDAR data exceeded those of GF-2 or LiDAR data alone. GLCM textures significantly improved the classification performance whether in GF-2 data or LiDAR height data. A fusion of GF-2 data, NDVI, LiDAR data and their texture features (102 RF variables) achieved the best classification accuracy in seven scenarios. Total accuracy and kappa coefficient were 93.32% and 0.91, respectively. Almost all classes in producer's accuracy and user's accuracy were greater than 90%.*

1 INTRODUCTION

Land cover refers to the surface covering of Earth under the influences of both natural and the man-made factors. Land cover and its changes caused by human exploitation of land resources are one of the important factors of global environmental change. Dynamically monitoring land use and land cover is always a hot topic (Salehi et al. 2012; Yan, Shaker, and El-Ashmawy 2015).

In previous studies, high or very high spatial and spectral resolution optical satellite sensors (such as QuickBird, SPOT, WorldView, GeoEye, and the GaoFen-1) or the fusion of these and LiDAR data have been reported to be used in land cover mapping of urban, agricultural, forest, wetland environment, and so on (Chen et al. 2009; Duro, Franklin, and Dubé 2012; Agarwal et al. 2013; Rasel et al. 2016; Fu et al. 2017). The GF-2 satellite as the first civilian optical remote sensing satellite with a resolution superior to 1 m was independently developed by China and has made it possible to identify complex terrestrial features with high accuracy (Li et al. 2016; Wang, Wang, and Wu 2016). Although the data from this satellite is relatively new, some studies have already estimate its performance of land cover classification at present (Zhang et al. 2017; Uamkasem, Huang, and Bi 2017; Zheng et al. 2017). However, few studies have

compared and assessed the classification performance based on GF-2 and LiDAR data alone or fused data from both or fused data from GF-2, LiDAR data with their textures.

In the article, we selected one of machine learning algorithms-RF as a classifier. The spectral bands of GF-2, NDVI, nDSM derived from LiDAR data, and their textures including mean, variance, homogeneity, contrast, dissimilarity, entropy, second moment and correlation, were generated to create different scenarios with different combination of RF input variables. Based on these study data, we respectively compared the classification map accuracy of seven scenarios using the total accuracy and class-level accuracies as metrics. This study aims to provide a reference for the efficient improvement of land cover classification and offer support for extending the applications of classification algorithms and data sources.

2 MATERIALS AND METHODS

2.1 Study area

The study area is located in Xuchang City, Henan Province, China (Figure 1). It contains numerous natural landscapes and artificial structures, including vegetation, buildings and roads. The city has a warm temperate and sub-humid monsoon climate with

abundant heat resource and sufficient sunlight, and it is characterized by spring droughts that increase sand, hot summers with rainfall concentrations, fine autumns with extended sunshine, and cold winters with little rain and snow. The mean annual temperate is 15°C, and the mean annual precipitation is 700 mm.
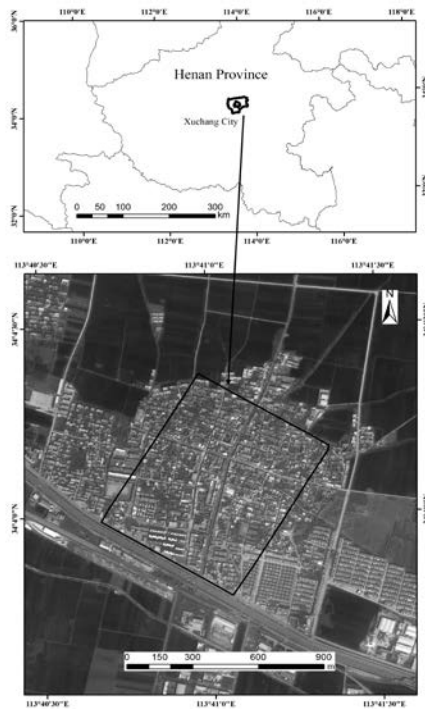
Figure 1 Location of the study area

2.2 LiDAR data

The raw LiDAR data for this study was acquired using a Riegl VZ-1000 LiDAR scanner system mounted to a fixed wing aircraft on March 16, 2016. The system recorded a single pulse return and intensity. The density of the point cloud for the study area was 8 points per m^2. The horizontal and vertical resolutions of the point clouds were 0.38 m and 0.4 m, respectively. The final LiDAR point clouds were all georeferenced to the Universal Transverse Mercator (UTM) Zone 49N/WGS-84 projection coordinates system.

We first removed noise points (low, isolated and air points) via filtering. Then, the point clouds were classified into non-ground and ground points using Terrasolid software. The ground and all points were respectively interpolated into a digital elevation model (DEM) and digital surface model (DSM) with 1 m resolution using ArcGIS software. A normalized digital surface model (nDSM) was created though raster calculation subtracting DEM from DSM.

2.3 Satellite GF-2 and ancillary data

GF-2 was the first civilian optical remote sensing satellite with a resolution superior to 1m, and it was independently researched and developed by China. GF-2 was successfully launched on August 19, 2014. It is equipped with two multispectral scanners, 1 m panchromatic and 4 m high resolution, respectively.

We obtained one scene from the GF-2 image data corresponding to the study area. The image contains both panchromatic and multispectral bands and was acquired on February 16, 2017. The pre-processing applied to the GF-2 images included radiometric calibration, atmospheric correction, and orthorectification. The above three processes were implemented using ENVI software. Atmospheric correction was performed using the Fast Line-of-sight Atmospheric Analysis of Spectral Hypercubes (FLAASH) module. Thus, the digital numbers (DN) of the raw images were converted into real reflectance values. Then, we respectively performed orthorectification of the panchromatic and multispectral bands using an RPC Orthorectification module. In addition, the multispectral bands were pan-sharpened with the panchromatic band using the Gram-Schmidt Pan-Sharpening model to generate Very-high-resolution (VHR) multispectral images at 1 m resolution. Finally, we selected the nDSM derived from the LiDAR data as a reference image for VHR multispectral images registration and resampling to achieve a total root-mean-square error of less than one pixel. The data were spatially subset to include only the study area. The normalized difference vegetation index (NDVI) was then calculated from the VHR multispectral images by Equation (1).

$$NDVI = \frac{R_{NIR} - R_{RED}}{R_{NIR} + R_{RED}} \quad (1)$$

where R_{NIR} and R_{RED} are the reflectance value in the near-infrared bands and the red bands of GF-2, respectively.

2.4 Textural Analysis

In this study, 8 GLCM textures from GF-2 bands (blue, green, red and near-infrared bands), ancillary data (NDVI) and LiDAR-derived height data (nDSM), including mean, variance, homogeneity, contrast, dissimilarity, entropy, second moment, correlation, were calculated for classification. After a number of experiments, the window sizes with the best performance were selected for the subsequent classifications, including 7×7 pixels, 9×9 pixels.

2.5 Random Forest classifier

A random forest is an ensemble of classification trees in which each tree contributes with a single vote for the assignment of the most frequent class to the input data (Breiman, 2001; Rodriguez-Galiano and Chica-Olmo 2012). Random Forest algorithm efficiently runs on large data sets and handle thousands of input variables. RF assesses the importance of input variables based on the permutation importance measure, which has been shown to be a reliable indicator in classification (Guo et al. 2011). The RF model requires two important parameters during execution: the number of variables in the random sampling used at each split to grow a decision tree (mtry) and the numbers of decision tree (ntree). The mtry parameter is not critical and is often set to the square root of the number of inputs (Guo et al. 2011). The ntree parameter values was set to the upper limit of 1000 because that value has been shown to be effective for many RF applications (Diaz-Uriarte and Andrés 2006; Gao et al. 2015). In this paper, we optimized the ntree and mtry parameters to improve the RF classifier efficiency based on the OOB (out-of-bag) error values. The RF model was performed using R project here.

2.6 Data fusion

We fused the GF-2 multispectral image data, its ancillary data (NDVI), nDSM and their 8 texture features to assess differences in classification accuracy. We used layer-stacking to combine abovementioned data sources into eight scenarios of composite images: (1) scenario 1: 4 input variables generated by the GF-2 multispectral data (blue, green, red and near-infrared bands); (2) scenario 2: 5 input variables generated by the GF-2 multispectral data and its ancillary data (NDVI); (3) scenario 3: 85 input variables generated by the GF-2 multispectral data, its ancillary data (NDVI), their texture features (7×7 pixels) and their texture features (9×9 pixels); (4) scenario 4: 1 input variable generated by the nDSM; (5) scenario 5: 17 input variables generated by the nDSM, its texture features (7×7 pixels) + its texture features (9×9 pixels); (6) scenario 6: 6 input variables generated by the GF-2 multispectral data, its ancillary data (NDVI) and nDSM; (7) scenario 7: 102 input variables generated by the GF-2 multispectral data, its ancillary data (NDVI), nDSM, their texture features (7×7 pixels) and their texture features (9×9 pixels).

2.7 Accuracy assessments

The scenes of the study area contain imbalanced classes: building, pavement/road and tree are predominant land cover types, while grass and cropland are minor classes. The available reference samples of six classes were randomly selected (see Table 1). 70% of samples were used as training data for RF model, the other 30% were used as testing data. A confusion matrix was used to evaluate the accuracy of the classification results. Based on the abovementioned scenarios, we differentiated between six classes, namely, building, pavement/road, tree, grass, cropland and shadow.

Table 1 The total numbers of training and testing samples for the six classes

Class	Total samples (pixels)
Building	2495
Pavement/Road	2020
Tree	2141
Grass	684
Cropland	172
Shadow	1529

3 RESULTS

In this study, we used the grid search approach based on the OOB error values to optimize the mtry and ntree parameters in the abovementioned scenarios (Eisavi et al. 2015). When OOB error rate was lowest in every scenario, we selected the mtry and ntree parameters (the optimum values) to run the RF model. Based on the total classification accuracy and kappa coefficient, scenario 7 outperformed the other scenarios (see Table 2). Total accuracy and kappa coefficient of scenario 7 were highest, 93.32% and 0.91, respectively. Land cover discrimination at the class level revealed general uptrends with fusion data using GF-2, NDVI, LiDAR and textures (see Table 3).

Table 2 Comparison of total accuracy and kappa coefficient among the scenarios

Scenario	Total Accuracy (%)	Kappa Coefficient
1	76.86	0.70
2	77.11	0.71
3	83.33	0.79
4	57.59	0.44
5	80.13	0.74
6	89.97	0.87
7	93.32	0.91

Comparing scenario 1 with scenario 2, the total accuracy increased from 76.85% to 77.10%, kappa coefficient increased from 0.70 to 0.71. Compared to scenario 1 and scenario 2, scenario 3 yielded good results, with a total accuracy of 83.33% and kappa coefficient of 0.79. The producer's accuracy and user's accuracy on building, road, tree, grass and shadow classes showed larger increases. Cropland was precisely identified in all three scenarios, the producer's accuracy and user's accuracy were 100% and showed no changes (see Table 2 and 3).

Table 3 Comparison accuracy of scenarios at the class-level

Scenario	Class	Producer's accuracy (%)	User's accuracy (%)
1	Building	77.07	78.24
	Road	69.42	70.23
	Tree	79.29	73.24
	Grass	51.87	64.53
	Cropland	100.00	100.00
	Shadow	91.65	89.92
2	Building	78.67	79.67
	Road	71.04	71.77
	Tree	75.99	74.96
	Grass	50.25	60.61
	Cropland	100.00	100.00
	Shadow	91.72	84.38
3	Building	82.80	85.17
	Road	78.28	78.96
	Tree	88.57	77.82
	Grass	55.56	87.59
	Cropland	100.00	100.00
	Shadow	94.18	90.66
4	Building	74.02	71.41
	Road	94.44	51.15
	Tree	59.08	57.06
	Grass	0.99	100.00
	Cropland	0.00	0.00
	Shadow	10.71	35.29
5	Building	95.36	94.61
	Road	76.24	69.65
	Tree	89.29	90.50
	Grass	30.00	50.81
	Cropland	69.44	38.46
	Shadow	70.74	70.59
6	Building	92.27	95.02
	Road	92.16	92.16
	Tree	87.38	84.74
	Grass	75.69	80.88
	Cropland	100.00	97.87
	Shadow	92.52	89.72
7	Building	95.67	97.46
	Road	94.28	92.72
	Tree	92.22	93.73
	Grass	83.66	79.72
	Cropland	100.00	100.00
	Shadow	93.31	92.34

In comparison, the classification results from scenario 4 were sufficiently poor, the total accuracy and kappa coefficient were only 57.59% and 0.44, respectively. The classification accuracy of cropland was the lowest in all the scenarios. The total accuracy from scenario 5 was 22.54% higher than that of scenario 4, and the kappa coefficient was 0.30 higher. Comparing scenario 4 to scenario 5, the producer's accuracy of building increased from 74.02% to 95.36%, and the user's accuracy increased from 71.41% to 94.61%, respectively. The improvement in producer's accuracy exceeded 29.01% for grass, 30.21% for tree, 60.03% for shadow and 69.44% for cropland, while the producer's accuracy for road class decreased by 18.20%. The improvement in user's accuracy exceeded 18.50% for road, 33.44% for tree, 35.30% for shadow and 38.46% for cropland, however, the grass class accuracy decreased sharply, from 100% to 50.81%.

The total accuracy and kappa coefficient for scenario 3 was higher than that for scenario 5. Comparing scenario 5 to scenario 3, the total accuracy increased from 80.13% to 83.33% and kappa coefficient increased from 0.74 to 0.79, respectively. Increases in the producer's and user's accuracies were realized for road, grass, cropland and shadow classes. However, building and tree classes showed decreases in the producer's and user's accuracies.

Scenario 6 produced a higher total accuracy (89.97%), improving on scenarios 2 and 4 by 12.87% and 32.38%, respectively. The kappa coefficient showed increase of 0.16 and 0.43, respectively. The producer's accuracy and user's accuracy at the class-level were greater than 80% except for grass class, where the producer's accuracy was 75.69 %.

Scenario 7 resulted in better performance than scenario 6, with 3.35% and 0.05 increases in total accuracy and kappa coefficient, respectively. The producer's accuracy and user's accuracy for building, road, tree, cropland and shadow classes were greater than 90%, which was an improvement compared to scenario 6. While grass was less than 85%, the producer's accuracy increased by 7.97%, the user's accuracy decreased slightly 1.16%. Scenario 7 was applied to a RF model for land cover mapping (see Figure 2).
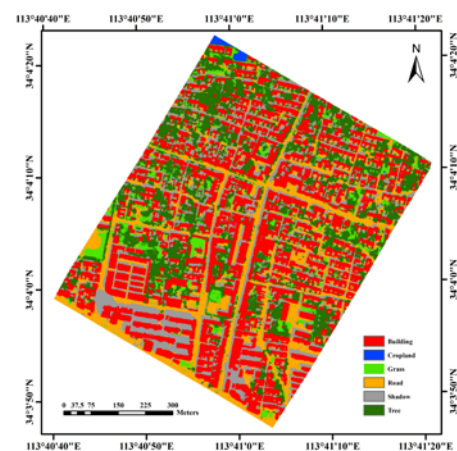
Figure 2 Land cover mapping based on the RF classifier

4 DISCUSSIONS

A comparison of the results listed in Section 3 showed that GF-2 multispectral data or fusion of GF-2 data and others sources can provide relatively good classification mapping accuracy in complex urban environments, where such data had the advantage to discriminate spectral difference among land covers, in particular distinguish shadow from cropland and grass. Compared to other VHR optical satellite sensors, for example, Chen et al. (2009) estimated urban land cover classification accuracy using QuickBird imagery only based on pixel-based classification method, resulting in a total accuracy and kappa coefficient of 69.12% and 0.6219, respectively. Hamedianfar et al. (2014) assessed the classification of urban areas based on both LiDAR data and WorldView-2 imagery using the support vector machine (SVM) and maximum likelihood (ML) methods. The ML and SVM classifications yielded overall accuracies of 72.46% and 75.69%, respectively. Besides, fusing nDSM data and its texture features exhibited the performance for discriminate classes that vertical difference was obvious, such as building and tree.

The GLCM texture significantly improved the classification performance when using in GF-2 satellite data or LiDAR height data. This finding was consistent with those of other studies, where texture features are commonly adopted in satellite remote sensing to improve the classification accuracy (Yan, Shaker, and El-Ashmawy 2015).

Compared to the other scenarios, LiDAR data alone yielded poor classification results. For example, cropland was not completely separable from other classes. The reason may have occurred because the structural differences were not distinct when the LiDAR data was collected in February. Therefore, we may conduct a further comparative study if LiDAR data are acquired during the growing season in future. The results also highlighted the importance of integrating optical remote sensing data (Singh et al. 2012); the results obviously showed that cropland was precisely identified in scenario 1 and 2 while achieving a producer's accuracy and user's accuracy of 100%. It demonstrated that GF-2 performs extremely well in distinguishing cropland from other classes.

The classification accuracy from using GF-2 satellite and LiDAR fusion data exceed that from using GF-2 or LiDAR data alone, resulting in a total accuracy and kappa coefficient of 89.97% and 0.87, respectively, and in classification accuracies on most classes above 80%. The use of LiDAR data was complementary for land-cover classification applications and improved classification accuracy (Singh et al. 2012; Yan, Shaker, and El-Ashmawy 2015; Wu et al. 2017). In addition, as seen in Table 3,

large net increases in producer's and user's accuracies were realized for most classes, this demonstrated that nDSM can efficiently help in differentiating between classes in which vertical features are relatively obvious (Singh et al. 2012).

The fusion of the GF-2 multispectral data, NDVI, LiDAR data and texture features results in the best classification accuracy in all scenarios. The producer's accuracy and user's accuracy of all classes (except for grass) were greater than 90%. This result seems to indicate that multi-source data fusion is a feasible solution for improving land cover classification. However, it also involves greater dimensionality and increased data volume. This phenomenon was also found in previous studies (Singh et al. 2012; Gao et al. 2015). Further studies should quantify the computational time and assess the efficiency of using increased amounts of data in urban classification.

5 CONCLUSIONS

In this study, we first estimated the potential classification accuracy of GF-2 satellite data using a RF classifier, found that GF-2 multispectral data or fusion of GF-2 data and other sources result in relatively good classification mapping accuracy in complex urban environments. Then, we compared classification accuracies for nDSM alone and fusion data of nDSM and its texture features, found that the latter performed better than the former. The total accuracy of both were poorer than fusion data of GF-2 data and its texture features. However, fusion data of nDSM and its texture features enhanced the ability to discriminate between classes with obvious vertical difference: in particular, building and tree. Meanwhile, our results suggested that GLCM textures can significantly improve land cover classification performance whether using in GF-2 satellite data or LiDAR height data. The fusion of GF-2 data and nDSM yielded higher results than either GF-2 or LiDAR height data alone. Fusing GF-2 data, nDSM and their texture features produced the highest total accuracy (93.32%), improving on fusion data of GF-2 data and nDSM by 3.35% and resulting in a producer's accuracy and user's accuracy on most classes of greater than 90%.

REFERENCES

Agarwal, S., Vailshery, L. S., Jaganmohan, M., Nagendra, H., 2013, Mapping Urban Tree Species Using Very High Resolution Satellite Imagery: Comparing Pixel-Based and Object-Based Approaches. *ISPRS International Journal of Geo-Information*, **2**, 220-236.

Breiman, L., 2001. Random forests. *Machine Learning*, **45**, 5-32.

Chen, Y., Su, W., Li, J., Sun, Z., 2009, Hierarchical object oriented classification using very high resolution imagery and lidar data over urban areas. *Advances in Space Research*, **43**, 1101-1110.

Diaz-Uriarte, R. and Andrés, S. A. D., 2006, Gene selection and classification of microarray data using random forest. *BMC Bioinformatics*, **7**, 3.

Duro, D. C., Franklin, S. E., Dubé, M. G., 2012, A Comparison of Pixel-Based and Object-Based Image Analysis with Selected Machine Learning Algorithms for the Classification of Agricultural Landscapes Using SPOT-5 HRG Imagery. *Remote Sensing of Environment*, **118**, 259-272.

Eisavi, V., Homayouni, S., Yazdi, A. M., Alimohammadi, A., 2015, Land cover mapping based on random forest classification of multitemporal spectral and thermal images. *Environmental Monitoring & Assessment*, **187**, 291.

Fu, B., Wang, Y., Campbell, A., Li, Y., Zhang, B., Yin, S., Xing, Z. F., Jin, X. M., 2017, Comparison of object-based and pixel-based random forest algorithm for wetland vegetation mapping using high spatial resolution GF-1 and SAR data. *Ecological Indicators*, **73**, 105-117.

Gao, T., Zhu, J., Zheng, X., Shang, G., Huang, L., Wu, S., 2015, Mapping spatial distribution of larch plantations from multi-seasonal landsat-8 oli imagery and multi-scale textures using random forests. *Remote Sensing*, **7**, 1702-1720.

Guo, L., Chehata, N., Mallet, C., Boukir, S., 2011, Relevance of airborne LiDAR and multispectral image data for urban scene classification using random forests. *ISPRS Journal of Photogrammetry and Remote Sensing*, **66**, 56-66.

Hamedianfar, A., Shafri, H. Z. M., Ahmad, N., Ahmad, N., 2014, Improving detailed rule-based feature extraction of urban areas from worldview-2 image and LiDAR data. *International Journal of Remote Sensing*, **35**, 1876-1899.

Li, X., Wu, T., Liu, K., Li, Y., Zhang, L., 2016, Evaluation of the Chinese fine spatial resolution hyperspectral satellite tiangong-1 in urban land-cover classification. *Remote Sensing*, **8**, 438.

Rasel, S. M. M., Chang, H. C., Diti, I. J., Ralph, T., and Saintilan, N., 2016, Comparison of very near infrared (vnir) wavelength from EO-1 hyperion and worldview 2 images for saltmarsh classification. 2016 XXIII ISPRS Congress held in Prague, Czech, on 12-19 July.

Rodriguez-Galiano, V., and Chica-Olmo, M., 2012, Land cover change analysis of a mediterranean area in spain using different sources of data: multi-seasonal landsat images, land surface temperature, digital terrain models and texture. *Applied Geography*, **35**, 208-218.

Salehi, B., Zhang, Y., Zhong, M., Dey, V., 2012, Object-based classification of urban areas using vhr imagery and height points ancillary data. *Remote Sensing*, **4**, 2256-2276.

Singh, K. K., Vogler, J. B., Shoemaker, D. A., Meentemeyer, R. K., 2012, Lidar-Landsat data fusion for large-area assessment of urban land cover: balancing spatial resolution, data volume and mapping accuracy. *ISPRS Journal of Photogrammetry & Remote Sensing*, **74**, 110-121.

Uamkasem, B., Huang, L. C., Bi, J. T., 2017, Regional land use dynamic monitoring using Chinese GF high resolution satellite data. IEEE International Conference on Applied System Innovation held in Sapporo, Japan, on 13-17 May.

Wang, H., Wang, C., Wu, H., 2016, Using GF-2 imagery and the conditional random field model for urban forest cover mapping. *Remote Sensing Letters*, **7**, 378-387.

Wu Q., Zhong, R. F., Zhao, W. J., Fu, H., Song, K., 2017, A comparison of pixel-based decision tree and object-based Support Vector Machine methods for land-cover classification based on aerial images and airborne lidar data. *International Journal of Remote Sensing*, **38**, 7176-7195.

Yan, W. Y., Shaker, A., El-Ashmawy, N., 2015, Urban land cover classification using airborne lidar data: a review. *Remote Sensing of Environment*, **158**, 295-310.

Zhang, Y., Li, Q., Huang, H., Wu, W., Du, X., Wang, H., 2017, The combined use of remote sensing and social sensing data in fine-grained urban land use mapping: a case study in Beijing, china. *Remote Sensing*, **9**, 865.

Zheng, X. Y., Wu, B., Weston, M. V., Zhang, J., Gan, M. Y., Zhu, J. X., Deng, J. S., Wang, K., Teng, L. M., 2017, Rural settlement subdivision by using landscape metrics as spatial contextual information. *Remote Sensing*, **9**, 486.

Assessment of MODIS daily snow albedo on Livingston Island, Antarctica

Javier F. Calleja[1], Alejandro Corbea-Pérez[1], Susana Fernández[2], Carmen Recondo[3], Juanjo Peón[3]

[1]*RSApps Research Group, Department of Physics, University of Oviedo, Spain.*
[2]*GIS-Forest Research Group, Department of Geology, University of Oviedo, Spain.*
[3]*RSApps Research Group, Department of Mining Exploitation and Prospecting, University of Oviedo, Spain.*
Email addresses: jfcalleja@uniovi.es, alejandrocorbea@gmail.com, fernandezmsusana@uniovi.es, mdrecondo@uniovi.es, juanjopeon@gmail.com

The aim of this work is to evaluate the MODIS daily snow albedo product MOD10A1 at a site on Livingston Island, Antarctica. Although there are albedo maps of Antarctica, they have a spatial resolution of 5 km. In addition, the daily MOD10A1 snow product has not been tested on Antarctica yet. The MOD10A1 daily product provides: cover type (snow, ice, land, cloud), snow cover fraction, snow albedo and a quality factor, at 500-m spatial resolution. The cloud mask of MOD10A1 was compared to in-situ cloud index data, and to data obtained from the NDSI of Landsat 7 and Landsat 8 images and assessed using four quality indices: proportion correct, false alarm ratio, hit rate and frequency bias. Finally, the temporal evolution of the albedo was analysed, based on the daily values and the monthly maximum values, comparing MOD10A1 albedo data to in-situ data. The results show that MOD10A1 on Livingston Island has a similar behaviour to that described for Greenland. MOD10A1 cloud mask can be used for the detection of clouds, although it does not always provide optimal results. As for the temporal evolution of the albedo, MOD10A1 on Livingston Island shows the expected increase of albedo during winter and a decrease of albedo during summer, but exhibits a greater variability than in-situ data.

1 INTRODUCTION

Permafrost is one of the elements most affected by global warming. The permafrost active layer thickness functions as an essential element in the formation of various forms of periglacial landscapes (de Pablo, 2016). The PERMASNOW project (Characterization of snow cover and its effects on the thermal evolution of frozen soils on Livingston and Deception Islands (Antarctica)) studies the influence of the snow cover on the permafrost active layer thickness. We intend to characterize the snow cover using satellite data, in particular, albedo data. The albedo is one of the key factors in climate change, especially in polar areas. The albedo decrease causes an increase of solar radiation absorption, and therefore a heat absorption increase and ice layer decrease (Moritz, 2002). The snow albedo depends on the snow state: when the surface of snow or ice begins to melt, the albedo decreases. In addition, the range of albedo values may indicate differences between sea ice types (Seo, 2016). Also, snow albedo generally decreases with snow aging, which allows to snowfall events. Although the research on snow albedo in the North hemisphere is abundant, few studies have focused on Antarctica,

probably because of its extreme climatic conditions. Monthly and annual albedo changes between 1982 and 1998 in the Arctic Ocean, the Kara and Barents Seas, the Greenland Sea, the Labrador Sea, Hudson Bay, and the Canadian archipelago have been analyzed using NOAA AVHRR data (Laine, 2004). The albedo has also been used to evaluate the energy balance (Foley, 2005). MODIS data have been available since 2000 and there have been numerous terrestrial, oceanic and atmospheric studies based on the data. However, MODIS snow products accuracy should be studied to optimize their use (Hall, 2007). A snow albedo algorithm has been developed (Klein, 2002), which was incorporated in the processing of Terra and Aqua MODIS snow products (MOD10A1 and MYD10A1, respectively). MODIS snow albedo products have been compared to in-situ data over Greenland: (Stroeve, 2005; Moustafa, 2015). It has been shown that MODIS MOD10A1 albedo product over Greenland exhibits the same seasonal variability as in-situ data although it presents occasional problems with the detection of clouds (Stroeve, 2006). Snow depth and snow duration have been investigated in Colorado, USA, comparing MODIS data with in-situ data (Malik, 2012). Moreover, an albedo database for the

Arctic Archipelago Svalbard has been created for the period 1979-2015 with MODIS albedo values (Möller, 2014). The albedo spatial and temporal variation has also been investigated on the Arctic with Melt Pond Detection (MPD) for MERIS (Medium Resolution Imaging Spectrometer) satellite data (Istomina, 2015).

Regarding Antarctica, the albedo has been analyzed in five sectors around Antarctica (Laine, 2008): the Weddell Sea, the Indian Ocean, the Pacific Ocean, the Ross Sea and the Bellingshausen-Amundsen Sea. The study of the long-term variability of albedo and its correlation with climatic variables on this polar zone has also been carried out (Seo, 2016), and different trends have been found depending on the region: positive in the eastern zone but negative in most part of the west. All these studies were carried out using AVHRR data of 5 km spatial resolution.

As a summary, previous results show that, first, there are albedo maps of Antarctica at 5 km resolution, and secondly, there is a MODIS daily snow albedo product with a spatial resolution of 500 m, but it has not been evaluated on Antarctica yet. It is our aim to investigate if this product can be used over Antarctica.

2 MATERIALS AND METHODS

2.1 Study area

The study area is located on Livingston Island, in the South Shetland Islands (SSI) Archipelago in Antarctica. Livingston Island (974 km^2) is 110 km northwest of Cape Roquemaurel in Antarctica, 90 % of the island surface is permanently covered with ice and only the west region and some coastal areas are snow free during the summer. There are two Spanish Antarctic stations on Livingston Island: Juan Carlos I (JCI) and Johnson Glacier (JG). Both stations are 1500 m apart, Juan Carlos I is 50 m from the coastline, Johnson's Glacier is inland. JCI was opened in the summer of 1987-88 and is currently located at 62 ° 39 '48' 'S, 60 ° 23' 19 " W, 13 m above sea level (Bañón, 2016). JG is provided with an automatic weather station (AWS) Campbell CR3000 and was installed in December 2006 at the Johnson Glacier. It was initially located at 62° 40 '16"S, 60° 21 '51"W, 178 m altitude. In January 2015 this AWS was transferred to the Hurd Glacier. JCI data indicates an average annual temperature of -1.2 ° C, with maximum values exceeding 0 ° C throughout the year, and minimum temperatures of -22.6 ° C in winter. The mean annual relative humidity is 83%, the average pressure is relatively low (988.7 hPa) and the average rainfall days (mainly solid, in the form of snow or granular snow, although in the summer liquid precipitations may be frequent) per year is 162. This conditions make Livingston Island a favorable environment for monitoring the permafrost active layer in Antarctica.

2.2 In-situ data

Average daily albedo was measured by a KIPP-ZONEN CNR-1 pyranometer. In-situ radiation data to determine cloud cover were obtained from JCI, which provides diffuse, direct and global radiation every 30 minutes. This station is equipped with KIPP-ZONEN CM11 sensors (for global and diffuse radiation) and KIPP-ZONEN CH1 (for direct radiation). JG provides only global radiation values. Solar zenith angle (SZA) filter was applied to the data: days for which SZA > 75° were eliminated (Wang, 2011). Diffuse and direct radiation data have already been used to study daily and annual albedo variations in Antarctica and the Arctic (Wang, 2011). In the present study, the mean daily cloud index was calculated using daily mean values of dif and dir using the equation:

$$clr = dif / (dif + dir) \qquad (1)$$

In previous studies, a day was classified as cloud-covered if clr > 0.7 (Wang, 2011). In this work we assume that the cloud index calculated with JCI data can be used to characterize the JG location (Manuel Bañón García, private communication).

2.3 Satellite data

MODIS MOD10A1 product data was downloaded from the Google Earth Engine page. The data used in this work corresponds to the pixel on which JG is placed, since the pixel where JCI is located includes water surface, providing misleading results. A total of 1546 snow albedo values were obtained from December 2006 to January 2015. We also obtained 22 Landsat 7 and 62 Landsat 8 whose dates coincided with the days in which MODIS data were available. In this work we are concerned with the daily snow product MOD10A1 evaluation. This product provides type of cover (snow, cloud or other), snow cover fraction, snow albedo value and a quality factor of the product generated. Two filters were applied: MOD10A1 quality filter (Snow_Spatial_QA Field) and the SZA filter as in the in-situ data. All the data with QA ≠ 0 were eliminated. With the resulting data, the albedo daily behavior is represented and analyzed. In order to evaluate the MOD10A1 cloud mask, the results obtained were compared to the standardized method based on the NDSI (Normalized Difference Snow Index) using Landsat 7 and Landsat 8 images. Landsat 7 and Landsat 8 were converted to TOA reflectance. Subsequently, the DOS (Dark Object Substraction) algorithm was applied. Dark pixels were selected from the Drake Pass or Hoces Sea, because they have depths above 4000 m in several areas. Then, the (NDSI) was calculated (Dozier, 1989; Hall, 1995). This index is based on the fact that snow is highly

reflective in the visible, but it reflects very little in the SWIR. For Landsat 8 data, the mean value of the NDSI was calculated on a 17×17 window centered at the Landsat pixel where JG was located in order to obtain the same pixel size as MODIS (500 m). It was not possible to calculate the mean value in the case of Landsat 7, due to the presence of the well-known no data stripes. NDSI threshold values have been used to discriminate cloud and snow. A threshold of 0.4, above which the pixel is classified as snow, has been proposed (Hall, 1995). Other authors (Park, 2016) take 0.6 as a threshold based on the fact the optimal threshold of the snow cover varies depending on the season of the year in a range between 0.4 and 0.6 (Vogel, 2002). Landsat's official website indicates that pixels with NDSI < 0.7 should be classified as cloud. In this article, for the comparison of the MODIS cloud mask versus Landsat 7 and Landsat 8, two thresholds were selected: 0.4 and 0.7.

2.4 Data processing

Four quality indices used for the cloud mask performance (Jolliffe, 2003). Proportion correct, False alarm ratio, Hit rate, and Frequency bias. Regarding the albedo, a 16-day window moving average was applied on both satellite and in-situ data. We also calculated MOD10A1 and in-situ data standard deviation, as previously done in the evaluation of MOD10A1 product on Greenland (Stroeve, 2006). In our work, the standard deviation was calculated every 15 days. We also calculated monthly maximum values. We selected the maximum value and not the mean value, because the data showed a great dispersion when approaching winter. Two temporal series were then obtained: MOD10A1 monthly maximum values and in-situ monthly maximum values. Subsequently, temporal series components were analyzed. For this article we analyzed the trend, which shows the movement of the series in the long term, and seasonal variations or seasonality, which indicate the fluctuations contained in the series with a duration equal to or less than one year.

3 RESULTS AND DISCUSSION

3.1 Cloud mask performance

Quality indices for MOD10A1 vs in-situ data are given in Table 1. From the total number of days between December 1, 2006 and January 25, 2015 (2978) there are 1546 with MOD10A1 data, 557 days with in-situ data and 464 days with both in-situ and MOD10A1 data. The best MOD10A1 hit rate is obtained for the threshold values 0.5 and 0.7. However, 0.5 threshold is also the highest false alarm ratio. The false alarm ratio diminshes when increasing clr. On the other hand, the probability of MODIS

detecting clouds is in all cases above 75%, so we conclude that MOD10A1 cloud mask can be used for the detection of clouds on Livingston Island, although the results are not optimal, as already noted in Greenland (Stroeve, 2006). The best clr threshold seems to be 0.5, in agreement with the value used before by other authors (Wang, 2011).

Table 1: Cloud mask quality indices results for MOD10A1 vs in-situ measurements.

Quality Indices	clr thresholds			
	0.5	0.7	0.9	0.99
Proportion correct (%)	78.2	72.8	58.8	40.1
False alarm ratio	0.85	0.74	0.59	0.39
Hit rate	80.7	81	80.1	76.8
Frequency bias	0.85	0.95	1.26	2.2

Quality indices for MOD10A1vs Landsat 7 are shown in Table 2.

Table 2: Cloud mask quality indexes results for MOD10A1 vs Landsat 7.

Quality index	NDSI threshold	
	0.4	0.7
Proportion correct (%)	59.1	63.6
False alarm ratio	0.2	0.8
Hit rate	90	76.5
Frequency bias	1.7	1.0

The results indicate that the hit rate for a NDSI threshold of 0.4 is higher than for 0.7, although in both cases this index exceeds 75. The false alarm rate approaches 0. The proportion correct is around 60% for both threshold values. In summary, these results show that cloud detection on Livingston Island using the MOD10A1 cloud mask is very similar to cloud detection using Landsat 7 NDSI, especially for a NDSI threshold of 0.4.

Quality indices for MOD10A1 vs Landsat 8 are shown in Table 3.

Table 3: Cloud mask quality indices results for MOD10A1 vs Landsat 8.

Quality index	NDSI threshold	
	0.4	0.7
Proportion correct (%)	67.7	74.2
False alarm ratio	0.4	0.6
Hit rate	82	78
Frequency bias	1.2	0.9

The proportion correct is higher than 60 % for both thresholds, exceeding 70 % for 0.7 threshold. In contrast, the 0.4 threshold gives a higher hit rate and a lower value in the false alarm ratio. Although the frequency bias is close to 1 for 0.7 threshold, the difference with the 0.4 threshold is only 0.1. For a

NDSI threshold of 0.4, cloud detection using MOD10A1 cloud mask produces nearly the same results as using Landsat 8 NDSI.

3.2 Albedo time series

The temporal evolutions of in-situ and MOD10A1 daily albedo are show in Fig. 1. There are long time spans without data. In addition to the missing data in the original series, the application of the quality filter and the SZA filter increased the number of days without data significantly, especially in the winter season, making the analysis even more difficult. In fact, there are no data from the months of May, June and July. It can be observed that both in-situ and MOD10A1 show an increase in albedo values when approaching winter, which are usually above 80% and a decrease in summer, where they are usually below 70%. We analyzed the time series from the monthly maximum values, and the trend and the seasonality components were obtained (Fig. 2). The in-situ data show monthly maximum albedo values in the range of 60% to 100%. The trend does not show a clear pattern, while seasonality shows a decline in albedo in the summer, with values ranging from less than 5% to more than 10% below the annual average. In the winter there is an increase of up to 5% above the annual average. It is worth noting that MOD10A1 albedo exhibits a similar behavior to in-situ data. Monthly values also fluctuate between 60% and 100%,

but more dispersion is observed than in the in-situ data. The trend of MOD10A1 albedo does not show any apparent pattern, and seasonality shows the same pattern as in-situ data: a decrease in albedo values in the summer, and an increase in winter.

To complete the albedo daily behavior analysis, the standard deviation was calculated, in order to determine the variability. As can be seen in Fig. 3, the standard deviation is higher when we approach winter while it decreases in the summer. The lowest average values of standard deviation are found in the period from October to March. In addition, the average standard deviation of MODIS albedo values is 7.3 while in-situ albedo values show an average standard deviation of 5.0, which shows that MOD10A1 presents greater variability than in-situ data, a result similar to that obtained on Greenland (Stroeve, 2006), where it was found that MOD10A1 tracks the seasonal variability in the albedo but presents a greater variability than that observed in the terrestrial stations. Moreover, the results obtained in the albedo analysis on Livingston Island show a behavior similar to that obtained in the Arctic (Wang, 2011). However, for both in-situ and MODIS data, it is important to emphasize the marked influence of the large number of missing values in the analysis. We conclude that MODIS daily snow albedo product MOD10A1 can be used on Livingston Island to characterize the time evolution of the snow albedo.
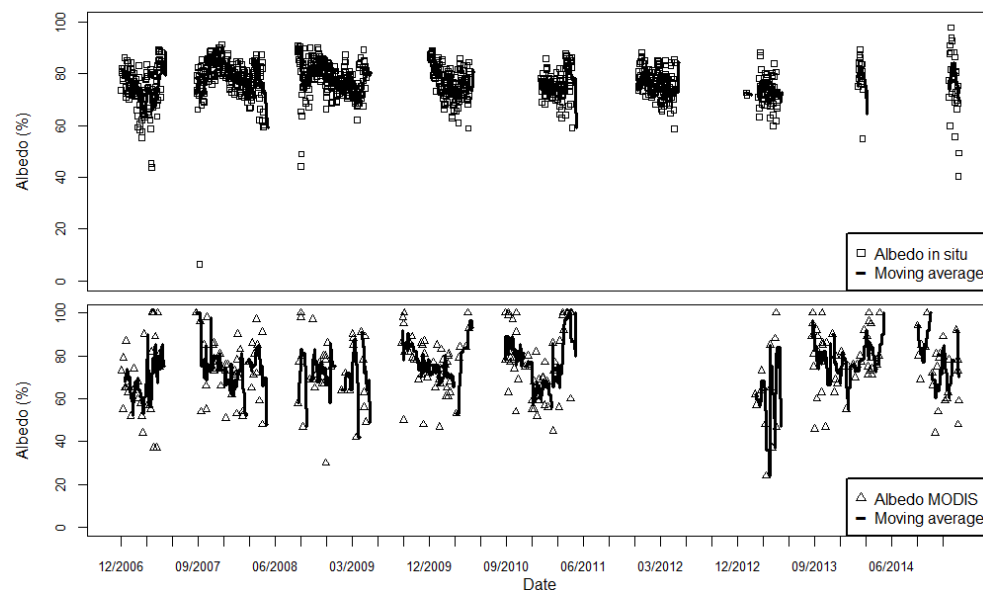
Figure 1. Snow daily albedo (open symbols) and the 16-window moving average (solid line) for in-situ measurements (top) and MOD10A1 product (bottom).
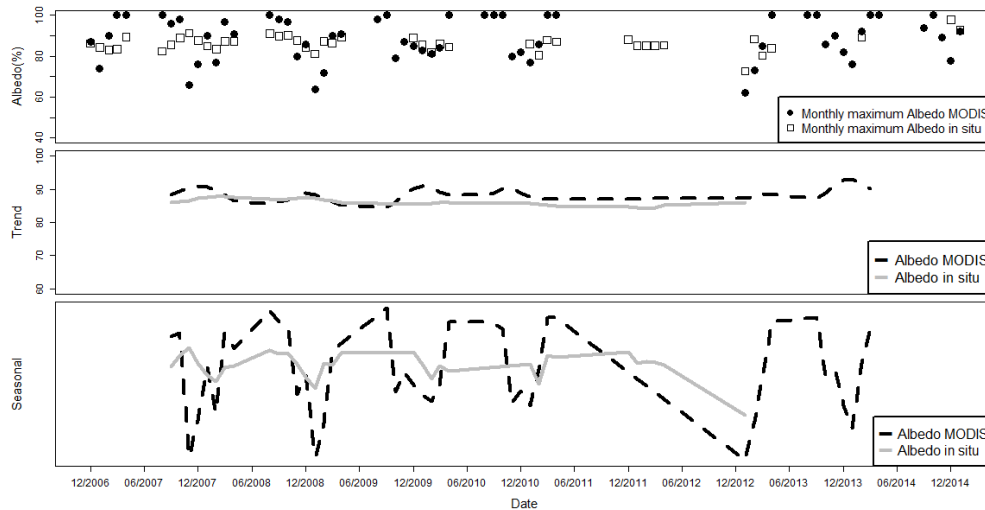
Figure 2. In-situ and MOD10A1 maximum monthly albedo (top), trend (middle) and seasonal (bottom) components.
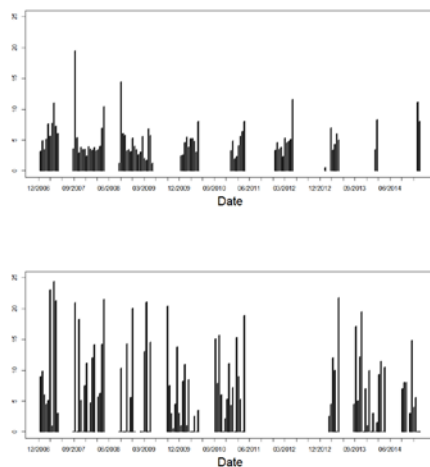
Figure 3. Albedo standard deviation calculated every 15 days for in-situ measurements (top) and MOD10A1 (bottom).

4 CONCLUSIONS

We have carried out an assessment of MODIS MOD10A1 daily snow albedo product at a site on Livingston Island, Antarctica, for the period 2006-20014. The cloud mask output has been compared to the classification obtained using the in-situ cloud index and to cloud masking output from NDSI data from Landsat 7 and 8. The results show that the MOD10A1 cloud mask performance is comparable to that obtained over Greenland and that, although it provides acceptable results, it must be used with caution. The albedo temporal behaviour was also analysed. The trend and the seasonal time series of MOD10A1 were compared to those obtained in-situ. The trend does not show a clear pattern, and the seasonal component exhibits in both cases the same regular pattern consisting of an increase of albedo in winter and a decrease in summer. Moreover, the standard deviation of albedo increases in winter in both MOD10A1 and in-situ data, a fact that needs further investigation. As a summary, we conclude that MOD10A1 snow albedo shows a temporal behaviour similar to that of in-situ albedo, and it can be used to study the time evolution of albedo on Livingston Island.

5 REFERENCES

Bañón, M., and Vasallo, F., 2016, AEMET en la Antártida. Climatología y meteorología sinóptica en las estaciones meteorológicas españolas en la Antártida AEMET, Madrid: Agencia Estatal de Meteorología.

Dozier, J., 1989, Spectral signature of Alpine snow cover from the Landsat Thematic Mapper, *Elsevier Science Publishing*, **28**, 9–22.

Foley, J., 2005, Tipping points in the tundra, *Science*, **310**, 627-628.

Hall, D.K., Riggs, G.A., and Salomonson, V.V., 1995, Development of methods for mapping global snow cover using moderate resolution imaging spectroradiometer data, *Remote Sensing of Environment*, **54**, 127–140.

Hall, D.K., and Riggs, G.A., 2007, Accuracy assessment of the MODIS snow products, *Hidrological Processes*, **21**, 1534–1547.

Istomina, L. et al., 2015, Melt pond fraction and spectral sea ice albedo retrieval from MERIS data-Part 1: Validation against in situ, aerial, and ship cruise data, *The Cryosphere*, **9**, 1567–1578.

Jolliffe, I.T., and Stephenson, D.B., 2003, Forecast Verification: A Practitioner's Guide in Atmospheric Science, New Jersey: Wiley.

Klein, A.G., and Stroeve, J., 2002, Development and validation of a snow albedo algorithm for the MODIS instrument, *Annals of Glaciology*, **34**, 45–52.

Laine, V., 2004), Arctic sea ice regional albedo variability and trends, 1982–1998, *Journal of Geophysical Research*, **109(C6)**, C06027.

Laine, V., 2008, Antarctic ice sheet and sea ice regional albedo and temperature change, 1981-2000, from AVHRR Polar Pathfinder data, *Remote Sensing of Environment*, **112**, 646–667.

Malik, M.J. et al., 2012, Assimilation of satellite-observed snow albedo in a land surface model, *Journal of Hydrometeorology*, **13**, 1119–1130.

Möller, M. and Möller, R., 2014, Modeling glacier-surface albedo across Svalbard for the 1979-2015 period: The HiRSvaC500-a data set, *Journal of Advances in Modeling Earth Systems*, **6**, 513–526.

Moritz, R.E., 2002, Dynamics of recent climate change in the Arctic. *Science*, **297**, 1497–1502.

Moustafa, S.E. et al., 2015, Multi-modal albedo distributions in the ablation area of the southwestern Greenland Ice Sheet, *Cryosphere*, **9**, 905–923.

de Pablo, M.Á. et al., 2016, Frozen ground and snow cover monitoring in the South Shetland Islands, Antarctica: Instrumentation, effects on ground thermal behaviour and future research. *Cuadernos de investigación geográfica*, **42**, 475-495.

Park, S.-H. et al., 2016, Spatiotemporal analysis of snow cover variations at Mt. Kilimanjaro using multi-temporal Landsat images during 27 years, *Journal of Atmospheric and Solar-Terrestrial Physics*, **143–144**, 37–46.

Seo, M. et al., 2016, Long-Term Variability of Surface Albedo and Its Correlation with Climatic Variables over Antarctica, *Remote Sensing*, **8**, 981.

Stroeve, J. et al., 2005, Accuracy assessment of the MODIS 16-day albedo product for snow: comparisons with Greenland in situ measurements, *Remote Sensing Remote Sensing of Environment*, **94**, 46–60.

Stroeve, J. et al., 2006, Evaluation of the MODIS (MOD10A1) daily snow albedo product over the Greenland ice sheet, *Remote Sensing of Environment*, **105**, 155–171.

Vogel, S.W., 2002, Usage of high-resolution Landsat 7 band 8 for single-band snow-cover classification, *Annals of Glaciology*, **34**, 53–57.

Wang, X. and Zender, C.S., 2011, Arctic and Antarctic diurnal and seasonal variations of snow albedo from multiyear Baseline Surface Radiation Network measurements, *Journal of Geophysical Research: Earth Surface*, **116**, 1–16.

Synergy between satellite and ground-based estimates of the cloud cover

Freile-Aranda M.D., Gómez-Amo J.L., Utrillas M.P., Martínez-Lozano J.A.
Dpt. Earth Physics and Thermodynamics, University of Valencia (Spain)
M.Dolores.Freile@uv.es, Jose.L.Gomez-Amo@uv.es, Maria.P.Utrillas@uv.es,
Jose.A.Martinez@uv.es

ABSTRACT – *Clouds play an important role in the Earth's energy budget and water cycle. The cloud-radiation interaction, through scattering or absorption, modifies the amount of radiation that reaches the Earth's surface or that goes out to space. The cloud cover is one the most important parameters regarding to the energy budget at regional or planetary level. Observations of the cloud cover are routinely made by satellites and from ground-based measurements. However, in most cases satellite and surface observations do not agree with the desired confidence level. Therefore, the aim of this work is to compare ground-based and satellite results of the cloud cover over Valencia (Spain). To do this we use two different methodologies to estimate the cloud cover from ground-based measurements: a) The automatic partial cloud amount detection algorithm (APCADA) using the terrestrial radiation and; b) The automated method presented by Long et al. (2006) using shortwave radiation. Ground-based estimates of the cloud cover have been compared against the determination provided by the Clouds and the Earth's Radiant Energy System (CERES) instrument. Different spatial windows, for the satellite data, and temporal windows around the satellite overpass, for ground-based measurements have been tested in the comparison. All datasets used in the study show similar cloud cover distributions. The correlation between ground-based and satellite cloud cover is always higher than the 90%, although the best coincidence is found from the pyranometer and Aqua comparison.*

1 INTRODUCTION

Clouds cover an appreciable portion of the sky and have an important impact on the Earth's energy budget and on the hydrological cycle (Chen et al, 1999; Lin et al., 2000). The magnitude of their impact is related to their interaction with radiation through the scattering of shortwave radiation and the absorption of longwave radiation. Typically, clouds interaction with radiation can produce cooling (shortwave effect) or warming (longwave effect) of the Earth-atmosphere system.

For all this reasons, it is essential to know their distribution in the sky. Several techniques have been developed using ground-based instruments as: pyranometers (Long et al., 2000; Long et al., 2006), pyrgeometers (Marty and Philipona, 2000; Dürr et al., 2004) and all-sky cameras (Calbó and Sabburg, 2008; Wacker et al., 20015).

Nowadays, satellites represent a powerful tool that help to have a better spatial description of the Earth surface and atmosphere conditions. The Clouds and the Earth's Radiant Energy System (CERES) instrument, on board Terra, Aqua and TRMM, provide information about cloud cover, cloud properties and radiation fluxes around the world.

In this work, the synergies between ground-based and satellite estimates of the cloud cover are analyzed. In section 2, the data used is described, while in section 3 the methodology followed is explained. Section 4 show the results obtained and, finally, section 5 contains the conclusions of this study.

2 DATA

2.1. GROUND-BASED

Ground-based data are registered by a series of instruments placed on the roof of the Faculty of Physics, on the Burjassot campus at the University of Valencia (39º30'N, 0º25'W). Longwave radiation measurements are taken by a CGR4 Kipp & Zonen pyrgeometer working in a spectral range between 4.5 and 42 µm. On the other hand, the components of the shortwave radiation are measured by two CMP21 Kipp & Zonen pyranometer (for global and diffuse, from 0.285 to 2.8 µm) and a CHP1 Kipp & Zonen pyrheliometer (for the direct within the 0.28-4 µm spectral range). All instruments are mounted in a SOLYS-2 sun-tracker and the data are stored with 1-minute resolution.

2.2. SATELLITE

The Clouds and the Earth's Radiant Energy System (CERES) instrument, on board of Terra and Aqua satellites, was developed to improve the understanding of the Earth's energy budget and the role of clouds in it. CERES has three detectors working in different spectral ranges: total (0.3-100µm), shortwave (0.3-5µm) and IR window (8-12µm). The spatial resolution at nadir is 20 km. The Single Scanner Footprint (SSF) product provided by CERES is used (Wielicki et al., 2006; Minnis et al, 2011). This is a Level 2 product that provides measurements of longwave, shortwave and window radiation and also includes cloud and aerosols

properties measured by the Moderate Resolution Imaging Spectroradiometer instrument (MODIS) on board of Terra and Aqua satellites too. Considering that CERES is on board of two platforms and both overpass our site twice a day, four satellite measurements are usually available every day.

3   METHODOLOGY

3.1. GROUND-BASED TECHNIQUES

The automatic partial cloud amount detection algorithm (APCADA) was developed by Dürr and Philipona (2004) to obtain the cloud cover using measurements of longwave downward radiation, temperature and relative humidity. To calculate the cloud cover, APCADA uses the variation of the longwave radiation during an hour and the cloud free index (CFI). The CFI is the quotient between the apparent emittance and the apparent cloud free emittance of the sky. It allows to distinguish clear sky situations (CFI≤1) from cloudy skies (CFI>1). Authors present a set of rules using the CFI and the longwave radiation variation to obtain the cloud cover in octas. APCADA provides continuous results 24 hours a day. This technique have some limitations detecting high clouds because of their low temperature and thus their longwave emission.

Long and Ackerman (2000) presented and automated method to identify cloudy and clear skies using global and diffuse radiation. To do this, they apply four tests to radiation data. The tests are based on the magnitude and variation of the radiation and allow the identification of clear skies. Then, overcast skies are identified through their effects on diffuse radiation and the ratio between diffuse and global radiation (Long et al., 2006). Finally, the fractional cloud cover is calculated with the remaining cases using a power law equation. Thin clouds present at large solar zenith angles are not detected by this method.

This technique provides the cloud cover values between 0 and 1. A conversion to octas is done following the rules shown in Table1:

Table 1 - Unit conversion of cloud cover

Fraction	Octas
0	0
0 < Cloud cover < 0.1875	1
0.1875 ≤ Cloud cover < 0.3125	2
0.3125 ≤ Cloud cover < 0.4375	3
0.4375 ≤ Cloud cover < 0.5625	4
0.5625 ≤ Cloud cover < 0.6875	5
0.6875 ≤ Cloud cover < 0.8125	6
0.8125 ≤ Cloud cover < 1	7
1	8
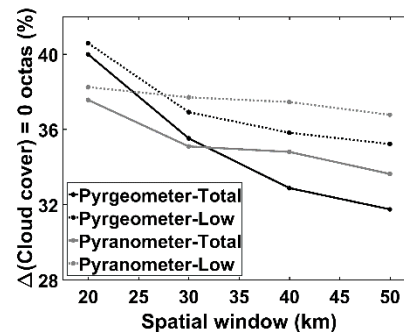
Figure 1 - Number of coincidences between Aqua and ground-based cloud cover for a temporal window of 60 minutes as a function of the spatial window.

3.2. SATELLITE

The CERES instrument provide the cloud cover up to two cloud layers. Independently of the layer height, the first layer is the lowest and the second the highest. In this work the low layer cloud cover and the total cloud cover are used, obtained as the sum of the low layer and high layer minus its overlap. These two datasets are used in order to analyse some limitations of the ground-based techniques related with the detection of high clouds.

CERES cloud cover is presented in percentage. To do the comparison, cloud cover values are converted to octas using the intervals included in Table 1, but multiplied by 100.

3.3. COMPARISON OF THE DATA

To do the comparison, a temporal and spatial window are defined. The temporal window defines the time interval used to average the ground-based data around the satellite overpass time. The spatial window sets the area (or number of pixels) around the ground-based site to average the satellite data used in the comparison. Spatial and temporal windows of different sizes are used to analyse which windows give the best results. The sizes for the spatial window are 20km x 20km, 30km x 30km, 40km x 40km and 50km x 50km around the site. On the other hand, the time intervals used as temporal windows are 15min, 30min and 60min, centered on the satellite overpass time.

4   RESULTS

4.1. SPATIAL AND TEMPORAL AVERAGES

First of all, an analysis is done to determine which spatial and temporal window are the most appropriate for the ground-satellite comparison. The number of coincidences (0 octas differences) between satellite and ground-based cloud cover is determined. All the datasets available are used: pyrgeometer, pyranometer, CERES total cloud cover and CERES low layer cover

from TERRA and AQUA. Figure 1 shows the number of coincidences as a function of the spatial window using CERES data on board Aqua. The four cases studied here show the same results. The best satellite and ground-based agreement is achieved when a spatial window of 20km x 20km is used.

Different sensitivities to the spatial window are observed in the comparison for the pyranometers and pyrgeometres methodologies. Pyrgeometers show a higher sensitivity to the spatial window than the pyranometer. The same results are obtained using Terra data (not shown).
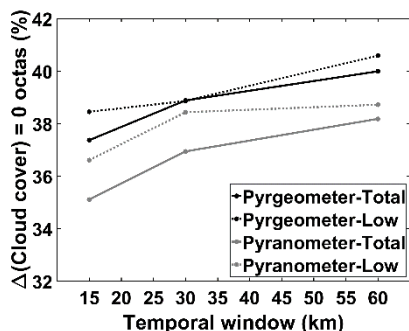
Figure 2 - Number of coincidences between Aqua and ground-based cloud cover for a temporal window of 60 minutes as a function of the temporal window.

The same procedure followed with the spatial window is now used with the temporal window. Fig. 2 presents the number of coincidences between ground-based cloud cover and CERES Aqua cloud cover in percentage. All four comparisons exhibit the same behaviour: the maximum number of coincidence appears always when a spatial window of 60 min selected. The same conclusion is obtained using Terra data (not shown).

4.2. CLOUD COVER DISTRIBUTION

After the results obtained in the previous section, ground-based and satellite cloud cover is compared using a spatial window of 20km x 20km and a temporal window of 60 minutes around the satellite overpass time.

Figure 3 represent the distribution of the cloud cover determined by the pyrgeometer, the pyranometer and the total and low layer cloud cover provided both by CERES Aqua. The four datasets present their maximum in 1octa and similar distribution for the rest of cloud cover values. The only exception is found in 7 octas for the total cloud cover. At this cloud cover value, Aqua total cloud cover presents a frequency higher than the other datasets in more than a 10%. Considering that this difference is not present in Aqua low layer cloud cover, it has to be a consequence of high clouds that are not identified by ground-based

techniques. Figure 4 represent the same that Fig. 3 but using CERES Terra data. The results shown are the same that using CERES Aqua data.
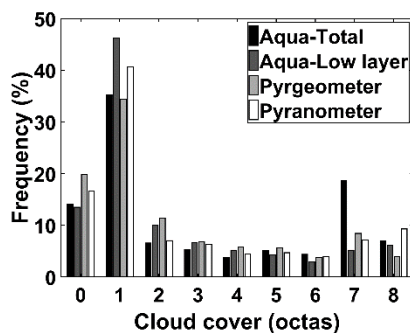
Figure 3 - Distribution of the cloud cover obtained by a pyrgeometer, pyranometer and the CERES instrument on board Aqua satellite.
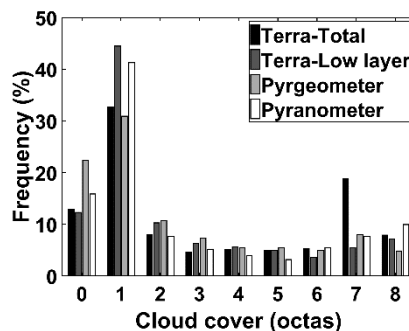
Figure 4 - Distribution of the cloud cover obtained by a pyrgeometer, pyranometer and the CERES instrument on board Terra satellite.

4.3. RELATIONSHIP BETWEEN GROUND-BASED AND SATELLITE CLOUD COVER

A linear regression analysis has been done to evaluate the agreement between ground-based and satellite determination of the cloud cover. All the available data-pairs have been used in the linear fit and the correlation coefficient, slope and intercept are shown in Tables 2 and 3. Mean ground-based cloud cover is calculated for each satellite cloud cover value.

Table 2 show the relationship between the pyrgeometer cloud cover and the Aqua total, Aqua low layer, Terra total or Terra low layer cloud cover. A correlation higher than the 90% between the two datasets considered is observed in all cases. So indicating a good agreement between pyrgeometer and satellite cloud cover. However, the slope is around the 70% in all cases, the intercept is never higher than 1 octa. As an example, Fig. 5 shows the linear fit obtained when pyrgeometer cloud cover is compared with Terra low layer cloud cover.

Table 2 - Relationship between pyrgeometer and satellite cloud cover.

Pyrgeometer	Slope	Intercept	r^2
Aqua Total	0.62 ± 0.04	0.3 ± 0.2	0.97
Aqua Low layer	0.73 ± 0.05	0.6 ± 0.3	0.96
Terra Total	0.67 ± 0.05	0.2 ± 0.2	0.96
Terra Low layer	0.79 ± 0.06	0.5 ± 0.3	0.96

Table 3 contains the same information that Table 2 but using the pyranometer cloud cover. In this case, the slopes are closer to 1 than in the pyrgeometer comparison. The intercept values are similar to the values presented in Table 2. The correlation between pyranometer and satellite cloud cover is always higher than the 90%. This confirms the good agreement between the two datasets. In Fig. 6 is plotted the relationship of the pyranometer and the Terra low layer cloud cover.

Besides, the results presented in Table 2 and 3 show that ground-based techniques have a better correspondence with satellite low layer cloud cover than with the total cloud cover. This effect is a consequence of the limitations of the ground-based techniques to identify high and thin clouds. Furthermore, high clouds are better detected by satellite instruments than by ground-based instruments, which are more influenced by low clouds.

Table 3 - Relationship between pyranometer and satellite cloud cover.

Pyranometer	Slope	Intercept	r^2
Aqua Total	0.79 ± 0.11	-0.5 ± 0.5	0.87
Aqua Low layer	0.90 ± 0.06	-0.2 ± 0.3	0.97
Terra Total	0.80 ± 0.13	-0.5 ± 0.6	0.84
Terra Low layer	0.93 ± 0.07	-0.1 ± 0.3	0.96
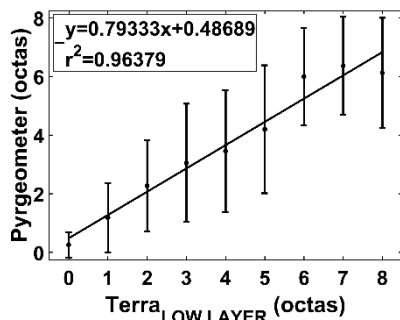
Figure 5 - Relationship between pyrgeometer and Terra total cloud cover.
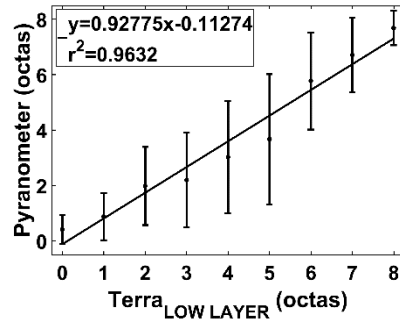
Figure 6 - Relationship between pyrgeometer and Terra low layer cloud cover.

Table 2 and 3 show that some differences exist between CERES Aqua and CERES Terra cloud cover, although both platforms carry the same instrument. As noted in (Minnis et al., 2004), these differences are related to diurnally dependent changes in clouds.

5   CONCLUSIONS

Synergies between satellite and ground-based cloud cover are analysed in this work. The satellite data used is provided by CERES, and the ground-based data registered by a pyrgeometer and a pyranometer.

The highest coincidence between ground-based and satellite cloud cover is obtained when a spatial window of 20km x 20km and temporal window of 60 minutes around the satellite overpass time are used.

All datasets present similar cloud cover distributions except the total cloud cover (Terra and Aqua). This data present a frequency of almost 20% that does not appear in the other datasets, probably caused by high clouds.

Results show a high agreement between satellite and ground-based cloud cover, although the best correlation is found for the pyranometer and Aqua low layer cloud cover. Pyrgeometer and Aqua (Terra) cloud cover coincide on a 40% (35%) of the data analysed, approximately. On the other hand, pyranometer present a 38% of coincidence with both Aqua and Terra.

6   ACKNOWLEDGEMENTS

7   REFERENCES

Calbo, J., and Sabburg, J., 2008, Feature extraction from whole-sky ground-based images for cloud-type recognition. *Journal of Atmospheric and Oceanic Technology*, 25(1), 3-14.

Chen, T., Rossow, W. B., and Zhang, Y, 2000, Radiative effects of cloud-type variations. *Journal of Climate*, 13, 264-286.

Durr, B. and Philipona R., 2004, Automatic cloud amount detection by surface longwave downward radiation measurements. *Journal of Geophysical Research: Atmospheres,* 109(D5), 2156-2202. doi: 10.1029/2003JD004182.

Lin, X., Randall, D., and Fowler, L., 2000, Diurnal Variability of the Hydrologic Cycle and Radiative Fluxes: Comparisons between Observations and a GCM, *Journal of Climate*, 13, 4159–4179.

Long, C. N., and Ackerman, T. P., 2000, Identification of clear skies from broadband pyranometer measurements and calculation of downwelling shortwave cloud effects. *Journal of Geophysical Research: Atmospheres,* 105(D12), 15609-15626. doi:10.1029/2000JD900077.

Long C. N., Ackerman T. P., Gaustad K. L. and Cole J. N.S., 2006, Estimation of fractional sky cover from broadband shortwave radiometer measurements. *Journal of Geophysical Research: Atmospheres,* 111(D11), 2156-2202. doi:10.1029/2005JD006475.

Marty, C., and Philipona, R., 2000, The clearsky index to separate clearsky from cloudysky situations in climate research. *Geophysical Research Letters*, 27(17), 2649-2652.

Minnis, P., Sun-Mack, S., Young, D.F., Heck, P.W., Garber, D.P., Chen, Y., Spangenberg, D.A., Arduini, R.F., Trepte, Q.Z., Smith, W.L., Ayers, J.K., Gibson, S.C., Miller, W.F., Hong, G., Chakrapani, V., Takano, Y., Liou, K. N., Xie, Y. and Yang, P., 2011, CERES Edition-2 Cloud Property Retrievals Using TRMM VIRS and Terra and Aqua MODIS Data - Part I: Algorithms. *IEEE Transactions on Geoscience and Remote Sensing*, 49(11), 4374-4400.

Minnis, P., Young, D. F., Sun-Mack,S., Heck, P. W., Doelling, D. R. and Trepte, Q. Z., 2004, CERES cloud property retrievals from imagers on TRMM, Terra, and Aqua. *Proceedings of SPIE Remote Sensing of Clouds and the Atmosphere VIII*, 5235, 37-49. doi: 10.1117/12.511210.

Wacker, S., Gröbner, J., Zysset, C., Diener, L., Tzoumanikas, P., Kazantzidis, A., Vuilleumier, L., Stöckli, R., Nyeki, S. and Kämpfer, N., 2015, Cloud observations in Switzerland using hemispherical sky cameras. *Journal of Geophysical Research: Atmospheres*, *120*(2), 695-707.

Wielicki, B. A., Barksotrm, B. R., Harrison, E. F., Lee III, R. B., Smith, G. L. and Cooper, J.E., 1996, Clouds and the Earth's Radiant Energy System (CERES): An Earth Observing System Experiment. *Bulletin American Meteorological Society* 77, 853-868.

Validation of the Climate Data Record of EUMETSAT LSA SAF SEVIRI/MSG LAI, FAPAR and FVC products

B. Fuster[1], J. Sánchez-Zapero[1], F. Camacho[1], F. J. García-Haro[2], M.Campos-Taberner[2]

[1]*EOLAB, Parc Científic Universitat de València. C/Catedrático Agustín Escardino, 9. 46980 Paterna (Valencia), Spain.*
[2]*Departament de Física de la Terra i Termodinàmica, Universitat de València, Spain.*
beatriz.fuster@eolab.es

ABSTRACT - *The EUMETSAT LSA SAF service generates and disseminates a suite of vegetation products (LAI, FAPAR and FCOVER) derived from SEVIRI/MSG observations for the whole Meteosat disk at two different time resolutions (daily products and 10-day products). LSA SAF service has recently reprocessed the entire MSG archive with the recent version of the several retrieval algorithms in the processing chain in order to obtain a continuous and homogeneous Climate Data Records (CDR) of Land-SAF suite of land products suitable for many environmental and climate application. This paper presents the validation of the CDR of vegetation parameters (LAI, FAPAR and FCOVER) from 2004 to 2016. The analysis is focused on the assessment of spatial and temporal consistency, precision, accuracy and stability of the time series. As validated references, the MODIS/TERRA C5 and the Copernicus Global Land SPOT/VGT V1 were used. Likewise, as ground references, the CEOS DIRECT (2000-2011) and the FP7 ImagineS ground databases (2013-2016) were used.*

1. INTRODUCTION

The LSA SAF service has recently reprocessed the entire SEVIRI/MSG archive (2004-2012), with the latest version of the several retrieval algorithms in the processing chain (VEGAv3.0 for daily LAI, FAPAR and FVC and v2.0 for the equivalent 10-day products) in order to obtain a continuous and homogeneous dataset of Climate Data Records (CDR) of vegetation products. These products are produced in near real time at a spatial resolution of 3 km at nadir in the geostationary grid (see more details in García-Haro et al., this issue).

The CDR dataset includes only 10-day VEGA products. However, a similar dataset of reprocessed daily products has been produced as "internal products". Although the daily products are not foreseen to be distributed as CDR, they may be made available upon request. It is worth mentioning that the VEGA algorithms of the daily products and the 10-day products are identical, differing only in the composition window of the BRDF input.

The 2004-2012 period has been considered for the temporal analysis and stability of the time series. Inter-comparison exercises have been performed using as reference SPOT/VGT V1 products and NASA MODIS C5 LAI, FAPAR products using a two year period (2008-2009). Finally, the accuracy assessment is achieved against matchups with ground-based reference maps coming from the OLIVE tool hosted at CEOS cal/val portal, and the ImagineS ground database. For this test, the whole period (2004-2016) was used to increase the number of observations.

The objective of this work is to validate the CDR of vegetation parameters (LAI, FAPAR and FCOVER) derived from SEVIRI/MSG data in the LSA SAF service.

2. METHODOLOGY

Several criteria of performance were assessed in agreement with previous global LAI validation exercises (Camacho et al., 2013), the OLIVE (On Line Validation Exercise) tool hosted by CEOS cal/val portal (Weiss et al., 2014), the recent CEOS LPV Global LAI product validation protocol (Fernandes et al., 2014) and additional metrics proposed to validate similar products in the Copernicus Global Land Service. First, an intercomparison with the existing global validated products was conducted to examine the spatial and temporal consistency, the precision and the stability of MSG VEGA products. Second, a direct validation approach was conducted using ground reference maps to quantify the overall uncertainties of the products.

2.1. Validation protocol

The reference global satellite products used are the Copernicus Global Land SPOT/VGT V1 observations (Baret et al., 2013), produced at 1 km spatial resolution and 10-days temporal frequency (using a temporal window of 30 days), and Terra MODIS LAI/FAPAR (MOD15A2) collection 5 (Knyazikhin et al., 1998), with 1 km spatial resolution and 8 days step over a sinusoidal grid.

The products were intercompared over the MSGVAL network composed of 478 sites that represents globally

the variability of land surface types (Figure 1): 239 BELMANIP-2.1 (Weiss et al., 2014) sites covering the MSG disk, 120 EUVAL sites located over Europe and North of Africa (Camacho et al., 2017a), 29 African validation sites used by JRC NARMA (Natural Resources Monitoring for Africa) user during geoland-2 project, 8 Enviro-Net sites (www.enviro-net.org/) across South of America, 63 sites coming from OLIVE DIRECT (http://calvalportal.ceos.org), and 19 coming from ImagineS.
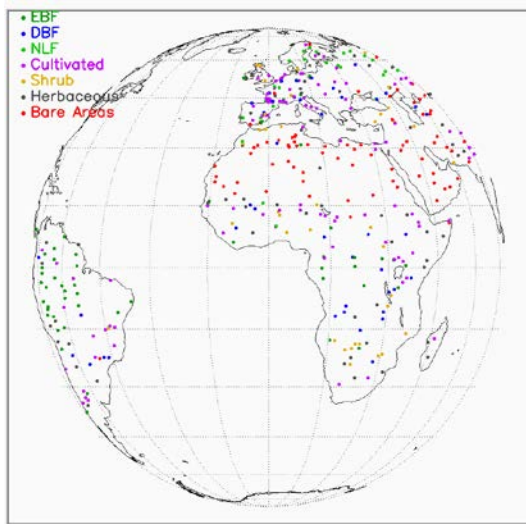
Figure 1: Location of the 478 MSGVAL sites.

The following criteria of performance and metrics were assessed:

- Product Completeness: corresponds to the absence of spatial and temporal gaps in the data. Temporal variations of missing values for SPOT/VGT V1 and MSG SEVIRI VEGA 10-day products have been computed.
- Spatial Consistency: can be quantitatively assessed by comparing the spatial distribution of a reference validated product with the product biophysical maps under study. Histograms of differences at a monthly basis were analyzed.
- Temporal Consistency: The consistency of temporal variations of the vegetation variables are compared to reference validated products.
- Precision: Intra-annual precision (smoothness) shows temporal noise assumed to have no serial correlation within a season. In this case, the anomaly of a variable from the linear estimate based on its neighbours can be employed as an indicator of smoothness or intra-annual precision. It can be characterized as suggested by Weiss et al., (2007): for each triplet of consecutive observations, the absolute value of the difference between the centre

P(dn+1) and the corresponding linear interpolation between the two extremes P(dn) and P(dn+2) was estimated:

$$\delta = \left| P(d_n+1) - P(d_n) - \frac{P(d_n) - P(d_{n+2})}{d_n - d_{n+2}}(d_n - d_{n+1}) \right| \quad (1)$$

Histograms of the smoothness are presented adjusted to a negative exponential function and the exponential decay constant is used as quantitative indicator of the smoothness value.

Inter-annual precision (i.e., dispersion of FAPAR values from year to year) was evaluated providing a box-plot of the median absolute deviation of anomalies versus product per bins until the maximum product value (Fernandes et al., 2014) using the upper 95th and lower 5th percentiles over MSGVAL sites. Note that cultivated sites were not considered in this analysis due to the large inter-annual variability in this land cover type. Broadleaf Evergreen Forest sites were also removed from this computation to avoid noisy temporal trajectories.

- Stability of the time series: can be investigated displaying Hovmöller plots (Hovmöller, 1949) of the bias between two products, providing the temporal evolution of bias and their latitudinal variation.
- Overall statistical consistency: The inter-comparison of products offers a means of assessing the relative uncertainties (systematic or random) between products. The global statistical analysis is performed over MSGVAL sites considering all dates available. Note that VEGA pixels with estimated error higher than 1.5 in case of LAI and higher than 0.15 in case of FVC/FAPAR have been discarded from this computation in order to avoid unreliable estimations. In case of GEOV1 and MODIS C5, only good quality pixels according to the Quality Flag were used.

2.2. Direct Validation

For the Accuracy Assessment, MSG VEGA daily products instead of MSG VEGA 10D were used as these products are more suitable to compare with ground values in terms of temporal frequency.

The accuracy assessment of MSG VEGA daily satellite products was performed against ground truth data processed according to CEOS LPV guidelines for validation of LAI products.

The data used to validate from 2004 to 2013 comes from the OLIVE DIRECT database (Camacho et al., 2013b), available at CEOS Cal/Val portal (http://calvalportal.ceos.org). Those forest DIRECT sites were understory was not characterized were discarded (Camacho et al., 2013). Finally, for the MSG coverage and the period under study, 22 LAI ground references over 16 sites were available.

Furthermore, from 2013 to 2016 were used references from the FP7 ImagineS project (http://www.fp7-imagines.eu/) over the MSG disk. Specifically, 44 LAI ground references over 18 new sites. Ground data was up-scaled by EOLAB using either SPOT-5 Landsat or imagery. Field data collection and up-scaling procedures for all the sites were done according to well-established guidelines (Camacho et al., 2014) in agreement with the VALERI protocols and the CEOS LPV recommendations. Only mean values compatible with MSG pixel resolution were used (see Camacho et al., 2017).

In addition, 3 sites coming from BELMANIP2.1 network were selected over the Sahara desert in order to increase the sampling over this specific biome type. Finally, note that pixels of MSG VEGA Daily with error higher than 1.5 for LAI, and higher than 1.2 for FAPAR or FVC are discarded. In the same way, pixels of GEOV1 and MODIS C5 flagged as 'low quality' were also removed.

3. RESULTS

3.1 Product Completeness

The temporal evolution of the fraction of missing values for the two products under study is showed in Figure 2. Over the 2008-2009 period, SPOT/VGT V1 and VEGA 10D provided consistent results, with VEGA 10D showing generally better slight fraction of valid observations, mainly during summer time (around 3% better). The larger fraction of missing values for VEGA 10D (around 14%) was found for the end of January whereas the lower fraction (around 5%) was found during the period of June to September. In conclusion, VEGA 10D improves the completeness mainly in summer period.
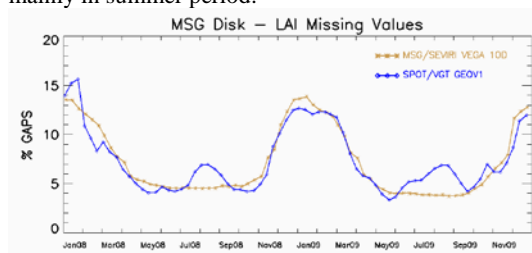
Figure 2: Percentage of missing values for MSG MTLAI and SPOT/VGT V1 products.

3.2 Spatial consistency

Histograms of differences between VEGA 10D and reference products are displayed monthly during the whole 2009 year in Figure 3. Just LAI and FAPAR results are shown as example.

For LAI differences, a good spatial consistency was found between VEGA 10D and SPOT/VGT V1 products with around 85% of cases lower than ±0.5

LAI units, and only 7% of pixels shows differences larger than ±1 LAI units. VEGA 10D and MODIS C5 LAI differences are larger with around 71% of differences ranging between ±0.5 and around 82% between ±1 LAI units, which means also good consistency in most cases, but showing an histogram with a slight tendency towards positive values (larger values in MSG).
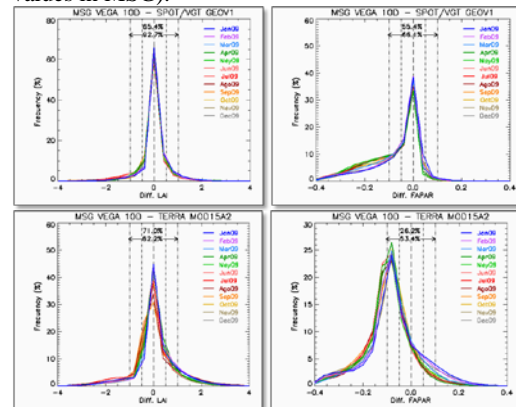
Figure 3: Distribution of differences between VEGA 10D and SPOT/VGT V1 (Top) and between VEGA 10D and MODIS C5 (Bottom) for LAI (Left side) and FAPAR (right side) products.

For FAPAR, larger discrepancies were observed in both cases. The histograms between VEGA 10D and SPOT/VGT V1 products are centered at zero for all dates, but a clear tendency to provide lower values in MSG VEGA was observed. Between VEGA 10D and MODIS histograms of differences are centred on -0.08 for all dates showing a systematic negative bias between both products, partly explained by the different definition of FAPAR in the satellite products. The accuracy assessment will provide further insight on the quality of the FAPAR product.

3.3. Temporal Consistency

Temporal consistency of MSG VEGA (10D and daily), as compared to SPOT/VGT V1 and MODIS C5 products over the 2004-2012 period was shown on Figure 4. In general, good consistency of MSG VEGA temporal variations was found for all the different biomes as compared to reference products.

On the other hand, similar temporal variations were observed for all biome types between MSG VEGA 10D and daily products, showing smoother trajectories in case of 10D due to the monthly composites as compared to daily products which are NRT products with a temporal compositing window (semi-Gaussian) of 5 days (see Camacho et al., 2017 for more details).
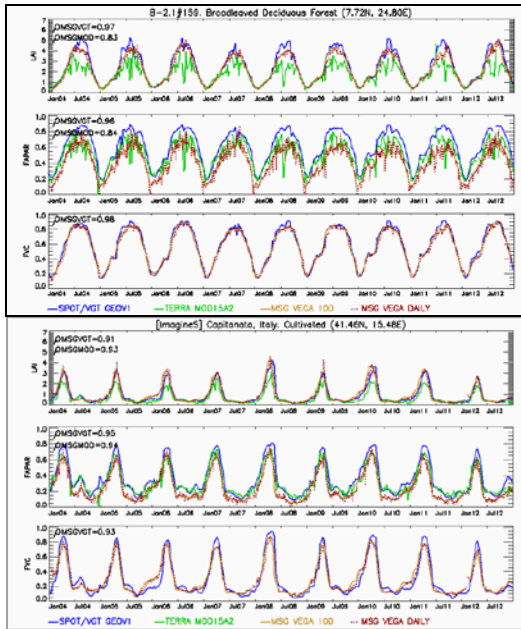
Figure 4: Temporal profiles of LAI (top), FAPAR (middle) and FCV (bottom) values of each product (SPOT/VGT V1, MODIS C5, MSG VEGA (10D and Daily) for selected sites.

3.4. Precision

3.4.1. Intra-Annual Precision

Figure 5 shows the histograms of smoothness for LAI and FAPAR products during the 2008-2009 period. The histograms fit a negative exponential function, showing the best results for MSG VEGA 10D and SPOT/VGT V1 (almost the same), with lower decay constant (τ) than MODIS for LAI and FAPAR.
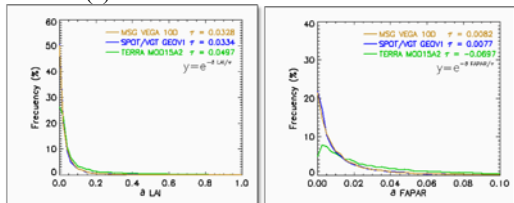
Figure 5: Histograms of the delta function (smoothness) for LAI and FAPAR products for MSGVAL sites during the 2008-2009 period. The curves are adjusted to an exponential function and the exponential decay constant is presented in the figure.

3.4.2. Inter-Annual Precision

Figure 6 shows the box-plots of absolute inter-annual anomalies (year 2009 versus 2008) of MSG VEGA 10D and SPOT/VGT V1 products. Just LAI and FAPAR results are shown as example, with FVC showing similar results to LAI.

Median absolute anomalies (95th and 5th percentiles) match the GCOS stability requirements for all variables. Good results were found for MSG VEGA 10D mainly for LAI products, with median absolute anomalies of 3.5%, improving the performance of SPOT/VGT V1 and MODIS C5 (around 4.5%). However, for FAPAR, is the opposite, due to the larger uncertainties in the BRDF k2 input data.
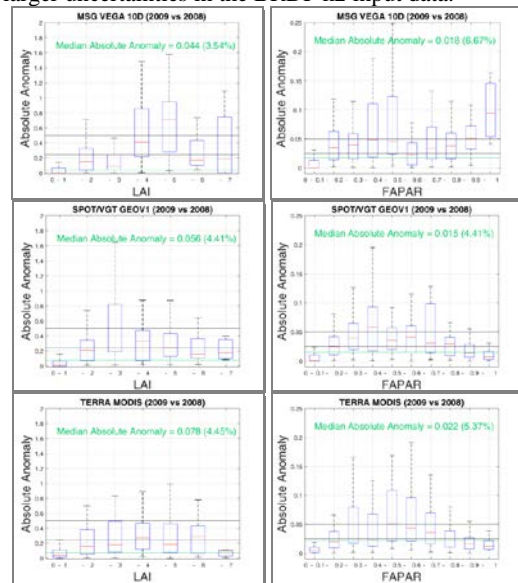
Figure 6: Box-plots of inter-annual absolute anomalies (2009 versus 2008) per bin. Red bars indicate median residuals; blue boxes stretch from the 25th percentile to the 75thpercentile the data; green line corresponds to the median absolute anomaly including all ranges.
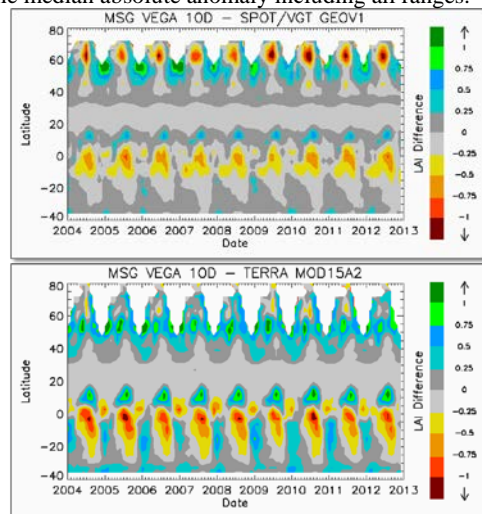
Figure 7: Hovmöller diagrams of the Bias between MSG VEGA 10D and reference products for LAI during the 2004-2012 period.

3.5. Spatio-Temporal Consistency

Figure 7 shows the Hovmöller plots during the 2004-2012 period. Only LAI diagrams are shown as example.

Very stable patterns of differences between MSG VEGA 10D and references products (SPOT/VGT GEOV1 and MODIS C5) were found along the whole time series. No trends are observed which indicates the good stability of the MSG CDR. Main differences are observed around the equatorial belt and northern latitudes.

3.6. Overall Statistical Consistency

The consistency of MSG VEGA 10D with the reference products was evaluated over MSGVAL sites during the 2008-2009 period. Uncertainty metrics are shown in Table 1.

	R^2	RMSE	Bias
LAI			
MSG VEGA 10D vs SPOT/VGT V1	0.8	0.72	0.005
MSG VEGA 10D vs MODIS C5	0.6	1.1	0.062
FAPAR			
MSG VEGA 10D vs SPOT/VGT V1	0.87	0.16	-0.102
MSG VEGA 10D vs MODIS C5	0.74	0.16	-0.104
FVC			
MSG VEGA 10D vs SPOT/VGT V1	0.91	0.09	0.003

Table 1: Performance between the different products over MSGVAL sites for 2008-2009 period.

MSG VEGA 10D and SPOT/VGT V1 are good correlated, with R^2 better than 0.8 for LAI, FAPAR and FVC. Low bias and RMSE is observed for LAI and FVC, for FAPAR a larger RMSE= 0.16 and Bias=-0.10 is found. On the other hand, the performance between MSG VEGA 10D and MODIS C5 is similar for FAPAR, but a little worse for LAI with R^2 of 0.6. Note that FAPAR shows negative bias in both cases, partly explained because SPOT/VGT V1 is based on MODIS C5 products (Baret et al., 2013).

3.7 Direct Validation

Scatter-plots between ground data and MSG VEGA are displayed to show the accuracy assessment (Figure 8). Scatter-plots between ground data and SPOT/VGT V1 are also shown for comparison.

MDLAI shows an overall accuracy (RMSE) of 0.98, and a low positive mean bias (0.126). Compared to reference products, MDLAI presents better overall accuracy than MODIS (1.02) but slight worse than SPOT/VGT V1 (0.84). Also, note that more than 56% of the samples are within the optimal level (Table 2).
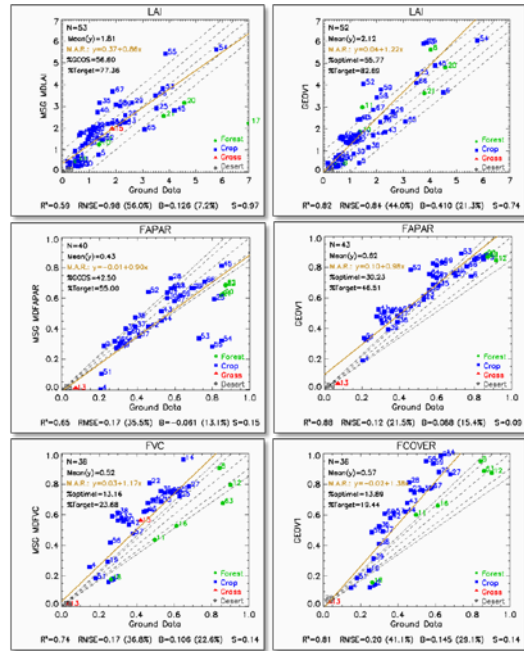
Figure 8: Comparison of satellite LAI, FAPAR and FVC products (MSG VEGA and SPOT/VGT V1) with the ground-based maps. Forest refers to Broadleaf Evergreen, Broadleaf Deciduous and Needle-leaf Forests; Crops stands for Cultivated; Grass stands for Herbaceous, Shrubs and Sparse; and Desert refers to Bare Areas.

MDFAPAR shows an overall accuracy (RMSE) of 0.17, a bit larger than SPOT/VGT V1 (RMSE=0.12) and MODIS C5 (RMSE=0.14). That could be explained mostly due to the estimations in Albufera rice site (#53, #54 and #55) which tend to underestimate largely FAPAR measurements during the peak of the season. Nevertheless, for the remaining of the cropland sites, MDFAPAR shows accurate measurements, whereas SPOT/VGT V1 tends to overestimate the ground measurements, and MODIS C5 presents large scattering because of its noisier retrievals. Also, MDFAPAR has 43% of the estimates within the GCOS requirements, better than the two reference products (Table 2).

Better overall accuracy was observed for MDFVC (RMSE=0.17) as compared to SPOT/VGT V1 (RMSE=0.2). Also, MDFVC provides a mean bias of 0.106 with a trend to overestimate croplands and to underestimate forest measurements, whereas SPOT/VGT V1 provides more accurate estimations over forest sites but larger bias over croplands. Just 13.2% of the samples are within the optimal level (Table 2).

		LAI	FAPAR	FVC
MSG VEGA Daily vs Ground Data	**N**	53	40	38
	R²	0.59	0.65	0.74
	Bias	0.126	-0.061	0.106
	RMSE	0.98	0.17	0.17
	% GCOS	56.6	42.5	13.2
SPOT/VGT V1 vs Ground Data	**N**	52	43	36
	R²	0.82	0.88	0.81
	Bias	0.41	0.088	0.145
	RMSE	0.84	0.12	0.2
	% GCOS	55.8	30.2	13.9
MOD15A2 C5 vs Ground Data	**N**	53	43	N/A
	R²	0.66	0.75	N/A
	Bias	-0.022	0.012	N/A
	RMSE	1.02	0.14	N/A
	% GCOS	60.4	37.2	N/A

Table 2: Performance of MSG VEGA Daily, SPOT/VGT V1 and MOD15A2 C5 products against ground data.

4 CONCLUSIONS

In this paper, a validation of MSG/SEVIRI VEGA LAI, FAPAR and FVC V3.0 Climate Data Record of VEGA 10D products, for the period 2004-2012 (extended to 2016 for accuracy assessment), was performed. The methodology used follows the guidelines proposed by the CEOS LPV group for validation of remote sensing vegetation products.

In summary, the validation results of the MSG VEGA CDR products show overall good results, with good spatial and temporal consistency as compared to validated satellite products. It is noticeable the good inter-annual precision of the products and the stability of the time series. The main discrepancy was found for the FAPAR product where MSG provides lower values than both references products but more accurate results for croplands, which is explained by the different definition of the FAPAR. Most of the criteria evaluated shows in overall positive results, with some limitations in the accuracy of FVC product.

5 REFERENCES

Baret, F., M. Weiss, R. Lacaze, F. Camacho, et al., 2013, GEOV1: LAI and FAPAR essential climate variables and FCOVER global time series capitalizing over existing products. Part1: Principles of development and production. *Remote Sensing of Environment* 137: 299–309.

Camacho, F., Cernicharo, J., Lacaze, R., Baret, F., Weiss, M., 2013. GEOV1: LAI, FAPAR essential climate variables and FCOVER global time series capitalizing over existing products. Part 2: Validation and intercomparison with reference products. *Remote Sens. Environ*. 137, 310–329. doi:10.1016/j.rse.2013.02.030

Camacho, F., C. Latorre, R. Lacaze, F. Baret, et al., 2014. A Network of Sites for Ground Biophysical Measurements in support of Copernicus Global Land Product Validation. Proceedings of the IV RAQRS conference, Torrent, September 2014.

Camacho, F., J. García-Haro, J. Sánchez-Zapero and B. Fuster, 2017. Validation Report MSG/SEVIRI Vegetation Parameters (VEGA). SAF/LAND/UV/VR_VEGA_MSG, Issue 3.0. (available on-line at landsaf.meteo.pt).

Fernandes, R., Plummer, S.E., Nightingale, et al., 2014. Global Leaf Area Index Product Validation Good Practices. CEOS Working Group on Calibration and Validation - Land Product Validation Sub-Group. Version 2.0. doi:10.5067/doc/ceoswgcv/lpv/lai.002.

García-Haro, F.J., M. Campos-Taberner, F. Camacho, B. Martínez, J. Sánchez-Zapero, G. Camps-Valls, S. Sánchez-Ruíz, M. A. Gilabert. The geostationary and polar orbit LSA SAF vegetation products. This issue.

Hovmoller, E., 1949. The Trough-and-Ridge diagram. Tellus 1, 62–66. doi:10.3402/tellusa.v1i2.8498

Knyazikhin, Y., Martonchik, J. V., Myneni, R.B., et al., 1998. Synergistic algorithm for estimating vegetation canopy leaf area index and fraction of absorbed photosynthetically active radiation from MODIS and MISR data. . *Journal of Geophysical Research*. 103, 32257. doi:10.1029/98JD02462

Weiss, M., Baret, F., Block, T., Koetz, B., et al., 2014. On line validation exercise (OLIVE): A web based service for the validation of medium resolution land products. Application to FAPAR products. *Remote Sens*. 6, 4190–4216. doi:10.3390/rs6054190

The geostationary and polar orbit LSA SAF vegetation products

Francisco Javier García-Haro[1]*, Manuel Campos-Taberner[1], Fernando Camacho[2], Beatriz Martínez[1], Jorge Sánchez-Zapero[2], Gustau Camps-Valls[3], Sergio Sánchez-Ruíz[1], María Amparo Gilabert[1]

[1] *Environmental Remote Sensing Group (UV–ERS), Faculty of Physics, Universitat de València, Spain.*

[2] *EOLAB, Parc Científic Universitat de València, Paterna (Valencia). Spain.*

[3] *Image Processing Laboratory (IPL), Universitat de València, Paterna,València, Spain.*

*j.garcia.haro@uv.es

ABSTRACT- *The Satellite Application Facility on Land Surface Analysis (LSA SAF) aims to provide land surface variables for environmental and meteorological purposes from EUMETSAT constellation satellites. The suite of LSA SAF vegetation products includes two different data sets, one from SEVIRI/MG geostationary satellites, and other from AVHRR/METOP polar orbit EPS data. The vegetation products are distributed in near real time from the LSA SAF website hosted at IPMA (http://landsaf.ipma.pt). Furthermore, the uncertainty of each retrieval is also provided to users in the form of error bars along with a quality flag and other relevant information. The LSA SAF vegetation products are routinely validated against in situ data and through comparisons with similar products such as those provided by the Copernicus Global Land Service and MODIS. This work provides detailed information on the suite of LSA SAF vegetation products. Furthermore, it provides updated validation results as well as evaluation of their temporal and spatial consistency.*

1 INTRODUCTION

The Satellite Application Facility on Land Surface Analysis (LSA SAF) is part of the SAF Network, a set of specialised development and processing centres, serving as EUMETSAT (European organization for the Exploitation of Meteorological Satellites) distributed Applications Ground Segment. The main purpose of the LSA SAF is to take full advantage of remotely sensed data, particularly those available from EUMETSAT sensors, to measure land surface variables.

The SEVIRI instrument onboard MSG has a 3 km resolution at nadir, 12 spectral channels and an imaging-repeat cycle of 15 minutes. On the other hand, the EUMETSAT Polar System (EPS), with the series of three Meteorological-Operational (MetOp) satellites, is Europe's first polar orbiting operational meteorological satellite.

The LSA SAF Team has a set of consolidated algorithms, used to generate Land Surface Products in an operational mode, archived and disseminated in near real time or off-line. These include retrievals of surface radiative components, vegetation parameters and snow cover (Trigo et al. 2011). Product distribution policy is wide open to the users community. The LSA SAF system is fully centralized at Portuguese Institute for the Ocean and Atmosphere (IPMA), which generates and disseminates the operational products by EUMTETCast and off-line from LSA SAF website (http://landsaf.ipma.pt) that contains products as well as updated information.

Although the LSA SAF is primarily targeted to meteorology applications, it addresses a wide community, ranging from surface processes modelling to agriculture and forestry applications. This community greatly benefits from products generated from a reliable observation system designed to ensure long-term operations.

The LSA SAF generates and disseminates daily and 10-day Fractional Vegetation Cover (FVC), the Leaf Area Index (LAI) and the Fraction of Absorbed Photosynthetically Active Radiation (FAPAR) derived from SEVIRI/Meteosat BRDF data for the whole Meteosat disk. More recently, the LSA SAF has developed a set of global 10-day FVC, LAI and FAPAR products from AVHRR/Metop. All LSA SAF vegetation products are distributed with quality control information and an error bar, indicative of the expected accuracy of the retrieved fields, on a pixel-by-pixel basis, supported by sensitivity studies and product validation.

The aim of this work is two-fold. Firstly, it presents detailed information on the suite of LSA SAF vegetation products, which in turn will also be of interest to assist the successful use of the data in research and applications. Secondly, it provides updated validation results as well as evaluation of their temporal and spatial consistency.

2. REFERENCE SATELLITE PRODUCTS

Validation activities consist basically on inter-comparison of LSA SAF products with ground observations obtained through international initiatives (e.g., OLIVE, IMAGINES) and with similar parameters retrieved from other satellite data (e.g., vegetation parameters from SPOT, PROBA-V or MODIS), which are briefly described as follows:

(i) The first version of global biophysical products (i.e., LAI and FCOVER), namely GEOV1, developed in the framework of Copernicus Global Land Service from SPOT/VGT and PROBA-V data at 1 km spatial resolution and 10-days temporal frequency (using a temporal window of 30 days). GEOV1 products have reached a validation stage level of 2 according to CEOS LPV criteria. Full validation results can be found in Camacho et al. (2013; 2014a).

(ii) Terra MODIS LAI/FAPAR (MOD15A2) is produced at 1 km spatial resolution and 8 days step over a sinusoidal grid. The MODIS LAI products have been extensively validated (Yang et al., 2006; Garrigues et al., 2008).

3 THE SEVIRI/MSG VEGETATION PRODUCTS

3.1 Product content

The current SEVIRI/MSG vegetation products are FVC, LAI and FAPAR. These products are produced in near real time from the MSG/SEVIRI observations at a spatial resolution of 3 km at equator (~5 km over central Europe) on a daily and 10-day basis, in the geostationary grid. The high rate of acquisition provided by the SEVIRI instrument guarantees the availability of spatially consistent cloud-free data for adequately monitoring both the seasonality of vegetation and the long-term trends in the state of vegetation.

The characteristics of SEVIRI based FVC, LAI and FAPAR products provided by the LSA SAF are summarized in Table 1. The coverage of the products is the MSG disk. The technical properties of final products (spatial and temporal resolution, thematic accuracy, etc.) depend on the input data, and the retrieval algorithms. For a detailed description we refer to García-Haro et al. (2016).

The products are spatially and temporally consistent and present practically no missing data except for areas that are usually covered by snow. The SEVIRI/MSG vegetation products have been reprocessed, in order to obtain a long time series of homogeneous Climate Data Records (2004-present) suitable for many environmental and climate applications.

During the current phase, a 10-day MSG based Gross Primary Production (GPP) related to the carbon uptake of terrestrial vegetation by photosynthesis will be will be operationally delivered (ORR foreseen for early 2018). We refer for details to Martinez et al. (2017, this issue).

a)   b)
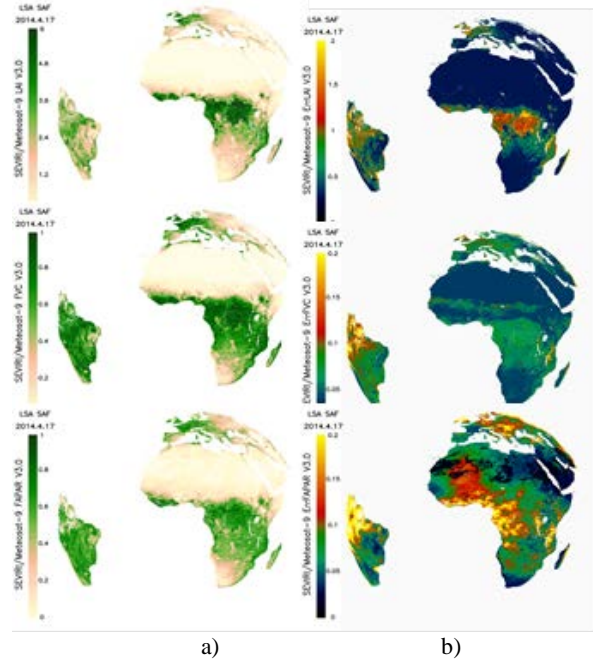
Figure 1 – MSG Daily LAI (top), FVC (middle) and FAPAR (bottom) LSA SAF VEGA corresponding to mid April 2014. A) products; B) respective error estimates.

Table 1. Main characteristics of the SEVIRI/MSG vegetation products

Products	LAI, FVC, FAPAR, GPP(*)
Coverage	MSG full disk (Continental pixels over land)
Spatial resolution	3km×3km (at nadir)
Projection	SEVIRI instrument projection (MSG-Disk)
Size (col, row)	3712 x 3712
Format	HDF signed integer 16 bits: products & errors 8 bits: Quality Flag
Frequency	Daily and 10-day
Temporal coverage	2004-present
Accuracy(**)	0.5 (LAI) 0.10 for FVC/FAPAR
(*) GPP is currently in development (**) achieved in about 70-75% of land pixels	

3.2 Product validation

The SEVIRI/MSG products are continuously validated using a limited number of ground measurements available from international initiatives such as CEOS/OLIVE, IMAGINES FP7 and ESA validation campaigns (Weiss et al. 2014; Camacho, 2014b). Indirect validation includes inter-comparison with equivalent satellite products from different sensors (MERIS, VGT, MODIS), as well as evaluation of their temporal and spatial consistency.
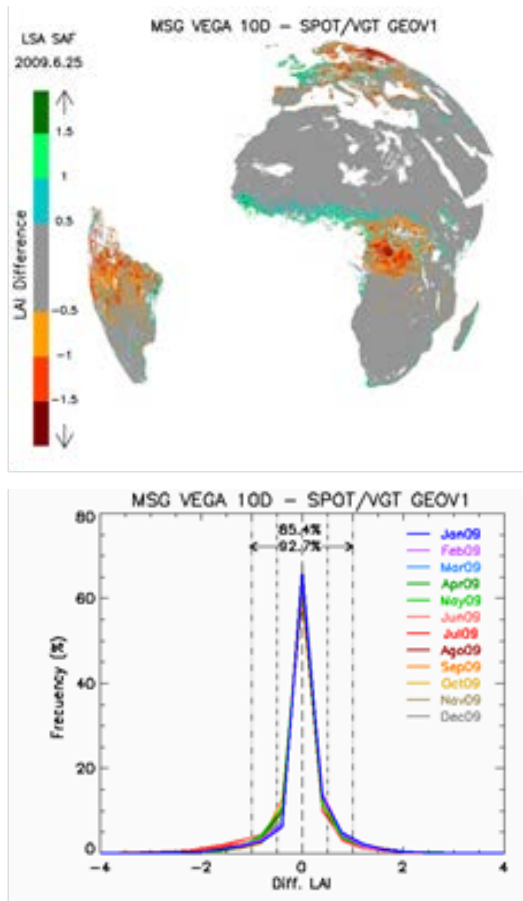
Figure 2. Comparison between SEVIRI LAI version 3.0 and Copernicus Global Land (SPOT/VGT GEOV1). Top: Image difference on mid June, 2009. Bottom: Histograms of products difference for all month during year 2009.

The validation exercises have shown the consistency of spatial and temporal FVC, LAI and FAPAR distributions per main biomes, with values within the baseline of equivalent reference products (see examples of validation results in figures 2 and 3). The SEVIRI products have shown to be temporally more stable regarding polar orbit products (e.g.

MODIS, VGT), which often present considerable multi-temporal noise and gaps over large areas and long temporal periods. The validation results are highly significant and allow concluding that SEVIRI/MSG vegetation products have reached a validation stage level 2 according to CEOS LPV criteria (e.g., Camacho et al., 2010; Martínez et al., 2013; García-Haro et al., 2016).

The fraction of valid pixels (i.e. processed with reliability) for LSA SAF FVC and LAI products over Africa zones is nearly 100% through the whole year which is clearly one of the main advantages of using MSG data, instead of polar-orbiting satellite products thanks to the high-frequency of observations that allows getting a much higher number of cloud-free observations.
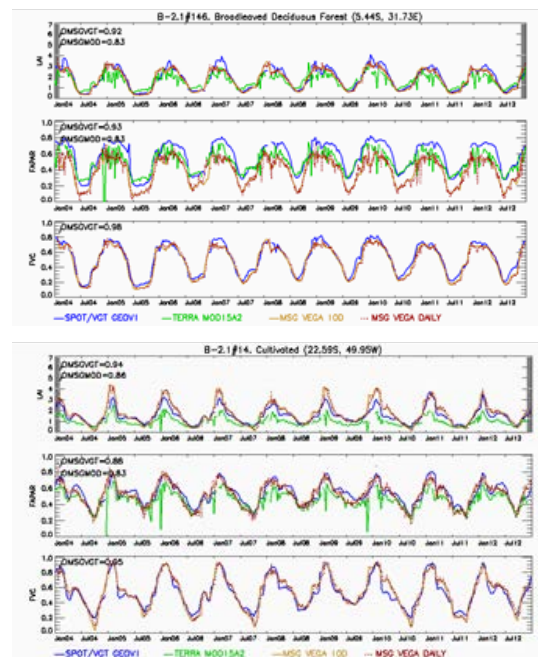
Figure 3. Temporal profiles of LSA SAF v3.0, Copernicus GEOV1 and NASA MODISC5 LAI (top), FAPAR (middle) and FVC (bottom) products over two sites representative of Broadleaved deciduous forest (BDF) and cultivated areas.

4 THE EPS VEGETATION PRODUCTS

4.1 Product content

The LSA SAF has recently developed a set of global 10-day FVC, LAI and FAPAR products from Advanced Very High Resolution Radiometer (AVHRR) instrument onboard MetOp, which permits a global coverage of the surface, being the complement of SEVIRI at high latitudes (see

characteristics in Table 2). Examples of the EPS product are given in figure 4. Product provide error uncertainty estimates. Completeness is good except for areas usually covered by snow. For a detailed description of EPS products we refer to García-Haro et al. (2017b).

The algorithm relies on a hybrid method through the generation of a reflectance radiative transfer model simulations to train powerful machine learning methods (García-Haro et al. 2017a). This emphasizes the use of physically based methods for a joint retrieval of vegetation variables. Future work is to assess the feasibility of including a new AVHRR/MetOp Canopy Water Content (CWC) product, targeted for fire risk monitoring and drought monitoring.

Table 2. Main characteristics of the AVHRR/MetOp vegetation products

Products	LAI, FVC, FAPAR, CWC(*)
Coverage	EPS global (Continental pixels over land)
Spatial resolution	EPS/AVHRR full resol. (0.01°)
Projection	EPS/AVHRR sinusoidal
Size (col, row)	36001 x 18000
Format	HDF signed integer 16 bits: products & errors 8 bits: Quality Flag, Z_Age
Frequency	Daily and 10-day
Temporal coverage	Now: 2015-present Foreseen: 2008-present
Accuracy(**)	0.5 (LAI) 0.10 for FVC/FAPAR
(*) CWC is currently in development	
(**) (achieved in about 60% of land pixels)	
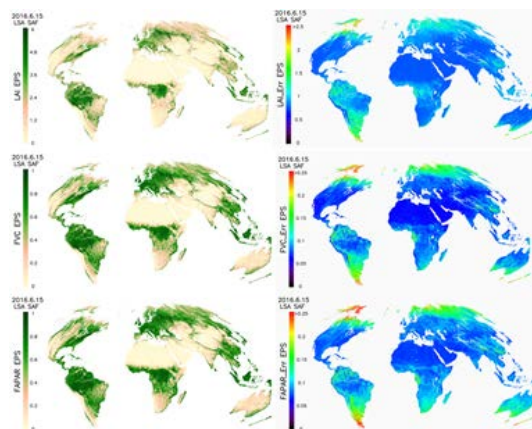
Figure 4 – EPS 10-daily LAI (top), FVC (middle) and FAPAR (bottom) LSA SAF products corresponding to mid June 2015. A) products; B) respective error estimates.

4.2 Validation of EPS vegetation products

The preliminary validation results of LSA SAF EPS vegetation products have shown in overall good performance of the EPS products as compared with both references (PROBA-V GEOV1 and MODIS C5) in terms of the statistical analysis over the network, with little systematic trends as compared to GEOV1 (see examples of validation results in figures 5 and 6).
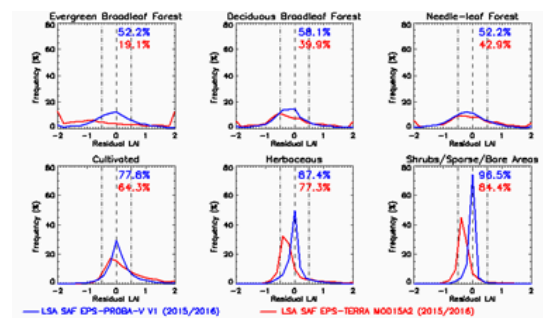
Figure 5. Histogram of differences for the main global biomes between EPS LAI and two reference products, Copernicus Global Land (PROBA-V GEOV1 and MODIS C5).
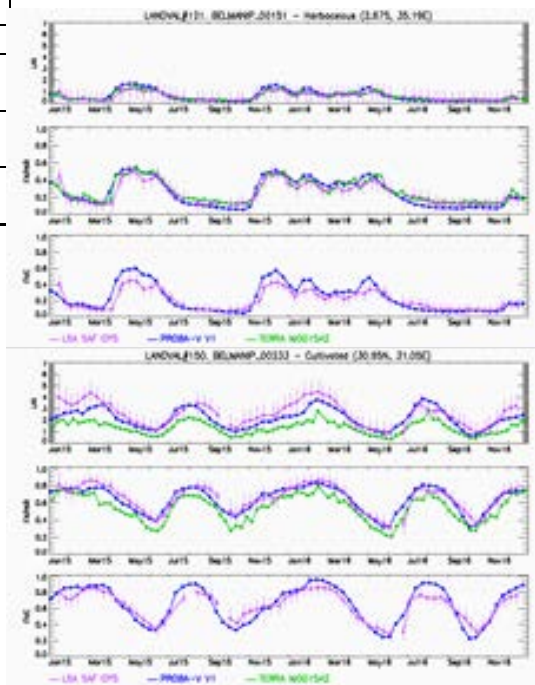
Figure 6. Temporal profiles of LSA SAF v3.0, Copernicus GEOV1 and NASA MODISC5 LAI (top), FAPAR (middle) and FVC (bottom) products over two sites representative of Herbaceous cover and cultivated areas.

5. CONCLUSIONS

The LSA SAF vegetation products are distributed in near real time from the website hosted at IPMA. Furthermore, the uncertainty of each retrieval is also provided to users in the form of error bars along with a quality flag, which provides information on the product expected performance, taking into account the retrieval conditions

The LSA SAF disseminates daily and 10-day FVC, LAI and FAPAR products derived from SEVIRI/MSG BRDF data for the whole Meteosat disk. The products are spatially and temporally consistent and present practically no missing data except for areas that are usually covered by snow. The availability of long time series of homogeneous MSG vegetation products (since January 2004 to present) offers new tools for a broad range of environmental, climate and weather applications.

The LSA SAF project recently entered its Continuous Development and Operational Phase-3 (CDOP-3), which will last until 2022. The validation activities will be continued during CDOP3 to consolidate the quality of products and extend them to a longer period. It is foreseen that the suite of 10-day FVC, LAI and FAPAR products from AVHRR/MetOp be reprocessed (from January 2008 onwards) during CDOP3. Future work will also include reprocessing from 2008 onwards of global EPS vegetation products in order to obtain a long time series of homogeneous Climate Data Records.

6. ACKNOWLEDGMENTS

7. REFERENCES

Camacho F.; J. Cernicharo; F.J. García-Haro; A. Verger; J. Meliá, (2010), Consistency assessment of FVC and LAI operational products over Africa, Proceedings of the RAQRS2010, 3rd International Symposium on Recent Advances in Quantitative Remote Sensing, Torrent, Spain, 27 Sept-1 Oct. 2010, (Publ. Univ. Valencia: Valencia), Ed. J. Sobrino, ISBN 978-84-370-7952-3, pp: 694-699.

Camacho, F., Cernicharo, J., Lacaze, R., Baret, F., Weiss, M., 2013, GEOV1: LAI, FAPAR essential climate variables and FCOVER global time series capitalizing over existing products. Part 2: Validation and intercomparison with reference products. *Remote Sensing of Environment*, **137**, 310–329.

Camacho, F., Sánchez, J., 2014a, GIOGL1 Quality Monitoring Report January – June 2014. LAI-FAPAR-FCOVER GEOV1, GEOV0. GIO-GL Lot 1, GMES Initial Operations, 77 pp.

Camacho F.; R. Lacaze; F. Baret; C. Latorre; F. De la Cruz; V. Demarez; C. Di Bella; H. Fang; F.J. García-Haro; M. Pat Gonzalez; N. Kussul; E. López-Baeza; C. Mattar; E. Nestola; E. Pattey; I. Piccard; C. Rudiger; I. Savin; A. Sanchez-Azofeifa; M. Zribi (2014b), A Network of Sites for Ground Biophysical Measurements in support of Copernicus Global Land Product Validation, 4th International Symposium on Recent Advances in Quantitative Remote Sensing: RAQRS'IV, 22-26 September 2014 (Publ. Univ. Valencia: Valencia), Ed. J. Sobrino, ISBN: 978-84-370-9808-1, pp: 410-414.

García-Haro, F.J., F. Camacho, (2016), The EUMETSAT Satellite Application Facility on Land Surface Analysis. Product User Manual of Vegetation Parameters (VEGA), (SAF/LAND/UV/PUM_VEGA/3.0), 52 pp. available from https://landsaf.ipma.pt/.

García-Haro F.J.; M. Campos-Taberner; J. Muñoz-Marí; Valero Laparra; F. Camacho; J. Sanchez-Zapero; G Camps-Valls, Derivation of global vegetation biophysical parameters from EUMETSAT Polar System, (2017a), ISPRS Journal of Photogrammetry and Remote Sensing, in revision.

García-Haro, F.J., Campos-Taberner, M., Camacho, F., (2017b), The EUMETSAT Satellite Application Facility on Land Surface Analysis (LSA SAF) Product User Manual EPS-AVHRR Vegetation Parameters, (SAF/LAND/UV/EPSVEGA_PUM/1.0), 32 pp., in revision.

Garrigues, S., Lacaze, R., Baret, F., Morisette, J. T., Weiss, M., Nickeson, J. E., et al., 2008, Validation and Intercomparison of Global Leaf Area Index Products Derived From Remote Sensing Data. *Journal of Geophysical Research*, **113**, G02028, doi: 10.1029/2007JG000635.

Martínez, B., Camacho, F., Verger, A., García-Haro, F.J., Gilabert, M.A., 2013, Intercomparison and quality assessment of MERIS, MODIS and SEVIRI FAPAR products over the Iberian Peninsula. *International Journal of Applied Earth Observation and Geoinformation*, **21**, 463-476.

B. Martínez, S. Sánchez-Ruiz, M. Campos-Taberner, F.J. García-Haro, M.A. Gilabert., 2017, Ten-day gross primary production (GPP) using SEVIRI/MSG data in the framework of LSA SAF project, this issue.

Trigo, I. F., DaCamara, C., Viterbo, P., Roujean, J.L., Olesen, F., Barroso, C., Camacho-de Coca, F., Carrer, D., Freitas, S.C., García-Haro, F.J., Geiger, B., Gellens-Meulenberghs, F., Ghilain, N., Meliá, J., Pessanha, L., Siljamo, N., Arboleda, A., 2011, The Satellite Application Facility on Land Surface Analysis, *International Journal of Remote Sensing*, **32**, 2725-2744.

Weiss, M, Baret, F., Block, T., Koetz, B., Burini, A., Scholze, B., Lecharpentier, P., Brockmann, C., Fernandes, R., Plummer, S., Myneni, R., Gobron, N., Nightingale, J., Schaepman-Strub, G., Camacho, F., Sanchez-Azofeifa, A., 2014, On Line Validation Exercise (OLIVE): A Web Based Service for the Validation of Medium Resolution Land Products. Application to FAPAR Products. *Remote Sensing*, **6**, 4190-4216.

Yang, W., Tang, B., Huang, D., Rautiainen, M., Shabanov, N.V, Wang, Y., et al., 2006, MODIS Leaf Area Index products: from validation to algorithm improvements. *IEEE Transactions on Geoscience and Remote Sensing*, **44**, 1829-1842.

New MODIS LST product for the monitoring of Amazonian tropical forests

Gomis-Cebolla, J., Jiménez-Muñoz,J.C., Sobrino, J.A., Soria, G., Julien, Y., Skokovic, D.
Global Change Unit, Image Processing Laboratory (University of Valencia)
Jose.gomis@uv.es

ABSTRACT *Amazonian tropical forests including approximately 50% of global tropical forests play a crucial role in the global water and carbon cycle. Additionally, these forests host about the 25% of world's terrestrial species. Taking into account the importance of this biome and the current global warming scenario the monitoring of the changes in these forests becomes of special importance. In this context, the use of satellite imagery is presented as the only viable means to observe the Amazon in a spatially comprehensive and temporally frequent fashion. Particularly, the use of optical imagery derived from medium resolution sensors such as MODIS, has been the most widely adopted solution. In addition to the use of vegetation indexes derived using VIS and NIR information, recent studies highlight the role of vegetation temperature in the understanding of the changes produced in these forests. Nevertheless, the use of thermal data still has some limitations being of special importance the possible cloud contamination effect in the estimation of LST. In this work a MODIS daytime LST product is presented aimed at reducing the current limitations of its MODIS counterparts. This product encompasses the benefits of updated split-window coefficients for the region and the use of MAIAC cloud mask. This alternative MODIS LST has been validated using in-situ data and has been compared to current MODIS LST products. The results obtained prove the utility of this new product in the monitoring of the Amazonian tropical forests.*

1 INTRODUCTION

In the current global warming scenario, the monitoring of forestry is of special importance. In this context globally forests are showing signs of stress that can be directed link to the combination of drought and/or high temperatures. (Allen et al., 2010) Additionally recent studies have highlighted the potential of warmer temperatures in the exacerbation of forest stress and die-back. (Williams et al., 2013) For the Amazonian tropical forests several studies have investigated the relationship between this variable and the CO_2 absorption capacity, showing that an increase in temperature could result in a negative impact on tropical forest CO_2 uptake and productivity (Clark et al., 2003). Additionally, anomalous high values have been proved to be more important than precipitation deficits in causing losses of biomass during drought periods (Galbraith et al., 2010)

In spite the vegetation temperature being a variable linked with plant physiology that can be routinely estimated from satellite imagery there is still scarce literature about the use of surface temperature products derived from satellite data over the Amazonian tropical forests. In particular, the studies of Toomey et al. (2011) and Jiménez-Muñoz et al. (2013-2015) were the major contributions. In their studies a significant and sustained warming was revealed from an analysis of land surface temperatures anomalies using MODIS LST products (MOD11) and climatic data. This helps to prove the valuable information that could be derived from monitoring LST anomalies over the region. Nevertheless, the use of thermal data for monitoring of tropical forests has some limitations regarding the estimation accuracy and the possible temperature alteration introduced by cloud-contamination effect. In particular, for the MODIS sensor, recent studies have shown how a land cover bias in the MODIS cloud mask and how it could interfere in the derived LST products (Wilson et al., 2014). Additionally, cloud contamination for MOD11 were reported in the literature, although for different biomes (Otsby et al., 2014). Recent efforts have been done in order to quantify this effect and provide accurate cloud filtered LST data (Gomis-Cebolla et al., 2016)

In the current work a daytime LST product which could help to refine the LST estimations over the region is presented. This product benefits for the development of updated split-window coefficient and the introduction of MAIAC cloud mask. This cloud mask has shown promising results in comparison with MODIS cloud mask over the tropical forests. Additionally, this product has been validated using in-situ data and compared with current MODIS LST products in order to report the existing differences.

The paper is organized as follows: in section 2 data and methods used are presented. In section 3 results of validation and comparison are resumed. And finally in section 4 the discussion and conclusions derived from the results are presented.

2 DATA AND METHODS

2.1 Data

Ground in-situ LST was derived from a permanent validation station situated in a relatively homogeneous tropical forest area at Tambopata (12.818 S, 69.281 W) in the Peruvian Amazon. The time period of data recording considered in this work is from December 2014 since October 2016.

Satellite data is resumed in Table 1. In particular, MYD07_L2 was used for the derivation of the LST algorithm (creation of simulated brightness temperatures database). MODIS Brightness temperatures for bands 31 and 32 were extracted from the MYDTBGA product. MAIAC cloud mask was extracted from the Status QA layer of MAIACATBRF product. Additionally, in order to ensure the validity of the algorithm over the region a vegetation mask was created in order to delineate the tropical forests. This was obtained by the intersection of a geographical and the class 2 of the IGBP classification in the MCD12Q1 product.

Table 1. MODIS products and layers used.

MODIS Products	Layers used
MYD07_L2	Temperature, Dew Point and Geopotential Height Profiles
MYDTBGA	Band 31,32
MAIACATBRF	Status QA
MCD12Q1	Land Cover Type 1 (IGBP)

2.2 LST algorithm

In this study in order to test an alternative LST retrieval algorithm we suggest the use of the theoretical Split-window model developed by Sobrino et al. (1996). For the particular consideration of tropical forests two assumptions are being considered: 1) dependence on emissivity terms results in a constant value which can be integrated in the c_0 term (tropical forests with dense green vegetation are well represented by typical vegetation emissivity), and 2) dependence on water vapour is considered implicitly in the derivation of c_1 and c_2 terms, thus eliminating the need of introducing water vapour information in the algorithm. Doing this, the mathematical structure results in:

$$T_s = T_i + c_0 + c_1(T_i - T_j) + c_2(T_i - T_j)^2 \qquad (1)$$

where T_i and T_j are the brightness temperatures of MODIS bands 31 and 32 respectively and c_i are derived from simulated data. The Split-Windows take the following values: 1.461 (K), 1.638 and 0.774 (K^{-1}) for c_0, c_1 and c_2 respectively.

In particular the Split-Window coefficients were derived by statistical linear regression of a simulated dataset of brightness temperatures (T_i, T_j) over different surface and atmospheric conditions. For the surface conditions three different vegetation spectra from the ASTER (Baldrige et al., 2009) spectral library were considered. For the atmospheric conditions MYD07 cloud-free profiles were collected from 1118 spatial reference points within the study area for the 2014-2016 time period. These atmospheric profiles were input to the MODTRAN (v5.20) radiative transfer code (Berk et al., 2008). The simulated database was generated by forward simulations driven by the Radiative Transfer Equation (RTE), the emissivity spectra and MODTRAN atmospheric outputs. All the spectral magnitudes were convolved to the spectral response functions of MODIS bands.

3 RESULTS

3.1 Validation results

Ground LST was derived by correcting the downwelling sky irradiance and the surface emissivity effects in the radiometric temperatures. The ground LSTs was compared against MODIS LSTs extracted for the pixel located at the test site using both standard products (MYD11) and the SW based product. Such comparison was performed at three different levels of cloud masking: i) the MOD35 cloud mask as included in the MYD11 without any additional QA discrimination (LST not produced due to clouds), ii) the MOD35 cloud mask and the additional filter based on the QC layer (LST not produced due to clouds + LST other quality), iii) the MAIAC cloud mask. For simplicity, we will refer to these three cases as MOD35, QC and MAIAC respectively.

Validation results are presented in Figure 1 for the three cases. These results are complemented with basic error metrics (bias, standard deviation and Root Mean Square Error) included in Figure 2. Error metrics were derived considering $(T_s - T_{alg})$.

The Split-Window LST algorithm is able to reduce the bias metric in comparison to MODIS (Figure 2, left). In particular, with values closer to 0 when considering an additional cloud filtering. The difference (MODIS minus SW) is of 1.36 K, 1.55 K, 1.61 K for the MOD35, QC and MAIAC case respectively. In terms of standard deviation SW is able to provide similar results when considering the additional cloud filtering. In terms of RMSE, SW is able to provide similar values to MOD35, and to improve them in the QC and MAIAC case with a difference of 0.7 and 0.6 K respectively. And finally, the combination of SW and MAIAC is able to reduce the RMSE in 0.2 and 2.4 K when compared to QC and MOD35 respectively.
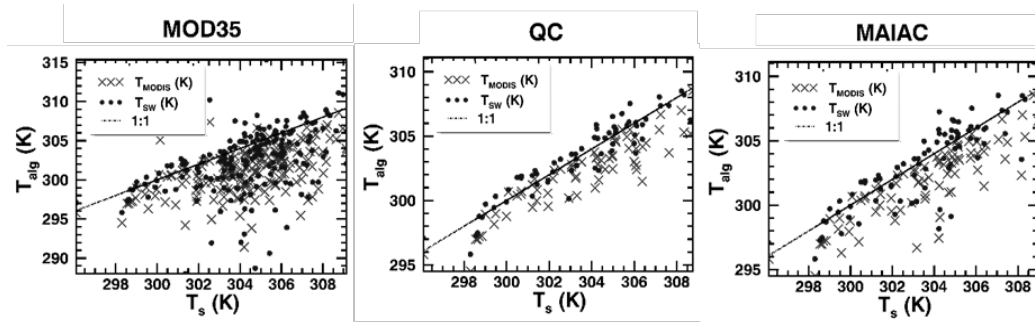
Figure 1. Ground measured T_s against T_{MODIS} (cross) and T_{SW} (filled circle) for the three cloud mask stages of comparison: left column (LST not produced due to clouds), middle column (LST good quality), right column (MAIAC cloud mask) and for the LST products considered: MYD11A1. The line 1:1 is also represented.
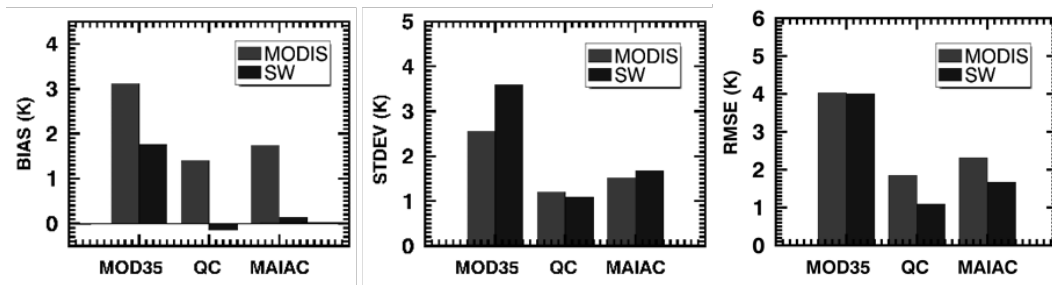
Figure 2. Error metrics for the three stages of comparison, LST not produced due to clouds (MOD35), LST having good quality (QC) and MAIAC cloud mask (MAIAC) considering the LST values derived from the MODIS LST products (MYD11) (lighter) and split-window algorithm (darker). Error metrics were calculated considering the difference T_s-T_{alg}.

3.2 Spatial analysis

For the spatial comparison analysis seasonal mean LST values together with number of clear sky days per season for the year 2014 are considered. Seasons included in the analysis were JFM (January-February-March), AMJ (April-May-June), JAS (July-August-September) and OND (October-November-December). Comparison was performed at the same three different levels of cloud masking than section 5.1 (MOD35, QC and MAIAC).

In Figure 3 and Figure 4 the boxplot diagrams for the LST and number of clear sky days representing the spatial mean values over the Amazon tropical forests (as denoted by the vegetation) are presented. In Figure 3 it can be appreciated the importance of properly address the cloud-contamination effect as it can introduce temperature alterations (colder-than-true values) (Otsby, 2014).
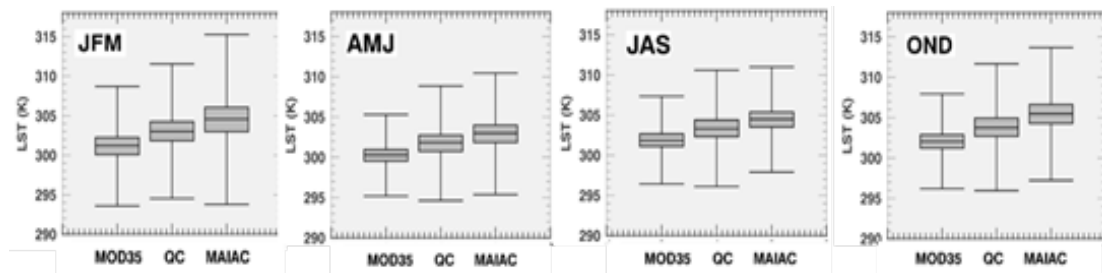
Figure 3. Boxplot diagrams for the seasonal LST values over the Amazon tropical forests considering the seasons JFM (January-February-March), AMJ (April-May-June), JAS (July-August-September) and OND (October-November- December) and for the three cloud mask stages of comparison: MOD35, QC and MAIAC.
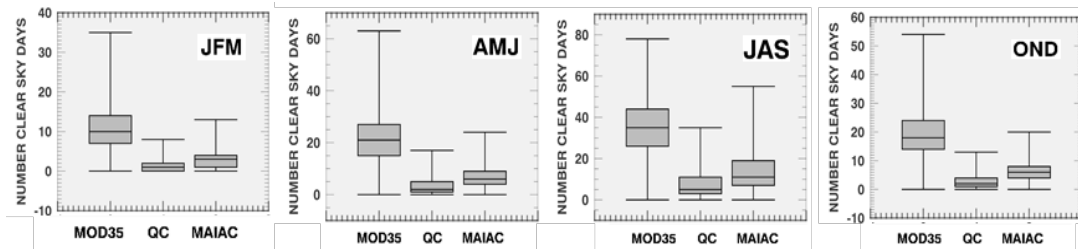
Figure 4. Boxplot diagrams for the seasonal number of clear sky days over the Amazon tropical forests considering the seasons JFM (January-February-March), AMJ (April-May-June), JAS (July-August-September) and OND (October-November- December) and for the three cloud mask stages of comparison: MOD35, QC and MAIAC.

In particular mean LST are shifted to higher temperatures (>1K) after applying the additional cloud filtering (for both QC and MAIAC). However, the use of an additional cloud filtering however considerably reduces the number of available clear-sky-days (Figure 4). Additionally, MAIAC is able to provide more cloud-free data for the different seasons (Figure 4). These results agree well with previous studies (Hilker et al, 2012) in which MAIAC was shown to provide about 20-80% more cloud-free pixels depending on season than MYD09 surface reflectance product.

For the comparison of QC and MAIAC we see that MAIAC provide similar values to QC (high rate of intersection in comparison with MOD35 and QC). However, MAIAC LST spatial values are shifted towards hotter values in comparison to QC (1-1.5K). Nevertheless, due to the low number of available data the possible discrepancies are difficult to properly being addressed.

4 DISCUSSION AND CONCLUSIONS

In this work a comparative analysis between a MODIS daytime LST product resulting from the combination of updated split-window coefficients and the introduction of MAIAC cloud mask, and current MODIS LST products version 6 (MYD11A1), was presented. MODIS LST product (MYD11A1) was found to be severely cloud contaminated when additional QC is not considered, with overall RMSEs around 4 K. The deficient cloud detection is partly solved when using two alternative cloud filtering approaches: the QC layer and the MAIAC cloud mask. However, the accuracy is improved at expenses of the reduction in data amount. Validation against in situ measurements showed a decrease of the RMSE for MODIS LST products (MOD11) when additional QC filtering or MAIAC is considered, with RMSEs around 2-3 K. The combination of the LST product presented in this paper with the MAIAC cloud mask was able to improve the RMSE, with RMSE differences in the range 0.2-2 K.

5 REFERENCES

Allen, C. D.,Macalady, A. K., Chenchouni, H., Bachelet, D.,McDowell, N. G., Vennetier,M., ...Cobb, N.,2010, A global overview of drought and heat-induced tree mortality revealsemerging climate change risks for forests. *Forest Ecology and Management*,259, 660–684.

Clark, D., Piper, S., Keeling, C. and Clark, D. (2003). Tropical rain forest tree growth and atmospheric carbon dynamics linked to interannual temperature variation during 1984-2000. *Proceedings of the National Academy of Sciences*, 100, 5852-5857.

Galbraith, D., Levy, P., Sitch, S., Huntingford, C., Cox, P., Williams, M. and Meir, P. (2010). Multiple mechanisms of Amazonian forest biomass losses in three dynamic global vegetation models under climate change. *New Phytologist*, 187, 647-665.

Gomis-Cebolla, J., Jiménez-Muñoz, J. and Sobrino, J. (2016). MODIS-Based Monthly LST Products over Amazonia under Different Cloud Mask Schemes. *Data*, 1, .2.

Hilker, T., Lyapustin, A., Tucker, C., Sellers, P., Hall, F. and Wang, Y. (2012). Remote sensing of tropical ecosystems: Atmospheric correction and cloud masking matter. *Remote Sensing of Environment*, 127, 370-384.

Jiménez-Muñoz, J. C., Sobrino, J., Mattar, C. and Malhi, Y. (2013). Spatial and temporal patterns of the recent warming of the Amazon forest. *Journal of Geophysical Research: Atmospheres*, 118,5204-5215.

Jiménez-Muñoz, J. C., Mattar, C., Sobrino, J. and Malhi, Y. (2015b). Digital thermal monitoring of the Amazon forest: an intercomparison of satellite and reanalysis products. *Int. Journal of Digital Earth*, 9, 477-498.

Østby, T., Schuler, T. and Westermann, S. (2014). Severe cloud contamination of MODIS Land Surface Temperatures over an Arctic ice cap, Svalbard. *Remote Sensing of Environment*, 142, 95-102.

Toomey, M., Roberts, D., Still, C., Goulden, M. and McFadden, J. (2011). Remotely sensed heat anomalies linked with Amazonian forest biomass declines. *Geophysical Research Letters*, 38.

Wilson, A., Parmentier, B. and Jetz, W. (2014). Systematic land cover bias in Collection 5 MODIS cloud mask and derived products — A global overview. *Remote Sensing of Environment*, 141, 149-154.

Williams, A. P., Allen, C. D., Macalady, A. K., Griffin, D., Woodhouse, C. A., Meko, D. M., …McDowell, N. G.,2013, Temperature as a potent driver of regional forest drought stress and tree mortality. Nature Climate Change, 3, 292–297.

Early validation results of the land surface temperature product derived from Sentinel-3 SLSTR instrument

J. C. Jimenez, J. A. Sobrino, G. Soria, Y. Julien, D. Skokovic, J. Gomis-Cebolla, C. Mattar, A. Santamaría-Artigas, J. J. Pasapera-Gonzales
Global Change Unit, Image Processing Laboratory (University of Valencia)
jcjm@uv.es

ABSTRACT *In this work we present results of an early validation of the Land Surface Temperature (LST) product retrieved from the Sea and Land Surface Temperature Radiometer (SLSTR) on board the Sentinel-3 satellite (S3/SLSTR). Validation results were obtained from comparison of S3/SLSTR retrievals against in situ measurements of surface temperature collected over different instrumented sites in Spain and Chile. The test sites include agricultural and marshland land covers. The validation exercise was performed on the standard S3/SLSTR Level-2 LST product as well as on a dedicated LST split-window algorithm with an explicit dependence on surface emissivity. Methods for LST retrieval from the synergy between SLSTR and Sentinel-2 Multispectral Scanner Imager (S2/MSI) data are also discussed. For this purpose, surface emissivity maps obtained from the high spatial resolution of S2/MSI are presented over some test areas.*

1 INTRODUCTION

Sentinel-2 (S2) and Sentinel-3 (S3) missions were developed by the European Space Agency (ESA) to support the European Copernicus programme. The S2 missions was designed to provide systematic global acquisitions of high-resolution multispectral imagery with a high revisit frequency through the Multi Spectral Instrument (MSI) with 13 spectral bands. MSI covers the Visible and Near Infra-Red (VNIR) and the Short Wave Infra-Red (SWIR) spectral ranges with a spatial resolution ranging from 10 m to 60 m.

The S3 mission provides continuity to ENVISAT's capabilities to cover ocean and land applications. Its main instruments are the Ocean and Land Colour Imager (OLCI) and the Sea and Land Surface Temperature Radiometer (SLSTR). OLCI operates in the 0.4-1 μm range at 300m spatial resolution, whereas SLSTR extends the spectral range to the Thermal Infra-Red (TIR) with two spectral bands roughly located at 11 and 12 μm.

In this context, ESA funded the project "Synergistic Use of The Sentinel Missions For Estimating And Monitoring Land Surface Temperature (SEN4LST)", which had the main objective to develop a SLSTR based LST algorithm that benefits from synergy between SLSTR and other Sentinels instruments (e.g. S3/OLCI and S2/MSI) to improve the atmospheric correction and the surface emissivity characterization. A LST algorithm based on the split-window technique with explicit dependence on emissivity was developed

in the framework of the SEN4LST project (Sobrino et al., 2016), as well as a toolbox denoted as LST Processor (Ruescas et al., 2016).

On another level, ESA implemented a different LST algorithm to generate the S3 Standard LST level-2 product. This algorithm was based on the heritage of the LST algorithm used to generate the Standard LST product from ENVISAT imagery. The level-2 LST algorithm uses a set of coefficients for different land covers, so it is not including an explicit dependence on the surface emissivity.

The main objective of this work is twofold: an early validation of the S3 level-2 LST product over different test sites and land covers is presented, and level-2 LST retrievals are compared to LST retrievals from the algorithm developed in the framework of the SEN4LST project. Additionally, we explore the feasibility of surface emissivity characterization from high resolution S2/MSI data and uncertainties linked to this characterization.

2 TEST SITES

2.1 Spain: Doñana and Almería

Doñana test site (36.998N, 6.434W) is located in the south west of Spain near the Atlantic Ocean coast. Approximately half of its area is marshland. The marshes undergo a yearly cycle of inundation in autumn and drying out during the spring season. The topography of the marshes is extremely flat, with a maximum elevation difference of 2.5 m. Continuous

radiometric temperatures are measured with a Campbell Scientific IR120 radiometer.

Almería test site (36.939N,2.034W) is located in Cabo de Gata, south Spain near the Mediterranean Sea. This region is characterized by a semi-arid climate with low rainfall, and the surface is covered mainly by soil and perennial vegetation. Radiometric temperatures are continuously measured by Apogee SI-120 radiometer.

Figure 1 shows the location of the two Spanish test sites, including also RGB compositions from Sentinel-2. More information about the sites can be found in Sobrino and Skokovic (2016).
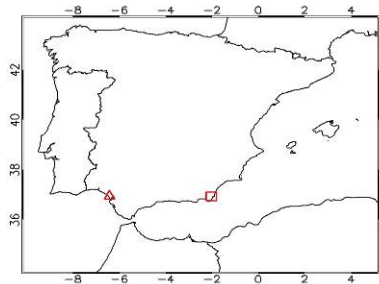
DOÑANA

ALMERIA

Figure 1. Doñana (triangle) and Almería (square) test site in Spain.

2.2 Chile: Oromo

Oromo test site is located over a pasture grass field (40º53'6.07''S,73º6'31.41''W) in southern Chile. The land cover of this area is characterized by its greenness and wet soils during the whole year. The LAB-net station in this site is configured to store 5 min averages of the different variables, including surface radiometric temperature with an Apogee SI-111 instrument (Mattar et al., 2016). Figure 2 shows the

location of the test site and RGB compositions from Sentinel-2.
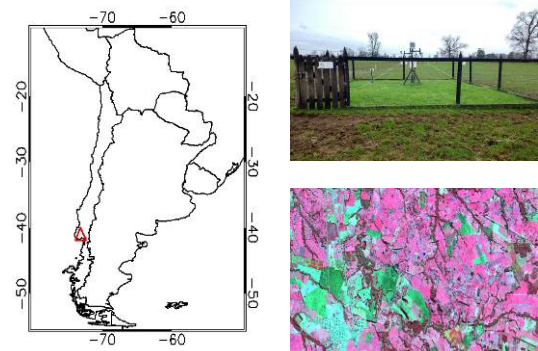
Figure 2. Oromo test site in Chile.

3 SENTINEL 2/3 IMAGERY

Sentinel-3 imagery was downloaded *via* the Sentinel Data Hub for the period July-August 2017. Sentinel-3 data included Brightness Temperatures from the SLSTR instrument (level 1 RBT) and the level 2 LST product. L1/RBT data was used to apply the SW algorithm to brightness temperatures. Pixels located at the test sites coordinates were identified to extract the L1/RBT and L2/LST values.

Sentinel-2 MSI imagery was also downloaded via the Sentinel Data Hub only for single dates for each test site (2017-07-31 for Doñana, 2017-08-04 for Almería, and 2017-05-09 for Oromo). Acquisitions dates were selected based on the cloud cover over the scenes to guarantee clear sky conditions at least over the test site. S2/MSI images were atmospherically corrected using the Sen2Cor module. At-surface reflectances were then used to estimate surface emissivity.

4 LST ALGORITHMS

The SW LST retrieval algorithm developed in the framework of the SEN4LST project is based in the mathematical structure suggested by Sobrino et al. (1996):

$$T_s = T_i + c_1(T_i - T_j) + c_2(T_i - T_j)^2 + c_0 + \quad (1)$$
$$+ (c_3 + c_4 W)(1 - \varepsilon) + (c_5 + c_6 W)\Delta\varepsilon$$

where T_i and T_j are the brightness temperatures of SLSTR bands 8 and 9, respectively, W is the total column atmospheric water vapour, ε the mean emissivity and $\Delta\varepsilon$ the emissivity difference. Algorithm

coefficients c_i are derived from simulated data, and its values are provided in Sobrino et al. (2016).

The LST algorithm used in the SLSTR level 2 product is a heritage of the LST algorithm used in the Envisat's AATSR level 2 product:

$$T_s = a_0 + b_0(T_i - T_j)^n + (b_0 + c_0)T_j \qquad (2)$$

This algorithm does not include W and ε in the formulation, but they are indirectly included in the coefficients a_0, b_0, c_0 which depend on the land cover, vegetation fraction and water vapour (Prata, 2002).

5 VALIDATION RESULTS

Figure 3 shows the results obtained in the comparison between LST retrievals using the two algorithms (Eqs. 1 and 2) and LST measured in situ over the three test sites (Doñana, Almería, Oromo). Overall, the SW (SEN4LST) algorithm provided better results than the Level-2 product, especially over Almería and Oromo, where the bias was reduced by more than 1 K. In the case of the Doñana test site, the bias was slightly lower for the Level-2 product, but the standard deviation was reduced by 0.7 K in the case of the SW algorithm.

The highest variability was observed over Doñana and Oromo, with standard deviation values ranging from 2 to 3 K for both algorithms. This result may be attributed to the high thermal heterogeneity over the Doñana test site in summer, when the surface is covered by dry vegetation and dry soil. In the case of Oromo, the surface is permanently covered by green grass, but the site has a high cloud cover occurrence. Therefore, it may be possible that some validation results were affected by the presence of clouds.

Figure 4 includes some illustrative examples of the spatial patterns observed in the S3 LST product over the Iberian Peninsula and northern regions of Africa, and South America (Chile and Argentina).
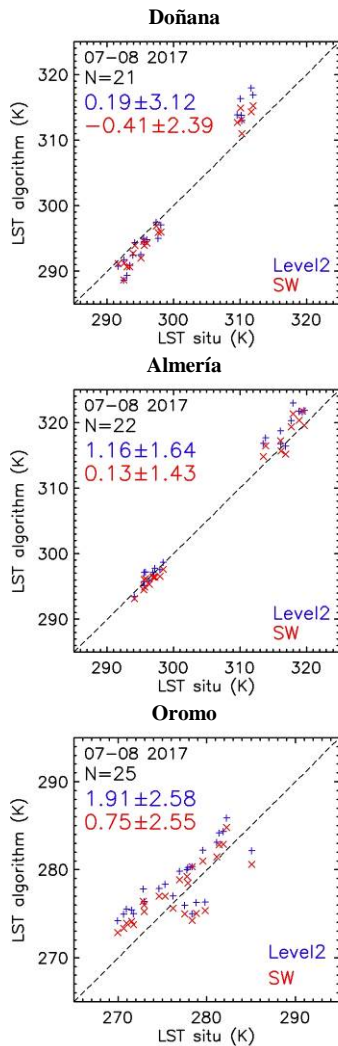
Figure 3. Validation results over the three test sites (Doñana, Almería, Oromo).
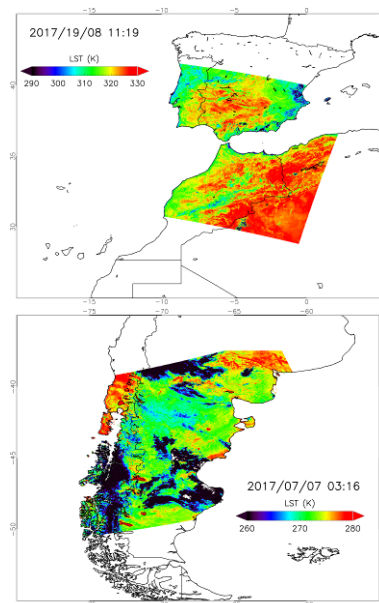
Figure 4. Visualization of the Sentinel-3 Level 2 LST product over the Iberian Peninsula (top) and South America (bottom).

6 SURFACE EMISSIVITY FROM S2/MSI

In order to explore the feasibility of estimating surface emissivity at high spatial resolution, the NDVI thresholds method (NDVI-THM) (Sobrino et al., 2008) was applied to S2/MSI data. For this purpose, S2 images were atmospherically corrected with the Sen2Cor module, which also provides a basic classification and cloud identification.

The NDVI-THM identifies pixels of bare soil, vegetation, and mixed pixels (soil+vegetation) using specific NDVI values for soil and vegetation surfaces, NDVIs and NDVIv, respectively. These values are also used to compute the Fractional Vegetation Cover (FVC) from the scaled NDVI. Pixel emissivities are estimated using a weighted mean between soil and vegetation emissivities (ε_s and ε_v, respectively):

NDVI<NDVIs:
$$\varepsilon = m\rho_{red} + n \qquad (3)$$
NDVIs<NDVI<NDVIv:
$$\varepsilon = \varepsilon_s(1\text{-}FVC) + \varepsilon_v FVC + C \qquad (4)$$
NDVI>NDVIv:
$$\varepsilon = \varepsilon_v + C \qquad (5)$$

where C is a term that takes into account the cavity effect (multiple reflections over a rough surface). For bare soil pixels (NDVI<NDVIs), an empirical relationship between emissivity and reflectance in the red band is proposed, although the red band can be replaced by other band combinations to improve the statistical fit.

Pixel emissivity uncertainty was also estimated through propagation of individual uncertainties using partial derivatives.

Maps of surface emissivity and uncertainty for S3 TIR band 8 (10.8 μm) are illustrated in Figure 5 over the three test sites.

7 CONCLUSIONS

The S3 Level-2 LST product was validated over three test sites using in situ measurements. Results show an optimal performance of the L2 product, but LST retrievals were improved when using a SW algorithm with explicit dependence on the emissivity, especially over semi-arid areas. Surface emissivity maps at high spatial resolution were also derived from S2 MSI data, thus showing the potential synergy between S2 and S3 data. Validation results presented in this work refer to a limited period of time. Longer validation periods are required to obtain robust statistics.
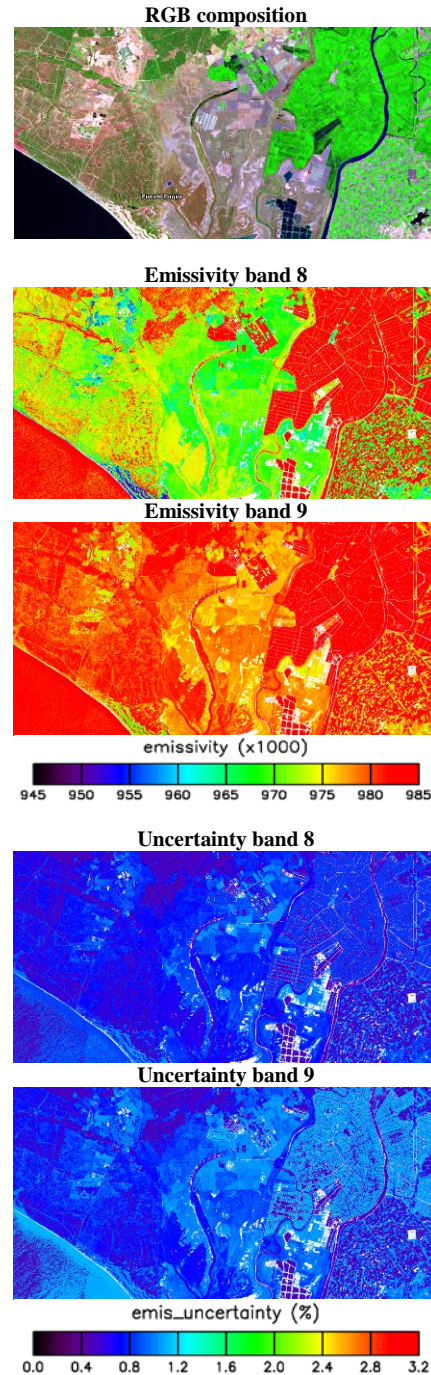
Figure 5. Surface emissivity maps at Sentinel-3 SLSTR bands 8 (10.9 μm) and 9 (12 μm) derived from Sentinel-2 MSI data over the Doñana test site.

9 REFERENCES

Mattar, C., Santamaría-Artigas, A., Durán-Alarcón, C., Olivera-Guerra, L., Fuster, R. and Borvarán, D. (2016). The LAB-Net Soil Moisture Network: Application to Thermal Remote Sensing and Surface Energy Balance. *Data*, 1, 6.

Prata, F. (2002). Land Surface Temperature Measurment From Space: AATSR Algorithm Theoretical Basis Document, Aspendale, Australia: CSIRO Atmospheric Research.

Ruescas, A. B., Danne, O., Fomferra, N. and Brockmann, C. (2016). The Land Surface Temperature Synergistic Processor in BEAM: A Prototype towards Sentinel-3. *Data*, 1, 3.

Sobrino, J. A., Li, Z.-L., Stoll, M. P. and Becker, F. (2016). Multi-channel and multi-angle algorithms for estimating sea and land surface temperature with ATSR data. *International Journal of Remote Sensing*, 17, 11, 2089-2114.

Sobrino, J. A., Jiménez-Muñoz, J. C., Sòria, G., Romaguera, M., Guanter, L., Moreno, J., Plaza, A., Martínez, P. (2008). Land surface emissivity retrieval from different VNIR and TIR sensors. *IEEE Transactions on Geoscience and Remote Sensing*, 46, 2, 316-327.

Sobrino, J. A. and Skokovic, D. (2016). Permanent Stations for Calibration/Validation of Thermal Sensors over Spain. *Data*, 1, 10.

Sobrino, J. A., Jiménez-Muñoz, J. C., Sòria, G., Ruescas, A. B., Danne, O., Brockmann, C., Ghent, D., Remedios, J., North, P., Merchant, C., Berger, M., Mathieu, P. P. and Göttsche, F.-M. (2016). Synergistic use of MERIS and AATSR as a proxy for estimating Land Surface Temperature from Sentinel-3 data. *Remote Sensing of Environment*, 179, 149-161.

Uncertainty Analysis of the Automated Radiometric Calibration over Baotou Cal&Val Site in China

Lingling Ma[1], Yongguang Zhao[1], Emma R. Woolliams[3], Yaokai Liu[1, 2], Ning Wang[1], Xinhong Wang[1], Caihong Dai[4], Caixia Gao[1], Chuanrong Li[1,*], Lingli Tang[1]

[1]*Key Laboratory of Quantitative Remote Sensing Information Technology, Academy of Opto-Electronics, Chinese Academy of Sciences, Beijing, China*
[2]*University of Chinese Academy of Sciences, Beijing, China*
[3]*National Physical Laboratory, Hampton Road, Teddington, Middlesex, TW11 0LW, UK*
[4]*National Institute of Metrology, Beijing, China*
First author (llma@aoe.ac.cn)   *corresponding author (crli@aoe.ac.cn)

ABSTRACT - An automated radiometric calibration system was established on the Baotou Cal&Val test site in China to provide an operational high-accuracy and high-stability vicarious calibration and validation site for high resolution remote sensing instruments. The composition of the system is described in this paper, which provides bottom-of-atmosphere (BOA) reflectance in 30 minute intervals in 10 nm steps over the spectral range from 400 nm to 1000 nm. The paper also provides an initial uncertainty analysis of the automated radiometric calibration considering three aspects: uncertainty associated with the spectrometer (ground viewing instrument) measurements; uncertainty associated with the BOA reflectance calculation; and the uncertainty associated with averaging this to the requirements of the Radiometric Calibration Network, RadCalNet. Preliminary analysis shows that the combined uncertainty associated with RadCalNet BOA reflectance would be approximatively 3.0 % within the spectral range 500 nm ~ 900 nm. The uncertainty associated with the TOA reflectance propagated from BOA reflectance measured by single observation is approximatively estimated as 4 % ~ 4.5 %, ignoring the influence of the surrounding pixels.

1 INTRODUCTION

Satellite-derived Earth observation data provide information about environmental and climate changes that is of immense value to society. However, the analysis of long term trends requires high accuracy data that can be reliably compared across time. This increasing need for high accuracy remote sensing data and information products in turn creates the need for reliable, stable ground references that can be used for the in-orbit characterisation, calibration and validation of satellite radiometric instrumentation.

Field vicarious calibration is a classic on-orbit calibration method, which provides field references for sensor full-chain calibration and performance evaluation, and is an effective way to compare satellite observations with a laboratory measurement standard (Naughton, et al., 2011). The principles of field calibration can be summarized as: simultaneously measuring the reflectance of the ground target and the atmospheric profile when the satellite overpasses; simulating the top-of-atmosphere (TOA) spectrally-resolved reflectance through a radiation transfer model based on the observing geometry of the sensor and measured surface & atmosphere characteristics; and finally comparing the simulated TOA radiance and the satellite observation value to determine the radiometric calibration coefficients. However, normal field calibration campaigns are expensive and require cooperation of ground observations by teams of scientists with the satellite overpass, along with clear weather conditions and expensive field equipment. In general, the radiometric accuracy of field calibration at solar reflective bands is approximately 5 % ~ 7 %. Automating the process of field observations increases the number of satellite overpasses that can be matched, is cheaper and has the potential for higher accuracy.

To realise automatic high frequency satellite radiometric (and geometric) calibration and validation, the Academy of Opto-Electronic (AOE), Chinese Academy of Sciences has designed the automated radiometric calibration system, and deployed it on the Baotou Cal&Val site (Li, et al., 2015). The system comprises operational ground-viewing radiometers, operational atmospheric measurement real-time transfer of measured data, data processing and radiation transfer modelling. It can obtain dynamic information of target surface reflectance, aerosol optical thickness, water vapour content, etc. The system can provide sensor-independent TOA spectral reflectance product with a 2 nm spectral interval every 2 minutes. This TOA spectral radiance product can be

combined with the sensor-specific spectral responsibility to obtain the band-integrated radiance of the sensor, which can be directly compared with the sensor observation. The automated radiometric calibration system can effectively improve both the frequency and stability of on-orbit radiometric calibration for those optical remote sensing sensors.

In this paper the Baotou Cal&Val site will be briefly introduced in section 2, and after that the system and methodology of the automated radiometric calibration are described in section 3. Emphasis is laid on the uncertainty analysis to the automated radiometric calibration in sections 4. And a preliminary analysis applied to the Sentinel-2A sensor is given in section 5.

2 DESCRIPTION OF THE BAOTOU CAL&VAL SITE

2.1 General Information

The Baotou Cal&Val site ("Baotou site" in brief) is located at the Ming'an township, Urad Front Banner, Bayannur prefecture, Inner Mongolia Autonomous Region, China. The city of Baotou is about 50 km away from the Baotou site. The geographic coordinate of the permanent target area in the site is 40.85°N, 109.6°E and the overall Baotou site extends over a region up to 35 km along the east-west axis, and 16 km along the north-south axis, with total area 292.5 km^2 and is about 1270 m above sea level.

A series of targets and infrastructure has been built in the Baotou site in order to provide effective support for sensor aerial test flight, satellite sensor on-orbit calibration & performance evaluation, and RS product validation (Li, et al., 2015).

In 2014, the Baotou site was chosen as one of the four prototype sites for the new RadCalNet (radiometric calibration network of automated instruments, sponsored by the Committee on Earth Observation Satellites) (Czapla Myers, et al., 2016).

RadCalNet has its own data processing system and requires ground reflectance data in 10 nm intervals every 30 minutes along with atmospheric conditions. The data are processed to provide TOA reflectance products with the same spectral and temporal resolution.

2.2 Permanent Target Region and Desert Area

To meet the requirements of a wide dynamic range and stability of the ground targets in sensor radiometric calibration, multi-greyscale permanent artificial optical targets and a flattened desert area were built in the Baotou site (see Fig.1).

Fig.1 Google image of the permanent target region and desert area (marked in circles)

In the permanent target region, the gray-scale artificial target is composed of 2 white, a gray and a black uniform gravel squares, each of which covers an area of 48 m × 48 m. There are three reflectance levels for the four squares, i.e. approximately 10 %, 20 % and 60 %. For the automated radiometric calibration and validation of moderate/high resolution satellite sensors, a desert area (300 m × 300 m) was established in October 2015. It is 1.8 km away from the permanent target region to the north-west and has been flattened.

3 METHODOLOGY OF AUTOMATED RADIOMETRIC CALIBRATION

3.1 Automatic Observation System of Ground Reflected Radiance (AOSGRR)

At the Baotou site, the surface-reflected radiance is measured by several automatic observation systems of ground reflected radiance (AOSGRR) developed by AOE (Academy of Opto-Electronics), CAS (Chinese Academy of Sciences); Fig. 2. Each system consists of a spectrometer unit, a control and data transfer unit, and a support and protective shell. The current system uses CR series spectrometers which cover the spectral region from 380 nm to 1080 nm, with a spectral resolution of 2 nm. The system can directly record the radiance in W m^{-2} sr^{-1} μm^{-1} and adjusts the integration time to ensure a high signal to noise ratio. The spectrometer has a 3º field of view (FOV) and was mounted at a height of 1.5 m. It observes the ground at nadir.

Fig.2 AOSGRR set on the white target and desert area

3.2 CE318 Sun Photometer

A sun photometer, the CIMEL CE318, has been fixed on the Baotou site. The CE318 instrument is a member of AERONET (Aerosol Robotic Network). The scanning model includes direct sun and sky measurements. Direct measurements of the sun and the sky can be made with several programmable sequences. The direct sun measurement is made in eight spectral bands and the measurement sequence takes approximately 10 s.

3.3 Reflectance Inversion Method from AOSGRR Measurement

The surface reflectance of the target can be derived from the following equation:

$$\rho = \frac{\pi L_g}{E_{solar}^{direct} + E_{sky}^{diffuse} + E_{sky}^{scat}} \quad (1)$$

Where, the L_g is the measured surface reflected radiance of the target by AOSGRR. E_{solar}^{direct} is the direct solar radiance arrived at ground, $E_{sky}^{diffuse}$ and E_{sky}^{scat} are the total sky irradiance reaching the ground. Both of the solar and sky irradiance reaching the ground are estimated with MODTRAN code (Berk, et al., 2011), with the observed atmospheric parameters provided by the Baotou AERONET station.

4 UNCERTAINTY ANALYSIS OF THE AUTOMATED RADIOMETRIC CALIBRATION

4.1 Uncertainty Associated with Spectrometer Measurements

The first step in obtaining the TOA reflectance of the Baotou targets is the measurement of the surface reflectance by the AOSGRR. During the actual operation of AOSGRR, the measurement is affected by several factors such as the uncertainty of spectrometer calibration and change of spectrometer working environment.

(a) Spectrometer Calibration. The spectrometer used in AOSGRR was calibrated by the National Institute of Metrology (NIM), China. The radiometric calibration was performed using a reference lamp and reflective diffuser (Dai, et al., 2017). The uncertainties associated with several sources were estimated through laboratory measurements. These sources are repeatability of spectrometer, lamp, lamp aging and current set, alignment for lamp, distance, diffuser panel, uniformity, nonlinearity of spectrometer, and stray light. The total uncertainty of spectrometer calibration was estimated by NIM, ranging in the order of 1.19 % ~ 2.3 % within the spectral range 500 nm ~ 1000 nm.

(b) Change of spectrometer working environment. Since rigorous measurements have not yet been conducted, it is estimated that the uncertainty associated with the change of the working environment (e.g. temperature sensitivity, transportation to the site) for the spectrometer is 0.5 %.

The total uncertainties associated with spectrometer measurements are summarised in Table.1.

Table.1 Uncertainties associated with measurements

Uncertainty Contributor (%)	Wavelength/nm						
	400	500	600	700	800	900	1000
Spectrometer Calibration	28.40	2.30	1.19	1.20	1.25	1.32	1.41
Change of working environment	0.5	0.5	0.5	0.5	0.5	0.5	0.5
Total uncertainty	28.40	2.35	1.29	1.30	1.35	1.41	1.50

4.2 Uncertainty associated with BOA reflectance calculation

The bottom-of-atmosphere (BOA) reflectance is calculated from the ground-reflected radiance measured by AOSGRR, the direct solar irradiance, and the total sky irradiance reaching the ground. The solar and sky irradiances are simulated by MODTRAN. In the simulation, several factors will increase the uncertainty of BOA reflectance, such as uncertainty of the solar irradiance model, uncertainty of the radiative transfer model, measurement uncertainties for the atmospheric parameters and other factors.

(a) Uncertainty of the solar irradiance model. The uncertainty of exoatmospheric solar irradiance model used in MODTRAN is estimated to be (standard uncertainties) 1.5 % at 450 nm, 0.9 % at 650 nm, 1.1 % at 850 nm, and 0.8 % at 1550 nm (Thuillier, et al., 1998, 2003). These values were linearly interpolated to provide intermediate wavelength uncertainties. (b) Uncertainty of the radiative transfer model. According to the MODTRAN user manual

(Berk, et al., 2011), the uncertainty associated with the radiative transfer code MODTRAN-5 is 2 % for radiance predictions.

(c) Uncertainty of the atmospheric parameter retrieval. To estimate the uncertainty associated with the BOA reflectance due to uncertainties in the atmospheric parameters, Monte Carlo simulations were performed, adding errors of 12 % and 0.01 to the water vapour content and aerosol optical thickness respectively (Holben, et al., 1998; Sinyuk, et al., 2012). The corresponding direct solar and total sky irradiances were simulated 1000 times by MODTRAN. The standard deviation of the 1000 sets of simulated irradiance is determined to be caused by measurement errors of water vapour content (WVC) and aerosol optical thickness (AOT). This process was repeated for different standard conditions, e.g. for a summer condition and a winter condition. Fig.3 shows the determined uncertainty caused by measurement error of the water vapour atmospheric parameter for summer and winter conditions. Similar analyses were carried out for AOT.
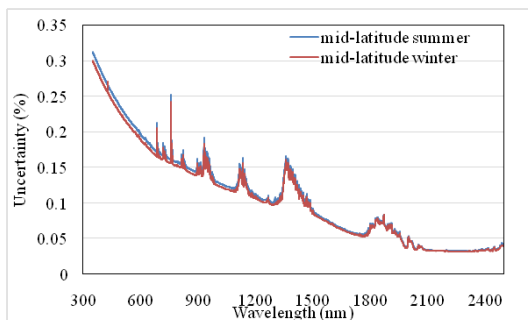
Fig.3 Uncertainty caused by error of WVC

(d) Other factors. The MODTRAN-5 radiative transfer model also requires classification, e.g. of aerosol type or atmospheric model. Some analysis was performed varying the classification and the uncertainty associated with the model choices was estimated conservatively to be within 1 %.

The separate uncertainties shown in Table.2 are calculated by assuming that the aerosol is rural, the atmospheric model is mid-latitude summer, the water vapour content is 0.5 g cm^{-2}, the aerosol optical thickness is 0.2, the solar zenith angle is 30, and the view zenith angle is 0.

The BOA reflectance computed from the surface-reflected radiance measured by AOSGRR is provided in 2 nm steps over the spectral range 380 nm ~ 1080 nm every 2 minutes. To generate the standard RadCalNet product with 10 nm spectral intervals and every 30 minutes, temporal averaging and spectral resampling processes are used. The uncertainties caused by this process should also be considered.

Table.2 Uncertainties associated with BOA reflectance calculation (Measured radiance from Table 1)

Uncertainty Contributor (%)	Wavelength/nm						
	400	500	600	700	800	900	1000
Measured radiance	28.40	2.35	1.29	1.30	1.35	1.41	1.50
Solar irradiance model	1.50	1.35	1.05	0.95	1.05	1.08	1.04
MODTRAN	2	2	2	2	2	2	2
AOT	0.28	0.23	0.20	0.17	0.16	0.15	0.13
WVC	0.001	0.001	0.027	0.18	0.12	0.80	0.03
Other factors	1.0	1.0	1.0	1.0	1.0	1.0	1.0
Total uncertainty	28.53	3.52	2.79	2.77	2.82	2.97	2.89

4.3 Uncertainty Associated with BOA Reflectance at 10 nm, 30 Minute Intervals

(a) Temporal average. To obtain BOA reflectance every 30 minutes, the reflectance averages of 15 minutes before and after a given time (i.e. 9:00, 9:30, 10:00, etc.) are used as the final BOA reflectance. Since the measurement interval of AOSGRR is 2 minutes, fifteen BOA reflectance values are averaged. The uncertainties caused by temporal average process is estimated by the standard deviation of the fifteen BOA reflectance values. The value thus obtained ranged from 0.32 % at 700 nm to 11 % at 400 nm. This will be caused by several factors, including instrument noise, and the motion of the sun and changes in environmental condition. The average of 15 values will have a smaller uncertainty than any individual reading but it is unlikely to be a purely random effect. Therefore, we determined the uncertainty associated with the average of the 15 readings by dividing the standard deviation by the square root of 15 and then adding, in quadrature, a base level of 0.3% to account for common errors between the different measurements.

(b) Spectral resampling. AOSGRR uses a hyperspectral spectrometer with 2 nm spectral sampling interval. There is no spectral resampling process in generating nadir BOA Reflectance at 10 nm intervals, the data are simply subsampled. So, the uncertainty caused by spectral resampling process is estimated to be zero.

Total uncertainties associated with nadir BOA reflectance at 10 nm, 30-minute intervals are shown in Table.3.

214

Table.3 Uncertainties associated with nadir BOA reflectance at 10 nm, 30-minute intervals

Uncertainty Contributor (%)	Wavelength/nm						
	400	500	600	700	800	900	1000
BOA reflectance	28.53	3.52	2.79	2.77	2.82	2.97	2.89
Temporal average	2.97	0.34	0.31	0.31	0.32	0.42	1.33
Total uncertainty	28.68	3.54	2.81	2.79	2.84	3.00	3.18

4.4 Final Uncertainty Associated with BOA Reflectance

The total uncertainty associated with BOA reflectance is shown in Fig.4, which is calculated by assuming that the aerosol is rural, the atmospheric model is mid-latitude summer, the water vapour content is 0.5 g cm^{-2}, the aerosol optical thickness is 0.2, the solar zenith angle is 30º, and the view zenith angle is 0º.
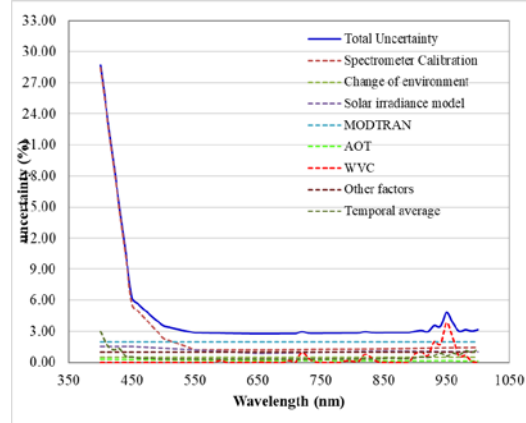
Fig.4 Total uncertainty associated with RadCalNet BOA reflectance

5 UNCERTAINTY ANALYSIS APPLIED TO SENTINEL-2A/MSI SPECTRAL BANDS

The aim of the analysis is to determine the spectral reflectance for comparison with satellite sensors. As an example of the uncertainty associated with the ground measurements in such a comparison, we obtained an average uncertainty for the bands of Sentinel-2 multispectral imager (MSI) (Martimort, et al., 2012); Table.4 weighted by the spectral response function of the Sentinel-2 bands. The weighted average is calculated using the higher spectral resolution product directly from the Baotou site processing, rather than the 10 nm data of RadCalNet.

Table.4 Uncertainties associated with the bands of Sentinel-2A/MSI

Uncertainty Contributor (%)	Channels			
	Blue	Green	Red	NIR
Spectrometer measured radiance	2.84	1.31	1.29	1.37
Simulated solar and sky irradiance	2.63	2.53	2.42	2.50
Temporal average	0.34	0.31	0.31	0.35
Total Uncertainty	3.88	2.87	2.76	2.88

6 FUTURE WORK

This paper described the automated radiometric calibration system deployed on the Baotou site, and the uncertainty analysis which has been undertaken for the BOA reflectance. In future we will further explore the uncertainty associated with TOA reflectance, considering the propagation to TOA. We will also include a model, under development, for correcting the spectrometer for thermal effects. The uncertainty associated with the non-uniformity and bi-directional reflectance distribution function (BRDF) effect of the targets should be analysed. In addition, due to the adjacency effect in estimating the TOA reflectance, the uncertainty associated with the adjacency effect correction will be also estimated. More detailed analysis work is in progress, and the corresponding joint manuscript between AOE, NPL and NIM is in preparation and will be published in future.

ACKNOWLEDGMENT

REFERENCES

Berk, A.; Anderson, G.; Acharya, P.; Shettle, E. MODTRAN5 5.2.1 user's manual; Spectral Sciences Inc., Air Force Research Laboratory: Burlington, MA, USA and Hanscom AFB, MA, USA. 2011.

Czapla Myers J, Bouvet M, Wenny B N. The Radiometric Calibration Network (RadCalNet): a Global Calibration and Validation Test Site Network[C]// AGU Fall Meeting. AGU Fall Meeting Abstracts, 2016:40-46.

Dai, C. H., Khlevnoy, B., Wu, Z. F., et al. Bilateral Comparison of Spectral Irradiance Between NIM and VNIIOFI from 250 to 2500 nm[J]. MAPAN, 2017:1-8.

Holben B N, Eck T F, Slutsker I, et al. AERONET—A federated instrument network and data archive for aerosol characterization[J]. Remote sensing of environment, 1998, 66(1): 1-16.

Li, C.; Tang, L.; Ma, L.; Zhou, Y.; Gao, C.; Wang, N.; Li, X.; Wang, X.; Zhu, X. A comprehensive calibration and validation site for information remote sensing. ISPRS Archives, 2015, Vol. 40, No. 7W3, pp. 1233-1240.

Martimort P, Fernandez V, Kirschner V, et al. Sentinel-2 MultiSpectral imager (MSI) and calibration/validation[C]// Geoscience and Remote Sensing Symposium. IEEE, 2012:6999-7002.

Naughton D, Czaplamyers J S. Absolute radiometric calibration of the RapidEye multispectral imager using the reflectance-based vicarious calibration method[J]. Journal of Applied Remote Sensing, 2011, 5(1):3544.

Sinyuk A, Holben B N, Smirnov A, et al. Assessment of error in aerosol optical depth measured by AERONET due to aerosol forward scattering[J]. Geophysical Research Letters, 2012, 39(23).

Thuillier, G.; Hersé, M.; Labs, D.; Foujols, T.; Peetermans, W.; Gillotay, D.; Simon, P.; Mandel, H. The solar spectral irradiance from 200 to 2400 nm as measured by the SOLSPEC spectrometer from the Atlas and Eureca Missions. Sol. Phys. 2003, 214, 1-22.

Thuillier, G.; Hersé, M.; Simon, P.; Labs, D.; Mandel, H.; Gillotay, D.; Foujols, T. The visible solar spectral irradiance from 350 to 850 nm as measured by the solspec spectrometer during the Atlas I Mission. In Solar Electromagnetic Radiation Study for Solar Cycle 22; Pap, J.M., Fröhlich, C., Ulrich, R.K., Eds.; Springer: Berlin, Germany, 1998, pp. 41–61.

Independent Analysis of Seasonal Surface Temperature Trend by Simultaneously Satellite Data and Numerical Simulations over Tibetan Plateau in the Last Decade

Xiaoying Ouyang[1,2], Yonghui Lei[1], Dongmei Chen[2]

1. *State Key Laboratory of Remote Sensing Science, Institute of Remote Sensing and Digital Earth, Chinese Academy of Sciences, Beijing 100101, China;*
2. *Department of Geography and Planning, Queen's University, Kingston, ON, K7L 3N6, Canada;*

Email addresses: ouyangxy@radi.ac.cn, xo@queensu.ca

ABSTRACT - We aggregate the Advanced Along-Track Scanning Radiometer (AATSR) land surface temperature (LST) 1 km dataset to the 10 km High Asian Refined analysis (HAR) surface temperature (TSK) and 2-meter air temperature (T2) grid to avoid the cloud effect and data sampling gap on the satellite observations. Meanwhile, we use the diurnal temperature cycle (DTC) model to fit the HAR datasets time to the AATSR overpassing time. Then, we investigate seasonal trend, spatial variability and elevation dependent of LST and T2 over TP for 2003-2011 by the independent simultaneously AATSR and HAR datasets over Tibetan Plateau (TP) region. The common used linear regression method is applied to both the AATSR data and the HAR data for the temperature trend and variability analysis over the study area. The consistent results from both satellite observations and numerical outputs show that the warming trend over the entire TP is not obvious during last decade, especially at the areas higher than 4000 m. The temperature of the region around Namco is warming during last decade. The results at site Qomolangma show clearly cooling trend, especially during day. Meanwhile, the discrepancy between the different datasets show that the simulation outputs warming trend is higher than the observation trend, especially in autumn and winter. Moreover, the increase of air temperature+ was more distinct than that of the surface temperature over TP for the last decade.

1 INTRODUCTION

The place of Tibetan Plateau (TP) is always treasured due to its significant geography and climatology position in Asia as well as the whole world. The research on the warming trend of the TP region is one of the main challenges in regional and global climate studies. However, the ground stations in TP are very limited and patchy, especially in the western TP region and elevations higher than 4,800 m (Qin *et al.*, 2009). Meanwhile, thermal remote sensing satellite observations and numerical simulations can give the chance of broad spatial coverage of the land surface temperature (LST) product independently (Li *et al.*, 2013). The elevation dependency on temperature trend, owing to its beneficial to understand mountain environmental variations, has been paid more attentions during global climate change studies in recent years (Fyfe and Flato, 1999; Liu and Chen, 2000; Qin *et al.*, 2009).

Several studies have been carried out in the temperature trend analysis on both global mean surface temperature and regional high mountain areas. Some of them show the clearly warming trend in their studies. For example, Fyfe and Flato (Fyfe and Flato, 1999) discovered an elevation dependency of the simulated surface screen temperature increase over the Rocky Mountains in the winter and spring seasons. Liu et al. (Liu and Chen, 2000) used a linear regression model to detect the temperature trend over TP and confirmed the warming trend increasing with elevation. Over the TP regions, the warming trend is also observed. Oku (Oku *et al.*, 2006) analysed the hourly LST geostationary observations over TP during the period of 1996 to 2002 and concluded an increasing trend. Qin et al. (Qin *et al.*, 2009) investigated the recent warming trend in TP with respect to the altitude using monthly MODIS LST data of 2000 – 2006 and concluded that no increasing trend was observed for elevations higher than 5000 m. Wu et al. (Wu *et al.*, 2013) revealed a statistically warming in ground surface temperature during 1980-2007 from 16 meteorological stations over central TP region. Zhang et al.(Zhang *et al.*, 2014) showed the increase surface temperature of warming lake in TP during 2001-2012 is caused by the increase of land and air temperature ; meanwhile, the temperature change of cooling lakes, most of which located at elevations higher than 4200 m, results from cold water from melted glacier. By analysing surface air temperature, Gao et al. (Gao *et al.*, 2014) showed a significant warming trend over the TP in the period of 1979-2010.

However, the probability of warming hiatus on global temperature trend is also reported by recent studies (Mears *et al.*, 2003; Fyfe *et al.*, 2013; An *et al.*, 2017). Mears et al. (Mears *et al.*, 2003) discovered the trend discrepancy between satellites based temperature and in situ observations. Fyfe et al. (Fyfe *et al.*, 2013) also found that recent observed global warming trend is significantly less than that of climate models simulation. An et al. (An *et al.*, 2017) detected a warming hiatus over the TP regions lower than 4000 m since the late 1990s as well as a delayed warming hiatus higher than 4000 m from mid-2000s.

Although various studies on the surface temperature trend analysis over the world using these two data sources have been done for the last decades, it is still controversial whether it is a warming trend or a warming hiatus over the earth due to the estimation and integration bias of different data sources. Meanwhile, the satellite based LST datasets are seldom used in the global climate change studies due to some limitations, such as the lack of high quality long-term climate record (Good *et al.*, 2017), satellite sampling and impact from the clouds (Jin and Dickinson, 1999; Vinnikov *et al.*, 2012). Although the integration of satellite observations and numerical simulations could intimidate the limitations to a certain extent, the merged processes and uncertainty of representation of LST still caused unprecedented discrepancies (Karl *et al.*, 2006; Good *et al.*, 2017).

In recent years, we have thoroughly investigated the potential usage of the quality-assured Advanced Along-Track Scanning Radiometer (AATSR) derived land surface temperature (LST) performance with ground measurements and numerical weather simulations (Ouyang *et al.*, 2017) over Heihe river basin and TP. In this paper, we first time use the AATSR dataset and High Asian Refined analysis (HAR) simulations to study the temperature trend over TP region from 2003-2011. We make a revision on the AATSR spatial aggregation from 1 km to 10 km to avoid the cloud effect and data sampling gap on the satellite observations. Meanwhile, we use the diurnal temperature cycle (DTC) model to fit the HAR simulations and the AATSR observations passing time. We then give an independent overview of the surface temperature trend over TP region for the last decade. It is an attempt analysing the temperature trend of both LST and T2 air temperature over TP region and could guarantee avoiding the integration of differences data sources.

2 DATA AND METHODOLOGY

2.1 Data

The study area of the TP region is between 26°-40ºN, 74°-101ºE. The TP region is always referred as the

region above 3000 m and the average elevation of TP is 4000 m. We analyse two independent data sources including AATSR LST products, HAR TSK and HAR T2 datasets from TP region for 2003-2011 in this study for the seasonal analysis. The three datasets are validated using a systematic evaluation framework proposed by our previous work. AATSR derived 1 km LST is one of the most accurate satellite LST data produced by GlobTemperature project of European Space Agency (ESA) Data User Element (DUE) (Ghent, 2012; Good *et al.*, 2017) which is derived using the "split-window" method from the AATSR sensors. AATSR and its precedents ATSR series could provide over twenty years' precise observation over the earth surface. HAR outputs are hourly 10 km gridded datasets dynamically downscaled from the global analysis data using the Weather Research Forecasting (WRF) model (Maussion *et al.*, 2014). HAR outputs provide over 10 years of high resolution atmospheric datasets including surface skin temperature (TSK) and 2 meter above ground air temperature (T2) over TP region. Elevation data used for the discrimination for the area higher than 4000 m are also from HAR datasets. Table 1 gives a general idea of the three datasets.

2.2 Methodology

We use the independent AATSR observation data and HAR simulation data to analyse the surface temperature trend of 2003-2011. The AATSR overpass the TP region at around 11:30 a.m. /p.m. Beijing Time. The hourly HAR datasets are normalized to the AATSR overpassing time by the DTC model.

Table 1. The temporal and spatial details of the three datasets original information.

Dataset name	Temporal resolution	Spatial resolution	Time Period	Source
AATSR LST	Twice per day	1 km	2002-2012	GlobTemperature
HAR TSK	Hourly	10 km	2001-2014	WRF
HAR T2	Hourly	10 km	2001-2014	

Meanwhile, the AATSR 1 km datasets are aggregated to 10 km HAR grid by the aggregated weighting method. Note that the AATSR and HAR datasets are all processed to the same clear-sky spatial and temporal conditions, which could guarantee that these datasets are all in the same temporal and spatial resolutions conditions although they are compared independently. After the data preparation processes of temporal and spatial matching, a linear regression model is used in the trend analysis (Ouyang et al., 2017). The trend is also calculated at different elevation range. The following equation is used to detect the temperature trend:

$$y=a+bx \qquad (3)$$

where y denotes the surface temperature (LST/TSK/T2); x is the time in years; a is the intercept; b is the slope i.e., the warming rate.

We investigate both seasonal trend and spatial variability of LST and T2 over TP for 2003-2011 by the day and night AATSR and HAR datasets. In addition, the LST and T2 trends at two specific sites are analysed to figure out the trend variations in different land surface type and different surface elevation.

The main processes in this paper are based on the linear regression model of equation 1. The calculation basis x is 9 years and each calculation is based on the four different seasons. We give an independent analysis of TP surface temperature trend from four aspects: first, we give an annual seasonal average temperature trend slope 1 on each 10 km grid in the whole study area for 2003-2011 to give a spatial variation on each season. Second, we consider the study area as a whole and give 9-year regression. Third, we choose the grid higher than 4000 m and calculate the grid of which slope is higher than 0 (warming). Finally, we compute the two specific validation sites statistics on the average temperature trend.

3 RESULTS

3.1 Spatial warming trend variation on each grid in the study area

Fig.1 shows the spatial seasonal variations result from both satellite observations (AATSR LST) and numerical outputs (HAR TSK/T2). For simplify, only the spring and winter day seasonal trend variations are shown. For the following results analysis, we only show the most representative figures to give a general idea of the trend. In general, the trend from AATSR LST is similar to that from HAR TSK/T2. Both of the two datasets show that the warming trend over the entire TP is not distinct during 2003-2011, especially for the satellite observations during autumn and winter. In fact, the simulations outputs are warmer than the observations for all the seasons except a little colder in the summer day. The overestimate of the simulation outputs has also been found by Jin et al. (Jin *et al.*, 1997) in low and mid-latitude and Fyfe et al. (Fyfe *et al.*, 2013) in global mean surface temperature analysis. Note that, the satellite observed spring and winter day trends are similar to the numerical outputs. Moreover, the Namco area and surroundings (around 30°N, 92.5°E) show the warming trend for all the seasons from all the datasets.
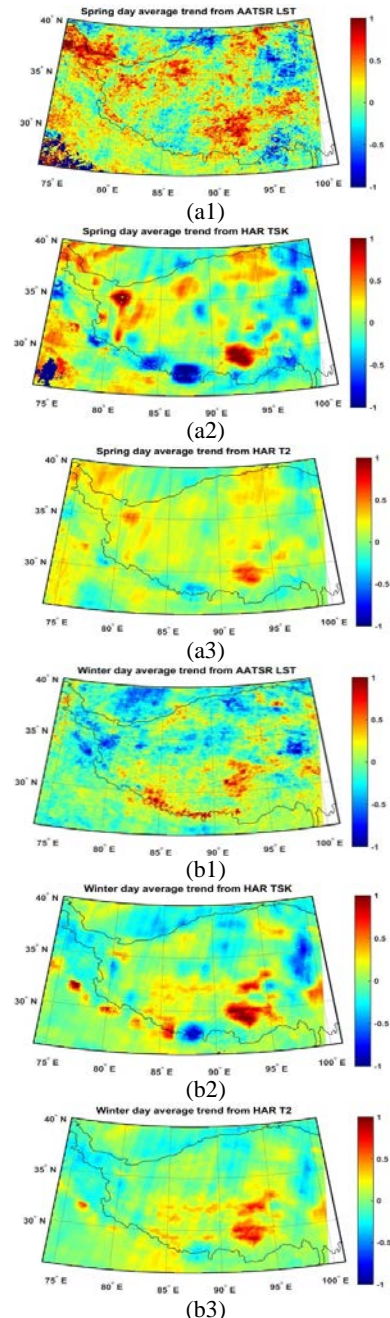
Figure 1. The spatial seasonal variations result from AATSR LST and HAR TSK/T2 warming trend over the entire during 2003-2011. Spring day average trend from (a1) AATSR LST, (a2) HAR TSK, (a3) HAR T2; winter day average trend from (b1) AATSR LST, (b2) HAR TSK, (b3) HAR T2. Some texture is evident for the swath of the AATSR is 500 km and the HAR sampling is also the same path as AATSR.

3.2 The whole study area averaged trend

Further studies are also conducted for the total average temperature trend over TP region both at day and night during last decade (Fig.2). From our former studies, the night AATSR LST trend is more similar to the HAR T2 than HAR TSK. The exception occurred at autumn night, where the AATSR LST shows no warming trend, while both HAR TSK and T2 show warming trend of 0.20 and 0.31 (b value), respectively. These results match the results in section 3.1 (not shown in figure), where the warming is clear from HAR datasets, especially in the HAR TSK. Except this inconsistent, the simulations and observations show nearly the similar results: the warming trend is not distinct, where the largest b value is 0.15 (excluded the autumn night. Both AATSR and HAR datasets even show the minus value for during spring night. In consideration of the unprecedented extreme climate events, cloud contamination, satellite noise and simulation bias in the computation, the rate is not distinct at all.

(a)

(b)
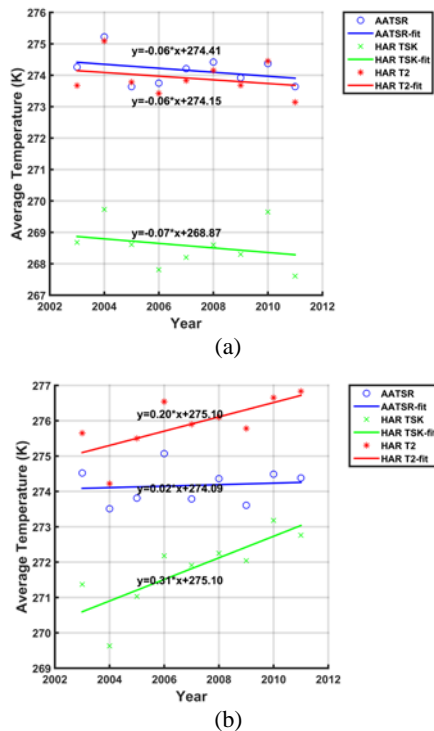
Figure 2. The total average temperature trend over TP region both at night during 2003-2011. (a) spring night, (b) autumn night.

3.3 Warming trend of areas higher than 4000 m

The area higher than 4000 m with a warming rate higher than 0 (warming trend) is analysed and shown in Fig.3. The results show that in these areas the frequency of warming rate higher than 0 (warming trend) is less than 50% except for the autumn day from HAR datasets. The HAR datasets show a more distinct warming trend than AATSR observations, especially for the HAR T2 datasets. The frequencies of warming trend from HAR T2 datasets are higher than that from AATSR observations and HAR TSK for almost all seasons except winter night. It means the increase of air temperature is more distinct than that of surface temperature over TP region for the last decade.

(a)

(b)
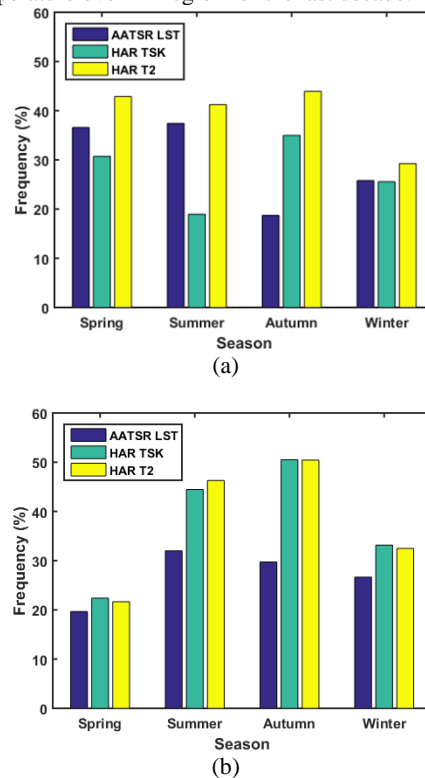
Figure 3 The area higher than 4000 m warming rate higher than 0 (warming trend) during 2003-2011. (a) day average, (b) night average.

3.4 Warming trend of two typical sites

We choose two typical ground sites for the different land surface type warming trend analysis: Namco (4730 m) for the near lake alpine steppe land surface type and Qomolangma (4293 m) for the riverbed gravel land surface type. The Namco site show clearly warming trend at both day and night for the observations and numerical outputs (Fig. 4). The results that the area around Namco is warming for all the datasets during all seasons are consistent with the results from Section 3.1. During spring and summer, the pattern of day and night for all datasets are similar.
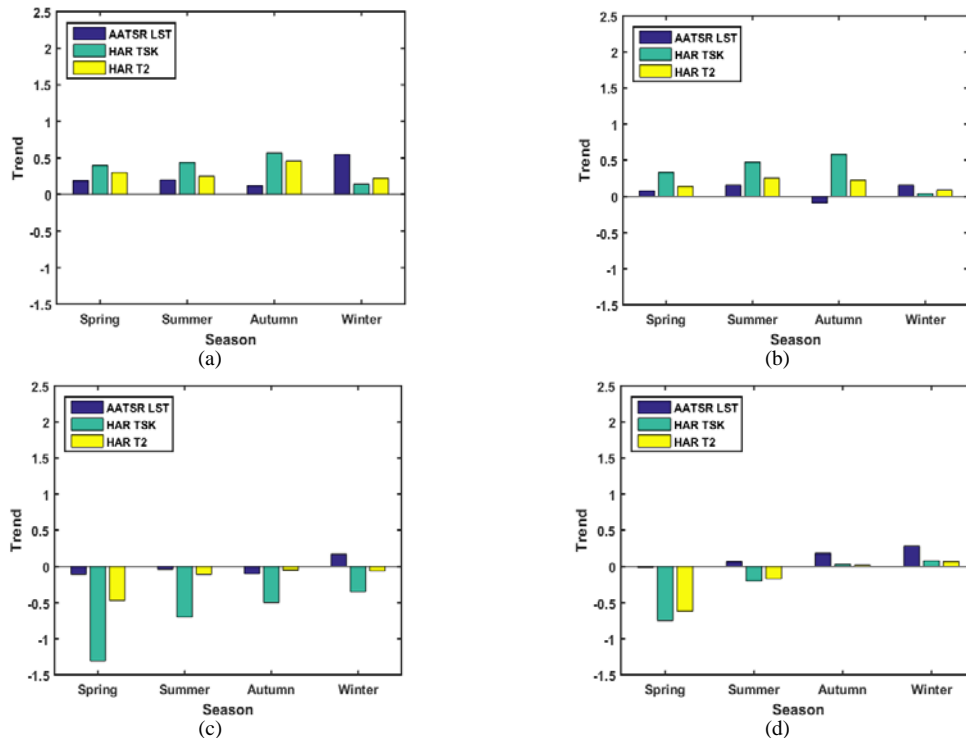
Figure 4 Two typical ground sites for the different land surface type warming trend analysis during 2003-2011. Day average trend for (a) Namco, (c) Qomolangma; Night average trend for (b) Namco, (d) Qomolangma.

The discrepancy is that the trend observed from AATSR show a little cooling (-0.1) during autumn night, whereas the warmer trend (0.5) is observed by AATSR during winter day than HAR outputs (~0.3).

In contrast, the Qomolangma site show a distinct cooling trend, especially from simulation outputs during day. During day, the HAR TSK show a cooling trend of higher than -0.5 for spring, summer and autumn. Although the trend of autumn and winter night is not distinct, the Qomolangma site is warming during last decade in general.

4 CONCLUSION

This study first time uses independent and simultaneous quality assured satellite observations and numerical datasets to analyse the temperature trend over TP for the last decade. We analysed the seasonal and spatial TP region temperature trend independently, as well as the characteristics of areas higher than 4000 m.

The results include two parts: the first part is the consistent results from different datasets and the second part is the discrepancies among them. The consistent results from both satellite observations and numerical outputs show that 1) the warming trend over the entire TP is not distinct during last decade, especially at the areas higher than 4000 m. 2) The

spring day average AATSR LST trend is consistent with the HAR TSK and T2 trend. 3) The temperature of the region around Namco is actually increasing during last decade in all seasons from all the datasets. 4) The results at site Qomolangma show distinct cooling trend, especially during day.

Meanwhile, the discrepancy between the different datasets shows that the warming trend from simulation outputs is higher than that from observation, especially in autumn and winter. Moreover, the increase of air temperature is more distinct than that of surface temperature over TP for the last decade.

The limitation of the studies also includes two parts: First, the clear-sky satellite observations sampling without cloudy-sky temperature information might mask the true LST trends (Wang and Key, 2003; Westermann *et al.*, 2012); Second, the 9-year trend comparison is not enough for the climatic change studies. In the future studies, we will focus on the long-term temperature analysis from different sources of datasets under all sky conditions. The urgent need for the inclusion of long-term remote sensing-based LST data in the global change studies has been mentioned in the Intergovernmental Panel on Climate Change (IPCC) (Change, 2001; Oku *et al.*, 2006). This work gives a clearer picture of climate change patterns through satellite derived LST data.

REFERENCES

An, W., Hou, S., Hu, Y., Wu, S., 2017, Delayed warming hiatus over the Tibetan Plateau. *Earth and Space Science*, 4, 128-137.

Change, C., 2001, The Scientific Basis. Intergovernmental Panel on Climate Change. *by JT Houghton, Y. Ding, DJ Griggs, et al.*

Fyfe, J.C., Flato, G.M., 1999, Enhanced climate change and its detection over the Rocky Mountains. *Journal of Climate*, 12, 230-243.

Fyfe, J.C., Gillett, N.P., Zwiers, F.W., 2013, Overestimated global warming over the past 20 years. *Nature Climate Change*, 3, 767-769.

Gao, L., Hao, L., Chen, X.W., 2014, Evaluation of ERA-interim monthly temperature data over the Tibetan Plateau. *Journal of Mountain Science*, 11, 1154-1168.

Ghent, D., 2012, Land surface temperature validation and algorithm verification. *Report to European Space Agency*, 1-17.

Good, E.J., Ghent, D.J., Bulgin, C.E., Remedios, J.J., 2017, A spatio‐temporal analysis of the relationship between near‐surface air temperature and satellite land surface temperatures using 17 years of data from the ATSR series. *Journal of Geophysical Research: Atmospheres*.

Jin, M., Dickinson, R., Vogelmann, A., 1997, A comparison of CCM2–BATS skin temperature and surface-air temperature with satellite and surface observations. *Journal of Climate*, 10, 1505-1524.

Jin, M., Dickinson, R.E., 1999, Interpolation of surface radiative temperature measured from polar orbiting satellites to a diurnal cycle: 1. Without clouds. *Journal of Geophysical Research: Atmospheres*, 104, 2105-2116.

Karl, T.R., Hassol, S.J., Miller, C.D., Murray, W.L., 2006, Temperature trends in the lower atmosphere. steps for understanding and reconciling differences.

Li, Z.L., Tang, B.H., Wu, H., Ren, H.Z., Yan, G.J., Wan, Z.M., Trigo, I.F., Sobrino, J.A., 2013, Satellite-derived land surface temperature: Current status and perspectives. *Remote Sensing of Environment*, 131, 14-37.

Liu, X.D., Chen, B.D., 2000, Climatic warming in the Tibetan Plateau during recent decades. *International Journal of Climatology*, 20, 1729-1742.

Maussion, F., Scherer, D., Molg, T., Collier, E., Curio, J., Finkelnburg, R., 2014, Precipitation Seasonality and Variability over the Tibetan Plateau as Resolved by the High Asia Reanalysis. *Journal of Climate*, 27, 1910-1927.

Mears, C.A., Schabel, M.C., Wentz, F.J., 2003, A reanalysis of the MSU channel 2 tropospheric temperature record. *Journal of Climate*, 16, 3650-3664.

Oku, Y., Ishikawa, H., Haginoya, S., Ma, Y., 2006, Recent trends in land surface temperature on the Tibetan Plateau. *Journal of Climate*, 19, 2995-3003.

Ouyang, X., Chen, D., Duan, S.-B., Lei, Y., Dou, Y., Hu, G., 2017, Validation and Analysis of Long-Term AATSR Land Surface Temperature Product in the Heihe River Basin, China. *Remote Sensing*, 9, 152.

Qin, J., Yang, K., Liang, S.L., Guo, X.F., 2009, The altitudinal dependence of recent rapid warming over the Tibetan Plateau. *Climatic Change*, 97, 321-327.

Vinnikov, K.Y., Yu, Y.Y., Goldberg, M.D., Tarpley, D., Romanov, P., Laszlo, I., Chen, M., 2012, Angular anisotropy of satellite observations of land surface temperature. *Geophysical Research Letters*, 39.

Wang, X., Key, J.R., 2003, Recent trends in Arctic surface, cloud, and radiation properties from space. *Science*, 299, 1725-1728.

Westermann, S., Langer, M., Boike, J., 2012, Systematic bias of average winter-time land surface temperatures inferred from MODIS at a site on Svalbard, Norway. *Remote Sensing of Environment*, 118, 162-167.

Wu, T., Zhao, L., Li, R., Wang, Q., Xie, C., Pang, Q., 2013, Recent ground surface warming and its effects on permafrost on the central Qinghai‐Tibet Plateau. *International Journal of Climatology*, 33, 920-930.

Zhang, G.Q., Yao, T.D., Xie, H.J., Qin, J., Ye, Q.H., Dai, Y.F., Guo, R.F., 2014, Estimating surface temperature changes of lakes in the Tibetan Plateau using MODIS LST data. *Journal of Geophysical Research-Atmospheres*, 119, 8552-8567.

Production of 10-days fCover, FAPAR and LAI maps from Sentinel-3 OLCI data

H. Poilvé, C. Bruschini, A. Roumiguié, A. Jacquin, Th. Binant
Airbus Defence and Space
contact email address: herve.poilve@airbus.com

ABSTRACT   *The OLCI sensor of Sentinel-3 satellites is the successor of MERIS sensor aboard Envisat (2002-2012). Although primarily designed for Ocean applications, OLCI data are very valuable for global and regional Land applications, lands being systematically acquired in Full Resolution mode (300 m).*
During the geoland FP7 project, a production chain of Land biophysical parameters at 300 m from MERIS data was developed and demonstrated by producing a full year of 10-days fCover, FAPAR and LAI maps over Europe. Such products are input to regional Agriculture applications, like the service helping to insure farmers against pastures drought in France, developed with an Insurance company partner; this service is based on a Forage Production Index (FPI) computed from the full-year time series of the fCover maps. The loss of Envisat in 2012 led to use MODIS data as a back-up solution, plan being now to migrate back to the S3 OLCI data.
Integration of OLCI data started as soon as first S3 products were made available; specific features implemented to best process the OLCI data are described, the set of 21 VNIR spectral bands making it highly powerful to get robust biophysical information on vegetation.
Results of the qualification of S3 OLCI data for the FPI service are presented here. This consists in performing comparison of the fCover maps produced from OLCI and MODIS on a 10-days periods and checking the achieved consistency and precision between these 2 data sets, which is needed in order to make near-perfect continuity between MODIS-based historic data and the new Copernicus based service.

1 INTRODUCTION

1.1 Context

The OLCI sensor aboard the Sentinel-3 satellites is the successor of MERIS sensor of the Envisat mission (2002-2012). In the frame of geoland2 FP7 project and in preparation to Copernicus, a processing chain was developed to produce 300 m biophysical maps from MERIS Full Resolution (FR) data. It was initially demonstrated by providing a full year of fCover, FAPAR and LAI 10-days products over Europe. In 2012, the sudden loss of Envisat forced to switch to MODIS Level 1 data as a back-up solution; for that sake, multi-resolution techniques were applied to generate similar 300 m products from bundle MOD02 250 m and 500 m products.

1.2 Operational applications

Since 2012, the 10-days fCover maps produced by this processing line were used to develop the Forage Production Index (FPI) and the associated service (Roumiguié, 2015), the FPI being used as a reference index for insurance of farmers against grassland drought.
FPI has been validated at national level by an independent experts committee acting on behalf of French Ministry of Agriculture; it is now used by the main insurance companies in France. In order to build up the FPI from long-term history, the whole series of

MODIS and MERIS images were processed over France, since 2000 and 2003 respectively.

1.3 Copernicus and the Sentinel-3 constellation

With the start of Copernicus operational phase and the availability of OLCI products from the first S3 satellite since early 2017, objective is now to migrate this processing chain back to the OLCI data.
Although OLCI was primarily designed for Ocean applications, characteristics of the OLCI sensor (21 spectral bands in the VNIR domain, 300 m spatial resolution, 1270 km swath width, with bands perfectly registered and data precisely calibrated and geo-located) make this EO data source highly valuable for global and regional Land applications. Once completed the constellation of 3 Sentinel-3 satellites will provide a system with unrivalled performances.

2 PROCESSING METHODS AND TOOLS

2.1 Biophysical processing

In geoland2 project, the processing chain to produce 300 m vegetation maps from the MERIS data was based on Overland, a biophysical processing suite developed by Airbus and applicable to a wide range of optical sensors. Overland integrates widely proven core models, such as the SAIL/PROSPECT models for canopy reflectance and the LOWTRAN model for atmospheric transfer, and applies advanced techniques that inverse the coupled scene-atmosphere models.

This approach is especially efficient with rich spectral data such as the OLCI images, with allows pixel-wise correction of aerosols, water vapour column and of cloud veils when present in the scene. To cope with the large pixel size (300 m) which makes that the pixel often combines different landscape elements, a composite canopy model was specifically developed to simulate mosaic conditions of agricultural landscapes.

Main components of the used vegetation model are presented in Figure 1, and the overall process to generate the vegetation maps from the source TOA image is illustrated in Figure 2. Detailed description of the processing algorithms developed for these MERIS biophysical products is given in (Poilvé, 2010).
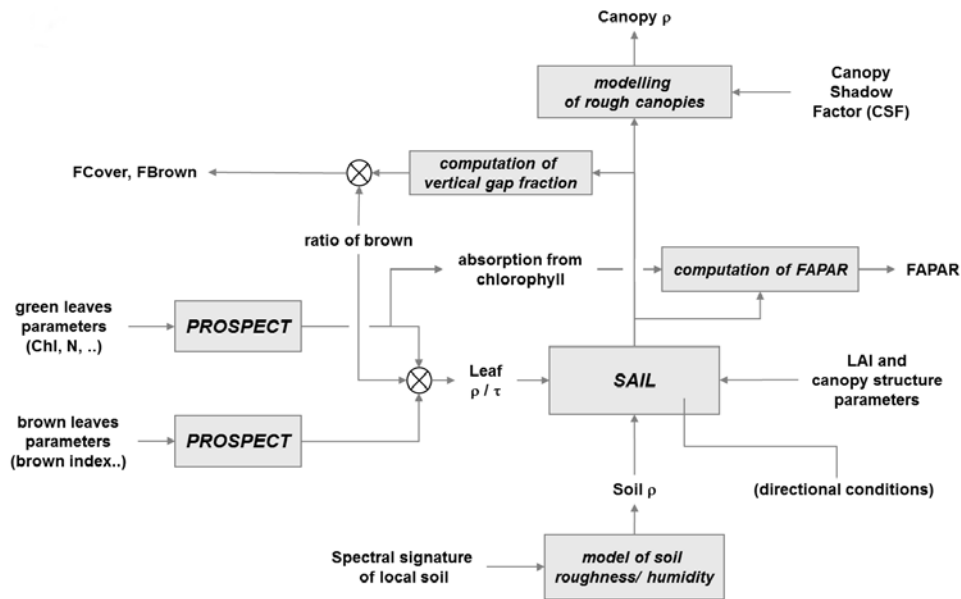
Figure 1 – Core vegetation models used in the S3 OLCI processing line to retrieve LAI, FAPAR, and fCover
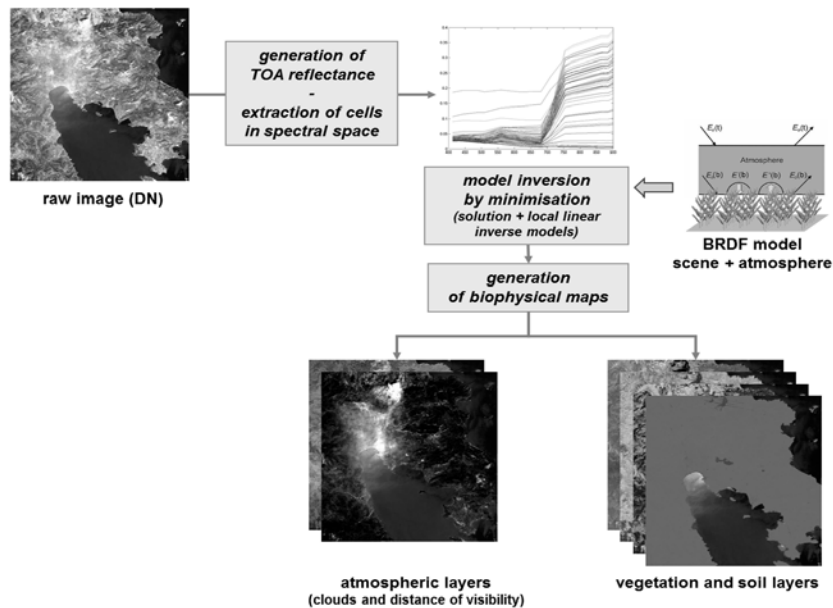
Figure 2 – Principle of biophysical processing from TOA reflectance to vegetation parameters maps by inversion of the coupled scene/atmosphere models
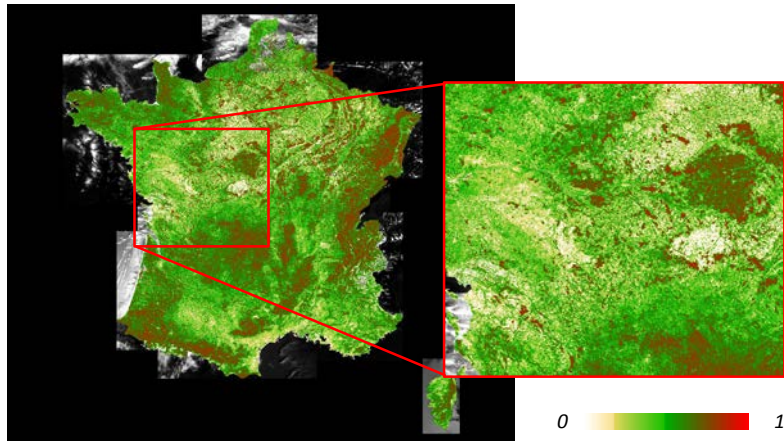
MODIS FAPAR 10-days map (01-10/07/2017)
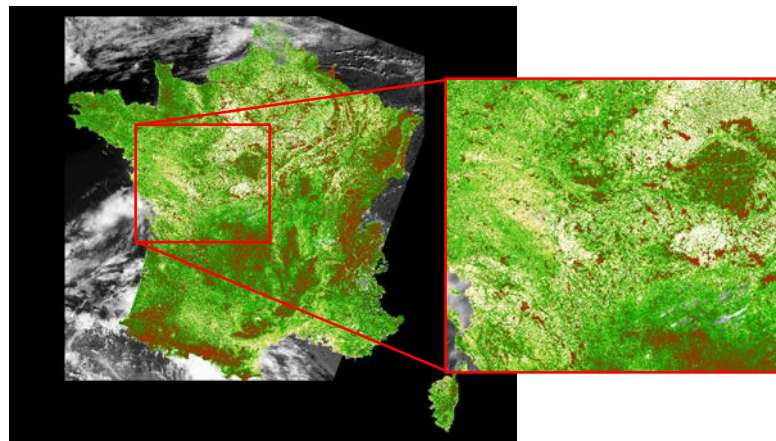
S3A FAPAR 10-days map (01-10/07/2017)

Figure 3 – Visual comparison of FAPAR 300 m maps produced from MODIS and S3 OLCI data for the same 10-days period

2.2 Processing line

The geoland2 MERIS/MODIS processing line was designed to routinely provide 10-days 300m vegetation maps over Europe and made fully automatic:

- it imports individual images, project them to LAEA projection and clip to target ROI (e.g. France or Europe) and merges images on same orbit pass when necessary
- then it performs automatic cloud masking and processes each image up to the biophysical level. This generates a whole set of maps, including fCover, FAPAR and LAI maps plus some more prospective parameters: fraction of non-photo-synthetic vegetation (fNPV), Canopy Shade Factor (CSF) and Chlorophyll maps.

- finally it applies an optimized compositing algorithm to generate the 10-days seamless products.

2.3 Integration of OLCI data

Integration of the OLCI data in the existing MERIS /MODIS chain was rather straight forward:

- The format of the OLCI products (using NetCDF) is convenient and fully descriptive; it includes precise pixel-wise geo-location (no more need of post-correction like the AMORGOS tool that was used for the MERIS data). Visual assessment of the consistency between OCLI and MODIS images (MODIS being projected with the MRTSwath tool) shows a correct co-registration, better than 1 pixel.
- all 21 bands of the OLCI data except band #01 (< 400 nm) are exploited by the Overland processor; band #13 (O2 absorption) is not used in the

225

reflectance model inversion but for estimating apparent O2 altitude/pressure through a dedicated processing. Thanks to the high quality of S3 radiometric calibration, a strong agreement was immediately found between model-based and OLCI measured reflectance

- tilt of the 5 OLCI cameras set (to stay clear of sun glint as recommended by the Ocean community) is not favourable to the Land applications. To avoid the too much degraded resolution of the extreme West camera, ultimately the image part acquired with viewing incidence beyond 40° will not be exploited here for target 300 m products, this will thus reduce usable swath to 900 km but will be soon compensated by the additional data from S3-B and S3-C data.

The full set of the 21 spectral bands enables to have a highly robust atmospheric correction and detection of clouds and cloud veils. Thanks to spectral richness we can even produce vegetation pigments maps (chlorophyll and secondary pigments) that can be interpreted as far as canopies are homogeneous enough at the size of OLCI pixel.

3 VALIDATION

3.1 Methods

Several 10-days periods of year 2017, with contrasted vegetation development conditions (i.e. post-winter, green peak of vegetation during spring, and summer) were selected for the first tests between OLCI and MODIS. 10-days consolidated fCover and FAPAR maps were produced from both sensors and compared, both visually to check spatial consistency, and by measuring the parameters RMS differences on values aggregated on 3km × 3km meshes (to minimize effects from residual mis-registration), this being performed on whole France (about 60 000 plotted values).

3.2 Results

High visual consistency was found between maps from the two sensors, as illustrated on Figure 3.
Quantitative analysis (illustrated in scatter plots of Figure 4) showed that RMS difference is close to the 3-5% performance objective.

4 CONCLUSION AND PERSPECTIVES

First validation results confirmed the high capabilities of OLCI data.
For the FPI service, objective is now to operate a progressive transfer to Sentinel-3 as a higher quality and a long-term secured data source, once having ensured seamless transition with the historical record that was produced from MODIS.
Another major evolution of the processing is the migration to a Cloud-based processing line, using

direct access to Sentinel-3 images on the Cloud infrastructures and a dockerized version of the core biophysical processor (Overland). This should be operational by year 2018.
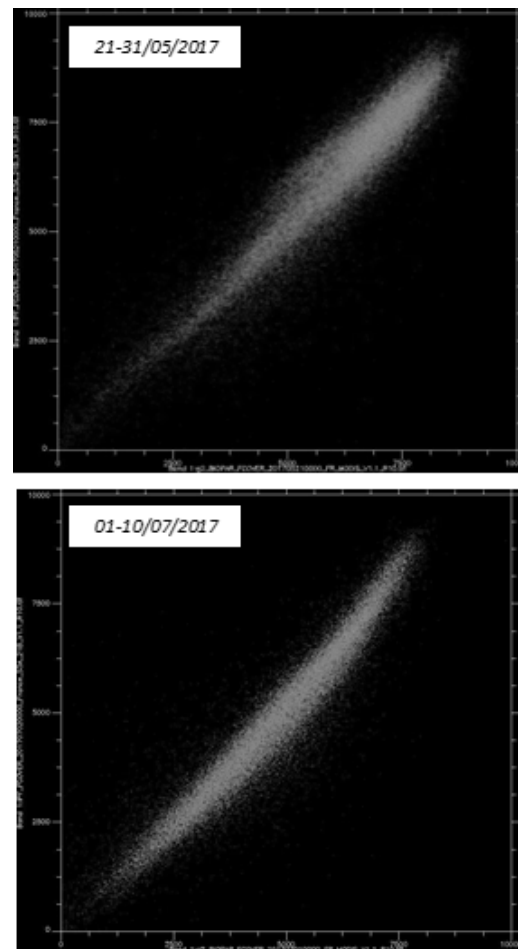
Figure 4 – Scatter plots comparing fCover values of MODIS (x-axis) and S3 (y-axis), extracted on 3 km ×3 km meshes for whole France from same 10-days periods; fCover range is 0-1 for both axes

5 REFERENCES

Poilvé, H., 2010: BioPar methods compendium of the MERIS FR biophysical products, *geoland2 FP7 project* (ref. FP-7-218795)

Roumiguié, A., Jacquin, A., Sigel, G., Poilvé, H., Hagolle, O. & Daydé, J. (2015). "Validation of a forage production index (FPI) derived from MODIS fCover time series using high-resolution satellite imagery: methodology, results and opportunities." *Remote Sensing*, 7-(9): 11525

Comparison of MODIS-derived Land Surface Temperatures with in situ Temperatures measured in the Hurd Peninsula, Livingston Island, Antarctica: *First results*

Carmen Recondo [1], Juanjo Peón [1], Enrique Pendás [2], Alejandro Corbea-Pérez [1,3], Miguel Ángel de Pablo [4], Miguel Ramos [5], Javier F. Calleja [3] and Susana Fernández [6]

[1]*Remote Sensing Applications (RSApps) Research Group. Area of Cartographic, Geodesic and Photogrammetric Engineering. Department of Mining Exploitation and Prospecting. University of Oviedo. Campus de Mieres. C/ Gonzalo Gutiérrez Quirós, s/n, 33600 Mieres, Asturias, Spain.*

[2]*AEMET-Galicia. C/ Canceliña 8, 15011 A Coruña, Galicia, Spain.*

[3]*RSApps Research Group. Department of Physics. University of Oviedo. Campus de Mieres. C/ Gonzalo Gutiérrez Quirós, s/n, 33600 Mieres, Asturias, Spain.*

[4]*Department of Geology, Geography and Environment. University of Alcalá. Campus Científico-Tecnológico. Ctra. A-II Km 33.6, 28871 Alcalá de Henares, Madrid, Spain.*

[5]*Physics and Mathematics Department. University of Alcalá. Campus Científico-Tecnológico. Ctra. A-II Km 33.6, 28871 Alcalá de Henares, Madrid, Spain.*

[6]*GIS-Forest Research Group. Department of Geology. University of Oviedo. Campus de Oviedo (Llamaquique). C/ Jesús Arias de Velasco s/n, 33005 Oviedo, Asturias, Spain.*

Emails: mdrecondo@uniovi.es, juanjopeon@gmail.com, enrique@pendas.es, alejandrocorbea@gmail.com, miguelangel.depablo@uah.es, miguel.ramos@uah.es, jfcalleja@uniovi.es, fernandezmsusana@uniovi.es

In the framework of the PERMASNOW project, we are comparing MODIS-LST data (1 km of spatial resolution) with in situ temperatures obtained at the AEMET meteorological stations, and our team's stations in the Hurd Peninsula, Livingston Island (Antarctica). This article shows the first results obtained for T_a at the AEMET stations: Juan Carlos I (JCI), Johnson Glacier (JG) and Hurd Glacier (HG) in the period between March-2000/July-2002 and February-2016. The daily LST data were compared with the daily mean values of T_a. A slightly decreasing linear trend of T_a in the studied period was confirmed. LST data only exist in cloud-free days (~1/3 of the studied days), but the main problem is the quality of these data: those with no "good quality" usually underestimate LST and are not reliable. The daily MODIS-albedo product (500m) was also used for eliminating the data with "other quality" and "cloud", besides of classifying the cover. Filtering reduced the LST data at JCI and JG (<10% of the studied days), and eliminated all in HG. A simple linear fit did not explain well the relationship T_a-LST ($R^2 \leq 0.4$), appealing to multiple linear regressions to take into account the annual/seasonal variations in this relationship. Thus, R^2 went up to 0.4-0.6, being better at JCI ($R^2 = 0.6$ and RSE~2°C). It is concluded that the MODIS-LST data are useful for estimating long-term trends in T_a at a global level in the Livingston Island. Improving the quality of the LST data in this type of cold environments is essential.

1 INTRODUCTION

Antarctic Peninsula (AP) climatic variability is extremely complex both at a spatial and temporal scale. Turner et al. (2005) showed that AP suffered a strong warming between 1950 and 2000, obtaining the maximum increase of T_a at the Faraday/ Vernadsky station (at the south of the western AP; +0.56 °C decade[-1]). This warming extended, but decreasing, from Faraday to the South Shetland Islands (SSI) (+0.35 °C decade[-1] at the Bellingshausen station, at the King George Island). Steig et al. (2009) used T_a measurements from stations but also NOAA-AVHRR Land Surface Temperature (LST) data for concluding that both types of data showed similar results: a West Antarctic's warming that exceeded 0.1°C decade[-1] between 1957 and 2006. O'Donnell et al. (2011) found that the warming in the same period was more concentrated in the AP ($\approx$ +0.35 °C decade[-1]) than in the West Antarctic. However, recent studies show that the T_a temporal trend at the AP has changed, and that

the most of the stations have suffered a cooling during the first decades of this century. Turner et al. (2016) observed that the change of trend in the northern AP started between 1998 and 1999, obtaining a cooling of −0.47 ℃ decade[-1] in the period 1999-2014. Oliva et al. (2017) studied the T_a trends from ten stations distributed across the AP in the period 1950-2015, obtaining that the cooling initiated in 1998/1999 was more significant in the N and NE of the AP and the SSI (>0.5 °C between the two last decades), and absent in the SW of the AP.

The T_a variations (and those in the permafrost or frozen ground, snow cover, etc.) in and around the AP must follow being monitored for understanding the occurred changes and prevent the future ones. For the monitoring, both *in situ* data and data from satellites are necessary, because both have advantages and disadvantages. Under this perspective, we work in the PERMASNOW research project (de Pablo et al., 2016) in the Livingston and Deception Islands, where the team of the University of Alcalá have been working since 1991, and in particular after 2006, with the inclusion of several stations that belong to the International Permafrost Association (IPA) networks. These islands belong to the SSI, archipelago at 120 km of the western side of the AP. The team works on and around the Spanish Antarctic Stations (SAS) Juan Carlos I (in the Hurd Peninsula on Livingston) and Gabriel de Castilla (in Deception). In particular, the monitoring sites in Livingston are in the Hurd and Byers Peninsulas. In all these areas, there are also Spanish meteorological stations of *Agencia Estatal de Meteorología* (AEMET, meaning State Meteorological Agency in English). In the PERMASNOW project (between 2015 and 2019) new *in situ* data will be analysed, but also radar (as in Mora et al., 2017), optical, and thermal data. This article focuses on the thermal data and, in particular, we will use MODIS-LST data, available since 2000/2002. Our team measures T_a and soil temperature in our stations, whereas the AEMET´s Antarctic stations (Bañón y Vasallo, 2015) only have T_a. This work only shows the first results related to the comparison between the AEMET T_a and the MODIS-LST data.

There are few studies in which a comparison between T_a and MODIS-LST data in polar areas is performed, especially in the Antarctica. The majority of these studies found correlation between both temperatures, although it is variable depending on the stations. For example, in the East Antarctica, Wang et al. (2013) found a stronger correlation in the East stations (R^2=0.83-0.98) than in the West stations (R^2=0.41-0.83). They used diurnal and nocturnal Terra images, observing that the R^2 values were similar for both type of images. They obtained errors between SD=1.3-8.5℃, with LST< T_a. At our best knowledge,

studies of comparison between T_a and MODIS-LST data have not been done in the SSI, hence the interest of this work. No MODIS-LST data exists in the Deception Island, neither in the Byers Peninsula, so that our comparison will be restricted to the Hurd Peninsula of the Livingston Island.

The aim of this work is to obtain algorithms that allow the estimation of T_a from MODIS-LST data in cold environments, as it has been possible in warner areas, for example, in Spain (Recondo et al., 2013; Peón et al., 2014). It would allow to obtain T_a in the whole of the Livingston Island, or even in other nearby islands, and to perform T_a temporal maps at 1 km of spatial resolution. Other objective is to study in detail the utility and limitations of the MODIS-LST data in so cold areas, to learn how future sensors can be improved.

2 STUDY AREA

Our study area is the Hurd Peninsula of the Livingston Island, one of the areas where we work in the PERMASNOW project (Figure 1; area D).
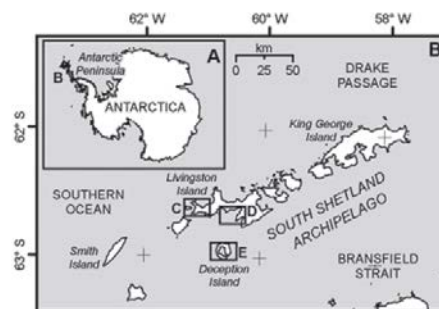
Figure 1. PERMASNOW project´s study areas: Byers (Area C) and Hurd (Area D) Peninsulas, Livingston Island, and Deception Island (Area E). The image is courtesy of de Pablo et al. (2016).

3 DATA

The T_a data used in this work were those obtained in the AEMET stations in the Hurd Peninsula of the Livingston Island: Juan Carlos I (JCI), Johnson Glacier (JG) and Hurd Glacier (HG), in the period between January of 2000 and February of 2016. The JCI station is the oldest, with data since 1988. The JG station was located in the Johnson Glacier more than eight years ago, being after moved to the Hurd lobule and called since then HG station. The geographical coordinates, altitude and dates of operability of each station are shown in Table 1. The T_a data are collected in JCI each 10 minutes (10[m]) along all the year, whereas those from JG and HG are obtained every 10[m] in the Antarctic summer (December-February) and every half an hour (0.5[h]) the rest of the year.

Table 1: Name, location, height about sea level (h) and dates of operability of the AEMET stations used in this study.

AEMET station	Latitude	Longitude	h (m)	Dates of operability
Juan Carlos I (JCI)	62°39′47′′S	60°23′16′′W	12	16/02/1988 31/12/2009
	62°39′48′′S	60°23′19′′W	13	31/12/2009 Actually
Johnson Glacier (JG)	62°40′16′′S	60°21′51′′W	178	01/12/2006 24/01/2015
Hurd Glacier (HG)	62°41′48′′S	60°24′44′′W	93	25/01/2015 Actually

T_a is measured in these AEMET stations at two different heights over the ground, 1.8 m and 20 cm. In order to avoid confusion, along this article the first temperature will be called simply T_a (because it is the most usual at the meteorological stations) and the second one, T_s (because it was measured close to the soil).

The MODIS data used were the daily MODIS-LST data (1 km of spatial resolution) from Terra and Aqua (MOD11 and MYD11 standard products, respectively; version 5), and both diurnal and nocturnal data. The quality control (QC) assessments of these data were also collected. These LST data were available in our study area since 5 March 2000 for Terra and since 8 July 2002 for Aqua. The daily MODIS-snow albedo data (MOD10/MYD10 products; 500 m of spatial resolution) were also used and its quality assessment (QA) data as well. These products include a classification of the cover type for each pixel, allowing the distinction among snow, land (no snow), water and cloud. This information has been used to improve the discrimination of the clouds (500 m is better resolution than 1 km) and to test if the cover has influence on the results.

The T_a-LST comparison was done until 21 February 2016, when the Spanish Antarctic summer campaign 2015/2016 finished. Thus, we have compared 16/14 years of T_a and MODIS-LST data.

4 METHODOLOGY

The daily mean T_a (and T_s) was performed using the data from each station only if all the daily data were taken (n=144 for the 10^m data, and n=48 for the 0.5^h data). The MODIS data were extracted in the location of each AEMET station using the Application Programming Interface (API) of Google Earth Engine (http://earthengine.google.org). The statistical analyses and most of the graphics were constructed using the free software R (http://www.r-project.org/). Most of the analyses were based on linear regressions (simple or multiple). In all cases, we used robust regressions, with the MASS library in R. The parameters used for

quantify the goodness of the models were the coefficient of determination (R^2) and the residual standard error (RSE). The models have not been validated yet.

5 RESULTS

5.1 Comparison between the AEMET air temperatures

The comparison between T_a (air temperature measured at 1.8 m over the ground) and T_s (air temperature measured at 20 cm over the ground, i.e., T measured near the soil) has been made to prove that they are correlated, as expected, and to decide which is better for the comparison with the MODIS-LST data. The comparison showed that both have a similar behaviour of sinusoidal type, varying both in phase and with similar amplitude (see example for JCI in Figure 2).
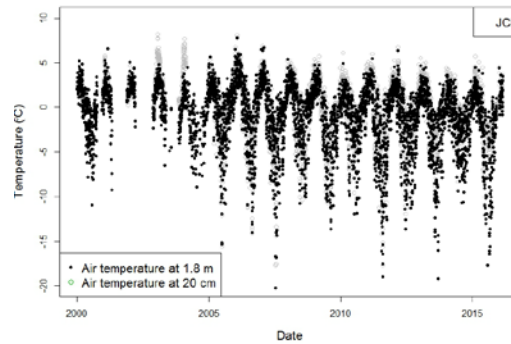
Figure 2: Daily mean T_a and T_s temporal variation for the study period in JCI station.

T_a and T_s also show a slightly decreasing linear trend along the studied period in most of the stations (see example for T_a in Table 2). This confirms the decreasing trend observed by our team in previous projects, and the general trend of cooling observed since 1998/1999 in the northern AP and the SSI by Turner et al. (2016) and Oliva et al. (2017).

Table 2: ΔT_a for the study period in the AEMET stations.

Station	Time period	T_{ini}, T_{fin}, ΔT_a (°C)
JCI	01-Jan-2000/ 21-Feb-2016	-0.03, -1.63, -1.60
JG	01-Dec-2006/ 24-Jan-2015	-2.37, -2.37, 0.0
HG	25-Jan-2015/ 15-Feb-2016	-0.32, -2.00, -1.68

T_a and T_s are strongly correlated (R^2=0.80 for JCI and HG, and R^2=0.66 for JG), with a linear slope (α) ~1 and RSE ~1°C in all the stations (see example for JCI in Figure 3). However, it is clear of Figure 3 that

the difference between both temperatures exceeds up to 10 °C some days. In these days, the sensor at 20 cm is probably covered of snow, maintaining T_s stable whereas T_a varies. These T_s data should be eliminated because they are not reliable (Bañón, private communication). Thus, for the purpose of our work, we will use T_a in the comparison with MODIS-LST.
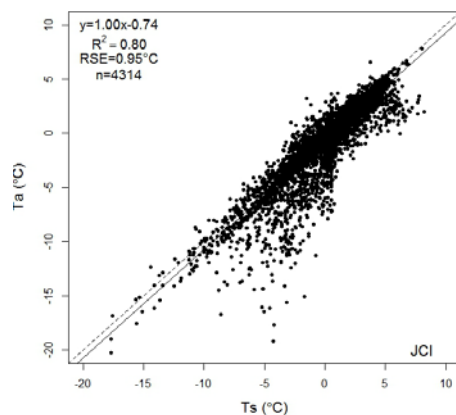
Figure 3: Linear regression between daily mean T_a and T_s in JCI in the period 1 January 2000 and 21 February 2016.

5.2 Comparison between T_a and LST

The availability of MODIS-LST data in the study area is limited, due to the frequent cloud coverage. Thus, there are only LST data in a 24-35%, 18-28% and 3-13% of the studied days in JCI, JG and HG, respectively (being the lower values for the nocturnal data). However, the main problem is the quality (QC) of these data, because those of lower quality according to Wan (2006) give LST<< T_a and should be eliminated. Therefore, only the LST data with "*good quality*" are reliable and they were the selected ones. Besides, the quality (QA) and the classification of the product MODIS-snow_albedo help us to filter the data with "*other quality*" and "*cloud*". Regarding the data classified as "*snow-covered land*", "*snow-free land*" and "*open water*" (melted snow in our case), they were taken jointed in the analyses because their relationship T_a-LST was found similar. All the applied filters (especially the one concerning to the quality of the LST data) significantly reduces the number of data consider as "*good*" in JCI and JG (at a 3-8% and 4% of the studied days, respectively) and eliminated all of them in HG.

A simple linear regression using the "*good*" data is not enough to explain the relationship T_a-LST ($R^2 \le 0.4$) (see example for JCI and diurnal Terra-MODIS data in Figure 4).
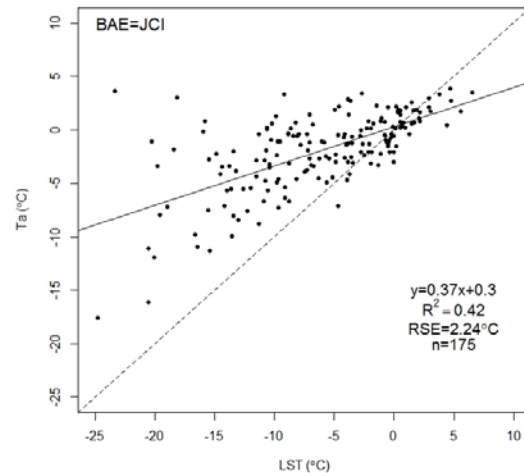
Figure 4. T_a versus "*good*" LST (Terra/Day) data in JCI.

Then, we used multiple linear regressions to take into account the annual and seasonal variations in the relationship T_a-LST. So, our first models for estimating T_a include, besides LST, the time (t) as a linear trend, and with two harmonics. Thus, R^2 goes up to 0.4-0.6, with RSE=2-3°C. The fits are better for JCI (R^2=0.5-0.6, RSE=2.1-2.3 °C, n=125-355) than for JG R^2=0.4-0.5, RSE=1.7-2.7 °C, n=53-55). There are hardly differences in terms of R^2 and RSE between the Terra and Aqua data, and between the diurnal and the nocturnal data, especially for JCI.

6 CONCLUSIONS

A moderate correlation (R^2=0.4-0.6 and RSE=2-3 °C) was found between the daily mean T_a and the LST from MODIS in the Hurd Peninsula of the Livingston Island between 2000 and 2016. Similar results were found in other areas within Antarctica West. Better results were obtained for JCI (R^2=0.6 and RSE~2 °C) than for JG.

Multiple linear regressions (MLR) work better than simple linear regressions (SLR), taking account annual and seasonal variations in the relationship T_a-LST.

The lack of LST data due to cloudiness is an important limitation, but more so the fact that most of the available data are not of good quality, which should be improved.

Even so, adequate LST data can be used to estimate long-term trends and to map globally Livingston Island.

8 REFERENCES

Bañón, M., and Vasallo, F., 2015, AEMET en la Antártida: Climatología y meteorología sinóptica en las estaciones meteorológicas españolas en la Antártida. *AEMET,* Madrid, 152 pp. ISBN: 978-84-7837-093-1.

de Pablo, M.A., et al., 2016, Frozen ground and snow cover monitoring in the South Shetland Islands, Antarctica: Instrumentation, effects on ground thermal behaviour and future research. *Cuadernos de Investigación Geográfica,* 42:2, 475-495.

Mora, C., Jiménez, J. J., Pina, P., Catalao, J., and Vieira, G., 2017, Evaluation of single-band snow-patch mapping using high-resolution microwave remote sensing: an application in the maritime Antarctic. *The Cryosphere*, 11,139-155.

O'Donnell, R.., Lewis, N., McIntyre, S., and Condon, J., 2011. Improved methods for PCA–based reconstructions: case study using the Steig et al. (2009) Antarctic temperature reconstruction. *Journal of Climate*, 24(8), 2099-2115.

Oliva, M., et al., 2017, Recent regional climate cooling on the Antarctic Peninsula and associated impacts on the cryosphere. *Science of the Total Environment*, 580, 210-223.

Peón, J., Recondo, C., and Calleja, J. F., 2014, Improvements in the estimation of daily minimum air temperature in peninsular Spain using MODIS land surface temperature. *International Journal of Remote Sensing*, 35:13, 5148-5166.

Recondo, C., et al., 2013, Empirical models for estimating daily surface water vapour pressure, air temperature, and humidity using MODIS and spatiotemporal variables. Applications to peninsular Spain. *International Journal of Remote Sensing*, 34:22, 8051-8080.

Steig, E. J., et al., 2009, Warming of the Antarctic ice-sheet surface since the 1957 International Geophysical Year. *Nature*, 457, 459-463.

Turner, J., et al., 2005, Antarctic climate change during the last 50 years. *International Journal of Climatology*, 25, 279-294.

Turner, J., et al., 2016, Absence of 21st century warming on Antarctic Peninsula consistent with natural variability. *Nature*, 535:7612, 411-415.

Wan, Z., 2006, Collection-5. MODIS Land Surface Temperature Products Users' Guide, Sep 2006. http://www.icess.ucsb.edu/modis/LstUsrGuide/MODIS_LST_products_Users_guide_C5.pdf

Wang, Y., et al., 2013, A comparison of MODIS LST retrievals with in situ observations from AWS over the Lambert Glacier Basin, East Antarctica. International Journal of Geosciences, 4, 611–617.

SALVAL: Surface ALbedo VALidation tool

L. de la Madrid [(1)] , **J. Sánchez-Zapero**[(1)], **F. Camacho** [(1)]

[(1)] *EOLAB, Spain*

lorena.delamadrid@eolab.es   jorge.sanchez@eolab.es   fernando.camacho@eolab.es

ABSTRACT- In this paper SALVAL (Surface ALbedo VALidation) tool is introduced. It allows the validation of global albedo products derived from satellite in accordance with the international validation standards. It is a Matlab-based Graphical User Interface (GUI) with the following main objectives: (i) to provide transparency and traceability to the validation process ;(ii) to integrate the different validation metrics into a tool in which the user can analyze the different validation criteria; (iii) to provide consistency in evaluating comparatively the new versions and new products; (iv) and finally, to provide a tool to achieve Committee for Earth Observation Satellites (CEOS) Land Product Validation (LPV) level 4 of validation. The different quality criteria will be assessed over a representative global network of homogeneous sites coming from a database of global reference sites to support validation of satellite surface albedo (Loew et al., 2016), desert calibration sites and additional sites to complete under sampled areas and biome types (LANDVAL network). The accuracy of the satellite products is assessed by direct comparison with ground measurements.

1 INTRODUCTION

The land surface albedo is defined as the fraction of incident solar irradiance reflected by Earth's surface over the whole solar spectrum (Dickinson, 1983); moreover, it is one of the terrestrial essential climate variables (ECV) introduced by the Global Climate Observing System (GCOS).

It is a potential variable in the control of climatology, as well as a sensitive indicator to the degradation of the environment, which makes that many space agencies, such as ESA, NASA, NOAA, and earth observation programs (e.g. Copernicus or LSA SAF) are interested in monitoring albedo derived from several sensors including VEGETATION/SPOT, MODIS/TERRA+AQUA, VEGETATION/PROBA-V, and many others.

Satellite products need to be evaluated and their uncertainties have to be well characterized for a proper exploitation. Thus, the products need to be validated to ensure that they meet user requirements on accuracy and stability (e.g. GCOS-154, 2016). Validation for the land product domain is defined as " the process of evaluating by independent means the accuracy of satellite-derived land products and quantifying their uncertainties by analytical comparison with reference data " (Justice et al, 2000).

The work described in this paper, is framed under the context of Copernicus Climate Change Service (C3S) and Copernicus Global Land Service (CGLS). The objective of this work is to develop a tool (SALVAL), that allows the validation of Albedo products derived from satellite data in accordance with the international validation standards CEOS-LPV and Quality Assurance for Earth observation (QA4EO). The aims of SALVAL are:

- To provide transparency and traceability to the validation process.
- To integrate the different validation metrics, allowing the user to analyze the different validation criteria as well as the requirement assessment in order to verify whether the results fit for purpose.
- To provide consistency when comparing either new versions or new albedo products.
- To provide a tool able to achieve CEOS LPV level 4 validation that defines an operational component to ensure that land product time-series are systematically validated (Nightingale et al, 2011).

2 FUNCTIONALITIES

SALVAL has three main functionalities implemented: (i) to configure the validation exercise by selecting a set of the given products, user's requirements, spectral region, spatial domain as well as temporal domain; (ii) run a validation exercise according to the previously set configuration; and (iii) the ability to import either a new product dataset or a new ground reference data in order to be included within the tool.
Figure 1 shows a diagram of SALVAL as a conceptual view.
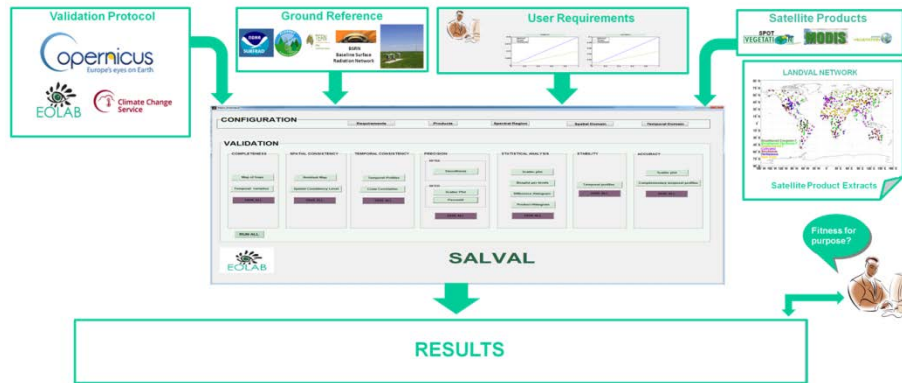
Figure 1. Conceptual view of SALVAL

2.1 Configuration of the validation exercise

The validation exercise has many parameters to be configured in order to allow a customized validation exercise according to the user.

SALVAL allows the configuration of the user requirements (accuracy and stability) within three different levels: optimal, target and threshold in order to verify whether the results fit for purpose. Default user requirements are set according to the Global Climate Observing System specifications (GCOS-154, 2016) as an optimal level, and a Key Performance Indicator (KPI) defined by the C3S as a target level as shown Figure 2 and Table 1. However, those requirements are not fixed values since the user is able to modify and/or add a new one. On the other hand, the user is able to select the reference products as well as the product under evaluation. In addition, the tool allows to select the spectral region, time period and the spatial domain.

	Stability	**Accuracy**
Optimal	Max(1%,0.001)	Max(5%,0.0025)
Target	Max(2%,0.002)	Max(10%,0.01)

Table 1. Stability and accuracy default values in regard to optimal and target levels.
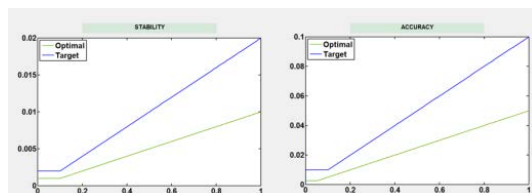
Figure 2. Default stability and accuracy requirements within SALVAL tool as a function of albedo values (x axis) according to values in Table 1.

2.2 Run validation

The validation exercise is performed over LANDVAL, a network of sites design by EOLAB. In order to identify potential reference sites, 2186 sites coming from SAVS 1.0 network (Loew et al., 2016) were analyzed, and besides, additional sites were included to complete under sampled areas and biome types. Several selection criteria were applied in terms of land cover and topography homogeneity and sites located over latitudes higher than 80ºN and 60ºS were dismissed due to the lower percentage of land pixels over those latitudes. As a result, an amount of 725 sites is achieved with a good representativeness per biome as shown in Figure 3.
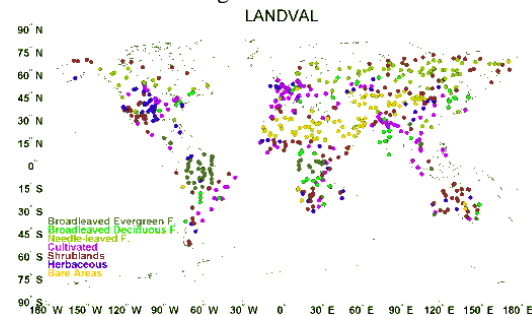
Figure 3. LANDVAL site locations map aggregated into 7 main biomes.

On the other hand, the products may not be spatially and/or temporal consistent which leads to the necessity of homogenize the data accomplishing a spatial and/or temporal support that is described in Table 2.

Once the configuration of the validation exercise has been applied, the user could run the validation over LANDVAL sites into two different ways:

Standard validation: All parameters for all the results are assessed with default values.

Custom validation: Several parameters such as graphical values, file name, file format (.png, .tiff, .jpeg) could be customized.
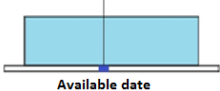
Spatial/ temporal consistency	
Spatial support	Spatial resolution: 3x3 pixels (1km) The median value of the valid pixels over the central 3x3 pixels window is computed if at least 6 out of the 9 pixels are valid.
	Projection: Plate Carrée
Temporal support	Temporal window: centered **Available date**
	Pair-wise comparison: The closest date to the product to be evaluated.
	Independent evaluation of the product: The original temporal frequency

Table 2. Spatial and temporal support applied within SALVAL.

2.3 Importing new data

Two different data types can be imported within the tool: new satellite land products to be validated or to be used as reference products and new ground data references used for accuracy and stability assessment.

Import new product: It allows to evaluate the performance of new products as compared with existing ones in the system. The extracts must be over LANDVAL in binary format with the spatial support described in Table 2. In addition, product parameters such as temporal resolution, temporal frequency and product name are requested.

Add new ground data reference: The tool described in this paper includes ground reference data for accuracy assessment, and besides, it allows to add new ground data reference in .txt format.

2.4 Maintenance service

SALVAL is under supervision in order to provide a maintenance service enabling to improve the validation process through updating some functionalities and enhancing the metrics already used.

3 ILLUSTRATION OF SALVAL FUNCTIONALITIES

This section shows some of the main results of SALVAL tool applied to three available albedo products: MODIS C5 (MCD43A3), PROBA-V (PROBAV_TDS_V1.5) and SPOT VGT (SPOTVGT_V1). The temporal and spatial characteristics for each product is shown in Table 3:

Product	Temp. Freq.	Temp. Resol.	Period	Spat. Resol.
MODIS C5	8 days	16 days	2013-2014	1 km
PROBA-V	10 days	30 days	Dec2013-2014	1km
SPOT-VGT	10 days	30 days	2013-May2014	1 km

Table 3. Temporal and spatial characteristics of the products considered for the validation in order to illustrate the functionalities of the tool.

3.1 The Validation Exercise

Table 4 shows all metrics included within SALVAL. In this section, only few of them are shown for the sake of shortness.

Validation Criteria		Metrics
Completeness		- Map of gaps - Length of gaps (histogram + temporal variation)
Spatial consistency		- Residual map - Consistency spatial level
Temporal consistency		- Cross correlation (histogram) - Temporal profiles
Precision	Intra	- Smoothness (histogram)
	Inter	- Median absolute anomaly (95%, 5% percentiles) - Scatter plot (calibration sites)
Overall analysis		- Difference histogram - Product histogram - Scatter plot - Box plot per bin (bias RMSD)
Stability		- Slope of bias
Accuracy		- Scatter plot (ground data reference)

Table 4 Validation criteria defined within the validation protocol

❖ Completeness

Completeness is assessed as the fraction of gaps as well as their spatial distribution, which is represented as a map of gaps (Figure 4) . In addition, in order to provide temporal information the length of gaps along the selected period is assessed (Figure 5).
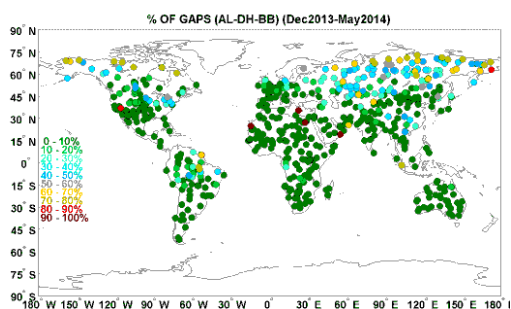
Figure 4. Percentage of gaps during December,2013 and May,2014 for PROBAV_TDS_V1.5 (AL-DH-BB) over LANDVAL.
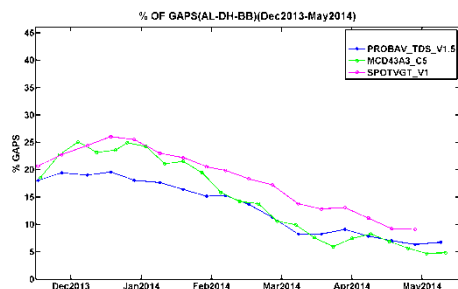
Figure 5. Temporal evolution of the percentage of gaps during December,2013 and May,2014 for PROBAV_TDS_V1.5 (AL-DH-BB) over LANDVAL.

❖ Spatial consistency

Spatial consistency refers to the realism and repeatability of the spatial distribution of retrievals over LANDVAL.

This analysis is assessed by residual maps between two different products. In addition, the percentage of residual values within the accuracy requirements defined by the user is quantified (Fig. 6) .
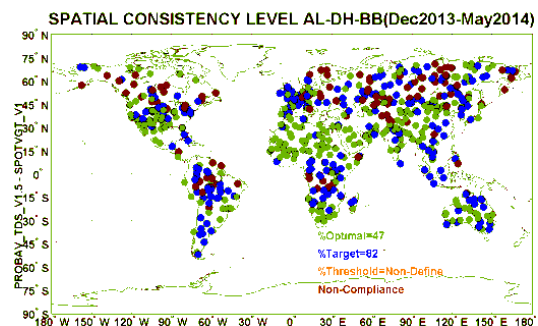
Figure 6. Percentage of values within the optimal and target requirement , during December, 2013 and May, 2014 for the residual values between PROBAV_TDS_V1.5 (AL-DH-BB) and SPOTVGT_V1(AL-DH-BB) over LANDVAL.

❖ Temporal consistency

Temporal variations over the whole LANDVAL network can be qualitatively assessed in order to evaluate the temporal trend of the products. Figure 7 shows one example of temporal profile, on which the user can analyze temporal response of the products against rapid changes in albedo values and under stable temporal situations.
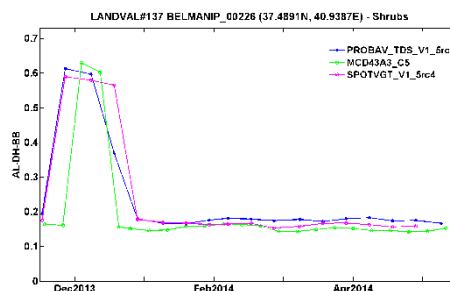
Figure 7. Temporal profile during December,2013 and May,2014 for PROBAV_TDS_V1_5rc9 (AL-DH-BB) over a BELMANIP site (37.4891N, 40.9387E).

❖ Intra annual precision

The smoothness used as intra annual precision measurement corresponds to temporal noise assumed to have no serial correlation within a season (Figure 8). In this case, the anomaly of a product value from the linear estimate based on its neighbours can be used as an indication of intra-annual precision (delta function). It can be characterized as suggested by (Weiss et al., 2007).
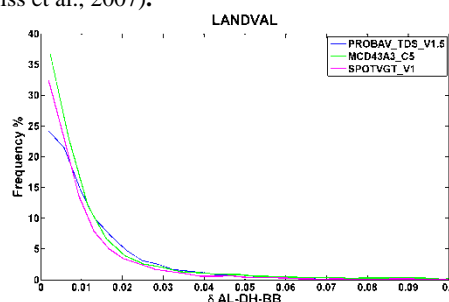
Figure 8. Smoothness (histograms of delta function), during December, 2013 and May, 2014 for PROBAV_TDS_V1.5 (AL-DH-BB) over LANDVAL.

❖ Inter annual precision

Inter-annual precision aims to measure the error between two different years of stable observations. Figure 9 shows a box plot graph for the absolute anomaly (percentiles 95% and 5% has been used) per bin between two different years, suggested as inter annual precision for another land products (Fernandes et al., 2014).
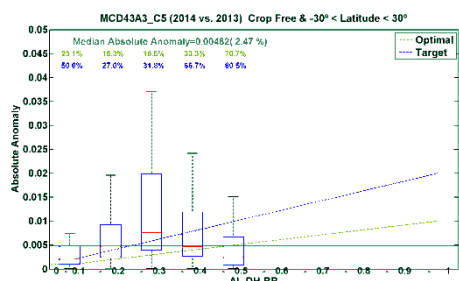
Figure 9. Median absolute anomaly per bin between 2014 and 2015 excluding data above 30º latitudes and below -30º latitudes as well as crop, including percentage of values within the optimal and target requirement.

❖ Overall analysis

Overall analysis lies in the inter-comparison between products in order to estimate the discrepancies between those products, as shown in Figure 10 and 11. To allow pair-wise comparison , the same temporal and spatial resolution has to be used.
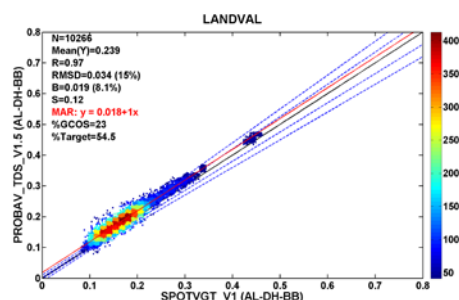
Figure 10. Scatter plot between PROBA_TDS_V1.5 and SPOTVGT_V1 over LANDVAL
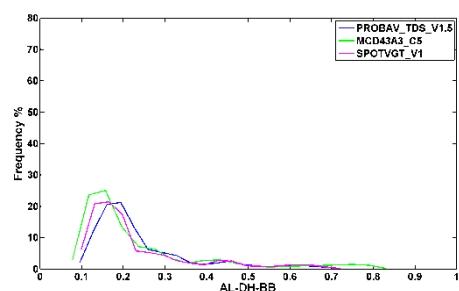
Figure 11. Product histograms

❖ Stability

The temporal stability of satellite data records is a key requirement for their applicability for climate change studies. It is defined as the property of a measuring instrument or data set to provide consistent measurements of a geophysical variable which is

known to remain constant over time (JCGM, 2012). In this case of study, Desert Rock site which belong to SURFace RADiation network (SURFRAD), is used as stable reference measurement. The slope of the bias is used as estimator for the stability since the reference measurement show changes on timescales as shown in Figure 12:
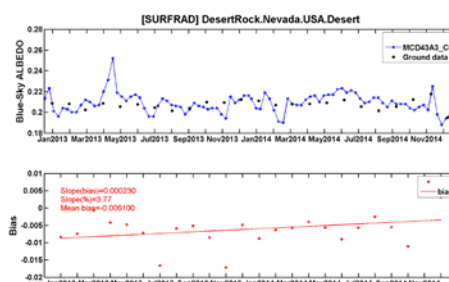
Figure 12. Temporal profile during 2013 and 2014 for MCD43A3_C5 (Blue-Sky albedo: See Ec.1) vs. Ground data retrieval over Desert Rock site (SURFRAD) as well as the bias temporal profile, including the bias slope as a temporal stability measurement.

❖ Accuracy

Accuracy is quantified by several metrics reporting the goodness of fit between the products and the corresponding ground measurements as shown Figure 13.

On the other hand, SALVAL provides the functionality to make ground data reference and satellite product data consistent. This functionality is bases on the following formula:

Surface Albedo = D*AL-BH + (1-D) *AL-DH   (1)

where D corresponds to the ground data reference diffuse value adjust to the satellite product temporal support; AL-BH is the broad band white-sky albedo and AL-DH is the broad band black-sky albedo for satellite data.
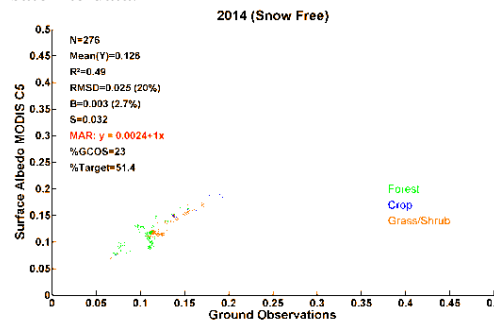
Figure 13 Scatter plot between ground observations and Surface albedo (MCD43A3_C5) during 2014

236

4 CONCLUSIONS

In this paper, SALVAL has been propounded as a graphical user interface that allows to provide transparency and traceability to the validation process.

SALVAL allows the configuration of user requirements (accuracy and stability) as well as to verify whether the results fit for purpose. In addition, it allows to evaluate new products in a robust and interactive way, since the user can define in addition to the requirements, the geographical area (global or continental) and the temporal domain.

SALVAL allows the validation results to be updated periodically after a temporary extension of the product and the reference data, allowing the maximum level of validation (Level 4) to be reached in the CEOS LPV hierarchy, a level not yet reached in albedo products (CEOS). SALVAL has the potential to extend to other satellite products such as surface reflectivity (TOC-R), or biophysical vegetation products (LAI, FAPAR). Finally, it presents a structure by modules for each metric in order to facilitate the incorporation of new metrics for the validation exercise, promoting a continuous updating of both the tool and the validation criteria given that there is no defined methodology of good practices as if it were for LAI (Fernandes, et al. 2014).

5 REFERENCES

CEOS Working group on calibration and validation: Validation hierarchy, https://lpvs.gsfc.nasa.gov/

Dickinson, R.E., 1983. Land surface processes and climate-surface albedo and energy balance. Advance in Geophysics, 25, 305-353

Fernandes, R., Plummer, S., and Nightingale, J., 2014 , Global leaf area index product validation good practices.

GCOS-154, 2016. Systematic Observation Requirements for Satellite-based Products for Climate Supplemental details to the satellite-based component of the Implementation Plan for the Global Observing System for Climate in Support of the UNFCCC - 2016 Update, WMO, Geneva, Switzerland.

Joint Committee for Guides in Metrology (JCGM), 2012. International vocabulary of metrology—Basic and general concepts and associated terms, BIPM, Sèvres, France

Justice, C.O.; Starr, D.; Wickland, D.; and Privette, J.; 1998, Suttles, T.EOS land validation coordination: An update. Earth Observ., 10,55-60.

Loew, A., Bennartz, R., Fell, F., Lattanzio, A., Doutriaux-Boucher,M., and Schulz,J., 2016, A database of global reference sites to support validation of satellite surface albedo datasets (SAVS 1.0). Earth Syst. Sci. Data, 8, 425–438, https://doi.org/10.5194/essd-8-425-2016

Nightingale, J.; Schaepman-Strub, G.; and Nickeson, J.; 2011,leads, L.F.A. Assessing Satellite-Derived Land Product Quality for Earth System Science Applications: Overview of the CEOS LPV Sub-Group. In Proceedings of the 34th International Symposium on Remote Sensing of Environment, Sydney, NSW, Australia, 10–15.

Weiss, M., F. Baret, S. Garrigues, and Lacaze, R., 2007. LAI and Fapar CYCLOPES global products derived from VEGETATION. part 2: Validation and intercomparison with MODIS Collection 4 products. *Remote Sensing of Environment*, 110 (3), 317–331.

Validation of LST Remote Sensing Products Based on IoT

Yaoqiang Wang[1], Kun Shao[1], Xing Huo[1,*], Yonghua Yang[2,3]

1. HeFei University of Technology, HeFei 230009, China
2. AnHui WanKen Food Group, BengBu 233426, China
3. AnHui LongKang Farm, BengBu 233426, China

huoxing@hfut.edu.cn

Abstract - *Land Surface temperature is a critical parameter to the studies in geography, resources, agriculture and other disciplines. In recent years, with the rapid development of Internet of Things, it is possible to take advantage of Internet of Things to verify remote sensing product's accuracy. Due to the large dimensional difference between the satellite pixel and the ground direct measurement, the nonuniform style of upper coverings type and the huge temperature difference caused by diverse coverings, it is extremely difficult to verify the correctness of the land surface temperature by measuring the surface temperature directly. The existing experiments and studies are generally carried out on the surface of the lake, snow or other uniform coverings. This paper proposes a method of detecting the correctness of surface temperature remote sensing products based on Internet of Things called LSTDIoT to solve this problem. First, the experimental area is divided according to its covering's type, and then measure each puzzle's temperature and the weights respectively. Then the average temperature of the lesser uniform surface type can be calculated, then the crossing validation of these data is carried out with the corresponding remote sensing temperature. Furthermore, an experimental model based on Internet of Things technology is designed, which significantly saves labor force and material resources, and improves the efficiency of the experiment.*

1 INTRODUCTION

1.1 LST and LST Measurement

LST is an important parameter in the study of geography, resources, agriculture and other disciplines, which contributes to the assessment of surface energy and hydrological balance, thermal inertia and soil moisture (Kalma, 2008). Conventional fixed-point measurement of LST is relatively simple, which can be completed by ordinary infrared detection equipment or even by a thermometer. However, conventional fix-point measurement cannot obtain LST in regional or global scale, and satellite remote sensing will be the only possible solution (Li, 2013).

Satellite inversion of LST needs to be completely validated. General methods are Temperature-based, Radiation-based and cross-validation (Li, 2016). The Temperature-based method is a kind of ground-based method. By directly comparing the temperature retrieved from satellite data with the one measured at the time of the satellite transiting. But due to the dimensional difference between immediate measurement and remote-sensing, and the huge changes in tiny cells of each area, studied areas are confined to lakes, grassland and snow-field, which are homogeneous areas in some means.

This paper proposes a method called LSTDIoT(Land Surface Temperature Detection based on Internet of Things), which can be used for surface temperature remote-sensing in lesser heterogeneous land.

1.2 Related Research

Measuring the LST at the experimental site is a complex and difficult task due to the dimensional difference between the satellite pixels (several square kilometers) and the experimental sensors (several square meters or several square centimeters). In addition, the natural surface covering and its temperature and emissivity values vary widely in the kilometer level. As evidence, Snyder pointed out that the surface which was uniform and flat, is easy to be measured and characterized, and can be used as a verification site in 1997 (Snyder, 1997). Also Wan made experiments in grassland, rice field and other uniform places in 2002 (Wan, 2002); Sobrino measured the temperatures in an agricultural region of Spain in 2004 (Sobrino, 2004).

2 METHOD DESCRIPTION

2.1 Internet of Things Technology

The Internet of things is not only an inevitable part of the new generation of information technology, but also an important stage of development of the information era. By using intellisense, identification technology, pervasive computing and other communication sensing technology, IoT is widely used in the integration of the network. Therefore, IoT is known as the world's third wave of information industry development after the invention of computer and application of internet.

With the use of IoT technology in other areas such as specific experiments and research, lots of manpower and resources could be saved, and it's more efficient.

In this paper, we try to use IoT technology to assist in correctness verification of LST remote sensing product to steeply improve the efficiency of our experiments and research.

2.2 LSTDIoT

In order to explore the possibility of verifying remote sensing LST of uneven ground surface, this paper proposes a method called LSTDIoT(Land Surface Temperature Detection based on Internet of Things), and try to do an experiment in areas where contain several kinds of coverings and each covering's weight can be calculated easily.

The main idea of LSTDIoT is to find a square area a on the ground according to satellite pixel's latitude and longitude, then divide a into several blocks according to its covering type and obtain each block's proportion and temperature. Based on the data above, we can estimate the covering's temperature Ta by using the following formula: $Ta = \sum_{k=1}^{n} \rho k \bullet \varepsilon k \bullet Tk$. When Pk is the covering's proportion, Ti is the covering's temperature, εk is the covering's weight. However, εk needs to be determined by a specific experiment. Assuming that Tpe is the temperature value of the satellite pixel. Let $Tpe = Ta$ we can get the equation $Tpe = \sum_{k=1}^{n} \rho k \bullet \varepsilon k \bullet Tk$. By this way we can get a equation set and then find out $\varepsilon k(k = 1,2,3...)$. εk can be applied to nearby satellite pixel and calculate nearby area's temperature for cross-validation, compared with the actual temperature of said satellite pixel.

The high resolution images (ASTER images of Terra) were used as satellite remote sensing data. We selected a large farm in Anhui Yangtze-Huaihe area which contains cropland, soil, lawn, river, building and other coverings as an experimental site, as shown in Figure 2 in Section 3.1. There are three main ways to obtain the area of various coverings: farm official data, measurement on-site by tools and calculated area using satellite surface covering information. While the surface temperature of the covering was measured by suspending the infrared temperature sensor at each location, and each covering was measured by multiple times and then the averaged value is taken. Unquestionably, in order to avoid the impact of sunlight, data collection would be carried out at night. The sensor would transmit the acquired temperature value to the server via the data base station and GPRS/GSM network. Finally, we designed a computer program to call these original data and calculate the value to obtain the value of each variable.

According to the method described above, in farms with n kinds of coverings, we can select n regions and measure for n times, and compare these data with the corresponding satellite pixel temperature values to get the block weight $\varepsilon k(k = 1,2,3...,n)$. Applying εk to other regions and the pixel, the cross-validation can be done.
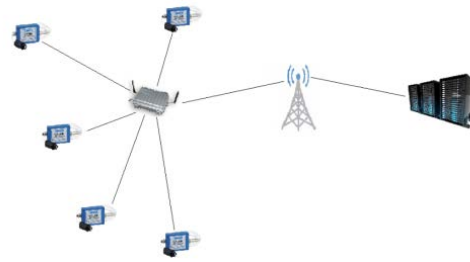
Figure 1: Diagram of data transmission of IoT

2.3 Construction of Experimental Model

In order to save manpower and material cost, while improve the efficiency of experiment, this paper constructs a kind of IoT experiment model to assist the experiment described above.

2.3.1 The Layout of Sampling Points

Using the latitude and longitude of the pixel on the satellite image, we select an experimental area, which is about 1km × 1km scale in the farm. The experimental area has lawn, cropland, soil, building and river. Assuming that it has N blocks and N is more than 5, so different blocks may be with the same covering. We tried to measure the surface temperature of each block separately. To avoid the mistake of incorrect temperature, multiple sensors were placed in each block and then took its averaged value. The number of sensors placed in each block was determined by the weight of the area and the shape of the block.

Assuming that the name of each block is $li(i = 1,2,3...,L)$, $ci(i = 1,2,3...,C)$, $si(i = 1,2,3...,S)$, $bi(i = 1,2,3...,B)$ or $ri(i = 1,2,3...,R)$, and set the weight of each block as $Pli(i = 1,2,3...,L)$, $Pci(i = 1,2,3...,C)$, $Psi(i = 1,2,3...,S)$, $Pbi(i = 1,2,3...,B)$, $Pri(i = 1,2,3...,R)$. While l, c, s, b and r represent the covering type of the blocks of lawn、cropland、soil、building and river. And L, C, S, B and R represent the number of blocks covered with lawn, cropland, soil, building and river, and the total of L, C, S, B and R is N.

2.3.2 Infrared Temperature Sensor

The temperature of the covering surface was measured by a suspended infrared temperature sensor. The infrared temperature sensor is to detect the infrared of the object.

As the infrared temperature sensor measures the surface temperature of the covering without contacting with the covering directly, which can effectively avoid the sensor's influence on the covering's temperature. Additionally, the infrared temperature sensor can be powered by lithium batteries for a long time without being charged in this networking model. So we don't have to read data after deploying these sensors, which effectively avoids the human impact on the temperature of the covering.

2.3.3 Data Transmission

Data transmission is the process of collecting temperature data measured by all infrared temperature sensors, and then sending it to the specified server (stationary IP address and port). Undoubtedly, the server has a corresponding program to receive these data. As shown in Figure 1.

The whole system of data transmission is completed by the corporation of infrared temperature sensors, data base station and server. And a data base station was arranged at the center of the experiment area. Communication between infrared temperature sensors and data base station uses AM 433MHz band, abbreviated as 433M.

The role of the data base station is to encapsulate and transmit data. The data base station mainly consists of receiving module, control module, transmitting module and power supply system. The receiving module can receive data as long as its parameters are the same as that of the infrared temperature sensor, such as frequency band and baud rate. The function of the control module is to control every running process of the entire data base station, including listening, encapsulating and sending data. The transmitting module needs to be connected to the GSM/GPRS network, so the data base station requires a SIM card to support this function. Generally, power supply system is consisted of co-operation of solar and batteries, which is one of the best ways for the long-term and stable power supply outdoors.

Infrared temperature sensor broadcasts the collected data through 433M module, and the signal transmission distance after amplifying can reach to 800m. The data base station locating at the center of the experiment area would keep listening, immediately encapsulating it and sending it through the GSM/GPRS network to the specified server once it receives the data. The format of the data follows the mainstream modbus protocol.

2.3.4 Data Processing

Data processing includes analysis, warehousing entry and classified counting of the data received by the server side.

The server receives data packets sent from data base station which are encapsulated according to modbus protocol with the information of sensor No., sensor's electric quantity, base station's electric quantity and the CRC check code as well as the temperature data that are needed to be deciphered.

Once the data has been successfully stored in the database, it is easy to carry out any calculations.

Assuming that the average temperature of each block is $Tli(i = 1,2,3...,L)$, $Tci(i = 1,2,3...,C)$, $Tsi(i = 1,2,3...,S)$, $Tbi(i = 1,2,3...,B)$, $Tri(i = 1,2,3...,R)$ So we can conclude that

$$Tk = \frac{\sum_{i=1}^{K} Tli \cdot Pli}{\sum_{i=1}^{K} Pli} \qquad (1)$$

$$\rho k = \frac{\sum_{i=1}^{K} Pli}{8100} \qquad (2)$$

here K means the number of each kind of covering block, taking L, C, S, B, and R. Then combined with the equation

$$Tpe = \sum_{k=1}^{n} \rho k \bullet \varepsilon k \bullet Tk \qquad (3)$$

in the LSTDIoT method, We can calculate the weight of the covering $\varepsilon k(i = 1,2,3...)$. Finally, according to $\varepsilon k(i = 1,2,3...)$ and formula (1) and (2), we can calculate the average temperature of other square area after measuring the blocks' temperature. Then compare the average temperature with the corresponding value of satellite pixel temperature, so as to complete cross validation.

3 APPLICATION OF THE METHOD

3.1 Study Area

We selected a large farm in Jianghuai, Anhui as the experimental site, whose name is Long Kang farm which locates in Huaiyuan County, Bengbu City, Anhui Province.

Long Kang farm is higher in the northwest, while lower in the southeast. The ground is 22.7 ~ 25.9 meters higher than the altitude, and the terrains looks like a ribbon. The farm is 17.5 km long from east to west, 1.6 km wide from south to north, and it's kind of flat as a whole.

The farm contains a small number of coverings including cropland, soil, lawn, river and building. The distribution of coverings is uniform, and the range of every covering is large, which is suitable for our experiment. As is shown in Figure 2.

Table 1: data collected by infrared temperature sensors

Sensor No.	1	2	3	4	5	6	7	8	9	10	11	12	13	14	15	16	17	18	19	20	21	22
Sampling data	25.5	29.9	26.4	20.1	31.5	23.5	27.1	23.7	26.8	22.6	30.2	19.9	32.1	25.8	22.9	31.5	23.1	24.0	26.6	20.5	31.0	26.1

Figure 2: Diagram of sampling in the experimental site

3.2 Satellite Image Data

The experiment uses data from ASTER sensor carried on Terra satellite as the data source. Five bands of ASTER data from 10 to 14 can be used for LST inversion, and the resolution from ground of these 5 bands can reach to 90m.

3.3 Experimental Data Collection

According to Figure 2, infrared temperature sensors and data base stations are deployed in the experimental area. Table 1 shows the data collected by infrared temperature sensors at 1:00 am.

4 RESULTS AND DISCUSSION

4.1 Experimental Results

According to formulas (1), (2) and (3) in Section 2.4, combining with the field data collected in section 3.3 and the ASTER sensor data, we can get a system of quaternion linear equations. After calculating, we obtained the weights of lawn, cropland, soil and river as follows: $\varepsilon lawn$ is equal to 12.2792, $\varepsilon cropland$ is equal to 13.9719, $\varepsilon soil$ is equal to 11.9938, $\varepsilon river$ is equal to 10.2850.

4.2 Cross-Validation

The basic idea of cross validation is to classify the original data in a certain sense, and set a part of them as training set and the others as verification set. Firstly, train the classifier with the training set, and then use the verification set to verify the trained model. The result will be used as a performance index for classifier evaluation.

Here, we use four of the pixel data as training set, the other two pixels' data as test set. Using the weights of the four types of coverings $\varepsilon lawn$ 、 $\varepsilon cropland$ 、 $\varepsilon soil$ 、 $\varepsilon river$ obtained in Section 4.1 and formulas (1), (2) and (3) in Section 2.4, we can figure out the average temperature of the other two square areas of 298.78K and 297.91K. Fortunately, their corresponding pixel temperature data are 296.85K and 296.15K.

4.3 Results Discussion

In Section 4.2, we derived average temperatures of the other two square areas by using parameters calculated by equations. And then we figured out the difference are 1.93K and 1.76K after comparing the average temperature with the corresponding pixel temperature data.

In the experiment, the data error mainly comes from three factors: the inevitable error of the infrared temperature sensor, the estimation error of the size of each block and the inversion error of Terra satellite ASTER sensor's data.

5 CONCLUSIONS

This paper proposed a detection method of the correctness of surface temperature remote sensing products based on Internet of Things called LSTDIoT to explore the possibility of verifying remote sensing LST of uneven surface types. And we selected a region in Long Kang farm located in Anhui Province Bengbu City Huaiyuan County for the experiment.

The experimental results indicate that, the surface temperature measured and calculated by LSTDIoT method has less than 2K error compared with the corresponding remote sensing temperature data. The error of the data mainly comes from measurement error of the infrared temperature sensor, estimation error of the size of blocks and inversion error of Terra satellite ASTER sensor's data. These three aspects, especially the resolution of the satellite thermal infrared sensor is worth being improved lately.

REFERENCES

Kalma J D, Mcvicar T R, Mccabe M F. Estimating Land Surface Evaporation: A Review of Methods Using Remotely Sensed Surface Temperature Data[J]. Surveys in Geophysics, 2008, 29(4):421-469.

Li Z L, Tang B H, Wu H, et al. Satellite-derived land surface temperature: Current status and perspectives[J]. Remote Sensing of Environment, 2013, 131(8):14-37.

Li Z L, Duan S B, Tang B H, et al. Review of methods for land surface temperature derived from thermal infrared remotely sensed data[J]. Journal of Remote Sensing, 2016, 20(5):899-920.

Snyder W C, Wan Z, Zhang Y, et al. Requirements for satellite land surface temperature validation using a silt playa ☆[J]. Remote Sensing of Environment, 1997, 61(2):279-289.

Wan Z, Zhang Y, Zhang Q, et al. Validation of the land-surface temperature products retrieved from Terra Moderate Resolution Imaging Spectroradiometer data[J]. Remote Sensing of Environment, 2002, 83(1–2):163-180.

Sobrino J A, Jiménez-Muñoz J C, Paolini L. Land surface temperature retrieval from LANDSAT TM 5[J]. Remote Sensing of Environment, 2004, 90(4):434-440.

Evaluation of ASTER AST05 product with field emissivity measured using a portable Fourier transform infrared spectroradiometer

Bo-Hui Tang[1, 2], Zhao-Liang Li[1, 2, 3, *], Hua Wu[1, 2], and Ronglin Tang[1, 2]

[1.] *State Key Lab of Resources and Environmental Information System, Institute of Geographic Sciences and Natural Resources Research, Chinese Academy of Sciences, Beijing, 100101, China.*

[2.] *University of Chinese Academy of Sciences, Beijing 100049.*

[3.] *Key Laboratory of Agri-informatics, Ministry of Agriculture / Institute of Agricultural Resources and Regional Planning, Chinese Academy of Agricultural Sciences, Beijing, 100081, China..*

[*.] Corresponding to whom should be addressed: lizhaoliang@caas.cb

ABSTRACT- *This work evaluates the accuracy of the ASTER emissivity product AST05 with field spectral radiance measurements by using a handheld portable Fourier transform infrared (FT-IR) spectroradiometer Model 102F for several natural surfaces. Considering that the 102F operates in the 2-16 µm spectral domain, with spectral resolutions of 4 cm^{-1}, the LST and LSE are decoupled by using a piecewise linear spectral emissivity method. The method derives reasonable emissivity spectra for four natural surfaces: sand, bare soil, alfalfa, sea water. The channel emissivity are derived by convolving the spectral emissivity with the spectral response function of ASTER five TIR channels. Comparisons of channel LSEs from field measurements with those from AST05 show that good agreements are obtained for sand and bare soil while big differences are existed for alfalfa and sea water with maximum bias up to 0.045 in channel 10 for sea water, which demonstrates that AST05 product provides accurate LSEs for higher spectral contrast surfaces but inaccurate LSEs for low spectral contrast surfaces.*

Keywords: Emissivity, field measurements, natural surfaces, 102F, ASTER

1 INTRODUCTION

Land surface emissivity (LSE) has long been seen as an indicator of material composition [1-3]. However, different materials in the terrestrial ecosystem (e.g., rock, soil, vegetation, water, and snow/ice) have different spectral features. The knowledge of LSE spectral variation is very important in many applications, such as the Earth's surface energy budget estimation, land surface temperature (LST) retrieval, land cover types discrimination, and so on [4-10]. It is therefore very necessary to analyze the spectral variation of LSE in the thermal infrared (TIR) domain (8-14 µm window).

The Advanced Spaceborne Thermal Emission and Reflection Radiometer (ASTER) surface emissivity product (AST05) provides five thermal infrared (TIR) channels emissivities derived with the Temperature Emissivity Separation (TES) method [11]. However, many researches reported that the AST05 product underestimated the emissivity for low spectral contrast surfaces (such as vegetation and water) with uncertain up to 7% for channel 10 at 8.3 µm [12].

To further evaluate the accuracy of the ASTER emissivity product AST05, this work measures several natural surfaces with a handheld portable Fourier transform infrared (FT-IR) spectroradiometer Model 102F at a field in-situ site. Section 2 introduces the study area and field experimental measurements. The method for deriving spectral emissivity from measured spectral radiance are described in Section 3. The results are presented in Section 4 where the verifications of derived spectral emissivity with spectral library data for several natural surfaces are given. The evaluation of the ASTER emissivity product AST05 are also given in this Section. Finally, the conclusions are drawn in section 5.

2 STUDY AREA AND FIELD MEASUREMENTS

2.1 Study area

The experimental measurements were conducted at Baotou field site, located in Urad Qianqi, Inner Mongolia, in northern China, between latitudes 40° 45′ N and 40° 54′ N and longitudes 109° 15′ E and 109° 40′ E. The location of the study site is shown in Figure 1. The study site is approximately 10 km2, and the average altitude is 1290 m above sea level. The site has a semi-arid temperate continental climate with a mean annual temperature of 6℃ and a mean annual rainfall of approximately 288 mm. Most

of the soil in the site is sandy loam and silt loam, and the primary vegetation is the shrub Caragana microphylla. Plots of 90 m×90 m were established on three natural surfaces, sand, bare soil, and alfalfa, in the study site.
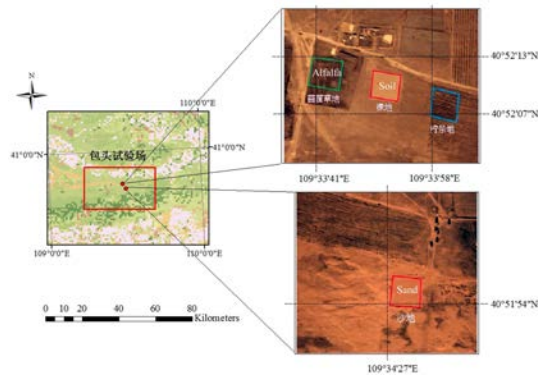
Fig.1. Location of the study site.

2.2 Field measurements

The spectral radiances for several natural surfaces were measured by a handheld portable Fourier transform infrared (FT-IR) spectroradiometer Model 102F, manufactured by the Designs & Prototypes Company, Simsbury, USA. It is a rugged and practical field instrument weighing less than 7 kg. The 102F portable field spectroradiometer operates in the 2-16 μm spectral domain, with selectable spectral resolutions of 4, 8, or 16 cm^{-1}. The overall interferometer dimensions are 36 cm×20 cm×23 cm, excluding the input optics. It runs on a compact battery, a 12 volt auto cigarette lighter, or a worldwide universal AC supply/battery charger. It is therefore suitable for field measurement of the spectral radiance of natural or man-made materials.

To reduce the influence of the environment on the radiance measurements, the experimental campaigns were conducted on March 16, July 14, and October 15 and 17, 2014 when there were with moderate ambient temperature, low humidity, and calm winds, free of visible cloud cover. Figure 2 shows three measurement images of field campaigns for grass land, bare soil and lake water in the field site, respectively.

2.3 ASTER emissivity product AST05

ASTER, a multispectral sensor providing 15 spectral channels (4 VNIR channels, 6 SWIR channels and 5 TIR channels), was launched on 19 December 1999 aboard Terra satellite. ASTER offers high spatial resolution imagery of 90 m for five thermal infrared (TIR) channels, as well as LST and emissiviy products (AST08 and AST05, respectively), derived with the

Temperature Emissivity Separation (TES) method [11]. The ASTER surface emissivity product (AST05) over the experimental site covering different surface types are used in this work.
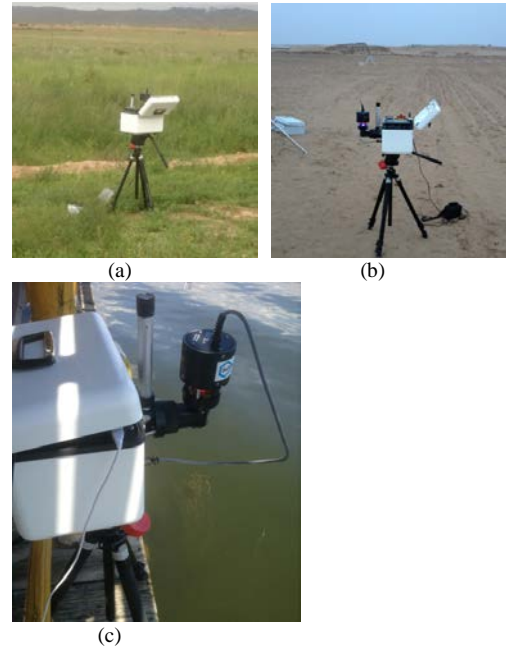
Fig.2. Measurement of emissivity with a handheld portable FT-IR spectroradiometer Model 102F in the study site: (a) for alfalfa grass land, (b) for bare soil land and (c) for inland lake.

3 METHOD

3.1 Radiative Transfer Theory in the TIR

According to the radiative transfer theory, for a cloud-free atmosphere under thermodynamic equilibrium, the spectral radiance R_λ measured at the ground level in a TIR sensor, is given with a good approximation as [13]:

$$R_\lambda(\theta,\varphi) = \varepsilon_\lambda(\theta,\varphi)B_\lambda(T_s) + (1-\varepsilon_\lambda(\theta,\varphi))R^\downarrow_{at_\lambda} \quad (1)$$

in which all variables depend on the wavelength λ. θ is the viewing zenith angle and φ is the viewing azimuth angle. B is the Planck function, and $B_\lambda(T_s)$ is the spectral radiance emitted by a blackbody at temperature T_s. $R^\downarrow_{at_\lambda}$ is the spectral downwelling radiance reflected from the target into the spectroradiometer with reflectance $(1-\varepsilon_\lambda)$. ε_λ is the spectral emissivity. To calculate ε_λ, according to equation (1), both $R^\downarrow_{at_\lambda}$ and T_s must be known.

3.2 Determination of Spectral Downwelling Radiance

To determine the spectral downwelling radiance $R_{at_\lambda}^\downarrow$, a gold plate with known emissivity is used. If we assume that a small error is caused by ignoring the scattered downwelling radiance of the gold plate in the measurement, the $R_{at_\lambda}^\downarrow$ can then be calculated as [14]

$$R_{at_\lambda}^\downarrow = \frac{R_\lambda^{gold}(\theta,\varphi) - \varepsilon_\lambda^{gold}(\theta,\varphi)B_\lambda(T_s^{gold}(\theta,\varphi))}{1 - \varepsilon_\lambda^{gold}(\theta,\varphi)} \quad (2)$$

in which R_λ^{gold} is the measured radiance for the gold plate, $\varepsilon_\lambda^{gold}$ is the known spectral emissivity of the gold plate, calculated from directional hemispherical reflectance measurements. T_s^{gold} is the gold plate's temperature, which can be obtained by a thermocouple during the radiance measurements.

It is worth noting that the measurements of downwelling radiances must be conducted immediately before or after that of target radiance measurement. The measured location, observation geometry of the gold plate should be the same to that of the target measurement. Then, the downwelling spectral radiance determined from the gold plate measurement is substituted for that of the target.

3.3 Determination of Spectral Emissivity

If the spectral downwelling radiance $R_{at_\lambda}^\downarrow$ is appropriately determined, the spectral emissivity ε_λ in equation (1) can be calculated by

$$\varepsilon_\lambda(\theta,\varphi) = \frac{R_\lambda(\theta,\varphi) - R_{at_\lambda}^\downarrow}{B_\lambda(T_s) - R_{at_\lambda}^\downarrow} \quad (3)$$

when the target temperature T_s is known.

Note that the temperature and emissivity are coupled in the TIR radiative transfer equation, to determine the spectral emissivity, the temperature and emissivity must be separated from the radiance measurements. Consequently, a piecewise linear spectral emissivity constraint method [15], which assumes that N bands corresponding to N emissivities in the hyperspectral data, is adopted to decouple the LST and LSE from the field radiance measurements.

4 RESULTS AND DISCUSSION

4.1 Results of Derived Spectral Emissivity

Sixteen places were measured for each natural surface to reduce the effects of instrumental noise and other systematic errors. Once the radiance of the natural surface is measured, the downwelling radiances are determined, and then the temperature/emissivity separation algorithm described above is performed to derive the spectral emissivity. Figure 3 shows the spectral emissivity curves derived for each measurement of three natural surfaces. The average and standard deviation spectral emissivity curves are also shown in this figure.
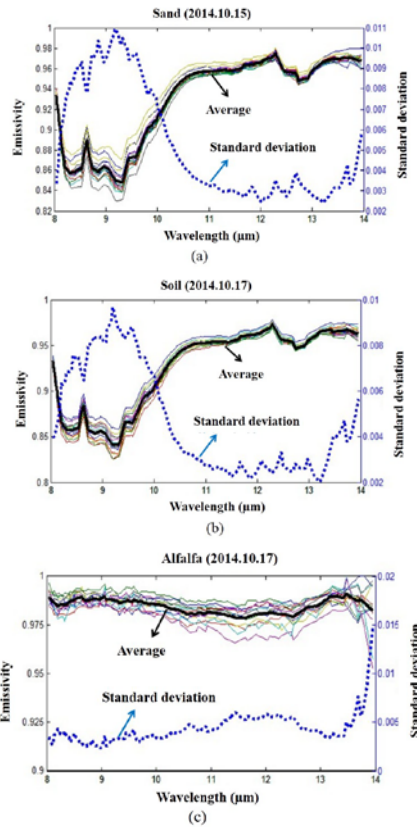
Figure 3. Spectral emissivity measured in the study site and derived with the proposed temperature/emissivity separation algorithm for three natural surfaces: (a) for sand, (b) for soil, and (c) for alfalfa.

In Figure 3, we can see that the maximum standard deviation for sand emissivity is below 0.011 and that for soil emissivity is below 0.01 in the spectral domain 8-14.0 µm. Most of the standard deviations are below 0.005 for both emissivity measurements in the spectral domain of 10-14.0 µm. For the alfalfa, the standard deviations at the spectral domain of 8-13.5 µm are less than 0.005. All of the values of spectral emissivity for alfalfa are above 0.97 in the 8-14 µm spectral domain. The spectral emissivity of bare soil is relatively low, with minimum below 0.93. The spectral emissivity for sand has a significant variance, especially in the spectral domain of 8-11 µm, with minimum below 0.85.

4.2 Comparisons with spectral library data

As a preliminarily test, the spectral emissivity derived from the field measurements, are compared with emissivity spectra of similar materials as provided by the MODIS UCSB emissivity library of the MODIS LST group. To assess the reliability of the comparison, the emissivity spectrum of materials with similar content are chosen. Comparisons between the emissivity spectra measured in the field and those obtained from the UCSB library are shown in Figure 4. The solid curves represent the spectral emissivities derived with the proposed scheme, and they are similar to the dashed curves obtained from the UCSB library. As shown in this figure, the change trends of different materials' emissivity spectra are approximate.
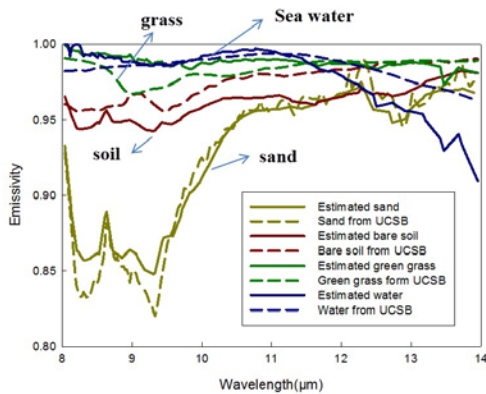
Figure 4. Emissivity spectrum curves derived from the field measurements (solid lines) and those obtained from the UCSB library (dashed lines).

Table 1 provides summary statistics of the comparison. The RMSEs are calculated for the derived and obtained emissivities in the 8-14 μm spectral domain. To better compare the two different datasets, the spectral resolution of emissivity spectra are resampled to 4 cm^{-1}. As given in this table, the minimum RMSE is 0.0101 for alfalfa. The maximum RMSE is 0.0135 for sea water, perhaps because the sea water we measured was from an inland water body, Ulansuhai Lake in Western Inner Mongolia, China. Differences in water quality may exist between this water and the sea water used in the UCSB. Due to all the RMSEs below 0.02 in the comparisons, we can conclude that the proposed scheme in this paper is appropriate to determine the emissivity spectrum of natural surfaces from field radiance measurements.

4.3 Evaluation of AST05 emissivity

To evaluate the accuracy of the ASTER emissivity product AST05, an image of AST05 data were obtained through the Earth Remote Sensing Data Analysis Center (ERSDAC). For each natural surface, the emissivity of ASTER five TIR channels for the pixels closest to the measurement site was extracted. Figure 5 shows, as an example, the comparisons between the emissivity spectra derived from the field measurements and those obtained from AST05 product for sand, soil, alfalfa, and water, respectively.

Table 1. Statistics of RMSE for the derived and obtained emissivity in 8-14 μm region for different materials.

Targets	Spectral domain (μm)	Spectral resolution (cm^{-1})	RMSE
Sand	8-14	4	0.0131
Soil	8-14	4	0.0140
Alfalfa	8-14	4	0.0101
Sea water	8-14	4	0.0135
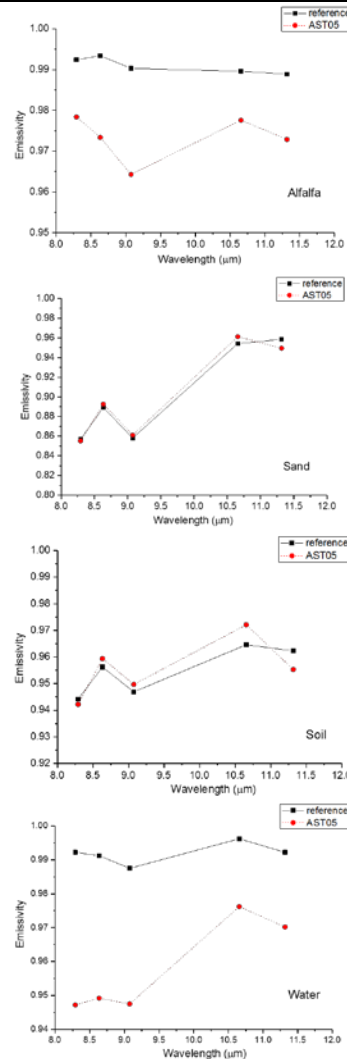
Figure 5. Comparisons of emissivity spectra derived from the field measurements (solid black lines) and those obtained from AST05 product (dashed red lines).

From figure 5, we can see a good agreements are obtained for sand and bare soil, with maximum bias of -0.0075 in channel 13 for soil. There are big discrepancies between the AST05 emissivities and the ground measured reference values for alfalfa and sea water, both in terms of magnitude and spectral shape, especially in channels 10-12, with maximum bias up to 0.045 in channel 10 for sea water, which demonstrates that AST05 product underestimate the channel emissivities for low spectral contrast surfaces.

5 CONCLUSIONS

A scheme was proposed in this paper to determine the longwave infrared emissivity spectra at the 8-14 μm window domain for natural surfaces from field radiance measurements with a portable FT-IR spectroradiometer. To determine the downwelling spectra radiances, a gold plate with known emissivity was used. Assuming that the downwelling spectra radiances for the measurements of the gold plate and the target were equal, the downwelling spectra radiance determined from the gold plate measurement was used to derive the target emissivity.

The ASTER emissivity product AST05 has been evaluated using field spectral measurements with a handheld portable spectroradiometer for several natural surfaces. The results showed that AST05 underestimated the five TIR channel emissivities for low spectral contrast surfaces, such as vegetation and water.

ACKNOWLEDGMENT

REFERENCES

Cuenca, J., and Sobrino, J. A., 2004, Experimental measurements for studying angular and spectral variation of thermal infrared emissivity. Applied Optics, 43(23), 4598-4602.

Li, Z.-L., Wu, H., Wang, N., Qiu, S., Sobrino, J. A., Wan, Z., Tang, B.-H., and Yan, G., 2013, Land surface emissivity retrieval from satellite data. International Journal of Remote Sensing, 34(9-10), 3084-3127.

Salisbury, J. W., and D'Aria, D. M., 1992, Emissivity of terrestrial materials in the 8-14 μm atmospheric window. Remote Sensing of Environment, 42(2), 83-106.

Tang, B.-H., and Li, Z.-L., 2008, Estimation of instantaneous net surface longwave radiation from MODIS cloud-free data. Remote Sensing of Environment, 112(9), 3482-3492.

Wan, Z., and Dozier, J., 1996, A generalized split-window algorithm for retrieving land-surface temperature from space. IEEE Transactions on Geoscience and Remote Sensing, 34(4), 892-905.

Zhao, E., Qian, Y., Gao, C., Huo, H., Jiang, X., and Kong, X., 2014, Land surface temperature retrieval using airborne hyperspectral scanner daytime mid-infrared data. Remote Sensing, 6(12), 12667-12685.

Jiang, G.-M., Zhou, W., and Liu, R., 2013, Development of split-window algorithm for land surface temperature estimation from the VIRR/FY-3A measurements. IEEE Geoscience and Remote Sensing Letters, 10(4), 952-956.

Sobrino J. A., and Raissouni, N., 2000, Toward remote sensing methods for land cover dynamic monitoring: application to Morocco. International Journal of Remote Sensing, 21(2), 353-366.

Tang, B.-H., Shao, K., Li, Z.-L., Wu, H., and Tang, R., 2015, An improved NDVI-based threshold method for estimating land surface emissivity using MODIS satellite data. International Journal of Remote Sensing, 36(19-20), 4864-4878.

Song, B., and Park, K., 2014, Validation of ASTER surface temperature data with in situ measurements to evaluate heat islands in complex urban areas. Advances in Meteorology, 2014, Article ID 620410, 12 pages.

Gillespie, A. R., Matsunaga, T., Rokugawa, S., and Hook, S. J., 1998, Temperature and emissivity separation from Advanced Spaceborne Thermal Emission and Reflection Radiometer (ASTER) images. IEEE Transactions on Geoscience and Remote Sensing, 36, 1113-1125.

Coll, C., Caselles, V., Valor, E., Niclos, R., Sanchez, J. M., Galve, J. M., and Mira, M., 2007, Temperature and emissivity separation from ASTER data for low spectral contrast surfaces. Remote Sensing of Environment, 110, 162-175.

Li, Z.-L., Petitcolin, F., and Zhang, R. H., 2000, A physically based algorithm for land surface emissivity retrieval from combined mid-infrared and thermal infrared data. Science in China Series E: Technological Sciences, 43, 23-33.

Tang, B.-H., Wang, J., Li, Z.-L., Wu, H., and Tang R., 2015, Measurements of natural surface emissivity with portable Fourier transform infrared spectroradiometer. Proceedings of SPIE, vol. 9808, pp. 98081B.

Wang, N., Wu, H., Nerry, F., Li, C., and Li, Z.-L., 2011, Temperature and emissivity retrievals from hyperspectral thermal infrared data using linear spectral emissivity constraint. IEEE Transactions on Geoscience and Remote Sensing, 49(4), 1291-1303.

Validation of Sentinel-2 LAI and FAPAR products derived from SNAP toolbox over a cropland site in Barrax and over an agroforested site in Liria (Spain)

D. Vinué [(1)*], F. Camacho [(1)], B. Fuster [(1)]

(1) EOLAB, Parc Científic Universitat de València, Paterna (Valencia). Spain.
*david.vinue@eolab.es

ABSTRACT - *Two field campaigns for the characterization of vegetation biophysical variables were conducted: first one in Las Tiesas-Barrax (Albacete, Spain) over the typical winter crop types as a part of the JECAM (Joint Experiment of Crop Assessment and Monitoring) activities to improve the retrieval of LAI (Leaf Area Index) and FAPAR (Fraction of Photosynthetically Active Radiation); second one in Liria (Valencia, Spain) over a forested area of* Pinus halepensis, *included in the project BIOSEN (BIOphysics variables of vegetation -LAI, FAPAR, FCover - and biomass from SENtinel-2 and Landsat-8). Ground data set was upscaled using Sentinel-2A top of canopy reflectance (L2A) data and transfer functions have been derived by multiple robust regressions between reflectance values and biophysical variables to generate empirical maps of biophysical variables. Furthermore, the L2B Biophysical Processor (BP) Toolbox of SNAP was used to estimate LAI and FAPAR over these two areas. This paper evaluates the performance of the Sentinel-2 LAI and FAPAR products derived from SNAP BP Toolbox over crops and forest areas using standard validation methodologies. Although FAPAR from SNAP shows a good consistency against field data and empirical maps, with an slight overstimation, LAI values from SNAP have been largely overestimated for NDVI values under 0.20 in agriculture areas, with RMSE values from 0.49 to 0.75 for several experiments and largely underestimated in forested areas over the full range of values with an adjust slope of 0.3.*

1 INTRODUCTION

Validation of satellite products are mandatory to make a proper use of this information. Protocols for validation of LAI global biophysical products are already developed in the context of Land Product Validation (LPV) group of the Committee on Earth Observation Satellite (CEOS) for the validation of satellite-derived land products (Fernandes *et al.,* 2014).

The direct validation strategy is based on the up-scaling of ground-data using high-spatial resolution imagery to match the coarse spatial resolution imagery. In addition, inter-comparison with equivalent products are performed to assess the consistency of the products over larger domains. These protocols were adapted for the validation of Sentinel-2 L2B prototype products using ESA campaigns datasets during the ESA VALSE-2 project (Camacho *et al.,* 2013). For direct validation, the ESU measurements is used directly, whereas empirical maps using robust regression techniques were used for intercomparison at the site extent.

The results of VALSE-2 project were used to develop a new toolbox -Biophysical Processor (BP)- by the European Space Agency (ESA) to calculate LAI and FAPAR from Sentinel-2 data (Baret *et al*., 2010) in the environment of the SNAP software.

The aim of this paper is to validate the Sentinel-2 LAI and FAPAR products of the BP toolbox. The Sentinel-2 BP products will be directly compared against the field data and against empirical maps obtained robust regression techniques, in one cropland site (Barrax) and one agro-forestal site (Liria), both located in Spain.

2 METHODOLOGY

2.1 Study areas

A field experiment to spatially characterize the vegetation, via its biophysical parameters, was performed over agricultural areas in Barrax (Albacete, Spain) on March, 2016. The collection of ground data in Barrax was performed as part of the JECAM experiment (Joint Experiment of Crop Assessment and Monitoring) concerning agriculture areas.

On February, 2017, a new field experiment was developed in Liria (Valencia, Spain) to collect biophysical variables over forested areas as part of the project developed by EOLAB "BIOphysics variables of vegetation -LAI, FAPAR, FCover - and biomass from SENtinel-2 and Landsat-8" (BIOSEN) for forested areas.

Experiments were performed in an area of 20x20 km^2 centred in the coordinates 39.05ºN and 2.11ºE in Barrax and 39.75ºN and 0.70ºE in Liria (WGS84).

The Barrax test site is located in a plateau 700 m above sea level with a flat morphology and large uniform land-use units. The region consists of approximately 65% dry land and 35% irrigated land. The typical crop types and rotation includes barley, alfalfa, papaver, onion among others (fig. 1). 24 Elementary Sampling Units (ESU) were sampled.
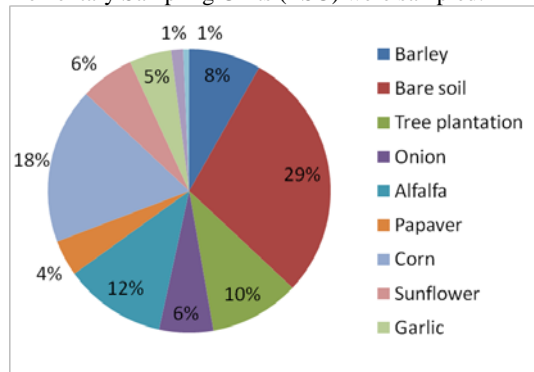
Figure 1: crop types sampled in Barrax.

Figure 2 shows an NDVI image of the Barrax site. Together with well-irrigated areas, senescent crops and bare soils can be observed. The presence of bare soils, senescent crops and irrigated crops makes of particular interest this cropland area for validation studies.
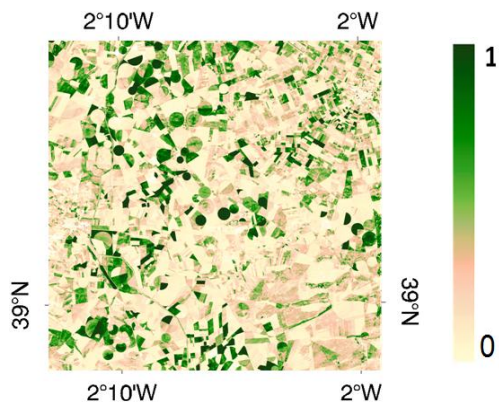
Figure 2: NDVI values in Barrax, 2016.

The site of Liria belongs to the Province of Valencia, 20 km inland far from the Mediterranean Sea. The area of study includes altitudes from 300 to 700 m above sea level. Sampling units comprise, overall, Aleppo pines (*Pinus halepensis*) at any stand age and bordering agrarian fields composed by orange trees (*Citrus x sinensis*) planted geometrically following well-distinguished rows with dense crowns. Traditional areas of olives (*Olea europaea*), locust trees (*Ceratonia siliqua*) and almond trees (*Prunus dulcis*) still remain between the majority of orange trees farms. The area is conformed as a typical

mediterranean forest-anthropic interface. 39 ESU were sampled.

Figure 3 shows a NDVI image of Liria study site. Well conformed forested areas and restored after burned areas occupy centre and North of the image, and agriculture areas can be noticed in South. In a general point of view, NDVI is relatively higher than in Barrax.
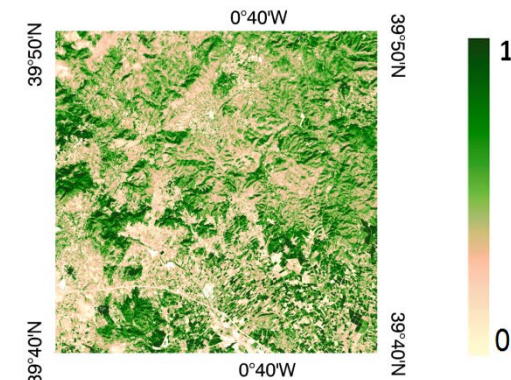
Figure 3: NDVI values in Liria, 2017.

2.2 Field data collection

Two field campaigns have been performed in the sites. Barrax area was sampled on 29th March, 2016 and Liria on 9th February, 2017.

Field data have been collected following the protocols of the ImagineS project (Camacho, 2013), using for this purpose Digital Hemispherical Photography (DHP), LP-80 Accupar Ceptometer and LAI2200 Plant Canopy Analyzer.

For DHP a pseudo-regular sampling in a square of 20x20 m2 was done, geolocating its center by GPS. Between 12 and 15 pictures have been taken, being processed afterwards with the CAN-EYE software developed by INRA[1].

For LP80 Accupar Ceptometer and for LiCOR-2000, each measurement was replicated three times, doing one measurement above and eight below the canopy in the same area as DHP.

2.3 Satellite imagery

Sentinel-2A data used for this study was atmospherically corrected from level L1C to L2A by using the SEN2COR[2] toolbox added to SNAP, both of them developed by ESA and freely available for all the users. Acquisition data was 12th of March, 2016 for Barrax (orbit 51, UTM 30SWJ) and 5th February, 2017 for Liria (UTM 30TKX).

---

[1] INRA: http://www6.paca.inra.fr/can-eye
[2] ESA: http://step.esa.int

2.4 Empirical transfer functions (TF)

Methodology to empirically estimate biophysical variables is compliant with existing guidelines (Morisette *et al.*, 2006). Following a validation strategy based on a bottom up approach, individual measurements are aggregated over an elementary sampling unit (ESU) corresponding with the pixel of those high resolution imagery used for the up-scaling of ground data. Radiometric values over a satellite image are also extracted over the ESUs that will be used to develop empirical transfer functions (TF) for up-scaling the ESU ground measurements (Martínez *et al.*, 2009).

As the number of sampled ESUs is enough, multiple robust regression between reflectance and biophysical variables can be applied (Martínez *et al.*, 2009). Several combinations of reflectance of 4 spectral bands of S2A from 540 nm to 1.660 nm were selected (bands related with green, red, near infrared and shortwave infrared zones of the spectrum), and NDVI, with a nadir ground sampling distance of 10 m.

For the transfer function analysis 'Robustfit' function from the Matlab® statistics toolbox was applied, using an iteratively re-weighted least squares algorithm and being the weights for each iteration computed by applying the bi-square function to the residuals from the previous iteration. This algorithm provides lower weight to ESUs that do not fit well.

The results are less sensitive to outliers in the data as compared with ordinary least squares regression. At the end of the processing, two errors are computed: weighted RMSE (using the weights attributed to each ESU - RW) and cross-validation RMSE (leave-one-out method - RC).

NDVI has been selected as the best input for the transfer function, as errors for this combination are enough good, while keep good consistency between both of the studied variables. Pre-established relationships were assumed for LAI and FAPAR, where NDVIs is the value of soil, and $NDVI_\infty$ the value for densest canopy, extracted from the image, as equations (1) and (2):

$$LAI = a + b \cdot ln\left(\frac{NDVI_\infty - NDVI}{NDVI_\infty - NDVI_s}\right) \qquad (1)$$

$$FAPAR = a + b \cdot NDVI \qquad (2)$$

2.5 Quality flag

The interpolation capabilities of the empirical transfer function used for up-scaling the ground data using decametric images is dependent of the sampling (Martinez *et al.*, 2009).

Data sampling was done over the most representative structures in the areas of study. However, because the method of TF has limited extrapolation capabilities, due linear functions, and to

ensure the quality of the data a test based on the convex hulls was also carried out additionally.

To characterize the representativeness of ESUs and the reliability of the empirical transfer function using the different combinations of the selected bands (green, red, NIR and SWIR) of the Sentinel-2A image, a flag image is computed over the reflectance values. The result on convex-hulls can be interpreted in figure 4 (for Liria, 2017) as:

    a)   well represented by the ground sampling, where transfer function will be used as an interpolator (clear blue);

    b)   the degree of confidence is quite good although the transfer function is used as an extrapolator (dark blue);

    c)   pixels where the transfer function behave as an extrapolator which makes the results less reliable (red).
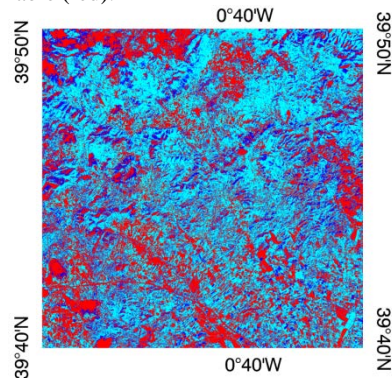
Figure 4: quality flag image for the transfer function in Liria, 2017.

2.6 L2B Biophysical Processor (BP)

After Level 2A of S2A imagery corresponding with reflectance at Top-Of-Canopy was achieved, level 2B (L2B) related to biophysical variables was obtained by performing these L2B biophysical processor (BP) installed in SNAP as a toolbox (Weiss and Baret, 2016). Values of LAI and FAPAR for individual ESU and for the whole scene were extracted.

2.7 Validation

Having then ground measurements and LAI and FAPAR results given by two methods (Transfer Functions -TF- and L2B processor -BP-) validation of both methods is conducted at the pixel level by direct comparison with ground measurements, and at the plot level over the site extent by comparison with the up-scaled maps.

3 RESULTS AND DISCUSSION

Sampling evaluation for TF shows a well represented sampling: 65.78% of pixels obtained by a strict- and

close to-interpolation in Barrax, 2016 and 67,63% of strict- and close to-interpolation obtained values in Liria, 2017.

3.1 Empirical maps

TF based on equations (1) and (2) using NDVI as input show for Barrax a RW=0.75 and RC=1.05 for LAI and values of RW=0.07 and RC=0.15 for FAPAR (table 1).

Table 1: TF applied in Barrax, 2016

Transfer function
LAI = 0,17 - 1,16 * ln[(0,95 - NDVI) / (0,95 - 0,12)]
FAPAR = -0,042 -1.099*NDVI

TF applied in Liria give errors for LAI of RW=0.75 and RC=1.15 and for FAPAR RW=0.13 and RC=0.13 (table 2).

Table 2: TF applied in Liria, 2017

Transfer function
LAI = 0,312 - 1,058 * ln[(0,97 - NDVI) / (0,97 - 0,12)]
FAPAR = -0,091 + 0,874*NDVI

In Barrax, application of TF gives a good correlation with field data for LAI, with an R^2=0.904. Although for FAPAR R^2=0.875, consistency of values for low NDVI areas is not enough to considerer the results in the experiment.

In Liria application of TF gives a good correlation with field data for LAI, with an R^2=0.867 and R^2=0.877 for FAPAR. In that case, both

3.2 Direct comparison

Biophysical values obtained by BP have been compared with ground measurements for each ESU. Figures 5 to 7 show the relation between variables for each data and site.

It is noticeable in Barrax that for low values of LAI, similar to bare soil, BP overestimate the results, but in general values are underestimated. In an agroforested area as Liria LAI results by BP are in accordance with this observation, as LAI is underestimated. FAPAR seems to be only slightly underestimated.

3.3 Intercomparison

Empirical maps obtained via TF application have been considered enough consistent to be used as a reference against BP values. A global scatter for the whole area has been processed in Barrax, 2016 (fig. 8).

Again, for low values of LAI, BP largely overestimate the empirical maps, better adjusted for bare soils and senescent crops which cover a significant area in Barrax. For other values, LAI BP values are underestimated compared to TF.

For the agroforestal area of Liria, a segmentation in two areas, one dominated by agriculture and one by pine forest. In agriculture areas, LAI behaviour obtained by TF or by BP of SNAP is similar to these one obtained in Barrax, 2016 (fig. 9). Low LAI values similar to bare soils are overestimated by BP whereas larger values are slightly underestimated. For FAPAR, however, a good correlation has been achieved with no overestimation for low values (fig. 10). This reveals a particular problem in LAI estimates.
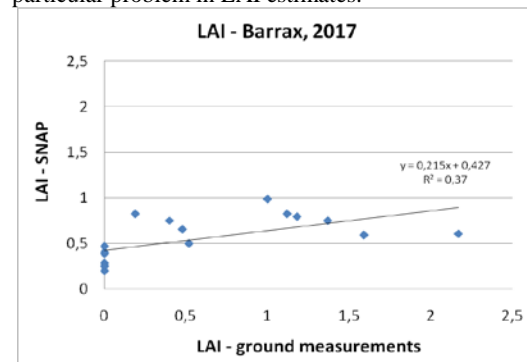
Figure 5: ground measurement of LAI compared with LAI from BP by ESU in Barrax, 2016.
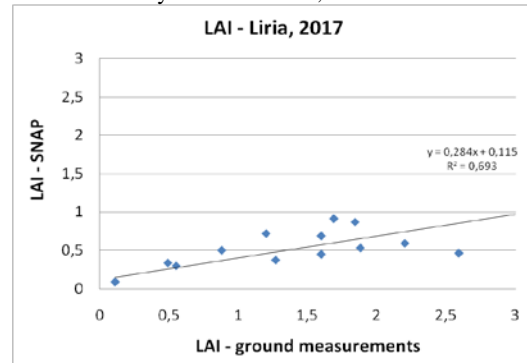
Figure 6: ground measurement of LAI compared with LAI from BP by ESU in Liria, 2017.
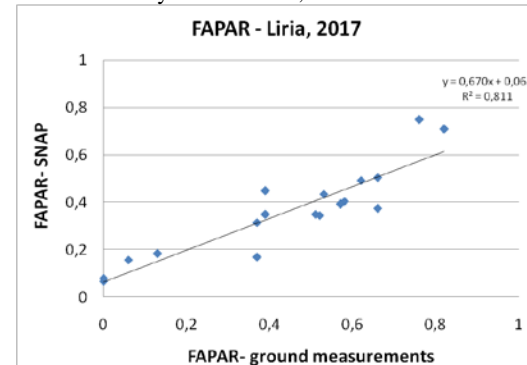
Figure 7: ground measurement of FAPAR compared with FAPAR from BP by ESU in Liria, 2017.
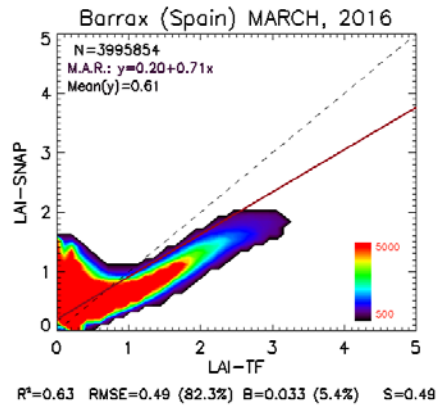
Figure 8: comparision of LAI. Barrax, 2016.
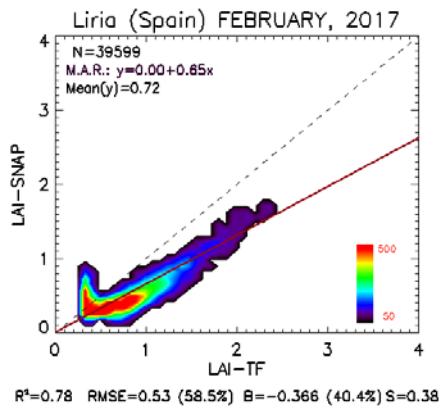
Figure 9: comparision of LAI value in agriculture areas. Liria, 2017.

In forested areas values of LAI derived from BP are underestimated for those forested and vegetated areas, with a low slope value of 0.30 (fig. 11). Differences can be explained either because radiative transfer simulations (PROSAIL) used in the BP are not well-suited for the three-dimensional structure of heterogeneous pine forest, and because the ground measurements refers to green PAI (Plant Area Index) rather than to green LAI. FAPAR values form BP are more similar with TF, although some underestimation is noticed. As a result, BP toolbox applied to forested areas seems to create some confusion .

4 CONCLUSIONS

High resolution ground-based maps of the biophysical variables have been produced over the sampling sites using Sentinel-2A Level-2A reflectance data, following the CEOS LPV recommendations, and used for validation of Sentinel-2 LAI and FAPAR products derived with the SNAP Biophysical Processor.

Over crops and farming areas it is noticeable that differences of LAI from BP of SNAP and transfer functions are major in low values related to bare soil. LAI from TF in areas of bare soil are closer to the null value than BP ones, that are normally overestimated for low values meanwhile other values are generally underestimated .
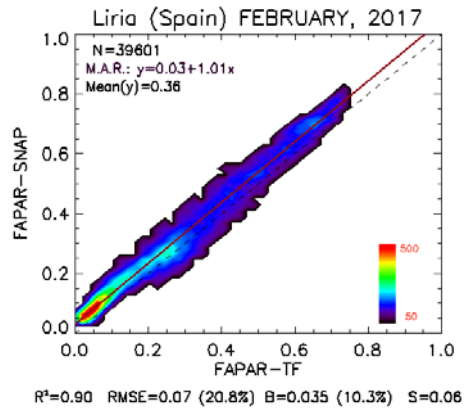
Figure 10: comparision of FAPAR values in agriculture areas. Liria, 2017.
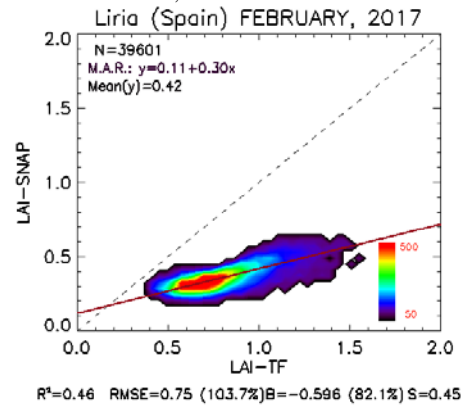
Figure 11: comparision of LAI value in forested areas. Liria, 2017.
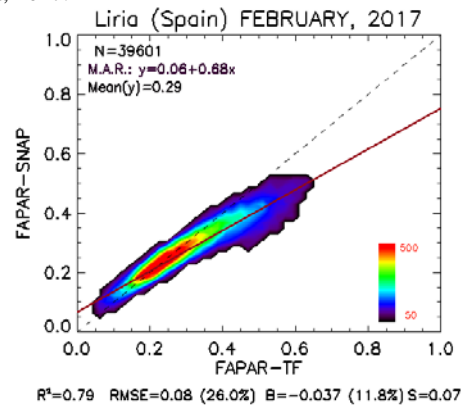
Figure 12: comparision of FAPAR value in forested areas. Liria, 2017.

252

In addition, in those forested areas analyzed, although FAPAR shows a slight better consistency against field data and empirical maps LAI values have been systematically underestimated, even after considering that LAI ground values in forest areas are slightly overestimated due to the contribution of non-leave elements to the photon interception.

Summarizing, LAI from BP presents a systematic inconsistency due a general underestimation and specifically over crops LAI values are non-reliable for areas with a low NDVI meanwhile FAPAR relations between two methods are softly better.

5 ACKNOWLEDGEMENTS

6 REFERENCES

Baret, F, Weiss, M., Bicheron, P., Berthelot, B. 2010. Sentinel-2 MSI Products. ATBD for product Group B. ESA SENTINEL 2 Products algorithms.

Camacho, F., Cernicharo, J., Lacaze, R., Baret, F., and Weiss, M., 2013. GEOV1: LAI, FAPAR Essential Climate Variables and FCOVER global time series capitalizing over existing products. Part 2: Validation and intercomparison with reference products. *Remote Sensing of Environment*, 137, 310-329.

Martínez, B., García-Haro, F. J., Camacho, F. 2009. Derivation of high-resolution leaf area index maps in support of validation activities: Application to the cropland Barrax site. *Agricultural and Forest Meteorology*, 149(1), 130-145.

Morisette, J. T., Baret, F., Privette, J. L., Myneni, R. B., Nickeson, J. E., Garrigues, S., et al. (2006). Validation of global moderate-resolution LAI products: A framework proposed within the CEOS land product validation subgroup. *IEEE Transactions on Geoscience and Remote Sensing*, 44, 1804–1817.

Weiss, M., Baret, F. 2016. S2ToolBox Level 2 products: LAI, FAPAR, FCOVER. Available for download at *http://step.esa.int/*. Last visit, October 2016.

A comparison between satellite and in situ SST data on a global scale

García-Monteiro, S.[1], Sobrino, J. A.[2]

[1] *Laboratorio de Procesado de Imágenes, Universidad de Valencia. C/ Catedrático José Beltrán, 2. 46980 Paterna, Valencia, España.*
[2] *Laboratorio de Procesado de Imágenes, Universidad de Valencia. C/ Catedrático José Beltrán, 2. 46980 Paterna, Valencia, España.*

[1] susana.garciamonteiro@gmail.com
[2] sobrino@uv.es

Sea Surface Temperature (SST) is a key variable that reflects and conditions natural processes which take place in the ocean and affect at a planetary scale. For this reason, there is a major interest in SST monitoring by using satellite data, with a periodic global coverage and a high precision. The present work used SST multi-temporal series, derived both from in situ and satellite data, to estimate SST, make a comparative analysis between these data sets and calculate the actual SST trend. The chosen data sets are: COBE (Japanese Meteorological Agency), ERSST version 4 (NOAA), and MODIS SST products (NASA) for the period 2002 to 2016 and the AATSR SST product, ARC SST v1.1 (ESA) for the period 2002 to 2011. Obtained SST trends show increases between 0.8 and 0.15 ºC per decade and an increase in the warming rate.

1. INTRODUCTION

The quantitative determination of the ocean temperature is crucial for global change studies. For this purpose, Sea Surface Temperature (SST) is selected as an indicator of climate processes associated to the ocean most superficial layer, reflecting possible warming-cooling trends, and has been determined as an Essential Climate Variable (ECV) by the Global Observing System for Climate (GCOS).

Until the 80s, SST monitoring was based on in situ data from buoys and oceanographic campaigns, basically with the support of oceanographic ships. Associated to this type of data, several problems appear. Firstly, these measurements are irregularly distributed in space and not necessarily representative of the real mean values of a determined area.

Both buoys and oceanographic campaigns use their own methodologies, generating intrinsic errors to each procedure. For this reason, the use of data from different sources as a homogeneous set, which could allow to establish the SST behaviour in time, is complex.

Satellite observations provide multi-temporal SST time series, averaged through spatial areas of an appropriate dimension for climate change studies and are potentially independent from in situ data (Mao *et al.*, 2017).

The main disadvantage is the need for making different corrections, for instance, atmospheric or geometric, in order to avoid errors because of the existent atmosphere between the observed surface and the sensor or the data collection by the satellite.

The present paper objective is to use remote sensing and in situ data to determine the SST evolution on a global scale, estimating trends by decades and comparing absolute SST data from the different data sets considered.

1.1. The importance of SST for climate change studies

Oceans are a fundamental energy reservoir in the Earth climate system. SST is a measurement of ocean's most superficial layer temperature and, once the influence of seasonal, regional or diurnal anomalies is removed, it can be used as a strong indicator of the ocean's surface climatology.

In figure 1, the contribution of different terrestrial components to the Earth climate system between years 1971 and 2010 is shown (IPCC, 2014). Energy values are a multiple of 10^{21} J.

These components are:

- The upper ocean above 700 m.
- Deep ocean below 700 m (including 2000 m estimates starting from 1992).
- Ice melt for glaciers and ice caps (Greenland and Antarctic ice sheet estimates starting from 1992, and Arctic sea ice estimate from 1979 to 2008).
- Continental (land) warming.
- Atmospheric warming (estimate starting from 1979)
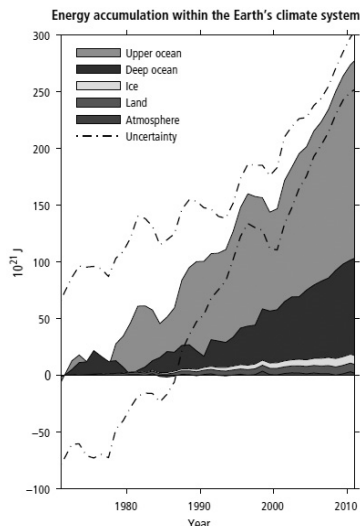
Figure 1. Energy accumulation within the Earth's climate system.

Uncertainty is estimated as the error from all five components at 90% confidence intervals.

Figure 1 shows that the most influential component to the Earth energy reservoir is the upper ocean, with an energetic contribution which increases through the years. SST behaviour reflects upper ocean processes, so it is important to monitor and study this variable correctly.

For this purpose, it is essential to obtain precise measurements of SST, as the offered by remote sensing techniques, which allow the detection of potential changes in SST evolution and offer a stable set of measurements that can be treated as an input parameter for numerical models, meteorological prediction models… and ease the understanding of different natural processes related to the ocean dynamics (Good *et al.*, 2007).

2. MATERIAL AND METHODS

An SST appropriate monitoring requires temporal data series for a minimum period of time of 10-15 years (Allen *et al.*, 1994). Another important issue to be taken into account is the maximum allowed error associated to measurements in climate change studies: in the case of a hypothetical increment SST trend of 0.25 K per decade, a stability of 0.1 K per decade is required for detecting changes with a minimum confidence level. (Llewellyn-Jones *et al.*, 2001), allowing in this way to determine the real SST evolution in time.

In the present paper, COBE SST and ERSST.v4 are the in situ SST data sets considered, and MODIS SST product and ARC.v1.1 SST AATSR product, the satellite data sets.

2.1 In situ data sets

Extended Reconstruction Sea Surface Temperature (ERSST) version 4

The ERSST multi-temporal series is a data set derived from ICOADS (International Comprehensive Ocean-Atmosphere Dataset), monthly averaged from January of 1854 until the present on a global scale. It is produced on a spatial 2º x 2º grid with spatial completeness enhanced using statistical methods (Huang *et al.*, 2015).

Version 4 is the most recent of the ERSST data produced by NOAA and includes absolute SST data and SST anomalies calculated respect a monthly climatology referred to years 1971-2000. It is presented in a 180 columns, 89 rows and 1961 bands format.

Centennial Observation-Based Estimates of SSTs (COBE-SST)

COBE-SST is the Japanese Meteorological Agency SST product produced on a 1º x 1º grid which includes data from 1891 to the present. It combines version 2.0 of ICOADS data set with the Japanese Kobe collection (NCAR, 2017).

The product is provided on a 360 column, 180 rows and 2004 bands format. Bands are associated to monthly averaged SST since January of 1981 to the present.

2.2. Satellite data sets

MODIS Terra/Aqua SST products

MODIS is an instrument aboard both Terra an Aqua satellites. Terra's orbit passes over the Equator from North to South in the morning at 10:30 a.m., whilst Aqua orbits over the Equator from South to North in the afternoon at 01:30 p.m.

SST products derived from MODIS are developed by the NASA Ocean Biology Processing Group (OBPG). For SST retrieval, two algorithms, long wave and short wave, are used. Data used in this study have been processed applying the long wave algorithm, which considers MODIS 31 and 32 bands.

Brightness temperatures are obtained from radiances, by an inversion of the relation between radiances and a black body temperature.

Data is available from 2001/2002 (Terra/Aqua) until the present. Images of a 4.63 km resolution, meaning an 8640x4320 pixels size, and monthly averaged have been used. Each pixel is also labelled according to its quality; for this study, only those with a value of 0 and 1, of good and acceptable quality, respectively, have been selected.

Along-Track-Scanning-Radiometer Reprocessing for Climate Sea Surface Temperature (ARC SST) version 1.1.

Climate change monitoring requires high precision level measurements. The ATSR programme pursues an absolute precision of 0.3 K in measurements with a stable error of 0.1 K during the whole mission (O 'Carroll *et al.*, 2006), averaged along areas of a 1º latitude and 1º longitude spatial resolution. Monthly averaged images have been used, for the period of time from year 1997 to 2011.

Measurements from ATSR instruments refer to the most superficial layer of the ocean, of a few micrometers depth (skin SST), slightly colder than water situated some centimeters deeper. In oceanography, SST is considered to be a measure of the temperature of the first 10 cm of the ocean water column (bulk SST), however, given the limitation of thermic radiation penetration in the water column, ATSR measurements refer to the first micrometers (Llewellyn-Jones *et al.*, 2011).

ARC SST version 1.1 SST data solves this difficulty as it is referred to a 20 cm depth (bulk SST), estimated by physic models which consider the original superficial temperature obtained by the sensor and making it ideal to be compared with in situ data. The averaged final values incorporate both diurnal (10:30) and night time data (22:30).

In figure 2, example images of the mentioned four SST data sets are shown.
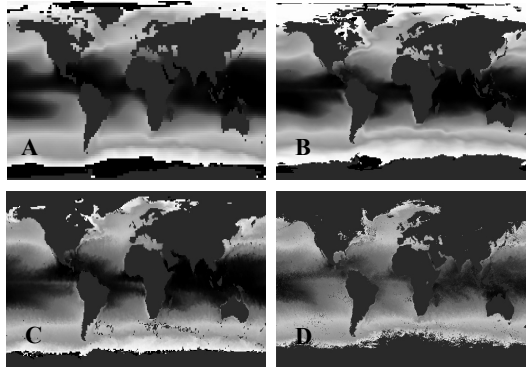
Figure 2. SST monthly averaged product examples: A, ERSST v.4 (NOAA); B, COBE-SST (Japanese Meteorological Agency); C, AATSR (ESA); D, MODIS (NASA)

2.3. Methodology

In general terms, mean SST is calculated by applying equation 2.1, where i is the number of columns, j the number of rows, SST_{ij}, is SST of one pixel for a given month, n is the number of measures considered and SST^t_{mean}, the mean temperature at a spatial range for a specific period of time.

$$SST^t_{mean} = \frac{1}{n} \sum_{i=1}^{i=n} \sum_{j=1}^{j=m} SST^t_{ij} \qquad (2.1)$$

For the MODIS case, SST for each pixel in every month is calculated as a mean between the four available measurements: MODIS Terra and Aqua, diurnal and nocturnal (Eq. 2.2). Observation times are symmetric, so the mean global SST estimated by equation 2.2 is similar to the absolute mean SST, as the temporal coverage of satellite data is continuous (Mao *et al.*, 2017). The uncertainty of these mean values is estimated by the standard deviation.

$$SST_{MODIS} = (T_m^{(01:30)} + T_m^{(10:30)} + T_m^{(13:30)} + T_m^{(22:30)})/4 \qquad (2.2)$$

Once the four data sets considered are processed, a comparison between the obtained results for years 2002-2011 is made.

MODIS SST product and the in situ data set, ERSST.v4, have temporal coverage up to the present, so the study will be extended until December of 2016, in order to estimate the actual SST trend by applying the minimum least squares method.

The uncertainty associated to SST trends ($\sigma\beta^2$) is calculated as the quotient of the data variance (σ^2) and the cubed size of the temporal period considered (Δt^3), multiplied by a factor (v) equal to 8 for satellite derived data and equal to 2, for ERSST.v4 (Hausfather *et al.*, 2017) (Eq. 2.3).

$$\sigma_\beta^2 = \frac{v\sigma}{\Delta t^3} \qquad (2.3)$$

Two programming languages have been used: IDL (Interactive Data Language), for data sets processing and variables extraction and Matlab, for the statistical analysis.

3. RESULTS AND DISCUSSION

3.1. Comparison between SST data sets: COBE-SST, ERSST v.4, MODIS and AATSR

Relations between the four SST data sets considered are shown in the next statistical analysis, in which a lineal adjustment by minimum squares is applied, considering monthly mean global SST data.

Several statistics are calculated: R^2 (determination coefficient), MBD (Mean Bias Deviation), RMBD (Relative Mean Bias Deviation) and RMSE (Root Mean Squared Error) (Table I).

Table I shows that, despite MBD, RMBD and RMSE are not high, determination coefficients show a week relation between most of the SST data sets considered, except for the pairs AATSR-ERSST, with a R^2 of 0.83, a -0.39 ºC bias, meaning an overestimation of satellite data respect in situ data, and a RMSE of 0.09 and MODIS-AATSR, with a R^2 of 0.69, a 0.91 ºC bias and an overestimation of MODIS respect AATSR.

Table I. Main statistics obtained by the lineal adjustment of SST data sets considered.

SST pairs Statistics	AATSR-COBE	AATSR-ERSST	MODIS-COBE	MODIS-ERSST	COBE-ERSST	MODIS-AATSR
R^2	0.08	0.83	0.04	0.06	0.27	0.69
MBD (ºC)	0.73	-0.39	-0.08	-1.20	-1.12	0.81
RMBD (%)	0.49	0.28	0.06	0.87	0.75	0.57
RMSE (%)	0.16	0.09	0.02	0.28	0.24	0.18
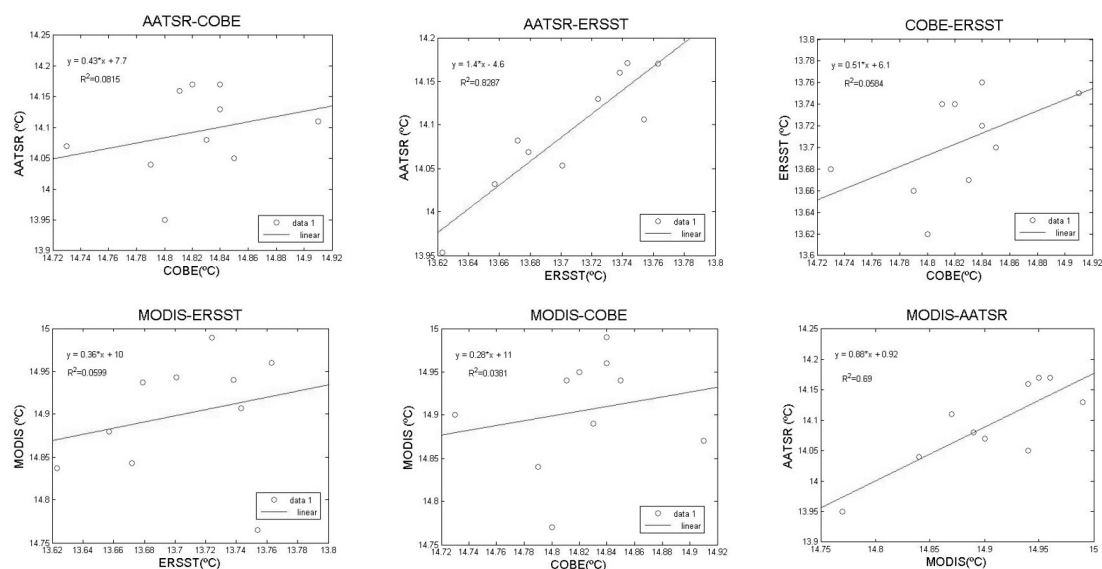
Figure 3. Lineal adjustments by SST data set pairs: AATSR-COBE, MODIS-COBE, COBE-ERSST, AATSR-ERSST, MODIS-ERSST, MODIS-AATSR.

The comparison between SST data sets show significant differences between generic absolute SST data available. Consequently, provided information by these multi-temporal absolute SST data series must be managed with caution, towards establishing any type of conclusions related to SST evolution. The adjustments can be visually observed in figure 3.

Several reasons generate such differences: errors in the satellite instruments calibration or the methodology used when taking samples, intrinsic of every oceanographic campaign and conditioned by the technicians in charge of the sampling. Furthermore, the fact that SST in situ data sets are a result of the interpolation of punctual measures in space, derived from buoys, and also punctual in time, when referring to oceanographic campaigns, must be taken into consideration. This will generate an associated error in the interpolated areas, in which direct measures are inexistent.

As in situ data sets, ERSST.v4 and COBE-SST, are derived, totally or partially, from the NOAA SST data set ICOADS (International Comprehensive Ocean-Atmosphere Data Set), the percentage of area sampled by ICOADS is shown in figure 4.

An oceanic coverage in SST sampling of between 40 and 60 % is registered, from years 1990 to 2014, revealing inexistent sampling in a minimum of 40% of the oceanic total area, which can introduce a significant error in interpolated zones
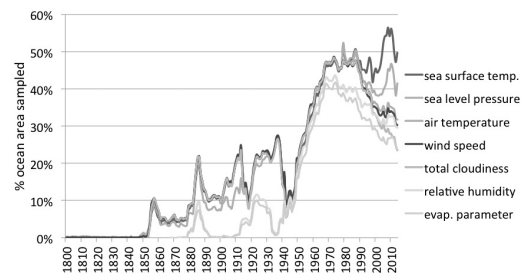
Figure 4. Percentage of sampled oceanic area between years 1800 and 2014 (NOAA, 2016).

For this reason, it is a clear necessity for using satellite data sets in SST monitoring, which offer continuous data at a global level, solving the problem of the in situ lack of data.

3.2. Current SST trend

Once analysed the relations between SST multi-temporal data series derived from ERSST.v4, MODIS, COBE-SST and AATSR, the parameter trend is estimated, considering ERSST.v4 and MODIS data from 1997 and 2002, respectively, to December of 2016. Results are shown in table II.

Table II. SST trend given by ERSST.v4 and MODIS data sets considering years 1997-2016, 2002-2016, 2007-2016 y 2011-2016.

Data Years	ERSST.v4 (ºC/decade)	MODIS (ºC/decade)
1997-2016	0.00(3) ± 0.00(0)	-
2002-2016	0.01 ± 0.00(0)	0.00(5) ± 0.00(0)
2007-2016	0.02 ± 0.00(2)	0.01(5) ± 0.00(1)
2011-2016	0.15 ± 0.01	0.08 ± 0.01

As observed in table II, the SST trends increase as a most recent period of time is considered in the estimations. The actual SST trend calculated in relation to years 2011-2016 is (0.15 ± 0.01) ºC/decade for ERSST.v4 data and (0.08 ± 0.01) ºC/decade for MODIS data.

Previous studies, which consider the period of time in between years 1997 and 2015, establish the SST trend on 0.12 ºC per decade for ERSST.v4 data (Hausfather *et al.*, 2017), with an increase of 0.03 ºC/decade during year 2016. These observations show that the SST trend is far from stability and it is increasing in time.

The SST trend resulting from analysing the ERSST.v4 data set is higher than the MODIS SST trend, nevertheless, in both cases an increase in the ocean absolute surface temperature and on the SST trend with the years is reflected, with the consequences that progressive changes on this parameter can cause on the global natural dynamic.

4. CONCLUSIONS

a. Significant differences exist between the four absolute SST data sets analysed, ERSST.v4, COBE-SST, MODIS and AATSR, as expected, due to in situ multi-temporal SST series are produced by combining measures from different sources (buoys, coastal measure stations, military data, oceanographic ships…), with its own sampling methodology, calibration and technicians. In consequence, although the application of quality controls and bias reductions, they will continue to show differences and data must be managed with caution.

b. Attending to sampling points distribution of in situ SST data sets, it is relevant the poor an irregular spatial coverage of measurements, which introduces errors in the global results and contributes to differences with satellite data sets.

c. Satellite data sets, offer measurements with an acceptable global temporal frequency and continuously in space, ensuring the whole Earth's surface coverage. The main problem associated to instruments which measure in the thermic range is the presence of clouds. However, a quality control variable is produced, at the same time as our variable of interes, SST, so that pixels with uncertain quality, can be filtered and eliminated from further calculations, improving results reliability, although there is still work to be done in this line.

d. In AATSR and MODIS cases, they offer global measures with a precision, estimated by standard deviation, of 0.1 ºC and 0.13 ºC, respectively. O'Carroll *et al.* (2006) had already determined a precision of 0.1 K for the whole ATSR mission, in agreement with this study's estimations.

e. In situ measurements are a complementary option to satellite data. The last ones, should reach the higher quality grade as possible, following an in situ data independent SST monitoring. ERSST.v4 and MODIS have been considered for trend estimations due to its present available data, resulting on (0.15 ± 0.01) ºC/decade and (0.08 ± 0.01) ºC/decade, respectively. 20 years ago, trends also showed a SST rising, but it was so low that the variable could be considered to be stable in time. This has changed and, currently SST is rising and should be continuously monitored to know its evolution in the short and middle time.

Given the rising and increasing SST trends, the topic of this paper is becoming a relevant investigation area, as SST is an Essential Climate Variable which conditions natural dynamics at a planetary scale. For this reason, a comprehensive knowledge of SST evolution and its relations with other oceanic variables will be required for making decisions about crucial matters, such as marine environment management and climate change attenuation.

REFERENCES

Allen, M. R., C. T. Mutlow, G. M. C. Blumberg, J. R. Christy, R. T. McNider, and D. T. Llewellyn-Jones, 1994. Global change detection. *Nature*, 370, 1–82.

Good, S. A., Corlett, G. K., Remedios, J. J., Noyes, E. J., Llewellyn-Jones, D. T., 2007. The Global Trend in Sea Surface Temperature from 20 Years of Advanced Very High Resolution Radiometer Data. *Journal of Climate*, 20, pp. 1255 1264, doi: 10.1175/JCLI4049.1

Hausfather, Z., Cowtan, K., Clarke, D. C., Jacobs, P., Richardson, M., Rohde, R., 2017. Assessing recent warming using instrumentally homogenous sea surface temperature records. *Science Advances 2017*, 3, doi: 10.1126/sciadv.1601207

Huang, B., Thorne, P., Smith, T., Liu, W., Lawrimore, J., Banzon, V., Zhang, H., Peterson, T., Menne, M., 2015. Further Exploring and Quantifying Uncertainties for Extended Reconstructed Sea Surface Temperature (ERSST) Version 4 (v4). *Journal of Climate,* 29, 3119–3142, doi:10.1175/JCLI-D-15-0430.1

IPCC, 2014. Climate Change 2014: Synthesis Report. Contribution of Working Groups I, II and III to the Fifth Assessment Report of the Intergovernmental Panel on Climate Change [Core Writing Team, R.K. Pachauri y L.A. Meyer (eds.)]. IPCC, Geneva, Switzerland, 151 pp.

Llewellyn – Jones, D., Corlett, G. K., Mutlow, C. T., 2001. AATSR: global-change and surface-temperature measurements from ENVISAT. *ESA Bulletin*, 105, 10-21.

Mao, K. B., Ma, Y., Tan, X. L., Shen, X. Y., Liu, G., Li, Z. L., Chen, J. M., Xia, L., 2017. Global surface temperature change analysis based on MODIS data in recent twelve years. *Advances in Space Research*, 59, 503-512.

Merchant, C. J., Embury, O., Rayner, N. A., Berry, D. I., Corlett, G. K., Lean, K., Veal, K. L., Kent, E. C., Llewellyn-Jones, D. T., Remedios, J. J. Saunders, R., 2012. A 20-year independent record of sea surface temperature for climate from Along-Track Scanning Radiometers, *Journal of Geophysics Research*, 117, C12013, doi:10.1029/2012JC008400.

National Center for Atmospheric Research Staff (Eds). Última modificación el 14 de abril de 2017. "The Climate Data Guide: SST data: COBE: Centennial in situ Observation-Based Estimates." Disponible en https://climatedataguide.ucar.edu/climate-data/sst-data-cobe-centennial-situ-observation-based-estimates.

NOAA. National Centers for Environmental Information. Extended Reconstructed Sea Surface Temperature (ERSST) v4. 2017. Último acceso: 4 de mayo de 2017, en https://www.ncdc.noaa.gov/data-access/marine

NOAA. ICOADS. 2016. Último acceso: 6 de julio de 2017, de http://icoads.noaa.gov/index_fig1.html

O'Carroll, A., Saunders, R.W., Watts, J.G., 2006. The measurement of the Sea Surface Temperature by Satellites from 1991 to 2005. *Journal of atmospheric and oceanic technology*, 23, 1573-1582.

Schluessel. P., Emery, W. J., Grassl H., Mammen, T., 1990. On the bulk-skin temperature difference and its impact on satellite remote sensing of sea surface temperature. J*ournal of Geophysical Research: Oceans*, 95(C8), 13341-13356.

Zeng, X. and Beljaars, A., 2005. A pronostic scheme of sea surface skin temperature for modelling and data assimilation. *Geophysical Research Letters*, 32, doi: 10.1029/2005GL023030

Estimation of land surface temperature from passive microwave data

Xiao-Jing Han[1,2,3], Si-Bo Duan[1,4], and Zhao-Liang Li[1,2,5,*]

1. Key Laboratory of Agri-informatics, Ministry of Agriculture/Institute of Agricultural Resources and Regional Planning, Chinese Academy of Agricultural Sciences, Beijing, 100081, China
2. ICube (UMR7357), UdS, CNRS, 300 Bld Sébastien Brant, CS10413, Illkirch, 67412, France
3. hanxiaojing_1988@163.com
4. duansibo@caas.cn
5. lizhaoliang@caas.cn

ABSTRACT *Land surface temperature (LST) plays an important role in land surface processes and is a key input for physically based retrieval algorithms of important hydrological states and fluxes such as soil moisture and evaporation. Compared to thermal signal, microwave signal can penetrate non-precipitating clouds, thereby providing a better representation of LST under nearly all sky conditions. However, previous study shows atmospheric impact on passive microwave brightness temperature is not negligible for the high frequency. A multi-channel method for retrieving LST is proposed using the passive microwave ground brightness temperature and a favorable accuracy with RMSE=1.58 K have been obtained in this study. To analyze the atmospheric impact on LST retrieval, the proposed method is performed using ground brightness and satellite measured brightness temperature, respectively. The results demonstrate that the atmospheric impact leads to an error of 0.73 K when retrieving LST using proposed method. Thus, the atmospheric correction is necessary.*

1 INTRODUCTION

Land surface temperature (LST) is a key physical measurement in surface energy and water balance processes at regional and global scales (Coll et al. 2016; Duan et al. 2014; Wan and Li 1997). It plays a key role in various studies, including studies of climatology, hydrology, meteorology, ecology, agriculture, public health, and environmental monitoring (Anderson et al. 2008; Li et al. 2009; Weng and Grody 1998). Currently, a number of studies have been performed to retrieve LST from remotely sensed data. Compared to the infrared signal, the passive microwave signal is not significantly affected by the atmosphere, thus, passive microwave remote sensing is widely used to estimate the LST without considering the atmospheric impact. For instance, Holmes et al. (2009) proposed an empirical algorithm for global land surface temperature retrieval using the vertically polarized brightness temperature at 37 GHz. However, previous study (Han et al. 2017; Liu et al. 2013) showed that the atmospheric impact on brightness temperature is not negligible for the high frequency. It leads to large error of LST which retrieved from the brightness temperature at high frequency.

Thus, the objectives of this study are (1) to retrieve the LST using ground brightness temperature and (2) analyze the atmospheric impact on the LST retrieval. This article is organized as follows. Section 2 describes the simulated data. Section 3 present the multi-channel method for retrieving LST. Section 4 provides an analysis of the atmospheric impact on the LST retrieval, and conclusions are presented in the last section.

2 SIMULATED DATA

To analyze the variation of emissivity over a spectrum of microwave frequencies, which plays a key role in the LST retrieval method, we used AIEM to simulate different surface conditions. To consider more land surface types, reasonable variations of sand volume content, clay volume content, surface roughness, soil moisture and land surface temperature are necessary; thus, 6 types of soil with different sand and clay volume content were selected, surface root mean square height was varied from 1.25 to 3 cm at steps of 0.25 cm, surface correlation length was varied from 12.5 to 30 cm at steps of 2.5 cm, soil moisture was varied from 0.02 to 0.38 m^3/m^3 at steps of 0.06 m^3/m^3 and land surface temperature was equal to the atmospheric bottom temperature. The output of this model is surface emissivity.

To analyze the atmospheric impact on the LST retrieval, we used Monortm to simulate different atmospheric conditions. We selected 4 atmospheric profiles from the TIGR dataset. The bottom temperatures varied from 273 K to 313 K, and water vapor varied from 0.09 to 6.02 cm. To consider both clear sky and cloudy

atmospheric conditions, reasonable CLW was added to atmospheric layers at the height less than 5 km and it was added to a single atmospheric layer for each situation. CLW is ranging from 0-0.5 mm at steps of 0.1 for the atmospheric layers at the height less than 2 km, 0-0.4 mm at steps of 0.1 mm for the atmospheric layers at the height from 2 km to 4 km, and 0-0.3 mm at steps of 0.1 mm for the atmospheric layers at the height from 4 km to 5 km. The clear sky conditions appear when CLW is equal to 0 and CLW larger than 0 describes the cloudy conditions. The outputs of this model are upwelling and downwelling atmospheric brightness temperature and transmittance.

Thus, the simulated dataset can be generated by combining the outputs from AIEM and Monortm using the radiative transfer model. It includes the satellite measured brightness temperature, ground brightness temperature, upwelling and downwelling atmospheric brightness temperature, transmittance, land surface temperature and emissivity (Figure 1). It is noted that the incidence angle at the surface was set as 53 ° according to the configuration of commonly used passive microwave sensors, and seven commonly used frequencies, i.e., 1.4 GHz, 6.93 GHz, 10.65 GHz, 18.7 GHz, 23.8 GHz, 36.5 GHz and 89.0 GHz, were selected when conducting the simulation.
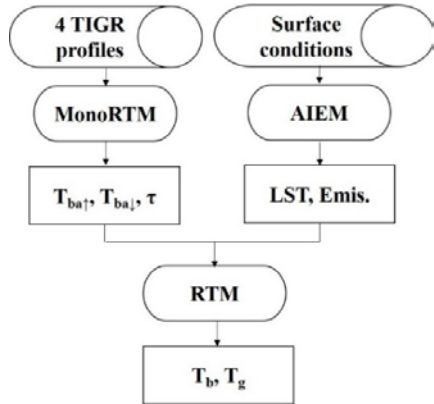
Figure 1. Flowchart for generating the simulated data.

3 MULTI-CHANNEL METHOD

Wang and Schmugge (1980) developed a model for computing the emissivity of wet surface based on the dielectric constant of water (which increase with the frequency) and the field capacity of the soil. The lowest emissivity occurs when the surface becomes saturated with water, as in the case of flooded land (Entekhabi et al. 1994). Figure 2 shows how emissivity changes as a function of frequency and the soil moisture. As the soil moisture increase, the emissivity decrease and the slope of emissivity between low and high frequencies increases.
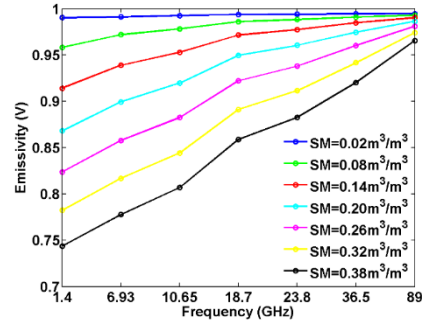
Figure 2. A relationship of emissivity over commonly used frequencies for eight surface soil moisture (the sand volume content is 0.14, the clay volume content is 0.57, the land surface temperature is 273.15 K, the correlation length is 12.5 cm, root mean square height is 1.25 cm).

Thus, for a given surface soil moisture, it is evident that the emissivity can be expressed as:

$$\varepsilon_s(\upsilon_1) = \varepsilon_0(\upsilon_1) - \left[\varepsilon_0(\upsilon_3) - \varepsilon_s(\upsilon_3)\right] - \left[\varepsilon_s(\upsilon_3) - \varepsilon_s(\upsilon_2)\right] \\ - \left[\varepsilon_s(\upsilon_2) - \varepsilon_s(\upsilon_1)\right] - \left[\varepsilon_0(\upsilon_1) - \varepsilon_0(\upsilon_3)\right] \tag{1}$$

where υ_1, υ_2 and υ_3 represent the 18.7, 36.5 and 89 channels, respectively, ε_s is the surface emissivity, ε_0 is the emissivity of dry surface (soil moisture=0.02 m^3/m^3).

To simplified this expression, we focused on the items $\left[\varepsilon_0(\upsilon_1) - \varepsilon_0(\upsilon_3)\right]$ and $\left[\varepsilon_0(\upsilon_3) - \varepsilon_s(\upsilon_3)\right]$. The item $\left[\varepsilon_0(\upsilon_3) - \varepsilon_s(\upsilon_3)\right]$ expresses the soil moisture impact on the emissivity, which is related to the slope of emissivity between two frequencies, figure 3 show the scatter plots of the $\left[\varepsilon_0(\upsilon_3) - \varepsilon_s(\upsilon_3)\right]$ and $\left[\varepsilon_s(\upsilon_3) - \varepsilon_s(\upsilon_2)\right]$ which indicates the slope of emissivity between two frequencies, it demonstrates that the relationship between $\left[\varepsilon_0(\upsilon_3) - \varepsilon_s(\upsilon_3)\right]$ and $\left[\varepsilon_s(\upsilon_3) - \varepsilon_s(\upsilon_2)\right]$ can be approximated by a quadratic relationship as follows:

$$\left[\varepsilon_0(\upsilon_3) - \varepsilon_s(\upsilon_3)\right] = \alpha\left[\varepsilon_s(\upsilon_3) - \varepsilon_s(\upsilon_2)\right]^2 \\ + \beta\left[\varepsilon_s(\upsilon_3) - \varepsilon_s(\upsilon_2)\right] + \gamma \tag{2}$$

The coefficients (α=5.9227, β=0.4002, γ=0.0011) were determined by polynomial fitting using the simulated data. A favorable accuracy with RMSE=0.003 is achieved, which can meet the accuracy requirement.

Figure 4 shows the histogram of the $\left[\varepsilon_0(\upsilon_1) - \varepsilon_0(\upsilon_3)\right]$, it indicates that this item is less than 0.01 for all the surface conditions, thus, it can be replaced using the mean C=-0.003.

261
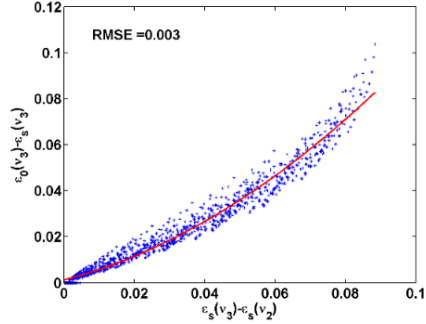
Figure 3. Scatter plots of $\left[\varepsilon_0(\upsilon_3)-\varepsilon_s(\upsilon_3)\right]$ vs $\left[\varepsilon_s(\upsilon_3)-\varepsilon_s(\upsilon_2)\right]$ (the fitting line is in red)
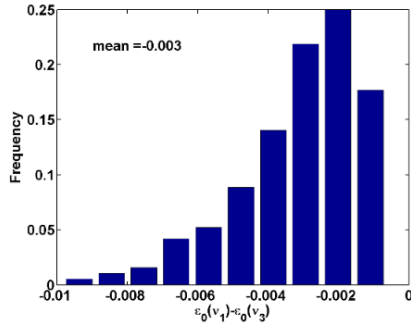
Figure 4. Histogram of the $\left[\varepsilon_0(\upsilon_1)-\varepsilon_0(\upsilon_3)\right]$.

The emissivity of υ_1 can be rewritten as:

$$\varepsilon_s(\upsilon_1)=\varepsilon_0(\upsilon_1)-\left[\varepsilon_s(\upsilon_2)-\varepsilon_s(\upsilon_1)\right]-(\beta+1)\left[\varepsilon_s(\upsilon_3)-\varepsilon_s(\upsilon_2)\right] \\ -\alpha\left[\varepsilon_s(\upsilon_3)-\varepsilon_s(\upsilon_2)\right]^2-(\gamma+C) \quad (3)$$

To formulate a surface temperature algorithm, we express the brightness temperature measurement as:

$$T_b(\upsilon)=\varepsilon_s(\upsilon)T_s \quad (4)$$

where T_b is the brightness temperature at frequency υ, T_s is the land surface temperature. This equation assumes negligible atmospheric effects over land compared to the variations in surface temperature and emissivity. Since the smallest variation in emissivity occurs for vertical polarization, this polarization is preferred when deriving surface temperature. Thus, substituting (4) into (3) and solving for T_s, we obtain:

$$T_s=\frac{\left\{\begin{array}{l}T_b(\upsilon_1)+\left[T_b(\upsilon_2)-T_b(\upsilon_1)\right]+(\beta+1)\left[T_b(\upsilon_3)-T_b(\upsilon_2)\right]\\+\alpha\left[T_b(\upsilon_3)-T_b(\upsilon_2)\right]^2\end{array}\right\}}{\varepsilon_0(\upsilon_1)-(\gamma+C)} \quad (5)$$

To reduce the error caused by above approximate expression, we added a coefficient of $\left[T_b(\upsilon_2)-T_b(\upsilon_1)\right]$ and a constant, and re-determinated all the coefficients by nonlinear fitting using the simulated data.

Thus, T_s can be expressed as:

$$T_s=\frac{\left\{\begin{array}{l}T_b(\upsilon_1)+a\left[T_b(\upsilon_2)-T_b(\upsilon_1)\right]+b\left[T_b(\upsilon_3)-T_b(\upsilon_2)\right]\\+c\left[T_b(\upsilon_3)-T_b(\upsilon_2)\right]^2+d\end{array}\right\}}{\varepsilon_0(\upsilon_1)-e} \quad (6)$$

The coefficients a=1.315, b=0.896, c=0.0315, d=0.55, e=-0.004 are achieved using the simulated data. Figure 5 shows the distributions of the differences between the actual and estimated values of T_s. It shows that a favorable accuracy was obtained with RMSE=0.83 K.
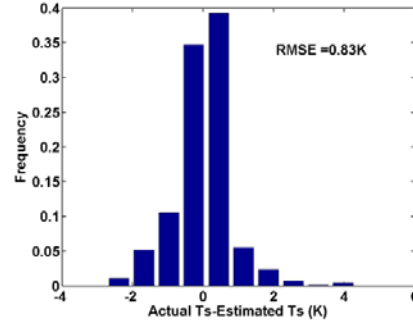
Figure 5. Histogram of the difference between the actual and estimated values of T_s from equation (6).

Since $\varepsilon_0(\upsilon_1)$ is related to the soil sand and clay volume content, and the surface roughness, it is difficult to accurately obtained. Moreover, the variation of $\varepsilon_0(\upsilon_1)-e$ is slight (Figure 6), we replace this item using the mean.
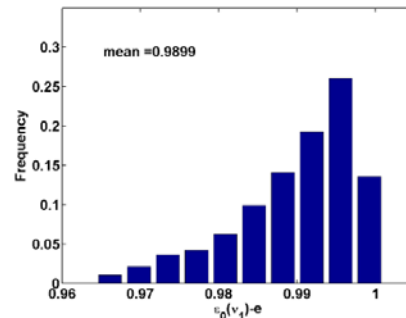
Figure 6. Histogram of the $\varepsilon_0(\upsilon_1)-e$.

Thus, T_s can be rewritten as:

$$T_s = T_b(\upsilon_1) + a' \left[T_b(\upsilon_2) - T_b(\upsilon_1) \right] + b' \left[T_b(\upsilon_3) - T_b(\upsilon_2) \right] + c' \left[T_b(\upsilon_3) - T_b(\upsilon_2) \right]^2 + d' \tag{7}$$

The coefficients a'=1.137, b'=1.186, c'=0.0270, d'=3.18 are obtained using the simulated data. Comparing the actual T_s and estimated T_s from equation (7), an accuracy of RMSE=2.53 K is obtained (Figure 7), which is a little worse than the accuracy of equation (6) due to the approximate expression of $\varepsilon_0(\upsilon_1)$. It is evident that multi-channel method can be used to retrieve LST and a favorable accuracy have been obtained using the simulated data.
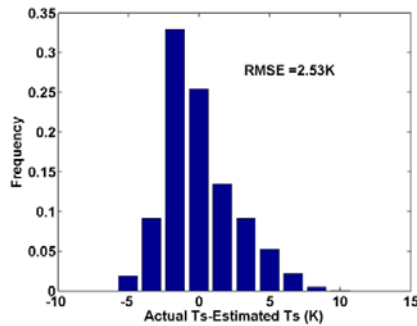
Figure 7. Histogram of the difference between the actual and estimated values of T_s from equation (7).

4 ATMOSPHERIC IMPACT ON LST RETRIEVAL

For the real earth-atmosphere system, previous study (Han et al. 2017) showed that the atmospheric impact on ground brightness temperature is not negligible, especially at high frequency. To analyze the atmospheric impact on LST retrieval, we performed the multi-channel method using the satellite measured brightness temperature and ground brightness temperature, respectively. We suppose the atmosphere is negligible, the three-channel method can be written as:

$$T_s = T_b'(\upsilon_1) + A \left[T_b'(\upsilon_2) - T_b'(\upsilon_1) \right] + B \left[T_b'(\upsilon_3) - T_b'(\upsilon_2) \right] + C \left[T_b'(\upsilon_3) - T_b'(\upsilon_2) \right]^2 + D \tag{8}$$

where T_b is the satellite measured brightness temperature. The coefficients A=1.366, B=0.555, C=0.0208, D=5.97 are obtained by nonlinear fitting using the simulated method. Comparing the actual T_s and estimated T_s from equation (8), an accuracy of RMSE=2.31 K is obtained (Figure 8).
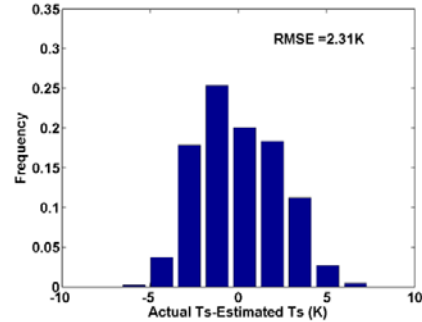
Figure 8. Histogram of the difference between the actual and estimated values of T_s from equation (8).

Assuming that atmosphere is not negligible, the multi-channel method can be rewritten as:

$$T_s = T_g(\upsilon_1) + A' \left[T_g(\upsilon_2) - T_g(\upsilon_1) \right] + B' \left[T_g(\upsilon_3) - T_g(\upsilon_2) \right] + C' \left[T_g(\upsilon_3) - T_g(\upsilon_2) \right]^2 + D' \tag{9}$$

where $T_g = \dfrac{T_b' - T_{ba\uparrow}}{\tau}$, $T_{ba\uparrow}$ is the upwelling atmospheric brightness temperature, τ is the transmittance. The coefficients A'=1.470 B'=0.722 C'=0.0112 D'=1.15 are determined using the simulated data. Comparing the actual T_s and estimated T_s from equation (9), an accuracy of RMSE=1.58 K is obtained (Figure 9). Obviously, atmospheric correction is necessary, and atmospheric impact leads to an error of 0.73 K for the LST.
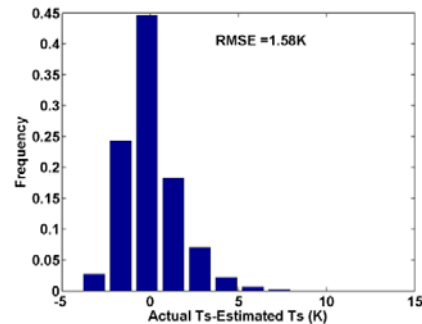
Figure 9. Histogram of the difference between the actual and estimated values of T_s from equation (9).

5 CONCLUSION

This article proposed a multi-channel method based on the relationship of emissivity over spectrum of commonly used frequencies. The results show that high accuracy with RMSE=0.83 K is obtained when $\varepsilon_0(\upsilon_1)$ is estimated accurately. If $\varepsilon_0(\upsilon_1)$ is approximately expressed using the

mean, the accuracy with RMSE=2.31 K is achieved when using the satellite measured brightness temperature, and RMSE= 1.58 K is obtained when using the ground brightness temperature. The atmospheric impact leads to an error of 0.73 K. It is evident that the atmospheric correction is necessary when retrieving LST from high frequency.

REFERENCES

Anderson, M.C., Norman, J.M., Kustas, W.P., Houborg, R., Starks, P.J., & Agam, N. (2008). A thermal-based remote sensing technique for routine mapping of land-surface carbon, water and energy fluxes from field to regional scales. Remote Sensing of Environment, 112, 4227-4241.

Coll, C., Garcia-Santos, V., Niclos, R., & Caselles, V. (2016). Test of the MODIS land surface temperature and emissivity separation algorithm with ground measurements over a rice paddy. IEEE Transactions on Geoscience and Remote Sensing, 54, 3061-3069.

Duan, S.B., Li, Z.L., Tang, B.H., Wu, H., & Tang, R.L. (2014). Generation of a time-consistent land surface temperature product from MODIS data. Remote Sensing of Environment, 140, 339-349.

Entekhabi, D., Nakamura, H., & Njoku, E.G. (1994). Solving the inverse problem for soil moisture and temperature profiles by sequential assimilation of multi frequency remotely sensed observations. IEEE Transactions on Geoscience and Remote Sensing, 32, 438-448.

Han, X.J., Duan, S.B., & Li, Z.L. (2017). Atmospheric correction for retrieving ground brightness temperature at commonly-used passive microwave frequencies. Optics Express, 25, A36-A57.

Holmes, T.R.H., De Jeu, R.A.M., Owe, M., & Dolman, A.J. (2009). Land surface temperature from Ka band (37 GHz) passive microwave observations. Journal of Geophysical Research-Atmospheres, 114.

Li, Z.L., Tang, R.L., Wan, Z.M., Bi, Y.Y., Zhou, C.H., Tang, B.H., Yan, G.J., & Zhang, X.Y. (2009). A Review of Current Methodologies for Regional Evapotranspiration Estimation from Remotely Sensed Data. Sensors, 9, 3801-3853.

Liu, Z.L., Wu, H., Tang, B.H., Qiu, S., & Li, Z.L. (2013). Atmospheric corrections of passive microwave data for estimating land surface temperature. Optics Express, 21, 15654-15663.

Wan, Z.M., & Li, Z.L. (1997). A physics-based algorithm for retrieving land-surface emissivity and temperature from EOS/MODIS data. IEEE Transactions on Geoscience and Remote Sensing, 35, 980-996.

Wang, J.R., & Schmugge, T.J. (1980). An empirical model for the complex dielectric permittivity of soils as a function of water content. IEEE Transactions on Geoscience and Remote Sensing, GE-18, 288-295.

Weng, F.Z., & Grody, N.C. (1998). Physical retrieval of land surface temperature using the special sensor microwave imager. Journal of Geophysical Research-Atmospheres, 103, 8839-8848.

ANALYSIS OF THE POTENTIAL OF GNSS-R MEASUREMENTS FOR THE MONITORING OF CONTINENTAL SURFACE CONDITIONS

Mehrez Zribi[1], Erwan Motte[1], Dominique Guyon[2], Jean Pierre Wigneron[2], Nicolas Baghdadi[3], Frédéric Baup[1], Sylvia Dayau[2], Remy Fieuzal[1],

[1]CESBIO (CNRS/UPS/IRD/CNES), 18 av. Edouard Belin, bpi 2801, 31401 Toulouse cedex9, France,
[2]ISPA, INRA-Bordeaux, Villenave d'Ornon 33140, France
[3]IRSTEA, UMR TETIS, 500 rue François Breton, 34093 Montpellier cedex 5, France.

E-mails
Mehrez.zribi@cesbio.cnes.fr
Erwan.motte@cesbio.cnes.fr
guyon@bordeaux.inra.fr
wigneron@bordeaux.inra.fr
nicolas.baghdadi@teledetection.fr

ABSTRACT- *The objective of this study is to analyze the sensitivity of airborne GNSS-R signals to the characteristics of the soil surface and vegetation over agricultural areas. Airborne polarimetric GNSS-R data were acquired in the context of the GLORI'2015 campaign along five flights performed over the June-July 2015 period. Ground measurements of soil surface parameters (moisture content and surface roughness) and vegetation characteristics (Leaf Area Index (LAI), Vegetation Water Content (VWC) and vegetation height) for different cover types (wheat, corn, sunflower …) were collected simultaneously to the airborne measurements. The GNSS-R observables (Signal to Noise Ratio (SNR), Reflectivity) illustrate a moderate to good correlation with the vegetation characteristics (more specifically vegetation height) or the surface soil moisture.*

1 INTRODUCTION

In agricultural areas, soil surface and vegetation cover conditions play an essential role in the understanding of processes related to the soil-vegetation-atmosphere interface and also for different applications related to agricultural management (Koster et al., 2004). Remote sensing has shown a high potential to retrieve land surface parameters (Baghdadi and Zribi, 2016). In this context, the GNSS-R technique based on bistatic radar observations, with the use of opportunity signals coming from global navigation satellite systems, has appeared in the beginning of the 1990s (Martin-Neira et al., 1993, Zavorotny et al., 2014). In the recent years, the GNSS-R technique has been increasingly tested and validated over the land surfaces, using either single antenna SNR measurements from commercial geodetic instruments or using dedicated multi-antennas based on the analysis of the correlation waveforms (Masters et al., 2004, Egido et al., 2012). The GLORI'2015 airborne campaign (Motte et al., 2016), summarized in the present paper, was designed to confirm the results from the previous studies illustrating high potential of GNSS-R to retrieve soil moisture and vegetation propperties. We consider an important ground database with important range of soil moisture, and vegetation cover types.

The main objective of this paper is to investigate interactions between the GNSS-R signals and the soil and vegetation cover at various incidence angles and for various crop types and soil moisture conditions.

In the second section, we present the study site, airborne and ground data. The third section is devoted to the presentation of GNSS-R data processing. The fourth section describes the correlation analysis between in situ data and GNSS-R measurements. Conclusions are gathered in the fifth section.

2 DATASET AND METHODS

2.1 Study site

The study sites are located in southwestern France (Figure 1). The region is governed by a temperate climate, with annual amount of rainfall close to 600 mm, and maximal mean daily air temperature near 25

°C in summer. The study area is highly anthropized, and the surfaces are mainly dedicated to agricultural activities. In our case, we consider two agricultural sites, La Masquère et Marcheprime, the two sites present complementarities in terms of irrigation, the agricultural fields in Marcheprime are irrigated and in Lamasquère are generally non irrigated. During the 20 days of airborne measurements, we consider reference fields with an important diversity of vegetation covers (wheat, sunflower, corn, carrots etc). The selected period of measurements correspond to the maximum of growth of all covers, except wheat cover at senescence. This allows analyzing effect of vegetation dynamic on GNSS-R measurements.

2.2 GNSS-R airborne data

The airborne GNSS-R data presented below was collected with the GLORI Instrument during the GLORI 2015 Campaign (Motte et al., 2016). The GNSS-R GLORI instrument is developed by CESBIO. It is a polarimetric instrument with four channels. Two antennas are connected to the receiver, a first at nadir with the RHCP polarization to receive the direct signal from the GNSS satellites, and a second at zenith for receiving the signals reflected in two polarizations (RHCP and LHCP). Five scientific flights were performed over the studied site on a two weeks span (Figure 1). The aircraft speed was ~100m/s and the altitude above ground was ~600m. The antenna radiation pattern allowed for measurements ranging between 45 and 90° of elevation.

The data was then processed offline to extract the GPS L1 signal waveforms, with a coherent integration time of 20 ms. After compensation for antenna radiation pattern and receiver noise, the individual waveform maxima were averaged incoherently for 240 ms in order to compute the apparent reflectivity as the ratio of incident signal to forward scattered signal.
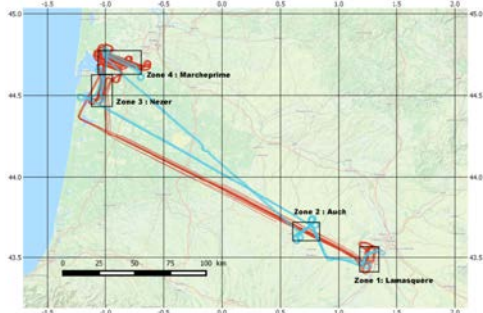
Figure 1: GLORI 2015 flight plan and ground truth collection zones.

2.3 In situ data

Intensive ground truth measurements were performed in collocation with the flights over the two agricultural zones presented above. In situ measurements over reference plots concern soil roughness, soil moisture, and vegetation characteristics (LAI, VWC, height).

3 DATA PROCESSING

The GLORI processing chain is composed of 4 main blocks using raw datastream, GPS ephemeris and flight ancillary data as inputs (Motte et al, 2016):

1. GNSS processing of raw datastream
2. Acquisition and tracking of modulated signal to compute correlation waveforms.
3. Time tagging and extraction of waveform maxima.
4. Processing of the navigation message to get transmission time and extraction of the correlation power.
5. Instrument corrections and incoherent averaging.
6. Correction for antenna gain and instrumental noise, incoherent averaging and computation of reflectivity.
7. Geolocalisation and merging of individual files ;
8. Computation of the footprint location and shape on the surface, merging of individual measurements in a consolidated file.

Three observables are considered for our analysis of GNSS-R sensitivity to land surface parameters:

The apparent reflectivity: it is related to the relative power reflected to the ground. For a polarization pq, the apparent reflectivity Γ_{pq} can be expressed as the ratio of the reflected $Y_{r,q}(\tau,f)$ to direct waveforms $Y_{d,p}(\tau,f)$. In the case of GNSS-R, the right-right and right-left ratios Γ_{rr} and Γ_{rl} represent the co- and cross-polar reflection coefficients. By assuming f to be aligned with the Doppler frequency shift of the direct signal, the apparent surface reflectivity Γ'_{pq} can be obtained as:

$$\Gamma'_{pq} = \left| \left\langle \frac{Y_{r,q}(\Delta\tau,f)}{Y_{d,p}(0,f)} \right\rangle \right|^2 \tag{1}$$

The processing Signal to Noise Ratio (SNR) of the reflected signal, defined as the signal power above the nose level divided by the noise level:

$$SNR = \left(\left| Y_{r,\max} \right| - B_r \right) / B_r \tag{2}$$

Where B_r is the waveform noise floor level.

4 STATISTICAL ANALYSIS

4.1. Sensitivity of GNSS-R observables to soil moisture

In order to limit effects due to elevation angles, The sensitivity of GNSS-R observables (LHCP reflected signal SNR and LHCP reflectivity) to soil moisture is discussed separately for two elevation angle intervals (30°-60° and 60°-90°).

Figure 2a illustrates the sensitivity of LHCP reflected signal SNR measurements over the different crop plots to soil moisture, with a sensitivity ranging from 0.35 to 0.39 dB/ [m^3/m^3] depending on the angle range. The SNR signal dynamic range is of the order of 15dB for the two cases. We observe a small decrease in the sensitivity to soil moisture with increasing elevation angles. This might be caused by the discrepancies in the transmitting signal strength at high elevation angle which is not taken into account in the SNR product. GNSS-R LHCP Reflectivity vs soil moisture is depicted in Figure 2b, with a sensitivity ranging from 0.35 to 0.45 dB/[m^3/m^3] depending on the angle range. The dynamics of GNSS-R signals is above 15dB for the two cases of angle ranges. We observe a small decrease of sensitivity of GNSS-R signals to soil moisture with

the decreasing of elevation angle. This is due to the increasing of vegetation effect for low elevation angles with more attenuation effect of soil scattering.

4.2. Sensitivity to vegetation parameters

In this section, the GNSS-R signals are analyzed as a function of vegetation parameter, namely the height of the plant cover. More precisely, the plant height is divided by the sine of the elevation angle, in order to account for the larger amount of vegetation through which the signal travelled. As for soil moisture, in order to see if elevation angle has an impact on the correlation, we consider two intervals of angles (30-60° and 60-90°), and two observables: LHCP SNR and LHCP Reflectivity.

Figure 3a shows GLORI LHCP SNR sensitivity to vegetation height over all the studied plots. First, we observe a clear signal decreasing trend with increasing vegetation, which is expected from signal scattering and attenuation (increasing optical thickness). We observe a dynamic range of about 10 dB for the 30-60° angles and 8 dB for angles 60-90°. This higher sensitivity at low elevation angle is probably related to the decrease of the effect of the soil component (roughness and moisture).

(a)

(b)
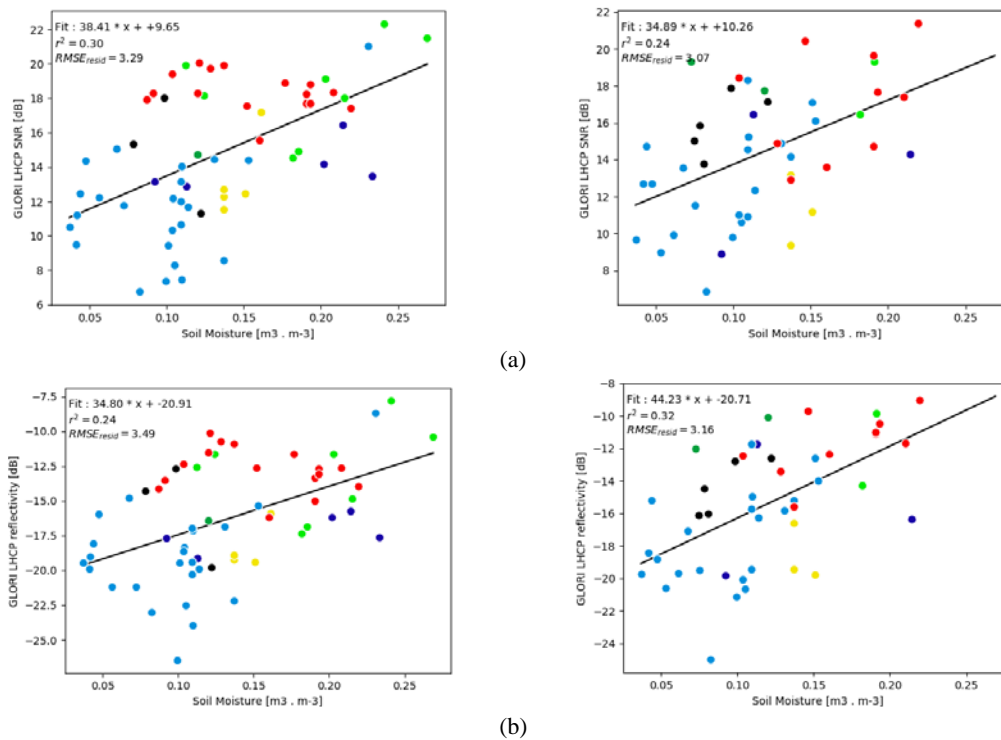
Figure 2: GLORI Observables vs Soil moisture. Left: Elevations 30-60°. Right: Elevation 60-90°. (a) LHCP Signal to Noise Ratio, (b) LHCP reflectivity

267
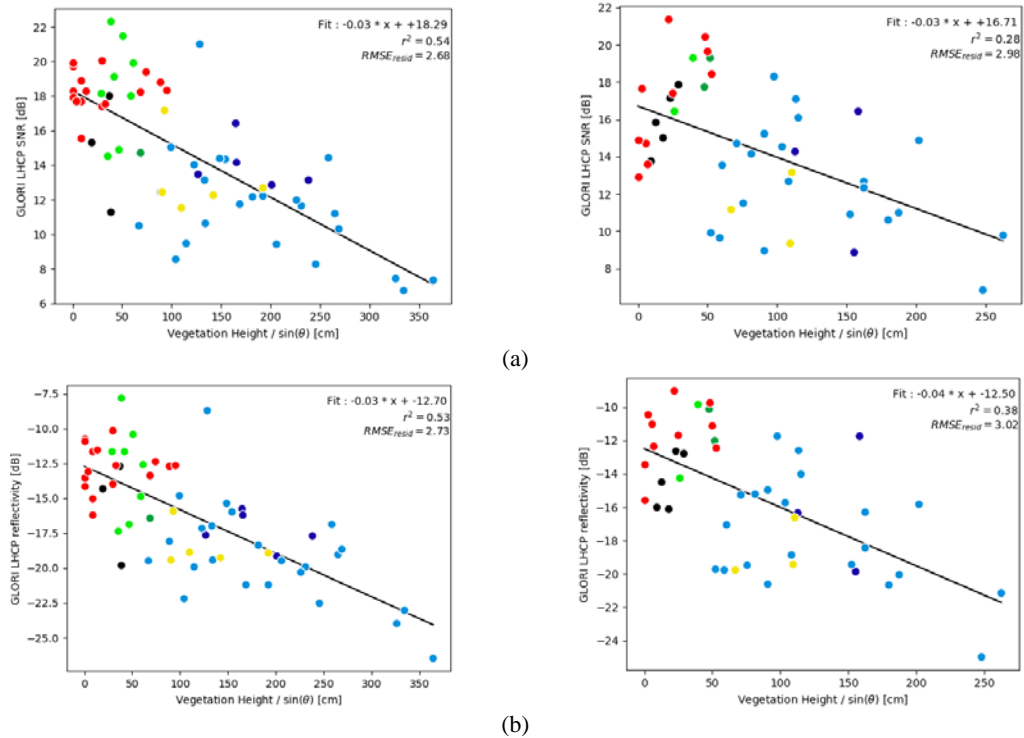
Figure 3: GLORI observables vs vegetation height. Left: Elevations 30-60°. Right: Elevation 60-90°. (a) LHCP Signal to Noise Ratio, (b) LHCP reflectivity

It is accompanied by an increase in the correlation between the GNSS-R signals and the vegetation height, with R^2 equal to 0.54 for low elevations, when it is only 0.28 at high elevations. Similar behavior is observed from LHCP reflectivity depicted on Figure 3 b, with about 10 dB of dynamic range, a sensitivity of about -3dB per meter and better performance at low elevation angles.

5 CONCLUSIONS

This study aimed to confirm the sensitivity of GNSS-R airborne measurements to soil moisture and vegetation parameters. For this purpose, an extensive campaign with collocated measurements of soil moisture and plant parameters was conducted. Sensitivity of GNSS-R measurement to soil moisture content is confirmed even for dense vegetation cover. GNSS-R observables (LHCP reflectivity (Γ), LHCP SNR) increase with the increasing of soil moisture. The sensitivity of GNSS-R observables is increased with increasing of elevation angle for LHCP reflectivity and LHCP SNR. GNSS-R observables are also sensitive to vegetation height parameter. We observe a clear decreasing of GNSS-R observables with vegetation growth. Highest correlation between

height and GNSS observables (LHCP reflectivity and LHCP SNR) are retrieved with low elevation angles. Sensitivities are approximately the same for the two elevation angle intervals.

6 References

Koster, R. D., P. A. Dirmeyer, Z. Guo, G. Bonan, Koster, R.D.; Dirmeyer, P.A.; Guo, Z.; Bonan, G.; Chan, E.; Cox, P.; Gordon, C.T.; Kanae, S.; Kowalczyk, E.; Lawrence, D., 2004, Regions of strong coupling between soil moisture and precipitation. Science, 305, 1138–1140.

Baghdadi, N., and Zribi, M., 2016, *Microwave Remote Sensing of Land Surface : Techniques and Methods.*, 1st ed. ISTE Press, London and Elsevier, Oxford.

M. Martin-Neira, "A Passive Reflectometry and Interferometry System(PARIS)- Application to ocean altimetry," *ESA J.*, vol. 17, no. 4, pp. 331–355, 1993.

Zavorotny, V. U., Gleason, S.? Cardellach, E., and Camps, A., 2014, Tutorial on Remote Sensing Using GNSS Bistatic Radar of Opportunity," *IEEE Geosci. Remote Sens. Mag.*, 2, 8–45.

Masters, D., Axelrad, P., and Katzberg, S.,2004, Initial results of land-reflected GPS bistatic radar measurements in SMEX02, *Remote Sensing of Environment*, 92, 4, 507–520.

Egido, E., Caparrini, M., Ruffini, G., Paloscia, S., Santi, E., Guerriero, L., Pierdicca, N. and Floury, N., 2012, Global navigation satellite systems reflectometry as a remote sensing tool for agriculture, *Remote Sens.*, 4, 2356–2372.

Motte, E., Zribi, M., Fanise, P, Egido, E., Darrozes, J., Al-Yaari, A., Baghdadi, N., Baup, F., Dayau, S., Fieuzal, R., Frison, P. L., Guyon, D., and Wigneron, J. P., 2016, GLORI: A GNSS-R Dual Polarization Airborne Instrument for Land Surface Monitoring, *Sensors*, 16, 5, 732.

A multi-sensor approach for the retrieval of canopy fluorescence and biophysical parameters by inversion of coupled radiative transfer models via optimization

Wouter Verhoef [1], Christiaan van der Tol [1], Elizabeth M. Middleton [2]

[1]*University of Twente, Faculty of Geo-Information Science and Earth Observation (ITC), Water Resources Dept., Enschede, The Netherlands*
[2]*NASA, Goddard Space Flight Center,*
Biospheric Sciences Lab., Greenbelt, MD 20771, USA
e-mail w.verhoef@utwente.nl; c.vandertol@utwente.nl; elizabeth.m.middleton@nasa.gov

ABSTRACT - *The FLuorescence EXplorer (FLEX) satellite mission, selected as ESA's 8th Earth Explorer, has been designed for the measurement of sun-induced fluorescence (SIF) spectra emitted by plants. This will be accomplished through a multi-sensor approach by placing it in a common orbit in tandem with the Sentinel-3 (S3) mission, featuring two sensors, namely OLCI (Ocean and Land Colour Instrument) and SLSTR (Sea and Land Surface Temperature Radiometer). These S3 instruments will be used in combination with the FLORIS imaging spectrometers on board FLEX to provide data useful for atmospheric correction of FLEX data. However, more synergism can be achieved by exploiting the spectral and directional information from all tandem mission instruments together, and this forms an attractive alternative which was explored in a numerical experiment. By employing all combined top-of-atmosphere (TOA) spectral radiance data, one can (i) characterize the relevant optical properties of the atmosphere, (ii) retrieve biophysical canopy properties including accounting for vegetation reflectance anisotropy, and (iii) retrieve a more accurate and consistent canopy SIF. A novel fluorescence retrieval method based on spectral radiative transfer (RT) modeling is proposed, in which coupled RT models are used to simulate TOA radiance spectra. These are then matched with 'measured' spectra in order to retrieve surface fluorescence, along with a suite of biophysical parameters, via model inversion through optimization. By applying coupled RT models of the soil-leaf-canopy and the surface-atmosphere systems, TOA radiance spectra can be simulated for all optical sensors of this tandem mission. In this way, complex effects due to surface reflectance anisotropy and the spectral sampling by the various instruments are properly taken into account by their incorporation in the forward modeling. Next, by model inversion of TOA radiance data via optimization, the most accurate SIF retrievals can be achieved in a consistent manner, along with important canopy level biophysical parameters that help interpret the SIF spectrum, such as chlorophyll content and leaf area index (LAI). The potential of this approach has been explored and the results are presented in this contribution. We found that, with the assumed well-characterized and plausible FLEX/S3 instrument performances, the simultaneous retrieval of biophysical canopy parameters and SIF spectra would be possible with a remarkable accuracy, provided the correct atmospheric characterization is available.*

1 INTRODUCTION

Sun-induced chlorophyll fluorescence (*F*) emitted by plant leaves and vegetation canopies is a sensitive indicator of plant physiological functioning, including photosynthetic activity (Lee et al., 2013). There is considerable interest in *F* for use as a direct measure of actual, rather than potential, photosynthetic activity, and as a unique early warning signal for detection of vegetation stress conditions that reduce primary production (ESA, 2015). Although coarse spatial resolution missions for atmospheric chemistry like GOSAT, OCO-2, GOME-2, SCIAMACHY and TROPOMI can provide global maps of *F* at a few NIR wavelengths, and after considerable aggregation over time and space, FLEX, recently selected as ESA's 8th Earth Explorer Mission and to be launched in 2022, will provide complete spectra of *F* at a spatial resolution of 300m, which is also more ecologically relevant for its application to vegetation functioning monitoring. FLEX will fly in tandem with one of the Sentinel-3 satellites to utilize its optical sensors OLCI and SLSTR (Donlon et al., 2012) for atmospheric correction of the FLEX data, thereby adopting the S3's 27-day repeat cycle and the overpass time of 10:00 a.m. local solar time.

Since the retrieval of *F* spectra from the FLORIS imaging spectrometer data of FLEX is expected to be a challenge, several algorithms have been explored in

the ESA study FLEX - Bridge. Traditional methods of F retrieval make use of the Fraunhofer Line Depth (FLD) principle (Plascyk, 1975) to discriminate F from surface reflectance R. Spectral fitting (SF) is a more advanced method which works over wider spectral intervals and uses mathematical functions to model the smooth spectra of both F and R (Cogliati et al., 2015). Both methods would work exclusively with FLORIS spectral data. However, better exploiting the possible synergy with the S3 optical sensors OLCI and SLSTR would allow the retrieval of biophysical parameters of the vegetation and from these their reflectance spectra R could be simulated using radiative transfer (RT) modeling, instead of using mathematical functions. This approach can be extended by including the atmospheric RT to model the TOA radiance spectra, so that these could be compared to measured spectra.

In this contribution, the SCOPE model (Van der Tol et al., 2009) was used to generate a database of 40 simulated observations of the TOA radiance as measured by the two spectrometers on board the FLEX satellite, FLORIS-WBS (wide band spectrometer) and FLORIS-NBS (narrow band spectrometer), supplemented by the OLCI and SLSTR sensors on board S3. To test the retrieval, a module of the SCOPE model dedicated specifically to soil-canopy RT in the solar-reflective domain, called RTMo, was used in combination with the leaf optical model Fluspect (Vilfan et al., 2016) and a soil spectral reflectance model called BSM, which is based on the Global Soil Vectors of Chongya & Hongliang (2012), enhanced with a soil moisture effect model. For the modeling of canopy fluorescence just four principal component (PC) spectra were used, which had been obtained previously from simulations with the full version of SCOPE. With the four soil parameters, five leaf biophysical parameters (Vilfan et al., 2016), four canopy structure parameters, and four fluorescence PC weights, the combined model has 17 variables in total, which are quite evenly divided over the various soil, leaf, canopy and fluorescence properties. After propagation of the modeled four-stream surface reflectance factors through the atmosphere using the T-18 system of atmospheric RT (Verhoef et al., 2014), the TOA radiance spectra were sampled at the known spectral bands of FLORIS, OLCI and SLSTR using the associate spectral response functions and a two-parameter generic noise model applicable to all optical sensors. For the modeling of atmospheric effects under various conditions, MODTRAN version 5.2.1 (Berk et

al., 2011) was used at a spectral resolution of $1\ cm^{-1}$ to generate the required set of T-18 transfer functions for each database case, including those for the backward looking of the SLSTR sensor under 55 degrees viewing angle.

2 DATABASE GENERATION

The FLEX-Bridge database that has been generated consists of simulated TOA radiance data and various other radiometric data (e.g. TOC reflectances and fluorescence) of interest to study atmospheric correction and alternative F retrieval approaches. Data were generated for five sensors, namely the FLORIS-WBS (187 bands), FLORIS-NBS (288 bands), OLCI (21 bands), SLSTR-N (nadir looking, 6 bands) and SLSTR-B (backward looking, 6 bands). For SLSTR only the six bands in the solar-reflective part of the spectrum were generated. In total 40 cases were defined, consisting of a standard case (no. 19) and 39 deviations from it. The standard case is described in Table 1.

Table 1. The standard case (no. 19)

Parameter	Value	Parameter	Value
Soil moisture	30% Vol.	LIDF	spherical
Leaf Cab	40 µg/cm^2	T_air	19.25 C
Leaf Ccar	10 µg/cm^2	P (surface pressure)	967 mbar
Leaf Cw	0.02 cm^{-1}	Humidity	15.0
Leaf Cdm	0.005 g/cm^2	CO$_2$ conc.	364.7 ppm
Leaf Cs	0.1	O$_2$ conc.	194.9 ppm
Leaf N	1.5	altitude	400m
Vcmax	40	SZA	45°
Rs (stomatal resistance)	5	Visibility	20 km
LAI	2	Aerosol type	Rural

The other cases of the database were generated by changing one or more parameters with respect to the standard case. Some parameters are common to SCOPE and MODTRAN and these were changed in concert to maintain consistency. Also, some changes invoke the simultaneous change of a whole group of parameters, for instance when surface altitude is changed from 400m to 1200m. All cases were labelled to facilitate their quick characterization. Table 2 gives a summary of all cases by means of their label.

Table 2. Summary of database cases

Case	Label	Case	Label
1	SM_5	21	Alt_1200
2	SM_55	22	Vis_05
3	Cab_20	23	Vis_80
4	Cab_80	24	Dry
5	Cw_01	25	Wet
6	Cw_03	26	Maritime
7	Cdm_025	27	Urban
8	Cdm_100	28	Winter
9	Cs05	29	Tropical
10	Cs20	30	SZA_30
11	Vcm_000	31	SZA_60
12	Vcm_100	32	plagio
13	Rs_2	33	extremo
14	Rs_9	34	Cab_5
15	LAI_0.5	35	Cab_10
16	LAI_6	36	LAI_0.25
17	plano	37	LAI_1
18	erecto	38	LAI_3
19	std	39	Vis_10
20	Alt_0000	40	Vis_40

From this summary one can see that first soil moisture, the leaf properties, Vcmax, stomatal resistance, LAI, and the LIDF were changed downward and upward with respect to the standard case, and next surface altitude, atmospheric visibility, humidity, aerosol type, atmospheric profile, solar zenith angle were changed twice as well. In the last nine cases a few more variations of the LIDF, leaf chlorophyll, LAI and atmospheric visibility were included. Leaf carotenoid was always slaved to chlorophyll by taking a quarter of Cab.

Each MODTRAN case was represented by a file containing the atmospheric transfer functions of the T-18 system corresponding to that case. These had been derived from MODTRAN tp7 output files containing simulated radiances at TOA and at BOA for two albedo values each. The TOA radiance is computed from four-stream surface reflectance and fluorescence terms, and 12 of the 18 atmospheric transfer functions according to Eq. (1).

$$L^{\text{TOA}} = T_1(T_2 + T_8 r_{so}) + F_t T_6 + \qquad (1)$$
$$\frac{T_1[(T_9 + T_{14}\overline{r_{sd}})r_{do} + (T_{10}\overline{r_{sd}} + T_{11}\overline{r_{dd}})] + \overline{F_d}(T_7 + T_{13}r_{do})}{1 - r_{dd}T_3}$$

The missing functions T_4 and T_5 are used for the solar and sky irradiance at BOA, and T_{15} to T_{18} are applied in the thermal domain. Why so many functions are needed is because surface anisotropy of reflectance and fluorescence are taken into account and because for finite spectral bands the products of transfer functions have to take into account the apparent violation of Beer's Law in atmospheric absorption bands. The functions T8 to T14 all comprise two or three photon paths, and in atmospheric absorption bands these functions are greater than the products of their corresponding primary functions, as can be clearly seen in Fig. 2 for the oxygen A band. Not taking this affect into account could easily cause errors in the predicted radiance of 100% or more! The greatest effects are found in the term T_{14}, which describes photons travelling directly from the sun to the ground, are reflected by the surroundings, scattered back to earth by the bottom of the atmosphere, are finally reflected by the target and transmitted directly through the atmosphere, to be detected at TOA.
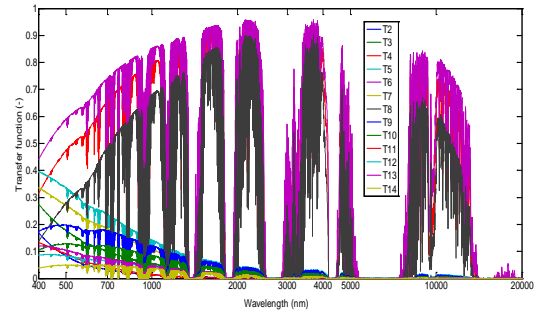
Fig. 1 Functions T_2 – T_{14} for the range 400 – 20000 nm, on a logarithmic scale for the wavelength and a linear scale for transmittance/reflectance
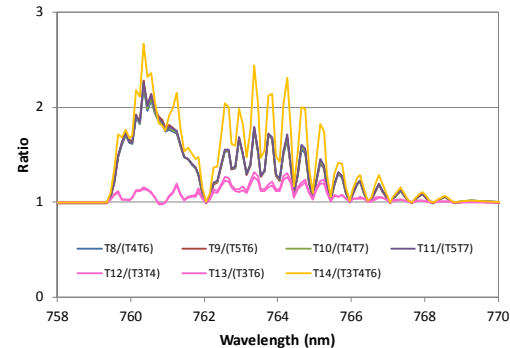
Fig. 2 Ratios of functions T_8 – T_{14} and the products of their corresponding primary functions in the O_2-A band

Realistic amounts of sensor noise were added to the computed LOA radiances by means of a generic signal-dependent two-parameter noise model that is suitable to describe most optical detector types. It is based on the assumption that the noise variance is a linear function of the radiance signal L, which gives a noise standard deviation, also called the noise-equivalent delta radiance, equal to

$$NE\Delta L = \sqrt{aL + b} \quad . \qquad (2)$$

The constants a and b can be fitted to represent a constant noise due to dark current, as well as the photon shot noise typical for electro-optical detectors, or a combination of both. For the sensors simulated in this study, data from which a and b could be derived for all bands have been provided by ESA, and the detector binning applied for the FLORIS spectrometers was mimicked by first generating the non-binned signals and then applying the binning in software. Binning leads to a lower spectral resolution but a higher signal-to-noise ratio. The generic noise model of Eq. (2) is very convenient, since the constants a and b depend mainly the instrument's design and are only slightly wavelength-dependent.

3 RETRIEVAL APPROACH

In the proposed retrieval approach, TOA radiance signals for all sensors are simulated by a chain of coupled models, of which the input parameters are optimized until a sufficient match with the "measured" spectral data (coming from the database) is reached. This approach allows incorporating irreversible effects due to surface anisotropy and spectral sampling over wider bands, such as those of the SLSTR sensor. In the chain of coupled models used during the retrieval, some elements are present that were not part of the set of models used during the generation of the database. The main differences are that (i) during the retrieval a soil spectral model called BSM (brightness-shape-moisture) is applied, while SCOPE used measured soil spectra as input. In SCOPE (ii) fluorescence was generated from the Fluspect leaf model and internal photosynthetic efficiencies, while during the retrieval a statistical model based on PCA was applied. The principal component spectra are shown in Fig. 4. Also (iii) during the retrieval, SCOPE was not used, but only the sub model RTMo in combination with Fluspect without F, which is equivalent to using PROSAIL. A simplified version of Eq. (1) was used to calculate TOA radiances (iv) and the T-18 functions

were convolved with SRFs in advance (v). Besides the addition of sensor noise, all five factors contribute to the independence of the retrieval model from the one used to generate the database, thus preventing "circularity".
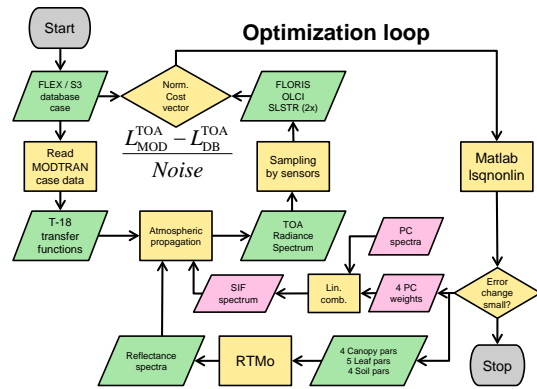
Fig. 3 Optimization loop illustrating the retrieval of F and biophysical parameters from spectra stored in the database
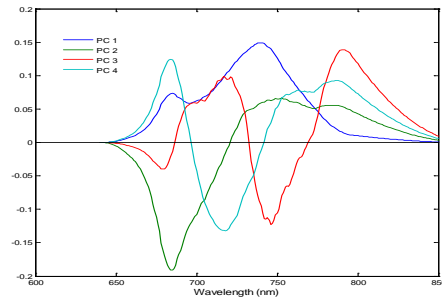
Fig. 4 Spectra of the first four left eigenvectors, PC 1 – 4. The four PCs express different spectral features, such as the overall F level (PC1), the difference between the peaks (PC2) and the depth of the valley between the peaks (PC4)

The cost function C that is minimized during the optimization comprises six parts, five for the five sensors, and one for the *a priori* information. Each part is normalized by its associated uncertainty, given by sensor noise and the uncertainties assumed about the *a priori* values of the 17 variables, as given by Eq. (3) as follows

$$C = \sum_{i=1}^{187}\left(\frac{L_i^{WBS} - L_i^{DB}}{S_i^{WBS}}\right)^2 + \sum_{j=1}^{288}\left(\frac{L_j^{NBS} - L_j^{DB}}{S_j^{NBS}}\right)^2 + \sum_{k=1}^{21}\left(\frac{L_k^{OLCI} - L_k^{DB}}{S_k^{OLCI}}\right)^2$$
$$+ \sum_{l=1}^{6}\left(\frac{L_l^{SLSTR-N} - L_l^{DB}}{S_l^{SLSTR-N}}\right)^2 + \sum_{m=1}^{6}\left(\frac{L_m^{SLSTR-B} - L_m^{DB}}{S_m^{SLSTR-B}}\right)^2 + \sum_{n=1}^{17}\left(\frac{p_n - \mu_n}{\sigma_n}\right)^2$$
$$(3)$$

For the optimization the Matlab function "lsqnonlin" was applied. Jacobians were calculated from the various sub models instead of from the complete model. This turned out to be much more efficient, since otherwise the complete model had to be executed once for each of the 17 input parameters.

4 BAYSIAN ERROR PROPAGATION

To limit the already high complexity of the algorithm, it was assumed that knowledge about the atmospheric transfer functions was perfect. In order to explore this dependence on knowledge about the atmospheric optical properties, a Bayesian error propagation (BEP) analysis was executed. From the results of this analysis it was concluded that the S3 sensors OLCI and SLSTR (both nadir and backward looking) provide sufficient information about the atmosphere as well as the surface to allow a fair estimation of atmospheric transfer functions and surface reflectance even if information about the atmosphere is not available *a priori*.

5 RESULTS

All 40 cases of the database were successfully retrieved by the optimization algorithm, although for some cases the residual radiance error remained higher than the one expected as a result of sensor noise only.

The number of iterations required to reach the solution was about 20, which for the given numbers of variables and spectral bands is encouraging. Fig. 5 shows the retrieved spectra of F as red solid lines, and the reference database spectra for the FLORIS-NBS and WBS spectrometers as circles and + signs, respectively. In the majority of cases the retrieved spectra are correct, and the RMS error is of the order of 0.1 mW m^{-2} sr^{-1} nm^{-1}, comparable to the noise level of the WBS and NBS spectrometers, with a SNR of about 1000. Systematic deviations were found for the planophile canopy and for the case of a hazy atmosphere with 5 km visibility.

A special benefit of the proposed retrieval approach is that biophysical parameters of the soil-leaf-canopy system are retrieved along with fluorescence, which facilitates a meaningful interpretation of the F signal in relation with canopy structure, fAPAR, etc. The quality of these retrievals depends on the parameter and the observational circumstances. Fig. 6 shows for each database case the associated parameter as a black solid line and the corresponding retrieved values as red circles. From this diagram it is clear that important parameters like LAI, the mean leaf inclination (LIDFa) and leaf chlorophyll are retrieved very well, soil moisture is mostly underestimated, and LIDFb (leaf angle distribution bimodality) is overestimated.
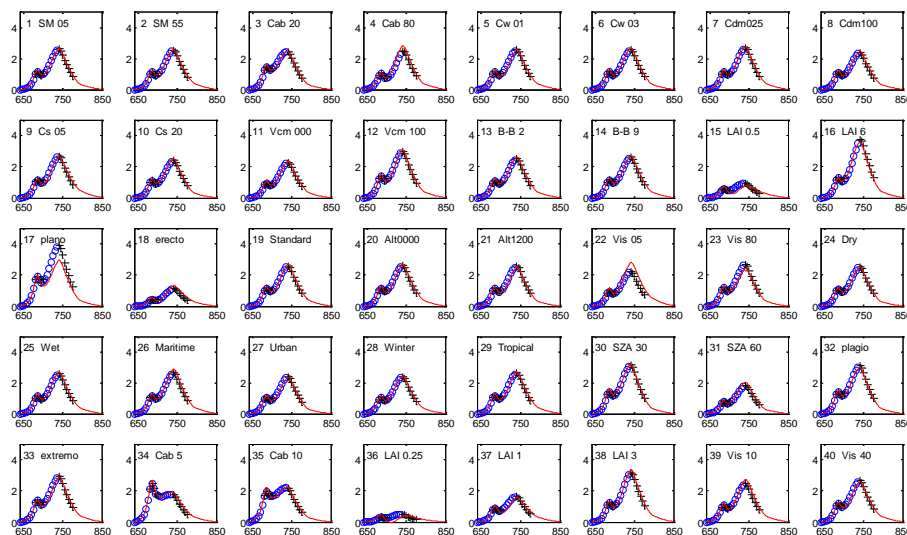
Fig. 5 Retrieved F spectra (red solid lines) compared to simulated FLORIS WBS (blue circles) and NBS (black +'s) data, plotted every 5 nm. The database cases (1 - 40) and their simulated condition/factor labels are indicated. Vertical axes show radiances in mW m^{-2} sr^{-1} nm^{-1}. Horizontal axes show the wavelength in nm
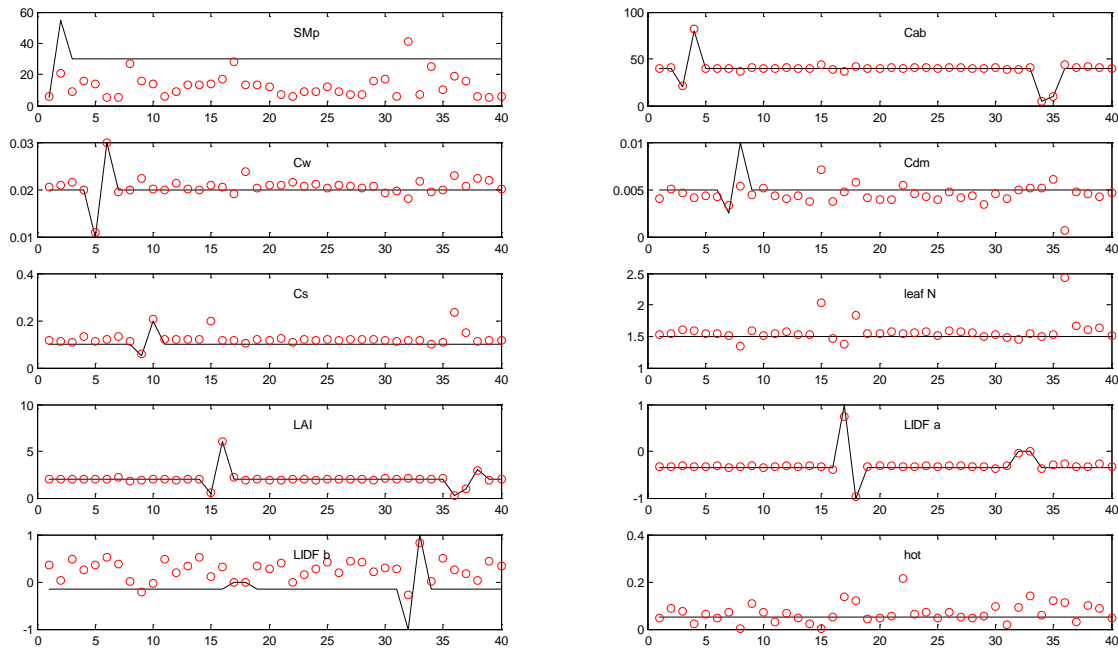
Fig. 6 Retrieved biophysical variables (red circles) and corresponding database inputs used in SCOPE (black solid lines) for the 40 cases

6 CONCLUSION

The integrated approach of combining all optical sensors from FLEX and S3 allows simultaneous retrieval of canopy fluorescence and biophysical parameters by numerical optimization and coupled RT modelling. Atmospheric properties were assumed known, but a BEP analysis indicates that S3 data allow their retrieval (and important canopy properties as well). Matlab takes ~30 s for one optimization, but using compiled code and parallel processing could improve this.

REFERENCES

Berk, A., Anderson, G.P., Acharya, P.K., Shettle, E.P., 2011, MODTRAN 5.2.1 User's Manual, Spectral Sciences Inc., Air Force Research Lab., USA.

Chongya Jiang, Hongliang Fang, 2012, Modeling soil reflectance using a global spectral library, *AGU Fall Meeting,* 3-7 December, 2012, San Francisco.

Cogliati, S., Verhoef, W., Kraft, S., Sabater, N., Alonso, L., Vicent, J., Moreno, J., Drusch, M., Colombo, R., 2015, Retrieval of sun-induced fluorescence using advanced spectral fitting methods, *Remote Sensing of Environment,* 169, 344-357. doi.org/10.1016/j.rse.2015.08.022.

Donlon, C., Berruti, B., Buongiorno, A., Ferreira, M.-H., Féménias, P., Frerick, J., Sciarra, R., 2012, The Global Monitoring for Environment and Security (GMES) Sentinel-3 mission. *Remote Sensing of Environment*, *120*, 37–57. doi:10.1016/j.rse.2011.07.024.

Lee, J.-E., Frankenberg, C., Van der Tol, C., Berry, J.A., Guanter, L., Boyce, C.K., Fisher, J.B., Morrow, E., Worden, J.R., Asefi, S., Badgley, G., Saatchi, S., 2013, Forest productivity and water stress in Amazonia: observations from GOSAT chlorophyll fluorescence. Proc. R. Soc. B. 280: 2130171.

Plascyk, J. A., finally1975, The MK II Fraunhofer line discriminator (FLD-II) for airborne and orbital remote sensing of solar-stimulated luminescence*, Opt. Eng.*, 14*,* 339–346.

Van der Tol, C., Verhoef, W., Timmermans, J., Verhoef, A. and Su, Z., 2009, An integrated model of soil - canopy spectral radiances, photosynthesis, fluorescence, temperature and energy balance. *Biogeosciences* 6 (2009)12 pp. 3109-3129.

Verhoef, W., Van der Tol, C., 2014, Optical-thermal surface-atmosphere radiative transfer modelling with direct-diffuse atmospheric transfer functions and surface reflectance factors, Proc. 4th Int. RAQRS Symposium, 22-26 Sept, 2014, Valencia, Spain.

Vilfan, N., Van der Tol, C., Müller, O., Rascher, U., Verhoef, W., 2016, Fluspect-B: a model for fluorescence, reflectance and transmittance spectra. *Remote Sensing of Environment, 186*, 596-615.

A new semi-empirical radar backscattering model for bare soil surfaces: Baghdadi model

M. Choker[1], Baghdadi N.[1], Zribi M.[2], El Hajj M.[1], Paloscia S.[3], Verhoest N.E.C.[4], Lievens H.[4], Baup F.[2], Mattia F.[5]

[1] *TETIS, IRSTEA, Université de Montpellier, Montpellier, France*
Email: mohammad.choker@teledetection.fr ; nicolas.baghdadi@teledetection.fr; mohammad.el-hajj@teledetection.fr
[2] *CESBIO, 18 av. Edouard Belin, bpi 2801, 31401 Toulouse cedex 9, France*
Email: mehrez.zribi@ird.fr; frederic.baup@cesbio.cnes.fr
[3] *CNR-IFAC, via Madonna del Piano 10, 50019 Sesto Fiorentino, Firenze, Italy*
Email: s.paloscia@ifac.cnr.it
[4] *Laboratory of Hydrology and Water Management, Ghent University, Ghent B-9000, Belgium*
Email: niko.verhoest@UGent.be; hans.lievens@UGent.be
[5] *CNR-ISSIA, via Amendola 122/D, Bari 70126, Italy*
Email: mattia@ba.issia.cnr.it

ABSTRACT - *The aim of this paper is to develop a new semi-empirical radar backscattering model (Baghdadi model) based on the Dubois model using a wide dataset of SAR data and experimental soil measurements for bare soil surfaces in HH, VV and HV polarizations. This dataset contains radar data in L-, C- and X-bands, with incidence angles ranged between 18° and 57°. The proposed model uses a formulation of radar signals based on physical principles that were validated in numerous studies.*
In comparison to Dubois model, results obtained with the new model are more accurate. The bias and the RMSE decrease for both HH and VV polarizations. The RMSE decreases from 3.8 dB to 2.0 dB for HH and from 2.8 dB to 1.9 dB for VV. In addition, the high over- and under-estimations of radar backscattering coefficients observed with the Dubois model according to soil moisture, surface roughness and radar incidence angle are clearly eliminated with the new model. Based on the same type of expression as that used for HH and VV, a radar signal in HV polarization was also proposed.

1 INTRODUCTION

Soil moisture content plays an important role in meteorology, hydrology, agronomy, agriculture, and risk assessment. This soil parameter can be estimated using synthetic aperture radar (SAR). Today, it is possible to obtain SAR data for global areas at high spatial and temporal resolutions with free and open access Sentinel-1 satellites (6 days with the two Sentinel-1 satellites, at 10 m spatial resolution).

The retrieval of soil moisture content and surface roughness requires the use of radar backscatter models capable of correctly modeling the radar signal for a wide range of soil parameter values. This estimation from imaging radar data implies the use of backscattering electromagnetic models, which can be physical, semi-empirical or empirical.

The aim of this study is to develop a robust, empirical radar backscattering model based on the Dubois model (Dubois et al., 1995). The performance of the Dubois model was firstly analyzed using a large dataset acquired at several study sites by numerous SAR sensors. Next, a new semi-empirical backscattering model (Baghdadi model) was proposed for bare soil in HH, VV, and HV polarizations.

The dataset is described in section 2. Section 3 analyzes the performance of Dubois model. The new model is proposed and its performance evaluated in section 4. Finally, section 5 presents the conclusion.

2 DATASET DESCRIPTIONS

2.1 Study Areas

A wide dataset composed of AIRSAR, SIR-C, JERS-1, PALSAR-1, ESAR, ERS, RADARSAT, ASAR and TerraSAR-X acquisitions over numerous agricultural sites in France, Italy, Germany, Belgium, Luxembourg, Canada and Tunisia have been used in this research work. In addition, in situ measurements of soil moisture and surface roughness were carried out simultaneously to SAR acquisitions over bare soil surfaces.

2.2 Satellite Data

A large number of L-, C- and X-band images (approximately 1.25 GHz, 5.3 GHz and 9.6 GHz, respectively) were acquired between 1994 and 2014 with different incidence angles (between 18° and 57°) and in HH, VV and HV polarizations. The spatial resolution of SAR images is between 1 m and 30 m (Table 1). Images were first radiometrically calibrated to enable the extraction of the backscattering coefficients (σ^0). Then, the mean backscattering coefficients were computed from calibrated SAR images by linearly averaging the σ^0 values of all pixels within the plot.

2.3 Field Data

Field measurements of soil moisture and surface roughness have been collected from bare plots selected over the study areas. Each plot is a homogeneous surface (similar soil type, moisture content and surface roughness) of around one hectare or more. In situ measurements of soil moisture (*mv*, in vol. %) were carried out for a soil layer of 5 cm or 10 cm in each reference plot by using both the gravimetric method or a calibrated TDR (time domain reflectometry) probe. For each bare soil reference field the average soil moisture (*mv*) of all samples was calculated. The soil moisture ranged between 2 vol. % and 47 vol. %.

Roughness measurements were carried out by using laser or needle profilometers (mainly 1 m and 2 m long, and with 1 cm and 2 cm sampling intervals); while for some in situ measurement campaigns, a meshboard technique was used. Several roughness profiles along and across the direction of tillage were acquired in each reference field. The standard deviation of surface heights (Hrms) and the correlation length (L) were calculated by using the mean of all experimental correlation functions. In our dataset, Hrms ranged from 0.2 cm to 9.6 cm.

A total of 1569 experimental data acquisitions with radar signal, soil moisture content and roughness were available for HH polarization, 930 for VV polarization, and 605 for HV polarization.

3 ANALYSIS OF THE DUBOIS MODEL

3.1 Description of the Dubois model

Dubois et al. (1995) proposed an empirical model to model radar backscatter coefficients in HH and VV polarizations (σ^0_{HH} and σ^0_{VV}) for bare soil surfaces. The expressions of σ^0_{HH} and σ^0_{VV} depend on the radar wave incidence angle (θ, in radians), the real part of the soil dielectric constant (ε), the rms surface height of the soil (Hrms), the radar wavelength (λ=2π/k, where k is the radar wavenumber):

$$\sigma^0_{HH} = 10^{-2.75} \left(\frac{\cos^{1.5}\theta}{\sin^5\theta} \right) 10^{0.028\varepsilon\tan\theta} \left(k\,Hrms\sin\theta \right)^{1.4} \lambda^{0.7} \qquad (1)$$

$$\sigma^0_{VV} = 10^{-2.35} \left(\frac{\cos^3\theta}{\sin^3\theta} \right) 10^{0.046\varepsilon\tan\theta} \left(k\,Hrms\sin\theta \right)^{1.1} \lambda^{0.7} \qquad (2)$$

σ^0_{HH} and σ^0_{VV} are given in a linear scale. λ is in cm. The validity of the Dubois model is defined as follows: kHrms ≤ 2.5, mv ≤ 35 vol. %, and θ ≥ 30°.

3.2 Comparison between simulated and real data

The analysis of the Dubois model shows an overestimation of the radar signal by 0.7 dB in HH polarization and an underestimation of the radar signal by 0.9 dB in VV polarization for all data combined (Table 1). The results show that the overestimation in HH is of the same order for L-, C- and X-bands (between 0.6 dB and 0.8 dB). For the L-band, a slight overestimation of approximately 0.2 dB of SAR data is observed in VV polarization. Also in VV polarization, Dubois model based simulations underestimate the SAR data in C- and X-bands by approximately 0.7 dB and 2.0 dB, respectively.

	Dubois for HH		Dubois for VV	
	Bias (dB)	RMSE (dB)	Bias (dB)	RMSE (dB)
FOR ALL DATA	-0.7	3.8	+0.9	2.8
L-BAND	-0.8	2.9	-0.2	2.3
C-BAND	-0.6	3.7	+0.7	2.6
X-BAND	-0.7	4.1	+2.0	3.2
KHRMS < 2.5	+0.4	3.4	+1.3	2.9
KHRMS > 2.5	-2.7	4.5	-0.1	2.5
MV < 20 VOL.%	-2.0	4.3	+0.9	2.8
MV > 20 VOL.%	+0.5	3.2	+0.9	2.8
θ < 30°	-4.1	5.4	-0.6	2.9
θ > 30°	+0.6	3.0	+1.5	2.7

Table 1. Comparison between the Dubois model and real data. Bias = real data – model.

The RMSE is approximately 3.8 dB and 2.8 dB in HH and VV, respectively (Table 1). The analysis of the RMSE according to the radar frequency (L, C and X separately) shows an increase of the RMSE with the radar frequency in HH (2.9 dB in L-band, 3.7 dB in C-band, and 4.1 dB in X-band). In VV polarization, the quality of Dubois simulations (RMSE) is similar for L- and C-bands but is less accurate in X-band (2.3 dB in L-band, 2.6 dB in C-band, and 3.2 dB in X-band).

Moreover, the analysis between Dubois model simulations and SAR data is done according to soil roughness, soil moisture and incidence angle (Figures 1 and 2).
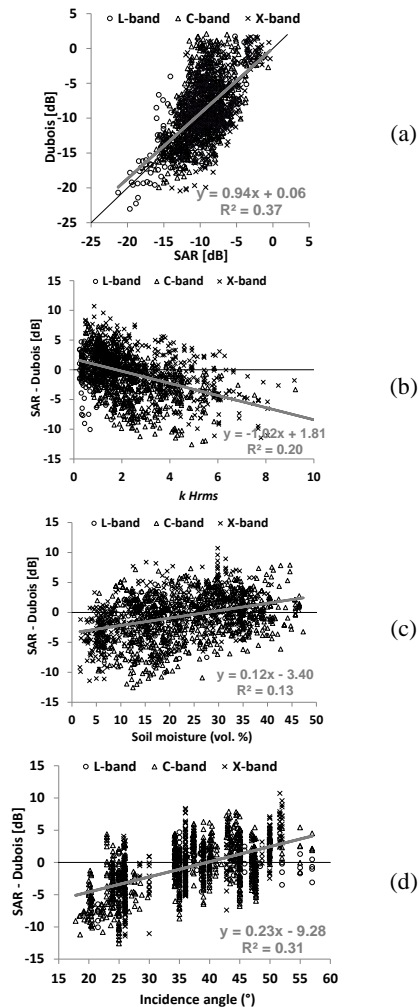
Figure 1. For HH polarization, (a) comparison between radar backscattering coefficients calculated from SAR images and estimated from the Dubois model, (b) difference between the SAR signal and the Dubois model relative to soil roughness (k*Hrms*), (c) difference between the SAR signal and the Dubois model relative to soil moisture (*mv*), (d) difference between the SAR signal and the Dubois model relative to incidence angle.

The results show a slight underestimation of the radar signal by the Dubois model in the case of kHrms lower than 2.5 (Dubois validation domain) for both HH and VV polarizations (Figures 1b, 2b; Table 1). For surfaces with a roughness kHrms greater than 2.5, an overestimation of the radar signal is obtained with the Dubois model in HH while the model simulates correctly in VV (Figures 1b, 2b; Table 1). Higher under- and overestimations are observed in HH than they are in VV (reach approximately 10 dB in HH).
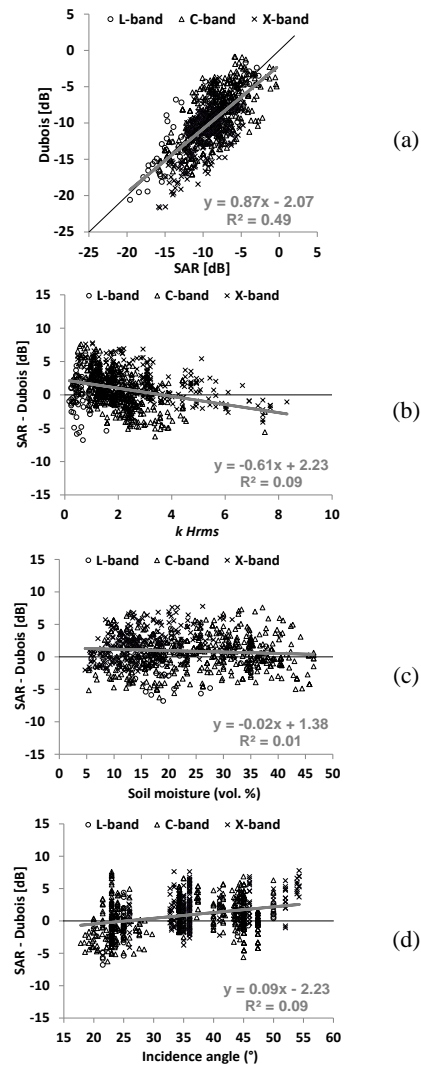
Figure 2. For VV polarization, (a) comparison between radar backscattering coefficients calculated from SAR images and estimated from the Dubois model, (b) difference between the SAR signal and the Dubois model relative to soil roughness (*kHrms*), (c) difference between the SAR signal and the Dubois model relative to soil moisture (*mv*), (d) difference between the SAR signal and the Dubois model relative to incidence angle.

Analysis of the error as a function of soil moisture (mv) shows that for both VV-polarized data, whatever the mv-values, and HH-polarized data with mv-values higher than 20 vol.%, the observed bias between real and simulated data is small (Figures 1c, 2c; Table 1). However, a strong overestimation of the radar signal is observed by the Dubois model in HH for mv-values lower than 20 vol.% (-2.0 dB, Table 1).

Finally, the discrepancy between SAR and the model is higher in HH for incidence angles lower than 30° (outside of the Dubois validity domain) than for incidence angles higher than 30° (Table 1). The Dubois model strongly overestimates the radar signal in HH for incidence angles lower than 30° but better agreement is found with the measured data for incidence angles higher than 30° (Figures 1d, 2d; Table 1). In VV polarization, the Dubois model slightly overestimates the radar signal for incidence angles lower than 30° and underestimates the signal for incidence angles higher than 30° by +1.5 dB (Figures 1d, 2d; Table 1).

In conclusion, the Dubois model simulates VV better than HH (RMSE=2.8 and 3.8 dB, respectively). The disagreements observed between the Dubois model and measured data are not limited to data that are outside the optimal validity domain of the Dubois model.

4 NEW EMPIRICAL MODEL

4.1 Methodology

The new model uses the dependency observed between the SAR signal and soil parameters. For bare soils, the backscattering coefficient depends on soil parameters (roughness and moisture) and SAR instrumental parameters (incidence angle, polarization and wavelength). The radar signal in pq polarization (p and q = H or V, with HV=VH) can be expressed as the product of three components:

$$\sigma_{pq}^{\circ} = f_{pq}(\theta)\, g_{pq}(mv, \theta)\, \Gamma_{pq}(kHrms, \theta) \qquad (3)$$

The relation between the radar backscatter and the incidence angle (θ) can be expressed by $f_{pq}(\theta) = \alpha(cos\,\theta)^{\beta}$ (Baghdadi et al., 2001).

In linear scale, the relationship $g_{pq}(mv, \theta)$ between the radar backscatter coefficient and soil moisture (mv) can be written as $\delta\, 10^{\gamma\, mv}$. (Baghdadi et al., 2006, 2008). The sensitivity of the radar signal to the soil moisture γ depends on θ. Higher sensitivity is observed for low than for high incidence angles (Baghdadi and Zribi, 2016). To include this dependence on incidence angle, the soil moisture value is multiplied with the term $cotan(\theta)$. Thus, $g_{pq}(mv, \theta)$ can be written as $\delta\, 10^{\gamma\, cotan(\theta)\, mv}$.

The last term $\Gamma_{pq}(kHrms, \theta)$ represents the behavior of σ° with soil roughness. For a logarithmic behavior of $\sigma°(dB)$ with kHrms, Γ_{pq} in linear scale can be written as $\mu(kHrms)^{\xi}$ (Baghdadi et al., 2006). Baghdadi et al. (2002) showed that at high incidence angles, radar return is highly sensitive to surface roughness and shows much larger dynamics than at a low incidence angle. In addition, the term $sin(\theta)$ is intended to include this dependence with the incidence angle: $\Gamma_{pq} = \mu(kHrms)^{\xi\, sin(\theta)}$.

Finally, the relationship between the radar backscattering coefficient ($\sigma°$) and the soil parameters for bare soil surfaces can be written by:

$$\sigma_{pq}^{\circ} = \delta(cos\,\theta)^{\beta}\, 10^{\gamma\, cotan(\theta)\, mv}\, (kHrms)^{\xi\, sin(\theta)} \qquad (4)$$

The coefficients δ, β, γ, and ξ are then estimated for each radar polarization using the method of least squares by minimizing the sum of squares of the differences between the measured and modelled radar signal:

$$\sigma_{HH}^{\circ} = 10^{-1.287}(cos\,\theta)^{1.227}\, 10^{0.009\, cotan(\theta)\, mv}\, (kHrms)^{0.86\, sin(\theta)}$$
$$\sigma_{VV}^{\circ} = 10^{-1.138}(cos\,\theta)^{1.528}\, 10^{0.008\, cotan(\theta)\, mv}\, (kHrms)^{0.71\, sin(\theta)} \quad (5)$$
$$\sigma_{HV}^{\circ} = 10^{-2.325}(cos\,\theta)^{-0.01}\, 10^{0.011\, cotan(\theta)\, mv}\, (kHrms)^{0.44\, sin(\theta)}$$

where θ is expressed in radians and mv is in vol.%. Equations (5) show that the sensitivity (γ) of the radar signal to the soil moisture in decibel scale is 0.25 dB/vol.% in HH polarization, 0.22 dB/vol.% in VV polarization and 0.30 dB/vol.% in HV polarization for an incidence angle of 20°. This sensitivity decreases to 0.09 dB/vol.% in HH, 0.08 dB/vol.% in VV and 0.11 dB/vol.% for an incidence angle of 45°.

4.2 Performance of the new model

Results show that the new proposed model provides more accurate results (biases and the RMSE decrease for both HH and VV polarizations). The RMSE decreases from 3.8 dB to 2.0 dB for HH and from 2.8 dB to 1.9 dB for VV. In addition, the high over- or underestimations of radar backscattering coefficients observed with the Dubois model according to soil moisture, surface roughness and radar incidence angle are clearly eliminated with the new model (Figures 3 and 4).

Analysis of the new model's performance for each radar wavelength separately (L-, C- and X-bands) shows that the most significant improvement is observed in X-band with an RMSE that decreases from 4.1 dB to 1.9 dB in HH and from 3.2 dB to 1.8 dB in VV. In L-band, the performance of the new model is not better than that of the Dubois model because the RMSE decreases slightly with the new model of 3.0 dB to 2.3 dB in HH and remains similar in VV (RMSE = 2.3 dB with the Dubois model and 2.7 dB with the new model). The improvement is also important for the C-band with an RMSE that decreases from 3.7 dB to 1.9 dB in HH and from 2.6 dB to 1.9 dB in VV. With respect to bias, the results show that it decreases with the new model for all radar

wavelengths. In addition, the new model does not show bias according the range of soil moisture, surface roughness, and radar incidence angle.
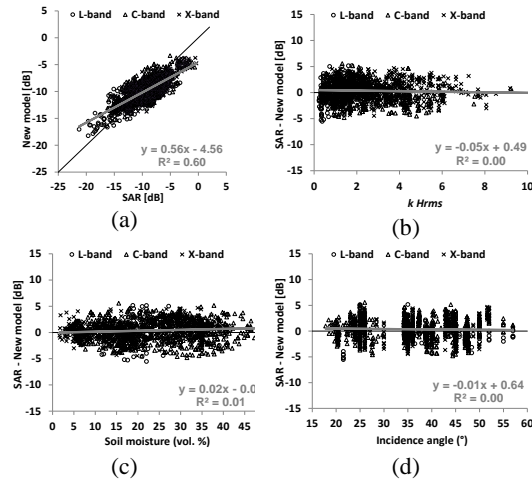
Figure 3. (a) Comparison between σ° modelled in the new model and σ° measured (for all SAR bands) for HH polarization, (b) difference between SAR and the new model as a function of surface roughness (*kHrms*), (c) difference between SAR and the new model as a function of soil moisture (*mv*), (d) difference between SAR and the new model as a function of incidence angle.
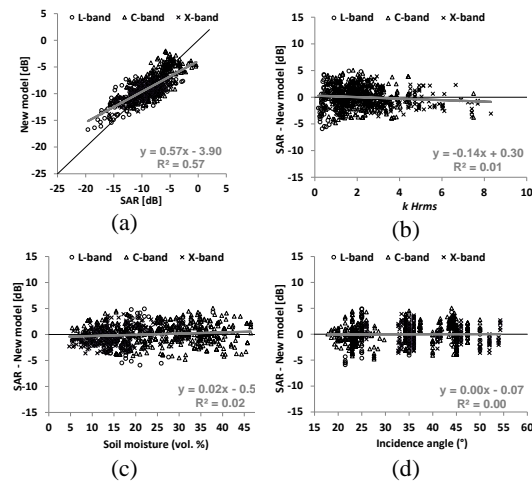
Figure 4. (a) Comparison between σ° in the new model and σ° measured (for all SAR bands) for VV polarization, (b) difference between SAR and the new model as a function of surface roughness (*kHrms*), (c) difference between SAR and the new model as a function of soil moisture (*mv*), (d) difference between SAR and the new model as a function of incidence angle.
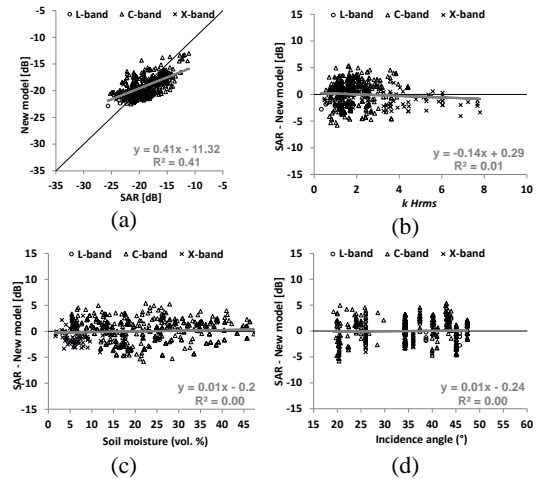
Figure 5. (a) Comparison between σ° in the new model and σ° measured (for all SAR bands) for HV polarization, (b) difference between SAR and the new model as a function of kHrms, (c) difference between SAR and the new model as a function of mv, (d) difference between SAR and the new model as a function of incidence angle.

The comparison between the new model simulations in HV polarization (Equation 5) and the real data (SAR data) shows an RMSE of 2.1 dB (1.6 dB in L-band, 2.2 dB in C-band, and 1.9 dB in X-band). The bias (σ°SAR - model) is -1.3 dB in L-band, 0.2 dB in C-band, and -1.3 dB in X-band. Figure 5 shows also that the new model correctly simulates the radar backscatter coefficient in HV for all ranges of soil moisture, surface roughness and radar incidence angle.

5 CONCLUSION

A new empirical model (Baghdadi model) was proposed for radar backscatter from bare soil surfaces. A large dataset was used, composed of ground measurements and SAR images over bare agricultural soils. Results show that the new model provides improved results in comparison to the Dubois model in the case of HH and VV polarization. Biases and RMSE have decreased for both HH and VV polarizations. Based on the same equation as that used for HH and VV, a radar signal in HV polarization was also proposed. Finally, the new empirical model proposed in the present study would allow more accurate soil moisture estimates using the new Sentinel-1A and -1B SAR data.

6 ACKNOWLEDGMENT

7 REFERENCES

Baghdadi, N., and Zribi, M. (2016). Characterisation of soil surface properties using radar remote sensing. Chapitre book: Baghdadi N. and Zribi M. (eds), Land surface remote sensing in continental hydrology, p. 1-40, Septembre 2016, Elsevier, 502 pp. (Elsevier).

Baghdadi, N., Bernier, M., Gauthier, R., and Neeson, I. (2001). Evaluation of C-band SAR data for wetlands mapping. Int. J. Remote Sens. 22, 71–88.

Baghdadi, N., King, C., Bourguignon, A., and Remond, A. (2002). Potential of ERS and RADARSAT data for surface roughness monitoring over bare agricultural fields: application to catchments in Northern France. Int. J. Remote Sens. 23, 3427–3442.

Baghdadi, N., Holah, N., and Zribi, M. (2006). Soil moisture estimation using multi-incidence and multi-polarization ASAR data. Int. J. Remote Sens. 27, 1907–1920.

Baghdadi, N., Zribi, M., Loumagne, C., Ansart, P., and Anguela, T.P. (2008). Analysis of TerraSAR-X data and their sensitivity to soil surface parameters over bare agricultural fields. Remote Sens. Environ. 112, 4370–4379.

Dubois, P.C., Van Zyl, J., and Engman, T. (1995). Measuring soil moisture with imaging radars. IEEE Trans. Geosci. Remote Sens. 33, 915–926.

Potential of synergy between sentinel1 and terrasar-X radar sensors to retrieve physical soil properties

Sandarbh Agrawal[1], Mehrez Zribi[2], Sekhar Muddu[1], Ahmad Albitar[2], Sylvain Ferrant[2], Nicolas Baghdadi[3], Mohammad El-Hajj[3]

[1]Department of Civil Engineering, Indian Institute of Science, Bangalore 560012, India; muddu@civil.iisc.ernet.in
[2]CESBIO (CNRS/UPS/IRD/CNES), 18 av. Edouard Belin, bpi 2801, 31401 Toulouse cedex9, France,
[3]IRSTEA, UMR TETIS, 500 rue François Breton, 34093 Montpellier cedex 5, France

Mehrez.zribi@cesbio.cnes.fr
sekhar.muddu@gmail.com
ahmad.albitar@cesbio.cnes.fr
nicolas.baghdadi@teledetection.fr
ferrants@cesbio.cnes.fr

ABSTRACT *The aim of this paper is to analyze the behavior of multi-frequency radar signals for the estimation of the vegetation covered surface characteristics in a tropical context. This analysis is based on radar measurements acquired by Sentinel-1 and TERRASAR-X radars over a period of two months (September-October 2016) at the site of Berambadi (South of India). Spatial measurements are accompanied by field measurements on reference plots, soil moisture and roughness and Leaf Area Index « LAI ». A sensitivity of the radar signals in the HH, VV and VH polarizations to the soil moisture and to the vegetation growth (through NDVI index) is observed. This sensitivity is higher in X band than in C band. In VH polarization, the sensitivity of the signal to surface properties appears very low.*

1 INTRODUCTION

Surface soil moisture and vegetation play an essential role in numerous environmental studies related to hydrology, meteorology and agriculture.

Radar remote sensing measurements of bare soil are very sensitive to the surface-layer water content, due to a pronounced increase in the dielectric constant of the soil or vegetation with increasing water content.

In the present paper, the objective is to analyze the potential of two radar sensor (TERRASAR-X and SENTINEL 1) potentials to estimate soil moisture and vegetation cover properties. Section 2 describes the studied site and database. Section 3 analyses results concerning sensitivity of radar signals to soil moisture and vegetation properties. Conclusions are gathered in section 4.

2 SITE AND DATABASE

2.1 STUDIED SITE

The study site is located in the Berambadi basin; it is close to the city of Gundlupet in Chamarajanagar district of Karnataka state in South India (Figure 1). The study site is semi-arid with an annual precipitation

of 800 mm mainly due to the South West monsoon rainfall. The main land use classes encountered in the area are: dense/closed forest, scrub forest, land with scrub, Kharif (summer) crop, double crop and plantation. During Kharif (summer) and Rabi (winter) marigold, sunflower, finger millet, maize, garlic, sugarcane, sorghum, water-melon, lentils, and groundnut etc., are grown.
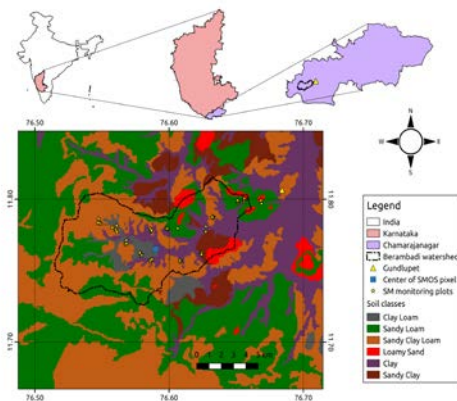
Figure 1: Illustration of studied site

2.2 SATELLITE DATA

a) Sentinel 1 radar data
The first S-1A satellite was launched on 3 April 2014. The second S1-1B Sentinel was launched on 22 April 2016. Both satellites offer a repeatability of 6 days for different parts of the globe (Europe, North Africa etc). They have a frequency of 5.4 GHz with standard operating modes: the Strip Map (SM), Interferometric Wide Swath (IW), Extra Wide Swath (EW), and WaVe (WV) modes. In this paper, we consider 4 IW S1 images with 10m X10m spatial resolution, a dual polarizations VV and VH, and an incidence angle about 39-40°, acquired from September 2016 to end of October 2016 (Table 1). All of these images were generated from the high-resolution Level-1 Ground Range Detected (GRD) product. The data was pre-processed with Sentinel-1 Toolbox with 3 steps:

- Thermal noise removal

- Radiometric calibration

- Terrain correction using SRTM DEM at 30m.

The calibration aims to convert digital number values of the raw images into backscattering coefficients (σ^0).

b) TERRASAR-X data
Five TerraSAR-X images (X-Band ~ 9.65 GHz) were acquired (in HH and VV polarizations, incidence angle of 36°). All of the images were acquired in the form of "Single Look Complex" products, with the TSX images produced in the Single Look Slant Range Complex (SSC) representation, having a ground pixel spacing of approximately 2 m. The images were then radiometrically calibrated to derive the backscattering coefficients $\sigma 0$, and then geo-referenced using the SRTM 3Sec as a DEM (Auto download in SNAP software). The mean radar signals were computed for each test field.

2.3 GROUND MEASUREMENTS

During September and October 2016 (two months), ground campaigns were carried out at the same time as the radar satellite acquisitions. Considered reference fields concern three types of land use (Turmeric, Sorghum and Maize). The ground measurements realized on the reference fields involved the characterization of the following soil parameters: soil moisture using a theta-probe instrument, soil roughness with just tortuosity estimation, and vegetation leaf area index.

Soil moisture
For each test field, approximately 20 handheld thetaprobe measurements were made at a depth of 5 cm. The samples were taken from various locations in each reference field, within a two-hour time frame, coinciding with the time of each overhead satellite acquisition. The volumetric moisture ranged between 1 vol.% and 32 vol.% for all thetaprobe measurements.

Soil roughness
Soil roughness is estimated through the use of a chain to calculate tortuosity. It is defined as the ratio of the length of the curve (*L*) to the distance between the ends of it (*C*). Results illustrate this parameter in the range 1.03-1.17, with limited variations between reference fields.

Leaf Area Index
LAI is defined as the total one-sided area of leaf tissue per unit ground surface area. According to this definition, the LAI is a dimensionless quantity. For each test field, we consider approximately twenty hemispherical digital photos processed to retrieve this vegetation parameter (Duchemin et al., 2008). These measurements were applied simultaneously to each TERRASAR-X data acquisition. During all measurement campaigns, the LAI measurements were ranged between 0 and 4.6.

For analysis of radar sensitivity to vegetation parameters, we choose to consider just NDVI vegetation index (from S2 satellite) because of limited number of LAI measurements during the studied period.

3 RESULT

3.1 SAR SENSITIVITY TO MOISTURE

During the studied period, we note the absence of precipitations. This induces very limited variations in soil moistures with values generally ranged between 0 and 7 cm3/cm3. For this reasons, analysis of radar signal sensitivity to soil moisture could not be discussed to all vegetation covers. It is considered just for irrigated turmeric cover. Figure 2 illustrates relationship between soil moisture and TERRASAR-X data in (HH and VV polarizations and S1 data in VV and VH polarizations. First, we observe highest sensitivity to soil moisture in X band than in C band. This behavior has been shown in other experimental studies (Baghdadi et al. 2012). This is due particularly to sensitivity of X band data to soil moisture in the first millimeters of soil and then to more extreme values, comparing to C band sensitive to moisture in 2-3 cm (Zribi et al., 2014). Values of NDVI for turmeric culture during this period seem not very high, for this reason, penetration of radar signal still not negligible and then sensitivity to soil moisture not weak.

(a)

(b)

(c)

(d)
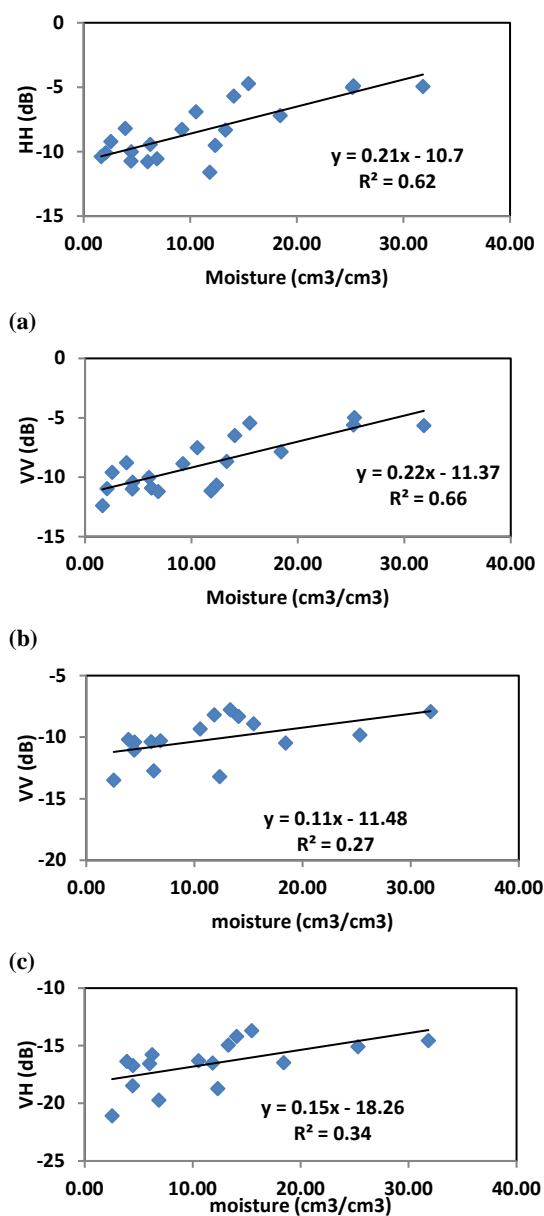
Figure 2: Sensitivity of radar data to soil moisture. a) TSX, HH polarization, b) TSX, VV polarization c) S1, VV polarization d) S1, VH polarization

3.2 SAR sensitivity to vegetation

In our case, we discuss sensitivity of radar signals to vegetation dynamic for three dominant vegetation covers, turmeric, sorghum and finally Maize.

a)   Turmeric cover

Figure 3 illustrates radar signals, TSX in HH and VV polarizations and S1 in VV and VH polarization, dynamic as a function of NDVI vegetation index. For the case of turmeric cover, NDVI is ranged between 0.1 and 0.55. First, for co-polarized signals (HH and VV), we observe an increasing of radar signal with NDVI increasing. The highest dynamic (about 2.5 dB) is observed in X band, with approximately the same dynamic for HH and VV polarizations. For C band, VH polarization does not show any sensitivity to vegetation dynamic. As observed in other experimental studies, this is probably due to limited volume scattering for this cover.
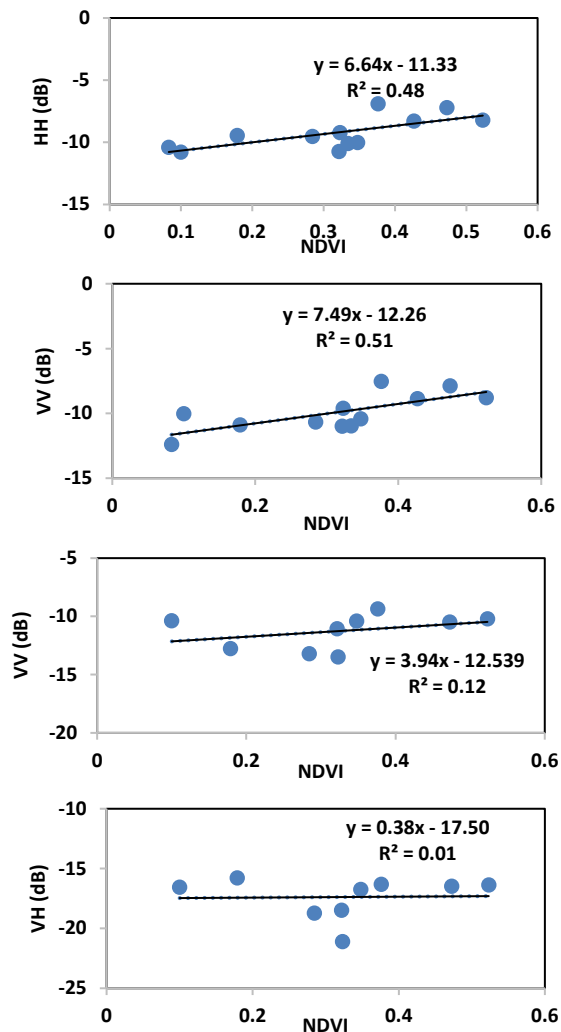
Figure 3: Sensitivity of radar data to vegetation NDVI index for Turmeric cover. a) TSX, HH polarization, b) TSX, VV polarization c) S1, VV polarization d) S1, VH polarization

b)   Sorghum

Figure 4 illustrates radar signals, TSX in HH and VV polarizations and S1 in VV and VH polarization, dynamic as a function of NDVI of Sorghum. NDVI values are weak and ranged approximately between 0.1 and 0.35. As for Turmeric, highest sensitivity is observed in X band, with a limited dynamic of radar signal as a function of NDVI. We note an increasing of just 1.2 dB for the 0.2 NDVI increasing. For C band, the sensitivity is completely absent; there is not tendency of radar signal as a function of NDVI.
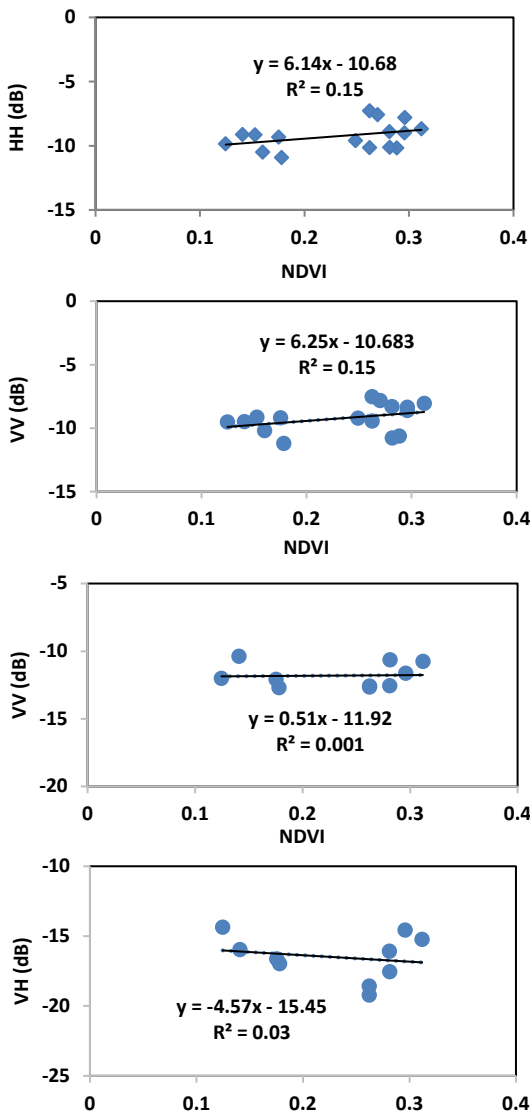
Figure 4: Sensitivity of radar data to vegetation NDVI index for Sorghum cover. a) TSX, HH polarization, b) TSX, VV polarization c) S1, VV polarization d) S1, VH polarization

c)   Maize

Figure 5 illustrates radar signals, TSX in HH and VV polarizations and S1 in VV and VH polarization dynamic as a function of NDVI of Maize. NDVI values are ranged approximately between 0.2 and 0.55. Inversely to the other covers, we observe an attenuation of radar signal with the increasing of NDVI, for all co-polarized signals. This behavior due to vegetation attenuation effect is observed also for cereals in other experimental studies (Fratanelli et al., 2013). The highest sensitivities are observed in X band, with approximately a dynamic of 2dB. In C band, VV polarization illustrates lower dynamic as a function of NDVI, around 1.5 dB. This decreasing trend is linked to the geometrical vertical structure of Maize, inducing attenuation of radar signal.

For VH data, we observe the inverse trend, with the increasing of radar signal with NDVI. This behavior is linked to the sensitivity of VH cross-polarization to volume component which increases with the growth of vegetation cover (increasing of NDVI).
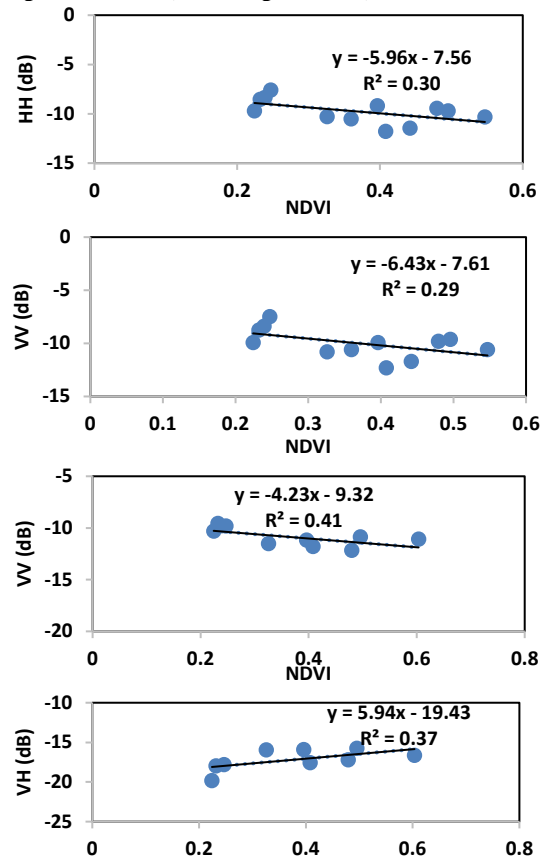
Figure 5: Sensitivity of radar data to vegetation NDVI index for Maize cover. a) TSX, HH polarization, b) TSX, VV polarization c) S1, VV polarization d) S1, VH polarization

285

4 CONCLUSION

This paper proposed an analysis of the sensitivity of TERRASAR-X/S1 radar signals for surface parameters (soil moisture and NDVI linked to vegetation cover dynamic) for three types of land use (Turmeric, Sorghum and Maize), in Berambadi site, in tropical conditions. For soil moisture, analysis is limited to irrigated Turmeric fields, illustrating a highest sensitivity to soil moisture for X band. For vegetation characterization, for the two polarizations HH and VV, and for the three covers, we observed a highest sensitivity of X band data to NDVI than with C band data. VH polarization illustrates the lowest potential to retrieve surface parameters.

5 REFERENCES

Koster, R.D.; Dirmeyer, P.A.; Guo, Z.; Bonan, G.; Chan, E.; Cox, P.; Gordon, C.T.; Kanae, S.; Kowalczyk, E.; Lawrence, D., 2004, Regions of strong coupling between soil moisture and precipitation. Science, 305, 1138–1140.

Manfreda, S.,Scanlon, T. M., Caylor K. K., 2009, On the importance of accurate depiction of infiltration processes on modelled soil moisture and vegetation water stress. Ecohydrol., 3, 155–165 .

Baghdadi, N., Zribi, M., 2016, Microwave Remote Sensing of Land Surfaces, Techniques and methods, ISTE Press, London and Elsevier, Oxford.

Baghdadi N., Dubois-Fernandez P., Dupuis X., and Zribi M., 2013. Sensitivity of multi-frequency (X, C, L, P and UHF-band) polarimetric SAR data to soil moisture and surface roughness over bare agricultural soils. IEEE Geoscience and Remote Sensing Letters, 10, 4, 731 - 735.

Zribi, M., Gorrab, A., Baghdadi, N., Lili-Chabaane, Z., Mougenot, B., Influence of radar frequency on the relationship between bare surface soil moisture vertical profile and radar backscatter, *IEEE Geoscience and Remote Sensing Letters*, 11(4) 848 - 852 10.1109/LGRS.2013.2279893.

Fratanellli, G., Paloscia, S., Zribi, M., Chahbi, A., 2013,Sensitivity analysis of X-band SAR to wheat and barley biomass in the Merguellil Basin, Remote Sensing Letters, 4, 11, 1107–1116.

Combined use of agro-meteorological model and multi-temporal satellite data (optical and radar) for monitoring corn biophysical parameters

M. Ameline [a, c]; R. Fieuzal [a]; J. Betbeder [b]; J-F. Berthoumieu [c]; F. Baup [a]

[a] *CESBIO, Université de Toulouse, CNES, CNRS, IRD, UPS, Toulouse, France*
[b] *Cirad, UPR BSEF, F-34398 Montpellier, France*
[c] *Association Climatologique de Moyenne-Garonne et du Sud-Ouest (ACMG)*
mael.ameline@gmail.com; remy.fieuzal@cesbio.cnes.fr; frederic.baup@cesbio.cnes.fr; betbederjulie@gmail.fr; acmg@acmg.asso.fr

ABSTRACT – *This work evaluates the assimilation of Green Area Index (GAI) derived from radar and optical imagery into an agrometeorological model named SAFY-WB (Simple Algorithm For Yield model combined with a Water Balance model) to retrieve corn biophysical parameters. Radar satellite information is provided by the Sentinel-1A (S1-A) mission through two angular normalized orbits allowing a repetitiveness from 12 to 6 days. Optical images are provided by Spot-5-Take-5 and Landsat-8 missions all along the crop cycle. A nonlinear relationship between GAI_{opt} (GAI derived from optical data) and the ratio radar signal ($\sigma°_{VH/VV}$), allows to create a GAI_{sar} (GAI derived from radar data) ($R^2 = 0.75$). Then, these GAI are assimilated into the model to optimize the simulations by using three configurations: GAI_{sar}, GAI_{opt} or a combination of radar and optical ($GAI_{sar+opt}$). Results show that in the calibration and validation steps, the GAI_{sar} is mainly suitable for initializing the model during the first crop stages. The GAI_{opt} is suited all along the crop cycle but limitations remains during the first phenological stages, when cloud cover is important over the studied region. The last configuration ($GAI_{sar+opt}$) uses the benefit of both sensors: GAI_{sar} to substitute GAI_{opt} at the beginning of the crop cycle and GAI_{opt} to retrieve the vegetation dynamic from flowering. Finally, the model, controlled by SAR and optical data, is able to accurately simulate the dynamic of GAI ($R^2<0.99$ and $rRMSE<11\%$), Dry Stem Mass (DSM), Total Dry Mass (TDM) and yield through Dry Grain Mass (DGM) ($R^2 = 0.82$).*
KEYWORDS: *maize, crop yield, microwave, Synthetic Aperture Radar (SAR), biomass, Sentinel-1*

1 INTRODUCTION

Cultivated throughout the world, corn is the most produced cereal with more than 1 billion of tons in 2013 (FAO, 2015). In France, corn is the second crop production, mainly cultivated in areas located in the south west (40% of the national production).

Among the wide range of monitoring tools (in situ measurements, human observations, weather stations, local modeling …), satellite images are fully suited for crop monitoring. Indeed, satellites images can be acquired at high spatial resolution, with medium to high temporal repetitiveness (few days), and with large swaths (several kilometers). However, the only use of satellite images (acquired in optical and/or microwaves domains) implies two main limitations. Firstly, they don't allow a continuous daily monitoring of crop parameters (being limited by their temporal sampling). Then, they can only be related to some specific crop biophysical parameters (Green or Leaf Area Index (GAI or LAI), height, mass of vegetation) during a limited period of the phenological cycle of the crop (Baup et al., 2016; McNairn and Brisco, 2004). To overcome these problems many studies have successfully combined optical and/or microwave images with a model of culture to daily estimate more crop parameters such as the water content, the GAI, the biomass, the evapotranspiration, or the grain yield during the whole crop cycle (Fieuzal et al., 2017; Battude et al., 2016; Betbeder et al., 2016; Claverie et al., 2012; Hadria et al., 2009; Duchemin et al., 2008; Maas, 1988). Such approach generally considers simple algorithm-crop models that are able to rapidly run over numerous and heterogeneous fields compared to more complex models that require a more detailed description of the surface (mechanistic description of vegetation and soil properties).

In this context, the objective is to evaluate the assimilation of Green Area Index (GAI) derived from radar (GAI_{sar}) and optical (GAI_{opt}) imagery into an agrometeorological model to retrieve corn biophysical parameters (GAI, Dry Stem Mass, Total Dry Mass and yield through Dry Grain Mass). The study area and data collection are presented in section 2, followed by the developed methodology (section 3) featuring the processing from satellite images to the parametrization of the model. The results and discussion are presented in section 4.

2 STUDY AREA AND DATA COLLECTION

2.1 Site description

The study area (centered at 44.06°N, 0.42°E, 110×140 km²) is located in the South-West of France over two French regions (Nouvelle-Aquitaine and Occitanie). Characterized by hilly and valley terrain, the open field agricultural landscape is by far the dominant land use system (Figure 1).
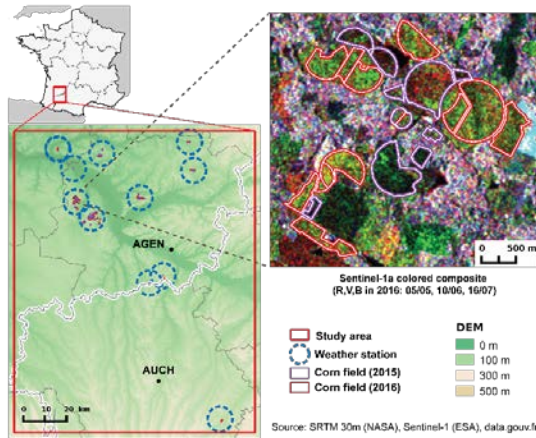
Figure 1: Location of the study site and inventoried corn fields in 2015 and 2016

2.2 Field surveys

The agricultural practices (variety, sowing, emergence and harvesting dates, irrigation information and yield per parcel) and the soil parameters (texture, depth) have been collected during two successive agricultural seasons (2015 and 2016) over 126 fields (Table 1).

Table 1 : Features of the corn field

Year	Number of fields	Area (ha) [min max mean]	Slope (°) [min max mean]
2015	65	[3.1 42.3 9.6]	[0.3 11.2 4.3]
2016	61	[3.1 62 11.9]	[0.4 9.7 4]

Among all the monitored fields, specific measurements are performed over 5 of them. Each three weeks from sowing to harvest, the total above ground biomass (fresh mass) is weighed in situ before being dried (at 65°C, at least 72h) to get Dry Stem Mass (DSM), Dry Grain Mass (DGM), Total Dry Mass (TDM) and Water Content (WC).
Climatic data are collected using a network of 11 weather stations located inside the study area (Figure 1). They acquire specific data related to the need of the model: global solar radiation, air temperature, rainfalls

2.3 Satellite images

a) Optical images

The Landsat-8 products are orthorectified and radiometrically corrected by the USGS. Spot-5 Take 5 and the Landsat images are processed by the level 2A processor named MACCS (Hagolle et al., 2015). All the images are available free of charge at the Theia land data services (https://www.theia-land.fr/en/). From April to November, it concerns 44 images in 2015 and 23 images in 2016. More detailed features of optical images are given in Table 2.

b) Radar images

Radar images are provided by Sentinel 1A (S1-A), freely available from the European Copernicus Services Data Hub (https://scihub.copernicus.eu/). Over the studied region, images are acquired in Ground Range Detected (GRD) mode and projected on Earth ellipsoid model, with an incidence angle ranged between 29.1° and 46°, following two orbits (#30 and #132) (Torres et al., 2012). For the same acquisition period as optical images, 50 and 68 images are respectively acquired in 2015 and 2016. Temporal sampling, size of the swath, spatial resolution and sensors features are given in Table 2.

Table 2: Satellite (radar and optical) features

Mission	Sentinel-1A	Landsat-8	Spot 5
Swath	250 km	185 km	60 km
Repetitivity	12 days	16 days	5 days
Spatial resolution	20×5 m	30 m	10 m
Sensor features	5.405 GHz	0.45-0.52 µm	0.50-0.59 µm
	Dual	0.53-0.60 µm	0.61-0.68 µm
	polarization	0.63-0.68 µm	0.79-0.89 µm
	(VV VH)	0.85-0.89 µm	

3 METHODOLOGY

3.1 Radar images processing

Sentinel 1-A GRD images are pre-processed (radiometric calibration, Range Doppler terrain correction and resampled at 10 m spacing) using the ESA's SNAP software to obtain the Sigma-naught for the VH and VV polarizations. The radar signal is sensitive to the antenna incidence angle, effect which can be reinforced by the local incidence angle observed over hilly landscape. Thereby an angular normalization (Betbeder et al., 2016; Fieuzal, 2013) is applied from sowing to harvest (equation 1).

$$\sigma^0_{norm} = (\theta_{\sigma^{0-}} \theta_{ref}) \times \tau_{mean} + \sigma^0_i \qquad (1)$$

Where σ^0_{norm} is the normalized radar signal, $\theta\sigma^0$ is the local incidence angle of the acquisition, θ_{ref} is the local incidence angle of reference (37.5°), τ_{mean} is the average angular sensitivity and σ^0_i is the initial radar signal ($\tau_{mean(VV)} = 0.06$ dB. $^{\circ-1}$, $\tau_{mean(VV)} = 0.07$ dB. $^{\circ-1}$).

Afterwards all the data are filtered using a moving-average fitting window to reduce the influence of external variables (e.g., precipitation, dew or irrigation) distorting the vegetation signal response.

3.2 Green Area Index (GAI) retrieval from optical and radar

The BVnet tool (Biophysical Variables Neural NETwork) is used to derive the GAI from optical images (GAI_{opt}). This algorithm is based on the inversion of the radiative transfer model PROSAIL using artificial neural network (Baret et al., 2007).

Empirical relationships are established between radar signals and GAI_{opt} to estimate GAI from S1-A images. Among the three tested radar configurations ($\sigma°_{VV}$, $\sigma°_{VH}$ and $\sigma°_{VH/VV}$), the ratio of polarizations gives the best empirical relationship from theoretical emergence (124°C.day) to the average radar saturation (1200°C.day), with a $R^2 = 0.75$ (Table 3).

Table 3: Coefficients of determination for nonlinear empirical relationships between radar configurations and GAI_{opt}

Radar	R^2	n
$\sigma°_{VV}$	0.21	592
$\sigma°_{VH}$	0.70	592
$\sigma°_{VH/VV}$	0.75	592

Finally, using a simple inversion of this nonlinear empirical relationship, GAI_{sar} is obtained from the $\sigma°_{VH/VV}$ ratio (equation 2).

$$GAI_{sar} = 167.97 e^{0.766 \times \sigma^0_{VH/VV}} \qquad (2)$$

3.3 Implementation of the agro-meteorological model

The SAFY-WB model (Simple Agro-meteorological For Yield estimate and Water Balance) (Duchemin et al., 2015) simulates the temporal evolution of the GAI and the aerial dry masses (more precisely: DSM, DGM and TDM) from the day of emergence until the harvesting day. The model runs at daily time steps, and physical processes are controlled by different climatic variables: the global solar radiation, the air temperature, the potential evapotranspiration and precipitation, and GAI-derived satellite data. Three configurations are evaluated when the model is controlled by GAI_{sar}, GAI_{opt} or $GAI_{sar+opt}$.

During the calibration step, the model is parameterized on one independent field of corn cultivated in 2016. During calibration, six parameters (Pl_a, Pl_b, Stt, Rs, D_0, ELUE (Duchemin et al., 2008) are optimized by comparing the GAI values simulated by the model (GAI_{sim}) and the GAI derived from satellite time series (GAI_{sar}, GAI_{opt} or $GAI_{sar+opt}$), using a method of simplex for the minimization of the cost function (i.e., RMSE between GAI_{sim} and $GAI_{satellite}$).

The validation step is performed over 65 fields of corn cultivated in 2015 (year independent of calibration). For this step, only two parameters of the six are optimized (D_0, ELUE), the others being constant. Model accuracy is investigated through the comparison between the maximum of DGM_{sim} and farmer's yield.

4 RESULTS AND DISCUSSION

4.1 Calibration performances of the model

Once calibrated, the trends of the GAI and the dry masses are globally well reproduced, as evidence by the example of simulation shown in Figure 2. In this example the model is controlled by $GAI_{sar+opt}$. Statistical performances are given in Table 4 depending on the GAI used to control the model.
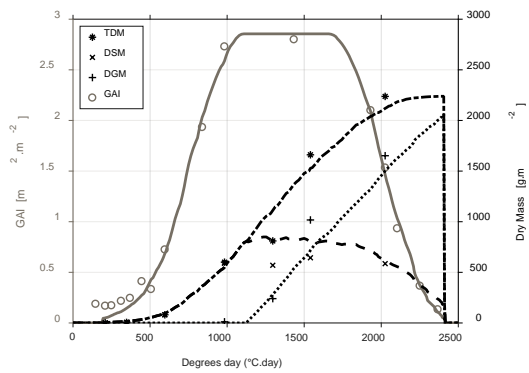
Figure 2: Comparison between observed and simulated GAI and dry masses (DSM, DGM and TDM). Lines represent simulations and punctual symbols the observations of GAI (GAI_{sar}: 0 - 500 °C.day or GAI_{opt}: 500 - 2500 °C.day) and dry masses

Table 4: Summary of statistical performances of the calibration step depending on the 3 satellites configurations (GAI_{sar}, GAI_{opt}, $GAI_{sar+opt}$) used to control the model

Configuration	Model output	R^2	rRMSE (%)	n
GAI_{sar}	GAI_{sim}	0.74	153	12
	DGM	0.94	43	7
	DSM	0.85	60	7
	TDM	0.98	19	7
GAI_{opt}	GAI_{sim}	0.99	11	13
	DGM	0.97	25	7
	DSM	0.93	34	7
	TDM	0.98	18	7
$GAI_{sar+opt}$	GAI_{sim}	0.99	10	15
	DGM	0.97	24	7
	DSM	0.94	30	7
	TDM	0.97	18	7

The poorest performances (mean rRMSE of 68%) are obtained when the model is controlled by GAI_{sar}. Although the assimilation of GAI_{sar} allows a faithfully estimation of the emergence date, the crop cycle is not fully recovered, inducing incoherent simulation of GAI,

DSM and DGM particularly (Ameline et al., 2016). At the opposite, the parameterization based on GAI_{opt} allows the model to well reproduce the temporal curve of the GAI_{opt} (R^2 = 0.99, rRMSE: 11%). The combination of radar and optical ($GAI_{sar+opt}$) gives comparable results to the optical case. In this case, GAI_{sar} provide essential information during the first phenological stages (from sowing till beginning of stem elongation) and GAI_{opt} overcomes the radar signal saturation problems to retrieve the vegetation dynamic especially from flowering to harvest. The dry masses simulations (DSM, DGM, and TDM) are in good agreement with measurements when the model is controlled by GAI_{opt} ($R^2 > 0.93$) or $GAI_{sar+opt}$ ($R^2 > 0.94$). Whatever the considered configuration, the DSM is estimated with a rRMSE superior or equal to 30%.

4.2 Validation

The assimilation of GAI_{sar} leads to aberrant estimates of GAI and DM (results not shown here). Contrariwise the simulation of dry mass is consistent with the literature ($754 < TDM < 2880$ g.m^{-2}), when the model is controlled by GAI_{opt} of $GAI_{sar+opt}$ data (Figure 3).
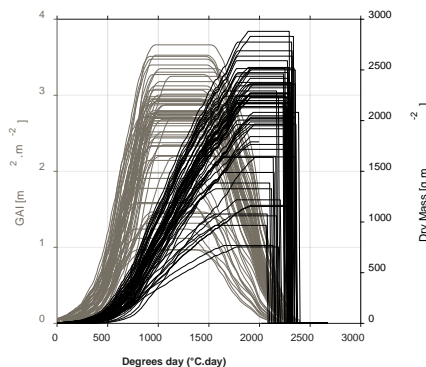
Figure 3: Model simulations of GAI and DGM obtained in the validation step for the 65 corn fields in 2015

The poorest performances for the yield estimation are observed by using the GAI_{sar} configuration (R^2 = 0.001), due to weak calibration performances. When the model is controlled by $GAI_{sar+opt}$, the estimates of yields offer the same high performance as the GAI_{opt} case (R^2 = 0.82) (Figure 4). In these two cases, the model is able to reproduce with confidence the yield heterogeneities (from 26 q.ha^{-1} to 145 q.ha^{-1}).

These results also highlight the difference in grain yield production due to irrigation practices, with higher values for irrigated fields.
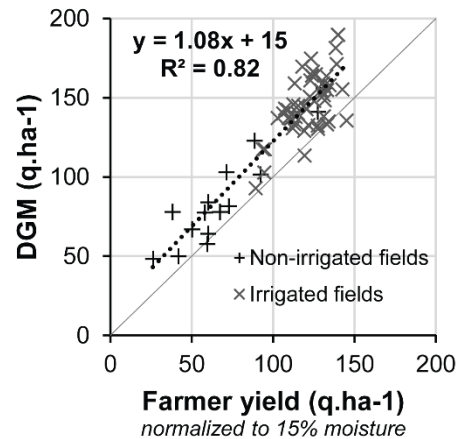
Figure 4: Comparison between the maximum of Dry Grain Mass simulated by the model and the farmer yields (over 65 corn fields in 2015)

5 CONCLUSION

The aim of this article was to evaluate the feasibility to assimilate GAI derived from radar and/or optical satellite data into the SAFY-WB model to estimate corn biophysical parameters. The results revealed that radar backscattering coefficients (especially the ratio VH/VV) have the potential to estimate the GAI only during the first phenological stages (until 500 °C.day), contrary to optical data which offer more possibilities all along the crop cycle (in condition of clear sky). Then the model was successfully controlled (calibration and validation steps) using three sources of satellite-derived GAI: GAI_{sar}, GAI_{opt} or $GAI_{sar+opt}$. Among these sources of GAI, best results in GAI (R^2 = 0.99), dry masses (R^2 = 0.93 to 0.97) and yield estimates (R^2 = 0.82) are obtained when the model is controlled by GAI_{opt} or $GAI_{sar+opt}$. In the first case, the GAI_{opt} can be used all along the crop cycle whereas in the combined case, the GAI_{sar} is only used during the first phenological stages (500 °C.day, when study area is often cloudy), followed by the GAI derived from optical data until harvest. These results demonstrate the efficiency of combining optical and radar images to monitor corn biophysical parameters.

In the future, this study must be extended to multi-year approach and the model should be improved to better simulate crop yield.

6 ACKNOWLEDGEMENTS

7 REFERENCES

Ameline, M., Fieuzal, R., Betbeder, J., Berthoumieu, J.-F., Baup, F., 2016. Assimilation of SAR and optical data into an agro-meteorological. International Congress on Environmental Modelling and Software.

Baret, F., Hagolle, O., Geiger, B., Bicheron, P., Miras, B., Huc, M., Berthelot, B., Niño, F., Weiss, M., Samain, O., Roujean, J.L., Leroy, M., 2007. LAI, fAPAR and fCover CYCLOPES global products derived from VEGETATION. Remote Sens. Environ. 110, 275–286. doi:10.1016/j.rse.2007.02.018

Battude, M., Al Bitar, A., Morin, D., Cros, J., Huc, M., Marais Sicre, C., Le Dantec, V., Demarez, V., 2016. Estimating maize biomass and yield over large areas using high spatial and temporal resolution Sentinel-2 like remote sensing data. Remote Sens. Environ. doi:10.1016/j.rse.2016.07.030

Baup, F., Villa, L., Fieuzal, R., Ameline, M., 2016. Sensitivity of X-Band (σ0, γ) and Optical (NDVI) Satellite Data to Corn Biophysical Parameters. Adv. Remote Sens. 05, 103–117. doi:10.4236/ars.2016.52009

Betbeder, J., Fieuzal, R., Baup, F., 2016. Assimilation of LAI and Dry Biomass Data From Optical and SAR Images Into an Agro-Meteorological Model to Estimate Soybean Yield. IEEE J. Sel. Top. Appl. Earth Obs. Remote Sens. 9, 2540–2553. doi:10.1109/JSTARS.2016.2541169

Claverie, M., Demarez, V., Duchemin, B., Hagolle, O., Ducrot, D., Marais-Sicre, C., Dejoux, J.-F., Huc, M., Keravec, P., Béziat, P., Fieuzal, R., Ceschia, E., Dedieu, G., 2012. Maize and sunflower biomass estimation in southwest France using high spatial and temporal resolution remote sensing data. Remote Sens. Environ. 124, 844–857. doi:10.1016/j.rse.2012.04.005

Duchemin, B., Fieuzal, R., Rivera, M., Ezzahar, J., Jarlan, L., Rodriguez, J., Hagolle, O., Watts, C., 2015. Impact of Sowing Date on Yield and Water Use Efficiency of Wheat Analyzed through Spatial Modeling and FORMOSAT-2 Images. Remote Sens. 7, 5951–5979. doi:10.3390/rs70505951

Duchemin, B., Maisongrande, P., Boulet, G., Benhadj, I., 2008. A simple algorithm for yield estimates: Evaluation for semi-arid irrigated winter wheat monitored with green leaf area index. Environ. Model. Softw. 23, 876–892. doi:10.1016/j.envsoft.2007.10.003

FAO, 2015. Statistical Pocketbook. World food and agriculture.

Fieuzal, R., 2013. Apports des données radar pour l'estimation des parametres biophysiques des surfaces agricoles. Université Toulouse III-Paul Sabatier.

Fieuzal, R., Marais Sicre, C., Baup, F., 2017. Estimation of Sunflower Yield Using a Simplified Agrometeorological Model Controlled by Optical and SAR Satellite Data. IEEE J. Sel. Top. Appl. Earth Obs. Remote Sens. 1–11. doi:10.1109/JSTARS.2017.2737656

Hadria, R., Duchemin, B., Baup, F., Le Toan, T., Bouvet, A., Dedieu, G., Le Page, M., 2009. Combined use of optical and radar satellite data for the detection of tillage and irrigation operations: Case study in Central Morocco. Agric. Water Manag. 96, 1120–1127. doi:10.1016/j.agwat.2009.02.010

Hagolle, O., Huc, M., Pascual, D., Dedieu, G., 2015. A Multi-Temporal and Multi-Spectral Method to Estimate Aerosol Optical Thickness over Land, for the Atmospheric Correction of FormoSat-2, LandSat, VENS and Sentinel-2 Images. Remote Sens. 7, 2668–2691. doi:10.3390/rs70302668

Maas, S.J., 1988. Use of remotely-sensed information in agricultural crop growth models. Ecol. Model. 41, 247–268.

McNairn, H., Brisco, B., 2004. The application of C-band polarimetric SAR for agriculture: a review. Can. J. Remote Sens. 30, 525–542. doi:10.5589/m03-069

Torres, R., Snoeij, P., Geudtner, D., Bibby, D., Davidson, M., Attema, E., Potin, P., Rommen, B., Floury, N., Brown, M., Traver, I.N., Deghaye, P., Duesmann, B., Rosich, B., Miranda, N., Bruno, C., L'Abbate, M., Croci, R., Pietropaolo, A., Huchler, M., Rostan, F., 2012. GMES Sentinel-1 mission. Remote Sens. Environ. 120, 9–24. doi:10.1016/j.rse.2011.05.028

Sensitivity of Sentinel-1 radar data to soil and vegetation parameters

Safa Bousbih[1,2], Mehrez Zribi[1] , Zohra Lili-Chabaane[2] , Pascal Fanise[1] , Bernard Mougenot[1], Nicolas Baghdadi[3]

[1]Centre d'Etude Spatiales de la Biosphère (CESBIO), Toulouse,
[2]Université de Carthage/Institut National Agronomique de Tunis (INAT), Tunisie,
[3]IRSTEA, UMR TETIS, Monpellier

Affiliations of all the authors
Email addresses

ABSTRACT *In semi-arid regions, climate is characterized by extended periods of drought. In this context , the characterization of surface parameters play a key role in the modeling of the water balance. The aim of this study is to analyze the potential of Sentinel-1 (S1) radar data to soil characteristics (roughness and water content) and to vegetation parameters (Leaf Area Index "LAI" and Vegetation Water Content "VWC") in agricultural areas. Simultaneously to several radar acquisitions over the Kairouan Plain (Tunisia, North Africa), acquired between 2015 and 2017 using S1 sensors, ground measurements (soil roughness, soil water content, LAI, VWC) were carried out. The NDVI (Normalized Difference Vegetation Index) index calculated from Landsat optical images revealed a strong correlation with in situ measurements of LAI and VWC. The sensitivity of the S1 measurements to variations in soil moisture, which has been reported in several scientific publications, is confirmed in this study. This sensitivity decreases with increasing vegetation cover growth (NDVI), and is stronger in the VV than in the VH polarization. The results also reveal a similar increase in the dynamic range of the radar signals observed in VV and VH polarizations, as a function of soil roughness. The sensitivity of S1 measurements to vegetation parameters (LAI and H) in the VV polarization is also determined, showing that the radar signal strength decreases when the vegetation parameters increase. No vegetation parameter sensitivity is observed in the VH polarization, probably as a consequence of volume scattering effects.*

1   INTRODUCTION

Hydrological process at regional and global scale play a key role in water balance modelling, particularly in climate change. These measurements have been based on field measurements and are incapable of restoring the spatial and temporal variability of these parameters and need to be extrapolated over larger areas.

Remote sensing data was widely to estimate surface parameters over agricultural areas (Baghdadi and Zribi, 2016). In this context, water content play a key component in these agricultural processes (Koster et al, 2004 ; Zhao et al, 2014 ; Manfreda et al, 2009).

Different spatial measurements have shown their potential for monitoring soil moisture like thermal infrared and microwave methods (Wagner, 1999 ; Paloscia et al, 2006).

Radar remote sensing data have also been developed for the estimation of soil parameters and have the advantage of being independent of weather conditions. Different inversion approaches have been proposed to restore these parameters based on different backscattering models (Baghdadi et al, 2006 ; Santi et al 2016)

The new C-band satellite was launched in April 2014 and offers free data with high temporal and spatial resolutions. This constellation allows achieving regular operational estimations of the characteristics of the continental surface.

In this context, the aim of this study is to analyse the potential of Sentinel-1 data for the assessment of different soil and vegetation parameters. The second section is experimental and describes the database over bare soil and cereals. The radar signals sensitivity to soil and vegetation parameters are analyzed in section 3. Section 4 describes the performance of the Water Cloud model. Our conclusion is provided in the last section.

2   DATABASE AND STUDY SITE

2.1 Study site
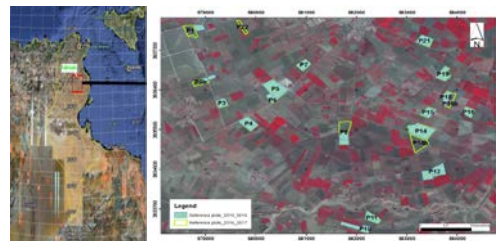
Figure 1 : Location of the Kairouan plain in Tunisia

The Kairouan plain is situated in Central Tunisia (9°23'-10°17'E, 35°1'-35°55'N). This semi-arid region is characterised by dry summer seasons and an annual average precipitation of 300 mm/year.

We selected about 20 reference fields between bare soils and cereal plots ranging in size between 2 and 8 ha. Over these plots, ground measurements were carried during two agricultural seasons (2015-2017).

2.2 Database

2.2.1 Radar data

The Sentinel-1A satellite was launched in April 2014. The satellite offers 12 days as a revisit time and 10 m of spatial resolution, co-polarization and incidence angle between 39° and 40°. The images were generated from Level-1 Ground Range Detected product with different pre processing as thermal noise removal, radiometric calibration, terrain correction and filtering of speckle.

Figure 2 : Setinel 1A satellite

2.2.2 Ground measurements

The ground measurements were carried over the fields which include handheld thetaprobe measurements, roughness measurements, and LAI measurements with hemispherical digital images.

The soil moisture content revealed a very high range between 3.9 vol.% and 45 vol.% during the experimental campaigns. Roughness measurements were made using a 1m long pin profiler. For each test plot, 5 parallel and 5 perpendicular profiles were compared to estimate the roughness parameters (the root mean square surface height (Hrms) and the correlation length (L)). Vegetation cover measurements are carried out to characterize several parameters: leaf area index (LAI) and water content. For each test field we consider approximately twenty hemispherical digital images, which are processed by analyzing the canopy gap fraction, in order to retrieve this vegetation parameter. The measurements were applied 4 times during each agricultural season. During all measurement campaigns, the computed

value of LAI ranged between 0 and 5. The VWC was measured three times in cereal fields for each vegetation cycle. For each reference field, measurements were made at three locations, each having a $1m^2$ surface area. The above ground biomass was removed, and wet and dry weights were used to estimate the VWC.

3 RADAR SIGNAL SENSITIVITY TO SOIL AND VEGETATION PARAMETERS

a) Radar signal sensitivity to soil moisture

The sensitivity of radar signal to soil moisture was analyzed for plots with NDVI<0.25 which corresponds to bare soils or poorly covered soils. The analysis of the two polarizations shows a higher sensitivity in VV than in VH which is explained by the sensitivity of the VH signals to the volume component in the surface scattering.
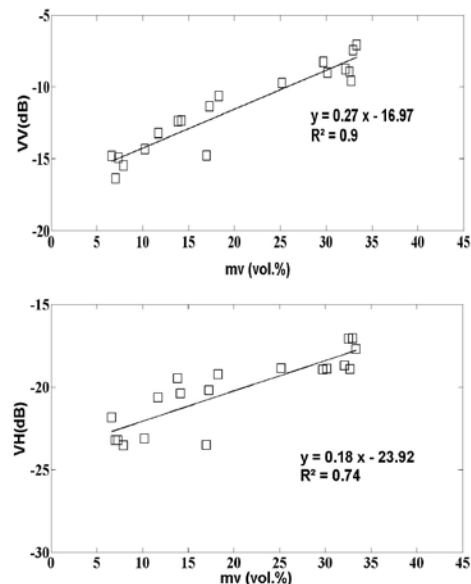
Figure 3 : Relationship between backscattering coefficient and soil moisture for: VV polarization (a) and VH polarization (b)

b) Radar signal sensitivity to soil roughness

For our case, we analyzed the relationship between the radar signal and Hrms parameters.

Soil moisture effect is very important on radar signal. VV and VH data show approximately the same behavior with a dynamic due to roughness approximately equal to 6 dB and shows good correlation, higher than 0.7.
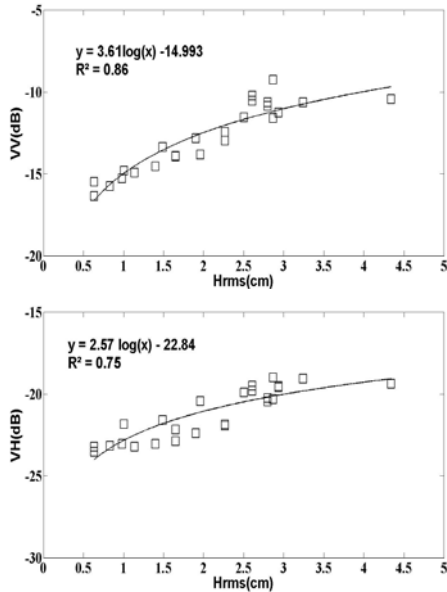
Figure 4: Relationship between backscattering coefficient and Hrms roughness parameter for: VV polarization (a) and VH polarization (b)

c) Radar signal sensitivity to vegetation parameters
d)

The behavior of the signal radar is different for VV and VH polarization. VV signal decreases with the increasing of LAI parameter. This behavior is the same for the vegetation water content. The effect of volume scattering component could explain this result.

4 METHODOLOGY

In this study, we proposed to use the "Water Cloud Model" (Attema and Ulaby, 1978) combined to a semi-empirical model for bare soil and calibrated using C-band radar data, NDVI, soil moisture, roughness parameter and incidence angle.
The NDVI was used as a vegetation descriptor, derived from LANDSAT8 images

$$\sigma^0 = \sigma^0_{canopy} + \sigma^0_{canopy+soil} + \tau^2 \sigma^0_{soil} \quad (1)$$

$$\text{With } \tau^2 = \exp(-2\,B\,.\,V1\,.\,\sec\theta) \quad (2)$$

$$\text{And } \sigma^0_{canopy} = A\,.\,V1\,.\,\cos\theta\left(1 - \tau^2\right) \quad (3)$$

$$\sigma soil = \alpha\,mv + \beta\,\log(Hrms) + \delta \quad (4)$$
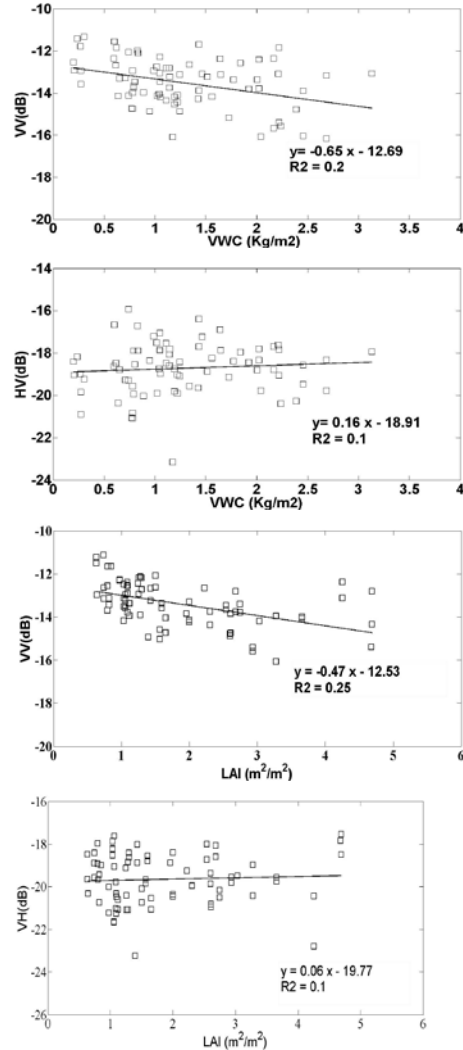
Figure 5: Relationship between backscattering coefficient and LAI for: VV polarization (a) and VH polarization (b)
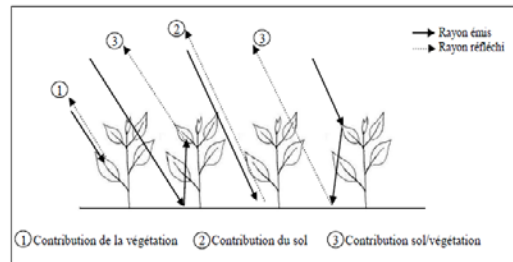
Figure 6: Contribution of the backscattering coefficient on a plot

5 RESULTS

The calibration process allows the empirical parameters A and B to be determined as: A = 0.06; B = 0.42.
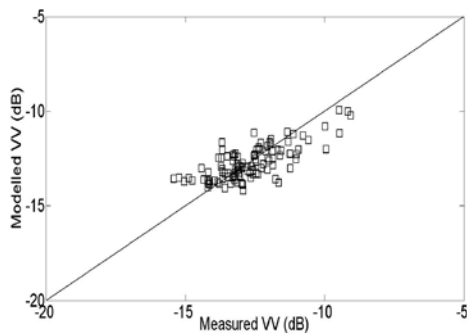
The figures provide the validation of the model's simulation of the radar signal and S-1 signal. A good degree of consistency is observed between the two outputs. Statistical parameters from the simulation are improved with a RMSE of 0.84 dB and a biais of 0.08 dB.

6 CONCLUSION

A calibrated Water Cloud Model (WCM), combined to an empirical backscattering model (Zribi et al., 2014) for simulating soil's contribution, is proposed in this study to simulate backscattering radar signal, applicable to agricultural fields. It combine C-band SAR data and optical images, using the NDVI as a vegetation descriptor in WCM. Bare soils and Cereals fields were considered in our study and the simulations are proposed during agricultural period (2015-2017). Results show that good correlation between the relationship of the radar signal and surface parameters, and also that the VV polarization is more sensitive to vegetation parameter.

7 REFERENCES

Attema, E. P.W.; Ulaby, F. T. Vegetation modeled as a water cloud. Radio Science 1978, 13, 357–364

Baghdadi, N.; Cresson, R.; El Hajj, M.; Ludwig, R.; la Jeunesse, I. Estimation of soil parameters over bare agriculture areas from C-band polarimetric SAR data using neural networks. Hydrol. Earth Syst. Sci. 2012, 16, 1607–1621.

Baghdadi, N., Zribi, M., 2016, Microwave Remote Sensing of Land Surfaces, Techniques and methods, ISTE Press, London and Elsevier, Oxford.

Koster, R.D.; Dirmeyer, P.A.; Guo, Z.; Bonan, G.; Chan, E.; Cox, P.; Gordon, C.T.; Kanae, S.; Kowalczyk, E.; Lawrence, D., 2004, Regions of strong coupling between soil moisture and precipitation. Science, 305, 1138–1140.

Manfreda, S.; Scanlon, T. M.; Caylor K. K., 2009, On the importance of accurate depiction of infiltration processes on modelled soil moisture and vegetation water stress. Ecohydrol., 3, 155–165 .

Paloscia, S.; Macelloni, G.; Santi, E. Soil moisture estimates from AMSR-E brightness temperatures by using a dual-frequency algorithm. IEEE Trans. Geosci. Remote Sens. 2006, 44 (11), 3135-3144.

Santi, E.; Paloscia, S.; Pettinato, S.; Fontanelli, G. Application of artificial neural networks for the soil moisture retrieval from active and passive microwave spaceborne sensors. International Journal of Applied Earth Observation and Geoinformation 2016,48, 61-73.

Wagner, W.; Lemoine, G.; Rott, H. A method for estimating soil moisture from ERS scatterometer and soil data. Remote Sens. Environ. 1999, vol. 70, no. 2, pp. 191–207.

Zhao, N.; Yu, F.; Li, C.; Wang, H.; Liu, J.; Mu, W., 2004, Investigation of Rainfall-Runoff Processes and Soil Moisture Dynamics in Grassland Plots under Simulated Rainfall Conditions. Water, 6, 2671-2689;

Using ground-based GNSS-IR to retrieval soil moisture

Chao Ren[1,2], Yueji Liang [1,2,*], Xianjian Lu[1,2], Hongbo Yan[1,2]
1 College of Geomatics and Geoinformation, Guilin University of Technology, Guilin 541004, China;
2 Research Center of Precise Engineering Surveying, Guangxi Key Laboratory of Spatial Information and Geomatics, Guilin 541004, China.
lyjayq@glut.edu.cn (Y.L.).

ABSTRACT- Considering the advantages of multi-satellite convergence and the time and space scale of soil moisture, a nonlinear sliding estimation method of soil moisture based on multi-satellite fusion is proposed. First, the direct and reflection signals of GNSS satellites are separated by means of a low order polynomial fitting, and then, by establishing the sinusoidal fitting model of reflection signals, the relative delay phase of the SNR interferogram is obtained. Finally, a linear regression model is used to analyse and select the phase of the SNR interferogram, and a sliding estimation method of soil moisture using the least squares support vector machine (LSSVM) based on multi-systems fusion is established. Based on the monitoring data, the feasibility and effectiveness of using single and multiple GNSS satellites to slide estimate soil moisture are compared and analysed. Theoretical analysis and experimentation show that, GNSS-IR can provide full play to the advantages of artificial intelligence and effectively integrate the performance of each satellite. The fitting process is stable, and the model needs less modelling data; the sliding mode can achieve a long time estimation, and the estimation error is relatively stable. Using satellites that have an R^2 value greater than 0.50, the results are better than when using single satellites, the correlation coefficient between the estimated results and the reference values of soil moisture was greater than or equal to 0.94, and RMSE and MAE are less than 0.06 and 0.05 respectively.

1 INTRODUCTION

Soil moisture is an important parameter in the research of hydrology, meteorology and the agricultural environment and is also one important index of the water resource cycle. The estimation of soil moisture is of great significance for climate prediction, flood disasters and the water resource cycle (Njoku et al., 2004; Sabater et al., 2008). In recent years, GNSS remote sensing technology based on the multi-path effect provides a new, efficient and high-resolution monitoring method for the acquisition of soil moisture. a GNSS multipath signal has been used to estimate the environmental parameters and their changes of station, such as snow depth, seawater height, soil moisture and vegetation water (Rodriguez-Alvarez et al., 2012;). According to the relationship between the soil dielectric constant and soil moisture, Wang et al. (Wang et al., 2010) proposed a simplified empirical or semi-empirical soil moisture model to verify the effectiveness of soil moisture estimation in different environments. Because these methods require numerous parameters and the modelling is complex, there are some deficiencies such as the need for manual measurement of data and the weak generalization property of the model. Larson et al. (Larson et al., 2010) took advantage of the amplitude, frequency and phase of the multipath reflection component at a certain satellite elevation to realize the

inversion of the trend of soil moisture change. Bilich et al. (Bilich, et al., 2007) studied the separation of the direct component and reflected component in SNR observations and the relationship between the reflected component and reflection environment value and then modified the phase observation value to get better results. Zavorotny et al. (Zavorotny, et al., 2010) used delay phase parameters to estimate soil moisture and verified that its correlation was more stable. By drawing from studies of vegetation scattering by other means of remote sensing, studies of the vegetation effect correction problem in the process of soil moisture detection and the derived parameter estimation of vegetation have been carried out step-by-step (Wu et al., 2012). Chew et al. developed a soil moisture retrieval algorithm for the influence of land surface soil moisture on the GPS multi-path and studied the influence of surface vegetation changes on SNR (Chew et al., 2015). Because the influence of soil surface roughness and vegetation information on microwave scattering differs, it is very difficult to establish an accurate soil moisture estimation model directly. The existing research is less concerned with the advantages of multi-satellite fusion estimation, and the estimation of soil moisture is affected by artificial interference, which is not conducive to the improvement of estimation accuracy. If soil moisture is changed with time scale and spatial scale, the

estimation of soil humidity using the GNSS-IR technique can be regarded as a nonlinear regression problem. It is possible to establish a nonlinear estimation model of soil moisture through the phase of the SNR interferogram.

Based on the aforementioned research, a method for estimating soil moisture is presented, using a least squares support vector machine based on multi-satellite fusion. The LS-SVM is introduced into soil humidity estimation, and a soil moisture estimation model based on multi-satellite fusion is established. Based on the monitoring data provided by the PBO network, the feasibility of using single and multiple satellites to estimate soil moisture was compared and analysed, and the effectiveness of the sliding type estimation was studied and verified.

2 THE THEORY OF SOIL MOISTURE SLIDING ESTIMATION

2.1 Satellite Signal Reflection

SNR is an indicator of receiver antenna signal quality, SNR can be described in plural form as follows:

$$\dot{SNR} = \dot{S}_d(0) + \dot{S}_m(\phi) \tag{1}$$

where $\dot{SNR}$, $\dot{S}_d(0)$ and $\dot{S}_m(\phi)$ are in plural form, and represent SNR, direct component and multipath reflection, respectively. Among them, '0' and 'ϕ' represent the initial phase value of direct component and the phase of the reflection component, respectively.

$$SNR^2 = S_d^2 + S_m^2 + 2S_d S_m \cos \psi \tag{2}$$

where ψ is the function variables associated with the geometry of the satellite receiver.

For one-time multi-path reflection, the signal received by the GNSS antenna is a composite signal of direct signal and reflected signal, as shown in Figure 1.
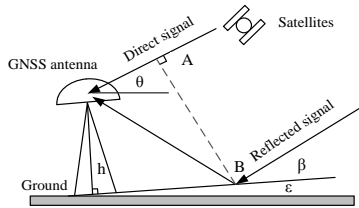
Figure 1. Geometric model of multipath error on the ground

In Figure 1, θ is the satellite elevation angle of the direct signal transmitted from the satellite; h is the vertical height of the antenna to the ground; ε is the incline angle of the slope; and β is the angle between the satellite signal and the slope. When ε is small, the formula can be expressed as follows:

$$\theta = \beta + \varepsilon \approx \beta \tag{3}$$

Combining with Figure 1, It can be concluded that

$$\frac{d\psi}{dt} = 2h \frac{2\pi}{\lambda} \cos \theta \frac{d\theta}{dt} = 2h \frac{2\pi}{\lambda} \frac{d\sin\theta}{dt} \tag{4}$$

There is a linear relationship between the relative phase ψ and $\sin\theta$.

Because there is a sine or cosine relationship between the observed SNR value and the relative phase ψ, GNSS soil moisture measurement is only related to multipath reflection components. Then, after removing the direct component, a sine or cosine relationship between SNR multipath reflection components and $\sin\theta$, with a fixed frequency, still exists (Larson et al., 2010):

$$SNR_{MP2} = A_{MP2}\cos(\frac{4\pi H}{\lambda} \sin \theta + \phi_{MP2}) \tag{5}$$

where θ, λ and H represent the satellite elevation angle, wavelength of carrier wave and GNSS antennas height, respectively; A_{MP2} is the relative amplitude of the multipath reflection components, and ϕ_{MP2} is the relative phase delay.

If $x = \sin \theta$ and $f = \frac{2\pi H}{\lambda}$, the aforementioned formula can be simplified as follows:

$$SNR_{MP2} = A_{MP2}\cos(2\pi f x + \phi_{MP2}) \tag{6}$$

2.2 The Soil Moisture Estimation Model Using The LS-SVM Based on Multi-satellite Fusion

Suppose the relative phase delay set of GNSS satellites is as follows:

$$x = [x_1^0, x_2^0, \ldots, x_i^0], (i = 1,2,\ldots, t1)$$
$$x_i^0 = [\phi_{MP2}^1, \phi_{MP2}^2, \ldots, \phi_{MP2}^j], (j = 1,2,\ldots,32) \tag{7}$$

where i is the day of the year (DOY), j is the satellite vehicle's ID, and is the length of time.

Suppose the soil humidity set corresponding to the relative phase delay set x is y. Because the relationship between the input vector x and soil moisture y is nonlinear in the application. GNSS satellite reflection signal to estimate soil moisture, mapping the sample input to a higher dimensional feature space by a nonlinear transformation is needed; thus, the nonlinear problem in input space is transformed into a linear problem in feature space. Then, a linear LS-SVM is used to fit the sample points in the feature space. The principle of LSSVM model is described (Suykens et al., 1999, Bishop et al., 2006).

2.3 The Process of Soil Moisture Estimation

1) Separating multi-path reflection components from the GNSS signal. SNR values were obtained by using TEQC software (Chew et al., 2016) to solve GNSS monitoring data, and the direct and reflection components were separated by low order polynomial fitting.

2) The resampling of multipath reflection components. Because the multipath reflection component changes with epochs, it is necessary to convert the problem to the relationship between the multi-path reflection components and the sinusoidal value of the incident satellite elevation.

3) Parameter estimation of multi-path reflection component. Fitting a sine to the component after resampling by a nonlinear least squares fitting algorithm (ohnson et al., 1981), a confidence interval algorithm (Powell et al., 1990) is used to determine the step length of the least-squares iteration and other parameters. Then, the values of amplitude and phase could be obtained.

4) Establishing a soil moisture estimation model. A linear regression model is adopted to establish the relationship between the phase of the SNR interferogram and soil moisture, selecting satellites by setting the threshold of the correlation coefficient R2. And then a nonlinear fitting model of multi-satellite fusion is established.

6) Sliding estimation. Supposing the former $t2$ period is selected as the training sample of the model and step size of estimation is τ, the total number of sliding times is $n = 1,2,\ldots,\dfrac{t1-t2}{\tau}$ and establishes the LS-SVM estimation: if the input training set is $X1 = \left\{x_1^0, x_2^0, \cdots, x_{n+b(t-1)}^0\right\}$, the output training set is $Y1 = \left\{y_1, y_2, \cdots, y_{n+b(t-1)}\right\}$; if the input training set is , the output training set is $X2 = \left\{x_{n+1}^0, x_{n+2}^0, \cdots, x_{n+bt}^0\right\}$. Thus, $Y1$ and $Y2$ could be treated as the output training set for the next model, and so on. The process is illustrated in Figure 2.

3 EXPERIMENT ANALYSIS

GNSS monitoring data of the P043 station, which is in the PBO network (http://xenon.colorado.edu/portal), was selected for the experiment. The station is located at Newcastle in Cheyenne, Wyoming, at 104.185702 W, 43.881146 N, and has an elevation of 1490.9 m.
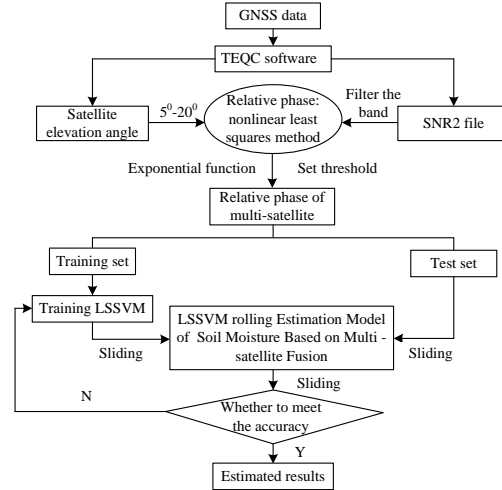
Figure 2. Flowchart depicting steps of the LS-SVM sliding estimation model based on multi-satellite fusion for soil moisture

The station can provide a high sampling rate and abundant meteorological data, and in 2011, the L2C observation data was opened to provide high quality L2 band SNR observation data. As shown in Figure 3 (left), the topography around the station is flat, open and sparsely vegetated (mainly grassland). The steel triangle bracket is adopted, and the receiver model is a TRIMBLE NERT9. The antenna cover of SCIT is adopted, and the antenna model is TRM59800.80. The change in soil moisture and rainfall at the site in the 73-294th days of 2015 (a total of 222 days) is shown in Figure 3 (right).
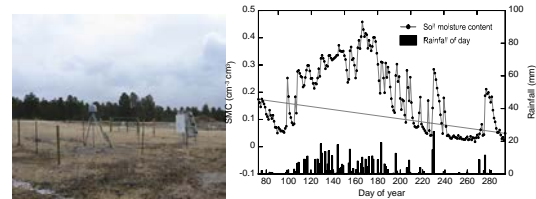
Figure 3. Digital elevation model around the GPS site p041 in southern California (left). The GPS site p041 environment (right).

Figure 3 (right) shows that rainfall is more significant, the largest rainfall is 26 mm. Corresponding to the rainfall, soil moisture increased significantly, especially from the 229-230th day and 275-276th day. Due to the continuous rainfall, the soil moisture changes more significantly and shows strong non-linearity and randomness. When the rainfall stops, soil moisture decreases gradually. It can be seen that rainfall is the main reason for the change in soil moisture. The station has abundant rainfall and is suitable for the study of soil moisture.
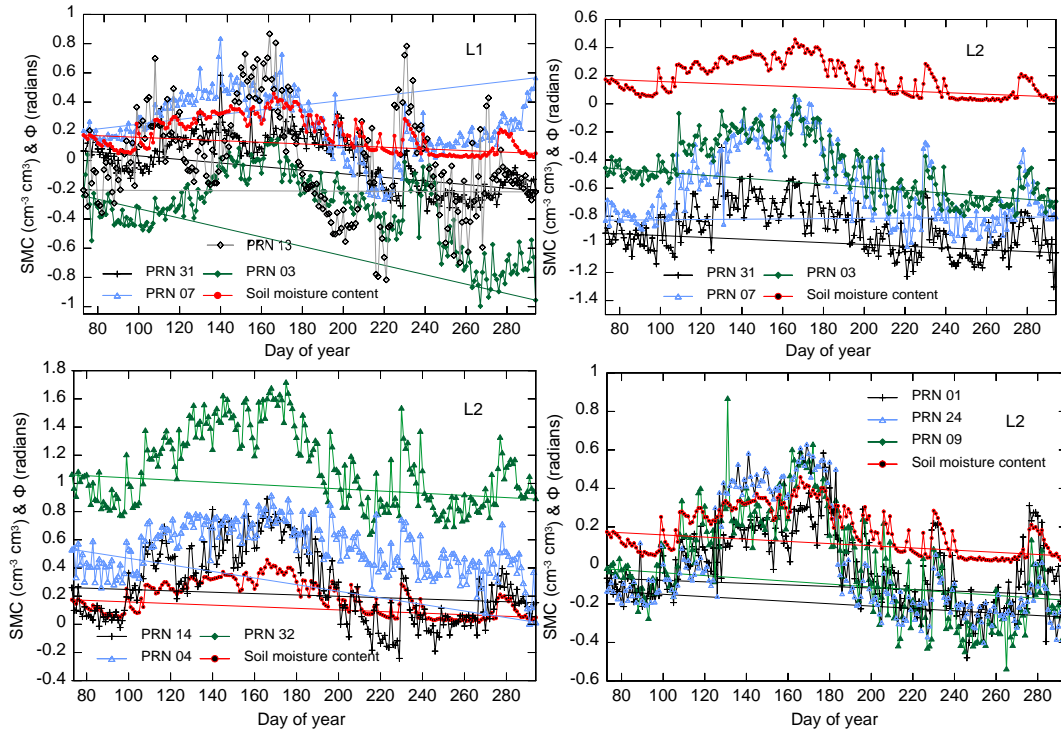
Figure 4. (top left) Delay phases of L1 for four satellite tracks: PRN03 (green triangles), 07 (blue triangles), 13 (black quadrilateral s) and 31 (black Crosses). (bottom left) Delay phases of L2 for three satellite tracks: PRN04 (blue triangles), 14 (black crosses), and 32(green triangles). (top right) Delay phases of L2 for three satellite tracks: PRN03 (green triangles), 07 (blue triangles), and 31(black crosses). (bottom right) Delay phases of L2 for three satellite tracks: PRN01 (black crosses), 09 (green triangles), and 24(blue triangles). Soil moisture content (red dots).

Therefore, the monitoring data from the 73rd-294th day of 2015 are selected, the sampling rate is 30 Hz, and the satellite elevation is between 5° and 20°. The SNR (L2 carrier) is obtained by using TEQC to calculate the GNSS receiver monitoring data, and separating the direct signal and reflection signal of each satellite by a quadratic polynomial separation. Then, the nonlinear least squares method is used to estimate the phase of SNR interferogram. Limited by space, only the L1 and L2 bands of some satellites are selected for analysis, and the relationship between the phase of the SNR interferogram of each satellite and soil humidity is shown in Figure 4.

Figure 4 shows that when the soil humidity rises or decreases, the phase of the SNR1 interferogram in the L1 carrier of each satellite has some outliers and has poor agreement with soil moisture, while the phase of the SNR1 interferogram in the L1 carrier of each satellite can have a good response to soil moisture. For the 229 ~ 231st day and 275 ~ 277th day, the phase of the SNR interferogram shows a large fluctuation. This is related to the sharp rise in soil humidity caused by continuous rainfall.
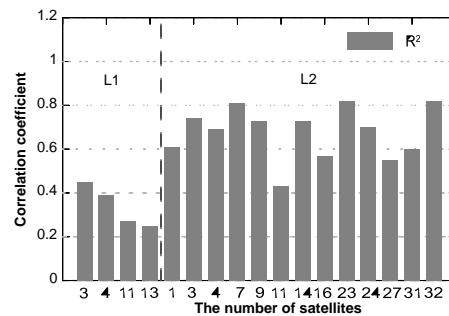
Figure 5. The correlation coefficient between delayed phase and soil moisture.

Combined with Figure 5, it shows that the correlation between the phase of the SNR1 interferogram and the soil moisture is poor, and the correlation coefficients between the phase of the SNR2 interferogram and soil moisture are more than 0.50. From the aforementioned analysis, we can see that the correlation coefficients between the phase of the SNR interferogram and soil moisture are different. Moreover, because the kinematical track of the

satellite and the different performance of different satellites, the response patterns of different satellites to changes in soil moisture are not consistent during the same periods. Therefore, the phase of the SNR interferogram in the L2 carrier is selected to establish the soil humidity estimation model in this paper.

To verify the feasibility and effectiveness of the soil moisture estimation method based on multi-satellite fusion, for the regression coefficient R^2 of the linear regression equation, this study set a threshold of 0.40. Phases of 13 satellite's SNR2 interferograms are selected to establish the soil moisture estimation model based on the LS-SVM, and 7 schemes are designed as follows: scheme 1 – sliding estimation based on a single satellite; scheme 2 - sliding estimation based on multi-satellite fusion with an $R^2 > 0.40$; scheme 3 - sliding estimation based on multi-satellite fusion with an $R^2 > 0.50$; scheme 4 - sliding estimation based on multi-satellite fusion with an $R2 > 0.60$; scheme 5 - sliding estimation based on multi-satellite fusion with an $R^2 > 0.70$; scheme 6 - sliding estimation based on multi-satellite fusion where $0.7 = < R^2 < 0.80$; and scheme 7 - sliding estimation based on multi-satellites fusion where $0.8 = < R^2 < 0.90$. To reduce the modelling error, each phase is pre-treated and normalized to [-1, 1], then reduced to the original interval after the estimation. The test samples are taken from the 73rd-119th days, the 120-294th days

are selected as the training samples, and the estimated step size was 1. For example, when the prediction step is, the 73rd-119th days are selected for establishing the model to estimate the 120th day. Then, when, the 73rd-120th days are selected for establishing the model to estimate the 121st day, and so on, until the 294th day is estimated. The estimated results of each scheme are shown in Figure 7. The linear regression analysis between the estimated results and the true values of soil moisture are shown in Figure 8. Limited by space, only partial satellite results are provided.

Figure 6 displays the soil moisture estimation based on a single satellite does not reflect the change in soil moisture accurately; the estimation error is large, and the fluctuation is obvious, in particular for the 240-270th day. Most of the estimation results based on a single satellite increase gradually, and even some estimation results of the satellites are distorted.

The comparison between Scheme 2 and Scheme 7 finds that the estimation error of the Scheme 2 days has an obvious distortion from the 120-180th day; estimated results of Scheme 3 and Scheme 4 are stable relatively, as the errors are within 0.10. For Schemes 5 through 7, because the number of satellites reduces gradually, the estimation error results in the phenomenon of sudden change, such as the 200 to 230th days.
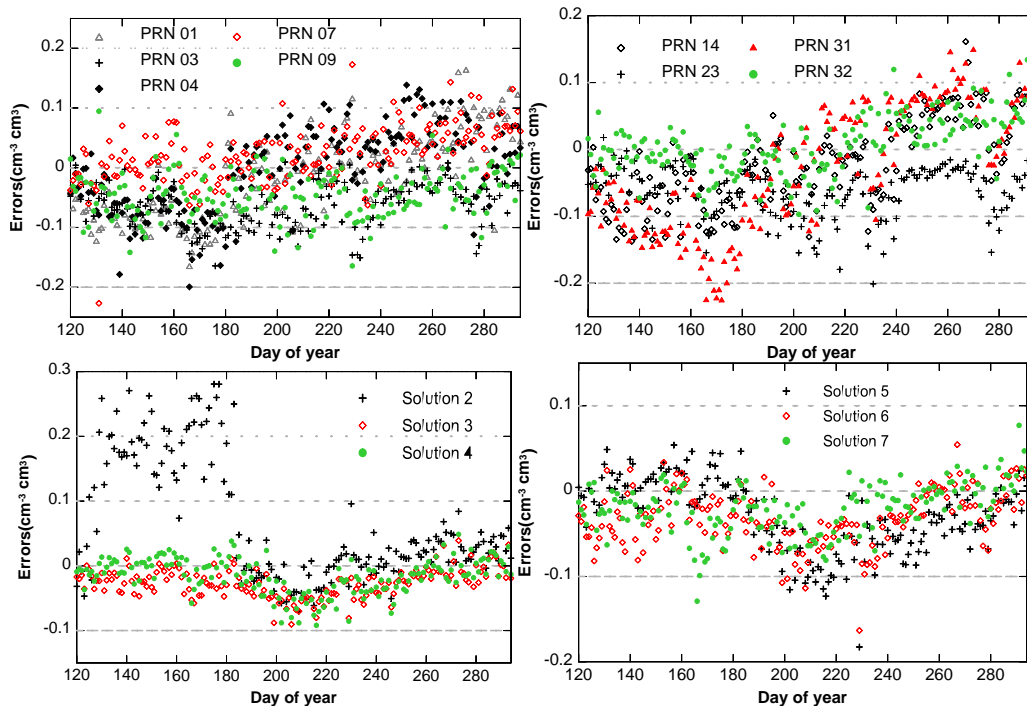
Figure 6. Top: Inversion error for Single satellite: PRN 01, 03, 04, 07, 09, 14, 23, 31 and 32. Bottom: Inversion error for Solutions: Solution 2, Solution 3, Solution 4, Solution 5, Solution 6 and Solution 7.

Combining Table 1, one can see that even though the correlation between the phase of the SNR2 interferogram and the estimation of soil moisture based on a single satellite is better, the estimation results still have major uncertainty. It is difficult to guarantee the stability of the error, and the maximum error is greater than 0.10. The estimation based on multi-satellite fusion can well reflect a change in soil moisture, and the correlation coefficient is greater than or equal to 0.94; by selecting the satellites where the R^2 is greater than 0.50 for fusion, the results of the estimation based on multi-satellite fusion are better. From scheme 4 ~ scheme 6, the estimation of soil moisture in different time periods is related to the number of satellites for fusion and the correlation coefficient. According to the analysis of the root mean square error and mean absolute error shown in Table 1, by selecting the satellites where the R^2 is greater than 0.50 for fusion, the estimation results have a better accuracy as most of the mean square error (RMSE) is less than 0.06, and the mean absolute error (MAE) is less than or equal to 0.04. Compared to the model based on multi-satellite fusion, the results of Scheme 3 and 4 are the best, with more stable accuracy and a maximum estimation error of less than 0.10, and the average error is 0.029 and 0.024, respectively.

Table 1. Estimation accuracy of soil moisture in each model (unit: cm^{-3} cm^3)

Satellites	R^2	RMSE	MAE	Max	Mean
PRN 01	0.74	0.072	0.060	-0.165	0.059
PRN 03	0.92	0.074	0.064	-0.164	0.084
PRN 04	0.78	0.070	0.058	-0.199	0.060
PRN 07	0.87	0.052	0.040	-0.227	0.064
PRN 09	0.91	0.060	0.050	-0.164	0.058
PRN 14	0.80	0.070	0.059	0.161	0.040
PRN 23	0.91	0.074	0.063	-0.201	0.050
PRN 31	0.69	0.097	0.084	-0.226	0.063
PRN 32	0.89	0.044	0.035	0.134	0.035
Scheme 2	0.94	0.115	0.080	0.281	0.080
Scheme 3	0.97	0.034	0.029	-0.090	0.029
Scheme 4	0.96	0.032	0.024	-0.092	0.024
Scheme 5	0.95	0.051	0.040	-0.183	0.040
Scheme 6	0.94	0.046	0.038	-0.163	0.038
Scheme 7	0.95	0.037	0.028	-0.129	0.028

Max is the maximum value of the model inversion error, Mean is the average of the model inversion results.

In conclusion, the sliding estimation method using the LS-SVM based on multi-satellite fusion integrates the performance of each satellite fully, and the phases of the SNR2 interferograms are complementary to each other; this method can improves the problem of a single satellite that has difficulty adapting to the multi-path effect of the surface. In addition, selecting the satellites for which the R^2 is greater than 0.50 for fusion can allow for better adaptation to different levels of soil moisture estimation compared to a single satellite. A fitting phenomenon does not occur in the process of estimating using the LS-SVM, and the performance of the models is well applied. The correlation coefficient R^2 between multi-satellite fusion and soil moisture is greater than the estimation results based on a single satellite. The sliding method is beneficial to the estimation of soil moisture, and over a long period, the estimation error is more stable.

4 CONCLUSIONS

The theoretical analyses and experiments show the following: 1) The GNSS antenna is affected by the kinematical track and the performance of satellites during observation, the phase of the SNR interferograms of different satellites have different response patterns to changes in soil moisture, and a linear regression equation can well describe the relationship between the two. 2) The proposed method provides full play to the advantages of artificial intelligence in measuring soil moisture, synthesizes the performance of each satellite effectively, and makes the phases of the SNR2 interferograms complementary to each other. Moreover, the model needs less modelling data, the sliding mode can realize the estimation over a long period of time, and the fitting process performance and the estimation error are stable. 3) Based on multi-satellite fusion, when the satellites for which the R^2 is greater than 0.50 are, the correlation coefficient between the results and the reference values of soil moisture is equal to or greater than 0.94. And the RMSE and MAE are less than 0.06 and 0.05, respectively. Therefore, the estimation of soil moisture can be treated as a nonlinear event, and multi-satellite fusion is more favourable to accurate estimation of soil moisture. To further improve the performance of this model, multi-station data in different environments, vegetation information, temperature, rainfall and other variables will be taken into account.

REFERENCES

Bilich, A., & Larson, K. M. (2007). Mapping the GPS multipath environment using the signal-to-noise ratio (SNR). Radio Science, 42(6).

Bishop, C. M. (2006). Pattern recognition and machine learning. Springer.

Chew CC, Small EE, Larson KM, Zavorotny VU. (2015). Vegetation sensing using GPS-interferometric reflectometry: theoretical effects of canopy parameters on signal-to-noise ratio data. IEEE Trans Geosci Remote Sens 53:2755–2764.

Chew, C., Small, E. E., & Larson, K. M. (2016). An algorithm for soil moisture estimation using GPS-interferometric reflectometry for bare and vegetated soil. GPS solutions, 20(3), 525-537.

Larson, K. M., Braun, J. J., Small, E. E., Zavorotny, V. U., Gutmann, E. D., & Bilich, A. L. (2010). GPS multipath and its relation to near-surface soil moisture content. IEEE Journal of Selected Topics in Applied Earth Observations and Remote Sensing, 3(1), 91-99.

Njoku, E. G., Lakshmi, V., & O'Neill, P. E. (2004). Soil moisture field experiment special issue. Remote Sensing of Environment, 92(4), 425-426.

ohnson, M. L., Correia, J. J., Yphantis, D. A., & HalvorSON, H. R. (1981). Analysis of data from the analytical ultracentrifuge by nonlinear least-squares techniques. Biophysical Journal, 36(3), 575-588.

Powell, M. J. D., & Yuan, Y. (1990). A trust region algorithm for equality constrained optimization. Mathematical Programming, 49(1), 189-211.

Rodriguez-Alvarez, N., Bosch-Lluis, X., Camps, A., Ramos-Perez, I., Valencia, E., Park, H., & Vall-Llossera, M. (2012). Vegetation water content estimation using GNSS measurements. IEEE Geoscience and Remote Sensing Letters, 9(2), 282-286.

Suykens, J. A., & Vandewalle, J. (1999). Least squares support vector machine classifiers. Neural processing letters, 9(3), 293-300.

Sabater, J. M., Rüdiger, C., Calvet, J. C., Fritz, N., Jarlan, L., & Kerr, Y. (2008). Joint assimilation of surface soil moisture and LAI observations into a land surface model. Agricultural and forest meteorology, 148(8), 1362-1373.

Wang qiang, Guo zhifeng, Sun guoqing, Luo chuan wen, & liu dandan. (2010). Construction of MGeoSAIL: A Hybrid BRDF mode for Discontinuous Vegetation nopies, 39 (2), 0-145.

Wu, X., Li, Y., & Xu, J. (2012). Theoretical study on GNSS-R vegetation biomass. In Geoscience and Remote Sensing Symposium (IGARSS), 2012 IEEE International (pp. 6380-6383). IEEE.

Zavorotny, V. U., Larson, K. M., Braun, J. J., Small, E. E., Gutmann, E. D., & Bilich, A. L. (2010). A physical model for GPS multipath caused by land reflections: Toward bare soil moisture retrievals. IEEE Journal of Selected Topics in Applied Earth Observations and Remote Sensing, 3(1), 100-110.

Comparison of Two Methods for Soil Moisture Mapping at 1km Resolution from Sentinel-1 and MODIS Synergy

Q. Gao, M. Zribi, M.J. Escorihuela, N. Baghdadi

isardSAT, Parc Tecnolo`gic Barcelona Activa, Carrer de Marie Curie, 8, 08042 Barcelona, Spain
CESBIO (CNRS/CNES/UPS/IRD), 18 av. Edouard Belin, bpi 2801, 31401 Toulouse cedex9, France.
Observatori de l'Ebre (OE), Univ. Ramon Llull CSIC, Spain
IRSTEA, UMR TETIS, 500 rue Franois Breton, 34093 Montpellier cedex 5, France
qi.gao@isardsat.cat

ABSTRACT - *This paper presents two methodologies retrieving soil moisture from SAR remote sensing data. The study is based on Sentinel-1 data in the VV polarization, over a site in Urgell, Catalunya (Spain). By modelling the backscatter difference w.r.t. NDVI, the soil moisture corresponding to a specific NDVI value can be retrieved. The first algorithm is already developed on West Africa (Zribi et al., 2008) from ERS scatterometer data to estimate soil water status. In this study, it is adapted to Sentinel-1 data and take into account the high repetitiveness of data in optimizing the inversion approach. Another new method is developed based on the backscatter difference be- tween two adjacent days of Sentinel-1 data w.r.t. NDVI, with smaller vegetation change, the backscatter difference is more sensitive to soil moisture. The validation of the two methods is done with field data acquired in study site, with an rms error about 0.08 m3/m3 for method 1 and 0.07m3/m3 for method 2 in volumetric moisture.*

1 INTRODUCTION

Surface soil moisture plays an essential role in numerous environmental studies related to hydrology, meteorology and agriculture. For hydrological and agricultural purposes, the estimation of soil moisture is crucial since it controls the quantity of water available for vegetation growth (Cook et al., 2006; Bezerra et al., 2013). The low resolution traditional passive remote sensing measures the surface soil moisture at a high temporal resolution about 2-3 days, but low spatial resolution (around 40 km) (Zribi et al., 2008). With SAR missions, although the temporal resolution is relatively low (eg. 12 days for Sentinel-1), but the spatial resolution is much higher. Radar remote sensing measurements of bare soil are very sensitive to water content in the surface layer due to   the pronounced increase in the soil dielectric constant with increasing water content (Baghdadi et al., 2016). Assuming the influence of vegetation variation and soil roughness change is small, we have the difference of backscatter related with the change of soil moisture. In the last twenty years, different inversion algorithms have been proposed to retrieve soil moisture. Change detection approaches have been widely used, particularly at low and medium spatial resolutions (Zribi et al., 2014; Wagner et al., 2008).

In this paper, we introduce two methodologies in which soil moisture is retrieved from Sentinel-1 data over the period from the end of 2014 until 2016 November for method 1 and method 2. In the two methodologies using change detection techniques, preprocessed radar data are combined with normalized difference vegetation index (NDVI) auxiliary data to estimate the mean soil moisture with a resolution of 1km. By modeling the relationship between the backscatter difference and NDVI, the soil moisture at a specific NDVI value is retrieved. The first method considering the backscatter difference between a certain value and the minimum value through- out the whole time period, while the second method considering the backscatter difference between two adjacent days of acquisition.

This paper is organized as follows. In Section 2, the studied site and data base are presented. Section 3 describes the two methodologies. Section 4 shows the validation with the ground measurements and the results of the retrieved soil moisture. Finally, the discussion and conclusions are presented in the last section.

2 SITE AND DATABASE

2.1 Site

The study area covers a 60x60km area and is located in Urgell, Catalunya. Urgell climate is typically Mediterranean with continental influence, mild in winter and warm in summer, with a very dry season in summer and two rainier seasons in autumn and spring (Escorihuela et al., 2016).

In the old irrigated district, the open channel leads water into the agricultural fields, makes the

vegetation flourishing in this area, which can be obviously recognized as the green area in the map in Fig.1. Surrounded the irrigated area, the land is much drier without irrigation. A new irrigated system is being developed surrounding the old irrigated system but is still not visible on satellite imagery.
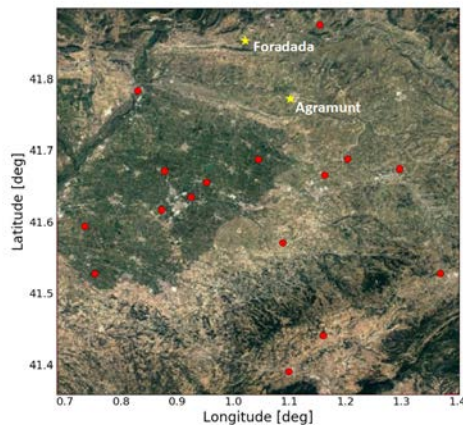
Fig. 1. Study area in Urgell, Catalunya (60km x 60km) with ground measurements (star points) and meteo stations (round points)

2.2 Data Base

2.2.1 Ground Measurements

In-situ measurements are acquired, continuously in two demonstrative fields belonging to the new irrigated district: Foradada and Agramunt.

Table 1. Ground measurement in the two demonstrative fields of Foradada and Agramunt.

Site	Foradada	Agramunt
Depths	3, 9, 10, 20 cm	5, 10, 20, 40 cm
Period	May-Aug. 2015	June-Oct. 2015
	Feb.-Oct. 2016	July-Nov. 2016
Sand	41.5%	52.1%
Silt	42.3%	35.3%
Clay	16.2%	12.6%

The meteorological data comes from 16 meteo stations in the study area and the nearest station is used for validation.

2.2.2 Satellite Data

1) Sentinel-1 data
The Sentinel-1 mission provides data from a dual-polarization C-band Synthetic Aperture Radar (SAR) instrument. In this study, three different tracks (110, 30, 132) of the Sentinel- 1A are used for retrieving soil moisture, with resolution of 10m and temporal resolution of 12 days for each track. VV polarization is used for our analysis. All the Sentinel-1 data is preprocessed with 3 steps: thermal noise removal, radiometric calibration, and terrain correction using SRTM DEM at 30m.

2) MODIS Data
The MODIS Normalized Difference Vegetation Index (NDVI) complements NOAAs Advanced Very High Resolution Radiometer (AVHRR) NDVI products and provides continuity for time series historical applications. In this study, the considered MODIS products (MOD13Q1 and MYD13Q1) coming from Aqua and Terra missions, have 16-day temporal resolution and 250m spatial resolution.

3 METHODOLOGIES

3.1 Method 1

The first method is to retrieve soil moisture by modeling of radar signal dependence on vegetation, which is already developed on West Africa with ERS Scatterometer to estimate soil water status (Zribi et al., 2008). In this study, the approach is adapted to Sentinel-1 data and takes into account the high repetitiveness of data in optimizing the inversion approach.

The signal received by the instrument from each spatial cell results from the sum of the backscattered signals contributed by both bare soil and vegetation cover (Zribi et al., 2008). The backscatter from bare soil is affected by soil moisture and soil roughness. If we assume that the influence of vegetation variation and soil roughness change are small compared to that of soil moisture, the backscatter difference between a given date and that at which the driest signal is estimated is related with the change of soil moisture. Three NDVI classes are divided evenly according to the minimum and maximum value in this area. Within each NDVI class, we assume the vegetation variation effect can be neglected. Take into account the all year round data, the minimum value for each pixel is found, which corresponding to the driest signal. With the increase of the NDVI value, the sensitivity of the signal to the moisture should decrease, which means the difference between satellite backscatter of a given date with that of the driest date is decreasing with NDVI.

3.1.1 Method 1 modeling

The modeling of backscatter difference as a function of NDVI for satellite track 110 is shown in Fig.2. To estimate the with- out being affected by noise effects due to rare events, for each value of the NDVI, we excluded the upper 1% of the corresponding values and we consider the 10% maximum (green points) to build the function, which is representing the maximum soil moisture.
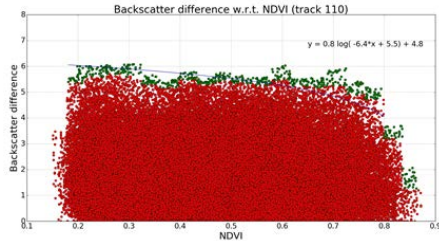
Fig. 2. Illustration of the processed radar signal as a function of NDVI over Urgell site

The soil moisture for each pixel can be retrieved by the following function.

$$Mv(i,j,t) = \frac{\Delta\sigma_{(i,j)}^{NDVI}}{f(NDVI)}(Mv_{\max}) + Mv_{\min}(i,j,d)$$

The soil moisture $Mv(i, j, t)$ for a specific cell (i, j) at a given date t can be derived by the difference between the backscatter for a given date and the minimum value for each pixel, divided by the function of NDVI, which corresponding with the maximum soil moisture, then multiplied by Mv_{max} which is set to be 0.3 according to SMOS data in this area. Mv_{min} is considered approximately equal to 5%.

3.2 Method 2

Another new method is developed based on the backscatter difference between two adjacent days of Sentinel-1 data w.r.t. NDVI, in this case the vegetation change is much smaller, thus the backscatter difference is more sensitive to soil moisture. The database for method 2 is from 2014 November until 2016 October, but data during April and May is excluded since the vegetation change is quite rapid causing big changes in radar signal.
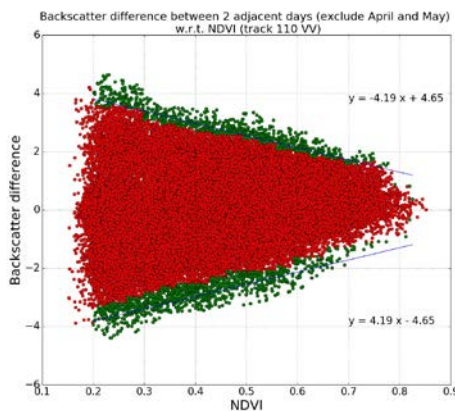
Fig. 3. Illustration of the backscatter difference between two adjacent dates as a function of NDVI over Urgell site

3.2.1 Method 2 modeling

In Fig.3, the difference between two adjacent days decrease with NDVI in a very symmetric pattern. Again, we set 20 NDVI steps, and for each step, we delete the 0.1% maximum, then consider the 10% maximum (green points) to build the linear function f(NDVI), which is corresponding to maximum soil moisture change between two dates.

The soil moisture for each pixel between date (t1) date (t2) can be retrieved by the following function.

$$Mv(i,j,t_2)) = H(\delta\sigma(t_1,t_2)) + Mv(i,j,t_1))$$

where H is equal to:

$$H(\delta\sigma(t,t+1)) = \frac{\delta\sigma NDVI}{g(NDVI)}(\delta Mv_{\max})$$

From the ground measurement statistics, the maximum soil moisture difference between two adjacent dates of Sentinel-1 data, $\delta Mv_{\max}$, is assumed to be equal to 0.15 m3/m3.
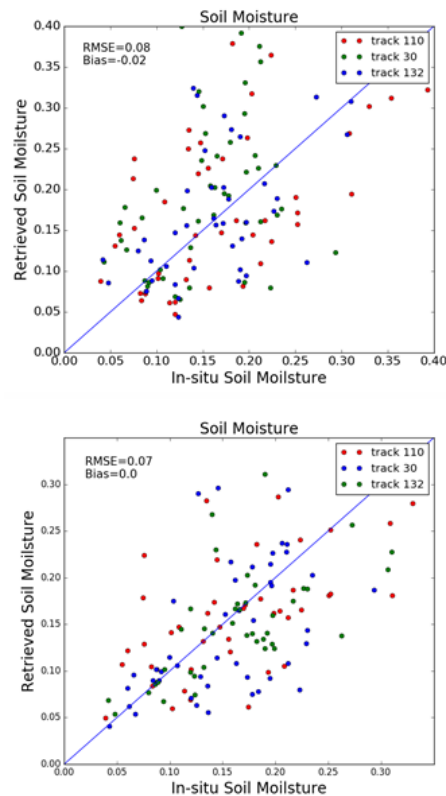
Fig. 4. Inter comparison between moisture Sentinel-1 estimations with all three satellite tracks for method 1 (up) and method 2 (bottom) and ground measurements in two demonstrative fields.

From a starting date t1, which in the present case is a date corresponding to a ground measurement, an

iterative calculation is used to determine the soil moisture for the following dates t1, t2, t3:

$$Mv(i, j, t_2)) = Mv(i, j, t_1)) + H(\delta\sigma(t_1, t_2))$$
$$Mv(i, j, t_3)) = Mv(i, j, t_2)) + H(\delta\sigma(t_2, t_3))$$

4. VALIDATION AND RESULTS

4.1 Validation

With the ground measurements available in two demonstrative fields (Foradada and Agramunt), the validation is done for retrieved soil moisture from Sentinel-1 data. The validation considers all three satellite tracks and two demonstrative fields for both methods. The Root Mean Square (RMS) error value is about 0.08 in volumetric soil moisture for method 1 and 0.07 for method 2 as shown in Fig.4. For method 2, the initial value for the starting point of iteration is based on ground measurement.

4.2. Results

The retrieved soil moisture for both methods are mapped for our studied site. Blue color represents wettest pixels and red color relatively dry. All the retrieved soil moisture values are scaled from 0 to 30%. The up 2 figures (a) and (b) in Fig.5 are the results of method 1, and figure (c) and (d) are the results of method 2. A high similarity is observed between the two method products. We retrieve approximately the same moisture spatial variations for the two analyzed dates. August 21st in 2015 is a very dry day, showing clearly the irrigated area. September 2nd of 2015 estimations are just after a rainfall more than 10 mm, resulting the soil moisture increased a lot in the whole area.

(a) Method 1 (2015-08-21)

(b) Method 1 (2015-09-02)

(c) Method 2 (2015-08-21)

(d) Method 2 (2015-09-02)
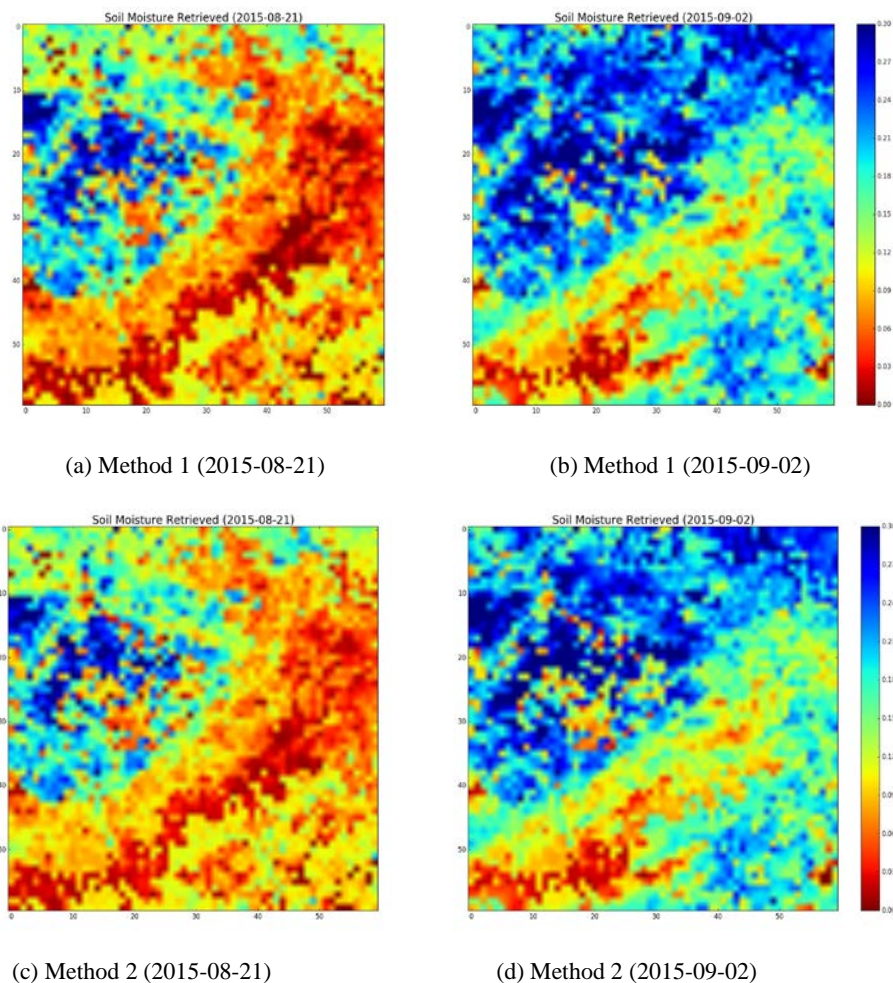
Fig. 5. Retrieved soil moisture map of method 1 and method 2.

5. DISCUSSION AND CONCLUSIONS

In this paper, two inversion approaches are developed based on the high repetitiveness of Sentinel-1 data. The proposed methodologies, using change detection techniques, have been validated with the ground measurement in two demonstrative fields with RMS value about 0.08 for method1 and 0.07 for method 2 (in volumetric moisture), and the coherence between soil moisture variations and rainfall events is observed. Soil moisture maps at 1km resolution are generated for the study area. These results demonstrate the potential of Sentinel-1 data for the retrieval of soil moisture at 1km or even better resolution.

6. REFERENCES

Zribi, M., Andre, C. and Decharme, B., 2008, A method for soil moisture estimation in Western Africa based on the ERS scatterometer. *IEEE Transactions on Geoscience and Remote Sensing*, **46** (2), 438 – 448.

Cook, B.I., Bonan, G.B. and Levis, S., 2006, Soil moisture feedbacks to precipitation in Southern Africa. *Journal of Climate*, **19**, 4198–4206,

Bezerra, B.G., Santos, C.A.C., Silva, B.B., Perez-Marin, A.M., Bezerra, M.V.C., Berzerra, J.R.C., and Rao, T.V.R., 2013, Estimation of soil moisture in the root-zone from remote sensing data. *Rev. Bras. Cilnc. Solo,* **37**, 596– 603.

Baghdadi, N., Zribi, M., 2016, Land Surface Remote Sensing in Continental Hydrology, *ISTE Press*, London and Elsevier, Oxford.

Zribi, M., Kotti, F., Amri, R., Wagner, W., Shabou, M., LiliChabaane, Z. and Baghdadi, N., Soil moisture mapping in a semiarid region, based on ASAR/wide swath satellite data, 2014, *Water Resources Research*, **50**, 823–835.

Wagner, W., Pathe, C., Doubkova, M., Sabel, D., Bartsch, A., Hasenauer, S., Bloeschl, G., Scipal, K., Martinez-Fernandez, J., and Loew, A., 2008, Temporal stability of soil moisture and radar backscatter observed by the Advanced Synthetic Aperture Radar (ASAR), *Sensors*, **8**, 1174–1197

Escorihuela, M. J. and Quintana-Segui, P., 2016, Comparison of remote sensing and simulated soil moisture datasets in mediterranean landscapes, *Remote Sensing of Environment*, **180,** 99–114.

Inland Water Level Retrieval with Radar Altimeters

Q. Gao, M.J. Escorihuela, A. Garcia-Mondejar, B. Martinez-Val, M. Zribi, P. Quintana-Segui, N. Baghdad,

isardSAT, Parc Tecnologic Barcelona Activa, Carrer de Marie Curie, 8, 08042 Barcelona, Spain

CESBIO (CNRS/CNES/UPS/IRD), 18 av. Edouard Belin, bpi 2801, 31401 Toulouse cedex9, France.

Observatori de l'Ebre (OE), Univ. Ramon Llull CSIC, Spain

IRSTEA, UMR TETIS, 500 rue Franois Breton, 34093 Montpellier cedex 5, France

qi.gao@isardsat.cat

ABSTRACT - *The inland water level plays an essential role in water balance management. This paper presents methodology to retrieve water level from radar altimeter data including Cryosat-2 and Jason-2 over lakes in Western Africa. The idea is to combine both Level-1 and Level-2 data to retrieve water level more precisely and automatically over small lakes. From Level-1 data, the waveform is analyzed for data filtering and the possibility of water level retrieval. Then an iteration method is proposed to retrieve the height from Level-2 altimeter data with a strict water mask. The preliminary results of water level time series, derived from Level-2 data, in Lake Volta and Lake Kainji are presented in this paper, and the results are compared with the data from DAHITI (Database for Hydrological Time Series of Inland Waters). The standard deviation is controlled below 0.3 meters.*

1 INTRODUCTION

The space-borne radar altimeter is an essential tool to monitor the oceans, and it can be also used for inland water surfaces including lakes and rivers. The space-borne radar altimeters transmit a short microwave pulse in the nadir direction, and the signal reflected by the surface is received by the instruments. The elapsed time corresponds to the range between the satellite and the Earth's surface (Calmant et al., 2008). The water level from an altimeter is derived from the satellite range (R), subtracted from the altitude of the satellite (Halt), and by applying the different needed corrections. In this study, the corrections of wet troposphere, dry troposphere, ionosphere, solid earth tide and pole tide are made, and the geoid is applied.

$$H_{waterlevel} = H_{alt} - R + (C_{wet\_tropo} + C_{dry\_tropo} + C_{iono} + C_{solid\_earth\_tide} + C_{pole\_tide}) + C_{geoid}$$

Since all altimeters including Cryosat-2 and Jason-2, are designed initially for oceans, so there are some limits for in- land water level retrieval, which is influenced a lot by land contamination. Despite CryoSat-2 having different operating modes (SAR, SARin and LRM), over the Niger basin is operated in LRM being its spatial resolution equivalent to Jason-2 (over 1km). The aim of this study is to reduce the contamination and get a clear signal for inland water level retrieval.

This paper is organized as follows. In Section 2, the studied area and data base are presented. Section 3 analyzes the level 1 waveform over the lakes. Section 4 proposes an iteration methodology to retrieve the water level. Section 5 shows the results of the retrieved height and the comparison with the DAHITI database. Finally, the conclusions are presented in the last section.
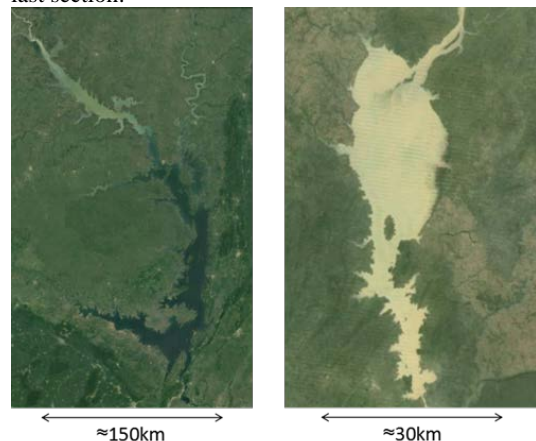
Fig. 1. Study areas including Lake Volta (a) and Lake Kainji (b).

2 STUDY AREA AND DATABASE

2.1 Study area

The study area is located in the Western Africa, and two lakes (Lake Volta and Lake Kainji) are chosen for

the study. For both lakes, the water level data time series is available in the DAHITI database. The water surface for both lakes is changing with seasons, and there are islands inside, irregular lakeshores, making it difficult to get a clean data. During dry seasons, the land reveals in the north part of Lake Kainji.

2.2 Data Base

1) Cryosat-2
CryoSat-2 is a European Space Agency environmental research satellite which was launched in April 2010. It is the first satellite with a high-resolution altimeter (Garcia Mondejar et al., 2014).
Although it is dedicated to monitoring of the ice change, the water level can also be retrieved from it. The new SAR mode provides an along track resolution of 250m. There are three operating modes of the payload SIRAL (SAR Interferometric Radar Altimeter): LRM (Low Rate Mode), SARIN (SAR Interferometric), SAR. Moreover, unluckily, the LRM is the operating mode over the study area. SARIN mode is only available since 2017 over Niger river basin.

2) Jason-2 and Jason PISTACH
The Ocean Surface Topography Mission (OSTM) on the Jason-2 satellite is a follow-on mission to Jason-1 measures the sea surface height since 2008. Jason PISTACH (Coastal and Hydrology Altimetry product) are the improved Jason-2 altimeter products for coastal areas and inland waters with specific processing, developed by CLS (Satellite Location Collection).

2.2.1. DAHITI

Database for Hydrological Time Series of Inland Waters (DAHITI) provides water level time series of lakes, reservoirs, rivers, and wetlands derived from multi-mission satellite altimetry for hydrological applications (Schwatke et al., 2015).

2.2.2. MODIS NDVI

The MODIS Normalized Difference Vegetation Index (NDVI) complements NOAA's Advanced Very High Resolution Radiometer (AVHRR) NDVI products and provides continuity for time series historical applications. The NDVI image is used for water mask generation over the study area.

3 METHODOLOGY

3.1. Level-1 Waveform Analysis

Level-1 data are calibrated waveforms with the engineering and Doppler corrections applied. For a rough surface, the leading edge of the return pulse is stretched because of scattering. For water surface, the power of signal received by the instrument is much larger than for the rough land, and the energy which is the total amount of waveform is larger as well. The power echo values are normally scaled to fit between a certain range. The scaling factors can change for each waveform, and it is given within the altimeter data (Cryosat product handbook, 2012).
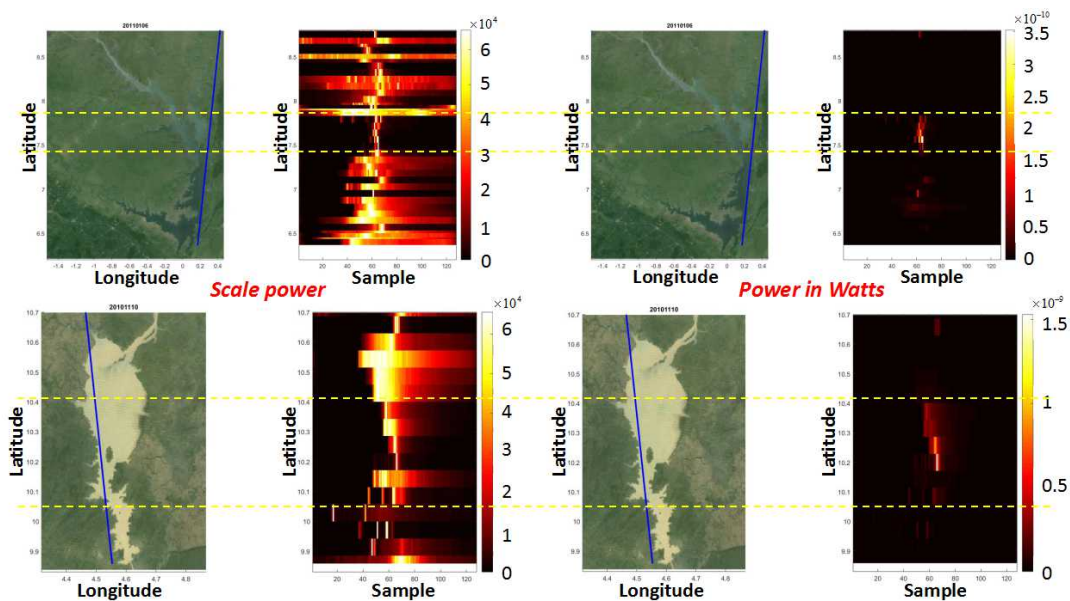
Fig. 2. Waveform analysis over Lake Volta and Lake Kainji.
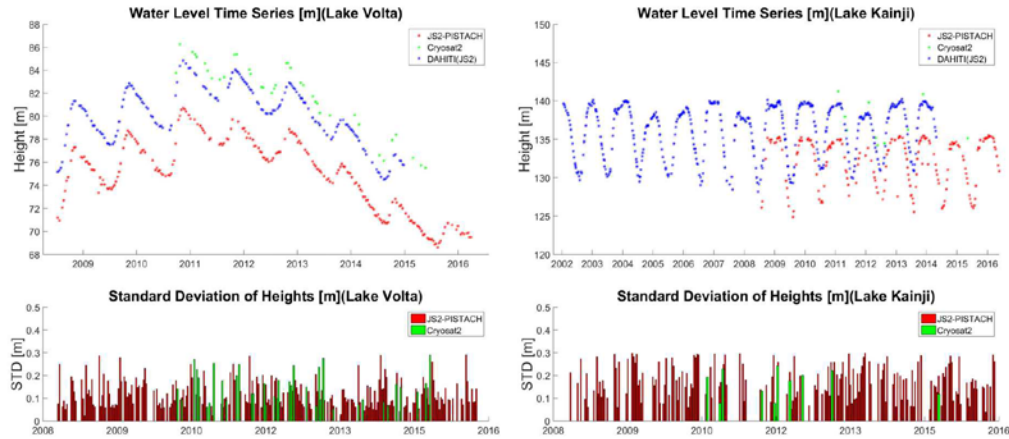
Fig. 3. Water level time series and Standard Deviation over Lake Volta (left) and Lake Kainji (right).

To convert these back to values in Watts the following equation is used.

Power_in_Watts=scaled_value*(scale_factor*e−9)* 2^scale_power

Fig.2 shows samples of waveform for each footprint over Lake Volta and Lake Kainji. The left figures show the scale power while the right figures show the power in Watts. When the satellite track passes through the water, the waveform is more peaky than for land, and after converted to power in watts, it is more clear where water is. For Lake Kainji, the land reveals in the north part. To get the water level from Level-1 data, a strict water mask is needed. It is possible to retrieve the height from waveforms by combining the conditions of the peak for the waveform and the energy amount, but the threshold needs to be defined depending on different situations. Level-1 data can be used for altimeter data filtering, together with Level-2 data, the height retrieved could be more precise.

3.2. Water level retrieval from Level-2 data

Level-2 data is the Level-1 data retracked and corrected for geophysical effects. The transmission time is included in the product which allows computing the satellite range easily. From Level-2 data, an iteration method is developed to control the standard deviation. For each track, start from the middle point within the lake, calculate the height standard deviation of the middle three points, add more points to the border if the standard deviation is smaller than 0.3 meters. In this case, the standard deviation is controlled below 0.3 meters and land contamination is restricted.

4. RESULTS

This study aims at estimating water level by combining Level-2 and Level-1 data, which can be used for data filtering. In this part, the preliminary results on elevation, done with Level-2 data only are presented, as shown in Fig.3.

The results of the height over Lake Volta and Lake Kainji are compared with DAHITI data (blue points). The heights retrieved from Cryosat-2 (green points) and Jason-2 PISTACH (red points) have the same yearly pattern but with a certain bias compared to DAHITI data since the geoid applied for the three types of data is different, with EGM96 geoid model for Cryosat-2, EGM08 geoid model for Jason-2 PISTACH, and EIGEN-6c3stat geoid model for DAHITI.

The standard deviations are smaller than 0.3 meters, which is set as the threshold.

5. CONCLUSION

The aim of the study is to retrieve inland water level from altimeter by combining both Level-1 and Level-2 data. In this paper, the Level-1 waveform is analyzed over lakes. To filter data for retrieving water levels, the conditions of the peak value of the waveform and the energy can be applied. To implement the Level-1 method, the threshold should be tested under different situations. The Level-2 data can be used for the retrieval by applying different corrections. The preliminary results from Level-2 data already show good agreement with DAHITI database.

For the future work, instead of using a strict mask, the method will be developed with the combination of Level-1 and Level-2 data, and will be applied to smaller lakes and rivers.

6 References

Calmant, S., Seyler, F., and Cretaux, J.F., Monitoring continental surface waters by satellite altimetry, 2008, *Surveys in Geophysics*, 29, pp. 247–269, December 2008.

Garcia-Mondejar, A., Martinez Val, B., Escorihuela, M. J., Garcia, P. N., Martin-Puig, C., Yang, J., and Liao, J., 2014, *Measuring the lake level evolution in the Qinghai-Tibet plateau with radar altimeters,* Proceedings of the conference, Dragon 3 Mid Term Results, ESA*, vol. 724.

Schwatke, C., Dettmering, D., Bosch, W., and Seitz, F. *Dahiti an innovative approach for estimating water level time series over inland waters using multi-mission satellite altimetry*, 2015, Hydrology and Earth System Sciences, vol. 19, pp. 4345–4364.

Cryosat product handbook, 2012, ESRIN –ESA and Mullard Space Science Laboratory - University College London.

Soil Moisture Inversion Using the Reflection Signals of GNSS Satellites

Yueji Liang [1,2], Chao Ren[1,2,*], Haoyu Wang[1,2], Zhongtian Zheng[1,2],
Hongbo Yan[1,2], Ninghui Xu[3], Jie Lu[3]

*1 College of Geomatics and Geoinformation, Guilin University of Technology, Guilin
541004, China; why@glut.edu.cn (W.H.); zhongtianzheng_13397735747@163.com (Z.Z.);
haifengliu_guilin@163.com (H.L.);
2 Research Center of Precise Engineering Surveying, Guangxi Key Laboratory of Spatial
Information and Geomatics, Guilin 541004, China;
3 Nanning Exploration & Survey Institute, Guangxi Nanning 530001, China.*
renchao@glut.edu.cn (R.C.)

ABSTRACT-Global Navigation Satellite System Interferometric Reflectometry (GNSS-IR) is a new remote-sensing technique, and it can be used to estimate near-surface soil moisture from signal-to-noise ratio (SNR) data. Considering the effects of vegetation changes on GNSS-IR soil moisture in some environments and the time and space scale of soil moisture, a non-linear inversion method for soil moisture is proposed that takes into account the effects of vegetation changes. First, the SNR data and satellite elevation angles are solved using TEQC. The direct and reflected signals are separated using a low-order polynomial; then, a sinusoidal fitting model of the reflection signal is established to obtain the amplitude and phase of the SNR interferogram. Finally, an estimation model of vegetation water content (VWC) and prediction model of the vegetation phase changes was established to modify the original phase and weaken the influence of the vegetation changes. Based on the corrected phase, a Genetic Algorithm-BP neural network model is established for soil moisture inversion.

1 INTRODUCTION

Near-surface soil moisture has been the subject of numerous climate and land surface-atmosphere studies, and it is of great significance on climate meteorological forecasting, flood disaster prediction, water resource cycling studies and other related research (Njoku et al., 2004; Sabater et al., 2008). Soil moisture affects precipitation via the partitioning of energy between the land and the atmosphere into sensible and latent heat fluxes (Betts et al., 1996; Robock et al., 2000). In recent years, GNSS remote sensing technology developed based on multi-path effect has provided a new high-efficiency and high-resolution monitoring method for obtaining soil moisture content. Chew et al. (Chew et al., 2016) further confirmed that the relative phase is the best measure of soil-moisture changes, and there is a linear relationship with surface soil moisture, in theory. Zavorotny et al. (Zavorotny et al., 2010) used the delayed phase to estimate soil moisture, and verified that the correlation was more stable than the amplitude. Furthermore, quantifying the vegetation extent, such as the vegetation water content, is important to soil scientists interested in using remote-sensing data products for soil moisture estimation, because soil moisture estimations are affected by changes in vegetation cover (Jackson et al., 2004; Pan

et al., 2012). Studies on vegetation change affect SNR, Rodriguez-Alvarez et al. (Rodriguez-Alvarez et al., 2012; Rodriguez-Alvarez et al., 2011) have used antennas or receivers that are specifically designed for the task. It has been suggested that geodetic-quality antennas/receivers could be used for vegetation sensing (Small et al., 2016). The phase of the SNR interferogram is also affected by vegetation. It is possible to account for vegetation effects on soil moisture retrieval algorithms by considering aspects of the SNR interferogram other than phase. The amplitude decreases as vegetation grows (Wan et al., 2015). A subsequent modeling study indicates that the effects of changing vegetation canopies on SNR data and how these effects could obfuscate soil moisture estimation (Chew et al., 2015). Chew et al. (Chew et al., 2014) described a method of estimating vegetation effects on soil moisture estimation by comparing observations of A, Heff, and ALSP with model simulations. However, the effects of vegetation on GNSS -IR must be considered in some environments. Therefore, quantifying or removing the effects of vegetation changes on the phase is more conducive to the accurate analysis of soil water content. If the soil moisture changes over temporal and spatial scales, the estimation of soil moisture using GNSS-IR can be regarded as a non-linear regression problem. It is possible to construct a non-linear inversion model for

soil moisture estimation using the relative phase of each satellite.

Based on the above research, considering the effects of vegetation changes on phase, an inversion method based on a GA-BP neural network for soil moisture, is proposed. Considering the effects of vegetation changes on SNR, the estimation model of vegetation moisture content and the prediction model of vegetation phase changes are established. The inversion model for soil moisture is constructed using the corrected phase. Using the measured data from the PBO website, the feasibility of soil moisture inversion by a nonlinear fitting method is studied, and the validity of soil moisture inversion is verified based on the effect of modified vegetation change on the phase.

2 THE PRINCIPLE OF SOIL MIOSTURE INVERSION

2.1 SNR Data

SNR is an indicator of the signal quality of the receiver's antenna. Direct and reflected signals between the interference or multipath effects have an obvious impacts on the direct signal, and the direct signal often show oscillating phenomenon(Figure 1). The direct and reflected signals are separated by a low-order polynomial. The low-order polynomial is then fitted to the data to retain only the interference pattern, and the amplitude of the reflected component is larger at a satellite elevation angle of less than 30 degrees (Figure 1).
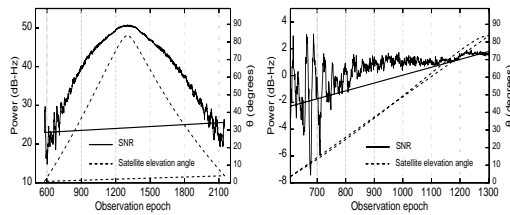
Figure 1. SNR interferogram observed on day 318 in 2011 at the South California GPS station (p041). An SNR interferogram from PRN 31 (left). The same SNR data from a rising part of PRN 31, but detrended with a low-order polynomial (right).

Initial studies characterized the SNR interferogram using the following equation (Larson et al., 2010)：

$$SNR = A\cos(\frac{4\pi H}{\lambda}\sin\theta + \phi)\qquad(1)$$

where θ、λ and H represent the elevation angle of the satellite, the GNSS wavelength and the a priori reflector height, respectively. A is an amplitude term, and ϕ represents the phase shift. A and ϕ are the

amplitude and phase of the demand, respectively, which are calculated using the nonlinear least-squares fitting algorithm (ohnson et al., 1981).

2.2 Modify the Impact of Vegetation Changes

Chew et al. (Chew et al., 2014) found that vegetation changes had a significant effect on phase. The effects of vegetation changes must first be quantified or removed before estimating the soil moisture. Moreover, there is a linear relationship between amplitude and vegetation change. Therefore, the veg-simple model described by Small et al. (Small et al., 2016) was used to estimate the vegetation water content and its phase change. The process was as follows.

First, amplitude A was normalized, the first 20% of A was used to calculate the mean for each year and each track; then, the mean was subtracted from the phase time series to obtain Anorm. The 20% value was a parameter that may decrease or increase depending on the amount of noise present in the data. Then, Anorm was smoothed using a Savitzky–Golay filter, and a least-squares smoothing method was used to remove high-frequency noise associated with soil moisture fluctuations from A norm. Modeling studies have shown that soil moisture-induced variations in amplitude are small compared to those from vegetation alone, but they are not negligible (Chew et al., 2014; Chew et al., 2015).

Second, the vegetation water content (VWC) was estimated using a smoothed amplitude sequence:

$$VWC(t) = \alpha_1 A_{norm}^4 + \alpha_2 A_{norm}^3 + \alpha_3 A_{norm}^2 + \alpha_4 A_{norm} + \alpha_5\qquad(2)$$

where $\alpha_1 = 10.6$, $\alpha_2 = -39.4$, $\alpha_3 = 41.8$, $\alpha_4 = -22.6$, $\alpha_5 = 5.24$.

Third，the estimated VWC was used to predict the phase shift ($\Delta\phi_{veg}$) resulting from the vegetation canopy:

$$\Delta\phi_{veg}(t) = \beta_1 VWC^4 + \beta_2 VWC^3 + \beta_3 VWC^2 + \beta_4 VWC + \beta_5\qquad(3)$$

where $\beta_1 = -5.65$, $\beta_2 = 43.9$, $\beta_3 = -101$, $\beta_4 = 20.4$, $\beta_5 = -2.37$.

Finally, the phase was adjusted for the predicted effects of vegetation, as follows:

$$\phi_r(t) = \phi(t) - \Delta\phi_{veg}(t)\qquad(4)$$

Equations (3) and (4) are based on model simulations of GPS reflections using a uniform vegetation canopy (Chew et al., 2014). The parameter values used in the veg-simple algorithm are based on model simulations. They were designed to replicate collocated GPS and vegetation data from only five sites (Chew et al., 2016).

2.3 Soil Moisture Inversion Process

The phase is set after modifying the effect of vegetation changes as follows:

$$x = [\phi_r(1), \ \phi_r(2), \ldots, \ \phi_r(t)], \ (t = 1,2,\ldots,n) \quad (7)$$

where t is on behalf of years, and n is the length of time.

y is the soil moisture set corresponding to the phase set, and the n time period of x is used as the training sample of the model; then, n − m is the test sample. The inversion process is shown in Figure 2.
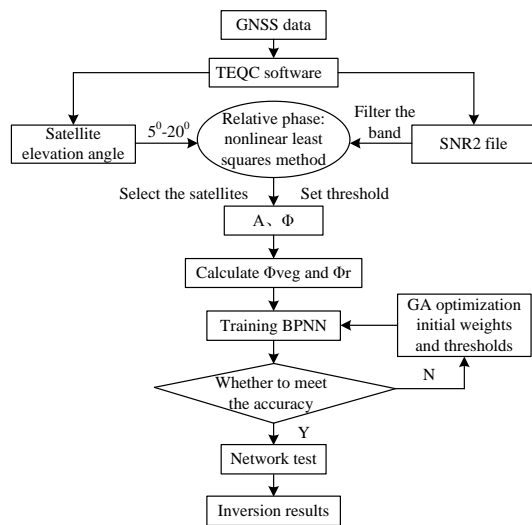
Figure 2. Flowchart depicting steps of soil moisture inversion

3 EXPERIMENT ANALYSIS

The GNSS monitoring data provided by the P041 station for the continental plate boundary observation network (PBO: http: //xenon.colorado.edu/portal) in South Carolina, USA were experimentally analyzed. The station is located in Marshall, Boulder and Colorado, at 105.1942673 W, 39.9494934 N and 1728.8 m above sea level. An earlier study of soil moisture provided a high sampling rate and rich meteorological data, and the first observation of L2C observations was carried out to improve the high quality L2-band SNR observation data. Fig. 3 (right) indicates that the station around the terrain is flat, open and that has scarce vegetation, and it is mainly grass-based. The station is supported by steel triangular brackets. The receiver model is a TRIMBLE NERT9, and the TRM59800.80 SCIT Radome was used in station P041, as shown (Fig. 3 (b)). The changes in soil moisture and rainfall from day 70-290 of 2011 are shown in Figure 4.

Figure 4 shows that significant rainfall occurred 13 times during this period, which included days 88, 100, 104, 115, 131 ~ 132, 137 ~ 140, 143 ~ 144, 171, 186 ~ 195, 207 ~ 211, 231 ~ 232, 250, 255 to 258, of which the maximum rainfall was 2.67 cm.

Corresponding to the rainfall, the soil moisture increased significantly, especially on days 131 ~ 132, 137 ~ 140 and 186 ~ 195. Due to the continuous rainfall, the soil moisture changed more intensely and exhibited a nonlinear and random patter; when the rainfall stopped, the soil moisture gradually reduced and descended. The rainfall is the clearly the main reason for the changes in soil moisture; the study area was rich in rainfall and suitable for soil moisture research.
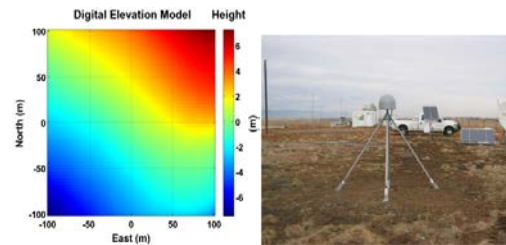
Figure 3. Digital elevation model around the GPS site p041 in southern California (left). The GPS site p041 environment (right).
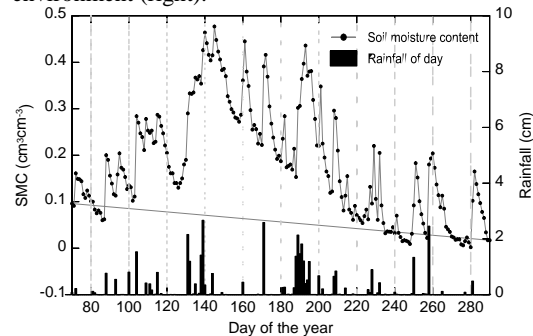
Figure 4. Soil moisture and rainfall from the southern California GPS site P041. Line：SMC in cm3 cm−3 time series. Bar: Daily precipitation in mm from NLDAS for the grid cell containing site P041.

Therefore, the selected monitoring data from the GNSS receiver occurred from days 70-290 in 2011, and the sampling rate was 30Hz. The SNR2 value (L2 carrier) was obtained by solving the monitoring data with TEQC. The straight and reflected signals of the satellites were separated by the quadratic polynomial, and the relative phase of each satellite was deduced by the nonlinear least squares method. Not all of the satellite tracks could be used for GPS-IR. The tracks should have consistent reflections between satellite elevation angles of . Due to limited space, only the selected PRN18, 21, 22 and 31 satellites were used for analysis, and the relationship between amplitude, phase and vegetation change of each satellite is shown (Figure 5).
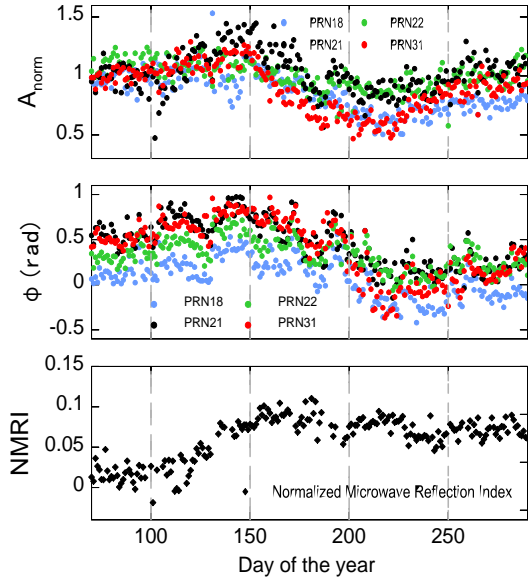
Figure 5. Top: Delay phases of four satellite tracks: PRN 18 (blue points), 21 (black points), 22 (green points) and 31 (red points). Middle: amplitudes of the same satellite tracks. Bottom: vegetation information from

Figure 5 indicates that the amplitude is linearly related to the vegetation information. When the vegetation change increased to 0.05, the amplitude of each satellite fluctuated greatly, such as on days 150 ~ 290. From the research of Chew et al. (Chew et al., 2014), using the Savitzky–Golay filter to smooth and remove the high-frequency information of the original amplitude, and calculate the vegetation caused by the phase change, the original phase was corrected to obtain a more realistic phase, as shown in Fig. 6. The correction of the original phase mainly focused on the 160th to 270th day, which corresponds to the coefficient of vegetation change, and the degree of phase fluctuation after the correction is weakened.

Therefore, to verify the feasibility and effectiveness of the proposed algorithm, the PRN 18, 21, 22 and 31 were selected for experimental analysis, and the GA-BPNN inversion model for soil moisture was established. Two solutions were established: solution 1 – a GA-BPNN inversion model based on the original phase, solution 2 – a GA-BPNN inversion model based on modified vegetation. To reduce the modeling error, the phase was preprocessed, the data were normalized to the interval [-1, 1], and the data were restored to the original intervals after modeling inversion. A training sample was taken on days 70-219, and the samples were tested on days 220-290. The inversion results for each solution are shown in Figure 7.
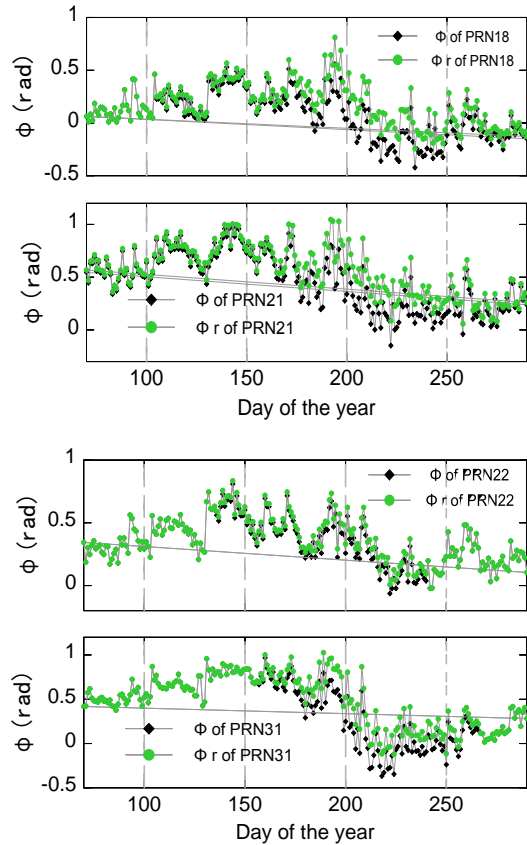
Figure 6. Compared and analyzed delayed phases for four satellite tracks: PRN 18, 21, 22 and 31. Green points: original phase. Black points: corrected phase data for vegetation effects

Figure 7 shows that the inversion of soil moisture was carried out using solution 1, the error was unstable and the fluctuation was large, especially from day 250 to 290; the inversion error was extremely unstable. Furthermore, the inversion result in solution 2 improved better than solution 1. From Figure 9's analysis, using Φr to invert the soil moisture, the correlation between the inversion result and the real value has been improved, especially the PRN 21 and 31; they increased by 17.3% and 23.4%, respectively. From the accuracy statistics of Table 1, the inversion result of Φr is superior to the inversion result using the original phase, whether it is the root mean square error (RMSE) or the mean absolute error (MAE), and the improvement of the maximum error also improved. It can be seen that it is necessary to modify the effect of vegetation changes and improve the accuracy of soil moisture inversion.
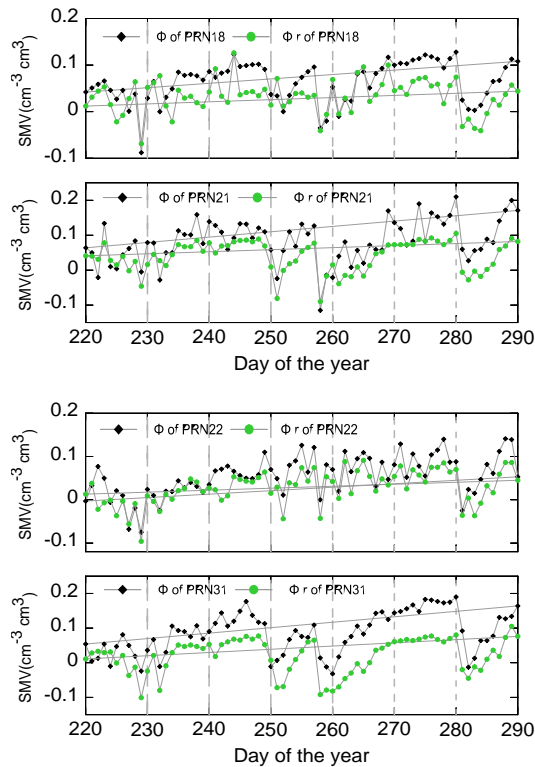
Figure 7. Inversion error for four satellite tracks: PRN 18, 21, 22 and 31. Green points: original phase. Black points: corrected phase data for vegetation effects.

Table 1 Inversion accuracy of each satellite (unit: cm-3 cm3)

Satellite	PRN18		PRN21		PRN22		PRN31	
number	Φ	Φr	Φ	Φr	Φ	Φr	Φ	Φr
RMSE	0.077	0.049	0.103	0.059	0.072	0.048	0.105	0.054
MAE	0.068	0.041	0.090	0.050	0.062	0.040	0.090	0.047
max	0.128	0.126	0.210	0.105	0.141	0.096	0.190	0.105

In short, the nonlinear model of soil moisture inversion was established using the phase of each satellite. In the process of inversion, BPNN was not fitted, and the performance of the model was improved. The phase reversal of soil moisture is feasible. And inverse soil moisture is feasible to determine based on the phase. Using Φr to inverse the soil moisture, the correlation between the obtained soil moisture and the monitoring value was better than the original phase inversion model, and the accuracy of the model inversion further improved. The correlation between soil moisture and the monitored value was better than that of the original phase inversion model, and the accuracy of the model inversion further improved. Thus, the effect of vegetation changes on soil moisture should be considered by quantifying or removing the phase of vegetation change to improve the inversion accuracy. It is feasible and effective to introduce a nonlinear model into soil moisture inversion.

4 CONCLUSIONS

Long-term monitoring of soil moisture and accurate analysis of its changes in environmental science research has great significance. A GA-BPNN soil moisture inversion method, using the effect of vegetation changes, was proposed herein. The theoretical analysis and experiments indicate the followings: 1) the GNSS antenna was affected by the geometric trajectory of the satellite and the satellite's own performance. The relative phase of the different satellites was different, and the amplitude was linearly related to the vegetation information. 2) Introducing a neural network into the soil moisture inversion made full use of the advantages of artificial intelligence, and the ability of non-linear fitting was effectively improved, and the fitting process performance was more stable. 3) the effect of vegetation changes on soil moisture and the accuracy of soil moisture inversion have been improved. The correlation coefficient between the inversion result and the reference value of soil moisture has been greatly improved, and the RMSE and MAE were less than 0.06 and 0.05. Therefore, applying the nonlinear model to the inversion of soil moisture was feasible and effective, and the problem of soil moisture was solved as a nonlinear event. To further improve the performance of the model, a follow-up study of vegetation modification in different environments and multi-satellite fusion inversion are necessary.

REFERENCES

Betts, A. K., Ball, J. H., Beljaars, A., Miller, M. J., & Viterbo, P. A.,1996,The land surface‐atmosphere interaction: A review based on observational and global modeling perspectives. Journal of Geophysical Research: Atmospheres, 101(D3), 7209-7225.

Chew, C. C., Small, E. E., Larson, K. M., & Zavorotny, V. U.,2015,Vegetation sensing using GPS-interferometric reflectometry: theoretical effects of canopy parameters on signal-to-noise ratio data. IEEE Transactions on Geoscience and Remote Sensing, 53(5), 2755-2764.

Chew, C. C., Small, E. E., Larson, K. M., & Zavorotny, V. U.,2014,Effects of near-surface soil moisture on GPS SNR data: development of a retrieval algorithm for soil moisture. IEEE Transactions on Geoscience and Remote Sensing, 52(1), 537-543.

Chew, C., Small, E. E., & Larson, K. M.,2016,An algorithm for soil moisture estimation using GPS-interferometric reflectometry for bare and vegetated soil. GPS solutions, 20(3), 525-537.

Jackson, T. J., Chen, D., Cosh, M., Li, F., Anderson, M., Walthall, C., ... & Hunt, E. R.,2004, Vegetation water content mapping using Landsat data derived normalized difference water index for corn and soybeans. Remote Sensing of Environment, 92(4), 475-482.

Larson, K. M., Braun, J. J., Small, E. E., Zavorotny, V. U., Gutmann, E. D., & Bilich, A. L.,2010,GPS multipath and its relation to near-surface soil moisture content. IEEE Journal of Selected Topics in Applied Earth Observations and Remote Sensing, 3(1), 91-99.

Njoku, E. G., Lakshmi, V., & O'Neill, P. E.,2004,Soil moisture field experiment special issue. Remote Sensing of Environment, 92(4), 425-426.

ohnson, M. L., Correia, J. J., Yphantis, D. A., & HalvorSON, H. R.,1981,Analysis of data from the analytical ultracentrifuge by nonlinear least-squares techniques. Biophysical Journal, 36(3), 575-588.

Pan, M., Sahoo, A. K., Wood, E. F., Al Bitar, A., Leroux, D., & Kerr, Y. H.,2012,An initial assessment of SMOS derived soil moisture over the continental United States. IEEE Journal of Selected Topics in Applied Earth Observations and Remote Sensing, 5(5), 1448-1457.

Robock, A., Vinnikov, K. Y., Srinivasan, G., Entin, J. K., Hollinger, S. E., Speranskaya, N. A., ... & Namkhai, A.,2000,The global soil moisture data bank. Bulletin of the American Meteorological Society, 81(6), 1281-1299.

Rodriguez‐Alvarez, N., Bosch‐Lluis, X., Camps, A., Aguasca, A., Vall‐llossera, M., Valencia, E., ... & Park, H.,2011, Review of crop growth and soil moisture monitoring from a ground‐based instrument implementing the Interference Pattern GNSS‐R Technique. Radio Science, 46(6).

Rodriguez-Alvarez, N., Bosch-Lluis, X., Camps, A., Ramos-Perez, I., Valencia, E., Park, H., & Vall-Llossera, M,2012,Vegetation water content estimation using GNSS measurements. IEEE Geoscience and Remote Sensing Letters, 9(2), 282-286.

Small, E. E., Larson, K. M., Chew, C. C., Dong, J., & Ochsner, T. E.,2016,Validation of GPS-IR soil moisture retrievals: Comparison of different algorithms to remove vegetation effects. IEEE Journal of Selected Topics in Applied Earth Observations and Remote Sensing, 9(10), 4759-4770.

Sabater, J. M., Rüdiger, C., Calvet, J. C., Fritz, N., Jarlan, L., & Kerr, Y.,2008,Joint assimilation of surface soil moisture and LAI observations into a land surface model. agricultural and forest meteorology, 148(8), 1362-1373.

Wan, W., Larson, K. M., Small, E. E., Chew, C. C., & Braun, J. J.,2015,Using geodetic GPS receivers to measure vegetation water content. Gps Solutions, 19(2), 237-248.

Zavorotny, V. U., Larson, K. M., Braun, J. J., Small, E. E., Gutmann, E. D., & Bilich, A. L.,2010,A physical model for GPS multipath caused by land reflections: Toward bare soil moisture retrievals. IEEE Journal of Selected Topics in Applied Earth Observations and Remote Sensing, 3(1), 100-110.

Monitoring an Alpine glacier through Ground Based SAR Interferometry: a case study

G. Luzi[1], N. Dematteis[2], D. Giordan[2], F. Zucca[3], P. Allasia[2], O. Monserrat[1],

1 Geomatics Division - Centre Tecnòlogic de Telecomunicacions de Catalunya (CTTC/CERCA) Av. Gauss 7, E-08860 Castelldefels (Barcelona), Spain
2 Geohazard Monitoring Group, Research Institute for Hydro-Geological Protection, National Council of Research of Italy, Torino, Italy.
3 Department of Earth Science and Environment, University of Pavia, Pavia, Italy.
gluzi@cttc.cat

ABSTRACT *This paper reports the results of an experimental campaign carried out with a Ground Based Synthetic Aperture Radar (GB-SAR), aimed at monitoring the behaviour of an Alpine glacier. The apparatus is an Ibis-L® system, a commercial interferometric radar operating at Ku-band. It has been installed in a valley in front of the Planpincieux glacier, located on the Italian side of the Mont Blanc massif, about 3 km far from the glacier surface. The images, acquired with a temporal frequency of approximately five minutes, were processed correcting the atmospheric effect using a simple model which takes into account the variation of the atmospheric parameters with the altitude. The study enhances the importance of a satisfactory evaluation of the atmospheric behaviour to achieve an estimate of the deformation, and finally evaluates the mean velocity of the glacier in the order of 20-30 cm per day.*

1 INTRODUCTION

Ground Based Synthetic Aperture Radar (GB-SAR) interferometry has consolidated in the last years as an operational tool for landslides and mines monitoring, and has achieved a fine dissemination as a tool also for glaciers and snow covered areas studies. The use of SAR interferometry for terrain monitoring is based on the same principle of most popular spaceborne Differential Interferometric SAR, DInSAR, but with different performances in terms of spatial and temporal resolution. Radar aboard satellites are potentially able to monitor very large area, at basin scale, while ground-based installation can observe single landslides, and give information on the movement or deformation of the monitored terrain with repetition time shorter than an hour, while satellite observations can be not fully satisfactory because of a too long repeat pass time. This is for example the case of an Alpine glacier, where the understanding of its behaviour, especially during the seasons where the meteorological conditions make them more active, demands at least daily observations. The ground based approach can be a valid and complementary tool to compensate the time gap between satellite observations or for calibration purposes, and as a monitoring and alerting system. GB-SAR interferometry is able to provide only a partial estimate of the terrain deformation; in the case of a glacier, for example, we obtain a partial estimate of the actual ice flow, because interferometric techniques provide only the Line of Sight component (LOS) of the displacement. Despite this limitation in the actual deformation and motion retrieval, the capability to provide information without the installation of artificial reflectors represents a valuable opportunity, especially for scenarios where the walk through the area under monitoring is not viable or safe. A GB-SAR can provide displacement maps of glaciers of a few square kilometres, from up to 3-4 km distance. In addition, in the case of Alpine glaciers, affected by cryosphere changes, the studies of glaciers' dynamics can largely benefit from the high spatial and temporal sampling available from terrestrial radar survey, with respect to satellite observations. Finally, the installation of a terrestrial radar is not affected by slope orientation, limitations that can occur for spaceborne observations.

In this paper, we present the results of an experimental campaign and the related interferometric data processing, aimed at monitoring an Alpine glacier, the Planpincieux glacier, located on the Italian side of the Mont Blanc massif. The GB-SAR employed is a commercial system working at Ku-band (an operating frequency corresponding to a 1.74 cm wavelength), installed in front of the glacier area for five weeks. The study of glacier monitoring faces some difficulties in radar data interpretation: the main issues are unwrapping errors, and high amplitude dispersion, mainly due to the high velocity and

dielectric heterogeneity of the backscattering surface. The atmospheric phase screen (APS) estimation, which can compromise the reliability of the retrieved interferometric data, is also a very important issue. For this reason, on the bases of the approaches available from literature a simple APS model which includes the elevation of the radar bin has been implemented. The availability of observations obtained through a different system monitoring observing the same area, allowed verifying the reliability of the radar data.

2 THE TECHNIQUE AND THE MONITORED SITE

2.1 GB-SAR Interferometry

When a series of SAR images acquired at different times is available, interferograms can be obtained by comparing pairs of images. Assuming that the dielectric characteristic of the pixels of the SAR image remain unchanged between two acquisitions, avoiding the occurrence of phase wrapping, and neglecting atmospheric effects on the signal propagation, the displacement along the radar LOS, d_{LOS}, associated to a pixel can be recovered using the following simple equation:

$$d_{\mathrm{LOS}} = \frac{\lambda}{4\pi} \cdot \Delta\varphi \qquad (1)$$

where λ is the wavelength of the radar sensor and $\Delta\varphi$ is the phase difference (interferometric phase) obtained for the same pixel. In real cases, to retrieve from the interferometric phase, the actual displacement, different factors must be taken into account (Caduff et al. 2015); a general expression for the interferometric phase, in the standard "zero baseline" condition of GB-SAR installation, is given by the sum of at least four terms, as shown in eq. 2:

$$\varphi_{\mathrm{int}} = \varphi_{\mathrm{displ}} + \varphi_{\mathrm{atm}} + \varphi_{\mathrm{noise}} + 2\mathrm{k}\pi \qquad (2)$$

where φ_{displ} is the term related to the geometric LOS displacement of the pixel; φ_{atm} is related to the change of the atmospheric parameters, especially air humidity and temperature; φ_{noise} contains possible thermal or/and scattering noise. The term $2k\pi$ refers to the case where measured phases values are wrapped, in fact the phase values are constrained within the range $[-\pi,\pi]$. To estimate, and correct, the contribution of these terms, some processing procedures are applied to the radar data. The first step of the processing consists in applying a 2D unwrapping algorithm (Costantini, 1998) to all the images.

The points whose interferometric phase can be used for retrieving the displacement with sufficient accuracy are usually selected with different criteria; one of this is calculating the dispersion of amplitude (DA) of the signal and using a threshold to discriminate good points (Ferretti et al., 2001): the lower is DA the better the accuracy of the phase measurement. The other critical factor is coherence, varying between zero and the unity. A high coherence means that disturbing effects are negligible and the measured phase is statistically reliable. Finally, the φ_{atm} term, related to APS, is introduced by the optical path change that is driven by meteorological variables, i.e. humidity temperature, and pressure (Luzi et al., 2004). Solutions to take into account this factor, are discussed in several papers: see for example: Noferini et al. (2005); Iannini and Guarnieri (2011), Iglesias et al. (2014). Monitoring stable surfaces like rocks, allows assuming that φ_{noise} changes negligibly between different acquisitions, and, after unwrapping, the only contribution to the right side of eq. 2 is in φ_{atm}.

Differently, a glacier surface, especially at temperate climate and during the intermediate seasons, is subject to melting and sublimation processes with consequent changes of the dielectric properties, snowdrift and snow metamorphism with possible collapses (Riesen et al., 2011). It is worth to note also that liquid and solid precipitation events can affect the phase of the propagating signal. For this reason, this term must be evaluated and the measured phase corrected.

Fig. 1: GB-SAR installation. In the small rectangle a description of the two main sectors of the glacier flow, with indicated the radar LOS. In red the western side mainly moving along the LOS; in yellow the eastern one whose motion is along the yellow arrow.

2.2 The radar apparatus

The GB-SAR system used in this study is the Ibis-L® from IdS spa (Rodesbereg et al., 2010). The system is composed of four separate modules: a radar sensor able to transmit and receive microwave signals, a mechanical scanning rail, 2-m long, along which the sensor moves providing synthetic aperture imaging, a laptop for data acquisition and processing, and a power supply module that allows continuous measurements. Many types of GB-SAR systems have been developed in the last decades: a review of the GB-SAR systems can be found in Caduff et al., 2015 and Monserrat et al., 2014. Fig. 1 shows a picture of the installation with a view of the monitored area from the radar site. In table 1 the main parameters of the radar are listed.

Table 1: Parameters of IBIS-L during the experimental campaign

GB-SAR Parameters	
Central frequency/Wavelength	17.1 GHz/1.75 cm
Length of the synthetic aperture	2 m
Maximum distance from target	3000 m
Range resolution	0.75 m
Azimuth resolution	4.4 mrad
Azimuth resolution at 3000m	13 m
Image acquisition rate	4 images/hour
Total duration of monitoring	From 09.04.2015 to 10.14.2015 (40 days).

2.3 The monitored glacier

The Planpincieux glacier is located approximately at 45.85°N 6.97°E, in the Aosta Valley Region (North-Western Italy). The glacier lies on the southern side of the Mont Blanc massif, towards the Ferret Valley, and it is part of the composite Grandes Jorasses-Planpincieux glacier, at an elevation between 2530-3700 m asl, covering approximately 1 km^2. As described in Giordan et al. 2016, the lower part of the Planpincieux glacier is intensely crevassed. The morphological analysis evidences that this part is separated in two different ice flows by a central ridge of bedrock. The Research Institute for Hydro-geological Protection of the National Council of Research of Italy (CNR IRPI) considers the Grandes Jorasses massif an open-air laboratory for the development of monitoring systems and techniques. Since 2013, CNR IRPI is monitoring the glacier with low-cost vision-based equipment, installed in the opposite side of the valley.

The apparatus location maximizes the parallel condition of the LOS to the estimated direction of the western flow. This choice affected the measurement of the eastern tongue that deviates from the measured component and appears as an increasing distance (see also fig. 1). The mean distance of the glacier is about 2700 m with differences in elevation of 1200-1400 m (Figure 2). Radar images are georeferenced on a 1 m-resolution digital surface model (DSM).

During this study, an Ibis-L, IDS™ is used, with a revisiting time of 16 minutes; the total amount of processed images is 3567. The survey lasted 40 days, from 4th September to 14th October 2015. Figures 3a-b represent the mean amplitude (MA) and the DA maps respectively. APS estimate is applied in the area within the frames.
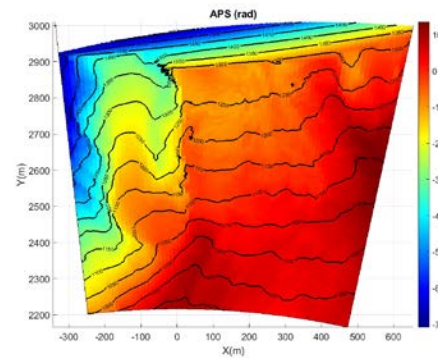
Fig. 2: Calculated cumulative APS in radians, as a function of the radar coordinates (range and elevation), obtained according to Equation (3) and projected on the DSM. 1 radian corresponds to a virtual displacement of λ/4 (approx. 4.4 mm). Contours map draws the altitude of the glacier surface.

2.4 Processing chain

The first step after checking the quality of the SAR images, was to study the role of the APS, analysing first the meteorological data of an automatic weather station: air temperature, air relative humidity, cumulative rainfall in 30 minutes, and snow deposit at ground. The station is placed at 2290 m asl, in the same valley side of the Planpincieux glacier. These data have been provided by the Centro Funzionale della Valle d'Aosta. The period of the survey coincided with the beginning of the Alpine cold season. Temperature was close to 0°C and some snowfall events occurred. Cold temperature and high

humidity affect the radar signal with an increased APS. On these bases, an estimate of APS from the radar data acquired in the stable surroundings of the glacier, considering stable points pixels with DA<0.35, was carried out; here the measured phase can be associated uniquely to APS. Using a regression formula that depends of range and altitude of the pixel, shown as eq. 3, we estimate the APS for the whole monitored surface; more details about its formulation in Dematteis et al., 2017. The calculated APS, projected on the Digital Surface Model is shown in fig. 2.

$$\varphi_{atm} = a_0 + a_1 r + a_2 z^2 \qquad (3)$$

The coherence threshold used to discard noisy interferograms is 0.65. This cleaning rejected some 16% of the total number.

As far as the DA is concerned, it is worth noting that the amplitude of the glacier response is very low and highly variable, so that the DA of the glacier is comparable to that of shadowed areas. In fig. 3 a map of the DA in radar coordinates is shown.
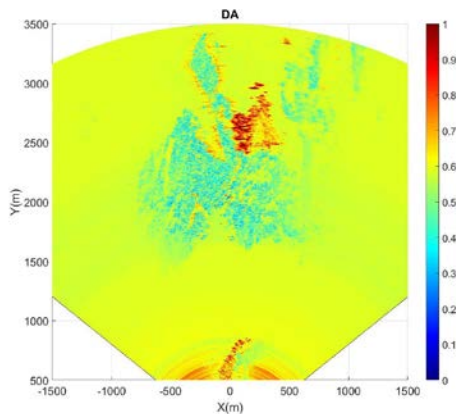
Fig. 3: Calculated DA in radar coordinates.

The unwrapping is performed on pixels selected with a coherence-driven criterion (Berardino et al. 2002), with a mean coherence higher than 0.55. Coherence is computed averaging 5 pixels in azimuth and 7 pixels in range.

3 THE EXPERIMENTAL RESULTS

To obtain a deformation map of the monitored area, the first step is a to calculate the mean amplitude (MA) map using all the selected images. Glacier and rocks in

general feature high amplitude while lower values are present in shadowed areas. A coherence-based mask is then applied to the pixels. The final outcome of the processing consists in a map of cumulative deformation projected on the DSM of the glacier, shown as fig. 4. To interpret the map legend, negative and positive values correspond to motion toward and away from the radar respectively. The eastern flow appears moving away because the motion direction is slanted with respect to the LOS.
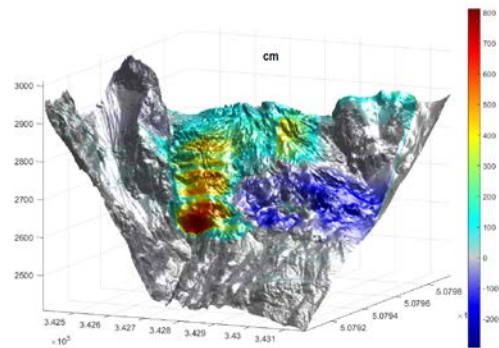
Fig. 4 Cumulative deformation map in cm projected on the DSM of the monitored area. Positive values indicate points moving toward the observer.

The general behaviour obtained through radar acquisitions, and some morphological observations of the glacier discussed in Giordan et al. 2016, agree. Two main streams with different kinematics are present. The western sector flows downstream almost parallel to the LOS, while the eastern part flows with a remarkable horizontal component towards east, resulting in a not LOS-aligned motion.

The deformation obtained through radar observations have been also compared with estimates obtained through an optical system (Giordan et al., 2016). Considering as error of the radar retrieval the standard deviation of the cumulative motion on the bedrock (σ=8.42 cm), i.e. a stable area, we obtain the following numerical results. For the front sector a 29.2 ±3.8cm/day velocity is estimated, with respect to 31,4±10.3 cm/day obtained from optical independent data. Also the crevasses, 23.0±2.6 cm/day, and middle sector, 20.8±3.9 cm/day, deformation velocities are very close to values obtained through the optical technique: 29.9±4.5 cm/day and 26±7.2 cm/day respectively. These results confirmed that, despite the need to operate a careful correction of the data affected by APS, GB-SAR monitoring over Alpine glaciers demonstrated to be reliable and accurate.

4 CONCLUSIONS

An experimental campaigns carried out with a GB-SAR to monitor an Alpine glacier has been reported. To improve the correction of the significant effect of the atmosphere on the radar data, mainly due to the large distance of the observed surface, and the difference in elevation, an experimental derived formula has been implemented using data acquired on stable points, and applied to the acquired data. Results obtained from the radar survey, mainly consisting in glacier velocity of three different sectors of the glacier, have been compared to estimates achieved in a recent study based on the use of optical images, showing a good agreement. The study confirmed that the GB-SAR technique can be successfully applied to the monitoring of Alpine glaciers, provided that atmospheric effects are carefully considered.

References

Berardino P., G. Fornaro, R. Lanari, and E. Sansosti, 2002. A New Algorithm for Surface Deformation Monitoring Based on Small Baseline Differential SAR Interferograms; IEEE Transactions on Geoscience and Remote Sensing 40 (11): 2375–2383.

Caduff R., F. Schlunegger, A. Kos, and A. Wiesmann, 2015. A Review of Terrestrial Radar Interferometry for Measuring Surface Change in the Geosciences; Earth Surface Processes and Landforms 40 (2): 208–228.

Costantini, Mario, 1998. A Novel Phase Unwrapping Method Based on Network Programming; IEEE Transactions on Geoscience and Remote Sensing 36 (3): 813–821.

Dematteis N., G. Luzi , D. Giordan , F. Zucca, P. Allasia, 2017. Monitoring Alpine glacier surface deformations with GB-SAR, Remote Sensing Letters, 8:10, 947-956, DOI: 10.1080/2150704X.2017.1335905.

Ferretti A., C. Prati, and F. Rocca, 2001. Permanent Scatterers in SAR Interferometry; IEEE Transactions on Geoscience and Remote Sensing 39 (1): 8–20.

Giordan D., Allasia P., Dematteis N., Dell'Anese F., Vagliasindi M., E. Motta, 2016; A Low-Cost Optical Remote Sensing Application for Glacier Deformation Monitoring in an Alpine Environment." Sensors 16 (10): 1750.

Iglesias R., X. Fabregas, A. Aguasca, J. J. Mallorqui, C. López-Martínez, J. A. Gili, and J. Corominas, 2014. Atmospheric Phase Screen Compensation in Ground-Based SAR with a Multiple-Regression Model over Mountainous Regions. IEEE Transactions on Geoscience and Remote Sensing 52 (5): 2436–2449.

Iannini L. and A. Monti Guarnieri, 2011. Atmospheric Phase Screen in Ground-Based Radar: Statistics and Compensation. IEEE Geoscience and Remote Sensing Letters 8 (3): 537–541.

Luzi G., M. Pieraccini, D. Mecatti, L. Noferini, G. Macaluso, A. Tamburini, and C. Atzeni. 2007. Monitoring of an Alpine Glacier by Means of Ground-Based SAR Interferometry. IEEE Geoscience and Remote Sensing Letters 4 (3): 495–499.

Luzi G., M. Pieraccini, D. Mecatti, L. Noferini, G. Guidi, F. Moia, and C. Atzeni, 2004. Ground-Based Radar Interferometry for Landslides Monitoring: Atmospheric and Instrumental Decorrelation Sources on Experimental Data. IEEE Transactions on Geoscience and Remote Sensing 42 (11): 2454–2466.

Monserrat, O., M. Crosetto, and G. Luzi, 2014. A Review of Ground-Based SAR Interferometry for Deformation Measurement." ISPRS Journal of Photogrammetry and Remote Sensing 93: 40–48.

Noferini, L., M. Pieraccini, D. Mecatti, G. Luzi, C. Atzeni, A. Tamburini, and M. Broccolato. 2005. "Permanent Scatterers Analysis for Atmospheric Correction in Ground-Based SAR Interferometry." IEEE Transactions on Geoscience and Remote Sensing 43 (7): 1459–1471.

Riesen P., T. Strozzi, A. Bauder, A. Wiesmann, and M. Funk, 2011. Short-Term Surface Ice Motion Variations Measured with a Ground-Based Portable Real Aperture Radar Interferometer." Journal of Glaciology 57 (201): 53–60.

Rödelsperger, S., G. Läufer, C. Gerstenecker, M. Becker, 2010. Monitoring of displacements with ground-based microwave interferometry: IBIS-S and IBIS-L. Journal of Applied Geodesy, 4(1), pp. 41-54. doi:10.1515/jag.2010.005

ASSESSMENT OF FULLY POLARIMETRIC RADARSAT-2 IMAGERY FOR SOIL PARAMETER ESTIMATION IN ARID REGIONS

Xiaodong Feng[1], Liping Yang*[,2], Fei Liu[2], Jing Liu[2], Xiaohui Sun[2]

[1] *School of Earth Science and Resources, Chang'an University, Xi'an, 710054, China*

[2] *School of Geological Engineering and Geomatics,Chang'an University, Xi'an, 710054, China*

* Correspondence author

E-mail: zylpyang@chd.edu.cn

ABSTRACT - *Fully polarimetric SAR (PolSAR) data contain not only the geometric and backscattering information, but also the polarization information of the scattering target. It has become the main data source for estimation of surface parameters such as soil moisture and surface roughness. A fully polarimetric RADARSAT-2 SAR data was used in this study to qualitatively evaluate the potential of PolSAR data at C-band frequency for the retrieval of surface roughness. Five polarimetric parameters including the entropy H, anisotropy A, mean scattering angle α, the single-bounce eigenvalue relative difference (SERD) and double-bounce eigenvalue relative difference (DERD) were calculated and were compared with measured root mean square height S (rms height S) and the correlation length L, the two most acknowledged parameters describing the surface roughness. Results show that the polarimetric parameter is nearly not relevant with both the rms height S and the correlation length L for all the correlation coefficients are less than 0.3. However, the sensitivity of each polarimetric parameter has demonstrated a certain difference especially with the rms height S in this preliminary study. The entropy H, mean scattering angle α and SERD seem to be more sensitive to surface roughness. Further discussion is required to explore the combination potential of polarimetric parameters with relatively higher sensitivity for the estimation of surface roughness in the following study.*

1 INTRODUCTION

As the key factors affecting the surface conditions, soil surface parameters, such as soil moisture and surface roughness, play an important role in hydrology, meteorology, agronomy and other application fields (Engman, 1991; Jackson et al., 1996; Bissonnais et al., 1998). SAR in particular provides one of the most effective and reliable means for estimation of these parameters.

With the rapid development of SAR systems, fully polarimetric SAR (PolSAR) data has been widely used in classification, target recognition and surface parameter retrieval (Oh et al., 1992; Zribi and Dechambre, 2003; Srivastava et al., 2003; Oh, 2004; Baghdadi et al., 2006; Fallahpour et al., 2017). Compared with the single polarization data, PolSAR image contains not only the geometric and backscattering characteristics, but also the polarization characteristics of the scattering target. Diverse polarimetric parameters such as scattering energy, entropy *H*, anisotropy *α*, mean scattering angle *α*, polarization power and polarization ratio, as well as coherence coefficient have been proposed to characterize the target objects (Cloude, 1999; Hajnsek, 2001; Allain et al., 2004). However, the potential of polarimetric parameter for the estimation of surface roughness was investigated in only few studies

(Hajnsek, 2001; Allain et al., 2004; Baghdadi et al., 2012). As we know that on the bare surface the return signal of SAR is mainly affected by the dielectric constant and surface roughness. The moisture content affects the return signal by affecting the dielectric constant, and the surface roughness determines the type of the return signal. A perfectly smooth surface has zero backscatter, while the rough surface diffuses signals in all directions (Ulaby et al., 1986). Therefore, soil moisture and surface roughness have close ties with each other. It is of great significance to explore the relationship between polarimetric parameter and surface roughness for accurate estimation of soil moisture.

This work presents a first qualitative comparison of PolSAR parameter at C-band with respect to surface roughness. It is organized in five parts. Section 2 introduces the study area and dataset. Section 3 describes the methodology. Results and discussion are given in Section 4, and finally conclusions are presented in section 5.

2 STUDY AREA AND DATASET

Juyanze (Latitude: 41°44′~42°00′N, Longitude: 101°30′~102°01′E) is located in the Inner Mongolia Autonomous Region of China. It is at the northeastern corner of the Ejina alluvial fan, and is one of the

terminal lakes of the Heihe River. Extensive land use and irrigation in the upper valley of the Heihe River has reduced modern flow to these terminal lakes. The average annual precipitation and evaporation are 37 *mm* and 3841.81 *mm*, respectively, indicating extremely dry climate and severe adverse nature environment at present.

A C-band fully polarimetric Radarsat-2 image was used in this study (Fig. 1). The single look complex (SLC) SAR image is acquired on July 6, 2014 with a width of $25km \times 25km$ and an incidence angle of 20.17°. Radiometric calibration, multi-look, filtering and terrain correction were performed using PolSARpro 4.2 (http://earth.eo.esa.int/polsarpro/), followed by polarimetric decomposition to obtain the following polarimetric parameters: entropy *H*, anisotropy *A*, mean scattering angle *α*, SERD and DERD.
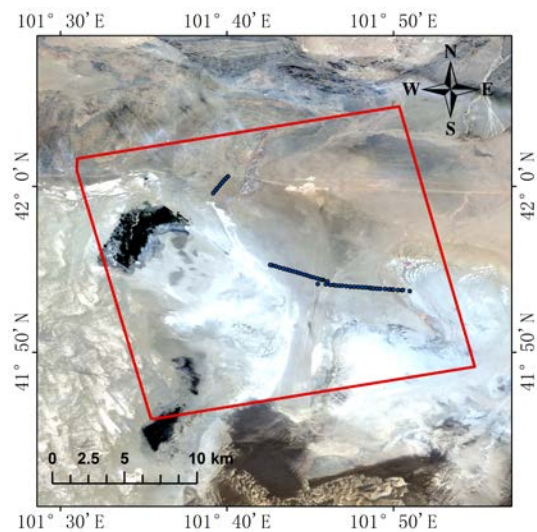
Fig.1 The study area and the sampling sites. The rectangle indicates the coverage of RADARSAT-2 SAR image acquired on Jul. 6, 2014. The dots indicate the sampling sites.

Simultaneously with the satellite overpass, surface roughness was measured using a *2m* long needle profilometer and a digital camera. 48 sites were measured, at each sampling site, 4 field photographs were taken, two were along and the rest were across the row direction. The photographs were processed by GetData Graph Digitizer software later on. The *rms* height *S* and correlation length *L* were calculated.

3 METHODOLOGY

3.1 Surface roughness

As mentioned above, soil moisture and surface roughness are two key factors affecting radar signal over bare surface. The moisture content affects the return signal by affecting the dielectric constant, and the surface roughness determines the type of the return signal. The *rms* height *S* and correlation length *L* are two commonly used parameters to describe surface roughness from the vertical and horizontal dimensions respectively. The equations can be found in Ulaby et al. (1986) and will not be shown here.

3.2 Polarization theory

Cloude and Pottier (1996) proposed a polarimetric decomposition theory based on eigenvector / eigenvalue of the coherent matrix (single, double and volume scattering) to determine the total scattering mechanism.

Using the eigenvectors and eigenvalues, three main parameters are used to express the decomposition results: scattering entropy *H*, anisotropy *A* and mean scattering angle *α*. The entropy *H* is an eigenvalue of the coherent matrix *T* defined by logarithms, which represents the random behavior of the scattering phenomenon. The anisotropy *A* reflects the relatively important minor scattering mechanism. If the scattering mechanism is equal, then *A* is equal to 0. The larger the value of *A*, the more anisotropic scattering is (Cloude and Pottier, 1996). The mean scattering angle *α* represents the dominant scattering mechanism and is calculated from the eigenvectors and eigenvalues of *T*. In addition, Allain et al. (2004; 2005) introduced two parameters, the single-bounce eigenvalue relative difference (SERD) and double-bounce eigenvalue relative difference (DERD), to better reflect the natural surface.

4 RESULTS AND DISCUSSION

Sensitivity of different polarimetric parameters, including the entropy *H*, anisotropy *A*, mean scattering angle *α*, SERD and DERD, to surface roughness parameters, the *rms* height *S* and the correlation length *L* are shown in Fig.2, and Fig.3 is the corresponding fitting lines by polynomial algorithm.

As Fig.2 demonstrated, the correlation between each polarimetric parameter and both the *rms* height *S* and the correlation length *L* is not obvious and all the correlation coefficients are less than 0.3. Among the five polarimetric parameters, entropy *H* is most sensitive to the slight variation of the *rms* height *S* and DERD is the least sensitive one. No great difference was detected in the sensitivity of SERD and the mean scattering angle *α* to *rms* height *S*. Meanwhile, it is found that SERD is the most sensitive one to the correlation length *L*, followed by anisotropy *A*. The other three parameters have approximate sensitivity to the correlation length *L*. From the polynomial fitting lines in Fig.3, it is discernible that there is a reverse

trend between anisotropy *A*, SERD and both surface roughness parameters. DERD presents a reverse trend only with the *rms* height *S*. In general, relatively complex changing trend are exhibited in the fitting lines with the correlation length *L*.
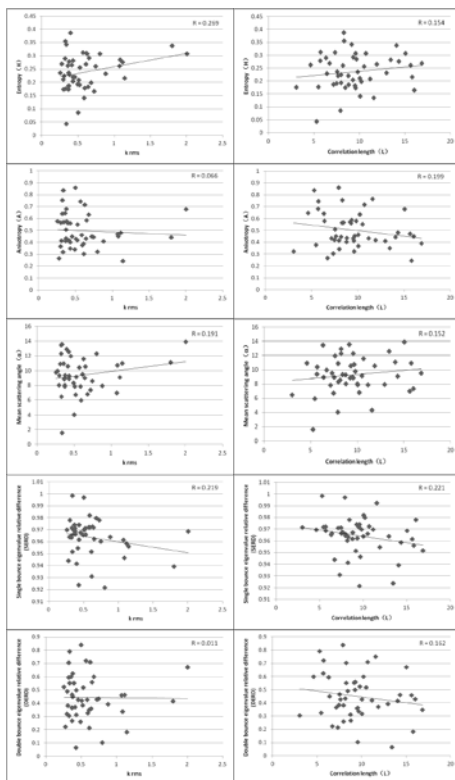
Fig.2 Sensitivity of different polarimetric parameters to the *rms* height *S* and the correlation length *L*.

Previous studies (Cloude, 1999; Hajnsek et al., 2001) show that the entropy *H*, the anisotropy *A* and mean scattering angle *α* are very sensitive to surface parameters values. They considered that the anisotropy *A* and combined *H*/*α* values offered the possibility of a straightforward inversion of roughness and dielectric constant. ERD, SERD and DERD are shown to have great relevance for roughness characterization (Allain et al. 2004, 2005). Although not very relevant with individual surface roughness parameter, the sensitivity of each polarimetric parameter has demonstrated a certain difference especially with the *rms* height *S*. The entropy *H* , mean scattering angle α and SERD seem to be more sensitive to surface roughness. Combination potential of entropy *H* , mean scattering angle α and SERD will be further investigated in future study.
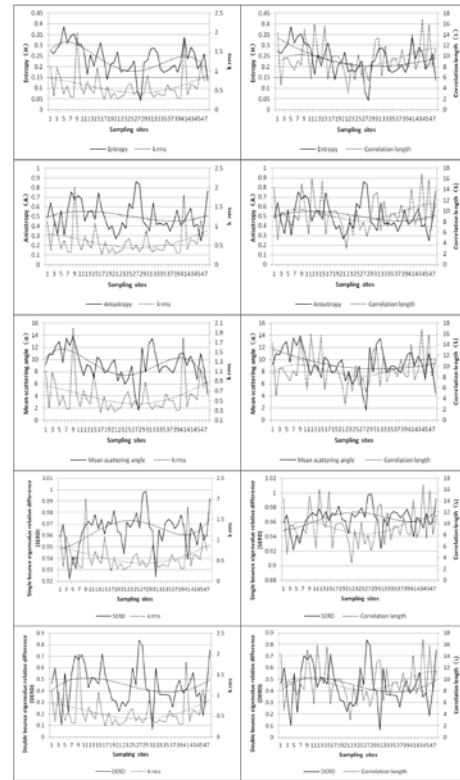
Fig.3 Polynominal fitting lines of different polarimetric parameters to the *rms* height *S* and the correlation length *L*.

5 CONCLUSIONS

Fully polarimetric RADARSAT-2 SAR data was used in this study to qualitatively evaluate the potential of PolSAR data at C-band frequency for the retrieval of surface parameters. Five polarimetric parameters including entropy *H*, anisotropy *A*, mean scattering angle *α*, SERD and DERD were calculated and the sensitivity to the *rms* height *S* and the correlation length *L*, the two most acknowledged parameters describing the surface roughness, was investigated. Results show that the polarimetric parameter is nearly not relevant with both the *rms* height *S* and the correlation length *L* for all the correlation coefficients are less than 0.3. However, the sensitivity of each polarimetric parameter has demonstrated a certain difference especially with the *rms* height *S* in this preliminary study. The entropy *H*, mean scattering angle *α* and SERD seem to be more sensitive to surface roughness. In the following study, further discussion is required to explore the combination potential of polarimetric parameters with relatively higher sensitivity for the estimation of surface roughness.

ACKNOWLEDGEMENT

REFERENCES

Allain, S., Ferro-Famil, L., and Pottier, E., 2004, Two novel surface model based inversion algorithms using multi-frequency polSAR data. In Proceedings of the IEEE International Geoscience and Remote Sensing Symposium held in Alaska, USA, on 20–24 Sep 2004, pp. 823–826.

Allain, S., Ferrofamil, L., and Pottier, E., 2005, New eigenvalue-based parameters for natural media characterization. European Radar Conference IEEE held in Paris, France, 2005, pp. 177–180.

Baghdadi, N., Cresson, R., Pottier, E., Aubert, M., Zribi, M., Jacome, A., and Benabdallah, S., 2012, A potential use for the C-band polarimetric SAR parameters to characterize the soil surface over bare agriculture fields. *IEEE Transactions on Geoscience and Remote Sensing*, 50(10), 3844–3858.

Baghdadi, N., Holah, N., and Zribi, M., 2006, Soil moisture estimation using multi-incidence and multi-polarization ASAR data. *International Journal of Remote Sensing*, 27(10), 1907-1920.

Bissonnais, Y. L., Benkhadra, H., Chaplot, V., Fox, D., King, D., and Daroussin, J., 1998, Crusting, runoff and sheet erosion on silty loamy soils at various scales and upscaling from m2 to small catchments. *Soil and Tillage Research*, 46(1-2), 69-80.

Cloude, S. R., and Pottier, E., 1996, A review of target decomposition theorems in radar polarimetry. *IEEE Transactions on Geoscience and Remote Sensing*, 34(2), 498-518.

Cloude, S. R., 1999, Eigenvalue Parameters for Surface Roughness Studies. *Proc. SPIE Conf. polarization: Measurement, Analysis and Remote sensing II held in Denver, USA*, on 25 Otp 1999, vol.3754，0277–786X.

Engman, E. T., 1991, Applications of microwave remote sensing of soil moisture for water resources and agriculture. *Remote Sensing of Environment*, 35(2-3), 213-226.

Fallahpour, M. B., Dehghani, H., Jabbar Rashidi, A., and Sheikhi, A, 2017, SAR Target Recognition Using Behavior Library of Different Shapes in Different Incidence Angles and Polarizations. *International Journal of Electronics*, (just-accepted).

Hajnsek, I., 2001, Inversion of Surface Parameters using Polarimetric SAR. *Doctoral Thesis Universität Jena, DLR – Science Report*. ISSN, pp. 1434-8454.

Jackson, T. J., Schmugge, J., and Engman, E. T., 1996, Remote sensing applications to hydrology: soil moisture. *Hydrological Sciences Journal*, 41(4), 517-530.

Oh, Y., Sarabandi, K., and Ulaby, F. T., 1992, An empirical model and an inversion technique for radar scattering from bare soil surfaces. *IEEE transactions on Geoscience and Remote Sensing*, 30(2), 370-381.

Oh, Y., 2004, Quantitative retrieval of soil moisture content and surface roughness from multipolarized radar observations of bare soil surfaces. *IEEE Transactions on Geoscience and Remote Sensing*, 42(3), 596-601.

Srivastava, H. S., Patel, P., Manchanda, M. L., and Adiga, S., 2003, Use of multiincidence angle radarsat-1 sar data to incorporate the effect of surface roughness in soil moisture estimation. *IEEE Transactions on Geoscience and Remote Sensing*, 41(7), 1638-1640.

Ulaby, F. T., Moore, R. K., and Fung, A. K., 1986, Microwave Remote Sensing: Active and Passive. Volume Scattering and Emission Theory, Advanced Systems and Applications. Dedham, MA: *Artech House*.

Yang, L. P., Li, Y. F., Li, Q., Sun, X. H., Kong, J. L., and Wang, L., 2017, Implementation of a multiangle soil moisture retrieval model using RADARSAT-2 imagery over arid Juyanze, northwest China. *Journal of Applied Remote Sensing*, 11(3), 036029.

Zribi, M., and Dechambre, M., 2003, A new empirical model to retrieve soil moisture and roughness from C-band radar data. *Remote Sensing of Environment*, 84(1), 42-52.

Photochemical Reflectance Index (PRI) as a proxy of Light use Efficiency (LUE) and transpiration in Mediterranean olive grove

Wafa Chebbi* (1,2), Valérie Le Dantec (1), Gilles Boulet (1), Alexandre Désiré (1), Zohra Lili Chabaane (2), Bernard Mougenot, Pascal Fanise
(1) Université de Carthage / Institut National Agronomique de Tunisie, Tunis, Tunisia.
(2) CESBIO, UMR5126 (CNRS, Université Toulouse 3, CNES, IRD), Toulouse, France.
* chebbiwafa15@gmail.com

ABSTRACT - *An early tracking of water stress with plant-based measurements using indices based on the near-infrared and the visible spectral bands is very important to monitor the plant water status and increase the water use efficiency. The photochemical reflectance index (PRI) provides an assessment of leaf physiological properties. It is based on the short term reversible xanthophyll pigment changes as a response to water deficit and the activity of the photosynthesis. It is able to track water stress before changes on the structure of vegetation (Suárez, et al., 2008). It may be used for a wide range of species. Strong relationships between PRI and LUE were shown at leaf and canopy scales (Garbulsky et al., 2011). However, there is a little information about its relationship with the plant water status. This study will investigate the PRI as a water stress index. First, we identified the factors of changes of transpiration from sap flow measurements at different time steps under rain-fed olive orchard in Tunisia and characterized the different water stress levels. . At canopy scale, we have not found any clear relationship between LUE and PRI as reported in several previous works. Then, at plant scale, we analyzed the relations between plant-based measurements (sap flow, PRI, the leaf turgor pressure, surface temperature) and the environmental variable (solar radiation, relative air humidity and vapour pressure deficit, soil water content..). There is no clear relationship between LUE and PRI. In clear sky conditions, the PRI was best correlated with sap flow especially over periods characterized by a moderate soil water deficit and thus when transpiration is governed by Vapor Pressure Deficit. Finally, under a high soil water deficit, the surface temperature was more closely associated with sap flow.*

1 INTRODUCTION

In Mediterranean regions, climate change is expected to increase air temperatures and might decrease rainfall. The main crop in this area (Olive orchard), is known as drought tolerant, but a moderate water deficit (i.e., a decrease in summer rainfall) may enhance water stress and limit its productivity by 40% (Hsiao et al., 1983). In this context, there is an increasing interest to adjust the water supplies to the plant water requirements. Remote sensing has potential in providing timely information on crop conditions. The assessment and the early detection of the water status is thus crucial since water stress is one of the main factors limiting water (transpiration) and carbon (photosynthesis and primary productivity) exchanges. Water stress also induces stomatal closure, which reduces the transpiration rate, thus decreasing evaporative cooling and increasing leaf temperature. To monitor the plant water status, indices based on the observed surface temperature have been proposed (Jackson et al., 1977). Jackson et al. (1977) used the difference between canopy temperature and air temperature (Tv-Ta) as an index to characterize the water status of the crops. Another index was defined by Gamon et al (1992) related to the state of foliar pigments. Moreover, This Photochemical Reflectance Index (PRI) is calculated as follows:

$$PRI=(R_{531}-R_{570})/(R_{531}+R_{570})$$

Where R_{531} and R_{570} are the reflectance at the 531nm and 570nm wavelength.

The PRI is sensitive to the epoxidation state of the xanthophyll cycle pigments which is related to the photosynthetic efficiency. The xanthophyll cycle pigment is de-epoxidized under conditions of excess light since this reaction is readily reversed under limiting light (Gamon et al., 1990). Winkel et al. (2002) demonstrated the sensitivity of PRI to water stress conditions, although structural effects caused by the water stress would also affect the reflectance signal over Chenopodium quinoa. Thenot et al. (2002) showed the clear difference given by the PRI between well-watered and water-stressed Sajama, a cultivar of Chenopodium quinoa. Thus, the de-epoxidation state may be used as an indicator of short-term changes in photosynthetic activity. Photosynthetic light-use efficiency (LUE), which is one of the widely used concepts to model carbon assimilation by plants, was demonstrated to be successfully estimated with PRI over Mediterranean holm oak forest (Serrano & Peñuelas, 2005), over Mediterraneen forest (Garbulsky

et al., 2008) and over olive trees (Suarez et al., 2008), although inconsistencies were found in the PRI/LUE relationship as function of drought conditions over Sky Oaks Field (Sims et al, 2006). These inconsistencies at the canopy scale can be explained by the difficulty of measurement in forest ecosystems especially at low fraction cover, as well as the high sensitiveness of the sensor to the tree structure. The sparse nature of the olive grove is a challenge in using remote sensing data for water stress monitoring, because the fraction of vegetation is such that the surface is dominated by the bare soil interaction with the atmosphere. But, to our knowledge no previous works have explored the comparaison of the effectiveness of the PRI and Tv-Ta.

The objective of this study is to evaluate the ability of the PRI and TIR (Thermal InfraRed) indices to early detect the water stress over a sparse olive orchard in semi-arid area. In this study, we choose different periods of well-defined climatic and water conditions to determine the relevance of the PRI and TIR indices. The level of water stress affecting the functioning of olive trees will be determined by analyzing different diagnostic parameters such as CO_2 and water vapour fluxes and sap flow.

2 Materials and methods

2.1 site description

Our study is conducted in an olive orchard covering an area of 39 ha in the plain of Kairouan, central Tunisia (35°18'17.14"; 9°54'56.62"). It is a semi-arid region with average annual precipitation of 300 mm. Rainfall varies largely in space and time a flood-generating peak of 700 mm in 1969 and a marked seasonal pattern (a wet season from October till April and a dry season from May till September). Olive trees in our site were planted with a spacing of 20 m resulting in a fractional vegetation cover of about 0.07. The trees are 80 years old. The soil is loamy sand.
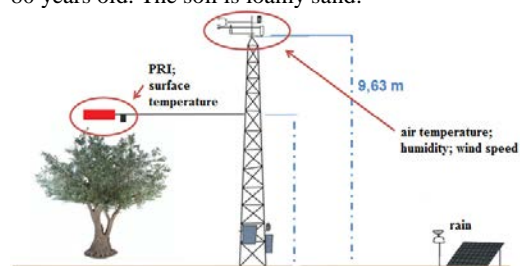
Fig.1: the site's instrumentation: the flux tower and the sensors installed above the tree.

The site was instrumented as shown in Fig.1. We measured weather variables such as temperature, wind speed, relative humidity, net radiation, and the rainfall; variables related to plant functioning such as PRI, surface temperature (Tv), sap flow and evapotranspiration and variables related to the bare soil functioning such as temperature and humidity at different depths, albedo and soil heat flux.

2.2 The observed and the potential transpiration

Sap flow measurements were performed using the heat dissipation technique, HDT (Granier, 1985). The GRANIER method consists in inserting, radially in the sapwood of the trunk, a sensor to measure the sap flow. This sensor (TDP 50) is composed of two needles inserted in the sapwood one above the other; The upper needle is heated with constant temperature, the other is not heated. The system allows to measure the temperature difference between the two needles. At zero flow conditions, this difference reaches its maximum. The temperature difference is highly correlated with the sap flow velocity. In this study, four olive trees are considered as representative of the olive orchard and are equipped with 2 sap flow sensors for each tree. The half-hourly sap flow of the olive tree in L dm^{-2} of sapwood is calculated from the mean of its two sensors. To estimate the half-hourly transpiration (Tobs), it is necessary to convert sap flow values to mm day-1. To do so, we estimated the conductive sapwood area as discussed by Ramos and Santos (2009) and then we multiplied the sap flow per tree by the ratio between the number of trees and the whole surface of the orchard. To estimate the water status of the tree, we calculated using the Penman Monteith equation (FAO 56) a potential transpiration (Tpot), which is defined as the amount of transpiration that would occur if a sufficient water source were available. In order to identify the plant water stress level, we applied the equation (3) to give the potential transpiration index (ITP).

$$ITP= 1- (Tobs/ Tpot) \qquad (3)$$

When water is not a limiting condition for evapotranspiration, the observed transpiration is close to the potential transpiration, the ITP is close to 0. ITP increases with the olive tree water stress level.

2.3 proxy for water stress detection

2.3.1 surface Temperature above the Vegetation (Tv)

An infra-red thermal radiometer (IR 120) was placed over the instrumented tree in order to continuously monitor crown temperature. (Tv-Ta) was calculated over the years of the study. Tv-Ta values were averaged over the 11h-13h time slot which corresponds to the maximum daily radiation.

2.3.2 The Photochemical Reflectance Index (PRI)

The PRI was recorded half hourly since June 2014. Data of reflectance at 531nm and 570nm as well were

collected and then the PRI was calculated. The crown of the tree instrumented with sap flow sensors has been seen from the PRI sensor (SKYE instrument). The outliers values (usually at the beginning and the end of each day) are removed due to the low elevation angles of the sun.

2.5 The Plant Available Water (PAW) estimation

In order to measure the vegetation stress level, we estimated the plant available water. The maximum PAW is the maximum amount of extractable water from the soil by roots. It represents the difference of soil water contents at the field capacity level and at the wilting point for a specified soil thickness. The horizon 0-40cm contains 70% of rooting according to in-situ root density measurements that allows the maximum of water extraction for the olive trees. Thus, the PAW of the horizon 0-40 cm has been calculated as follows:

$$PAW_{0\text{-}40cm} \text{ (mm)} = PAW_{0\text{-}10cm} + PAW_{10\text{-}20cm} + PAW_{20\text{-}40cm}$$

$$PAWmax_{0\text{-}40cm} \text{ (mm)} = (H_{FC} - H_{Wilt}) * 400$$

The fraction of the PAWmax of the 0-40 cm horizon first calculated using the following equation.

$$PAW_{0\text{-}40cm} \text{ (\%)} = (PAW_{0\text{-}40cm} \text{ (mm)}/PAW_{max}) \text{ x } 100 \quad (4)$$

The fraction of the PAWmax is needed to define the plant water stress levels due to soil moisture deficit. The PAW value below 60% correspond to moderate water stress. When the PAW becomes less than 40%, the plant water stress becomes high (Phillips et al., 1984).

3 Results and discussion

The study was carried out from April 2014 to September 2016. 2014 is considered as a "wet" year with frequent rainfall. Precipitation is less frequent in 2015 and 2016 with a stochastic distribution. The three contrasting years allow us to study the sensitivity of the PRI and IRT indices in different water stress conditions (High VPD and soil water deficit). But the choice of the studied periods was based on the fraction of PAWmax. After a large rain event, the PAW decreases simultaneously with the soil water content. During the drydown, it is relevant to monitor the plant functioning and to study response of both indices to the water deficit slope.
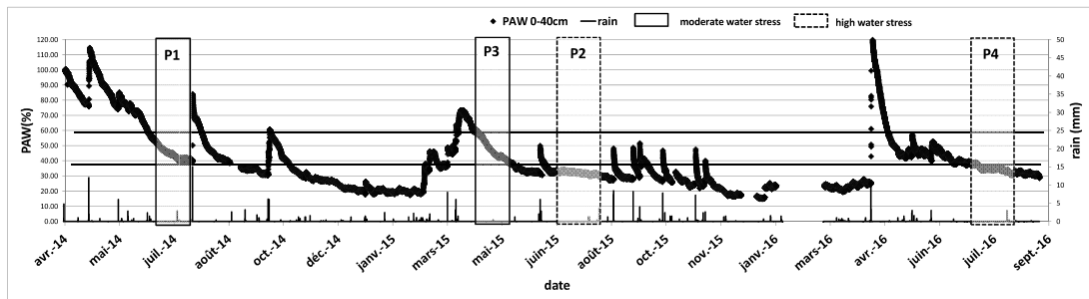
Fig.2: the dynamics of the plant available water (PAW) between 0 and 40 cm of soil over the period of study
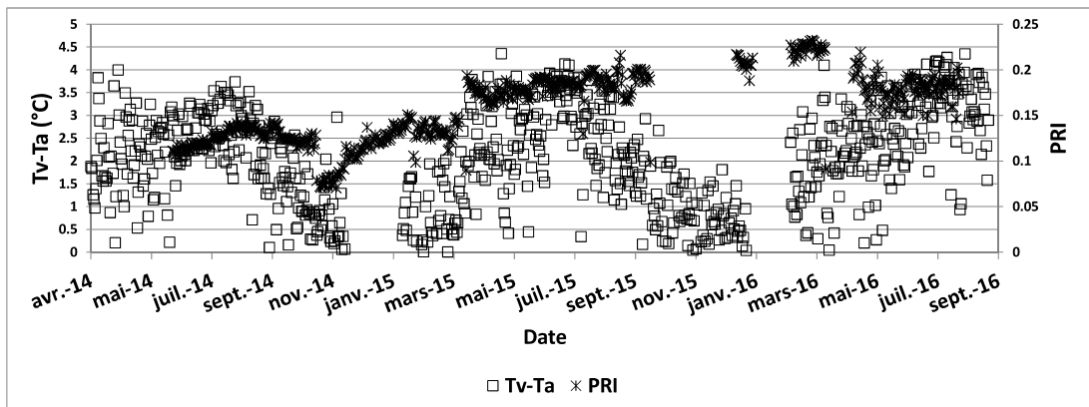
Fig.3: the seasonal dynamics of the PRI and Tv-Ta over the period of study

We selected four study periods when all data are available: P1 from 30/07/2014 to 30/08/2014, P2 from 15/06/2015 to 30/07/2015, P3 from 07/04/2015 to 08/05/2015 and P4 from 13/06/2016 to 03/08/2016. P1 and P3 are characterized by moderate soil water stress conditions and P2 and P4 are characterized by high soil water stress conditions.

3.1 the daily and seasonal dynamics of PRI and Tv-Ta

Beside two gaps in the dataset in November 2014 and in November 2015 due to technical problems, pruning was performed at the end of March. The increase in the order of magnitude of the PRI values after this tree pruning is due to the decrease in the fraction cover included in the field of view of the PRI sensor. PRI values range from 0.12 to 0.15 before the tree pruning and from 0.15 to 0.24 during the remaining period. The PRI, was, as expected, usually larger in 2015 and in 2016 in response to a change in xanthophyll pigments caused by high water deficit conditions. However, The Tv-Ta dynamics were widely scattered and values ranged from 1.2 to 5 degrees during clear days. The maxima in 2015 and 2016 were relatively higher and reach 4.5 ° C.
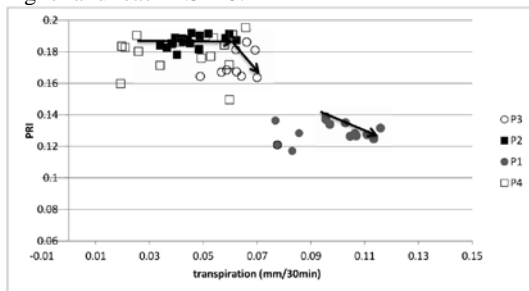
Fig. 4 : the relationship between the transpiration and PRI for the four periods.
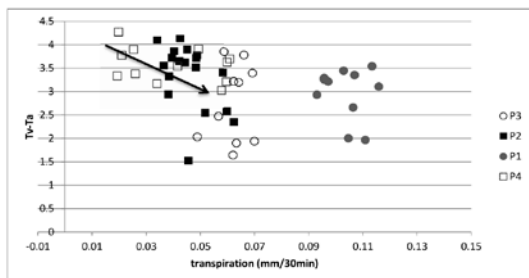
Fig. 5: the relationship between the transpiration and Tv-Ta for the four periods.

At the daily scale, the relationship between the sap flow and the PRI is linear during the period P1 and in the expected direction under moderate water deficit (Fig. 4). The relationship is less strong during P3 which can be explained by phenological stage of the olive tree during the spring (the flowering). The PRI

curve of P2 and P4 flattens to the top at low values of transpiration (between 0.01 and 0.05 mm/30min). These values were affected by the increase of the bare soil fraction included in the field of view of the PRI sensor and the decrease of the evaporative leaf area. In contrario, the relationship between Tv-Ta and sap flow is more marked during P2 and P4 (Fig. 5) due to the increase of the crown temperature at high water deficit conditions.
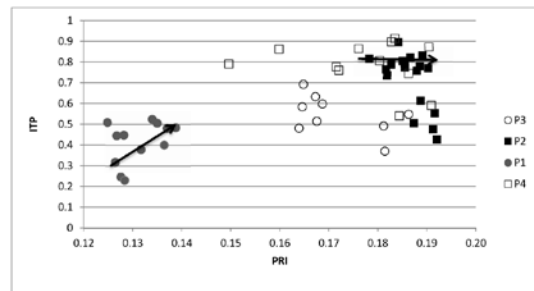
Fig. 6: scatter plot of daily PRI vs ITP at the rainfed olive tree site
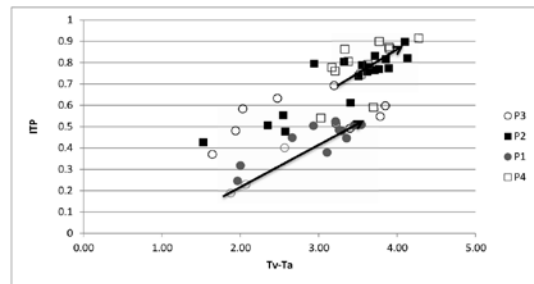
Fig. 7: scatter plot of daily Tv-Ta vs ITP at the rainfed olive tree site

As reported by Thenot et al. (2002), the correlation between the PRI and the water deficit indicator ITP was clear at moderate water stress conditions (i.e, during P1). The pigment changes are effective in response to moderate water deficit. In contrario, at high water stress conditions (P2 and P4) (Fig. 6), no relationship has been established. The PRI values did not vary for ITP values higher than 0.7. This behavior reflects complete de-epoxidation of xanthophyll. On the other hand, (Tv-Ta) is correlated with the ITP at moderate and high water stress conditions (Fig. 7). During P3, the relationship between (Tv-Ta) and ITP was not clear. The vegetation temperature was thus more sensitive to meteorological conditions (during the spring: lower temperature and radiation) which explain the high variability of the values of (Tv-Ta) found over this period. Sepulcre-Canto et al. (2006) shows that the correlation between crown temperature and in-situ measurements of the water potential is higher early in the morning because the soil thermal effects at midday affect the crown temperature.

4 CONCLUSION

The present study focus on two indicators for monitoring the olive tree water stress: PRI and Tv-Ta. However, the relevance of these indicators in monitoring the functioning of the plant depends on the water deficit level. The moderate soil water deficit is difficult to track and the PRI can be a good indicator. (Tv-Ta) gave positive and significant results under different soil water deficit levels and the correlation is higher at high water deficit levels but it is sensitive to weather conditions. The prediction of the transpiration from these indicators will be relevant. A ZIM sensors for measuring the turgor pressure were also installed at the leaf level and data will be investigated in further study.

6 REFERENCES

Gamon, J. A., Field, C. B., Bjorkman, O., Artree, A., & Peñuelas, J. (1990). Remote sensing of the xantophyll cycle and chlorophyll fluorescence in sunflower leaves and canopies. Oecologia, 85, 1–7

Garbulsky MF, Penuelas J, Papale D, Filella I (2008) Remote estimation of carbon dioxide uptake by a Mediterranean forest. Global Change Biology, 14, 2860–2867.

Garbulsky, M.F., Peñuelas, J., Gamon, J., Inoue, Y., & Filella, I. (2011). The photochemical reflectance index (PRI) and the remote sensing of leaf, canopy and ecosystem radiation use efficiencies: A review and meta-analysis. Remote Sensing of Environment, 115 (2), 281-297.

Granier A., Une nouvelle méthode pour la mesure du flux de sève brute dans le tronc des arbres. Annales des Sciences Forestieres, 42 (1985), pp. 193-200

Hsiao C., Braddord K.J. (1983) Physiological consequences of cellular water deficits, ASA- CSSA-SSSA.

Phillips, R.E., Ronald, I., Phillips, E., 1984. Plant Available Water and Plant Water Stress. Plant Soil Sci. 5, 1–5.

R.D. Jackson, S.B. Idso, R.J. Reginato, W.L. Ehrier Crop temperature reveals stress. Crop Soils, 29 (1977), pp. 10-13

G. Sepulcre-Cant, P. Zarco-Tejada, J. Jimnez-Muoz, J. Sobrino, E. de Miguel, F. Villalobos, "Detection of water stress in an olive orchard with thermal remote sensing imagery", Agric. For. Meteorol., vol. 136, no. 1/2, pp. 31-44, Jan. 2006.

Serrano, L., & Peñuelas, J. (2005). Assessing forest structure and function from spectral transmittance measurements: A case study in a Mediterranean holm oak forest. Tree Physiology, 25, 67−74.

Sims, D. A., Luo, H., Hastings, S., Oechel, W. C., Rahman, A. F., & Gamon, J. A. (2006). Parallel adjustment in vegetation greenness and ecosystem CO2 exchange in response to drought in a Southern California chaparral ecosystem. Remote Sensing of Environment, 103, 289−303.

Suárez, L., Zarco-Tejada, P. J., Sepulcre-Cantó, G., Pérez-Priego, O., Miller, R. J., Jiménez-Muñoz, J. C., et al. (2008). Assessing canopy PRI for water stress detection with diurnal airborne imagery. Remote Sensing of Environment, 112(2), 560-575.

Thenot, F., Méthy, M., & Winkel, T. (2002). The photochemical reflectance index (PRI) as a water-stress index. International Journal of Remote Sensing, 23 (23), 5135–5139.

Winkel, T., Méthy, M., & Thénot, F. (2002). Radiation use efficiency, chlorophyll fluorescence , and reflectance indices associated with ontogenic changes in water-limited Chenopodium quinoa leaves. Photosynthetica, 40 (2), 227−232.

Scaling Effect on Radar Sensing of Rough Surface

Du-Gang Xi[1], Kun-Shan Chen[2], Zhao-Liang Li[3], and Yu Liu[2]

1, The PLA Information Engineering University, Zhengzhou, 450001, P.R. China;
2, The State Key Laboratory of Remote Sensing Science, Institute of Remote Sensing and Digital Earth, Chinese Academy of Sciences, Beijing 100101, China;
3, Key Laboratory of Agri-informatics, Ministry of Agriculture / Institute of Agricultural Resources and Regional Planning, Chinese Academy of Agricultural Sciences, Beijing 100101, China.
E-Mail: chenks@radi.ac.cn

ABSTRACT - *In radar sensing of natural surface, which in nature is multi-scale, it is of practical importance to understand the control mechanisms over the different spatial scales in order to maximize the information content that may attain. It has been known that the multi-scale entropy (MSE), by incorporating interrelationship of entropy and scale, is capable of revealing long-range correlations on multi-scale random process. In this paper, we apply the MSE to quantitatively characterize the information content in radar sensing of random surface. The dependence of the surface size, auto-correlation function (ACF), correlation length (l), and root-mean-square (rms) height on the radar scattering signal is examined. Results shows that the MSE is a simple and yet effective approach to measuring the effect of sampling scales in sensing random surface, and thus to choosing the proper resolution cell size in term of radar wavelength. Moreover, the choice of spatial resolution is more sensitive for surface with smaller correlation length, and No rms height effect on the resolution scaling is observed. In addition, finer resolution is required for surface with exponential ACF compared to that with Gaussian ACF.*

1 INTRODUCTION

Rough surface observation is a subject of extensive research for its wide applications in remote sensing of terrain and ocean. With rapidly increasing availability of high-resolution airborne and space-borne radar sensors, studies have found that measuring signals (amplitude and phase) are always poised to sampling size effects as far as information content is concerned (eg., Nesti et al., 1996). It is of practically important to understand the control mechanisms over the different spatial scales in radar sensing of natural surface to ensure better use of microwave scattering data in natural surface monitoring.

In the past decades, there has been some works concerning scaling effect on radar sensing of rough surface, such as experiment analyses (eg., Nesti et al., 1996), and numerical simulations (Sarabandi and Oh, 1995; Allain et al., 2003; Park et al., 2008). Those studies were always carried out based on some qualitative analysis with casual cases. The scale effects identified by various researchers are inconsistent. Considering that, in radar sensing of natural surface, the goal is to preserve the maximum information content, among others, of the parameters of interest that are transferred from inputs to outputs of the radar response. Thus, the information theory, which is capable characterize the information content, is expected to be able to quantitatively and objectively evaluate the information in radar observation, and thus to maximize the information content that may attain.

In addition, considering that the rough surface in nature is multi-scale, the multi-scale entropy (MSE) (Costa et al., 2005), a typical information parameter concerning scale characters, is expected to be applicable to indicate the scaling effect of radar sensing of rough surface. The reason lies in that, the MSE, using scale factor to construct consecutive coarse-grained data series, incorporates interrelationship of entropy and scale, and reveals long-range correlations on multi-scale random process. It has been widely used to characterize the information content in multi-scale time series of physical and biological systems. Theoretically, for rough surface profile, the scale factor in MSE analysis is consistent with spatial resolution size. Motivated by this fact, in this paper, we apply MSE to characterize quantitatively, the information content in observing random surface, in order to gain deeper insights into the control mechanisms over the different spatial scales, as well as to figure out proper spatial resolution in term of radar wavelength.

In this study, Section 2 introduces the method to describe random surface. Section 3 gives the formulation of the problem of scale effect. Section 4, the main body of this paper, the dependence of surface size, auto-correlation function (ACF), correlation

length (l), and root-mean-square (*rms*) height are examined. Finally, in Section 5, a summary and the conclusion are drawn to close the paper.

2 ISOTROPIC SURFACE DESCRIPTIONS

For naturally occurring surfaces, such as terrain and sea, are best and, perhaps, only can be modelled by random processes. To describe such random surface, we adopted the $\sigma\text{-}l$ approach, which is a classical and commonly used statistical approach. It used two roughness parameters: the *rms* height σ , and the correlation length l , which measure the horizontal- and vertical- roughness scale, respectively. The ratio of σ to l is the surface *rms* slope.

Specifically, assuming a randomly rough surface $z(x,y)$ and a real stationary process with zero mean and standard deviation σ , then

$$\langle z(x,y)z(x+\tau_x,y+\tau_y)\rangle = \sigma^2 \rho(\tau_x,\tau_y)$$

where $\sigma^2 = \langle z^2 \rangle - \langle z \rangle^2$ and z follows a Gaussian distribution such that:

$$p(z) = \frac{1}{\sigma\sqrt{2\pi}} e^{-z^2/2\sigma^2} \tag{1}$$

For an isotropic surface, we have $\tau_x = \tau_y = \tau$. In what follows, for simplicity, but without loss of generality, we have only discussed the isotropic surface. Thus, the joint probability density function between two points on the surface can be written as,

$$p(z,z') = \frac{\exp\left\{-\left(z^2 - \rho zz' + z'^2\right)/\left(2\sigma^2\left(1-\rho^2\right)\right)\right\}}{2\pi\sigma^2\sqrt{1-\rho^2}} \tag{2}$$

The correlation function ρ is defined as:

$$\rho(\tau) = \lim_{L\to\infty} \frac{1}{L} \int_0^{L-\tau} z(r)z(r+\tau)dr \tag{3}$$

where $r = \sqrt{x^2 + y^2}$; and L is the surface length.

According to the Wiener Khintchine Theorem, the surface spectrum and correlation function ACF are related to form a Fourier transform pair:

$$W(k,\varphi) = \int_0^{2\pi}\int_0^\infty \rho(\tau,\phi)e^{jk\tau\cos(\varphi-\phi)}\tau d\tau d\phi \tag{4}$$

For an isotropic surface, the autocorrelation function $\rho(\tau,\phi)$ is independent of direction and dependent only on lag distance τ . The relation reduces to:

$$W(k,\varphi) = \int_0^\infty \rho(r)J_0(Kr)rdr \tag{5}$$

where J_0 is zero[th] order Bessel function.

For natural surfaces, because of their formation mechanisms, the actual ACF from field measurements are complicated and usually vary between Gaussian and exponential functions (Oh et al., 1992). Their ACF and corresponding surface spectrum are given as:

For the Gaussian function

$$\rho(r) = e^{-r^2/l^2}, W(K) = \frac{l}{\pi}e^{-K^2l^2/2} \tag{6}$$

Similarly, for the exponential function

$$\rho(r) = e^{-|r|/l}, W(K) = \frac{1}{\pi l\left(1+K^2l^2\right)} \tag{7}$$

Note that, for simplicity, we only consider 1-D rough surface in this study.

3 FORMULATION OF THE PROBLEM OF EFFECTIVE RESOLUTION

In (Costa et al., 2005), the authors considered the multi-scale characters of biological signals based on the MSE analysis. Following the same procedure elaborated in the formulation of MSE (Costa et al., 2005), to analyze the effect of spatial resolution on radar sensing rough surface, we first produce a one-dimensional discrete rough surface series , $\{x_i\} = \{x_1,\ldots,x_i,\ldots,x_N\}$, with the sample segment length of τ . Then we construct consecutive coarse-grained series of surface, $\{y^{(\tau)}\}$, corresponding to the scale factor, τ , as shown in Fig.1.
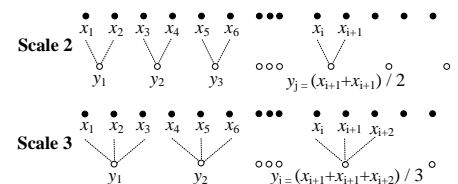
Fig.1 Schematic illustration of the coarse-graining. Adapted from Ref. (Costa et al., 2005).

In general, each element of a coarse-grained series is calculated according to the equation

$$y_j^{(\tau)} = \frac{1}{\tau}\sum_{i=(j-1)\tau+1}^{j\tau} x_i, \qquad 1 \le j \le N/\tau \tag{8}$$

For scale one, the series $\{y^{(1)}\}$ is simply the original series. From the definition in Eq.(8), we can obviously see that the scale factor is corresponding to the spatial observation resolution. From the Fig.1, it can be found that statistical properties of random rough surfaces vary with spatial resolution cell size. For example, when the scale factor increases, the topography tends to be more flat due to coarse-grained series progressively "smoothed out" .
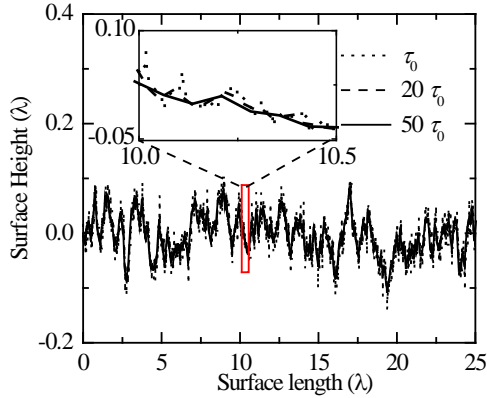
Fig.2 A generated random surface with scale factor $\tau = \tau_0, 20\tau_0, 50\tau_0$. The surface ($\sigma = 0.06\lambda$ and $l = 0.5\lambda$) has exponential ACF and the profile length of 25λ with $\tau_0 = 0.0016\lambda$. The scale factor, τ, is corresponding to the spatial observation resolution.

Then, we calculate an entropy measure S_E for each coarse-grained series which is equal to the negative of the natural logarithm of the conditional probability. Taking the scale one $\left\{ y^{(1)} \right\}$ as an example, which is composed of m-length vectors $u_m(i) = \left\{ x_i, x_{i+1}, \ldots, x_{i-m+1} \right\}$, $1 \leq i \leq N - m + 1$. The Euclidean distance between two vectors as the maximum absolute difference between their components can be written as,

$$d\left[u_m(i), u_m(j) \right] = \max \left\{ \begin{array}{l} \left\| x(i+k) - x(j+k) \right\| \\ 0 \leq k \leq m-1 \end{array} \right\} \quad (9)$$

Let $n_i^m(r)$ represents the number of vectors $u_m(j)$ that are close to the vector $u_m(i)$, i.e., the number of vectors that satisfy $d\left[u_m(i), u_m(j) \right] \leq r$. The probability that any vector $u_m(j)$ is close to the vector $u_m(i)$ can be written as

$$C_i^m(r) = n_i^m(r) / (N - m + 1) \quad (10)$$

Then the average of the C_i^m is

$$C^m(r) = 1/(N - m + 1) \sum_{i=1}^{N-m+1} C_i^m(r) \quad (11)$$

Thus, the S_E can be written as,

$$S_E(m, r, N) = -\ln \frac{C^{m+1}(r)}{C^m(r)} \quad (12)$$

In general, the MSE reflects the variance of data series as well as their correlation properties. It incorporates interrelationship of entropy and scale, and is capable of revealing long-range correlations on multi-scale random process. Generally, data sets with higher variability or greater randomness tend to be more entropic. Moreover, a monotonic decrease of the entropy values indicates the original signal contains information only in the smallest scale, and vice versa.

In this paper, unless otherwise specified, S_E are calculated based on 50 generated infinite random surfaces with length of $\geq 100l$, sampling point $N = 83600$, and $m = 2$. The r is sets as 15% of the original data series, with reference to similar MSE analysis in (Costa et al., 2005).

4 RESULTS

In order to quantifying the scale effect on radar sensing of rough surface for different resolution and illustrate the optimal resolution selection, we analyzed the dependence of profile length, as well as the effect of roughness characterization associated, including the correlation length, ACFs and *rms* height.

4.1 The effect of Surface length

In theory simulation, the random surface is always treated as infinite. However, in practical measurement, roughness profile for the resolution cell is truncated with rectangular window. To illustrate the effect of truncated length on surface information and optimal resolution selection, we plot the MSE as a function of surface length, as shown in Fig. 3.
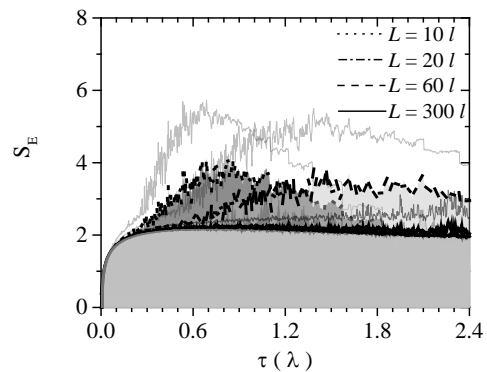
Fig.3 MSE as a function of resolution cell size for infinite surface ($L = 300l$) and truncated surfaces ($L = 10l, 20l, 60l$). Solid line represents the mean values of S_E for 50 simulated surfaces, and error region represent the standard deviation. The surface ($\sigma = 0.06\lambda$ and $l = 0.5\lambda$) has exponential ACF. $\tau = l = 0.5\lambda$.

The surface ($\sigma = 0.06\lambda$ and $l = 0.5\lambda$) has exponential ACF and τ_0=0.0016λ. The result shows that the MSE generally increase as spatial scale increases. For infinite surface ($L = 300l$), the observation of surface parameters are almost insensitive to measurements with different resolution, if only the pixel cell greater than 0.2λ . For truncated surfaces, entropy fluctuates greatly, and decreases slightly at greater cell scales, which indicates that, the observation may lose some information when resolution is coarse.

4.2 The effect of Surface ACF

Fig. 4 shows MSE for surface with exponential and Gaussian ACF. The result shows that, both for infinite and truncated surface, the largest difference between the entropy values of two ACFs is obtained at high resolution, and the MSE Curve almost overlap at coarse cell. Moreover, it can be seen that, comparatively, observation of surface with exponential ACF is less dependent on the resolution cell due to its relatively flat MSE curve. This result is consistent with the fact that, unlike Gaussian, exponential surface contains complex structures across small scales.

(a)

(b)
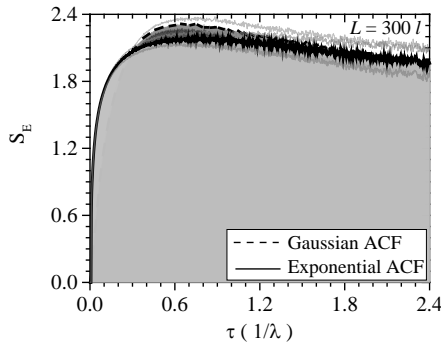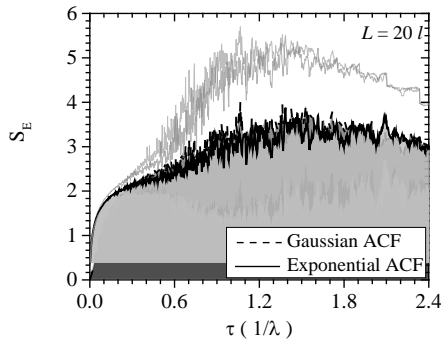
Fig.4 Similar to Fig.3 but for surface with exponential and Gaussian ACF. (a) truncated surface (*L*=20*l*), and (b) infinite surface (*L*=300*l*)).

4.3 The effect of Surface correlation length

Fig.5 is the MSE for infinite surface with different correlation length. It can be observed, in the case of surface with small correlation length (eg., $l \leq 0.6\lambda$), MSE increase firstly, and then decease with increasing cell size, and it arrives at the peak around with $\tau = l$. For surface with greater correlation length $(l = 0.8\lambda)$, MSE keeps stable at coarse resolution. This suggests that the spatial resolution choice is comparably more important for surface with small correlation length, while resolution cell size around correlation length $(\tau = l)$ is preferable to observe random surface.
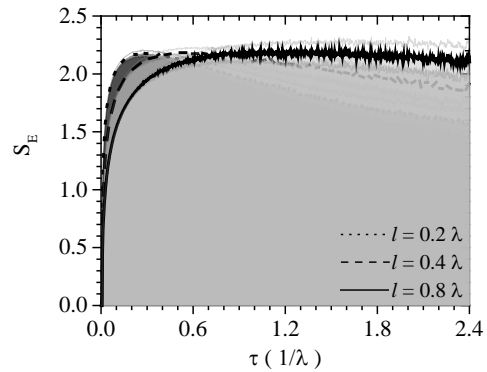
Fig.5 Similar to Fig.3 but for infinite surface with different correlation length

4.4 The effect of Surface *rms* height

Fig. 6 shows MSE for surface with different *rms* height. The results show that the *rms* height do not change the information observed in high-resolution images, for almost all lines are overlapped. Thus, there is no need to consider *rms* height in the optimal resolution selection.
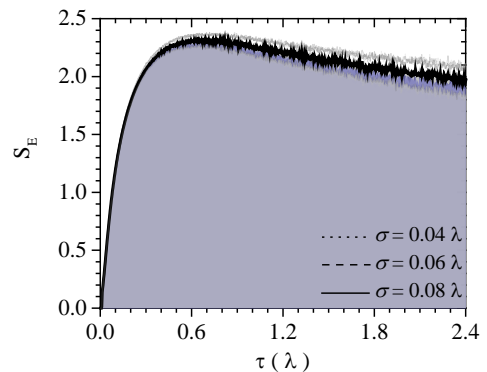
Fig.6 Similar to Fig.3 but for infinite surface with different *rms* height

5 CONCLUSIONS

In this paper, we introduces MSE concept, which incorporates the interrelationship of entropy and scale, to understand the control mechanisms over the different spatial scales in order to maximize the information content that may attain. The effect of roughness characterization associated, including the correlation length, *rms* height and ACF is estimated, and the dependence of profile length is investigated which is always treated as infinite. The results show that the information content contained for different resolution cell size varies greatly over different surface correlation length, ACF, surface length, and is strongly dependent on surface length. In general, the choice of spatial resolution is more sensitive for surface with smaller correlation length. No *rms* height effect on the resolution scaling is observed. In addition, finer resolution is required for surface with exponential ACF compared to that with Gaussian ACF. From the results, we can see that, the MSE is a simple, as well as effective approach to measuring the effect of sampling scales in sensing random surface, and thus to choosing the proper resolution cell size in term of radar wavelength.

6 ACKNOWLEDGMENTS

7 REFERENCES

Allain, S., Ferro-Famil, L., Pottier, E., and Fortuny, J., 2003, Influence of resolution cell size for surface parameters retrieval from polarimetric SAR data. In *Geoscience and Remote Sensing Symposium, 2003. IGARSS'03. Proceedings. 2003 IEEE International* (Vol. 1, pp. 440-442). IEEE.

Costa, M., Goldberger, A. L., and Peng, C. K., 2005, Multiscale entropy analysis of biological signals. Physical review E, 71(2), 021906.

Nesti, G., Fortuny, J., and Sieber, A. J.,1996, Comparison of backscattered signal statistics as derived from indoor scatterometric and SAR experiments. *IEEE transactions on geoscience and remote sensing*, *34*(5), 1074-1083.

Oh, Y., Sarabandi, K., and Ulaby, F. T., 1992, An empirical model and an inversion technique for radar scattering from bare soil surfaces. *IEEE transactions on Geoscience and Remote Sensing*, *30*(2), 370-381.

Park, S. E., Ferro-Famil, L., Allain, S., and Pottier, E., 2008, Analysis of polarimetric surface scattering in high resolution SAR. In *Geoscience and Remote Sensing Symposium, 2008. IGARSS 2008. IEEE International* (Vol. 3, pp. III-394). IEEE.

Sarabandi, K., and Oh, Y., 1995, Effect of antenna footprint on the statistics of radar backscattering from random surfaces. In *Geoscience and Remote Sensing Symposium, 1995. IGARSS'95. 'Quantitative Remote Sensing for Science and Applications', International* (Vol. 2, pp. 927-929). IEEE.

Operational light source and luminance determination methodology by using hyperspectral and mapping cameras at very high spatial resolution

Ramon Alamús, Vicenç Palà, Anna Tardà, Luca Pipia, Jordi Corbera
Institut Cartogràfic i Geològic de Catalunya (ICGC). Barcelona, Spain
ramon.alamus@icgc.cat, vicenc.pala@icgc.cat, anna.tarda@icgc.cat, luca.pipia@icgc.cat, jordi.corbera@icgc.cat

ABSTRACT - *Metropolitan areas account for 75% of the world's energy consumption and much of its CO_2 emissions. In some Spanish towns and cities, public lighting is responsible for 50% of power consumption. As lighting and management systems are nowadays being developed and improved, street lighting is one of the sectors with a larger potential in energy savings. The current auditing process to evaluate the level of lighting systems of municipalities is costly and tedious. Night-light remote sensing provides data concerning luminance and type of light source. Satellite and space platform, as DMSP and SUOMI satellites or the International Space Station (ISS), provide data with moderate spatial and spectral resolution. Airborne hyperspectral imaging spectrometers can achieve data with better spatial and spectral resolution. At the Institut Cartogràfic i Geològic de Catalunya (ICGC) we have developed a data fusion methodology by using our own airborne VNIR hyperspectral sensors and photogrammetric cameras to provide local authorities with data at a very high spatial resolution (up to 25 cm GSD) concerning luminance and sources of lighting (incandescent, mercury vapour, high pressure sodium vapour, metal halide and light-emitting diode-LEDs). The paper presents operational and practical results over large urban areas. Transforming this quantitative information into knowledge will become a key issue for a better and sustainable urban planning at next future.*

1 INTRODUCTION

Nocturnal light pollution is a side effect of industrial civilization and accounts for excessive, misdirected or undesired artificial light produced by dwellings, factories, offices, sport fields, billboards, street lights and so on. Metropolitan areas account for 75% of the world's energy consumption and much of its CO_2 emissions. For instance, in Spain, in some towns and cities, public lighting is responsible for 50% of power consumption. Thus, street lighting is one of the sectors with a larger potential in energy saving (between 30% and 40%): lighting and management systems are nowadays being developed and improved, by using more efficient lights with less energy consumption.

Reliable methods to quantify the amount of artificial light radiation are a prerequisite to detect light/energy waste and to assess the effectiveness of policies and actions. Current auditing processes based on field campaigns are time consuming, thus costly and tedious. Field campaigns are unable to provide a synoptic view over a large area. In this work, remotely sensed night-lights observations are used to distinguish different sources of lighting depending on their spectral signature and to quantify their level of light emission.

Concerning data acquisition as a part of such methods, space-borne imagery provides a moderate spatial and spectral resolution (currently available from instruments on board satellites and space platforms, such as the data taken by DMSP and SUOMI satellites or taken from the International Space Station). Such data have limited spectral bands and coarse spatial resolution, and the dynamic range of the sensors is optimized for daytime rather than nocturnal capture. Accurate quantification and characterization of artificial light radiated at ground level from remote sensing imagery requires high spectral and spatial resolutions, with a high dynamic range. Images with these characteristics can be achieved with airborne hyperspectral imaging spectrometers.

At the ICGC we have developed a methodology to fusion data simultaneously recorded with a hyperspectral sensor (an AISA Eagle II from SPECIM), which combines a synoptic view with multiple narrow spectral bands, and a digital photogrammetric camera (a DMC-I from Z/I-Hexagon). As a result we are providing to local authorities luminance maps at a resolution up to 0.25 cm and maps of main source of lights (incandescent, mercury vapour, high pressure sodium vapour, metal

halide and light-emitting diode-LEDs) at a resolution up to 1.5 m.

2 SENSORS AND DATA ACQUISITION

2.1 AISA Eagle II

The AISA Eagle II is a hyperspectral VisNIR pushbroom imager with a reflection grating and a two-dimensional CCD (charge coupled device) solid-state array detector, manufactured by SPECIM. The instrument operates by looking down in a fixed direction and imaging successive lines of the flown scene, building up a two-dimensional image as the platform moves forward (main parameters are described in table 1). One dimension of the CCD covers the across-track spatial direction (configurable in 512 or 1024 spatial pixels); the other one accounts for the spectral domain (configurable up to 256 bands covering the spectral range 400-1000 nm).

Table 1. AISA Eagle II main parameters

FOV [°]	37.7
no. FOV pixels	Configurable 512 or 1024
no. spectral pixels	Configurable up to 256
spectral range [nm]	400-1000
Focal length [mm]	17.8
GSD @ 2500 m [m]	1.5

2.2 DMC-I

DMC is a high-resolution photogrammetric frame camera, manufactured by Z/I imaging (currently Hexagon) (Dörstel 2003), which simultaneously captures one high-resolution (HR) panchromatic and four low-resolution (LR) multi-spectral (red, green, blue and near-infrared) images (main parameters are described in table 2). The across-track and along-track ratio between multispectral and panchromatic imaging is 1:4. The high resolution image is the result of mosaicking four sub-images acquired by four inclined panchromatic camera heads. Each of them covers approximately a quarter of the final image, called virtual image. The four low resolution multi-spectral images in the red, green, blue and near-infrared colour bands are acquired with four additional nadir-looking camera heads with a focal length of 25 mm. Note that the four images completely cover the virtual high resolution image.

Table 2. DMC-I main parameters

FOV [°]	69.9x42
no. FOV pixels (HR)	13824x7680
no. FOV pixels (LR)	3072 x1920
no. spectral bands	1 panHR / 4(RGBNir)LR
Focal length [mm]	120(panHR)/25(LR)
GSD @ 2500 m [m]	0.25(panHR)/1(LR)

2.3 Data acquisition

Data is acquired in a single nocturnal flight where both sensors (AISA and DMC) are operated simultaneously in an airborne platform, which is able to carry both sensors.

As the goal is the analysis of artificial nocturnal lights, it is required to avoid natural light sources, which means avoid moon light. Night flights must be ideally performed close to the New Moon phase when moon has been already set.

Moreover, due to safety reasons according to aerial control authorities, nocturnal flights may have some operational restrictions, which depend on capabilities of the airplane, terrain and distance to the nearest airport. Such restrictions may limit the resolution of the resulting luminance map.

3 LUMINANCE MAP

This section is dedicated to the description of the retrieval of luminance from the hyperspectral sensor and the subsequent fusion with the photogrammetric camera data. A more detailed explanation can be found in Pipia et al. 2014.

3.1 Luminance Map (retrieved from the Hyperspectral sensor)

For each pixel, the VisNIR sensor collects a spectral sampling of the radiation in 400-900nm spectral range emitted by the surface. Since the luminance map should represent how the human visual system perceives the radiance of light at ground level, the radiance values of the 126 bands must be converted to luminance values at ground level and then combined to retrieve the visual perception of human beings. The spectral sensitivity of the human visual system is described by the photopic luminosity function which indicates the sensitivity of human eye to incoming light radiation at different wavelengths (CIE 1931). The conversion from measured radiance to luminance at ground level is performed in several steps. Firstly, a radiometric calibration converts digital numbers captured by VisNIR sensor into radiances at flying height. These radiances are transferred to radiances at ground level by compensating for the atmospheric hyperspectral attenuation and combining the 126 band radiances using the photopic luminosity function. Finally, a low resolution luminance map (at a resolution of 1.5 m GSD) of the entire area is created by mosaicking the imagery from the different flight tracks of the hyperspectral sensor. Figure 1 shows a detail of the low resolution luminance map segmented into 10 classes from 0.35 to 10 cd/m^2.

3.2 DMC and AISA data fusion

The dynamic range of the DMC panchromatic band is higher compared to the VisNIR sensor as the DMC spectral bands are much broader and, consequently, more photons can reach the charge-coupled device (CCD) in the image plane. The fusion consists of fitting the radiance values of the DMC images to the luminance map retrieved from the hyperspectral sensor. Once this calibration process has been completed, the luminance map at 0.25m GSD can be computed from DMC imagery alone. Figure 2 shows a detail (the same area that in figure 1) of the high resolution luminance map segmented into 10 classes from 0.35 to 10 cd/m^2.

| ■ [.35,.65[| ■ [.65,.85[| ■ [.85,1.25[| ■ [1.25,1.75[| ■ [1.75,3[| |
| ■ [3,4[| ■ [4,5[| ■ [5,7.5[| ■ [7.5,10[| □ >10 | [cd^{m-2}] |
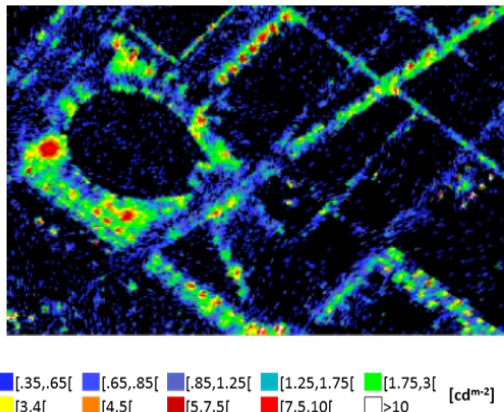
Figure 1. Low resolution luminance map derived from AISA Eagle II hyperspectral sensor.

| ■ [.35,.65[| ■ [.65,.85[| ■ [.85,1.25[| ■ [1.25,1.75[| ■ [1.75,3[| |
| ■ [3,4[| ■ [4,5[| ■ [5,7.5[| ■ [7.5,10[| □ >10 | [cd^{m-2}] |
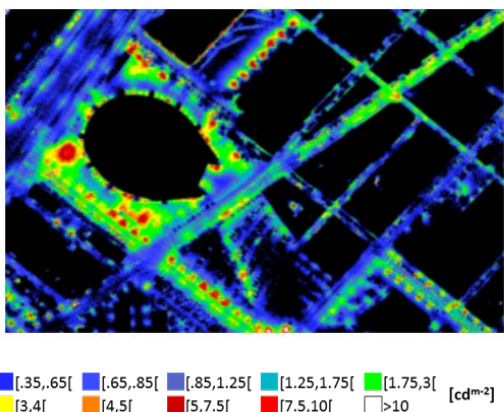
Figure 2. High resolution luminance map derived from the AISA Eagle II and DMC-I fusion.

A visual comparison of the retrieved luminance at the two spatial resolutions (1.5 m, AISA luminance map, and 0.25 m, DMC-I luminance map, respectively shown in figures 1 and 2) stress the noteworthy improvement in the quality of the images in terms of spatial resolution. The slight geometrical discrepancies between AISA and DMC are due to two main reasons: the different way the pushbroom and frame sensors observed the same pixels on the ground, and the coarser resolution of the hyperspectral sensor, which is expected to introduce some distortions. Yet, the details contained the high resolution map, may become extremely useful in order to activate any artificial illumination optimization strategy. The blurred description provided by AISA at 1.5 m sharpens in the HR luminance map, where single street lamps are detectable. The high resolution map allows giving a step further. In fact, it becomes feasible to move from the detection of the brightest point close to the light source to the characterization of a wider crown around this bright spot, where the illumination decreases proportionally to the distance from the source.

Concerning the luminance absolute estimation, the radiometric information was preserved in the DMC map generation process. This can be observed in figures 1 and 2. It is clearly observed that the information that was recovered using AISA has been well preserved for luminance values higher than 1.5 cd/m^2. Moreover, the lower noise floor of DMC has enhanced the dynamic range of the retrieved luminance from 1.5 cd/m^2 down to 0.35 cd/m^2.

4 LIGHT SOURCE TYPE MAP

In the literature, hyperspectral and multispectral airborne sensors have been often used for nocturnal image analysis. Yet, all these studies have been focused on the detection of artificial light sources or classification based on specific spectral signature detection (Aubé et al. 2005, Barducci et al. 2006, Elvidge et al. 2010 and Tardà et al. 2011).

As shown in figure 3, artificial light sources have specific spectral signatures. The hyperspectral capabilities of the AISA Eagle II sensor allow deriving a set of spectral indexes focusing in particular features of the light spectral signatures, which are used to discriminate them.

The hyperspectral instrument AISA Eagle II has been designed for recording reflected sunlight and not for capturing artificial light at night. Then, the relatively low intensity of artificial light at night and the limited exposure time by operational restrictions causes hyperspectral images to be affected by high noise level.
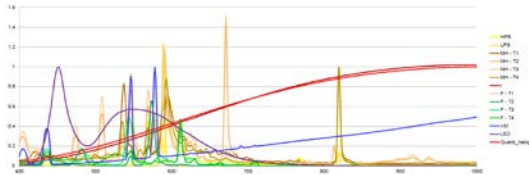
Figure 3. Spectral signature of usual different types of artificial light sources. (Units on x-axis are nanometers)

In order to overcome with this handicap a two steps strategy has been designed. Firstly, punctual source lights and their illuminated neighborhood are detected in the DMC nocturnal images. Afterthat, a set of light spectral indexes is computed as a weighted average of spectral indexes derived from the AISA hyperspectral data.

Punctual source lights are detected as the point (pixel) with the highest light intensity in its neighborhood. In a first step, for each image pixel the pixel with a maximum light intensity is detected in a 6 m radius neighborhood. Finally, for each pixel that is a local maxima in a 6 m radius neighborhood (punctual light source), its neighborhood is grown up to the area that is mainly illuminated by the punctual light source. Such point-like source describes the position where light intensity is the highest in its neighborhood, and is likely to correspond to the lamp center.
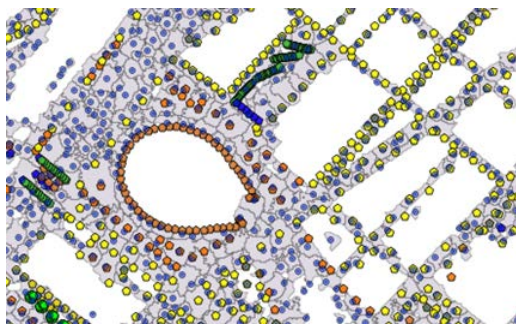
Figure 4. Detection of punctual source lights and their illuminated neighbourhood.

Figure 4 shows a detail of detected punctual source lights (grey-blue dots) and their illuminated neighborhood (grey polygons). The theoretical locations of public lamps (colored circles) are superimposed on the image. Notice that most of the public lamps are close to a detected punctual source light. Nevertheless, in low light intensity area there are punctual source lights that correspond to vehicles lights or reflective surfaces (for example, ground painted lanes, metal surfaces…) instead of known public lamps.

Taking advantage of the different spectral signatures of the light sources (fig 3), a set of indexes has been derived.

For each neighborhood of a punctual source light a set of light spectral indexes is computed as a weighted (by the light intensity over the whole light intensity in the neighborhood) average of the spectral indexes derived from AISA data. This set of indexes is used to derive the main type of the light source in the neighborhood of the punctual source light. Notice that each neighborhood may be mainly influenced by the principal light source: the maximum in the neighborhood. Despite of this, such neighborhood may be also influenced by other light sources as car lamps or showcase lights and light source type will be also influenced by the reflectivity features of the imaged surface. Figure 5 shows a detail of the resulting light source type map. The classification categories are the following: in yellow high pressure sodium lamps, in orange metal-halide lamps, in blue mercury vapor lamps, in green fluorescent lights, in violet LED lamps, in red halogen or incandescent lamps and in grey not classified lamps.
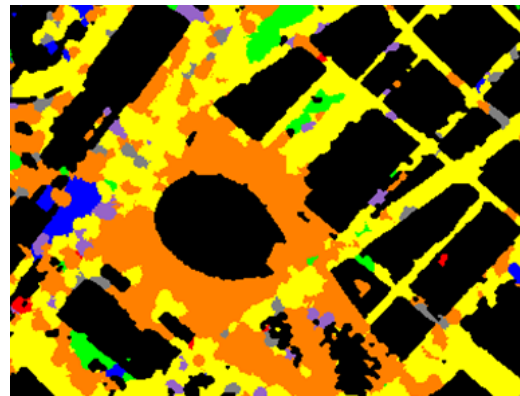
Figure 5. Light source type map derived from hyperspectral sensor.

5 CONCLUSIONS

The operational approach of the ICGC is providing high resolution luminance maps (up to 25 cm GSD) and light source typology maps (up to 1.5 m GSD). Such maps are generated from simultaneous hyperspectral and photogrammetric airborne acquisitions. As acquisitions are carried out in a single flight session, these maps provide a synoptic view of the public and private illumination of whole municipalities, urban and peri-urban areas.
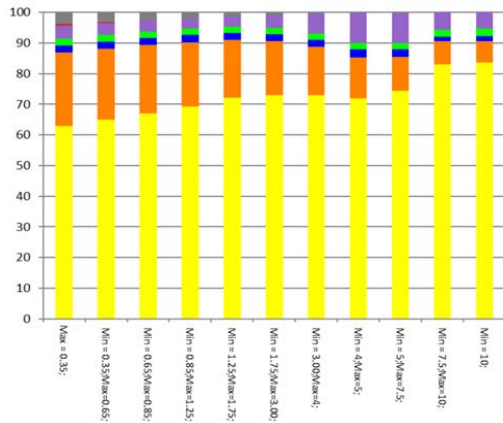
Figure 6. Distribution of type of light source versus light intensity in cd/m^2. Legend is the same that in figure 5.

These maps are thematic information of the nocturnal urban landscape and become a tool to: analyse and monitor both public and private illumination, check whether policies on light pollution are fulfilled in terms of intensity (mainly excess of light emitted towards the sky due to reflection or misdirection of the lamps) or typology of light sources, in particular the detection of unwanted type of lamps as mercury vapour lamps, cross usage of typology of light versus intensity or facilities (as in figure 6 where it can be seen that LED lamps has a larger deployment in the range of intensities between the 3 and 7.5 cd/m^2) and the ICGC approach offers a decision support tool to evaluate street lighting policies and actuations.

6 REFERENCES

Aubé, M., Franchomme-Fossé, L., Robert.Staehler, P., Houle, V., "Light Pollution Modelling and Detection in a Heterogeneous Environment," Proceedings of SPIE 5890. Atmospheric and Environmental Remote Sensing Data Processing and Utilization, (2005).

Barducci, A., Benvenuti, M., Bonora, L., Castagnoli, F., Guzzi, D., Marcoionni P., Pippi, I., "Hyperspectral remote sensing for light pollution monitoring," Annals of Geophysics vol. 49(1), 305-310, (2006).

CIE, "CIE Commission Internationale de l'Eclairage Proceedings", Cambridge University Press, (1931).

Dörstel, C., "DMC- Practical Experiences and Photogrammetric System Performance," Proceedings of the 49th PhoWo, 59-65, (2003).

Elvidge, C.D., Keith, D.M., Tuttle, B.T., Baugh, K.E., "Spectral Identification of Lighting Type and Character," Sensors 10,3961-3988, (2010).

Pipia, L., Alamús, R., Tardà, A., Pérez F., Palà, V., Corbera, J., "A methodology for luminance map retrieval using airborne hyperspectral and photogrammetric data", Proc. SPIE 9245, Earth Resources and Environmental Remote Sensing/GIS Applications V, 92450O (Nov 4, 2014).

Tardà A., Palà V., Arbiol, R, Pérez F., Viñas O., Pipia L., et al., "Detección de la iluminación exterior urbana nocturna con el sensor aerotransportado CASI-550," International Geomatic Week, Barcelona, Spain, (2011).

Aerial Research Platforms: ICTS-PAI

J.A. Gómez Sánchez, J. Ortiz Muñoz, A. Corrales Sierra, N. Seoane Vieira, G. Vega López,
B. Marqués Balaguer
Aerial Platforms for Research. INTA
gomezsj@inta.es

ABSTRACT- *INTA Aerial Platforms for Research is a large infrastructure which main component is a fleet of instrumented aircraft suited to collect airborne data. Its priority goal is to attend the demand of access coming from the technical and scientific community, that require a suitable and flexible aerial platform to carry out studies in fields so diverse as aeronautical science, Earth observation, atmospheric research or R & D of new airborne devices that need to be tested in actual flight conditions. The infrastructure so configured was acknowledged in November 2009 by the Spanish Ministry of Economy, Industry and Innovation (MINECO) as to National Large Scale Facility to support Science and Research (ICTS-PAI).*

1 INTRODUCTION

An aerial research platform is an aircraft modified for the installation and operation of scientific instrumentation, which is prepared to perform flight campaigns to collect data used in scientific experiments, and the testing of equipment and systems under real flight conditions.

INTA (National Institute for Aerospace Technology) has three manned platforms: two C212-200 aircraft, manufactured by CASA-EADS, and a motorglider Stemme S15, all modified and adapted as aerial platforms to provide service support for scientific activities. They provide support for the needs of the technical and scientific communities so as to undertake trials with aircraft in flight, atmospheric research, data collection from remote sensing/observation of the Earth and tests for the development and qualification of new scientific instrumentation, among others.

Since November 2009 INTA aircraft belong to the Spanish network of unique scientific and technical infrastructures (ICTS), coordinated by the Ministry of Economy, Industry and Competitiveness (MINECO). They are managed and operated by the Institute with the collaboration of the Spanish Air Force.

The complete system is offered to the scientific community nationally and internationally through agreements and public and private partnership programs without discarding commercial operations.

2 COMPONENTS OF THE ICTS-PAI

The ICTS-PAI infrastructure consists of facilities and equipment which, depending on their location can be grouped into:

- ✓ Air segment. Includes aircraft, the onboard scientific instrumentation: sensors, detectors, etc.; for monitoring, pre-processing and registration of all data and all of the auxiliary modules needed to perform the data acquisition campaigns: power supplies, racks, stands, mission communications systems , etc.

- ✓ Ground segment. Consists of a base located in the Rozas Centre for Airborne Research (CIAR) located in the aerodrome of Rozas, Lugo, that features all of the required aviation infrastructure so as to allow for the safe operating of the aircraft: operations control centre, taxiway, platforms, hangars, etc. In addition, we have planned to also install the facilities required to support the activities of the ICTS-PAI, such as laboratories, workshops, offices, meeting rooms, warehouses, additional halls, etc. The ground segment includes also the necessary fixed and mobile instrumentation to acquire complementary field data to those taken from the air: weather station, instrumentation for the calibration data and the maintenance of the sensors, modules for the analysis and validation of the data, etc.

The data obtained by the instrumentation of the PAI are often complex and unique in their format, structure, variable measure, technique of measurement, etc. INTA in association with the PAI staff provides the users of ICTS with the support necessary to exploit and interpret the data generated, and extract from them useful information.

The PAI also includes a facility for processing, analysis and archiving (PAF) of data from airborne sensors.

Figure 1. C212 "Aviocar".

Figure 2. Motorglider Stemme S15.

Figura 3. Probe PCAPS mounted under the left wing of the C212 s/n 30 airplane.

.

Figura 4. Control tower and auxiliary buildings in Research Center airborne Rozas - CIAR Castro de Rei, Lugo
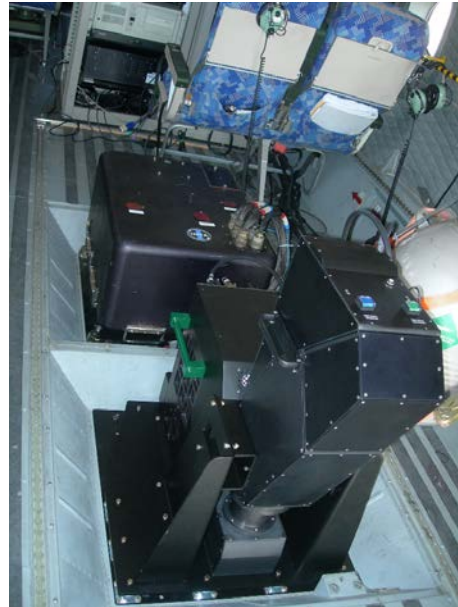
Figura 5. Detectors modules of the AHS (above) and CASI 1500i (bottom) hyperspectral imaging sensors mounted on the C212 n/s 270 cabin.

3 APLICATIONS OF ICTS-PAI

The primary fields of application in which the ICTS develops its activity and gives support to users who request access to it are:

- ✓ **Flight testing**. Undertaking flights to test the characteristics and performance of the C212 aircraft in flight was the original mission that motivated putting in operation PAI. The objective is to test the aircraft in multi-mission settings, with distinct flight configurations, under real world operational conditions, on occasion to the limit of the flight envelope to which it has been certified safe and thus learn about its behaviour in such circumstances.

- ✓ **Atmospheric research**. In this case, the objective is monitor the physics and chemistry of the atmosphere during flights, in which atmospheric data is taken on-site. The aircraft is configured as a airborne lab with the appropriate team and measurement instruments to collect the data in the environmental conditions that are required and will depend on the atmospheric environment being studied. In particular, our team has specialized in measuring the characteristics of atmospheric particles in suspension: size, composition, shape and

concentration. Another line of research that is increasingly active is that related to the study of the formation and accretion of ice on aeronautical surfaces, under real flight conditions.

- ✓ **Remote sensing in the optical spectrum**. An activity that has acquired some relevance in recent years is the support provided by the ICTS-PAI for campaigns of remote sensing sensors of imaging hyperspectral to monitor the Earth's surface, objects and the phenomena on it. In this case, there are sensors that collect passive imagery covering the entire optical spectrum and provide calibrated data with high spectral, radiometric and geometric detail.

- ✓ **SAR campaigns**. This activity aims to make the flights needed to qualify, the SAR (Synthetic Aperture Radar) sensors developed by the Institute's Area of radio frequency in real operating conditions. This support extends to undertaking "production" flights for SAR images of the Earth's surface and the objects located there.

- ✓ **Assistance in the installation and qualification in flight of new instrumentation**. A support activity for the R&D of instruments for data collection, whose purpose is to adapt the prototypes developed and already tested on land for flight operations mounted on aerial platforms. This includes support for installation, certification and qualification of new instrumentation, as and when appropriate.

4 HOW TO ACCESS ICTS-PAI

The capabilities of the ICTS-PAI are offered to the scientific and research community, both nationally and internationally, with the only limitation being the distance between the base of operations (CIAR, Castro de Rei, Lugo) and the proposed location of the area that is to be studied. Currently the PAI fleet consists of aircraft with a maximum speed of 200 knots (370 km/h) cruise and whose maximum autonomy is that of 5 hours, this being the factor that determines the 'reasonable' operating radius that for all practical purposes, covers the Central-European space.

The ICTS-PAI is part of the European consortium of aircraft instrumented for environmental research, EUFAR (European Facility for Airborne Research) www.eufar.net. EUFAR is supported by the European Commission through the successive R&D European framework programmes, which is made up of 24 operators from 11 countries and since the year 2000, through the transnational access instrument or TA funds the implementation of proposals that pass a selection process, covering the costs to access an aircraft and the instruments offered by its operators, who are also consortium members.

It is important to mention that the capabilities of the ICTS-PAI are among the most sought after by European users, especially among those of the Earth observation community, and that as a result, there have been numerous campaigns throughout the European space: GREASEMH, CALABRIA, T-Mapp-FP7, Edocros, Hymoweb, Biohype, HyperForest, CalValHyp, UrbSense, DehesHyRe are some of them.

Among the campaigns whose purpose was the study of the atmosphere and of the phenomena occurring within it, those of note include EURICE, TRUMPET, validate, EXTICE, VERDRILLT, MISPALIDAR, VOAS, TECOAGUA, CLIMARENO, etc; these have been financed with funds from the European R&D programmes in some cases, and in others, with funds allocated within the framework of national R&D programmes.

It is also relatively frequent for access to be financed by specialized public entities which select proposals and projects of the greatest interest among those presented by universities and research centres. As it is the case of BELSPO in Belgium that has funded the activities of successive editions of the STEREOs program and in 2005 and 2007 were entrusted to the ICTS-PAI.

The European Space Agency (ESA) has since 2004 been one of the primary users of the ICTS-PAI, an agency with which it frequently collaborates with in campaigns of remote sensing as support for future Earth observation missions from space: SPARC, CEFLES2, AgriSAR, SEN2FLEX, DESIREX, THERMOPOLIS, SEN3EXP, etc.

At the national level, the ICTS-PAI provides competitive access to the projects selected by the national R&D Plan, proposals that often involve the Institute, some of which mentioned previously.

Finally, mention that the ICTS-PAI is also available to companies requiring an aerial platform to complete studies and trials.

5 CONCLUSIONS

The ICTS-PAI should be seen and understood as a key infrastructure that is unique in its scope, whose purpose is to give support and boost air instrumentation research and development.

The primary objective of the Strategic Plan 2016-2020 is the increase of the number of users that get access to the ICTS-PAI, increase access in absolute terms while maintaining or improving the quality of the performed service.

Under this Plan, the obsolescence of the fleet of the ICTS has been identified as the main risk factor in maintaining the continuity of the service. FENYX "Future Aircraft for Research and Experimentation" a proposal selected by MINECO in March 2017 is to be co-financed and emerges as a response to that critical analysis.

The financing of access to ICTS-PAI is a key factor to consider to promote and "democratize" its use between the different communities within the scientific and research fields, with often limited and always scarce economic resources, to cover the high costs associated with the operation of complex manned aircraft.

Also of note is the situation created by the instrument of "transnational access" offered by EUFAR, which finances users access to the aerial research platforms from States that are part of the Consortium and which expressly excludes the co-national researchers of each operator, in our case not including Spanish applicants to the ITS-PAI. An agency similar of that of EUFAR but on national level allowing us avoid such asymmetry is expected.

The current European scene, dominated by the EUFAR2 program of FP7 (EUFAR continued) and that it will end January 31, 2018, according to the recommendations of the Commission, will give way to a new collaboration model based on the creation of the AISBL* " EUFAR" and the establishment of the figure of the "open access" that will regulate the exchange of resources and access to infrastructures, model which is currently in the phase of design and discussion among the participants in the Consortium, and that once agreed and approved is expected to attract new public financing of State authorities and the European Commission.

* AISBL, *Association Internationale Sans But Lucratif.*

6 BIBLIOGRAPHY

INTA, 2016. Strategic Plan 2016-2020. Unique Scientific & Technical Infrastructure - Aerial Platforms ICTS-PAI.

MINECO, 2015. Map of Unique Scientific and Technological Infrastructures (ICTS).

Brenguier, J. L. 2009. *Programa EUFAR. Una oportunidad para la teledetección aérea en Europa.*

Reusen, I. 2007. Towards an improved access to hyperspectral data across Europe (HYRESSA).

7 THANKS

Optimization of an Experimental Cloud Infrastructure for Earth Observation Services

J. Becedas, M. M. Núñez, D. González

Elecnor Deimos Satellite Systems, Puertollano, Spain

jonathan.becedas@elecnor-deimos.es, maria-del-mar.nunez@elecnor-deimos.es, david.gonzalez@elecnor-deimos.es

ABSTRACT- *Processing and distribution of big space data still implies the treatment of massive and large-sized data obtained from Earth Observation satellite recordings. Remote sensing industries implement on-site conventional infrastructures to acquire, store, process and distribute the geo-information generated. However, these solutions present several drawbacks: (i) the cost of acquiring recent Earth images is limiting, (ii) clients have no direct and fast access to needed data as information is processed and distributed spontaneously, and (iii) the service is not flexible, in other words, it does not cover significant changes in the demand of services and the access to the information presents large latencies. Deimos' research focuses on the development of future internet technologies in order to improve Earth Observation (EO) services and reduce the associated costs. In particular, a cloud infrastructure based on OpenNebula is used, and the Deimos-2 PDGS is optimised by using the ENTICE open source middleware. Experimental results of the implemented system are presented.*

1 INTRODUCTION

Until now, Earth Observation (EO) satellite systems have commonly been operated by public organizations. However, in recent years the Earth Observation from space paradigm is changing. The market is being boosted, mainly due to the increased performance of the commercial satellites, the agreements signed between private and public customers and the appearance of the New Space paradigm (Denis, 2017). Besides, new countries (not traditionally involved with the Earth Observation industry) are investing in EO, while those countries with EO programmes are increasing their budgets in this field (Keith, 2015). These facts together with the fast evolution of the information and communication technologies during the last decade, and the increase of revenues in the market of the generated data (Keith, 2016) are contributing to the evolution of the space sector because there is a better performance of the systems at a lower cost. In addition, the launch of satellite constellations is a spreading trend to reduce the revisit time, which is one of the main limitations to develop new applications.

Nevertheless, the infrastructures commonly used to manage EO data are still based on traditional IT technology, i.e. systems that were designed to be monolithic, completely controllable and localized in a single and specific location. This requirement of full controllability of the traditional Earth Observation Payload Data Ground Segments (PDGS) made the systems present the following limitations:

a) Traditional infrastructures are not flexible neither easily scalable to operate.
b) There exists the risk of oversizing/undersizing the infrastructure to offer services when highly variable demand exists.
c) They make the cost of acquiring recent images of the Earth very high.
d) The customers cannot access directly neither fast to the information they need because this has to be processed and ad-hoc distributed.

The use of cloud computing technology can eliminate the previous drawbacks because it is elastic, scalable, it works on demand through virtualization of resources (Armbrust, 2010), offers virtually unlimited storage and computation capability, it is worldwide connected and it is based on a pay per use model (Botta, 2016).

Nevertheless, the current cloud computing technology still presents some limitations (Ramos, 2016):
a) The virtual machine images (VMIs) are not optimized, being highly over-sized, impacting in the costs of using the infrastructure and in the dynamic resources provisioning.
b) The deployment of Virtual Machines (VM) in cloud is not in real time. The deployment normally takes between 10 and 20 minutes, which directly affects to the flexibility and dynamic scalability of the system.
c) The costs of using cloud computing are still high.
d) Cloud infrastructure vendor lock-in limits the democratization of services.

We propose the cloud-based implementation of the Deimos-2 PDGS to optimize the system and increase the efficiency by using the ENTICE middleware. The system is named as Earth Observation Data (EOD) pilot (Prodan, 2016). The EOD pilot is optimized and results of parallel processing of satellite imagery are presented.

2 EARTH OBSERVATION DATA PROCESSING AND DISTRIBUTION PILOT

2.1 ENTICE environment

The EOD pilot makes use of the ENTICE middleware, which facilitates auto-scaling and flexibility to the ingestion of satellite imagery, its processing and distribution to end users with variable demands (Kecskemeti, 2016). The ENTICE environment consists of a ubiquitous repository-based technology which provides optimised Virtual Machine (VM) image creation, assembly, migration and storage in federated clouds. The expected ENTICE features are the following:

a) Reduction of up 80% storage.
b) 95% elastic Quality of Service.
c) VMIs creation 25% faster.
d) Reduction on the costs of deployment.
e) VMIs optimization up to 60%.
f) VMIs delivery 30% faster.
g) Scalability and elasticity.
h) Elimination of cloud infrastructure vendor lock-in.

In the EOD pilot, ENTICE is used as a middleware between the federated cloud infrastructure and the adapted gs4EO application software.

2.2 EOD pilot description

The Earth Observation Data Processing and Distribution Pilot (EOD) consists of the implementation of the Elecnor Deimos' gs4EO software, which is a software developed for the processing, storage and distribution of satellite imagery. It was implemented for the Deimos-2 satellite, and here we adapted it and implemented in cloud. Its architecture is composed by the following components:

a) monitor4EO: it is a ground station monitor which ingests the available raw data from the ground stations to the Cloud system.
b) process4EOserver: it generates the Job Orders that contain all the necessary information that the processors need, and controls the processing chain by communicating with the product processors.
c) process4EOnode: it includes one product processor for each level of processing: L0 (raw data decoded), L0R (transformation of

L0 into image), L1A (geolocated and radiometric calibrated image), L1BR (resampled image and more precise geolocation) and L1CR (orthorectification).
d) archive4EO: stores and catalogues the processed images in a Catalogue Service for the Web (CSW) interface.
e) user4EO: it is a web service in which the end users can access to the products.
f) Shared Storage: it is a storage in which all the inputs and outputs of all the modules of the architecture are stored.
g)

Figure 1 depicts the EOD pilot architecture with all the elements and their interrelations by means of the work and data flows.
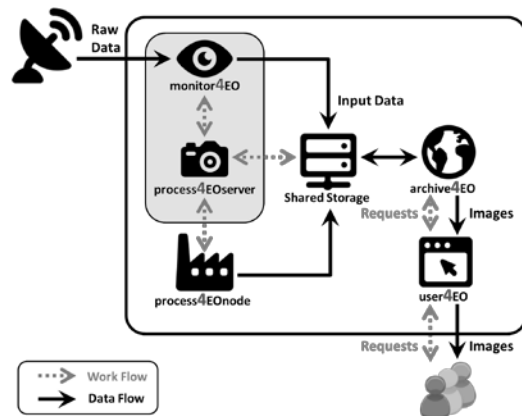
Figure 1. EOD pilot architecture.

3 EXPERIMENT SETUP

3.1 Testing infrastructure

The federated cloud infrastructure implemented for testing purposes was based on OpenNebula. The Kernel-based Virtual Machine (KVM) was used as hypervisor. The virtual machines were created with Packer, and Ansible was used to automate the deployment of the virtual machines generated. Figure 2 shows a scheme of the automatic generation of the virtual machines. The process was the following:

1. The Python script received the configuration file and launched the Packer command after configuring some parameters in the Kickstart file in order to build the VMIs required to deploy the EOD pilot.
2. Packer made use of the template and built all the VMIs by using KVM. The Packer template had the provisioners which defined the recipes in Ansible for configuring the machines and installing the applications.
3. Once the image was built, Packer launched all the provisioners. Thus, Ansible carried out

several steps: it configured all the repositories, installed all the dependencies and software packages of the EOD modules, configured the EOD software, and installed a context package to deploy the VMI in OpenNebula.

The hardware of the infrastructure used in the experiment was constituted by different nodes, distributed in three different countries and managed in a federated manner: DMU infrastructure in United Kingdom, DMS infrastructure in Spain and DME infrastructure in Portugal. The DMU infrastructure was the master of the infrastructure. It had the ENTICE middleware installed, an object store with interface to Amazon S3, and the cloudware of OpenNebula. DMS and DME infrastructures were slaves of the DMU infrastructure. Both of them had an object store with interface to Amazon S3 and the cloudware in OpenNebula. Table 1 shows the features of the hardware integrating the federated cloud for testing. The operative system installed in the different resources was CentOS 7.2.1511.

In addition, two different tools were used to record the experimental data and to monitor the cloud resources. On the one hand, the open source application Apache Jmeter[TM] was used to measure the behaviour of the EOD system functionality in the runtime. On the other hand, Nagios[®] was used to monitor the infrastructure.

Table 1. Hardware Infrastructure.

Place	Name	CPU	RAM (GB)	HD (GB)
DMU	Node-1	Intel Core i7 – 2600 3.4 GHz	8	160
	Node-2	Intel Core i7 – 2600 3.4 GHz	16	250
	Open-nebula-fe	Intel Core 2 6300 1.86 GHz	4	250
DMS	Node-2	Intel 8 Core 2.37 GHz	16	2048
	Node1	Intel 2 Core 3 GHz	6	230
DME	Node1	AMD Athlon 64 X2 Dual Core 3800+	4	256

3.2 Experiment description

The aim of this experiment is to demonstrate the feasibility of implementing the EOD system in cloud and evaluate the benefits obtained. For that purpose, the VM containing the processing chain (process4EO) of the EOD pilot was optimized and experiments were carried out with both optimized and not optimized VMs to facilitate comparison. The scenario was that of a common image acquisition with the Deimos-2 satellite. In the emulation, the recording in raw data was ingested into the EOD system and it was automatically processed in the different levels to obtain the imagery products: L0, L0R, L1A, L1BR and L1CR. To validate the scalability of the system, parallel processing of ten images was done. The testing image used in the processing had the following features: 3MB size, four multispectral bands (R, G, B and NIR), one panchromatic band, and the recorded area was a rectangle of 8.86 x 16.59 km^2.

To establish a comparison in the performance of the system the following evaluation metrics were defined: VMI size, VMI creation time, VMI delivery time and VMI deployment time. These were measured in the EOD pilot with optimised and not optimised VMs. Notice that all previous metrics are not runtime related. However, in order to demonstrate that the functionality of the system remained intact after the optimisation process, the processing time and the size of the imagery produces were measured.

4 EXPERIMENT RESULTS

The virtual machine image was created, delivered and deployed in the cloud infrastructure. This VMI had a size of 2 GB. Then, the virtual machine image was optimized and created, delivered and deployed as an optimized application. In this case, the optimized VMI
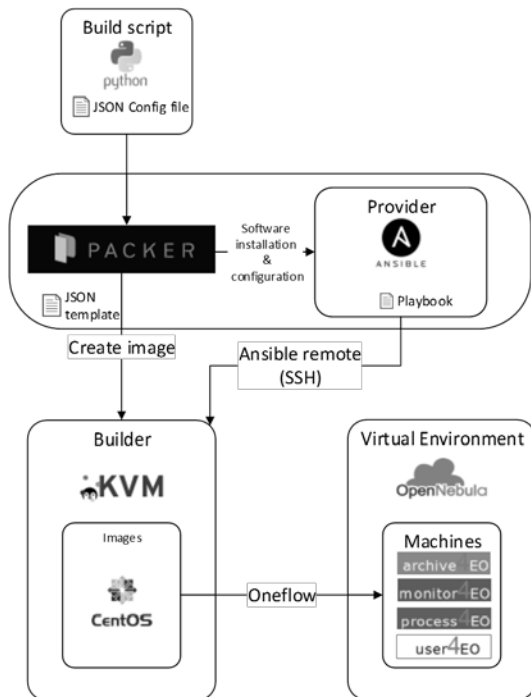
Figure 2. Diagram of the automatic genereation of the EOD virtual machines.

had a size of 1.4 GB, i.e 30% less. The results obtained in the creation, delivery and deployment of the not optimized virtual machine are presented in Figure 3. On the one hand, The VMI creation of the not optimized VM was done in 19.70 minutes, the VMI delivery in 20.42 minutes and the VMI deployment in 6.78 minutes. The whole process was done in 46.90 minutes. On the other hand, in the case of the optimized VM, the time to create the VMI was 12.35 minutes, the delivery time was 13.37 minutes and the deployment time was 3.12 minutes, the sum of them being 28.84 minutes (see Figure 4). Then, the reduction in the creation, delivery and deployment times of the optimized VM were 37.31%, 34.52% and 53.98% respectively, the difference in the total time required from the creation time to the deployment time being 38.51%.

Next, for both optimized and not optimized EOD pilots ten images in raw data were ingested in the shared storage. Then ten processing chains started running in parallel. They were monitored and their statistics were measured. The processing time required to obtain the imagery products, i.e the processing time per processing stage obtained are depicted in Table 2.
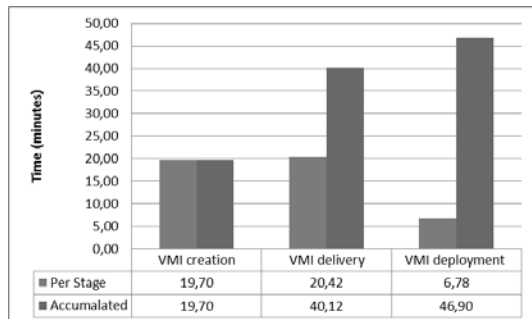
Figure 3. VMI creation, delivery and deployment time of the not optimized VM.
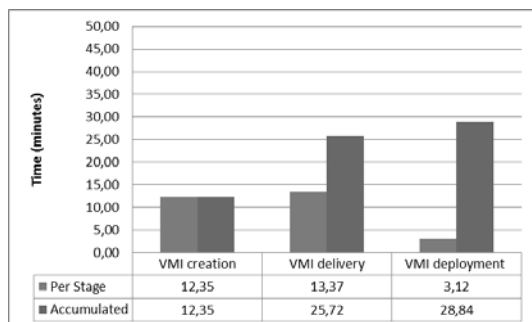
Figure 4. VMI creation, delivery and deployment time of the optimized VM.

The processing time of the imagery products with the not optimized EOD pilot was of 50.20 minutes mean with 7.69 minutes standard deviation, while the processing time with the optimized EOD pilot was a of 49.19 minutes mean with 7.94 minutes standard deviation. Although slightly different, we can affirm that the processing time of the EOD pilot was similar in both cases. The processing time per processing stage of the not optimized system is shown in Figure 5 and that of the optimized system in Figure 6.

Table 2. Processing time per stage.

Stage	Not optimized		Optimized	
	Mean (min)	STD (min)	Mean (min)	STD (min)
L0	6.41	0.83	5.69	0.72
L0R	7.74	0.96	7.70	1.00
L1A	3.87	0.30	3.68	0.82
L1BR	22.32	4.57	22.42	3.98
L1CR	9.86	1.03	9.69	1.41
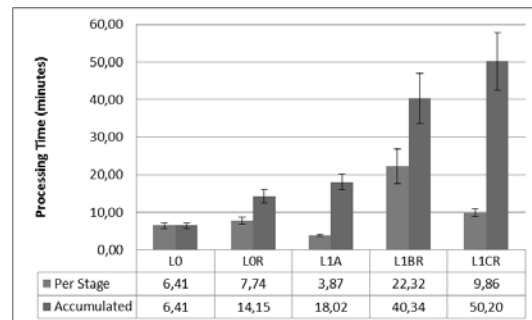
Figure 5. Processing time of the not optimized pilot.
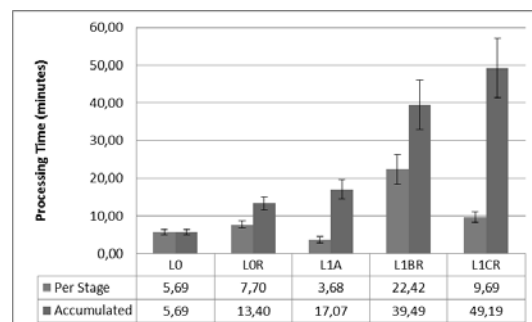
Figure 6. Processing time of the optimized pilot.

Notice that the parallel processing of ten images was done. In a monolithic system without scalability the processing of ten images could have taken ten times more, more than 8 hours of continuous processing. This demonstrates the benefits in time to user terms of distributing and making scalable an application.

Finally, the size of the different imagery products obtained in all the tests was the following:

- L0: 764MB
- L0R: 789MB
- L1BR: 749MB
- L1CR: 1140MB

5 CONCLUSIONS

In this work a PDGS was implemented in a federated cloud with the support of the ENTICE middleware. The virtual machine containing the processing chain of the PDGS was optimized and results were obtained with the not optimized and the optimized system. The optimization of the virtual machine provided a virtual machine image with 30% less size, i.e. the VMI passed from 2GB to 1.4GB. Furthermore the creation, delivery and deployment time of the optimized VMI was 38.51% less, with respect to the not optimized VMI. These results indicate that the optimization of the system can reduce the costs of storage, the size of the repository and the time to deploy the application in the cloud.

Furthermore, it was demonstrated that the optimization of the system did not affect its functionality, providing a correct execution of the system: the different imagery products were correctly obtained and in a similar time.

In addition, the scalability of the system was tested by processing in parallel ten images at the same time. This demonstrates (independently from the optimization of the system) that making the application distributed in cloud can dramatically reduce the processing of several recordings at the same time. In a monolithic system, the system would wait until the system has finished the processing of one image to start with the processing of a new one. The parallelization thus presents a clear advantage over the traditional application.

6 ACKNOWLEDGEMENTS

7 REFERENCES

Armbrust M, Fox A, Griffith R, Joseph AD, Katz R, Konwinski A, Lee G, Patterson D, Rabkin A., Stoica I, Zaharia M, 2010, A View of Cloud Computing. *Communications of the ACM*, 53 (4), pp. 50-58.

Denis, G., Claverie, A., Pasco, X., Darnis, J. P., de Maupeou, B., Lafaye, M., & Morel, E., 2017, Towards disruptions in Earth observation? New Earth Observation systems and markets evolution: Possible scenarios and impacts. *Acta Astronautica*, 137, pp. 415-433.

Keith A., 2015, Emerging Programs, Markets Drives Earth Observation Growth. *Earth Imaging Journal*. Online available: http://eijournal.com/print/articles/emerging-programs-markets-drive-earth-observation-growth.

Keith A, Larrea Brito N and Manjunath S., 2016, Satellite-Based Earth Observation: Market Prospects to 2025 (9th edition. Euroconsult).

Botta, A., De Donato, W., Persico, V., & Pescapé, A., 2016. Integration of cloud computing and internet of things: a survey. *Future Generation Computer Systems*, 56, pp. 684-700.

Kecskemeti, G., Marosi, A. C., & Kertesz, A., 2016, The ENTICE approach to decompose monolithic services into microservices. IEEE International Conference on High Performance Computing & Simulation (HPCS), pp. 591-596.

Prodan R, Fahringer T, Kmovski D, Kecskemeti G, Csaba A, Stankovski V, Becedas J, Ramos JJ, Sheridan C, Whigham D, Rodrigo C., Use Cases towards a Decentralized Repository for Transparent and Efficient Virtual Machine Operations. IEEE 25th Euromicro International Conference on Parallel, Distributed and Network-based Processing (PDP'2017); 6-8 March 2017, St. Petersburg, Russia. pp. 478-485.

Ramos J.J. and Becedas J., Deimos' gs4EO over ENTICE: A cost-effective cloud-based solution to deploy and operate flexible big EO data systems with optimized performance. Proceedings of the 2016 conference on Big Data from Space (BiDS'16), (Santa Cruz de Tenerife, Spain: European Space Agency), pp. 107-110.

Multi-year monitoring of rice crop using Sentinel-1 time series

Hoa Phan*[1], Thuy Le Toan[1], Alexandre Bouvet[1], Lam Dao Nguyen[2], Mehrez Zribi[1]

[1] *Centre d'Etudes Spatiales de la Biosphère (CESBIO), Toulouse, France*

[2] *STAC, VNSC, VAST, Ho Chi Minh City, Vietnam*

*thi-hoa.phan@cesbio.cnes.fr

ABSTRACT - *Rice is the staple food for more than half of humanity - over 90% of the world's rice crop produced and consumed in Asia. In the context of price instability and threatened food security, accurate information are needed on the spatial distribution of rice fields, water use, risk occurrence, annual production projections. Long term inter-annual monitoring is also required in order to study impacts of environmental issues and of changes in cultural practices on the rice grown area and the production. With the launch of Sentinel-1 (S1) in April 2014, C-band SAR data are available worldwide, which present an unprecedented opportunity to monitor the rice growth at high spatial and temporal resolution (10 m, every 12 or 6 days). This is particularly important for rice grown regions under frequent cloud cover. In this paper, the methods are developed for rice monitoring in the Mekong River Delta (MRD) in Vietnam, one of the most important rice growing region. The methods are based on the temporal change of the backscatter intensity at VV, VH and VH/VV ratio of S1 time series. The results on rice area and rice crop density (every 6 days at present) have shown good agreement with in-situ data. The methods have been discussed regarding the generality of the methods to be applied for a diversity of rice growing practices.*

1 INTRODUCTION

Among EO data, SAR data have been proved efficient for rice monitoring since late 80's (Le Toan, 1989) with all-weather capacity and also are well adapted to distinguish rice from the other land cover types because of the specific response of the radar backscatter from the rice fields. Rice area mapping, rice production estimation (Mosleh, 2015) and retrieval of rice parameters (Inoue, 2014) were well demonstrated, but applications have been hampered by lack of systematic and cost effective data. The Sentinel-1A satellite launched in April 2014 presents an unprecedented opportunity for rice monitoring applications over large areas. Over the Mekong River Delta, (MRD) in Vietnam, S1 IW with dual-polarization data are currently acquired every 6 days over a 300 km x 300 km. In this study, the time series data are analysed and interpreted using knowledge of the SAR scattering mechanisms. The results lead to a development of mapping methods for rice monitoring. The results obtained in 2015, 2016 and 2017 are used to assess the inter-annual changes in rice grown areas in the region, under the impact of El Niño in 2016.

2 MATERIALS

2.1 Study site

The study site is the MRD, a region constituted by 13 provinces in the southern tip of Vietnam, covering around 40000 km², 275 km from North to South, 260 km from West to East, where the Mekong River empties into the sea through a network of nine main distributaries. The topography is very flat, with most of the land below 5m. The MRD is the major rice- area in Vietnam producing more than half of national production. Rice farmers in the region have relatively small farms that are of 1 to 2 hectares on average and generally cultivate three major cropping seasons during a year: winter-spring or early season; summer-autumn or midseason; and autumn-winter or a longer rainy season crop. It can be noted that the crop calendar, rice varieties and water management are very diverse, changing from one region to another, and from one field to the next.

2.2 SAR Data

The data used in this study are Sentinel 1 (S1), images at C-band (5.405 GHz) operating in Interferometric WideSwath Mode at VV+VH polarizations, high resolution (10 m), large coverage (up to 300 km), having short revisit time (every 12 days for S1-A and every 6 days with S1-A and B) and rapid and free of charge data delivery. A processing chain has been developed at CESBIO for automatically collecting and preprocessing a stack of time series S1 data. In this study, time series of 108 S1 scenes have been preprocessed and analyzed.

2.3 Ground Data

Ground data are necessary to the understanding of the radar backscatter for algorithm development, and also for result validation. For algorithm development, 60 rice fields located in the An Giang province were surveyed during each rice season in 2015 and 2016.

General parameters include rice varieties, date of sowing, planting methods (direct sowing, line sowing), date of harvesting, and final yield. Moreover, data collected randomly for rice/non-rice validation (100 independent samples of rice fields and 30 samples of other LULC) in the major rice regions across the Mekong delta in 2016 and 2017. For validation of rice grown area per season, statistics in rice planted areas from the 13 provinces in the MRD in the Summer-Autumn rice season 2016 have been used.

3 METHODS

3.1 Analysis of the SAR data

In order to derive the temporal variation of the backscattering coefficient of rice fields, the S1 VV and VH polarization have been analyzed over 60 sampled fields, in the An Giang province, Vietnam. The backscatter values have been derived from series of S1 (A + B) including 108 acquisitions from 06 October 2014 to 08 September 2017.
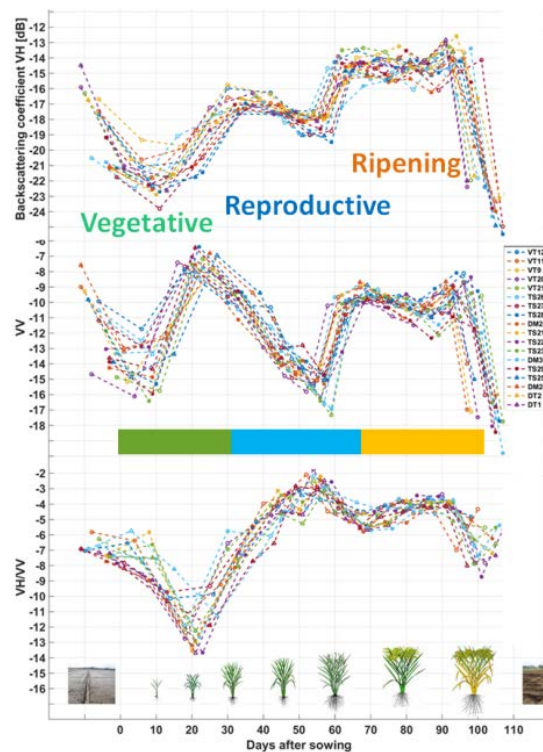
Figure 1. Variation of VH, VV backscattering coefficient, and polarization ratio VH/VV of the 18 sampled fields extracted from S1 images of 15 dates, versus the sowing date of each field.

It is noted that the planting calendar differs among the 60 rice fields under study, depending on the varieties, planting practices and farmer schedule. As a result, at a given date, rice fields are displayed on S1 images with a large range of backscatter values. To understand the polarisation and temporal behaviour of rice field backscatter, the sampled fields following the same calendar were selected for analysis. Fig. 1 shows the VH, VV and VH/VV backscatter analysed as a function of plant age (days after sowing) of 18 rice sampled fields in the Autumn-Winter 2016 rice season in An Giang province.

The temporal variation differs between VH and VV between 10 days after sowing and until the end of the reproductive stage. The rice is sown on wet soil and the fields are flooded at 10 days, when the backscatter values are the lowest during this first period. Before the sowing, the ploughed soil has been smoothed, this explains the early decrease of the backscatter. After 10 days, VV backscatter increases during 10 days, both due to the double bounce scattering and the volume scattering. At 20 days, when the plants are developed, the attenuation increases in double bounce scattering, causing a decrease in the backscatter. Towards the end of the reproductive stage, around 60 days, the rice grain increases in biomass, contributing to an increase of the volume scattering until maturation stage. After harvest, the backscatter decreases to values corresponding to smooth bare soil. After 10 days, VH backscatter increases until 40 days, then decreases slightly until 60 days, toward the end of reproductive phase.

The most interesting feature is the ratio between VH and VV, which shows an increase from 20 to 60 days, then decrease to 70 days. The VH/VV ratio (or difference in dB) in Fig. 1 shows that two periods can be distinguished during each rice season: on the first period (up to 50-60 days) where the ratio increases with plant age (from about -12 dB to -4 dB), and the second period where the ratio slightly increases or keeps a stable evolution during the ripening stage then decreases until harvest. This large increase in VH/VV can be interpreted as caused by the differential contribution of the double bounce scattering, and the differential attenuation in VH and VV. As a consequence, the ground contribution is minimised in the ratio, and it is expected that the backscatter ratio has higher correlation with the plants parameters such as biomass or LAI, as reported by (Bernardis, 2016, Veloso, 2017). Fig. 2 shows the backscatter of rice fields compared to that of the main other land use classes present in the Mekong Delta, here, forest, water, and urban areas, which have much more temporal stability, and which have very different VH backscatter levels. These observations lead to the use of the VH and VH/VV temporal change as a classifier of rice fields.
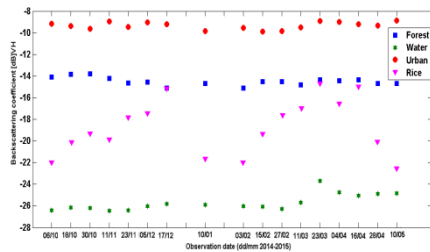
Figure 2. Variation of VH backscatter of forest, river, urban and rice extracted from S1 images versus observation date in the Mekong Delta.

Since the beginning of the acquisitions of Sentinel-1 data over the Mekong Delta around October 2014, time-series covering almost 9 growing seasons have been acquired. Fig. 3 shows the VH, VV and VH/VV backscatter profiles of 60 rice fields situated in the An Giang province. Three rice seasons per year are clearly shown by the backscattering coefficient trend in the Fig. 3.
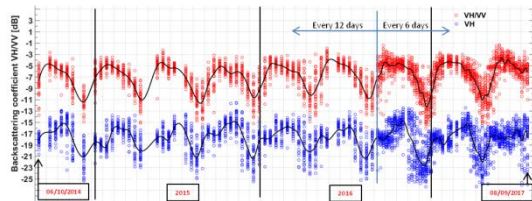
Figure 3. Temporal variation of S1 VH (blue) and VH/VV (red) of the 18 experimental fields in the province of An Giang. The data are from 6/10/2014 to 08/09/2017, with 12 day repeat frequency with S1A until October 2016, followed by 6 day repeat frequency of both S1A and S1B.

Fig. 3 shows similar temporal behaviour of VH/VV backscatter across rice seasons, with maximum values of about -3 dB and minimum of about -17 dB, making the largest dynamic range in backscatter (maximum – minimum of 14 dB) as compared to other crops or LULC types. These analyses reveal that the VH and VH/VV maximum temporal change are robust classifier of rice fields, and they could be used for phenological stage estimation.

Effect of incident angle

The incidence angle (in degrees) of the IWS data used for rice mapping corresponding to the 3 different sub-swaths. As the range of incidence angle is quite large (roughly 31° to 46°), it is necessary to assess the variability of the rice backscatter profiles across the incidence range. The analysis shows that the maximum temporal increase of VV rises with the incidence, from about 4.5 - 5.5 dB in near range to about 8.5 - 11.5 dB in far range, due to the difference in both the backscatter of smooth surface at the start of the season, and that of the multiple scattering at the

peak season. Similar analysis results are obtained with VH, where 3 - 4 dB was found at near range and 8 – 9 dB at far range. In all cases however, the maximum temporal increase is high (above 4 dB) compared to other land use land cover types. The maximum temporal increase of the other targets is found to be around 1 – 2 dB. A threshold of 4 dB could be used to map rice at different incidence angles. However, confusion with other targets is expected to be more important at near range. The methodology to calculate the optimal threshold is described in (Bouvet, 2010). In this work in the Mekong Delta, the threshold was determined for each of the beams of S1 images. For this purpose, rice fields have been located within each incidence range and their temporal change is analysed to define the relevant threshold. These thresholds can be used for rice mapping in the Mekong Delta using S1 images acquired every 12 days. To extend the method to other regions, there is a need to assess experimentally these thresholds, which depend on the backscatter temporal change of other land use land cover types, and also on the time interval between acquisitions (6 days, 12 days to 24 days).

3.2 Rice monitoring methods

The methods for rice mapping and monitoring is backscatter temporal change using maximum increase, which is shown in the previous section that the VH backscattering coefficients increase 8-14 dB during the rice growth cycle.

The Fig. 4 has shown the optimized rice mapping algorithms, which follows (Bouvet, 2011). A pre-processing is needed as a first step in order to reduce the speckle noise by calibration, registered, terrain correction, multi-temporal filter by using the automatically processing chain. To avoid confusion of the rice map, other land cover maps are created: water map, tree map and urban map have been created. The analysis shows the difference temporal change of each cover types. The tree map based on the low temporal change of backscatter (1-2 dB). The backscatter of water shows lower than -24 dB as seen in Fig. 2.
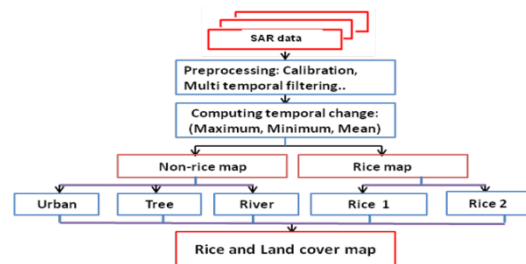
Figure 4. Rice mapping methodology

The retained rice mapping algorithm is composed of the three following rules:

1. If VH_max_inc > (Threshold) dB then rice
2. Else if VH_min > -18 dB then trees/built-up areas
3. Else if VH_mean < -22 dB then water.

The first rules describe the typical backscatter increase of rice fields in each rice season, from the flooding stage to the mature stage, with the optimal threshold for each S1 incidence angle range mentioned in 3.1. Only VH is used here, because of its robustness to discriminate rice from the other major classes (trees, built-up areas, water) in the region. An additional test using time series of VH, VV and VH/VV of pixels (or polygons) is performed, to assess the consistency of the rice backscatter temporal profiles. Until now, this test is performed manually. The second rule accounts for the fact that built-up areas and trees have a consistently high backscatter at cross-polarization compared to the other land use types in this area. The third rule is based on the fact that the backscatter of water bodies, though slightly variable, is consistently low.

When applying the threshold algorithms to Sentinel-1 images, we need to consider the various imperfections that may affect the rice map accuracy and must take them into account while evaluating the performance of such algorithms; therefore the thresholds are defined within each incidence range, their temporal change and the time interval between acquisitions (6 days vs 12 days). Probability of error (PE) in classification methods between rice and non-rice classes used to assess the accuracy (Bouvet, 2010).

4 RESULTS AND DISCUSSIONS

The analysis results in the previous section have shown that the method using the backscatter temporal change is a good classifier for rice mapping during the period of rice cycle. The method makes use of temporal change of the backscatter intensity at VH and provides mapping results every 6 days at present. Nine maps of nine rice seasons since October 2014 to present have been derived. They can be used to observe the temporal evolution of rice cultivation in the Mekong River Delta in Vietnam. Fig. 5 shows the comparison of rice mapping results in 2015, 2016 and 2017 winter-spring rice season in the MRD. The rice areas in Winter-Spring season in 2016 decreases of 283000 ha or 16.8%; i.e. 1.39M ha vs 1.67M ha as compared to Winter-Spring season in 2015 and 1.69M ha in Winter-Spring season in 2017. The decrease of rice areas in Winter-Spring in 2016 is interpreted as due to El Niño effect. This is attributed to by shortage of water and saline water intrusion (CCAFS-SEA, 2016).

The rice/non-rice map has been validated using 413 check points including 299 rice fields during the campaign, 23 fields before or after the rice season and

91 check points of other crops (pepper, sweet potatoes, corn, etc.), during the 3-8 July 2016 campaign in 9 provinces in the Mekong Delta. The comparison has shown good agreement (407/413 check points), that is 98,5% of good rice detection.

For the rice grown area estimates, the rice map in the Summer-Autumn rice season based on S1 data from April to August 2016 is used to calculate the number of rice pixels, and the area of rice planted area in each of the 13 provinces. Fig. 6 shows the comparison between the estimated area and the Province Agency statistics of rice planted areas for the Summer-Autumn 2016 rice season.
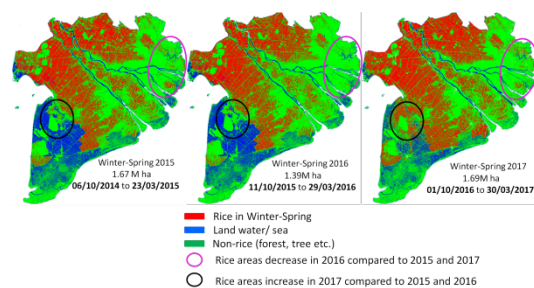
Figure 5. Comparison of rice mapping results in 2015, 2016 and 2017 winter-spring rice season in the Mekong River Delta, Vietnam.
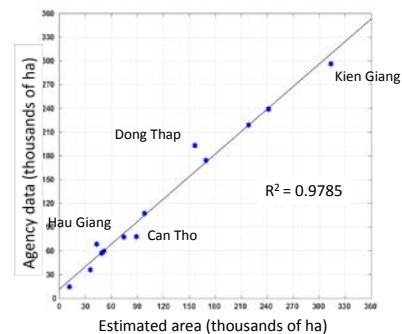
Figure 6. Comparison in rice planted areas estimated from the Sensinel-1 rice map and the Province Agency statistics for the Summer-Autumn 2016 rice season.

The result provides good agreement in the overall comparison (95,6% for the 13 provinces in the Mekong Delta). Two important under estimated areas were found in Dong Thap and Hau Giang, that could be interpreted as due to the early start of season in 2016 (in January and February instead of March-April, to avoid the impact of El Niño), whereas the test was done using S1 data starting in April 2016. The start of the season is important (as well as the peak period of the season) because the method is based on the backscatter maximum variation (maximum –

minimum for peak and start of the season). For the other 11 provinces, the error due to the crop calendar is reduced. The estimated areas using S1 product for these 11 provinces (with Dong Thap and Hau Giang excluded) account for 99.3% of the Agency data.

The estimates could be improved when the crop calendar is automatically determined at province level by the time series of data, e.g. the temporal curves of VH/VV. Also to be tested is the use of medium resolution optical data such as Sentinel-3, to determine the start of the season. To apply the method to other regions, the knowledge of the duration of the rice growing season and the phenological development of rice plants are required.

5 Conclusion

This study evaluates the use of earth observation data for a large-scale near-real-time monitoring system of rice crops in the Mekong Delta, Vietnam and provides results for rice area, rice cropping density and the assessment the inter-annual changes in rice grown areas in the region. The resulting information on rice crop extent is essential for planning, monitoring and food security applications. Results from this study have demonstrated that Sentinel-1 data can provide useful information for mapping rice crops at near real time and high accuracy. Especially the very short revisit time (6 days at present), high resolution (10m) and large coverage demonstrate the advantages of Sentinel-1 data for operational mapping of rice fields at region and national level.

Finally, further works need to be carried out to bring the methodology towards operational rice monitoring: (1) experiments and analysis across sites in different regions and countries, (2) refinement of methods for the retrieval of rice parameters (biomass, sowing date, phenological stages, inundation status), and (3) integration of EO products in crop production models.

Remote sensing of crops is of prime interest for social-economic and global environmental aspects. The current methods and techniques may be applied to national scale to assess their capabilities in monitoring rice growth and production under different effects of diverse environmental and field management conditions.

REFERENCES

A. Bouvet and T. Le Toan, 2011, Use of ENVISAT/ASAR wide-swath data for timely rice fields mapping in the Mekong river delta, Remote Sensing of Environment, vol. 115, pp. 1090-1101.

A. Bouvet, A., Le Toan, T., Floury, N., & Macklin, T. 2010, "An end-to-end error model for classification methods based on temporal change or polarization ratio of SAR intensities". IEEE Transactions on Geoscience and Remote Sensing, 48(9), 3521-3538.

De Bernardis, Caleb, et al. 2016, "Contribution to real-time estimation of crop phenological states in a dynamical framework based on NDVI time series: Data fusion with SAR and temperature." IEEE Journal of Selected Topics in Applied Earth Observations and Remote Sensing 9.8: 3512-3523.

F. Ribbes and T. Le Toan, "Rice field mapping and monitoring with RADARSAT data," International Journal of Remote Sensing, vol. 20, pp. 745-765, 1999.

N. Torbick, D. Chowdhury, W. Salas, and J. Qi, 2017, "Monitoring Rice Agriculture across Myanmar Using Time Series Sentinel-1 Assisted by Landsat-8 and PALSAR-2," Remote Sens, vol.9, no. 2, p. 119, 2017.

M. K. Mosleh, Q. K. Hassan, and E. H. Chowdhury, "Application of remote sensors in mapping rice area and forecasting its production: a review," Sensors (Basel)., vol. 15, no. 1, pp. 769–791, 2015.

S. Quegan et J. J. Yu, 2001, " Filtering of multichannel SAR images", IEEE Trans. Geosci. Remote Sens., vol. 39, no 11, p. 2373‑2379.

T. Le Toan, and N. Lam Dao, 2009, Monitoring of the Rice Cropping System in the Mekong Delta Using ENVISAT/ASAR Dual Polarisation Data, IEEE Transactions on Geoscience and Remote Sensing, vol. 47, pp. 517-526.

T. Le Toan, F. Ribbes, L.-F. Wang, N. Floury, K.-H. Ding, J. A. Kong, M. Fujita, and T. Kurosu, "Rice crop mapping and monitoring using ERS-1 data based on experiment and modelling results," IEEE Transactions on Geoscience and Remote Sensing, vol. 35, pp. 41-56, January 1997.

T. Le Toan, H. Laur, E. Mougin, and A. Lopes, "Multitemporal and dual-polarization observations of agricultural vegetation covers by X-band SAR images," IEEE Transactions on Geoscience and Remote Sensing, vol. 27, pp. 709-718, November 1989.

Veloso, A., Mermoz, S., Bouvet, A., Le Toan, T., Planells, M., Dejoux, J. F., & Ceschia, E. (2017). Understanding the temporal behavior of crops using Sentinel-1 and Sentinel-2-like data for agricultural applications. Remote Sensing of Environment, 199, 415-426.

Y. Inoue, E. Sakaiya, and C. Wang, 2014, "Capability of C-band backscattering coefficients from high-resolution satellite SAR sensors to assess biophysical variables in paddy rice," Remote Sens. Environ., vol. 140, pp. 257–266.

A high performance GPU implementation for multitemporal analysis of huge satellite remote sensing databases

N. Ben Achhab[1], N. Raissouni[1], J. A. Sobrino[2], A. Chahboun[1], A. Azyat[1], M. Lahraoua[1] &
S. El Adib[1]

1 Remote Sensing & Geographic Information System Unit (RS&GIS),
University Abdelmalek Essaadi, Morocco
2 Global Change Unit (GCU). Imaging Processing Laboratory (IPL).
University of Valencia (UV). Spain.
*corresponding author: nbenachhab@gmail.com, nraissouni@uae.ma

ABSTRACT - *The Multitemporal analysis of the huge quantities of satellite remotely sensed data (i.e., Pathfinder AVHRR land database, LTDR database, MODIS database, Landsat database, etc.) need an enormous increasing in both hardware power and algorithms architecture development. Nowadays, using Graphics Processing Units (GPU) computing, a substantial amounts of compute power and time optimization is provided. It has been done so by making it possible for enormous numbers of compute cores to work in parallel. However, GPU Hardware architectures (i.e., Fermi, Kepler, Maxwell, etc.), advanced memory Hierarchy (i.e., Cache, Unified, Shared, Local and Global memories, etc.), and bottlenecks management programming have made software development a very hard and heavy charge. In this paper, The Multi-temporal, Multi-threading Multi-core computation framework (3MCF) has been extended to support Compute Unified Device Architecture (CUDA) optimized GPU remote sensing algorithms computing biophysical indices (i.e., Split-Window Land Surface Temperature (LST), Normalized Difference Vegetation Index (NDVI), etc.). Thus, to improve performance and reduce computing time of multitemporal analysis and using the most commune GPU graphics cards like GeForce GTX1080 and GeForce GTX480 with respectively 2560 cores running at 1,6 GHz and 480 cores running at 1.4GHz. In order to study the improvement of the computation time performance, 336 benchmarking tests was applied (i.e., 2 hardware architectures, 2 algorithms, 7 image sizes, one year monthly temporal resolution). Final adapted benchmark results show a gain reaching more than 700% for the GTX1080 and more than 500% for the GTX480 depending on hardware architecture, image size and algorithm complexity.*

1 INTRODUCTION

The exponential growing of satellite data during the last two decades (due to the use of increasingly number of satellites and continuously higher resolutions), and the development of more than 40 biophysical indices (i.e., Land Surface Temperature (LST), Thermal Inertia (TI) (Sobrino et al., 1998), emissivity (ε) (Sobrino et al., 2001), Normalized Difference Vegetation Index (NDVI), Leaf Area Index (LAI), atmospheric Water vapour (W), Global Environmental Monitoring Index (GEMI), Soil Adjusted Vegetation Index (SAVI) (Baret et al.,1989), etc.), has transformed multitemporal study into very complex task. Hens, a huge quantity of satellite remotely sensed data has been accumulated waiting for new software and hardware capability treatments. These treatments are both time and memory consuming for the huge amount of data (Ben Achhab et al. 2010). Therefore, the need of new High Performance Computing (HPC) techniques able to compute Remote Sensing (RS) algorithms on such

huge quantity of data has been intensified. Therefore, computer hardware industry has provided more computational power with computer systems containing powerful Graphics Processing Units (GPU) (Glenn and rtun, 2009) used as co-processors firstly designed for gaming and then well used by the scientific community (Kingyens, 2009).

With the push of the GPU systems, software developers are confronted with an increasing complexity: i) complex transferring and loading data to the GPU, ii) GPU caches memory are more pipelined as more cores are implemented (Brodtkorb, Hagen, and Sætra 2013), and iii) software developers must implement parallel programming instead of serial one. Thus, using techniques such as: multiprocessing, MultiTHreading (MTH), special libraries (i.e. CUDA, OpenCL. etc.), etc.

In this work, a framework has been built to implement Remote Sensing (RS) algorithms with Simultaneous MultiThreading (SMT) on GPU architectures. It has been integrated into the core of Multitemporal Multithreading on Multicore Computations

Framework (3MCF). 3MCF proposes an approach to compute automatically whole RS databases -in order to carry out multitemporal studies- to:

    i) avoid the memory overflow,

    ii) accelerate the execution with full and/or partial parallelization,

    iii) optimize system and device memory reservations,

    iv) maximize the speedup, and

    v) exploit the full hardware power.

2 GPU overview

2.1 Hardware architecture

NVIDIA's Fermi architecture have marked an important change in GPUs architecture design involving many Graphics Processing Clusters (GPCs) (Xuan, Li, and Han 2018), each one encompassing numerous Streaming Multiprocessors (SM), and each SM contains several processors called SM Cores (SMC) (see Figure 1).
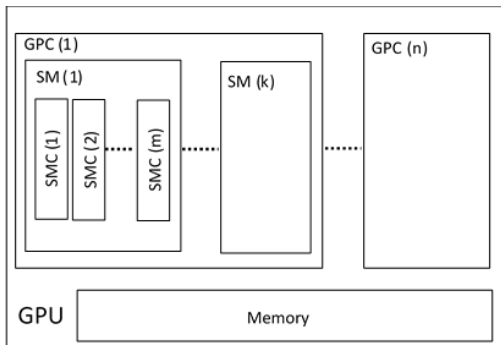
Fig.1. Modern Graphics Processing Architecture

This architecture has been also adopted for both Kepler (Purawat et al., 2017) and pascal (Peternier, et al., 2017) architectures and changing the number of GPC, SM, and SMC to increase the Total Number of Cores (TNC). During the last few years, GPU architectures have implemented from 2 to 4 GPC each one encompassing from 2 to 20 SM. Table1 gives an overview of some commune Nvidia graphics cards.

Table1. Overview of some Nvidia's graphics cards.

Architecture	Nvidia graphics card	GPC	SM	SMC	TNC
Fermi	GeForce GTX480	4	4	32	480
Kepler	GeForce GTX680	4	2	192	1536
	GeForce GTX980	4	16	32	2048
Pascal	GeForce GTX1060	2	20	32	1280
	GeForce GTX1070	3	20	32	1920
	GeForce GTX1080	4	20	32	2560

2.2 CUDA architecture

The Compute Unified Device Architecture (CUDA) is a programming model (Kalaiselvi et al., 2017) created by Nvidia to assist software developers to use the GPU cores. It is also a parallel computing platform designed to work using programming languages like C and C++. CUDA uses multithreading coarse and fine-grained models to enable execution of many concurrent threads. Commands are distributed to a collection of threads called a warp. This last is a part of block mapped to SM. Finally, the grid is number of blocks (See Fig.2).
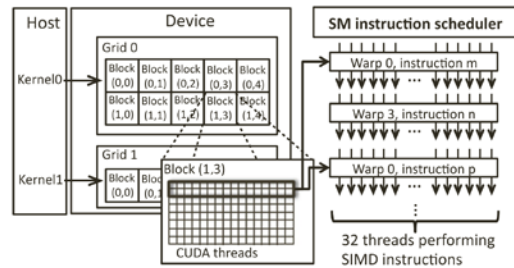
Fig.2. Compute Unified Device Architecture

The number of threads per block and the number of blocks per grid is limited by the GPU hardware. In the case of Nvidia GeForce GTX1080Ti the maximum number of threads per multiprocessor is 2048 and the maximum number of threads per block is 1024. It is true that every block of threads can work together by sharing data through device shared memory and thread-synchronisation but just inside a single block. More generally, the computer or commonly called Host send data and instructions to the graphics card called Device, it wait executions on the Device to be done, and the computed data is sent to the Host.

3 FRAMEWORK FOR MULTITEMPORAL GPU COMPUTATION

3.1 Huge Remote sensing databases

Nowadays, collecting data from a variety of satellite - and aircraft- based sensors some RS databases store huge amounts of data every day (i.e., Landsat8 with 86.15 Tera byte/year, Radarsat-2 with 20.56 Tera bytes/year, SPOT5 with 19.58 Tera bytes/year, etc.) (Ma et al., 2014). Hence, Actual RS databases have reached thousands of Tera bytes (i.e., MODIS-TERRA/AQUA, Landsat OLI/TIRS, Landsat TM, etc.) and numerous RS databases have reached hundreds of Tera bytes (i.e., ASTER/TERRA, PALSAR Radar, Sentinel-2, etc.). Table 2 resumes some archived huge remote sensing databases sorted by total data size.

Table 2. Some archived huge remote sensing databases.

Platform/Sensor	Acquisition Dates	Number of images /files	Total size (Tera Bytes)	Notes / Relevant Citations
MODIS - TERRA/AQUA NASA	2001-2017	94907847	8571.4	NASA/-EROS
Landsat OLI/TIRS	2013-2017	1080003	3732.6	NASA / USGS -EROS
Landsat ETM+	1999-2017	2375646	2206.7	NASA / USGS -EROS
Landsat TM	1982-2012	2414179	1211.1	USGS -EROS
Sentinel-2	2016-2017	2181595	912.7	ESA -ESA/EROS
ASTER - TERRA	2001-2017	7838585	755.7	NASA -NASA/EROS
HRO original data files	2008-2017	3694381	434.1	USGS -MCMC/EROS
ASF PALSAR Radar Consortium Data Pool	2006-2017	563230	290.1	USGS -ASF
Landsat MSS	1972-1992	1312592	80.1	USGS -EROS
Earth Observation EO-1 Hyperion	2000-2017	91398	50.6	USGS -EROS
Indian Space Research Organisation	2016-2017	31329	34.2	ISRO -ISRO/EROS
Scanned Satellite Film (CORONA, ARGON, LANYARD)	1960-1972	24505	30.8	USGS -EROS
SPOT	2009-2013	941945	29.0	USGS -EROS
Earth Observation EO-1 ALI	2000-2017	91613	18.8	USGS -EROS
Landsat OLI	2013-2017	4069	11.9	NASA / USGS -EROS
DOQ - QUARTER QUAD (3.75 MINUTE) CIR	1997-2009	74776	10.1	USGS -WMC/EROS
DOQ - QUARTER QUAD (3.75 MINUTE) B/W	1997-2009	205201	9.1	USGS -WMC/EROS
LAC Data Received via FTP	1980-2017	176395	8.7	NOAA -NOAA/EROS
Declassification II (KH-7, KH-9)	1963-1980	3109	8.1	USGS -EROS
AVHRR 1-KM Orbital Segment	1992-2017	32008	4.3	USGS -EROS
The Atmospheric Infrared Sounder (AIRS/EOS)	2002-2016	5147	2.65	(AIRS Science Team 2013)
Landsat TIRS	2013-2017	3363	2.3	NASA / USGS -EROS
Global gridded monthly/daily precipitation averages	2009-2017	3165	0.83	(GPM Science Team 2016)
AIRX3SPD: AIRS/Aqua L3 Daily (AIRS+AMSU)	2002-2016	5141	1.88	(AIRS Science Team 2013)
Long Term Data Record MODIS 2 LTDR	2000-2016	14219	5.8	(Pedelty et al. 2007)
Long Term Data Record version 4 - NOAA07	1981-1985	38002	0.43	(Pedelty et al. 2007)
Long Term Data Record version 4 - NOAA09	1985-1988	4082	0.47	(Pedelty et al. 2007)
Long Term Data Record version 4 – NOAA11	1988-1994	6253	0.73	(Pedelty et al. 2007)
Long Term Data Record version 4 – NOAA14	1995-1999	5426	0.64	(Pedelty et al. 2007)
Long Term Data Record version 4 – NOAA16	2000-2005	5638	0.70	(Pedelty et al. 2007)
Long Term Data Record version 4 – NOAA18	2005-2009	4664	0.59	NASA- GSFC
Long Term Data Record version 4 – NOAA19	2009-2017	9051	1.2	NASA- GSFC
GLS 1990	1984-1997	7375	2.6	USGS -EROS
TM Scene-based	1984-1997	7106	2.8	NASA -EROS
SIR-C Precision Processed	1994	19402	3.0	USGS -EROS
ETM+ Pansharpened Uncompressed Mosaics	1999-2003	2489	3.2	NASA -EROS
GLS 2010	2008-2012	8555	4.2	USGS -EROS
GLS 2005	2003-2008	9718	5.2	USGS -EROS
GLS 2000	1999-2003	8756	5.4	USGS -EROS
ETM+ Scene-based	1999-2003	8756	5.9	NASA -EROS
ETM+ Pansharpened Scene-based	1999-2003	8767	6.7	NASA -EROS
AVHRR EDC-HRPT Data	1981-2017	138859	6.9	NOAA -NOAA/EROS

3.2 Remote sensing algorithms

In order to choose two types of algorithms, we have selected the most important RS algorithms: The NDVI algorithm using two images and LST using five images. The NDVI can be defined by the following equation:

$$NDVI = (NIR - Red)/ (NIR + Red) \qquad (1)$$

where NIR and Red are radiances in the near-infrared band (AVHRR Channel 2, Landsat8 band 5, etc.) and the red band (AVHRR Channel 1, Landsat8 band 4, etc.), respectively. The LST using the split-window algorithm for AVHRR images is as follow.

$$LST = T_4 + 1.40(T_4 - T_5) + 0.32(T_4 - T_5)^2 + \\ 0.83 + (57 - 5W)(1 - \varepsilon) - (161 - 30W)\Delta\varepsilon \qquad (2)$$

where T4 and T5, are the total atmospheric transmittances in Channels 4 and 5 of the AVHRR, ε and Δε are the effective emissivity and the difference emissivity respectively and W (g cm-2) the atmospheric water vapour. Similarly, LST algorithm for Landsat images is given by the following equation.

$$LST = T_i + 1.378(T_i - T_j) + 0.183(T_i - T_j)^2 - 0.268 \\ + (54.30 - 2.238W)(1 - \varepsilon) - (16.40W - 129.20)\Delta\varepsilon \qquad (3)$$

where Ti and Tj are the Landsat8 at-sensor brightness temperatures at the SW bands i and j.

3.3 3MCF Framework

The Multi-temporal, Multi-threading Multi-core computation framework (3MCF) (BenAchhab et al.,

358

2010), 3MCF has been designed to: a) Automation: automatic computation for a whole temporal database, b) Performance: system performance increases by fully using multicore and GPU capabilities, c) Low cost: hardware cost reduction by running on a common personal computer, d) Portability: compatibility with multiple hardware and software platforms, e) Simplicity: remote sensing software parallelism complexity minimization. Designed for multithreaded implementation, 3MCF is basically composed of C++ classes structured following the multiple layers architecture shown in Fig.3.
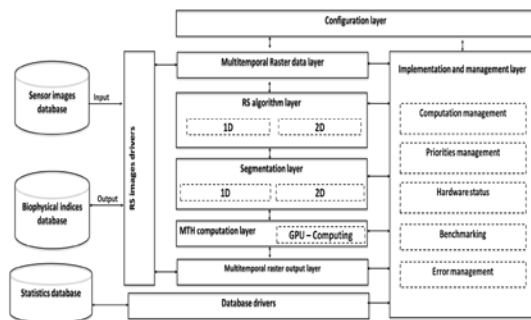
Fig. 3: 3MCF architecture diagram

Due to portability intend, threads scheduling are given in part to the operating system with a high priority require. The configuration layer permits an automatic computation of RS images. It is also responsible of the accomplishment of user preferences (i.e., maximum number of threads to execute over a CPU, threads priorities, algorithm to be executed, RS database to compute, memory reservation depending on the number of images to be integrated in the corresponding RS algorithm). The core implementation and management layer is charge of all computations executed over this framework, it includes GPU computing core which is in charge of all GPU computations. It is also in charge of transferring computed images to and from the Device.

Default, preferences load RS images from the sensor images database using the multitemporal raster data layer, and store the computed images (using MTH computation layer) in the biophysical indices database using multitemporal raster output layer. Sensor images and biophysical indices databases structure has been designed on the basis of separating and storing the data within folders classed by years and months. This data, can be stored under different formats (i.e., Raster, Hierarchical Data Format, GeoTIFF, Erdas Imagine, Oracle Spatial GeoRaster, VTK, etc.) using RS images drivers layer. This last, is based on some developed files drivers and the Geospatial Data Abstraction Library (GDAL). RS algorithm layer regroups the most used algorithms subdivided in two categories: i) 1D

algorithm section compute the biophysical indices requiring pixel by pixel computation (i.e., NDVI, LAI, GEMI, WDVI, SAVI, LST, etc.), and ii) 2D algorithm section compute the biophysical indices requiring multiples pixels by multiples pixels computation like water vapour algorithm. The 3MCF framework computational approach is built up from a divide-and-conquer approach, by dividing the remote sensing image into regions and the algorithm application into multiples simultaneous threads. Instead of cropping the image into sub images with corresponding reserved memory, the 3MCF segmentation layer has been structured on the basis of executing multiple CUDA threads on the original image itself which is already reserved in the Device and Host memories.

4 PERFORMANCE ANALYSIS

To evaluate the performance of the 3MCF remote sensing GPU computation core 7 RS image types have been used as shown in Table 3.

Table 3. RS images used in the tests performance.

Remote sensing image type		Lines	Rows	NDVI Elements	LST Elements
IM1	Landsat data (North of Morocco)	7061	6781	95761282	287283846
IM2	Landsat data (North of Morocco)	6820	3580	48831200	146493600
IM3	Landsat data (North of Morocco)	6432	2530	32545920	97637760
IM4	NOAA/AVHRR Global PAL Data	5004	2168	21697344	65092032
IM5	NOAA/AVHRR Cropped PAL Data	4250	1850	15725000	47175000
IM6	NOAA/AVHRR Cropped PAL Data	4048	1296	10492416	31477248
IM7	NOAA/AVHRR Cropped PAL Data	2703	970	5243820	15731460

where the number of elements is total number of image pixels multiplied by the number of images used by the algorithm. For accuracy commitment, i) all execution have been made using the same system: Intel Core i7-960 3.2GHz. ii) the execution time is the average computing time of 12 algorithm executions. The different picked time positions are indicated in Fig. 4. t_S is indicating the start pick time directly after memory reservation, t_E the end pick time directly after file result saving, t_{SC} the start computation pick time indicating the start of running on the GPU Device and t_{EC} the end pick time computation just after ending of all the algorithms' parts computation and before file result saving.

GPU Execution diagram
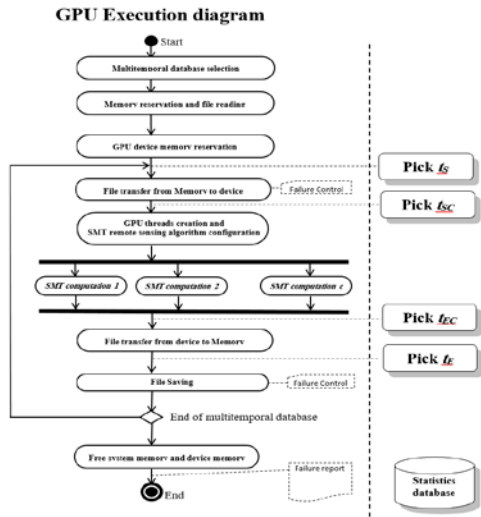
Fig. 4. 3MCF execution diagram and picked time positions.

5 RESULTS

Results show an important gain in computing time for both NDVI and LST algorithms. See Table4 and Table5

Table 4. NDVI average computation time

Images	CPU (GTX1080) (ms)	GTX1080 (ms)	CPU (GTX480) (ms)	GTX480 (ms)
IM1	1370.89	181.32	1245.63	359.68
IM2	604.26	91.05	604.00	130.37
IM3	410.00	68.79	407.11	78.58
IM4	272.42	49.84	275.63	56.68
IM5	200.00	42.37	195.26	41.74
IM6	133.05	33.05	132.11	38.26
IM7	67.16	23.58	67.95	28.21

Table 5. LST average computation time

Images	CPU (GTX1080) (ms)	GTX1080 (ms)	CPU (GTX480) (ms)	GTX480 (ms)
IM1	1245.37	371.42	1268.47	470.95
IM2	637.74	197.95	632.16	248.74
IM3	429.32	139.32	434.16	169.89
IM4	1245.37	445.63	288.79	117.58
IM5	211.21	77.11	211.53	88.95
IM6	140.63	58.42	140.58	69.32
IM7	71.42	36.21	73.89	66.47

The SpeedUp, as non unit index, is defined as a ratio of execution times with the aim of quantifying the gain in time comparing the serialized and parallelized programs. It is given by the following equation.

$$SpeedUp = t_{serial} / t_{GPU} \qquad (4)$$

where t_{serial} is the computing time using the CPU, t_{GPU} is the computing time running on the GPU including loading and transferring times. In order to show the linear tendency with the image elements increasing, Figures 5 and 6 has been constructed for all the images.
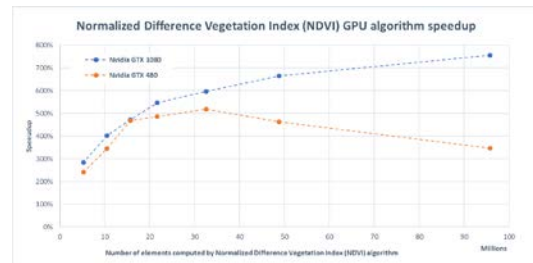
Fig. 5. 3MCF execution diagram and picked time positions.
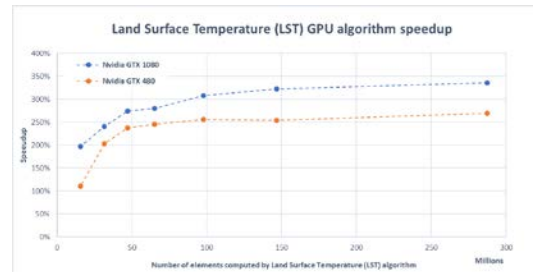
Fig. 6. 3MCF execution diagram and picked time positions.

6 CONCLUSION

The potential of the developed Multitemporal Multithreading on Multicore Computations Framework (3MCF) GPU core applied to Remote Sensing (RS) algorithms computations has been shown (in our case NDVI and LST algorithms). The GPU approach has potentially increases the multitemporal performance computing of the huge quantity of satellite remotely sensed data.

7 REFERENCES

AIRS Science Team, Joao Texeira. 2013. AIRS/Aqua L3 8-day Support Multiday Product (AIRS+AMSU) 1 degree x 1 degree V006, Greenbelt, MD, USA, Goddard Earth Sciences Data and Information Services Center (GES DISC).

Baret, E, G. Guyot, and D.J. Major. 1989. TSAVI: A vegetation index which minimizes soil brightness effects on LAI and APAR estimation. In 12th Canadian Symposium on Remote Sensing, 1355-58.

BenAchhab, Nizar, Naoufal Raissouni, Abdelilah Azyat, Asaad Chahboun, and Mohammed Lahraoua. 2010. High performance computing software package for multitemporal Remote-Sensing computations, Inter. Journal of Engineering and Technology, 2: 6.

Brodtkorb, André R., Trond R. Hagen, and Martin L. Sætra. 2013. Graphics processing unit (GPU) programming strategies and trends in GPU computing, Journal of Parallel and Distributed Computing, 73: 4-13.

Glenn, Bakke, and Ruben. 2009. Programming graphic processing units (GPUs).

GPM Science Team. 2016. GPM MHS on NOAA19 (GPROF) Radiometer Precipitation Profiling L3 1 month 0.25 degree x 0.25 degree V05, Greenbelt, MD, USA, Goddard Earth Sciences Data and Information Services Center (GES DISC).

Kalaiselvi, T., P. Sriramakrishnan, and K. Somasundaram. 2017. Survey of using GPU CUDA programming model in medical image analysis, Informatics in Medicine Unlocked, 9: 133-44.

Kingyens, Jeffrey Richard Code. 2009. A GPU-inspired soft processor for high-throughput acceleration (Library and Archives Canada : Ottawa).

Ma, Yan, Haiping Wub, Lizhe Wang, Bormin Huang, Rajiv Ranjand, Albert Zomaya, and Wei Jie. 2014. Remote sensing big data computing: Challenges and opportunities, Future Generation Computer Systems.

Pedelty, Jeffrey, David Roy, Eric Vermote, and Crystal Schaaf. 2007. Generating a Long-term Land Data Record from the AVHRR and MODIS Instruments. In IGARSS2007. Barcelona, Spain: IEEE Geoscience and Remote Sensing Society.

Peternier, Achille, John Peter Merryman Boncori, and Paolo Pasquali. 2017. Near-real-time focusing of ENVISAT ASAR Stripmap and Sentinel-1 TOPS imagery exploiting OpenCL GPGPU technology, Remote Sensing of Environment.

Purawat, Shweta, Pek U. Ieong, Robert D. Malmstrom, Garrett J. Chan, Alan K. Yeung, Ross C. Walker, Ilkay Altintas, and Rommie E. Amaro. 2017. A Kepler Workflow Tool for Reproducible AMBER GPU Molecular Dynamics, Biophysical Journal, 112: 2469-74.

Sobrino, J.A., M.H. El Kharraz, J. Cuenca, and N. Raissouni. 1998. Thermal inertia mapping from NOAA-AVHRR data, Advances in Space Research, 22: 655-67.

Sobrino, J.A., N. Raissouni, and Zhao Liang Li. 2001. A Comparative Study of Land Surface Emissivity Retrieval from NOAA Data, Remote Sensing of Environment, 75: 256-66.

Xuan, Yubo, Dayu Li, and Wei Han. 2018. Efficient optimization approach for fast GPU computation of Zernike moments, Journal of Parallel and Distributed Computing, 111: 104-14.

Sea Surface Height Monitoring Of Multi-GNSS-MR Based on Wavelet Denoising

Fade Chen [1,2,] Lilong Liu [1,2,3,*,] Junyu Li [1,2,*,] Liangke Huang [1,2,] and Linbo Liu [1,2,]

1 College of Geomatics and Geoinformation, Guilin University of Technology, Guilin 541004, China;
fadechen666@163.com (F.C.); 13077651398(F.C.);lkhuang666@163.com
(L.H.); 924134799@qq.com (L.L.);
2 Guangxi Key Laboratory of Spatial Information and Geomatics, Guilin 541004, China
3 College of Resources and Environment, Qinzhou University, Qinzhou 535011, China
* Correspondence: fadechen666@163.com(F.C.) 13077651398 (F.C.);
lijunyu@glut.edu.cn(J.L.) 15676331890 (J.L.);
hn_liulilong@163.com (L.L.); 13367835262 (L.L.)

ABSTRACT:Sea Surface Height is an important parameter that affecting human living environments. Since GNSS-MR owns long-term stability and high temporal and spatial resolution as well as other characteristics, the SNR data of BDS (L1, L5, L7), GPS (L1, L2, L5), and GLONASS (L1, L2) over a period of seven days were used to estimate the SSH. The results show that the RMSE is better than 32.3cm, the correlation coefficient is better than 0.83. To improve the accuracy of the estimated results, a new method was proposed that using the estmated results to reconstructe the tidal waveforms by applying wavelet denoising. The results demonstrated that the wavelet denoising result shows a high precision with the correlation coefficient and RMSE of 0.95 and 18.7cm, which is improved about 14.5% and reduced by 42.1% compared with the results from the SNR method.
Keywords: Multi-GNSS-MR • Sea Surface Height • SNR • wavelet denoising • accuracy

1 INTRODUCTION

Sea Surface Height (SSH) is an important physical parameter in oceanography, ocean shipping, marine fisheries and ocean engineering. It can be used for the establishment of oceanic and oceanic tidal models and the study of mesoscale climate models and tsunami warning. In recent years, with the continuous development of GNSS technique,GNSS-R (Global Navigation Satellite System Reflectometry) remote sensing technique could be applied in many fields such as soil moisture, snow thickness and earth power in addition to sea level, sea surface wind, wave height and sea surface salinity Learning and so on. GNSS-R has a high temporal and spatial resolution, which is important in the real-time monitoring of SSH.This remore sensing technique is also termed GNSS interferometry reflectometry (GNSS-IR), GNSS interference pattern technique (GNSS-IPT), or GNSS multipath reflectometry (GNSS-MR), when the direct and reflected signals are received by the same antenna such as a zenith-looking geodetic antenna. The GNSS-MR remote sensing technique can monitor the surface environment parameters changes such as snowfall, soil moisture, vegetation growth and SSH by using the SNR or carrier phase observation recorded by the conventional GNSS receiver, which makes this technique become GNSS remote sensing the latest research hot spots. At present, the use of GNSS-MR technology for surface environmental monitoring has a certain research foundation. (Larson *et al*., 2008; Larson *et al*., 2008; Larson *et al*., 2010) first demonstrated how to make positive use of multipath signals observed by the existing geodetic GPS network. They pointed out that the amplitude and phase of a multipath signal change with surface soil moisture around the receiver antenna. Later, (OZEKI M *et al.*, 2011) put forward a new snow depth estimation method base on GPS L4 observation no geometric distance due to the problem of lack of observation using GPS-MR technique, and it is consistent with SNR's inversion results. And then, (Yu K *et al.*, 2015) proposed a snow depth estimation method by using a linear phase combination of GPS triple-frequency(L1, L2, L5) signals, which is not affected by ionospheric delay. (Jin S *et al.*, 2017) first use the SNR and phase combination of BDS to obtain a high correlation coefficient of 0.81-0.91 and RMSE over 0.5m for estimating sea surface height changing compared to tide gauge observations.

With the steady progress of BDS, Galileo and other systems, it is possible to make multi-GNSS-MR to monitor global environmental change. In this paper, the SNR data of BDS (L1, L5, L7), GPS (L1, L2, L5) and GLONASS (L1, L2) are used to estimate SSH, with elevation angles between 5°~20° over a period of

seven days. The SNR method results are further evaluated by comparing with tide gauge observations. Some effects are also discussed. Then reconstructing the tidal waveform with the discrete data of the SNR results by using wavelet denoising, and then processing the residual data, and obtaining the height sequence statistics after processing. Finally, conclusions are given.

2 THE THEORY OF MONITORING THE SSH OF GNSS-MR

GNSS multipath is the main source of error that constrains high-precision positioning of GNSS. The multipath is caused by the difference of the phase between the direct signals and the reflected signals, which is related to the antenna height h in Fig.1. Fig.1 illustrates the case where both direct and reflected signals arrive at zenith-looking GPS antenna. The interference between the direct and reflected signals will affect GNSS observations and cause oscillations in observations. This interference phenomenon is recorded in the form of amplitude in the Signal Noise to Ratio (SNR), which can reflect the SSH change. Fig.2 shows the SNR Variations of BDS.
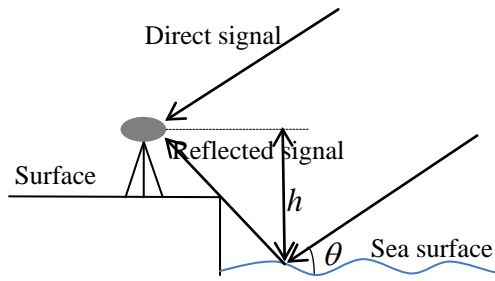
Fig.1 Diagram of GNSS-MR for SSH Variation.The h is the antenna height from reflected surface, θ is the angle between the direct signal and the instantaneous sea surface.
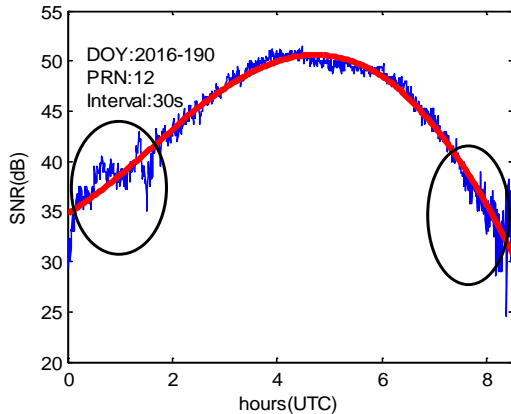
Fig.2 SNR Variations of BDS

2.1 Signal-Noise to Ratio (SNR) method

SNR is one of main observables of GNSS receiver, which mainly related to the satellite signal transmission power, antenna gain, the distance between satellite and receiver and multipath effect. When the elevation angle is high, the antenna gain increases cause increasing of SNR. When the elevation angle is low, SNR is reduced due to the multipath effect and the decreasing of the antenna gain. So if there is no multipath effect, the SNR value will rise smoothly with the increasing of elevation angle. In this paper, we use the observed SNR data from the receiver to estimate SSH, which is proportional to the squared amplitude, i.e.,

$$SNR = \frac{A^2}{2P_n} = \frac{1}{2P_n}\begin{pmatrix} A_d^2 + A_r^2 + \\ 2A_d A_r cos\delta\varphi(t) \end{pmatrix} \quad (1)$$

Where P_n is the noise power, A_d is amplitude of direct signal, A_r is amplitude of reflected signal, $cos\delta\varphi(t)$ is the reflection excess phase with respect to direct phase to direct phase(also known as the interferometric phase),where

$$\delta\varphi(t) = \frac{4\pi h}{\lambda}\sin\theta(t) \quad (2)$$

In order to receive the direct signal effectively, the receivers suppress the multipath reflected signal, the relationship between A_d and A_r as following:

$$A_d \gg A_r \quad (3)$$

In combination with Fig. 2, Eq.(1) and Eq.(3), the direct signal determines the overall trend of the SNR observations (Fig.2). So we can use low-order polynomial to obtain SNR detrended time series formed by the multipath, which can be used to estimate the surface parameters such as SSH. After removing the SNR trend, the multipath pattern can be expressed as following:

$$dSNR = A\cos(\frac{4\pi h}{\lambda}\sin\theta + \phi) \quad (4)$$

Where

$$A = \frac{A_d \cdot A_r}{P_n} \quad (5)$$

h is antenna height from the reflected surface in Fig. 1. λ is the carrier wavelength, θ is the elevation angle and ϕ is the phase. We can definit: $t = \sin\theta$ and $f = 2h/\lambda$ in Eq.(4), which can expressed as following:

$$dSNR = A\cos(2\pi ft + \phi) \quad (6)$$

Supposed that the reflector height h in Fig.1 does not change during the period of satellite arc and the reflected surface is horizontal, the frequency of multipath is pattern is a constant with respect to the Sine of satellite elevation angle. Though the SSH change with the time, this constant frequency model is sufficient for this station whose maximum tide range is 4m, which is less than the tide range 7m that should consider the varying reflector height. Through Eq.(6), the frequency of multipath pattern can be obtained as following:

$$h = f\lambda / 2 \qquad (7)$$

From Eq.(7), it is clear to see that h is proportional to f. Spectral analysis is applied to obtain the spectral peak frequency of the $dSNR$ time series. The estimated peak frequency and Eq.(7) are applied to obtain the antenna height and hence SSH in a straightforward way. In this paper, the Lomb Scargle method was used to obtain the peak frequency.
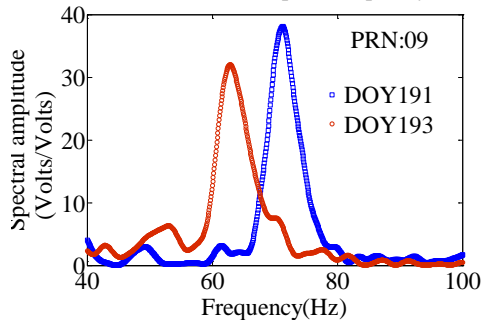
Fig.3 L-S Result

3 SSH MONITORING ANALYSIS OF Multi-GNSS-MR

To verify the feasibility and effectiveness of monitoring SSH based on Multi-GNSS-MR, the the observation data of MAYG station, which is located in Mayotte, France near the Indian Ocean, are used to be experimented. The TRIMBLE NETR9 receiver and TRM59800.00(latitude: -12.78°,longitude: 45.26°and height: -16.35m) antenna are installed in MAYG station, and the data sampling rate is 1Hz. Because MAYG is one of the Multi-GNSS Experiment (MGEX) stations, it receives not only the GPS and GLONASS signals but also BDS signals with three frequencies (L1, L5 and L7). In this paper, the observation and navigation data published by IGS are applied to estimate the SSH. According to evaluating the circumference of the receiver and the sky view of the observation satellite, the azimuths is used from 20° ~ 80° and 110° ~ 170°.

The SNR data of BDS (L1, L5, L7), GPS (L1, L2, L5), and GLONASS (L1, L2) with elevation angles between 5°~20° over a period of seven days from 191 to 196 in 2017 were used to estimate the antenna height from reflected surface base on the L-S spectral analysis. Fig.5 shows the results of L-S spectral analysis of PRN09 of BDS. In order to verify the accuracy of estimating SSH of Multi-GNSS-MR, the Dzaoudzi tide gauge observations, which is about ten meters from the MAYG station, are compared and analyzed.
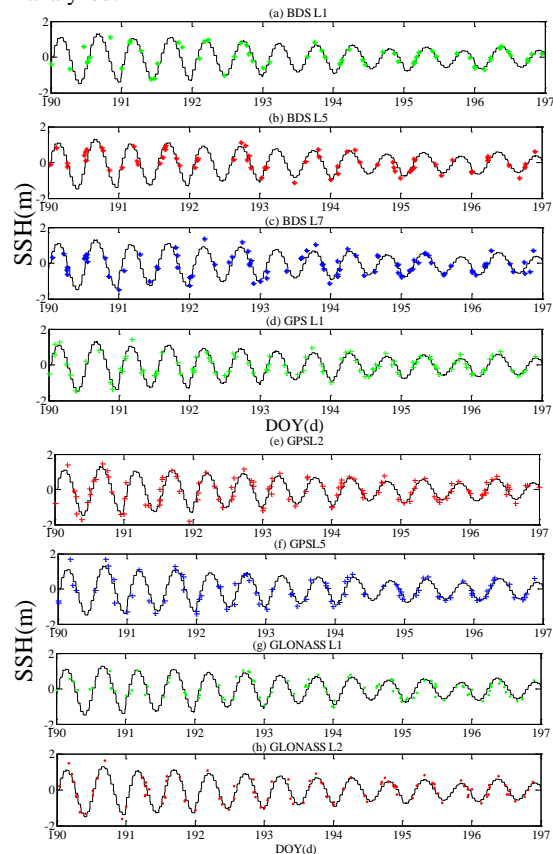
Fig.4 The BDS-MR、GPS-MR and GLONASS-MR Inversion Results

Fig.4 shows the results of SSH, which obtained by the above method, and truth comparison. Where the horizontal axis represents the day of year (DOY), and the black line is the relative average (low) tidal surface of the SSH estimated by GNSS-MR and the asterisk is the estimated SSH.

As observed in Fig.4, there is a significant daily periodicity of SSH changes monitored by tide stations, which mainly due to tidal effects. There is a good agreement with tide gauge observtions based on BDS, GPS, GLONASS inversion in the 190-196 days.
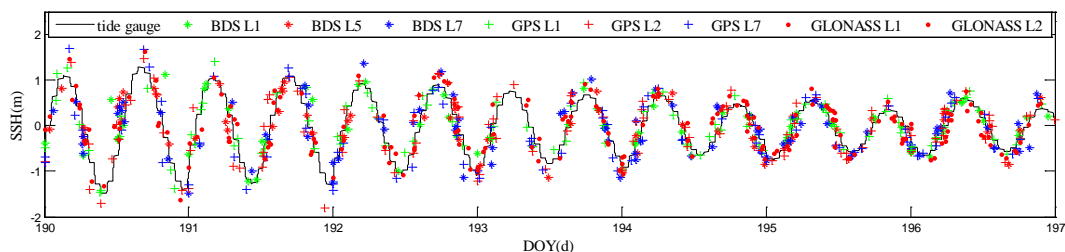
Fig.5 The BDS-MR、GPS-MR and GLONASS-MR Inversion Results
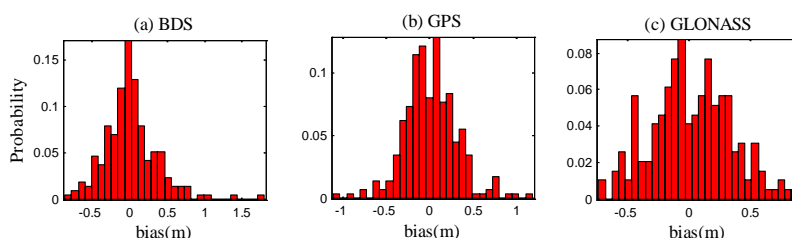
Fig.6 The BDS-MR、GPS-MR and GLONASS-MR Inversion Results

Because of a limited number of satellites' signals reflected from sea surface, each carrier did not monitor the SSH changes in a certain period of time. The time resolution of GPS is better than GLONASS, BDS, the reason may be the number of satellites of each GLONASS and BDS less than GPS. In order to better analyze the effect of the monitoring of three systems, the statistical results of the three systems are shown in Fig.5.
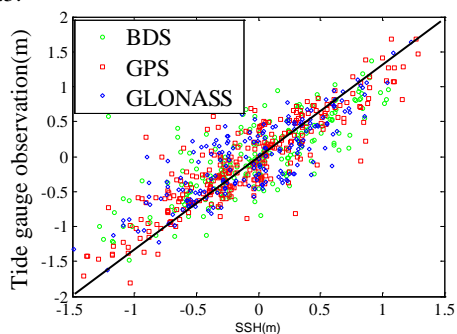
Fig.7 Histogram of sea surface height estimates by BDS-MR, GPS-MR and GLONASS-MR. Tide gauge data are treated as ground-truth.

As observed from Fig.5, the monitoring sampling time of three systems is complementary, thus monitoring the time resolution to be greatly improved. What's more, when the observation period is shorter and the observation environment is poor, the superiority of multi-GNSS-MR monitoring SSH is more obvious. Tab.1 presents detailed correlation and RMSE (root-mean-square) values for BDS, GPS, GLONASS estimate results, then the bias probalility distribution of estimated SSH are shown in Fig.6.

Tab.1 The Accuracy of Inversion base on BDS-MR、GPS-MR and GLONASS-MR

Carrier	RMSE/m	R
BDS L1	0.357	0.78
BDS L5	0.317	0.80
BDS L7	0.368	0.77
GPS L1	0.226	0.91
GPS L2	0.340	0.87
GPS L5	0.336	0.88
GLONASS L1	0.310	0.80
GLONASS L2	0.331	0.84

In table 1, the estimations from GPS L1 with the correlation(R) of 0.91 and RMSE of 0.226m are better than the others. From Fig.6, the estimated results is similar to the normal distribution.Fig.6 and Fig.7 show a good correlation with tide gauge observations. In summary, by using the SNR data of BDS, GPS and GLONASS to estimate the SSH not only improves the continuity and time resolution of monitoring, but also has good global inversion accuracy.

4 WAVELET DENOISING AND IMPROVEMRNT

As observed from Fig.5, there are some noise in the results. In order to improve the accuracy of the estimated results, tidal waveforms are reconstructed after wavelet denoising base on the acquired discrete estimated results. In order to get a better denoising effect, different wavelet basises and time of decompositions used to be compared. The results shows that when using db6 wavelet basis and 6 time of decomposition we can get the best denoising results. And Fig.8, Fig.9 shows the results by using this method.
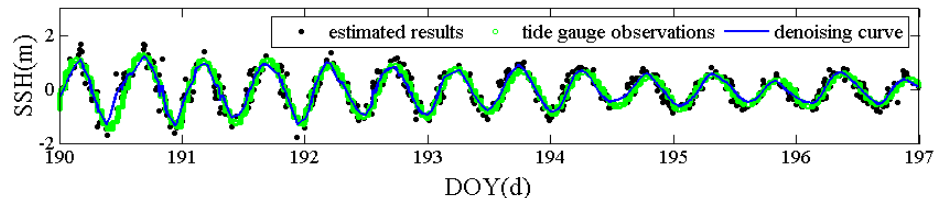
Fig.8 SSH from estimated results and denoising results
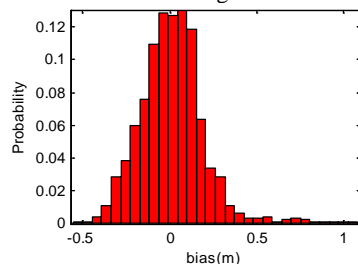
Fig.9 Bias between Denoising results and tide gauge observations

After wavelet denoising, it is clear that the denoising curve shows a good agreement with the tide gauge observations. The correlation coefficient and RMSE of this method is respectively 0.95, 0.187m, which is improved about 14.5% and reduced by 42.1% compared with the results from the SNR method. Furthermore, the temporal resolution of monitoring is greatly increased.

5 CONCLUDING REMARKS

In this paper, the SNR data of BDS (L1, L5, L7), GPS (L1, L2, L5), and GLONASS (L1, L2) to estimate the sea surface height (SSH). After obtaining the SSH,we use the inversion results to reconstructe the tidal waveforms by wave filtering. Compared with tide gauge observations, the results demonstrated that the estimated SSH show a high precision and after wave filtering, the RMSE reach 0.153m, which is reduced by 42.1% compared with the SNR method.

6 ACKNOWLEDGMENT

7 REFERENCE

A. Bilich and K. M. Larson, 2007, Mapping the GPS multipath environment using the signal-to-noise ratio (SNR). Radio Sci., 6, 1-16.

F. G. Nievinski, K. M. Larson, 2014, Forward modeling of GPS multipath for near-surface relectometry and positioning applications. *GPS Solutions*, 2, 309-322.

F. G. Nievinski, K. M. Larson, 2014, Inverse modeling of GPS multipath for snow depth estimation—Part II: Application and validation. IEEE Trans. Geosci. Remote Sens., 10, 6564-6573.

Johan S. LÖfgren, Rüdiger Haas, Hans-Georg Scherneck, 2014, Sea level time series and ocean tide analysis from multipath signals at five GPS site in different parts of the world. *Journal of Geodynamics*, 80, 66-80.

Jin S, Qian X, Wu X, 2017, Sea level change from BeiDou Navigation Satellite System-Reflectometry(BDS-R):First results and evaluation. *Global & Planetary Change*, 149, 20-25.

Jin S, Qian X, Kutoglu H, 2016, Snow Depth Variations Estimated from GPS-Reflectometry: A Case Study in Alaska from L2P SNR Data. *Remote Sensing*, 1, 63.

Jin S G, Jin R, Li D, 2016, Assessment of BeiDou differential code bias variations from multi-GNSS network observations. *Annales Geophysicae*, 2, 259-269.

K. M. Larson *et al.*, 2010, GPS multipath and its relation to near-surface soil moisture content. IEEE J. Sel. Topics Appl. Earth Observ. Remote Sens., 1, 91-99.

K. M. Larson *et al.*, 2008, Using GPS multipath to measure soil moisture fluctuations: Initial results. GPS Solutions, 3, 173-177.

K. M. Larson *et al.*, 2008, Use of GPS receivers as a soil moisture network for water cycle studies. Geophys. *Res. Lett.*, 35, Art. ID. L24405.

Kristine M.Larson, Johan S.lofgren,Rudiger Haas, 2013, Coastal Sea Level Measurements Using a Single Geodetic GPS Receiver. *Advances in Space Research*, 8, 1301-1310.

OZEKI M, HEKI K, 2011, GPS Snow Depth Meter with Geometre-Free Linear Combinations of Carrier Phases. *Journal of Geodesy*, 3, 209-219.

S. Katzberg, O. Torres, M. Grant, D. Masters, 2006, Utilizing calibrated GPS reflected signals to estimate soil reflectivity and dielectric constant: Results from SMEX02. *Remote Sens. Environ.*, 1, 17-28.

Yu K, Ban W, Zhang X, *et al.*, 2015, Snow Depth Estimation Based on Multipath Phase Combination of GPS Triple-Frequency Signals. *IEEE Transactions on Geoscience & Remote Sensing*, 9, 5100-5109.

Yu K, 2015, Tsunami-wave parameter estimation using GSS-based sea surface height measurement. *IEEE Trans. Geosci. Remote Sens.*, 5, 2603-2611.

Yu K, Rizos C, Dempster A G, 2014, GNSS-Based Model-Free Sea Surface Height Estimation in Unknown Sea State Scenarios. *IEEE Journal of Selected Topics in Applied Earth Observations & Remote Sensing*, 5, 1424-1435.

The Spatial Upscaling Algorithm of Leaf Area Index Based on Discrete Wavelet Transform

Hong Chen[1,2], Hua Wu[1,2,*], Zhao-Liang Li[3,4], Bohui Tang[1,2], Ronglin Tang[1,2], Guangjian Yan[5]

[1]State Key Laboratory of Resources and Environmental information System, Institute of Geographic Sciences
and Natural Resources Research, Chinese Academy of Sciences, Beijing, 100101, China
[2]University of Chinese Academy of Sciences, Beijing, 100049, China
[3]Key Laboratory of Agri-informatics, Ministry of Agriculture/Institute of Agricultural Resources and Regional Planning, Chinese Academy of Agricultural Sciences, Beijing 100081, China
[4]ICube, UdS, CNRS, Bld Sebastien Brant, BP10413, 67412, Illkirch, France
[5]State Key Laboratory of Remote Sensing Science, School of Geography, Beijing Normal University, Beijing 100875, China;
*Corresponding author: wuhua@igsnrr.ac.cn

ABSTRACT- *Leaf Area Index (LAI) provides key information for earth surface process simulations and climate change research from local to global scale. However, when the LAI retrieval model built at local scale (high resolution) was directly applied at a large scale (low resolution), a spatial scaling bias may be caused. In this study, we try to explore the potential application of wavelet transform in spatial up-scaling. Hence, an algorithm based on the relation between the bias rate in scaling and the detail lost rate in Discrete Wavelet Transform (DWT) was proposed to remove scaling bias at a large scale. To evaluate the proposed algorithm, a study site with high heterogeneity from Validation of Land European Remote Sensing Instruments (VALERI) database was chosen. Additionally, the up-scaling accuracy between the algorithm based on Taylor Series Expansion (TSE) and that based on DWT was compared. Generally speaking, both two algorithms can provide a good performance on the correction of the scaling bias at four different scales. However, unlike the method based on TSE, the proposed method is simpler and is not constrained by the characteristic of the retrieval model. Over high heterogonous landscape, the accuracy of the proposed algorithm is more obvious, with the root mean square error (RMSE) from 0.36 to 0.09 with the corresponding synchronous prior knowledge. When the synchronous prior knowledge is not available, the RMSE can also be reduced to 0.13.*

1 INTRODUCTION

The Leaf area index (LAI) is a significant variable for many land surface biophysical and biogeochemical models and serves as a useful indicator of the vegetation cover change. It can be obtained from ground measurements (Chen et al. 1992) or remote sensing methods (Chen 1996; Garrigues et al. 2006; Jacquemoud 2009). Advanced satellite systems and sensors provide us massive information covering large spatial and temporal range, which is critical to the modeling of natural phenomena both at local and global scales. Estimating LAI with remote sensing technique has become one of the primary methods. Although the LAI can be estimated from remotely sensed measurements by using various retrieval methods, there is an inevitable and critical scaling problem in the retrieval process (Raffy 1992; Chen 1999; Garrigues et al. 2006; Wu et al. 2013). Generally, most retrieval models are mainly derived at a local scale, assuming that the land surface at that scale is homogeneous. When those models are directly applied for heterogeneous land surface at a large scale (low resolution), unforeseeable scaling errors may be induced (Wu et al. 2013). These errors will have obvious influence on the quality of the products and make the LAI products unreliable. It was reported that the relative scaling bias of the LAI may be up to 50% if these scaling effects are ignored (Chen 1999). Additionally, Zhang et al. (2006) indicated that the mixing of distinctive surfaces of vegetation and water may result in a relative scaling bias of up to 400%. The existence of scaling effects has prevented the improvement in the accuracy of retrieval and the development of remote-sensing applications (Wu and Li 2009). Therefore, when the retrieval models are used in other scales, it is completely necessary to take the scaling effect into account in generating LAI products. There are a lot of studies focused on where the scaling effect comes from, finding that the scaling errors are mainly caused by the nonlinearity of retrieval model and heterogeneity of land surface. (Hu and Islam 1997a)

For decades, to solve the scaling issue, several spatial up-scaling algorithms have been developed to eliminate the scaling errors. Raffy (1992) proposed the computational geometry method (CGM), using the lower and upper boundaries of the retrieval model to correct for the products at large scales to reduce the scaling effects. Hu and Islam (1997a) proposed the method based on Taylor Series Expansion (TSE) with textural parameters to characterize the scaling effects. Chen (1999) focused on the ground contextual characteristics and built the relation between the scaling effects and land-cover component fractions. Garrigues et al. (2006) further extended the TSE-based scaling method to analytically compute the scaling bias for the retrieval model with two or more variables. All of those methods have already been employed to correct for the scaling errors of various remotely sensed products (Hu and Islam 1997b, 1998; Raffy and Gregoire 1998; Pelgrum et al. 2000; Simic et al. 2004; El Maayar and Chen 2006; Garrigues et al. 2006; Ma et al. 2008; Wu et al. 2013). Because of the clear physical interpretation and high correction accuracy, the TSE-based scaling method is more widely used than the other up-scaling methods. However, the TSE-based up-scaling method will be subject to many other restrictions. It is shown that when the degree of nonlinearity is large, ignoring the items higher than three-order may cause great error (Pelgrum 2000). When applied in complicated retrieval models with a large number of variables, it would be difficult to get the derivatives of the model. Moreover, the variance and covariance among each variable would also be difficult to be estimated because very few synchronous high- and low-resolution data exist in reality. Generally speaking, the difficulty of obtaining the scaling correction item would greatly reduce the applicability of that method.

As well known, Wavelet Transform is a mathematical tool widely used to dissect the signal or image into different frequency components in many subjects (Mallat 1989). In remote sensing, with the Discrete Wavelet Transform (DWT) the image can be decomposed into the low-frequency components representing the information kept at large scale and the high-frequency components corresponding to the details lost during scaling. Those high- and low-frequency components contain important information between different scales, which may be useful for the study of spatial up-scaling.

In this paper, we try to present a new up-scaling method based on DWT to eliminate the scaling effect instead of the TSE-based up-scaling method when the retrieval model is not continuous or derivable. Section 2 describes the three contrasted landscapes with different degrees of heterogeneity extracted from the Validation of Land European Remote Sensing Instruments (VALERI) database and used in this study. A semi-empirical retrieval model is also built to relate the normalized difference vegetation index (NDVI) directly to the LAI. In Section 3, two different processes of spatial aggregation for remote sensing products are provided to indicate the scale problems. In addition, a new up-scaling method that correct for the scaling effects is proposed on the basis of the DWT. In Section 4, the DWT-based method is applied to the multi-scale data of VALERI to evaluate the accuracy of spatial up-scaling. The performance of the proposed method is analysed under two conditions: with and without the corresponding synchronous high-resolution images. Finally, conclusions are given in Section 5.

2 DESCRIPTION OF THE DATA

VALERI is a European remote sensing validation program launched by the European Space Agency (ESA) in early twenty-first century. There are 21 sites located in 11 countries, providing plenty of *in situ* observed data and high-resolution satellite image data for validating the biophysical products (LAI, fAPAR and fCover). Since the scaling characteristics would change with different LAI retrieval model and heterogeneity of the study area, one site (Fundulea in Romania) with high spatial heterogeneity are selected in this study. This site is flat topography and covered by one or two types of vegetation. The SPOT NDVI imagery for this site is shown in Figure 1.
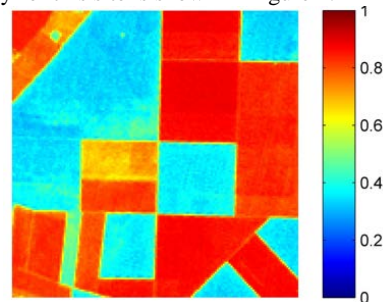
Fig.1 the selected study site of Fundulea

The high spatial resolution (20m) SPOT images with cloud-free conditions on May 2 2001 for Fundulea were selected. The original SPOT image is simple aggregated from 20m to 40m, 80m, 160m and 320m to form a nested hierarchy, corresponding to the four different aggregated scales of 2×2、4×4、8×8 and 16×16. Here, the SPOT image will be used to evaluate the up-scaling performance where the corresponding synchronous high-resolution images are assumed to be available and are used as a priori knowledge. Two days of Landsat 8 TM images with spatial resolution of 30m on April 13 and May 15 2015 for Fundulea were also selected for further study.

The aggregated scales are consistent with those for SPOT images. For TM images, the corresponding synchronous high-resolution images are assumed to be not available. One TM image will be used to evaluate the up-scaling performance, while the other will be used to get the required information for the proposed DWT-based method.

For this study site, an NDVI value is first calculated for its sensitivity to the vegetation cover as following:

$$NDVI = \frac{\rho_{nir} - \rho_{red}}{\rho_{nir} + \rho_{red}} \quad (1)$$

where ρ_{nir} and ρ_{red} represent the near infrared and red reflectance, respectively. With the ground measurement LAI data and corresponding NDVI value for each study site, an exponential empirical model representing the relation between NDVI and LAI is built for simplicity as:

$$LAI = a \times e^{b \times NDVI} \quad (2)$$

where a and b are model coefficients, depending on the characteristics of sites. The accuracy and applicability of the retrieval model will not be discussed because the model is just taken as a case study to analyse the scaling effect of LAI caused by the nonlinearity of retrieval model and spatial heterogeneity. The exponential model is chosen for it has higher fitting accuracies than other models. Additionally, for simplicity we only consider the retrieval model with univariate variable, ignoring the scaling effect caused by the nonlinearity of the NDVI as a function of red and near infrared reflectance.

3 METHODOLOGY

3.1. Procedure of the scaling aggregation

To fully show the reason why scaling bias would happen, the spatial aggregation processes shown in Figure 2 should be first recalled. Here, a semi-empirical retrieval model between the NDVI and the LAI is also used in this demonstrating example. The non-linearity of the NDVI as a function of the near infrared and red reflectances is ignored. Obviously there are two distinguished path to get LAI at a large scale (coarse resolution). The first path is applying the retrieval model f at a local scale (high resolution) and then aggregating the result to get the distributed LAI_D (path A in Fig. 2). The second path is the aggragation of NDVI befor use in the retrieval model f to get the lumped LAI_L (Path B in Fig.2).

Generaly, aggregation procedure takes the arithmetic average of corresponding high-resolution results. Thus, LAI_D and LAI_L can be rewritten in math as:

$$LAI_D = \frac{1}{N}\sum_{i=1}^{N} LAI_i = \frac{1}{N}\sum_{i=1}^{N} f(NDVI_i)$$
$$LAI_L = f(\overline{NDVI}) = f\left(\frac{1}{N}\sum_{i=1}^{N} NDVI_i\right) \quad (3)$$

where N is the number of aggregated pixels, $\overline{NDVI}$ is the arithmetic average value of pixel at large scale, f is the retrieval model built at a high spatial resolution at which the surface is assumed to be homogeneous within each pixel. Acocording to the defniniton of LAI, the distributed LAI_D is considered to be the exact value of the LAI at a large scale. Corespondingly, LAI_L is thought as the approximation value of the LAI at large scale. The change of scale will cause the discrepancy between the LAI_D and LAI_L. This discrepancy is regarded as the scaling bias:

$$Bias = LAI_D - LAI_L \quad (4)$$

Only when the surface is homogenous or the retrieval model is linear, the LAI will be scale-invariant without any scaling bias. However, this rarely happens because of spatial heterogeneity and model nonlinearity (Raffy 1992; Hu and Islam 1997a; Chen 1999; Wu & Li, 2009). The goal of scaling is to make the LAI values calculated from coarse resolution data equal to the arithmetic average values derived independently at local scale. To ensure that the LAI derived at coarse spatial resolutions are of better accuracy and consistency, the scaling bias in Eq. (4) must be corrected for.
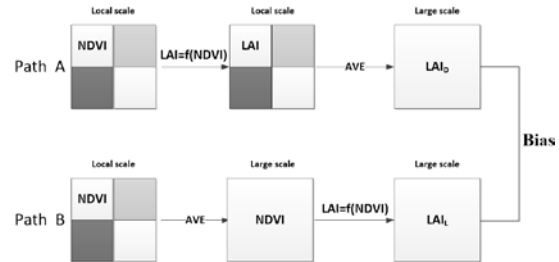
Fig.2 Sketch map of spatial aggregation and scaling bias

3.2. Wavelet transform theory

Wavelets are mathematical functions that are used to dissect data into different frequency components, each of which is characterized with a resolution appropriate to its scale (Mallat 1989). DWT analyzes the image in a discrete set of scale, wildly used in data fusion, especially that among multi-sensor images with different resolutions (Amolins et al., 2007). DWT is also suitable for remote sensing image data processing technology reflecting the characteristics of surface ecological environment. As shown in Figure 3, DWT provides a framework to decompose a signal or image into a multi-resolution representation with a low-frequency approximation image and a set of high-

frequency detail images. With the DWT, the LAI image at local scale can be decomposed into an orthogonal wavelet representation at a given coarser resolution. No extra data are produced in the decomposition procedures because of the orthogonality of the wavelet representation (Mallat,1989). According to the wavelet theory, an inclusion relation exists in the adjacent scales that the information at a local scale consists of the information in a larger scale and the loss of information during scaling as well. With the DWT, we can find where changes take place and simultaneously measure the rate of the change. Therefore, DWT is a suitable tool to analyse the multi-scale relationships in remote sensing scaling.

During the DWT decomposition, the resolution decreases exponentially at the base of two, the original image can be decomposed into four parts (as shown in Fig.3), including a low-frequency coefficient (A_1) and high-frequency coefficients (D_1^H , D_1^V , D_1^D) in horizontal, vertical and diagonal direction. In the second decomposition, the low-frequency coefficient (A_1) from the first decomposition will continue to be decomposed into a new low-frequency coefficient (A_2) and three new high-frequency coefficients (D_2^H, D_2^V, D_2^D). The low-frequency coefficient represents the approximate value at a large scale, while the high-frequency coefficients represent the information lost between adjacent scales.
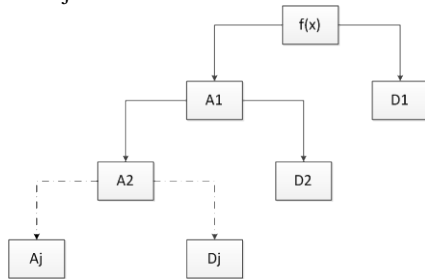
Fig.3 The decomposition of the image (the approximation and details coefficients)

3.3. DWT-based scaling bias modeling

To build the DWT-based scaling bias model, two parameters (R_{bias} and $R_{detlost}$) are first defined. The R_{bias} describes the bias rate in scaling, while $R_{detlost}$ indicates the detail lost rate in wavelet transform. Those two parameters are calculated as following:

$$R_{bias} = \frac{LAI_D - LAI_L}{LAI_D} \qquad (5)$$

$$R_{detlost} = \frac{\sqrt{(D_i^H)^2 + (D_i^V)^2 + (D_i^D)^2}}{A_i + \sqrt{(D_i^H)^2 + (D_i^V)^2 + (D_i^D)^2}} \qquad (6)$$

where LAI_D and LAI_L are the exact value and the approximation value of the LAI at a large scale, respectively. A_i represents the low-frequency coefficient. D_i^H , D_i^V and D_i^D represent the high-frequency coefficients in horizontal, vertical and diagonal direction, respectively. The subscript i represents the DWT decomposition level.

As reported previously, there is intrinsic relation between the wavelet coefficients and the scaling bias. Therefore, the bias rate R_{bias} can be expressed as the function of the detail lost rate $R_{detlost}$ as following:

$$R_{bias} = f(R_{detlost}) \qquad (7)$$

where f represents the transfer function from $R_{detlost}$ to R_{bias}.

Consequently, the corrected LAI, LAI_{cor}, based on the low-frequency coefficient and the high-frequency coefficients at the larger scale, can be estimated by combining Eq. (5)-(7) to give:

$$LAI_{cor} = \frac{LAI_L}{1 - f(R_{detlost})} = \frac{LAI_L}{1 - f\left(\frac{\sqrt{(D_i^H)^2 + (D_i^V)^2 + (D_i^D)^2}}{A_i + \sqrt{(D_i^H)^2 + (D_i^V)^2 + (D_i^D)^2}}\right)} \qquad (8)$$

4 RESULTS

4.1. Application with the priori knowledge

To fully verify the reliability, the proposed DWT-based scaling model is applied to four different aggregation scales. Here, $R_{detlost}$ are calculated from the corresponding synchronous high-resolution images. Fig. 4 shows the scaling performance at the 4 × 4 aggregation scale based on the proposed scaling models.
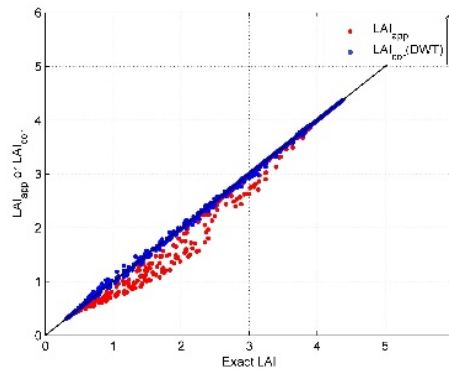
Fig.4 The scatter plot between actual LAI and estimated LAI, actual LAI and corrected LAI in Fundulea
(at 4×4 aggregation scale)

It could be easily seen that the correlation between LAI_L and LAI_D after correction was greatly improved in this site after scaling. These results demonstrate that the spatial scaling algorithms developed using the proposed method could greatly reduce the error of LAI at four aggregation scales.

To evaluate the accuracy of proposed scaling model (Eq. (8)), the RMSE (Root Mean Square Error) are used to analyze the scaling performance.

Fig.5 show the model performance of LAI estimation at four different aggregation scales based on the DWT and TSE methods. One can easily find that the scaling effect of LAI generally increases with the aggregation scale. With the proposed method, the RMSE of retrieved LAI are both reduced rapidly.
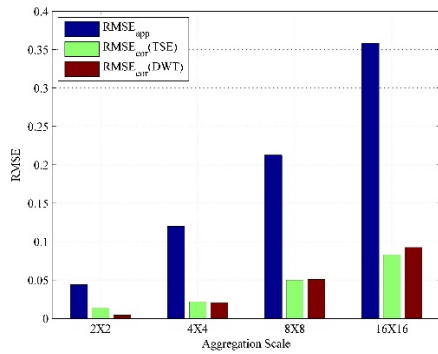
Fig.5 RMSE of retrieved LAI at 4×4 aggregation scales

As shown in Fig.5, our proposed scaling models can correct for the scale effects caused by spatial heterogeneity and model nonlinearity. If the wavelet coefficients within a large pixel are known, the scaling effect can be corrected effectively. Using either of the correction method shows great improvement. Our method can decrease the RMSE from 0.36 to 0.09 at the 16×16 aggregation scale. Thus, if wavelet coefficients are available at large scale, the proposed DWT-based method could be used to correct the coarse resolution LAI product.

4.2. Application without the priori knowledge

To further verify the reliability, the proposed DWT-based scaling model is also applied to the Fundulea site. However, the prior knowledge about $R_{detlost}$ is gained from different time. The Landsat 8 TM image on May 15 2015 is used to estimate $R_{detlost}$ and that on April 13 2015 is to evaluate the scaling performance (Fig. 6). Fig.6 shows the scatter plot between actual LAI and estimated LAI at 4×4 aggregation scale in Fundulea site. The estimated LAI after scaling bias correction become closer to the 1:1 line.
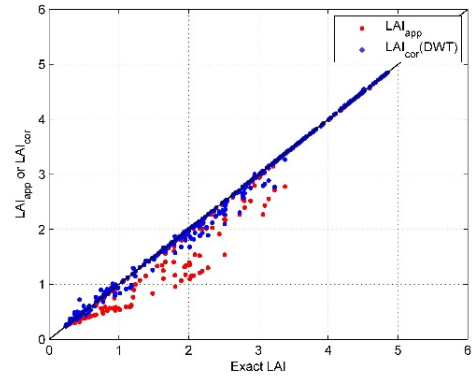
Fig.6 The scatter plot between actual LAI and estimated LAI at 4×4 aggregation scale in Fundulea site

Here, the TSE- and DWT- based methods are also compared and shown in Fig. 7. RMSE for the DWT method shows a better result at the 16×16 aggregation scale. However, the above results of TSE are under the condition that complete high-resolution data at the same time are available. In contrast, the proposed DWT-based method can achieve a good performance without the high-resolution data at the same time.
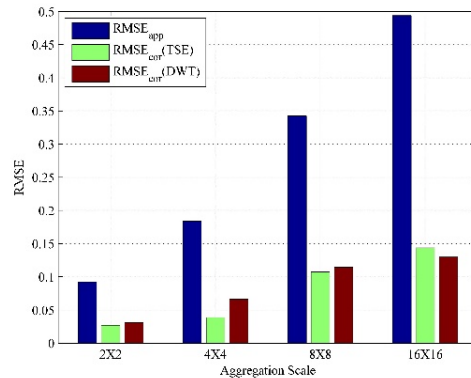
Fig.7 RMSE of retrieved LAI at different aggregation scales

5 CONCLUSIONS

In this study, we propose a new method for correcting the spatial scaling bias caused by nonlinearity of LAI retrieval model and the spatial heterogeneity. Based on characteristics of the binary discrete wavelet transform, a new DWT-based method is proposed to analyse the scaling bias. We investigated the possibility of using the relation to eliminate the scaling bias. The validation of the proposed method was carried out in different areas chosen from the VALERI database. The results show that the proposed DWT-

based method behaved a satisfactory estimation and strong flexibility, because wavelet coefficients and scaling bias have a good consist power-law relationship at different aggregation resolutions. The wavelet coefficients are adopted to represent the loss rate of scaling. It is found that it is possible to resolve the scaling bias with DWT.

ACKNOWLEDGEMENTS

REFERENCES

Amolins, K., Y. Zhang, and P. Dare. 2007. "Wavelet based image fusion techniques — an introduction, review and comparison." ISPRS Journal of Photogrammetry and Remote Sensing 62: 249-263.

Chen, J. M., and T. A. Balck. 1992. "Defining leaf area index for non-flat leaves." Plant Cell and Environment 15: 421-429.

Chen J. M. 1996. "Optically-based methods for measuring seasonal variation of leaf area index in boreal conifer stands." Agricultural and Forest Meteorology 80: 135-163.

Chen, J. M. 1999. "Spatial Scaling of a Remotely Sensed Surface Parameter by Contexture." Remote Sensing of Environment 69: 30–42.

El Maayar, M., and J. M. Chen. 2006. "Spatial Scaling of Evapotranspiration as Affected by Heterogeneities in Vegetation, Topography, and Soil Texture." Remote Sensing of Environment 102: 33–51.

Hu, Z. L., and S. Islam. 1997a. "A Framework for Analyzing and Designing Scale Invariant Remote Sensing Algorithms." IEEE Transactions on Geoscience and Remote Sensing 35: 747–55.

Hu, Z. L., and S. Islam. 1997b. "Effects of Spatial Variability on the Scaling of Land Surface Parameterizations." Boundary-Layer Meteorology 83: 441–61.

Hu, Z. L., and S. Islam. 1998. "Effects of Subgrid-Scale Heterogeneity of Soil Wetness and Temperature on Grid-Scale Evaporation and Its Parametrization." International Journal of Climatology 18: 49–63.

Garrigues, S., D. Allard, F. Baret and M. Weiss. 2006. "Influence of landscape spatial heterogeneity on the non-linear estimation of leaf area index from moderate spatial resolution remote sensing data." Remote Sensing of Environment 105: 286-298.

Jacquemoud, S., W. Verhoef, F. Baret, C. Bacour, P. J. Zarco-Tejada, G. P. Asner, C. Francois, and S. L. Ustin. 2009. "PROSPECT+SAIL models: a review of use for vegetation characterization." Remote Sensing of Environment 113: S56-S66.

Ma, L. L., C. R. Li, B.-H. Tang, L. L. Tang, Y. Y. Bi, B. Y. Zhou, and Z.-L. Li. 2008. "Impact of Spatial LAI Heterogeneity on Estimate of Directional Gap Fraction from SPOT-Satellite Data." Sensors 8: 3767–79.

Mallat S G. 1989, "A theory for multiresolution signal decomposition: the wavelet representation." IEEE Transactions on Pattern Analysis and Machine Intelligence 11:674-693.

Pelgrum, H., T. Schmugge, A. Rango, J. Ritchie, and B. Kustas. 2000. "Length-Scale Analysis of Surface Albedo, Temperature, and Normalized Difference Vegetation Index in Desert Grassland." Water Resources Research 36: 1757–65.

Raffy, M. 1992. "Change of Scale in Models of Remote Sensing: A General Method for Spatialization of Models." Remote Sensing of Environment 40: 101-112.

Raffy, M., and C. Gregoire. 1998. "Semi-Empirical Models and Scaling: A Least Square Method for Remote Sensing Experiments." International Journal of Remote Sensing 19: 2527–41.

Simic, A., J. M. Chen, J. Liu, and F. Csillag. 2004. "Spatial Scaling of Net Primary Productivity Using Subpixel Information." Remote Sensing of Environment 93: 246–58.

Wu, H., B.-H. Tang and Z.-L. Li. 2013. "Impact of nonlinearity and discontinuity on the spatial scaling effects of the leaf area index retrieved from remotely sensed data." International Journal for Remote Sensing 34: 3503-3519.

Wu, H., and Z.-L. Li. 2009. "Scale Issues in Remote Sensing: A Review on Analysis, Processing and Modeling." Sensors 9: 1768–93.

Zhang, X., G. Yan, Q. Li, Z.-L. Li, H. Wan, and Z. Guo. 2006. "Evaluating the Fraction of Vegetation Cover Based on NDVI Spatial Scale Correction Model." International Journal of Remote Sensing 27: 5359–5372.

Spatiotemporal cropland monitoring based on optical microwave and thermal infrared remote sensing data complementarities

B. Cheul*, B. Coudert*, R. Fieuzal*, F. Baup*, J. Cros, V. Rivalland*, M. Huc*

CESBIO, Université de Toulouse, CNES, CNRS, IRD, UPS, Toulouse, France
benoit.cheul@cesbio.cnes.fr

Abstract : Several methodological studies have shown the interest of using thermal infrared, microwave and optical remote sensing to constrain land surface models, more particularly water and energy budget models. Studies based on non simulated remote sensing data are however sparse because of the lack of a suitable dataset. We study the behavior of thermal infrared and C-band radar signals with time over several crops of the south-west of France, wheat and sunflower mainly, at the field level. Our objective is to make use of the strength of each wavelength domain to provide information about field heterogeneity on the same crop to take advantage of the synergy between Sentinel suite and Landsat 8 (and future TIR satellite missions in preparation as TRISHNA). We aim to identify discrepancies between remote sensing data in order to better point out specific signatures of surface and crop behavior. Remote sensing data is compared to in situ measurement, such as top soil moisture, texture, plant height, realized during the MCM'10 experiment, which covered an entire crop cycle, and coupled in-situ acquisition with satellite overpass. Visible optical remote sensing is also used for signal interpretation with green area index values recovered from the NDVI vegetation index. The heterogeneities highlighted between fields thanks to the remote sensing signals dynamics aim us to precise and distribute the value and ranges of parameters of a Soil-Vegetation-Atmosphere-Transfer (SVAT) model in order to constrain it better when it is distributed at landscape scale.

1. Introduction

Remote sensing data are widely used in continental surface modeling, whether as input or assimilation data. Among the surface models types using these data are Soil-Vegetation-Atmosphere-Transfer (SVAT) models. Two families can be distinguished (Crow et al, 2005): Water and energy balance (WEB-SVAT) and remote sensing (RS-SVAT) models. The former relying on a more detailed description of the processes to estimate surface states (e.g., soil water root zone dynamic) and energy and water budget partitioning, and the later requiring remote sensing data in input, more precisely thermal infrared (TIR) one, to simulate the surface fluxes.

Different wavelength domains can inform surface models, most of the time there are optical and TIR. The information provided is specific to the observation wavelength. Visible provide reflectance information from which are derived vegetation indexes while thermal infrared measure surface temperature and can inform about water stress (Jackson et al, 1981;Sandholt et al, 2002). Among the other type of sensor available is radar. Such data are mostly used to retrieve information such as soil moisture, and surface roughness (Zribi et al, 2005) and to provide additional information to classification (McNairn et al, 2009).

The combined use of TIR and radar data has been studied in the literature (Barret et al, 2009; Li et al, 2010 among others) to improve the monitoring of crops water budget over agricultural areas. Most of the studies focus on assimilating model output to surface properties inverted from remote sensing, generally top soil and root zone moisture, using Kalman ensemble filtering.

Another approach to better constrain SVAT model is to dynamically limit the variation interval of modeling parameters. Minimization methods based on Pareto ranking have shown an increase in model performances using the best set and ranges of parameters (Bastidas et al, 1999; Gupta et al, 1999; Demarty et al, 2005, Coudert et al., 2006).

We aim to use the second method using TIR, C-band radar and optical data to identify heterogeneities within fields of a same crop for wheat, sunflower and maize.

First we use data from the MCM'10 experiment (Baup et al, 2012) to relate TIR and C-band radar remote sensing signals evolution along multi-dates series to surface and vegetation properties and heterogeneities. Then we plan to use such temporal signatures and complementarities between radar and TIR to i) better select parameters set and ranges values for simulations, ii) improve the use of TIR to constrain the model during specific temporal windows and iii) propose a new methodology of radar and TIR dynamic coupling in order to select the better scenarios of SVAT simulation for crop water budget monitoring.

2. Dataset

Most of our data originates from the MCM'10 experiment conducted by CESBIO in the south-west of France (Figure 1). The purpose was to collect multispectral data in optical and radar domains to study the behavior of the signal over crops in each domain. Images have been collected in optical domain with SPOT4/5 and FORMOSAT-2, in radar with TERRASAR-X (X band), Radarsat-2 (C band) and ALOS (L band). A survey of thermal images available, from LANDSAT 5/7 was also conducted. Enough images are available to allow a characterization of surface changes (vegetation geometry, surface water status, water stress)
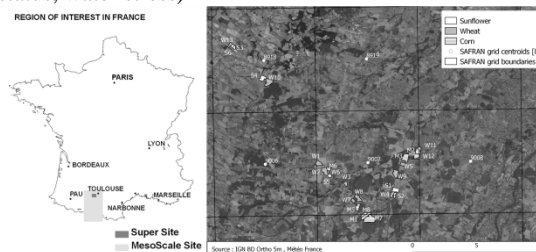
Figure 1: Localization of the studied sites

In situ information has also been compiled, with qualitative data over 300 fields and quantitative data for 37 fields. The crops studied are wheat, rapeseed, soybean, maize and sunflower. They represent the majority of the cultivated surface in this area (Dejoux et al, 2012).

Quantitative data collected range from top soil moisture (TSM) (Figure 2), aerial biomass measurements, height and soil texture. They will be used to understand the dynamics and variations of the signal between fields.
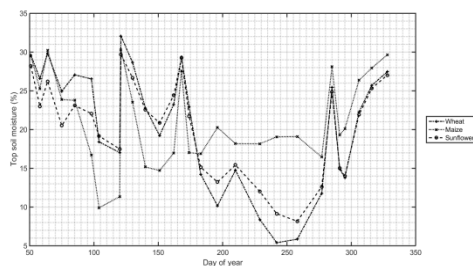
Figure 2: In-situ Mean Top Soil Moisture measured per crop type

For the work presented in this paper, thermal infrared images have been corrected from atmospheric radiation using the LANDARTS tool (Tardy, 2015). Corrected images are available at a 30 m resolution, compared to the original resolution at 120m. This resampling is obtained with the emissivity image which is created using the visible bands of the instrument (Sobrino et al. 2004). We kept 30 m resolution to maximize our number of points on each field and to leave the opportunity to study intra-fields variability available assuming the associated uncertainties.

In the radar domain, we use the quad-polarization images from Radarsat-2 (C-band). These images have been normalized for the incidence angle effect using an empirical relationship based on NDVI (Fieuzal et al, 2012), in order to be able to compare successive acquisition dates independently from the view angle. We then extracted the backscattering coefficients by fields, choosing the polarization providing the better dynamic (Fieuzal, 2013).

This work is focused on wheat, maize and sunflower, one winter crop and two summer crops (Table 1). It allows sampling different culture practices, some fields are irrigated, other are not. The fields will be described using the first letter of the crop and the number of the field (eg W5 for the fifth field of wheat).

Crop	Number of fields
Wheat	13
Maize	8
Sunflower	6

Table 1: Number of fields studied by crop

Two weather stations are situated in fields W10 and M3. Reanalysis from SAFRAN Meteo-France (Quintana-Segui et al. 2008) have also been used. It provides meteorological variables (temperature, global and atmospheric radiation, precipitations) on a 8km by 8km grid (Figure 1) with an hourly resolution.

Remote sensing surface temperature measurement has been normalized using SAFRAN air temperature in Kelvin using the relation (1).

$$T_{norm} = \frac{T_{surf} - T_{air}}{T_{air}} \qquad (1)$$

As the LANDSAT overpass of the studied area is around 10:30, we used the average air temperature of the day between 9:00 and 12h00.

Lastly, an extraction of the green area index (GAI) over the studied fields was performed (Figure 3). The GAI was calculated using the BVnet method (Baret et al, 2007).

In the two following parts, we study the behavior of the C-band radar and thermal infrared signal over wheat and sunflower more specifically. The cultural cycle is separated into 4 parts representing the main stages of the cultural cycle. The division is the following: bare soil before emergence, growth, maximum of vegetation and senescence.
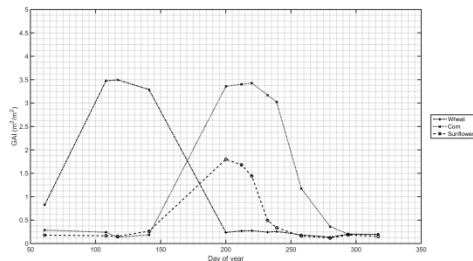
Figure 3: Mean GAI per crop from the BVnet method

3. Analysis of radar C-band and thermal infrared signature on wheat crop

To study the heterogeneity between wheat fields, we analyzed the dynamics of multidates radar backscatter coefficient versus normalized relative temperature. The objective was to pick up global and more specific behaviors in signals responses in order to be intercompared in terms of heterogeneities. To do so, each of the radar and thermal signature where first of all interpreted according to their stage of development, GAI dynamics and top soil moisture in situ measurement.

The normalized relative surface temperature versus backscattering coefficient plots were obtained assuming acceptable interpolation of the backscattering coefficient on the day of thermal infrared acquisition.
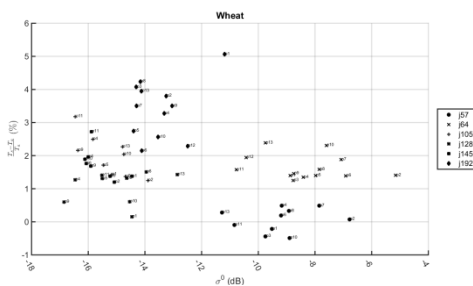
Figure 4: Normalized relative surface temperature versus C-band backscattering coefficient for wheat

Such representation (Figure 4) illustrates the evolution of the backscattered radar signal with the changes of the vegetation and hints at the water stress periods with normalized relative temperature. It has been shown (Mattia et al, 2003 that in VV polarization the backscattering coefficient decreases with the vertical development of the plant. It then increases slowly as the canopy is drying. However, even when wheat is the densest there is still some sensitivity to soil moisture (Mattia et al, 2003).

During the early stages of growth, before DoY 70, the plant height is still low (<30 cm), the GAI is also

small (Figure 6) and the radar signal is dominated by the response from soil moisture. During this period, surface temperature cannot provide information on soil moisture status because of the mixed response of soil and vegetation. On the other hand C-band backscattering signal allows identifying three types of behaviors. The first one is field W2 which displays a higher than average backscattering coefficient on days 57 and 64, hinting at higher top soil moisture. In an opposite fashion, fields W11, W12 and W13 have a backscatter coefficient about 1dB lower which indicates lower soil moisture.
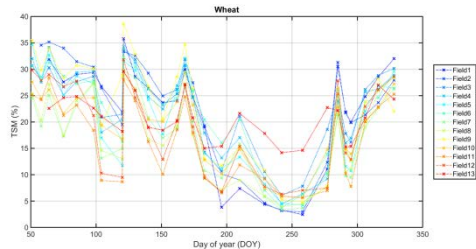
Figure 5: In-situ measurement of TSM for wheat fields
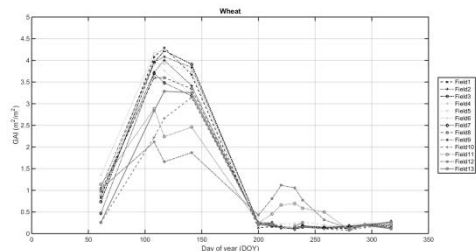
Figure 6: GAI profiles for wheat fields

Soil moisture and precipitations indicate that between DOY 105 and DOY 120, fields experiment a drought episode. As we are at the maximum of plant development, variations between fields are likely to be related to a difference in soil water status. During this period, field W2 shows a lower relative surface temperature, about 1%, and a higher backscattering coefficient, of 1dB. This would suggest a higher TSM for this field during this period, as the plant has access to more water and is then more capable of transpiration and to regulate its temperature. The radar indicator confirms this tendency, as a higher soil moisture results in more energy being backscattered. On the other hand Field W11 shows the opposite behavior, which we relate to a higher water stress level. This observation is confirmed two ways. First by the in-situ measurements, which show that field W2 consistently has higher soil moisture and W11 a lower one (Figure 5). Then the data from DoY 128 corroborate our reasoning. Indeed, the region experienced a large precipitation event on DoY 123

(≈30mm), with a direct repercussion on top soil moisture, and most of the fields show the same tendency on relative surface temperature, which decreases, and backscattering coefficient, which increases. Different hydrodynamic properties, such as water reserve and hydraulic conductivity, would then be attributed based on the tendencies observed during this time window.

The analysis can also be done between main stages of development to precise tendencies we observed. For example during growth, fields W11 and W13 signals indicated lower soil moisture, which we could have related to the same origin. Nevertheless, the data from DoY 105, with W13 presenting a lower relative temperature difference and a higher backscattering signal, shows a different response to the water stress period. In situ measurement confirms that field W13 keeps a higher TSM, about 10%, compared to W11. Additional data shows that W13 has a higher clay percentage, which would result on a higher water reserve and a higher hydraulic conductivity limiting vertical water transfer in soil. The initial assumption that both fields would have similar soil properties can then be nuanced and precised.

4. Analysis of radar C-band and thermal infrared signature on sunflower crop

The methodology used for sunflower is the same than for wheat, we used the same relative surface temperature versus backscattering coefficient representation (Figure 7). However the temporal sampling is not as good as the one we had for wheat, with a large time period, from DoY 145 to 192 without thermal images.

We used the VV polarization from Radarsat-2 images. The evolution of the signal is different than the one presented for wheat. Here, plant growth is accompanied by an increase of the backscattering coefficient, followed by a plateau during the maximum of vegetation. Senescence is marked by a decrease of the backscattering coefficient.
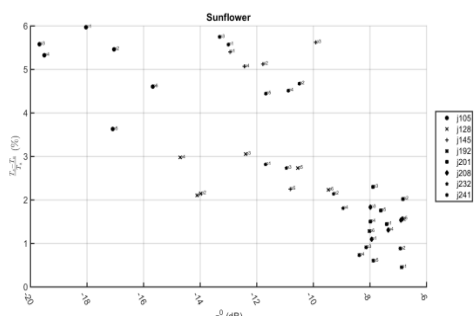
Figure 7: Normalized relative surface temperature versus C-band backscattering coefficient for sunflower

On DOY 105 and 128 three groups can be identified: S3 and S4, S1 and S2, S5 and S6. These groups are consistent during this period but no clear relation to TSM can be made. The only observation possible is the effect of the rain even on DoY 123, which causes the decrease of temperature and increase of the backscattering coefficient.

On DOY 145, field S5 displays a lower surface temperature of about 4%. This is related to the higher top soil moisture observed during this period. No clear relation appears between backscattering coefficient and TSM (Figure 8). Our GAI vales are of no use at this time, as they under sample the growing period and can't inform development discrepancies that could be exposed by the different backscattering coefficients.

During senescence, on DoY 232 and 241, two groups can be identified: S1 and S3, S2 and S4. The signal is evolving the same way, with an increase of relative temperature difference caused by the drying of the plant and the decrease on the backscattered coefficient, because leaves are falling. However the magnitude of the evolution is different, S1 and S3 show a larger evolution than S2 and S4 for the same dates. This would indicate a later senescence phase for the latter fields. This evolution is confirmed by the GAI data (Figure 9), where fields S3 and S1 have a decreasing GAI at least from DoY 212. Fields S2 and S4 display a higher GAI from this day to the end of the cultural cycle. In our modeling perspective, we would start using parameters optimized for senescence sooner for fields S1 and S3.
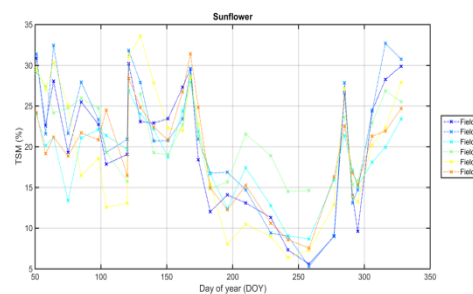
Figure 8: In-situ measurements of TSM for sunflower fields
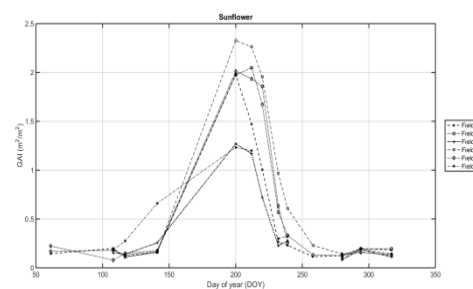
Figure 9: GAI profiles for sunflower fields

5. Conclusion

This paper presented the dataset used to study the combined use of thermal infrared and C-band radar remote sensing data to distinguish heterogeneities between fields of the same crop. Examples of analysis and possible model parameterizations have been presented. Our aim is now to make use of the differences between fields to run a model simulation of the water and energy budget in order to better constrain them.

References:

Bastidas, L. A., Hoshin Vijai Gupta, S. Sorooshian, W. James Shuttleworth, and Z. L. Yang. "Sensitivity Analysis of a Land Surface Scheme Using Multicriteria Methods." *Journal of Geophysical Research: Atmospheres* 104, no. D16 (1999): 19481–90.

Baret, Frédéric, Olivier Hagolle, Bernhard Geiger, Patrice Bicheron, Bastien Miras, Mireille Huc, Béatrice Berthelot, Fernando Niño, Marie Weiss, and Olivier Samain. "LAI, fAPAR and fCover CYCLOPES Global Products Derived from VEGETATION: Part 1: Principles of the Algorithm." *Remote Sensing of Environment* 110, no. 3 (2007): 275–86.

Barrett, Damian J., and Luigi J. Renzullo. "On the Efficacy of Combining Thermal and Microwave Satellite Data as Observational Constraints for Root-Zone Soil Moisture Estimation." *Journal of Hydrometeorology* 10, no. 5 (2009): 1109–27.

Baup, Frédéric, Remy Fieuzal, Claire Marais-Sicre, Jean-Francois Dejoux, Valérie Le Dantec, Patrick Mordelet, Martin Claverie, Olivier Hagolle, Ana Lopes, and Pascal Keravec. "MCM'10: An Experiment for Satellite Multi-Sensors Crop Monitoring from High to Low Resolution Observations." In *Geoscience and Remote Sensing Symposium (IGARSS), 2012 IEEE International*, 4849–52. IEEE, 2012.

Crow, Wade T., Fuqin Li, and William P. Kustas. "Intercomparison of Spatially Distributed Models for Predicting Surface Energy Flux Patterns during SMACEX." *Journal of Hydrometeorology* 6, no. 6 (2005): 941–53.

Dejoux, J.-F., Gérard Dedieu, Olivier Hagolle, Danièle Ducrot, Jean-Claude Menaut, Eric Ceschia, Frédéric Baup, Valérie Demarez, Claire Marais-Sicre, and Mohamed Kadiri. "Kalideos OSR MiPy: Un Observatoire Pour La Recherche et La Démonstration Des Applications de La Télédétection à La Gestion Des Territoires." *Revue Française de Photogrammétrie et de Télédétection*, no. 197 (2012): 17–30.

Demarty, Jérôme, Catherine Ottlé, Isabelle Braud, Albert Olioso, Jean Pierre Frangi, Hoshin V. Gupta, and Luis A. Bastidas. "Constraining a Physically Based Soil-vegetation-atmosphere Transfer Model with Surface Water Content and Thermal Infrared Brightness Temperature Measurements Using a Multiobjective Approach." *Water Resources Research* 41, no. 1 (2005).

Fieuzal, Rémy. "Apports Des Données Radar Pour L'estimation Des Parametres Biophysiques Des Surfaces Agricoles." Université Toulouse III-Paul Sabatier, 2013.

Fieuzal, Remy, Frédéric Baup, and Claire Marais-Sicre. "Sensitivity of TERRASAR-X, RADARSAT-2 and ALOS Satellite Radar Data to Crop Variables." In *Geoscience and Remote Sensing Symposium (IGARSS), 2012 IEEE International*, 3740–43. IEEE, 2012.

Gupta, Hoshin Vijai, L. A. Bastidas, S. Sorooshian, W. James Shuttleworth, and Z. L. Yang. "Parameter Estimation of a Land Surface Scheme Using Multicriteria Methods." *Journal of Geophysical Research: Atmospheres* 104, no. D16 (1999): 19491–503.

Jackson, Ray D., S. B. Idso, R. J. Reginato, and P. J. Pinter. "Canopy Temperature as a Crop Water Stress Indicator." *Water Resources Research* 17, no. 4 (1981): 1133–38.

Li, Fuqin, Wade T. Crow, and William P. Kustas. "Towards the Estimation Root-Zone Soil Moisture via the Simultaneous Assimilation of Thermal and Microwave Soil Moisture Retrievals." *Advances in Water Resources* 33, no. 2 (2010): 201–14.

Mattia, Francesco, Thuy Le Toan, Ghislain Picard, Francesco I. Posa, Angelo D'Alessio, Claudia Notarnicola, Anna Maria Gatti, Michele Rinaldi, Giuseppe Satalino, and Guido Pasquariello. "Multitemporal C-Band Radar Measurements on Wheat Fields." *IEEE Transactions on Geoscience and Remote Sensing* 41, no. 7 (2003): 1551–60.

McNairn, Heather, Catherine Champagne, Jiali Shang, Delmar Holmstrom, and Gordon Reichert. "Integration of Optical and Synthetic Aperture Radar (SAR) Imagery for Delivering Operational Annual Crop Inventories." *ISPRS Journal of Photogrammetry and Remote Sensing* 64, no. 5 (2009): 434–49.

Quintana-Segui, P., Le Moigne, P., Durand, Y., Martin, E., Habets, F., Baillon, M., ... & Morel, S. (2008). Analysis of near-surface atmospheric variables: Validation of the SAFRAN analysis over France. *Journal of applied meteorology and climatology*, 47(1), 92-107.

Sandholt, Inge, Kjeld Rasmussen, and Jens Andersen. "A Simple Interpretation of the Surface Temperature/vegetation Index Space for Assessment of Surface Moisture Status." *Remote Sensing of Environment* 79, no. 2 (2002): 213–24.

Zribi, Mehrez, Nicolas Baghdadi, Noha Holah, and O. Fafin. "New Methodology for Soil Surface Moisture Estimation and Its Application to ENVISAT-ASAR Multi-Incidence Data Inversion." *Remote Sensing of Environment* 96, no. 3 (2005): 485–96

Estimating grassland above-ground biomass using Landsat8 OLI imagery and regression kriging method in Hulunber, China

Lei Ding†, Zhenwang Li †, Beibei Shen, Xu Wang, Ruirui Yan, Xiaoping Xin*

National Hulunber Grassland Ecosystem Observation and Research Station, Institute of Agricultural Resources and Regional Planning, Chinese Academy of Agricultural Sciences, Beijing 100081, China

First author: dinglei0206@126.com

Corresponding author: xinxiaoping@caas.cn

† These authors contributed equally to this work.

ABSTRACT - *Accurate estimating grassland above-ground biomass (AGB) is important to estimate grassland productivity and to assess global carbon balance. This study used the regression kriging (RK) method to estimate grassland AGB in northeast China based on the Landsat8 OLI images, three remote sensing variables (band4, normalized difference vegetation index (NDVI), and enhanced vegetation index (EVI)) were used to build RK models separately and to explore their capability for modeling spatial distribution of grassland AGB. The results were validated using the ground measurements and compared with the results of the simple regression (SR) method. The results showed an improved performance of the RK method compared to the SR method. For the SR method, model based on band4 had the best performance in terms of root mean square errors (RMSE, 21.37 g/m2), while for the RK method, models based on NDVI (RMSE=17.78 g/m2) and EVI (RMSE=17.48 g/m2) had a similar performance and provided a better estimation than that of band4 (RMSE=20.14 g/m2). The total grassland AGB in the study region is 1681.20 kiloton and mean AGB density is 100.85 g/m2, the density is decreasing with an order of mountain meadow steppe, temperate meadow steppe, lowland meadow steppe, temperate steppe, and desert steppe.*

1 INTRODUCTION

Above ground biomass (AGB) is defined as the dry weight of all above ground live mass per unit area (Dong et al., 2003). it provides the basis to estimate aboveground net primary productivity (Lauenroth et al., 1986). In the pasture area, the amount of grassland AGB determines forage availability and herbivore carrying capacity (Jobbágy et al., 2002;Mutanga and Skidmore, 2004;Yahdjian and Sala, 2006). Timely and accurate monitoring of the quantity of grass-land AGB can provide the scientific data to regulate stocking rates for sustainable use of grassland resources (Tucker, C. and Sellers, 1986;Wang et al., 2006). Traditional method to estimate AGB is mainly conducted by field surveys, although it can provide a better estimation of vegetation AGB, they are too labor- and time-consuming over large areas (Xie et al., 2009;Paul et al., 2013) which limited its use over large areas (Viana et al., 2012). Remotely sensed data, which are endowed with high temporal resolution and the capacity for large-scale observation, are widely used for large area AGB estimation.

A number of AGB estimation methods have been developed from remote sensing data. The most popular and commonly used approaches are empirical statistical methods, which link various predictor variables derived from remotely sensed data to AGB

values measured on the ground. Another approach widely used is the machine learning method, such as artificial neural networks, support vector machines, and random forests (RFs). Geostatistical prediction methods, including ordinary kriging (OK), universal kriging (UK), and regression kriging (RK), which model the data structure of spatial autocorrelation and incorporate this information in the response variables for unsampled locations, have also been used to map environmental variables (Li et al., 2016). Recent studies have shown the superiority of RK when compared to the other two methods (Hernández-Stefanoni et al., 2011;Li et al., 2016).

To better estimate grassland AGB, this study used the RK method to build models with three remote sensing variables (band4, normalized difference vegetation index (NDVI), and enhanced vegetation index (EVI)) from Landsat8 OLI images. The model for each variable was then validated using the ground measurements, a simple regression (SR) model for each variable was also built to compare the result with that of RK method.

2 METHODS AND DATA

2.1 Study Area

Hulunber is located in the northeastern part of Inner Mongolian, China, and is a part of Mongolian

Plateau in central Asia. Chenbarhu Banner is located in the backland of Hulunber (48º48'-50º12' N, 118º22' –121º02' E), this region is characterized by a semi-arid inland climate with an annual mean precipitation of 300-550 mm and annual mean temperature about 1 ℃(Nie et al., 2005). The average elevation is 677 m, and rise from the west to the east. The length of growing season is approximately 140 days and lasts from May to September (Tang et al., 2015). Grassland is the biggest ecosystem in this region and five main grassland types are included: lowland meadow steppe, mountain meadow steppe, temperate steppe, temperate meadow steppe and desert steppe. The total area of available steppe is about $1.67 \times 10^6 \, hm^2$.
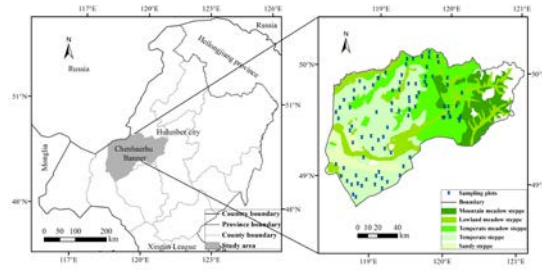
Figure 1. Study area and sampling plots

2.2 Sample Design and Field Measurements

Field survey was performed from July 9 to July 16 in 2015. The 1:1,000,000 digital vegetation map of People's Republic of China was used to guide the location of the survey plots relative to the different vegetation types. Each survey sample plot was 30 m × 30 m with homogeneous canopy, which is well-suited for the 30 m resolution Landsat data. Three 1 m × 1 m quadrats were randomly selected in each sample plot. The grassland AGB was obtained using the harvest method. Firstly, cut off the fresh grass from the ground with a stubble no more the 0.5 cm, and then brought the fresh grass to the laboratory, dried it under the temperature of 65℃ for 48h in the oven, finally, measured and recorded the weight. The quadrat's AGB is the total dry grass weight of each species. The sample plot's AGB is the average weights of three quadrats. A Global Positioning System (GPS) receiver, capable of providing real-time positioning with 2m accuracy, was used to obtain the coordinates for these sample plots. In total, data for 89 sample plots were obtained. Then, 56 samples (2/3 of the total) was randomly selected to train the models, and the remaining of 28 sample plots (1/3 of the total) was independently used to validate model performance.

2.3 Satellite Data

Landsat8 OLI lever-1 standard data products were acquired from USGS Earth Explorer website (http://earthexplorer.usgs.gov/). The images were radiometrically and geometrically corrected and were projected as UTM coordinates (WGS84 datum, Zone 51N). In order to cover the study area, four scenes of Landsat8 images corresponding to the dates of the field survey were collected in this study. Two of the images (Path 123, row 25 and 26) were acquired on July 5; the other two scenes (Path 124, row 25 and 26) were acquired on July 12. All images were with high quality, and minimal (<10%) or no cloud contamination. To obtain the reflectance of the top of canopy (TOA), the images were atmospherically corrected using the FLAASH (Fast Line-of-sight Atmospheric Analysis of Spectral Hypercubes) program embedded in ENVI 4.8 software (Agrawal et al., 2011).

Two vegetation indices were calculated from the TOA reflectance images and were used in this study for regression and geostatstical analysis, they are Normalized Difference Vegetation Index (NDVI) (Rouse et al., 1974) and Enhanced Vegetation Index (EVI) (Huete, A.R. et al., 1997;Huete, A. et al., 1999). The indices were computed using the following equations:

$$NDVI=(NIR-R)/(NIR+R) \qquad (1)$$

$$EVI=(2.5(NIR-R))/(1+NIR+6R-7.5B+L_2) \qquad (2)$$

Where B, R, NIR refers to the reflectances in the blue, red and near infrared bands, respectively.

2.4 Regression Kriging

RK is a hybrid geostatistics method that combines a linear regression method with the ordinary kriging of the residuals (Castillo-Santiago et al., 2013). In the process of RK, the predictions are combined from two parts: one is the predictied trend (obtained by regressing the primary variable on the auxiliary predictor using generalized least-squares regression, the other is the residuals, which are interpolated using OK (Viana et al., 2012). Finally, predictions at unvisited locations $\hat{z}_{RK}(s_0)$ are performed by summing the predicted trend and residuals(Hengl et al., 2007).

$$\hat{z}_{RK}(s_0) = \sum_{k=0}^{p}\hat{\beta}_k \, q_k(s_0) + \sum_{i=1}^{n}\lambda_i \times \varepsilon(s_i) \qquad (3)$$

where $\hat{\beta}_k$ corresponds to the estimated trend model coefficients, $q_k(s_0)$ represents the predictive variables at the location s_0, $\varepsilon(s_i)$ is the regression residual, λ_i is the kriging weight determined by the spatial autocorrelation structure of the residual, and *p* is the number of auxiliary predictors. The analysis was accomplished using the "gstat" package (Pebesma, 2004) within the statistical software package R 3.3.3.

2.5 Model Assessment

The results were validated with data from the field sampling. The root mean square error (RMSE) was used to determine which models have more precision in the estimation of grassland AGB in the.

$$RMSE = \sqrt{\frac{1}{n}\sum_{i=1}^{n}(y_i - \hat{y}_i)^2} \qquad (4)$$

where $\hat{y}_i$ the predicted AGB value, y_i is the measured AGB value, i is the number of the sample plot, and n is the number of measured values in the validation data.

3 RESULTS AND DISCUSSION

3.1 Correlation and Regression Analysis

The linear correlation analysis is shown as Table 1. All spectral bands are significantly correlated with AGB, the band4 (red band) was nore noticeable for its highest negative coefficient value. The B5 (NIR band) is the only one have a positive correlation. NDVI and EVI also showed a strong correlation with AGB with the correlation coefficients larger than 0.7, NDVI has higher correlation values than EVI. The band4, NDVI, and EVI were chosen for the following regressing and geostatstical analysis.

Table 1. Correlation coefficients between image variables and AGB

Variable	Correlation coefficients (n=84)
band1	-0.731**
band2	-0.735**
band3	-0.719**
band4	-0.746**
band5	0.471**
band6	-0.744**
band7	-0.721**
NDVI	0.731**
EVI	0.708**

**refers to a significant correlation between image variables and AGB ($P < 0.01$).

3.2 Geostatistical Analysis

The empirical variograms built from the residuals of the regression models clearly show spatial autocorrelation, the variance of residuals increasing with distance between plots reaching an inflection point at different range for the three variables (Table 2 and Figure. 2). The three theoretical models fit the data well, independently of the variables employed: band4, NDVI and EVI. The adjusted theoretical models ranged from 13.05 to 43.68 km, distances at which the observations were independent.

Table 2. Parameters of the fitted empirical variogram models built from the residuals for RK

Variable	RK			
	Model	Sill	Range	Nugget
band4	Exponential	595.29	14111.75	456.80
	Gaussian	599.20	17408.81	487.52
	Spherical	583.10	24559.61	448.08
NDVI	Exponential	631.22	33950.91	375.91
	Gaussian	583.69	24498.59	416.30
	Spherical	563.05	43684.25	374.03
EVI	Exponential	647.71	15222.55	66.67
	Gaussian	616.79	13046.56	240.11
	Spherical	605.59	37128.79	181.53
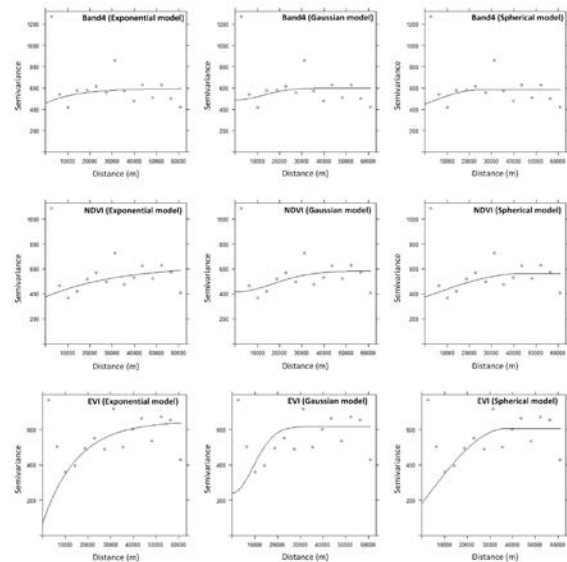
Figure 2. Plot of experimental and theoretical variograms of residuals.

3.3 Model Accuracy

Validated using ground measurements, the models based on RK method presented the least error (Table 3), and all had an improved accuracy from the SR method. The exponential model of the RK method for the three variables produced lowest RMSE and MAE and was chosen for kriging interpolation. For the SR method, model based on band4 had the best performance in terms of root mean square errors (RMSE, 21.37 g/m²), while for the RK method, models based on NDVI (RMSE=17.78 g/m²) and EVI (RMSE=17.48 g/m²) had a similar performance and provided a better estimation than that of band4 (RMSE=20.14 g/m²).

Table 3. Validation of the regression kriging and simple regression methods using the ground measurements.

Variable	RK		SR
	Model	RMSE (g/m²)	RMSE (g/m²)
band4	Exponential	20.14	21.37
NDVI	Exponential	17.78	22.19
EVI	Exponential	17.48	23.75

3.4 Biomass Distribution in Different Grassland Types

According to the regression and accuracy analysis, the result of exponential model of the RK method built with EVI was used to estimate grassland AGB (Table 4). In general, the AGB shows an increasing trend from west to east. The total grassland AGB in the study region is 1681.20 kiloton and mean AGB density is 100.85 g/m², the AGB density is decreasing with an order of mountain meadow steppe, temperate meadow steppe, lowland meadow steppe, temperate steppe, and sandy steppe.Temperate meadow steppe was estimated to have the largest AGB, sandy steppe have the smallest AGB.
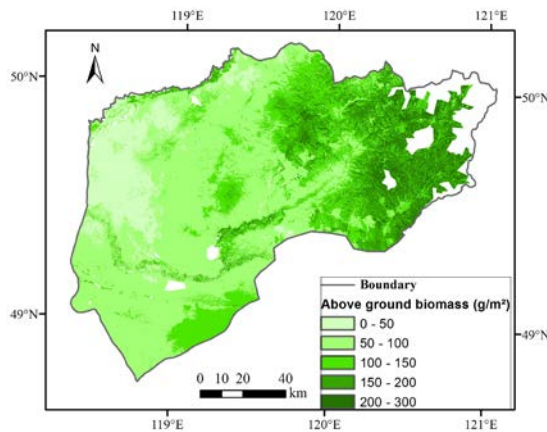
Figure 4. The above ground biomass spatial distribution of Chenbarhu Banner

Table 4. The above ground biomass of different grassland types

Grassland types	Area (10⁴ hm²)	AGB density (g/m²)	Total AGB (kt)
MMS	18.64	179.79	335.19
LMS	29.95	108.97	326.34
TMS	42.78	110.92	474.51
TS	63.72	72.82	463.99
SS	11.61	69.92	81.17
WR	166.70	100.85	1681.20

MMS, LMS, TMS, TS, SS, WR represent Mountain meadow steppe, Lowland meadow steppe, Temperate meadow steppe, Temperate steppe and Sandy steppe respectively.

4 CONCLUSION

This study explored the RK method in estimating grassland AGB in northeast China, the band4, NDVI and EVI were used as the indenpent variables to built RK models separately. Validation results showed that RK models for the three variables all had an improved accuracy than the SR method, the exponential model of the RK method produced better estimation.

REFERENCES

Agrawal, G., Sarup, J.Bhopal, M., 2011. Comparision of QUAC and FLAASH atmospheric correction modules on EO-1 Hyperion data of Sanchi, Int. J. Adv. Eng. Sci. Technol, 4, 178-186.

Castillo-Santiago, M., Ghilardi, A., Oyama, K., Hernández-Stefanoni, J.L., Torres, I., Flamenco-Sandoval, A., Fernández, A.Mas, J.-F., 2013. Estimating the spatial distribution of woody biomass suitable for charcoal making from remote sensing and geostatistics in central Mexico, Energy for Sustainable Development, 17, 2, 177-188.

Dong, J., Kaufmann, R.K., Myneni, R.B., Tucker, C.J., Kauppi, P.E., Liski, J., Buermann, W., Alexeyev, V.Hughes, M.K., 2003. Remote sensing estimates of boreal and temperate forest woody biomass: carbon pools, sources, and sinks, Remote Sensing of Environment, 84, 3, 393-410.

Hengl, T., Heuvelink, G.B.M.Rossiter, D.G., 2007. About regression-kriging: From equations to case studies, Computers & Geosciences, 33, 10, 1301-1315.

Hernández-Stefanoni, J.L., Gallardo-Cruz, J.A., Meave, J.A.Dupuy, J.M., 2011. Combining geostatistical models and remotely sensed data to improve tropical tree richness mapping, Ecological Indicators, 11, 5, 1046-1056.

Huete, A., Justice, C.Leeuwen, W.V., 1999. MODIS Vegetation Index (MOD13). Algorithm theoretical basis document,

Huete, A.R., Liu, H.Q., Batchily, K.Leeuwen, W.V., 1997. A comparison of vegetation indices over a global set of TM images for EOS-MODIS, Remote Sensing of Environment, 59, 3, 440-451.

Jobbágy, E.G., Sala, O.E.Paruelo, J.M., 2002. Patterns and controls of primary production in the Patagonian steppe: a remote sensing approach, Ecology, 83, 2, 307-319.

Lauenroth, W., Hunt, H., Swift, D.Singh, J., 1986. Estimating aboveground net primary production in grasslands: a simulation approach, Ecological Modelling, 33, 2-4, 297-314.

Li, Z., Wang, J., Tang, H., Huang, C., Yang, F., Chen, B., Wang, X., Xin, X.Ge, Y., 2016. Predicting Grassland Leaf Area Index in the Meadow Steppes of Northern China: A Comparative Study of Regression Approaches and Hybrid Geostatistical Methods, Remote Sensing, 8, 8, 632.

Mutanga, O.Skidmore, A.K., 2004. Narrow band vegetation indices overcome the saturation problem in biomass estimation, International Journal of Remote Sensing, 25, 19, 3999-4014.

Nie, H.G., Yue, L.P., Wen, Y., Li, Z.P.Yang, X.K., 2005. Present Situation, Evolution Trend and Causes of Sandy Desertification in Hulunbuir Steppe, Journal of Desert Research, 25, 5, 5.

Paul, K.I., Roxburgh, S.H., England, J.R., Ritson, P., Hobbs, T., Brooksbank, K., Raison, R.J., Larmour, J.S., Murphy, S.Norris, J., 2013. Development and testing of allometric equations for estimating above-ground biomass of mixed-species environmental plantings, Forest Ecology and Management, 310, 483-494.

Pebesma, E.J., 2004. Multivariable geostatistics in S: the gstat package, Computers & Geosciences, 30, 7, 683-691.

Rouse, J.W., Jr, Haas, R.H., Schell, J.A.Deering, D.W., 1974. Monitoring Vegetation Systems in the Great Plains with Erts, Nasa Special Publication, 351, 309.

Roy, D.P., Wulder, M.A., Loveland, T.R., C.E, W., Allen, R.G., Anderson, M.C., Helder, D., Irons, J.R., Johnson, D.M., Kennedy, R., Scambos, T.A., Schaaf, C.B., Schott, J.R., Sheng, Y., Vermote, E.F., Belward, A.S., Bindschadler, R., Cohen, W.B., Gao, F., Hipple, J.D., Hostert, P., Huntington, J., Justice, C.O., Kilic, A., Kovalskyy, V., Lee, Z.P., Lymburner, L., Masek, J.G., Mccorkel, J., Shuai, Y., Trezza, R., Vogelmann, J., Wynne, R.H.Zhu, Z., 2014. Landsat-8: Science and product vision for terrestrial global change research, Remote Sensing of Environment, 145, 154-172.

Tang, H., Li, Z., Zhu, Z., Chen, B., Zhang, B.Xin, X., 2015. Variability and climate change trend in vegetation phenology of recent decades in the Greater Khingan Mountain area, Northeastern China, Remote Sensing, 7, 9, 11914-11932.

Tucker, C.Sellers, P., 1986. Satellite remote sensing of primary production, International Journal of Remote Sensing, 7, 11, 1395-1416.

Tucker, C.J., 1979. Red and photographic infrared linear combinations for monitoring vegetation, Remote Sensing of Environment, 8, 2, 127-150.

Viana, H., Aranha, J., Lopes, D.Cohen, W.B., 2012. Estimation of crown biomass of Pinus pinaster stands and shrubland above-ground biomass using forest inventory data, remotely sensed imagery and spatial prediction models, Ecological Modelling, 226, 22-35.

Wang, R., Qin, Z., Jiang, L.Ye, K. (2006). Valuation of rangeland ecosystem degradation with remote sensing technology in China. Proceedings of SPIE, the International Society for Optical Engineering, Society of Photo-Optical Instrumentation Engineers.

Xie, Y., Sha, Z., Yu, M., Bai, Y.Zhang, L., 2009. A comparison of two models with Landsat data for estimating above ground grassland biomass in Inner Mongolia, China, Ecological Modelling, 220, 15, 1810-1818.

Yahdjian, L.Sala, O.E., 2006. Vegetation structure constrains primary production response to water availability in the Patagonian steppe, Ecology, 87, 4, 952-962.

Cirrus cloud removal in Sentinel-3 SLSTR images using an empirical algorithm in the Cirrus band

J.C. Fortea and J. Moreno
Laboratory for Earth Observation, University of Valencia
juan.fortea@uv.es

ABSTRACT   *Cloud identification is one of the first tasks usually carried out when using satellite imagery for land and ocean applications. Cirrus clouds are thin, transparent, or semi-transparent in most visible spectral bands and so they are one of the most elusive cloud types.*

A spectral band centred near the strong 1.38 μm water vapor absorption band is useful for monitoring cirrus clouds (Gao et al. 1993), thus that band has been incorporated into the latest sensors and platforms. Cirrus clouds comprise ice crystals and form at high altitudes at the highest layers of the troposphere, normally 7-20 km above the Earth's surface. Recent observations have shown that cirrus cover can reach as high as 30% of the globe, and has doubled over the past 40 years.

This work contributes to how the effect of cirrus clouds can be removed from the surface reflectance at the top of the atmosphere instead of eliminating pixels identified as being covered by cirrus clouds. Here we apply an empirical algorithm (Gao et al. 2002) to the SLSTR sensor on board the Sentinel-3A satellite, using the cirrus spectral band.

1. INTRODUCTION

Because of the absorption of water vapor, which is mainly concentrated in the lower atmospheric layers, reflected solar radiation in the cirrus band is mainly absorbed at these wavelengths. This approach attempts to detect light from this spectral region, i.e. light reflected by high-altitude cirrus clouds and not completely absorbed by the small amount of atmospheric water vapor above these cirrus clouds (figure 1).
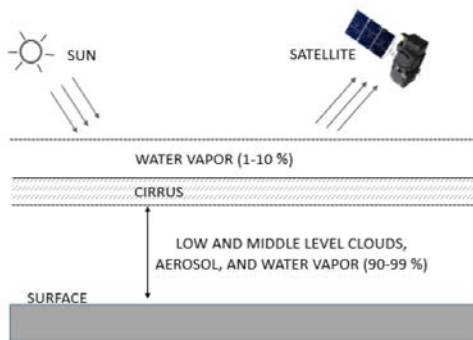
Figure 1. Solar and view geometry. The atmosphere-earth system can be viewed as comprising three layers.

Thus, this empirical algorithm (Gao et al. 2002) uses the information from the cirrus band to correct other spectral bands for the effects of cirrus clouds. This methodology is based on the quasi-linear relationship between the reflectance of cirrus clouds in the cirrus band and the cirrus reflectance in other visible and shortwave IR bands. Here we combine this algorithm with cirrus band information to eliminate the effects of these clouds in SLSTR Sentinel-3 images, therefore obtaining surface parameters from pixels previously defined as cirrus clouds.

2. MATERIAL AND METHODOLOGY

2.1. Methodology

The top of the atmosphere (TOA) reflectance can be expressed for each band as:

$$\rho^* = (\pi \cdot L)/(\mu_0 \cdot E_0) \tag{1}$$

where L is the band radiance, μ_0 is cosine solar zenith angle, and E_0 is the solar irradiance at the TOA. Thus, in the case of a cirrus cloud, for each spectral band we have:

$$\rho^* = \rho_c + T_c \cdot \rho \tag{2}$$

where ρ_c is the cirrus reflectance, T_c is the two-way transmission (direct and diffuse) through the cirrus cloud, and ρ is the reflectance of the surface. With the linear relationship between the cirrus reflectance in the cirrus band ρ_c (1378 nm) and another selected band, ρ_c (λ):

$$\rho_c(1378 \text{ nm}) = K_\lambda \cdot \rho_c(\lambda) \tag{3}$$

where K_λ is the empirical parameter, we can obtain the 'cirrus-path-radiance corrected image' as:

$$T_c \cdot \rho = \rho^* - \rho_c (1378 \text{ nm}) \tag{4}$$

2.2. Material

We applied this methodology to the SLSTR Copernicus Sentinel-3 images acquired on the January 31, 2017 at 10:23 h (UTC) over the south-east of the Iberian Peninsula (figure 2).
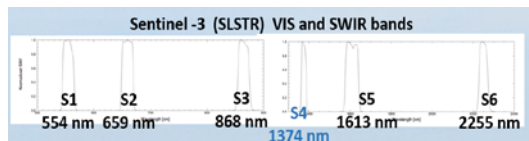
Figure 2. SLSTR-Sentinel-3 spectral bands. The cirrus band is at S4 (1374 nm).

The meteorological situation was defined by a cold front arriving to the west of the Iberian Peninsula, pushing the air mass over the Peninsula to the east, with the presence of low, medium, and high clouds (figures 3 and 4).
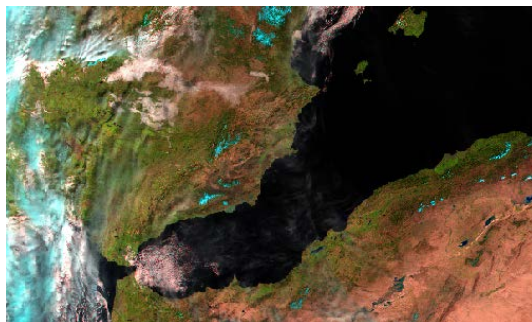
Figure 3. Image of the south-east of the Iberian Peninsula on January 31, 2017. SLSTR Sentinel-3 RGB(S5-S3-S2).
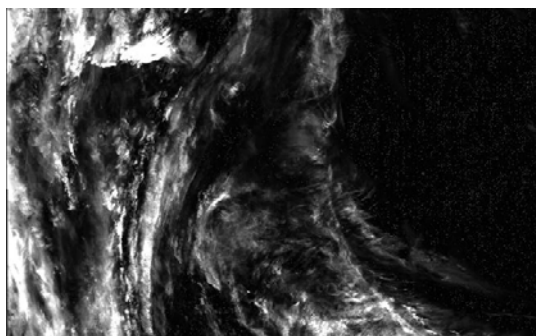
Figure 4. Cirrus band image (S4 SLSTR Sentinel-3) for the same zone and time as in figure 3. Only cirrus reflectance was detected, and no surface or low-level cloud reflectance was detected in cirrus band.

3. RESULTS

There is a linear relationship between cirrus reflectance in bands S2, S3, and S5 with cirrus reflectance in the S4 (cirrus band) channel. We estimated and corrected the cirrus contribution to the S2, S3, and S5 spectral bands and the effect of cirrus correction in the normalized differential vegetation index (NDVI) was calculated.
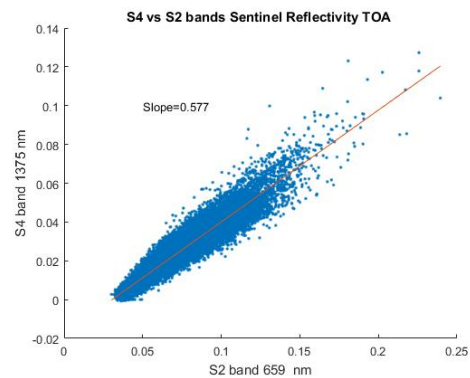
Figure 5. S4 vs. S2 spectral band SLSTR Sentinel-3 reflectivity at the TOA.
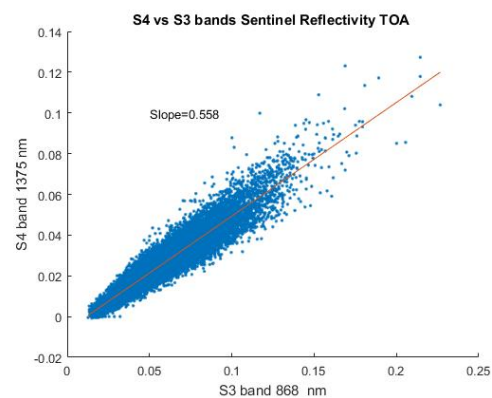
Figure 6. S4 vs. S3 spectral band SLSTR Sentinel-3 reflectivity at the TOA.
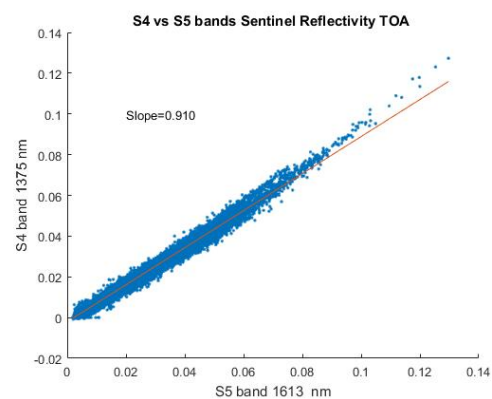
Figure 7. S4 vs. S5 spectral band SLSTR Sentinel-3 reflectivity at the TOA.

We also estimated the effect of cirrus correction on the NDVI as: (S3-S2)/(S3+S2), as shown in figure 8.
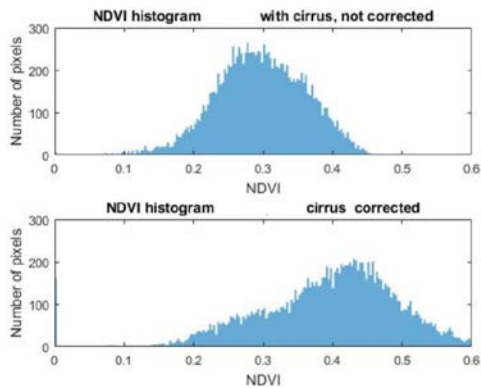
Figure 8. Histograms of NDVI in a zone of Valencian Region, with and without cirrus correction.

The magnitude of the cirrus-induced change on the NDVI normally depends on the thickness of the clouds. Cirrus clouds decrease the NDVI values which causes loss of variability. With this correction the pixels covered with cirrus clouds can again become useful information.

4. CONCLUSIONS

We applied an empirical methodology (Gao et al. 2002) to remove the effects of cirrus clouds in SLSTR Sentinel-3 images using the cirrus band information. In this work we highlight the utility of the SLSTR cirrus band on the Sentinel-3 for correcting the cirrus effect in its visible and shortwave infrared spectral bands. Cirrus clouds significantly affect the satellite estimations of different surface parameters. The information from the S4 cirrus band on board Sentinel-3 was used to correct other spectral bands and thus, to obtain surface parameters from pixels that had already been defined as cirrus clouds.

5. REFERENCES

Gao, B.C., A.F.H. Goetz, and W.J. Wiscombe. 1993, Cirrus clouds detection from airborne imaging spectrometer data using the 1.38 µm water vapor band. Geophys. Res. Lett.

Gao B.C., P. Yang, W. Han, R.-R. Li, and W. J. Wiscombe, August 2002. An algorithm using visible and 1.38 µm channels to retrieve cirrus cloud reflectance from aircraft and satellite data. IEEE Trans. Geosci. Remote Sensing.

Downscaling of the seasonal evolution of various crops in the Versailles plain (France), based on MODIS 250m EVI vegetation index and a Bayesian approach inversion

M.A. Ghribi[1,2], F. Maignan[1], C. Ottlé[1], A. Kallel[2], E. Vaudour[3], J.M. Gilliot[3], N. Delbart[4], C. Bacour[5] and J.Y. Peterschmitt[1]

(1) LSCE-IPSL, Orme des Merisiers, 91191, Gif-sur-Yvette, France
(2) CRNS, RSSA Group, Technopole de Sfax, BP 275, Sakiet Ezzit, 3021 Sfax - Tunisie
(3) UMR ECOSYS, INRA, AgroParisTech, Université Paris-Saclay, 78850 Thiverval-Grignon, France
(4) UMR PRODIG, Université Paris Diderot, UFR GHES, case 7001, 75205 PARIS Cedex 13, France
(5) NOVELTIS, 153 rue du Lac, 31670 Labège, France
fabienne.maignan@lsce.ipsl.fr
catherine.ottle@lsce.ipsl.fr

ABSTRACT:

This study carried out in the framework of the CNES TOSCA-PLEIADES-CO project of the French Space Agency, evaluates the relevance of remote sensing data acquired at medium resolution for the monitoring of seasonal cycles at the agricultural plot scale. The developed methodology uses a downscaling approach based on Least Squares estimation. The medium resolution data are derived from MODIS Aqua products MYD09GQ, which are surface reflectances acquired at a spatial resolution of 250m. These data are supplemented by the high-resolution land cover map and field contours of the study area (agricultural plots of the plain of Versailles) at a 5m spatial resolution.

The seasonal cycles of the main agricultural species present in the study area (winter wheat, winter barley, maize and rapeseed) were first analysed using the Enhanced Vegetation Index 2 (EVI2) index combining RED and NIR bands. The method is based on three sequential steps: (i) selection of homogeneous MODIS pixels (covered by one single crop type), (ii) cloud filtering and (iii) temporal interpolation of EVI2 data at a daily time step. The seasonal variations of pure winter and summer cereals could be separated.

The seasonal variations of the EVI2 for the various crops composing mixed pixels were then extracted by applying the downscaling method. The MODIS pixels composed of only two different crops (winter and summer crops) were selected and the downscaling method was applied. The comparison between the seasonal cycles of the homogeneous pixels and those inversed from the downscaling of the mixed pixels, showed a good agreement.

1 INTRODUCTION

The region under study is the Alluets Plateau in the plain of Versailles in France. This is a cropland area dominated by winter wheat (49%) and winter barley (10%), oilseed rape (20%). Summer crops like maize (10%) or summer barley (10%) can also be found.

2 CLOUDS FILTERING AT PIXEL SCALE

The EVI2 « Enhanced Vegetation Index » was used in this study to assess the crops seasonal cycle during the Year 2013.

$$EVI2 = 2.5 * \left(\left(Ref_{NIR} - Ref_{Red} \right) / \left(Ref_{NIR} + 2.4 * Ref_{Red} + 1 \right) \right) \quad (1)$$

Where *Ref* are the surface reflectances acquired in the Red and NIR domain respectively.

Two clouds filtering algorithms were tested and applied. The first one is based on thresholds applied on the surface reflectances and on combinations of them

(NDVI, NIR/Red ratio, Ishida and Nakajima, 2009): observations are flagged as cloudy if NDVI is lower than -0.1, or if the red reflectance is higher than the minimum of the former 30-day period + 0.26, or if the NIR/Red ratio is lower than 0.70. Figure 1 (top) illustrates the results for one MODIS pixel, the most discriminating test is the one on the red reflectance. All cloudy observations are further discarded.

The second filter, developed in this study, uses the 16-day EVI MODIS product to diagnose cloudy data. The 16-day EVI is interpolated at a daily time step. Various interpolation algorithms were tested (polynomial, univariate spline functions, sinusoids…) and the best results were obtained with the CCGRV algorithm (Bacour et al., 2006), which combines polynomial and sinusoidal functions and demonstrated previously high performances for the interpolation of long time series of vegetation indices (Maignan et al., 2008).
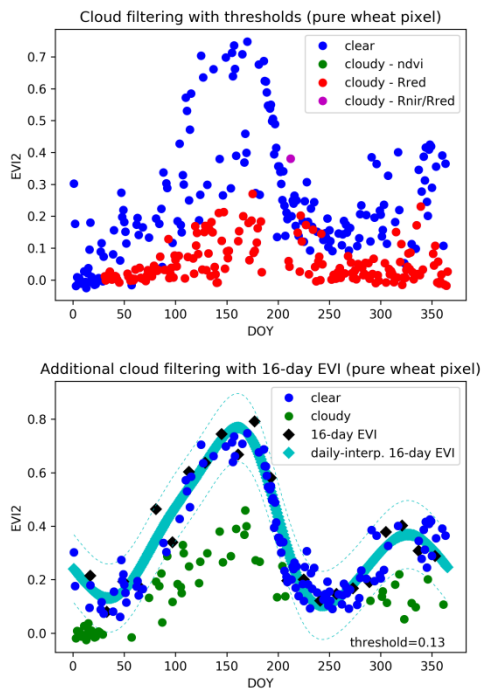
Figure 1 - Cloud filtering. Top: Different thresholds are applied on NDVI (green dots), the red reflectance (red dots) and the ratio NIR reflectance to Red reflectance (violet dots), to flag cloudy observations following Ishida and Nakajima (2009). Bottom: Use of the 16-day EVI product to discard remaining cloudy observations (green dots).

We compute a weighted mean absolute distance between the clear EVI2 observations and the interpolated EVI (with a weight of 0.5 for observations above the interpolated EVI and a weight of 1 for observations below): we indeed assume that the 16-day EVI is mostly cloud-free and that cloudy EVI2 observations will have lower values. All observations that are below the interpolated EVI and farther than the mean distance are discarded as cloudy ones. This is illustrated in Figure 1 (bottom) for the same MODIS pixel.

3 INTERPOLATION AT FIELD SCALE AND DAILY TIME STEP

After cloud filtering, the EVI2 signal was interpolated at a daily time step using the CCGRV algorithm.

In order to assess the seasonal variations of the EVI2 signal for the main crop types of the study region (winter wheat, winter barley, oilseed rape and maize), the MODIS-EVI2 were extracted for each pixel considered as pure (i.e. covered by a single crop) and cloudy observations were filtered following the algorithm presented in section 2.

For each crop type, a daily median signal was generated. This median cycle was then interpolated at a daily time step with the CCGRV method.

The results are illustrated in Figure 2 for the four main crops.
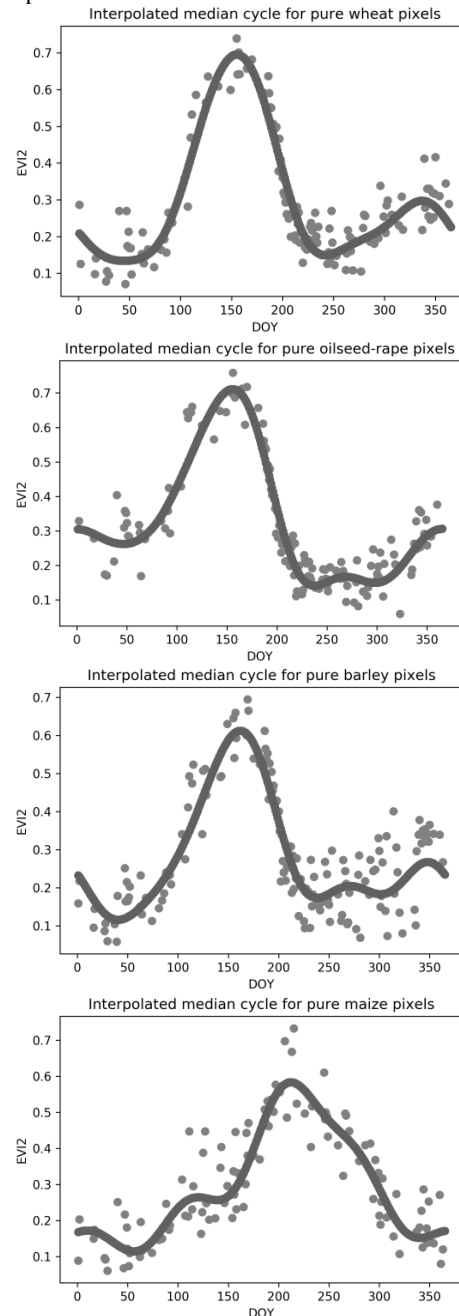
Figure 2 – Median cycles for the four main crops present in the study area. The dots represent the median observations, while the line shows the daily-interpolated signal.

They show expected cycles in agreement with the *in situ* observations. Winter crops like oilseed rape, wheat and barley present a growing season ranging between DOY 50 and DOY150 and a senescent period starting around DOY 170 and ending around DOY 230. Summer crops like maize show a delayed cycle with a peak around DOY 220 and a senescence ending around DOY 310.

4 DOWNSCALING METHOD AND RESULTS

As a first approach, we have tested a least square inversion method to assess the reflectances of the main components of a mixed pixel, assuming linear properties and stationarity (i.e., the spatial variations of the surface reflectances only depend on the vegetation type).

Then, the inversion problem comes down to the minimization of the discrepancies between the aggregated signal (weighted by the fractions of the various vegetation classes composing a mixed pixel) and the low resolution signal.

Applied to the EVI2 signal and to a number of n pixels composed of m land cover types, the inversion problem sum up to the minimization of the following equation:

$$\sum_{i=1}^{n}(\dot{q}_i^2) = \sum_{i=1}^{n}(\sum_{j=1}^{m}(F_{i,j}r_j) - R_i)^2 \qquad (2)$$

Where $F_{i,j}$, is the fraction of each land cover type in the considered pixel, r_j is the unknown EVI2 of crop j, R_i is the EVI2 of the mixed pixel i,
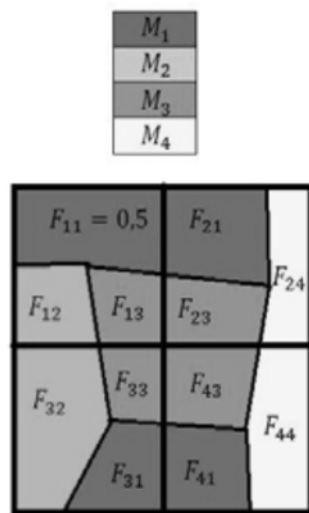
Figure 3 – Representation of 4 neighboring pixels composed of various fractions $F_{i,j}$ of 4 different crops.

As a first step, we have applied the inversion method to the MODIS pixels covered by only two different crops (winter and summer crops which present very differentiate seasonal cycles). Then, two pixels covered partly by winter wheat and maize were selected.

The minimization was then applied to these two pixels to estimate the respective EVI2 of the two mixed crops (in our case, wheat and maize) at each date when a MODIS image was available. The respective EVI2 have been computed, interpolated and compared to the one calculated previously on the pure pixels.

Figure 4 presents the preliminary results obtained. The EVI2 seasonal cycles inversed are in good agreement with the one extracted previously on the pure pixels of wheat and maize, even though the inversion was performed on only two pixels. We can see that the estimated maize cycle is noisier than the wheat one, which reflects the larger spatial variability of the phenology of summer crops compared to winter crops.
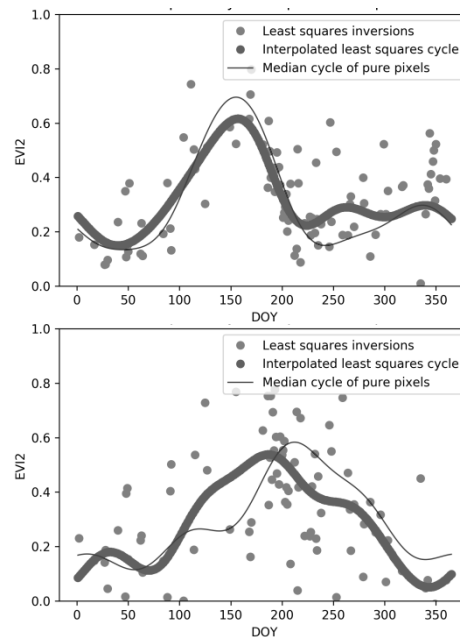
Figure 4 – Seasonal cycle downscaled for mixed « wheat-maize » MODIS-250m pixels. The dots represent the least square inversion of the observations over the mixed pixels, to get the signal of the pure crops (top: wheat, bottom: maize). The thick line shows the daily-interpolation of the inverted cycle. The thin line shows for comparison the seasonal cycle derived from the observations of pure pixels only.

5 CONCLUSION AND PERSPECTIVES

The contribution of a prior estimate given by the pure pixels should increase the performances of the methodology.

The next step is indeed to add constraints in the inversion process and to apply the methodology to the other mixed pixels covered by oilseed-rape and barley, and to a larger number of endmembers (more than 2).

The interpolation methodology could also be slightly improved to better assess the peak of the cycle. This could be achieved by introducing time-varying weights on the data.

6 FUNDING

7 REFERENCES

Bacour, C., Bréon, F. M. and Maignan, F., 2006, Normalization of the directional effects in NOAA–AVHRR reflectance measurements for an improved monitoring of vegetation cycles. *Remote Sensing of Environment*, 102(3), 402-413.

Ghribi, M.A., 2016, Suivi de la phénologie des cultures à partir d'images MODIS sur la plaine de Versailles, Rapport de fin d'études d'Ingénieur INIT, Sfax, Tunisie, Septembre 2016.

Ishida, H. and Nakajima, T. Y., 2009, Development of an unbiased cloud detection algorithm for a spaceborne multispectral imager. *Journal of Geophysical Research: Atmospheres*, 114(D7).

Maignan, F., Bréon, F. M., Bacour, C., Demarty, J., and Poirson, A., 2008, Interannual vegetation phenology estimates from global AVHRR measurements: Comparison with in situ data and applications. *Remote Sensing of Environment*, 112(2), 496-505.

Advances in statistical cloud screening: the Proba-V case study

Gonzalo Mateo-García, Luis Gómez-Chova, Jordi Muñoz-Marí, Gustau Camps-Valls,
Image Processing Laboratory, Universidad de Valencia
gonzalo.mateo-garcia@uv.es

ABSTRACT - *Accurate and automatic detection of clouds in optical Earth observation satellite scenes is a key issue for a wide range of remote sensing applications. With no accurate cloud masking, undetected clouds are one of the most significant sources of error in both sea and land biophysical parameter retrieval. We present recent advances in statistical cloud detection for Proba-V imagery.*
The objective of the cloud masking algorithms is to detect clouds accurately providing a cloud flag per pixel. We first approach the problem from the classical machine learning perspective based on feature extraction plus supervised classification with neural networks (NN). Using this approach we significantly improve the cloud detection accuracy compared to the operational Proba-V algorithm. Then we approach the problem using deep learning methods based on convolutional neural networks (CNN). Experimental results show that CNN are a promising alternative for solving cloud masking problems.

1 INTRODUCTION

The main objective of this work is to propose a cloud detection algorithm for Proba-V (Dierckx, 2014). Images acquired by Proba-V instrument, which works in the visible and infrared (VIS-IR) ranges of the electromagnetic spectrum, may be affected by the presence of clouds. Cloud masking is the process of identifying the pixels in an image which are cloud contaminated. Cloud masking can be tackled as a two-class classification problem. In its simplest approach, cloud detection can be done using a set of static thresholds (e.g. over reflectance) applied to every pixel in the image. This is the case of the current Proba-V cloud masking algorithm (Wolters, 2015) which uses a set of dynamic thresholds defined using monthly composites of cloud-free reflectance on the blue band depending on the land cover of the underlying pixel.

Proba-V instrument presents a limited number of spectral bands (Blue, Red, NIR and SWIR) which makes cloud detection particularly challenging since it does not present thermal channels or a dedicated cirrus band. In this context, the European Space Agency (ESA) carried out a 'Proba-V Cloud detection Round Robin' (PV-CDRR) experiment (Iannone 2017) in order to propose and compare different cloud detection methodologies for Proba-V. This paper presents our contribution in the framework of this experiment as well as further improvements obtained using convolutional neural networks.

In the context of the PV-CDRR, we present an algorithm that follows what we call the *machine learning classical approach* (ML). This is a supervised, pixel-based, classification algorithm trained on top of a set of manually designed set of features. This approach, which does not use any kind of ancillary data, ended up increasing the accuracy

2.5% points over the operational algorithm on the external validation provided by Brockmann Consult (Stelzer, 2017).

We further improve those results using convolutional neural networks (CNN) in what we called the deep learning approach (DL). The deep learning approach aims to automatically learn the feature extraction step directly from the data. Using convolutions we exploit the spatial information of the nearby pixels improving the classification accuracy. We present two deep learning approaches: one using patch classification to predict the label of the center pixel. The second one is a fully convolutional network that aims to predict the labels of the complete image patch.

All in all, we show that our proposed methodologies are capable of exploiting the information of Proba-V features beyond the limits of the operational threshold based approach. The current work summarizes and extends the previous authors' work presented in Gómez-Chova (2017) and Mateo-García (2017).

The paper is organized as follows: first we explain both methodologies in the context of cloud detection, then we introduce the dataset together with the manual labelling process of the images to create a ground truth. We then present the results of the validation assessment from Brockmann Consult, the improvements using CNN and some illustrative examples of the generated cloud masks.

2 METHODOLOGY

Statistical machine learning methodologies for cloud detection can be divided into supervised and unsupervised methods. Supervised methods assume you have a sufficiently large set of pixels labelled; that is, for those pixels you have a label that indicates if the pixel is whether or not affected by cloud

contamination. On the other hand, unsupervised methods attempt to distinguish the underlying class directly from the data. Supervised methods, when provided with diverse and large enough amount of data perform better than unsupervised approaches. Both of our proposed methodologies can be framed into the supervised classification framework. Thus we rely on having a *large enough* set of pixels labelled as 'cloud free' or 'cloudy', i.e. the *ground truth*.

2.1 Machine learning classical approach

The first of our proposed cloud masking methodologies works pixel-wise. It relies on the extraction of meaningful physically-based spectral features (e.g. brightness and whiteness) that are combined with a set spatial features to increase the cloud detection accuracy. Then, a supervised pixel-based classification is trained in top of those features using a manually labelled training set.

The set of extracted features can be divided into spectral and spatial features. For the spectral features we used physically-inspired features proposed in previous researches (Mei, 2017). Table 1 summarizes the spectral features considered. We also extract basic spatial features at different scales: we computed the mean and standard deviation for each feature on 3×3 and 5×5 windows. Thus, we ended up having 70 features for each pixel conformed by the four (4) Proba-V reflectance channels, the spectral features of Table 1 (10) and the mean and standard deviation computed at both scales: (4+10)×4. We selected the 40 top most relevant features using several feature ranking methods.

Table 1. Cloud features extracted from Proba-V images

Cloud Feature	Feature
Brightness	x_{Br}
Brightness VIS	$x_{Br,VIS}$
Brightness NIR	$x_{Br,NIR}$
Whiteness	x_{Wh}
Whiteness VIS	$x_{Wh,VIS}$
Whiteness NIR	$x_{Wh,NIR}$
Snow NDSI	$x_{(Blue-NIR)/(Blue+NIR)}$
Snow NDSI	$x_{(Blue-SWIR)/(Blue+SWIR)}$
Red-SWIR ratio	$x_{Red/SWIR}$
NDVI	$x_{(NIR-Red)/(NIR+Red)}$

The set of the selected 40 best features constitutes the inputs of the supervised classification algorithms. In this context we assume we are given a set of l labelled training samples $\{x_i, y_i\}$, where x_i is the observed vector in the input space and y_i is the observation label in the output space. In our problem, each pair $\{x_i, y_i\}$ in that set is a pixel where x_i is the 40 dimensional feature description of the pixel and y_i is the label of such pixel (0: 'cloud free' or 1: 'cloudy').

The selected supervised classification algorithm for the current task is the standard multilayer perceptron neural network (MLP); which has been a traditional approach for cloud classification (Torres Arriaza, 2003; Hughes, 2014).

Summarizing, for the machine learning classical approach we trained an MLP on top of a set of 40 relevant spatio-spectral features. Those 40 features can be extracted directly from the four top of atmosphere (TOA) reflectance channels of the Proba-V images; thus the method does not require any kind of ancillary data to be deployed. Results of this approach compared against the operational Proba-V algorithm are shown in Section 4.

2.2 Deep learning approach

Convolutional neural networks (CNN) have proven to be state of the art methods for image classification, image segmentation, and object detection. Beyond their high classification accuracy shown in many problems, CNN present interesting properties for remote sensing data. For instance, hierarchical spatio-spectral feature extraction step is automatically learned from the data. Therefore, previous custom feature extraction step is not needed provided enough training data. In addition, convolutional filters are specially designed to exploit the spatial information of images. This is specially relevant to our problem since the amount of spectral information is scarce (only four spectral bands and no cirrus or thermal infrared bands).

Cloud masking problem is an image segmentation problem where every pixel of the image has to be predicted. A simple deep learning approach for image segmentation is patch classification: for classifying a pixel a patch of image surrounding it is taken. Thus the segmentation problem is transformed into image classification where there is a set of patches and each patch has a label corresponding to the tag of the center pixel. Alternatively a multi-output approach can be taken where, for each image patch, the prediction of the full patch is provided. This approach has been popularized with the fully convolutional networks (FCN), which are CNN architectures without any fully connected layer at the output. These architectures allow much faster predictions compared to the patch classification approach.

For this work we tried both approaches:

- *Patch classification*. We used small patches of the 4 Proba-V channels, the goal is to provide the label of the center pixel of the patch. We test two input configurations: 4-channel 17×17 and 4-channel 33×33.
- *Fully convolutional*. For practical purposes the network was trained on 32×32 4-channel Proba-V image patches.

We used a modified version of the 'Xception' architecture (Chollet, 2016) for the patch classification

approach. The 'Xception' architecture is a deep architecture designed for image classification. Our modified version has 7 layers formed by standard convolutions and separable convolutions. We employed residual connections (He, 2016) and batch normalization (Ioffe, 2015). The network was trained with Adam optimizer (Kingma, 2015) which is a mini-batch stochastic gradient descent algorithm with adaptive estimates of higher order moments.

For the fully convolutional scheme we used a simplified version of the 'UNet' architecture (Ronneberger, 2015). We used 2 sets of 2 separable convolutions followed by max-pooling for the downsampling path and deconvolutions (also called transpose convolutions) for the upsampling path. We employed residual connections from the downsampling to the upsampling path and batch normalization (Ioffe, 2015).

All networks were trained to minimize binary cross entropy between predictions and the corresponding labels. In the multi-output approach we minimize the mean binary cross entropy along all outputs in the patch.

One of the major problems when training big convolutional neural networks is their tendency for overfitting. In order to avoid overfitting, regularization has to be imposed. In this work, we employed dropout, weight decay, and data augmentation by rotations and flips of the patches.

3 PROBA-V DATASET

We consider as input data Proba-V Level 2A products with TOA reflectance. This comprises the four Proba-V bands which are radiometrically and geometrically corrected and resampled at 333m.

For the round robin experiment, ESA released 331 products. Those images conformed a complete globe acquisition from four different dates covering the four seasons along the year 2014.

In order to apply our proposed methodologies we need ground truth data to train our supervised classifiers. For this purpose we manually labelled 72 from the original 331 images using a semi-automatic user driven methodology proposed in (Gómez-Chova, 2007). The aforementioned methodology consists on clustering the pixels of the images using Gaussian Mixture Model clustering algorithm (GMM). Clusters are afterwards labelled by an expert on different categories: ice, soil, vegetation, clouds, sand, water or mixture. The last one is used when the cluster contains different covers, and mixed clusters are discarded and a posteriori probabilities are recomputed for each cluster class. The final manual cloud mask comprises the pixels whose highest probability is the cloud class and it exceeds a predefined threshold. If the highest probability is cloud but it is below the threshold the

pixel is labelled as uncertain. Since the ground truth has to be as accurate as possible, uncertain pixels are not taken into account neither for training nor for testing.

The spatial location of the labelled dataset is shown in Fig.1. We split the 72 labelled images into 48 for training and 24 for testing. In order to fairly compare the DL and the ML methodologies, we randomly selected 100,000 pixels from the training images for training and 200,000 pixels from the remaining 24 test images for testing.
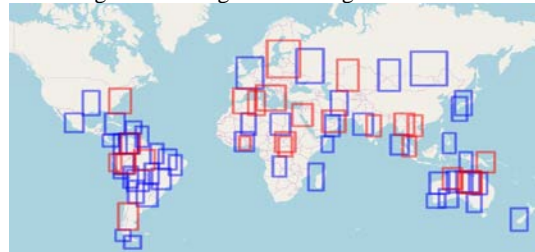
Figure 1. Location of labelled Proba-V images used for training (blue squares) and testing (red squares).

4 EXPERIMENTAL RESULTS

4.1 Results of the PV-CDRR experiment

Our proposed classical machine learning methodology for cloud detection was presented in the context of the PV-CDRR experiment. The participants had to provide a cloud mask for all the 331 images using their proposed methodology. Afterwards a validation study was carried out by Brockmann Consult (Stelzer , 2017). For this validation study, 10,000 individual pixels were manually tagged by an expert and accuracy metrics were computed comparing the different approaches. In addition, visual examination of cloud masks was undertaken by an expert to provide qualitative information about the cloud masks.

Figure 2 shows the performance of the different algorithms in the 10,000 unseen labelled pixels. Our approach ended up in second position in terms of accuracy and with clear advantages in terms of the algorithm implementation. It improves the current operational approach in 2.5 points which a total cloud detection accuracy of 91.57%.

4.2 Results of the Deep Learning approach

CNN models where implemented in python using 'keras' library. We used the GPU (Tesla K80) for training. Training time highly depends on the chosen architecture and in the size of the patches. The 17×17 patch classification model based on 'Xception' architecture can be trained in less than 12 hours. The 33×33 patch classification took around 2 days for the patch classification 'Xception' model as well as for the fully connected approach based on 'UNet'. The total

number of parameters of the 17×17 patch classification model is 11,845. It increases to 70,885 for the 33×33 model while the fully connected approach has a total of 217,317 parameters.
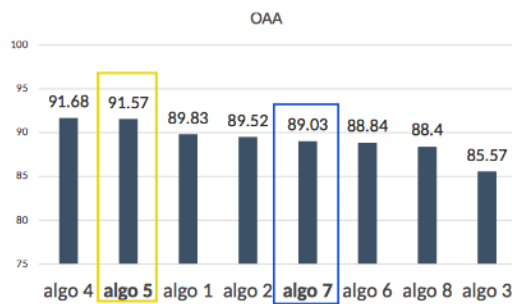
Figure 2. Cloud detection performance (overall average accuracy) of the algorithms analysed within the PV-CDRR (Algo5: our ANN; Algo7:operational Proba-V cloud mask)

Figure 3 shows the accuracy of the different proposed methodologies on our manually labelled test set of 24 images described in the previous section. We see that the patch classification approach has the highest accuracy improving in 1 point the classification accuracy of the classical approach. The 17×17 approach has similar performance than the 33×33 one; thus we will prefer the former since it has lower computational complexity. The fully connected approach in this case yields similar performance than the standard pixel based classical approach so the patch classification approach is preferred in terms of accuracy. Finally it is worth noting that the operational Proba-V yields considerably worse than our algorithms this difference is even higher than the reported by Brockmann. This highlights the differences between the Brockmann validation set and ours. We conjecture this is due to, on the one hand, our semiautomatic labelling procedure which is noisy since we tag clusters of pixels, on the other hand, differences might come from different cloud class assignments for semitransparent clouds, cloud borders etc. This is an inherent problem of cloud detection in general.

Finally, Fig. 4 shows our best performing cloud mask based on the 17×17 deep learning patch classification approach compared with our manually labelled ground truth. We see a high overall visual agreement in both figures being the most significant differences on the contours of the clouds. Figure 4b is a challenging snowy region in Kazakhstan. We see again that the proposed solution works fairly well and it is able to distinguish between snow and clouds with near human precision.
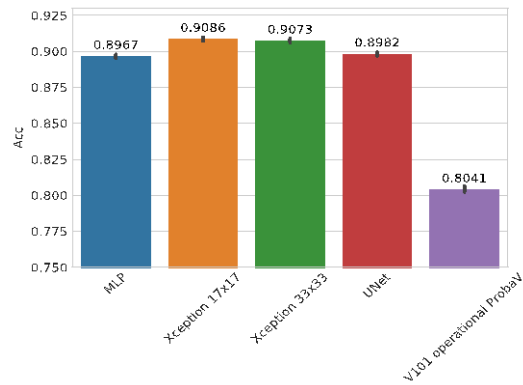
Figure 3. Cloud detection performance of the proposed networks on the manually labelled Proba-V images.
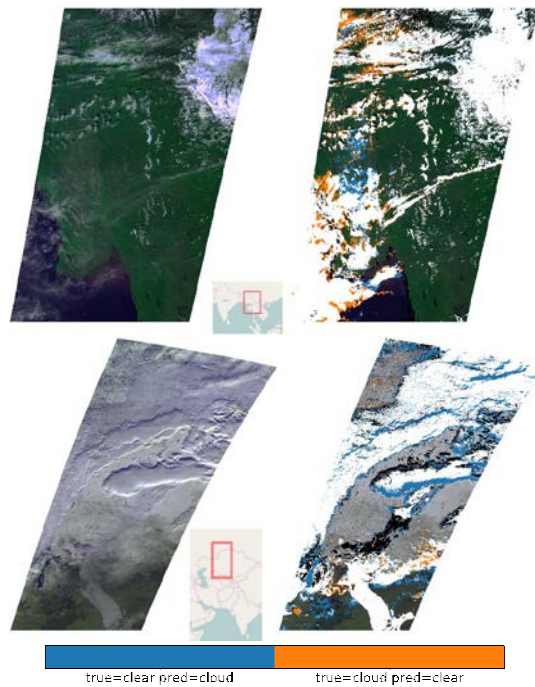
Figure 4. Cloud detection examples showing the RGB false color composite, and the comparison of the 'manual ground truth' with the proposed network: discrepancies are shown in blue when proposed method detects cloud and in orange when pixels are classified as cloud-free.

5 CONCLUSIONS AND FUTURE WORK

We presented an end-to-end implementation of cloud detection algorithms based on machine learning. We proved that machine learning approaches to cloud detection yield state-of-the-art performance for Proba-V. We showed that the deep learning approach simplifies the design of the cloud detection algorithm since no feature extraction step is required, this approach also slightly improves the final performance

of the algorithm. Finally, we provide a labelled dataset of Proba-V cloud masks that could be exploited for further studies.

The future lines of this work are wide open. We would like to explore the transfer capability of the deep learning approaches to different satellites. We would also like to compare our manually labelled dataset to the less noisy one from Brockmann since this could bring insight in the learning with noisy labels problem. It also remains open further validation of the current algorithms for their implementation in the ground segment.

ACKNOWLEDGEMENTS

REFERENCES

Chollet, François. 2016. "Xception: Deep Learning with Depthwise Separable Convolutions." *CoRR* abs/1610.02357. http://arxiv.org/abs/1610.02357.

Dierckx, Wouter, Sindy Sterckx, Iskander Benhadj, Stefan Livens, Geert Duhoux, Tanja Van Achteren, Michael Francois, Karim Mellab, and Gilbert Saint. 2014. "PROBA-V mission for global vegetation monitoring: standard products and image quality." *International Journal of Remote Sensing* 35 (7): 2589–2614.

Gómez-Chova, L., G. Camps-Valls, J. Calpe-Maravilla, L. Guanter, and J. Moreno. 2007. "Cloud-Screening Algorithm for ENVISAT/ MERIS Multispectral Images." *IEEE Transactions on Geoscience and Remote Sensing* 45 (12): 4105–4118.

Gómez-Chova, Luis, Gonzalo Mateo-García, Jordi Muñoz-Marí, and Gustau Camps-Valls. 2017. "Cloud detection machine learning algorithms for PROBA-V." In *IGARSS 2017. IEEE 2017 International Geoscience and Remote Sensing Symposium.*

He, Kaiming, Xiangyu Zhang, Shaoqing Ren, and Jian Sun. 2016. "Deep Residual Learning for Image Recognition." *2016 IEEE Conference on Computer Vision and Pattern Recognition (CVPR)*, Las Vegas, NV, 2016, pp. 770-778. doi: 10.1109/CVPR.2016.90.

Hughes, M. Joseph, and Daniel J. Hayes. 2014. "Automated Detection of Cloud and Cloud Shadow in Single-Date Landsat Imagery Using Neural Networks and Spatial Post-Processing." *Remote Sensing* 6 (6): 4907–4926.

Iannone, R. Q., P. Goryl S. Dransfeld B. Hoersch K. Stelzer G. Kirches M. Paperin C. Brockmann L. Gómez-Chova G. Mateo-García R. Preusker J. Fischer U. Amato C. Serio U. Gangkofner B. Berthelot M. D. Iordache L. Bertels E. Wolters W.Dierckx I. Benhadj E. Swinnen, F. Niro. 2017. "Proba-V Cloud Detection Round Robin: Validation Results and recommendations." In *9th International Workshop on the Analysis of Multitemporal Remote Sensing Images (MultiTemp 2017)*, Brugge, 2017, pp. 1-8. doi: 10.1109/Multi-Temp.2017.8035219.

Ioffe, Sergey, and Christian Szegedy. 2015. "Batch Normalization: Accelerating Deep Network Training by Reducing Internal Covariate Shift." In *International Conference on Machine Learning (ICML 2015)*, Lille, France, 2015.

Kingma, Diederik P., and Jimmy Ba. 2015. "Adam: A Method for Stochastic Optimization." In *International Conference on Learning Representations (ICLR)*, San Diego, 2015.

Mateo-García, Gonzalo, Luis Gómez-Chova, and Gustau Camps-Valls. 2017. "Convolutional Neural Networks for multispectral image cloud masking." In *IGARSS 2017. IEEE 2017 International Geoscience and Remote Sensing Symposium.*

Mei, Linlu, Marco Vountas, Luis Gómez-Chova, Vladimir Rozanov, Malte Jäger, Wolfhardt Lotz, John P. Burrows, and Rainer Hollmann. 2017. "A Cloud masking algorithm for the XBAER aerosol retrieval using MERIS data." *Remote Sensing of Environment* 197 (Supplement C): 141–160.

Ronneberger, Olaf, Philipp Fischer, and Thomas Brox. 2015. "U-Net: Convolutional Networks for Biomedical Image Segmentation." In *Medical Image Computing and Computer-Assisted Intervention – MICCAI 2015. Lecture Notes in Computer Science, vol 9351. Springer, Cham pp 234-241.*

Stelzer, Kerstin, Michael Paperin, and Grit Kirches. 2017. *PROBA-V cloud round robin validation report*. Technical Report Technical Note, 02/05/2017. ESA.

Torres Arriaza, José Antonio, Francisco Guindos Rojas, Mercedes Peralta López, and Manuel Cantón. 2003. "An Automatic Cloud-Masking System Using Backpro. Neural Nets for AVHRR Scenes." *IEEE Trans. on Geoscience and Remote Sensing* 41 (4): 826–831.

Wolters, E.L.A., E. Swinnen, I. Benhadj, and W. Dierckx. 2015. *PROBA-V cloud detection evaluation and proposed modification*. Technical Report Technical Note, 17/7/2015. QWG.

FPGA-based implementation of detection and matching of feature points

Jingjin Huang[1, 2, 3], Guoqing Zhou[1, 2, 3,*], Guangyun Zhang[3], Rongting Zhang[1], Dianjun Zhang[3],

[1] *School of Precision Instrument & Opto-electronics Engineering, Tianjin University, Tianjin 300072, China;*

[2] *GuangXi Key Laboratory for Spatial Information and Geomatics, Guilin University of Technology, Guilin, Guangxi 541004, China;*

[3] *The Center for Remote Sensing, Tianjin University, Tianjin 300072, China.*

Corresponding author: Guoqing Zhou (gzhou@glut.edu.cn)

ABSTRACT - *The objective of this paper is to achieve real-time detection and matching of feature points in remote sensing image. To realize the real-time detection and matching, a FAST detector and a BRIEF descriptor are adopted, and a FPGA architecture is designed to speed up the processing because of the parallel and pipeline property of FPGA. The whole architecture is consist of a DDR3 write-read module, a FAST detector module, a BRIEF descriptor module, and a Hamming distance module. In DDR3 storage module, the series images were written and read through DDR3 which is working on the ping-pong operation mode. In corner detection module, a multichannel parallel comparison strategy was implemented. In descriptor generation module, 256 channels parallel comparison were designed to generate a 256 bits binary vector named as BRIEF descriptor. In matching module, a Hamming distance was computed by two descriptors, which one descriptor in the prior image, and the other one for the next image. Furthermore, the parallel strategy is also adopted in this module. The whole architecture is implemented on XC7325T FPGA, which is simulated by six sub-image pairs with the known Homography matrixes. The experiment results indicated that the accuracy was satisfactory, especially in the image pairs covering with artificial structures. The utilization of FPGA resources was also acceptable.*

1 INTRODUCTION

Feature detection and matching is one of the basic image processing operations in remote sensing, and its performance directly influence the final results produced by the aforementioned applications (Rosten, 2010). Especially in the environment with a high real time, such as on-board processing of satellite image, satellite attitude determination, object tracking & recognition, and unmanned vehicle etc. (Zhou, 2004; Zhang, 2011). Hence, how to implement the detection and matching in real time is becoming extremely important. To meet the requirement of high real time, this paper presented a hardware architecture to implement the corner detection and matching in a high frame rate. This proposed hardware architecture can also be used in on-board tracking & recognition, space junk trapping and so on.

A Field Programmable Gate Array (FPGA) architecture is adopted, because of its excellent characteristics in pipeline structure and fine-grained parallelism. Furthermore, the size and speed of FPGA are competitive when compare with Application Specific Integrated Circuit (ASIC), especially in design flexibility and development cycle (Torres-Huitzil, 2000). More importantly, this paper implemented the whole algorithm on a single FPGA. The proposed algorithm includes corner detection, descriptor generation, and matching. The main contributions of this paper are: (1) A complete solution for FPGA implementation of the detection and matching; (2) A FAST detector and a BRIEF descriptor are combined to achieve corner detection and matching; (3) Various images with different terrestrial landscapes are used to evaluate the FPGA implementation of the proposed algorithm.

The remainder of this paper is organized as follows: Section II presents relative work. Section III overviews the proposed algorithm. Section IV gives a detailed procedure about the FPGA implementation. Section V shows the experimental results and evaluates the performance of FPGA implementation. Section VI summarizes the conclusion.

2 RELATIVE WORK

To our best knowledge, many researchers used FPGAs to accelerate detection and matching algorithms for real-time applications.

Several work only focus on feature point detection, for example: Yao et al. (2009) proposed a Xilinx Virtex-5 FPGA implementation of optimized SIFT

feature detection (Yao, 2009). Mehra et al. (2012) conducted a FPGA-based implementation of Sobel edge detector for image processing applications (Mehra, 2012). Bi et al. (2012) firstly proposed a FPGA-based system for real-time corner and polygon detection (Bi, 2012). In detection phase, the detection of multi-scale feature point, line feature, and polygon feature will consume huge FPGA resources and lead to a poor real-time performance, because of high complexity of algorithm and the float-pointing operation.

Most work focus on the detection and matching, for instance: Svab et al. (2009) implemented multi-scale SURF on FPGA (Svab, 2009); Schaeferling et al. (2011) implemented a complete SURF-based system on Xilinx Virtex 5 FX70T FPGA for object recognition (Schaeferling, 2011); Sledevic et al. (2012) proposed an FPGA-based implementation of a modified SURF algorithm (Sledevic, 2012); Battezzati et al. (2012) proposed a FPGA architecture for implementation SURF algorithm (Battezzati, 2012); Weberruss et al. (2015) proposed a hardware architecture of ORB on FPGA (Weberruss, 2015); Huang and Zhou (2017) achieved SURF+BRIEF on FPGA for satellite imagery on-board processing (Huang, 2017). In matching phase, the descriptor generation and matching are the most time-consuming stages when they are implemented on PC (Fan, 2013). While the running time can dramatically reduce by avoiding large computation, serial execution, and floating-point operation in FPGA implementation. SIFT descriptor is one of the most excellent descriptors, while it is also hardest to implemented on FPGA, because of the complex algorithm and the float-point operation (Fularz, 2015). SURF descriptor can achieve a similar performance compared with SIFT descriptor (Fan, 2013). The SURF descriptor can be implemented on FPGA with a relative large resources consumption. The BRIEF descriptor, which consists of a set of binary vectors, is easier to be achieved on FPGA when compared with SIFT descriptor and SURF descriptor.

This paper proposed a FAST+BRIEF algorithm to be implemented on FPGA for the corner detection and matching.

3 OVERVIEW OF THE PROPOSED ALGORITHM

3.1 Corner detector and its descriptor

The FAST detector first proposed by Rosten (Rosten, 2006) are widely used in corner detection for computer vision. The segment test criterion operates by considering a circle of sixteen pixels around the corner candidate p, as illustrated in Fig. 1, the original detector classifies p as a corner if there exists a set of n contiguous pixels in the circle which are brighter than

the intensity of the corner candidate Ip plus a threshold t, or all darker than Ip minus the t. The n was chosen to be 12 because a very large number of non-corners can be removed by this test.
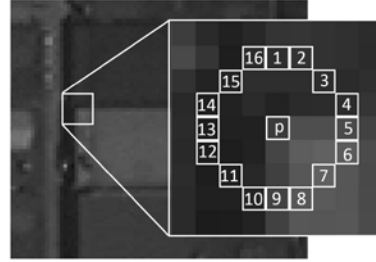
Fig. 1. FAST detector

The formula of FAST detector is presented as follows.

$$S_{p \to x} = \begin{cases} d, & I_{p \to x} \leq I_p - t \\ s, & I_p - t < I_{p \to x} < I_p + t \\ b, & I_p + t \leq I_{p \to x} \end{cases} \quad (1)$$

where I_p is the intensity of corner candidate p, $I_{p \to x}$ is the intensity of the sixteen pixels around the corner, t is a threshold. If $S_{p \to x}$ equals to d, it means that the pixel belongs to "d", if $S_{p \to x}$ equals to s, it means that the pixel belongs to "s", if $S_{p \to x}$ equals to b, it means that the pixel belongs to "b". If there exists continuous 12 pixels which belong to "d" or "b", the corner candidate p is regarded as a corner.

When all pixels are tested by the above operations, the corners are located. While the corners will get together in some cases. To find the stronger robustness corners, a non-maximal suppression method based on a score function is adopted in this paper. The score value is computed by:

$$s = max\left(\sum_{x \in S_{bright}} \left| I_{p \to x} - I_p \right| - t, \sum_{x \in S_{dark}} \left| I_p - I_{p \to x} \right| - t \right) \quad (2)$$

where I_p is the intensity of corner candidate p, $I_{p \to x}$ is the intensity of the sixteen pixels around the corner, t is a threshold.

The BRIEF descriptor first proposed by M. Calonder (Calonder, 2010) is adopted for description of the detected corner. The form of BRIEF descriptor is consisted of "1" and "0" and the length of BRIEF descriptor is generally defined as 128 bits, 256 bits, and 512 bits, which are efficiently implementation by FPGA with a low consumption. The following formula clearly shows the definition of BRIEF descriptor:

$$\lambda\left(p; r_1, c_1, r_2, c_2 \right) = \begin{cases} 1 : I\left(r_1, c_1 \right) < I\left(r_2, c_2 \right) \\ 0 : I\left(r_1, c_1 \right) \geq I\left(r_2, c_2 \right) \end{cases} \quad (3)$$

where $I(r_1, c_1)$ and $I(r_2, c_2)$ are the intensity of pixels at (r_1, c_1) and (r_2, c_2). If $I(r_1, c_1)$ is less than $I(r_2, c_2)$, then $\lambda=0$, otherwise, $\lambda=1$. The length of λ is selected as 256

bits in this paper. The locations (r_i, c_i) of the 256 point pairs are determined by the Gaussian distribution. Details for how to determine the locations of 256 point pairs can refer (Calonder, 2010).

3.2 Matching

To find out the pairs in two images, a hamming distance between two BRIEF descriptors is computed by "*XOR*" operation. The basic steps of matching based on hamming distance are listed as follows:

- Select a BRIEF descriptor in first image as a candidate;
- Select all BRIEF descriptors in second image as comparison objects;
- Compute all hamming distances between the candidate and the comparison objects;
- Find out the minimum value of all hamming distances.

Once the minimum value is determined, it means that the corresponding two BRIEF descriptors are the most similar which indicate that the corresponding corners are matching.

4 FPGA-BASED IMPLEMENTATION

4.1 FPGA architecture

This paper design a complete FPGA architecture for the detection and matching in real time. The whole FPGA architecture is presented in Fig. 2. As seen from Fig. 2, the architecture consists of four modules. The functions of the four modules are summarized as follows:

- DDR3 storage module: Image data are stored into DDR3 for detection, matching;
- Corner detection module: The image data read out from DDR3 are used to detect the corner;
- Descriptor generation module: According to the location corner, the sub-image read out from DDR3 are used to generate the BRIEF descriptor;
- Matching module: BRIEF descriptors in two image are matching by Hamming distance with pixel precision.
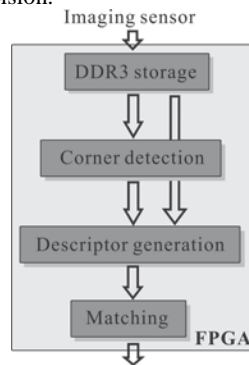
Fig. 2. FPGA architecture of the proposed algorithm

4.2 FPGA implementation of writing and reading of DDR3

The image sequence should be written into DDR3 for corner detection, BRIEF generation. The FPGA implementation of writing and reading is presented in Fig. 3. As seen from Fig. 3, in the process of writing, the 8 image cells with 8 bits are combined into a writing data with 64 bits, meanwhile a writing address is generated. According to the writing data and address, the 8 image cells can be stored into a blank of DDR3. The other image cells are stored into DDR3 in the same way; In the process of reading, the data are read out from DDR3 according to the reading address, then the reading data with 64 bits are read out from a blank of DDR3 and separated into 8 image cells with 8 bits. The other image cells are read out from DDR3 in the same way.
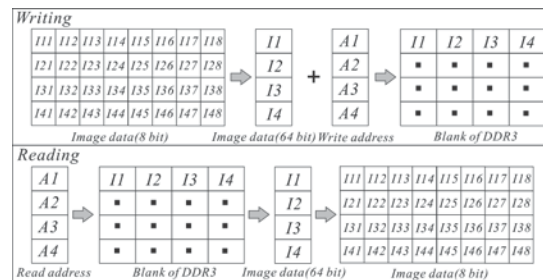
Fig. 3. FPGA implementation of writing and reading

4.3 FPGA implementation of FAST detector

According to the Fig. 1 and Eq. 1, corner candidate (c) and its Bresenham circle of sixteen pixels (x_i) are selected from the reading data. The "*corner detec.*" module is implemented based on Eq. 1. In this module (Fig. 4), if there exists contiguous 12 "b_i" or "d_i", then the corner candidate is outputted as a brighter or a darker. The "*corner score*" module is implemented based on Eq. 2. The score of corner candidate is determined by searching the maximum one. The score are sent into a "*nonmax. supper.*" module to select the most robust corner.
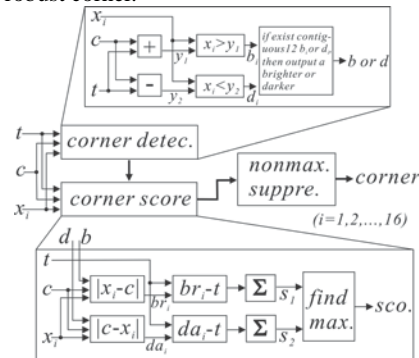
Fig. 4. FPGA implementation of FAST detector

4.4 FPGA implementation of BRIEF descriptor

To generate a BRIEF descriptor, a sub-image centred on the detected corner is read out from DDR3. To read this sub-image, a corresponding reading address is generated by the row and column of the detected corner. In FPGA implementation (see Fig. 5), a sub-image with a size of 35×35 is read. Meanwhile, because of the image noise, a sliding window (the black box) with a size of 5×5 is used in the sub-image to generate a new sub-image with a size of 31×31. The binary vector with a length of 256 bits are generated by comparing with the 256 pairs (p_i, q_i, $i=1$, 2… 256). Finally, a binary vector with a length of 256 bits is outputted as a BRIEF descriptor.
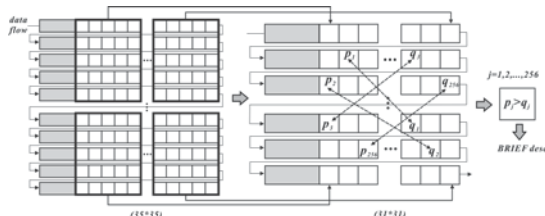
Fig. 5. FPGA implementation of BRIEF descriptor

4.5 FPGA implementation of matching

In FPGA implementation (see Fig. 6), two BRIEF descriptors are computed by "*XOR*" operation and its Hamming distance is computed by summating each bits of the operation result. In matching phase, when one BRIEF descriptor in first image are compared with all BRIEF descriptors (n) in second image, there will generate n Hamming distances and the minimal Hamming distance is the matching.
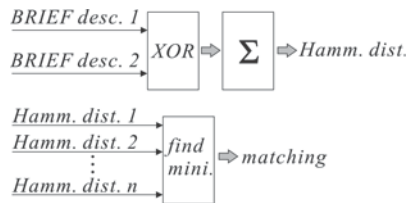
Fig. 6. FPGA implementation of matching

5 EXPERIMENT RESULTS AND PERFORMANCE ANALYSIS

5.1 Hardware platform

The selected FPGA has a 326080 Logic Cells, 4000 kb Block RAMS and 840 DSP Slices (Xilinx, 2016). The resources of board are enough to implement the whole design. In addition, the design tool is Vivado2014.2, the simulation tool is Modelsim-SE 10.4, and the hardware design language is Verilog HDL.

5.2 Image dataset

An image pair produced by GJ-1-01/02 on May 6, 2017 are used to evaluate the FPGA implementation of FAST+BRIEF algorithm. In Fig. 7, the image pair with a spatial resolution of 0.5 m are located at Mentougou District, Beijng, China. In this work, six sub-image pairs covering with different ground objects are used as test fields, and Homography matrixes of the six sub-image pairs are prior computed by OpenCV (2.4.9 version) (OpenCV, 2017) on PC. The computed results are listed as follows.
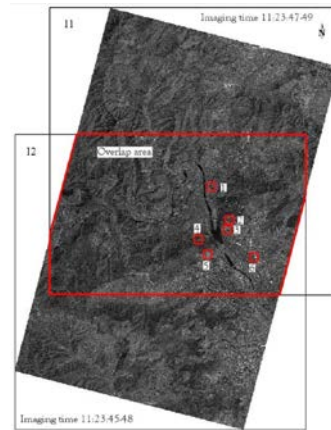
Fig. 7. Test field in Mentougou district, Beijing, China
(1) expressway; (2) rural road; (3) bungalow; (4) tree; (5) bare soil; (6) high building.

$$H_1 = \begin{bmatrix} 1.006367 & -0.002508 & -5.360394 \\ 0.002415 & 1.000690 & 1.070197 \\ 2.354719e\text{-}05 & -1.406829e\text{-}05 & 1 \end{bmatrix} \quad (4)$$

$$H_2 = \begin{bmatrix} 1.001888 & -0.002281 & -2.841617 \\ 0.001323 & 0.997152 & 9.514452 \\ 9.935040e\text{-}06 & -9.588419e\text{-}06 & 1 \end{bmatrix} \quad (5)$$

$$H_3 = \begin{bmatrix} 1.000939 & -0.000179 & 3.060421 \\ 0.000623 & 0.999503 & 0.038150 \\ 2.765602e\text{-}06 & -2.605087e\text{-}06 & 1 \end{bmatrix} \quad (6)$$

$$H_4 = \begin{bmatrix} 1.000715 & 0.000696 & 3.125068 \\ -0.001212 & 0.999692 & 2.427667 \\ -1.145561e\text{-}06 & 2.446546e\text{-}06 & 1 \end{bmatrix} \quad (7)$$

$$H_5 = \begin{bmatrix} 0.987162 & -0.003653 & 1.444455 \\ -0.007780 & 0.989969 & 5.676099 \\ -4.523469e\text{-}05 & -5.933579e\text{-}06 & 1 \end{bmatrix} \quad (8)$$

$$H_6 = \begin{bmatrix} 1.001664 & 0.000919 & -0.956221 \\ 0.000693 & 1.000989 & -1.912867 \\ 4.016018e\text{-}06 & 2.346683e\text{-}06 & 1 \end{bmatrix} \quad (9)$$

5.3 Experiment results

Six sub-image pairs are sent to FPGA architecture, respectively. The image data flow are fist stored in DDR3, then sent to detection module to produce corners. According to the locations of corners, sub-sub-images centred on corners are read out from DDR3. The reading image data flow and the locations of corners are both sent to matching module. The matching corners of image pairs are outputted as the final results. To keep the same situation before comparison, 100 corners are detected and matching in each sub-image pairs.

The experimental results are displayed in Fig. 8 by Matlab software (R2014a version). As seen from Fig. 8, most of the point pairs are correct matching, especially a seldom are false matching. The experimental results also indicate that the correct matching rate is impacted by the coverages, especially when the image covers with artificial structures (such as high building and bungalow), a high matching rate is achieved in this paper. A further analysis of the matching performance is depicted in next sections.
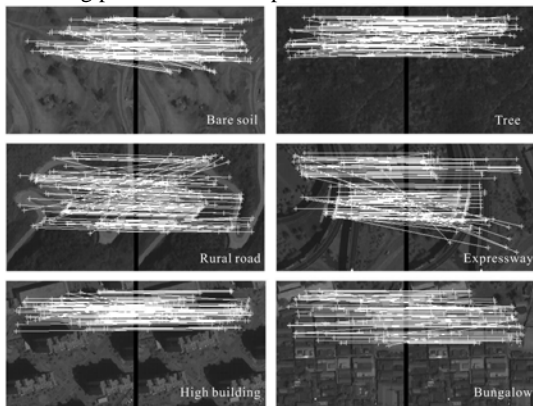
Fig. 8. Detection and matching by FPGA architecture

5.4 Accuracy analysis

A standard evaluation method has been proposed to assess the matching performance, which is presented as a curve of *recall* vs. *1-precision* (Mikolajczyk, 2005). The curve is generated below a threshold *t* which determined if two descriptors are matched. Given two images representing the same scene, the formulas of *recall* and *1-precision* are depicted in Eq. 10:

$$\begin{cases} recall = N_1/N_2 \\ 1\text{-}precision = N_3/(N_1 + N_3) \end{cases} \quad (10)$$

where N_1 is the number of correctly matched points; N_2 is the number of corresponding matched points, which are determined by overlapping of the points in different images; N_3 is the number of the falsely matched points. The higher *recall* and lower *1-precision* means the better performance of matching.

For instance, with the changes of threshold, if *recall* is increasing and *1-precision* is still equal to *0*, it means that the point pairs are all correctly matching; if *recall* keeps stable and *1-precision* is increasing, it means that most of point pairs are falsely matching.

The accuracy of detection and matching of six sub-image pairs are presented in Fig. 9. We find that the image pairs with expressway, high building and bungalow with higher accuracy. With the image pairs with natural coverages (such as bare soil, tree and rural road), the accuracy is relative low. These findings indicate that the artificial structures have a better performance in detection and matching.
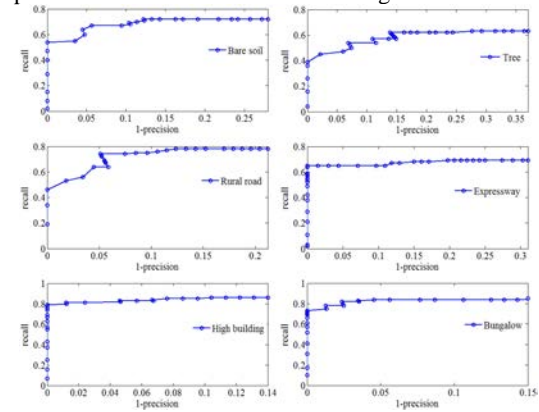
Fig. 9. 1-precision vs recall

5.5 Resource usage

The FPGA resource usage of the proposed method is analysed in this section. The results of comparison are listed in Table 1. As seen from Table 1, the usage of FFs and LUTs in this work are 28% and 39%. The usage of BRAMs in this work is about 0%. The usage of FPGA resources in this work can be reduced when the whole system are further optimized.

Table 1 Comparison of FPGA resource usage

Resource	FFs	LUTs	BRAMs
FAST+BRIEF	112,166 (28%)	80,472 (39%)	1 (~0%)

6 CONCLUSION

This paper proposes a FPGA implementation of FAST and BRIEF algorithm for detection and matching of feature points. The proposed algorithm, which realize the corner detection by pixel level processing and achieve the matching by fix-point operation, is different from the traditional detection and matching methods. These traditional methods have an excellent performance on PC, while they are time-consuming and large consumption of resource on FPGA.

This paper proposed a whole hardware architecture for FAST and BRIEF algorithm. In this architecture, the data flow are firstly sent into DDR3 for storing, then storing data are sent to detection module for corner detection. Based on the location of detected corner, a sub-image centred on corner are sent into matching module from DDR3. In matching, a hamming distance of two candidate descriptors is computed, and a point pair is determined by finding a minimal hamming distance from the candidate hamming distances.

A high-resolution satellite image pair of Mentougou district, Beijing is used as the experimental area. Six sub-image pairs covering with different coverages are used to evaluate the performance of the FPGA implementation of the proposed algorithm. The experimental results find that (1) If image pairs cover with artificial structure (such as expressway, building, and bungalow), the accuracy of matching is higher than those cover with natural terrain; (2) When the image with a size of 256×256, the speed of FPGA-based implementation can reach 500 fps, which is 19 times speedup when compare with PC-based implementation (about 38 ms per frame); (3) The consumption of FPGA resources is acceptable for the selected FPGA platform. When the whole FPGA architecture is further optimized, the usage of resource will be reduced.

7 ACKNOWLEDGMENT

8 References

Rosten, E., Porter, R., & Drummond, T., 2010, Faster and better: A machine learning approach to corner detection. IEEE transactions on pattern analysis and machine intelligence, 32(1), 105-119.

Zhou, G.Q.; Baysal, O.; Kaye, J.; Habib, S.; Wang, C., 2004, Concept design of future intelligent earth observing satellites. Int. J. Remote Sens. 25, 2667–2685.

Zhang, B., 2011, Intelligent remote sensing satellite system. J. Remote Sens. 15, 415–431.

Torres-Huitzil, C., & Arias-Estrada, M., 2000, An FPGA architecture for high speed edge and corner detection. In Computer Architectures for Machine Perception, 2000. Proceedings. Fifth IEEE International Workshop on (pp. 112-116). IEEE.

Yao, L.; Feng, H.; Zhu, Y.; Jiang, Z.; Zhao, D., 2009, An architecture of optimised SIFT feature detection for an FPGA implementation of an image matcher. In Proceedings of the International Conference on FieldProgrammable Technology, Sydney, Australia, pp. 30–37.

Mehra, R., & Verma, R., 2012, Area Efficient FPGA Implementation of Sobel Edge Detector for Image Processing Applications. International Journal of Computer Applications, 56(16).

Bi, C., & Maruyama, T., 2012, Real-time corner and polygon detection system on FPGA. In Field Programmable Logic and Applications (FPL), 2012 22nd International Conference on (pp. 451-457). IEEE.

Svab, J.; Krajnik, T.; Faigl, J.; Preucil, L., 2009, FPGA based speeded up robust features. In Proceedings of the IEEE International Conference on Technologies for Practical Robot Applications, Woburn, MA, USA, pp. 35–41.

Schaeferling, M.; Kiefer, G., 2011, Object recognition on a chip: A complete SURF-based system on a single FPGA. In Proceedings of the 2011 International Conference on Reconfigurable Computing and FPGAs, Cancun, Mexico, pp. 49-54.

Sledevič, T.; Serackis, A., 2012, SURF algorithm implementation on FPGA. In Proceedings of the 2012 13th Biennial Baltic Electronics Conference, Tallinn, Estonia, pp. 291–294.

Battezzati, N.; Colazzo, S.; Maffione, M.; Senepa, L., 2012, SURF algorithm in FPGA: A novel architecture for high demanding industrial applications. In Proceedings of the Conference on Design, Automation and Test in Europe, Dresden, Germany, pp. 161–162.

Weberruss, J.; Kleeman, L.; Drummond, T., 2015, ORB feature extraction and matching in hardware. In Proceedings of the Australasian Conference on Robotics and Automation, the Australian National University, Canberra, Australia, pp. 1–10.

Huang, J., Zhou, G., 2017, On-Board Detection and Matching of Feature Points. Remote Sensing, 9(6), 601.

Fan, X.; Wu, C.; Cao, W.; Zhou, X.; Wang S.; Wang L., 2013, Implementation of high performance hardware architecture of OpenSURF algorithm on FPGA. In Proceedings of the 2013 International Conference on Field-Programmable Technology, Kyoto, Japan, 152–159.

Fularz, M.; Kraft, M.; Schmidt, A., & Kasiński, A., 2015, A high-performance FPGA-based image feature detector and matcher based on the FAST and BRIEF algorithms. International Journal of Advanced Robotic Systems, 12(10), 141.

Rosten, E., & Drummond, T., 2006, Machine learning for high-speed corner detection. Computer Vision–ECCV 2006, 430-443.

Calonder, M., Lepetit, V., Strecha, C., & Fua, P., 2010, Brief: Binary robust independent elementary features. Computer Vision–ECCV 2010, 778-792.

Available online: https://china.xilinx.com/support/documentation/selection-guides/7-series-product-selection-guide.pdf (accessed on 15 July 2016).

OpenCV library. Available online: http://opencv.org/ (accessed on 12 June 2017).

Mikolajczyk, K.; Schmid, C., 2005, A performance evaluation of local descriptors. IEEE Trans. Pattern Anal. Mach. Intell. 27, 1615–1630.

Super-resolution reconstruction of remote sensing image based on neural network with barycentric weight function

Xing Huo[1,2], Wenxuan Huang[1], Lingling Ma[3,*], Kun Shao[1], Ronglin Tang[4], YongHua Yang[5]

[1] Hefei University of Technology , Hefei, Anhui 230009,PR China;
 huoxing@hfut.edu.cn

[2] University of Science and Techbology of China, Hefei, Anhui 230000,PR China;
huoxing@ustc.edu.cn

[3] Key Laboratory of Quantitative Remote Sensing Information Technology, Academy of Opto-Electronics, Chinese Academy of Sciences, Beijing 100094, PR China;
llm_2017@outlook.com

[4] Institute of Geographic Sciences and Natural Resources Research, CAS, Beijing,100101,PR China;trl_wd@163.com

[5]Long Kang Farm, Huaiyuan, Anhui 233426,PR China

ABSTRACT (OF 200-250 WORDS)-*An accurate super-resolution image(SI) reconstruction of remote sensing images (RSI) for preserving the quality during the process of super-resolution conversion is crucial for many scientific and operational applications. Recent studies in supervised and unsupervised machine learning methodologies of SI reconstruction have demonstrated their great potential for higher reconstruction performance in obtaining the accuracy and quality. In this paper, a novel neural network with barycentric weight function(BWFNN) was proposed as a non-linear mapping function selected from the features of reference images. The whole process includes online reconstruction phase and offline training phase, the innovation falling in three respects:(1) a new neural network based on barycentric weight function (BFWNN)for mapping was proposed; (2) an edge oriented based pre-learned kernel was introduced to subscribe the reference prior information; (3) a simple interpolation-like structure was taken in the proposed method which does not require any conventional iterative computation and leads to fast reconstruction. Compared with most of the conventional reconstruction approaches, the proposed algorithm performs better in terms of peak signal to noise ratio (PSNR) and structural similarity (SSIM) which shows its significant ability of reconstructing the image details. In addition, our algorithm is naturally robust to noise, and therefore, the proposed algorithm can handle low resolution with noisy inputs in a more unified framework.*

1 INTRODUCTION

In recent years, more and more remote sensing applications and projects rely on the moderate or high-resolution satellite images[1,2]. However, with the constraints of satellite orbital characteristics and atmosphere conditions, degraded scenes are usually obtained resulting in difficulties in identifying the objects[3-5].

The super-resolution (SR) reconstruction task is identified as a inverse problem of recovering the high-resolution image by a set of low-resolution images guided by reasonable assumptions or prior knowledge of specific model which maps the high-resolution images to low-resolution ones. This could be presented as the formula below,

$$L = SBH \tag{1}$$

where S is a down-sampling operator, and B is a blurring operator. The SR image reconstruction always known as a severely ill-posed problem[6]for the sake of the insufficient number of low-resolution images, ill-conditioned registration and unknown blurring operators, leading to an infinite number of resolutions. Traditional SR image reconstruction algorithms generally accomplish the SR image reconstruction based on various prior knowledge for the precise estimation.

Many studies focus on high resolution(HR) image up-scaling which can be concluded as two categories: low complexity and high quality. For lowing the computation complexity, interpolation algorithms are always taken to fill the missing pixels during the enlargement [7,8]. Although this kind of approach is very fast and practical, it produces low-quality HR images. A better solution is selective SR method[9] which is an improvement of conventional SR method. Compared to the traditional methods, it has

lower computation. In these approaches, specific image patches are selected based on human visual perception metrics for SR. Conventional SR methods always aims at generating high quality results other than the complexity. Machine learning techniques are utilized in these methods. Most famous SR method including:

(1) SR methods based on convolutional neural networks. The most popular algorithm in this category is SRCNN[10] which introduces deep convolutional neural networks to learn the mappings. These methods outperform others in quality, but accompanying with high-complexity. (2) SR methods based on sparse representation. ANR is both based on the sparse learned dictionary and cluster centroids[11]. (3) SR methods based on the examples. LR-HR correspondences are generated from certain examples in the dictionaries by certain searching strategy. Two kinds of dictionaries are utilized: external and internal. External dictionary is built from various external HR images[6] while internal dictionary is built from internal LR image itself [14].However this approach also have much higher complexity than interpolation methods. The SI method was proposed first in[12]. Unlike the conventional SR methods, this approach doesn't require any intermediate bicubic interpolation and overlapping processing , directly maps an LR image patch to its HR one via edge-orientation based linear mapping which is a unified transformation of edge-orientation based interpolation and linear mapping based SR, thus makes the SR processing less complex. Although this method is satisfying , it still can be improved in a few ways.

In this paper, we intend to gain a high-resolution image for the sake of visual recognition with lower complexity and an effective SI method based on the barycentric neural network was presented. The proposed SI method generates HR images of better or comparable quality compared to the SI method and other state-of-the-art SR methods. The whole paper is organized as follows: Section II gives the whole framework of the proposed approach and the core structure of the SI method; Section III presents the training phase of the framework including the construction of the training set which based on the edge-oriented clustering of the patches and the non-linear mapping which based on the BFWNN.; We describe our proposed SI method in Section IV by presenting how we elegantly reconstruct the HR image; Section V shows a plenty of experimental results for our SI method in comparison with SI method and other state-of-the-art SR methods; Section VI draws the conclusion.

2 PROPOSED ALGORITHM

2.1 The Framework of Proposed Algorithm

The whole amework includes two phases: training phase and reconstruction phase. In training phase, external images are used for constructing the training set. Like SR method based on examples, images are decomposed to LR-HR pairs based on an interpolation structure, then clustered and indexed according to the edge-oriented analysis, finally, for each indexed cluster an non-linear mapping results are learned based on the BFWNN. In reconstruction phase, The LR image (the image needs up-scaling) is separated into LR patches and each patch is indexed by the edge-oriented analysis and looked up by the index for a reasonable mapping result, finally, by applying such mapping result the HR image is obtained. The entire procession is shown in Fig 1,
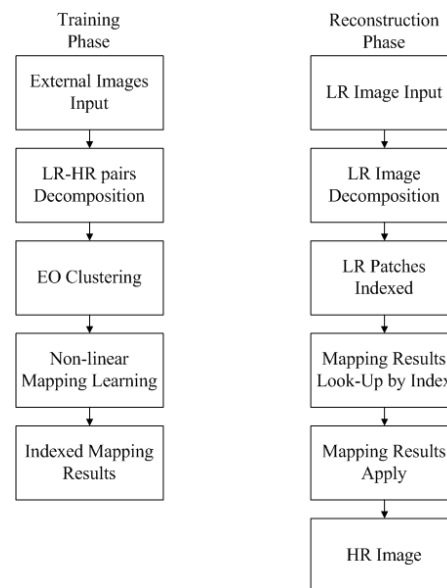
Fig 1 Flowchart of proposed framework

2.2 The Core Structure

In conventional SR reconstruction, an intermediate interpolated image is generated first, then converts the interpolated image into high resolution image by patch-wise strategy. Therefore, the overlapping is inevitable when placing the generated HR patch back to the image which leads to the additional operations. SI can effectively resolve these problems. The Core structure of SI is an interpolation one, peripheral information of the surrounding pixels from LR image is utilized to better estimate 4 HR pixels by an interpolation-like structure. An 3x3-2x2 structure of SI used for generating HR image is shown in fig 2 which generates x2 upscale result,

Fig 2 3x3-2x2 structure of SI

Table 1   Quantized Patch Indices

Gradient Direction Value	Quantized Value	Code Value
Low gradient magnitude	--	0
-22.5-22.5	0	1
22.5-67.5	45	2
67.5-112.5	90	3
112.5-157.5	135	4
157.5-202.5	180	1
202.5-247.5	225	2
247.5-292.5	270	3
292.5-337.5	315	4
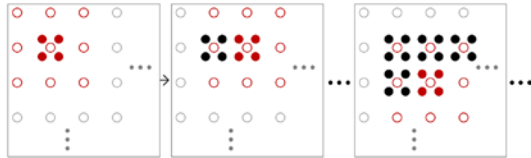
where 3x3-2x2 structure means four HR pixels are generated by the 3x3 LR patch with an interpolation structure. Although the padded LR patches are used, the generated HR patches are non-overlapped. more - over, the templates of LR patches are also flexible. In the following section, we will discuss the training phase and reconstruction phase of our proposed approach based on this structure.

3 TRAINING   PHASE

3.1 Construction of the Training Set

External images with high resolution are utilized for constructing the training set in this phase. In SI approach, all of the external images are down-scaled and blurred first by eq(1) to generate the LR images set. Thus, for each HR external image has one corresponding LR image. Then, LR-HR patch pairs are extracted from the external images according to the 3x3-2x2 SI structure. Finally, LR-HR patch pairs set are generated from the external images set which used as the training set.

Before applying the learning procession, the training set requires some refinement. LR-HR patch pairs in the training set are indexed by edge-oriented strategy which used for the preserving of the texture features. For each LR patch, two 2x2 gradient operators (vertical and horizontal) are applied to the LR patch in four diagonal directions. For each direction, the gradient magnitude (2 norm of the gradient values) and direction (tangent value) are computed. Then, the gradient magnitude is compared to a threshold (15 in SI) to judge whether there is an edge or not. If there is no edge, the index of this direction is set to 0. If edge exits, then assigned the four indices according to the gradient direction values. Otherwise, these values are required quantization and the quantization rule utilized in SI is shown in table 1

Four indices can represent the texture feature of this LR patch. For convenience, four indices are coded into one single quainary code which used as the EO index.

Since each pair has an index, patch pairs from training set with similar texture structure could be clustered by the indices. With the indices, a look-up table can be formed. For each index, a new training sub-set is generated and this set is used for the learning of the HR patch mapping.

3.2 BFWNN Construction

For each cluster a non-linear Mapping from LR patch to HR patch can be learned from the training set by some kind of interpolation. A novel neural network is proposed in this paper which is based on the barycentric interpolation.

There is supposed to be one mapping function corresponds to one specific cluster. LR-HR patch pairs from one cluster could be used to learn the mapping. Since the size of LR patch is 3x3, the size of HR patch is 2x2, if we convert the patches into one dimensional gray value vector in column-major order, the mapping is supposed to project the vector with nine elements to the vector with four elements in an interpolation-like form.

Suppose $L_1 \cdots L_9$ are values of non-linear mapping functions at input LR image patch pixels $l_1^{In} \cdots l_9^{In}$. These non-linear mapping functions have barycentric rational interpolation structure, they are learned from the training set. $H_1 \cdots H_4$ are pixels' values of generated high resolution patch which are given by equation (2),

$$H_m = \sum_{n=1}^{9} \eta_n L_n, m = 1 \cdots 4, n = 1 \cdots 9 \quad (2)$$

Where, η_n is the weight of interpolation for generating HR patch. η_n is also taken as a projection factor, it represents the importance of a specific surrounding pixel. Therefore, the selection of η_n depends on the contribution of the pixels from the LR patch.

The non-linear mapping functions for generating the L_n are constructed from the training set (actually from a certain EO cluster of the training set, thus each cluster corresponds to one non-linear mapping (BFWNN)).

Suppose the number of LR-HR pairs in i^{th} cluster is denoted as num_i, the LR patches in i^{th} cluster is denoted as LR_j^i and the HR patches in i^{th} cluster is denoted as HR_j^i.

$$LR_j^i = \{l_{n,j}\}, n = 1\ldots 9, j = 1\cdots num_i \qquad (3)$$
$$HR_j^i = \{h_{m,j}\}, m = 1\ldots 4, j = 1\cdots num_i$$

where l, h respectively represent the gray value of pixels in LR patch and HR patch.

To construct the training samples, the dimension should be unified. Reverse mapping of the proposed network is utilized, suppose $\eta_n^{'(m)}, m = 1\ldots 4, n = 1\ldots 9$ is the reverse mapping factor which is preselected. Suppose $HR_i^{'}$ denotes the unified HR patch of ith cluster, then,

$$HR_j^{i'} = \eta_n^{'(m)} \cdot HR_j^i = \{h_{n,j}^{'(m)}\},$$
$$m = 1\ldots 4, n = 1\ldots 9, j = 1\ldots num_i$$

where the multiply represents row vectors of $\eta_{m,n}^{'}$ multiply the corresponding column elements of HR_j^i. For each pixel of HR patch, four sample sets are represented by $\{l_{n,j}, h_{n,j}^{'(1)}\}, \{l_{n,j}, h_{n,j}^{'(2)}\}, \{l_{n,j}, h_{n,j}^{'(3)}\}$, $\{l_{n,j}, h_{n,j}^{'(4)}\}$, each set is used to construct the barycentric rational interpolations. The barycentric rational interpolation form is given by,

$$L_n = BF_n(l_n^{In}) = \frac{\sum_{j=0}^{num_i - d} \mu_{n,j}(l_n^{In}) h_{n,j}^{'(m)}}{\sum_{j=0}^{num_i - d} \mu_{n,j}(l_n^{In})}$$

Where, $\mu_{n,j}(l_n^{In}) = \prod_{r=0}^{j-1}(l_n^{In} - l_{n,r}) \prod_{k=j+d+1}^{num_i}(l_{n,k} - l_n^{In})$

d is an integer with $0 \le d \le num_i$. In this paper d is chosen as 1.

The whole procession is shown in fig 3,
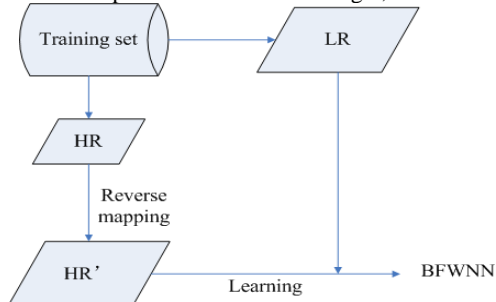
Fig 3 The construction of BFWNN

4 RECONSTRACTION PHASE

Compared to the training phase, the reconstruction phase is a reverse procession. In reconstruction phase, the LR input image is divided to the 3x3 patches, then each patch's edge feature is computed to find EO cluster it belongs to, the non-linear mapping(BFWNN) of the corresponding EO cluster is applied to the LR patch and generates the HR patch. Finally, by using the SI structure, filling such HR patches back to the LR image to construct the HR version.

5 EXPERIMENTS

To validate the proposed method, five popular super-resolution reconstruction algorithms were taken. The performance comparisons were carried out on six HR images from Berkeley Segbench database and remote sensing image with an ordinary resolution(322x482-512x512). These images were down-sized by bicubic interpolation method and up-scaled by different reconstruction methods where SI,SI- BFWNN used 3x3-2x2 structure. The training set for the methods mentioned above contained 69 images used in [6]. Comparisons among these methods in terms of PSNR，SSIM and TIME are listed in table1. The reconstructed up-scaling images are showed in fig1.

Table 2 The perform comparisons of different SR methods

Images	Bicubic		NEDI		ICBI	
	PSNR	SSIM	PSNR	SSIM	PSNR	SSIM
Lena	34.28	0.929	34.01	0.921	34.96	0.931
Woman	28.13	0.838	27.56	0.813	28.26	0.836
Monarch	31.94	0.957	31.72	0.953	32.91	0.961
Caps	33.67	0.924	33.88	0.922	34.04	0.926
Bikes	27.11	0.842	27.01	0.832	27.60	0.856
Parrots	35.01	0.954	35.11	0.951	35.69	0.955

Images	SRCNN-15		SI		SI- BFWNN	
	PSNR	SSIM	PSNR	SSIM	PSNR	SSIM
Lena	36.02	0.945	35.54	0.939	35.72	0.940
Woman	29.55	0.871	28.72	0.865	28.98	0.871
Monarch	36.98	0.973	34.87	0.969	35.40	0.970
Caps	36.01	0.941	35.43	0.936	35.77	0.937
Bikes	29.98	0.903	28.11	0.857	28.53	0.859
Parrots	38.12	0.962	36.75	0.957	37.02	0.960

As shown in Table1, SRCNN gives best performance since a deep neural network is used, the proposed method is less performance than SRCNN and better than SI method using linear mapping and other methods. Results indicate that the proposed method can keep both colour and structure information.
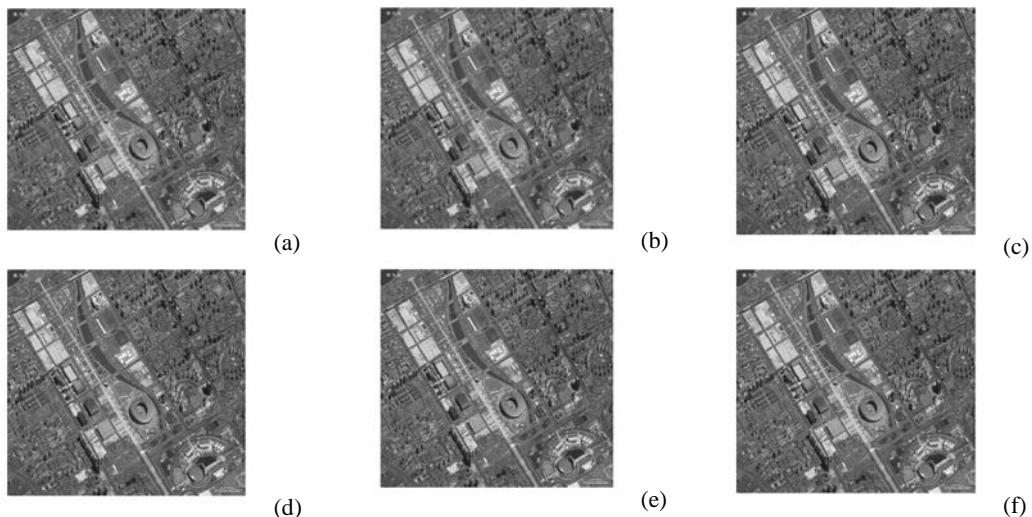
Fig 4 Remote sensing image enlarged by six methods.(a)bicubic (b)NEDI (c)ICBI (d)SRCNN (e)SI (f)SI-BFWNN

We also compared the time consuming among these methods. Bicubic is the fastest, ICBI is the lowest. SRCNN is a little faster than NEDI. Compared to SRCNN, SI method performances much better, between them is the proposed method.

6 CONCLUSION

As shown in Table 3 and Fig 4, the proposed method is good at preserving the colour and texture structure of the image for its non-linear mapping network and the time cost is also acceptable. The future work will focus on more accurate mapping strategy and reducing the time consuming.

7 REFERENCE

Inglada J.,Vincent A.,Arias M.,Tardy B.,Morin D.and Rodes I.,2017,Operational High Resolution Land Cover Map Production at the Country Scale Using Satellite Image Time Series, *Remote Sensing,* 9,pp.95-140.

Lu H.Y., Wei J.B.,Wang L.Z.,Liu P.,Liu Q.G., Wang Y.H. and Deng X.H.,2016,Reference Information Based Remote Sensing Image Reconstruction with Generalized Nonconvex Low-Rank Approximation, *Remote Sensing,* 8,pp.499-519.

Seto, K.C.,Woodcock, C.E.,Song, C.,Huang, X., Lu, J.,Kaufmann, R.K.,2002,Monitoring land-use change in the pearl river delta using landsat tm. *International Journal of Remote Sensing,*23, pp.1985–2004

Narasimhan, S.G., Nayar, S.K.,2002, Vision and the atmosphere. *International Journal of Computational Visualization,* 48, pp.233–254.

Narasimhan, S.G., Nayar, S.K.,2003, Contrast restoration of weather degraded images. *IEEE Transactions on Pattern Analaysis and Machine Intelligences,*25, pp.713–724.

Giachetti A. and Asuni N.,2011,Real-time artifact-free image upscaling, *IEEE Transactions on Image Processing,*20(10), pp.2760–2768.

Kang W. et al.,2013, Real-time super-resolution for digital zooming using finite kernel-based edge orientation estimation and truncated image restoration, *in Proc. 20th IEEE International Conference of Image Processing,* pp.1311–1315

Liang L.,Luo P., Cheung W. K., and Chiu K. H., 2013,Fast single rame super-resolution using perceptual visibility optimization, *in Proc. IEEE Int. Symp. Circuits Syst.* pp.2716–2719.

Zhang K.,Tao D.,Gao X.,Li X.,and Xiong, Z. , 2015,Learning multiple linear mappings for efficient single image super-resolution, *IEEE Transaction on Image Processing,*24(3), pp.846–861.

Timofte R.,De V., and Van L. Gool, 2013,Anchored neighborhood regression for fast example-based super-resolution, i*n Proc. IEEE International Conference of Computational Visualization,* pp.1920–1927.

Li B., Chang H., Shan S., and Chen X., 2009,Locality preserving constraints for super-resolution with neighbor embedding, *in Proc. 16th IEEE International Conference of Image Processing,* pp.1189–1192.

Choi J.S. and Kim M.,2016, Super-Interpolation With Edge-Orientation-Based Mapping Kernels for Low Complex 2× Upscaling, *IEEE Transactions on image processing,* 25(1), pp.469-483

Assessment of the zenith tropospheric delay derived from GGOS Atmosphere data with GNSS ZTD over China

Junyu Li [1,2,*], Lilong Liu [1,2,3,*], Liangke Huang [1,2,*], Shaofeng Xie [1,2,] Fade Chen [1,2] and Linbo Liu [1,2,]

1 College of Geomatics and Geoinformation, Guilin University of Technology, Guilin 541004, China;

lijunyu@glut.edu.cn (J.L.); 15676331890 (J.L.); xieshaofeng@glut.edu.cn (S.X.); 1182913264@qq.com (F.C.); 874086451@qq.com (W.Z.);

2 Guangxi Key Laboratory of Spatial Information and Geomatics, Guilin 541004, China

3 College of Resources and Environment, Qinzhou University, Qinzhou 535011, China

* Correspondence: lijunyu@glut.edu.cn(J.L.) 15676331890 (J.L.);
lkhuang666@163.com(L.H.); 15578360626 (L.H.);hn_liulilong@163.com (L.L.); 13367835262 (L.L.)

ABSTRACT: The tropospheric delay of GNSS signals from the zenith to the horizon (ZTD) is about 2-20 m. In this work, we initially used gridded ZTD data from Global Geodetic Observing System Atmosphere products (GGOS ZTD) to calculate ZTD at studied sites. We also implemented the Global Navigation Satellite System observed ZTD (GNSS ZTD) to compare the precision and simplicity of GGOS ZTD interpolated by different methods to establish a model for interpolating GGOS ZTD at any site. At the same time, the stability of interpolated GGOS ZTD in space and time was validated. The results are as follows: (1) Relative to GNSS ZTD, the yearly bias and RMS for the GGOS ZTD were determined to be -0.40 cm and 2.30 cm, respectively. (2) The GGOS ZTD showed good correction performance and reliability. (3) GGOS ZTD is sufficient for ZTD correction and to establish a ZTD prediction model for GNSS navigation and positioning in China.

Keywords: GNSS·ZTD·GGOS ZTD·Refinement·CMONOC

Introduction

Currently, it is necessary to improve the accuracy of ZTD corrections for in high precision GNSS applications, since tropospheric delay is a primary error source for satellite navigation and can be mapped onto the zenith direction using the mapping function (Li et al., 2010; Jin et al., 2010). Over the past few decades, a number of mitigation approaches have been developed for ZTD correction. Such approaches are split into meteorological parameter models (Hopfield, 1969; Saastamoinen, 1973; Black, 1978; et al.) and non-meteorological parameter models (Dodson et al., 1999; Penna et al., 2001; Krueger, 2005; Leandro et al., 2008; Lagler et al., 2013; Schüler, 2014; Li et al.,2015; Möller et al., 2015; Yao et al., 2016; Huang et al., 2017). Another approach includes deriving ZTD from numerical forecast data (Pany T et al., 2001; Ghoddousi-Fard et al., 2009; Chen et al., 2012) from the European Center for Medium-Range Weather Forecasts (ECMWF), the United States National Centers for Environmental Prediction (NCEP), et al. However, the ZTD derived from this method is integrated based on the pressure-level meteorological data, which is time consuming and complicated. The GGOS ZTD is of high temporal and spatial resolution, and ZTDs can be obtained by simply adding up the ZHDs and ZWDs at the same point and time. For instance, Yao et al. (2017) conducted a global performance evaluation of GGOS ZTD for satellite navigation and positioning. However, the China region has not been a focus in such studies. With the development of navigation and positioning and the large land mass covering various climate zones, it is necessary to check the feasibility of GGOS ZTD for ZTD correction over China. The GNSS ZTD, which was derived from the observed data in the year 2015 at 205 GNSS sites distributed in China, was used to build the appropriate method for deriving GGOS ZTD in any site and to assess the feasibility and accuracy of GGOS ZTD for ZTD correction. The work presented in this paper provides a valuable reference for fellow researchers needing to compute ZTD and establish the ZTD prediction model based on GGOS ZTD, which is specifically significant for the massive GNSS users and manufacturers in China.

Data sets

The GGOS provides ZHDs and ZWDs (Boehm et al., 2006) on a global grid with 2.5°×2° (lon×lat) sampling

at 00:00, 06:00, 12:00, and 18:00 UTC per day, which was derived from the reanalysis data provided by the ECMWF. The range for GGOS ZTD data in this study is from 18°N to 54°N and from 72.5°E to 135°E. The reference GNSS ZTDs were observed from the measured data in the year 2015 at 205 GNSS sites, including 8 IGS (International GNSS Service) sites and 197 CMONOC (The Crustal Movement Observation Network of China) sites distributed in China, with a temporal resolution of 2 hours. The locations of the GNSS sites are shown in Figure 1; the asterisk and square denote the IGS site and CMONOC site, respectively.
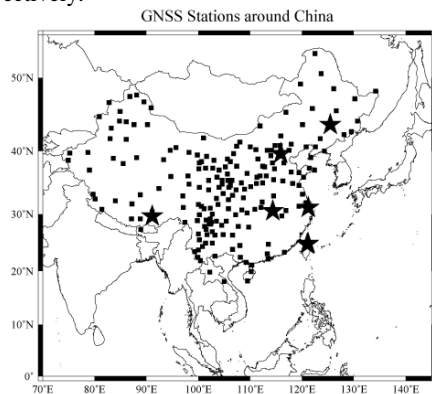
Figure 1 Distribution of the GNSS sites in China

ZTD of a GNSS station elevation from GGOS ZTD data

The ZTD variation is complex due to the strong correlation between ZTD and elevation and the comprised area of complex terrain with great undulations over China. Therefore, it is necessary to establish an altitude difference correction model for correcting the altitude difference between GGOS ZTD grids and GNSS sites in China. The characteristics of GNSS ZTD variation in height over China were studied, and the results are shown in Figure 2.
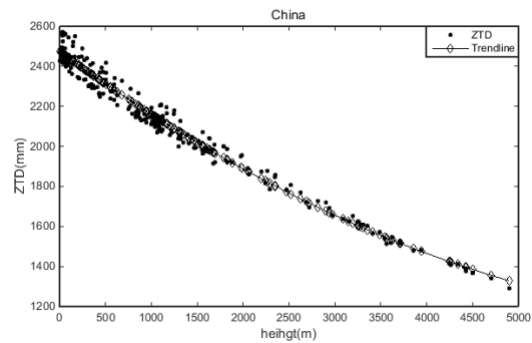
Figure 2 Characteristics of GNSS ZTD variation in height over China

It is obvious that the annual GNSS ZTD decreased with increasing altitude. The decreasing rate and acceleration were estimated based on the nonlinear least squares method using one year annual GNSS ZTD in the year 2015, and the parameters were used in the altitude difference correction (ADC). The GGOS ZTD at a specific elevation can be obtained by adding the initial GGOS ZTD with ADC.

ZTD at the GNSS station from the ZTDs of the same elevation grid points

Most of the GNSS sites were not collocated with the GGOS ZTD grid points, thus four methods were used to derive GGOS ZTD at GNSS stations. One method selects the GGOS ZTD from the grid point nearest to the GNSS station (named NER), then adds ADC. A second method selects ZTDs of four grid points near the GPS station, adds ADC, and then interpolates the ZTD to the GNSS site by an arithmetic mean method (named AVE). The third method differs from the second method only by a bilinear interpolation (named BIL). The fourth method is equivalent to the former, but implements a distance-weighted algorithm (named IDW). Comparison of the results of the four methods is shown in Table 1, where it is clear that the latter three methods are similar in accuracy compared to the first method.

Table 1 Agreement between the GNSS ZTD and the GGOS ZTD derived by different methods (cm)

Methods	A NEA	B NEA+ADC	C AVE	D AVE+ADC	E BIL	F BIL + ADC	G IDW	H IDW + ADC
Yearly-bias	-4.91	-0.85	-14.37	-0.80	-15.47	-0.77	-6.45	-0.77
min-bias	-55.84	-9.65	-75.44	-6.32	-61.41	-7.84	-66.24	-7.89
max-bias	35.86	3.00	26.12	2.59	19.44	2.32	20.85	2.12
Yearly-RMS	7.79	2.78	15.77	2.63	16.14	2.53	8.20	2.52
min-RMS	1.25	0.79	1.32	0.91	1.28	0.87	1.07	0.84
max- RMS	55.96	9.82	75.56	7.21	61.52	8.00	66.36	8.05

The agreement between GNSS ZTDs and GGOS ZTDs derived by the first method is worse than those derived by the other three methods. We also found that the maximum absolute values of the bias and RMS from the BIL+ADC and IDW+ ADC were larger than that of AVE+ADC, where the AVE+ ADC is more stable than BIL+ADC and IDW+ ADC in accuracy. Thus, we preferred to use the AVE+ADC to derive GGOS ZTD in the GNSS stations. To refine the GGOS ZTD, we obtained the bias and RMS of AVE+ADC distributed in China. Figure 3 shows that the AVE+ADC with correction accuracy was worse than 4 cm in some areas of the Qinghai-Tibetan Plateau (range from 10°N~63°N and 30°E~160°E), and the ZTD estimation error from existing precision models was about 4 cm (Yao et al., 2017). Therefore, it is essential to refine the GGOS ZTD derived by AVE+ADC. Considering the absence of ADC, a significant improvement can be achieved in the precision of all four methods using altitude difference correction, which again demonstrates that it is necessary to add the ADC for deriving GGOS ZTD.

Figure 3 Distributions of bias and RMS for the GGOS ZTD interpolated by AVE + ADC in China

Determination of the refinement model

Figure 3 reveals that the bias of AVE+ADC at all sites in the Qinghai-Tibetan Plateau is equal to about -5 cm, suggesting that there may be some systematic difference between the GNSS ZTD and GGOS ZTD. Linear regression analysis was performed for GNSS ZTD and GGOS ZTD from all sites in Qinghai-Tibetan Plateau, which were used to analyze the systematic difference.

The results in Table 2 indicate that there is a significant linear relationship between GNSS ZTD and GGOS ZTD, whose correlation coefficient almost equals 1. The relationship is expressed in Equation (1), where y denotes GNSS ZTD; x is the derived ZTD; a and b are extracted from Table 2. GGOS ZTD derived by AVE+ADC can be refined by multiplying it by a then adding b.

$$y = ax + b \qquad (1)$$

Table 2 Results of the linear regression analysis between GNSS ZTD and the ZTD derived based on AVE+ADC

a	b	R^2
0.9718	8.8470	0.9912

Validation and analysis of the GGOS ZTD

After the GGOS ZTDs were processed by the AVE+ADC and refinement discussed above, the bias and RMSD were computed between GNSS ZTD and GGOS ZTD.

Table 3 Errors of GGOS ZTD validated by GNSS ZTD (cm)

bias			RMS		
max	min	mean	max	min	mean
2.59	-3.64	-0.40	3.98	0.92	2.30

The Temporal Variation of the Bias and RMS

Table 3 displays the yearly bias and RMS at GNSS stations for 2015. As seen from Table 3, compared to GGOS ZTD without refinement, the bias and RMS of the refined GGOS ZTD were reduced by 50% and 12.5%, respectively. The absolute bias and absolute RMS had maximums of 3.64 cm and 3.98 cm, respectively, and the refined GGOS ZTD is comparable to the most accurate and complicated models. The monthly bias and RMS were calculated to analyze their seasonal changes. Figure 4 presents variations in the monthly bias and RMS and shows that there is a significant season-varying feature in these factors. The bias had negative maximum in summer, positive maximum in spring with a minimum in autumn, but even distribution around zero without systematic
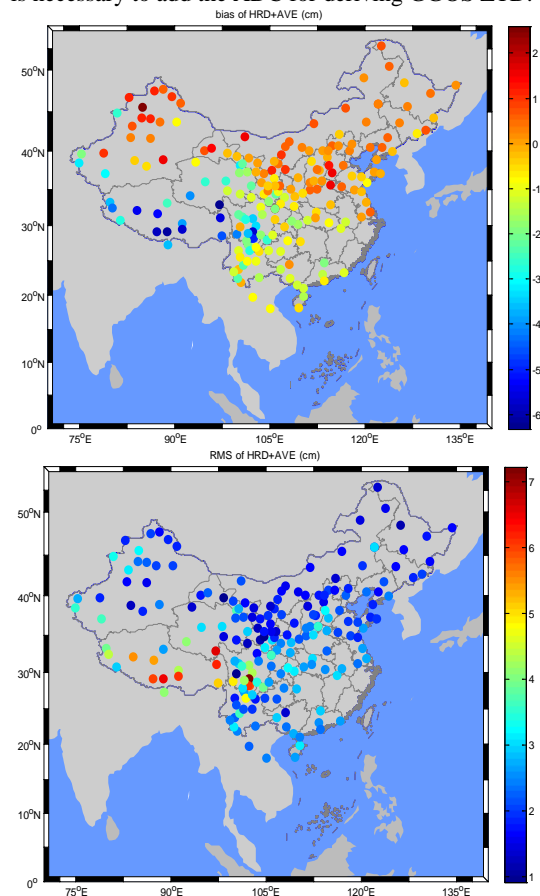
differences. There was a larger RMS in summer months and smaller RMS in winter months. The maximum bias and RMS occurred in summer due to the effect of the changeable atmospheric water. The daily bias and RMS of the sites (JSLS, XJBC, GDZH, NMDW), which are respectively located in eastern, western, southern, and northern China, were analyzed to probe their subtle variation. Statistical analyses are shown in Figure 5, which indicate that the daily bias and RMS had seasonal variations at the JSLS, XJBC, and GDZH sites where there were larger values and dramatic changes in summer. The daily bias and RMS of the NMDW site mildly changed without obvious seasonal features due to its far distance from the ocean and less change in atmospheric water vapor.
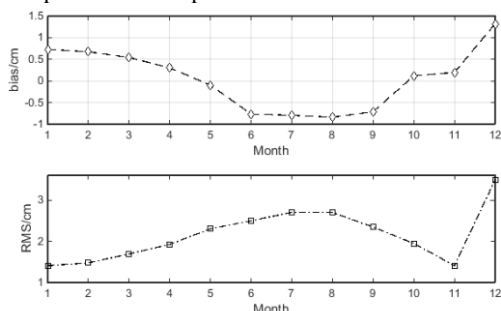
Figure 4 Variation in the monthly bias and RMS in 2015 over China
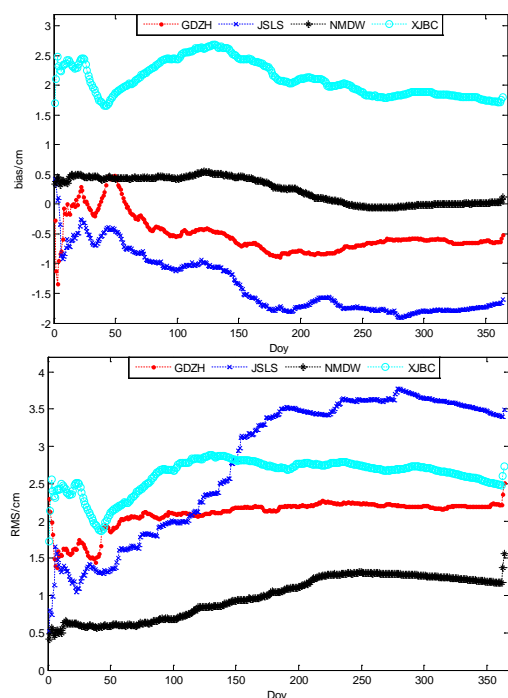
Figure 5 Variation in the daily bias and RMS in 2015 at JSLS, XJBC, GDZH and NMDW sites

The Spatial Characteristics of Bias and RMS

Variations in the bias and RMS with latitude and altitude were analyzed to research the spatial characteristics of both variables. The altitude range was organized into five categories, namely below 20°, 20-30°, 30-40°, 40-50°, and above 50°. The corresponding bias and RMS are listed in Figure 6, which shows that there is no obvious trend for the bias with increasing altitude. RMS showed an apparent decreasing trend with increasing latitude. The elevations were sorted using 500-m intervals (less than 500 m, 500-1000 m, 1000-1500 m, 1500-2000 m, 2500-3000 m, 3000-3500 m, 3500-4000 m, 4000-4500 m, and above 4500 m) to display the characteristics of bias and RMS with altitude. Figure 7 shows the bias and RMS with altitude sorted by ascending order. Figure 7 displays the increase in bias with increasing elevation in the range 0-3500 m and shows a significant reduction in the trend for elevations greater than 3500 m. RMS undulates with elevation changes without obvious trend. The RMS differences between each height interval are less than 1 cm. It can be seen that the height correction model established in this paper has a better correction for ZTD of each elevation interval.
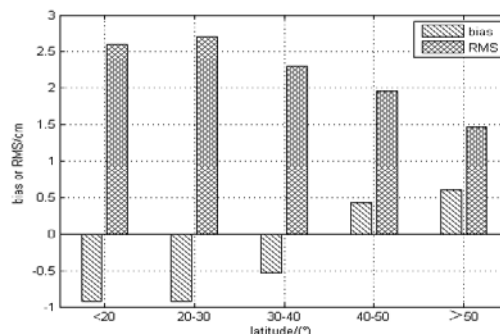
Figure 6 Distribution of bias and RMS with respect to altitude
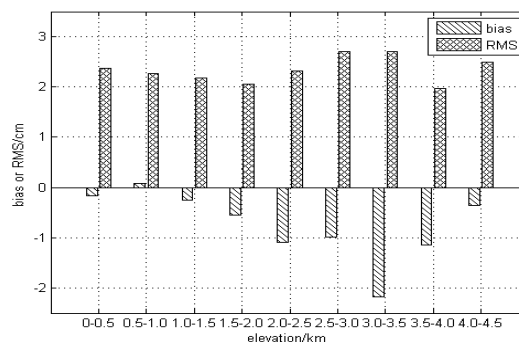
Figure 7 Distribution of bias and RMS with respect to height

Summary

The ZTD data from 205 GNSS sites distributed in China were used to investigate the performance of the GGOS ZTD. We conducted AVE+ ADC interpolation to derive GGOS ZTD at all sites due to its better accuracy and stability compared to other methods. Its systematic difference in the Qinghai-Tibetan Plateau can be corrected by Equation (1), where y demotes GNSS ZTD, x is GGOS ZTD, a and b are equal to 0.9534 and 12.4377, respectively. After refinement, the yearly bias had a maximum of 2.59 cm and average of -0.40 cm, while the yearly RMS had a maximum of 3.98 cm and average of 2.30 cm. Bias and RMS showed good stability with respect to time and position. It is suggested that the derived GGOS ZTD can be used for most ZTD corrections and to establish a ZTD prediction model for GNSS navigation and positioning.

References

Black, H. D., 1978, An easily implemented algorithm for the tropospheric range correction. Journal of Geophysical Research, 83, 1825–1828.

Chen, Q. M., Song, S. L., Zhu, W. Y., 2012, An analysis for the accuracy of tropospheric zenith delay calculated from ECMWF/NCEP data over ASIA. Chinese journal of geophysics, 55(3), 275-283.

Dodson, A. H., Chen, W., Baker, H. C., et al., 1999, Assessment of EGNOS tropospheric correction model. Proceedings of the 12th International Technical Meeting of the Satellite Division of The Institute of Navigation (ION GPS 1999), 1401–1408.

Ghoddousi-Fard, R., Dare, P., Langley, R. B., 2009, Tropospheric delay gradients from numerical weather prediction models: effects on GPS estimated parameters. GPS Solutions, 13(4), 281–291.

Hopfield, H. S., 1969, Two tropospheric refractivity profile for correcting satellite data. Journal of Geophysical Research, 74, 4487–4499.

Huang, L. K., Xie, S. F., Liu, L. L., 2017 SSIEGNOS: A New Asian Single Site Tropospheric Correction Model. International Journal of Geo-Information, 6(20), 1-18.

Jin, S. G., Luo, O., Ren, C., 2010, Effects of physical correlations on long-distance GPS positing and zenith tropospheric delay estimates. Advances in Space Research, 46, 190-195.

Krueger, E., Schueler, T., Arbesser-Rastburg, B., 2005, The standard tropospheric correction model for the European satellite navigation system. Proc. General Assembly URSI, New Delhi, India.

Lagler, K., Schindelegger, M., Böhm, J., et al., 2013, GPT2: Empirical slant delay model for radio space geodetic techniques. Geophysical Research Letters, 40, 1069–1073.

Leandro, R. F., Langley, R. B., Santos, M. C., 2008, UNB3m_pack: a neutral atmosphere delay package for radiometric space techniques. GPS Solutions, 12, 65–70.

Li, B. F., Feng, Y. M., Shen, Y. Z., et al., 2010, Geometry-specified troposphere decorrelation for subcentimeter real-time kinematic solutions over long baselines. Journal of Geophysical Research Solid Earth, 115 (B11), 226-234.

Li, W., Yuan, Y. B., Ou, J. K., et al., 2015, New versions of the BDS/GNSS zenith tropospheric delay model IGGtrop. Journal of Geodesy, 89, 73–80.

Möller, G., Weber, R., Böhm, J., 2014, Improved troposphere blind models based on numerical weather data. Navigation, 61, 203–211.

Pany, T., Pesec, P., Stang, G., 2001, Elimination of tropospheric path delays in GPS observations with the ECMWF numerical weather model. Physics and Chemistry of the Earth, Part A: Solid Earth and Geodesy, 26(6–8):487–492.

Penna, N., Dodson, A., and Chen, W., 2001, Assessment of EGNOS tropospheric correction model. Journal of Navigation, 54, 37–55.

Saastamoinen, J., 1973, Contributions to the theory of atmospheric refraction. Bulletin Géodésique (1946–1975), 107, 13–34.

Schüler, T., 2014, The TropGrid2 standard tropospheric correction model. GPS solutions, 18, 123–131.

Yao, Y. B., Hu, Y. F., Yu, C., et al., 2016, An improved global zenith tropospheric delay model GZTD2 considering diurnal variations. Nonlinear Processes in Geophysics, 23, 127–136.

Yao, Y. B., Xu X. Y., Hu, Y. F., 2017, Precision analysis of GGOS tropospheric delay product and its application in PPP, Acta Geodaetica et Cartographica Sinica, 46(3), 278-287.

Vegetation dynamics in the Iberian Peninsula from GIMMS NDVI 3g 1982-2011 and its relation to the advance of the summer season

B. Martínez[a], S. Sánchez-Ruiz[a], M.J. López García[b], M.A. Gilabert[a]

a) *Departament de Física de la Terra i Termodinàmica, Facultat de Fisica, Universitat de València. Dr. Moliner, 50, 46100-Burjassot (España).*
b) *Departament de Geografia, Universitat de València, Ap 22060, 46080 Valencia, España*
e-mail: beatriz.martinez@uv.es

ABSTRACT-*This work aims to analyse the trends observed in the start of growing season (SOS) for the vegetation canopy over the Mediterranean area of the Iberian Peninsula, as well as its relation with the temperature increase shown in the coastal Valencia region. The global and longest image time series Global Inventory Modelling and Mapping Studies (GIMMS) NDVI have been used. This archive corresponds to more than 30 years record (1982–2011) with a spatial resolution of approximately 8 km and a bi-weekly temporal resolution. The SOS has been computed from a smooth NDVI time series derived from a Multi-Resolution Analysis (MRA) based on the wavelet transform (WT). The MRA provides a temporal decomposition of the original series, where different components of the signal are derived removing the contribution of specific temporal resolutions. The detail component of level 4 has been selected since it provides the intra-annual variability of the original signal with a temporal resolution between 90 and 180 days. Moreover, two types of profiles were considered potentially unstable in our method and were therefore discarded from our analysis: firstly, pixels for which there is no distinct seasonality (e.g., more than ten years with NDVI mean value lower than 0.1) and secondly, pixels with double (or more) growing seasons. The results show an advance in the SOS parameter that could be related to the trend towards an earlier onset of the summer observed both from sea surface temperature (SST) data and from air temperature records in the Balearic Sea and its surroundings. The records indicate a significant temperature increase during the months of April, May and June, with a temperature variation of 0.5°C -1°C between the periods 1993-2009 and 1985-92 which show a recent tendency towards an earlier and longer summer.*

1 INTRODUCTION

Changes in start of vegetation growing season (SOS) can modify vegetation activity and ecosystem functions during the entire year that follows (Richardson et al., 2009), affecting even land–atmosphere energy and carbon budgets (Piao et al., 2008). Studies have reported pronounced changes in the SOS in northern middle and high latitudes in response to accelerated warming since the early 1980s (Richardson et al., 2009).

Longer variations in the growing seasons of temperate vegetation and changes over the Northern Hemisphere are mainly explained by changes in temperatures and precipitation during the last decades. However, uncertainties regarding this conclusion exist since the time scale considered in many of the studies has been limited (i.e., mostly between 1981 and 1999). Many authors have analysed satellite time series from the normalized difference vegetation index (NDVI) derived from the advance very high-resolution radiometers (AVHRRs) on NOAA's polar- orbiting satellites. Indeed, with some satellite observations now spanning more than 40 years, the value of this information for climate monitoring purposes is becoming increasingly evident. This is the case of the NASA Global Inventory Monitoring and Modeling Systems (GIMMS) group, which offers NDVI long time series with a spatial resolution of 8 km × 8 km and 15-day temporal resolution for a minimum period of 30 years (1981-2015).

In the Iberian Peninsula seems to be an agreement on an increase of temperature from the 1970s onward. Different rates are given depending on spatial scale (global, regional or local), the geographical area and the period of time considered in every study. However, the impression that the higher warming rates observed in recent decades are due to the increment of temperature during spring and summer seasons seems to be extending (López García, 2015).

The main objective of this study is to evaluate long-terms variation in the vegetative growing season over the Iberian Peninsula for a minimum period of 30 years (1982-2011) by using bi-weekly temporal resolution NDVI data at 8 km from the GIMMS archive. We will try to identify the possible impacts of spring temperature increase on spring vegetation greening.

2 MATERIALS

The used NDVI data set was produced at a spatial resolution of 8 km by the 15-day maximum-value composition technique using observations made by the AVHRR instrument on board the NOAA satellite series. This NDVI data set has been corrected for instrument calibration, viewing geometry, volcanic aerosols, and other effects not related to vegetation changes (Tucker et al., 2005).

3 METHODS

Although compositing techniques were used for synthesizing bi-weekly GIMMS products, the time series is still being affected by artifacts related to the presence of clouds and residual atmospheric effects. Previous to using phenological detection techniques, filtering the noise is essential. A smooth time series using the multi-resolution analysis (MRA) based on the wavelet transform (WT) was derived. This technique has demonstrated its ability in a wide range of remote sensing applications (Fonseca et al., 1998; Sakamoto et al., 2005; Martínez & Gilabert, 2009). Particularly, the MRA has demonstrated its high performance to derive relevant information from non-stationary time series about vegetation dynamics at regional scale, such as the mean and minimum NDVI value, the amplitude of the phenological cycle, the timing of the maximum NDVI (t_{max}) and the magnitude of the land-cover change (Martínez & Gilabert, 2009).

The MRA decomposes the signal into different temporal scales by successively translating and convolving the elements of a high-pass filter and low-pass scaling filter associated with the mother wavelet. These filters retain the small- and largescale components of the signals also known as detail (D) and approximation (A) series. The D component of level 4 has been selected since it provides the intra-annual variability of the original signal with a temporal resolution between 90 and 180 days.

The signal $f(t)$ can be reconstructed from the approximation and detail components as:

$$f(t) = A_m(t) + \sum_{j=1}^{m} D_j(t), \quad (1)$$

where m is the highest decomposition level considered. In the first level of the decomposition, $f(t)=A_1+D_1$, the signal has a low-pass filtered component, A_1, and a high-pass filtered component, D_1. In a second step, the approximation A_1 is split as $A_1=A_2+D_2$, and so on. The relationship $D_j=A_{j-1}-A_j$ gives us information about the portion of the signal that can be attributed to variations between the scales

[$j-1$, j]. In summary, the detail component D_j is a N-dimensional vector that depends on the wavelets coefficients and hence is associated with changes on averages in a scale j. The final term in the MRA is A_m, an N dimensional vector that depends only on the scaling coefficients. The approximation vector A_m is associated with averages over scales 2^m and longer and, therefore captures the slowly varying portion of the original signal (Percival & Walden, 2000).

3.1 Experimental procedure.

In this study, the SOS has been derived as the time when the left edge has increased to 20% of the amplitude. The threshold (20%) has been used extensively and was determined by Yu et al. (2010) from *in situ* observations. Although the typical evolution of modern SOS extraction methods has become more complicated, it has been found that more complex algorithms may not be able to produce better estimates of either SOS as expected, at least at a coarse spatial scale encompassing several sites. This threshold method has been chosen because of its low computation cost.

Figure 1 shows an example of the MRA derived for a pixel located in Almeria. The A_1 (red box) component belongs to the original NDVI series where the first-level has been discarded since it accounts for high frequency variations (<1 month), which are mostly due to temporal noise. The A_5 component belongs to the NDVI time series were the temporal changes due to low frequency variations (<1 year) have been discarded (i.e., the season variations) and only the inter-annual variations are remaining. According to the interpretation of Eq. (1), the detail component at levels j=2, ..., 5 are attributable to changes at scales: D_2(24-48 days), D_3(49–96 days), D_4(97–192 days), and D_5(193–384 days).

Instead of using the original NDVI time series, the D_4 (Figure 1) component from the MRA has been used since it demonstrated to represent a major contribution to the intra-annual variability and its suitability for detecting timing phenological parameters (Martínez & Gilabert, 2009).

The SOS for each year will be determined as the time when the 20% of the D_4 amplitude occurs for the period 1982-2011. The advance or delay of the SOS will be analysed by means of the slope of the SOS over the period. The timing which appears most often (i.e., the mode) is also computed for the SOS and the t_{max}. First, pixels with NDVI average values from June to September should be higher than 0.10. Second, only pixels with an annual maximum NDVI were considered.
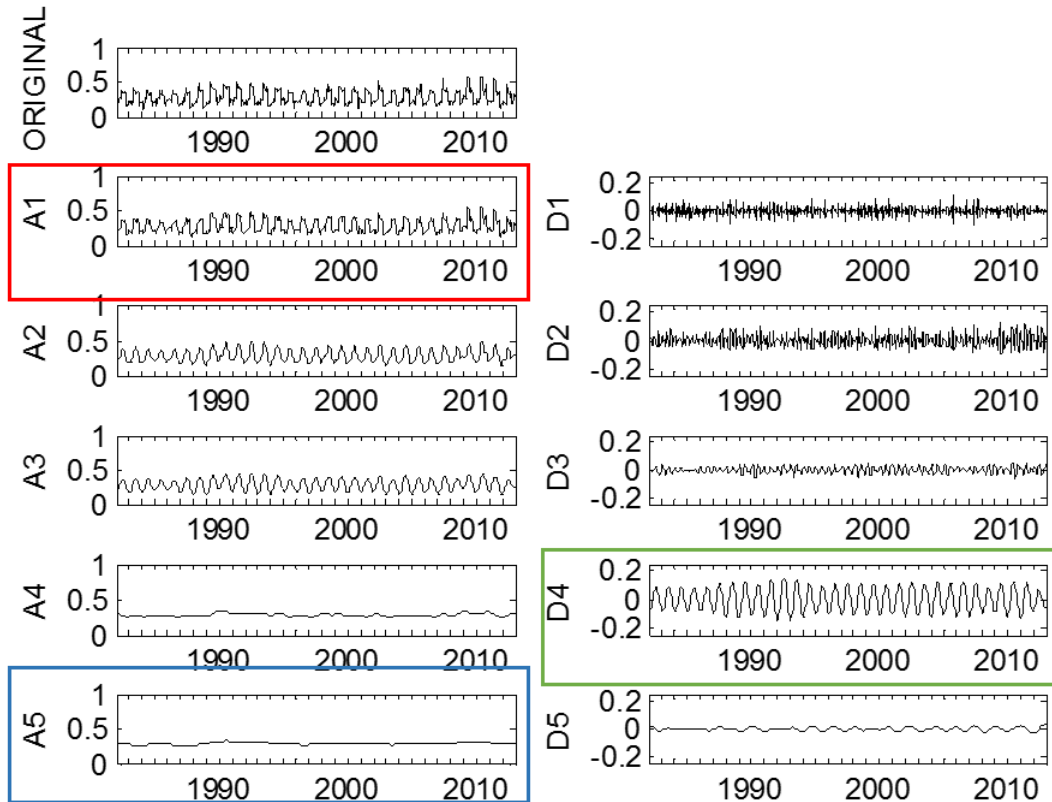
Figure 1. Example of the MRA for a pixel located in Almeria. The A_1 (red box) component belongs to the NDVI times series without high frequency variations (<1 month) whereas the A_5 component (blue box) component shows the NDVI signal with only the inter-annual variations. The D_4 component (green box) gives us information concerning to variations related to changes between three and six months.
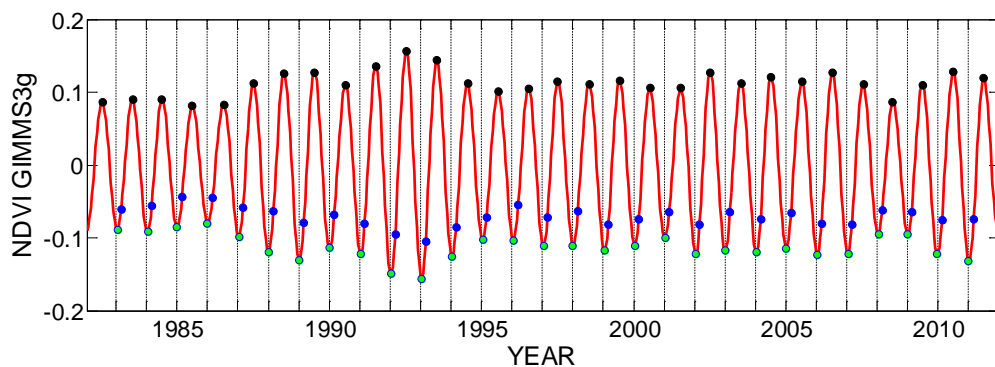
Figure 2. Example of the SOS (blue), time of maximum growing (black) and time of minimum growing (green) for the selected Almeria pixel of Figure 1. y-axis belongs to the D_4 NDVI component.

4 RESULTS

Major positives inter-annual changes over all the Mediterranean region and northern Spain (NDVI A_5 component) for the period 1982-2011 are observed (top Figure 3). Negative SOS changes over the major part of Spain explain a general advance in the SOS (centre) figure 3 for the considered period. The pixels with the highest positive inter-annual NDVI trend (top Figure 3) and most advance in the SOS are located in the Mediterranean coastline.
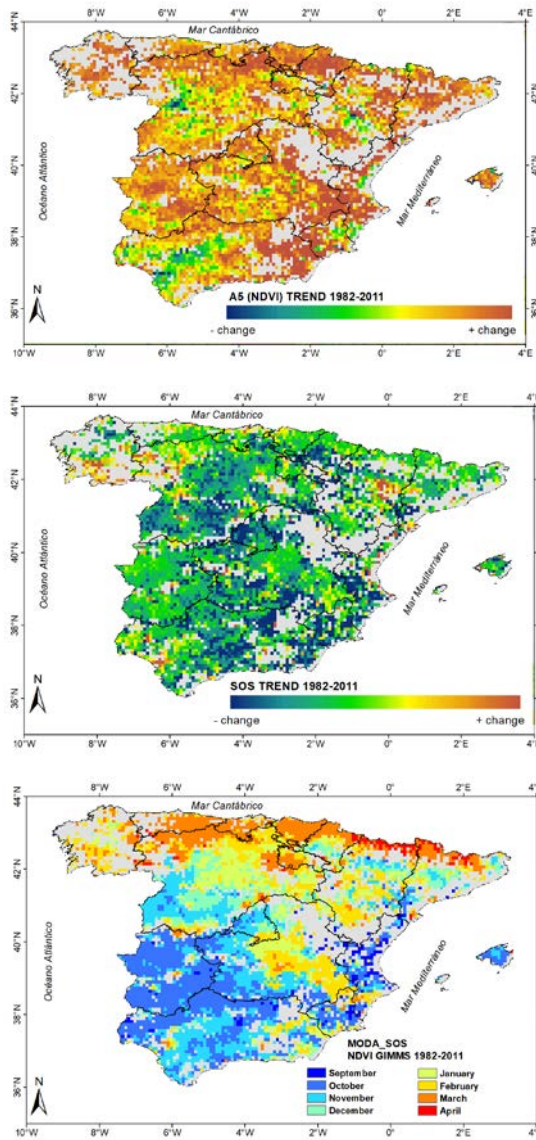
Figure 3. Inter-annual NDVI trend (top), SOS trend (centre) and mode values for the SOS (bottom) along the period 1982-2011. Grey color refers to non-significant pixels.

These results agree with those observed over the same area with other satellite products (Giner et al., 2012). A positive and different trend in the 3-month Standardized Precipitation Index (SPI) was observed for the 2000-2009 decade regarding the negative trends during the decade before (Giner et al., 2012; Martínez & Gilabert, 2009). Those pixels mainly correspond to citrus crops (east of Valencia region), herbaceous and shrub cover areas, mainly located at

the south of Murcia and Almeria regions. All of them reach the t_{max} between February and April, with the most often SOS around autumn season. The citrus crops along with the olive groves (concentrated in Extremadura region) show important changes during the year since in winter it is covered by herb (*Oxalis sp.*) that is eliminated by tilling in summer. This agricultural practice determines a higher NDVI value in February and SOS between September and October. The non-irrigated crops such those located in Castilla-Leon region shows a moderated advance in the SOS (dark green colors). These crops show a t_{max} in May with the most often SOS occurring between January and February. Forested areas in north Spain shows a low advance in the SOS (light green and yellow) with the most often SOS in March.

4.1 Relationship between vegetation dynamics and temperature.

Studies of sea surface temperature (SST) in western Mediterranean from AVHRR data in recent decades (López-García & Camarasa, 2011) as well as the analysis of longer land-temperature series for coastal Mediterranean stations in Spain have obtained an average warming trend of 0.039ºC/year for land for the period 1960-2010 and 0.026ºC/year for sea surface temperature during 1985-2009. The seasonal analyses showed a recent tendency towards earlier and longer summers both on land and at sea. In the last 25 years, the higher trends were registered during the transition spring to summer, with the highest warming rates in June (0.12ºC/year on land and 0.08ºC/year in sea temperatures) (López-García, 2015) (Figure 4).
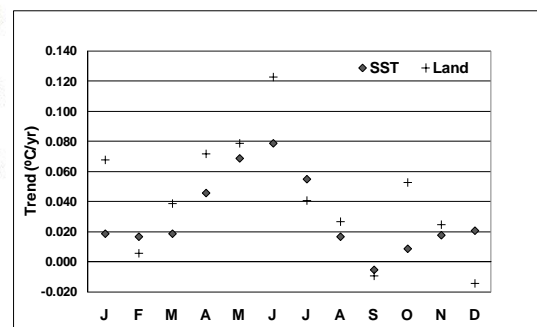
Figure 4. Linear trends (ºC/year) for every month for land and SST calculated for the period 1985-2009. SST trends have been obtained from AVHRR monthly data from the Physical Oceanography Distributed Active Archive Center (PO. DAAC) for the western Mediterranean sea. Land trends have been derived from three coastal stations (Valencia, Barcelona and Tortosa) in the Spanish Mediterranean coast.
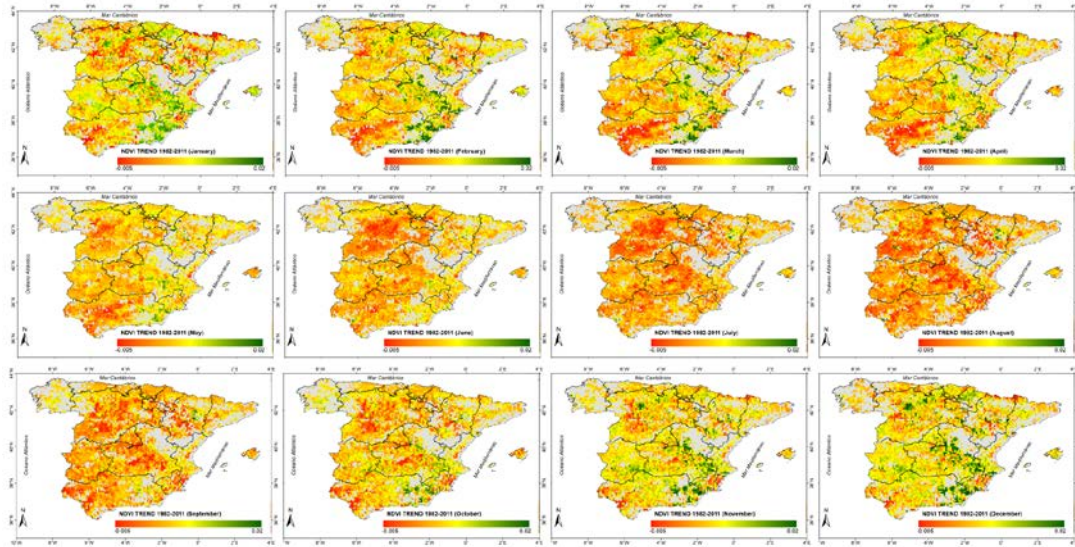
Figure 5. Ratio between the monthly trend and mean NDVI over the considered period for every pixel. Positive values (green colors) refer to an increase in the NDVI values for a particular month during the studied period.

In order to find whether there is a relationship between vegetation dynamics and temperature over the Mediterranean region, the monthly NDVI trend over the considered period is analysed. A linear trend using the monthly NDVI A_2 component is computed. Figure 5 shows the ratio between the monthly trend and mean NDVI over the considered period for every pixel. Positive values (green colors) refer to an increase in the NDVI values for a particular month during the studied period. Moderate positive trends are observed for all the Mediterranean coastline (yellow colors) except the Murcia region where negative trend values are obtained for most of the months. The highest trend is observed during February, March, and April in south Valencia and Almeria regions (dark green colors) as well as during October, November and December. These positive trends are in agreement with those observed in Figure 4.

Figure 6 shows the example of three pixels located over the Mediterranean region. Pixel 1 refers to a particular rice field located in the Ebro River Delta. The paddy fields are flooded towards the end of April and the sowing is carried out in the first half of May. The fields develop a green canopy through the water in June/July, and flower from mid-August. An increased in the NDVI is beginning during the flowering. The harvest takes place approximately the last week of September after draining the paddy fields, so the trends obtained for November and December have to be taken with caution. Pixel 2 belongs to a

non-irrigated crop in Valencia region, which shows an increase of NDVI in the preceding months to spring, where the maximum was expected. Lastly, pixel 3 belongs to a shrub cover in Almería region very close to the coast. This pixel highly agrees with the SST behavior observed in Figure 4, where a maximum increase in NDVI is observed in May and October.

5 CONCLUSIONS

The main goal of this paper has been to analyse the trends observed in the start of growing season (SOS) for the vegetation canopy over the Mediterranean area of the Iberian Peninsula along a 30 year period.

Negative SOS changes for the period 1982-2011 are observed over the major part of Spain explaining a general advance in the SOS. The analysis of monthly NDVI tendency also shows moderate positive trends in the Mediterranean coast with the highest trends in spring and autumn in the south of Valencia and Almeria regions. The tendency found towards earlier and longer summers both on land and sea surface temperature is in agreement with that found for the pixel 3 (a shrub cover) in Almería region very close to the coast.

6 ACKNOWLEDGMENTS
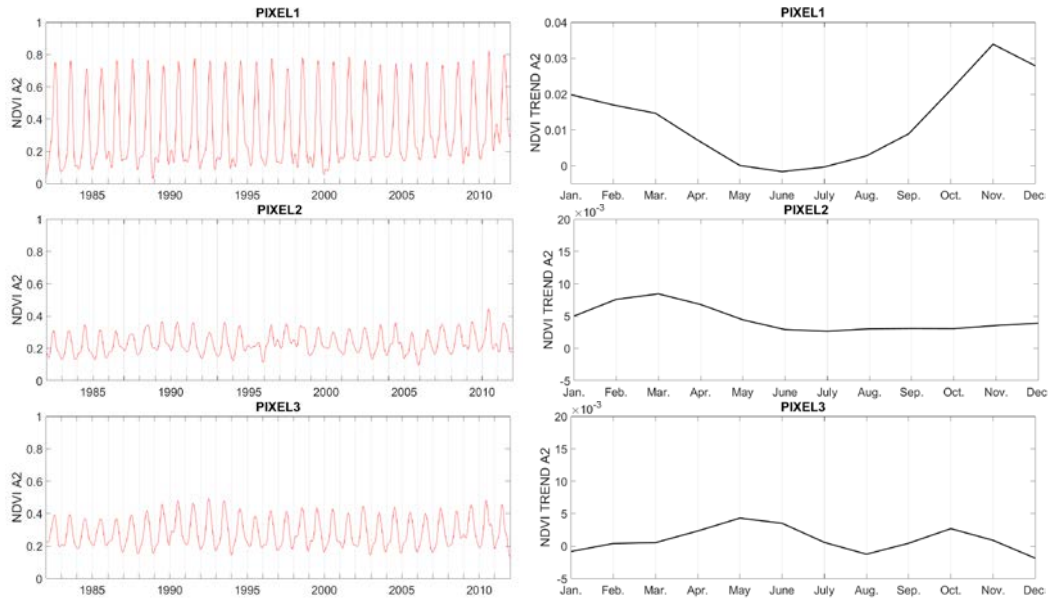
Figure 6. Example of three pixels located over the Mediterranean region. Pixel 1 refers to a particular rice field located in the Ebro River Delta. Pixel 2 belongs to a non-irrigated crop in Valencia region whereas pixel 3 is a to shrub cover in Almería region very close to the coast.

7 REFERENCES

Fonseca, L.M.G., Costa, M.H.M., Manjunath, B.S., Kenny, C. 1998. Automatic registration of satellite imagery. Proceedings of "Image Registration Workshop". (Greenbelt: NASA Goddard Space Flight Center), 13–27.

Giner, C., Martínez, B., Gilabert, M.A., Alcaraz-Segura, D. 2012. Tendencias en el verdor de la vegetación y en la producción primaria bruta de las áreas forestales en la España peninsular (2000-2009). *Revista de Teledetección,* 38, 51-64.

López-García, M.J. & Camarasa, A. 2011. Recent trends of SSS in the Western Mediterranean basins from AVHRR Pathfinder data (1985-2007). *Global Plane. Change,* 78, 127-136.

López-García, M.J. 2015. Recent warming in the Balearic Sea and Spanish Mediterranean coast. Towards an earlier and longer summer. *Atmófera,* 28(3), 149-160.

Martínez, B., and Gilabert, M.A. 2009. Vegetation dynamics from NDVI time series analysis using the wavelet transform. *Remote Sensing of Environment*, **113**, 1823-1842.Percival, D. B., & Walden, A. T. 2000. Wavelet methods for time series analysis. Cambridge University Press, 594 pp.

Piao, S., et al., 2008. Net carbon dioxide losses of northern ecosystems in response to autumn warming. *Nature*, **451**: 49–52.

Richardson, A. D., et al., 2009. Influence of spring phenology on seasonal and annual carbon balance in two contrasting New England forests. *Tree Physiology*, 29: 321–331.

Sakamoto, T., et al., 2005. A crop phenology detection method using time-series MODIS data. *Remote Sensing of Environment*, 96, 366−374.

Tucker, C.J., et al., 2005. An extended AVHRR 8-km NDVI dataset compatible with MODIS and SPOT vegetation NDVI data. *International Journal of Remote Sensing*, 26, 4485–4498.

Yu, H.Y., Luedeling, E., Xu, J.C. 2010. Winter and spring warming result in delayed spring phenology on the Tibetan Plateau. Proceedings of the National Academy of Sciences of the United States of America, 107: 22151–22156.

LST Split-Window algorithm FPGA implementation for Cubesats onboard computations purposes

N. Raissouni[1], S. El Adib[1], J. A. Sobrino[2], N. Ben Achhab[1], A. Chahboun[1], A. Azyat[1] &
M. Lahraoua[1],
1 Remote Sensing & Geographic Information System Unit (RS&GIS),
University Abdelmalek Essaadi, Morocco
2 Global Change Unit (GCU). Imaging Processing Laboratory (IPL).
University of Valencia (UV). Spain.
*corresponding author: nraissouni@uae.ma & raissouni.naoufal@gmail.com

ABSTRACT - *Nano, pico, and so named CubeSat satellites are taking place due to the emergent improvements in both high performance nano and pico electronics and computational technologies. More than 1600 Nanosats and CubeSats are existing nowadays (i.e., 685 nanosats launched, 613 cubesats launched, 405 nanosatellites in orbit, 321 operational nanosatellites, 71 nanosats destroyed on launch, etc), with an incredible panoply of different constellations, governmental and non-governmental, high and easy to reach technologies, instruments in miniatures and missions from military to universities and schools. This paper describes an approach to the implementation of the Land Surface Temperature Split-Window (LST-SW) (Sobrino J. & Raissouni N., IJRS 2000) algorithm structure based on the Field Programmable Gate Array (FPGA) technology. Due to ever-increasing integrated circuit fabrication capabilities, the future of FPGA technology promises both higher densities and higher speeds for Cubesats onboard computations purposes. The application research shows the advantages of the used Xilinx Virtex-5 LX50 series FPGA approach to the LST-SW implementation with higher sampling rates than are available from existing Digital Signal Processing (DSP) chips, lower costs than an Application Specific Integrated Circuits (ASIC) for moderate volume applications and more flexibility than the alternate approaches. Since many current FPGA architectures are in-system programmable, the configuration of the device may be changed to implement different functionality if required depending on the LST-SW parameters for each corresponding authors. Finally, preliminary results show that the proposed LST-SW Xilinx Virtex-5 LX50 FPGA implementation approach is exceedingly flexible. Moreover, this implementation provides considerable and promising performance suitable for future Cubesats onboard LST-SW computations purposes.*

1 INTRODUCTION

The processing work on a satellite can range from simple storing and relay to a ground station for later processing or processing the data onboard and streaming only the important bits of data later to a ground station. Most current remote sensing satellites operate on a store-and-forward paradigm, where imagery is captured, stored on board, and then transmitted to a ground station when it comes into view. Due to the high volumes of data collected by satellite imaging systems, tremendous demand is placed on the onboard storage resources. Furthermore, these large images require significant downlink time to transmit them to ground stations. Due to bandwidth constraints and limited satellite visibility time, it may take more than one pass to complete the downloading of the acquired imagery (Dawood, A. S., et al, 2002). With onboard processing, the data can be altered, processed and compressed resulting in smaller amounts of data to be transferred.

A trend in the design of hardware modules for remote sensing missions has been using hardware devices with small size and cost, but with flexibility and high computational power. Onboard processing, as a solution, allows for a good reutilization of expensive hardware resources. Furthermore, it allows making autonomous decisions onboard that can potentially reduce the delay between the image capture, analysis, and the related action. Implementations of onboard processing algorithms to perform data reduction can dramatically reduce data transmission rates. Moreover, satellite-based remote sensing instruments can only include chips that have been certified for space operation. This is because space-based systems must operate in an environment in which radiation effects have an adverse impact on integrated circuit operation. Field Programmable Gate Array (FPGA) was certified by international remote sensing agencies, which was frequently used in remote sensing missions and space-borne Earth observation missions (González, C., et al, 2012). FPGA also offers exact results with compact size, which makes the reconfigurable system interesting for onboard data processing.

The objective of this work is to implement the Land Surface Temperature Split-Window (LST-SW) algorithm structure (Sobrino J. & Raissouni N., 2000) on FPGA for Cubesats onboard computations purposes.

Onboard computation has become a bottleneck for advanced science instrument and engineering capabilities. Currently available spacecraft processors have high power consumption, are expensive, require additional interface boards, and are limited in their computational capabilities. Recently developed hybrid FPGAs, such as the Xilinx Virtex-5, offer the versatility of running diverse software applications on embedded processors while at the same time taking advantage of reconfigurable hardware resources, all on the same chip package. In fact, radiation hardened FPGAs are in great demand for military and space applications (Compton, K. et al, 2002; Lysaght, P., et al, 2006). For instance, industrial partners such as Xilinx have been producing radiation-tolerant antifuse FPGAs for several years, intended for high-reliability space-flight systems. Xilinx FPGAs have been used in more than 50 missions. In this paper, a Xilinx Virtex-5 LX50 FPGA have been used, with the aim of implementing the Land Surface Temperature Split-Window (LST-SW) algorithm, by using LabVIEW FPGA Module.

2 THE ROLE OF RECONFIGURABLE HARDWARE IN REMOTE SENSING MISSIONS

Reconfigurable Hardware (RH) provides a flexible medium to implement hardware circuits. The RH resources are reconfigurable post-fabrication, allowing a single-base hardware design to implement a variety of circuits. The RH that combines the flexibility of traditional microprocessors with the performance of Application Specific Integrated Circuits (ASIC) devices, is very promising for remote sensing missions, and can be used to increase the fault-tolerance of designs. RH can be reconfigured to avoid hardware faults (Laplante, P. A., 2005), whether they result from fabrication or the environment. The trend in remote sensing missions has always been towards using hardware devices with smaller size, lower cost, more flexibility, and higher computational power (Heinz, D. et al, 2001; Plaza, A., 2004). On-board processing, as a solution, allows for a good reutilization of expensive hardware resources. Instead of storing and forwarding all captured images, remote sensing data interpretation can be performed on orbit prior to downlink, resulting in a significant reduction of communication bandwidth as well as simpler and faster subsequent computations to be performed at ground stations. In this regard, FPGAs combine the flexibility of traditional microprocessors with the power and performance of ASICs. Therefore, FPGAs are a promising candidate for on-board remote sensing data processing.

The transmission of high-dimensional information collected by a satellite-based instrument to a control station on Earth for subsequent processing may turn into a very slow task, mainly due to the reduced bandwidth available and to the fact that the connection may be restricted to a short period of time. The ability to interpret remote sensing data onboard can significantly reduce the amount of bandwidth and storage space needed in the generation of science products. Subsequently, on-board processing has the potential to reduce the cost and the complexity of ground control systems. Furthermore, it allows autonomous decisions (to be taken on board) that can potentially reduce the delay between image capture, analysis, and action.

Recently, FPGAs have become a viable target technology for implementation of remotely sensed hyperspectral imaging algorithms (Plaza, A. et al, 2007). These computing systems combine the flexibility of general-purpose processors with the speed of application-specific processors.

Reconfigurable hardware offers the necessary flexibility and performance with reduced energy consumption compared to other high performance processors. By mapping functionality to FPGAs, the computer designer can optimize the hardware for a specific application resulting in acceleration rates of several orders of magnitude over general-purpose computers. In addition, these devices are characterized by lower form/wrap factors compared to parallel platforms and by higher flexibility than ASIC solutions. Reconfigurable computing technology further allows new hardware circuits to be uploaded via a radio link for physical upgrade or repair (Chang, C.I, 2007).

Moreover, satellite-based remote sensing instruments can only include chips that had been certified for space conditions. This is because space-based systems must operate in an environment in which radiation effects have an adverse impact on integrated circuit operation (Neil, B. et al, 1999). Ionizing radiation can cause soft-errors in the static cells used to hold the configuration data. This will affect the circuit functionality and can cause system failure. Therefore, it requires special FPGAs that provide on-chip reconfiguration error-detection and/or correction circuitry. High-speed, radiation-hardened FPGA chips with million gate densities have recently emerged can support the high throughput requirements for the remote sensing applications. Radiation-hardened FPGAs are in great demand for military and space applications. For instance, industrial partners such as Actel Corporation (www.actel.com) or Xilinx (www.xilinx.com) have been producing radiation-

tolerant antifuse FPGAs for several years for high-reliability space-flight systems. Actel FPGAs have been on board more than 100 launches and Xilinx FPGAs have been used in more than 50 missions. In this work, we use a Xilinx Virtex-II PRO xc2vp30 FPGA as a baseline architecture since it is similar to the existing FPGAs (Fischman, M. A., et al, 2003) that have been certified by several international agencies for remote sensing applications. They are based on the same architecture so we could immediately implement our design on them.

3 LST SPLIT-WINDOW ALGORITHM

Land Surface Temperature (LST) is one of most key parameters in the biophysics of land surface processes (Morrow, N., et al., 1998). LST plays an important role in the cycle of the natural ecosystem evolution and global change. LST determination from satellite data is mainly influenced by the atmosphere and surface emissivity. In our case, the LST Split-Window (LST-SW) algorithm proposed by Sobrino J. & Raissouni N. (IJRS, 2000) has been used for implementation purpose on FPGA (see eq. 1):

$$LST = T_4 + 1.40 (T_4\text{-}T_5) + 0.32 (T_4\text{-}T_5)^2 + 0.83 + (57\text{-}5W) (1\text{-}\varepsilon) - (161\text{-}30W) \Delta\varepsilon \qquad (1)$$

where T_4 and T_5 in (K) are the brightness temperatures measured in the Advanced Very High Resolution Radiometer (AVHRR) Channels 4 and 5 on board the National Oceanic and Atmospheric Administration (NOAA) satellite series, W is the total amount of atmospheric water vapour in (g cm^{-2}). ε and $\Delta\varepsilon$ are, respectively, the average effective emissivity in both channels and the spectral variation of emissivity.

4 FPGA IMPLEMENTATION OF THE LST-SW ALGORITHM

4.1 Materiel: CompactRIO system

CompactRIO system of the National Instruments (NI) used consists of four main components: an Intelligent Real-Time Embedded Controller NI cRIO-9022, a reconfigurable field-programmable gate array (FPGA)-based chassis cRIO-9014, C Series I/O modules, and software. This cRIO-9014 reconfigurable embedded chassis (Carroll, D., et al, 2006; Maciej, R., et al, 2010) contains the Xilinx Virtex-5 LX50 FPGA that offers ultimate processing power to implement LST-SW algorithm using NI-LabVIEW FPGA software (Figure 1).

The Xilinx Virtex-5 FPGA offers a number of performance enhancements over previous generations of FPGA. Another important benefit that the new Virtex-5 architecture provides is the ability to compile code at faster rates, increasing the processing capabilities of NI-LabVIEW FPGA hardware. Additionally, all chips are processed using a 65 nm lithographic process. The cRIO-9022 is used for image controlling/storing and for configuring the FPGA chassis. This is an embedded real-time controller module featuring an industrial 533 MHz Freescale MPC8347 real-time processor for deterministic, reliable real-time applications and contains 256 MB of DDR2 RAM and 2 GB of non-volatile storage for holding: programs and logging data. These two modules provide a complete platform to implement LST-SW algorithm based on FPGA Xilinx Virtex-5. The chassis containing the FPGA has 8 slots to connect external hardware modules, used for signal acquisition. The modules are interfaced to the FPGA in order to enable transferring data directly to the chip. The real-time controller contains a 10/100 Base T/TX Ethernet port to communicate with Personal Computer (PC) or other systems.

FPGAs are really just blank silicon canvases that you can program to be any type of custom digital hardware. Traditionally, programming these FPGA chips has been difficult and, therefore, only possible by experienced digital designers and hardware engineers. NI has simplified programming these devices through graphical system design with NI-LabVIEW FPGA so that nearly anyone can take advantage of these powerful reconfigurable chips. Because NI-LabVIEW FPGA Virtual Instruments (VIs) are synthesized down to physical hardware, the FPGA compile process is different from the compile process for a traditional LabVIEW for Windows or LabVIEW Real-Time application.
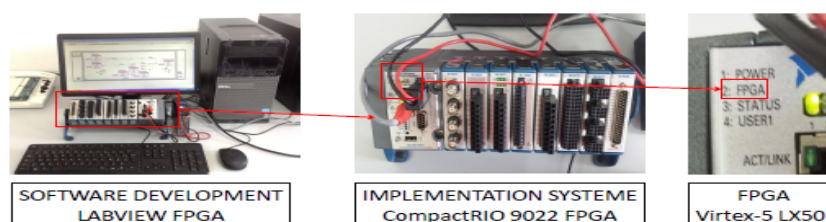
Figure 1. Material implementation: NI cRIO-9022 embedded real- time controller
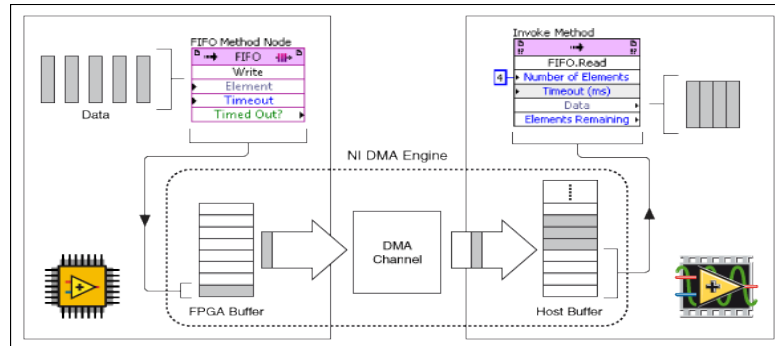
Figure 2. Illustration of communication between host computer VI and FPGA VI.

4.2 VIs Synchronisation: Computer and FPGA

One of the advantages of the CompactRIO system are the three Direct Memory Access (DMA) channels, which provide data streaming from the FPGA target to the host application by means of First In First Out (FIFO) tables. DMA-FIFOs are an efficient mechanism for streaming data from the FPGA to the host processor without involving processor resources. LabVIEW provides an interface that makes it uncomplicated to setup DMA channels for data streaming between the FPGA hardware and the software running on the host computer. DMA channels can be created to operate in both directions, FPGA to host computer or host computer to FPGA see Figure 2. This property only can be set before compile-time. The direction of the DMA channel cannot be changed during run-time (after synthesis). The advantage of using DMA channels is the high data throughput rate that they can obtain. That makes them suitable for streaming of measurement data. However, there are only a limited number of DMA channels that can be setup for data communication, which makes them unsuitable for status data from the FPGA and command data to the FPGA.

4.3 Methodology: Implementation of the LST-SW algorithm using NI-LabVIEW FPGA

The proposed implementation is divided into two parts: i) writing the code in FPGA mode and, ii) controlling it through host computer. Here cRIO-9022 has been taken as an intelligent real-time embedded controller for CompactRIO. Figure 3 shows the FPGA VI in charge of computing the LST-SW image. Image pixel values are stored in memory, and then the DMA-FIFO is used to transfer the data into the host computer. Images T_4, T_5, W and ε (see eq. 1) are stored on hard disk and then transferred to FPGA VI which calculates the LST-SW (in our case we consider $\Delta\varepsilon = 0.005$). In the whole process, images data is stored in memory separately and delivered coherently to the host computer in 1024 element frames by checking the DMA-FIFOs status before writing to them, so that the FPGA DMA buffer never overflows. The advantage of DMA is that the host computer processor can perform calculations while the FPGA target transfers data to the host computer memory through bus mastering. A DMA-FIFO allocates memory on both the host computer and the FPGA target, but acts as a single FIFO. The FPGA VI writes to the DMA-FIFO one element at a particular instant of time with the Write method of the FIFO Method Node or reads from the FIFO one element at a particular instant of time with the Read method. While invoking, the host computer VI reads from or writes to the FIFO one or more elements at a time. A DMA Engine is used by LabVIEW to transfer DMA-FIFO data between the FPGA and the host computer.

Finally, a host computer VI has been written using the FPGA code see Figure 4. The values of the pixels stored in memory are transferred to the host computer through FIFO type Target to Host-DMA. The open FPGA reference opens a reference to the FPGA VI without running it, in order to avoid generating data before DMA is configured. Reset the VI to guarantee that FIFOs are in a known state on the target. The size of the image can be given manually or it can be determined by the loop by using different scaling VIs present in LabVIEW. There are two DMA-FIFOs named as Host to Target DMA1 and Host to Target DMA2 being used to transport the images stored in the hard disk to the FPGA respectively. Prior to the main loop in the host computer VI, DMA1-FIFO and DMA2-FIFO has been configured so that the main loop will run after the DMA-FIFO get 1024 values from FPGA VI, will be used at a time. This ensures that there will be a continuous execution of the main loop in host computer VI without any data insufficiency. The values are converted to 16-bit non-signed integer numeric (U16) from FXP (fixed point). Finally, the Close FPGA VI reference closes the reference to the FPGA.

421
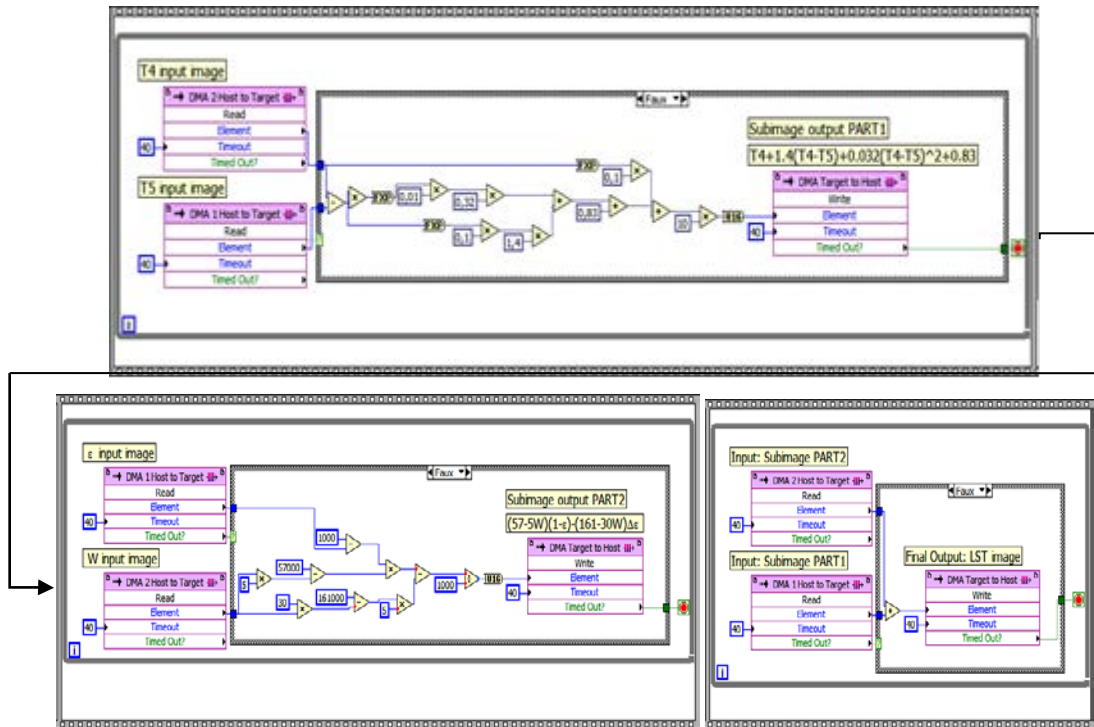
Figure 3. FPGA VI for the proposed implementation in NI-LabVIEW FPGA
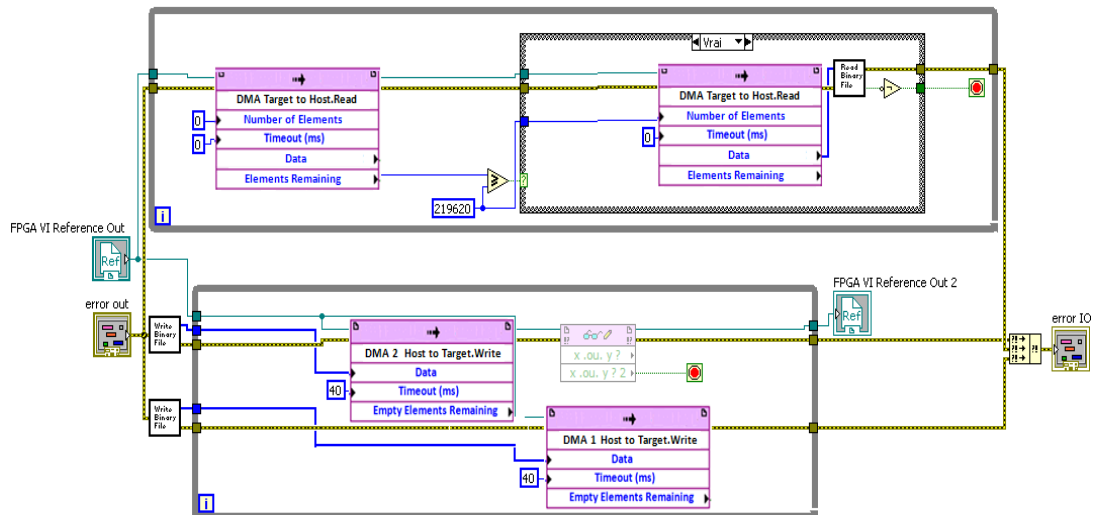
Figure 4. Host computer VI for the proposed implementation in NI-LabVIEW FPGA

5 EXPERIMENTAL RESULTS

5.1 Satellite data and LST-SW results

The study area is the Mediterranean Basin. This particular geographical position gives the area a great bioclimatic diversity and important temperature gradient between north and south.

The Pathfinder AVHRR Land (PAL) satellite dataset has been used for the study of the Mediterranean Basin. NOAA and National Aeronautics and Space Administration (NASA) are the

sponsors of the PAL project responsible of producing a set of global data calibrated and processed regularly for the investigation on climatic change. The AVHRR data used are the Global Area Coverage GAC with a resolution at nadir view of 4 Km. In this application we have used the images (Format: 695 columns, 316 rows, Integer Host (Intel), Homolosine projection) corresponding to the composite period from 21 to 30 of August, September, October, November and December of 1982.
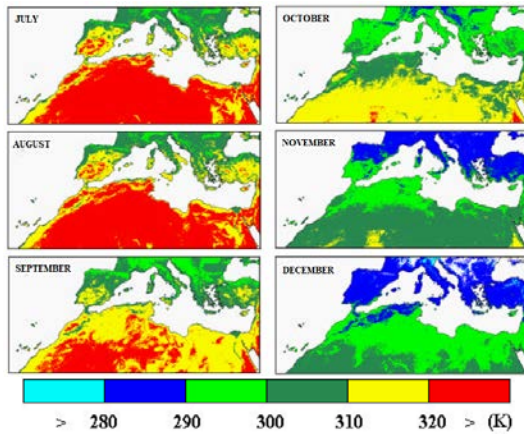
Figure 5. SW-LST images computed using LST-SW NI-LabVIEW FPGA implementation

Figure 5 shows the LST-SW images computed using the LST-SW NI-LabVIEW FPGA proposed implementation. An important LST variability is shown for the area and period in total coherence with the biodiversity of the same.

5.2 LST-SW FPGA Performance Evaluation

In this subsection, we conduct an experimental evaluation of the computational performance of the proposed FPGA implementation. Table 1 shows the resources used for our hardware implementation of the proposed LST-SW algorithm design, conducted on the Virtex-5 LX50 FPGA of the NI cRIO-9014 reconfigurable embedded chassis. This FPGA has a total of 7200 slices, 28800 slice flip-flops, and 28800 four input look-up tables available. In addition, the FPGA includes some heterogeneous resources, such as 48 DSP48s, and 48 Block RAMs. In our implementation, we took advantage of these resources to optimize the design. The Block RAMs are used to implement the FIFO, so the vast majority of the slices are used for the implementation of the LST-SW algorithm with the DSP48s multipliers.

TABLE. 1. Summary of resource utilization for the NI-LabVIEW FPGA-based implementation of the LST-SW algorithm.

Target FPGA	Virtex-5 LX50		
Device Utilization	Used	Total	%
Total Slices	1169	7200	16.2
Slice Registers	2425	28800	8.4
Slice LUTs	2590	28800	9.0
DSP48s	16	48	33.3
Block RAMs	3	48	6.2
Maximum Frequency	83.33 MHz		

We have applied a perfecting approach to hide the communication latency using DMA. Basically, while the LST-SW module is processing a set of image, the DMA is fetching the following set and storing it in the FIFO. Having in mind the proposed optimization concerning the use of available resources. It is important to find a balance between the number of DMA operations and the capacity of the destination FIFO. In other words, we need to fit enough information in the FIFO so that the LST-SW module never needs to stop. In addition, the greater the FIFO capacity, the fewer DMA operations will be required. We have evaluated several FIFO sizes and identified that, for 1024 positions or more, there are no penalties due to reading of the input data.

6 CONCLUSION

The number of remote sensing applications requiring fast response of algorithm analysis has been growing exponentially in recent years. Current sensor design practices can greatly benefit from the inclusion of radiation-hardened FPGAs, which can be easily mounted or embedded in the sensor due to its compact size and low-weight, which does not compromise mission payload. In this paper, we have discussed the role of FPGAs in remote sensing missions and presented the experimental results of first FPGA implementation of the Land Surface Temperature Split-Window (LST-SW) algorithm, one of the most well-known approaches for determination of Land Surface Temperature from satellite data in the remote sensing community. Finally, experimental results show that the proposed LST-SW Xilinx Virtex-5 LX50 FPGA implementation approach is exceedingly flexible and able to provide accurate results in real time. Moreover, this implementation provides considerable and promising performance suitable for future Cubesats onboard LST-SW computations purposes (e.g., PICASSO 3U CubeSat Science Mission, www.clyde.space/our-missions/12-picasso). The mission also serves as an ESA in-orbit-

demonstrator of CubeSat technology and a pioneer for small satellite missions. PICASSO will demonstrate the capability of low-cost nanosatellites to perform remote and in-situ scientific measurements of physiochemical properties of the Earth's atmosphere as well as enhancing the technology readiness level of the instruments on-board.

7 REFERENCES

Carroll, D., Jeannie, S., Brain, M., 2006, Motorcycle Control Prototyping Using an FPGA-Based Embedded Control System, IEEE Control Systems Magazine, pp.17-21.

Chang, C.-I., Hyperspectral Data Exploitation: Theory and Applications, New York: Wiley, 2007.

Compton, K. and Hauck, S., 2002, Reconfigurable computing: A survey of systems and software, ACM Comput. Surveys, vol. 34, pp. 171–210.

Dawood, A. S., Williams, J. A. and Visser, S. J., 2002, On-board satellite image compression using reconfigurable FPGAs, IEEE International Conference on Field-Programmable Technology, (FPT). Proceedings. pp. 306-310.

Fischman, M. A., Berkun, A. C., Cheng, F. T., Chun, W. W., Im, E., and Andraka, R., 2003, Design and demostration of an advanced on-board processor for the second-generation precipitation radar, in Proc. IEEE Aerosp. Conf., vol. 2, pp. 1067–1075.

González, C., Mozos, D., Resano, J., Plaza, A., 2012, FPGA implementation of the N-FINDR algorithm for remotely sensed hyperspectral image analysis, IEEE Transactions on Geoscience and Remote Sensing 50 (2), 374-388.

Heinz, D. and Chang, C.-I., 2001, Fully constrained least squares linear mixture analysis for material quantification in hyperspectral imagery, IEEE Trans. Geosci. Remote Sens., vol. 39, no. 3, pp. 529–545.

Laplante, P. A., 2005, Computing requirements for self-repairing space systems, Journal of Aerospace Computing, Information and Communication, vol. 2, no. 3, pp. 154–169.

Lysaght, P., Blodget, B., Mason, J., Young, J., and Bridgford, B., 2006, Enhanced architectures, design methodologies and CAD tools for dynamic reconfiguration of Xilinx FPGAs, in Proc. Int. Conf. Field Programmable Logic Appl., pp. 1–6.

Maciej, R., Adam, P., Andrzej, T., 2010, Real- time controller design based on NI Compact-RIO, Proceedings of the International Multiconference on Computer Science and Information Technology, pp. 825–830.

Morrow, N. & Friedl, MA., 1998, Modelling biophysical controls on land surface temperature and reflectance in grasslands, Agricultural and Forest Meteorology. 92. 147-161.

Neil, B. and Dawood, A., 1999, Reconfigurable computers in space: Problems, solutions and future directions, in Proc. Military Aerosp. Appl. Programmable Logic Devices Conf., pp. 1–2.

Plaza, A., Martinez, P., Perez, R., and Plaza J., 2004, A quantitative and comparative analysis of endmember extraction algorithms from hyperspectral data, IEEE Trans. Geosci. Remote Sens., vol. 42, no. 3, pp. 650–663.

Plaza, A. and Chang, C.-I., 2007, High Performance Computing in Remote Sensing. Boca Raton, FL: CRC Press.

Sobrino, J. A. and Raissouni, N., 2000, Toward remote sensing methods for land cover dynamic monitoring. Application to Morocco, International Journal of Remote Sensing, vol. 21, no. 2, pp. 353-366.

The fusion of satellite and UAV data. The accuracy analysis of data fusion results.

Agnieszka Jenerowicz, Katarzyna Jenerowicz, Malgorzata Woroszkiewicz, Rafal Dabrowski

Military University of Technology, Faculty of Civil Engineering and Geodesy, Geodesy Institute, Department of Remote Sensing, Photogrammetry and Imagery Intelligence, gen. S. Kaliskiego 2, 00-908 Warsaw, Poland

agnieszka.jenerowicz@wat.edu.pl, katarzyna.siok@wat.edu.pl

ABSTRACT - *Remote sensing techniques that apply imagery data obtained with sensors mounted on UAV platforms became more popular in the last few years due to the availability of low- cost UAV platforms and low-cost sensors. To enrich the spectral information of imagery data acquired with low- cost sensors, the authors proposed the fusion of RGB data obtained with UAV platform with multispectral satellite imagery. The fusion is based on the pansharpening process, that aims to integrate the spatial details of the high-resolution panchromatic image with the wide spectral information of lower resolution multispectral imagery. The key of pansharpening is to accurately estimate the missing spatial details of multispectral or hyperspectral images while preserving their spectral properties. Depending on the temporal gap between the acquisition of low- and high- resolution image, and panchromatic image simulated from RGB image, the spectral quality and accuracy of the pan-sharpened image can vary significantly. In the research, the authors presented the fusion of RGB images (with high spatial resolution) obtained with sensors mounted on low- cost UAV platforms and multispectral satellite imagery. As a result of the fusion, the authors obtained several multispectral images with very high spatial resolution and then analysed the spatial and spectral accuracies of processed images. The authors analysed the influence of time shift between UAV and satellite imagery acquisition on the spectral accuracy of selected land cover forms. The proposed fusion of low- cost UAV imagery with open source satellite imagery allows obtaining imagery of high spectral and spatial resolution, which could be used for the quality and quantitative analysis of land cover.*

1 INTRODUCTION

Data obtained from low altitudes with low- cost sensors can be characterised by high spatial and radiometric resolution but quite low spectral resolution. High spectral resolution and many spectral bands allow not only distinguish land cover types and objects types but also give the possibility of sensing a variety of spectral reflectance characteristics of many different object types at once, e.g. nitrogen, leaf area index, biomass, vegetation stress, soil's moisture level, organic matter, nutrients, anthropogenic objects etc., due to the fact that specific wavelengths are most sensitive to each type of objects. Unfortunately, imagery data obtained with low- cost technology is quite limited due to lack of high spectral resolution (Goel et al., 2003; Zarco-Tejada et al., 2005). Therefore it is essential to enrich the spectral information of imagery data acquired from UAV.

Many methods allow adding spectral information. One of the most popular is based on pansharpening, which is data is one of the most popular data integration method for remote sensing applications (Jenerowicz & Woroszkiewicz, 2016; Siok et al., 2017).

The pansharpening process aims to integrate the spatial details of the high-resolution panchromatic image with the wide spectral information of lower resolution multispectral or hyperspectral imagery to obtain multispectral or hyperspectral images with high spatial resolution. The key of pan-sharpening is to correctly estimate the missing spatial details of multispectral or hyperspectral images while preserving their spectral properties (Alparone et al., 2007; Hervieu et al., 2016; Siok et al., 2017).

Depending on the pansharpening method, spatial resolution and quality of RGB image, temporal gap between the acquisition of low- and high- resolution image, and panchromatic image simulated from RGB image, the spectral quality and accuracy of the pan-sharpened image can vary significantly.

The research presents preliminary results of the fusion of imagery obtained from the low- cost RGB sensor platform mounted on UAV and open- source data from multispectral satellite- Landsat 8 OLI.

This research aimed to analyse the influence of time gap between satellite and UAV data on the accuracy of the pansharpening process, for different land cover types.

2 DATA AND METHODOLOGY

2.1 Data

In this study, two datasets (A and B) containing high-spatial resolution RGB image acquired with low- cost sensor mounted on the UAV platform and set of satellite images acquired by Landsat 8 OLI sensor, were used. In order to analyse the time gap influence between the images, six satellite images acquired (± two; ±four, and ± six weeks after and before) were used for each data set.

The RGB imagery was obtained with digital camera Canon 700D with fixed focal length (35 mm) mounted on the UAV system X-8. The X-8 UAV is a light system made from the elapor foam with the single electric engine.

Satellite data were acquired by Landsat 8 OLI sensor. Landsat 8 OLI imagery have a spatial resolution of 30 m (multispectral). Data from Landsat platform are open source. Therefore authors had decided to use them for the study and to show the potential of fusion of satellite and UAV imagery.

Dataset A- Fig. 1, consist of one RGB image with 0.04 m spatial resolution acquired on 30th may 2015, and seven multispectral satellite imagery with 30m spatial resolution, acquired on:

- T_{-3}=30.05.2015 – 6 weeks
- T_{-2}=30.05.2015 – 4 weeks
- T_{-1}=30.05.2015 – 2 weeks
- T_0= 30.05.2015
- T_{+1}=30.05.2015 + 2 weeks
- T_{+2}=30.05.2015 + 4 weeks
- T_{+3}=30.05.2015 + 6 weeks.
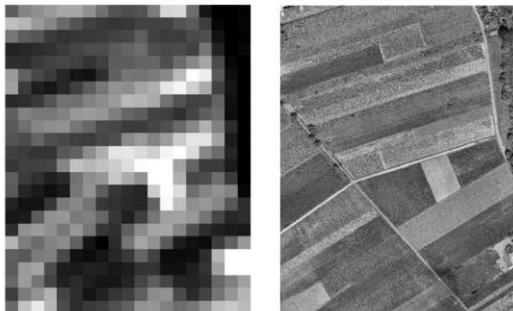
Fig. 1. Satellite and UAV imagery of test site A

Dataset B- Fig. 2, consist of one RGB image with 0.05 m spatial resolution acquired on 27th July 2016, and seven multispectral satellite imagery with 30m spatial resolution, acquired on:
- T_{-3}=08.08.2016– 6 weeks
- T_{-2}=08.08.2016– 4 weeks

- T_{-1}=08.08.2016– 2 weeks
- T_0= 08.08.2016
- T_{+1}=08.08.2016+ 2 weeks
- T_{+2}=08.08.2016+ 4 weeks
- T_{+3}=08.08.2016+ 6 weeks

Unfortunately for this data set, imagery data from 27th July were not available, then imagery from 8th August were used.
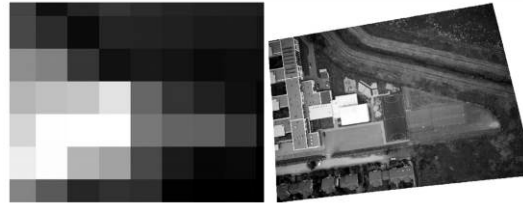
Fig. 2. Satellite and UAV imagery of test site B

2.2 Data processing

The full methodology of data processing is presented in the graph below- Fig. 3.

The first stage of data processing has been preceded by process of orthorectification of UAV and satellite imagery. UAV and satellite imagery were orthorectified in order to eliminate errors associated with the occurrence of differences in the data geometry. For the orthorectification of aerial imagery, some control and checkpoints were used, and for Landsat 8 OLI data, DEM obtained from the SRTM mission was used.

Next, the panchromatic band was simulated. The simulation on new panchromatic images was made by the weighting sum of RGB channels of UAV image (Kanan & Cottrell, 2012) - equation (1).

$$PAN_{NTSC} = 0.299 * R + 0.587 * G + 0.114 * B \quad (1)$$

Simultaneously to panchromatic band simulation from RGB high- spatial resolution data, the atmospheric correction of multispectral data was conducted by application of QUAC algorithm (Bernstein et al., 2006).

Then, the pansharpening process was applied to all datasets. The Gram- Schmidt method was used to fuse UAV and satellite imagery. The Gram- Schmidt pan-sharpening generates a synthetic lower resolution panchromatic image through a weighted sum of blue, green, red and near-infrared multispectral bands. The weights are calculated based on the relative spectral response of the four multispectral bands and the panchromatic band. The Gram- Schmidt is a generalisation of PCA method, in which PC1 may be arbitrarily chosen, and the remaining components are calculated to be orthogonal to one another and PC1. Like PCA method, this method also requires forward

and backward transformation of multispectral image (Arfken, 1985; Laben & Brower, 2000). As a result, seven enhanced images were obtained in two data sets.
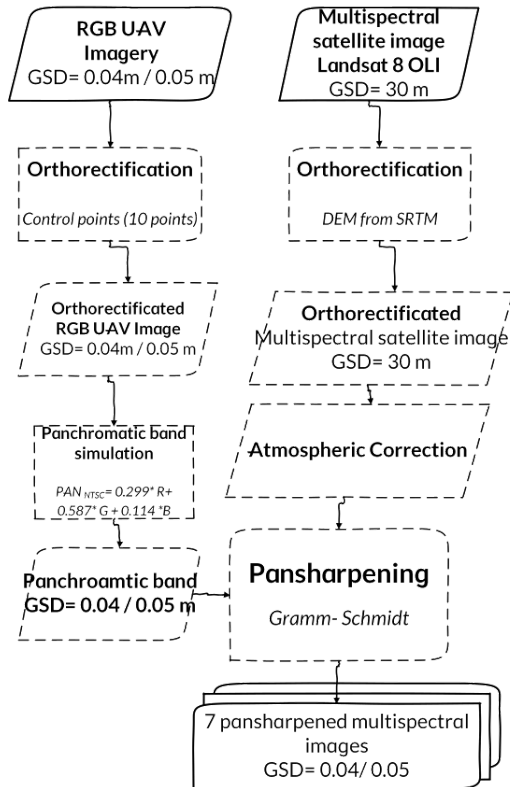
Fig. 3. Block diagram showing the process of data preparing and processing

3 RESULTS

With the application of the Gram- Schmidt pansharpening method there were fused images from two data sets, i.e. Landsat 8 OLI images with panchromatic image simulated from high- spatial resolution UAV image- Fig. 4 and Fig. 5. As a result, seven enhanced images were obtained in two data sets. First, the visual assessment of pansharpening results was conducted. Second, to verify the spectral properties of the photographed objects for data acquired on different dates, the spectral characteristics of two objects located in the input images: natural, i.e. vegetation for data set A, and artificial for data set B, were analysed.

Based on visual assessment of results it can be concluded that obtained results for the fusion of UAV and Landsat data are good, however visual analysis of results for datasets A, and B, shows that better results are obtained for data set A.

In the images that are results of satellite and UAV data fusion- dataset A; it is possible to distinguish

different types of vegetation (meadows, cereals, cabbage, bushes, trees, etc.)- in comparison to original multispectral data. Also, it is possible to separate vegetation from the ground easily. As it can be observed, this fusion was very successful regarding the spatial quality improvement of multispectral image.

Fig. 4. Results of data fusion with the Gram- Schmidt method- data set A

Fig. 5. Results of data fusion with the Gram- Schmidt method- dataset B

In the images obtained after the fusion of data from set B, it is possible to distinguish different types of land cover, i.e. buildings, vegetation, athletic track, in comparison to original multispectral data. However, edges of buildings are blurred, and the colour reproduction of anthropogenic objects is not ideal.

In order to verify the spectral properties of the photographed objects, the spectral characteristics of two types objects located in the input images natural, i.e. vegetation for data set A, and artificial for data set B, were analysed. Spectral reflectance characteristics were obtained from enhanced images and in-situ measurements. The results are presented in the figures 6 and 7.

For the anthropogenic object, the results are similar for all dates. However, in the case of a natural object, the best results of pansharpening process were obtained when time gap is no bigger than two weeks.
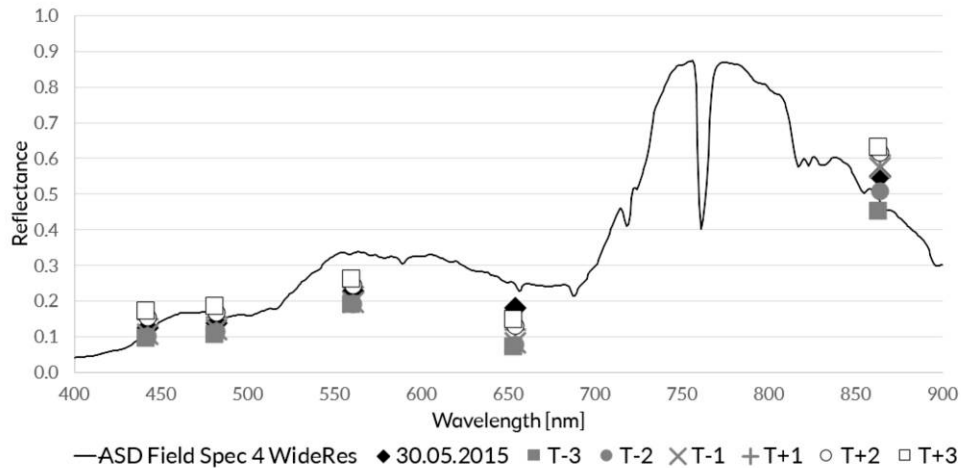
Fig. 6. Spectral reflectance characteristic of vegetation- data set A
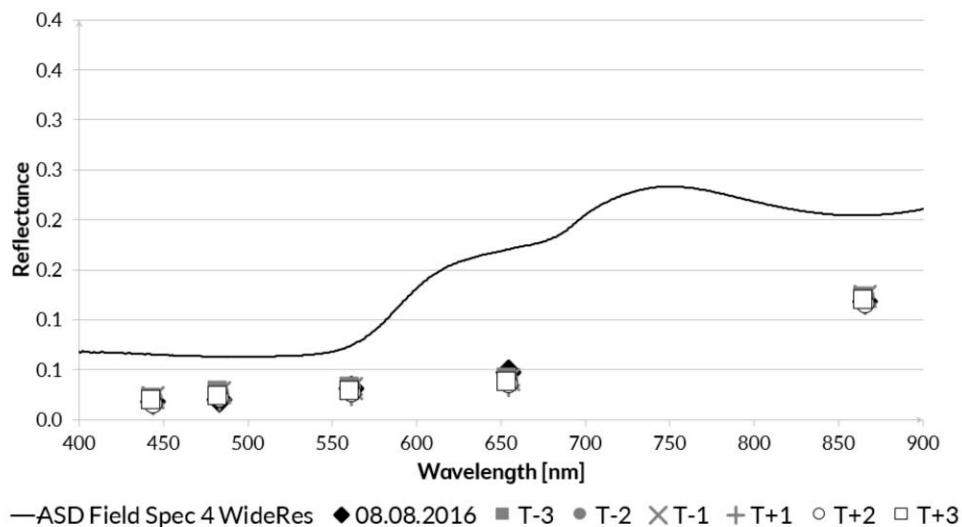
Fig. 7. Spectral reflectance characteristic of urban area- data set B

4 SUMMARY AND CONCLUSIONS

In the presented study, the analysis of the influence of time gap between satellite and UAV data on the accuracy of the pansharpening process, for different land cover types was presented. The fusion of UAV and satellite allows to obtain not only high spatial resolution images but also maintain correct spectral response of objects in the new pan-sharpened image.

The best results of data fusion are the best when the time gap is less than two weeks for vegetation. The results for the urban area are very similar even if the time gap is quite high. The similar shape of the

spectral characteristics of objects obtained from the enhanced image, and obtained with an ASD spectroradiometer, and high SI values are confirmation of good results of data fusion.

The method can be useful in the remote sensing analyses especially for more precise land cover identification and classification for precision agriculture purposes.

5 ACKNOWLEDGEMENTS

6 REFERENCES

Alparone L, Wald L, Chanussot J, Thomas C, Gamba P, Bruce LM. Comparison of pansharpening algorithms: Outcome of the 2006 GRS-S data-fusion contest. *IEEE Transactions on Geoscience and Remote Sensing*. 2007;45(10):3012–21.

Arfken, G., 1985, Gram–Schmidt orthogonalization. Mathematical methods for physicists, 3rd ed. Orlando, FL: Academic Press, 516–520.

Bernstein LS, Adler-Golden SM, Sundberg RL, Ratkowski AJ. Improved reflectance retrieval from hyper- and multispectral imagery without prior scene or sensor information . Vol. 6362, Proc. SPIE. 2006. p. 63622P–63622P–8.

Goel, P.K, Prasher, S.O, Landry, J.A, Patel, R.M, Bonnell, R.B, Viau, A.A, Miller, J.R, 2003, Potential of airborne hyperspectral remote sensing to detect nitrogen deficiency and weed infestation in corn, *Computers and Electronics in Agriculture*, Volume 38, Issue 2, February 2003, 99-124.

Hervieu A, Le Bris A, Mallet C. Fusion of Hyperspectral and Vhr Multispectral Image Classifications in Urban Areas. ISPRS Annals of Photogrammetry, *Remote Sensing and Spatial Information Sciences*. 2016;3(3):457–64.

Jenerowicz A, Woroszkiewicz M. The pan-sharpening of satellite and UAV imagery for agricultural applications. In: Neale CMU, Maltese A, editors. Proc SPIE 9998, Remote Sensing for Agriculture, Ecosystems, and Hydrology XVIII. 2016. p. 99981S.

Kanan C, Cottrell GW. Color-to-grayscale: does the method matter in image recognition. PloS one. 2012;7(1):e29740.

Laben, C.A., Brower, B.V., 2000, Process for enhancing the spatial resolution of multispectral imagery using pan-sharpening, Technical Report, US Patent No. 6011875. Eastman Kodak Company.

Siok K, Jenerowicz A, Woroszkiewicz M. Enhancement of spectral quality of archival aerial photographs using satellite imagery for detection of land cover. *Journal of Applied Remote Sensing*. 2017;11(3):36001.

Zarco-Tejada, P., Berjón, A., López-Lozano, R., Miller, J., Martín, P., Cachorro, V., et al., 2005, Assessing vineyard condition with hyperspectral indices: leaf and canopy reflectance simulation in a row-structured discontinuous canopy, *Remote Sensing of Environment*, 99, 271- 287.

The simulation of new spectral bands for the purpose of data pansharpening

Katarzyna Siok, Ireneusz Ewiak, Agnieszka Jenerowicz
Military University of Technology, Faculty of Civil Engineering and Geodesy, Geodesy Institute, Department of Remote Sensing, Photogrammetry and Imagery Intelligence, gen. S. Kaliskiego 2, 00-908 Warsaw, Poland
katarzyna.siok@wat.edu.pl, ireneusz.ewiak@wat.edu.pl , agnieszka.jenerowicz@wat.edu.pl

ABSTRACT - *In many applications of remote sensing, it is required to preserve both high spatial resolution and high spectral resolution of images. Therefore, many methods of pan-sharpening that use the original high spatial resolution panchromatic image and low spatial resolution multispectral images had been developed. Due to the limited range of sensitivity of panchromatic data, the authors indicate that the simulation of new panchromatic high-spatial-resolution images for the pan- sharpening purpose is highly recommended. That is related to the possibility to obtain more reliable results of the sharpening of the data in both the visible and infrared range spectrum. This paper presents the method of simulation of new panchromatic images with high spatial resolution. The method allows obtaining enhanced images of a higher spectral quality in reference to the original panchromatic data. The algorithm was invented by WorldView-2 and Landsat-5 data. The new visible images had been simulated based on analysis of the results of weighting sum of channels. Next, the authors applied commonly used Gram-Schmidt algorithm of pan-sharpening. Several accuracy assessment indices to determine the accuracy of the data integration processes were used: Universal Image Quality Index, Peak Signal To Noise Ratio Index, Correlation Coefficients and ERGAS. The proposed method of simulation of the new panchromatic channel allows to obtain not only high spatial resolution images but also maintain the correct spectral response of objects in the new pan- sharpened image. Concerning this, it will enable efficient detection of various forms of land cover contained in images.*

1 INTRODUCTION

Both, high-spatial resolution and high-spectral resolution data are significant for environmental studies, such as precision agriculture, high-resolution land cover mapping, plant species, and change detection (Goel et al. 2003; Gevaert et al., 2015; Heim et al. 2015; Lehmann et al., 2015). For global analyses, it is required to have satellite imagery, which is characterised by a large size of the scene, regularity of acquisition and free access (e.g. Landsat, Sentinel). Such requirements are not met for aerial photos or UAV data. Unfortunately due to the trade-off between spatial resolution, spectral resolution and Signal to Noise Ratio (SNR), satellite sensors register low-spatial resolution images (e.g. Proba-1 CHRIS or EO-1 Hyperion). In addition, currently, there are few satellites on which were mounted both hyperspectral (HS) and multispectral (MS) sensors. Therefore, it is necessary to integrate images from different sensors selected depending on the application. With the increasing number of high-resolution satellites, it is possible to register images of the same area from several sensors in a similar vegetation period. Satellite data fusion from different sensors can be accomplished through pansharpening process (Yokoya et al., 2017).

The pansharpening is a process, that is widely used for the enhancement of the spatial quality of multispectral or hyperspectral images with relatively low Ground Sampling Distance (GSD). Different methods of pansharpening allow for integration of multispectral data with panchromatic data from the same area as well as for the fusion of hyperspectral images with multispectral images. In the second case, it is assumed that multispectral data have higher spatial resolution compared to hyperspectral data. Therefore it is possible to obtain enhanced images with better spatial quality that preserve spectral information, that could be next used for target detection and identification (Alparone et al., 2007; Winter et al., 2007; Hervieu et al., 2016; Siok et al., 2017).

In order to carry out of reliable analysis of natural land cover, it is essential to retain high spatial and spectral quality of the images in the pansharpening process. That is strictly related not only to the time shifts between registration time of input images but also to the spectral, radiometric and spatial resolution of the input data, as well as to the used pansharpening method. Some methods of pansharpening allow

maintaining higher spatial resolution while other higher spectral resolution (Hill et al., 1999; Alparone et al., 2007; Sarp 2014; Grochala & Kedzierski, 2017; Siok et al., 2017). The authors of the article do not focus on the determination of the best fusion method but the analysis of the spectral quality of pansharpening results using different simulations of the panchromatic band. Consequently, the Gram-Schmidt method was chosen because of the speed and ease of implementation, and sufficiently preserving spectral information (Chen et al., 2014; Jenerowicz & Woroszkiewicz, 2016).

Authors aim to preserve the original spectral features of photographed objects, as many as possible, by applying different modifications to the high spatial image during the pansharpening process. In the research, the case of multisource multispectral data without a panchromatic band is considered. Such situation can be found in the case of Sentinel- 2 sensors. Authors aim to simulate panchromatic channel for a satellite that physically does not acquire such channel. The developed methodology will also be useful in the process of sharpening of hyper- and multispectral data.

In this article, the authors show the need for simulation of new panchromatic bands that could be used to increase the interpretation, identification and classification capabilities of land cover and objects.

2 SIMULATION OF NEW SPECTRAL BANDS

When integrating high-spatial multispectral data with high-spectral hyperspectral data, and there is lack of physically acquired panchromatic band it is necessary to simulate the high-resolution panchromatic image (Yokoya et al., 2017). Regardless of the method of panchromatic image simulation, pansharpening process allow to obtain an enhanced image, that can be used in various applications. However, the efficiency of the obtained image depends on the method of data simulation.

The most common data simulation method is based on the arithmetic mean of four multispectral bands, i.e. Blue, Green, Red, and NIR (Hill et al., 1999). Moreover, the mean is also used for band simulation from hyperspectral bands (Chen et al., 2014).

The pansharpening process can be applied separately for different ranges of the electromagnetic spectrum. Price (Price, 1987) fused the panchromatic band with the visible (VIS) channels and separately with NIR channel. The applied spectral partition is related to the nonlinear relationship between visible and near-infrared bands.

The new spectral band is also simulated based on the assumption that spectral reflectance coefficients of the same terrain objects are practically identical in two spectral ranges (Zhang & He, 2007). In other studies, authors propose weighting sum of the channels for the simulation purpose (Mayumi & Iwasaki, 2011). The weight factors are connected to the mutual spectral response. Moreover, the authors suggest simulation of the new spectral band based on the estimated linear regression value between hyperspectral and multispectral bands.

3 DATA AND METHODOLOGY

3.1 Data and pre-processing

In this study, two multispectral images from different sensors were used: WorldView-2 (WV-2) and Landsat-5 TM- Fig. 1. The data selection for the research purpose was based on images availability, cloud cover, the small time difference in data acquisition, and diversification of land cover. The WorldView-2 image was registered on 10th August 2010 and image from Landsat-5 TM on 15th August 2010.
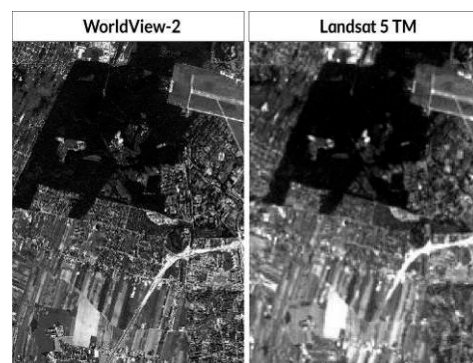
Fig. 1. Imagery data used in the study, i.e. WorldView-2, and Landsat 5 TM images

The selected imagery data are characterised by lack of clouds, relatively small temporal shift and registration of many natural and anthropogenic objects, i.e. forest, meadows, farmland, soil without vegetation, building, roads, courts etc.

Both images were georeferenced (UTM, Zone 34), and radiometrically corrected. First, the imagery was radiometrically calibrated with coefficients provided by the data provider. Next, QUAC (Bernstein et al., 2006) atmospheric correction was applied.

3.2 Methodology

The study was conducted to evaluate the spectral quality of results of pansharpening when various panchromatic channel simulations were used. It was assumed that the chosen satellites could not register the panchromatic band. The original WV-2 panchromatic image was used only to evaluate the pansharpening results. The influence of the image with

higher spatial resolution on preserving the spectral characteristics of the photographed objects was also investigated.

In this work, the WV-2 data were considered as imagery with high-spatial and low-spectral resolution, and Landsat-5 TM image was used as high-spectral and low-spatial resolution one. Panchromatic channel simulations were limited to VIS bands modifications of WV-2 data. First, the integration of Landsat multispectral data and the original Red, Green and Blue bands of WV-2 was made. Next fusion of Landsat MS and modifications of original VIS channels of WV-2 was carried out. The simulation on new panchromatic images was made by calculating the arithmetic mean of Red, Green, and Blue bands of WV-2 (Zhang et al., 2007; Chen et al., 2014) - equation (1), and the weighting sum of these channels (Kanan & Cottrell, 2012) - equation (2).

$$PAN_{MEAN} = \frac{R + G + B}{3} \qquad (1)$$

$$PAN_{NTSC} = 0.299 * R + 0.587 * G + 0.114 * B \qquad (2)$$

The weight factors used in the equation (2) correspond to the values used by NTSC in the YUV colour model, and their values are related to human perception (Pratt 2001; Kanan & Cottrell, 2012).

The pansharpening was performed using the Gram-Schmidt algorithm. The results of that process were evaluated based on visual analysis of enhanced images and statistical analysis using four coefficients: Universal Image Quality Index (UIQI), Peak Signal To Noise Ratio Index (PSNR), and Correlation Coefficient (CC) (Hill et al., 1999; Otazu et al., 2005; Karathanassi et al., 2007; Yokoya et al., 2017).

The degree of preservation of the spectral features of selected objects was also checked by comparing their spectral characteristics obtained from enhanced images and the in-situ measurements conducted with ASD FieldSpec 4 WideRes spectroradiometer.

4 RESULTS

The multispectral data of WV-2 and Landsat-5 TM were fused to obtain six enhanced images with 2 m spatial resolution, i.e.:

a) one image resulting from the integration of Landsat-5 TM data and original WV PAN degraded to 2m – it is reference data for quality evaluation of results;

b) three images resulting from the integration of Landsat TM data with original WV-2 Red, Green and Blue bands separately;

c) two images resulting from the integration of Landsat TM data with bands simulated, based on equations (1), and (2).

First, the visual assessment of pansharpening results was conducted. Contrast, artefact occurrence, and degree of preservation of colour and details were investigated using different colour compositions.

When applying the pansharpening using the original panchromatic band, it was possible to preserve the highest level of detail. On the other hand, using the original Red or Green bands, allowed to obtain images with more intense colours, as opposed to using the Blue channel.

Due to the high spatial resolution ratio between the WV-2 and Landsat-5 data colour propagation between neighbouring elements is significant- Fig. 2. However, not always a sharpened image, that is optimal for human eyesight or automatic classification, will be suitable for the accurate detection of objects (Winter et al., 2007).

The statistical evaluation was performed by comparison of enhanced images with original Landsat TM data by calculating the coefficients: UIQI, PSNR, ERGAS, and CC.

Fig. 2. Results of pansharpening process

SHARPENED BANDS	PANCHROMATIC BAND											
	UIQI – Universal Image Quality Index						PSNR – Peak Signal To Noise Ratio Index					
	PAN_{WV2}	PAN_{NTSC}	PAN_{MEAN}	PAN_{RED}	PAN_{GREEN}	PAN_{BLUE}	PAN_{WV2}	PAN_{NTSC}	PAN_{MEAN}	PAN_{RED}	PAN_{GREEN}	PAN_{BLUE}
Red	0.56	0.60	0.58	0.61	0.60	0.49	18.71	19.07	18.87	19.14	19.09	17.95
Green	0.55	0.59	0.57	0.60	0.59	0.48	20.20	20.55	20.35	20.62	20.58	19.43
Blue	0.62	0.65	0.64	0.66	0.65	0.56	22.94	23.29	23.10	23.36	23.32	22.18
NIR	0.99	0.97	0.97	0.97	0.97	0.96	32.68	32.41	32.27	32.39	32.47	31.67
NIR II	0.56	0.58	0.56	0.59	0.58	0.45	21.30	21.63	21.43	21.70	21.66	20.51
MIR	0.54	0.58	0.56	0.59	0.58	0.46	20.09	20.44	20.24	20.52	20.46	19.32

SHARPENED BANDS	PANCHROMATIC BAND											
	ERGAS						CC – Correlation Coefficients					
	PAN_{WV2}	PAN_{NTSC}	PAN_{MEAN}	PAN_{RED}	PAN_{GREEN}	PAN_{BLUE}	PAN_{WV2}	PAN_{NTSC}	PAN_{MEAN}	PAN_{RED}	PAN_{GREEN}	PAN_{BLUE}
Red	8.51	8.17	8.36	8.10	8.14	9.29	0.84	0.86	0.85	0.86	0.86	0.82
Green	7.29	7.00	7.16	6.95	6.98	9.44	0.87	0.88	0.88	0.89	0.88	0.85
Blue	6.15	5.91	6.04	5.87	5.89	6.72	0.90	0.91	0.91	0.91	0.91	0.89
NIR	0.75	0.77	0.78	0.77	0.77	0.84	1.00	1.00	1.00	1.00	1.00	1.00
NIR II	4.18	4.03	4.12	3.99	4.01	4.58	0.95	0.95	0.95	0.95	0.95	0.94
MIR	7.19	6.91	7.07	6.85	6.89	7.86	0.87	0.89	0.88	0.89	0.89	0.85

Table. 1. Results of the statistical evaluation, i.e. UIQI, PSNR, ERGAS, and CC coefficients

The highest UIQI, PSNR and CC coefficients, as well as the lowest values of the ERGAS coefficient, were obtained when PAN_{RED}, PAN_{NTSC} and PAN_{GREEN} bands were used during the pansharpening process. Application of those bands shows the best spectral quality preservation - Table 1.

In order to verify the spectral properties of the photographed objects, the spectral characteristics of two objects located in the input images: artificial - treadmill and natural - pine were analysed. Characteristics were obtained from enhanced images and in-situ measurements. The results are presented in the figures 3 and 4.
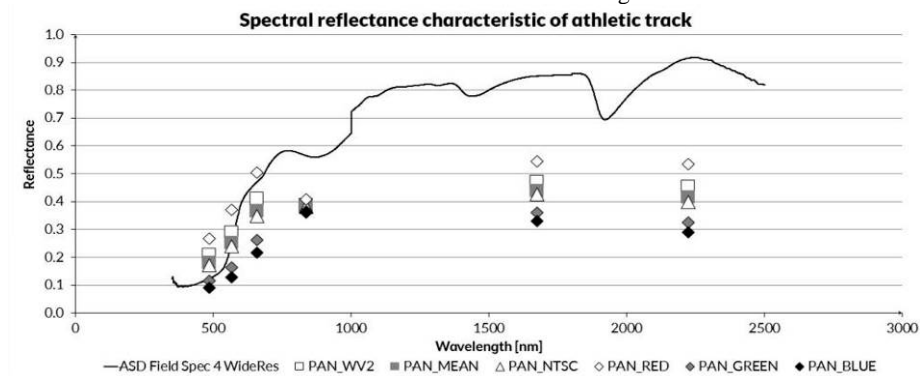

Fig. 3. Spectral reflectance characteristic and coefficients of athletic track
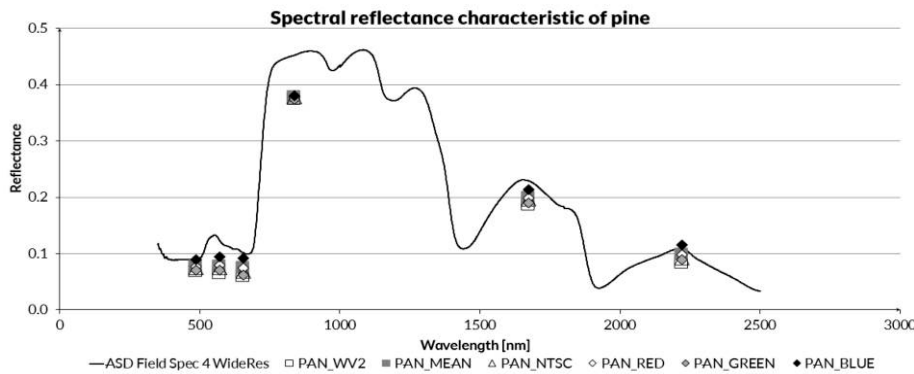

Fig. 4. Spectral reflectance characteristic and coefficients of pine

For the artificial object- the athletic track, the use of the Red channel instead of the original PAN resulted in better preservation of spectral information in the Red, NIR, NIR II and MIR ranges. The use of the Green channel resulted in better maintenance of the spectral properties of the objects in the Blue range, while for the Green range, the best results were received by simulating the PAN channel by the arithmetic mean of the R, G, and B bands.

In the case of a natural object- pine, the best results of pansharpening process were obtained when PAN$_{BLUE}$ channel was used.

For both objects types, i.e. pine, and athletic track, the spectral reflectance coefficients received from enhanced images are similar to those obtained with a spectroradiometer during in-situ measurements. Observed differences, may be caused by atmospheric conditions, inaccurate radiometric correction or relatively small image sample size.

5 SUMMARY AND CONCLUSIONS

In the presented study, the usefulness of the panchromatic band simulation was investigated, to preserve high spectral properties of the photographed objects during the pansharpening process. The preliminary research was carried out using the multispectral data of WV-2 and Landsat TM. The WV-2 imagery was used as lower-spectral resolution (only three channel Red, Green and Blue were taking into account) and high-spatial-resolution data, while Landsat-5 TM images were used as high-spectral and low-spatial resolution data. In the future work, the authors intend to implement a developed methodology to simulate panchromatic band for sensors that physically do not register panchromatic data, e.g. Sentinel-2.

As a result of pansharpening process with the application of different panchromatic simulated bands, enhanced images with 2 m spatial resolution were obtained.

The use of appropriate spectral quality coefficients, or a comparison of reliably acquired spectral reflectance coefficients of individual objects, allow assessing the usefulness of the simulation methods in a global context (whole image with a diversity of photographed objects) or local (an only specific group of objects).

Confirmation of the research results requires the analysis of more samples and the use of different sets of image data. Nevertheless, the authors point the need of simulation of the panchromatic band depending on the type of land cover that will be analysed finally. The selection of suitable bands that would be registered in narrower spectral ranges than the original PAN, or the use of an appropriate modification of multispectral channels to simulate PAN band could improve spectral properties of enhanced objects. The improved spectral quality of enhanced images is of particular importance in the interpretation and classification process of the land cover.

6 ACKNOWLEDGEMENTS

7 REFERENCES

Alparone L, Wald L, Chanussot J, Thomas C, Gamba P, Bruce LM. Comparison of pansharpening algorithms: Outcome of the 2006 GRS-S data-fusion contest. *IEEE Transactions on Geoscience and Remote Sensing*. 2007;45(10):3012–21.

Bernstein LS, Adler-Golden SM, Sundberg RL, Ratkowski AJ. Improved reflectance retrieval from hyper- and multispectral imagery without prior scene or sensor information . Vol. 6362, Proc. SPIE. 2006. p. 63622P–63622P–8.

Chen Z, Pu H, Wang B, Jiang G-M. Fusion of hyperspectral and multispectral images: A novel framework based on generalization of pan-sharpening methods. *IEEE Geoscience and Remote Sensing Letters*. 2014;11(8):1418–22.

Gevaert CM, Suomalainen J, Tang J, Kooistra L. Generation of Spectral- Temporal Response Surfaces by Combining Multispectral Satellite and Hyperspectral UAV Imagery for Precision Agriculture Applications. *IEEE Journal of Selected Topics in Applied Earth Observations and Remote Sensing*. 2015;8(6):3140–6.

Goel PK, Prasher SO, Landry JA, Patel RM, Bonnell RB, Viau AA, et al. Potential of airborne hyperspectral remote sensing to detect nitrogen deficiency and weed infestation in corn. *Computers and Electronics in Agriculture*. 2003;38(2):99–124.

Grochala A, Kedzierski M. A Method of Panchromatic Image Modification for Satellite Imagery Data Fusion. *Remote Sensing*. 2017;9(6).

Heim RH-J, Jürgens N, Große-Stoltenberg A, Oldeland J. The Effect of Epidermal Structures on Leaf Spectral Signatures of Ice Plants (Aizoaceae). *Remote Sensing*. 2015;7(12):16901–14.

Hervieu A, Le Bris A, Mallet C. Fusion of Hyperspectral and Vhr Multispectral Image Classifications in Urban Areas. ISPRS Annals of Photogrammetry, *Remote Sensing and Spatial Information Sciences*. 2016;3(3):457–64.

Hill J, Diemer C, Stöver O, Udelhoven T. A local correlation approach for the fusion of remote sensing data with different spatial resolutions in forestry applications. *International Archives of Photogrammetry and Remote Sensing*. 1999;32(Part 7):3–4.

Jenerowicz A, Woroszkiewicz M. The pan-sharpening of satellite and UAV imagery for agricultural applications. In: Neale CMU, Maltese A, editors. Proc SPIE 9998, Remote Sensing for Agriculture, Ecosystems, and Hydrology XVIII . 2016. p. 99981S.

Kanan C, Cottrell GW. Color-to-grayscale: does the method matter in image recognition. PloS one. 2012;7(1):e29740.

Karathanassi V, Kolokousis P, Ioannidou S. A comparison study on fusion methods using evaluation indicators. *International Journal of Remote Sensing*. 2007;28(10):2309–41.

Lehmann JRK, Große-Stoltenberg A, Römer M, Oldeland J. Field Spectroscopy in the VNIR-SWIR Region to Discriminate between Mediterranean Native Plants and Exotic-Invasive Shrubs Based on Leaf Tannin Content. *Remote Sensing*. 2015;7(2):1225–41.

Mayumi N, Iwasaki A. Image sharpening using hyperspectral and multispectral data. In: Geoscience and Remote Sensing Symposium (IGARSS), 2011 IEEE International. IEEE; 2011. p. 519–22.

Otazu X, González-Audícana M, Fors O, Núñez J. Introduction of sensor spectral response into image fusion methods. Application to wavelet-based methods. *IEEE Transactions on Geoscience and Remote Sensing*. 2005;43(10):2376–85.

Pratt WK. Image enhancement. Digital Image Processing: PIKS Scientific Inside, Fourth Edition. 2001;247–305.

Price JC. Combining panchromatic and multispectral imagery from dual resolution satellite instruments. *Remote sensing of environment*. 1987;21(2):119–28.

Sarp G. Spectral and spatial quality analysis of pan-sharpening algorithms: A case study in Istanbul. *European Journal of Remote Sensing*. 2014 Jan 17;47(1):19–28.

Siok K, Jenerowicz A, Woroszkiewicz M. Enhancement of spectral quality of archival aerial photographs using satellite imagery for detection of land cover. *Journal of Applied Remote Sensing*. 2017;11(3):36001.

Winter ME, Winter EM, Beaven SG, Ratkowski AJ. Hyperspectral image sharpening using multispectral data. In: Aerospace Conference, 2007 IEEE. IEEE; 2007. p. 1–9.

Yokoya N, Grohnfeldt C, Chanussot J. Hyperspectral and Multispectral Data Fusion: A comparative review of the recent literature. *IEEE Geoscience and Remote Sensing Magazine*. 2017;5(2):29–56.

Zhang Y, He M. Multi-spectral and hyperspectral image fusion using 3-D wavelet transform. *Journal of Electronics* (China). 2007;24(2):218–24.

Comparison of spatial sampling schemes for winter wheat acreage estimation using remotely sensed images in a large regional scale

Di Wang[1,2], Zhaoliang Li[1,2], Qingbo Zhou[1,2], Peng Yang[1,2]

1. Key Laboratory of Agricultural Remote Sensing, Ministry of Agriculture, Beijing 100081, P.R.China

2. Institute of Agricultural Resources and Regional Planning, Chinese Academy of Agricultural Sciences, Beijing 100081, P.R.China

Email addresses: wangdicaas@126.com；*Corresponding author: lizhaoliang@caas.cn

ABSTRACT-*Crop acreage information is an important basis for formulating national food policies and economic planning. Spatial sampling schemes have been widely used for crop acreage estimation in the large regional scale. However, the efficiencies of different spatial sampling schemes have not been quantitatively evaluated so that the optimum sampling scheme has not still been proposed. This study's aim is to make a comparison among the different spatial sampling schemes using remotely sensed data for improving the efficiency of crop acreage estimation. In this study, Shandong Province, China is selected as the study area. Moderate Resolution Imaging Spectroradiometer (MODIS) images from 2010 are used to extract the winter wheat. 13 spatial sampling schemes are formulated to draw samples, then extrapolate population values and estimate the sampling error, combining remotely sensed data, Geographic Information Systems, Geostatistics and traditional sampling methods. The Relative Error (RE), Coefficient of Variation (CV) and Sampling Fraction (SF) are selected as the index for evaluating sampling efficiency. The results demonstrate that the stratification criterion has a significant effect on the sampling efficiency, but the sample layout within the strata is not yet. For 13 spatial sampling schemes, the efficiency of spatial stratified sampling is the maximum (RE, CV and SF is 0.76%, 2.42% and 24.24%, respectively), comprehensively considering the population extrapolation accuracy, stability and sampling cost. In this way, this research can provide a theoretical basis for improving the efficiency of spatial sampling survey for crop sown acreage estimation in a large regional scale.*

1 INTRODUCTION

Information on crop area is an important basis for the formulation of national food policies and economic planning (Chen et al 2005; Qian et al 2007). Timely and accurate estimating crop sown acreage is one of key technologies of crop yield monitoring by remote sensing, it has become an important subject in national agricultural condition monitoring field (Yang et al 2002; Quarmby et al 1993; Reynold et al 2000). With the development of "3S" technology (Remote Sensing, Geographic Information System, Global Positioning System), spatial sampling methods constructed by combining traditional sampling methods and "3S" technology have been gradually used for estimating the crop area at large scales(Wu and Li 2004; Tsiligrides 1998; Delince 2001; Pradhan 2001; Gallego 1999; Carfagna and Gallego 2005; Wu et al 2014). For example, crop area was monitored by combining the stratified sampling method and "3S" technology in the LACIE (Large Area Crop Inventory and Experiment) and AGRISARS (Agriculture and Resources Inventory Surveys through Aerospace Remote Sensing) programs sponsored by the United States (US) (Benedetti et al 2010). So far, the method has been still employed by NASS (National Agricultural Statistics Service) for estimating the main crops acreage in the US (Boryan, Yang and Muller 2011). In addition, the stratified sampling method has also been combined with "3S" technology to estimate 17 crop sown acreages across the European Union (EU) in the MARS (Monitoring Agriculture with Remote Sensing) program (Gallego 1999; Carfagna and Gallego 2005). In recent years, the spatial sampling method has also been used to estimate crop acreage for large-scale areas in China; the selected sampling method is mainly stratified sampling, and the involved crops include wheat, rice and cotton. Jiao (2006) et al used the stratified sampling scheme to estimate the interannual change in paddy field area in China. In the study, a standard topographic map with a scale of 1:50000 was selected as the sampling units, and remote sensing and field surveys were employed to obtain the rice planting area in the sampled units. To improve the accuracy of winter wheat area estimation, Zhang (2010) et al incorporated stratified sampling and remotely sensed data into a spatial sampling scheme. Compared with the result retrieved only using images, the spatial sampling method obtains an improved estimation accuracy of 5% for winter wheat areas. Although spatial sampling methods have been widely used to estimate crop acreage in previous

studies, the focus has been on testing the efficiency of single spatial sampling scheme, which constructed by only one traditional sampling method (e.g., stratified sampling) combining "3S" technology. However, the efficiencies of different spatial sampling methods have not been quantitatively compared, furthermore sampling schemes for crop area have not been optimized yet, consequently hindering the improvement of spatial sampling efficiency.

To solve this problem, we conducted a study on the comparison of spatial sampling schemes in a large-scale region to improve the efficiency of the current sampling survey for crop area estimation. Shandong Province, China was selected as the study area, and winter wheat acreage was selected as the study object. "3S" technology and the traditional sampling methods are used in the study.

2 MATERRIALS AND METHODS

2.1 Technical route

The technical route consist of 4 steps: the first step is preparation of basic data used to formulate the spatial sampling scheme, the data include basic geographic information data, land use, crop spatial distribution and planting regionalization data of the study area; the second step is the design of spatial sampling schemes. It includes the formulation of sampling unit size and geometric shape, the design of sampling methods using the basic data; the third step is samples selection and population extrapolation. Samples are drawn using the spatial sampling scheme formulated in the second step, and then population value are extrapolated and sampling error are estimated; The last step is comparison of different sampling scheme efficiencies. The relative error, coefficient of variation (*CV*) and sampling cost are selected as the index of efficiency evaluation.

2.2 Study area

Shandong Province is situated between 34°22′54″N and 38°27′00″N and between 114°47′30″E and 122°42′18″E, on the verge of the Bohai Sea and the Yellow Sea and apart from Korean peninsula and Japanese archipelago by sea. The total land area of the whole province is 157,000 Km2; the offshore sea area is over 170, 000 Km2. The whole province is divided into 17 prefecture-level administrative regions with 139 county-level administrative regions. Shandong province is located in warm temperate zone and semi-humid monsoon region, with moderate climate, concentrated rainfall and four distinctive seasons. The annual mean temperature is from 11℃ to 14℃, the amount of precipitation is from 550 to 590 mm and the frost-free period is more than 200 days. Shandong province is

located in Huang-Huai plain and is the main producing area of winter wheat in our country.

2.3 Data

The experimental data consist of 4 parts: 1) Basic geographic information data. It refers to administrative boundary data of Shandong Province (the scale is 1:250000, vector format); 2) The land use data of the study area (the scale is 1:250000, vector format, 3 levels land use types); 3) The crop spatial distribution data. It refers to winter wheat spatial distribution data of the study area in 2011(derived from MODIS image, spatial resolution is 250m); 4) winter wheat planting regionalization data. Fig.1, Fig. 2 and Fig. 3 presents the spatial distribution of cultivated land, winter wheat and its planting regionalization in the study area, respectively.
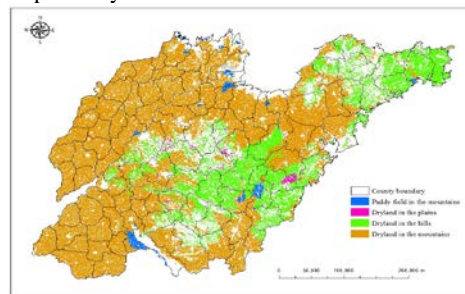

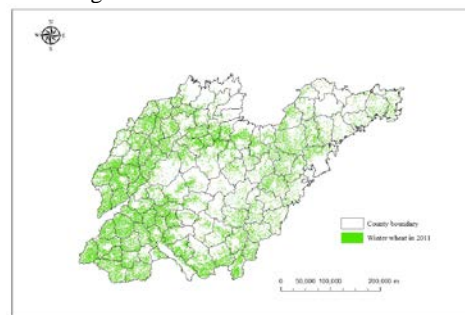Fig. 1. Spatial distribution of cultivated land in Shandong Province

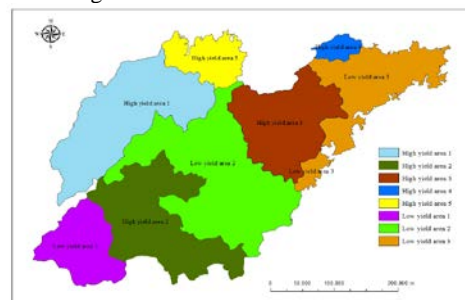Fig. 2. Spatial distribution of winter wheat in Shandong Province in 2011

Fig. 3. Winter wheat planting regionalization in Shandong Province

2.4 Spatial sampling scheme

The square grid is served as the geometric shape of sampling basic units to facilitate the analysis of spatial correlation and variability of sampling. Considering that the study area is very large, therefore, the size of the sampling basic unit, that is the square gird, is 40 Km × 40 Km, in order to improve the availability of satellite images. Then, the study area is separated by the square grid (the size is 40 Km × 40 Km) to construct sampling frame. The winter wheat sown area in each square grid is calculated as the population unit value using the ArcGIS software, based on the results of overlapping the sampling frame with the spatial distribution data of winter wheat sown area. Fig. 4 presents the distribution map of all sampling units coded by the ID number in the study area.

Fig. 4. The distribution map of sampling units coded by the ID number in the study area

2.4.1 Basic sampling units

2.4.2 Spatial sampling methods

6 different categories sampling methods are formulated to compare their efficiencies: they are simple random sampling (SRS), spatial random sampling (SPR), traditional systematic sampling (TSY), spatial systematic sampling (SSY), traditional stratified sampling (TST) and spatial stratified sampling (SST).

a) Simple random sampling: Sample size is calculated according to Eq. (1) ~ Eq. (4).

$$n_\mathrm{o} = (\frac{t}{r})^2 \frac{S^2}{\bar{Y}^2} \tag{1}$$

$$n = \frac{n_\mathrm{o}}{1 + \dfrac{n_\mathrm{o}}{N}} \tag{2}$$

$$\bar{Y} = \frac{1}{N} \sum_{i=1}^{N} Y_i \tag{3}$$

$$S^2 = \frac{1}{N} \sum_{i=1}^{N} (Y_i - \bar{Y})^2 \tag{4}$$

where n_0 is the initial sample size; n is modified sample size, when $n_0 / N > 0.05$, n_0 is modified according to Eq. (2); t is the sampling probability degrees, when the confidence level is 95%, t is equal to 1.96; r is the relative error, 5% is designed as r in the study; $\bar{Y}$ is the population mean; S^2 is the population variance; N is the population size; Y_i is the i-th population unit observations.

The procedure of samples selection using simple random sampling is that all population units are first encoded in 1−N order using ArcGIS9.3 software. Pseudo random numbers are then generated by SPSS16.0 software and used to code each successive sampling unit during its spatial location assignment.

b) Spatial random sampling: Sample size is calculated according to Eq. (5) ~ Eq. (8).

$$n_\mathrm{spatial} = n_\mathrm{simple} (1 - r) \tag{5}$$

$$r = \frac{C(Z_i, Z_{i+h})}{\sigma^2 p} \tag{6}$$

$$C(Z_i, Z_{i+h}) = \frac{1}{N(h)} \sum_{i=1}^{N(h)} [Z(X_i, Y_i) - \overline{Z(X_i, Y_i)}][Z(X_{i+h}, Y_{i+h}) - \overline{Z(X_{i+h}, Y_{i+h})}] \tag{7}$$

$$\sigma_p 2 = \frac{1}{N} \sum_{i=1}^{N} (Z_i - \overline{Z_i})^2 \tag{8}$$

where $n_{spatial}$ is sample size using spatial random sampling; n_{simple} is that of simple random sampling; r is spatial correlation coefficient; $C(Z_i, Z_{i+h})$ is covariance between the population units in the sampling frame; $N(h)$ is the numbers of population units with a distance of h; $Z(X_i, Y_i)$ is winter wheat sown area in i-th population unit; σ^2_p is dispersion variance of all population units.

For the spatial random sampling, the procedure of sample selection is the same with that of the simple random sampling.

c) Traditional systematic sampling: In order to compare the efficiencies of the two sampling methods, sample size of traditional systematic sampling is nearly the same with that of spatial random sampling, therefore, 3 is formulated into the sampling interval k, which equal to the integer value of the population size N divided by the sample size n.

Two patterns are used to draw the samples: one is that the ID numbers of all sampling units are sorted in ascending order. If the population is divided into n sections, then each section includes k population units. One population unit is drawn randomly from the k population units in the first section as the starting point, and one sampled unit is drawn every k units until all of the sampled units have been drawn. The

other is that the winter wheat area in every sampling unit is sorted in ascending order, the rest procedures is same with those of the former.

    d) Spatial systematic sampling: the space intervals between adjacent sampled units are the same in the horizon and vertical direction, furthermore, the samples are evenly distribute into the whole study area, accordingly, the sample size can be determined. Comprehensively considering the scope of the study area and population size, 80Km and 120 Km are selected as the spatial sampling interval.

    e) Traditional Stratified sampling: 3 auxiliary variables are selected as the stratification criterions: the first is the winter wheat proportion within one sampling units (WPS), and 5 strata are formulated to decrease the variance of population units in each stratum and reduce the sampling cost; the second is winter wheat planting regionalization, and 5 strata is still used; the last is cultivated land types. 4 strata are used, considering the quantity and distribution of cultivated land types in the study area. Two patterns are selected to draw samples within the strata: one is systematic isometric sampling; the other is simple random sampling. Sample size is calculated referring to (Cochran 1977).

    f) Spatial Stratified sampling: Stratification criterions are the same with those of traditional stratified sampling. The sample size is calculated according to Eq. (9) and Eq. (10).

$$n_{h,ss} = n_{h,ts}(1 - r_h) \qquad (9)$$

$$r_h = \frac{C_h(Z_i, Z_{i+h})}{\sigma_h^2 p} \qquad (10)$$

where $n_{h,ss}$ is the sample size in the h-th stratum for spatial stratified sampling; $n_{h,ts}$ is sample size of the h-th stratum for traditional stratified sampling; r_h is spatial correlation coefficient of the h-th stratum.
The spatial correlation threshold of sampling units, that is range A referred to in Geostatistics, is served as sampling interval to distribute the sampled units in each stratum.

2.4.3 Samples observation

    The winter wheat planting acreage in the sampled units is measured by overlapping the maize spatial distribution data of the study area in 2011 and square grids, and then the acreage is served as samples observation to extrapolate population value and estimate sampling error.

2.4.4 Population extrapolation and error estimation

    Simple estimator is used to extrapolate population and estimate error in the 6 sampling methods. With regard to simple random sampling, traditional systematic sampling, spatial systematic sampling and traditional stratified sampling, population inference and error estimation can be conducted referring to (Cochran 1977) and literature (Du 2005). For the spatial random sampling and stratified sampling, population total and sampling error estimation can be estimated according to Eq. (11) and Eq. (12).

$$v(\hat{Z})_{spr} = N^2 \frac{1-f}{n} s^2(1-r) = N^2 \frac{1-f}{n} \left[s^2 - COV(z(x, y) \right] \qquad (11)$$

$$v(\hat{Z})_{sst} = \sum_{h=1}^{L} N^2_h (1 - f_h) \left[s^2_h - COV(z_h(x, y)) \right] \qquad (12)$$

where $v(\hat{Z})_{srs}$ is the variance of population total estimate for spatial random sampling; $v(\hat{Z})_{sss}$ is the variance of population total estimate for spatial stratified sampling; f is sampling fraction; f_h is sampling fraction in the h-th stratum; s^2_h is discrete variance in the h-th stratum; $COV(z_h(x, y))$ is the covariance of sampled units in the h-th stratum.

    Relative error (r) and coefficient of variation (CV) are selected as index to quantitatively evaluate the efficiency of spatial sampling scheme for winter wheat acreage estimation.

3 RESULTS AND ANALYSIS

3.1 Impacts of sample selection methods on sampling efficiency

    Fig. 5 shows the histogram of sampling fraction (f), relative error (r) and CV of population extrapolation of winter wheat acreage using simple random sampling, spatial random sampling, traditional systematic sampling and spatial systematic sampling methods, in order to analyze the influence of sample selection methods on the sampling efficiency. It may be observed that r and CV increase with decreasing the f for 6 sampling methods. Although the r and CV of simple random sampling is the minimum, accordingly, the f is the maximum (nearly 90%) among the 6 methods. For the spatial systematic sampling, although the f is less than 15%, r and CV are more than 10% yet. As for the rest of 4 sampling methods, although the r and CV are almost less than 10%, however, the f is still high, it is more than 30%. It indicates that sample selection methods have no significant effect on the improvement of the sampling efficiency, comprehensively considering f, r and CV of population extrapolation of winter wheat acreage by 6 sampling methods.
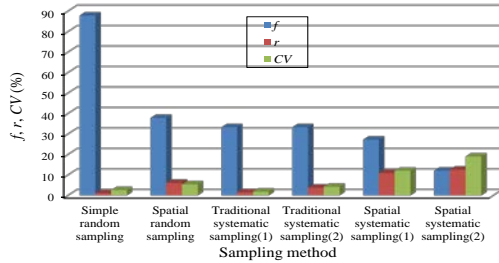
Note: *f* is sampling fraction; *r* is relative error between the true and estiamted value of population total; *CV* is the coefficient of variation; Traditional systematic sampling(1) means that the winter wheat area in every sampling unit is sorted in ascending order, then the samples are drwan according to the order ; Traditional systematic sampling(2) means that ID numbers of all sampling units are sorted in ascending order; Spatial systematic sampling(1) and (2) mean that the sampling interval is 80Km and 120Km, respectively.
Fig. 5. Histograms of sampling fraction, relative error and CV of population extrapolation of winter wheat acreage for the different random and systimatic sampling methods

3.2 Impacts of stratification criterion and sample layout on the stratified sampling efficiency

In order to analyze the influence of stratification criterion and sample layout on the sampling efficiency, Fig. 6 shows the histogram of *f*, *r* and *CV* of population extrapolation of winter wheat acreage using 7 stratified sampling methods. It may be observed that the f of the stratified sampling using WPS as the stratification criterion is the minimum, and that of the stratified sampling using winter wheat planting regionalization as the stratification criterion is the maximum for 5 sampling methods (TST(1), TST(2), TST(3), TST(4) and SST(1)), when r and CV of the five methods are almost the same(less than 5%).

Furthermore, for the TST(1), TST(2) and SST(1), when the f is nearly equal, although the stratification criterion of the three methods are the same, however, r and CV of population extrapolation are still close to equal. In addition, for SST(1) SST(2)and SST(3), when sample layout and the f are almost the same, the difference of r and CV are obvious among the three methods. It indicates that the stratification criterion has a significant effect on the sampling efficiency, but the sample layout within the strata is not yet.
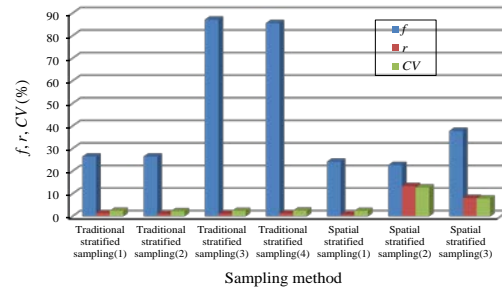
Note: Traditional stratified sampling(1) and (2) mean that WPS is selected as the stratification criterion, but systematic isometric and simple random sampling are used to draw samples within the strata for (1) and (2), respectively. Traditional stratified sampling(3) and (4) mean that simple random sampling is used to draw samples within the strata, but winter wheat plant regionalization and cultivited land types are seleted as the stratification criterion for (3) and (4), respectively. For the Spatial stratified sampling(1), (2) and (3), the spatial correlation threshold (A) of sampling units is selected as the sampling interval.WPS, winter wheat plant regionalization and cultivited land types are seleted as the stratification criterion for (1), (2)and (3), respectively.
Fig. 6. Histograms of sampling fraction, relative error and CV of population extrapolation of winter wheat acreage for the different stratified sampling methods

Table 1. Results of population extrapolation and error analysis of winter wheat acreage estimation using 13 spatial sampling methods in the study area in 2011.

No.	Sampling method	Population size	Sample size	Sampling fraction	Relative error	Coefficient of variation
				(%)	*(%)*	*(%)*
1	Simple random sampling	132	116	87.88	1.08	2.64
2	Spatial random sampling	132	50	37.88	6.17	5.42
3	Traditional systematic sampling(1)	132	44	33.33	1.58	1.88
4	Traditional systematic sampling(2)	132	44	33.33	3.83	4.24
5	Spatial systematic sampling(1)	132	36	27.27	10.98	12.06
6	Spatial systematic sampling(2)	132	16	12.12	12.59	19.04
7	Traditional stratified sampling(1)	132	35	26.52	1.39	2.48
8	Traditional stratified sampling(2)	132	35	26.52	1.03	2.28
9	Traditional stratified sampling(3)	132	115	87.12	1.13	2.44
10	Traditional stratified sampling(4)	132	113	85.61	1.29	2.56
11	Spatial stratified sampling(1)	132	32	24.24	0.76	2.42
12	Spatial stratified sampling(2)	132	30	22.73	13.41	12.78
13	Spatial stratified sampling(3)	132	50	37.88	8.15	7.92

a.　Simple random sampling

d.　Spatial systematic sampling

b.　Spatial random sampling

e.　Traditional stratified sampling

c.　Traditional systematic sampling

f.　Spatial stratified sampling
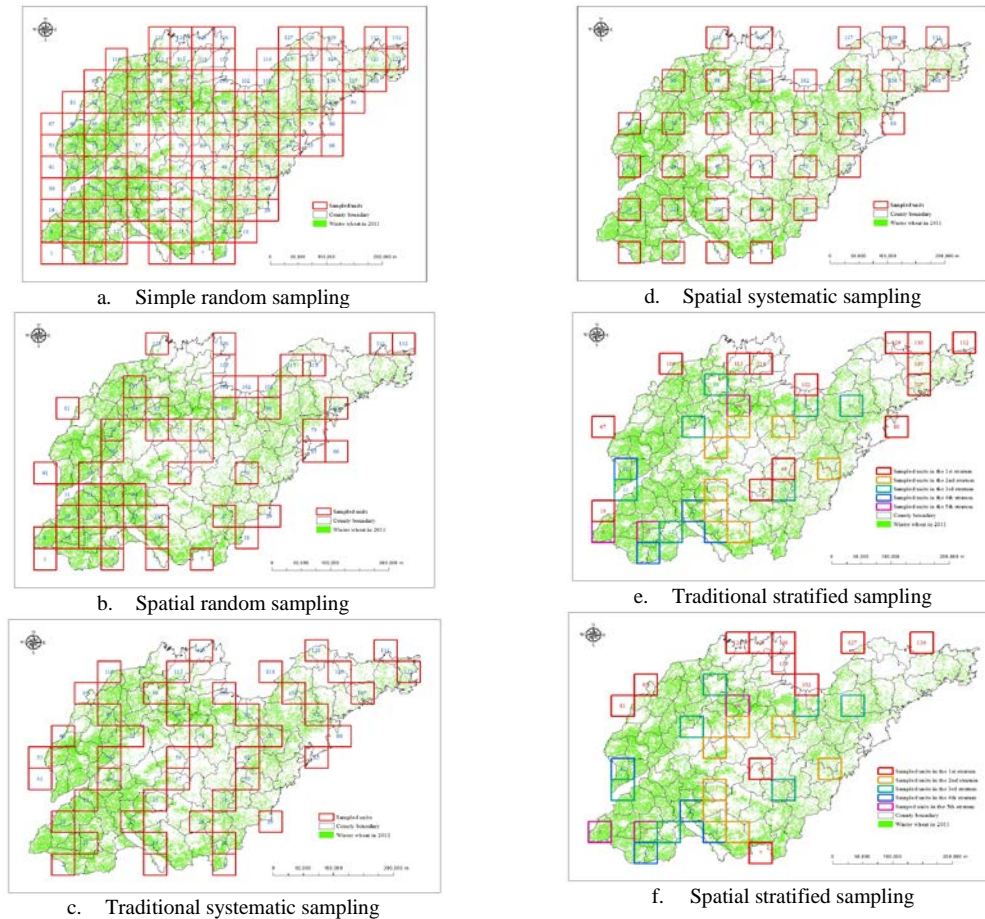
Fig. 7.　The spatial distribution of sampled units drawn by 6 spatial sampling methods for winter wheat acreage estimation in the study area

3.3 Comparison of the efficiencies for the different spatial sampling schemes

In order to compare the efficiencies of the different spatial sampling schemes for winter wheat acreage estimation, Table 1 presents the results of sample size, sampling fraction, population extrapolation and error analysis of winter wheat area using 13 sampling methods. It may be observed that the efficiency of the spatial stratified sampling, which the stratification criterion is WPS and the spatial correlation threshold of sampling units is selected as the sampling interval, is the maximum(f, r and CV is 24.24%, 0.76% and 2.42%, respectively) for 13 sampling methods, comprehensively considering the population extrapolation accuracy, stability and sampling cost. Sorted in descending order of the sampling efficiency, the rest of sampling methods are traditional stratified sampling, spatial systematic sampling, traditional

systematic sampling, spatial random sampling and simple random sampling. Fig. 7 shows the spatial distribution of sampled units drawn by 6 spatial sampling methods for winter wheat acreage estimation in the study area.

4 CONCLUSIONS

The experiments on comparison the efficiencies of different spatial sampling schemes are conducted to improve the efficiency of sampling survey for crop planting acreage estimation. Shandong Province was selected as the study area and winter wheat planting acreage as the study object. Spatial analysis, "3S" technology, Geostatistics and traditional sampling method are used. 6 sampling methods and 13 spatial sampling schemes are formulated, and square grid is served as the geometric shape of sampling units in this study. The experimental results demonstrate as follows:

1) Comprehensively considering *f*, *r* and *CV*, sample selection methods have no significant effect on the improvement of the sampling efficiency, when random or systematic sampling is used to estimate winter wheat acreage.

2) No matter traditional stratified or spatial stratified sampling, the stratification criterion has a significant effect on the sampling efficiency, but the sample layout within the strata is not yet.

3) For 13 spatial sampling schemes, the efficiency of spatial stratified sampling (stratification criterion is WPS, and sampling interval is the spatial correlation threshold of sampling units) is the maximum, in view of the population extrapolation accuracy, stability and sampling cost of winter wheat acreage.

Acknowledgements

References

Chen, S. S., Liu, Q. H., Chen, L.F., Li, J., and Liu, Q., 2005, Review of research advances in remote sensing monitoring of grain crop area. *Transactions of the CSAE*, 21(6): 166-170. (in Chinese with English abstract)

Qian,Y. L., Yang, B. J., and Jiao, X. F., 2007, Accuracy assessment on the crop area estimating method based on RS sampling at national scale. T*ransactions of the CSAE*, 23(11): 180-187. (in Chinese with English abstract)

Yang, B. J., Pei, Z. Y., and Zhou, Q. B., 2002, Key technologies of crop monitoring using remote sensing at a national scal: Progress and problems. *Transactions of the CSAE*, 18(3): 191-194. (in Chinese with English abstract)

Quarmby N. A., Milnes, M. and Hindle, T. L., 1993, The use of multi-temporal NDVI measurements from AVHRR data for crop yield estimation and prediction. *International Journal of Remote Sensing*, 14, 199-210.

Reynolds, C. A., Yitayew, M., and Slack, D. C., 2000, Estimating crop yields and production by integrating the FAO crop specific water balance model with real-time satellite data and ground-based ancillary data. *International Journal of Remote Sensing*, 21, 3487-3508.

Wu, B. F., and Li, Q. Z., 2004, Crop acreage estimation using two individual sampling frameworks with stratification. *Journal of Remote Sensing*, 8(6): 551-569). (in Chinese with English abstract)

Tsiligrides, T. A., 1998, Remote sensing as a tool for agricultural statistics: A case study of area frame sampling methodology in Hellas. *Computers and Electronics in Agriculture*, 20(1): 45-77.

J. Delince, "A European approach to area frame survey," Processing of the Conference on Agricultural and Environmental Statistical Applications in Rome(CAESAR), 2:463-472, European Commission GI & GIS, Rome, 2001.

Pradhan, S., 2001, Crop area estimation using GIS, remote sensing and area frame sampling. *International Journal of Applied Earth Observation*, 3(1): 86-92.

Gallego, F. J., 1999, Crop area estimation in the MARS project. Conference on ten years of the MARS Project, 1-11, European Commission GI & GIS, Brussels.

Carfagna, E., and Gallego, F. J., 2005, Using remote sensing for agricultural statistics. *International Statistical Review*, 73(3): 389-404.

Wu, M. Q., Yang, L. C. and Yu, B., 2014, Mapping crops acreages based on remote sensing and sampling investigation by multivariate probability proportional to size. *Transactions of the CSAE*, 30(2): 146-152. (in Chinese with English abstract)

Benedetti, R., Bee, M., Espa, G., Piersimoni, F., 2010, Agricultural survey methods. Chippenham: John Wiley and Sons.

Boryan, C., Z. W. Yang, R. Mueller, and M. Craig. 2011. Monitoring US agriculture: the US Department of Agriculture, National Agricultural Statistics Service, Cropland Data Layer Program. *Geocarto International* 26(5): 341-358.

Jiao, X. F., Yang, B. J., and Pei, Z. Y., 2006, Paddy rice area estimation using a stratified sampling method with remote sensing in China. *Transactions of the CSAE*, 22(5): 105-110. (in Chinese with English abstract)

Zhang, J. S., Shen, K. J., Pan, Y. Z., .Li, L. L., and Hou, D., 2010, HJ-1Remotely sensed data and sampling method for wheat area estimation. *Scientia Agricultura Sinica*, 43, 3306-3315. (in Chinese with English abstract)

Cochran, W. G., 1977, *Sampling Techniques* (3rd ed.). Singapore: John Wiley and Sons,

Du, Z. F. 2005. *Sampling Techniques and Practices*. Beijing: Tsinghua University Press.

Prediction of GNSS TEC Based on improved BP Neural Network

Yin Xing [1,2], Chuang Chen[3], Lilong Liu [1,2,4] *, Liangke Huang [1,2] *, Jun Chen[1,2], Wei Zhou [1,2]

[1]College of Geomatics and Geoinformation, Guilin University of Technology, Guilin 541004, China ;

[2]Guangxi Key Laboratory of Spatial Information and Geomatics, Guilin University of Technology, Guilin 541004, China ;

[3]College of Electrical Engineering and Control Science, Nanjing Tech University, Nanjing 211816, China ;

[4]College of Resources and Environment, Qinzhou University, Qinzhou 535000, China .

*Correspondence: lkhuang666@163.com; hn_liulilong@163.com

The detailed mailing address: College of Geomatics and Geoinformation, Guilin University of Technology, 12 Jian'gan Road, Guilin, Guangxi, China, 541004

 Fax and tel. numbers: Tel: +86(773)5891135; Fax: +86(773) 5893995

Abstract: The ionosphere is present in the Earth's high-level atmospheric airspace with a height of about 60 km to 100 km, containing more free electrons that can significantly affect the propagation of radio waves. Due to the influence of the free electrons in the ionosphere, when the satellite signal passes through the ionosphere, the ionospheric signal will produce the ionospheric delay error. Therefore, in order to improve the prediction accuracy of Total Electron Content (TEC), a new prediction model based on genetic algorithm to optimize Back Propagation (BP) neural network is proposed. Genetic Algorithm(GA) is a global optimization search algorithm based on natural selection and genetic theory. Through the selection, crossover and mutation operation of GA, the initial weights and thresholds of BP neural network are optimized deeply, which can be used to generalize BP neural network Mapping ability, so that BP neural network has fast convergence and strong learning ability. In this paper, TECs, from Internation Global Naviagation Satellite System(GNSS) Service center, in high, medium and low latitudes from 2013 to 2015 are selected as experimental data. BP neural network and BP neural network optimized by genetic algorithm are trained and simulated respectively. The results show: (1) Regardless of active period or quiet period ,the GA-BP model has smaller prediction residuals, and the standard deviation of active period is lower than the standard deviation of quiet period .(2) The recognition accuracy in the mid latitude region is higher, and the prediction accuracy in the high latitude region is low. In particular, the prediction accuracy of the GA-BP model in the mid latitude region is 93.53%, while the accuracy of the GA-BP model in the low latitude region is only about 74.28%. (3) The GA-BP model can improve the prediction accuracy of the ionospheric TEC value by 1-3 percentage points, which has a high fitting degree to the GNSS Service Center Observation data.

Key word: GNSS ; TEC ; prediction ; BP neural network

INTRODUCTION

The ionosphere is in the high-level atmospheric airspace at a height of about 60 km to 100 km. It contains a lot of free electrons. When the electromagnetic wave passes through the ionosphere, its propagation path will be significantly affected [1]. The total electron content (TEC) of the ionosphere is an important parameter to characterize the ionosphere in navigation and positioning, and its research has become an important subject. There are two ways to predict TEC values nowadays. One is the empirical model, including Bent model, IRI model, Klobuchar model and other classical models, only to obtain the actual TEC values of 50%~60%. The second is to directly establish the TEC model with TEC observation data as the data source. A number of time series prediction models, local linear model, RBF neural

network model and some combination prediction models are established by direct simulation of TEC data. But these models are susceptible to the length of sample data and prediction time.

For the ionospheric TEC with non-linear, non-stationary characteristics in time and space, the neural network has achieved remarkable results in its prediction. BP neural network has a complex nonlinear mapping ability through the combination of neurons with simple processing ability. But in the process of use, there are defects such as slow convergence rate and easy to fall into the local minimum. Therefore, many experts and scholars have adopted various methods to improve the neural network [2-4]. Genetic algorithm is a global optimization algorithm with good convergence and fast random search ability. It can make up the stochastic defects of BP neural network in weights and threshold selections, making BP neural network have

fast convergence and strong learning ability [5]. At the same time, combining genetic algorithm with BP neural network to predict non-stationary time series has achieved good results in some fields [6-7], but few achievements have been made in TEC prediction. Therefore, this paper will explore the BP neural network optimized by genetic algorithm. In this paper, the global TEC values provided by IGS are used to evaluate the prediction results.

1 BASIC THEORY

1.1 BP Neural Network

BP neural network is also called back propagation neural network. It is a non-federated network with three or more layers [8]. BP neural network not only has input layer and output layer, but also has multiple hidden layers. It implements the full connection between the nerves of each layer, but there is no connection between the neurons in the same layer.
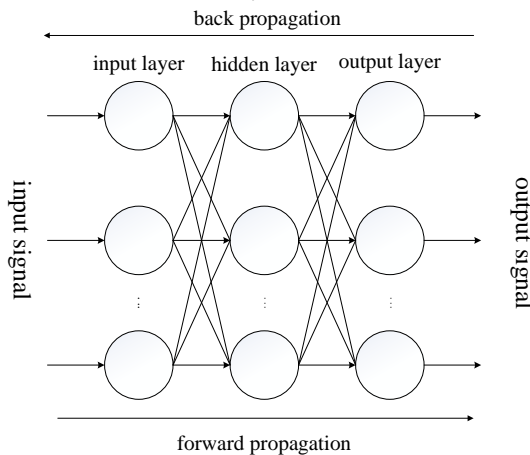

Figure 1 the learning process of BP neural network with three layers

The learning process of BP neural network is shown in figure 1. It consists mainly of two parts, that is, the forward propagation of the input signal and the back propagation of the error signal. In forward propagation, the input signal is input from the input layer, which is then processed by the hidden layer, and finally it is passed to the output layer to get the actual output. If the actual output does not match the expected output, then the error is propagated backwards. The process of back propagation is to correct the connection weights from the output layer to the input layer, so that the error is reduced [9]. The two propagation processes are carried out cyclically. The connection weights of the BP network are continually trained to meet the set target accuracy or to the maximum number of iterations.

1.2 Genetic Algorithm (GA)

GA is a computational model for simulating the natural elimination of organisms in natural evolution. It is a kind of algorithm with strong global search ability and global optimization performance, mainly including selection, crossover and mutation operation. For details, please refer to reference [10].

1.3 BP Neural Network Optimized By Genetic Algorithm

Due to the randomness of the generated weights and thresholds in network training, it may lead to unstable results. In order to improve the prediction accuracy and stability, this paper uses the genetic algorithm to optimize the initial weights and thresholds of the network. The basic steps are as follows:

- Individual coding. Since the weights and thresholds of BP networks are decimals between (-1, 1) and their number is large, it is not suitable for binary encoding. Therefore, the real coded rule is adopted in this paper.

- Evolutionary parameters of BP neural network are determined by the individual evaluation function. The weights and thresholds of the BP neural network are assigned by the coding obtained in the above, so that the accuracy of the training sample is set in the neural network, obtaining the output values of network training. Here, the reciprocal of mean square error is taken as the fitness of the individual.

- The selection of the operator is carried out, that is, the optimal chromosome quality in each generation is selected according to the selection strategy of fitness proportion. The selection probability is as follows:

$$p_i = f_i / \sum_{i=1}^{p} f_i, i = 1, 2, ..., p. \tag{1}$$

Where f_i is the fitness value; p is the population size.

- Because the individual uses real number coding, crossover operation is performed by real number crossing method. For example, the crossover between the $k\text{-}th$ Gene w_k and the $l\text{-}th$ gene w_l in the j bit is as follows:

$$\begin{aligned} w_{kj} &= w_{kj}(1-b) + w_{lj}b, \\ w_{lj} &= w_{lj}(1-b) + w_{kj}b. \end{aligned} \tag{2}$$

Where b is the random number between 0 and 1.

- Mutation operation. Select the $j\text{-}th$ gene of the $i\text{-}th$ individual to perform the mutation operation as follows:

$$w_{ij} = \begin{cases} w_{ij} + (w_{ij} - w_{max})f(g), r \geq 0.5; \\ w_{ij} + (w_{min} - w_{ij})f(g), r < 0.5. \end{cases} \quad (3)$$

$$f(g) = r_2(1 - g / G_{max}). \quad (4)$$

Where w_{max} and w_{min} are the upper and lower bounds of the w_{ij} value of the gene; r and r_2 are the random numbers between 0 and 1; g is the current iteration number; and G_{max} is the maximum evolution number.

- The optimal individual obtained by GA is decomposed into initial weights and thresholds of BP neural network.

2 EXPERIMENTAL ANALYSIS

2.1 Data Sampling

In this paper, the TEC data provided by IGS from 2013 to 2015 are used as sample sequences. The TEC data are modeled on the first 10 days using the BP model and the GA-BP model, and the TEC data are predicted 5 days later (that is, the first 120 data are used to predict the 60 data). Specifically, the annual TEC data of low latitude (10 ˚N, 115 ˚E), mid latitude (40 ˚N, 115 ˚E) and high latitude (70 ˚N, 115 ˚E) in three years are selected as experimental data.
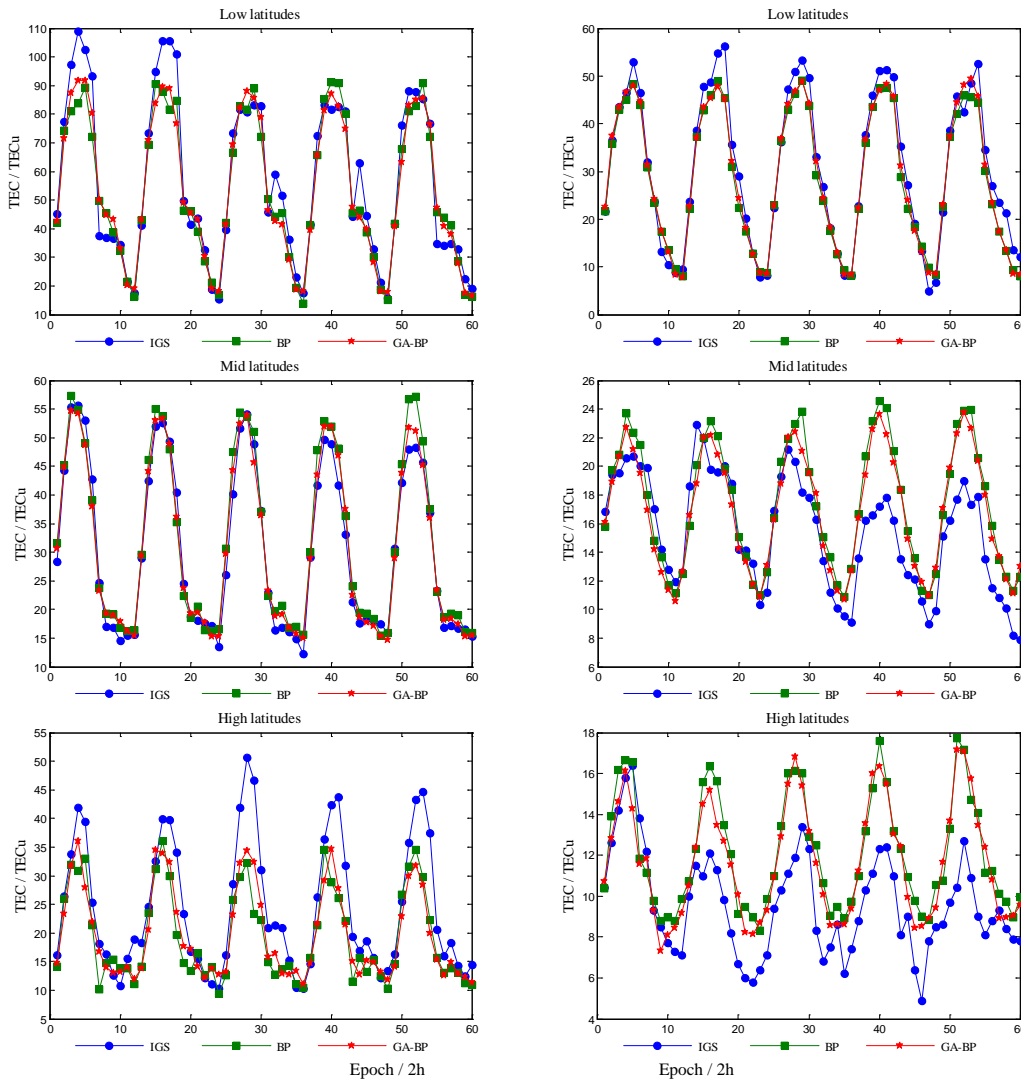

Figure 2 TEC prediction results of the active period (left) and the quiet period (right) at different times

IGS releases the TEC values every two hours, so there are 12 values per day, with a total of 4380 TEC values per year. Since using TEC data for the first 10 days to predict TEC data after 5 days, such a total of 3159 sample data are established. In this experiment, the TEC data of 50-64 days in 2014 are used as the test samples of active period. The TEC data of 236-250 days in 2015 are used as the test samples of quiet period. The data in the 2013, 2014 and the remainder of 2015 are used as training samples.

At the same time, this paper uses the data provided by the IGS center as the truth value, and uses relative precision P and standard deviation SDE to evaluate the prediction result. The formulas are as follows:

$$SDE_{day} = \sqrt{\frac{\sum_{i=12n-11}^{12n} (K_{pre[i]} - K_{igs[i]})^2}{12}} \qquad (5)$$

$$P_{pre-day} = \frac{\sum_{i=12n-11}^{12n} (1 - \frac{\left| K_{pre[i]} - K_{igs[i]} \right|}{K_{igs[i]}})}{12} \qquad (6)$$

Where $K_{pre[i]}$ is the prediction result; $K_{igs[i]}$ is the TEC observation value provided by the IGS center; n is the n-th day of the predicted days.

2.2 Results Analysis

BP neural network with three layers is selected in this paper. After a constant attempt, the final parameters are selected as follows: the number of input layer nodes is 120; the number of output layer nodes is 60; the number of hidden layer nodes is 20; the maximum number of iterations is 3000; the target precision is 0.01; and the learning rate is 0.1. The GA-BP network parameters are set such that the initial population size is 50; the generation is 100; the crossover rate is 0.8; the mutation rate is 0.05, and the other parameters are the same as the BP network.

Two models are constructed and trained. The experimental results are shown in figure 2. In figure 2, the abscissa represents the prediction epoch while every 2h is 1 epoch; the ordinate indicates the TEC values while the unit is TECu. From Figure 2, we can see that both in the quiet period or active period, TEC values predicted by the BP model and GA-BP model in different latitudes (low, medium and high) are better able to follow the actual values. In particular, the prediction results using the GA-BP model are closer to the observed values than the BP model.

The overall residual distribution of the two models is shown in Table 1 and Table 2. According to Table 1 and Table 2, it can be seen that when the mean values of 5-day prediction residuals are lower than 1 TECu, the percentage content mean of GA-BP model is higher than that of BP model in both the active period and

quiet period. When the mean values of 5-day prediction residuals are higher than 3 TECu, the percentage content mean of GA-BP model is lower than that of BP model in both the active period and quiet period. Therefore, the prediction residuals of the GA-BP model are smaller and the prediction results are better.

Table 1 Residuals distribution of two models in active period (low, middle, high latitudes)

Forecast day	BP/GA-BP /%		
	$\Delta<1$TECu	1TECu$\leq\Delta<$3TECu	$\Delta\geq$3TECu
1	16.67/13.89	38.89/41.67	44.44/44.44
2	16.67/30.56	27.78/36.11	55.56/33.33
3	22.22/27.78	16.67/22.22	61.11/50.00
4	25.00/16.67	30.56/33.33	44.44/50.00
5	16.67/22.22	22.22/30.56	61.11/47.22
Mean	19.45/22.22	27.22/32.78	53.33/45.00

Table 2 Residuals distribution of two models in quiet period (low, middle, high latitudes)

Forecast day	BP/GA-BP /%		
	$\Delta<1$TECu	1TECu$\leq\Delta<$3TECu	$\Delta\geq$3TECu
1	38.89/52.78	50.00/41.67	11.11/5.56
2	30.56/30.56	33.33/38.89	36.11/30.56
3	27.78/33.33	38.89/41.67	33.33/25.00
4	11.11/16.67	33.33/33.33	55.56/50.00
5	2.78/8.33	33.33/30.56	63.89/61.11
Mean	22.22/28.33	37.78/37.22	40.00/34.45

In order to further illustrate that the prediction results of GA-BP model are better than the prediction results of BP model, the standard deviations and relative precision are statistically shown in Table 3 and Table 4. Table 3 discusses the TEC in the active period. It can be seen that the prediction accuracy in the mid-latitude region is the highest, followed by the low latitude region and the lowest in the high latitude region. The standard deviation of GA-BP model in different latitude regions is less than that of BP model. In addition, both the BP model and the GA-BP model have a large positive standard deviation for the first day in the high latitude region, which may be caused by excessive fluctuations in the TEC values of the ionosphere in high latitude region on March 1, 2014. Table 4 discusses the TEC in the quiet period. It can be seen that the prediction accuracy is the highest in the low latitude region, followed by the mid-latitude region

and the lowest in the high latitude region. The prediction accuracy of GA-BP model is higher than that of BP model. Combined with Table 3 and Table 4, we can see that

- The prediction accuracy of the GA-BP model is superior to the BP model in either active or quiet period.
- The recognition accuracy in the mid latitude region is higher, and the prediction accuracy in the high latitude region is low. In particular, the prediction accuracy of the GA-BP model in the mid latitude region is 93.53%, while the accuracy of the GA-BP model in the low latitude region is only about 74.28%. The possible reason for this is that the low latitudes are strongly influenced by the earth's magnetic field and solar activity. It leads to an anomalous ionosphere over the $\pm 20^{\circ}$ geomagnetic, greatly increasing its electronic content. At the same time, the variation law of the ionosphere in the mid-latitude region is relatively simple and no abnormal changes can occur. In the high latitudes, the electronic content is low, and the abnormal plasma changes make the edge of the electrons change drastically in the short term.

In Table 1-4, we can find that the relative accuracy of the active period is slightly higher than that of the quiet period, but the prediction residuals are the opposite. The reason is that the magnitude of the base values will affect the calculation results of relative accuracy to a certain extent. If the initial value is different, the relative accuracy will be quite different for the same or similar prediction residuals. Taking into account the initial value, the active period is greater than the quiet period, so even if it contains a large difference, the relative accuracy can still be maintained at a higher level.

3 CONCLUSION

In view of the nonlinear and non-stationary characteristics of the ionospheric total electron content, this paper introduces genetic algorithm to optimize the weights and thresholds of BP neural networks. Then, the two models are used to predict the TEC values. The experimental results show that the relative accuracy of the active period is slightly higher than that of the quiet period, but the prediction residuals are larger than that of the quiet period. Compared with the BP model, the GA-BP model improves the prediction accuracy and has good stability, so as to better explain the change characteristics of ionosphere.

Table 3 Comparison of the prediction accuracy using BP and GA-BP models in the active period

Grid point	Model	Evaluation index	Day					Mean
			1	2	3	4	5	
Low latitude	BP	SDE_{day}	0.3897	0.4479	1.0226	0.1655	0.8824	0.5816
		$P_{pre-day}$	0.8641	0.8886	0.8854	0.9162	0.8585	0.8826
	GA-BP	SDE_{day}	0.3816	0.7931	0.1816	0.6147	0.7209	0.5384
		$P_{pre-day}$	0.8728	0.9047	0.9015	0.8999	0.8804	0.8918
Mid-latitude	BP	SDE_{day}	0.2255	0.8798	0.9665	0.0131	0.1688	0.4507
		$P_{pre-day}$	0.9242	0.9224	0.8850	0.9202	0.9178	0.9139
	GA-BP	SDE_{day}	0.0525	0.5491	0.7693	0.3718	0.0270	0.3539
		$P_{pre-day}$	0.9229	0.9494	0.9196	0.9309	0.9539	0.9353
High latitude	BP	SDE_{day}	2.2536	0.2510	0.0264	0.8647	1.0409	0.8873
		$P_{pre-day}$	0.8039	0.8235	0.7584	0.8017	0.8101	0.7995
	GA-BP	SDE_{day}	1.9922	0.7053	0.2272	0.4427	0.8886	0.8512
		$P_{pre-day}$	0.8513	0.8361	0.7680	0.8217	0.7940	0.8142

Note: the unit of SDE_{day} is TECu; the unit of $P_{pre-day}$ is %.

Table 4 Comparison of the prediction accuracy using BP and GA-BP models in the quiet period

Grid point	Model	Evaluation index	Day					Mean
			1	2	3	4	5	
Low latitude	BP	SDE_{day}	0.4052	0.1958	0.0270	0.4575	1.1593	0.4490
		$P_{pre-day}$	0.9068	0.8953	0.9307	0.8295	0.8314	0.8787
	GA-BP	SDE_{day}	0.4596	0.1434	0.0872	0.5500	1.0545	0.4589
		$P_{pre-day}$	0.9113	0.9086	0.9501	0.8600	0.8387	0.8937
Mid-latitude	BP	SDE_{day}	0.0413	0.4080	1.0768	0.7407	1.2671	0.7068
		$P_{pre-day}$	0.9263	0.9170	0.8536	0.7286	0.7046	0.8260
	GA-BP	SDE_{day}	0.0148	0.5368	1.0463	0.8649	1.4811	0.7888
		$P_{pre-day}$	0.9223	0.9195	0.8804	0.7564	0.7148	0.8387
High latitude	BP	SDE_{day}	0.7994	0.8009	0.6790	0.5883	0.6160	0.6967
		$P_{pre-day}$	0.8851	0.6408	0.6965	0.6457	0.6748	0.7086
	GA-BP	SDE_{day}	0.6044	0.6346	0.5783	0.2639	0.5036	0.5170
		$P_{pre-day}$	0.9115	0.7047	0.7380	0.6880	0.6717	0.7428

Note: the unit of SDE_{day} is TECu; the unit of $P_{pre-day}$ is %.

4 ACKNOWLEDGEMENT

REFERENCES

Jiao M L, Jiang T C, Wang X P, 2008, Research development of ionospheric models based on GNSS. *Science of Surveying and Mapping*, 33(5):91-93.

Yuan M U, 2007, Hydraulic turbine temperature model establishment based on improved BP neutral network. *Journal of Shenyang Institute of Aeronautical Engineering*.

Zhang Y, Liu J, 2002, Improvement of Sensor′s Performance by Using BP Neutral Network and It′s New Algorithms. *Journal of Transcluction Technology*.

Sun X, Yang Z, Wang Z, 2010, The application of BP neutral network optimized by genetic algorithm in transportation data fusion, *Proceedings of 2010 2nd Advanced Computer Control (ICACC)*, IEEE, 560-563.

Dong H K, Abraham A, Cho J H, 2007, A hybrid genetic algorithm and bacterial foraging approach for global optimization, *Information Sciences*, 177(18):3918-3937.

Li S, Luo Y, Zhang M R, 2011, Prediction method for chaotic time series of optimized BP neural network based on genetic algorithm, *Computer Engineering and Applications*, 47(29):52-55.

Li H B, 2009, Research on the application of chaotic time series prediction, *University of Science and Technology of China*.

Hecht-Nielsen R, 1989, Theory of the backpropagation neural network. *Proceedings of International Joint Conference on Neural Networks (IJCNN)*, IEEE, 593–605.

Chen B Y, Dai W J, Cai C S, *et al*, 2012, Ionospheric modeling and forecasting based on tomographic and neural network method. *Geomatics and Information Science of Wuhan University*, 37(8):972-975.

Wang Q, Liu C, Huang J, 2011, Prediction of VLF electric strength based on waveguide mode theory using GA, *Proceedings of 2011 International Conference on Electric Information and Control Engineering(ICEICE)*, IEEE, 605-608
.

GIS-based Landslide Susceptibility Mapping Using an Integrated Model

Yaning Yi[1,2], Wanchang Zhang[1*], Cai Deng[1,3], Xiangpeng Yang[4] and Qi Xu[4]

[1] *Key Laboratory of Digital Earth Science, Institute of Remote Sensing and Digital Earth, Chinese Academy of Sciences, Beijing 100094, China*

[2] *University of Chinese Academy of Sciences, Beijing, 100049, China*

[3] *State Key Laboratory of Pollution Control & Resource Reuse, School of the Environment, Nanjing University, Nanjing 210023, China*

[4] *Institute of Karst Geology, Chinese Academy of Geological Sciences, Guilin 541004, China*

*Corresponding author: zhangwc@radi.ac.cn

ABSTRACT - *As catastrophic events, landslides can cause human injury, loss of life and economic devastation, and destroy construction works and cultural and natural heritage. To develop strategies for landslide risk assessment and management, an effective landslide susceptibility, hazard, and risk model is necessary to mitigate or even avoid the resulted disastrous consequences from landslides. For this purpose, an integrated model combining frequency ratio (FR) and analytical hierarchy process (AHP) method was attempted to map the landslide susceptibility in the Southwestern part of Qushan town near the Wenchuan earthquake-stricken area in 2008, South West China. The relationships between landslide susceptibility and causative factors were analysed with the FR method and the weights of causative factors were assigned by the AHP method based on the availability of existing data resources. The causative factors incorporated into the model were: elevation, slope, aspect, lithology, distance to rivers, normalized difference vegetation index (NDVI) and peak ground acceleration (PGA). The weighted overlay analysis was conducted to produce the susceptibility map of landslides in the study area by using GIS software. The landslide susceptibility was categorized into five levels: very low, low, moderate, high and very high. The results obtained in this study showed that the integrated model can be used as an effective tool in assessment of landslide susceptibility, the results obtained provide the basis for hazard assessment and regional planning.*

1 INTRODUCTION

A landslide, also known as a landslip, is a form of mass wasting that includes a wide range of ground movements, such as rock-falls, deep failure of slopes, and shallow debris flows. As a major geological hazard, Landslides cause significant life losses and property damage, destruction of infrastructure and damages to natural ecosystems (Dai and Lee, 2002; Saha et al., 2010). Landslides occur when the slope changes from a stable to an unstable condition. A change in the stability of a slope can be caused by a number of factors, acting together or alone, mainly influenced by geological, meteorological and human factors, especially the rainfall and earthquake. To mitigate the impact of landslides, many studies have been carried out to map the intensity and locations that are prone to landslides.

In the recent years, various approaches have been proposed to produce the landslide susceptibility map based on statistical analysis and expert knowledge. Among which frequency ratio (FR) method (Pradhan B, 2010; Anbalagan R, 2015), logistic regression (Bai et al, 2010; Mathew et al, 2007), weights of evidence (Althuwaynee et al, 2012; Regmi et al, 2010), AHP

(Pourghasemi et al, 2012; Yalcin, 2008), information valued method (Jun et al, 2010; Lin and Tung, 2004) have been utilized in disaster prevention practise. Landslide susceptibility mapping based on statistical analyses assumes that landslide susceptibility can be assessed through analysis between landslides occurrence and causative factors. However, the relationships obtained through analysis between landslides occurrence and causative factors can't fully reflect the inner relations among causative factors. Furthermore, statistical methods require a large amount of field samples and such intensive field activity is almost impossible to carry out in most cases.

With the rapid advances of remote sensing and GIS, quick acquirement of high resolution remote sensing images makes it possible to interpret various disasters effectively. Remote sensing techniques have been approved very success in landslides interpretations in many studies (Sato et al, 2007; Xu et al, 2015). In this paper, an integrated model by combining FR and AHP methods was proposed to map landslide susceptibility of the study area. In this model, the FR method was used to depict relationships

between landslide occurrence and causative factors, and the AHP method was adopted to reflect relationships among causative factors. Landslide causative factors mainly including elevation, slope, aspect, lithology, distance to rivers, NDVI and PGA, were used to map the landslide susceptibility of the study area damaged by the Ms 8.0 Wenchuan earthquake in 2008, Southwestern China.

2 STUDY AREA

The study area is located in the southwest of Qushan town in the Sichuan province of China (Figure 1). The total area of this study site is about 53.66 km^2 with central longitude/latitude at 104.457°E and 31.835°N. The topography of the region is undulated with terrain featured by successive hills and mountains of elevations ranging from 570 m to 2100 m above mean sea level. Jian River, the largest river channel flows through the region. According to the local climate record provided by China Meteorological Administration, the long term average annual temperature in this area is about 15.6℃ and average annual precipitation is around 1472 mm, which characterizes this region a typical subtropical moist monsoon climate.

The study area is closed to the epicentre of 2008 Wenchuan earthquake, about 133 km from each other. The Yingxiu–Beichuan fault, one of three main faults of the Long Menshan tectonic belt (Zhen et al., 2008), just developed in this area. Landslides seriously threaten the living and productive activities of the people living there, especially after the Wenchuan earthquake. Landslide susceptibility mapping is therefore of great significance to be implemented in the region.
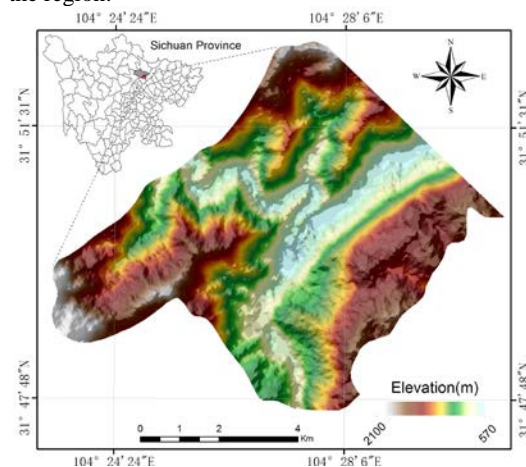
Figure 1 Geographic map showing the location and topography of the study area.

3 DATA

Landslide hazard analysis and mapping can provide useful information for catastrophic loss reduction, and assist in the development of guidelines for sustainable land use planning. The analysis is used to identify the factors that are related to landslides, estimate the relative contribution of factors causing slope failures, establish a relation between the factors and landslides, and to predict the landslide hazard in the future based on such a relationship. The factors that have been used for landslide hazard analysis can usually be grouped into geomorphology, geology, land use/land cover, and hydrogeology. Slope, aspect, elevation, lithology, distance to rivers and NDVI. PGA is the dynamic factor of landslides triggered by earthquake, and it has a great impact on landslides. Seven causative factors were used for the landslide susceptibility mapping.

To extract the landslide causative factor layers for the area, we used 1: 200,000-scale geologic map, 30×30 m Digital Elevation Model (DEM), and SPOT remote sensing images of May 2008 (10 m spatial resolution). All the additional data on the terrain morphology (elevation, slope, and aspect) were derived from the DEM. The lithology map was extracted from the 1:200,000-scale geologic map. SPOT image of 10 m spatial resolution was used to generate the NDVI map. Aerial photographs of 4 m spatial resolution were further used to identify the location of landslides by means of visual image interpretation, and 64 landslides triggered by the Wenchuan earthquake were interpreted in the study area. PGA is important causative factor which can download from the United States Geological Survey (USGS, https://www.usgs.gov). Prior to produce the susceptibility map of landslide, all data set were converted into raster format and processed by ArcGIS10.2 and ENVI5.3 software, and all images and layers were projected on a UTM (Universal Transverse Mercator) zone 48 North projection with WGS84 datum. Finally a spatial data set of causative factor maps were prepared. Figure 2 refers to the data layers worked out in this study.

4 LANDSLIDE SUSCEPTIBILITY MAPPING

4.1 Methodology

In the present study, an integrated model combining frequency ratio and AHP method was used to perform landslide susceptibility mapping. This model consists of three generic steps: (1) characterization of relationships between causative factors and landslide occurrences using FR method, (2) determination of weights among the causative factors with AHP approach, (3) producing landslide susceptibility map of the study area by means of GIS techniques.
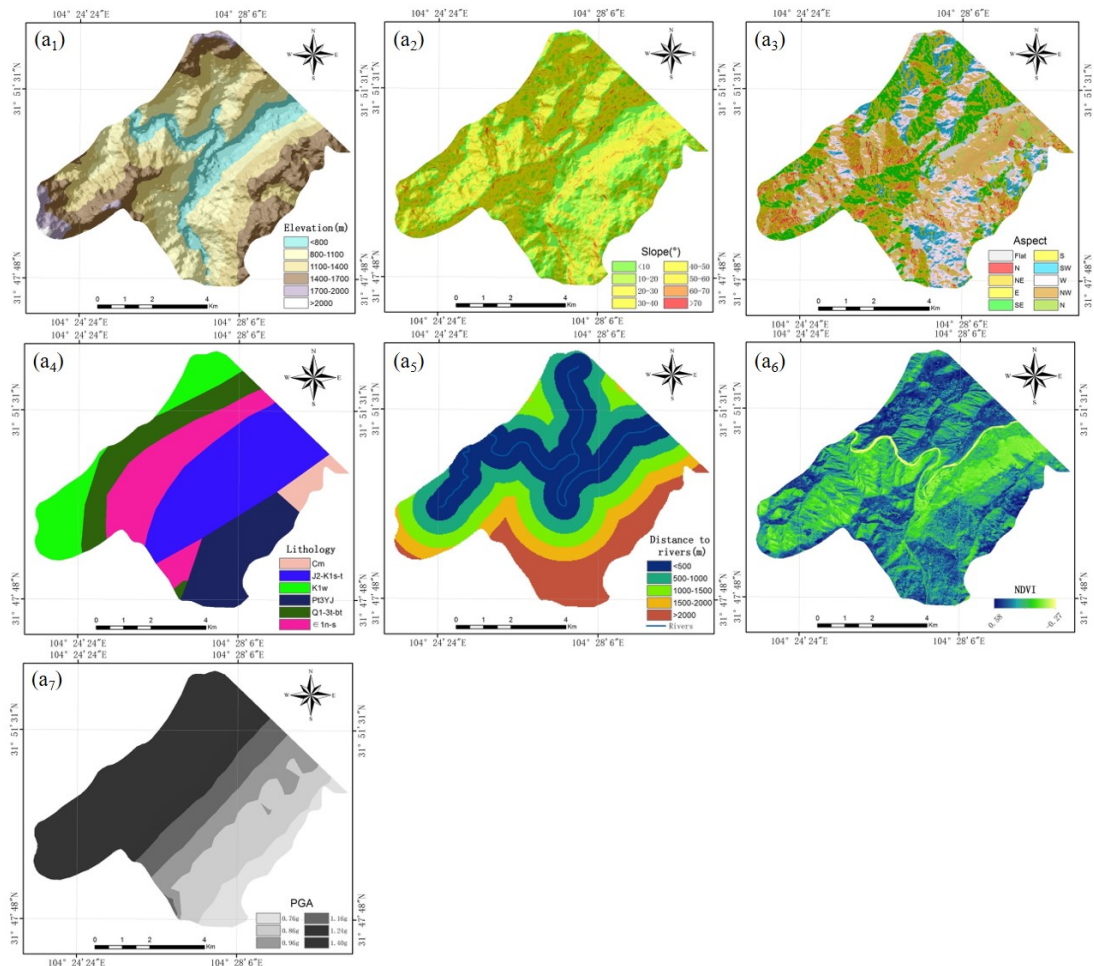
Figure 2 Descriptive map of causative factor layers. a_1: elevation; a_2: slope; a_3: aspect; a_4: lithology; a_5: distance to rivers; a_6: NDVI; a_7: PGA.

The assumption behind landslide susceptibility mapping is that susceptibility can be evaluated if the causative factors and the relationships between the causative factors and landslide susceptibility are known (Zhu, 2014). Following the same assumption, the relationships can be quantified between landslides related causative factors with the landslide occurrences spatially using FR method. The FR method is the ratio of the area/probabilities where landslides occurred in the total study area for given attributes (Lee and Talib, 2005). It follows the principle of conditional probability, in which if the ratio >0 then there is a positive correlation between landslides and factor classes whereas ratio <0 represents negative correlation.

Next step of the integrated model is to assess the relationship between causative factors by using AHP method. The AHP method, developed by Saaty (Saaty,

1977), has been applied for assessing landslide susceptibility (Komac, 2006; Pourghasemi et al, 2012) originally but now it was used to define the relationships between the different causative factors and to derive their weights. In this study, the values from local landslide experts were used to characterize relationships between different causative factors. These values were later imported into the AHP matrixes to compute weights of causative factors using MATLAB software. The weights with the Consistency Ratio less than 0.1 were accepted. Table 1 refers to the weights of each causative factors.

For the landslide susceptibility mapping, causative factors with certain weights obtained from previous process were integrated for estimating landslide susceptibility values. GIS data layers for these seven causative factors and the landslide distribution map were spatially analysed by using ArcGIS10.2. Each

GIS factor data layer was multiplied by weights to obtain the landslide susceptibility values of the study area by using weighted overlay analysis tool in GIS for producing landslide susceptibility map. The landslide susceptibility values were classified in five data ranges corresponding to five susceptibility zones namely, very low, low, moderate, high and very high using the Natural Breaks (Jenks) method in the ArcGIS10.2.

Table. 1 The relative importance, factor weights, and consistency ratio estimated in this study

CF	a_1	a_2	a_3	a_4	a_5	a_6	a_7	W
a_1	1	1/4	1/2	1/4	1/3	1/2	1/5	0.0436
a_2	4	1	4	2	2	3	1	0.2463
a_3	2	1/4	1	1/3	1/2	1/2	1/4	0.0606
a_4	4	1/2	3	1	2	3	1/2	0.1756
a_5	3	1/2	2	1/2	1	2	1/3	0.1162
a_6	2	1/3	2	1/3	1/2	1	1/4	0.0769
a_7	5	1	4	2	3	4	1	0.2808

Consistency Ratio: 0.0188

Note: CF means the causative factors; W means the weights of causative factors. When a factor is more important than another, the score varies between 1 and 9. Conversely, the score varies between 1/2 and 1/9. a_1: elevation; a_2: slope; a_3: aspect; a_4: lithology; a_5: distance to rivers; a_6: NDVI; a_7: PGA.

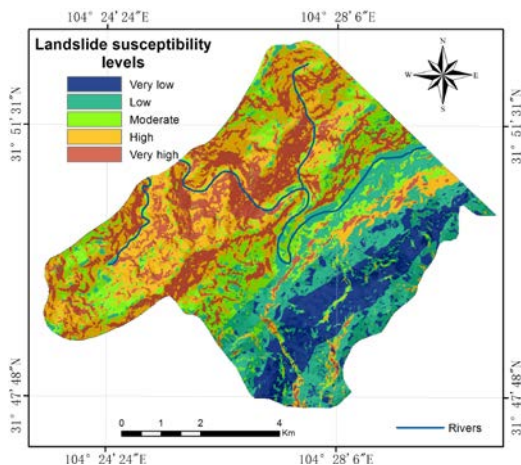**Figure 3** The susceptibility map of landslides in the study area

4.2 Results and Discussions

Finally, a susceptibility map of landslides in the study area was generated through the above described steps (Figure 3). Statistical analysis on landslide susceptibility map suggested a clear correlation between landslides and susceptibility levels (Table 2). Most landslides were identified in the high and very high susceptibility regions, and very few landslides were identified in the very low susceptibility region, as shown in Fig. 3.

In our study area, very high, high, moderate, low, very low susceptibility occupied about 21.07%, 26.43%, 17.20%, 23.00%, 12.30% of the study area, approximately about 11.31km^2, 14.18km^2, 9.23km^2, 6.60 km^2, correspondingly. Results indicated that high susceptibility zone predominately developed in the middle mountainous region. Settlement area, where the old Beichuan county located, are generally situated on the plain of the eastern part and were less prone to the landslides. On the contrary, the extensive middle mountainous region in the western part of the study area are made up of siltstone or shale and may be easily subjected to mass movements such as sheet erosion in case of intense rain. Very High susceptibility zones were also found along rivers in the central part of the study area and the over barren steep slopes with less vegetation. Low susceptibility zones were generally found in settlement area and medium mountains of the southern part of the study area.

5 VERIFICATION of LANDSLIDE SUSCEPTIBILITY MAP

To evaluate the validity of results, the landslide susceptibility map was further verified through a statistical analysis. The landslide density of each class was computed (Table 2). From the table, it can be found that the very high susceptibility level has a very high landslide density value, which is remarkably higher than the other levels. On the contrary, the very low susceptibility level has a very low landslide density value. In general, as the landslide density decreases, the landslide susceptibility level also decreases. Large difference in landslide density values between the susceptibility levels can be recognized evidently, which implied that the occurrence of landslides is highly correlated the level of the landslide susceptibility. This indirectly demonstrated the reliability of the landslide susceptibility map with existing slope instability conditions.

6 CONCLUSIONS

As an attempt to use an integrated model combining frequency ratio and AHP method to assess the landslide susceptibility of the Qushan town, which is highly prone to the occurrence of landslides, the integrated model incorporated most of the landslide causative factors of the area including elevation, slope, aspect, lithology, distance to rivers, NDVI and PGA.

Table. 2 Landslide susceptibility levels and the density of landslides in the study area

Susceptibility level	Area (km^2)	Area (%)	Landslide quantity	Landslide quantity (%)	Density (no./km^2)
Very Low	6.60	12.30	2	3.13	0.25
Low	12.34	23.00	5	7.81	0.34
Moderate	9.23	17.20	7	10.94	0.64
High	14.18	26.43	17	26.56	1.01
Very High	11.31	21.07	33	51.56	2.48
All	53.66	100.00	64	100.00	--

Satellite images and geo-informatics tools were used in landslide susceptibility mapping for the study area, and the results obtained suggested that it is possible to produce satisfactory landslide susceptibility maps with the integrated model when applied at regional scale. With the integrated model much extensively tested, feasibility of the model for landslide susceptibility mapping can be much conformed. At present, it can be concluded that the model developed in this study is satisfactory for our study goals and the results from this study can provide the scientific suggestions for hazard assessment and regional planning.

ACKNOWLEDGMENT

REFERENCES

Althuwaynee OF, Pradhan B, Lee S, 2012, Application of an evidential belief function model in landslide susceptibility mapping. *Computers & Geosciences*, **44**, 120-135.

Anbalagan R, Kumar R, Lakshmanan K, et al., 2015, Landslide hazard zonation mapping using frequency ratio and fuzzy logic approach, a case study of Lachung Valley, Sikkim. *Geoenvironmental Disasters*, **2**, 1-17.

Bai S-B, Wang J, Lü G-N, Zhou P-G, Hou S-S, Xu S-N, 2010, GIS-based logistic regression for landslide susceptibility mapping of the Zhongxian segment in the Three Gorges area, China. *Geomorphology*, **115**, 23-31.

Dai FC, Lee CF, 2002, Landslide characteristics and slope instability modeling using GIS, Lantau Island, Hong Kong. *Geomorphology*, **42**, 213-228.

Jun DU, Yang QH, Yan J, 2010, Hazard Evaluation of Secondary Geological Disaster Based on GIS and Information Value Method. *Earth Science*, **35**, 324-330.

Komac M, 2006, A landslide susceptibility model using the Analytical Hierarchy Process method and multivariate statistics in perialpine Slovenia. *Geomorphology*, **74**, 17-28.

Lee S, Dan N T, 2005, Probabilistic landslide susceptibility mapping in the Lai Chau province of Vietnam: focus on the relationship between tectonic fractures and landslides. *Environmental Geology*, **48**,778-787.

Lin M-L, Tung C-C, 2004, A GIS-based potential analysis of the landslides induced by the Chi-Chi earthquake. *Engineering Geology*, **71**, 63-77.

Mathew J, Jha VK, Rawat GS, 2007, Application of binary logistic regression analysis and its validation for landslide susceptibility mapping in part of Garhwal Himalaya, India. International *Journal of Remote Sensing*, **28**, 2257-2275.

PeiZhen Z et al., 2008, Slip rates and recurrence intervals of the Longmen Shan active fault zone, and tectonic implications for the mechanism of the May 12 Wenchuan earthquake, 2008, Sichuan, China. *Chinese Journal of Geophysics*, **51**, 1066-1073.

Pourghasemi HR, Pradhan B, Gokceoglu C, 2012, Application of fuzzy logic and analytical hierarchy process (AHP) to landslide susceptibility mapping at Haraz watershed, Iran. *Nat Hazards*, **63**, 965-996.

Pradhan B, Saro L, 2010, Delineation of landslide hazard areas on Penang Island, Malaysia, by using frequency ratio, logistic regression, and artificial neural network models. *Environmental Earth Sciences*, **60**, 1037-1054.

Regmi NR, Giardino JR, Vitek JD, 2010, Modeling susceptibility to landslides using the weight of evidence approach: Western Colorado, USA. *Geomorphology*, **115**, 172-187.

Saaty TL, 1977, A scaling method for priorities in hierarchical structures. *Journal of Mathematical Psychology*, **15**, 234-281.

Saha AK, Gupta RP, Arora MK, 2010, GIS-based Landslide Hazard Zonation in the Bhagirathi (Ganga) Valley, Himalayas. *International Journal of Remote Sensing*, **23**, 357-369.

Sato H P, Hasegawa H, Fujiwara S, et al., 2007, Interpretation of landslide distribution triggered by the 2005 Northern Pakistan earthquake using SPOT 5 imagery. *Landslides*, **4**, 113-122.

Xu C, Xu X, Shyu J B H, et al., 2015, Landslides triggered by the 20 April 2013 Lushan, China, Mw 6.6 earthquake from field investigations and preliminary analyses. *Landslides*, **12**, 365-385.

Yalcin A, 2008, GIS-based landslide susceptibility mapping using analytical hierarchy process and bivariate statistics in Ardesen (Turkey): Comparisons of results and confirmations. *Catena*, **72**, 1-12.

Zhu A X et al., 2014, An expert knowledge-based approach to landslide susceptibility mapping using GIS and fuzzy logic. *Geomorphology*, **214**, 128-138.

Comparative Study on Remote Sensing Estimation Methods of Grassland Fractional Vegetation Coverage: A case study of grassland in Ili Prefecture, Xinjiang, China

Wenbo Zhang[a], Xiuchun Yang[a], Asiya Manlike [b], Yunxiang Jin[a], Fengling Zhen[b], Jian Guo[a], Ge Shen[a], Yujing Zhang[a] and Bin Xu[a*]

a. Key Laboratory of Agri-informatics of the Ministry of Agriculture Institute of Agricultural Resources and Regional Planning, Chinese Academy of Agricultural Sciences, Beijing, China
b. Grassland research institute, Xinjiang Academy of Animal Sciences, Urumchi, China
Email: zhangwenbowww@163.com
CONTACT Bin Xu, xubin@caas.cn Chinese Academy of Agricultural Sciences, Beijing, China

ABSTRACT - *Fractional vegetation cover (FVC) is an important biophysical parameter of terrestrial ecosystems. This study made use of GF-1 MFV satellite data (growing seasons of grass in 2014), based on the grassland type and soil type vector data, using empirical model method, sub-pixel method, linear spectral unmixing method and maximum three bands gradient difference method estimate the FVC of grassland in Ili prefecture of Xinjiang, and then the estimation accuracy of the four methods was compared in different types of grassland. After verification of the ground sampling points obtained from the grassland supervision departments, the four methods were 89.86%, 87.31%, 88.01% and 75.21% on the estimation accuracy of Xinjiang grassland vegetation coverage. The empirical model method achieved the highest estimation accuracy, while the maximum three bands gradient difference method had the lowest accuracy. For the grassland types, the highest accuracy was the FVC estimation of temperate meadow steppe area using the empirical model method, the RMSE value was 5.88. And the average estimation accuracy of alpine meadow was lowest. The results of this study showed that the empirical model method has some advantages in evaluating the vegetation coverage in the small-scale area, the maximum three band gradient difference method needed further improvement and perfection.*

1 INTRODUCTION

Terrestrial ecosystem, as an important component of the earth system, plays an important role in maintaining the structure, function and environment of the entire Earth system and regulating it to suit the direction of human existence (Steffen, 2004). Vegetation is the most basic part of terrestrial ecosystems, and all other organisms depend on vegetation. Fractional vegetation coverage (FVC), as an important quantitative index of vegetation, reflects the basic situation of vegetation to a great extent. Fractional vegetation coverage refers to the percentage of the vertical projection area of all vegetation canopies and branches in the growing area, which accounts for the statistical area of the study area. It is an important parameter to describe the vegetation cover of the earth, and also a basic indicator of ecological environment change (Qi, 2000; Zhang, 2010). The grassland area of the world is about 1/2 of the total land area, and it is the most basic production material and base for the development of grassland animal husbandry. Grassland occupies a very important position in the global ecosystem. Therefore, regional and global estimation of grassland vegetation coverage is of great significance to the study of vegetation and related fields.

The calculation method of the FVC can be divided into two types of field measurement and remote sensing monitoring, the vegetation coverage has a significant spatial and temporal variation characteristics of measured surface method is not only time-consuming. But for large scale research, this method is neither realistic nor possible, so remote sensing monitoring has become the main means of FVC estimation (Liang, 2012).

At present, the remote sensing measurement method of FVC can be categorized into the regression model, mixed pixel decomposition method and machine learning method and so on. Regression model established the empirical estimating models by regression analysis of one band, band combination, vegetation index of remote sensing data with FVC (Voorde, 2008; Xiao, 2005; Boyd, 2002). The mixed pixel decomposition method assumes that each component of the pixel contributes to the information observed by the sensor, establish a mixed pixel decomposition model to estimate the FVC. Sub-pixel model is the simplest linear pixel unmixing model. Machine learning methods mainly include neural networks, decision trees, support vector machines, etc. Hansen et al. (Hansen, 2007) established the MODIS

standard product Vegetation Continuous Fields algorithm by using decision tree model. Although the FVC algorithm is rich and diverse, there are few studies for grassland area, without considering the heterogeneity of study area to establish the partition model. In this study, the estimation of FVC in grassland of Xinjiang, Ili was studied, and the establishment of subarea estimation model was explored.

2 STUDY AREA

Ili Kazak Autonomous Prefecture is located in the northwest part of Xinjiang Uygur Autonomous Region, between 40°14' and 49°10'N and 80°09' and 90°01'E. The total area of the whole state is 350 thousand square kilometers, and the mountains, plains, basins and valleys are distributed in the territory. The "three mountains, two basins and two valleys" constitute the main geomorphic unit. The main features of grassland resources in Ili are good grassland quality and high yield of grassland, and the total grassland area is 35,933 km2, representing 64% of the total area of the region. The Ili grassland is primarily dominated by mountain meadow, alpine meadow, temperate meadow steppe temperate steppe and temperate desert steppe (Fig.1).
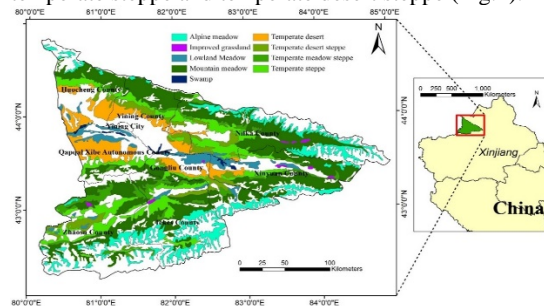

Fig.1. The location map of Ili, China

3 DATA AND METHODS

3.1 Study Data and Pre-treatment

WFV 16 m multispectral data From July to August in 2014 is the main data source of this study, including 6 images covering Ili prefecture. GF-1 is the first satellite of China's high resolution earth observation system, carrying two 2m resolution panchromatic /8m resolution multispectral cameras, and four 16m resolution multispectral cameras. The remote sensing data used in the study also include the LANDSAT8 OLI panchromatic image of the same phase in the study area as the reference image of ortho rectification and geometric correction of the GF-1WFV image. Non remote sensing data for ground sampling data and vector data base, including 125 ground sampling points of vegetation coverage data (from the field investigation of the Ili prefecture in 2014, in part

provided by the grassland supervision center, Ministry of agriculture), 1:100 million grassland type distribution data and vector data of administrative divisions.

Choosing 6 scenes of GF-1 WFV data (low cloud-cover) of study area in July and August which is the growing season of grassland vegetation (roughly matched the acquisition time of ground verification points). After ortho correction, geometric correction, radiometric calibration, atmospheric correction, image mosaic and cropping pretreatment, obtained the surface reflectance image of research area. In order to eliminate the influence of clouds, water, snow, forest and other features in the study area, before estimating the FVC of grassland we needed to mask the aforementioned objects. Respectively used HOT threshold method, normalized difference water index (NDWI) threshold method and decision tree method to carry on the mask processing.

3.2 Empirical Model (EM)

In this paper, the FVC value of partial ground verification points and NDVI value of corresponding pixel were used for regression analysis, and established regression equation, so as to establish empirical estimation model. Through regression analysis, the regression model of FVC and NDVI was established as logarithmic model.

3.3 Partition Sub-pixel Model (PSP)

The sub-pixel model assumed that the pixels were only composed of two parts: vegetation and non-vegetation cover, and the spectral information was only synthesized by the two groups. The proportion of their respective areas in the pixels was the weight of each factor, and the percentage of the vegetation covering the earth surface was FVC of the pixel. The expression of two pixel model was as follows:

$$FVC = (NDVIi - NDVIsoil)/(NDVIveg - NDVIsoil) \quad (1)$$

Among them, *NDVIi* represented the pixel NDVI value of I time, *NDVIveg* was the pixel NDVI value of whole vegetation cover, and *NDVIsoil* was the NDVI value of naked soil pixel.

For temperate steppe, temperate desert steppe and temperate desert, theoretically there was no uniform pixel full of vegetation cover, the maximum NDVI value of image would not be able to instead the *NDVIveg*, needing to calculate *NDVIveg* and *NDVIsoil* by the equation composed with two ground validation points at least within the region . For the two pixels a1 and a2 in the region, their FVC was known as *fvc1* and *fvc2*, and the formula (1) for these two pixels can be obtained:

$$fvc1 = (NDVIa1 - NDVIsoil)/(NDVIveg - NDVIsoil) \quad (2)$$

$fvc2 = (NDVIa2 - NDVIsoil)/(NDVIveg - NDVIsoil)$ (3)

Calculated the *NDVIveg* and *NDVIsoil* of above equation set, and obtained:

$NDVIsoil = (fvc2 * NDVIa1 – fvc1 * NDVIa2) / (fvc2- fvc1)$ (4)

$NDVIveg = [(1 – fvc2) * NDVIa2 – (1 – fvc1) * NDVIa1)] / (fvc2- fvc1)$ (5)

After the analysis and calculation, we got the *NDVIveg* and *NDVIsoil* of each grassland type partition, which was shown in table 1.

3.4 Linear Spectral Unmixing (LSU)

The mixed spectrum refers to the integrated information of ground reflectance spectrum composed of vegetation spectrum and underlying surface spectrum (Li, 2013). By solving the proportion of each component in the mixed pixels, the proportion of the vegetation branch was the required FVC (Kenneth, 2000).

Firstly, MNF (Minimum Noise Fraction) transform was applied to the image. The essence of MNF transform was two stacked principal component transform, which can effectively eliminate the noise. And then selected the bands without noise obtained from MNF transform to calculate the spectral purity index (PPI). The computation of PPI was achieved by projecting the N dimensional scatter to the random unit vector and recording the number of pixels falling into the unit vector, the more the number, the more likely the pixel was pure. Then selected the pixel whose PPI values were greater than a certain threshold as a training area. Observed the distribution of pixels in the training area in the space by the N dimensional visualization, and chose the corresponding endmembers, then obtained the average spectral curve of endmembers (Fig 2). There were four endmembers obtained in this study: vegetation, bare sand, soil, forest. The spectral curve of endmembers were used as input parameters to decompose the mixed pixels of reflectance image, and the distribution of endmember and error were obtained. Fig 3 showed the vegetation endmember proportion distribution. Fig 4 was the error distribution map.
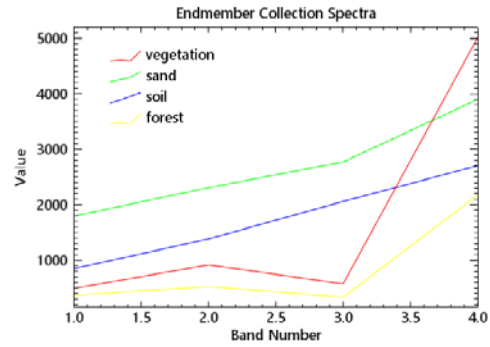

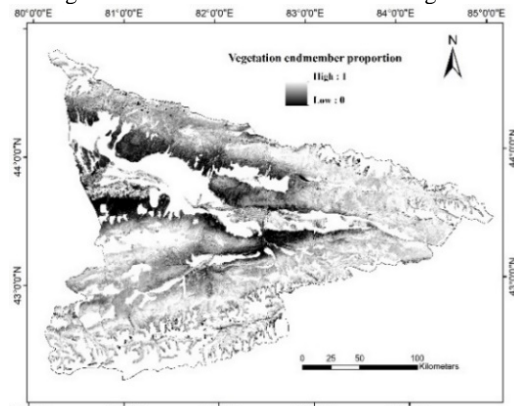Fig 2 Endmember reflectance curve diagram
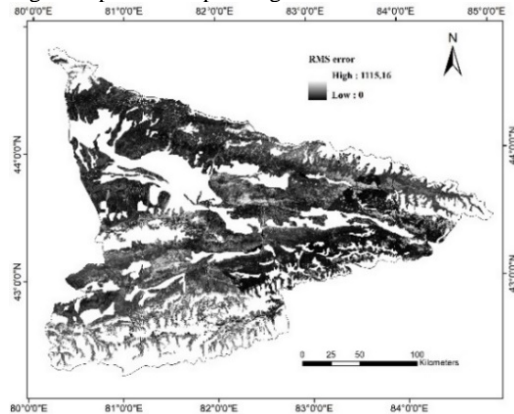

Fig 3 Proportion map of vegetation endmember

Fig 4 RMS error distribution map of LSU

Table 1 Parameters List of Sub-pixel Method

Grassland type	*NDVIsoil*	*NDVIveg*	Grassland type	*NDVIsoil*	*NDVIveg*
Alpine meadow	0.11	0.823	Mountain meadow	0.3	0.843
Improved grassland	0.166	0.86	Temperate meadow steppe	0.19	0.813
Lowland meadow	0.173	0.85	Temperate desert	0.14	0.79
Swamp	0.17	0.852	Temperate steppe	0.174	0.747
Temperate desert steppe	0.167	0.71			

3.5 Maximum Three Bands Gradient Difference (MTGD)

As was known to all, the vegetation reflectance spectrum had a low reflection peak in the green band, and had a high reflection peak in the near infrared band. There was an absorption peak in red light band, while the soil spectrum changed approximately linearly in green to near infrared band. For the reflectance image, the slope of green to red reflectance and red to near infrared reflectance reached the maximum at the pixel full of vegetation coverage, while the slope of reflectance of soil pixels was the same in each band. In order to highlight the changes of soil reflectance curve caused by vegetation in a certain pixel, we introduce the concept of gradient difference d:

$$d = (\frac{Rir - Rr}{\lambda ir - \lambda r}) - (\frac{Rr - Rg}{\lambda r - \lambda g}) \qquad (6)$$

Among them, R_{ir}, R_r and R_g represent near infrared, red, green band reflectance, λ_{ir}, λ_r and λ_g represent near infrared, red and green wavelengths.

For any pixel of the image, its fractional vegetation coverage:

$$FVC = d / d_{max} \qquad (7)$$

$$d_{max} = max(d) \qquad (8)$$

For the GF-1 WFV data used in this study, the formula of FVC was:

$FVC = d / d_{max}$

$$FVC = 0 \quad if \quad FVC < 0 \qquad (9)$$

$$FVC = 1 \quad if \quad FVC > 1 \qquad (10)$$

$$d = (\frac{Rir - Rr}{789 - 675}) - (\frac{Rr - Rg}{675 - 555}) \qquad (11)$$

R_{ir}, R_r and R_g represent near infrared, red, green band reflectance of GF-1 WFV data. λ_{ir}, λ_r and λ_g in formula (6)were replaced by the corresponding wavelengths of GF-1 WFV data.

4 RESULTS AND ANALYSIS

Through the above steps, the grassland FVC in the study area was estimated by four methods, and the results obtained by each method were shown in figure 7- 10.

4.1 Analysis of Calculation Results

From Fig 5- 8, the results of FVC calculated by the four methods were consistent in the overall spatial distribution trend. The calculated by linear spectral unmixing method was obviously higher than the other three methods, the distribution range of high coverage area was also more than the other three methods. The average value of FVC calculated by the maximum three band gradient method is the lowest, and the low coverage area was the most widely distributed.
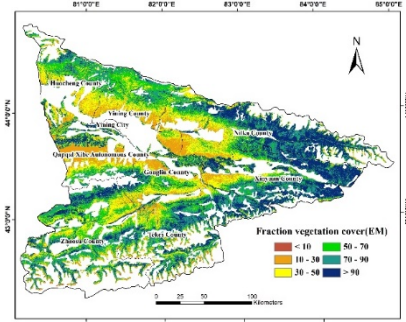

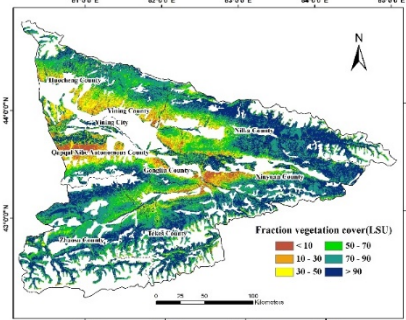Fig 5 FVC Distribution map by EM method

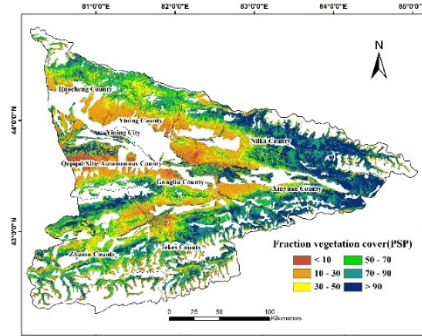Fig 6 FVC Distribution map by LSU method
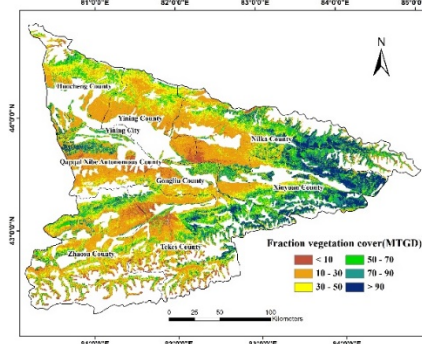

Fig 7 FVC Distribution map by PSP method

Fig 8 FVC Distribution map by MTGD method

Table 2 Accuracy of Estimation Table

Methods	Pearson correlation	RMSE (%)	Average error (%)
Empirical model	0.94	10.14	7.66
Sub-pixel model	0.94	12.69	10.10
Linear spectral unmixing	0.92	11.99	8.64
Maximum three bands gradient difference	0.81	24.88	19.20

From the section of estimation accuracy verification in next part of this paper, the estimation accuracy of FVC calculated by empirical model was the highest. In this part, this paper took empirical model results as the standard to study grassland FVC spatial distribution characteristics.

The spatial distribution of grassland FVC in study area was characterized by high coverage areas were mainly concentrated in mountain meadow and Lowland Meadow of the eastern and southern, low coverage areas were mainly distributed in the temperate desert steppe and temperate desert located in the central region. The extreme high vegetation coverage area (>90%) accounted for 31.4% of the total grassland area of the study area, the medium high vegetation coverage area (70%-90%) accounted for 15.25%, while the high vegetation coverage area (50%-70%) accounted for 15.3%. The total areas of three types above accounted for 61.95% of the total grassland area, while the area with extremely low vegetation coverage (<10%) accounted for only 7.62% of the total area. The situation of grassland vegetation coverage in the study area was dominated by the high coverage.

4.2 Verification of Ground Sample Points Accuracy

In this paper, Pearson correlation coefficient, RMSE (root mean square error) and error were used as evaluation contents of calculation accuracy. And the results of calculation accuracy were shown in Table 2.

The Pearson correlation coefficient of the empirical model and the partition sub-pixel model was the highest, reaching 0.94, and the RMSE and the average error of empirical model method were the minimum,

with the values of 10.14 and 7.66. In general, the empirical model method had the highest precision. Compared with the other three methods, the maximum three band gradient difference method has low calculation accuracy, and the RMSE was 24.88. The scatter degree was also the highest from the scatter diagram.

4.3 Evaluation of Different Grassland Types Accuracy

After comparing the overall accuracy of each method, the accuracy of the main grassland types was analyzed and compared to show the applicability of different methods to different grassland types. From the Table 3, it can be seen that the minimum RMSE was the temperate meadow steppe using empirical model, with a value of 5.88. For partition sub-pixel model, the highest accuracy type was temperate desert, and its RMSE was 7.43. For linear spectral unmixing method, the highest accuracy type was mountain meadow, with RMSE of 9.34. For the maximum three band gradient difference method, the highest precision was temperate desert, and the RMSE was 12.88.

From the average value column of Table 3, it can be seen that the highest average precision was temperate desert, and the RMSE was 10.21. The RMSE of alpine meadow was 36.41, which was the maximum in the main grassland types. The reasons why the alpine meadow estimation accuracy was low were uncertain. Parts of accumulated snow region had been identified and masked in the data pretreatment, but due to the influence of complex terrain and snow the estimation error were still larger than other types of grassland.

Table 3 Accuracy of Estimation Table

Methods / Grassland type	Empirical model	Sub-pixel model	Linear spectral unmixing	Maximum three bands gradient difference	Average value
Alpine meadow	27.19	23.95	25.50	14.38	36.41
Mountain meadow	7.84	11.48	9.34	22.90	12.89
Temperate desert	9.01	7.43	11.50	12.88	10.21
Temperate desert steppe	8.34	12.33	14.00	16.04	12.68
Temperate meadow steppe	5.88	8.96	14.34	35.63	16.20
Temperate steppe	8.27	13.74	12.39	30.43	16.21

5 CONCLUSION AND DISCUSSION

In this paper, based on the domestic GF-1 WFV 16 meter multi-spectral data, eliminating interference of snow and forest to grassland FVC, using the model method, partition sub-pixel method, linear spectral unmixing method and maximum three band gradient difference method, we retrieved the grassland FVC of Ili prefecture. A method of Estimating grassland FVC based on partition sub-pixel model was proposed, and the maximum three band gradient difference method was tentatively applied to the inversion of grassland FVC. The accuracy of each method was analyzed by the accuracy test with ground verification points, and the calculation accuracy of the main grassland types was also analyzed. Among them, the accuracy of FVC estimated by empirical model was the highest, reaching 89.86%. The maximum three band gradient difference method had the lowest estimation, which was 75.21%. For the accuracy of all grassland types, the temperate meadow steppe with empirical model was the highest, reaching 94.12%; the average precision was the highest in temperate desert, reaching 89.79%, the lowest was alpine meadow, the average accuracy was only 63.59%.

Through the inversion of Ili grassland FVC, we found that the high coverage areas are mainly distributed in the mountain meadow and lowland meadow area of eastern and southern regions, low coverage area was mainly distributed in temperate desert steppe and temperate desert of central region. The overall situation of grassland FVC in the study area was dominated by high vegetation coverage (>50%).

Due to the high quality of ground verification points used in this study, the empirical model method possessed enough measured values for modeling. For a certain region, the empirical model had certain advantages with substantial ground measured data, so its estimation accuracy was higher. For the maximum three band gradient method, because the method was affected by complex soil background and the image brightness of different phase, its estimation accuracy was low. And subsequent research will continue to improve and optimize this method. For alpine meadow, the reasons for low estimation accuracy may be that the areas were influenced by complex topography and snow cover. On the other hand, due to the difficult sampling in the alpine region, the accuracy and representativeness of ground verification point data were affected inevitably.

GF-1 satellite data, as an important component of domestic high resolution satellite system, had good spatial resolution and multi-spectral characteristics, which can provide necessary supplement and continuation for MODIS and LANDSAT data. It is of great significance to continuously explore and evaluate the use effect of GF-1 satellite data for the development and improvement of high resolution satellite system.

REFERENCES

Steffen, W., Sanderson A., Tyson P. D., et.al. 2004, Global Change and the Earth System: A Planet under Pressure. *Berlin: Springer*.

Qi, J., Marsett, R. C., Moran M. S., et al. 2000, Spatial and temporal dynamics of vegetation in the San Pedro river basin area. *Agricultural and Forest Meteorology*, 105(1): 55 - 68.

Zhang, X., Wu, B., Ling, F., et.al. 2010, Identification of priority areas for controlling soil erosion. *Catena*, 83(1): 76-86.

Liang, S., Li, X., and Wang J., 2012, Advanced Remote Sensing: Terrestrial Information Extraction and Applications. *Pennsylvania: Academic Press*.

Voorde, T., Vlaeminck, J., and Canters F., 2008, Comparing different approaches for mapping urban vegetation cover from Landsat ETM + data: A case study on Brussels. *Sensors*, 8: 3880-3 902 .

Xiao, J. F., and Moody, A., 2005, A comparison of methods for estimating fractional green vegetation cover within a desert-to-upland transition zone in central New Mexico, USA. *Remote Sensing of Environment*, 98: 237-250.

Boyd, D. S., Foody, G. M., and Ripple, W. J., 2002, Evaluation of approaches for forest cover estimation in the Pacific Northwest, USA, using remote sensing. *Applied Geography*, 22: 375-392.

Hansen, M. C., and De Fries, R. S., 2007, Global percent tree cover at a spatial resolution of 500 meters: First results of the MODIS vegetation continuous fields algorithm. *Earth Interactions*, 2007, 7: 1-15.

Li, J.Y., X.C., Yang, B, Xu.et.al. 2013, Monitoring and analysis of grassland desertification dynamics using Landsat images in Ningxia, China. *Remote Sensing of Environment*, 138: 19-26.

Kenneth, M. G., Timothy M., Lynn F., 2000, Hyperspectral mixture modeling for quantifying sparse vegetation cover in arid environments. *Remote Sensing of Environment*, 72(3): 360-374.

Real-time ortho-rectification for remote sensing images

Rongting Zhang[1,2,3], Guoqing Zhou[1,2,3,*], Jingjin Huang[1,2,3], and Xiang Zhou[2,3]

[1] *College of Precision Instrument and Opto-Electronic Engineering, Tianjin University, Tianjin 300072, China;*

[2] *Guangxi Key Laboratory for Spatial Information and Geomatics, Guilin University of Technology, Guilin, Guangxi, 541004, China;*

[3] *The Center for Remote Sensing, Tianjin University, Tianjin, 300072, China*

[*] glitezhou@yahoo.com

ABSTRACT - *Orthophoto is different from general maps. It has no distortion, and reflects affluent true and objective information. The orthophoto not only contains geometric accuracy of map, but also has the features of remote sensing image. Thus, orthophoto has been applied in different fields, such as preventing disaster, planning public facilities construction, and so on. How to quickly acquire the ortho-rectified remote sensing image has become an urgently issue. However, conventional ortho-rectification techniques for remotely sensed imagery, which are performed on the basis of ground image processing platform, have been unable to meet the timeliness requirements. The speed of image processing can't catch up with the speed of obtaining remote sensing images because of the limitation of image processing technology. Conventionally, to ortho-rectify the acquired images, these images need to be sent back to the ground perform systems. Moreover, the traditional image processing systems, such as ENVI and ERDAS IMAGINE, are serial instruction systems based on desk computer. Thus, these image processing systems hardly meet the demand in response of the time-critical disasters, which makes the abundant image resources be not fully used. To solve this problem, this paper presents the research on ortho-rectification technique based on field programmable gate array (FPGA) platform, which can be implemented on-board and spaceborne for a real-time processing. Through comparing the correction accuracy and the time consuming of traditional ortho-rectification method with the proposed method, it shows that the proposed FPGA-based on-board ortho-rectification has great advantage over improving the image ortho-rectification speed and can reach the requirements of correction accuracy.*

1 INTRODUCTION

Ortho-rectification is an image correction method, which aims to remove the geometric distortion and obtain the correct geographic coordinates of the remotely sensed image. However, the technology for processing remotely sensed (RS) images at a real-time manner is facing a bottleneck due to the limitation of image processing technology. The traditional image processing systems (such as ENVI and ERDAS IMAGINE) are serial instruction systems based on personal computer. However, since the demand in response of the time-critical disasters, the traditional method cannot meet this demand.

An effective solution for real-time processing of image ortho-rectification is to perform the ortho-rectification on hardware. In recent several decades, field programmable gate array (FPGA) has been widely used in image processing filed, which make the real-time processing come true. For example, Klupsch *et al.* (2002) proposed a substantial speed up of image processing methods on 2D and 3D images making use of FPGA technology. The proposed method can enable the use of those flexible image processing methods in application s where real time performance is indispensable. Qu *et al.* (2013) designed a real-time

image system based on FPGA and multi-DSP (digital signal platform), which solved complex algorithm that was difficult to achieve real-time processing of multiband image fusion within large amount of data. Greisen *et al.* (2011) presented a real-time processing platform for high-definition stereo video. In the hybrid FPGA-GPU-CPU platform, a high-density FPGA was used to perform the low-level image processing tasks and to carry out radial undistortion, image rectification, and disparity estimation. Tomasi *et al.* (2012) proposed a real-time implementation of stereo algorithm on FPGA, which was a phase-based model that allowed computation with sub-pixel accuracy. Colodro-Conde *et al.* (2014) presented an evaluation of area-based algorithms used for calculating distance in stereoscopic vision system, their hardware architectures for implementation on FPGA and the cost of their accuracies in terms of FPGA hardware resources. Abdul Waheed Malik *et al.* (2014) described a hardware architecture for real-time image component labelling and the computation of image component feature descriptors. The developed architecture could process 390 video frames per second of size 640 × 480 pixels and the dynamic power consumption was 13mW at 86 frames per second.

To our knowledge, the hardware system for image correction is mainly about the field of video image real-time correction, stereopair real-time correction, and so on. There is few research on RS image orthorectification which has high requirement in RS community. Thus, this paper develops a hardware platform based on FPGA for RS image ortho-rectification. Through decomposing the ortho-rectification algorithm, several basic algorithms of image processing can be obtained, which can reduce the complexity of algorithm and reach the purpose of real-time correction.

2 FPGA-BASED IMPLEMENTATION FOR ORTHO-RECTIFICATION ALGORITHM

2.1 A Brief Review of the Collinearity Condition Equation

In recent decades, a lots ortho-rectification methods have been proposed, such as (Yang *et al.*, 2013; Reinartz *et al.*, 2011; Aguilar *et al.*, 2013). In this paper, the collinearity condition equation (CCE) is chosen to implement the ortho-rectification of RS images, according to the type of image and the covered area. The CCE is suitable for various resolutions of images and the situation where the parameters of orbit are known or unknown. The indirect method of CCE is used to perform the ortho-rectification of RS images. The processes of the indirect method based on CCE can be divided into the following four parts:

(1) Calculate the geodetic coordinates for pixels in the orthophoto:

$$\begin{cases} X_{geo} = X_0 + S \bullet (I + 0.5) \bullet \Delta x \\ Y_{geo} = Y_0 + S \bullet (J + 0.5) \bullet \Delta y \end{cases} \quad (1)$$

where (X_{geo}, Y_{geo}) are the geodetic coordinates of a pixel in the orthophoto; (X_0, Y_0) are the geodetic coordinates of marginal point on the left bottom of the orthophoto; S is the scale denominator; (I, J) are the column and row coordinates of a pixel in the orthophoto; $(\Delta x, \Delta y)$ are the sampling interval of column and row.

(2) Calculate the image plane coordinates:

$$\begin{cases} u = x_0 - f \dfrac{o_1(X_{geo} - X_e) + p_1(Y_{geo} - Y_e) + q_1(Z_{geo} - Z_e)}{o_3(X_{geo} - X_e) + p_3(Y_{geo} - Y_e) + q_3(Z_{geo} - Z_e)} \\ v = y_0 - f \dfrac{o_2(X_{geo} - X_e) + p_2(Y_g - Y_e) + q_2(Z_{geo} - Z_e)}{o_3(X_{geo} - X_e) + p_3(Y_{geo} - Y_e) + q_3(Z_{geo} - Z_e)} \end{cases} \quad (2)$$

where (u, v) are the image plane coordinates of a pixel of orthophoto in the original image; (x_0, y_0, f) are the interior orientation elements; (X_e, Y_e, Z_e) are the exterior orientation elements; o_h, p_h, q_h (h=1, 2, 3) are the coefficients of rotation matrix, which can be calculated by rotational angles (φ, ω, and κ) along the x-, y- and z-axis; Z_{geo} can be got by digital elevation model (DEM).

(3) Calculate scanning coordinates:

$$\begin{bmatrix} i' \\ j' \end{bmatrix} = \begin{bmatrix} a_1 & b_1 \\ a_2 & b_2 \end{bmatrix} \begin{bmatrix} u \\ v \end{bmatrix} + \begin{bmatrix} c_1 \\ c_2 \end{bmatrix} \quad (3)$$

where (i', j') are the scanning coordinates; a_t, b_t, and c_t (t=1, 2) are the coefficients of affine transformation.

(4) Calculate gray-scale for pixels in the orthophoto. Since the obtained scanning coordinates may not only be in the center of a pixel, a gray-scale interpolation process is required. In this paper, the bilinear interpolation method is applied.

$$f(i+r, j+s) = (1-r)(1-s)f(i, j) + (1-r)sf(i, j+1) + r(1-s)f(i+1, j) + rsf(i+1, j+1) \quad (4)$$

where i and j are nonnegative integers; r and s are in the range of (0, 1); and $f(i, j)$ are gray values.

2.2 FPGA-based Modelling for CCE Model

By analysing the structuer of CCE algorithm and optimizing it, an FPGA-based hardware architecture for implementing CCE algorithm was designed. As shown in Figure 1, the designed architecture can be divided into three parts: the first part is the input data model; the second part is the coordinate transformation model; and the third part is the interpolation model. In this paper, a pipe-line structure is applied, which can ensure that data are processed in real time. The details of these models are described as follows.
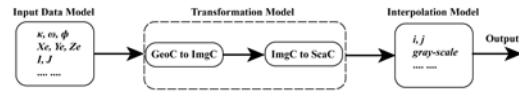

Figure 1. The designed architecture based on FPGA for implementing CCE algorithm. GeoC: geodetic coordinate; ImgC: image plane coordinate; SanC: scanning coordinate.

(1) Input data model.

The raw image data and parameters (such as interior orientation elements, exterior orientation elements, and affine transformation coefficients) are stored in the random-access memory (RAM). They are sent to transformation model and interpolation model in the same clock cycle, when the enable signal is being received.

(2) Transformation model.

i) The transformation from geodetic coordinate to image plane coordinate.

According to Eq. (2), it can be divided into the following three parts. The parallel computation is implement in each parts. The first part is

$$P_1 = X_{geo} - X_e; \qquad P_2 = Y_{geo} - Y_e; \qquad P_3 = Z_{geo} - Z_e \quad (5)$$

The second part is

$$\begin{aligned} P_4 &= o_1 P_1 + p_1 P_2 + q_1 P_3 \\ P_5 &= o_2 P_1 + p_2 P_2 + q_2 P_3 \\ P_6 &= o_3 P_1 + p_3 P_2 + q_3 P_3 \end{aligned} \quad (6)$$

The third part is

$$P_7 = P_4 / P_6; \qquad P_8 = P_5 / P_6 \quad (7)$$

According to Eq. (5), (6), and (7), the hardware implementation architecture can be designed as the following Figure 2.
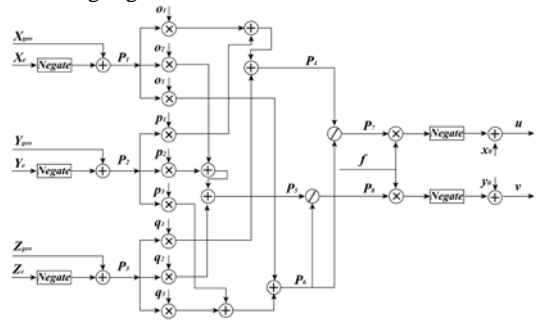

Figure 2. The hardware architecture for the transformation from geodetic coordinate to image plane coordinate.

ii) The transformation from image plane coordinate to scanning coordinate.

To implement the parallel computation for Eq. (3), it can be divided into two parts: the first part is

$$g_1 = A_1 B; \qquad g_2 = A_2 B \qquad (8)$$

where $A_1 = [a_1, b_1]$, $A_1 = [a_2, b_2]$, and $B = [u, v]^T$.
The second part is:

$$i' = g_1 + c_1; \qquad j' = g_2 + c_2 \qquad (9)$$

According to Eq. (8) and (9), the hardware implementation architecture can be designed as the following Figure 3.
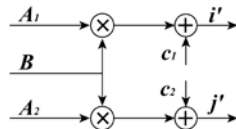

Figure 3. The hardware architecture for the transformation from image plane coordinate to scanning coordinate.

(3) Interpolation model.

According to Eq. (4), it can be rewritten as the following Eq. (10).

$$\begin{cases} D_{11} = D_1 + s \square (D_2 - D_1) \\ D_{12} = D_3 + s \square (D_4 - D_3) \\ D_{out} = D_{11} + r \square (D_{12} - D_{11}) \end{cases} \qquad (10)$$

where D_1 to D_4 are the values of gray-scale of input image; D_{11} and D_{12} are the intermediate variables; D_{out} is the interpolation result; $r = |i' - \text{INT}(i')|$ and $s = |j' - \text{INT}(j')|$ are the weights.

According to Eq. (8) and (9), the hardware implementation architecture can be designed as the following Figure 4.
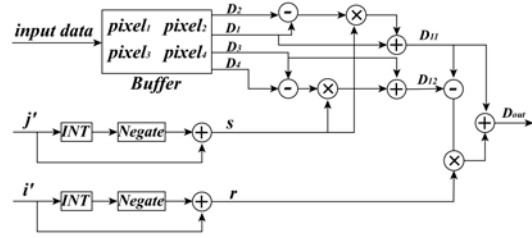

Figure 4. The hardware architecture for collinearity interpolation algorithm.

3 EXPERIMENT

3.1 Hardware, Software, and Data

In this paper, the AC701 Evaluation Kit of Artix-7 series produced by Xilinx company is used. The version of FPGA is Xilinx Artix-7 XC7A200T FBG676ACX1349 D4658436A ZC. The design tool is ISE 4.7 and System Generator. The simulation tool is ModelSim SE10.1a. FPGA Evaluation Kit can be connected with computer by using the UART and JTAG ports.

The data is acquired from an ERDAS IMAGINE example dataset, i.e., ps_napp.img (2294 × 2294) (see Figure 5) and ps_dem.img (see Figure 6).

Figure 5. The original aerial image covering the study area (from ERDAS IMAGINE 9.2).

The ortho-rectified results by the proposed FPGA-based platform and PC-based platform are shown in Figure 7.

Table 1. Statistics of difference value of geodetic coordinate.

#	Max	Min	Mean	Standard Deviation
X coordinates	1.31 m	0.41 m	1.11 m	0.14 m
Y coordinates	1.94 m	0.80 m	1.59 m	0.38 m

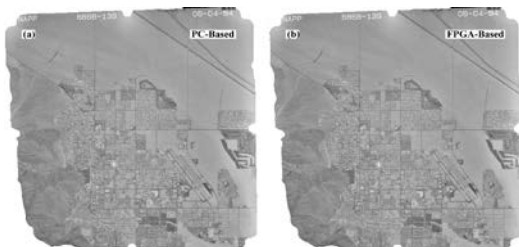Figure 6. Digital elevation model (DEM) covering the study area (from ERDAS IMAGINE 9.2).

Figure 7. The ortho-rectified results by (a) the PC-based platform; and (b) the proposed FPGA-based platform.

3.2 Analysis

To validate the rectified accuracy of the proposed FPGA-based platform, ninety check points were selected. Through computing the differences of coordinates obtained by the PC-based platform and the proposed FPGA-based platform, some statistics (such as maximum value, minimum value, standard deviation, and mean of difference value) are calculated (see Tab.1)

Additionally, the consuming time of processing between the PC-based platform and the proposed FPGA-based platform. The total consuming time of the proposed FPGA-based platform and the PC-based platform are 0.47 seconds and 2.04 seconds, respectively. The total time decreases by about 77% using the proposed FPGA-based platform.

4 CONCLUSION

In this paper, an FPGA-based ortho-rectification method is proposed, and the data acquired from an ERDAS IMAGINE example dataset are used to validate the proposed method. Compared to traditional method based on PC platform, the ortho-rectification accuracy of our method can meet the requirement of correction, and the total consuming time of ortho-rectification decreases by 77%. This research can quickly provide reliable results for ortho-rectification.

6 REFERENCES

Aguilar, M. A., Saldaña, M. d. M., and Aguilar, F. J., 2013, Assessing geometric accuracy of the orthorectification process from GeoEye-1 and WorldView-2 panchromatic images. *International Journal of Applied Earth Observation and Geoinformation*, 21, 427-435.

Colodro-Conde, C., Toledo-Moreo, F. J., Toledo-Moreo, R., Martínez-Álvarez, J. J., Garrigós Guerrero, J., and Ferrández-Vicente, J. M., 2014, Evaluation of stereo correspondence algorithms and their implementation on FPGA. *Journal of Systems Architecture*, 60, 22-31.

Greisen, P., Heinzle, S., Gross, M., and Burg, A. P., 2011, An FPGA-based processing pipeline for high-definition stereo video. *EURASIP Journal on Image and Video Processing*, 2011, 1-13.

Klupsch, S., Ernst, M., Huss, S. A., Systeme, I. S. u., Rumpf, M., and Strzodka, R., 2002, Real time image processing based on reconfigurable hardware acceleration. *In Workshop Heterogeneous Reconfigurable Systems on Chip (SoC)*, 1.

Malik, A. W., Thornberg, B., Imran, M., and Lawal, N., 2014, Hardware architecture for real-time computation of image component feature descriptors on a FPGA. *International Journal of Distributed Sensor Networks*, 2014, 14.

Qu, F., Liu, B., Zhao, J., and Sun, Q., 2013, Image fusion real-time system based on FPGA and multi-DSP. *Optics and Photonics Journal*, 3, 76-78.

Reinartz, P., Müller, R., Schwind, P., Suri, S., and Bamler, R., 2011, Orthorectification of VHR optical satellite data exploiting the geometric accuracy of TerraSAR-X data. *ISPRS Journal of Photogrammetry and Remote Sensing*, 66, 124-132.

Tomasi, M., Vanegas, M., Barranco, F., Diaz, J., and Ros, E., 2012, Real-time architecture for a robust multi-scale stereo engine on FPGA. *IEEE Transactions on Very Large Scale Integration (VLSI) Systems*, 20, 2208-2219.

Yang, G. D., and Zhu, X., 2013, Ortho-rectification of SPOT 6 satellite images based on RPC models. In *Applied Mechanics and Materials*, 808-814.

Retrievals of all-weather daytime land surface temperature from FengYun-2D data

Xiaoyu Zhang,[1]* Chenguang Wang,[1] Hong Zhao[1] and Zehui Lu[2]

[1]School of Environment and Resources, Shanxi University, Taiyuan, Shanxi, China; Postcode: 030006

[2]School of physic and electronic engine, Shanxi University, Taiyuan, Shanxi, China; Postcode: 030006

* zhang_xyhz@sxu.edu.cn

Abstract: *Land surface temperature (LST) is a key parameter in the interaction of the land-atmosphere system. Nevertheless, on the regional scale, the actual weather is cloudy for half a year in most regions. Therefore, how to get all-weather LST from thermal-infrared remote sensing data is necessary and urgent. In this paper, an approach with multi-temporal and spatial neighboring-pixel in combination with diurnal solar radiation and surface temperature evolution is proposed to estimate daytime all-weather LST using FY-2D data. Evaluation of the accuracy of the algorithm is performed against the simulated data and the in situ measurements. The root mean square error (RMSE) between the actual and estimated LSTs under cloud-free condition is approximately 1.84 K for the simulated data, while the RMSE of LST under cloud-free condition varies from 3.42 to 5.1 K for the in situ measurement, and RMSE of LST under cloudy sky is approximately 7 K. The results indicate that the new algorithm is practical for retrieving the daytime all-weather LST at high-temporal resolution without any auxiliary field measurement, although some uncertainties exist.*

1 Introduction

Land surface temperature (LST) is one of the most important variables in monitoring surface energy and global climate change, and it controls many biological and physical processes between atmosphere and land.

Due to the characteristic of the remote sensing, such as simultaneous observation, speediness and comprehensiveness, the technology is the only means to observe LST over the entire globe with some temporal resolution and spatial coverage. Because of the simplicity and practicality of the general split window method (GSW), currently, LST is obtained from thermal infrared remote sensing data. But the method is only used to estimate LST under the cloud-free condition (T_{clear}) and many products only supply the LST for clear pixels while invalid value was filled for cloudy pixels. However, on the regional scale, the actual weather is cloudy for half a year in most regions (Duan et al, 2017). Therefore, how to get all-weather LST is necessary and urgent.

At present, some methods have been developed to estimate all-weather daytime LST. Due to the penetrability of the microwave, LST under the cloudy-sky condition (T_{cloud}) is retrieved using the data. Many researchers proposed some methods to estimate LST, especially under the cloudy-sky condition (Shwetha and Kumar, 2016), but the accuracy is poor.

Most methods are used to estimate LST using thermal infrared data. In order to obtain the real LST

under the cloudy-sky condition, Jin et al. (2000) proposed a 'spatial neighboring-pixel' approach to estimate the T_{cloud} from polar-orbiting satellite data, in which T_{cloud} is interpolated from LST observations of surrounding T_{clear} pixels within 100 to 300 km or within two days based on the surface energy balance. However, the method is limited if the clear and cloudy pixels are not homogeneous or the atmospheric conditions are non-uniform. To overcome this deficiency, a method is proposed using temporal-based T_{clear} to estimate T_{cloud} (Lu et al., 2011). At the same time, the result is also compared with the LST estimated using the spatial-based neighboring-pixel method. The result shows that the temporal 'neighboring-pixel' method is better than a spatial approach, and the absolute error is within 1.5 K. However, some disadvantages of this approach are inevitable. First, the method is proposed based on the same or similar T_{clear} of temporal neighboring-pixel. In fact, because the difference of T_{clear} at two times is obvious especially for the longer time interval, large estimation errors of T_{cloud} will be produced if the time interval is longer between the time that cloud appears and that the sky is clear. Second, some errors can be caused due to the inconsistence that T_{cloud} is interpolated from T_{clear} of temporally neighboring pixels, whereas the difference in net solar shortwave radiation (NSSR) is obtained from spatially neighboring pixels. Third, auxiliary field measurements like solar radiation need to be input in the method. To avoid the weakness, Yu et al. (2014)

proposed a spatially and temporally neighboring-pixel method to reconstruct cloud-contaminated pixels using daily MODIS LST products based on the consideration of the surface energy balance. Nevertheless, ground-based measurements are often needed to calculate T_{cloud}, which makes it difficult to implement for the fewer observation regions. In order to reduce the input of the in-situ measurement data, Zhang et al. (2015) proposed a method to estimate T_{cloud} based on a one-dimensional heat transfer equation and the evolution of daily temperatures and NSSR. The method only uses multi-temporal satellite data to obtain T_{cloud}, but it is invalid when T_{clear} on one day is less than six observations.

To reduce the dependence on auxiliary field measurements, this study aims to develop an improved flexible and effective method to retrieve all-weather daytime LST. The advantage of the improved approach is that it can generate more accurate LST for all the pixels, without depending on ground-based ancillary data and the amount of T_{clear} on one day and the method can provide LST at high-temporal resolution. This approach could be valuable in meteorological and hydrological studies and applications. In the following sections, the methodology is firstly put forward in section 2; next, the data including simulated data, satellite data and field measurement are described in section 3; then, the method's performance is demonstrated based on both simulated and field measurement in section 4; Finally, the conclusion is drawn in section 5.

2 Methodology

All-weather daytime LST is retrieved with two steps: one step is to estimate the T_{clear} using GSW method; the other step is to estimate the T_{cloud} using multi-temporal pixel or spatial neighboring-pixel method in combination with the diurnal solar radiation and the surface temperature evolution.

2.1. Estimation of LST under the cloud-free condition

Due to the simplicity and operability of GSW method, LST is retrieved using the GSW method for most satellite data including polar-orbiting and geostationary satellite. Considering that onboard S-VISSR sensor of FY-2D has two adjacent thermal infra-red channels, LST under the cloud-free condition is estimated using GSW algorithm proposed by Sobrino et al.(1999). The specific formula can be expressed as following:

$$T_s = a_0 + a_1 T_i + a_2(T_i - T_j) + a_3(T_i - T_j)^2 + a_4(1-\varepsilon_i) + a_5 \Delta\varepsilon \quad (1)$$

where T_s is LST, T_i and T_j are the top of the atmosphere (TOA) brightness temperatures measured in channels i (11.0μm) and j (12.0 μm), respectively,

$\Delta\varepsilon=(\varepsilon_i-\varepsilon_j)/2$, ε_i and ε_j are the land surface emissivities (LSEs) in channels i and j, respectively. a_0-a_5 are unknown coefficients which will be obtained through statistical regression method from simulated data mentioned in section 3.1.

2.2. Estimation of LST under the cloudy-sky condition

If the pixel is overcast by cloud, the LST cannot be obtained through GSW method. LST under the cloudy-sky condition can be derived using multi-temporal pixel method in combination with diurnal solar radiation and surface temperature evolution if the clear-sky LSTs observations on one day are more than 6 and the clear-sky LSTs observations in the morning are more than 2 (Zhang et al. 2015b). However, if the conditions cannot be met, LST under cloudy-sky condition should be estimated using spatial neighboring-pixel method in combination with diurnal solar radiation and surface temperature evolution.

2.2.1. Estimation of cloudy LST using multi-temporal pixel method

Assuming the variation in the LST is caused by variations in insolation (ΔS), Zhang et al. (2015b) proposed a method to calculate the LST under cloudy-sky condition.

$$T_{cloud}=T_{clear}-10*\Delta S/P \quad (2)$$

where T_{cloud} is the LST under cloudy–sky condition, T_{clear} is the hypothetic LST under cloud-free condition at the same time, and ΔS is the difference between a hypothetic clear-sky NSSR and real NSSR under cloudy–sky condition at the same time, and P represents the resistance to a temperature change in the upper few centimeters of the surface throughout the day. The estimation of ΔS and P are described in detail by Zhang (2015b) if there are more than six observations including T_{clear} and NSSR (at least include two observations in the morning) in one day can be obtained.

If the condition cannot be met, T_{cloud} cannot be obtained using this method. At this time, a novel algorithm which uses spatial neighboring-pixel method to estimate T_{cloud} in combination with diurnal solar radiation and surface temperature evolution is proposed.

2.2.2. Estimation of cloudy LST using spatial neighboring-pixel method

If there are less than six LST observations under a clear sky in one day or less than two clear-sky LST observations in the morning, retrievals of LST under cloudy condition need to use spatial neighboring-

pixel method in combination with diurnal solar radiation and surface temperature evolution. The specific process is as follows: first, spatial neighboring-pixels which met the conditions (more than six T_{clear} observations in one day and more than two T_{clear} observations in the morning) are searched within 50*50 windows (within 250 km); then, the distance between estimated pixel and searched pixel is calculated using Eq. (3), and the nearest pixel which met the condition is selected as spatial neighboring-pixel; third, assuming that the coefficients of diurnal temperature cycle (DTC) for the estimated pixel are the same as that for the spatial neighboring-pixel, and LST at any time in one day for the estimated pixel can be obtained to be regarded as hypothetic clear-sky LST; at the same time, the coefficient in the expression of TOA solar irradiation is related to the declination and longitude just as shown in Eq. (4), so, the coefficients in the diurnal solar cycle (DSC) model fitted by the spatial neighboring-pixel clear-sky NSSR observations are adjusted as the actual coefficients of estimated pixel using the declination and longitude which is shown in Eq. (5), thereby, the hypothetic clear-sky NSSR at any time in one day for the estimated pixel can be obtained; meanwhile, assuming the P of the estimated pixel is the same as that of the spatial neighboring-pixel; last, LST can be estimated with Eq. (2).

$$D_{i,j} = \sqrt{(x_i - x_j)^2 + (y_i - y_j)^2} \qquad (3)$$

where x and y are the spatial coordinate of a pixel, i and j are the estimated and spatial neighboring-pixel respectively.

$$NSSR = (1-A)S\tau\cos(Zn) = (1-A)S\tau(\cos(\lambda)\cos(\delta_s)\cos(wt) + \sin(\lambda)\sin(\delta_s)) \quad (4)$$

where S is the solar constant, τ is the transmission, A is the broadband albedo, Zn is the solar zenith, λ is the latitude, δ_s is the solar declination, NSSR is the net shortwave solar radiation (W/m²).

$$S_{min} = \frac{\sin(\lambda_{est})\sin(\delta_{s\_est}) * S_{min\_near}}{\sin(\lambda_{near})\sin(\delta_{s\_near})}$$

$$S_{max} = \frac{\cos(\lambda_{est})\cos(\delta_{s\_est}) * S_{max\_near}}{\cos(\lambda_{near})\cos(\delta_{s\_near})} \qquad (5)$$

where S_{min_near} and S_{max_near} represent the S_{min} and S_{max} fitted by the spatial neighboring-pixels NSSR observations under cloud-free sky, respectively, λ_{est} and δ_{est} represent the longitude and declination of estimated pixels respectively, λ_{near} and δ_{near} represent the longitude and declination of the spatial neighboring-pixels.

3 Data

3.1. Simulated data

For clear pixels, the popular method to estimate LST is the GSW method (Wan and Dozier. 1996). The coefficients of GSW should be estimated using bright temperature (BT) and corresponding LST under various kind of atmospheric and surface conditions. So far, there is no available database of field LST measurement in coincidence with FY-2D. Therefore, it is more effective to make radiative transfer simulation for wide ranges of atmospheric and surface conditions. In this work, the top of the atmosphere (TOA) radiance and the atmospheric parameters (Latm↑, Latm↓, τ) ranging from 0.3 to 5 µm and 8.5 to 14.5 µm at an interval of 1 µm were simulated using atmospheric radiative transfer model (MODTRAN 5.2) under various kinds of atmospheric conditions obtained from the European Centre for Medium-Range Weather Forecasts (ECMWF) reanalysis and nine types of surface cover including soil, vegetation canopy, grassland, wetland, city, desert and ocean surface, new snow and sea ice. In addition, the view zenith angle (VZA) ranging from 0° to 60° at an interval of 1°, relative azimuth angle (RAA) ranging from 0° to 120° at an interval of 60° and the solar zenith angle (SZA) ranging from 0° to 60° at an interval of 10° and atmospheric water vertical content (WVC) ranging from 0 to 6.5 g/cm² at an interval of 1 g/cm² are all inputted into the MODTRAN5 as input parameters. In order to make the simulation more representatives, according to the atmospheric temperature T_a in the first boundary layer, LST are varied in a wide range from T_a-5K to T_a+15K. Moreover, according to the character of the most land covers, the averaged emissivity ranges from 0.90 to 1.0 with a step of 0.01 and the emissivity difference ranges from -0.01 to 0.01 with a step of 0.005.

Then, the TOA radiance and the atmospheric parameters (Latm↑, Latm↓, τ) corresponding to the upgraded Stretched-Visible and Infrared Spin-Scan Radiometer (S-VISSR) onboard FY-2D were obtained with the appropriate thermal infrared and VIS channel response function of the S-VISSR onboard FY-2D. Last, for given LST, in combination with the atmospheric parameters (Latm↑, Latm↓, τ) obtained from the output result of MODTRAN 5.2 and the emissivity of two thermal infrared channels, the channel brightness temperature (BT) at the TOA can be determined with the inverse of Planck's law. So far, the database including LST and BT corresponding to different WVC, view zenith angle, solar zenith angle, emissivity, and surface condition is set up and 4755135 different situations are included in the database.

3.2. Satellite data

3.2.1. MODIS data

MODIS (Moderate Resolution Imaging Spectro-radiometer) is a key instrument carried on the Terra and Aqua satellites. Terra's orbit around the Earth is timed so that it passes from north to south across the equator in the morning, while Aqua passes south to north over the equator in the afternoon.

MODIS data products have been available and widely used in many studies and applications since 2000. In the study, the required MODIS data products include the MODIS/Aqua LST Daily L3 Global 1 km Grid product (MOD11A, Collection 6) which was used to provide LST and daily emissivity and land use product (MCD12) which is used to discriminate different land. In order to match MOD11A product and FY-2D data in a consistent system, the MODIS Re-projection Tool (MRT) is used to re-project MOD11A product and MCD12 from a sinusoidal projection to a geographical projection.

3.2.2. FY-2D data

In this study, FY-2D data downloaded from the China Meteorological website (http://satellite.cma.gov.cn/PortalSite/Data/Satellite.aspx) was used to evaluate the proposed work-frame. FY-2D, a geostationary meteorological satellite developed by Shanghai Academy of Space Flight Technology and China Academy of Space Technology was launched on 8, December 2006 and is located above the Equator at longitude 86.5° E and 35,800 km away. The S-VISSR as the main sensor are loaded on the satellite, and it can acquire one full disc image covering the Earth surface from 60° N to 60° S in latitude and from 45° E to 165° E in longitude per hour and 30 min per acquisition for flood season. S-VISSR consists of 5 channels, including a VIS channel and 4 infrared channels. Latitude, longitude, VZA, SZA, and RAA besides radiances of VIS and thermal infrared channel were also provided by the downloaded disc image file. Considering the method is different for the clear and cloud pixels, cloud products of FY-2D were also used to discriminate the different weather conditions. Meanwhile, geolocation files are used to provide the latitude and longitude for each pixel.

3.3. Ground data

Field measurements were collected to evaluate the proposed method from Taiyuan Xiaodian meteorological station (112°33′ E, 37°47′ N) with the elevation of 780m and Changwu ecological station (107°40′E, 35°12′N) with the elevation of 1300m, which is located in Shaanxi Province and joined the Chinese Ecosystem Research Network in 1991. In this study, LST data are detected using PTB100 and collected at 1minute intervals from March 1 to April 26, 2012. In situ LST data corresponding to the image time of FY-2D are selected for validation.

4 Results and Validation

4.1 Retrieval of LST under clear conditions

As is shown in Eq. (1), LSEs are required as a model input in GSW algorithm. In the following, the method to obtain LSEs is described.

LSEs in channels IR1 and IR2 of S-VISSR can be obtained from the daily MODIS LST product (MOD11A1) at 1 km resolution. Due to the slight difference between the two split-window channels of MODIS and S-VISSR, the relationships between MODIS and S-VISSR on LSEs are proposed using the spectral databases from the Johns Hopkins University (JHU) (http://speclib.jpl.nasa.gov/), which were shown in Eqs. (6) and (7).

$$\varepsilon_{IR1} = 0.0068 + 0.9942\varepsilon_{31} \qquad (6)$$

$$\varepsilon_{IR2} = 0.0042 + 0.9981\varepsilon_{32} \qquad (7)$$

Due to the difference of spatial resolution of S-VISSR and the MODIS, they should be matched accurately. First, LSEs from MOD11A1 were aggregated into WGS 84 (World Geodetic System 1984) coordinate system with the spatial resolution of 5KM using weighed averaged method. Then, LSEs were extracted using spatial nearest neighboring method according to the geolocation from FY-2D.

In order to improve the accuracy of estimation of LST, WVC is divided into some sub-ranges ranging from 0 to 6.5 g/cm^2 at an interval of 1 g/cm^2 while determining the a_0-a_5 coefficients in Eq. (1). The retrieval of WVC using three methods is compared by Zhang et al. (2015a) with MSG2-SEVIRI Thermal-IR data and the better result is got from split window co-variance ratio method. So, WVC is obtained using this method in this study assuming that the ratio of two adjacent thermal infra-red channel emissitivities equals to 1.

The determination of coefficients a_0-a_5 is performed after dividing the WVC into six sub-ranges with an overlap of 0.5 g/cm^2: [0, 1.5], [1.0, 2.5], [2.0, 3.5], [3.0, 4.5], [4.0, 5.5], and [5.0, 6.5] g/cm^2. Meanwhile, a_0-a_5 is interpolated according to θ at an interval 1°. T_{clear} is calculated using the GSW algorithm with the coefficients corresponding to kinds of the sub-range WVC under view zenith angle. The result shows that the RMSE between the actual T_{clear} and estimated T_{clear} is 1.82K with a mean error of 1.43K for all conditions. Meanwhile, the errors between the actual and estimated LST is distributed within ±6 K. Due to errors in the parameters inputted

in the algorithm cause the increasing of estimated T_{clear}, in the following, T_{clear} errors caused by the uncertainty in instrumental noises (NEΔT) and LSEs (i.e. sensitivity analysis) are performed.

An error from -0.5 to 0.5 K at an interval of 0.1 K is respectively added to the TOA brightness temperatures T_i and T_j, the RMSE of LST under kinds of θ is obtained and the results show that 1) The RMSE of actual and estimated LST is increasing with the increase of the absolute (δT_i-δT_j); 2) The RMSE reached minimums when the WVC ranges from 2 to 3.5 g/cm^2, whereas the RMSE reached maximums when the WVC ranges from 4 to 5.5 g/cm^2, and the RMSE reached 8 K when (δT_i-δT_j) is $\pm$1 K; 3) The RMSE is all less than 4K when the WVC is less than 4.5 g/cm^2; 4) The RMSE is less than 4 K when the absolute (δT_i-δT_j) is less 0.4 K.

Similarly, an error from -0.01 to 0.01 K at an interval of 0.005 is respectively added to LSEs (ε_i and ε_j), the RMSE of LST is obtained and results show that RMSE of actual and estimated LST are all less than 0.5 K, and a conclusion that the sensitivity caused by the uncertainty in LSEs is unobvious can be drawn.

In addition, the in situ LST measurement at two sites (Taiyuan Xiaodian and Changwu station) is used to evaluate the accuracy of LST under the cloud-free conditions. The RMSEs of measured LST and estimated LST are 3.42 and 5.12 K with a mean error (ME) of 0.004 and 3.03 K, respectively for Taiyuan Xiaodian and Changwu station, which is shown in Figs. (1) and (2). Three reasons can explain the relatively large RMSE values associated with Tclear. One reason is due to the spatial scale inconsistency between the all-weather LST and the in situ LST measurements. The in situ LST were measured within a very small area (4m*4m), while the satellite measurement was collected in a very large region (nearly 5 km * 5 km) and reflected an integrated response over a heterogeneous area. The second reason is the uncertainty of the measurement and that of GSW algorithm caused by the errors of the input parameters. Just as shown in sensitivities analysis, the RMSE of LST reached 8K when the difference of NEΔT between IR1 and IR2 channel is $\pm$1 K for WVC more than 4 g/cm^2. The last reason is associated with the quality of FY-2D cloud product. The misjudgment of cloud will affect the right choice of the algorithm.

4.2 Estimation of LST under cloudy conditions

Figs. (1) and (2) show a comparison of the estimated daytime all-weather LST using the proposed method and the daytime all-weather LST measured at the Changwu Ecosystem experimental station and Taiyuan Xiaodian meteorological observation station from March 1 to April 26 in 2012.

The scatter plot shows that the RMSE is 7.59 K and 7.87 K with a mean error of -3.84K and 3.15K under cloudy condition, respectively for Taiyuan and Changwu station. Compared to the results presented in previous studies, the error appears relative larger, such as, the errors of LST under cloudy sky obtained using spatial neighboring-pixel method proposed by Jin et al. (2000) are 2K for most situations and some errors reached 8-10K. But the result is performed based on the simulated data and shows a better.
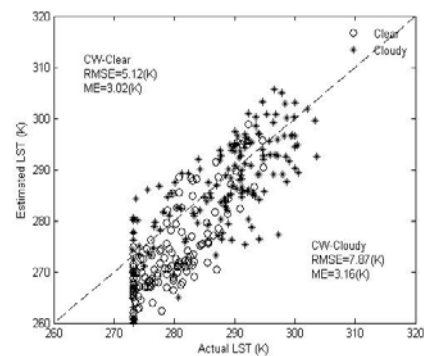

Figure 1. Comparison of LST estimated using proposed method and in situ LST from Taiyuan experiment station
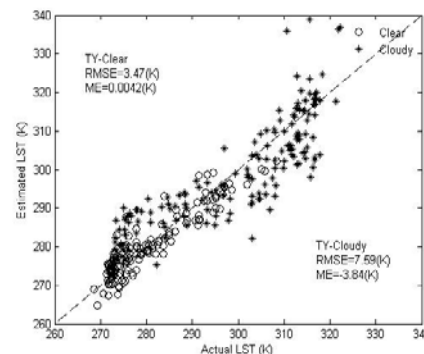

Figure 2. Comparison of LST estimated using proposed method and in situ LST from Changwu experiment station

The bias of LST under the cloudy sky is mainly caused by four reasons. The first reason is the spatial scale inconsistency between the estimated LST and in situ LST measurements which the spatial resolution of 4 m for in situ LST measurement and the spatial resolution of 5 km for the estimated LST in evaluating the T_{clear}. The second reason is the uncertainty of some parameters (T_{clear}, NSSR, WVC, LSEs, θ etc.) input in the proposed algorithm. The third reason is the uncertainty in the proposed algorithm, such as some assumption in the algorithm (e. g. the parameters of DTC of estimated pixel are

the same as that of the spatial neighboring-pixel. In fact, due to the heterogeneity of surface and atmospheric conditions, the parameters will display difference and it will yield more uncertainty in estimating T_{cloud}). The last reason is associated with the quality of FY-2D cloud product. The choice of algorithm depends on the cloudy judgment and cloudy misjudgment will decrease the accuracy of T_{cloud}. In addition, uncertainty of field measurement also affects the result.

5 Conclusion

With increasingly more geostationary meteorological satellites in operation, it is possible and realized to obtain all-weather LST at high-temporal resolution using multi-temporal satellite data without any auxiliary field measurement. In this paper, we proposed a method to estimate daytime all-weather LST by combining diurnal solar radiation with diurnal surface temperatures under different conditions without any auxiliary field measurement. The method consists of two steps, including the estimation of LST under cloud-free sky using general split window method and the estimation of LST under cloudy sky using multi-temporal data in combination with spatial neighboring-pixel method. Data collected S-VISSR sensor aboard the FY-2D was used as an example data for input into the proposed algorithm.

Considering the retrieval of Tcloud is based on the Tclear, in this study, first, the GSW method is used to obtain Tclear, and the coefficients of the GSW for FY-2D data is calculated using simulated data obtained from atmospheric radiative transfer model (MODTRAN 5.2) under various kinds of atmospheric and surface condition. The RMSE between the actual T_{clear} and estimated T_{clear} is 1.82K with a mean error of 1.43K for all the condition and most scatters are concentrated on [-1,1] for the simulated data. Meanwhile, in situ measurements from Taiyuan Xiaodian and Changwu station were used to evaluate the accuracy of the algorithm under the cloudy-free condition. The RMSE of LST under the cloudy-free condition varies from 3.42 to 5.12 K with a mean errors varying from 0.004 to 3.02K. At the same time, the RMSEs of LST under cloud condition are calculated and the value varies from 7.59 to 7.87 K with the mean errors varying from -3.84 to 3.15 K. Considering the spatial scale inconsistency between the LST from satellite data and the in situ measurements and the sensitivity to instrumental noises, the error can be accepted and the proposed method can be used to retrieve the daytime all-weather LST at high-temporal resolution using geostationary meteorological satellite data without any auxiliary field measurement. The availability of all-weather LST at a high temporal resolution would benefit many research field including climate change, soil moisture and evapotranspiration etc.

Notably, the proposed method assumes that the variation in the LST is caused by variations in insolation (which is related to cloudiness) during the daytime and the parameters of the DTC model of estimated pixel are the same as that of the spatial neighboring-pixel. Therefore, the approach can only be used during the daytime. Furthermore, the DTC parameters should display some differences especially for heterogeneity pixels. How to calibrate the parameters and retrieve the all-weather nighttime LST at high-temporal resolution need to be further deepened and explored.

References

Duan, S.-B., Li, Z.-L. and Leng, P. 2017, A framework for the retrieval of all-weather land surface temperature at a high spatial resolution from polar-orbiting infrared and passive microwave data. Remote Sens. Environ., 195, 107-117..

Jin.M.-L. 2000, Interpolation of surface radiative temperature measured from polar-orbiting satellites to a diurnal cycle 2. Cloudy-pixel treatment. J.Geophys. Res. 105 (D3), 4061–4076.

Lu, L., Venus,V., Skidmore,A., Wang, T., and Luo, G. 2011, Estimating land-surface temperature under clouds using MSG/SEVIRI observations. Int. J. Appl. Earth Obs. 13, 265–276.

Shwetha, H. and Kumar, D. 2016, Prediction of high spatio-temporal resolution land surface temperature under cloudy conditions using microwave vegetation index and ANN. ISPRS J. Photogramm. Remote Sens. 117, 40–55.

Sobrino , J.A., Li, Z.-L., Stoll, M.P., and Becker, F. 1993, Determination of the surface temperature from ATSR data. In Proceedings of 25th International Symposium on Remote Sensing of Environment,Graz, Austria, April 4-8. pp. II-19 - II-109.

Wan, Z., and Dozier, J. 1996, A generalized split-window algorithm for retrieving land surface temperature from space. IEEE Trans. Geosci. Remote Sens. 34, 892–905.

Yu, W.-P., Ma, M.-G., Wang, X.-F., and Tan, J.-L. 2014, ,"Estimating the land-surface temperature of pixels covered by clouds in MODIS products. J. Appl. Earth Obs. 8(1), 083525.

Zhang, X., and Pang, J. 2015a, A comparison between atmospheric water vapour content retrieval methods using MSG2-SEVIRI thermal IR data. Int. J. Remote Sens. 36(19-20), 5075-5086.

Zhang, X., Pang, J. and Li, L. 2015b, Estimation of Land Surface Temperature under Cloudy Skies Using Combined Diurnal Solar Radiation and Surface Temperature Evolution. Remote Sens. 7(1), 905-921.

Thank you for attending the RAQRS 2017 symposium, we hope to see you in the next edition.